Rubber Nanocomposites

Preparation, Properties and Applications

Sabu Thomas | Ranimol Stephen

WILEY

RUBBER NANOCOMPOSITES

RUBBER NANOCOMPOSITES

PREPARATION, PROPERTIES, AND APPLICATIONS

Editors

Sabu Thomas

Mahatma Gandhi University, India

Ranimol Stephen

Cochin University of Science and Technology, India

John Wiley & Sons (Asia) Pte Ltd

Copyright © 2010

John Wiley & Sons (Asia) Pte Ltd, 2 Clementi Loop, # 02-01, Singapore 129809

Visit our Home Page on www.wiley.com

All Rights Reserved. No part of this publication may be reproduced, stored in a retrieval system or transmitted in any form or by any means, electronic, mechanical, photocopying, recording, scanning, or otherwise, except as expressly permitted by law, without either the prior written permission of the Publisher, or authorization through payment of the appropriate photocopy fee to the Copyright Clearance Center. Requests for permission should be addressed to the Publisher, John Wiley & Sons (Asia) Pte Ltd, 2 Clementi Loop, #02-01, Singapore 129809, tel: 65-64632400, fax: 65-64646912, email: enquiry@wiley.com.

Designations used by companies to distinguish their products are often claimed as trademarks. All brand names and product names used in this book are trade names, service marks, trademarks or registered trademarks of their respective owners. The Publisher is not associated with any product or vendor mentioned in this book. All trademarks referred to in the text of this publication are the property of their respective owners.

This publication is designed to provide accurate and authoritative information in regard to the subject matter covered. It is sold on the understanding that the Publisher is not engaged in rendering professional services. If professional advice or other expert assistance is required, the services of a competent professional should be sought.

Other Wiley Editorial Offices

John Wiley & Sons, Ltd, The Atrium, Southern Gate, Chichester, West Sussex, PO19 8SQ, UK

John Wiley & Sons Inc., 111 River Street, Hoboken, NJ 07030, USA

Jossey-Bass, 989 Market Street, San Francisco, CA 94103-1741, USA

Wiley-VCH Verlag GmbH, Boschstrasse 12, D-69469 Weinheim, Germany

John Wiley & Sons Australia Ltd, 42 McDougall Street, Milton, Queensland 4064, Australia

John Wiley & Sons Canada Ltd, 5353 Dundas Street West, Suite 400, Toronto, ONT, M9B 6H8, Canada

Wiley also publishes its books in a variety of electronic formats. Some content that appears in print may not be available in electronic books.

Library of Congress Cataloging-in-Publication Data

Thomas, Sabu.
Rubber nanocomposites: preparation, properties, and applications / editors, Sabu Thomas, Ranimol Stephen.
p. cm.
Includes bibliographical references and index.
ISBN 978-0-470-82345-3 (cloth)
1. Rubber. 2. Nanocomposites (Materials) I. Stephen, Ranimol. II. Title.
TA455.R8T46 2010
678′.72–dc22

2009053136

ISBN 978-0-470-82345-3 (HB)

Typeset in 10/12pt Times by Thomson Digital, Noida, India.
Printed and bound in Singapore by Markono Print Media Pte Ltd, Singapore.
This book is printed on acid-free paper responsibly manufactured from sustainable forestry in which at least two trees are planted for each one used for paper production.

Contents

List of Contributors xv

Preface xix

Editor Biographies xxi

1 Nanocomposites: State of the Art, New Challenges and Opportunities 1
Ranimol Stephen and Sabu Thomas

1.1 Introduction 1
1.2 Various Nanofillers 2
1.2.1 Layered Silicates 2
1.2.2 Nanotubes 3
1.2.3 Spherical Particles 5
1.2.4 Polyhedral Oligomeric Silsesquioxanes 6
1.2.5 Bionanofillers 7
1.3 Rubber Nanocomposites 8
1.4 Future Outlook, Challenges and Opportunities 11
References 12

2 Manufacturing Techniques of Rubber Nanocomposites 21
Jun Ma, Li-Qun Zhang and Li Geng

2.1 Introduction 21
2.1.1 Conventional Manufacturing Techniques 22
2.1.2 Rubber Nanocomposites 22
2.1.3 Reinforcing Agent 23
2.2 Melt Compounding 25
2.2.1 Manufacturing Factors Control 25
2.2.2 Filler Surface Modification 34
2.3 Solution Blending 39
2.3.1 Manufacturing Factors Control 39
2.3.2 Preparing Exfoliated/Intercalated Nanocomposites 46
2.4 Latex Compounding 47
2.4.1 Manufacturing Factors Control 48
2.4.2 The Effect of Rubber Type 57

2.5 Summary 61
Acknowledgments 61
References 61

3 Reinforcement of Silicone Rubbers by Sol-Gel *In Situ* Generated Filler Particles 63
Liliane Bokobza and Amadou Lamine Diop

3.1 Introduction 63
3.2 Synthetic Aspects 64
3.2.1 General Considerations 64
3.2.2 Adopted Protocols 65
3.3 Properties of the Hybrid Materials 71
3.3.1 State of Dispersion 71
3.3.2 Stress-Strain Curves 71
3.3.3 Low Strain Dynamic Properties 74
3.3.4 Mullins Effect 76
3.3.5 Characterization of the Polymer-Filler Interface 78
3.3.6 Thermal Properties 80
3.4 Conclusions 82
References 82

4 Interface Modification and Characterization 87
Jun Ma, Li-Qun Zhang and Jiabin Dai

4.1 Introduction 87
4.1.1 Particle Size 87
4.1.2 Surface Activity 88
4.2 Rubber Nanocomposites Without Interface Modification 89
4.2.1 Hardness and 300% Tensile Modulus 89
4.2.2 Tensile Strength 89
4.2.3 Tensile Strain 92
4.2.4 Tear Strength 92
4.2.5 Rebound Resilience 92
4.2.6 Processing Properties 92
4.2.7 Advantages 92
4.2.8 Disadvantages 92
4.3 Interface Modification by Nonreactive Routes 93
4.4 Interface Modification by Reactive Routes 100
4.5 Characterization of Interface Modification 104
4.5.1 Direct Methods for Interface Characterization 105
4.5.2 Indirect Methods for Interface Characterization 106
4.6 Conclusion 110
List of Abbreviations 110
Acknowledgments 111
References 111

5 Natural Rubber Green Nanocomposites **113**
Alain Dufresne

5.1 Introduction 113
5.2 Preparation of Polysaccharide Nanocrystals 114
5.3 Processing of Polysaccharide Nanocrystal-Reinforced Rubber Nanocomposites 115
5.4 Morphological Investigation 116
5.5 Swelling Behavior 118
5.5.1 Toluene Swelling Behavior 119
5.5.2 Water Swelling Behavior 127
5.5.3 Influence of the Chemical Modification of the Filler 128
5.6 Dynamic Mechanical Analysis 131
5.7 Tensile Tests 134
5.8 Successive Tensile Tests 137
5.9 Barrier Properties 143
5.10 Conclusions 143
References 144

6 Carbon Nanotube Reinforced Rubber Composites **147**
R. Verdejo, M.A. Lopez-Manchado, L. Valentini and J.M. Kenny

6.1 Introduction 147
6.2 Functionalized Carbon Nanotubes 148
6.3 Elastomeric Nanocomposites 152
6.3.1 Natural Rubber 152
6.3.2 Styrene-Butadiene Rubber 155
6.3.3 Polyurethane Rubber 157
6.3.4 Silicone Rubber 160
6.4 Outlook 161
References 162

7 Rubber/Clay Nanocomposites: Preparation, Properties and Applications **169**
K.G. Gatos and J. Karger-Kocsis

7.1 Introduction 169
7.2 Clays and Their Organophilic Modification 170
7.3 Preparation of Rubber/Clay Nanocomposites 171
7.3.1 Solution Intercalation 173
7.3.2 Latex Route 173
7.3.3 Melt Compounding 174
7.4 Properties of Rubber/Clay Nanocomposites 176
7.4.1 Crosslinking 176
7.4.2 Mechanical Performance 179
7.4.3 Barrier Properties 184
7.4.4 Fire Resistance 186
7.4.5 Others 187

7.5 Applications 189
7.6 Outlook 189
Acknowledgments 190
References 190

8 Cellulosic Fibril–Rubber Nanocomposites 197
Maya Jacob John and Sabu Thomas

8.1 Introduction 197
8.2 Cellulose 198
8.3 Cellulosic Nanoreinforcements 199
8.3.1 Cellulosic Microfibrils 199
8.4 Studies on Cellulosic/Latex Nanocomposites 204
8.5 Conclusions 207
References 207

9 Nanofillers In Rubber–Rubber Blends 209
Rosamma Alex

9.1 Introduction 209
9.2 Types of Nanofillers 209
9.2.1 Spherical Fillers 210
9.2.2 Tubular Fillers 210
9.2.3 Layered Clays 211
9.3 Role of Nanofillers in Reinforcement 213
9.3.1 Particle Size 213
9.3.2 Rubber–Filler Interaction 215
9.3.3 Filler–Filler Interactions 216
9.3.4 Shape and Structure of Filler 216
9.3.5 Filler Reinforcement with Reference to Concentration and Cure 217
9.4 Methods to Enhance Polymer–Filler Interaction and Reinforcement 218
9.4.1 Micromechanical Interlocking 218
9.4.2 Physical and Chemical Interactions – Modification of Nanofillers 218
9.5 Role of Nanofiller as Compatibilizer 220
9.6 Structure Compatibility Concept of NR-Based Latex Blends 222
9.6.1 Forms of NR Suitable for Blend Nanocomposites 222
9.6.2 Important Synthetic Latices used in Blend Nanocomposites 224
9.7 Solubility Parameter and Mixing of Latices 225
9.7.1 Particle Size and Molecular Weight 225
9.7.2 Nonrubber Solids and Total Solids Content 226
9.8 Preparation of Nanocomposites 226
9.8.1 Solution Blending 226
9.8.2 Latex Stage Compounding 226
9.8.3 Melt Intercalation 229
9.9 Rubber Blend Nanocomposites Based on Skim NR Latex and Fresh NR Latex: Preparation, Characterization and Mechanical Properties 229

9.10 Advantages of Nanocomposites and Application of Rubber Nanocomposites 231
References 234

10 Thermoplastic Polyurethane Nanocomposites 239
S.K. Smart, G.A. Edwards and D.J. Martin

10.1 Introduction 239
10.2 Market 240
10.2.1 Styrene Block Copolymers 240
10.2.2 Thermoplastic Olefins 240
10.2.3 Thermoplastic Vulcanizates 240
10.2.4 Copolyester Elastomers 240
10.2.5 Thermoplastic Polyurethanes 241
10.3 TPU Chemistry, Morphology and Properties 241
10.4 TPU Nanocomposites 242
10.5 Layered Silicate/TPU Nanocomposites 243
10.6 Carbon Nanotube/TPU Nanocomposites 247
10.7 Future Perspectives 250
References 250

11 Microscope Evaluation of the Morphology of Rubber Nanocomposites 255
Hiroaki Miyagawa

11.1 Introduction 255
11.2 Optical Microscopy 256
11.3 Scanning Electron Microscopy 259
11.3.1 Micrographs with Secondary Electron 259
11.3.2 Energy Dispersive X-Ray Spectroscopy (EDX) 262
11.3.3 Electron Probe Microanalysis 263
11.3.4 X-Ray Ultramicroscopy 264
11.4 Transmission Electron Microscopy 265
11.4.1 Sample Preparation for TEM Observations 266
11.4.2 Bright-Field TEM Micrographs 268
11.4.3 Scanning Transmission Electron Microscopy and EDX 272
11.4.4 Electron Spectroscopy Imaging in Transmission Electron Microscopy 273
11.4.5 3-D Transmission Electron Microtomography 274
11.5 Scanning Probe Microscopy 276
11.5.1 Atomic Force Microscopy 277
11.5.2 Other AFM-Related Techniques 281
11.6 Summary 285
References 285

12 Mechanical Properties of Rubber Nanocomposites: How, Why ... and Then? 291
L. Chazeau, C. Gauthier and J.M. Chenal

12.1 Introduction 291
12.2 Typical Mechanical Behavior of Rubber Nanocomposites 292

12.2.1 The Fillers and Their Main Characteristics 292
12.2.2 Filler Reinforcement (Modulus Increase) 295
12.2.3 Mechanical Behavior at Small Strain: the Payne Effect 297
12.2.4 Mechanical Behavior at Larger Strains 299
12.2.5 Aging, Fatigue and Ultimate Properties 300
12.2.6 Conclusion 304
12.3 How to Explain Reinforcement in Rubber Nanocomposite? 304
12.3.1 Filler Morphology and Filler–Filler Interactions 305
12.3.2 Filler–Matrix Interactions 307
12.3.3 Indirect Influence of Fillers on Matrix Crosslinking 311
12.3.4 Influence of Fillers on Rubber Crystallization 312
12.3.5 Conclusion 316
12.4 Modeling Attempts 316
12.4.1 Polymer Network Contribution: Modeling Rubber Behavior 316
12.4.2 Filler Contribution: How to Describe the Composite Effect? 318
12.4.3 Account for the Filler–Filler and Filler–Matrix Interactions 321
12.4.4 Conclusion 323
12.5 General Conclusions 323
References 324

13 Nonlinear Viscoelastic Behavior of Rubbery Bionanocomposites 331
Alireza S. Sarvestani and Esmaiel Jabbari

13.1 Introduction 331
13.2 Rubbery Bionanocomposites 333
13.2.1 Biofiber–Natural Rubber Composites 333
13.2.2 Hydrogel Nanocomposites 334
13.3 Nonlinear Viscoelasticity of Hydrogel Nanocomposites 335
13.3.1 Filler–Gel Interfacial Structure 337
13.3.2 Dynamics of the Adsorbed Layer 338
13.3.3 Macroscopic Properties 341
13.3.4 Model Predictions 342
13.4 Conclusions 345
Acknowledgments 345
References 346

14 Rheological Behavior of Rubber Nanocomposites 353
Philippe Cassagnau and Claire Barrès

14.1 Introduction 353
14.2 Linear Viscoelasticity 355
14.2.1 General Trends 355
14.2.2 Percolation Threshold 357
14.2.3 Equilibrium Shear Modulus 361
14.3 Payne Effect 363
14.3.1 The Limit of Linearity 365
14.3.2 Thixotropy and Recovery 367
14.4 Flow Properties of Rubber Nanocomposites 368
14.4.1 Shear Viscosity 369
14.4.2 Rubber Nanocomposites Based on Nanoclays 376
14.4.3 Extensional Viscosity 378

14.4.4 Yield Stress 382
14.4.5 Wall Slip 383
14.4.6 Extrudate Swell 384
14.5 Conclusions 384
References 385

15 Electron Spin Resonance in Studying Nanocomposite Rubber Materials 391
S. Valić

15.1 An Approach to the Study of Polymer Systems 391
15.1.1 Introduction 391
15.1.2 Theoretical Background 393
15.2 ESR – Spin Probe Study of Nanocomposite Rubber Materials 397
15.3 Summary 403
References 404

16 Studies on Solid-State NMR and Surface Energetics of Silicas for Improving Filler–Elastomer Interactions in Nanocomposites 407
Soo-Jin Park and Byung-Joo Kim

16.1 Introduction 407
16.2 Surface Modification of Silicas 408
16.2.1 Thermal Treatment 408
16.2.2 Silane Coupling Method 409
16.2.3 Direct Fluorination 409
16.3 Solid-State NMR Analyses of Silicas 409
16.3.1 Thermally Treated Silicas 409
16.3.2 Silane-Treated Silicas 409
16.3.3 Fluorinated Silicas 411
16.4 Surface Energetics of Silicas 411
16.5 Other Surface Analyses of Modified Silicas 413
16.5.1 Thermally Treated Silicas 413
16.5.2 Fluorinated Silicas 414
16.6 Mechanical Interfacial Properties of the Compounds 417
16.6.1 Thermally Treated Silicas 417
16.6.2 Silane-Treated Silicas 419
16.6.3 Fluorinated Silicas 422
16.7 Conclusions 422
References 423

17 Wide-Angle X-ray Diffraction and Small-Angle X-ray Scattering Studies of Rubber Nanocomposites 425
Valerio Causin

17.1 Introduction 425
17.2 WAXD: An Overview 426
17.3 SAXS: An Overview 427
17.4 Lamellar Fillers 429
17.5 Nonlamellar Fillers 445
17.5.1 Carbon Black 445

17.5.2 Carbon Nanotubes 451
17.5.3 Silica 454
17.5.4 Polyhedral Oligomeric Silsesquioxane 460
17.5.5 Rubber as a Filler or Compatibilizer in Nanocomposites 464
17.6 Characterization of the Matrix in Polymer-Based Nanocomposites 464
17.6.1 Strain-Induced Crystallization 464
17.6.2 Thermoplastic Elastomers 472
References 486

18 Barrier Properties of Rubber Nanocomposites 499
Changwoon Nah and M. Abdul Kader

18.1 Introduction 499
18.2 Theoretical Consideration 501
18.2.1 Fundamental Permeation Theories 501
18.2.2 Diffusion through Polymer Membrane Filled with Particulate and Layered Fillers 503
18.3 Experimental Studies 510
18.4 Applications 520
18.5 Conclusions 522
Acknowledgments 523
References 523

19 Rubber/Graphite Nanocomposites 527
Guohua Chen and Weifeng Zhao

19.1 Introduction and Background 527
19.2 Graphite and its Nanostructure 529
19.2.1 Basic Issues on Graphite 529
19.2.2 Graphite Intercalation Compounds 530
19.2.3 Expanded Graphite 533
19.2.4 Graphite Nanosheets 535
19.2.5 Graphene and Graphite Oxide 537
19.3 Rubber/Graphite Nanocomposites 538
19.3.1 Preparation, Processing and Characterization 539
19.3.2 Properties and Applications 540
19.4 Future Outlook 546
Acknowledgments 546
References 546

20 Aging and Degradation Behavior of Rubber Nanocomposites 551
Suneel Kumar Srivastava and Himadri Acharya

20.1 Introduction 551
20.2 Types of Fillers Used in Rubber Nanocomposites 552
20.2.1 Clay Minerals 552
20.2.2 Layered Double Hydroxide 553
20.2.3 Carbon Nanotubes and Other Inorganic Nanofillers 554
20.3 Aging of Rubber Nanocomposites 554
20.3.1 Natural Rubber 555

20.3.2 Ethylene Propylene Diene Terpolymer 559
20.3.3 Styrene Butadiene Rubber 559
20.3.4 Nitrile Butadiene Rubber 561
20.3.5 Hydrogenated Nitrile Butadiene Rubber 561
20.3.6 Silicone Rubber 563
20.4 Degradation of Rubber Nanocomposites 563
20.4.1 Natural Rubber 563
20.4.2 Ethylene Vinyl Acetate 566
20.4.3 Ethylene Propylene Diene Terpolymer 568
20.4.4 Acrylonitrile Butadiene Rubber 579
20.4.5 Hydrogenated Nitrile Butadiene Rubber 581
20.4.6 Styrene Butadiene Rubber 582
20.4.7 Silicone Rubber 583
20.4.8 Butyl Rubber 587
20.5 Summary 588
References 588

21 Positron Annihilation Lifetime Spectroscopy (PALS) and Nanoindentation (NI) 595
Dariusz M. Bieliński and Ludomir Ślusarski

21.1 Introduction 595
21.2 Positron Annihilation Lifetime Spectroscopy 597
21.2.1 Introduction 597
21.2.2 Application of PALS to Study Rubber Morphology 599
21.2.3 Final Remarks 618
21.3 Nanoindentation 621
21.3.1 Introduction 621
21.3.2 Application of Nanoindentation to Study Rubber Morphology 623
21.3.3 Application of Nanotribology to Study Rubber Morphology 624
21.3.4 Final Remarks 626
References 627

22 Thermoelasticity and Stress Relaxation Behavior of Synthetic Rubber/Organoclay Nanocomposites 631
K.M. Sukhyy, E.G. Privalko, V.P. Privalko and M.V. Burmistr

22.1 Introduction 631
22.2 Experimental 632
22.2.1 Materials 632
22.2.2 Methods 633
22.3 Polychloroprene/Organoclay Nanocomposites 633
22.3.1 Structural Characterization of Unstretched Samples 633
22.3.2 Thermoelastic Behavior 634
22.3.3 Stress Relaxation 638
22.3.4 Conclusions 642
22.4 Styrene-*co*-Butadiene Rubber/Organoclay Nanocomposites 642
22.4.1 Structural Characterization of Unstretched Samples 642
22.4.2 Thermoelastic Behavior 643
22.4.3 Stress Relaxation 645
22.4.4 Conclusions 648
References 648

23 Theoretical Modeling and Simulation of Rubber Nanocomposites **651**
Jan Kalfus and Josef Jancar

23.1 Introduction 651
23.2 Brief Theory of Conformation Statistics and Chain Dynamics 653
23.3 Basic Aspects of Rubber Elasticity 657
23.4 Mechanisms of Nanocomposite Reinforcement 659
23.5 Chains at Rubber–Filler Interfaces 664
23.5.1 Structural Aspects 664
23.5.2 Dynamical Aspects 666
23.6 Structural Peculiarities of Rubbery Nanocomposites 668
23.7 Concluding Remarks 672
Acknowledgments 672
References 672

24 Application of Rubber Nanocomposites **675**
Miroslawa El Fray and Lloyd A. Goettler

24.1 Introduction 675
24.1.1 Rubbery Matrices 676
24.1.2 Nanofillers 676
24.2 Rubber Nanocomposites in Tire Engineering Applications 682
24.2.1 Tread 682
24.2.2 Innerliner 684
24.2.3 Other 687
24.3 Rubber Nanocomposite Membranes 687
24.4 Applications of Rubber Nanocomposites in Sporting Goods 689
24.5 Advanced Nanocomposites for Airspace Applications 690
24.6 Nanorubbers in Medicine and Healthcare 691
24.7 Conclusions 693
References 693

Index **697**

List of Contributors

Himadri Acharya, Indian Institute of Technology, Kharagpur, India.

Rosamma Alex, Rubber Research Institute of India, Kerala, India.
Email: rosammaalex2000@yahoo.com

Claire Barrès, INSA-Lyon, Villeurbanne, France; CNRS UMR5223, Villeurbanne, France.
Email: claire.barres@insa-lyon.fr

Dariusz M. Bielinski, Institute for Engineering of Polymer Materials & Dyes, Piastów, Poland. Email: d.bielinski@ipgum.pl; Technical University of Lodz, Lodz, Poland.
Email: dbielin@p.lodz.pl

Liliane Bokobza, ESPCI, Paris Cedex, France. Email: Liliane.Bokobza@espci.fr

M.V. Burmistr, Ukrainian State Chemical Technology University, Dnepropetrovsk, Ukraine.

Philippe Cassagnau, Université de Lyon 1, Lyon, France; CNRS UMR5223, Villeurbanne, France. Email: cassagno@univ-lyon1.fr

Valerio Causin, Università di Padova, Padova, Italy. Email: valerio.causin@unipd.it

Laurent Chazeau, INSA de Lyon, Villeurbanne Cedex, France.
Email: laurent.chazeau@insa-lyon.fr

Guohua Chen, Huaqiao University, China. Email: hdcgh@hqu.edu.cn

Jean-Marc Chenal, INSA de Lyon, Villeurbanne Cedex, France.
Email: jean-marc.chenal@insa-lyon.fr

Jiabin Dai, School of Advanced Manufacturing & Mechanical Engineering, University of South Australia, SA, Australia.

Amadou L. Diop, Laboratoire PPMD, Paris Cedex, France.
E-mail: Amadou-Lamine.Diop@espci.fr

Alain Dufresne, Grenoble Institute of Technology, The International School of Paper, Print Media and Biomaterials (Pagora), Saint Martin d'Hères Cedex, France; Universidade Federal de Rio de Janeiro (UFRJ), Departmanto de Engenharia Matalúrgica e de Materiais, Coppe, Rio de Janeiro, Brail. Email: Alain.Dufresne@efpg.inpg.fr

G.A. Edwards, University of Queensland, Brisbane, Australia.

M. El Fray, West Pomeranian University of Technology in Szczecin, Szczecin, Poland. E-mail: mirfray@zut.edu.pl

K.G. Gatos, Megaplast SA, Athens, Greece. Email: kgatos@gmail.com

Catherine Gauthier, INSA de Lyon, Villeurbanne Cedex, France. Email: catherine.gauthier@insa-lyon.fr

Li Geng, University of South Australia, SA, Australia. Email: Li.Geng@postgrads.unisa.edu.au

Lloyd A. Goettler, The University of Akron, Akron, USA. Emails: lagoett@uakron.edu and goet30@aol.com

E. Jabbari, University of South Carolina, Columbia, USA. Email: jabbari@engr.sc.edu

J. Jancar, Brno University of Technology, Brno, Czech Republic. Email: jancar@fch.vutbr.cz

Maya Jacob John, CSIR Materials and Science Manufacturing, Polymers and Composites Competence Area. Email: mjohn@csir.co.za

M. Abdul Kader, B.S.A. Crescent Engineering College, Chennai, India.

J. Kalfus, Brno University of Technology, Brno, Czech Republic. Email: kalfus@fch.vutbr.cz

J. Karger-Kocsis, Tshwane University of Technology, Pretoria, Republic of South Africa; Budapest University of Technology and Economics, Budapest, Hungary. Email: karger@pt.bme.hu

José Maria Kenny, University of Perugia, Terni, Italy. Email: kenny@unipg.it

Byung-Joo Kim, Jeonju Institute of Machinery and Carbon Composites, Jeollabuk-do, Republic of Korea. Email: kimbj@jmc.re.kr

Miguel Angel Lopez-Manchado, Institute of Polymer Science and Technology, Madrid, Spain. Email: lmanchado@ictp.csic.es

Jun Ma, Beijing University of Chemical Technology, Beijing, China; University of South Australia, SA, Australia. Email: Jun.Ma@unisa.edu.au

D.J. Martin, University of Queensland, Brisbane, Australia. Email: darren.martin@uq.edu.au

Hiroaki Miyagawa, Nitto Denko Technical Corporation, Oceanside, USA. Emails: miyagaw2@msu.edu and hiroaki.miyagawa@gmail.com

Changwoon Nah, Chonbuk National University, Jeonju, Republic of Korea. Email: cnah@chonbuk.ac.kr

Soo-Jin Park, Inha University, Incheon, Republic of Korea. Email: sjpark@inha.ac.kr

E.G. Privalko, Institute for Macromolecular Chemistry, National Academy of Sciences of Ukraine, Kharkiv Chaussee 48, Kyiv, Ukraine.

V.P. Privalko, National Academy of Sciences of Ukraine, Kyiv, Ukraine.

Alireza S. Sarvestani, University of South Carolina, Columbia, USA.
Email: sarvesta@engr.sc.edu

Ludomir Slusarski, Technical University of Lodz, Lodz, Poland.
Email: ludomir.slusarski@p.lodz.pl

S.K. Smart, University of Queensland, Brisbane, Australia.

Suneel Kumar Srivastava, Indian Institute of Technology, Kharagpur, India.
Email: sunit@chem.iitkgp.ernet.in

R. Stephen, Cochin University of Science and Technology, Kerala, India.
Email: ranistephen@yahoo.com

K.M. Sukhyy, Ukrainian State Chemical Technology University, Dnepropetrovsk, Ukraine.
Email: ksukhyy@rambler.ru

S. Thomas, Mahatma Gandhi University, Kerala, India. Emails: sabupolymer@yahoo.com and sabuchathukulam@yahoo.co.uk

Luca Valentini, University of Perugia, Terni, Italy. Email: mic@unig.it

Srecko Valic, University of Rijeka, Rijeka, Croatia; Rudjer Bošković Institute, Zagreb, Croatia. E-mail: valics@medri.hr

Raquel Verdejo, Institute of Polymer Science and Technology, Madrid, Spain.
Email: rverdejo@ictp.csic.es

Li Qun Zhang, Beijing University of Chemical Technology, Beijing, China.
Email: zhanglq@mail.buct.edu.cn

Weifeng Zhao, Huaqiao University, China. Email: weifeng484@hqu.edu.cn

Preface

Rubber nanocomposites have attracted many researchers due to their unique properties. In rubbers, fillers are used to achieve products with improved properties for end use applications. It is well known that for most of the applications, rubber must be reinforced with certain fillers such as carbon blacks, silica, clay and so on. Rubber nanocomposites are prepared through different techniques such as melt mixing, mill mixing, solution mixing, latex stage mixing followed by a co-coagulation method and polymerization around the filler particles. As compared with microfiller-reinforced rubber, nanofiller-reinforced rubber exhibits high hardness, modulus, anti-aging and gas barrier properties. Therefore, the nanoconcept is highly relevant for rubber compounds since their applications require filler reinforcement.

The present book focuses on the synthesis, morphology, structure, properties and applications of natural and synthetic rubber nanocomposites. This book carefully debates the preparation of unmodified and modified nanofillers, various manufacturing techniques of rubber nanocomposites, structure, morphology, properties and applications of nanocomposites. The text reviews the processing; characterization and properties of 0D, 1D and 2D nanofiller-reinforced rubber nanocomposites. It examines the polymer/filler interaction, that is, the compatibility between matrix and filler using unmodified and modified nanofillers. The extraction of various nanofillers and nanocrystals from bioresources such as cellulose and starch and their incorporation in natural rubber for the development of eco-friendly green bionanocomposites is reviewed in detail. The book also examines the applications of rubber nanocomposites in various engineering fields.

This book consists of 24 chapters and each chapter covers various relevant topics in rubber nanocomposites. The state of the art, new challenges and opportunities in the area of rubber nanocomposites are discussed in Chapter 1. Chapter 2 is devoted to various aspects and technologies for the manufacture of rubber nanocomposites. The effect of various spherical fillers on the properties of rubber by *in situ* generated filler particles through sol-gel process is described in Chapter 3. Chapter 4 considers interface modifications in rubber nanocomposites through reactive and nonreactive routes. Chapter 5 reviews the preparation, characterization and properties of green rubber nanocomposites. It emphasizes the preparation of nanoparticles from natural resources which could be incorporated into natural rubbers to produce eco-friendly green composites. Chapter 6 surveys the effects of the incorporation of carbon nanotubes on the physical and mechanical properties of natural and synthetic rubbers. Chapter 7 deals with the preparation, properties and applications of rubber/clay nanocomposites. The preparation,

characterization and properties of nanocellulose fiber-reinforced rubber nanocomposites are discussed in Chapter 8.

Chapter 9 surveys the role of nanofillers for the interface modification and various other properties of rubber–rubber blends. Chapter 10 focuses on nanofilled thermoplastic elastomers and is exclusively dedicated to the properties of polyurethane nanocomposites. The major developments in the morphology of rubber nanocomposites are extensively reported in Chapter 11, with the morphology being analyzed using various microscopic techniques. Chapter 12 describes major achievements in the physical properties of nanofilled rubber as compared to microfilled systems. Chapter 13 deals with the nonlinear viscoelastic behavior of rubbery nanocomposites. The rheological properties of rubber nanocomposites are described in Chapter 14. An understanding of the rheological properties of polymer nanocomposites is crucial to gain a fundamental knowledge of the processability and structure–property relations. Chapter 15 discusses the electron spin resonance (ESR) method as an indirect method to characterize rubber nanocomposites by introducing stable free radicals into the matrix. Chapter 16 describes how solid-state nuclear magnetic resonance (NMR) and the surface energetics of silicas can be used to improve filler–elastomer interactions in nanocomposites. Chapter 17 deals with the characterization of rubber nanocomposites using wide-angle X-ray diffraction and small-angle X-ray scattering techniques.

Chapter 18 surveys the effect of nanofillers on the barrier properties of rubber nanocomposite membranes. Chapter 19 describes conducting rubbers incorporated with nanographite and graphite nanosheets as fillers. The aging and degradation of rubber nanocomposites under various atmospheres such as temperature, ozone, oxygen and so on is discussed in Chapter 20. The characterization of rubber nanocomposites, that is, the organization of filler particles and filler–matrix interactions using positron annihilation spectroscopy (PAS) and nanoindentation (NI) is discussed in Chapter 21. Chapter 22 describes the thermal properties of rubber nanocomposites. The theoretical approach to the properties of rubber nanocomposites is discussed in Chapter 23. Finally, the application of rubber nanocomposites in various fields based on their properties are described in Chapter 24. Rubber nanocomposites find a large number of applications in tire and non-tire engineering and also in biomedical field.

Sabu Thomas

Ranimol Stephen

Editor Biographies

Dr Thomas is a full Professor of Polymer Science and Engineering at the School of Chemical Sciences, Mahatma Gandhi University, Kottayam, Kerala, India and Director of Centre for Nanoscience and Nanotechnology, Mahatma Gandhi University. He received his BSc degree (1980) in Chemistry from the University of Kerala, India, B.Tech (1983) in Polymer Science and Rubber Technology from the Cochin University of Science and Technology, Cochin, India, and Ph.D (1987) in Polymer Engineering from the Indian Institute of Technology (IIT), Kharagpur, India.

Prior to joining the Mahatma Gandhi University in 1987, he worked in the industry for two years at Bata India Ltd (1983–1984) and Bayer India Ltd (1987). He established an excellent Polymer Science and Engineering research laboratory at the Mahatma Gandhi University from external funding from government and industry. He was the founding Director of the Polymer Engineering program at the School of Technology and Applied Sciences of the Mahatma Gandhi University and Center for Nanoscience and Nanotechnology. During his career at the Mahatma Gandhi University, he spent two years (1989–1991) as a post-doctoral fellow at the Macromolecular Science and Engineering Research Center (CERSIM) of Laval University, Quebec City, Canada, under the supervision of Professor P.E. Prud'homme. He was a senior visiting fellow at the Laboratory of Macromolecular Structural Chemistry (MSC), Department of Chemistry, Katholieke University of Leuven, Belgium, for two years in the group of Professor Groeninckx (1996–1998). He was also an invited visiting professor to many polymer research laboratories in Europe and Asia (Katholieke University, Leuven, Belgium, 2001, 2003 and 2004; CNRS, Thais, France, 2002; University of Orleans, France, 2005; University of South Brittany, France, 2005; Beijing University of Chemical Technology, Beijing, China, 2006; IPF Dresden, Germany, 2006; University Paris 12, France, 2007; University of Du Maine, Le Mans, France, 2008, University of Paris 12, France, 2009).

Currently, he is a fellow of the Royal Society of Chemistry, London; a member of the American Chemical Society, Rubber Division; a member of the New York Academy of Sciences; a member of the Polymer Society of India; and a lifetime member of the Society of Polymer Technologists, Cochin University of Science and Technology. He is a reviewer of numerous international journals and funding agencies. The research activities of Dr Thomas include surfaces and interfaces in multiphase polymer blend and composite systems, kinetics of phase separation in polymer blends, compatibilization of immiscible polymer blends, thermoplastic elastomers, phase transitions in polymers, nanostructured polymer blends, macro-, micro- and nanocomposites, polymer rheology, recycling, reactive extrusion, processing–

morphology–property relationships in multiphase polymer systems, double networking of elastomers, natural fibers and green composites, rubber vulcanization, interpenetrating polymer networks, diffusion and transport and polymer membranes. He has supervised 50 Ph.D theses, 20 MPhil theses and 10 Masters theses. The students of Dr Thomas occupy leading positions in academia, industry and R&D laboratories in India and abroad. His research has culminated in some 400 research publications in international refereed journals, several book chapters, three patents and six co-edited books which have been cited by others in many different polymer journals. The h index of Dr Thomas is 33. He has more than 4000 citations. His research accomplishments have been presented at local and international conferences, seminars, and workshops, in both oral and poster form. He has delivered several plenary and key note talks as well as invited lectures in international conferences held in India, USA, Japan, Germany, South Africa, Australia, Brazil, Malaysia, Singapore, China, Sweden, France and Taiwan. Dr Thomas has chaired many international conferences, seminars and workshops. He has several national collaborations with different polymer laboratories in India as well as many international collaborations with different countries. He has many external funded projects from government and industrial funding agencies. This has enabled him to establish an excellent center of polymer research at the Mahatma Gandhi University. He has been ranked no. 5 in India as one of the most productive scientists, with regards to the number of publications he has published. He also received the coveted Sukumar Maithy Award for the best polymer researcher in the country for the year 2008. Dr Thomas' research group has also received numerous awards and honors for excellent work in the field of polymer science and engineering.

Dr Ranimol Stephen, a budding polymer technologist is, at present, a Dr D.S. Kothari Post Doctoral Fellow (sponsored by University Grants Commission, New Delhi, India) at Cochin University of Science and Technology, Kerala, India. Before that, she had done a Post Doctoral Fellowship in the synthesis and properties of segmented block copolymers of engineering thermoplastic at University of Twente, The Netherlands, in collaboration with BASF, Germany. Dr Stephen received her Masters in Chemistry from Mahatma Gandhi University, Kerala, India. She joined the Ph.D in Dr Thomas' group at the School of Chemical Sciences, Mahatma Gandhi University, in the field of micro- and nano-filled rubber latices and their blends, and received her doctoral degree in the year 2006. She is an author of more than twenty research papers published in highly-rated international journals, in the field of polymer science and technology. She did an extensive investigation on the properties of micro- and nano-filled latices as part of her Ph.D work.

1

Nanocomposites: State of the Art, New Challenges and Opportunities

Ranimol Stephen[1] and Sabu Thomas[2]

[1] *Department of Polymer Science and Rubber Technology, Cochin University of Science and Technology, Cochin, Kerala, 682 022, India*

[2] *School of Chemical Sciences, Mahatma Gandhi University, Priyadarshini Hills P.O., Kottayam, Kerala, 686 560, India*

1.1 Introduction

Nanoscience and nanotechnology can be considered as a revolutionary science in the multidisciplinary area combining chemistry, physics, material science, electronics and biosciences. It is a fascinating technology of the twentyfirst century, ranging from novel building materials to medicine. Normally, the term nano encompasses the range 1–100 nm. With respect to diversity in technological applications, nanotechnology offers novelty and versatility not observed in any other field.

Nanoengineered polymeric materials are of great interest, rapidly growing new class of materials alternative to conventional filled polymers or polymer blends. The value of polymer nanocomposites (PNCs) not only solely based on the mechanical property enhancement but also value-added properties without sacrificing the inherent processability and mechanical properties of the polymer. The first industrial application of PNCs was provided by Okada *et al.* [1] They synthesized a Nylon-6 nanocomposite by polymerization in the presence of monomer. It was then marketed by UBE industries and Bayer; currently it is used to make the timing belt cover of Toyota's car engines and also for the production of packaging film.

Elastomers are filled with small and hard particles to improve the mechanical properties like elastic modulus or resistance to abrasion. A fine dispersion of filler resulting in good adhesion at the polymer/filler interface is the basic requirement for attaining optimum reinforcement and

Rubber Nanocomposites: Preparation, Properties and Applications Edited by Sabu Thomas and Ranimol Stephen
© 2010 John Wiley & Sons (Asia) Pte Ltd

low hysteresis in elastomers. Carbon black and mineral fillers such as silica has been widely used in rubber industry for the past many decades to improve properties. However, due to the high structure of carbon black strong shear fields or filler modification needed to ensure fine dispersion.

Over the past few years rubber nanocomposites have been widely discussed by scientists by considering the number of potential nanoelements such as layered silicates, talc, silica, nanobiofillers and carbon nanotubes. Although all these nanofillers have been in use in rubber nanocomposites for past 10 years, the major interest is on the use of layered silicates and carbon nanotubes. Incorporation of clay or layered silicates to polymer matrix provides four different structures: (i) conventional, (ii) partially intercalated and exfoliated, (iii) fully intercalated and dispersed and (iv) fully exfoliated and dispersed. It is interdependent on the clay concentration, the degree of clay layer separation and distribution in the composites [2]. In microcomposites or conventional composites the particles exist as aggregates with no insertion of polymer matrix. Hence it cannot impart any enhancement in properties. Intercalated nanocomposites consisting of a regular insertion of polymer in between the silicate layers in a crystallographically regular fashion [3–6]. In an exfoliated nanocomposite, the individual 1 nm silicate layers are separated and dispersed in a continuous polymer matrix, with average distances between layers depending on the clay concentration. Exfoliated nanocomposites exhibit better properties owing to the maximum polymer/filler interactions. In exfoliated structure, the entire surfaces of the layers are available for interactions with the polymer. Therefore, it is a major challenge in polymer nanocomposite field to achieve a fully exfoliated structure.

This chapter provides information about the developments in rubber nanocomposites. The discussion focuses on the different types of potential nanofillers and their reinforcement in various rubbers. Attempts have been made to establish the morphology-property correlations.

1.2 Various Nanofillers

1.2.1 Layered Silicates

Layered silicates (LS) are rock-forming minerals and are main active minerals in soils and clays. Nowadays, they are important raw material in many areas, like construction, ceramics, paper industry, cosmetic industry, biomaterials, electronic field and so on. The significant potential of this material captured various applications which include composite materials, molecular sieves, selective ion trap, catalytic support and so on.

LS/clay minerals are part of the class of silicate minerals, phyllosilicates. They include natural and synthetic clays such as mica, bentonite, magadiite, laponite, fluorohectorite and so on. LS are the most widely used 2-D nanofillers in various fields. The structure of LS consists of a 2-D layer of two fused silicate tetrahedral sheet with an edge-shared octahedral sheet of metal atoms, such as Al or Mg. The model crystal structure of LS was proposed by Hoffmann *et al.* [7] In the case of phyllosilicates the neighboring layers are separated by a weak van der Waals bond and the gap are called galleries or interstatum, the layers exist as small flake like structure. The galleries are occupied by cations and they counterbalance the excess of negative charges due to the isomorphous substitution of Si^{4+} for Al^{3+} in the tetrahedral sheet and Al^{3+} for Mg^{2+} in the octahedral sheet. This will result in the partial positive charge in the gallery, considered as the beauty of intercalation chemistry required for the dispersal of clay in the polymer on a nanometer scale. Figure 1.1 gives the schematic structure of layered silicates.

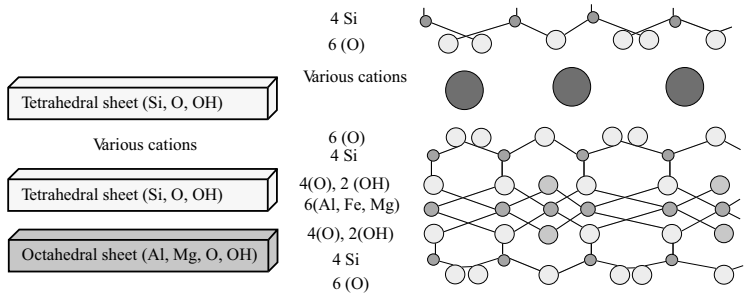

Figure 1.1 Schematic structure of LS, MMT 2:1 type (Reproduced with permission from S. Grunwald and K. McSweeney, ''Secondary Silicates,'' University of Wisconsin-Madison, Department of Soil Science, http://www.soils.wisc.edu/courses/SS325/silicates.htm#structsil (accessed July 3, 2007).)

These sheet-like nanofillers are ∼1 nm thick and 100s to 1000s of nanometers long; as a result they possess a high aspect ratio. Therefore, polymer/silicate nanocomposites provide an attractive method to improve the polymer properties such as stiffness, strength and barrier properties without any change in processing technique. Primarily, two types of microstructures could result from the interaction between polymer and the layered silicates: (i) intercalated and (ii) exfoliated structure. A regular pattern of insertion of polymer in between the galleries of silicates can be occurred in intercalated structure. However, in exfoliated structure, the individual silicate layers of approximately 1 nm are separated and dispersed in a continuous polymer matrix. The later system exhibits better properties due to the higher polymer/LS interactions. The dispersion of inorganic fillers in organic polymers is like oil in water. The way to overcome this drawback is by transforming the organophobic galleries to organophilic. This is achieved by replacing the cation originally present in the galleries with organic cation, which has long organic chains with a positively charged end. It will act as a compatibilising agent between organic and inorganic phase; since like dissolves like. Amino acids were the first compatibilising agents used for the synthesis of polymer nanocomposites [9]. Alkyl ammonium ions are the most widely used promising compatibilizing agent. It has the ability to lower the surface energy of the layered silicates and as a result it reduces the electrostatic interactions between the silicate layers and allow molecules to diffuse between the layers [10, 11]. The basic formula is $[(CH_3{=}CH_2{=})_nNH^{3+}]$, where n is between 1 and 18. It is interesting to note that the length of the ammonium ions has a strong influence on the resulting structure of nanocomposites. Lan *et al.* [12] observed that alkyl ammonium ions with a chain length larger than eight carbon atoms favored the synthesis of exfoliated nanocomposites whereas ammonium ions with shorter chains led to the formation of intercalated nanocomposites. Examples of other compatibilizing agents used for the organic modification of layered silicates include polyetheramines, dihydroimmidazolines, silanes and so on.

1.2.2 Nanotubes

Among different types of nanotubes, carbon nanotubes are the most widely used and accepted in polymer research field and industry. Carbon nanotubes are allotropes of carbon and belong to the fullerene structural family. As the name indicates, nanotubes are cylindrical in shape with at

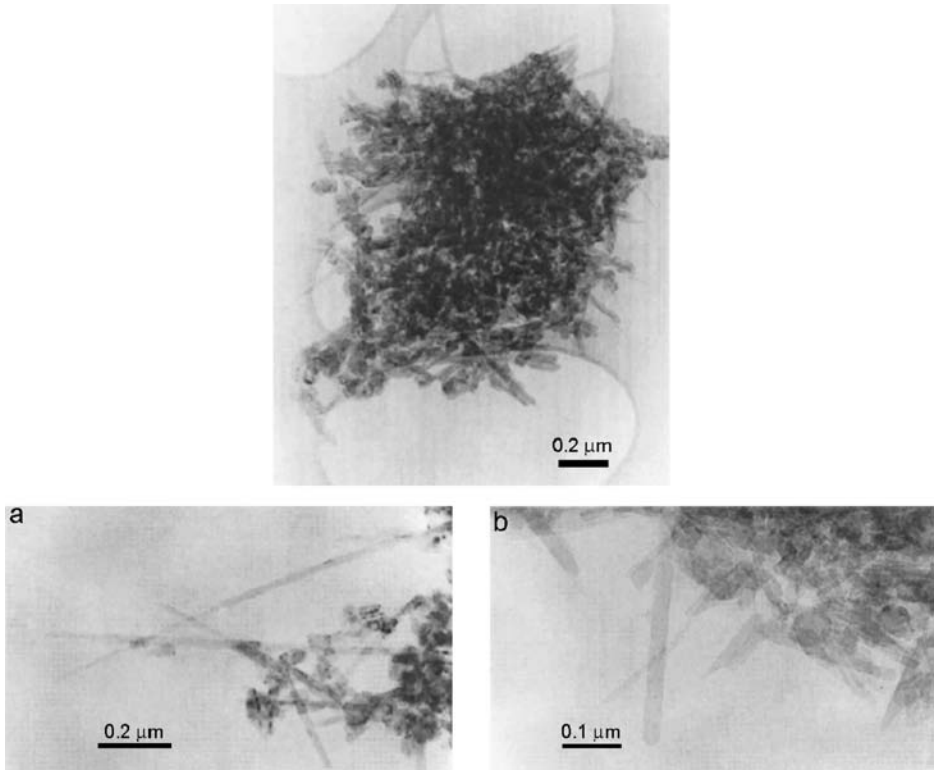

Figure 1.2 Upper image: cluster of nanotubes and nanoparticles on lacey carbon support film. Lower images: higher magnification images of nanotube/nanoparticle clusters (Reproduced with permission from P.J.F. Harris, "Carbon Nanotubes and Other Graphitic Structures as Contaminants on Evaporated Carbon Films," Journal of Microscopy, 186, 88–90, © 1997, Wiley-Blackwell.)

least one end capped with a hemisphere of the buckyball structure; it is spherical in shape. The structure of a carbon nanotube is shown in Figure 1.2 [13].

In nanotubes the diameters are in the order of a few nanometers; however, they are millimeters or even centimeters long. Therefore, these nanotubes possess a high aspect ratio, thereby imparting high strength to the polymer with a small weight percent. The excellent properties of carbon nanotubes are a consequence of its bonding nature. The chemical bonding of carbon nanotubes are sp^2 hybridized as seen in graphene, which is stronger than sp^3 as in diamond. Nanotubes are classified into: (i) single-walled nanotubes (SWNTs) and (ii) multi-walled nanotubes (MWNTs). Carbon nanotubes can be synthesized by different techniques, such as arc discharge, laser ablation, high-pressure carbon monoxide (HiPCO) and various catalytic chemical vapor deposition (CVD) techniques [14–20].

Carbon nanotube-reinforced composites are of particular interest in the field of material science to develop significantly lightweight strong materials. A major problem in this field is the failure to attain a homogeneous dispersion of nanotubes in the polymer matrix due to the aggregation of these tubes. Researchers have employed different techniques to attain optimum dispersion of nanotubes in the polymer matrix, including: (i) solution mixing [21],

(ii) sonication [22], (iii) coagulation [23], (iv) melt compounding [24–27], (v) *in situ* emulsion polymerisation [26, 27], (vi) the use of surfactants [28] and (vii) chemical functionalization of nanotubes [29, 30]. Chemical modification of carbon nanotubes is the best technique to get more homogeneous dispersion through covalent and noncovalent attachments of functional groups in nanotubes with the matrix. Various strategies of functionalisation of carbon nanotubes have been reported by researchers [31–37]. Among the different functionalisation methods electrochemical modification and surface initiated *in situ* polymerization are the appreciable means for the preparation of nanotubes reinforced polymers with maximum properties and minimum damage of CNTs [38–42]. Owing to their structural characteristics, electrical and mechanical properties, CNTs are used in a wide variety of applications in the automotive and aerospace industries [43, 44], as nanoelectronic devices [45–47], as tips for scanning probe microscopes [48–50] and so on.

A new class of naturally occurring nanotubes (silicates with a nanotubular structure) named halloysite nanotubes (HNTs) have been reported and used as reinforcing filler in various polymers [51, 52]. HNTs are aluminosilicates with nanodimensional tubular structure composed of siloxane groups on the surface along with a few hydroxyl groups; they possess a better dispersion property and the ability to form hydrogen bonding with the functionalized polymer matrix [53, 54].

1.2.3 Spherical Particles

Nanofillers of isodimensional, that is, with three dimensions in the nanometer regime are the spherical nanofillers generally obtained by a sol-gel process [55, 56]. In sol-gel processes the organic/inorganic hybrid materials can be formed by the condensation reaction between the functionalized prepolymers and the metal alkoxides, leading to the formation of a chemical bond between the polymer and the inorganic filler. Therefore, the incorporation of filler particles in polymers through the sol-gel process avoids the aggregation of filler. Peng *et al.* [57] have synthesized surface unmodified and modified silica nanoparticles from Stöber synthesis (Figure 1.3).

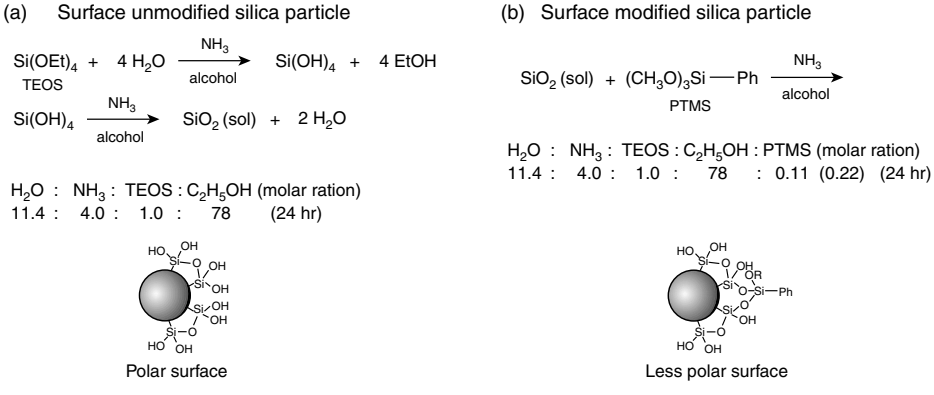

Figure 1.3 Synthesis and structure of "smart" nanosilica: (a) unmodified and (b) modified, where TEOS is tetraethoxysilane and PTMS is phenyl trimethoxy silane (Reproduced with permission from C-C. Peng, A. Gopfert, M. Drechsler and V. Abetz, "'Smart' Silica-Rubber Nanocomposites in Virtue of Hydrogen Bonding Interaction," Polymers for Advanced Technologies, 16, 770–782, © 2005, Wiley-Blackwell.)

The strategy behind the surface modification of fillers is to enhance its interaction with the polymer matrix through hydrogen bonding with the reactive site of polymer matrix. Various polymers with functional groups have been incorporated into a sol-gel process resulted in a material with high degree of homogeneity owing to the good interaction between the polymer and filler in this process [58–64]. Kickelbic [65] has extensively studied the concept behind the nanoscale incorporation of inorganic building blocks in organic polymer. Silica, TiO_2, ZnO, $CaSO_4$, $CaCO_3$, $ZnFe_2O_4$ and so on, are the widely used spherical inorganic nanofillers in the polymer field [66–68].

1.2.4 Polyhedral Oligomeric Silsesquioxanes

Polyhedral oligomeric silsesquioxane (POSS) chemical technology is the recent development in polymer science and technology. POSS molecules are considered as the smallest particles possible for silica. Conversely, each POSS molecule possesses covalently bonded reactive functionalities appropriate for polymerization or grafting POSS monomers to polymer chains. Also, POSS molecules have nonreactive organic active sites for solubility and compatibility of the POSS segments with various polymer systems. The anatomy of POSS molecule is displayed in Figure 1.4 [69].

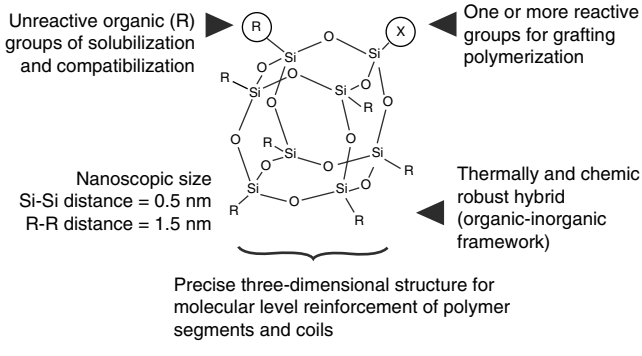

Figure 1.4 The structure of a POSS, where R represents unreactive organic groups for solubilization of the molecule and compatibility with other organic species. X represents reactive groups for grafting or copolymerization. The Si=Si distance is ~0.5 nm, and the R–R distance is ~1.5 nm (Reproduced with permission from J. Lichtenhan, "What is POSS Technology?" Hybrid Plastics Inc., http://www.hybridplastics.com/posstech.html (accessed December 17, 2008).)

The two unique features of POSS are the following: (i) the chemical composition is a hybrid intermediate (RSiO 1.5) between that of silica (SiO 2) and silicone (R 2SiO) and (ii) these molecules are physically large with respect to polymer dimensions and nearly equivalent in size to most polymer segments and coils [70]. A representation of the POSS polymer system is given in Figure 1.5 [70].

POSS chemical technology has been successfully employed in plastics. The advantages of POSS incorporation in polymers includes enhancement in physical properties, fire retardation, a higher use temperature, improved mechanical properties and lightweight endproducts [70].

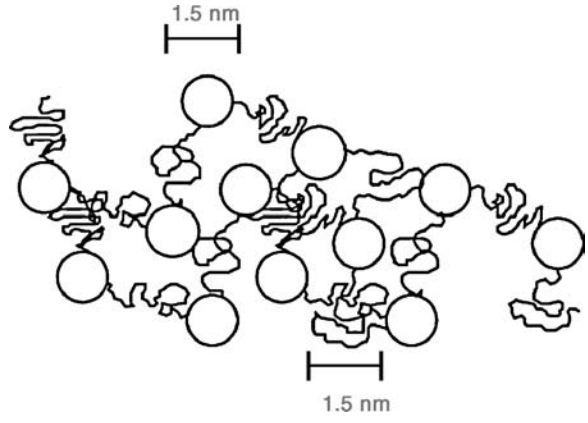

Figure 1.5 Schematic representation of POSS/polymer system (Reproduced with permission from J. Lichtenhan, "What is POSS Technology?" Hybrid Plastics Inc., http://www.hybridplastics.com/posstech.html (accessed December 17, 2008).)

Owing to the nanoscopic size and its relationship to polymer dimensions, the incorporation of POSS molecules in polymers results in an enhancement of properties. It has the ability to control the motions of polymer chains whilst maintaining the polymer processability and mechanical properties.

POSS was first developed by United States Air Force for aerospace applications. Research works are going on in large number of POSS monomers and polymers. POSS technology can incorporate into polymers through copolymerization and blending by the existing processing techniques due to its chemical nature. Li *et al.* [71] reviewed the synthesis and properties of homopolymers and copolymers of monomers containing inorganic/organic hybrid POSS structures.

1.2.5 Bionanofillers

Currently, there is an interesting demand for biobased fillers in polymer industry to produce low cost biodegradable materials. The instable price of petrochemicals also increases the demand for fillers from natural resources such as natural fibers (hemp, flax, rutabaga, wheat, and so on), wood fibers, starch and so on. These long fibers consist of stacks of strands with thin layers of polysaccharides, pectin and lignin. Nanofibrils can be synthesized from these natural fibers. Bhatnagar and Sain [72] have synthesized nanofibrils from various naturally occurring plant fibers, such as bast, hemp, kraft pulp and rutabaga by different chemical treatments. They have obtained nanofibers with diameters between 5 and 60 nm. They have observed superior properties of composite film comprising of 90% polyvinyl alcohol and 10% nanofibers.

Dufresne and coworkers [73, 74] have synthesized waxy maize starch nanocrystal platelets of 6–8 nm thickness, 40–60 nm length and 15–30 nm width. They have analyzed the properties of NR reinforced with these nanocrystals. Nanocrystals (rod-like) have been synthesized also from cellulose and chitin, with 6–8 nm thickness, 20–40 nm length and 15–30 nm width [75].

Nanofibers have been successfully synthesized and reinforced in polymer matrices by Nunes and coworkers [76].

1.3 Rubber Nanocomposites

According to the survey of 2006, the worldwide consumption of rubber rose to 21.5 million tonnes. This statistical report explored the inevitability of rubber goods in the day to day life of human beings. Worldwide, China is the largest consumer of rubber. Of the total vast consumption, NR accounts for 43.1%, while synthetic rubber (SR) accounts for 56.9%. The dominant market for rubber is the automotive industry, in the manufacture of tires and inner tubes. Other industrial rubber goods include various belts, hoses, oil seals, gaskets and so on. Table 1.1 presents regional total rubber consumption across the world.

Table 1.1 World rubber consumption

Region	Percentage
East Asia and India	48
European Union	17
North America	16
Rest of Europe	9
Latin America	6
Rest of the world	4

(Reproduced with permission from H.P. Smit, "Rubber nanocomposites: state of the art, new challenges and opportunities," Outlook for Elastomers 2004–2005 and Rubber Statistical Bulletin, Nov-Dec 2006.)

Albeit the consumption of synthetic rubber is increasing, it is an authentic truth that NR is the most fascinating and industrially relevant rubbery material. The foremost grounds behind it include its high green strength due to the presence of nonrubber components such as phospholipids and proteins, strain-induced crystallization behavior, easy vulcanization and its stereoregularity. SBR is the most widely used SR, followed by PBR. However, to attain good mechanical properties in accordance with the end use application the elastomers have to be reinforced with particulate fillers such as carbon black and silica. Usually a high percentage, around 20–40 wt% conventional fillers are needed to get adequate reinforcement depends on the application. There are certain drawbacks associated with these traditionally filled rubbers. A higher content of filler: (i) reduces the processability and (ii) increases the weight of the final product. Under these circumstances, the nano concept is highly relevant for rubber compounds since their application requires filler reinforcement [77–83]. Okada *et al.* [84] found that 10 phr of organoclay is enough to achieve a tensile strength of NBR as compared to 40 phr carbon black loaded NBR. Similarly, Arroyo *et al.* [81] have compared the reinforcement imparted on NR upon the addition of organoclay and carbon black. They observed that the mechanical properties of NR with 10 phr organoclay have been comparable to the compound with 40 phr carbon black. Based on the improvement in properties of nanofilled rubber, many researchers and industrialists have prepared various rubber nanocomposites through different methods such as melt mixing [85–88], two-roll mill mixing [89–94], solution mixing [95–101], latex

stage mixing followed by coagulation method [102–109] and polymerization around the filler particles [108, 109].

Rubber/clay nanocomposites have been of particular interest for the past few years due to their unique physical and chemical properties. It has been proved that the dispersion state of the clays and the polymer/clay interaction play a crucial role in the fine tuning of the ultimate properties of nanocomposites. Rubber/LS nanocomposites exhibited excellent properties due to the high aspect ratio of layered silicates arising from their platelet-like morphology (lamellar structure): 1 nm thick and 1000s of nanometers long. In the presence of LS, rubber nanocomposites can form either intercalated or exfoliated structure and partly intercalated and exfoliated structure [110, 111]. In an intercalated structure a well defined arrangements of rubber chains in between the layers of silicates leads to the formation of multilayered structure with alternative rubber and silicate layers with increased d-spacing between the silicate layers. However, in exfoliated structure the layers are highly disordered in rubber matrix. In principle, the morphology of rubber nanocomposites are in between these two structures, that is, with a partial intercalation and exfoliation. Due to the incompatibility between the organic (rubber) and inorganic (silicates) components the maximum properties can only be attained by the organic modification of the silicates. Thus the interaction between hydrophobic rubber and hydrophilic filler has been improved to get unique physical and chemical properties.

The most commonly used LS in rubber industry are montmorrillonite (MMT), hectorite, saponite and organically modified MMT. The literature reveals that unprecedented improvement in properties has been observed in elastomers with these nanofillers [81–83, 85–88, 95, 102, 112–114]. Jeon *et al.* [115] have synthesized a modified Na-MMT using poly(ethylene glycol)monooleate and poly(ethylene glycol) diacrylate as modifiers to enhance the fine dispersion in rubber matrix. An appealing result has been obtained for PEG-modified Na-MMT.

They have found that the 2θ of Na-MMT is 7.3° while that of Na-MMT intercalated with PEG-oleate and PEG-acrylate at 6.4° and 6.7° respectively. From Bragg's equation, the interlayer distance of MMT increased from 12.1 Å to 13.8 Å and 13.2 Å respectively for the intercalation of PEG-oleate and PEG-acrylate. They reported that the properties, morphology as well as the cure characteristics of rubber filled with these modified MMT have been improved. It has been revealed that the organic modification enhanced the fine dispersion of Na-MMT effectively in the hydrophobic rubber matrix. Jia *et al.* [116] have observed a significant improvement in the mechanical properties of SBR/organoclay nanocomposites. According to them, the modifiers can improve the strength of the nanocomposites. The modifiers of long chain alkyl ammonium salts mainly enhanced the tensile strength by physical entanglements with rubber molecules. For the past few years, researchers have employed various rubbers (both natural and synthetic) for the preparation of nanocomposites, viz, NR [81, 88, 98–101, 117–124], SBR and XSBR [91, 125–131], HNBR and NBR [104, 132–137], IR and ENR [85, 88], EPDM [80, 138, 139], EVA [140, 141] and so on. The developments in rubber/clay nanocomposites have been properly reviewed by Karger-Kocsis and Wu [142] and Sengupta *et al.* [143].

Owing to the high modulus, aspect ratio and excellent thermal and electrical properties of carbon nanotubes have been used as reinforcing filler in elastomers instead of conventional fillers such as carbon black and silica. Liliane *et al.* [144–148] have studied the reinforcing effect of multiwalled carbon nanotubes in SBR. They found that the elastic modulus of the matrix increases substantially with a small amount of filler. Recently, Liliane *et al.* [149] have

investigated and compared the reinforcement of SBR by single fillers of carbon black and multiwalled carbon nanotubes and by mixture of carbon black and MWNTs. A significant improvement in properties for samples containing dual phase as well as the electrical resistivity and percolation threshold were found to be lower for composite with blends of fillers. Jacob and coworkers [150] have synthesized the nanocomposite of crosslinked natural rubber and single-walled carbon nanotubes. The crosslink density of the nanocomposites have been determined by mechanical measurements and Raman spectroscopic analysis. They have compared the results obtained from the mechanical measurements and Raman spectroscopic measurements and found that the single walled nanotube Raman sensors are sensitive to the crosslinking density in natural rubber. Therefore, it can be used to evaluate the crosslinking process of rubbery materials. They also studied the effect of SiC nanoparticles and single-walled carbon nanotubes in natural rubber [151]. They found that the tensile strength of the nanocomposite was enhanced by incorporating SiC and SWNTs even at lower concentration (1.5 wt%). Researchers have paid much interest in nancomposites of various rubbers and carbon nanotubes (SWNTs and MWNTs) such as NR [152–156], SBR [157, 158], HNBR [159], EPDM [160], PUR [161–168] and silicone rubbers [169–171]. Bhattacharyya *et al.* [172] have reinforced natural rubber using carboxylated multiwalled carbon nanotubes (c-MWCNT) dispersed with sodium dodecyl sulfate. The c-MWNTs was characterized by TEM, Figure 1.6a. A 10-fold increase in Young's modulus was observed with 8.3 wt% of c-MWNTs. The stress-strain curves are presented in Figure 1.6b. Dielectric measurements at room temperature revealed a low percolation threshold (<1 wt%) associated with formation of an interconnected nanotube network.

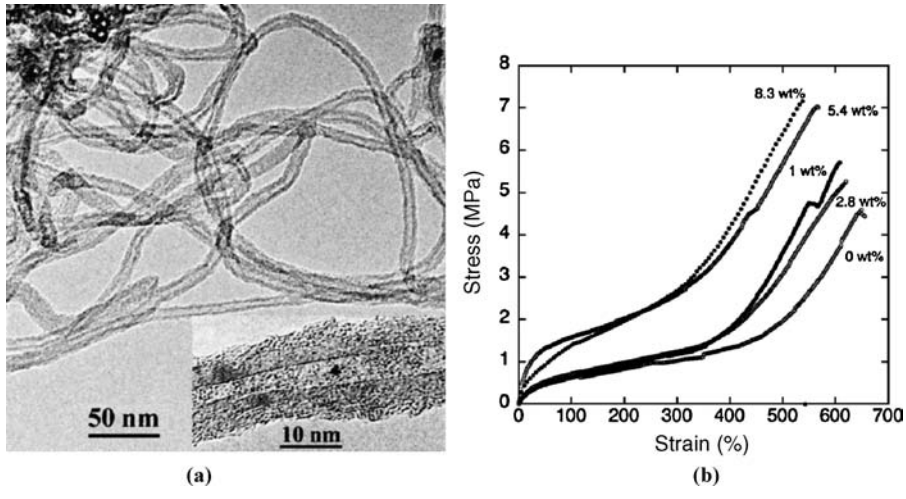

Figure 1.6 (a) TEM images of c-MWCNTs. Inset: HR image showing the damaged outer shells of c-MWCNTs and (b) Stress–strain curves for pure latex films and composites (Reprinted from Carbon, 46, S. Bhattacharyya, C. Sinturel, O. Bahloul, M-L. Saboungi and S. Thomas, "Improving Reinforcement of Natural Rubber by Networking of Activated Carbon Nanotubes," 1037–1045, © 2008, with permission from Elsevier.)

Nano inorganic spherical filler silica has been extensively used in the rubber industry. The introduction of Green Tire® has enhanced the demand for silica particles. Now scientists focus on the *in situ* generation of silica particles to synthesize nanocomposites of polymer and silica particles. Recently, Ikeda *et al.* [173] have synthesized nano silica particles up to approximately 80 parts per hundred rubber by weight *in situ* in the rubber matrix via sol-gel reaction of tetraethoxy silane. Moreover, more homogeneous dispersion of silica in the rubber matrix has been achieved than that of commercial silica dispersed by conventional method. Due to the high interaction between *in situ* generated silica and the rubber matrix the tensile stress was found to be higher.

Liu *et al.* [174] have used modified silica using basic cyclohexylamine incorporated into the natural rubber. According to them the damping values decreased significantly, which resulted in lower rolling resistance and heat generation of the filled natural rubber vulcanizates. Mishra *et al.* [68] have compared the effect of commercial and nano $CaSO_4$ filler particles on the mechanical, physical and thermal properties of SBR. The matrix SBR has been reinforced with nano filler via *in situ* deposition technique. They have observed an enhancement in properties of SBR with nano $CaSO_4$ up to a filler loading of 10 wt%. According to them at higher loading all properties of SBR decreased due to the agglomeration of filler particles. The physical properties of the copolymer of LDPE-EVA was improved by the incorporation of pristine nanosilica. The interaction of hydrophilic silica filler with the copolymer has been improved in the presence of silane coupling agents [175].

Polyhedral oligomeric silsesquioxane (POSS) is a new class of nanofillers with functional groups that are widely using in thermoplastics and thermosets as reinforcing agents. Sahoo *et al.* [176] have synthesized POSS with hydroxyl functional groups with an average diameter of 50 nm. They have used POSS nanoparticles as curing agent in certain functionalized rubbers such as fluorocarbon rubber (FKM) and carboxylated nitrile rubber (XNBR) and analyzed the physical properties. The results revealed that the POSS nanoparticles crosslinked effectively in FKM and XNBR. Composites of silicone rubber and POSS were prepared by melt blending with special interest in the thermal stability of POSS macromers and the effects of mixing temperature and the subsequent vulcanization of polysiloxane [177]. The results showed that the condensation reaction could be possible at higher temperature, leading to a partially amorphous structure of crystalline POSS; however, it was recrystallized upon cooling. Nowadays efficient and environmentally friendly nanofillers are developed from natural fibers and starch. NR filled with waxy maize starch nanocrystals showed that upto a loading of 20 wt% the physical properties found to be higher. At 20 wt% the relaxed modulus at room temperature was 75-fold higher than that of unfilled matrix [70].

1.4 Future Outlook, Challenges and Opportunities

For the past 10 years, polymer nanocomposites are the dominating field in polymer science and technology. The interest in polymer nanocomposites is due to the reinforcement effect of nanofillers, better mechanical properties, thermal stability and barrier properties. Nanotechnology emerged to improve the physical properties of traditional materials at the molecular level without affecting the processing. On reviewing the literature one can find that majority of the research work in the field of rubber nanocomposites has been carried out in rubber/layered silicates system, which includes unmodified and modified LS. In other words, we can say that

rubber/LS have been the first generation of rubber nanocomposites. Modification of the matrix rubber with LS can significantly improve the physical and barrier properties of the matrix even at lower wt%. Due to the higher aspect ratio of LS better polymer/filler interaction could be possible than conventional fillers. A major difficulty in rubber/LS nanocomposites is to attain homogeneous dispersion of filler in the matrix. Basically, it can form intercalated and exfoliated structure, while most of the nanocomposites form partially intercalated and exfoliated structure. Exfoliated structure can impart better properties in the polymer nanocomposites. Comparatively, this problem has been overcome by the chemical modification of LS. With the developments of nanotechnology, researchers have synthesized different types of carbon nanotubes and incorporated in polymer matrices as reinforcing fillers. Incorporation of carbon nanotubes to a lower scale of dimension to the matrix would significantly increase the modulus and strength. In elastomers, SWCNTs, MWCNTs and chemically modified nanotubes are employed to reinforce the matrix. From the literature it is clear that the percolation threshold increased even at a small wt% of carbon nanotubes.

Isodimensional nanofillers generated *in situ* through a sol-gel process in the polymer is of particular interest because it will reduce the filler aggregation. A breakthrough in nanotechnology is the introduction of POSS chemical technology. POSS nanostructured chemicals when incorporated in polymer can provide nanocomposite properties while maintaining the processability. Its chemical diversity offered unique properties to the polymer. Eventhough it has been incorporated in plastics successfully a few works have been carried out in rubber. But these promising nanostructured chemicals will revolutionize the entire technological society. The application of POSS chemical technology will cover the automobile, medical and electronic industry in the near future. Another area to be explored effectively in rubber nanocomposites is the incorporation of naturally derived nanofillers such as cellulose, starch and so on, in a rubber matrix. The development of rubber/bionanofillers is still in its infancy due to the difficulty in the extraction of nanofillers from naturally occurring fibers or from other sources.

There are several challenges in the area of rubber nanocomposites. Complete exfoliation and uniform dispersion of nanofillers in rubber matrix still remains to be a dream. Efficient surfactants have to be designed for the excellent dispersion. In the case of clay filled rubber nanocomposites, the extent of exfoliation/intercalation has not been quantified yet. The orientation of nanoplatelets in rubber matrix by special extrusion is also a major challenge. The *in situ* monitoring of the flow of rubber nanocomposites during processing needs a lot of attention. Finally, we still have to go a long way for the successful use of rubber nanocomposites in various commercial applications.

References

1. Okada, A., Fukoshima, Y., Inagaki, S. *et al.* (1988) Composite material and process for manufacturing same. US Patent 4.739.007.
2. Luo, J.-J. and Daniel, I.M. (2003) Characterization and modeling of mechanical behavior of polymer/clay nanocomposites. *Composites Science and Technology*, **63**, 1607.
3. Messermith, P.B. and Giannelis, E.P. (1993) Polymer-layered silicate nanocomposites: in-situ intercalative polymerization of ε-caprolactone in layered silicates. *Chemistry of Materials*, **5**, 1064.
4. Giannelis, E.P. (1996) Polymer layered silicate nanocomposites. *Advanced Materials*, **8**, 29.
5. Komarneni, S. (1992) Nanocomposites. *Journal of Materials Chemistry*, **2**, 1219.
6. Ruiz-Hitzky, E. (1993) Conducting polymers intercalated in layered solids. *Advanced Materials*, **5**, 334.

7. Hoffmann, U., Endell, K., and Wilm, D. (1933) Kristallstruktur und Quellung von Montmorillonit. (Das Tonmineral der Bentonittone). *Zeitschrift fur Kristallografie Mineral Petrografie Abteilung A*, **86**, 340.
8. http://www.soils.wisc.edu/courses/SS325/silicates.htm#structsil.
9. Okada, A., Kawasumi, M., Usuki, A. *et al.* (1990) Nylon 6-clay hybrid. *Materials Research Society Symposium Proceedings*, **171**, 45.
10. Jordan, J.W. (1949) Organophilic bentonites. I. Swelling in organic liquids. *Journal of Physical and Colloid Chemistry*, **53**, 294.
11. Weiss, A. (1963) Organic derivatives of mica type layer silicates. *Angewandte Chemie - International Edition*, **2**, 134.
12. Lan, T., Kaviratna, P.D., and Pinnavaia, T.J. (1995) Mechanism of clay tactoid exfoliation in epoxyclay nanocomposites. *Chemistry of Materials*, **7**, 2144.
13. Harris, P.J.F. (1997) Carbon nanotubes and related structures as contaminants on evaporated carbon films. *Journal of Microscopy*, **186**, 88.
14. Sumio, I. (1991) Helical microtubules of graphitic carbon. *Nature*, **354**, 56.
15. Ebbesen, T.W. and Ajayan, P.M. (1992) Large-scale synthesis of carbon nanotubes. *Nature*, **358**, 220.
16. Ting, G. (1995) Self-assembly of tubular fullerenes. *The Journal of Physical Chemistry*, **99**, 10694.
17. Ting, G. (1995) Electrical conductors comprising single-wall carbon nanotubes. *Chemical Physics Letters*, **243**, 49.
18. Walker, P.L. Jr. (1959) Carbon formation from carbon monoxide-hydrogen mixtures over iron catalysts. I. Properties of carbon formed. *The Journal of Physical Chemistry*, **63**, 133.
19. Jose-Yacaman, M. (1993) Catalytic growth of carbon microtubules with fullerene structure. *Applied Physics Letters*, **62**, 657.
20. Wendy, B. (2007) UC Researchers Shatter World Records with Length of Carbon Nanotube Arrays, University of Cincinnati, April 27, 2007.
21. Pham, J.Q., Mitchell, C.A., Bahr, J.L. *et al.* (2003) Glass transition of polymer/single-walled carbon nanotube composite films. *Journal of Polymer Science Part B Polymer Physics*, **41**, 3339.
22. Xie, H., Liu, B., Yuan, Z. *et al.* (2004) Cure kinetics of carbon nanotube/tetrafunctional epoxy nanocomposites by isothermal differential scanning calorimetry. *Journal of Polymer Science Part B Polymer Physics*, **42**, 3701.
23. Du, F., Fischer, J.E., and Winey, K.I. (2003) Coagulation method for preparing single-walled carbon nanotube/poly(methyl methacrylate) composites and their modulus, electrical conductivity, and thermal stability. *Journal of Polymer Science Part B Polymer Physics*, **41**, 3333.
24. Dondero, W.E. and Gorga, R.E. (2006) Morphological and mechanical properties of carbon nanotube/polymer composites via melt compounding. *Journal of Polymer Science Part B Polymer Physics*, **44**, 864.
25. Kim, J.Y. and Kim, S.H. (2006) Influence of multiwall carbon nanotube on physical properties of poly(ethylene 2,6-naphthalate) nanocomposites. *Journal of Polymer Science Part B Polymer Physics*, **44**, 1062.
26. Yu, Y., Ouyang, C., Gao, Y. *et al.* (2005) Synthesis and characterization of carbon nanotube/polypyrrole core-shell nanocomposites via in situ inverse microemulsion. *Journal of Polymer Science Part A Polymer Chemistry*, **43**, 6105.
27. Ham, H.T., Choi, Y.S., Chee, M.G., and Chung, I.J. (2006) Singlewall carbon nanotubes covered with polystyrene nanoparticles by in-situ miniemulsion polymerization. *Journal of Polymer Science Part A Polymer Chemistry*, **44**, 573.
28. Gong, X., Liu, J., Baskaran, S. *et al.* (2000) Surfactant-assisted processing of carbon nanotube/polymer composites. *Chemistry of Materials*, **12**, 1049.
29. Ramanathan, T., Liu, H., and Brinson, L.C. (2005) Functionalized SWNT/polymer nanocomposites for dramatic property improvement. *Journal of Polymer Science Part B Polymer Physics*, **43**, 2269.
30. Wu, H.L., Yang, Y.T., Ma, C.-C.M., and Kuan, H.-C. (2005) Molecular mobility of free-radical-functionalized carbon-nanotube/siloxane/poly(urea urethane) nanocomposites. *Journal of Polymer Science Part A Polymer Chemistry*, **43**, 6084.
31. Konya, Z., Vesselenyi, I., Niesz, K. *et al.* (2002) Production of carbon nanotubes on different metal supported catalysts. *Chemical Physics Letters*, **360**, 429.
32. Bahr, J.L., Yang, J., Kosynkin, D.V. *et al.* (2001) Functionalization of carbon nanotubes by electrochemical reduction of aryl diazonium salts: a bucky paper electrode. *Journal of the American Chemical Society*, **123**, 6536.

33. Zhang, N., Xie, J., Guers, M., and Varadan, V.K. (2004) Chemical bonding of multiwalled carbon nanotubes to polydimethylsiloxanes and modification of the photoinitiator system for microstereolithography processing. *Smart Materials & Structures*, **13**, N1.
34. Zhu, J., Kim, J.D., Peng, H. *et al.* (2003) Improving the dispersion and integration of single-walled carbon nanotubes in epoxy composites through functionalization. *Nano Letters*, **3**, 1107.
35. Zhu, J., Peng, H., Rodriguez-Macias, F. *et al.* (2004) Reinforcing epoxy polymer composites through covalent integration of functionalized nanotubes. *Advanced Functional Materials*, **14**, 643.
36. Wang, J., Fang, Z., and Gu, A. (2006) Effect of multi-walled carbon nanotubes dispersity on the light transmittancy of multi-walled carbon nanotubes/epoxy composites. *Polymer Engineering and Science*, **46**, 635.
37. Pompeo, F. and Resasco, D.E. (2002) Water solubilization of single-walled carbon nanotubes by functionalization with glucosamine. *Nano Letters*, **2**, 369.
38. Kooi, S.E., Schlecht, U., Burghard, M., and Kern, K. (2002) Electrochemical modification of single carbon nanotubes. *Angewandte Chemie International Edition*, **41**, 1353.
39. Balasubramanian, K., Friedrich, M., Jiang, C. *et al.* (2003) Electrical transport and confocal raman studies of electrochemically modified individual carbon nanotubes. *Advanced Materials*, **15**, 1515.
40. Bahun, G.J., Wang, C., and Andronov, A. (2006) Solubilizing single-walled carbon nanotubes with pyrene-functionalized block copolymers. *Journal of Polymer Science Part A Polymer Chemistry*, **44**, 1941.
41. Narain, R., Housni, A., and Lane, L. (2006) Modification of carboxyl-functionalized single-walled carbon nanotubes with biocompatible, water-soluble phosphorylcholine and sugar-based polymers: bioinspired nanorods. *Journal of Polymer Science Part A Polymer Chemistry*, **44**, 6558.
42. Ha, J.U., Kim, M., Lee, J. *et al.* (2006) A novel synthesis of polymer brush on multiwall carbon nanotubes bearing terminal monomeric unit. *Journal of Polymer Science Part A Polymer Chemistry*, **44**, 6394.
43. Breuer, O. and Sundararaj, U. (2004) Big returns from small fibers: a review of polymer/carbon nanotube composites. *Polymer Composites*, **25**, 630.
44. Wise, K.E., Park, C., Siochi, E.J., and Harrison, J.S. (2004) Stable dispersion of single wall carbon nanotubes in polyimide: the role of noncovalent interactions. *Chemical Physics Letters*, **391**, 207.
45. Rotkin, S.V. and Zharov, I. (2002) Nanotube light-controlled electronic switch. *International Journal of Nanoscience*, **1**, 347.
46. Derycke, V., Martel, R., Appenzeller, J., and Avouris, Ph. (2001) Carbon nanotube inter- and intramolecular logic gates. *Nano Letters*, **1**, 453.
47. Bachtold, A., Hadley, P., Nakanishi, T., and Dekker, C. (2001) Logic circuits with carbon nanotube transistors. *Science*, **294**, 1317.
48. Yenilmez, E., Wang, Q., Robert, R.J. *et al.* (2002) Wafer scale production of carbon nanotube scanning probe tips for atomic force microscopy. *Applied Physics Letters*, **80**, 2225.
49. Ye, Q., Cassell, A.M., Liu, H. *et al.* (2004) Large-scale fabrication of carbon nanotube probe tips for atomic force microscopy critical dimension imaging applications. *Nano Letters*, **4**, 1301.
50. Cheung, C.L., Hafner, J.H., Odom, T.W. *et al.* (2000) Growth and fabrication with single-walled carbon nanotube probe microscopy tips. *Applied Physics Letters*, **76**, 3136.
51. Liu, M.X., Guo, B.C., Du, M.L. *et al.* (2007) Properties of halloysite nanotube–epoxy resin hybrids and the interfacial reactions in the systems. *Nanotechnology*, **18**, 455703.
52. Du, M.L., Guo, B.C., Liu, M.X., and Jia, D.M. (2006) Preparation and characterization of polypropylene grafted halloysite and their compatibility effect to polypropylene/halloysite composite. *Polymer Journal*, **38**, 1198.
53. Joussein, E., Petit, S., Churchman, J. *et al.* (2005) Halloysite clay minerals - a review. *Clay Minerals*, **40**, 383.
54. Ye, Y.P., Chen, H.B., Wu, J.S., and Ye, L. (2007) High impact strength epoxy nanocomposites with natural nanotubes. *Polymer*, **48**, 6426.
55. Mark, J.E. (1996) Ceramic-reinforced polymers and polymer-modified ceramics. *Polymer Engineering and Science*, **36**, 2905.
56. Wen, J. and Wilkes, G.L. (1996) Organic/inorganic hybrid network materials by the sol-gel approach. *Chemistry of Materials*, **8**, 1667.
57. Peng, C.-C., Göpfert, A., Drechsler, M., and Abetz, V. (2005) Smart silica-rubber nanocomposites in virtue of hydrogen bonding interaction. *Polymers for Advanced Technologies*, **16**, 770.
58. Juangvanich, N. and Mauritz, K.A. (1998) Polyethersulfone-[silicon oxide] hybrid materials via in situ sol-gel reactions for tetra-alkoxysilanes. *Journal of Applied Polymer Science*, **67**, 1799.

59. Landry, C.J.T., Coltrain, B.K., Wesson, J.A. *et al.* (1992) In situ polymerization of tetraethoxysilane in polymers: chemical nature of the interactions. *Polymer*, **33**, 1496.
60. Wang, S., Ahmad, Z., and Mark, J.E. (1993) A polyamide–silica composite prepared by the sol-gel process. *Polymer Bulletin*, **31**, 323.
61. Zhao, M.X., Ning, Y.P., and Mark, J.E. (1991) *Ceramic Transactions*, **19**, 891.
62. Deng, Q., Moore, R.B., and Mauritz, K.A. (1995) Novel nafion/ORMOSIL hybrids via in situ sol-gel reactions. 1. Probe of ORMOSIL phase nanostructures by infrared spectroscopy. *Chemistry of Materials*, **7**, 2261.
63. Deng, Q., Jarrett, W., Moore, R.B., and Mauritz, K.A. (1996) Novel Nafion®/ORMOSIL hybrids via in situ sol-gel reactions: 2. Probe of ORMOSIL phase nanostructure by 29Si solid state NMR spectroscopy. *Journal of Sol-Gel Science and Technology*, **7**, 177.
64. Shao, P.L., Mauritz, K.A., and Moore, R.B. (1996) [Perfluorosulfonate ionomer]/[SiO2-TiO2] nanocomposites via polymer-in situ sol-gel chemistry: Sequential alkoxide procedure. *Journal of Polymer Science Part B Polymer Physics*, **34**, 873.
65. Kickelbick, G. (2003) Concepts for the incorporation of inorganic building blocks into organic polymers on a nanoscale. *Polymer*, **28**, 83.
66. Piña-Hernández, C., Flores-Vélez, L.M., del Castillo, L.F., and Domínguez, O. (2007) Processing and mechanical properties of natural rubber-$ZnFe_2O_4$ nanocomposites. *Journal of Materials Engineering and Performance*, **16**, 470.
67. Sahoo, S. and Bhowmick, A.K. (2007) Influence of ZnO nanoparticles on the cure characteristics and mechanical properties of carboxylated nitrile rubber. *Journal of Applied Polymer Science*, **106**, 3077.
68. Mishra, S. and Shimpi, N.G. (2007) Effect of the variation in the weight percentage of the loading and the reduction in the nanosizes of $CaSO_4$ on the mechanical and thermal properties of styrene-butadiene rubber. *Journal of Applied Polymer Science*, **104**, 2018.
69. http://www.hybridplastics.com/chem.html.
70. http://www.hybridplastics.com/posstech.html.
71. Li, G., Wang, L., Ni, H., and Pittman, C.U. Jr. (2001) Polyhedral oligomeric silsesquioxane (POSS) polymers and copolymers: a review. *Journal of Inorganic and Organometallic Polymers*, **11**, 123.
72. Bhatnagar, N. and Sain, M. (2005) Processing of cellulose nanofiber-reinforced composites. *Journal of Reinforced Plastics and Composites*, **24**, 1259.
73. Angellier, H., Molina-Boisseau, S., Lebrun, L., and Dufresne, A. (2005) Processing and structural properties of waxy maize starch nanocrystals reinforced natural rubber. *Macromolecules*, **38**, 3783.
74. Angellier, H., Molina-Boisseau, S., and Dufresne, A. (2005) Mechanical properties of waxy maize starch nanocrystal reinforced natural rubber. *Macromolecules*, **38**, 9161.
75. Putaux, J.L., Molina-Boisseau, S., Momaur, T., and Dufresne, A. (2003) Platelet nanocrystals resulting from the disruption of waxy maize starch granules by acid hydrolysis.. *Biomacromolecules*, **4**, 1198.
76. Lapa, V.L.da C., de Oliveira, P.D., Visconte, L.L.Y., and Nunes, R.C.R. (2008) Investigation of NBR-cellulose II nanocomposites by rheometric and equilibrium swelling properties. *Polymer Bulletin*, **60**, 281.
77. Heinrich, G. and Vilgis, T.A. (1993) Contribution of entanglements to the mechanical properties of carbon black-filled polymer networks. *Macromolecules*, **26**, 1109.
78. Westermann, S., Krutschmann, M., Hintzen, W.P. *et al.* (1999) Matrix chain deformation in reinforced networks: a SANS approach. *Macromolecules*, **32**, 5793.
79. Nakatani, Al., Cen, W., Schmidt, R.C. *et al.* (2001) Chain dimensions in polysilicate-filled poly(dimethyl siloxane). *Polymer*, **42**, 3713.
80. Usuki, A., Tukigase, A., and Kato, M. (2002) Preparation and properties of EPDM–clay hybrids. *Polymer*, **43**, 2185.
81. Arroyo, M., Lopez-Manchado, M.A., and Herrero, B. (2003) Organo-montmorillonite as substitute of carbon black in natural rubber compounds. *Polymer*, **44**, 2447.
82. Frogley, M.D., Ravich, D., and Wagner, H.D. (2003) Mechanical properties of carbon nanoparticle-reinforced elastomers. *Composites Science and Technology*, **63**, 1647.
83. Zheng, H., Zheng, H., Zhang Y.X.. *et al.* (2004) Influence of clay modification on the structure and mechanical properties of EPDM/montmorillonite nanocomposites. *Polymer Testing*, **23**, 217.
84. Okada, A., Usuki, A., Kurachi, T., and Kamigaito, O. (1995) in Hybrid organic-inorganic composites (eds J.E. Mark, C.Y.C. Lee, and P.A. Bianconi), *ACS Symposium Series 585*, ACS, Washington, D.C.

85. Vu, Y.T., Mark, J.E., Pham, L.H., and Engelhardt, M. (2001) Clay nanolayer reinforcement of cis-1,4-polyisoprene and epoxidized natural rubber. *Journal of Applied Polymer Science*, **82**, 1391.
86. Nah, C., Ryu, H.J., Han, S.H. *et al.* (2001) Fracture behaviour of acrylonitrile-butadiene rubber/clay nanocomposite. *Polymer International*, **50**, 1265.
87. Chen, Z. and Gong, K. (2002) Preparation and dynamic mechanical properties of poly(styrene-b-butadiene)-modified clay nanocomposites. *Journal of Applied Polymer Science*, **84**, 1499.
88. Varghese, S., Karger-Kocsis, J., and Gatos, K.G. (2003) Melt compounded epoxidized natural rubber/layered silicate nanocomposites: structure-properties relationships. *Polymer*, **44**, 3977.
89. Lopez-Manchado, M.A., Biagiotti, J., Valentini, L., and Kenny, J.M. (2004). Dynamic mechanical and Raman spectroscopy studies on interaction between single-walled carbon nanotubes and natural rubber, *Journal of Applied Polymer Science*, **92**, 3394.
90. Gonzalez, J.C., Retsos, H., Verdejo, R. *et al.* (2008) Effect of nanoclay on natural rubber microstructure. *Macromolecules*, **41**, 6763.
91. Liang, Y., Cao, W., Li, Z. *et al.* (2008) A new strategy to improve the gas barrier property of isobutylene- isoprene rubber/clay nanocomposites. *Polymer Testing*, **27**, 270.
92. Liu, Q., Zhang, Y., and Xu, H. (2008) Properties of vulcanized rubber nanocomposites filled with nanokaolin and precipitated silica. *Applied Clay Science*, **42**, 232.
93. Ismail, H. and Ramli, R. (2008) Organoclay filled natural rubber nanocomposites: the effects of filler loading and mixing method. *Journal of Reinforced Plastics and Composites*, **27**, 1909.
94. Wang, X., Huang, A., Jia, D., and Li, Y. (2008) From exfoliation to intercalation - changes in morphology of HNBR/organoclay nanocomposites. *European Polymer Journal*, **44**, 2784.
95. Ganter, M., Gronski, W., Reichert, P., and Mulhaupt, R. (2000) Rubber nanocomposites: morphology and mechanical properties of br and sbr vulcanizates reinforced by organophilic layered silicates. *Rubber Chemistry and Technology*, **74**, 221.
96. Pramanik, M., Srivastava, S.K., Samantaray, B.K., and Bhowmick, A.K. (2003) Rubber-clay nanocomposite by solution blending. *Journal of Applied Polymer Science*, **87**, 2216.
97. Jeon, H.S., Rameshwaram, J.K., Kim, G., and Weinkauf, D.H. (2003) Characterization of polyisoprene–clay nanocomposites prepared by solution blending. *Polymer*, **44**, 5749.
98. Stephen, R., Thomas, S., Raju, K.V.S.N. *et al.* (2007) Dynamic mechanical and dielectric properties of nanocomposites of natural rubber (NR) and carboxylated styrene butadiene rubber (XSBR) latices and their blend. *Rubber Chemistry and Technology*, **80**, 672.
99. Stephen, R., Varghese, S., Joseph, K., and Oommen, Z. (2006) Diffusion and transport through nanocomposites of natural rubber (NR), carboxylated styrene butadiene rubber (XSBR) and their blends. *Journal of Membrane Science*, **286**, 162.
100. Stephen, R., Ranganathaiah, C., Varghese, S. *et al.* (2006) Gas transport through nano and micro composites of natural rubber (NR) and their blends with carboxylated styrene butadiene rubber (XSBR) latex membranes. *Polymer*, **47**, 858.
101. Stephen, R., Alex, R., Cherian, T. *et al.* (2006) Rheological behavior of nanocomposites of natural rubber and carboxylated styrene butadiene rubber latices and their blends. *Journal of Applied Polymer Science*, **101**, 2355.
102. Zhang, L., Wang, Y., Wang, Y. *et al.* (2000) Morphology and mechanical properties of clay/styrene-butadiene rubber nanocomposites. *Journal of Applied Polymer Science*, **78**, 1873.
103. Wang, Y., Zhang, H., Wu, Y. *et al.* (2005) Preparation, structure, and properties of a novel rectorite/styrene-butadiene copolymer nanocomposite. *Journal of Applied Polymer Science*, **96**, 324.
104. Wu, Y.-P., Zhang, L.-Q., Wang, Y.-Q. *et al.* (2001) Structure of carboxylated acrylonitrile-butadiene rubber (CNBR)-clay nanocomposites by co-coagulating rubber latex and clay aqueous suspension. *Journal of Applied Polymer Science*, **82**, 2842.
105. Wang, Y., Zhang, L., Tang, C., and Yu, D. (2000) Preparation and characterization of rubber-clay nanocomposites. *Journal of Applied Polymer Science*, **78**, 1879.
106. Jia, Q.-X., Wu, Y.-P., Wang, Y.-Q. *et al.* (2008) Enhanced interfacial interaction of rubber/clay nanocomposites by a novel two-step method. *Composites Science and Technology*, **68**, 1050.
107. Du, M., Guo, B., Lei, Y. *et al.* (2008) Carboxylated butadiene–styrene rubber/halloysite nanotube nanocomposites: interfacial interaction and performance. *Polymer*, **49**, 4871.
108. Xiong, M., Wu, L., Zhou, S., and You, B. (2002) Preparation and characterization of acrylic-latex/nano SiO_2 composites. *Polymer International*, **51**, 693.

109. Pu, Z., Mark, J.E., Jethmalani, J.M., and Ford, W.T. (1997) Effects of dispersion and aggregation of silica in the reinforcement of poly(methyl acrylate) elastomers. *Chemistry of Materials*, **9**, 2442.
110. Wu, Y.-P., Wang, Y.Q., Zhang, H.F. *et al.* (2005) Rubber–pristine clay nanocomposites prepared by co-coagulating rubber latex and clay aqueous suspension. *Composites Science and Technology*, **65**, 1195.
111. Jeong, H.M., Choi, M.Y., and Ahn, Y.T. (2006) Morphology and properties of polyacrylonitrile/Na-MMT nanocomposites prepared via in-situ polymerization with macroazoinitiator. *Macromolecular Research*, **14**, 312.
112. Zanetti, M., Camino, G., THomann, R., and Mulhaupt, R. (2001) Synthesis and thermal behaviour of layered silicate–EVA nanocomposites. *Polymer*, **42**, 4501.
113. Arrighi, V., Mc Ewen, I.J., Qian, H., and Prieto, M.B.S. (2003) The glass transition and interfacial layer in styrene-butadiene rubber containing silica nanofiller. *Polymer*, **44**, 6259.
114. Chen, Y., Zhou, S., Yang, H., and Wu, L. (2005) Structure and properties of polyurethane/nanosilica composites. *Journal of Applied Polymer Science*, **95**, 1032.
115. Jeon, H.U., Lee, D.H., Choi, D.-J. *et al.* (2007) Characteristics of rubber/sodium montmorillonite nanocomposites prepared by a novel method. *Journal of Macromolecular Science, Part B: Physics*, **46**, 1151.
116. Jia, Q.-X., Wu, Y.-P., Lu, M. *et al.* (2008) Interface tailoring of layered silicate/styrene butadiene rubber nanocomposites. *Composition Interface*, **15**, 193.
117. Joly, S., Garnaud, G., Ollitrault, R., and Bokobza, L. (2002) Organically modified layered silicates as reinforcing fillers for natural rubber. *Chemistry of Materials*, **14**, 4202.
118. Magaraphan, R., Thaijaroen, W., and Lim-Ochakun, R. (2003) Structure and properties of natural rubber and modified montmorillonite nanocomposites. *Rubber Chemistry and Technology*, **76**, 406.
119. Lopez-Manchado, M.A., Herrero, B., and Arroyo, M. (2004) Organoclay-natural rubber nanocomposites synthesized by mechanical and solution mixing methods. *Polymer International*, **53**, 1766.
120. Wang, Y., Zhang, H., Wu, Y. *et al.* (2005) Structure and properties of strain-induced crystallization rubber-clay nanocomposites by co-coagulating the rubber latex and clay aqueous suspension. *Journal of Applied Polymer Science*, **96**, 318.
121. Varghese, S., Gatos, K.G., Apostolov, A.A., and Karger-Kocsis, J. (2004) Morphology and mechanical properties of layered silicate reinforced natural and polyurethane rubber blends produced by latex compounding. *Journal of Applied Polymer Science*, **92**, 543.
122. Lopez-Manchado, M.A., Arroyo, M., Herrero, B., and Biagiotti, J. (2003) Vulcanization kinetics of natural rubber-organoclay nanocomposites. *Journal of Applied Polymer Science*, **89**, 1.
123. Varghese, S. and Karger-Kocsis, J. (2004) Melt-compounded natural rubber nanocomposites with pristine and organophilic layered silicates of natural and synthetic origin. *Journal of Applied Polymer Science*, **91**, 813.
124. Teh, P.L., Mohd Isak, Z.A., Hashim, A.S. *et al.* (2006) Physical properties of natural rubber/organoclay nanocomposites compatibilized with epoxidized natural rubber. *Journal of Applied Polymer Science*, **100**, 1083.
125. Ganter, M., Gronski, W., Semke, H. *et al.* (2001) Surface-compatibilized layered silicates: a novel class of nanofillers for rubbers with improved mechanical properties. *Kautschuk Gummi Kunststoffe*, **54**, 166.
126. Sadhu, S. and Bhowmick, A.K. (2003) Effect of chain length of amine and nature and loading of clay on styrene butadiene rubber-clay nanocomposites. *Rubber Chemistry and Technology*, **76**, 860.
127. Sadhu, S. and Bhowmick, A.K. (2004) Preparation and properties of styrene-butadiene rubber based nanocomposites: the influence of the structural and processing parameters. *Journal of Applied Polymer Science*, **92**, 698.
128. Zhang, H., Wang, Y., Wu, Y. *et al.* (2005) Study on flammability of montmorillonite/styrene-butadiene rubber (SBR) nanocomposites. *Journal of Applied Polymer Science*, **97**, 844.
129. Jia, Q.X., Wu, Y.P., Xu, Y.L. *et al.* (2006) Combining in-situ organic modification of montmorillonite and the latex compounding method to prepare high-performance rubber-montmorillonite nanocomposites. *Macromolecular Materials and Engineering*, **291**, 218.
130. Mousa, A. and Karger-Kocsis, J. (2001) Rheological and thermodynamical behavior of styrene/butadiene rubber-organoclay nanocomposites. *Macromolecular Materials and Engineering*, **286**, 260.
131. Schon, F. and Gronski, W. (2003) Dynamic and viscoelastic behavior of natural rubber/layered silicate nanocomposites obtained by melt blending. *Kautschuk Gummi Kunststoffe*, **56**, 166.
132. Kojima, Y., Fukumori, K., Usuki, A. *et al.* (1993) Gas permeabilities in rubber-clay hybrid. *Journal of Materials Science Letters*, **12**, 889.

133. Wu, Y.P., Jia, Q.X., Yu, D.S., and Zhang, L.Q. (2003) Structure and properties of nitrile rubber (NBR)-clay nanocomposites by co-coagulating NBR latex and clay aqueous suspension. *Journal of Applied Polymer Science*, **89**, 3855.
134. Kim, J.T., Lee, D.Y., Oh, T.S., and Lee, D.H. (2003) Characteristics of nitrile-butadiene rubber layered silicate nanocomposites with silane coupling agent. *Journal of Applied Polymer Science*, **89**, 2633.
135. Kim, J.T., Oh, T.S., and Lee, D.H. (2003) Preparation and characteristics of nitrile rubber (NBR) nanocomposites based on organophilic layered clay. *Polymer International*, **52**, 1058.
136. Kim, J.T., Oh, T.S., and Lee, D.H. (2003) Morphology and rheological properties of nanocomposites based on nitrile rubber and organophilic layered silicates. *Polymer International*, **52**, 1203.
137. Nah, C., Ryu, H.J., Kim, W.D., and Chang, Y.W. (2003) Preparation and properties of acrylonitrile-butadiene copolymer hybrid nanocomposites with organoclays. *Polymer International*, **52**, 1359.
138. Zheng, H., Zhang, Y., Peng, Z., and Zhang, Y. (2004) Influence of the clay modification and compatibilizer on the structure and mechanical properties of ethylene-propylene-diene rubber/montmorillonite composites. *Journal of Applied Polymer Science*, **92**, 638.
139. Gatos, K.G., Thomann, R., and Karger-kocsis, J. (2004) Characteristics of ethylene propylene diene monomer rubber/organoclay nanocomposites resulting from different processing conditions and formulations. *Polymer International*, **53**, 1191.
140. Pramanik, M., Srivastava, S.K., Samantaray, B.K., and Bhowmick, A.K. (2002) Synthesis and characterization of organosoluble, thermoplastic elastomer/clay nanocomposites. *Journal of Polymer Science Part B-Polymer Physics*, **40**, 2065.
141. Lim, S.K., Kim, J.W., Chin, I.J., and Choi, H.J. (2002) Rheological properties of a new rubbery nanocomposite: polyepichlorohydrin/organoclay nanocomposites. *Journal of Applied Polymer Science*, **86**, 3735.
142. Karger-Kocsis, J. and Wu, C.M. (2004) Thermoset rubber/layered silicate nanocomposites. Status and future trends. *Polymer Engineering and Science*, **44**, 1083.
143. Sengupta, R., Chakraborty, S., Bandyopadhyay, S. *et al.* (2007) A short review on rubber/clay nanocomposites with emphasis on mechanical properties. *Polymer Engineering and Science*, **47**, 1956.
144. Bokobza, L. (2007) Multiwall carbon nanotube elastomeric composites: A review. *Polymer*, **48**, 4907.
145. Bokobza, L. and El Bounia, N.-E. (2008) Reinforcement effects of multiwall carbon nanotubes in elastomeric matrices: comparison with other types of fillers. *Composition Interface*, **15**, 1.
146. Bokobza, L. and Belin, C. (2007) Effect of strain on the properties of a styrene-butadiene rubber filled with multiwall carbon nanotubes. *Journal of Applied Polymer Science*, **105**, 2054.
147. Kolodziej, M., Bokobza, L., and Bruneel, J.-L. (2007) Investigations on natural rubber filled with multiwall carbon nanotubes. *Composition Interface*, **14**, 215.
148. Bokobza, L. and Kolodziej, M. (2006) On the use of carbon nanotubes as reinforcing fillers for elastomeric materials. *Polymer International*, **55**, 1090.
149. Bokobza, L., Rahmani, M., Belin, C. *et al.* (2008) Blends of carbon blacks and multiwall carbon nanotubes as reinforcing fillers for hydrocarbon rubbers. *Journal of Polymer Science Part B Polymer Physics*, **46**, 1939.
150. Zhao, Q., Tannenbaum, R., and Jacob, K.I. (2006) Carbon nanotubes as raman sensors of vulcanization in natural rubber. *Carbon*, **44**, 1740.
151. Kuesseng, K. and Jacob, K.I. (2006) Natural rubber nanocomposites with SiC nanoparticles and carbon nanotubes. *European Polymer Journal*, **42**, 220.
152. Sui, G., Zhong, W.H., Yang, X.P., and Yu, Y.H. (2008) Curing kinetics and mechanical behavior of natural rubber reinforced with pretreated carbon nanotubes. *Materials Science and Engineering*, **485**, 524.
153. Fakhru'l-Razi, A., Atieh, M.A., Girun, N. *et al.* (2006) Effect of multi-walled carbon nanotubes on the mechanical properties of natural rubber. *Composition and Structure*, **75**, 496.
154. Suil, G., Zhong, W.H., Yang, X.P. *et al.* (2008) Preparation and properties of natural rubber composites reinforced with pretreated carbon nanotubes. *Polymers for Advanced Technologies*, 1163. doi: 10.1002/pat
155. Sui, G., Zhong, W., Yang, X., and Zhao, S. (2007) Processing and material characteristics of a carbon-nanotube-reinforced natural rubber. *Macromolecular Materials and Engineering*, **292**, 1020.
156. Wang, J.D., Zhu, Y.F., Zhou, X.W. *et al.* (2006) Preparation and mechanical properties of natural rubber powder modified by carbon nanotubes. *Journal of Applied Polymer Science*, **100**, 4697.
157. Zhou, X., Zhu, Y., Gong, Q., and Liang, J. (2006) Preparation and properties of the powder SBR composites filled with CNTs by spray drying process. *Materials Letters*, **60**, 3769.

158. Zhou, X., Zhu, Y., and Liang, J. (2007) Effects of the vulcanizing reagent addition on the properties of CNTs/SBR powder composites. *Journal of Applied Polymer Science*, **106**, 1836.
159. Felhös, D., Karger-Kocsis, J., and Xu, D. (2008) Tribological testing of peroxide cured HNBR with different MWCNT and silica contents under dry sliding and rolling conditions against steel. *Journal of Applied Polymer Science*, **108**, 2840.
160. Valentini, L., Biagiotti, J., Kenny, J.M., and López Manchado, M.A. (2003) Physical and mechanical behavior of single-walled carbon nanotube/polypropylene/ethylene-propylene-diene rubber nanocomposites. *Journal of Applied Polymer Science*, **89**, 2657.
161. Jung, Y.C., Sahoo, N.G., and Cho, J.W. (2006) Polymeric nanocomposites of polyurethane block copolymers and functionalized multi-walled carbon nanotubes as crosslinkers. *Macromolecular Rapid Communications*, **23**, 126.
162. Wang, T.-L. and Tseng, C.-G. (2007) Polymeric carbon nanocomposites from multiwalled carbon nanotubes functionalized with segmented polyurethane. *Journal of Applied Polymer Science*, **105**, 1642.
163. Wang, X., Du, Z., Zhang, C. *et al.* (2008) Multi-walled carbon nanotubes encapsulated with polyurethane and its nanocomposites. *Journal of Polymer Science Part A Polymer Chemistry*, **46**, 4857.
164. Jana, R.N. and Cho, J.W. (2008) Thermal stability and molecular interaction of polyurethane nanocomposites prepared by in situ polymerization with functionalized multiwalled carbon nanotubes. *Journal of Applied Polymer Science*, **108**, 2857.
165. Buffa, F., Abraham, G.A., Grady, B.P., and Resasco, D. (2007) Effect of nanotube functionalization on the properties of single-walled carbon nanotube/polyurethane composites. *Journal of Polymer Science Part B Polymer Physics*, **45**, 490.
166. Xiong, J., Zheng, Z., Song, W. *et al.* (2008) Microstructure and properties of polyurethane nanocomposites reinforced with methylene-bis-ortho-chloroanilline-grafted multi-walled carbon nanotubes. *Composites Part A: Applied Science and Manufacturing*, **39**, 904.
167. Sahoo, N.G., Jung, Y.C., Yoo, H.J., and Cho, J.W. (2007) Influence of carbon nanotubes and polypyrrole on the thermal, mechanical and electroactive shape-memory properties of polyurethane nanocomposites. *Composites Science and Technology*, **67**, 1920.
168. Xiong, J., Zheng, Z., Qin, X. *et al.* (2006) The thermal and mechanical properties of a polyurethane/multi-walled carbon nanotube composite. *Carbon*, **44**, 2701.
169. Jiang, M.-J., Dang, Z.-M., Yao, S.-H., and Bai, J. (2008) Effects of surface modification of carbon nanotubes on the microstructure and electrical properties of carbon nanotubes/rubber nanocomposites. *Chemical Physics Letters*, **457**, 352.
170. Jiang, M.-J., Dang, Z.-M., and Xu, H.-P. (2007) Enhanced electrical conductivity in chemically modified carbon nanotube/methyl vinyl silicone rubber nanocomposite. *European Polymer Journal*, **43**, 4924.
171. Kim, G.-T. and Park, E.-S. (2008) Thermal reproducibility and voltage stability of carbon black/multiwalled carbon nanotube and carbon black/SnO2-Sb coated titanium dioxide filled silicone rubber heaters. *Journal of Applied Polymer Science*, **109**, 1381.
172. Bhattacharyya, S., Sinturel, C., Bahloul, O. *et al.* (2008) Improving reinforcement of natural rubber by networking of activated carbon nanotubes. *Carbon*, **46**, 1037.
173. Ikeda, Y., Poompradub, S., Morita, Y., and Kohjiya, S. (2008) Preparation of high performance nanocomposite elastomer: effect of reaction conditions on in situ silica generation of high content in natural rubber. *Journal of Sol-Gel Science and Technology*, **45**, 299.
174. Liu, J., Wu, C., Zhang, P., and Zhao, S. (2008) Effects of cyclohexylamine modified silica on the mechanical properties of filled natural rubber. *Journal of Macromolecular Science, Part B Physics*, **47**, 689.
175. Hui, S., Chaki, T.K., and Chattopadhyay, S. (2008) Effect of silica-based nanofillers on the properties of a low-density polyethylene/ethylene vinyl acetate copolymer based thermoplastic elastomer. *Journal of Applied Polymer Science*, **110**, 825.
176. Sahoo, S. and Bhowmick, A.K. (2007) Polyhedral oligomeric silsesquioxane (POSS) nanoparticles as new crosslinking agent for functionalized rubber. *Rubber Chemistry and Technology*, **80**, 826.
177. Liu, L., Tian, M., Zhang, W. *et al.* (2007) Crystallization and morphology study of polyhedral oligomeric silsesquioxane (POSS)/polysiloxane elastomer composites prepared by melt blending. *Polymer*, **48**, 3201.

2

Manufacturing Techniques of Rubber Nanocomposites

Jun Ma[1,2], Li-Qun Zhang[1] and Li Geng[2]
[1] *Beijing University of Chemical Technology, Beijing, 100029, China*
[2] *School of Advanced Manufacturing & Mechanical Engineering and Mawson Institute, University of South Australia, SA5095, Australia*

2.1 Introduction

Rubber, also called elastomer, is one of the most important commercial polymers. The polymer chains in rubber are long and flexible with a coiled and kinked nature. In the molecular structure of cured rubber, atoms are connected in long, randomly coil chains that are interlinked at a few points. Between a pair of links each bond can rotate freely regardless of its neighbor. Thus, rubber exhibits unique physical and chemical properties. Under stress the molecular chain uncoils and an aligned structure results. Upon release of the stress the molecules rapidly recover their coiled up randomness. This characteristic causes material stretch, large free volume fraction, and amorphous and non-orientated state, which result in unique properties, such as low hardness, high elasticity and high elongation at break. It swells to more than double its size in organic solvents but is impermeable to water. Unfortunately, these useful properties of rubber cannot be obtained unless the rubber is chemically modified by sulfur atoms or other curing agents, a process called vulcanization. Vulcanization of rubber creates more sulfide bonds between chains so it makes each free section of chain shorter. The result is that the chains tighten more quickly for a given length of strain. This increases the elastic force constant and makes rubber harder. Therefore raw rubber is often vulcanized for its applications in the real world.

Rubber Nanocomposites: Preparation, Properties and Applications Edited by Sabu Thomas and Ranimol Stephen
© 2010 John Wiley & Sons (Asia) Pte Ltd

2.1.1 Conventional Manufacturing Techniques

Traditionally, a typical manufacturing sequence comprises mixing, forming and vulcanizing in the rubber manufacturing industry.

2.1.1.1 Mixing

For dry rubber, the solid rubber and other materials (for example, softeners, fillers, pigments for color, vulcanizing agents, additives) have to be mixed together. This is achieved with either of two basic machines: (i) a two-roll mill in which the material is passed between two metal rollers mounted horizontally and (ii) an internal mixer in which the materials are sheared between the internal rollers and the inside of the casing.

For mixing via rubber latex, compounds added to the raw latex must be in the form of emulsions or dispersions. They can be prepared by milling the substances with distilled or softened water in ball or gravel mills, which revolve from a few hours up to several days. Gelatin, casein, glues, soaps and so on, are used as wetting or dispersing agents. The latex is stabilized with surfactants, which act by imparting a charge to the surface of the tiny rubber particles or by holding an envelope of water around the particle, thereby preventing any aggregation.

2.1.1.2 Forming

After mixing, the compounded rubber is plastic and is now ready to be formed into a shape for vulcanization. The most common process is by molding under pressure in a heated mould. There are three important variants of the process–compression, transfer and injection molding–of these, the compression mold is the most widely used.

2.1.1.3 Vulcanizing

The final step in the manufacturing sequence is vulcanization. Basically, the vulcanizing process applies heat at an elevated temperature for a given time to cure the product so it takes up a shape in mold. Curing involves the chemical reactions which occur in the rubber mixture to produce the crosslinking. There are various vulcanizing methods. The economically important method (that is, the vulcanization of tires) uses increased pressure and temperature. Other methods (for example, those used to make door profiles for cars) include hot air vulcanization or microwave vulcanization.

2.1.2 Rubber Nanocomposites

In recent years researchers both in industry and universities have focused their interest on polymeric nanocomposites, which represent a radical alternative to conventional filled polymers. In contrast to conventional systems, the reinforcement in the nanocomposites has at least one dimension in the nanometer size range, usually defined as 1–100 nm. Generally rubber nanocomposites show advantageous mechanical properties, lower water sensitivity and lower permeability to gases.

2.1.2.1 Advantages of Rubber Nanocomposites

In comparison with conventional composites, the main advantages of nanoreinforcements are summarized as follows:

1. Nanomaterials are more effective reinforcements because smaller fraction of nanomaterials causes a significant improvement of the matrix properties, leading to lightweight composites with lower cost and easy processability.
2. The load transfer from the matrix to the reinforcements is more efficient in case of nanocomposites due to their increased surface area, assuming good adhesion at the interface.
3. The crack propagation length at the interface becomes longer because of the size reduction of nanomaterials, which improves both strength and toughness.

It is well known that the particle size, structure and surface characteristics of reinforcing agents are three main factors that determine their reinforcing ability. Particle size is the primary determinant among these three factors and this point is supported by Hamed [1]. In fact reinforcement, especially reinforcement of nanofillers, is essential for rubber products.

2.1.2.2 Challenges of Rubber Nanocomposites

Although nanoreinforcements enhance overall material performance, there are still challenges facing nanocomposites.

1. Nanoparticles tend to aggregate during manufacturing processes. The severe particle aggregation is detrimental to the thermal and mechanical properties of the nanocomposites. The homogeneous dispersion of the nanoparticles in matrix is critical to obtain high performance nanocomposites.
2. Health and environmental threats can occur from the production, use and disposal of nanoparticles. Nanoparticles can damage the body's natural defenses or cause increased responses to common allergens. Workers in nanotech industries are at risk of exposure to high concentrations of nanoparticles. Nanoparticles used in consumer products may threaten public health. Already it is known that nanoparticles in air pollution can be up to 50 times more damaging to lung tissue than fine particles of the same chemicals.

2.1.3 Reinforcing Agent

The use of reinforcing agent in rubber is almost as old as the use of rubber itself. Figure 2.1 is the schematic diagram of sizes and shapes of typical rubber fillers.

2.1.3.1 Carbon Black

Among fillers, carbon black (nanoparticles, spherical) was the first taken as a reinforcing filler in 1904, and since then carbon black has been widely used in various rubber products, such as tires, tubes and so on. It is the excellent nanoreinforcing effect of carbon black that greatly upgrades the mechanical properties of rubber and produces a great many applications.

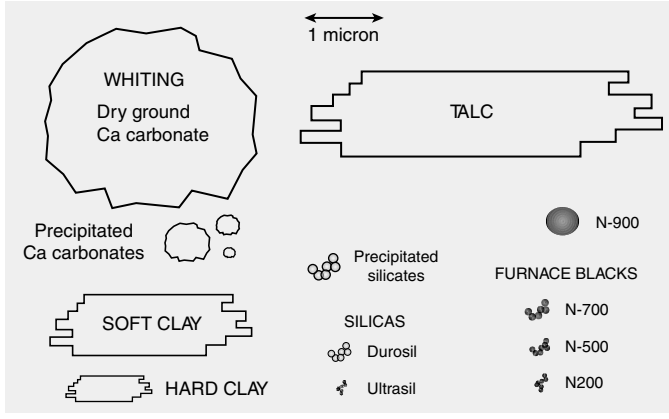

Figure 2.1 Schematic of sizes and shapes of rubber fillers

2.1.3.2 Clays and Clay Minerals

Although carbon black is an efficient agent used in the rubber industry, its polluting nature, its monotonous black color and its dependence on petroleum caused researchers to develop other reinforcement fillers. Clays such as montmorillonite and saponite, hectorite and so on, have been widely used as fillers for rubber and plastic for many years ever since the Toyota research group reported that nylon nanocomposites containing small amounts of clay (layered silicates) possessed exceptional properties. Moreover, clay is abundant, inexpensive and natural. Therefore clays have a great potential for use as rubber fillers.

As an inorganic, clay is hydrophilic in nature, and this makes it very difficult to disperse into most polymer matrices. Generally, the hydrophilic pristine layered silicates are intercalated using organic modifiers via cation exchange reaction. This is the most common way to improve the affinity of inorganic layered silicates with organic polymers. The most popular modifiers used are organic quarternized ammonium or phosphonium, preferably with long alkyl chains, for instance, hexadecyl trimethyl ammonium bromide, octadecyl trimethyl ammonium chloride, dodecyl trimethyl ammonium bromide and so forth. Silane coupling agents such as 3-aminopropyl triethoxy silane are also used. The effect of clay modification on NBR/organo-MMT nanocomposites was studied by Kim *et al.* [2]. Organoclays were modified by the use of alkylamine cations and these nanocomposites were characterized by XRD, TEM, DMA and a universal testing machine (UTM). These organoclay layers were uniformly dispersed in the polymer matrix. With increasing organo-MMT content, the NBR/organo-MMT nanocomposites showed a substantial improvement in mechanical properties compared with unfilled NBR. Zhang *et al.* combined *in situ* organic modification of montmorillonite (MMT) with the latex compounding method to prepare high-performance SBR/MMT nanocomposites [3]. Unsaturated organic ammonium chloride (UOAC), viz. N-allyl-N, N-dimethyloctadecyl ammonium chloride, was used to achieve an *in situ* organic modification of MMT. This modified MMT was co-coagulated with SBR latex. The tensile strength of the obtained nanocomposites was four times higher than that of SBR/MMT nanocomposites.

Organically modified clay (OMC) are now used as fillers in most polymer/clay nanocomposites. Melt blending organically modified clay with polymers has become popular, because of its processing convenience.

2.2 Melt Compounding

Different from thermoplastic polymer/clay nanocomposites, rubber/clay nanocomposites (RCNs) need vulcanization following the nanocompounding of rubber and clay. Given the high chain flexibility and possible difference in crosslinking rate between the inner and outer regions of clay galleries, the microstructures of RCNs are expected to change during vulcanization. Nowadays technologies for the preparation of rubber/clay nanocomposites mainly include the rubber melt or solution intercalation of organoclay and the latex route using pristine clay. Of these, the melt compounding may be of great practical relevance, because the current rubber processing facility can be used. From an industrial standpoint, it is the most direct, most cost-effective, and environment friendly method (no organic solvent is needed).

Since Vaia *et al.* [4] reported mixing polymers with clays without the use of organic solvents, there has been vigorous research in this field. Tian *et al.* reported the preparation of excellent properties and low-cost SBR nanocomposites based on attapulgite (AT), a natural fibrillar silicate clay material, by direct mill mixing [5]. The structure and properties of above composites were carefully investigated by TEM, SEM and RPA. It was found that most AT separated into dispersed units with diameters less than 100 nm in SBR. However, a few dispersion units as large as 0.2–0.5 μm and a clear network structure of dispersion units in SBR were observed. AT can be purified, but purified AT cannot be easily dispersed in the rubber matrix by melt blending. Silane coupling agent Si69 can improve the dispersion of AT and enhance the chemical interfacial adhesion. At the same loading, AT (pretreated with Si69) was found to have better reinforcing effect on SBR than: (i) carbon black SRF with particle size 60–100 nm and (ii) N330 with particle size 26–30 nm.

In a study conducted by Teh *et al.*, onium ion-modified MMT (organoclay) at 2–10 phr loading was melt compounded with NR in an internal mixer and cured using a CV system [6]. The stiffness of the nanocomposite was enhanced with increasing filler content. The addition of 10 phr ENR50 as the compatibilizer in the NR/organoclay nanocomposites significantly improved mechanical properties such as tensile strength, elongation at break, modulus and tear strength. This was attributed to the better dispersion of the MMT in the nanocomposite as supported TEM.

Kim *et al.* prepared nanocomposites of ODA-modified MMT and NBR by mixing at room temperature in an internal mixer [7]. 3-(Mercaptopropyl) trimethoxysilane was used as a coupling agent. TEM studies proved that the coupling agent was effective in enhancing the dispersion of the organoclay.

2.2.1 Manufacturing Factors Control

The most important consideration to achieve RCNs is the dispersion of organoclay particles in a rubber matrix. With such organoclay used as fillers, generally three types of composites materials are obtained: conventional composites, intercalated nanocomposites and exfoliated nanocomposites. Of the three types, the exfoliated structure is the most desired in terms of

reinforcement. As long as the organoclay layers fully delaminate (that is, exfoliate), dispersing less than 10 wt% of them may replace a three- to fourfold amount of traditional fillers for similar reinforcement. Furthermore, exfoliated clay strongly enhances the gas barrier property and swelling resistance compared to pristine polymer. However, fully exfoliated RCNs are difficult to produce. In most of reported RCNs prepared by melt compounding, the full exfoliation of organoclay layers in rubber matrix has not been obtained. There are many factors affecting the morphology of RCNs during melt compounding. Some previous works have disclosed that the dispersion state of organoclay in rubber matrix is influenced by the type of intercalates, compounding condition (shear rate and temperature) and the polarity of matrix rubber. It was also found that the microstructures of some RCNs were changed by curing processes and influenced by the type of curatives; this was attributed to the difference in curing reactions between the inter and outer galleries of silicates by some researchers.

The heat (or temperature), pressure and crosslinking reaction during the manufacturing process should be the main factors causing microstructural changes. Within the scorch period (the initial stage of curing), the crosslinking reaction starts but does not proceed considerably. Hence, most rubber macromolecules are still in the linear state and have mobility. The former two factors, heat and pressure, are dominant in this stage; while after the scorch period, the crosslinking reaction may also alter the microstructure and finally reserve the changed microstructure through crosslinking bonds. Undoubtedly, the final properties of RCNs should correspond to their final microstructures derived from vulcanization. Therefore, the knowledge of the vulcanization influence on the microstructures of RCNs is of great importance for the control of morphology and property of RCNs.

The influence of heat/temperature and pressure on intercalated structures is revealed by the study of melt-blended isobutyl-isoprene rubber/clay nanocomposites (IIRCNs) [8]. IIR and organically modified clay (OMC) were compounded for about 15 min using a laboratory 6-in (15-cm) two-roll mill. The temperatures of two rolls were within the range 30–60 °C. None additives were added to the mixture in order to avoid their disturbance on the morphology. The thermal treatments of OMC and IIRCNs under atmosphere pressure were carried out in an oven. By contrast, the thermal treatments of OMC and IIRCNs under high pressure were performed on a press, which exerted the predetermined temperature and pressure on to a standard mold containing the IIRCN and OMC samples.

The morphology of the IIRCN without thermal treatments is displayed in Figure 2.2, in which the silicates are shown as dark lines. The low magnification TEM photograph clearly shows that most intercalated silicate layers with about 15–30 nm in width and 100–300 nm in length are homogeneously dispersed in the IIR matrix. Moreover, the intercalated silicate layers are locally stacked in some regions of polymer matrix. The high magnification TEM photograph in Figure 2.2 displays that there are also some finer silicate particles dispersing in the IIR matrix; the width of the particles is within the range 4–7 nm. Because the width of most observed silicate particles are far larger than the width of single silicate layers (that is, $\sim$1 nm), the IIRCN should not belong to exfoliated PCN.

Figure 2.3 reveals the changes in the intercalated structures of IIRCN caused by a thermal treatment under atmospheric pressure (AP). In all treated IIRCN patterns, a broad intense peak appears at around $2\theta = 4.31^\circ$, corresponding to a spacing of 2.05 nm. The intensity of the reflection at $2\theta = 4.31^\circ$ is considerably stronger than other reflections at lower 2θ, and the order spacing for this reflection is not in integral proportion to those at lower 2θ. Therefore, this reflection should not be classified as a high order reflection, and herein it is attributed to the

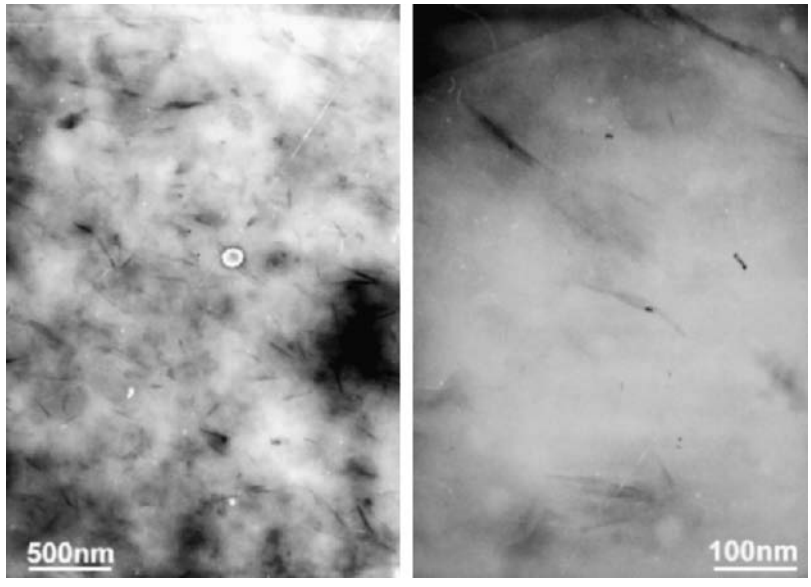

Figure 2.2 TEM morphologies of IIRCN. Left – low magnification; right – high magnification

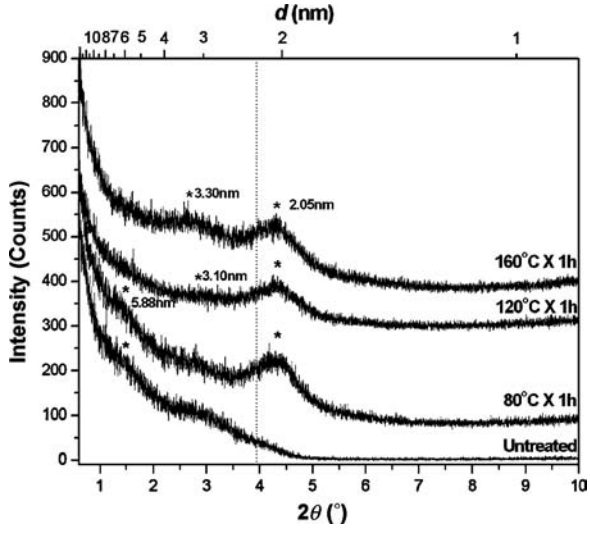

Figure 2.3 WAXD patterns of untreated IIRCN and IIRCN thermally treated at different temperatures and AP for 1 h. The asterisks indicate (0 0 1) peaks for OMC dispersed in IIR matrix. The dotted line indicates the location of the silicate (0 0 1) reflection of pure OMC. The curves are shifted vertically for clarity

coherent structures with a basal spacing of 2.05 nm, which is still less than that for the original OMC but much larger than that for pure clay. This means the formation of un-interacted silicate structures during the thermal treatment. It is also observed that with increasing the treating temperature, the reflection corresponding to a spacing of ~5.88 nm gradually disappears, and a new reflection corresponding to a spacing of ~3.30 nm appears. In the sample treated at medium temperature (that is, 120 °C), the original and new intercalated structures coexist. The new peak at $2\theta = 2.85°$ corresponding to the spacing of 3.10 nm in the pattern should be caused by the overlapping of the basal reflection of the new intercalated structure (~3.30 nm) and the (0 0 2) reflection of original intercalated one (~2.94 nm). It is also noticed that this evolvement of intercalation structures is strongly dependant upon the treating temperature. When thermally treated at 80 °C, the originally intercalated structure with a basal spacing of 5.88 nm is little destroyed. When the treating temperature is increased to 160 °C, however, this original intercalated structure is almost transformed to new intercalated structure with decreased gallery height. In the IIRCN treated at 120 °C, there is a mixture of these two intercalated structures. It should be pointed out that the appearance of the 2.05 nm reflection is little affected by treating temperatures applied in this work. Therefore, it is assumed that there might be two types of intercalated structures with different thermal stability existing in IIRCN prepared in this study.

Figure 2.4 shows the TEM photographs of IIRCN treated at the conditions of 80 °C × AP × 1 h and 160 °C × AP × 1 h, respectively. In the TEM photograph of the 80 °C × AP × 1 h sample (Figure 2.4a), the quantity of darker line-like materials are apparently reduced and are replaced by small flocculent dispersions, compared with the untreated IIRCN. This result implies that the assembly of intercalated silicates should occur more easily during the thermal treatment than the extrusion of IIR chains from silicate galleries. The enlarged observation reveals that most of flocculent structures were not comprised of orderly stacked silicate layers. Moreover, on the left bottom of the high magnification photograph of this sample, an extremely darker dispersion can be observed, representing that this area is composed of very high density of heavy elements (i.e., Si). This dispersion might correspond to the un-intercalated silicate structure with the basal spacing of 2.05 nm disclosed in Figure 2.3. When the treating temperature is increased to 160 °C, as shown in Figure 2.4b, some very large aggregations are obvious, whose length is around 1 μm and width is several hundred nanometers; small flocculent structures are reduced. The enlarged photograph discloses that many silicate layers orderly stack to form these large aggregations. This kind of structure formed by the flocculation of intercalated stacked silicate layers due to the hydroxylated edge-edge interactions was defined as an intercalated-flocculated structure.

Figure 2.5 represents the effect of the treating time on the intercalation structures of IIRCN treated at 120 °C and AP. It can be seen that the un-intercalated silicate layers with a basal spacing of 2.05 nm appear relatively quickly. After only a 10-min thermal treatment at 120 °C, a considerable amount of this kind of structure appeared. In contrast, it takes a longer time for transformation from the original intercalation structure with a basal spacing of 5.87 nm to the new intercalated structure with a basal spacing of 3.30 nm. The 10-min thermal treatment at 120 °C causes little change of these intercalated structures. These results imply that two types of intercalated structures with different features might exist in the untreated IIRCN.

The pressure is another important factor for curing process besides temperature (or heat) and time. Figure 2.6 represents the time dependence of intercalated structures of IIRCN treated at

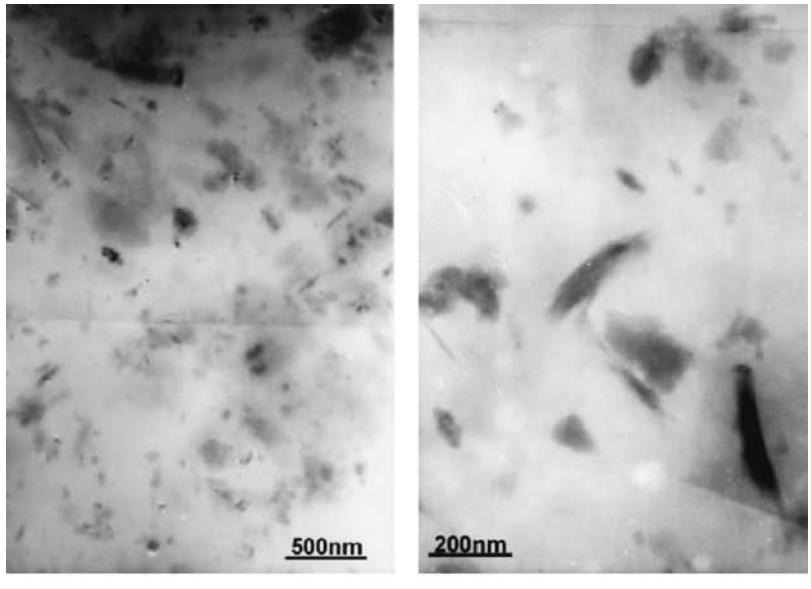

(a) Treated at 80°C x AP x 1h

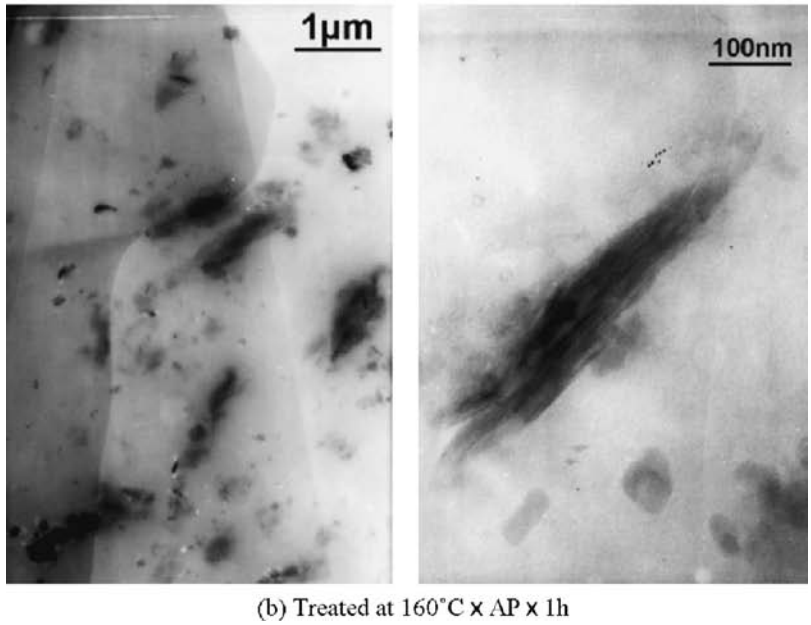

(b) Treated at 160°C x AP x 1h

Figure 2.4 TEM photographs of IIRCN treated at two temperatures and AP for 1 h: (a) 80 °C or (b) 160 °C. Left – low magnification; right – high magnification

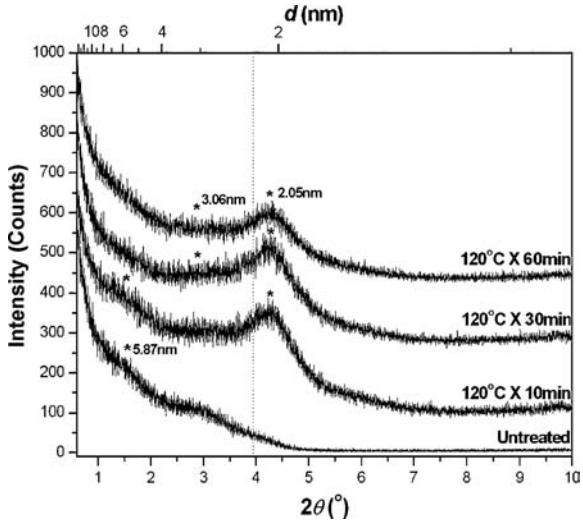

Figure 2.5 WAXD patterns of untreated IIRCN and IIRCN thermally treated at 120 °C and AP for different times. The asterisks indicate (0 0 1) peaks for OMC dispersed in IIR matrix. The dotted line indicates the location of the silicate (0 0 1) reflection of pure OMC. The curves are shifted vertically for clarity

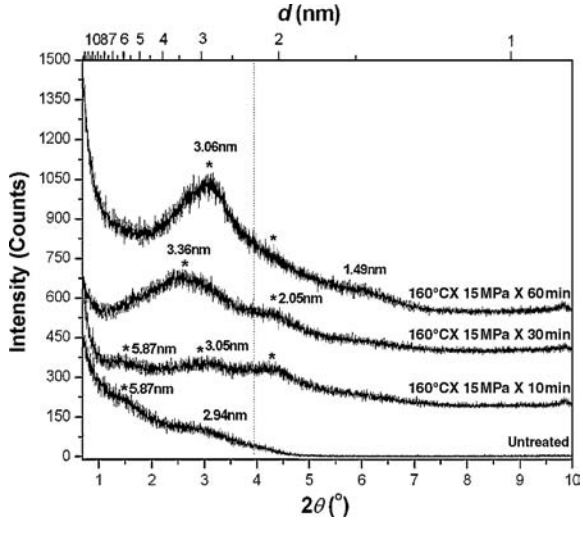

Figure 2.6 WAXD patterns for IIRCN treated at 160 °C and 15 MPa pressure for different times. The asterisks indicate (0 0 1) peaks for OMC dispersed in IIR matrix. The dotted line indicates the location of the silicate (0 0 1) reflection of pure OMC. The curves are shifted vertically for clarity

160 °C with 15 MPa pressure. Similar to the case of IIRCN treated at AP, un-intercalated silicate structures with a basal spacing of 2.05 nm formed more quickly than the transformation of original intercalated structures to new intercalated structures with smaller gallery height. In contrast, the thermal treatment at high pressure (that is, 15 MPa) results in a new intercalated structure having a smaller gallery height, with a basal reflection which is much stronger and sharper, compared with IIRCN treated at AP. Moreover, d_{002} reflection (=1.49 nm) of this basal reflection is also obvious in the pattern of the 160 °C × 15 MPa × 60 min sample. This result suggests that high pressure can significantly increase the coherence length of the silicate crystallites besides further extruding IIR chains out of the silicate galleries; this structural transformation should be also kinetic.

Figure 2.7 depicts TEM photographs of IIRCN treated at 160 °C with 15 MPa pressure for 1 h. In contrast to IIRCN thermally treated at AP, the dispersions are almost intercalated-flocculated structures from 300 nm to 1.5 μm in length and 100–300 nm in width. This extensive flocculation of intercalated and stacked silicates greatly improves the order coherency of silicate crystallites, causing a strong and sharp reflection peak in the WAXD pattern. It should note that the high pressure does not change the intensity and width of the reflection peak at ∼2.05 nm, meaning that un-intercalated silicate crystallites cannot be further assembled by high pressure.

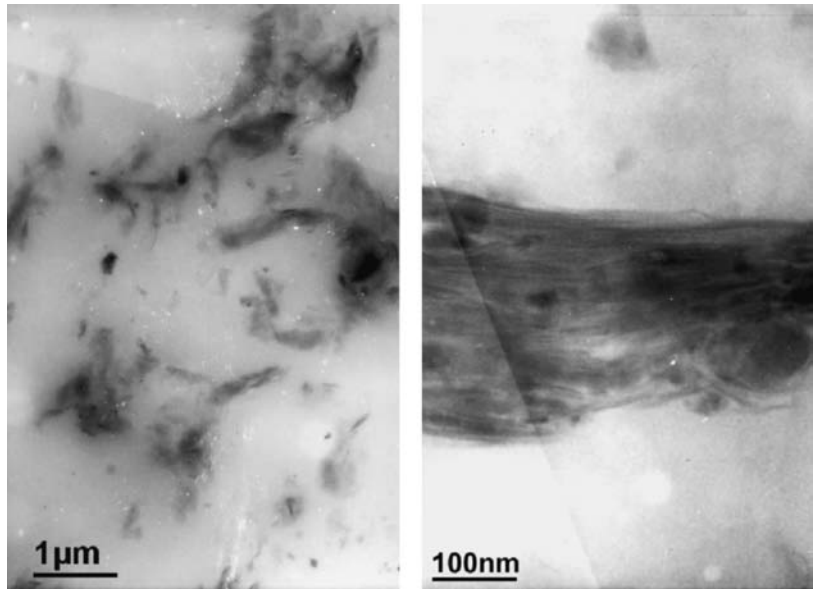

Figure 2.7 TEM photographs of IIRCN treated at 160 °C and 15 MPa for 1 h. Left – low magnification; right – high magnification

Figure 2.8 reveals that the magnitude of the extra pressure for thermal treatment has significant influence on the intercalated structures of the treated IIRCNs. With increasing pressure, the WAXD pattern of IIIRCN changes from the pattern of AP sample to that of 15 MPa sample. It should note that the difference in WAXD pattern between AP and 4.5 MPa samples are

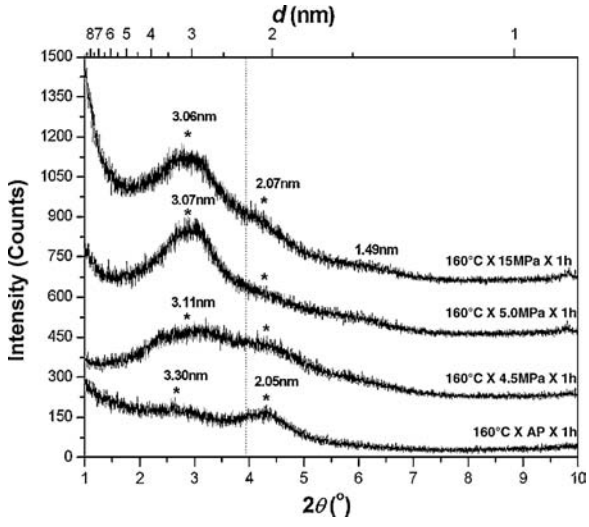

Figure 2.8 Influence of pressure on WAXD patterns of IIRCN treated at 160 °C for 1 h. The asterisks indicate (0 0 1) peaks for OMC dispersed in IIR matrix. The dotted line indicates the location of the silicate (0 0 1) reflection of pure OMC

much smaller than that between 4.5 MPa and 5.0 MPa samples; and if extra pressure is beyond 5 MPa, the further increase of extra pressure will impose little impact on WAXD patterns. The previous results (Figures 2.6 and 2.8) revealed that the strong and sharp reflection, corresponding to a basal spacing of ~3.06 nm, is mainly attributed to extensive stacking and flocculating of intercalated silicate layers. So there should exist a critical pressure value within the range 4.5–5.0 MPa for intercalated silicate layers starting to stack and flocculate across the full scale of the nanocomposite.

Combining the WAXD analyses with TEM observations, the possible structural models for untreated and treated IIRCNs are proposed in Figure 2.9. In untreated IIRCN, there are two types of dispersion silicate structures with different thermal stabilities. Obviously, one structure is intercalated silicate with a basal spacing of ~5.88 nm [structure (a) in Figure 2.9], which is transformed to new intercalated structures with decreased basal spacing by the treatments. We assumed that the other structure might be partially intercalated silicate [structure (b) in Figure 2.9], which is transformed to un-intercalated silicates with a basal spacing of 2.05 nm by the treatments. There is evidence from two experiments supporting our assumption: (i) Figures 2.6 and 2.8 show that the IIR chains in the fully intercalated silicate gallery cannot be extruded out completely, even though in the condition of high temperature and high pressure; (ii) Figures 2.3, 2.5–2.6 and 2.8 demonstrate that the un-intercalated structures form easily and quickly during the treatments. Only the partially intercalated structures, where the energy barrier against the extrusion of IIR chains out of silicate gallery is low, can result in these behaviors. Since this partial intercalation also disturbs the orderly stacking of silicate layers, no reflection signals can be observed in WAXD pattern of untreated IIRCN. Through thermal treatments, those IIR chains inserted in the edge region of silicate galleries are extruded completely and the orderly

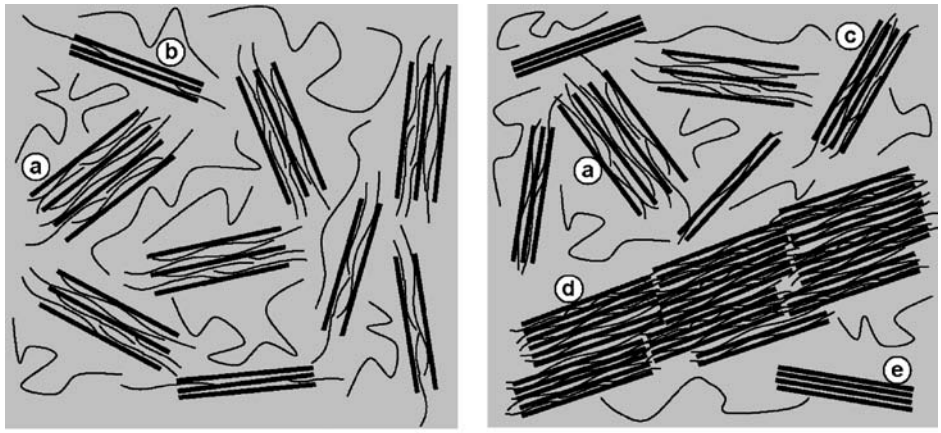

Figure 2.9 Schematic illustrations of possible types of dispersions in: (a) untreated and (b) treated IIRCNs. All possible structures are labeled by letters: (a) intercalated structure with a basal spacing of ~5.87 nm; (b) partially intercalated structure; (c) intercalated structure with decreased basal spacing; (d) intercalated–flocculated structure with decreased basal spacing; and (e) un-intercalated silicate with a basal spacing of ~2.06 nm

stacked silicate layers is regained, and as a result a corresponding WAXD reflection appears. The thermal treatments also cause the tethered aliphatic chains of alklammonium salt in the interlayer rearranging to pack at a more compact state, and as a result, the un-intercalated structures has a basal spacing even less than that for pure OMC. As shown in Figure 2.9b, there are four possible types of dispersion structures in the treated IIRCN. The fraction of each structure varies from the condition of the treatment, some tendencies of which are summarized as follows:

1. The fraction of un-intercalated structure is little affected by treating temperature, pressure and time used in this work.
2. Thermal treatment at AP can cause the transformation from the original intercalated structure to a new intercalated structure with a basal spacing of ~3.30 nm. Both increasing treating temperature and prolonging treating time can increase the extent of this structural transformation.
3. Thermal treatment at AP can also cause intercalated silicates assembling and decrease the homogenous degree of dispersion. With increasing the treating temperature, the assembling fraction is increased and more and larger aggregated structures appear. In the 160 °C × AP × 1° sample, some intercalated-flocculated structures are obvious.
4. The IIR chains can be further extruded from the interlayer by extra pressure, with the formation of other new intercalated structure with a basal spacing of 3.06 nm. The assembling extent of intercalated silicates can also be increased by extra pressure. If it is beyond a critical pressure between 4.5 and 5 MPa, the intercalated-flocculated structures are formed across the full scale of the IIRCN.

In conclusion, by a process of melt blending, an IIRCN mainly having the intercalated structure was obtained. This original intercalated structure is thermodynamically unstable but frozen at room temperature. The thermal treatment at AP can cause a transformation from the original intercalated structure to a new intercalated one with a smaller gallery height and assembling of some intercalated silicates. Exerting extra pressure during thermal treatment can cause the further collapse of the intercalated structures and assembling of intercalated silicates. The magnitudes of treating temperature, pressure and time have tremendous impacts on the morphology of treated IIRCN. If extra pressure is added beyond 5 MPa, the intercalated-flocculated structure forms across the full scale of the IIRCN. It is well accepted that the PCN having higher dispersion extent of silicate layers possesses the better performance. Based upon the above results and discussions, we proposed guidelines on how to obtain a desired morphology in the case of IIRCN prepared by melt blending. The curing system should be selected to ensure that curing process could occur at low temperature, the scorch period should be short and the curing rate should be high. Additionally, relatively low pressure should be used during vulcanization.

2.2.2 Filler Surface Modification

Fibrillar silicate (FS) is one type of hydrated magnesium aluminum silicate clay, composed of many single fibrillar nanocrystals. The dominant FS is attapulgite or palygorskite. FS has the structural formula $Mg_5[Al]Si_8O_{20}(HO)_2(OH_2)_4{\cdot}H_2O$. The primary structural unit is the fibrillar nano single crystal which is 100–3000 nm in length and 10–30 nm in diameter. Single crystals compactly arrange in parallel to form into crystal bundles and these crystal bundles then agglomerate into particles having diameters of 5–50 μm. According to Tian's [9] investigation, it was found that modified FS using silane coupling agent could also be directly separated into nano single crystals or crystal bundles (also called nanofibrils) in rubber matrix under mechanical shear during melt blending. In this way, various kinds of FS/rubber nanocomposites with excellent performances have been achieved. It is promising that the composites will be launched into future applications due to the cheap cost and simple preparation process.

2.2.2.1 Surface Modification of FS

In the experiments, 20–50 wt% FS aqueous solution was put into a high-speed agitator and agitated at the speed of 800 rpm to make FS separated into single crystals. Then a mixture of Si69/alcohol (ratio about 1 : 5) was added slowly and uniformly to the above solution, which was treated for 30 min at 60 °C. After removal of the solvent to get dry solid particles, these were then ground into powders. Herein the amount of Si69 alcohol solution added was calculated according to a weight ratio of Si69:FS = 2.4:100.

2.2.2.2 Preparation of FS/SBR Composites

Adjusting the two rolls of a two-roll mill to the smallest distance when rubber becomes fluidic, modified FS was then added into the rubber step by step to ensure good dispersion. Next, vulcanizer and accelerator were added (as shown in Table 2.1), and the compound was finally obtained and sliced at 1.5 mm two-roll spacing to prepare for vulcanization. Cure time was determined by a disc oscillating rheometer and the compound was vulcanized in a platen presser at 25 t pressure. The vulcanization temperature of SBR was 150 °C.

Table 2.1 Compositions of materials

Rubber (g)	100
Vulcanizer and accelerator (g)	10
Modified FS (g)	Variable

2.2.2.3 Properties of FS/SBR Composites

It can be seen from Table 2.2, FS/SBR composites prepared by direct blending possessed higher hardness, tensile stress at 100% strain, tensile strength and very high tear strength, which demonstrated that modified FS showed an excellent reinforcing effect. As the loading level of FS rose, the composites had a distinct increase in hardness and tear strength but a decrease in elongation at break and permanent set. When the amount of FS was more than 60 g/100 g SBR, the tensile stress at 100% strain and the tensile strength of the composites were remarkably enhanced once again.

As shown in Figure 2.10, most of modified FS could be separated into fibrils with diameters less than 100 nm and dispersed in SBR. Moreover, the greater the amount of FS added, the greater the number of nanofibrils, which implied the separation of FS and the dispersion of FS improved when the loading of FS was increased. As we observed, the uniformity of FS dispersion was better when the loading level of FS was 50 g/100 g SBR or 60 g/100 g SBR. This was likely explained that the maximal shear force acting on FS increased with the

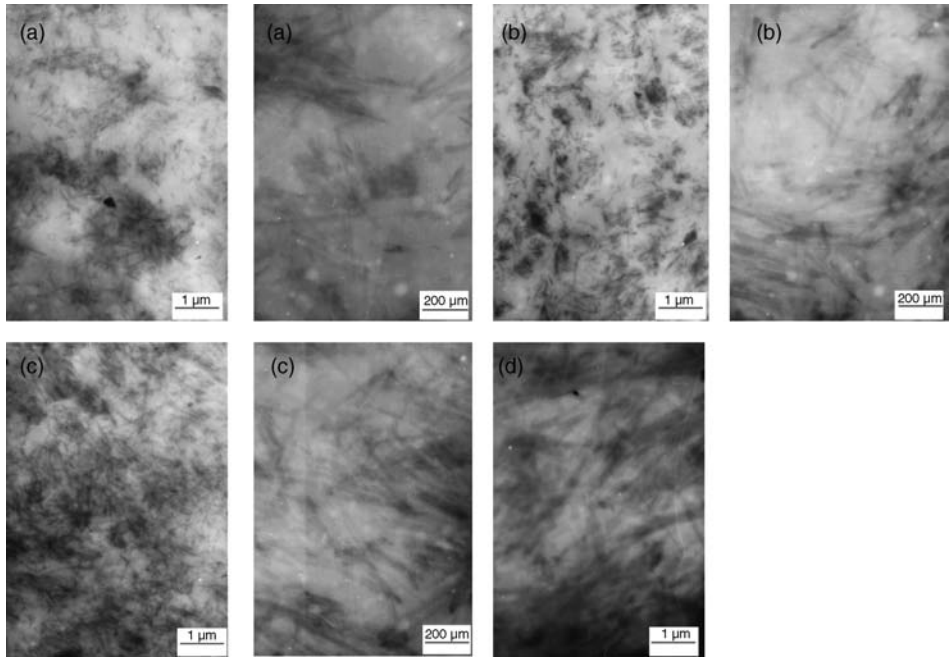

Figure 2.10 TEM observations of FS/SBR composites, containing x g/100 g SBR: (a) 30 g; (b) 40 g; (c) 50 g; and (d) 60 g

Table 2.2 Mechanical properties of composites

	Amount of modified FS							
	30		40		50		60	
	Unaged	Aged	Unaged	Aged	Unaged	Aged	Unaged	Aged
Hardness (shore A)	69	78	73	80	75	83	79	85
Tensile stress at 100% strain (MPa)	7.3	8.4	7.6	10.4	7.8	12.2	10.2	13.7
Tensile strength (MPa)	14.1	14.3	14.7	16.0	14.4	17.5	18.8	20.5
Elongation at break (%)	350	260	344	238	336	233	309	233
Permanent set (%)	20	12	20	12	12	8	12	8
Tear strength (KN m^{-1})	58.0		60.8		67.4		64.7	

increasing viscosity of matrix and thus improved the separation and dispersion of FS. It is true that the viscosity of matrix rose as the amount of FS increased.

Figures 2.11 and 2.12 show that, as the amount of FS increased, the dynamic elastic modulus (E') of the composites rose but the maximum loss tangent ($\tan\delta_{max}$) declined. This agreed with a spherical filler such as carbon black reinforced rubber. It was obvious that the rubber volume fraction decreased with increasing FS amount. The temperature corresponded to $\tan\delta_{max}$ could be thought as the glass transmission temperature (T_g) of SBR, about at $-50\,^{\circ}C$. It could be concluded that the content of FS had little effect on T_g. When the temperature is significantly less than T_g, the rubber molecules are glassy and cannot move, hence the loss tangent ($\tan\delta$) is very low while E' is very high. As the temperature rises but is less than T_g, the rubber molecules begin to move in limited volume, and $\tan\delta$ gradually increases while E' declines dramatically. When the temperature is more than T_g, the rubber molecules can freely move due to the rise in the free volume of rubber, and $\tan\delta$ begins to decline while E' decreases to a minimum value and changes little. Therefore, $\tan\delta$ of the composite appears to have a maximal value.

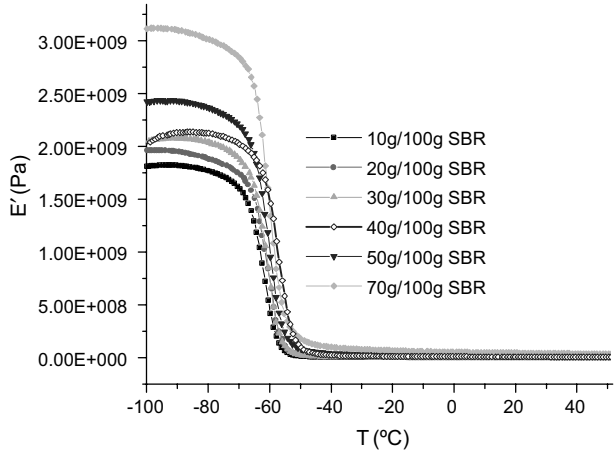

Figure 2.11 The relation of dynamic elastic modulus of FS/SBR composites and temperature

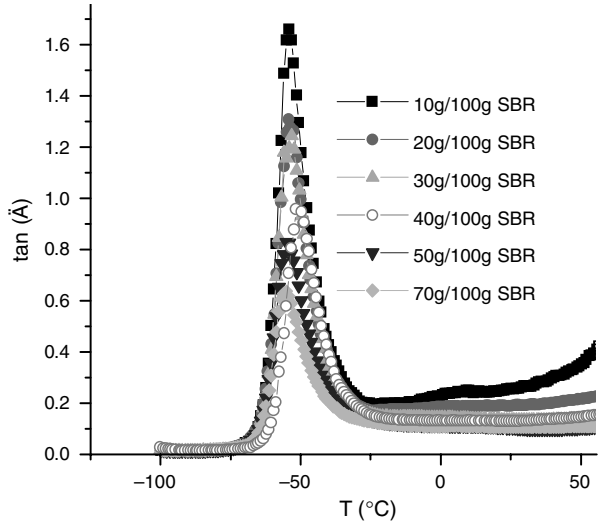

Figure 2.12 The relation of loss tangent of FS/SBR composites and temperature

In order to discuss the anisotropy of FS/SBR composites during the preparation of the composites, the two rolls were adjusted to the smallest interval so as to give maximal shear to make the nanofibrils oriented when the compound was sliced. As seen in Figure 2.13, FS/SBR composites exhibited higher stress in the tropism direction than that in the vertical to tropism direction at the same amount of FS. It was obvious that the stress difference in the two directions became more distinct with increasing FS content. Table 2.3 shows that it is also true for the tensile Young's modulus of the composites. The difference in tensile Young's modulus in the two directions became more visible when the content of FS was more than 60 g/100 g SBR. Like short microfibers, nanofibrils could also be oriented along the shear direction. The greater

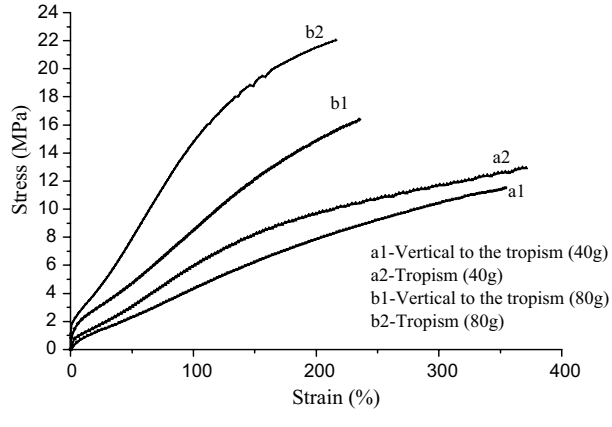

Figure 2.13 The stress and strain relation of FS/SBR composites in two different directions

Table 2.3 Tensile Young's modulus of FS/SBR composites

The content of FS (g/100 g SBR)	Tropism tensile Young's modulus (MPa)	Vertical tensile Young's modulus (MPa)
30	7.51	6.19
40	10.80	10.65
50	13.71	12.32
60	22.40	13.58
70	23.16	14.80
80	26.88	16.81

the amount of FS, the greater is the number of nanofibrils and the more distinct is the orientation of fibrils. As a result, the composites showed more evident anisotropy.

It could be concluded from Figure 2.14 that the Mooney viscosity of FS/SBR and WCB/SBR compounds increased with the increasing amount of filler but the increment of the former was more remarkable. It was very puzzling that the Mooney viscosity of the FS/SBR compound was lower at the same loading level of filler. In addition, it is very easy to mix FS with rubber, and FS/SBR composites show good appearance. As we knew, short microfiber-reinforced rubber usually exhibited an undesirable flow property and appearance due to its large dimension. Therefore, it is possible that FS can be used in some special rubber product instead of short microfibers to some extent.

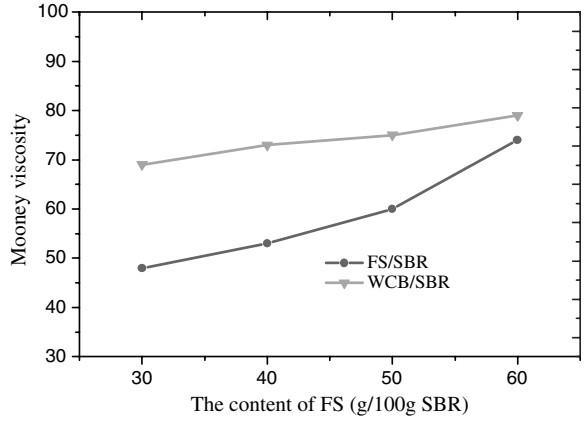

Figure 2.14 Mooney viscosity of FS/SBR and WCB/SBR compounds

Cheap FS fibrils showed excellent reinforcing effect for SBR. FS/SBR composites prepared by melt compounding exhibited the similar characteristics of short microfiber-reinforced rubber, for examples, high stress at definite strain, high tear strength, low elongation at break and anisotropy. In addition, the FS/SBR compound had a good flow property.

2.3 Solution Blending

Different from melt compounding, organic solvent is needed to prepare rubber/clay nanocomposites by solution blending. In this method, dry rubber is dissolved in a suitable solvent along with the organically modified clays or mixed together after dissolution in suitable solvents. The solvent is evaporated to obtain the nanocomposite.

Ganter *et al.* prepared rubber nanocomposites based on styrene–butadiene rubber (SBR) and butadiene rubber (BR) containing organophilic-layered silicates [10, 11]. They reported that the intergallery distance of the organoclay increased more than twofold when it was incorporated in SBR dissolved in toluene. The excellent dispersion of the organoclay (exhibiting both intercalated and partially exfoliated layers) in rubber was demonstrated by TEM and AFM. The organoclay vulcanizates exhibited enhanced hysteresis when compared with silica-filled vulcanizates, which was explained by the orientation and sliding of the anisotropic silicate layers.

In another study, Sadhu and Bhowmick studied the influence of the structural and processing parameters on rubber-based nanocomposites prepared with ODA-modified MMT and SBR with different styrene contents [12]. Toluene, chloroform and carbon tetrachloride were used as solvents and the composites were cured by dicumyl peroxide and sulfur cure systems. All the composites were characterized by TEM, indicating a uniform distribution of the organoclay in the SBR matrix. Even with a very low organoclay loading, the modified clay/SBR nanocomposites displayed improved mechanical properties and the styrene content of the rubber had a pronounced effect on the properties of the nanocomposites. Increasing the styrene content increased the tensile strength, modulus and elongation at break of SBR.

2.3.1 Manufacturing Factors Control

The effects of heat and pressure during solution blending on the microstructures of isobutylene-isoprene rubber/clay nanocomposites (IIRCNs) were investigated by Lu *et al.* [13]. To prepare the nanocomposites, organically modified clay (OMC) was dispersed in toluene with vigorous stirring, and then IIR/toluene solution was added into this suspension. The obtained mixture was vigorously stirred for 24 h. After the solvent was evaporated, the IIR/OMC (100/10) nanocomposite (IIRCN) was obtained. The vaporization of solvent was carried out in a vacuum oven at 40 °C for 24 h. No other additives were added to the mixture in order to avoid their disturbance of the morphology.

The thermal treatments of IIRCNs under atmospheric pressure (AP) were carried out in an electrically heated oven. However, the thermal treatments of IIRCNs under high pressure (HP) were performed on an electrically heated hydraulic press, which exerted the predetermined temperature and pressure on a standard mold containing the IIRCN sample.

Figure 2.15 compares WAXD patterns of OMC and untreated IIRCN. In the OMC pattern, there is a reflection signal at $2\theta = 3.92°$, corresponding to a basal spacing of 2.24 nm. Whereas, in that of S-IIRCN, the diffraction peak locates at $2\theta = 2.51°$, corresponding to a basal spacing of 3.50 nm, which is detectable of the intercalation structure. Additionally, there are no any other higher order reflections in the pattern, which implies that the order degree of intercalated structure in initial IIRCN is not high.

Figure 2.16 shows bright field TEM images of untreated IIRCN at two different magnifications, in which dark entities are the clay particles and bright areas are the matrix. From the TEM

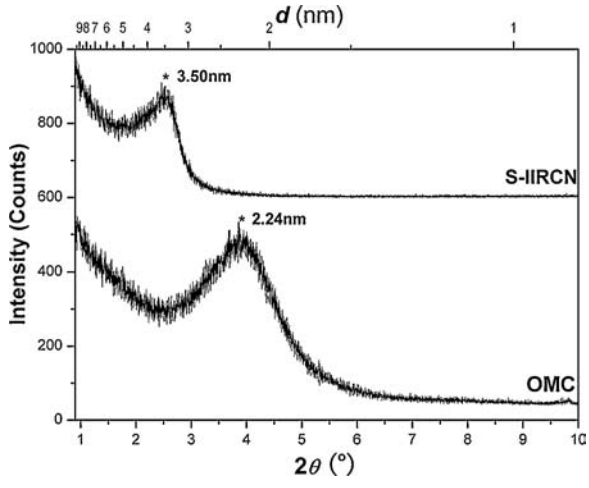

Figure 2.15 WAXD patterns of IIRCN (IIR/OMC = 100/10 wt) and pure OMC. The asterisks indicate (0 0 1) peaks for OMC dispersed in IIR matrix and pure OMC. The curves are shifted vertically for clarity

image of low magnification, it can be observed that silicate layers stacks and flocculates to form large agglomerates 100–200 nm in width and 400–600 nm in length. Moreover, the dispersion of these clay agglomerates in rubber matrix is inhomogeneous. The enlarged observation reveals that the agglomerates are composed of many silicate tactoids; and in many parts of the

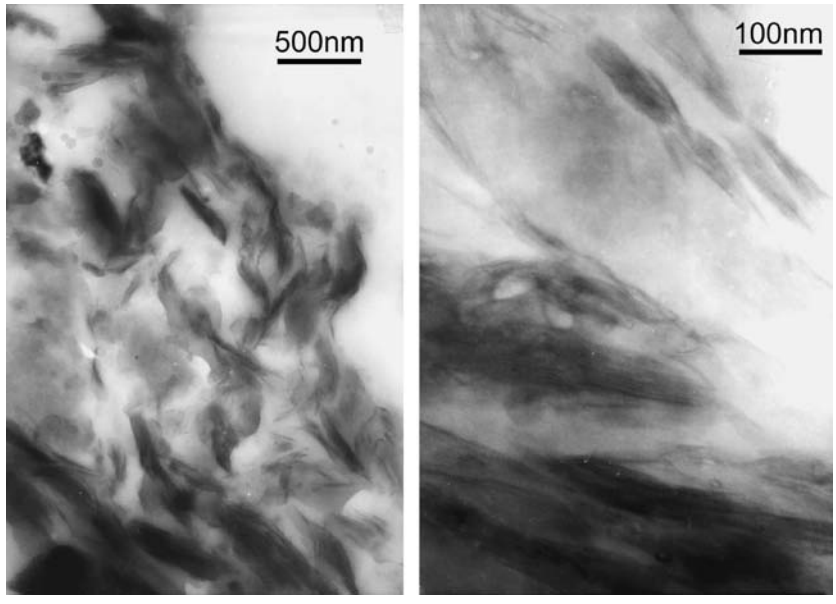

Figure 2.16 TEM photographs of IIRCN (IIR/OMC = 100/10 wt). Left – low magnification; right – high magnification

agglomerates, the silicate tactoids stacks in disrupted form. This observation is in accordance with the WAXD data (Figure 2.15).

The initial IIRCN was thermally treated in free state, that is, under AP, and at 80, 100, 120, 140 and 160 °C, respectively, for 1 h. These treated IIRCNs were denoted by AP80, AP100, AP120, AP140 and AP160, respectively. The WAXD patterns of these samples are shown in Figure 2.17. In general, the structural changes of polymer based clay nanocomposites can be determined by monitoring the position, intensity and full width at half maximum (FWHM) of the (0 0 1) basal reflection of OMC. First, the change in the intensity caused by AP thermal treatments is most apparent. Moreover, the intensity is strongly dependant on the thermal-treating temperature, as shown in Figure 2.18 [the method for the measurement of (0 0 1) peak intensity is shown in Figure 2.17]. This pattern can be divided into three regions. In the first region (80–100 °C), the reflection intensity increases with the treating temperature increasing. In the second region (100–140 °C), the intensity decreases sharply with the thermal-treating temperature increasing. In the third region (140–180 °C), the rate for the (0 0 1) peak intensity decreasing with the thermal-treating temperature becomes low. The (0 0 1) reflection peaks of OMC in AP80, AP100 and AP120 samples are obviously stronger than that of untreated IIRCN. Furthermore, the higher order reflections of the (0 0 1) basal peak are obvious in the WAXD patterns of these samples. These phenomena indicate that the intercalated structures in these IIRCNs are more ordered than those in the initial IIRCN. On the other hand, the (0 0 1) peak for AP140 and AP160 samples are much weaker than that for untreated IIRCN.

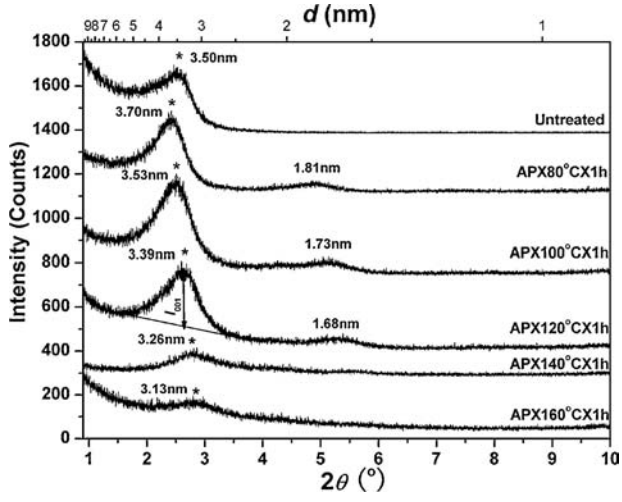

Figure 2.17 WAXD patterns of untreated IIRCN and IIRCNs treated at different temperatures and AP for 1 h. The asterisks indicate (0 0 1) peaks for OMC dispersed in IIR matrix. The curves are shifted vertically for clarity

There are two possible reasons resulting in the decrease in intensity of the (0 0 1) basal reflection: (i) the decrease in the degree of coherent silicate layer stacking and (ii) the occurrence of the exfoliation and destruction of some intercalated silicates. The FWHM of the (0 0 1) basal reflection peak is inversely proportional to the coherence length of the

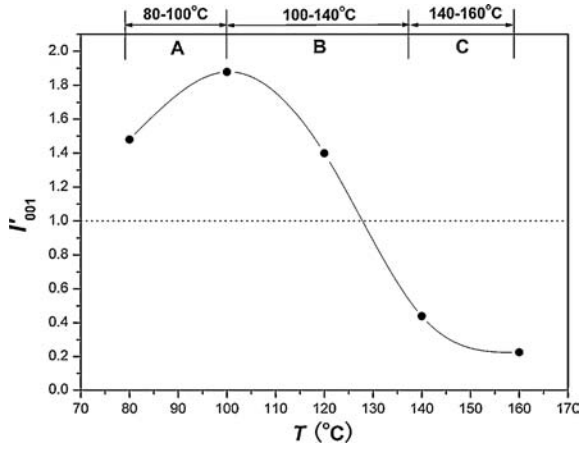

Figure 2.18 Influence of treating temperature (T) on relative intensity of (0 0 1) reflection peak ($I'_{001} = I^{T}_{001}/I^{\text{untreated}}_{001}$) for OMC dispersed in IIRCN thermally treated at AP for 1 h. The dotted line indicates the level for untreated IIRCN

OMC (L001) and therefore reflects the coherent order of the silicate layers. Table 2.4 summarizes the coherence lengths (L001) of the intercalated OMC for initial IIRCN and thermally treated samples calculated from FWHM by using Scherer equation. It can be seen that AP thermal treatments at different temperatures result in remarkable increase of L001, and the treating temperature has little influence on the L001 of interacted silicate structures in IIRCN treated under AP. Therefore, the increase in the intensity of the (0 0 1) reflection peak for AP80, AP100 and AP120 samples should be caused by the improvement in the coherence order degree of the intercalated OMC in these composites. The dramatic decrease in the intensity of the (0 0 1) reflection for AP140 and AP160 samples should be essentially due to the exfoliation of substantial OMC and the decrease in amount of intercalated structures. In these two treated IIRCNs, the residual intercalated silicates still have higher coherence order in comparison with the untreated IIRCN. Table 2.4 also compares the basal spacing of OMC

Table 2.4 The intensities of (0 0 1) peaks and crystalline parameters obtained from WAXD analyses of OMC dispersed in untreated IIRCN and IIRCNs treated at different temperatures and AP for 1 h

Temp (°C)	I_{001}[1] (Counts)	d_{001} (nm)	L_{001} (nm)	L_{001}/d_{001}[2]
Untreated	173	3.50	6.66	1.9
80	256	3.70	9.60	2.6
100	325	3.53	10.16	2.9
120	242	3.39	9.09	2.7
140	76	3.26	9.09	2.8
160	39	3.13	9.09	2.9

[1]The method for determining the intensity of (0 0 1) peak (I_{001}) is shown in Figure 2.3.
[2]This ratio represents the mean number of silicate layers in basic intercalated structure.

among initial and AP thermally treated IIRCNs. The result reveals that the gallery height of OMC in the AP thermally treated nanocomposite decreases with the treating temperature increasing and is smaller than that in untreated IIRCN when the treating temperature is beyond 100 °C. It should be pointed out that the change in the gallery height with treating temperature is not much.

Figure 2.19 represents the TEM images of AP80 and AP160, which demonstrate that the treating temperature possesses the essential influence on the dispersion state of silicate particles in IIR matrix. In the AP80 sample, the majority of OMC particles are still dispersed in stacked forms comprising several decade silicate layers, and the dispersion homogeneity of them is little improved, compared with the initial IIRCN. In contrast, the exfoliated silicates are dominant in the AP160 sample, but a small amount of stacked intercalated silicate structure still remains. Furthermore, the dispersion homogeneity of silicate layers in this nanocomposite is greatly improved. The high-magnification TEM images display that the intercalated silicates stack more orderly in the AP80 and AP160 samples than in the untreated IIRCN. These TEM observations are well consistent with the WAXD results.

On the basis of the WAXD patterns and TEM observation, the microstructural changes of IIRCN caused by AP thermal treatments can be determined. AP thermal treatments at low temperature (that is, 80, 100, 120 °C) mainly improve the coherence order of stacked intercalated silicates, but little change the spatial distribution of silicate particles in IIR matrix. However, AP thermal treatments at high temperature (that is, 140, 160 °C) not only cause the exfoliation of majority of silicates, but also result in a dramatic improvement in the dispersion homogeneity of silicate particles.

Figure 2.20 shows the effect of constant extra pressure (15 MPa) on the structural change of IIRCN treated at different temperatures. Among WAXD patterns of IIRCNs treated at different temperature under 15 MPa pressure, there might be a development of reflection signal from a large 2θ angle to a small one. In both patterns of IIRCN treated at 80 and 160 °C under 15 MPa pressure, only one reflection peak is obvious. The basal spacing of OMC in IIRCN treated at 80 °C under 15 MPa pressure is 2.08 nm, which is even smaller than that of original OMC (2.24 nm), indicating the existence of un-intercalated structures. The basal spacing of OMC in IIRCN treated at 160 °C under same pressure is 3.18 nm, which is considerably larger than that of the original OMC, revealing the existence of intercalated hybrid structures. In patterns of IIRCNs treated at 140 °C and 100 °C, there are two reflection signals. The position of the low 2θ angle reflection is stable at $\sim$2.12 nm, but its diffraction intensity decreases as the treating temperature increases. In contrast, the position of the high 2θ angle reflection shifts to a high angle and its intensity increases as the treating temperature increases. These results demonstrate that exerting extra pressure at low treating temperature leads to the extrusion of initially intercalated rubber chains out of silicate galleries to even form complete un-intercalated structures; but increasing treating temperature can effectively retard this extrusion.

Figure 2.21 displays the influence of magnitude of extra pressure on the microstructure of IIRCN when thermally treated at 160 °C. It can be seen that there is only one reflection signal in all patterns, and the reflection position does not change considerably with extra pressure changing. Figure 2.22 shows that the intensity of (0 0 1) reflection peak increases remarkably with extra pressure, but changes little when extra pressure exceeds 5.2 MPa. This phenomenon demonstrates that high extra pressure may be favorable to form intercalated structures rather than exfoliated ones.

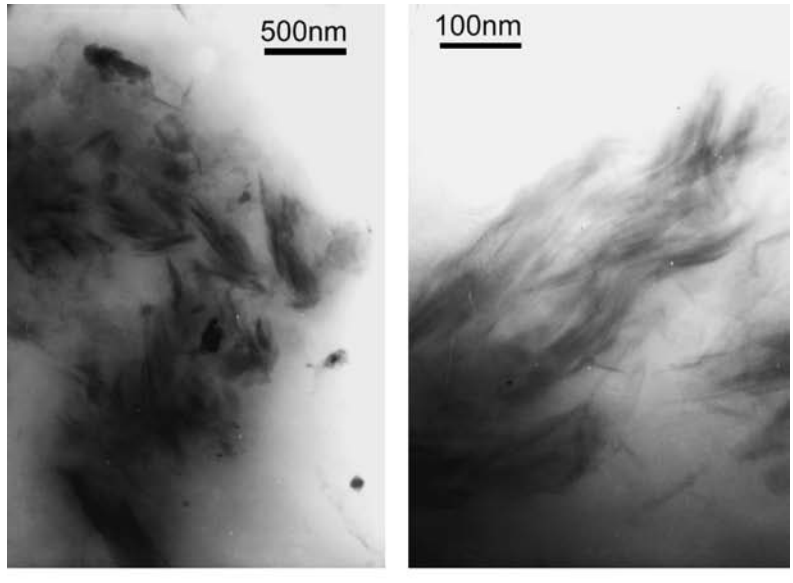

(a) AP ×80°C× 1h sample

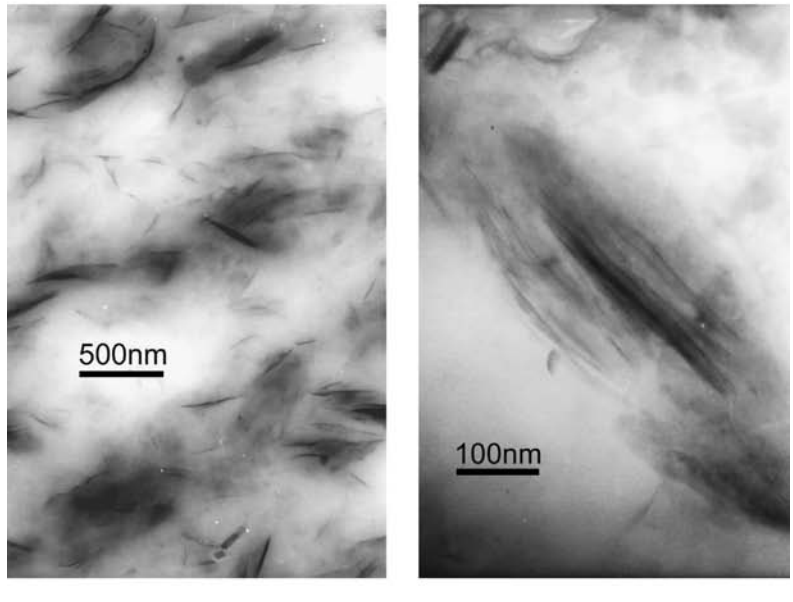

(b) AP×160°C × 1h sample

Figure 2.19 TEM photographs of IIRCN treated at the condition of: (a) AP × 80 °C × 1 h; and (b) AP × 160 °C × 1 h. Left – low magnification; right – high magnification

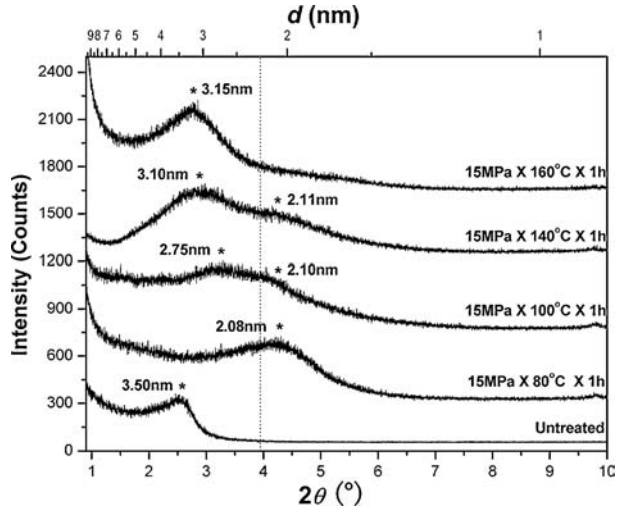

Figure 2.20 WAXD patterns of untreated IIRCN and IIRCNs treated by different temperatures and 15 MPa pressure for 1 h. The asterisks indicate (0 0 1) peaks for OMC dispersed in IIR matrix. The dotted line indicates the location of the silicate (0 0 1) reflection of pure OMC. The curves are shifted vertically for clarity

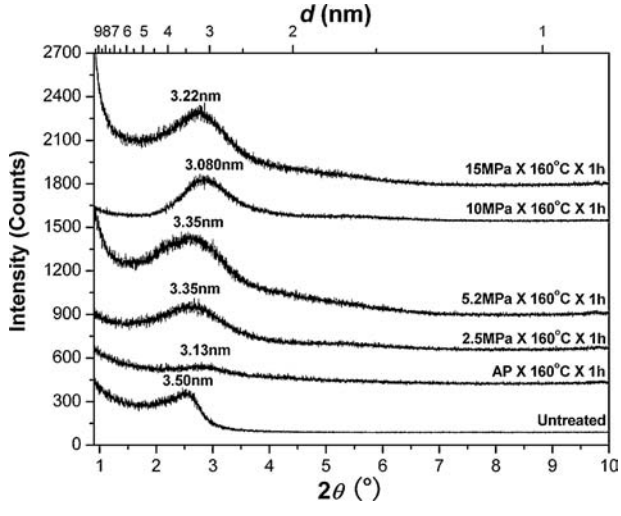

Figure 2.21 WAXD patterns of untreated IIRCN and IIRCNs treated at 160 °C and different pressures for 1 h. The curves are shifted vertically for clarity

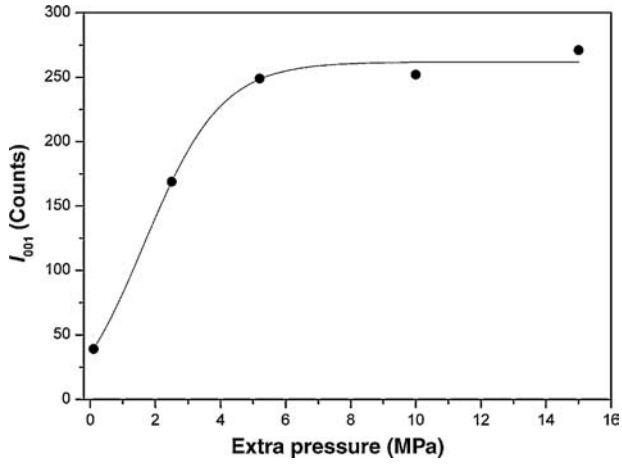

Figure 2.22 The relationship between the intensity of (0 0 1) reflection peak (I_{001}) and extra pressure exerted

On the basis of these experimental results, it can be concluded that:

1. By solution blending, an IIRCN having the intercalated-flocculated structures with low coherence order was obtained, and a considerable amount of solvent molecules remained within silicate interlayers.
2. The thermal treatment at AP and relatively low temperature considerably improves the coherency of intercalated silicates. However, the thermal treatment at AP and relatively high temperature can cause the exfoliation of silicate layers and improve the distribution homogeneity of silicate particles in IIR matrix. In these treated IIRCN, the intercalated structures with improved coherence order and exfoliated silicate layers coexist. When the treating temperature is beyond 140 °C, the exfoliated structure is dominant. The exfoliation of silicate layers is related to the vaporization of residual solvent molecules within silicate interlayers. In addition, the small dimension of dispersed silicate layers facilitates exfoliation during AP thermal treatment at high temperature. Exerting extra pressure during thermal treatment at relative low temperature can cause complete de-intercalation because the residual solvent molecules within silicate interlayers favor the motion of intercalated IIR chains. Increasing the treating temperature retards this de-intercalation, which is also attributed to the vaporization of residual solvent molecules.
3. To obtain a desired morphology in the case of IIRCN: (i) the pressure applied in vulcanization should not be high, (ii) the curing process should be performed at high temperature and (iii) the curing system should be selected to ensure that the curing process has a long scorch period and low curing rate, in order to allow the exfoliation of silicate layers to take place.

2.3.2 *Preparing Exfoliated/Intercalated Nanocomposites*

A novel method for preparation of exfoliated/intercalated nanocomposites is reported by Ma *et al.* based on two steps, that is, preparation of treated montmorillonite (MMT) solution

and solution blending with polymers [14]. After *in situ* polymerization of dimethyldichlorosilane between layers and separation of most polydimethylsiloxane (PDMS), the treated MMT solution shows good storage stability. Although the elemental analyzer shows no residue PDMS, NMR proves residue PDMS still exists in the solution. A lower relaxation time of end-capped CH_3 of alkyl ammonium grafted onto layer surface via ion exchange in the solution shows that the layer spacing was increased significantly or even exfoliated. When the solution was blended with some polar polymers, exfoliated nanocomposites were found. When it was blended with some nonpolar polymers, however, intercalated nanocomposites were obtained. The reason was explained in the light of compatibility between polymer matrix and MMT as well as alkyl ammonium and PDMS grafted on the layer surface. For intercalated nanocomposites, different layer spacing corresponds to different chain flexibility and the presence of multipeaks is caused by the processing of these blends.

2.4 Latex Compounding

Most of the rubbers are available in the form of latex. The layered silicates are able to suspend in water. The water swelling capability of the natural clays depends upon the type of clay and its cation exchange capacity [15]. Compared with the melt or solution method, the approach of co-coagulating rubber latex and clay aqueous suspension (namely LCM), where pristine clay (non-organoclay) is employed, is promising for industrialization due to the low cost of pristine clay, the simplicity of the preparation process and the superior cost/performance ratio.

Zhang *et al.* pioneered this technology by mixing SBR latex with a clay/water dispersion and coagulating the mixture [16]. The structure of the dispersion of clay in the SBR was studied by TEM. The mechanical properties of clay/SBR nanocomposites with different filling amounts of clay were studied. The results showed that the main structure of the dispersion of clay in the SBR was a layer bundle whose thickness was 4–10 nm and its aggregation formed by several or many layer bundles. Compared with the other filler, some mechanical properties of clay/SBR nanocomposites exceeded those of carbon black/SBR composites and were higher than those of clay/SBR composites produced by directly mixing clay with SBR through regular rubber processing means.

Wu *et al.* prepared NBR/clay nanocomposites with excellent mechanical and gas barrier properties by co-coagulating rubber latex and clay aqueous suspension [17]. TEM showed that the silicate layers of clay were dispersed in the NBR matrix at the nanometer level and had a planar orientation.

Rectorite/SBR nanocomposites were prepared by co-coagulating SBR latex and a rectorite/water suspension by Wang *et al.* [18]. TEM showed that the layers of rectorite were well dispersed in the SBR matrix and the aspect ratio (width/thickness) of it was higher than that of montmorillonite (MMT). X-ray diffraction indicated that the nanocomposite produced by this method was of neither intercalated type nor exfoliated type. The gas barrier properties and mechanical properties of the novel nanocomposites were excellent.

In general, polymer/clay nanocomposites are of two different types, namely intercalated structure and exfoliated structure. Carboxylated NBR (CNBR)/clay mixtures were prepared by LCM followed by traditional rubber compounding and vulcanization [19]. The silicate layers were aligned in a more orderly fashion during the compounding. The structure of the

clay/CNBR nanocomposites was a combination of exfoliated and intercalated silicate layers dispersed in the continuous CNBR matrix. The structure was different from intercalated and exfoliated clay nanocomposites, in which the rubber molecules "separated" the clay particles into either individual layers or just silicate layer aggregates of nanometer thickness without the intercalation of rubber molecules into clay galleries. Such a structure was found to result from the competition between separation of rubber latex particles and re-aggregation of single silicate layers during the co-coagulating process.

It was also reported that the flocculant cations, for instance H^+, Ca^{2+} and $RNH_3{}^+$, intercalated into silicate layers. At the same time, the interfacial compatibility was poor without special interfacial modification. It was also found in that way that there was a competition of intercalation between the modifier cations and the flocculant cations, and the amount of rubber-intercalated structure or modifier-intercalated structure strongly depended on the result of the above competition.

2.4.1 *Manufacturing Factors Control*

A novel way to increase the interfacial interaction between pristine clay and rubber was developed by Jia *et al.* [20]. First, a SBR/clay nanocomposite was prepared by LCM with diluted sulfuric acid solution and calcium chloride aqueous solution as flocculating agents. Then, hexadecyl trimethyl ammonium bromide (ab. C16) or 3-aminopropyl triethoxy silane (ab. KH550) was directly introduced into the SBR/clay nanocompounds on a two-roll mill with other ingredients to prepare SBR/clay nanocomposites. Compared with *in situ* modification in suspension, this method seems to be simpler and more feasible. The results acquired can provide some reference to the preparation of high performance rubber/clay nanocomposites with good interfacial interaction.

In experiments, about 2% aqueous suspension of clay and the SBR latex were mixed and vigorously stirred for a given period of time. After that, the mixture was co-coagulated in electrolyte solution (1% calcium chloride aqueous solution, or 2% sulfuric acid solution), washed in water and dried in an oven at 50 °C for 20 h, and then the SBR-clay nanocompound was obtained. (Here it must be made clear that the nanocompounds are referred to as uncured and the nanocomposites as cured.)

The modifier (hexadecyl trimethyl ammonium bromide, or 3-aminopropyl triethoxy silane), the vulcanizing ingredients and other additives were mixed into the nanocompound on a 6-in two-roll mill, according to the recipe listed in Table 2.5. Then the compound was vulcanized in a standard mold at about 15 MPa pressure at 150 °C. The vulcanizates are referred to as SBR/clay nanocomposites. Table 2.6 gives the sample designations of all the SBR/clay nanocomposites.

In order to reveal the effect of heat and pressure on the structure of clay in the rubber matrix, the uncured and cured modified SBR/clay nanocomposites were carefully studied by XRD. The XRD patterns of SBR/clay nanocomposites prepared by different flocculants and organic modifiers are shown in Figure 2.23.

Figure 2.23a gives the XRD patterns for the H^+-flocculated SBR/clay nanocomposites. On the curve of H-cured nanocomposite, there is one peak at $2\theta = 6.29°$, corresponding to a basal spacing of 1.43 nm, a little bit bigger than that of Na^+-MMT, which results from the intercalation of flocculant ions into the clay galleries during the flocculating process. However, this H^+-intercalated structure is a "separated" structure. Although there is no rubber

Table 2.5 Formulation of the mixes

Ingredients	Contents (phr[1])
SBR	100
Clay	10
Hexadecyl trimethyl ammonium bromide (or 3-aminopropyl triethoxy silane)	5 (or 4)
Zinc oxide	5.0
Stearic acid	2.0
Diphenyl guanidine	0.5
Dibenzothiazode disulfide	0.5
Tetramethyl thiuram disulfide	0.2
N-isopropyl-N′-phenyl-*p*-phenylene diamine	1.0
Sulfur	2.0

[1]phr is the abbreviation of weight parts per 100 weight parts rubber.

Table 2.6 Designation of the SBR-clay (100/10) nanocomposites

Flocculant ions	H^+	Ca^{2+}	H^+	H^+	Ca^{2+}	Ca^{2+}
Modifier	No modifier	No modifier	C16	KH550	C16	KH550
Nanocomposite designation	H	Ca	HC16	HKH550	CaC16	CaKH550

macromolecules intercalation, it is still a nanostructure, which can be proved by TEM. For the uncured SBR/clay nanocomposite with C16 added on the two-roll mill, there are three peaks, corresponding to basal spacings of 1.43 nm, 2.08 nm and 4.37 nm, respectively. Obviously the addition of C16 intensively changes the structures of clay in the SBR matrix. Although the H^+-intercalated structure remains, two new structures of C16-intercalated and SBR-intercalated emerge, which indicate that C16 can intercalate into part of silicate layers during general mechanical processing through ion exchange between H^+ and C16. And this C16-intercalation can further induce the intercalation of SBR macromolecules to clay galleries due to the strong shearing force. After vulcanization, similar peaks but with stronger intensity appear for the HC16-cured nanocomposite possibly because of the orientation and re-aggregate of clay layers by hot pressure during vulcanization. Compared with C16, KH550 can completely intercalate into the clay galleries during the compounding process, representing a single peak with a 1.82 nm layer spacing on the XRD patterns. Here the XRD peak of H^+-intercalated structure almost disappears. After vulcanization, this singe peak disappears, and as a result, two new peaks emerge corresponding to layer spacings of 4.41 nm and 1.45 nm. This can be explained by the strong intercalation between H^+ and amine group of KH550; KH550 easily intercalates into the H^+ clay layers. However, on the one hand the layer space of KH550 intercalated clay is small, and on the other hand the physical compatibility between KH550 and SBR rubber chains is not good enough. So the rubber intercalation does not evidently happen during mixing. During the curing process, the KH550 with amine group and ethyl hydroxyl group participates in vulcanization and connects with rubber macromolecules by chemical bonding, so the SBR macromolecules are drawn into some clay galleries and result in the small peak of 4.41 nm on the XRD patterns. For the same reason, part of KH550 is drawn out from the clay galleries. Thus a new peak with 1.45 nm layer spacing is observed.

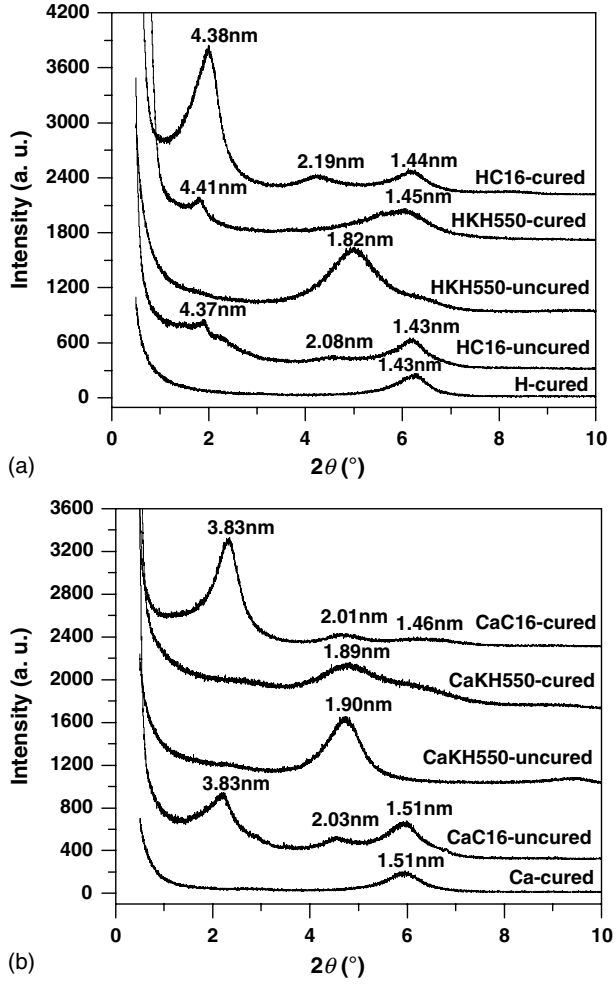

Figure 2.23 X-ray diffraction spectra of SBR-clay nanocomposites flocculated by different flocculating agents: (a) H^+-flocculated system and (b) Ca^{2+}-flocculated system

In the case of Ca^{2+} as flocculant, similar results can be gained except that the clay layer spacings of all kinds of intercalated structures are different. With the bigger size of Ca^{2+}, the layer spacing of a Ca^{2+}-intercalated structure is 1.51 nm. But for uncured and cured CaC16 nanocomposites, the layer spacing of a SBR-intercalated structure changes from about 4.40 nm to 3.83 nm, possibly on account of the strong layer-layer intercalation led by Ca^{2+}. In comparison with Figure 2.23a, the biggest difference in Figure 2.23b is the curve of CaKH550-cured nanocomposite, in which only a single peak is observed, weak but very broad, corresponding to the KH550-intercalated structure of 1.9 nm layer spacing. That is still because that the strong layer-layer interaction of clay led by Ca^{2+} makes it very difficult for KH550 to intercalate into clay galleries during the vulcanization process.

To investigate the effect of modifiers and flocculating agents on the dispersion of clay and interfacial interaction between clay and SBR matrix, the morphologies of a series of SBR/clay nanocomposites were observed with TEM, as shown in Figure 2.24. The dark lines in the photographs are the intersections of the dispersed silicate layers or layer aggregates. It is worth to note that the dispersion of clay in each photo is good. For un-modified SBR/clay nanocomposite, seen in Figure 2.24a and b, the dimensions of the dispersed clay layers are quite fine and their spatial distributions are homogeneous. All the clay layers exist in aggregation with 10–20 nm thickness. In Figure 2.24b, some cavities are observed near the interface between clay layers and rubber matrix, which is caused by the poor interfacial interaction between pristine clay and SBR. Compared with those of a nanocomposite of Ca, the clay layers of a nanocomposite of H disperse more finely and the interfacial strength seems a little better.

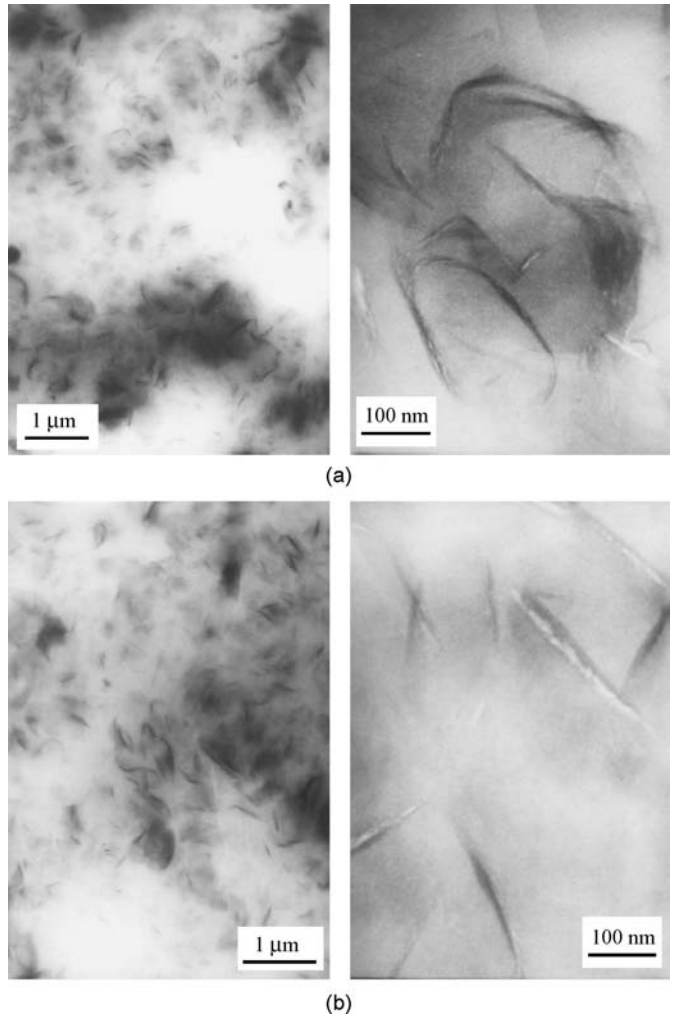

Figure 2.24 TEM photos of SBR-clay nanocomposites: (a) H; (b) Ca; (c) HKH550; and (d) KC16

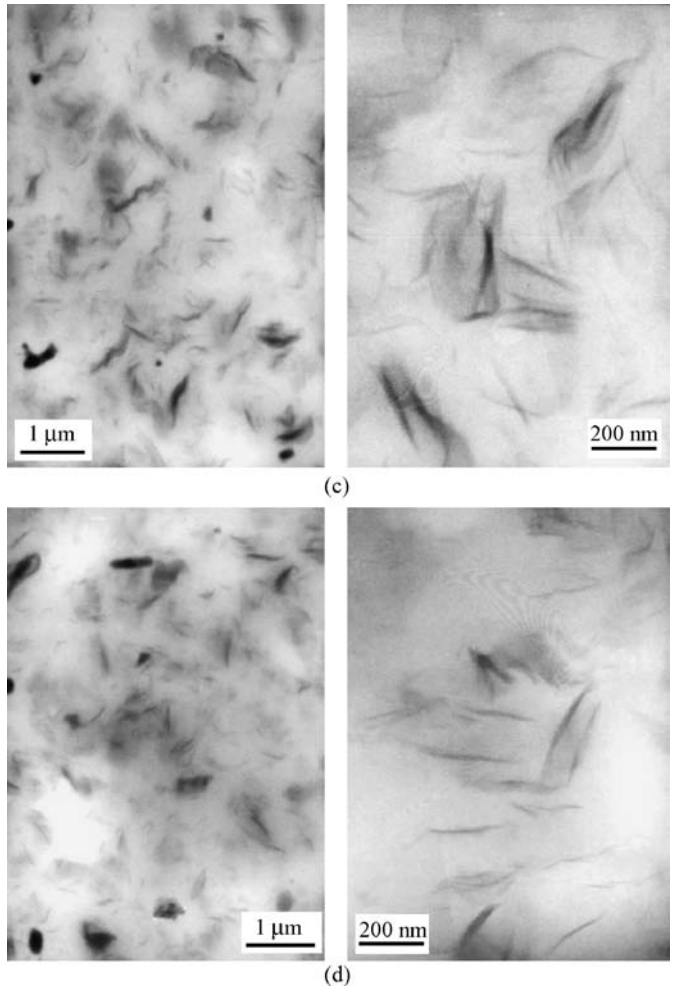

Figure 2.24 (*Continued*)

When KH550 or C16 is used to modify SBR/clay nanocomposites, the dimension of most dispersed clay layers and the amount of clay aggregates are larger. However, no cavity is found on the interface, and dispersion is homogenous. That not only means that the modifier improves the compatibility of nanodispersed clay and rubber, but that organic modifier assembles some layers or aggregates to form layer aggregates assisted by pressure during vulcanization. This implies KH550 and C16 are efficient compatibilizers of clay and SBR. With KH550 modification, in Figure 2.24c, the dispersion of clay is more homogeneous. Comparison of these photos initially demonstrates that KH550 is more efficient. All these results are consistent with that from XRD.

The effect of the amplitude-dependence of the dynamic viscoelastic properties of filled rubbers was performed using RPA2000, which can carry out strain and frequency scanning in a

board range, showing information on the dispersion of filler particles in the rubber matrix. Figure 2.25 shows the dependency of the storage modulus (G') of the uncured modified rubber nanocompounds on the strain amplitude, and a highly nonlinear behavior is observed for each one. It is found that the modulus decreases dramatically with increasing the strain amplitude for all the SBR/clay nanocompounds. This can be explained by "the Payne effect." The severe decrease in the modulus with increasing deformation ratio is due to the disentanglement of uncured rubber macromolecules, and the breakdown of filler-rubber network constructed by filler-filler interaction and filler-rubber interaction. Another observation is that compared with KH550 modified SBR/clay nanocompounds, C16 modified SBR/clay nanocompounds possess higher moduli. At the same time, the moduli of C16 modified SBR/clay nanocompounds decrease faster when the strain is over 40%. This is probably because that the longer alkyl chains of C16 provide strong entanglements with SBR chains or by themselves, which can be described by the sketch in Figure 2.26. However, compared with C16, KH550 has lower compatibility with SBR, thus its effect on helping constructing network is relatively weak. Different from the modified SBR/clay nanocompounds, the reason why the unmodified nanocompounds possess high moduli is that in those nanocompounds, although both the clay-rubber interaction and the compatibility between clay and SBR are weak, the filler-filler interaction is very strong due to filler aggregation.

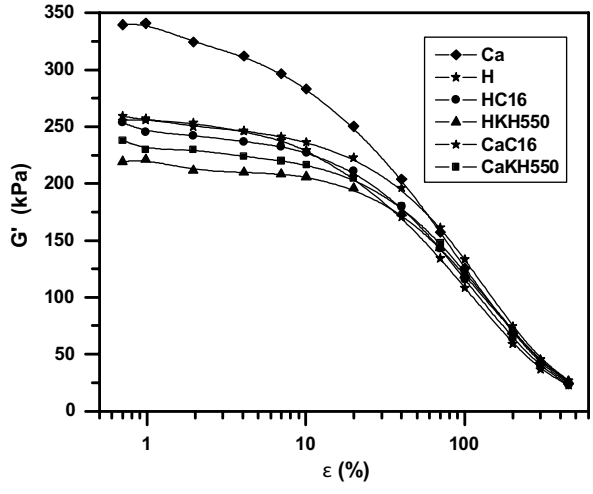

Figure 2.25 RPA analysis of uncured SBR-clay nanocompounds

In order to investigate the dynamic properties of cured modified SBR-clay nanocomposites, the dynamic storage modulus (G') and mechanical loss factor ($\tan\delta$) were also studied. Two zones are found in Figure 2.27a. Zone 1 is the modulus-strain pattern under the 100% strain, in which the dynamic shear storage modulus remains constant. When the strain is over 100%, zone 2 is formed, in which the modulus decreases dramatically, similar with what in Figure 2.25 due to the same reason. In contrast, it can be found that the order in G' of all the modified SBR/clay nanocomposites is HKH550 > CaKH550 > HC16 > CaC16 and the difference between them is very big, different from that observed in Figure 2.25. One must note that, compared with

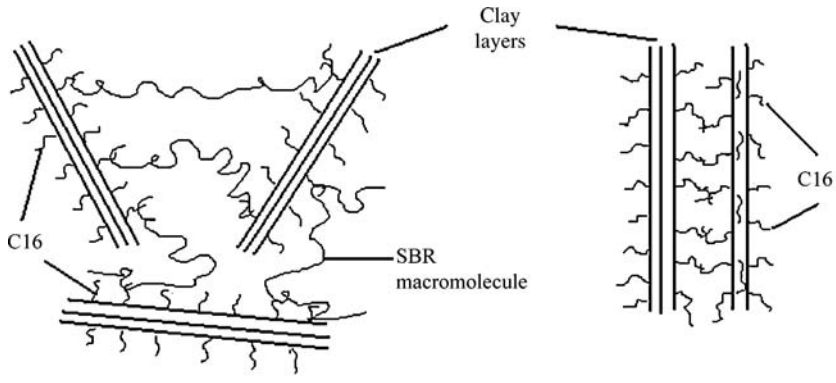

Figure 2.26 Sketch of the physical entanglement between C16 and SBR

Figure 2.27a, the order in the tanδ of all the modified SBR/clay nanocomposites is reversed in Figure 2.27b. Tanδ is dependent on the elasticity of the filled rubber nanocomposites. It is well known that the lower the tanδ, the higher the elasticity. High elasticity implies that the material has an excellent interface. To understand this, the interfacial interaction among these nanocomposites must be analyzed. At first, we must realize that the layer surface interaction is more important compared with edge interaction since the former is much bigger than the latter in area. C16 is physically absorbed on the clay layers, its long alkyl chains only physically interact with rubber molecules chains even after vulcanization. So the interfacial strength of C16 modified SBR/clay nanocomposites is not strong, which results in interface sliding during tensile and high hysteresis during dynamic deformation. However, the $=NH_2$ and $=OC_2H_5$ of KH550 can chemically bond with rubber molecules through participating in a complex curing reaction. Consequently, clay layers act as the chemical crosslinking points, which further markedly increase the modulus of nanocomposites and remarkably reduce the interfacial hysteresis.

In order to test this, the effect of modification on curing characteristics is given in Figure 2.28. Vulcanization is a vital step for rubber product, and the rubber modulus increases dramatically during curing; thus it is used as a monitor to investigate the progress of curing. In Figure 2.28, for unmodified SBR/clay nanocomposites, the occurrence of vulcanization is delayed. This is caused by the combination of the curing agents with fillers by hydrogen bonding. The combined agents do not crosslink SBR until the combination begins to vanish at the curing temperature. The existing of C16 and KH550 can evidently accelerate the occurrence of vulcanization, as shown in curves for modified nanocomposites. For C16-modified SBR/clay nanocomposites, the maximum torque is reached soon and remains constant. Different from this, KH550 can obviously shorten the scorch time at first. But as curing progresses, the curing speed decreases, and the cure time is protracted. Simultaneously the torque keeps increasing all the time. Thus it can be concluded that the existing KH550 participates in the curing reaction and significantly influences the intercrosslinking structure of SBR/clay nanocomposites.

Table 2.7 shows the mechanical properties of pure SBR, unmodified and modified SBR/clay nanocomposites; the corresponding stress-strain curves are presented in Figure 2.29. While the

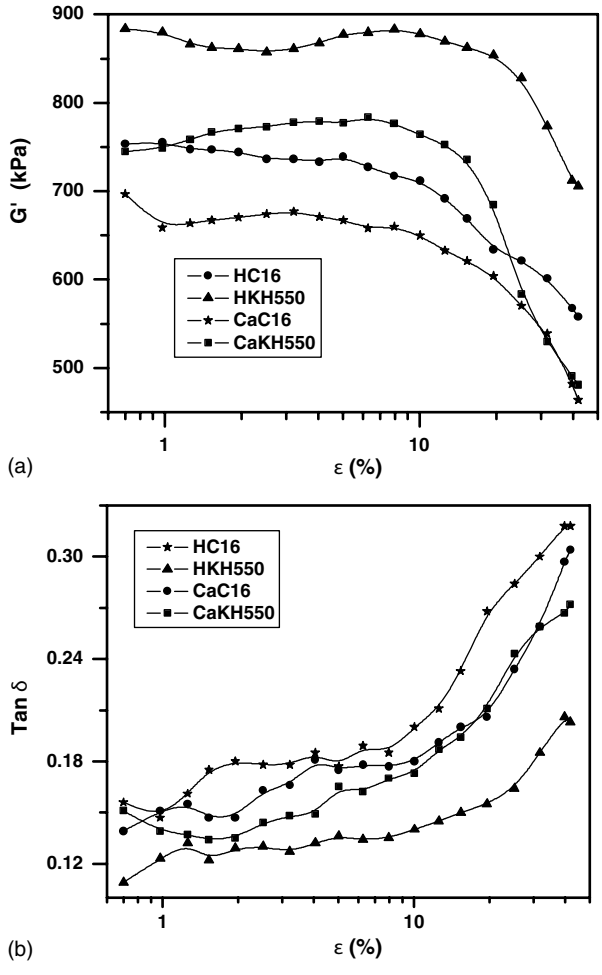

Figure 2.27 RPA analysis of cured SBR-clay nanocomposites

tensile strength of pure SBR is measured at 2.3 MPa, without organic modification, it is only improved to 4.3 or 4.4 MPa with the addition of 10 phr nanoclay by using H^+ or Ca^{2+} as the flocculating agent, respectively. This improvement is big but not enough for the application requirement. Compared with that of un-modified SBR/clay nanocomposite, no obvious improvement in tear strength, or stress at 100% or 300% elongation is found, but tensile strength is improved to about 9.0 MPa for the C16-modified nanocomposites, over 100% improvement, in both systems with H^+ or Ca^{2+} as flocculating agent. With almost the same amount of KH550, the tear strength and the modulus at 100% and 300% of the modified nanocomposites are improved more than 30%, and the tensile strength is also improved 2.5 times of that of un-modified nanocomposites.

As shown in Figure 2.29, the obvious difference appears even at a very small elongation with a value around 40%; and with further increase of elongation, the difference among all the

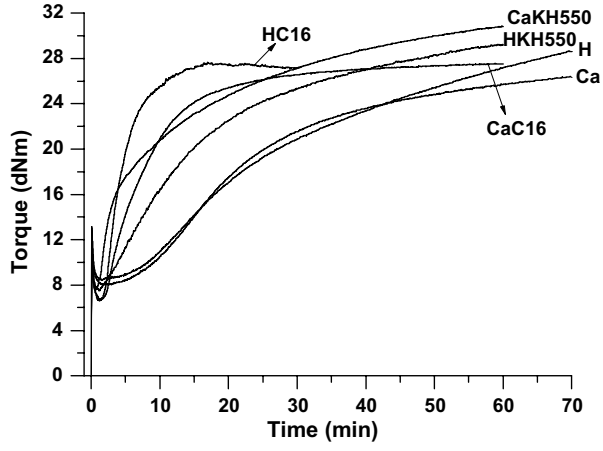

Figure 2.28 Curing curves of all the SBR-clay (100/10) nanocomposites

Table 2.7 Mechanical properties of SBR-clay nanocomposites

Nanocomposite	Shore A hardness	Modulus at 100% strain (MPa)	Modulus at 300% strain (MPa)	Tensile strength (MPa)	Elongation at break (%)	Permanent set (%)	Tear strength ($KN\,m^{-1}$)
Pure SBR	47	0.9	1.1	2.3	632	8	9
H	58	1.4	2.6	4.3	592	24	21
Ca	60	1.2	1.7	4.4	751	36	21
HC16	64	1.9	2.9	9.0	516	28	21
CaC16	62	1.7	2.3	9.4	598	40	20
HKH550	55	1.8	6.8	12.4	504	16	27
CaKH550	57	1.9	5.2	10.1	513	28	26

curves becomes more and more distinct. It can be concluded that in the range of median to large strain (for example, 300% elongation), the stress of H^+-flocculated nanocomposites are higher than that of Ca^{2+}-flocculated nanocomposites for each similar system in which the flocculating agent is the only difference. Likewise, the stress at 300% elongation of the modified nanocomposites is much higher than that of unmodified counterparts. Moreover, the stress at 300% elongation of KH550-modified nanocomposites is higher than that of C16-modified ones in each system using either H^+ or Ca^{2+}. In the following part, the mechanism of reinforcement is discussed from the point of interface sliding and interfacial interaction during the tensile process. It is well known that the modulus at a very small strain provides very important information. Here the modulus mainly relies on the strength of network, indicating the filler dispersion and hardness of the vulcanizate. With 100% elongation, the order of stress of cured nanocomposites is HC16 > CaC16 > CaKH550 > HKH550, which is consistent with the RPA result of uncured SBR/clay nanocompounds and the Shore A hardness of cured SBR/clay nanocomposites. For nanocomposites of H and Ca, the moduli of their uncured nanocompounds are higher than those of the modified nanocompounds because of higher

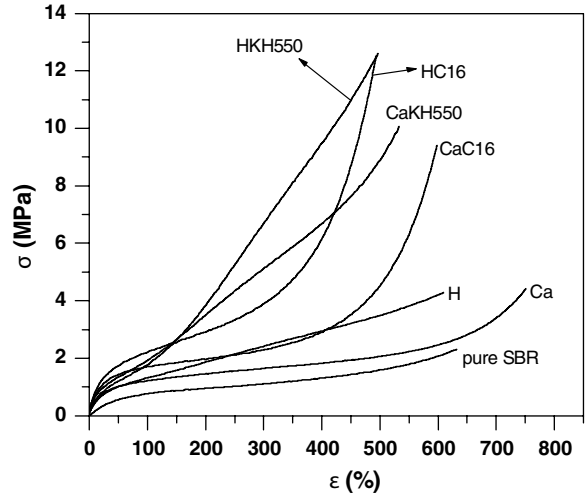

Figure 2.29 Stress-strain curve of cured SBR-clay nanocomposites

filler-filler interaction. However, the stress of their cured nanocomposites is the lowest among all of the SBR/clay nanocomposites because of the worst clay dispersion in the SBR matrix. With increasing strain, the interface interaction between filler and matrix dominates the increase in stress. In general, when the interfacial interaction between clay and rubber is chemical linking, the stress at a certain strain will be dramatically improved. That is why the curve of KH550-modified SBR/clay nanocomposites is in the highest position when the strain level is over 200% and takes on a steep rise. For C16 modified SBR/clay nanocomposites, the interaction between clay and SBR matrix is physical interaction, that is, weak Van der Waals forces. However, the interfacial compatibility between clay and SBR is improved due to the existing of C16. During the tensile process, interface sliding between clay layers and SBR matrix occurs, and the rubber macromolecules chains can gradually make an orientation. At that moment, C16 acts as a bridge, which can delay the detaching between clay and rubber molecules. Thus C16 improves the interfacial compatibility and promotes the rise of stress. For the same modifier-modified system, the stress at same strain level of H^+-flocculated nanocomposite is always higher than that of the Ca^{2+}-flocculated nanocomposite. The difference in stress-stain curves might attribute more to the influence of H^+ on the crosslinking degree of nanocomposites than Ca^{2+}.

2.4.2 The Effect of Rubber Type

To investigate the effect of rubber type on the dispersion of clay in the rubber/clay nanocomposites prepared by LCM, Wu *et al.* [21] prepared four rubber/clay nanocomposites containing 20 phr clay, NR-clay, SBR-clay, NBR-clay, and CNBR-clay by directly co-coagulating the rubber latex and clay aqueous suspension.

In the TEM micrographs shown in Figure 2.30, the dark lines represent the intersections of the silicate layers. Figure 2.30a–d shows that there are both individual layers and stacking

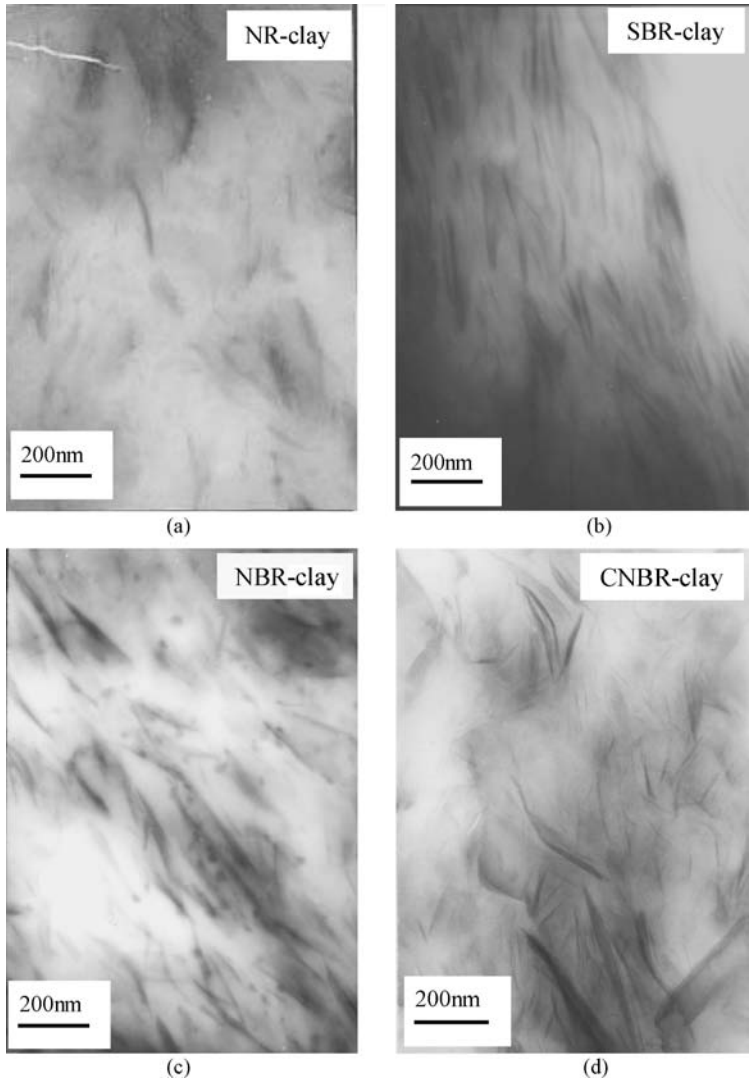

Figure 2.30 TEM micrographs of four rubber/clay nanocomposites: (a) NR-clay; (b) SBR-clay; (c) NBR-clay; and (d) CNBR-clay

silicate layers with a thickness of 10–30 nm. It is worth to note that the dispersion of clay in each of the four rubber matrices is excellent.

The mechanical properties of three rubber/clay nanocomposites, SBR-clay, NR-clay and CNBR-clay, are listed in Table 2.8. Compared to the corresponding conventional rubber/clay composites containing the equivalent amount of clay (20 phr), all three nanocomposites exhibit substantially higher 300% stress, shore A hardness, tensile strength and tear strength. Of particular note is that the tensile strength of SBR-clay nanocomposite exhibited a six times

Table 2.8 Mechanical properties of rubber-clay nanocomposites (NC samples) and conventional rubber-clay composites (MC samples) with 20 phr clay

Sample	SBR-clay		NR-clay		CNBR-clay	
	MC	NC	MC	NC	MC	NC
Stress at 300% strain (MPa)	2.1	7.4	2.7	12.3	5.2	—
Tensile strength (MPa)	2.4	14.5	11.6	26.8	9.0	18.0
Elongation at break (%)	400	548	568	644	444	228
Shore A hardness	52	60	41	54	60	82
Tear strength ($KN\,m^{-1}$)	16.5	45.3	22.8	44.1	24.4	46.5

higher value than that of the conventional SBR-clay composite. The largely increased reinforcement and the tear resistance of the nanocomposites should be ascribed to the dispersed structure of clay at the nano level, the high aspect ratio and the planar orientation of the silicate layers.

The gas permeabilities of SBR-clay, NR-clay and NBR-clay nanocomposites with 20 phr clay are presented in Table 2.9. Compared to the corresponding gum vulcanizates, the nitrogen permeability of SBR-clay, NR-clay and NBR-clay nanocomposites reduced by 54.1%, 46.7% and 47.8%, respectively, and the decrease amplitude is about 50% for all of the three nanocomposites. This implies that the dispersion of silicate layers in SBR, NR and NBR matrix is almost the same.

Table 2.9 Nitrogen permeabilities of clay/rubber nanocomposites with 20 phr clay ($10^{-17}\,m^2\,Pa^{-1}\,s^{-1}$)

Materials	Pure SBR	SBR-clay	Pure NR	NR-clay	Pure NBR	NBR-clay
Permeability	7.4	3.4	13.7	7.3	2.3	1.2

It can be seen that these novel nanocomposites exhibit excellent mechanical and gas barrier properties. Therefore, a conclusion can be made that the method of co-coagulation for preparing rubber/clay nanocomposites is widely applicable to rubbers that exist as a latex.

As mentioned above, the rubber/clay nanocomposites prepared by LCM are different from those of intercalated and exfoliated polymer/clay nanocomposites. They have a kind of partly exfoliated structure, in which the rubber molecules "separate" the clay into either individual layers or just silicate layer aggregates of nanometer thickness without the intercalation of rubber molecules into clay galleries. Therefore, the mechanism for forming nanocomposite structure by the latex route is put forward.

The non-exfoliated layer aggregates in rubber/clay nanocomposites prepared by co-coagulation are formed by the re-aggregation of exfoliated clay layers during the co-coagulating process. Therefore, it is according to the unique nanocompouding mechanism that this kind of structure prepared by co-coagulation is named "separated" structure, where the rubber molecules "separate" the clay into either individual layers or just silicate layer aggregates of nanometer thickness without the intercalation of rubber molecules into clay galleries. In addition, the concept of "separated" structure can also present the difference from partly exfoliated structure prepared by melt blending.

The formation mechanism of "separated" structure can be illustrated by a schematic of the mixing and co-coagulating process (Figure 2.31).

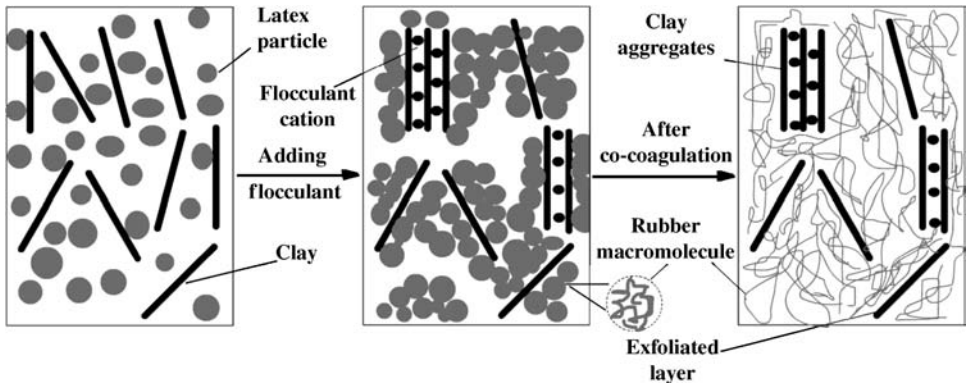

Figure 2.31 Schematic illustration of the mixing and co-coagulating process

At the stage of mixing, the rubber latex particles are mixed with the clay aqueous suspension, in which clay is dispersed as individual silicate layers. After adding a flocculant, the flocculant coagulates the rubber latex and the silicate layers simultaneously, but the rubber macromolecules do not exactly intercalate into the galleries of clay. This mainly results from the competition between separation of rubber latex particles and re-aggregation of single silicate layers upon the addition of flocculant. Since rubber latex particles are composed of several molecules, the existence of latex particles between the galleries of silicate layers in the water medium should result in a completely separated (exfoliated) silicate layers. However, cations of flocculant cause separated silicate layers to re-aggregate so that the rubber latex particles between the silicate layers may be expelled. As a result, there are some non-exfoliated layers in the nanocomposites. In the meantime, due to the fact that the amount of latex is greater than that of silicate layers and the latex particles agglomerate rapidly, the re-aggregation of silicate layers is evidently obstructed to some extent by the agglomerated latex particles around the silicate layers. Consequently, the size of aggregates of silicate layers is at the nanometer level, and the thus obtained nanocomposites contain both exfoliated silicate layers and non-exfoliated (not intercalated) aggregates of nanometer thickness in the rubber matrix.

According to the above nanocompounding mechanism, the factors affecting the final dispersion level of nanocomposites mainly include the size of rubber latex particles, the ratio of rubber latex to clay suspension and the speed of co-coagulation.

It can be expected that the smaller latex particles, the greater latex content and the faster speed of co-coagulating rubber latex and clay layers will provide nanocomposites with fewer non-exfoliated layer aggregates and even completely exfoliated nanocomposites.

Wang *et al.* compared the mechanical properties of clay (fractionated bentonite)/SBR nanocomposites prepared by the solution and latex blending techniques [22] and found that, at equivalent clay loadings, the nanocomposites prepared by the latex route were better than those prepared by the solution blending technique. Moreover, the set properties of the nanocomposites prepared by the latex route were lower than those prepared by solution blending. The TEM

shows that clay was dispersed as one or several layers. The XRD shows that the basal spacing in the clay was increased. It was evident that some macromolecules intercalated to the clay layer galleries. The clay layer could be uniformly dispersed in the rubber matrix on the nanometer level. The mechanical testing shows that the nanocomposites have good mechanical properties. Some properties exceeded those of rubber reinforced with carbon black, so the clay layers could be used as an important reinforcing agent in the same way as carbon black.

2.5 Summary

Rubber/clay nanocomposites can be prepared via melt compounding or solution blending. In the melt compounding method, it is difficult to exfoliate the clay because of the high viscosity due to the polymer high molecular weight. In the solution method, organized clay is mixed with a polymer solution, followed by the evaporation of solvents. However, it is difficult to intercalate polymer chains into the silicate layers in a solution state, and the solvent removal process is troublesome.

A new method named the latex method was developed recently by our group. In the latex method, a clay layer was dispersed in deionized water, followed by mixing with rubber latex. The mixture was then co-coagulated by flocculants. At this stage, exfoliated silicate layers re-aggregated to several layers of silicates of nanometer thickness, and rubber molecules dwelled between several layers of silicates during the co-coagulation process. The advantages of this method are (1) no solvent involved; and (2) readily available intercalation/exfoliation co-existence, leading to highly improved mechanical and barrier performance. In addition, the rubber supplied in the state of latex can be readily used, so that the dispersion effect of nanofillers can be maximized.

Acknowledgments

This research is supported by the National Science Foundation of China (Grant 50673010 and 50725310); J.M. thanks the Australian Research Council for the award of an Australian Postdoctoral Fellowship, tenable at the University of South Australia.

References

1. Hamed, G.R. (2000) Reinforcement of rubber. *Rubber Chemistry and Technology*, **73**(3), 524.
2. Kim, J.T., Oh, T.S., and Lee, D.H. (2003) Preparation and characteristics of nitrile rubber (NBR) nanocomposites based on organophilic layered clay. *Polymer International*, **52**, 1058.
3. Jia, Q.X., Wu, Y.P., Xu, Y.L. *et al.* (2006) Combining in-situ organic modification of montmorillonite and the latex compounding method to prepare high-performance rubber-montmorillonite nanocomposites. *Macromolecular Materials and Engineering*, **291**, 218.
4. Vaia, R.A., Ishii, H., and Giannelis, E.P. (1993) Synthesis and properties of two-dimensional nanostructures by direct intercalation of polymer melts in layered silicates. *Chemistry of Materials*, **5**, 1694.
5. Tian, M., Qu, C., Feng, Y., and Zhang, L.Q. (2003) Structure and properties of fibrillar silicate/SBR composites by direct blend process. *Journal of Materials Science*, **38**, 4917.
6. Teh, P.L., Mohd Isak, Z.A., Hashim, A.S. *et al.* (2006) Physical properties of natural rubber/organoclay nanocomposites compatibilized with epoxidized natural rubber. *Journal of Applied Polymer Science*, **100**, 1083.
7. Kim, J.T., Lee, D.Y., Oh, T.S., and Lee, D.H. (2003) Characteristics of nitrile-butadiene rubber layered silicate nanocomposites with silane coupling agent. *Journal of Applied Polymer Science*, **89**, 2633.

8. Liang, Y.R., Ma, J., Lu, Y.L. *et al.* (2005) Effects of heat and pressure on intercalation structures of isobutylene-isoprene rubber/clay nanocomposites. I. Prepared by melt blending. *Journal of Polymer Science Part B-Polymer Physics*, **43**(19), 2653.
9. Tian, M., Cheng, L.J., Liang, W.L., and Zhang, L.Q. (2006) Overall properties of fibrillar silicate/styrene-butadiene rubber nanocomposites. *Journal of Applied Polymer Science*, **101**(5), 2725.
10. Ganter, M., Gronski, W., Reichert, P., and Mulhaupt, R. (2001) Rubber nanocomposites: morphology and mechanical properties of BR and SBR vulcanizates reinforced by organophilic layered silicates. *Rubber Chemistry and Technology*, **74**, 221.
11. Ganter, M., Gronski, W., Semke, H. *et al.* (2001) Surface-compatibilized layered silicates: a novel class of nanofillers for rubbers with improved mechanical properties. *Kautschuk Gummi Kunststoffe*, **54**, 166.
12. Sadhu, S. and Bhowmick, A.K. (2004) Preparation and properties of styrene-butadiene rubber based nanocomposites: the influence of the structural and processing parameters. *Journal of Applied Polymer Science*, **92**, 698.
13. Lu, Y.L., Liang, Y.R., Wu, Y.P., and Zhang, L.Q. (2006) Effects of heat and pressure on microstructures of isobutylene-isoprene rubber (IIR)/clay nanocomposites. *Macromolecular Materials and Engineering*, **291**(1), 27.
14. Ma, J., Xu, J., Ren, J.H.,*et al.* (2003) A new approach to polymer/montmorillonite nanocomposites. *Polymer*, **44** (16), 4619.
15. Theng, B.K.G. (1979) *Formation and Properties of Clay-Polymer Complexes*, Elsevier Scientific, Amsterdam.
16. Zhang, L.Q., Wang, Y.Z., Wang,Y.Q. *et al.* (2000) Morphology and mechanical properties of clay/styrene-butadiene rubber nanocomposites. *Journal of Applied Polymer Science*, **78**, 1873.
17. Wu, Y.P., Jia, Q.X., Yu, D.S., and Zhang, L.Q. (2003) Structure and properties of nitrile rubber (NBR)-clay nanocomposites by co-coagulating NBR latex and clay aqueous suspension. *Journal of Applied Polymer Science*, **89**, 3855.
18. Wang, Y., Zhang, H., Wu, Y.P. *et al.* (2005) Preparation, structure, and properties of a novel rectorite/styrene-butadiene copolymer nanocomposite. *Journal of Applied Polymer Science*, **96**, 324.
19. Wu, Y.P., Zhang, L.Q., Wang, Y.Q. *et al.* (2001) Structure of carboxylated acrylonitrile-butadiene rubber (CNBR)-clay nanocomposites by co-coagulating rubber latex and clay aqueous suspension. *Journal of Applied Polymer Science*, **82**, 2842.
20. Jia, Q.X., Wu, Y.P., Wang, Y.Q. *et al.* (2007) Organic interfacial tailoring of styrene butadiene rubber-clay nanocomposites prepared by latex compounding method. *Journal of Applied Polymer Science*, **103**(3), 1826.
21. Wu, Y.P., Wang, Y.Q., Zhang, H.F. *et al.* (2005) Rubber-pristine clay nanocomposites prepared by co-coagulating rubber latex and clay aqueous suspension, *Composites Science and Technology*, **65**(7–8), 1195.
22. Wang, Y., Zhang, L.Q., Tang, C., and Yu, D.J. (2000) Preparation and characterization of rubber-clay nanocomposites. *Journal of Applied Polymer Science*, **78**, 1879.

3

Reinforcement of Silicone Rubbers by Sol-Gel *In Situ* Generated Filler Particles

Liliane Bokobza and Amadou Lamine Diop
E.S.P.C.I., Laboratoire PPMD, 10 rue Vauquelin, 75231 Paris Cedex, France

3.1 Introduction

During the past decade, organic-inorganic hybrid materials have attracted tremendous interest because they offer improved properties compared with the corresponding properties in pure organic or inorganic materials. In elastomeric composites, the incorporation of filler particles leads to an increase in stiffness resulting from the inclusion of rigid particles in the soft matrix and also from additional crosslinking sites at the particle-matrix interface. But besides the extent of interaction between the organic and inorganic phases, the level of matrix reinforcement depends on several filler parameters such as the volume fraction of the particles, their size and especially their state of dispersion within the host matrix. The reinforcing qualities of conventional fillers such as carbon blacks and silicas have been widely demonstrated in the literature. These fillers are physically mixed into the polymers before the crosslinking reaction, which tends to produce rather inhomogeneous materials. An alternative synthetic route based on the sol-gel method usually allows the precipitation of the reinforcing phase that is more finely dispersed than in the case of a mechanical mixture. Many organic-inorganic hybrids can be obtained through a sol-gel process, which has proved to be a very simple and efficient approach for the synthesis of composites where an inorganic network is formed within a polymer matrix. Further, this process allows a tailored manipulation of the organic and inorganic phases at a nanometer scale for the synthesis of new materials exhibiting synergistic mechanical and thermal responses.

Rubber Nanocomposites: Preparation, Properties and Applications Edited by Sabu Thomas and Ranimol Stephen
© 2010 John Wiley & Sons (Asia) Pte Ltd

The sol-gel process involves inorganic alkoxides ([M (OR)$_x$], where M = Si, Ti, Zr, Al,... and R is an aliphatic group) that are hydrolyzed and condensed in the presence of a catalyst, in order to form M−O−M bridging units.

The structure of the generated inorganic particles depends on the hydrolysis and condensation conditions and especially on the type of alkoxide and catalyst. The molecular weight of the polymer, the filler concentration and the nature of the interfacial interactions between the organic and inorganic phases are additional factors that have a significant effect on the morphology of the composite.

A controlled combination of the different factors that affect the composite structure leads to the synthesis of composite materials with tailored properties. But, incorporating particles through sol-gel *in situ* precipitations avoids agglomeration of the reinforcing filler frequently obtained by the usual blending of the filler into the polymer prior to its crosslinking into an elastomeric network.

The primary goal of this chapter is to give a better understanding of the structure-property relationships in some hybrid organic-inorganic materials obtained by means of a sol-gel process. Silica and titania are chosen as the inorganic phases and poly(dimethylsiloxane) (PDMS) as the organic phase.

3.2 Synthetic Aspects

3.2.1 General Considerations

Pioneered by Mark for essentially filling silicone rubbers [1–7], the sol-gel process has been successfully extended to various other polymers [8–20]. The *in situ* organic-inorganic systems are often called nanocomposites on account of the small size of the generated structures.

The work previously reported on the reinforcement of PDMS by *in situ* generated filler particles [1–7], is essentially related to silicone elastomers formed by the use of functionally terminated PDMS fluids that undergo catalyzed crosslinking reactions.

Typically, silica formation via the sol-gel process based on the polymerization of tetraethoxysilane (TEOS) used as the inorganic precursor can be carried out before or after or alternatively during curing [21]. In the third procedure, hydroxyl-terminated PDMS chains are blended with enough TEOS to simultaneously end-link the precursor chains and provide the silica particles.

Two reactions are generally used to describe the sol-gel synthesis of silica from TEOS:

$$Si(OC_2H_5)_4 \xrightarrow{\text{hydrolysis}} Si(OH)_4 + C_2H_5OH$$

$$Si(OH)_4 + Si(OH)_4 \xrightarrow{\text{polycondensation}} (OH)_3Si \cdots O \cdots Si(OH)_3 + H_2O$$

This process which can be carried out at relatively low temperatures in host polymeric matrices, leads to samples exhibiting excellent mechanical properties and optical transparency.

The generated inorganic structures highly depend on the hydrolysis and condensation conditions and essentially on the nature of the catalyst used to accelerate the gelation process. The role played by the catalytst in the sol-gel processing of silica has been thoroughly examined by Pope and Mackenzie [22]. Also, the mechanisms and kinetics of the hydrolysis-condensation

reactions have been widely discussed on the basis of the water content and on the pH dependence of the gelation process [23, 24].

Large spherical particles are expected in the case of base-catalyzed reaction while linear chain growth is suggested via acid catalysis. Silica polymerization in the solution precursor is generally described by models of nucleation, growth and aggregation. Kinetic models based on fractal geometry concepts were developed and applied for the analysis of small-angle X-ray scattering profiles in order to gain information on the morphology of the inorganic entities.

A wide range of complex structures were obtained for *in situ* silica-filled poly(dimethylsiloxane) networks prepared by various synthetic protocols [4, 7]. Nevertheless, the typical fractal patterns and morphologies described in the case of the polymerization of silica in solution are not exactly those observed when the polymerization is carried out in PDMS [4]. This is most probably due to the constraints provided by the polymer environment. Jackson *et al.* [25] have analyzed the changes in the morphology of organic-inorganic hybrid materials when the relative rates of polymerization of the organic and inorganic phases are changed. A strong phase separation has been observed when the polymerization is fast with respect to the sol-gel reaction while a faster sol-gel polymerization leads to a finer morphology and more diffuse interfacial regions between the two phases.

3.2.2 Adopted Protocols

This chapter concentrates essentially on the sol-gel process carried out under different catalytic conditions in already formed networks by using a synthetic protocole different from those previously reported. Generating silica structures within a preformed PDMS network is expected to prevent the formation of large silica aggregates. But the synthetic protocol for the filling process before the crosslinking reaction is also presented for purpose of comparison. We deal with the synthesis, characterization and properties of the filled systems with a special emphasis on the polymer-filler interface, which plays a crucial role on the mechanical properties of the resulting materials.

3.2.2.1 Synthesis of the Unfilled Networks

Unfilled PDMS networks can be obtained by end-linking polymer chains by means of a multifunctional crosslinking agent. This type of process using α,ω-bifunctional polymers of known molecular weight reacting with adequate multifunctional reagent are widely used to obtain elastomeric networks with structures expected to be as close as possible to ideality [21, 26, 27]. Samples can be obtained by the hydrosilylation reaction (that is, the addition of a silyl function $-$SiH of precursor chains of hydride-terminated PDMS to an unsaturated C=C bond of the crosslinking molecule [27] or the addition of vinyl functional polymers to a SiH group of a tetrafunctional siloxane [28]). In both cases, the hydrosilylation reaction is catalyzed by a platinum complex (that is, platinum-divinyltetramethyldisiloxane). Alternatively, terminal silanol functional PDMS are able to condense to alkoxy systems (the most widely used being TEOS) under a tin compound catalyst. Nevertheless the reaction between hydroxyl-terminated PDMS and TEOS is difficult to control and, to be efficient, requires, as often reported in the literature [29, 30], larger amounts of TEOS than the stochiometric equivalent. A typical synthesis started from OH-terminated precursor chains is described below.

Hydroxyl-terminated PDMS (molecular weight = 18 000) supplied by Gelest is mixed for 30 min with TEOS, in excess of 50%, and used here as the crosslinking agent. A small amount of stannous-2-ethyl-hexanoate used as catalyst, is then added to the mixture under mechanical stirring just for 5 min to avoid a crosslinking reaction during mixing. The reacting mixture is slowly cast into a Teflon mold and left for a few minutes at room temperature then at 80 °C for one day for complete curing. The films are extracted with toluene for 72 h to remove any unreacted materials. The sol fractions are between 4 and 5%.

In the previous studies, PDMS networks were synthesized by using a stochiometric balance between ethoxy groups of the tetrafunctional alkoxysilane crosslinker and the hydroxyl chain ends of the hydroxyl-terminated PDMS precursor chains in order to get model networks characterized by constant junction functionality and known molecular weight between crosslinks (close to the number average molecular weight of precursor chains) [1–7]. In fact, networks prepared at stoichiometric conditions have an elastic modulus lower than that deduced from the molecular weight between crosslinks and great soluble fraction (around 10%). This may be due to the volatility of TEOS thus reducing the amount of crosslinker required for the alkoxy-functional condensation reaction. Much greater ratios of crosslinker functions to chain ends than that required by stoichiometry have already been used in the literature [29, 30] but in our case, we carried out a systematic study of the effect of excess of TEOS on the mechanical properties of networks synthesized from OH-terminated chains. A 50% excess (and not higher values as already reported) are enough to ensure correct modulus and reasonable soluble fraction.

3.2.2.2 Procedures for Composite Preparation

In Situ *Filling Process of Already Formed Networks*

For silica *in situ* precipitation, the PDMS films are swollen in TEOS in the presence of a pH-neutral catalyst: dibutyltin diacetate (DBTDA) or an acid catalyst (HCl) used at 3 wt%. The swelling time determines the degree of TEOS absorption and thus the filler loading. Both the TEOS-swollen film and a beaker containing water are placed for 48 h into a desiccator maintained at a constant temperature (30 °C) thus exposing the swollen film to saturated water vapor. The film is then vacuum-dried at 80 °C for several days to constant weight in order to remove any alcohol generated from the reaction and also the remaining TEOS which has not been hydrolyzed.

Some samples are also prepared according to the procedure already reported [4, 7] which consists of immersing the TEOS-swollen network into an aqueous solution containing 3 wt% of a base catalyst (diethyl amine (DEA) or ammonia) for one day. The films were then removed from solution and vacuum-dried as described above.

The amount of filler incorporated into the network was calculated from the weights of the films before and after the generation of the filler.

PDMS elastomeric composites containing titania (TiO_2) instead of silica (SiO_2) can be also prepared by replacing the hydrolysis of TEOS by the hydrolysis of an organo-titanate. Titania is well known to improve weather resistance and heat stability of silicone rubbers [3]. But in comparison with silica alkoxides, titanium alkoxides have much higher reactivity, resulting in the formation of precipitates. It has been shown that the resistance to hydrolysis increases with the increase in chain length of the alkyl chain [31]. Therefore, as in other studies [32, 33] titanium *n*-butoxide (TBO) has been chosen as the precursor of TiO_2 in the sol-gel process.

Figure 3.1 compares the time dependence of the degree of swelling of PDMS films (around 1 mm thick) in the two alkoxides at room temperature. It has to be mentioned first that the swelling behavior of the film is not affected by the presence of the catalyst. Second, at a given swelling time, a much higher swelling ratio is obtained with TEOS most probably on account of the easier diffusion of TEOS into the elastomer due to its lower viscosity.

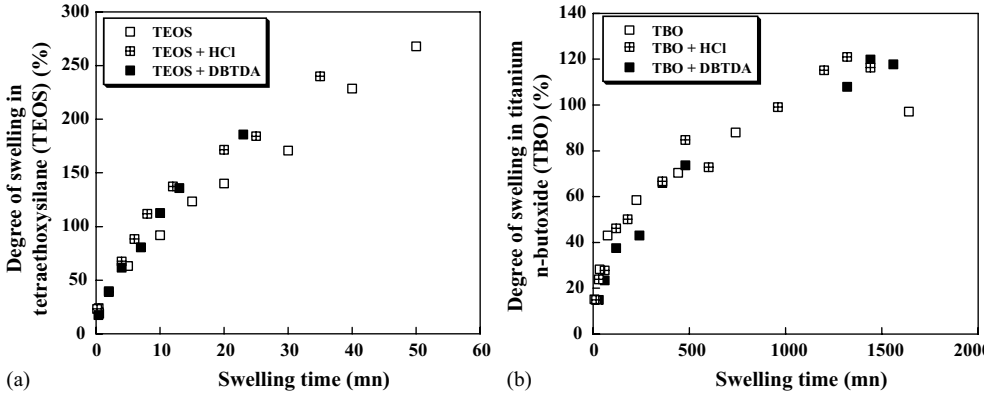

Figure 3.1 Time dependence of the degree of swelling of PDMS films around 1 mm thick in the pure respective alkoxides: (a) tetraethoxysilane (TEOS) or (b) titanium *n*-butoxide (TBO), and in the presence of HCl or dibutyltin diacetate (DBTDA) used as catalysts

One way to quantify the diffusion phenomenon of the alkoxide into the polymer film, is to plot the experimental data according to a Fick model (Figure 3.2):

$$m_{\text{alkoxide}}/m_{\infty} \propto D^{1/2}t^{1/2}e^{-1}$$

where m_{alkoxide} is the mass of absorbed alkoxide at a given time, m_{∞} is the mass of absorbed alkoxide at $t \rightarrow \infty$, D is the diffusion coefficient and e is the thickness of the sample. It can be seen that the rate of diffusion of TEOS is much faster than that of TBO in PDMS films.

Nevertheless, under the described experimental conditions, at small filler loadings the films are not swollen to equilibrium and one may expect the diffusion phenomenon to go on, once the film is removed from the alkoxide, in order to ensure a homogeneous distribution of the filler particles within the matrix. This point was checked by transmission electron microscopy (TEM) of a sample microtomed at $-140\,^{\circ}\text{C}$, without the use of any dye, to obtain the cross-section through the thickness of the sample. The TEM image of a PDMS film filled with 23 phr (phr = parts of filler per hundred parts of elastomer) of TiO_2 catalyzed by 3 wt% of DBTDA does not display any gradient of filler concentration, the filler particles being homogeneously dispersed throughout the thickness of the film (Figure 3.3).

Fourier transform infrared spectroscopy (FTIR) using attenuated total reflection technique (ATR), which is particularly well-suited for the study of thick films, allows the analysis of the changes in the infrared spectra occuring during the hydrolysis reaction. The *n*-butoxide displays two absorption bands located at 1461 and 1374 cm^{-1}, assigned to the deformation modes of the methyl and methylene groups [34] (1461 cm^{-1} corresponds to the scissoring vibration of the

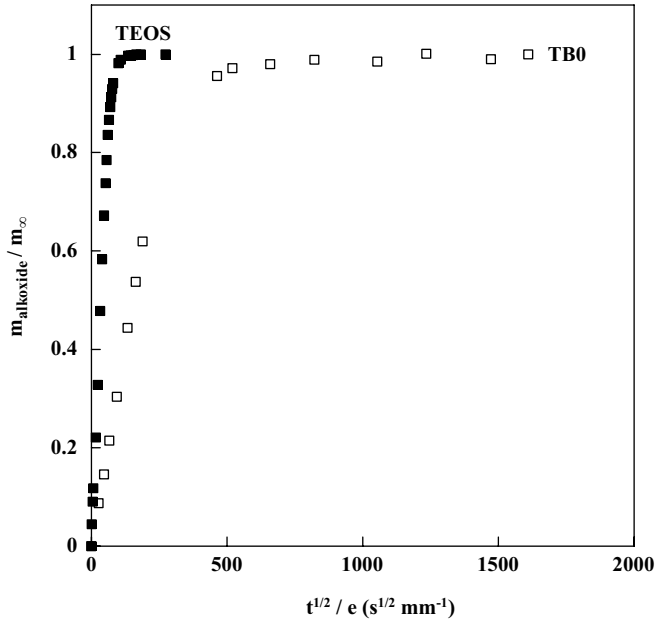

Figure 3.2 Ratios of alkoxide absorption at a given time, m_{alkoxide}, against m_{∞} (mass of absorbed alkoxide at $t \rightarrow \infty$) as a function of $t^{1/2}/e$, as suggested by the Fick model

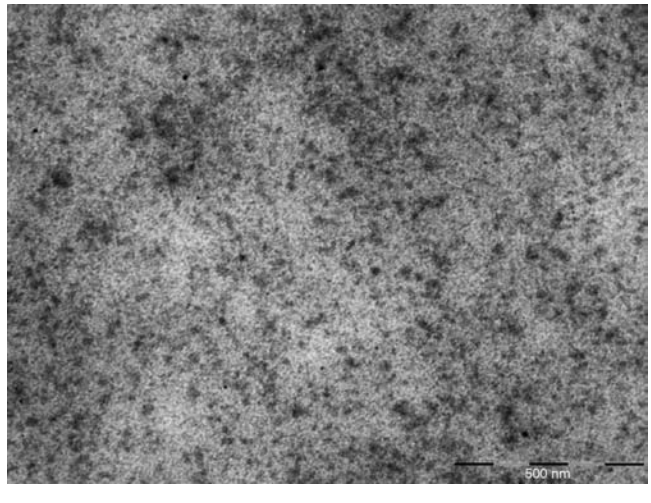

Figure 3.3 TEM image of a DBTDA-catalyzed PDMS composite containing 23 phr of TiO_2, sliced through the thickness of the film

CH_2 group and asymmetric CH_3 bending, while the band at 1374 cm^{-1} corresponds to symmetric CH_3 deformation; Figure 3.4). We note a progressive reduction in intensity of these two bands during the hydrolysis process and a total disapperance after total reaction.

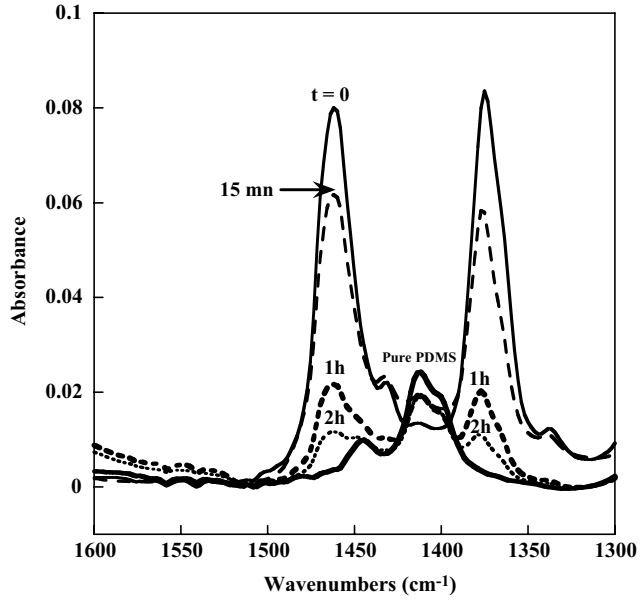

Figure 3.4 ATR spectra of a PDMS film swollen with titanium *n*-butoxide (TBO) and taken at different times (0 min, 15 min, 1 h, 2 h) during the hydrolysis process

In contrast, silica formation within the preformed PDMS network can be visualized in the infrared spectra of the silica-filled PDMS networks, where it is seen that the bands associated with silica increase with the silica content in the composite (Figure 3.5). It is interesting to mention that, on account of similar chemical structure, the matrix which is constituted of poly (dimethylsiloxane) polymer chains has an infrared spectrum very similar to that of the bulk spectrum of silica itself.

As seen in Figure 3.6, our synthetic protocols ensure that the real filler loading is very close to the theoretical one, represented as the straight lines and calculated by assuming a total conversion of the alkoxide into silica or titania.

In Situ *Filling Process Before the Crosslinking Reaction*

In the second protocol in which the sol-gel reaction is conducted before the crosslinking process, low viscosity silanol terminated PDMS fluids (viscosity $\leq$ 100 cSt and molecular weight $\leq$ 4000) are mixed with a given amount of TEOS (calculated in order to get a given filler loading) added with 3 wt% of dibutyl diacetate. A small beaker full of water is maintained on the top of the jar holding the reaction mixture. The jar is closed and the mixture is exposed for 48 h, under continuous magnetic stirring, to saturated water. A further addition of TEOS in excess of 50% with regard to the stoichiometric balance is carried out in order to proceed to the endlinking reaction and after further stirring for 30 min, followed by the incorporation of the

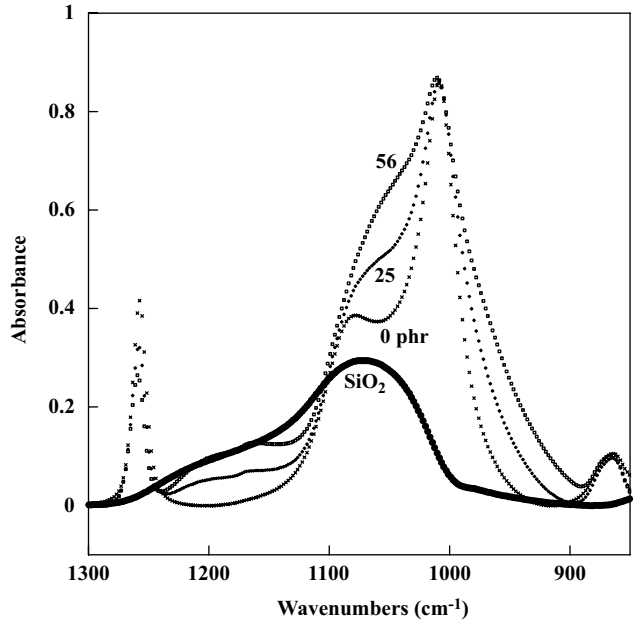

Figure 3.5 ATR spectra of pure silica, pure PDMS and of PDMS/SiO_2 composites: each curve is labeled with the amount of filler and all spectra are normalized at the band of PDMS, located at 1011 cm^{-1}

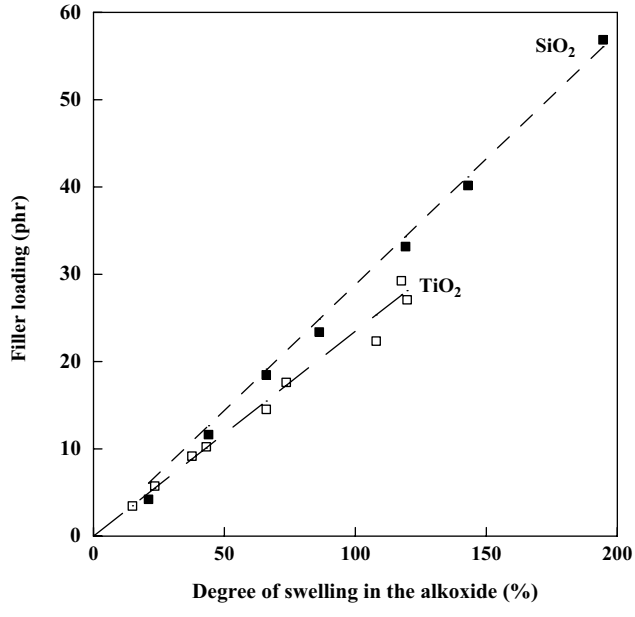

Figure 3.6 Dependence of the filler loading on the degree of swelling in the alkoxide (TEOS for SiO_2, TBO for TiO_2, both generated under DBTDA catalyst). The squares are the experimental points and the straight lines are the theoretical amounts of filler

catalyst (stannous-2-ethyl-hexanoate), the reacting mixture is cast into a Teflon mold and cured at 80 °C as described above.

The present chapter only concentrates on the sol-gel process carried out in already formed PDMS networks.

3.3 Properties of the Hybrid Materials

3.3.1 State of Dispersion

Filled elastomeric materials usually display improved bulk properties relative to the base polymer. In particular, the incorporation of filler particles leads to an increase in stiffness resulting from the inclusion of rigid particles in the soft matrix and also from additional crosslinking sites at the particle-matrix interface [35–37]. In addition to the volume fraction of the particles, filler parameters such as specific primary particle and aggregate size, spatial morphology or "structure" and surface characteristics are well known to have a strong influence on the mechanical response of the resulting material. However, full realization of the filler capability can only be achieved if the filler is well dispersed in the rubbery matrix.

Figure 3.7 shows TEM images of DBTDA-catalyzed composites filled with SiO_2 (Figure 3.7a and c) or TiO_2 (Figure 3.7b and d) particles *in situ* generated in already formed PDMS networks. The *in situ* technique is seen to give much better dispersions than simple blending of the particles into the polymers prior to the crosslinking process. But although *in situ* precipitated filler particles seem uniformly dispersed in both cases, different morphologies are revealed. The diameter of the generated silica particles is seen to be much smaller than that of titanium dioxide particles. The composite containing 10 phr of SiO_2 (Figure 3.7a) shows an excellent dispersion of the mineral phase in the polymer with small silica domains around $\sim$5 nm in diameter and rather diffuse interfaces. For the higher content, a fine morphology of the silicate structure is still obtained suggesting an interpenetrated polymer-silica structure. TEM images of titania-filled PDMS composites indicate an obvious two-phase structure with particles approximately spherical in shape and diameters between 20 and 40 nm in size. The interface between the polymer and the particles is better defined than in the case of silica-filled systems and even at the lowest filler content (Figure 3.7b), the titania particles are almost connected in a branched network structure.

3.3.2 Stress-Strain Curves

Stress-strain curves for pure PDMS and DBTDA-catalyzed PDMS composites are shown in Figure 3.8. The measurements were carried out simply by stretching strips of materials between two clamps by means of a sequence of increasing weights attached to the lower clamp. The distance between two marks was measured with a cathetometer after allowing sufficient time for equilibration.

With regard to the unfilled state which displays extremely poor mechanical strength, great improvements in modulus and rupture properties are achieved with the use of in-situ generated filler particles. For each type of particles, the stress increases with the increase in the amount of filler precipitated into the networks. In order to quantify the extent of reinforcement provided by each type of filler, values of stress at a given deformation are reported in Table 3.1. It is interesting to mention for both types of composites that at high filler loadings, a change in the

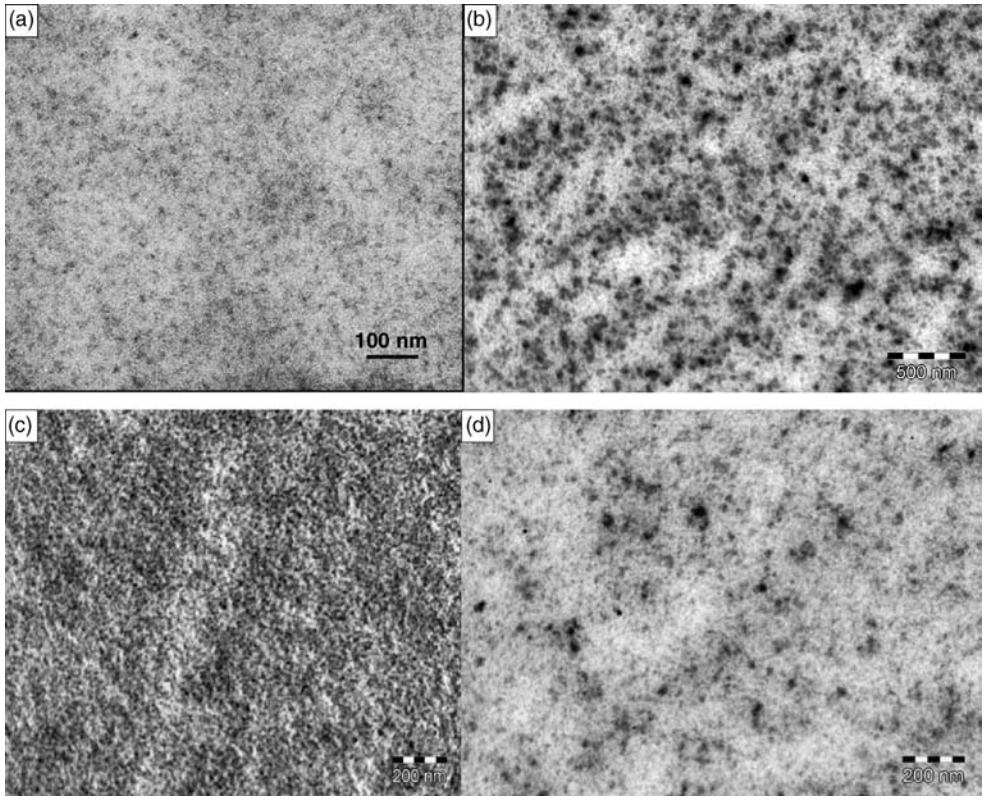

Figure 3.7 TEM images of DBTDA-catalyzed PDMS composites filled with *in situ* generated particles: (a) 10 phr of SiO_2; (b) 12 phr of TiO_2; (c) 28 phr of SiO_2; and (d) 25 phr of TiO_2 (Reprinted from *Polymer*, **46**, L. Dewimille, B. Bresson and L. Bokobza, "Synthesis, Structure and Morphology of Poly(dimethylsiloxane) Networks Filled with in situ Generated Silica Particles," 4135–4143, © 2005, with permission from Elsevier.)

shape of the curve is observed: the mechanical behavior is close to that of a thermoplastic polymer with a well defined yield point followed by a smaller strain dependence of the stress. This plastic behavior, which may be the result of the formation of an interconnecting filler network, is much more pronounced for the PDMS/TiO_2 composite as it can be seen in Figure 3.9 which compares the strain dependence of the nominal stress (Figure 3.9a) and the reduced stress, σ^*, ($\sigma^* = \sigma/[\alpha - \alpha^{-2}]$, where σ is the nominal stress and α is the extension ratio), for composites containing almost the same amount of filler. The PDMS/SiO_2 composite shows better reinforcement at large elongations which is also visualized by the higher value of the reduced stress (Figure 3.9b). But the large decrease in the reduced stress observed at small deformations for the sample filled with titania results from the destruction of the filler network upon application of the deformation. This "Payne effect" is generally demonstrated through the analysis of the low strain dynamic mechanical properties which describe the viscoelastic response of the rubbery material to periodic deformation. This effect will be discussed below.

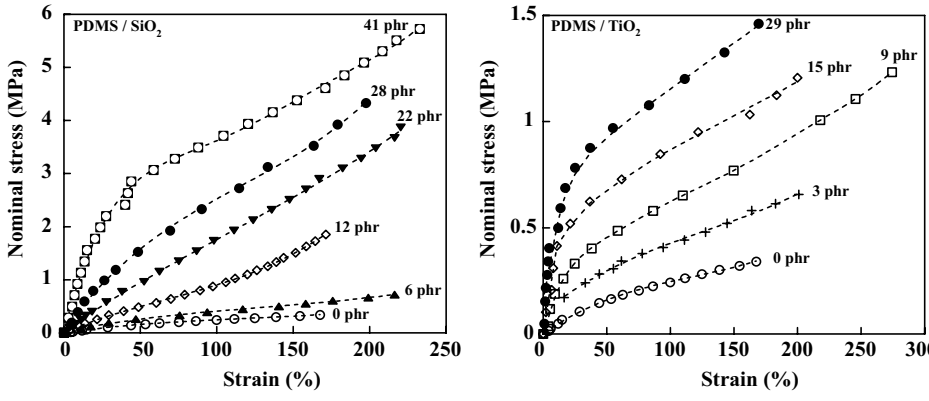

Figure 3.8 Stress-strain curves at room temperature for PDMS filled with *in situ* generated particles (SiO_2, TiO_2) in the presence of dibutyltin diacetate as catalyst

Table 3.1 Mechanical properties of PDMS and PDMS filled with *in situ* generated particles

Sample	Volume fraction of filler	Stress at 50% (MPa)	Stress at 100% (MPa)	Stress at 150% (MPa)
Pure PDMS	0	0.155	0.244	0.319
PDMS + 6 phr SiO_2	0.0283	0.259	0.399	0.518
PDMS + 12 phr SiO_2	0.0550	0.487	0.897	1.495
PDMS + 22 phr SiO_2	0.0964	0.957	1.754	2.551
PDMS + 28 phr SiO_2	0.1195	1.575	2.512	3.329
PDMS + 41 phr SiO_2	0.1660	2.950	3.688	4.266
PDMS + 3 phr TiO_2	0.0072	0.299	0.419	0.533
PDMS + 9 phr TiO_2	0.0214	0.454	0.618	0.770
PDMS + 15 phr TiO_2	0.0351	0.673	0.862	1.027
PDMS + 29 phr TiO_2	0.0657	0.942	1.146	1.365

Another interesting point appearing in Table 3.1 is the fact that, at constant wt% content, the TiO_2 composite has a somewhat lower volume fraction of filler because TiO_2 has a higher density than SiO_2. As the theoretical models intended to predict the mechanical properties of composite materials are essentially based on the volume fraction of filler, it was interesting to compare the dependence of the stress at a given strain value on the filler volume fraction (Figure 3.9c). The two sets of data do not significantly differ but there is a very large discrepancy between the experimental data and the Guth and Gold equation [38] which predicts the increase in the modulus imparted to the soft matrix by the inclusion of rigid spherical particles:

$$G = G_0(1 + 2.5\Phi + 14.1\Phi^2)$$

where G_0 is the modulus of the matrix and Φ is the volume fraction of filler. The difference arises from interactions between the elastomer and the filler leading to an increase in the effective degree of crosslinking.

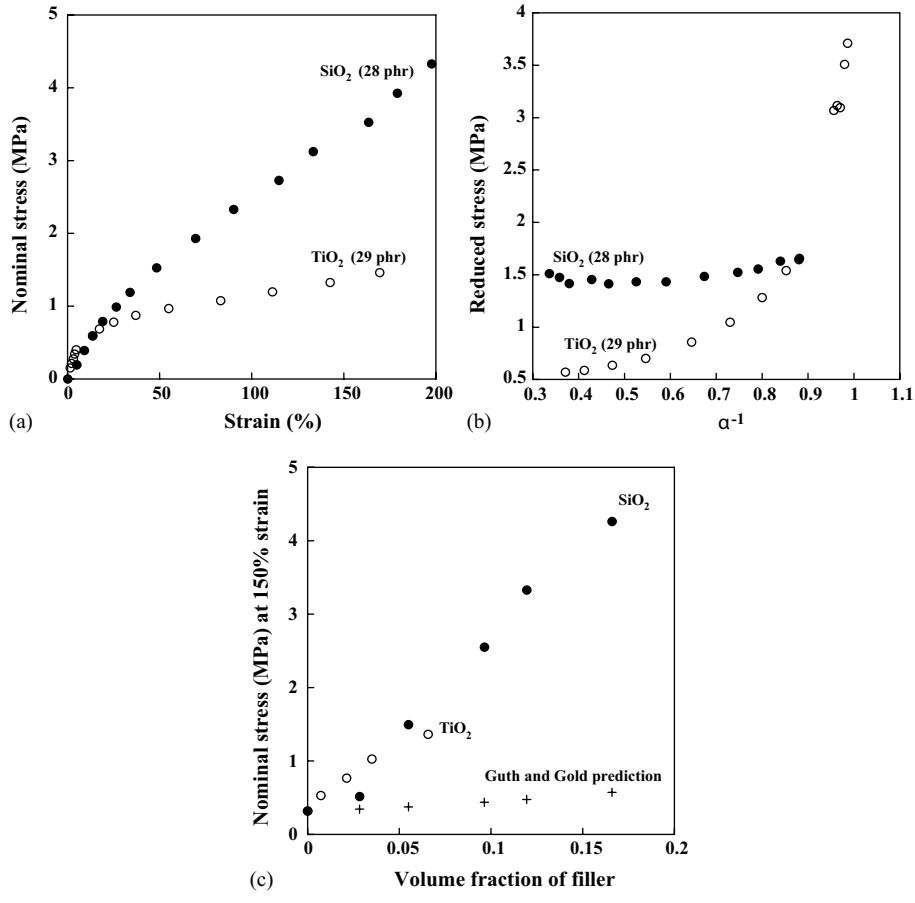

Figure 3.9 Effect of the filler nature on the stress-strain behavior of PDMS composites

3.3.3 Low Strain Dynamic Properties

The addition of mineral fillers into elastomeric matrices strongly modifies the viscoelastic behavior of the material at small strains and leads to the occurrence of a nonlinear behavior, the Payne effect [39], characterized by a drop in the elastic modulus G' with an increase in the amplitude of small-strain oscillations, while the loss modulus G'' passes through a maximum. The dynamic behavior of filled rubbers is of great importance in the performance of rubber engineering and is essential in tire applications thus explaining the considerable interest in the past decade for the Payne effect [40–44]. The amplitude $\Delta G' = (G'_0 - G'_\infty)$ of the Payne effect, where G'_0 and G'_∞ are the maximum and minimum values of the storage modulus respectively, depends on several filler parameters: concentration, surface area, surface characteristics, and temperature. At larger deformations, the difference between unfilled and filled rubber (G'_∞) contains the contribution arising from the inclusion of rigid particles (accounted for by the Guth and Gold expression [38] and also the contribution of the polymer-filler crosslinks to the network structure (Figure 3.10).

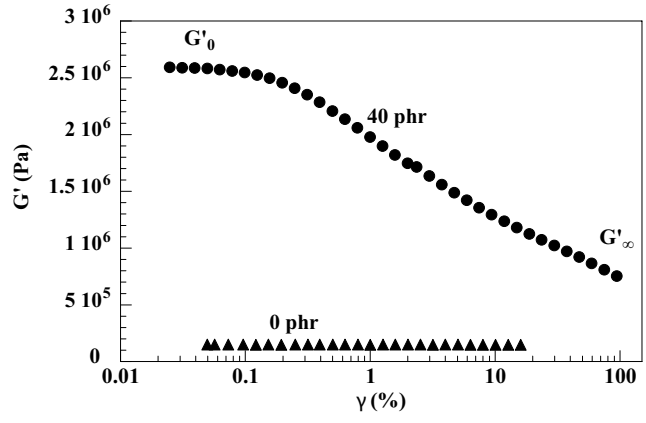

Figure 3.10 Strain dependence of the storage modulus of an unfilled PDMS and a PDMS filled with 40 phr of a treated pyrogenic silica

Based on an agglomeration-deagglomeration mechanism of the filler structures, Kraus [45] developed a model which describes the strain dependence of the dynamic storage and loss moduli of carbon black filled rubbers. Another analysis of the Payne effect based on interactions between network chains and the filler surface was proposed by Maier and Goritz [46]. This model explains the breakdown of the dynamic modulus of filled elastomers to a desorption of the chains with increasing amplitude. In a recent work of Ramier *et al.* [44], filler-matrix interactions via chemical grafting were tailored in order to evaluate the influence of the filler surface modification on the Payne effect in silica-filled SBR vulcanizates. The main idea was to discriminate between the two different pictures commonly used to explain the Payne effect and involving filler-filler interaction or filler-matrix interaction. Unfortunately, it was impossible to the authors to distinguish both scenarios because filler-filler and filler-matrix interactions are modified in the same manner by the grafting covering agent.

For PDMS filled with *in situ* generated silicas, no Payne effect is observed: G' increases with the filler content but remains constant in the whole range of deformation investigated (Figure 3.11a). This could be due to the excellent dispersion of the filler particles in the elastomeric matrix. In the description of the Payne effect based on agglomeration/disagglomeration of the filler structures, if no aggregates or agglomerates are formed, no destruction of the filler structures could occur by applying the oscillatory shear. At higher filler loadings, a continuous filler network is formed that is not broken either at least within the strain range. This would show that the silica network of generated particles is much more resistant to the applied mechanical work than that formed by conventional silicas. These behaviors, quite different from that observed with pyrogenic silicas [43], may be regarded as different nanocomposites morphologies: a common particle-matrix morphology where silica particles tend to form aggregates in the continuous matrix is expected for a classical material while an open mass-fractal silica structure believed to be bicontinuous with the polymer phase, at a molecular level, is expected in the case where the mineral part is synthesized *in situ*.

A Payne effect is observed for the PDMS/TiO_2 composites (Figure 3.11b) which is consistent with the analysis of the tensile properties and also with the TEM image of the

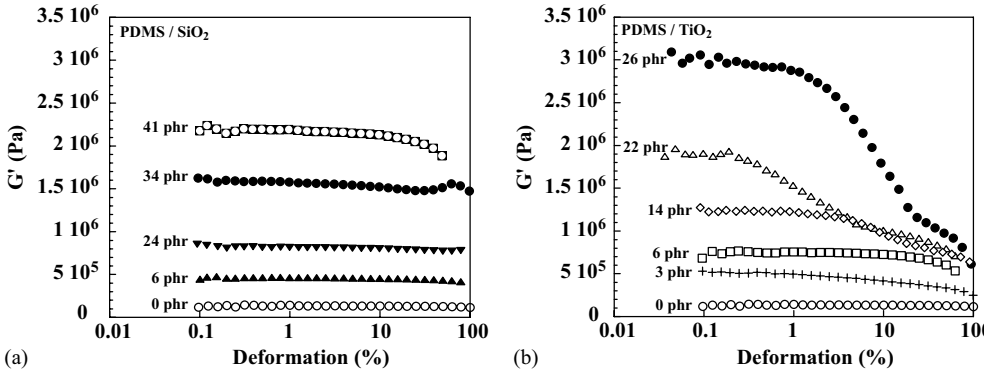

Figure 3.11 Strain dependence of the storage modulus of PDMS filled with various amounts of *in situ* generated particles: (a) silica and (b) titania

composite showing the for mation of a filler network even at a relatively low filler fraction of titania particles.

3.3.4 Mullins Effect

Filled elastomers display, at large deformations, a characteristic stress-strain behavior after a prestretching. After being stretched to a given strain then released and stretched again, the filled sample appears softer on the second stretch exhibiting the so-called stress-softening phenomenon, also known as the "Mullins effect" [47]. Bueche [48] has developed a molecular interpretation of the Mullins effect based on the breakage of elastomeric chains between filler particles. When the rubber is stretched, the network chains which are fastened at both ends to filler particles break when the filler particles are separated enough to stretch the chains to their limit of extensibility. The loss of these chains causes a prestretched rubber to exhibit a much lower modulus than the original rubber. The chains are expected to reach their limited extensibility by strain amplification effects. The Bueche model has the drawback to consider a unique interparticle distance, which is equivalent to consider that the strain amplification is uniform within the whole sample. Clément *et al.* [49] go beyond this simplified picture and show that the strain amplification factor and consequently the macroscopic strain at which chains reach their limit of extensibility strongly depends on the local volume fraction of filler around these chains, in other words on the state of filler dispersion. On account of strain amplification phenomenon, the rubber is much more deformed in regions of the sample of high volume fractions of filler and consequently the chains reach their limit of extensibility at low strains and detach from the filler surface thus causing the loss of elastic chains. The other regions of lower filler volume fraction are not concerned at this stage of deformation but become affected at increasing strains.

Figure 3.12 compares first and second stretchings, performed at different strain values, of a PDMS composite filled with fumed silica with those of composites prepared by the *in situ* sol-gel process. After stretching and release, the filled elastomers show a permanent deformation, which was assigned by Kilian *et al.* [50] to an irreversible deformation of the filler

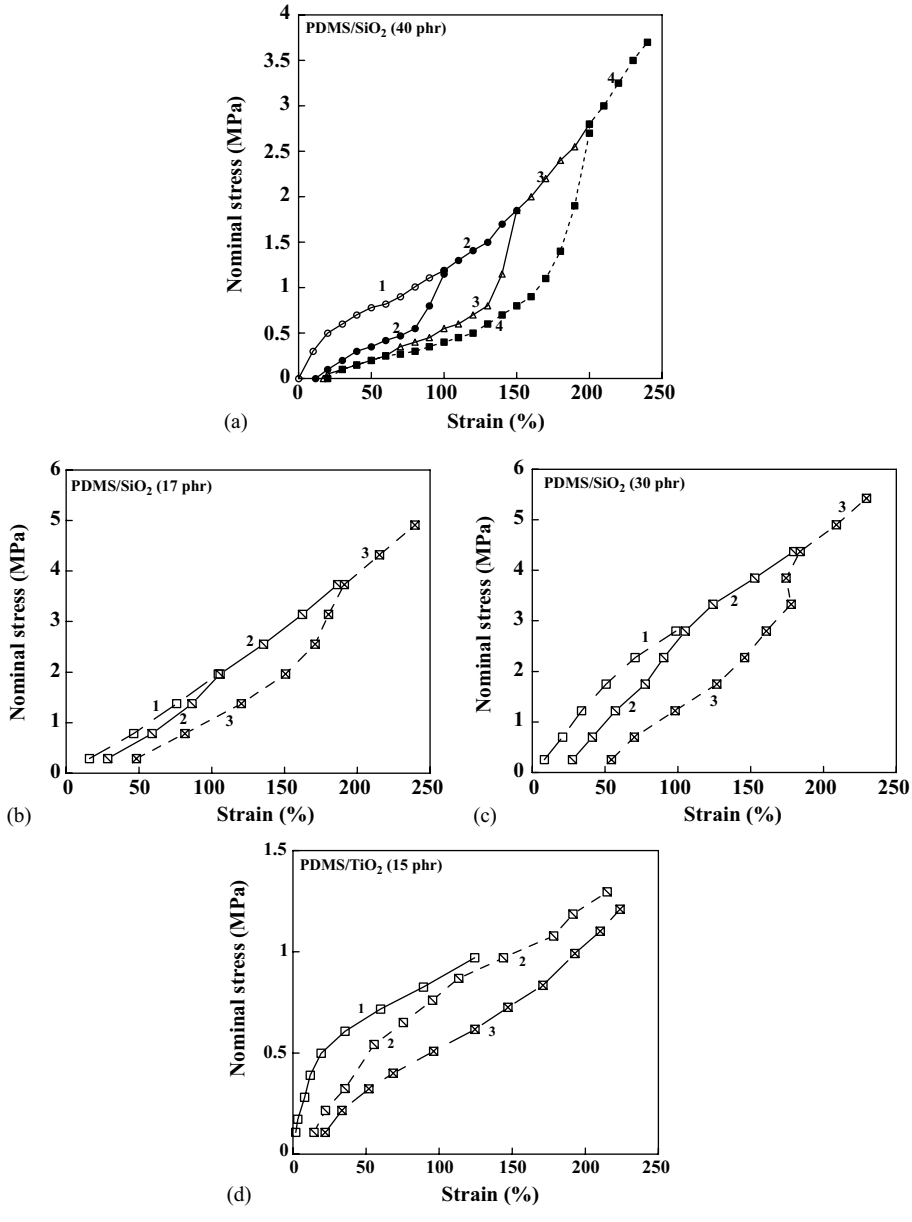

Figure 3.12 (a) Mullins effect for PDMS filled with 40 phr of fumed silica; (b,c) composites of PDMS/SiO_2; and (d) PDMS/TiO_2

network. After stretching at 200%, it is about 10% for the silica-filled PDMS sample obtained by the usual mechanical mixing (Figure 3.12a) and much more pronounced for the samples filled with *in situ* precipitated silicas (Figure 3.12b and c). The composites filled with *in situ* precipitated silicas possess a very fine and interpenetrated polymer-silica morphology. The

significant residual deformation obtained in that case, may be explained by the breaking up of both the filler network and the rubber:filler bonds. Moreover, the amount of stress-softening for the sample filled with 17 phr of silica (Figure 3.12b) is much smaller than that exhibited by the high loaded polymer. This may be due to the good dispersion of silica and consequently to a narrow distribution of chain lengths between fillers. Less residual deformation is obtained for the PDMS/TiO_2 composite which does not exhibit an interpenetrated polymer-filler morphology: the condensed titania structures are well distributed in the matrix in a classical organic-inorganic hybrid. In contrast, after stretching to 200% then release, the second stretching does not display the plastics behavior because the filler network has been destroyed during the first stretching.

3.3.5 Characterization of the Polymer-Filler Interface

Compared with a classical composite filled with fumed silica, the sol-gel process provides inorganic particles with greatly improved reinforcing properties on account of the small size of the particles and of the hydrophilic character of the filler surface thus allowing strong interactions with the polymer chains. In fact, the interfacial interaction between the organic and inorganic phases plays a crucial role in the reinforcement effects and in filled PDMS samples, hydroxyl species, present in the filler structure, are involved. The amount and the nature of the hydroxyl groups are expected to depend on the synthetic conditions. In a previous paper [28], solid-state ^{29}Si NMR spectroscopy has been shown to be particularly well suited for a detailed analysis of the surface silanol hydroxyl groups (isolated and geminal, also denoted Q_3 and Q_2, Q_4 being related to SiO_4 species). It was demonstrated that silica particles generated by the sol-gel process display a higher content of Q_3 species than that reported for fumed silica [51]. However, at a same filler loading, less Q_3 sites were found for the composite prepared under base catalysis, which would indicate that more condensed silica structures are obtained in the base-catalyzed samples.

Hydroxyl groups, present on the filler surface, are generally recognized as hydration sites and the water physisorption can induce a change in the mechanical properties of the filled compounds. So the surface hydration of silica, which depends on the surface silanol distribution, has received considerable interest [52, 53]. States of physisorbed water can be characterized by infrared spectroscopy through the bands associated with the OH stretching vibrations and located in the 3800–3200 cm^{-1} range. These vibrations usually give rise to very strong absorption bands, so it is convenient to analyze the band assigned to a combination of the bending (δ) and one of the stretching modes (v) of the water molecule located in the 5050–5350 cm^{-1} range (Figure 3.13). In both cases, the absorptions associated with the water molecule increase with the amount of filler but the two types of composites display a different water interface. In addition to a difference in the spectral pattern, the wavenumbers for the PDMS/TiO_2 composites are lower than those observed for the silica-filled sample, suggesting a clustering of water around the first adsorption sites. As explained by Burneau *et al.* [54], additional water adsorption can take place around the first layer of water molecules interacting with the solid surface. This can be understood by the fact that the titania particles are more condensed and thus more accessible to water molecules at the outer interface in contrast to the open-fractal structure of the silica particles.

The polymer-filler interactions which largely govern the mechanical properties of the composite material contribute to the formation of an adsorption layer whose thickness is

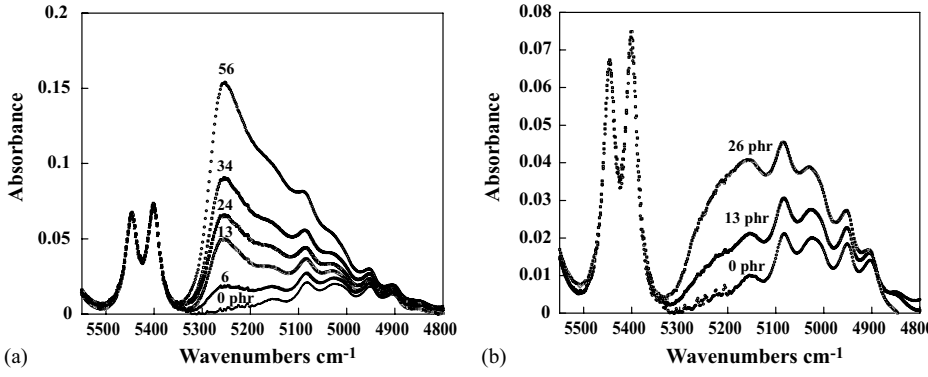

Figure 3.13 Infrared spectra in the 4800–5500 cm^{-1} range of pure PDMS and DBTDA-catalyzed (a) PDMS/SiO_2; and (b) PDMS/TiO_2 composites. Each curve is labeled with the amount of filler in phr

estimated around 2 nm for PDMS filled with *in situ* generated silica particles and where motions of chain units are more restricted than those in the mobile phase, as evidenced by ^{1}H NMR relaxation methods using spin-echo techniques. The transverse nuclear magnetic relaxation time, T_2, has been shown to be affected by physical and chemical crosslinks in filled elastomers and subsequently to give access to the determination of the proportion of polymer with restricted mobility, in the adsorption layer surrounding the filler particles [55–58]. In a filled system where strong interactions are established between the active sites on the filler surface and polymer chains, T_2 values for the individual components can be extracted from the transverse magnetization relaxation function and the thickness of the adsorption layer can be evaluated by the following expression [28]:

$$e = R\left[\left(1 + \frac{\omega(1-\phi)}{\phi}\right)^{1/3} - 1\right]$$

where R is the radius of the particles estimated by TEM, ω is the fraction of immobilized polymer and ϕ is the volume fraction of filler.

Dielectric techniques also give evidence that the segmental motions of a fraction of the polymer phase are retarded by filler particles. In addition to the α relaxation associated with the glass transition of the polymer matrix, an additional slower α relaxation, assigned to polymer chains close to the polymer-filler interface and whose mobility is restricted, has been observed for PDMS filled with silica particles synthesized *in situ* [59, 60].

The adsorption interactions taking place at the polymer-filler interface have also an impact on the thermal characteristics of the filled systems and essentially on the crystallization process. In fact, differential scanning calorimetry measurements (DSC) show that besides the low glass transition temperature, one important characteristics of PDMS is the exothermic peak ascribed to crystallization (Figure 3.14). In systems filled with silica or titania particles (Figure 3.15), it is seen that the temperature of crystallization as well as the degree of crystallinity (measured from the area under the peak) decrease in both cases with the filler content. Crystallization is obtained by cooling the sample at a cooling rate of 1.5 °C min^{-1} under N_2 atmosphere. This fact has already been reported by Aranguren [61] in an investigation

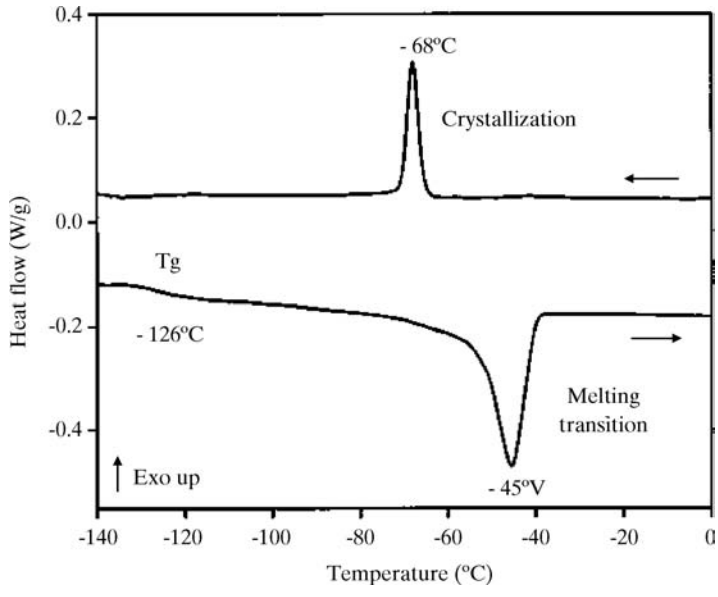

Figure 3.14 DSC thermogram for unfilled PDMS after cooling and heating at 1.5 °C min^{-1}

of unfilled PDMS and filled with pyrogenic silica in uncured and cured states. The decrease in crystallinity with the filler content may be regarded as the result of an increase in the apparent crosslinking density due to polymer-filler interactions, the ability of polymer to crystallize being reduced when the apparent molecular weight between crosslinks decreases. This interpretation is close to that reached by Patel *et al.* [62] in a study on the effect of the crosslinking density on the crystallization characteristics of PDMS.

3.3.6 Thermal Properties

Thermogravimetric analysis (TGA) is widely used to study the thermal stability of a polymer and its composites. TGA of unfilled PDMS and of composites, ramped at 10 °C min^{-1} from room temperature to 800 °C under nitrogen atmosphere at a flow rate of 100 ml min^{-1}, are shown in Figure 3.16. The neat PDMS shows a one-step weight loss as previously reported [63] and there is almost no residue at the end of the degradation. The thermal degradation of PDMS in inert atmosphere and under vacuum results in depolymerization to produce cyclic oligomers [64, 65]. The TGA curves of the two composites show that the two types of particles affect differently the thermal decomposition of the polymer. There is more residue left for the composites after the degradation with weight losses about 24 and 48% respectively for PDMS samples both filled with 18 phr of *in situ* silica and titania particles, which have been generated in the presence of dibutyltin diacetate as catalyst. Interestingly, the presence of *in situ* precipitated silica increases the onset of degradation with regard to the pure polymer. This delay to the depolymerization process may be due to the interaction by hydrogen bonding between the hydroxyl groups on the filler surface and the PDMS chains. Two stages of degradation are observed for the PDMS/TiO_2 composite: the first stage starts around 100 °C,

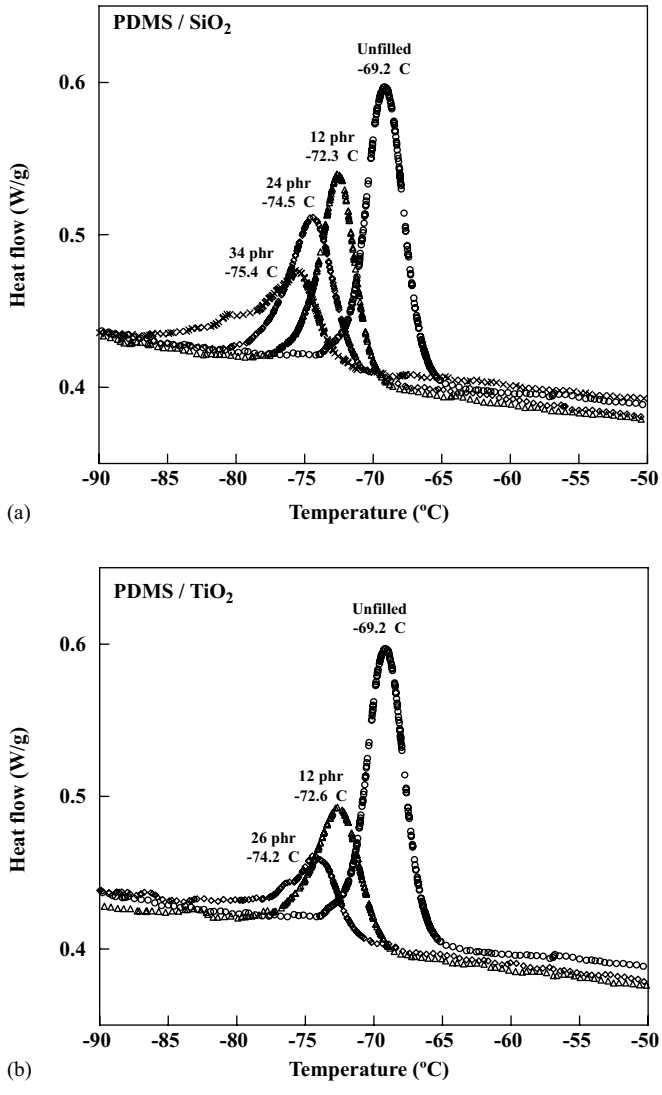

Figure 3.15 Influence of the amount of filler on the crystallization peak of PDMS: *in situ* generated (a) silica and (b) titania particles

which is well below the temperature at which the pure PDMS begins to degrade, whereas the second begins at a comparable temperature ($T \sim 410\,^{\circ}\mathrm{C}$) to that of the silica-filled composite. This result is quite similar to what was already published by Murugesan *et al.* [66] for PDMS/TiO_2 composites prepared by the sol-gel technique. The first step was expected to correspond to the loss of titanium butoxide not hydrolyzed [3] but in our case, we have demonstrated from infrared spectroscopy the absence of any organic precursor. One possible suggestion is to ascribe the first loss to the elimination of adsorbed water. This hypothesis has also been considered by other authors [67, 68]. The residue left above 700 °C is much larger than the

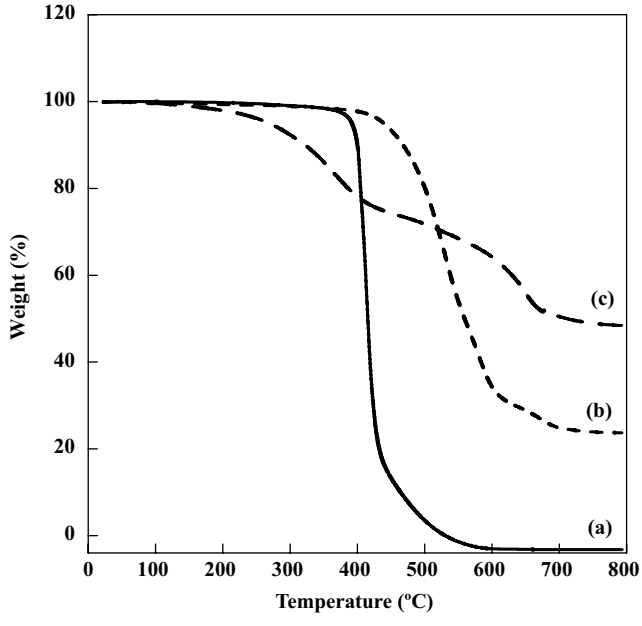

Figure 3.16 TGA thermograms under nitrogen for (a) unfilled PDMS and composites filled with 18 phr of *in situ* precipitated particles: (b) silica; and (c) titania

amount of filler contained in the PDMS network. This residue contains a small black powder and also silica (confirmed by an infrared analysis).

3.4 Conclusions

Silica and titania particles can be *in situ* precipitated into a PDMS elastomeric network by a sol-gel approach. After a description of the synthetic protocols, the respective reinforcing ability of each type of particles is discussed through the mechanical and thermal properties of the composites. Additional information from molecular spectroscopies bring new insights into the polymer-filler interface and allow a further understanding of the improvement of elastomeric properties of these filled systems.

References

1. Wang, S., Xu, P., and Mark, J.E. (1991) Shear and biaxial extension measurements of reinforcement from in-situ precipitated silica. *Rubber Chemistry and Technology*, **64**, 746.
2. Mark, J.E. (1992) Novel reinforcement techniques for elastomers. *Journal of Applied Polymer Science: Applied Polymer Symposium*, **50**, 273.
3. Wen, J. and Mark, J.E. (1994) Precipitation of silica-titania mixed-oxide fillers into poly(dimethylsiloxane) networks. *Rubber Chemistry and Technology*, **67**, 806.
4. McCarthy, D.W., Mark, J.E., and Schaeffer, D.W. (1998) Synthesis, structure, and properties of hybrid organic-inorganic composites based on polysiloxanes. I. Poly(dimethylsiloxane) elastomers containing silica. *Journal of Polymer Science: Part B: Polymer Physics*, **36**, 1167.

5. McCarthy, D.W., Mark, J.E., Clarson, S.J., and Schaeffer, D.W. (1998) Synthesis, structure, and properties of hybrid organic-inorganic composites based on polysiloxanes. II. Comparisons between poly(methylphenylsiloxane) and poly(dimethylsiloxane), and between titania and silica. *Journal of Polymer Science: Part B: Polymer Physics*, **36**, 1191.
6. Breiner, J.M., Mark, J.E., and Beaucage, G. (1999) Dependence of silica particle sizes on network chain lengths, silica contents, and catalyst concentrations in in situ-reinforced polysiloxane elastomers. *Journal of Polymer Science; Part B: Polymer Physics*, **37**, 1421.
7. Yuan, Q.W. and Mark, J.E. (1999) Reinforcement of poly(dimethylsiloxane) networks by blended and in-situ generated silica fillers having various sizes, size distributions, and modified surfaces. *Macromolecular Chemistry and Physics*, **200**, 206.
8. Tanahashi, H., Osanai, S., Shigekuni, M. *et al.* (1998) Reinforcement of acrylonitrile-butadiene rubber by silica generated in situ. *Rubber Chemistry and Technology*, **71**, 38.
9. Ikeda, Y. and Kohjiya, S. (1997) In situ formed silica particles in rubber vulcanizate by the sol-gel method. *Polymer*, **38**, 4417.
10. Hashim, A.S., Azahari, B., Ikeda, Y., and Kohjiya, S. (1998) The effect of bis(3-triethoxysilylpropyl)tetrasulfide on silica reinforcement of styrene-butadiene rubber. *Rubber Chemistry and Technology*, **71**, 289.
11. Hajji, P., David, L., Gérard, J.F. *et al.* (1999) Synthesis, structure, and morphology of polymer-silica hybrid nanocomposites based on hydroxyethyl methacrylate. *Journal of Polymer Science: Part B: Polymer Physics*, **37**, 3172.
12. Kohjiya, S. and Ikeda, Y. (2000) Reinforcement of general purpose grade rubbers by silica generated in situ. *Rubber Chemistry and Technology*, **73**, 534.
13. Kohjiya, S., Murakami, K., Iio, S. *et al.* (2001) In situ filling of silica onto "green" natural rubber by the sol-gel process. *Rubber Chemistry and Technology*, **74**, 16.
14. Murakami, K., Iio, S., Tanahashi, T. *et al.* (2001) Reinforcement of NR by silica generated in situ; comparison with carbon black stock. *KGK Kautschuk Gummi Kunststoffe*, **54**, 668.
15. Matejka, L., Dukh, O., and Kolarik, J. (2000) Reinforcement of crosslinked rubbery epoxies by in-situ formed silica. *Polymer*, **41**, 1449.
16. Matejka, L. and Dukh, O. (2001) Organic-inorganic hybrid networks. *Macromoleculare Symposia*, **171**, 181.
17. Yoshikai, K., Ohsaki, T., and Furukawa, M. (2002) Silica reinforcement of synthetic diene rubbers by sol-gel process in the latex. *Journal of Applied Polymer Science*, **85**, 2053.
18. Jang, J. and Park, H. (2002) In situ sol-gel process of polystyrene/silica hybrid materials: effect of silane-coupling agents. *Journal of Applied Polymer Science*, **85**, 2074.
19. Bandyopadhyay, A., De Sarkar, M., and Bhowmick, A.K. (2005) Polymer-filler interactions in sol-gel derived polymer/silica hybrid nanocomposites. *Journal of Polymer Science: Part B: Polymer Physics*, **43**, 2399.
20. Bokobza, L. and Chauvin, J.-P. (2005) Reinforcement of natural rubber: use of in situ generated silicas and nanofibres of sepiolite. *Polymer*, **46**, 4144.
21. Mark, J.E. and Erman, B. (1988) *Rubber Elasticity. A molecular Primer*, Wiley-Interscience, New York.
22. Pope, E.J.A. and Mackenzie, J.D. (1986) Sol-gel processing of silica. II. The role of the catalyst. *Journal of Non-Crystalline Solids*, **87**, 185.
23. Pouxviel, J.C., Boilot, J.P., Beloeil, J.C., and Lallemand, J.Y. (1987) NMR study of the sol/gel polymerization. *Journal of Non-Crystalline Solids*, **89**, 345.
24. Brinker, C.J. (1988) Hydrolysis and condensation of silicates: effects on structure. *Journal of Non-Crystalline Solids*, **100**, 31.
25. Jackson, C.L., Bauer, B.J., Nakatani, A.I., and Barnes, J.D. (1996) Synthesis of hybrid organic-inorganic materials from interpenetrating polymer network chemistry. *Chemistry of Materials*, **8**, 727.
26. Herz, J.E., Remp, P., and Borchard, W. (1977) Model networks. *Advances in Polymer Science*, **26**, 105.
27. Besbes, S., Cermelli, I., Bokobza, L. *et al.* (1992) Segmental orientation in model networks of poly(dimethylsiloxane): Fourier transform infrared dichroism measurements and theoretical interpretation. *Macromolecules*, **25**, 1949.
28. Dewimille, L., Bresson, B., and Bokobza, L. (2005) Synthesis, structure and morphology of poly(dimethylsiloxane) networks filled with in situ generated silica particles. *Polymer*, **46**, 4135.
29. Takeuchi, H. and Cohen, C. (1999) Reinforcement of poly(dimethylsiloxane) elastomers by chain-end anchoring to clay particles. *Macromolecules*, **32**, 6792.
30. Schmidt, D.F., Clément, F., and Giannelis, E.P. (2006) On the origins of silicate dispersion in polysiloxane/layered silicate nanocomposites. *Advanced Functional Materials*, **16**, 417.

31. Bradley, D.C., Mehrotra, R.C., and Gaur, D.P. (1986) *Metal Alkoxides*, Academic Press, London.
32. He, Y-q. and Ping, Y-h. (2003) Nano-composite TiO2-PI via sol-gel process. *Materials Chemistry and Physics*, **78**, 614.
33. Xiong, M., Zhou, S., You, B. *et al.* (2004) Effect of preparation of titania sol on the structure and properties of acrylic resin/titania hybrid materials. *Journal of Polymer Science: Part B: Polymer Physics*, **42**, 3682.
34. Colthup, N.B., Daly, L.H., and Wiberley, S.E. (eds) (1975) *Introduction to Infrared and Raman Spectroscopy*, 2nd edn, Academic Press, New York.
35. Bokobza, L. (2001) Reinforcement of elastomeric networks by fillers. *Macromolecular Symposia*, **169**, 243; (2001) Reinforcement of elastomeric networks by fillers. **171**, 163.
36. Bokobza, L. and Rapoport, O. (2002) Reinforcement of natural rubber. *Journal of Applied Polymer Science*, **85**, 2301.
37. Bokobza, L. (2095) Elastomeric composites. I. silicone composites. *Journal of Applied Polymer Science*, **93**, 2004.
38. Guth, E. and Gold, O. (1938) On the hydrodynamical theory of the viscosity of suspensions. *Physical Review*, **53**, 322.
39. Payne, A.R. (1962) The dynamic properties of carbon black-loaded natural rubber vulcanizates. Part I. *Journal of Applied Polymer Science*, **VI**, 57.
40. Wang, M.-J. (1998) Effect of polymer-filler and filler-filler interactions on dynamic properties of filled vulcanizates. *Rubber Chemistry and Technology*, **71**, 520.
41. Drozdov, A.D. and Dorfmann, A. (2002) The Payne effect for particle-reinforced elastomers. *Polymer Engineering and Science*, **42**, 591.
42. Klüppel, M. (2003) The role of disorder in filler reinforcement of elastomers on various length scales. *Advances in Polymer Science*, **164**, 1.
43. Clément, F., Bokobza, L., and Monnerie, L. (2005) Investigation of the Payne effect and its temperature dependence on silica-filled polydimethylsiloxane networks. Part I: Experimental results. *Rubber Chemistry and Technology*, **78**, 211; (2005) Investigation of the Payne effect and its temperature dependence on silica-filled polydimethylsiloxane networks. Part II: Test of quantitative models. **78**, 232.
44. Ramier, J., Gauthier, C., Chazeau, L. *et al.* (2007) Payne effect in silica-filled styrene-butadiene rubber: influence of surface treatment. *Journal of Polymer Science: Part B: Polymer Physics*, **45**, 286.
45. Kraus, G. (1984) Mechanical losses in carbon-black filled rubbers. *Journal of Applied Polymer Science: Applied Polymer Symposium*, **39**, 75.
46. Maier, P.G. and Göritz, D. (1996) Molecular interpretation of the Payne effect. *Kautschuk Gummi Kunstsoffe*, **49**, 18.
47. Mullins, L. (1969) Softening of rubber by deformation. *Rubber Chemistry and Technology*, **42**, 339.
48. Bueche, F. (1960) Molecular basis for the Mullins effect. *Journal of Applied Polymer Science*, **4**, 107.
49. Clément, F., Bokobza, L., and Monnerie, L. (2001) On the Mullins effect in silica-filled polydimethylsiloxane networks. *Rubber Chemistry and Technology*, **74**, 847.
50. Kilian, H.G., Strauβ, M., and Hamm, W. (1994) Universal properties in filler-loaded rubbers. *Rubber Chemistry and Technology*, **67**, 1.
51. Léonardelli, S., Facchini, L., Frétigny, C. *et al.* (1992) Silicon-29 nuclear magnetic resonance study of silica. *Journal of the American Chemical Society*, **114**, 6412.
52. Legrand, A.P., Hommel, H., Tuel, A. *et al.* (1990) Hydroxyls of silica powders. *Advances in Colloid and Interface Science*, **33**, 91.
53. Burneau, A. and Gallas, J.-P. (1998) Vibrational spectroscopies p. 147–234, in *The Surface Properties of Silicas* (ed. André P. Legrand), Wiley, Chichester, United Kingdom, p. 470.
54. Burneau, A., Barrès, O., Gallas, J.P., and Lavalley, J.C. (1990) Comparative study of the surface hydroxyl groups of fumed and precipitated silicas. 2. Characterization by infrared spectroscopy of the interactions with water. *Langmuir*, **6**, 1364.
55. Litvinov, V.M. (1988) Molecular-dynamic processes on the polydimethylsiloxane-filler interface. *Polymer Science USSR*, **30**, 2250.
56. Litvinov, V.M. and Spiess, H.W. (1991) ^{2}H NMR study of molecular motions in polydimethylsiloxane and its mixtures with aerosils. *Makromolekulare Chemie*, **192**, 3005.
57. Litvinov, V.M. and Spiess, H.W. (1992) Molecular mobility in the adsorption layer and chain orientation in strained poly(dimethylsiloxane) networks by ^{2}H NMR. *Makromolekulare Chemie*, **193**, 1181.

58. Litvinov, V.M. (1996) Poly(dimethylsiloxane) chains at a silica surface, in *Organosilicon Chemistry II, From Molecules to Materials* (eds N. Auner and J. Weis), VCH, Weinheim, pp. 779–814.
59. Fragiadakis, D., Pissis, P., and Bokobza, L. (2005) Glass transition and molecular dynamics in poly(dimethylsiloxane)/silica nanocomposites. *Polymer*, **46**, 6001.
60. Fragiadakis, D., Pissis, P., and Bokobza, L. (2006) Modified chain dynamics in poly(dimethylsiloxane)/silica nanocomposites. *Journal of Non-Crystalline Solids*, **352**, 4969.
61. Aranguren, M.I. (1998) Crystallization of polydimethylsiloxane: effect of silica filler and curing. *Polymer*, **39**, 4897.
62. Patel, M., Morrell, P.R., and Skinner, A.R. (2002) Physical and thermal properties of model polysiloxane rubbers: impact of crosslink density and tin concentration. *Macromoleculare Symposia*, **180**, 109.
63. Camino, G., Lomakin, S.M., and Lazzari, M. (2001) Polydimethylsiloxane thermal degradation. Part 1. Kinetic aspects. *Polymer*, **42**, 2395.
64. Thomas, T.H. and Kendrick, T.C. (1969) Thermal analysis of polydimethylsiloxanes. I. Thermal degradation in controlled atmospheres. *Journal of Polymer Science*, **A-2**, **7**, 537.
65. Camino, G., Lomakin, S.M., and Lageard, M. (2002) Thermal polydimethylsiloxane degradation. Part 2. The degradation mechanisms. *Polymer*, **43**, 2011.
66. Murugesan, S., Sur, G.S., Mark, J.E., and Beaucage, G. (2004) In-situ catalyst generation and controlled hydrolysis in the sol-gel precipitation of zirconia and titania particles in poly(dimethylsiloxane). *Journal of Inorganic and Orgametallic Polymers*, **14**, 239.
67. Brennan, A.B. and Wilkes, G.L. (1991) Structure-property behaviour of sol-gel hybrid materials: effect of a polymeric acid catalyst. *Polymer*, **32**, 733.
68. Whang, C.M., Yeo, C.S., and Kim, Y.H. (2001) Preparation and characterization of sol-gel derived SiO_2-TiO_2-PDMS composite films. *Bulletin of the Korean Chemical Society*, **22**, 1366.

4

Interface Modification and Characterization

Jun Ma[1,2], Li Qun Zhang[2] and Jiabin Dai[1]
[1] *School of Advanced Manufacturing & Mechanical Engineering, University of South Australia, SA 5095, Australia*
[2] *Beijing University of Chemical Technology, Beijing, 100029, China*

4.1 Introduction

Of all the ingredients used to modify the properties of elastomers, fillers occupy a dominant role because of their significant contribution to the reinforcement and processability of elastomers. Particle size and surface activity are the two main factors determining the interaction of fillers with elastomers.

4.1.1 Particle Size

Fillers with particles sizes larger than 1 μm in diameter usually have unobvious reinforcement effect on rubber products. Fillers ranging from 100 nm to 1 μm offer moderate reinforcement effect. Nanofillers, which range from 1 to 100 nm, are able to significantly improve the mechanical performance of the rubber products. The dependence of the reinforcement on particle size is explained from two aspects, that is, surface area and particle mass.

The surface area of a particle is inversely proportional to its particle size. If all particles are spheres of the same size, the surface area A_S per gram of filler is given by the equation:

$$A_S = \frac{\pi d^2}{\frac{1}{6}\pi d^3 \rho} = \frac{6}{d\rho}$$

Where d is the diameter and ρ is the density. The difference between micron-size and nanoscale filler surface area can be a factor of 10–100.

Rubber Nanocomposites: Preparation, Properties and Applications Edited by Sabu Thomas and Ranimol Stephen
© 2010 John Wiley & Sons (Asia) Pte Ltd

The mass of a particulate solid which directly relates to its particle size is given by the equation

$$G = \frac{4}{3}\pi\left(\frac{d}{2}\right)^3 \rho g$$

The effect of fillers on rubber reinforcement depends on the quantity of polymer chains physically or chemically attached to the filler surface and the mass and volume fraction of the particles. In comparison with microparticles, the high surface area of nanoparticles leads to more polymer chains attached to the surface. This restricts the movement of polymer chains under loading, resulting in high reinforcement. Therefore, nanoparticles are profoundly important to the reinforcement of elastomers.

4.1.2 Surface Activity

Significant reinforcement can be generated by compounding the nanofillers of high surface activity into elastomers. Carbon black has been remaining a dominant nanofiller in rubber industry due to its high surface activity: (i) Carbon black particles have carboxyl, lactone quinone and other organic functional groups which promote a high affinity of rubber to filler; (ii) it has chemically active sites (less than 5% of particle surface) that arise from broken carbon–carbon bonds as a consequence of manufacturing and that chemically react with the elastomer chains.The importance of the high surface activity of carbon black is evidenced by heat treatment at 1600–3000 °C, through which all the organic functional groups and the active sites are lost as a result of graphitization. Table 4.1 shows the dramatic effect of the loss of the surface activity on the mechanical properties. Upon heat treatment, both the modulus and the tensile strength significantly reduced. The abrasion loss was also obviously deteriorated by the treatment.

The foregoing example shows that high surface activity is dispensable to nanoparticles in rubber matrix. Nevertheless, it is argued that stronger interface by chemical bonding may be unnecessary. This argument is supported by an example in which micron-sized brass powder was used as a filler accompanied by a large amount of sulfur for curing rubber matrix as well as for producing chemical bond between the powder and the matrix. Final compound obtained a very higher modulus but poor tensile strength and elongation. In the authors' view, however, significant reinforcement may be obtained if nanoscale brass particles are used.

Table 4.1 Effect of surface activity of carbon black (ISAF[1]) on mechanical properties of rubber

Carbon black (ISAF)	Modulus at 300%, kg/cm^2	Tensile strength, kg/cm^2	Abrasion loss, cc/10^6 rev.
Original	105	280	67
Heat treated	30	230	142

[1]ISAF: Intermediate super abrasion furnace.

(Adapted with kind permission from Springer Science + Business Media: "Fillers: carbon black and nonblack," in M. Morton (ed.), *Rubber Technology*, 2nd ed., Table 3.3, Van Nostrand Reinhold Company, New York. © 1973 [1].)

Based upon the nanoparticle dispersion and interface adhesion, rubber nanocomposites can be divided into two types: miscible and immiscible nanocomposites. Miscible rubber

nanocomposite is characterized by uniform nanoparticle dispersion and strong interface adhesion, resulting in significant reinforcement and/or new functional properties. However, the vast majority of inorganic fillers are immiscible with rubbers. Due to the nanofiller high specific surface area and the hydrophilic surface, these fillers form aggregates or clusters during fabrication; the poor interface between hydrophilic fillers and hydrophobic rubbers leads to little improved mechanical properties. Therefore, a fundamental aspect in rubber nanotechnology is the interface modification which is accomplished by nonreactive routes and/or reactive routes as explained below.

This chapter attempts to classify representative interface modification by the different methods described in the open literature. The emphasis is on illustrating the scope of these typical methods, and not on presenting each known example of interface modification. The characterization of the interface modification is also introduced. Since the majority of the rubber nanocomposites developed in recent years sits in the category of rubber/clay nanocomposites, this chapter focuses on the nanoclay modification and characterization.

4.2 Rubber Nanocomposites Without Interface Modification

Clay is a widely used nanomaterial in material science and technology. Its structure and compounds with polymers were reviewed elsewhere [2]. Zhang *et al.* pioneered the field of rubber nanocomposites by creating a new manufacturing method – latex-coagulating montmorillonite (a main type of clay) with styrene-butadiene rubber (SBR), carboxylated acrylonitrile-butadiene rubber and natural rubber (NR) [3–5]. A typical procedure is to disperse 4 wt% clay in water by strong stirring, followed by mixing with SBR latex for a period of time. Then the mixture is coagulated by 2 wt% hydrochloric acid solution. The coagulation is washed with water until pH 7 and is then dried at 80 °C for 24 h. The remaining procedure proceeds on a two-roll mill, similar to common rubber processing. This method of producing an intercalation/exfoliation-coexisting structure is denoted LCM.

Figure 4.1 contains the mechanical properties of SBR/clay composites in comparison with a range of composites blended with conventional reinforcing fillers, including high-abrasion furnace carbon black (CB), silica, short fibre (SRF) and talc (TC). The effect of clay on the mechanical properties is discussed below in comparison with conventional fillers.

4.2.1 Hardness and 300% Tensile Modulus

With similar filler loading, as shown in Figure 4.1a and b, the hardness of SBR/clay nanocomposites is higher than other composites. It is attributed to the high specific surface of the clay. In particular the hardness of the nanocomposites is also much higher than that of SBR/clay composites, because the composites were prepared by melt mixing, which made intercalation/exfoliation unlikely to occur.

4.2.2 Tensile Strength

When clay loading is lower than 20 phr, in Figure 4.1c, the nanocomposite exhibits the highest tensile strength. With 10 phr filler content, the nanocomposite demonstrates higher

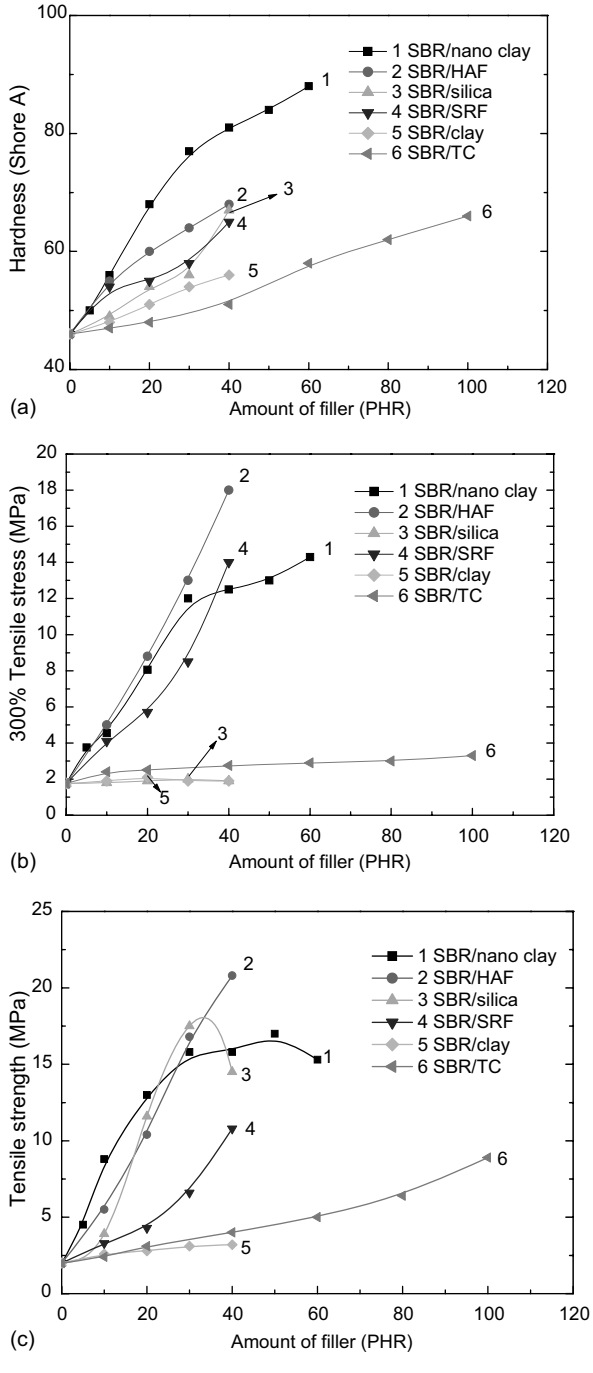

Figure 4.1 Mechanical properties of SBR/clay composites in comparison with composites filled with conventional reinforcing fillers

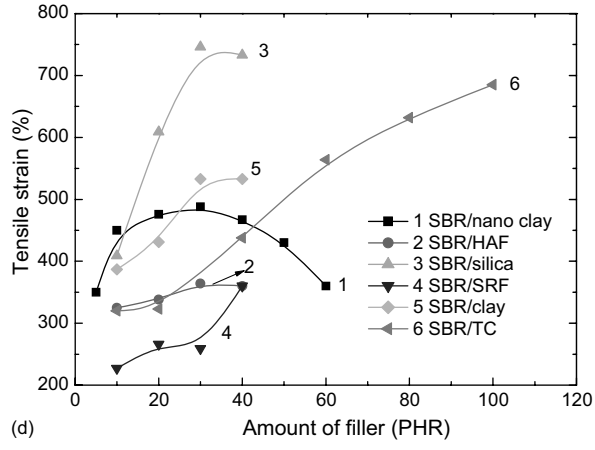

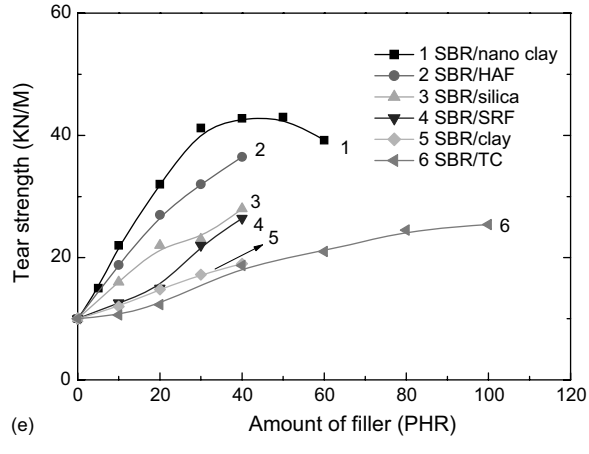

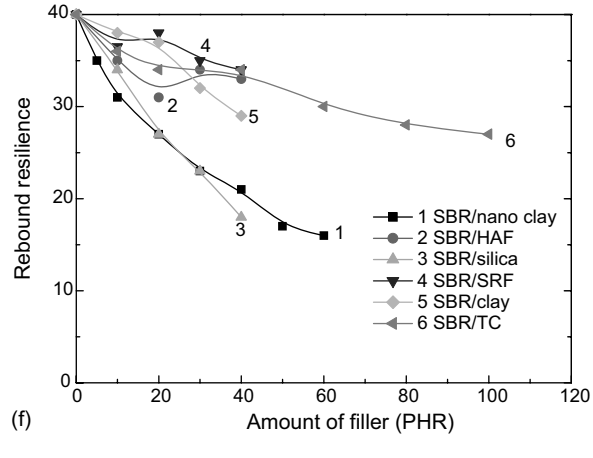

Figure 4.1 (*Continued*)

tensile strength than the other composites. When 40 phr of clay is used, however, the tensile strength of the nanocomposites is lower than SBR/HAF, but still higher than SBR/silica.

4.2.3 Tensile Strain

In Figure 4.1d, the tensile strain of the nanocomposites increases and then drops with increasing clay loading. With 40 phr clay, the tensile strain of the nanocomposites achieves the same reinforcement level as SBR/HAF.

4.2.4 Tear Strength

The nanocomposites exhibit excellent tear strength at all clay loadings in comparison with other composites in Figure 4.1e. This is due to the intercalation/exfoliation-coexisting structure of the nanocomposites, which could improve resistance to crack propagation.

4.2.5 Rebound Resilience

In Figure 4.1f, the rebound resilience of the nanocomposites reaches the level of SBR/silica but is lower than other composites.

4.2.6 Processing Properties

The Mooney viscosity of the nanocomposites is far higher than the SBR/TC composite. This is because the layered structure effectively restricted the macromolecular movement. The other phenomenon observed is that the mixing time was shortened during processing due to the presence of intercalated/exfoliated clay in the matrix.

4.2.7 Advantages

Most mechanical properties of the SBR/clay nanocomposite, including the hardness, 300% tensile stress, tensile strength, tear strength and tensile strain, reach the level of the SBR/HAF composites.

4.2.8 Disadvantages

Most of the properties of the nanocomposites reach maximum at the 40 phr loading and then decrease. The rebound resilience of the nanocomposites is not satisfied.

This LCM method produces an intercalation/exfoliation-coexisting structure with highly improved mechanical properties, which are superior to SBR/HAF composites at low filler loadings. However, it is noteworthy that no interface modification has been made in this method. Since hydrophilic clay is incompatible with hydrophobic rubbers, interface modification is essential to make them compatible. Significant improvement of mechanical properties

has been obtained through nanofiller-matrix interface modification, which is elaborated in the following discussion.

4.3 Interface Modification by Nonreactive Routes

Since exchangeable ions locate on hydrophilic clay surface, the most common modification method is to graft a low molecular weight surfactant to the clay surface via ion exchange. According to the arrangement of the silicate layers in a polymer matrix, two types of morphology are differentiated in terms of intercalation and exfoliation. Exfoliated structure has been well recognized as the best morphology for higher performance with lower clay loading. However, exfoliation is difficult to achieve.

LeBaron and Pinnavaia first modified clay (lithium fluorohectorite) with hexadecyl trimethyl ammonium bromide and obtained an intercalated structure [6]. With 5 wt% clay, the tensile strength of silicone elastomer increased from 152 to 361 MPa.

Ma proposed a strategy for clay modification based on a two-step procedure: preparation of treated clay (montmorillonit) solution and a subsequent solution blending with polymers [7].

A typical procedure is as follows.

1. Preparation of treated clay solution: 5 g of o-clay (montmorillonite modified by hexadecyl trimethyl ammonium bromide) were immersed in 50 g of chloroform for 10 h and then 25 g of monomer (dimethyldichlorosilane) were added to the solution followed by sonication using an ultrasonic generator for about 60 min. 10 ml of H_2O, 30 ml of CH_3OH and 30 ml of $CHCl_3$ were mixed in a three-neck reactor. The above sonicated solution was then dropped into this reactor at a speed of 1 drop/s at 0 °C while under vigorous stirring. After dropping, the obtained solution was washed with deionized water until no chloride ion was detected by one drop of 0.1 N $AgNO_3$ solution. The solution was then mixed with 200 ml of tetrahydrofuran, which is a good solvent for polydimethylsiloxane (PDMS, the product of reacted monomers) but a poor solvent for org-clay, under stirring for 5 min. Then the mixture was loaded into polypropylene tubes and centrifugated at 3000 rpm for 5 min. The opaque whitish layer accumulated at the bottom of the tubes was dissolved in 500 ml of $CHCl_3$ under stirring for 10 min. The obtained solution is named as the treated clay solution.
2. Preparation of polymer/clay nanocomposites: a given amount of the treated clay solution was added into a three-neck reactor. Polymer, such as PDMS, polyvinyl chloride (PVC), SBR, polystyrene (PS) and ethylene propylene diene monomer rubber (EPDM), was mixed into the solution and kept at 50 °C under stirring for 1 h. Then polymer/clay was precipitated by a large amount of methanol. Since polycarbonate (PC) was poorly dissolved in chloroform, toluene and higher blending temperature were employed to prepare PC/clay nanocomposites.

Figure 4.2 shows a series of XRD patterns of treated clay nanocomposites containing various polymer matrix. The featureless patterns of nanocomposites suggest that exfoliation hybrids might be present as opposed to the diffraction peak at 2 nm for org-clay in Figure 4.3, indicating the possibility of having exfoliated silicate layers of clay dispersed in polymer matrices.

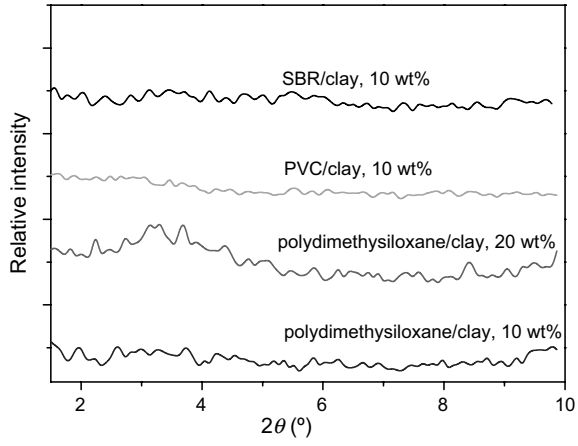

Figure 4.2 XRD patterns of PDMS/clay, PVC/clay and SBR/clay nanocomposites

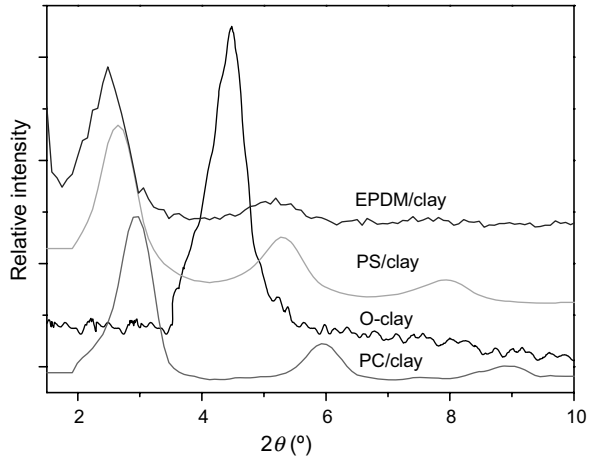

Figure 4.3 XRD patterns of o-clay and PC/clay, PS/clay and EPDM/clay nanocomposites containing 10 wt% clay

Figure 4.4 shows TEM images of SBR/clay nanocomposite prepared as above. The low magnification image in Figure 4.4a reveals that the clay is uniformly dispersed into matrix. Figure 4.4b shows a higher magnification image which reveals that clay is well exfoliated in the matrix and the individual layers are aligned along the flow axis during the crosslinking of SBR, corresponding to XRD pattern analysis. The dark lines in Figure 4.4a are the cross-sections of single or possibly multiple silicate platelets. The platelets are flexible and, thus, show some curvature. The average thickness of the clay platelets appears to be approximately 3 nm while the average length is about 120 nm. The thickness deduced from these photomicrographs is higher than that of a single clay layer of $\sim$1 nm. This is because that the microtoming direction

is not perpendicular to the surface of the platelets and therefore the image of such a tilted platelet appears thicker than it actually is.

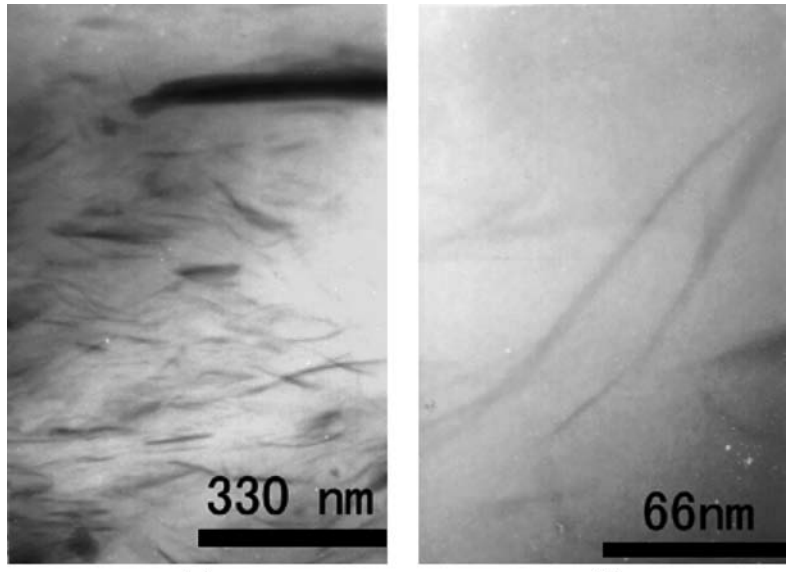

Figure 4.4 TEM images of SBR/clay nanocomposite

Table 4.2 shows the TGA analysis for both pristine SBS and PDMS and their nanocomposites containing 10 wt% clay. An increase in decomposition temperature of 68.2 °C was observed for PDMS/clay nanocomposite, while SBR/clay nanocomposite shows only 13.0 °C of increase in decomposition temperature with the same amount of clay. The nanocomposites show delayed decomposition temperature compared to the pristine polymers, as is attributed to hindered diffusion of the volatile decomposition products.

Table 4.2 Thermal decomposition temperatures of polymers and their nanocomposites with 10 wt% of clay

Polymer type	Decomposition temperature of pristine polymer, °C	Decomposition temp. of nanocomposite, °C	Increase of decomposition temp. after adding clay, °C
SBR	428.7	441.7	13.0
PDMS	395.4	463.6	68.2

The XRD patterns of intercalated polymer/clay are presented in Figure 4.2. It is notable that, although exfoliated SBR/clay, PDMS/clay and PVC/clay were obtained as discussed above, intercalated nanocomposites were still presented while using almost the same fabrication method.

The difference between them is explained by compatibility. Both the grafted PDMS on clay surface and the silicate layers that comprise silicone, oxygen and carbon are polar. Therefore, both are compatible with the polar chains of SBR, PDMS and PVC. The compatibility promoted the intercalation/exfoliation of the layers by the polymer chains, leading to exfoliation. PC, PS and EPDM are nonpolar polymers, which are not compatible with clay and the grafted molecules. The poor compatibility impedes intercalation/exfoliation and results in the intercalated nanocomposites.

As shown in Figure 4.3, the layer spacings of intercalate nanocomposites decrease in the order: EPDM/clay > PS/clay > PC/clay, which should be explained according to macromolecular flexibility. The EPDM macromolecules are flexible and its molecular weight is high, which facilitate the EPDM molecular movement into the silicate layer spacing during the solution blending. The PS chain is not flexible because it contains a styrene group and so it is difficult to intercalate into clay layers. The PC chain is so rigid that it is the most difficult to intercalate.

For PC/clay and PS/clay nanocomposites, multipeaks were shown in Figure 4.3 and the reason can be found in the processing of these nanocomposites. When nanocomposites were precipated from solution by a large amount of methanol, the polymer either stayed in the silicate layer space or moved out. It is well known that the layer spacing of clay increases from 1 to 2 nm after treatment using ammonium surfactants. In this study, the increase of clay layer spacing should be due to the existence of organic ammonium molecules and PDMS grafted onto the clay surface. When the polymer chains were moving out of the space, some grafted molecules might be also taken out of the space by this movement. Therefore, the layer spacing of some part of o-clay was decreased after precipitation.

The foregoing work yielded a range of polymer/clay nanocomposites taking advantage of the further modification of o-clay. However, matrix modification also promotes interface adhesion. Hasegawa developed exfoliated ethylene propylene rubber (EPR)/clay nanocomposites by melt mixing maleic anhydride-modified EPR with organophilic clay [8]. In comparison with conventional rubber/carbon black composites, the nanocomposite exhibited higher storage modulus, tensile strength and creep and swelling resistance.

Zhang further developed the LCM method for SBR/clay (montmorillonite) composites by mixing hexadecyl trimethylammonium bromide (C16) and 3-aminopropyl triethoxy silane (KH550) into the coagulated mixture via a two-roll mill [9]. The C16 and KH550 were used to improve the interface interaction. In Table 4.3, the tensile strength and the modulus at 300% elongation of interface-modified nanocomposites are significantly improved with 10 wt% clay.

Carbon-based surfactants were used in the majority of studies to improve the compatibility of clay with polymer matrix. As silicone polymer is incompatible with the carbon-based surfactant, it is imperative to employ silicone-based surfactants to modify clay. Thus, Ma proposed a unique siloxane surfactant with a weight-average molecular weight (M_w) of 1900 to modify clay [10].

Table 4.3 Mechanical properties of SBR/clay nanocomposites

	Shore A hardness	Tensile strength, MPa	Elongation at break, %	Tear strength, kN/m
Neat SBR	47	2.3	632	9
SBR/modified clay	55	12.4	504	27

A typical procedure is described as follows.

1. Preparation of modified clay: 1 g of sodium clay (montmorillonite with CEC 80 mequiv/100 g from Southern Clay Product) was added to 1 kg of boiling distilled water, mixed and heated for 5 min. 3 g of a siloxane surfactant (provided by Siltech Corporation), whose structure is shown in Figure 4.5, were dissolved in 100 g of water and then 0.3 ml of 2 M hydrochloric acid were added and stirred by a glass rod. The modified clay is denoted "sil-clay". The solution was slowly added to the sil-clay suspension and then the blend was vigorously stirred for 4 min at 80–90 °C. After modification, the suspension was repeatedly washed with water until no chloride ion was detected by $AgNO_3$. The suspension was then condensed until flowable sil-clay slurry was obtained.
2. Preparation of silicon rubber/clay nanocomposite: sil-clay slurry was mixed with silicone rubber (Dow Corning 3110) with a spoon for 3 min until a homogeneous blend with supernatant water obtained. Water was removed and then the compound was degassed at 100 °C for 1 h to get rid of the water residue. 5 g of curing agent (Catalyst F, Dow Corning Product) were added to 100 g of the compound, mixed and cured at room temperature for subsequent characterization.

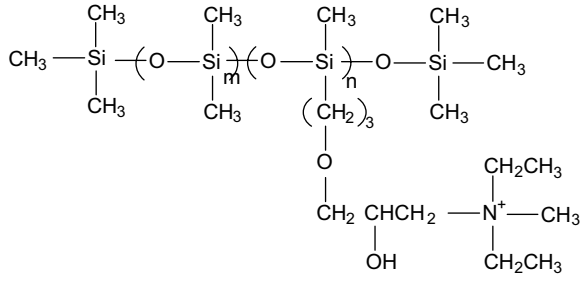

Figure 4.5 Silicone surfactant used in this study

In Figure 4.6, the XRD results of sodium clay indicate a diffraction pattern at about 7.5° for an interlayer spacing of 1.2 nm. After modification with the siloxane surfactant, a wide pattern is seen from 1.5 to 5.5° corresponding to interlayer spacing of 1.6 to 6.0 nm. This unique pattern shows a disordered arrangement of the siloxane surfactant grafted on the clay layer surfaces. The siloxane chain is flexible so that this high molecular weight surfactant can assume different conformations between the clay layers and hence different layer spacing is found after the surface modification. The XRD pattern, when the modified clay is mixed with silicon rubber before curing, shows that all the peaks have disappeared. This means that the silicone rubber macromolecules are fully embedded in the clay layer spacing driven by diffusion and intercalation. After curing, the featureless XRD pattern shows sil-clay is orderly exfoliated with layer spacing larger than 8 nm or even disorderly exfoliated. The exfoliation is confirmed by a TEM micrograph in Figure 4.7. Previous studies on silicone rubber/clay nanocomposites [6, 11–13] modified clay using a rigid carbon-based surfactant. LeBaron and Pinnavaia prepared silicone rubber/clay nanocomposites by mixing synthetic fluorohectorite with silicone rubber for 12 h [11]. However, the mixture still had an intercalated structure,

though exfoliation occurred during curing. Nonetheless, the method of milling and mixing clay with the matrix for 12 h is complicated and time consuming. Our simple method is to: (i) modify clay with the siloxane surfactant and (ii) mix the modified clay with silicone rubber manually just for 3 min.

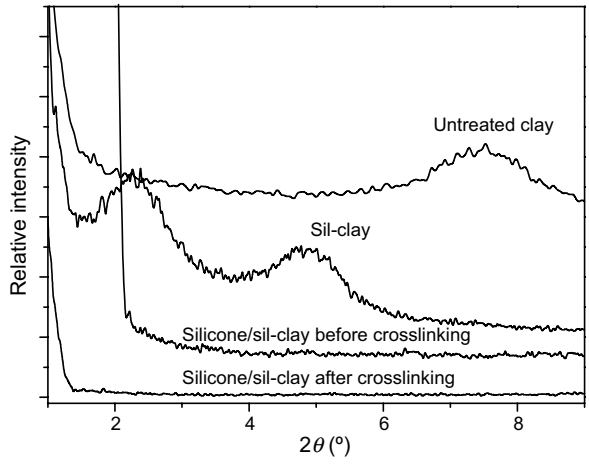

Figure 4.6 *In situ* XRDs of clay modified with siloxane surfactant and its compounding with silicon rubber before and after crosslinking

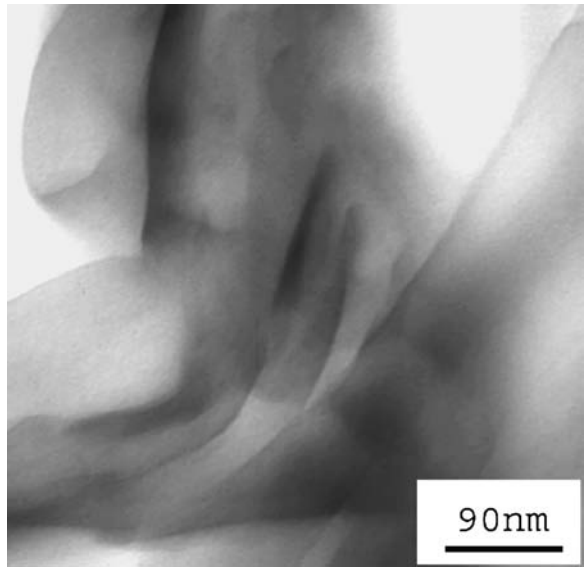

Figure 4.7 TEM micrograph of silicone rubber/sil-clay nanocomposite containing 2.0 wt% sil-clay

Exfoliated silicone rubber/clay nanocomposites were prepared in this work by modifying clay with a flexible, high molecular weight siloxane surfactant. This strategy is different to previous studies because of its special exfoliation mechanism. Traditionally, clay is modified by using carbon-based surfactants, such as hexadecyl trimethylammonium bromide. The molecular chains of this type of surfactant are stiffer and shorter than the siloxane surfactant adopted here. During mixing of the matrix polymers with the sil-clay, as confirmed in Figure 4.6, the grafted siloxane surfactants on the clay layer surfaces enable the diffusion and intercalation of the polymer chains in the inter-galleries causing exfoliation.

There are three main reasons associated with the siloxane surfactant.

1. High molecular weight: the siloxane surfactant used in this research has a higher molecular weight ($M_w = 1900$) than the common surfactants and is capable of molecular entanglement with the polymer matrix molecules, thus forming a thicker clay-matrix interface than the carbon-based surfactants.
2. Flexibility: Siloxane chain is more flexible than the carbon chain; this promotes molecular entanglement and facilitates intercalation and diffusion of the matrix molecules into the intergalleries.
3. Direct slurry-polymer compounding: the basic idea is first to increase the clay interlayer spacing through polymerization or suspension in water/solvents and then to intercalate the matrix polymer in this enlarged spacing. Here, direct clay slurry-polymer compounding was helpful to promote molecular entanglement. Thus, for the silicone rubber/clay nanocomposites, the clay slurry modified by the siloxane surfactant was hand-mixed with silicone rubber; during mixing, the water between layers was replaced by rubber and the supernatant water was finally removed.

Clay modified by carbon-based surfactants is not thermally stable and this impedes the application of polymer/clay nanocomposites, since various polymers are processed and/or used at above 200 °C. We found (not shown here) that the 5 wt% decomposition temperature of sil-clay is 46.7 °C higher than clay-30b (a conventional organic clay by Southern Clay Products). This means sil-clay prepared in this research has a higher thermal stability than the common organic clay modified by carbon-based surfactants.

Silicone rubber is one of the most thermal-resistant rubbers, but unfortunately its mechanical properties are poor. Previous work showed the tensile strength of neat silicone rubber could be increased 100% with addition of 2–5 wt% of clay depending on the types of clay and the matrix molecular weight [6, 11–13]. In this study, silicone rubber Dow Corning 3110 was chosen to compound with sil-clay as reported earlier. It is seen from Table 4.4 that both tensile strength and tear strength increase with sil-clay loading and reach maximum at 2.0 wt% clay. Since sil-clay modified by siloxane surfactant is very well compatible with silicone rubber, disorderly exfoliated structure can be readily achieved.

Li applied the sil-clay to fibre/silicone composite [14]. It shows an orderly exfoliated structure and much improved thermal stability. By incorporation of merely 0.3 wt% of the clay, the flexural modulus and strengths of fiber/PMSQ laminate are increased by 21 and 62%, respectively. This study illuminates the importance of the compatibility of the grafted siloxane surfactant with the matrix polymer in achieving both exfoliation and dispersion of clay as well as highly improved mechanical properties for silicone-based polymers.

Table 4.4 Mechanical properties of silicone rubber/sil-clay nanocomposites

Sil-clay content in silicone rubber, wt%	Tensile strength at 100% elongation, MPa	Tensile strength, MPa	Tear strength, kN/m	Elongation at break, %
0	0.47	0.79	2.71	162
0.5	0.91	1.23	2.91	140
1.0	0.82	1.45	3.20	150
2.0	1.22	1.62	4.55	149
3.0	1.05	1.53	4.45	145

The interface modification is able to produce superior reinforcement, but in a few cases it induced inferior mechanical properties to unmodified nanocomposites. Nair chemically modified the surface of chitin whiskers and compounded it into NR [15]. The mechanical properties were found to be inferior to those of unmodified chitin/NR composites. It is concluded that this loss of performance is due to the partial destruction of the three-dimensional network of chitin whiskers assumed to be present in the unmodified composites. Bhowmick prepared rubber/clay nanocomposites by mixing fluoroelastomers with unmodified clay and o-clay [16], respectively. Exfoliation was observed with both the unmodified and the modified clays at low loading in fluoroelastomer, but higher mechanical properties were found with the unmodified clay due to its best compatibility with the elastomer.

4.4 Interface Modification by Reactive Routes

Disorderly exfoliated structure of rubber/clay nanocomposite is well recognized for optimum reinforcement, but it is difficult to achieve due to the weak interface strength/toughness unless chemical reaction bridges clay with rubber molecules. Thus, Ma and Zhang adopted three types of surfactants (shown in Figure 4.8), that is, triisopropanolamine (TA), m-xylylenediamine (MXD) and allylamine (AA), to modify S-clay (sodium montmorillonite with a CEC of 85 mequiv/100 g, provided by Southern Clay Products). The three types of modified clay were denoted as TA-clay, MXD-clay and AA-clay, respectively.

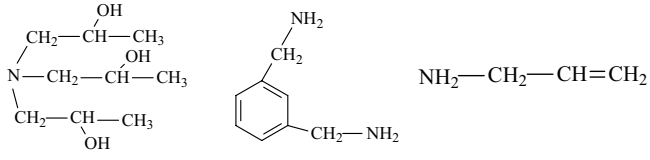

Figure 4.8 Three types of surfactants used in this study

The SBR/clay composites were prepared following the four steps below.

1. Modification of clay by TA and AA: 10 g of clay was added to 5 kg of boiling distilled water, mixed and heated for 10 min. Stoichiometric TA or AA was dissolved in 500 g of water and then a given quantity of hydrochloric acid was added and stirred by a glass rod. The solution

was added slowly to the clay suspension and then the blend was vigorously stirred for 10 min at 80–90 °C. After modification, the clay suspension was repeatedly washed with water until no chloride ion was detected by $AgNO_3$. Then, the suspension was condensed to 1500 ml by heating. The modification of clay by MXD was conducted according to Ma's previous work [17].

2. Emulsion compounding: the desired amount of the condensed suspension was added to a given quantity of SBR latex followed by mixing for 5 min. Then the mixture was coagulated by diluted H_2SO_4 solution and washed with water until neutral. After being dried at 60 °C for 6 h, the SBR/clay was ready for shear mixing with additives.
3. Shear mixing; 4. Vulcanization: since steps (3) and (4) are common techniques in rubber processing, both have been omitted.

Figure 4.9a shows the XRD patterns of various SBR/clay nanocomposites. As a benchmark, we prepared and characterized SBR/S-clay nanocomposite by the LCM method. A significant diffraction pattern was found for SBR/S-clay nanocomposite at $2\theta = 6.2°$, corresponding to a layer spacing of 1.4 nm, indicating that direct compounding achieved a nonexfoliated structure. For TA-treated clay, however, a diffraction peak was found at $2\theta = 5.9°$ for a layer spacing of 1.5 nm. The reduced pattern intensity suggests that some amount of clay was fully intercalated or even exfoliated in comparison with SBR/S-clay nanocomposite. As clay was treated by TA, a large quantity of hydroxyl group and organic units were introduced on the clay layer surface, which could endow TA-clay both good suspending ability in water and a certain compatibility between SBR and clay. Hence, parts of clay were fully intercalated or exfoliated. For SBR/MXD-clay nanocomposite, a decreased diffraction pattern was also found at $2\theta = 5.9°$, inferring the same layer spacing of 1.5 nm. This can be caused by the enhanced compatibility between SBR and MXD-clay. However, no obvious diffraction peak was observed on SBR/AA-clay nanocomposite, which might indicate fully intercalated structure or exfoliation. Figure 4.9b shows the changes of the layer spacing of clay during the various processing stages, indicating the layer spacing was increased each step and finally exfoliation was achieved and stabilized by the reaction of the double bonds of SBR and those on the clay layer surface, which consequently confers a strong interface to the nanocomposite.

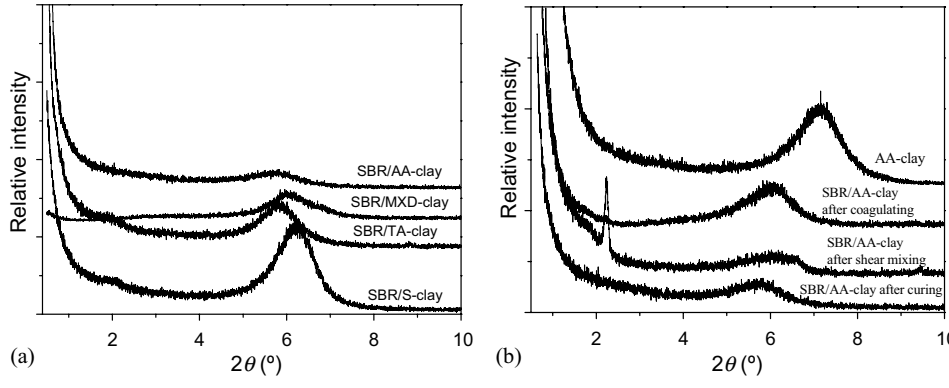

Figure 4.9 XRD patterns of: (a) various SBR/clay nanocomposites and (b) *in situ* characterization of SBR/AA-clay nanocomposites

Figure 4.10a is a low magnification TEM micrograph for SBR/AA-clay nanocomposite, in which exfoliated layers were observed. Some small aggregates were also found, which might comprise of exfoliated layers or intercalate layers. A typical aggregate was observed at higher magnification in Figure 4.10b, which indicates disorderly exfoliated structure. Based on the XRD result and TEM micrographs, it can be concluded that exfoliation has been achieved in SBR/AA-clay nanocomposite.

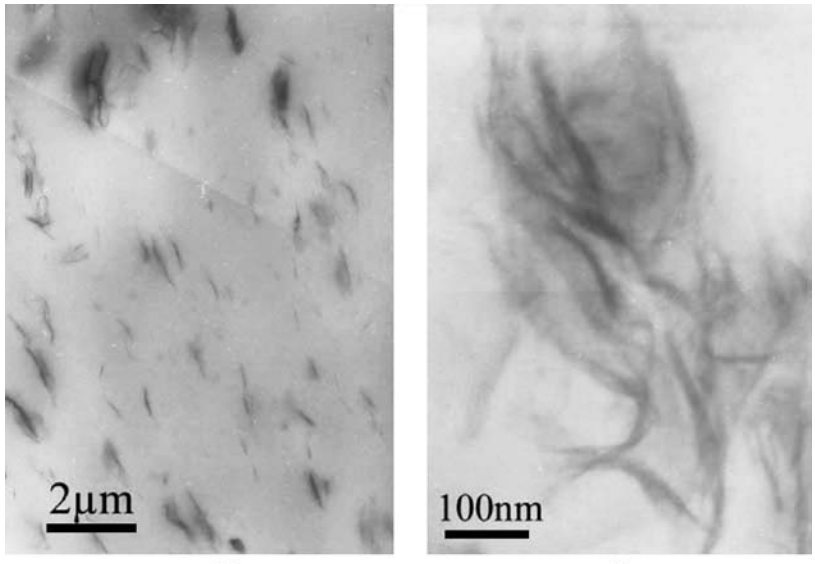

Figure 4.10 TEM images of SBR/AA-clay nanocomposite prepared by the novel approach, revealing the disorderly exfoliated silicate layer structure in SBR

Critical questions may now be asked, since disorderly exfoliated structure is obtained for SBR/AA-clay nanocomposite: when does the exfoliation occur and what is the exfoliation mechanism? The proposed mechanism is shown in Figure 4.11. After modification, the hydrophilic sodium clay becomes more or less hydrophobic depending on the surfactant molecular size and composition. The AA-clay prepared in this study is both hydrophobic and hydrophilic because the size of AA molecular is much smaller compared to other common surfactants, such as octadecylammonium. Thus, AA-clay could form a stable suspension in water even at a low concentration 0.05 wt%, which is the prerequisite for the emulsion compounding method. After coagulation, an initially intercalated structure will be obtained since rubber molecules trapped in latex particles have just a little chance to intercalate in the clay interlayer spacing during the stir mixing and the subsequent coagulating. When the dried SBR/clay is shear mixed with additives, more rubber molecules intercalate into the interlayer spaces. Ultimate exfoliation is achieved and stabilized during vulcanization in which a fierce driving force for exfoliation is provided by the reaction of the double bond of SBR molecule with that of AA grafted on clay.

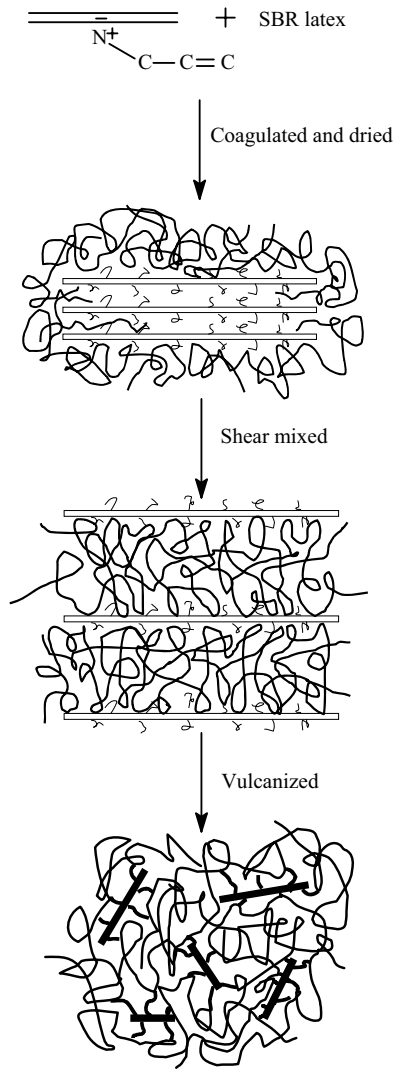

Figure 4.11 Schematic of exfoliation mechanisms

The proposed mechanism can be verified by tracking the gradual intercalation of SBR molecule into the clay layer spacing *in situ* as measured by XRD during the procedure shown in Figure 4.9b. AA-clay shows a strong diffraction pattern at $2\theta = 7.2°$, indicating a layer spacing of 1.2 nm. For SBR/AA-clay after coagulation, a down-shifted pattern occurs at $2\theta = 6.0°$, corresponding to a layer spacing of 1.5 nm, which may be caused by the intercalation of a small amount of SBR molecule into the interlayer spacing. After shear mixing, the intensity of the diffraction pattern at 6.0° is significantly decreased and this indicates more rubber molecule intercalate into the interlayer spacing due to the good compatibility between the matrix and the

surfactant grafted onto the clay layer. In addition, a new peak is found at $2\theta = 2.2^\circ$, which might show a much larger layer spacing of 4.0 nm. It is concluded that shear mixing is helpful to melt intercalation. In our recent study, shear mixing was found to be an efficient method for preparing rubber/clay nanocomposite, since no obvious XRD peak was found for butyl rubber/organic clay (90/10 by weight) nanocomposite. After curing, the intercalation pattern at 2.2° disappeared and exfoliated layers were shown on TEM, demonstrating that exfoliation had occurred and been stabilized finally.

The exfoliated SBR/AA-clay nanocomposite with strong interface shows promising mechanical properties. With only 4 wt% of AA-clay, the tensile strength improves from 2.2 to 9.0 MPa and the elongation at break from 261 to 588% while the hardness remains low at 51 Shore A. These property enhancements are equivalent to what would be achieved by addition of at least 10 wt% CB and also higher than that reported by our previous works [4]. It confirms that both full exfoliation and strong interface are crucial factors in achieving these results.

Zhang also introduced a method to modify clay (montmorillonite) based upon a reactive surfactant N-Allyl-N,N-dimethyl-octadecylammonium chloride ($CH_3CH{=}CHC_{18}H_{37}(CH_3)_2N^+Cl^-$) for the SBR using the LCM method [18]. An intercalation/exfoliation-coexisting structure was obtained. Nevertheless, it shows significantly improved mechanical properties in Table 4.5.

Table 4.5 Mechanical properties of SBR/clay nanocomposites

	Shore A hardness	Tensile strength, MPa	Elongation at break, %
Neat SBR	58	4.3	592
SBR/clay, 10 wt%	59	16.5	734
SBR/clay, 20 wt%	57	18.7	638

Adding a third reactive component is another method to improve the compatibility between rubber and o-clay. Liu mixed the resorcinol and hexamethylenetetramine complex (RH) with nitrile-butadiene rubber (NBR) and o-clay in a two-roll mill [19]. The clay layer spacing increased substantially with RH addition, resulting in highly improved thermal properties and mechanical performance. This is explained as the RH could enhance the interface between rubber and o-clay.

4.5 Characterization of Interface Modification

The interface modification of rubber nanocomposites was characterized by two categories of methods: direct and indirect methods. Direct methods are the use of instruments to identify specific reactions occurred on nanofiller surface, within matrix or between nanofiller and matrix. These methods include Fourier transform infrared (FTIR) spectroscopy, nuclear magnetic resonance (NMR) spectrometry, Elemental analysis (EA), and so on. As a result of interface modification, nanofiller dispersion and mechanical/funtional properties are expected to change dramatically (improve in most cases and deteriorate in rare cases). Indirect methods identify the interface modification by investigating the morphology, the mechanical property, the dynamic mechanical property, the swelling and other properties of the nanocomposites.

4.5.1 Direct Methods for Interface Characterization

Nanofiller modification is often made by a grafting reaction on nanofiller surface using an organic molecule which may contain functional groups for creating molecular entanglements with or producing chemical links to matrix. Upon grafting an organic molecule to nanofiller, the molecule units will demonstrate a distinctive absorption on FTIR [15] and NMR spectrum indicating the interface modification.

The following example is NMR characterization for the modification of clay by M-xylylenediamine (MXD) which subsequently reacted with diglycidyl ether of bisphenol A (DGEBA) [17]. Although it is derived from epoxy/clay nanocomposites, the characterization method is applicable to rubber/clay nanocomposites.

Figure 4.12 shows the ^{1}H NMR spectra of the reactive surfactant MXD and the modified clay. In the free MXD molecule the methylene protons are chemically equivalent and appear as a single resonance at 3.85 ppm. Upon grafting MXD to the clay layer surface via one quaternary ammonium center, the methylene units would no longer be equivalent, and a downfield shift in resonance would be expected for the methylene moiety adjacent to the grafted ammonium center. The ^{1}H NMR spectrum for m-clay exhibits two distinct resonances at 3.87 and 3.98 ppm, and this implies that the two ammonium groups on the MXD molecule are in different chemical environments, with one ammonium group grafted onto the clay layer surface and the other unchanged. This result confirms the reaction of the DGEBA with the dangling ammonium group. When the clay was further modified with epoxy, abundant epoxy signal in ^{1}H NMR (not shown here) was found due to a large amount of DGEBA grafted onto clay via MXD.

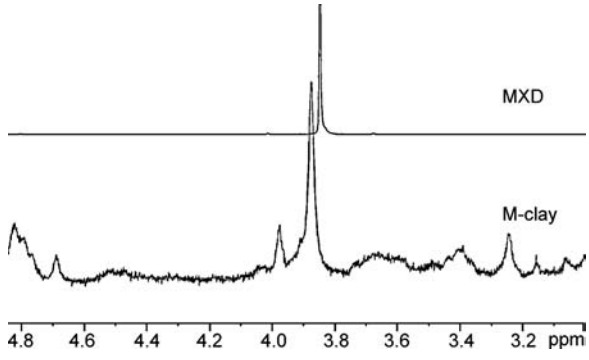

Figure 4.12 ^{1}H NMR spectra of MXD (top) and m-clay (bottom)

In the case of a large amount of or a high molecular weight surfactant grafted on the nanofiller surface, EA is used for characterization [7].

An important means to measure the degree of clay layer dispersion and exfoliation is usually obtained by XRD measurements. Generally intense reflections in the range $2\theta = 3$–9° indicate an orderly intercalated system with alternating polymer/silicate layers. In exfoliated nanocomposites, on the other hand, where single silicate layers (1 nm thick) are homogeneously dispersed in the polymer matrix, XRD patterns with no distinct features in the low 2θ range are anticipated due to the loss of structural registry.

Kim modified clay (montmorillonite) with octylamine $CH_3(CH_2)_7NH_2$ and the modified clay is denoted C8-clay. Similarly, the clay modified by dodecylamine amine $CH_3(CH2)_{11}NH_2$ is denoted C12-clay and the clay modified by octadecylamine $CH_3(CH_2)_{17}NH_2$ is denoted C18-clay [20]. The X-ray diffraction patterns of o-clay are shown in Figure 4.13. The peaks of C8-clay, C12-clay and C18-clay are shifted to lower angles compared with the unmodified clay, which shows a characteristic peak (d001 = 1.23 nm) at 7.16°. The d-spacings of the C8-clay, C12-clay and C18-clay correspond to 1.36, 1.52 and 2.18 nm, respectively. This clearly indicates the graftion of alkylammonium cations onto the silicate layer surface.

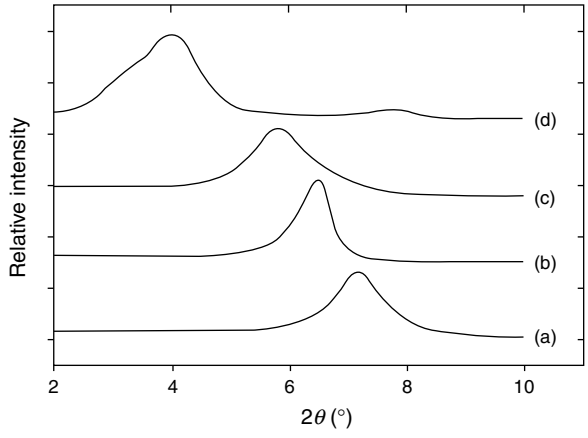

Figure 4.13 X-ray diffraction patterns of (a) Na^+-clay and organoclays: (b) C8-clay, (c) C12-clay and (d) C18-clay ("Preparation and characteristics of nitrile rubber (NBR) nanocomposites based on organophilic layered clay," J.T. Kim, T.S. Oh and D.H. Lee, *Polymer International*, **52**, no. 7, 1058, © 2003, Copyright Society of Chemical Industry. Reproduced with permission. Permission is granted by John Wiley & Sons Ltd on behalf of the SCI.)

Figure 4.14 shows the XRD patterns of NBR/neat clay and NBR/organoclay hybrids. The diffraction peak of NBR/C8-clay are observed at $2\theta = 3.92°$ (d001 = 2.25 nm) compared with C8-clay of 6.5° of 2θ (d001 = 1.36 nm). In the case of NBR/C12-clay and NBR/C18-clay nanocomposites, the characteristic peaks disappear. These results imply that the intercalated silicate layers are probably exfoliated through the melt compounding process.

4.5.2 Indirect Methods for Interface Characterization

Interface modification leads to the uniform dispersion of nanofiller and improved properties. Indirect methods for interface characterization are usually based on the morphology investigation using TEM and on the measurement of properties, such as mechanical property, swelling [19], dynamic mechanical property [20] and other properties of the nanocomposites.

Unmodified nanofillers are often incompatible with polymer matrices, leading to the agglomeration of nanofillers. Interface modification is able to improve the compatibility of nanofillers with polymer matrices, and thus nanofillers are often more separately dispersed in matrices. TEM is a

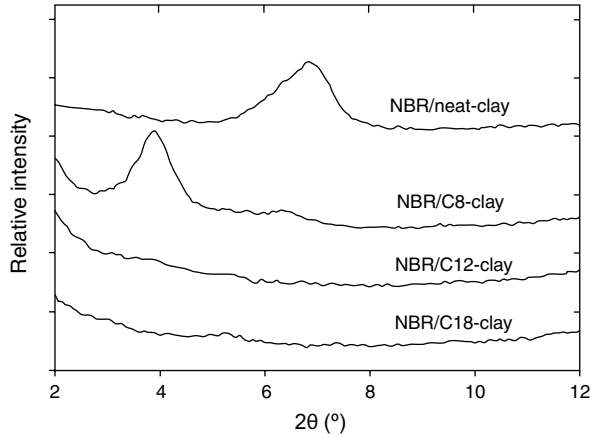

Figure 4.14 X-ray diffraction patterns of NBR hybrids with 4.52 wt% clay ("Preparation and characteristics of nitrile rubber (NBR) nanocomposites based on organophilic layered clay," J.T. Kim, T.S. Oh and D.H. Lee, *Polymer International*, **52**, no. 7, 1058, © 2003, Copyright Society of Chemical Industry. Reproduced with permission. Permission is granted by John Wiley & Sons Ltd on behalf of the SCI.)

powerful tool to monitor the nanofiller dispersion. It is the most authoritative method to characterize the clay exfoliation. Based on extensive TEM observation, Zhang *et al.* draw a conclusion that the structure of rubber/clay nanocomposites prepared by the LCM, method is different from conventional intercalated/exfoliated nanocomposites, because in LCM, the rubber molecules separate the clay particles into either individual layers or just silicate layer aggregates with several nm thickness without intercalation of rubber molecules. Such a structure resulted from the competition between separation of rubber latex particles and re-aggregation of single silicate layers during the coagulation process [21].

Mechanical property testing might be the most convenient characterization for the interface modification of rubber nanocomposites.

Continued from 4.5.1, Kim characterized the interface modification of clay using mechanical property investigation as shown in Figures 4.15–4.17. In the cases of C12-clay and C18-clay, the tensile strength increases rapidly with the clay content in the range 0–8.7 wt%. In the case of C8-clay, significant increase is found for clay content from 0 to 4.52 wt%, and the tensile strength changes less for clay content higher than 4.52 wt%. The tensile moduli of NBR/C12-clay and NBR/C18-clay nanocomposites increase rapidly with increasing clay content. In contrast, the tensile modulus increases slightly with increasing C8-clay content. The elongation at break of the nanocomposites approaches maximum at about 8.7 wt% loading and then decreases with further increase of the clay content. The differences in mechanical properties among the NBR/C8-clay, NBR/C12-clay and NBR/C18-clay hybrids are caused by the modification of organoclay. As illustrated in Figures 4.15–4.17, the mechanical properties of NBR/organoclay hybrids increase in the order: C8-clay < C12-clay < C18-clay, depending on the length of the alkyl chain in the alkyl ammonium, as a longer alkyl chain length means a higher level of interface modification towards compatibilization.

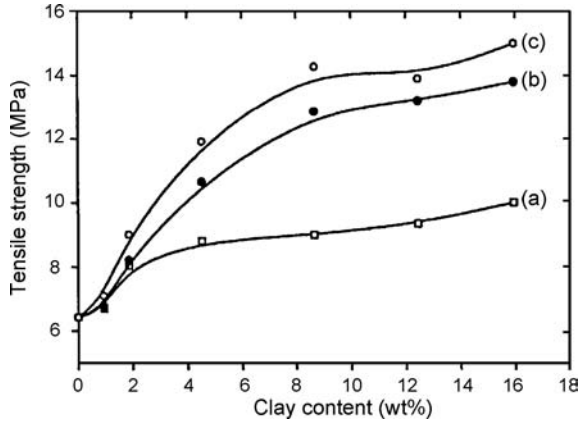

Figure 4.15 Effect of organoclay content on tensile strength of NBR nanocomposites at room temperature: (a) NBR/C8-clay; (b) NBR/C12-clay; and (c) NBR/C18-clay ("Preparation and characteristics of nitrile rubber (NBR) nanocomposites based on organophilic layered clay," J.T. Kim, T.S. Oh and D.H. Lee, *Polymer International*, **52**, no. 7, 1058, © 2003, Copyright Society of Chemical Industry. Reproduced with permission. Permission is granted by John Wiley & Sons Ltd on behalf of the SCI.)

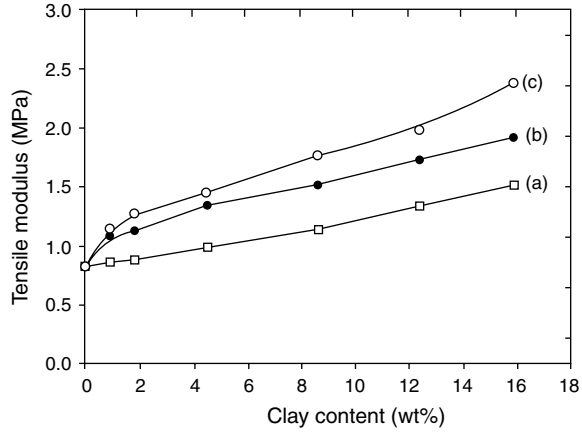

Figure 4.16 Effect of organoclay content on tensile modulus of NBR nanocomposites at room temperature: (a) NBR/C8-clay; (b) NBR/C12-clay; and (c) NBR/C18-clay ("Preparation and characteristics of nitrile rubber (NBR) nanocomposites based on organophilic layered clay," J.T. Kim, T.S. Oh and D.H. Lee, *Polymer International*, **52**, no. 7, 1058, © 2003, Copyright Society of Chemical Industry. Reproduced with permission. Permission is granted by John Wiley & Sons Ltd on behalf of the SCI.)

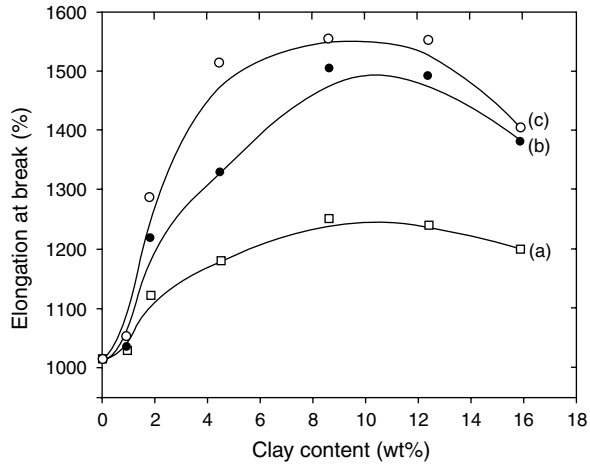

Figure 4.17 Effect of organoclay content on elongation at break of NBR nanocomposites at room temperature: (a) NBR/C8-clay; (b) NBR/C12-clay; and (c) NBR/C18-clay ("Preparation and characteristics of nitrile rubber (NBR) nanocomposites based on organophilic layered clay," J.T. Kim, T.S. Oh and D.H. Lee, *Polymer International*, **52**, no. 7, 1058, © 2003, Copyright Society of Chemical Industry. Reproduced with permission. Permission is granted by John Wiley & Sons Ltd on behalf of the SCI.)

The interface modification leads to a strong interaction between nanofillers and matrices, which can be measured as a free volume by Positron annihilation lifetime spectroscopy. Zhang *et al.* [22] prepared the rubber nanocomposites by LCM and melt blending methods as follows:

1. Latex compounding: about 3% clay aqueous suspension and SBR latex were mixed and vigorously stirred for 20 min. Afterwards, the mixture was co-coagulated in 2% dilute sulfuric acid solution, washed with water, and then dried in an oven at 70 °C for 24 h, and SBR/clay nanocompounds (SBRN/clay) were obtained.
2. Melt blending: organic clay was directly mixed with SBR (not latex) on a two-roll mill for 5 min to obtain SBR/clay nanocompounds (SBRN/o-clay).

The nanocompounds of SBRN/clay and SBRN/o-clay were mixed with other additives on a two-roll mill for 10 min, and then vulcanized at 150 °C in a hot press for the optimum cure time determined by a disk rheometer.

SBR/clay microcomposites (SBRM/clay) and SBR composites filled with carbon black N330 (SBR/N330) were prepared using the same melt-blending procedure as described above.

Figure 4.18 shows the dependence of the free volume of the nanocomposites on the filler volume fraction. SBRN/clay shows the highest free volume (I30), implying the lowest nanofiller interaction with the matrix. A lower free volume was found for SBRM/clay and SBRN/o-clay. SBR/N330 indicates the lowest free volume, meaning the highest interfacial interaction between nanofiller and matrix.

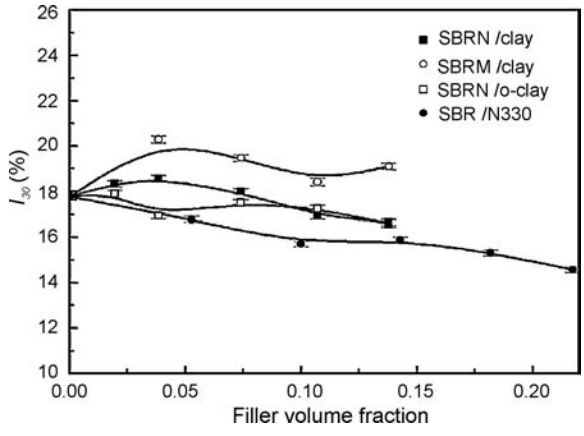

Figure 4.18 Effect of nanofiller volume fraction on the orthopositronium (o-Ps) intensity for nanocomposites

4.6 Conclusion

Although unmodified nanofillers might be able to disperse in rubber matrix, interface modification is preferred for the purpose of significant property enhancement. The interface modification can be accomplished by two routes: the reactive and the nonreactive route. The reactive route employed functional molecules, which would usually contain two reactive cites, one grated onto the nanofiller surface and the other reacted with matrix. This route achieved strong interface as well as clay exfoliation, but not many rubbers contain certain amount of reactive sites for grafting. The nonreactive route involves the filler surface modification using high molecular surfactants to form a core-shell structure. As these surfactants offer high levels of compatibility and chain entanglement with matrix polymers, it actually plays the role of compatibilizers, leading to the uniform dispersion of nanoparticles with good interface. This routine has no specific requirement in terms of the reactive sites for matrix rubber, and the modified nanofillers suit more classes of rubbers.

Mechanical property measurement is the most convenient indirect method to characterize the interface modification, as nonocomposites with strong interface often demonstrate distinctive improvement of mechanical properties. The other indirect methods include morphology observation using transmission electron microscopy (TEM), X-ray diffraction (XRD) testing, dynamic mechanical property measurement, swelling investigation and so on. The direct methods include Fourier transform infrared (FTIR) spectroscopy, nuclear magnetic resonance (NMR) spectrometry, elemental analysis (EA), and so on. These methods quantitatively measure the degree of interface modification.

List of Abbreviations

AA	allylamine
CB	carbon black
C8-clay	clay modified by octylamine $CH_3(CH_2)_7NH_2$

C12-clay	clay modified by dodecylamine amine $CH_3(CH_2)_{11}NH_2$
C16	hexadecyl trimethyl ammonium bromide
C18-clay	octadecylamine $CH_3(CH_2)_{17}NH_2$
DGEBA	diglycidyl ether of bisphenol A
EA	elemental analyser
EPDM	ethylene propylene diene monomer rubber
EPR	ethylene propylene rubber
FTIR	Fourier transform infrared spectroscopy
ISAF	intermediate super abrasion furnace
KH550	3-aminopropyl triethoxy silane
M_w	weight-average molecular weight
MXD	m-xylylenediamine
NBR	nitrile butadiene rubber
NMR	nuclear magnetic resonance
NR	natural rubber
PDMS	polydimethylsiloxane
PVC	polyvinyl chloride
PS	polystyrene
PC	polycarbonate
RH	resorcinol and hexamethylenetetramine complex
SBR	styrene butadiene rubber
S-clay	sodium montmorillonite
SRF	short fibre
TC	talc
TA	triisopropanolamine
XRD	X-ray diffraction

Acknowledgments

J.M. thanks the Australian Research Council for the award of an Australian Postdoctoral Fellowship, tenable at the University of South Australia.

References

1. Morton, M. (1973) *Rubber Technology*, Van Nostrand Reinhold Company, New York.
2. Pinnavaia, T.G. and Beall, G.W. (2000) *Polymer-Clay Nanocomposites*, Wiley, Chichester, England; New York.
3. Wang, Y.Z., Zhang, L.Q., and Wang, Y.Q. (2000) Preparation and characterization of rubber-clay nanocomposites. *Journal of Applied Polymer Science*, **78**(11), 1879–1883.
4. Zhang, L.Q., Wang, Y.Z., and Wang, Y.Q. (2000) Morphology and mechanical properties of clay/styrene-butadiene rubber nanocomposites. *Journal of Applied Polymer Science*, **78**(11), 1873–1879.
5. Wu, Y.P., Zhang, L.Q., and Wang, Y.Q. (2001) Structure of carboxylated acrylonitrile-butadiene rubber (CNBR)-clay nanocomposites by co-coagulating rubber latex and clay aqueous suspension. *Journal of Applied Polymer Science*, **82**, 2842–2848.
6. LeBaron, P.C. and Pinnavaia, T.J. (2001) Clay nanolayer reinforcement of a silicone elastomer. *Chemistry of Materials*, **13**(10), 3760–3765.
7. Ma, J., Xu, J., Ren, J.H. *et al.* (2003) A new approach to polymer/montmorillonite nanocomposites. *Polymer*, **44** (16), 4619–4624.

8. Hasegawa, N., Okamoto, H. *et al.* (2004) Preparation and properties of ethylene propylene rubber (EPR)-clay nanocomposites based on maleic anhydride-modified EPR and organophilic clay. *Journal of Applied Polymer Science*, **93**(2), 758–764.
9. Jia, Q.X., Wu, Y.P., Zhang, L.Q. *et al.* (2007) Organic interfacial tailoring of styrene butadiene rubber-clay nanocomposites prepared by latex compounding method. *Journal of Applied Polymer Science*, **103**(3), 1826–1833.
10. Ma, J., Kuan, H.Q., Dasari, A., Mai, Y.W. *et al.* (2005) A new strategy to exfoliate silicone rubber/clay nanocomposites. *Macromolecular Rapid Communications*, **26**, 830–833.
11. Bokobza, L. (2004) Elastomeric composites. I. Silicone composites. *Journal of Applied Polymer Science*, **93**, 2095.
12. Takeuchi, H., and Cohen, C. (1999) Reinforcement of poly(dimethylsiloxane) elastomers by chain-end anchoring to clay particles. *Macromolecules*, **32**, 6792.
13. Wang, C., Long, X., Wang, Q., and Li, Z. (1998) Synthesis and properties of silicone rubber/organomontmorillonite hybrid nanocomposites. *Journal of Applied Polymer Science*, **69**, 1557.
14. Li, B.Y., Ma, J., Xu, J., Mai, Y.W. *et al.* (2006) Siloxane surfactant-modified clay and its effect in reinforcing the laminate of polymethyl silsesquioxane. *Journal of Applied Polymer Science*, **100**, 3974–3980.
15. Nair, K.G. and Dufresne, A. (2003) Crab shell chitin whiskers reinforced natural rubber nanocomposites. 3. Effect of chemical modification of chitin whiskers. *Biomacromolecules*, **4**(6), 1835–1842.
16. Maiti, M. and Bhowmick, A.K. (2005) Structure and properties of some novel fluoroelastomer/clay nanocomposites with special reference to their interaction. *Journal of Polymer Science, Part B, Polymer Physics*, **44**(1), 162–176.
17. Ma, J., Yu, Z.Z., Zhang, Q.X. *et al.* (2004) A novel method for preparation of disorderly exfoliated epoxy/clay nanocomposite. *Chemistry of Materials*, **16**(5), 757–759.
18. Jia, Q.X., Wu, Y.P., and Zhang, L.Q. (2006) Combining in-situ organic modification of montmorillonite and the latex compounding method to prepare high-performance rubber-montmorillonite nanocomposites. *Macromolecular Materials and Engineering*, **291**(3), 218–226.
19. Liu, L., Jia, D.M., and Luo, Y.F. (2006) Preparation, structure and properties of nitrile-butadiene rubber-organoclay nanocomposites by reactive mixing intercalation method. *Journal of Applied Polymer Science*, **100**(3), 1905–1913.
20. Kim, J.T., Oh, T.S., and Lee, D.H. (2003) Preparation and characteristics of nitrile rubber (NBR) nanocomposites based on organophilic layered clay. *Polymer International*, **52**(7), 1058–1063.
21. Wu, Y.P., Wang, Y.Q., Zhang, L.Q. *et al.* (2005) Rubber-pristine clay nanocomposites prepared by co-coagulating rubber latex and clay aqueous suspension. *Composites Science and Technology*, **65**, 1195.
22. Wang, Y.Q., Wu, Y.P., Zhang, L.Q. *et al.* (2004) Free volume of montmorillonite/styrene-butadiene rubber nanocomposites estimated by positron annihilation lifetime spectroscopy. *Macromolecular Rapid Communications*, **25**(23), 1973–1978.

5

Natural Rubber Green Nanocomposites

Alain Dufresne[1,2]
[1]*Grenoble Institute of Technology, The International School of Paper, Print Media and Biomaterials (Pagora), BP 65, 38402 Saint Martin d'Hères cedex, France*
[2]*Universidade Federal de Rio de Janeiro (UFRJ), Departamento de Engenharia Metalúrgica e de Materiais, Coppe, Rio de Janeiro, Brazil*

5.1 Introduction

Latex from rubber trees (*Hevea brasiliensis*) is virtually the source of all commercial natural rubber (NR; *cis*-1,4-polyisoprene). Both NR and synthetic rubbers like styrene butadiene rubber (SBR) display mechanical properties which make them important and irreplaceable materials in dynamically loaded applications such as tires and engine mounts [1]. NR is mainly used in winter tires and truck tires. Small solid tires are usually made of SBR. The consumption of NR and SBR is equal and the materials can be used interchangeably. The unique mechanical properties of NR result from its highly stereo-regular microstructure, the rotational freedom of the α-methylenic C−C bonds and the entanglements which result from the high molecular weight and contribute to its high elasticity.

The properties of rubbers can be tailored by the addition of fillers [2, 3]. A wide range of fillers are used in the rubber industry to improve and modify the physical properties of elastomeric materials. The addition of the filler usually results in the improvement of the stiffness and hardness, and also of the resistance to abrasion, tear, cutting and rupture. The increase in the modulus is due to the inclusion of rigid filler particles in the soft matrix. Another contribution arises from filler-rubber interactions leading to additional crosslinks in the network structure. In addition, the physical performance of an elastomeric material strongly depends on a large number of parameters, such as volume fraction, as well as the shape, size and aspect ratio of the particles. Fillers are generally classified according to their average particle size. Particles larger than 1 μm do not have reinforcing capabilities (at best) or have a detrimental effect, and they generally increase viscosity by a mere hydrodynamic effect.

Rubber Nanocomposites: Preparation, Properties and Applications Edited by Sabu Thomas and Ranimol Stephen
© 2010 John Wiley & Sons (Asia) Pte Ltd

Reinforcement is readily obtained with sizes smaller than 100 nm, that is, in the range of nanocomposites. It is also found that particle structure is a decisive factor.

Carbon black and silica are the main fillers used in the compounding recipes [4, 5]. Short fibers can be used to reinforce polymers in order to improve or modify certain mechanical properties of the host matrix for specific applications [6]. The use of various natural fibers such as bamboo, coir and oil palm as reinforcing agents in rubber matrices has also been reported [7–12]. More recently, polysaccharide nanocrystals have been used to reinforce NR. The choice of NR as matrix for the processing of such nanocomposites is interesting because of the renewable nature of both components, because the matrix is available as aqueous dispersions (latex) and because the effect of these nanoparticles can be easily compared to any of the other fillers for NR published in the literature.

5.2 Preparation of Polysaccharide Nanocrystals

Stable aqueous suspensions of polysaccharide nanocrystals can be prepared by acid hydrolysis of the biomass (cellulose, chitin, starch). The literature uses different descriptors of the resulting colloidal suspended particles, including whiskers, monocrystals and nanocrystals. The designation "whiskers" is used to designate elongated rod-like nanoparticles. These crystallites are also often described in the literature as microfibrils, microcrystals or microcrystallites, despite their nanoscale dimensions. Most of the studies reported in the literature refer to cellulose nanocrystals. A recent review reported the properties and application in nanocomposite field of cellulosic whiskers [13]. A more general description of nanocrystals extracted from cellulose, chitin or starch can be found elsewhere [14].

The procedure for the preparation of such colloidal aqueous suspensions is described in detail in the literature for cellulose and chitin [15, 16]. The biomass is generally first submitted to a bleaching treatment with NaOH in order to purify cellulose or chitin by removing other constituents. The bleached material is then disintegrated in water, and the resulting suspension is submitted to a hydrolysis treatment with acid. The amorphous regions of cellulose or chitin act as structural defects and are responsible of the transverse cleavage of the microfibrils into short monocrystals under acid hydrolysis [17, 18], as schematically illustrated in Figure 5.1. Under controlled conditions, this transformation consists of the disruption of amorphous regions surrounding and embedded within cellulose or chitin microfibrils, while leaving the microcrystalline segments intact. It is ascribed to the faster hydrolysis kinetics of amorphous domains compared to crystalline ones. The resulting suspension is subsequently diluted with water and washed by successive centrifugations. Dialysis against distilled water is then performed to remove free acid in the dispersion. Complete dispersion of the whiskers is obtained by a sonication step. The dispersions are stored in the refrigerator after filtration to remove residual aggregates and addition of several drops of chloroform. This general procedure has to be adapted depending on the nature of the substrate. In the specific cases of chitin whiskers obtained from crab shell and cellulose whiskers extracted from date palm tree, the procedure is reported in Refs. [19, 20], respectively.

Aqueous suspensions of starch nanocrystals can be also prepared by acid hydrolysis of native starch granules. It can be performed in aqueous medium with hydrochloric or sulfuric acid but at lower temperature than for cellulose or chitin because gelatinization of starch in acid medium occurs at relatively low temperature. Response surface methodology was used by Angellier *et al.* [21] to investigate the effect of five selected factors on the selective sulfuric acid hydrolysis of waxy maize starch granules in order to optimize the preparation of aqueous

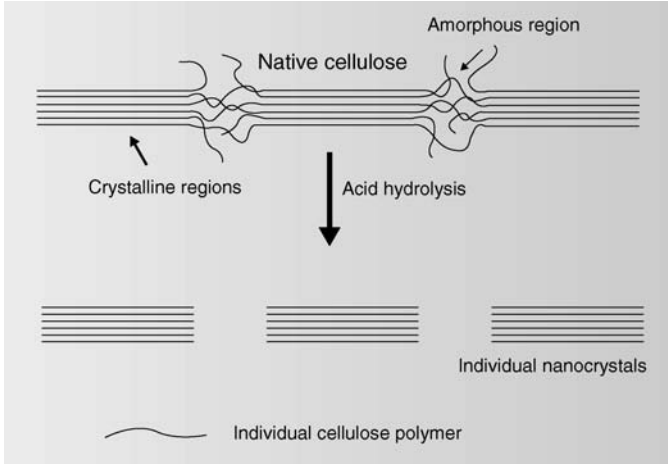

Figure 5.1 Schematic illustration of the effect of acid hydrolysis of cellulose or chitin: example of cellulose

suspensions of starch nanocrystals. These predictors were temperature, acid concentration, starch concentration, hydrolysis duration and stirring speed.

The stability of resulting suspensions depends on the dimensions of the dispersed particles, their size polydispersity and surface charge. The use of sulfuric acid rather than hydrochloric acid leads to a more stable aqueous suspension [22, 23]. Indeed, the H_2SO_4-prepared whiskers present a negatively charged surface, while the HCl-prepared whiskers are not charged. During acid hydrolysis of most clean cellulose sources via sulfuric acid, acidic sulfate ester groups are likely formed on the nanoparticle surface.

5.3 Processing of Polysaccharide Nanocrystal-Reinforced Rubber Nanocomposites

Because of the high stability of aqueous polysaccharide nanocrystals dispersions, water is the preferred processing medium. Rubber is not hydrosoluble but native NR occurs as an aqueous dispersed polymer, that is, latex. Then the processing of polysaccharide nanocrystal-reinforced NR is very simple and consists in mixing and casting the two aqueous suspensions. A solid nanocomposite film can be then obtained by water evaporation and particle coalescence (film casting) or by freeze-drying, followed by classical hot-pressing or extrusion processes.

For the present chapter, NR was kindly supplied as unvulcanized NR latex by the Technical Center, MAPA, Liancourt, France, for chitin whisker- and starch nanocrystal-reinforced composites. It contained spherical particles with an average diameter around 1 μm and had a total solid content (TSC) and a dry rubber content (DRC) of 61.58 and 60.1%, respectively. Sodium laurylsulfate (0.2 g per 100 g of dry rubber) and potassium (0.4 g per 100 g of dry rubber) were added as stabilizers. The density of dry NR was 1 g cm^{-3}. Unvulcanized NR latex used for date palm tree cellulose whisker-reinforced composites was kindly supplied by Michelin (Clermont Ferrand, France). It contained spherical particles with an average diameter around 1 μm and its weight concentration was about 50 wt%. The dry NR had a density, ρ_{NR}, of 1 g cm^{-3} and it contained more than 98% of *cis*-1,4-polyisoprene. Prevulcanized latex with low

degree of crosslinking was kindly provided by SAFIC ALCAN, Puteaux, France. Its TSC, DRC and density were 61.5%, 60% and 1 g cm^{-3}, respectively. Vulcanizing agents such as tetra methyl thiuram disulfide (TMTD) and zinc oxide (ZnO) were used as accelerator and activator, respectively, in this latex. The latex particle size was around 1 μm.

The processing of nanocomposite materials from an organic solvent solution instead of using aqueous suspensions can be also considered. It is necessary to proceed to an exchange solvent process or to chemically modify the surface of polysaccharide nanocrystals to reduce their surface energy. In the literature, the following reagents were used:

1. A commercial succinic anhydride (ASA, Accosize 18 from American Cynamid) consisting of a mixture of oligomers of different sizes, centered around C18 (Mn = 300), bearing the general structure:

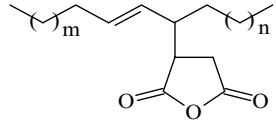

2. Phenyl isocyanate (PI, Aldrich):

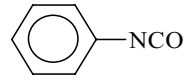

3. Isopropenyl-α,α′-dimethylbenzyl isocyanate (TMI, Aldrich):

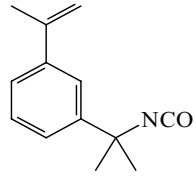

These were used to disperse chitin nanocrystals obtained from crab shell in toluene [24] whereas the two former were used for starch nanocrystals [25]. After mixing these suspensions with NR solution in toluene, solid films were obtained by toluene evaporation.

Sample details and codifications used in this chapter are listed in Table 5.1.

Attempts were made to extrude cellulosic whiskers directly with melt NR. However, the mixture was too viscous. In addition, the dispersion level of the filler within the NR matrix and then the performances of the ensuing composites will be certainly very poor, cellulose being highly polar.

5.4 Morphological Investigation

Figure 5.2a shows a transmission electron micrograph (TEM) of a diluted suspension of hydrolyzed crab shell chitin. The chitin fragments consist of slender rod-like nanoparticles with sharp points that have a broad distribution in size. The average length and width were estimated to be around 240 and 15 nm, respectively [19]. The average aspect ratio (L/d, L being the length and d the diameter) of these whiskers is therefore around 16. The diffraction pattern obtained for chitin whisker suspension using transmission microscopy studies is also depicted in Figure 5.1a. The sharp and well defined diffraction rings obtained indicate the crystalline

Table 5.1 Codification of the samples

Sample	Filler	Modification	Matrix	Medium	Processing technique	Filler content (wt%)
NRev			Unvulc. NR	Water	Water evaporation	
PNRev	None	None	Prevulc. NR	Water	Water evaporation	0
NRfd			Unvulc. NR	Water	Freeze-drying and hot-pressing	
NRtolev			Unvulc. NR	Toluene	Toluene evaporation	
NRevC2						2
NRevC5	Crab shell					5
NRevC10	Chitin whiskers	None	Unvulc. NR	Water	Water evaporation	10
NRevC15						15
NRevC20						20
PNRevC2						2
PNRevC5	Crab shell					5
PNRevC10	Chitin whiskers	None	Prevulc. NR	Water	Water evaporation	10
PNRevC15						15
PNRevC20						20
NRfdC5						5
NRfdC10	Crab shell	None	Unvulc. NR	Water	Freeze-drying and hot-pressing	10
NRfdC15	Chitin whiskers					15
NRfdC20						20
NRasaC10	Crab shell	ASA				10
NRtmiC10	Chitin whiskers	TMI	Unvulc. NR	Toluene	Toluene evaporation	10
NRpiC10		PI				10
NRevW2						2
NRevW5						5
NRevW10						10
NRevW15	Waxy maize starch					15
NRevW20	Nanocrystals	None	Unvulc. NR	Water	Water evaporation	20
NRevW25						25
NRevW30						30
NRevW40						40
NRevW50						50
NRasaW5						5
NRasaW10	Waxy maize starch	ASA	Unvulc. NR	Toluene	Toluene evaporation	10
NRasaW20	Nanocrystals					20
NRpiW5						5
NRpiW10	Waxy maize starch	PI	Unvulc. NR	Toluene	Toluene evaporation	10
NRpiW20	Nanocrystals					20
NRevCell1						1
NRevCell2.5	Date palm tree	None	Unvulc. NR	Water	Water evaporation	2.5
NRevCell5	Cellulose whiskers					5
NRevCell10						10
NRevCell15						15

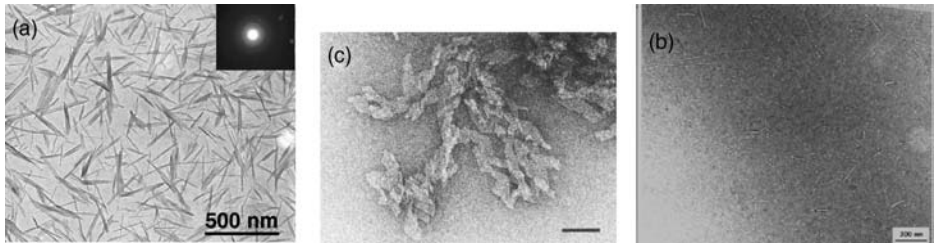

Figure 5.2 Transmission electron micrograph of a dilute suspensions. (a) Crab shell chitin whiskers (inset: typical electron diffractogram recorded on chitin fragments) [19] (Reprinted with permission from N.K. Gopalan and A. Dufresne, "Crab shells chitin whiskers reinforced natural rubber nanocomposites. 1. Processing and swelling behavior," *Biomacromolecules*, **4**, no. 3, 657–665, 2003. © 2003 American Chemical Society); (b) Waxy maize starch nanocrystals (scale bar: 50 nm) [26] (Reprinted with permission from J.L. Putaux, S. Molina-Boisseau, T. Momaur and A. Dufresne, "Platelet nanocrystals resulting from the disruption of waxy maize starch granules by acid hydrolysis," *Biomacromolecules*, **4**, no. 5, 1198–1202, 2003. © 2003 American Chemical Society); (c) Date palm tree cellulose whiskers [20] (Reprinted with permission from A. Bendahou, Y. Habibi, H. Kaddami and A. Dufresne, *Journal of Biobased Materials and Bioenergy*, **3**, 2009. Copyright © American Scientific Publishers, www.aspbs.com.)

nature (amorphous protein part and amorphous chitin domains have been removed during acid hydrolysis) of chitin whiskers present in the suspension.

Waxy maize starch nanocrystals consist of platelet-like particles with a thickness of 6–8 nm, a length of 40–60 nm and a width of 15–30 nm [26]. Such nanocrystals are generally observed in the form of aggregates (Figure 5.2b) having an average size around 4.4 μm, as measured by laser granulometry [21]. Despite the micrometric scale of the starch nanoparticles, the term nanocomposite is suitable for starch nanocrystal/NR materials since the primary particles are nanometric, as for carbon black-filled materials. In addition, we can suppose that at least one of the dimensions of the aggregates is at the nanometer scale.

Cellulose whiskers were extracted from the rachis of the date palm tree (Figure 5.2c). They consist of rod-like nanoparticles with an average length and width around 260 and 6.1 nm, respectively [20], giving rise to an aspect ratio of 43. For whiskers extracted from the leaflets of the date palm tree, the average length and diameter were around 180 and 6.1 nm, respectively (aspect ratio around 30). This difference was ascribed to the higher cellulose content of the rachis [20].

For all kinds of filler, scanning electron microscopy (SEM) displayed a uniform distribution of the filler within the elastomeric matrix when casting and water evaporation was used to process the nanocomposite films [19, 20, 27]. For crab shell chitin whisker-reinforced NR a poorer filler distribution was observed in freeze-dried and hot-pressed materials (NRfd series) [19]. When the surface of the polysaccharide nanocrystals was chemically modified, a nonuniform distribution of the filler was clearly observed [24, 27]. Large smooth unfilled domains were shown by SEM observation of the freshly fractured surface.

5.5 Swelling Behavior

The swelling process and its kinetics give an idea about the capacity of a linear or branched polymer to dissolve or of a crosslinked polymer to swell in different liquids and vapor media.

The interaction of polymeric materials with solvents is a huge problem from both academic and technological points of view. The mass and dimensions of polymer systems may be changed due to the penetration of solvents into swollen specimens. When a crosslinked polymer is brought into contact with a solvent, the network absorbs a certain amount of solvent, which strongly depends on the temperature, molecular weight of this solvent, crosslinking density of the polymer and polymer/solvent interactions, besides the ingredients added.

When an elastomer and reinforcing filler are mixed, strong interactions occur so that a good solvent of the polymer can extract only a free rubber portion, leaving a highly swollen rubber-filler gel. This fraction of bounded rubber (FBR) is, by definition, the rubber content of this gel. The choice of the solvent used for the experiment is of importance. It must be a good solvent of the matrix to allow its swelling or dissolution, but it must not be able to break the eventual links between the matrix and the filler. If this last condition is not respected, the experiments cannot be conclusive.

The kinetics of solvent absorption consists generally in first drying and weighing the sample, and then immersing it in the liquid solvent or exposing it to the vapor medium. The sample is then removed at specific intervals and weighed up to an equilibrium value is reached. The swelling rate of the sample can be calculated by dividing the gain in weight by the initial weight. Generally, the short-time behavior displays a fast absorption phenomenon whereas at longer times, the kinetics of absorption is low and leads to a plateau, corresponding to the solvent uptake at equilibrium. The diffusion coefficient can be determined from the initial slope of the solvent uptake curve as a function of time. Details of the calculation can be found elsewhere [28]. At short times, the mass (M) of absorbed liquid at time t ($M_t - M_0$) is given by:

$$\frac{M_t - M_0}{M_\infty} = \frac{2}{\pi}\left(\frac{D}{\pi}\right)^{1/2} t^{1/2} \tag{5.1}$$

where M_∞ is the mass of liquid sorbed at equilibrium and $2L$ is the thickness of the polymeric film. The diffusivity or diffusion coefficient, D, of the liquid in the material can be estimated from the slope of the plot of $(M_t - M_0)/M_\infty$ as a function of $(t/L^2)^{1/2}$ for $(M_t - M_0)/M_\infty \leq 0.5$.

5.5.1 Toluene Swelling Behavior

5.5.1.1 Chitin Whisker-Reinforced NR

The toluene uptake of crab shell chitin whisker/prevulcanized NR nanocomposites when immersed in toluene was determined (Table 5.2) [19]. It was found that as the whiskers content increased, the toluene uptake values decreased continuously with a sharp evolution of 5–10 wt%. The crosslink density of the evaporated matrix from prevulcanized latex (PNRev) was calculated from the classical equation [29] and it was found to be around 13 000 g mol^{-1}. The monomeric molecular weight of NR being 68 g mol^{-1}, the average number of monomer units between crosslinks is of the order of 190.

In Figure 5.3, the weight swelling rate, $\phi_p = M_\infty/M_0$ is plotted for the samples prepared from the prevulcanized latex as a function of chitin whisker content. For the unfilled matrix it was found to be around 5.9. For composite materials ϕ_p values were corrected to account for the fact that only the matrix phase can be swelled by the solvent. The filler weight must be removed from both M_0 and M_∞ data. As the whiskers content increases, ϕ_p decreases. The corrected

Table 5.2 Toluene uptake at equilibrium and toluene diffusion coefficients in chitin whiskers/prevulcanized NR and starch nanocrystals/unvulcanized NR composites immersed in toluene at room temperature

Sample	Toluene uptake at equilibrium (%)	Toluene diffusion coefficient ($cm^2\,s^{-1} \times 10^8$)
PNRev	488	14.1
PCH5ev	413	8.1
PCH10ev	331	5.0
PCH15ev	282	4.6
PCH20ev	239	4.4
NRev	$\propto$	40.0
NRevW2	$\propto$	38.0
NRevW5	3290	20.8
NRevW10	2660	7.9
NRevW15	2210	5.4
NRevW20	2020	5.1
NRevW30	1320	3.4
NRevW40	1110	3.8
NRevW50	750	1.6

value is only around 4 for the 20 wt% chitin whisker-filled composite. Therefore, the swelling of the material is strongly reduced in the presence of chitin whiskers within the NR matrix, and a decrease of around 50% is observed for the highly filled material (20 wt%). Similar results were reported for cellulose whisker-filled plasticized starch when submitted to high moisture conditions [28, 30]. This phenomenon was ascribed to the formation of a rigid cellulose network, which prevented the swelling of the starch and therefore its water absorption. This 3-D network was found to result from the establishment of strong hydrogen bonding between cellulose whiskers that can develop during the film formation (evaporation step). The reduction of the swelling rate for chitin whisker-reinforced NR most probably results from a similar

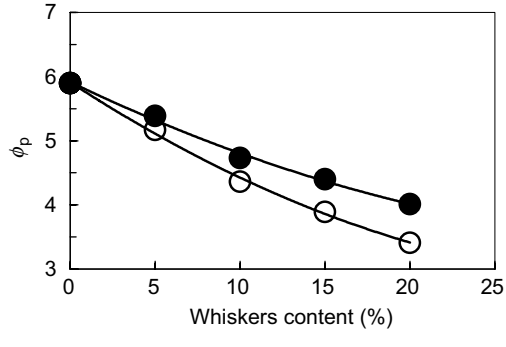

Figure 5.3 Raw (●) and corrected (○) weight swelling rate (ϕ_p) of vulcanized samples in toluene at room temperature (25 °C) as a function of chitin whiskers content. Solid lines serve to guide the eye [19] (Reprinted with permission from N.K. Gopalan and A. Dufresne, "Crab shells chitin whiskers reinforced natural rubber nanocomposites. 1. Processing and swelling behavior," *Biomacromolecules*, **4**, no. 3, 657–665, 2003. © 2003 American Chemical Society.)

phenomenon and can be ascribed, at least partially, to the formation of a chitin network within the vulcanized rubber. It can also result from strong interaction between the chitin filler and the crosslinked polymeric chains, preventing the swelling of the polymeric chains located in the interfacial zone.

The toluene diffusion coefficient, D, in these vulcanized NR-based composites was also determined (Table 5.2) [19]. The unfilled matrix presented the maximum diffusion coefficient (around $1.4 \times 10^{-7}\,cm^2\,s^{-1}$). Adding chitin whiskers within the NR matrix results in a progressive decrease of D with a sharp evolution between 0 and 10 wt%, down to 4.4×10^{-8} $cm^2\,s^{-1}$ for the 20 wt% filled system. This observation was attributed to the increasing stiffness of the hydrogen bonded chitin network by increasing the filler content. It was also supposed to result from strong interactions between the filler and the matrix, which limits the toluene diffusivity within the entangled polymer matrix.

Figure 5.4 shows photographs of unvulcanized NR/chitin whisker nanocomposites before and after 24 h swelling in toluene. It can be seen that all the samples swelled after immersion in toluene. It has also been observed that both neat unvulcanized NR and 5 wt% filled composite completely disrupted after 24 h of swelling hence they are not included in Figure 5.4. By comparing photographs of swelled evaporated samples (NRevC series) it clearly appears that swelling of the material systematically decreases with increasing amount of chitin whiskers within the NR matrix, as observed for vulcanized NR-based materials. This observation was quantified by measuring the diameter of the disk after 24 h swelling in toluene. Results are reported in Table 5.3. For some compositions, swelling was not isotropic in the radial direction and the diameter was averaged. The diameter of the 10 wt% filled composite increased by 67% upon swelling. For the 20 wt% filled material the diameter increase was only 33%. As for vulcanized NR-based composites, this phenomenon can be explained, at least partially, by the formation of a hydrogen-bonded whiskers network within the matrix. This stiff network hinders the swelling of the elastomer.

The effect of processing technique on swelling can be analyzed by comparing evaporated and hot-pressed samples for a given composition (Figure 5.4 and Table 5.3). It is clearly observed that the degree of swelling upon toluene immersion is much higher for hot-pressed sample than for evaporated sample regardless the composition. It is also observed that the diameter of the swelled 10 wt.-% filled evaporated specimen (NRevC10) is similar to that of 20 wt% filled hot-pressed (NRfdC20) composite. A possible explanation could be ascribed to the fact that not only the presence of a chitin-chitin network, but the amount of whiskers also affects the degree of swelling. From these results, it is assumed that the formation of a hydrogen-bonded network of whiskers within the matrix is a major reason for the lower degree of swelling exhibited by evaporated samples than hot pressed samples. The evaporation method is a slow step process, in which whiskers get enough time and mobility to establish a rigid chitin-chitin network within the host matrix. In contrast, in the freeze-drying and subsequent hot-pressing method, the mobility of rubber chains and whiskers are completely arrested all on a sudden during initial quenching process. It results in the formation of filler aggregates within the matrix and which in turn causes poorer dispersion of chitin whiskers in the medium. SEM analysis supported this assumption [19].

For crab shell chitin whisker-reinforced unvulcanized samples, the swelling experiments were more difficult to perform since part of the sample can dissolve in toluene during a long-term swelling experiment. Therefore instead of following the above procedure, the bound rubber content (FBR) and the fraction of NR dissolved in toluene were determined. It consisted in first weighing (M_0) thin disks of sample material that were then immersed in toluene for 48 h.

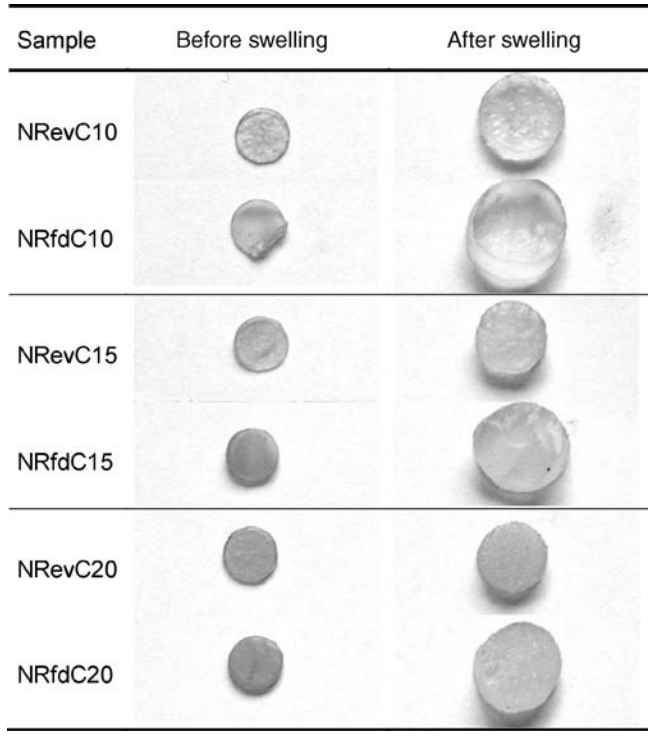

Figure 5.4 Photographs of unvulcanized samples (prepared by evaporation and hot-pressing methods) before and just after swelling in toluene for 24 h at room temperature (25 °C). The diameter of all samples before swelling was $d_0 = 7.5$ mm [19] (Reprinted with permission from N.K. Gopalan and A. Dufresne, "Crab shells chitin whiskers reinforced natural rubber nanocomposites. 1. Processing and swelling behavior," *Biomacromolecules*, **4**, no. 3, 657–665, 2003. © 2003 American Chemical Society.)

They were subsequently dried for 12 h at 55–60 °C and weighed again (M'_0). The "sol" fraction (M'_0/M_0) and relative weight loss (RWL $= [M_0 - M'_0]/M_0$) were then determined. This allowed estimating the fraction of NR bonded to the filler (FBR) and the fraction of NR dissolved in toluene.

Table 5.3 Diameter (d) of chitin whiskers/unvulcanized NR composite disks immersed for 24 h in toluene. The initial sample diameter (before swelling) was $d_0 = 7.5$ mm and the diameter variation was determined by $(d - d_0)/d_0$

Sample	Processing technique	d (mm)	Diameter variation (%)
NRevC10	Water evaporation	12.5	67
NRevC15		11.0	47
NRevC20		10.0	33
NRfdC10	Freeze-drying and hot-pressing	15.0	100
NRfdC15		13.5	80
NRfdC20		12.5	67

The bound rubber content and fraction of NR dissolved in toluene after 48 h for unvulcanized NR based materials were determined and data are collected in Table 5.4. Figure 5.5 displays the evolution of the relative weight loss (RWL) versus chitin whiskers content for both evaporated and hot-pressed unvulcanized NR based composites. Data show that about 50% of the unfilled material is dissolved in toluene. The dissolution of a limited amount of NR is ascribed to the fact that the experiment was performed at room temperature without any stirring. The RWL is slightly higher for the evaporated matrix (NRev) than for the hot-pressed one (NRfd). It could be due to the formation of short crosslinks developed in the NR during hot-pressing.

Table 5.4 Relative weight loss (RWL) and fraction of bound rubber matrix (FBR) of chitin whiskers/unvulcanized NR composite disks immersed for 48 h in toluene and dried for 12 h at 55–60 °C

Sample	Processing technique	RWL (%)	FBM (%)
NRev	Water evaporation	53.5	0
NRevC5		45.5	5.3
NRevC10		11.8	36.6
NRevC15		10.1	35.4
NRevC20		7.5	35.3
NRfd	Freeze-drying and hot-pressing	50.4	0
NRfdC5		46.2	1.7
NRfdC10		18.0	27.4
NRfdC15		13.6	29.2
NRfdC20		11.8	28.5

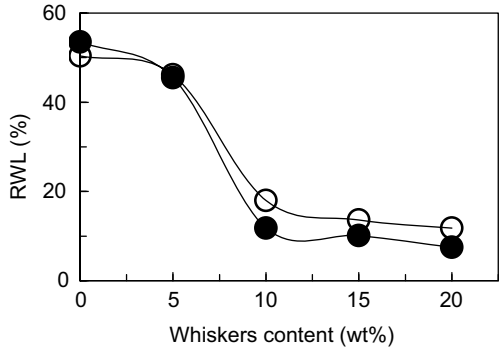

Figure 5.5 Relative weight loss of evaporated (○) and hot-pressed (●) unvulcanized samples after immersion in toluene at room temperature (25 °C) for 48 h and subsequent drying at 55–60 °C for 12 h. Solid lines serve to guide the eye [19] (Reprinted with permission from N.K. Gopalan and A. Dufresne, "Crab shells chitin whiskers reinforced natural rubber nanocomposites. 1. Processing and swelling behavior," *Biomacromolecules*, **4**, no. 3, 657–665, 2003. © 2003 American Chemical Society.)

As the whiskers content increases, the RWL of the sample decreases with a sharp evolution between 5 and 10 wt%. For all composites, the RWL values are higher for hot-pressed samples than for evaporated ones. This observation can be ascribed again to the formation of a rigid

chitin network within the evaporated materials. This network is expected to form above the critical volume fraction at the percolation threshold, v_{Rc}. For a 3-D network, v_{Rc} depends on the aspect ratio L/d of the fiber, as $v_{Rc} = 0.7/(L/d)$ [13, 14]. For chitin whiskers obtained from crab shells, the aspect ratio close to 16 leads to a value of $v_{Rc} = 4.4$ vol%, that is, around 6.4 wt%. This value is in the range 5–10 wt% for which the evolution of both the RWL and toluene uptake at equilibrium is fast. However, it seems that the influence of this network on the dissolution of NR chains is limited. The main parameter that is involved in this process, is the presence of chitin whiskers and their level of interaction with the matrix. That is, the filler-matrix interactions should be sufficiently strong to prevent the dissolution of NR chains and maintain them in the "sol" fraction of the sample.

The fraction of bonded matrix (FBR) was determined from RWL data. It is worth noting that FBR values correspond to the NR fraction, which is entrapped within the network of chitin and on the surface of the chitin whiskers. For the calculation it was assumed that the insoluble part of the unfilled matrix ($1 - \mathrm{RWL_o}$) should be present in the composites balanced by the matrix content ($1 - w_F$; w_F being the filler weight fraction). The "sol" fraction (% "sol") of each sample is therefore the sum of three terms:

$$\%\text{“sol”} = 1-\mathrm{RWL} = w_F + (1-\mathrm{RWL_0})(1-w_F) + \mathrm{FBR} \tag{5.2}$$

The first (w_F) corresponds to the whiskers content, the second [$(1 - \mathrm{RWL_0})(1 - w_F)$] to the insoluble part of the matrix and the third (FBR) to the fraction of NR in strong interaction with the surface of the chitin filler. The FBR values calculated from Equation 5.2 are collected in Table 5.4. It is interesting to see that FBR values first strongly increase with filler content and then stabilize for chitin whisker fractions higher than 5 wt%, that is, above the percolation threshold. For a low whiskers content, it seems quite normal that the fraction of bonded matrix increases with the filler content as a result of the increase of the interfacial area. Above the percolation threshold, the interfacial area increases continuously but the following two phenomena can be appeared at high filler loading. On the one hand, the overlapping of the whiskers restricts the filler/matrix interfacial area and, on the other hand, as the whiskers network closes up the entrapping matrix fraction decreases. These two effects are the responsible reasons for the stabilization of the FBR above the percolation threshold.

5.5.1.2 Starch Nanocrystal-Reinforced NR

The kinetics of toluene absorption was also determined for waxy maize starch nanocrystal-reinforced unvulcanized NR (NRevW series). Figure 5.6a shows the evolution of the toluene uptake (TU) versus time for different starch contents. All the compositions absorbed toluene during the experiment. Two zones can be distinguished. The first zone, corresponding to $t < 10$ h, is characterized by fast absorption kinetics. A clear trend is observed with respect to the starch content: the higher the starch content, the lower the absorption rate. In the second zone, associated with long times of experiments, the toluene uptake increases more slightly until reaching a plateau corresponding to the toluene uptake at equilibrium. For low starch contents (0 and 2 wt%), the second zone is not observed. A disruption of part of the films due to their repetitive manipulations rapidly occurred, preventing their weighing after several hours of immersion. Thereby, the TU at equilibrium for NRev and NRevW2 films was considered to be infinite. It is worth noting that only 5 wt% of starchy filler allows preventing the disruption of

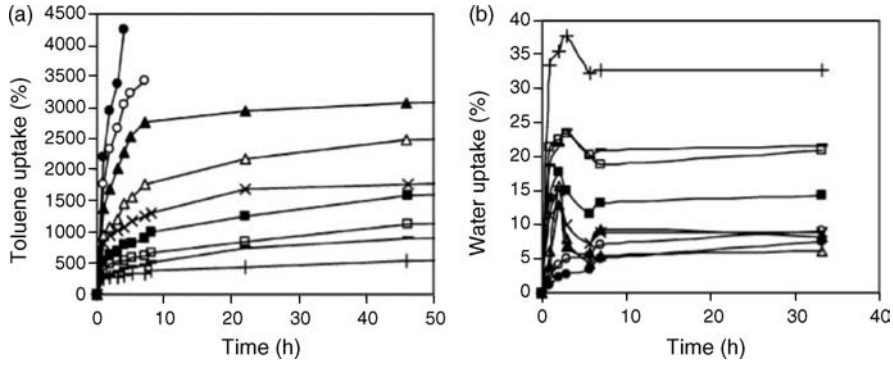

Figure 5.6 Evolution of: (a) toluene uptake and (b) water uptake as a function of time at room temperature for NRev (○), NRevW2 (●), NRevW5 (▲), NRevW10 (△), NRevW15 (×), NRevW20 (■), NRevW30 (□), NRevW40 (−), NRevW50 (+). Solid lines serve to guide the eyes [27] (Reprinted with permission from H. Angellier, S. Molina-Boisseau, L. Lebrun and A. Dufresne, "Processing and structural properties of waxy maize starch nanocrystals reinforced natural rubber," *Macromolecules*, **38**, no. 9, 3783–3792, 2005. © 2005 American Chemical Society.)

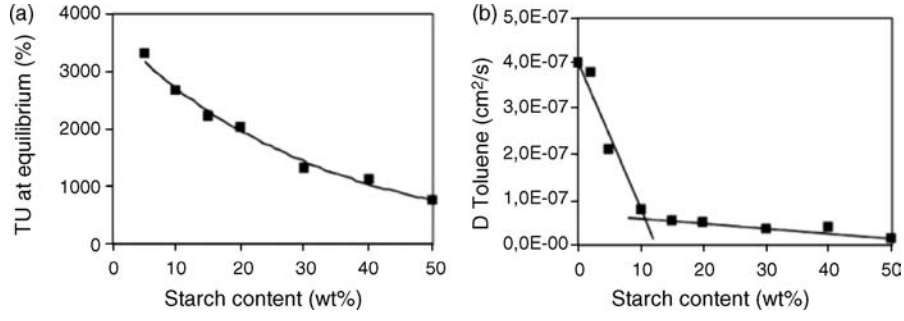

Figure 5.7 Evolution of: (a) toluene uptake at equilibrium and (b) diffusion coefficient of toluene for starch nanocrystals/NR nanocomposite films as a function of starch content. The solid lines serve to guide the eyes [27] (Reprinted with permission from H. Angellier, S. Molina-Boisseau, L. Lebrun and A. Dufresne, "Processing and structural properties of waxy maize starch nanocrystals reinforced natural rubber," *Macromolecules*, **38**, no. 9, 3783–3792, 2005. © 2005 American Chemical Society.)

the matrix. The toluene uptake values at equilibrium were measured after 7 days of immersion (170 h) and are given in Table 5.2. We can notice that TU values at equilibrium decrease continuously when increasing the starch content (Figure 5.7a).

The toluene diffusivities or diffusion coefficients of toluene, noted D_{toluene}, were estimated for all compositions. These values are collected in Table 5.2. The unfilled NR matrix displayed the highest toluene diffusion coefficient. Adding starch nanocrystals to the NR matrix first resulted in a dramatic decrease of the toluene diffusivity, followed by a more progressive linear decrease from 10 wt% of filler (Figure 5.7b).

All these results seem to show that starch nanocrystals may form a 3-D network, in agreement with TEM observations (Figure 5.1), that allows reducing the swelling capability of the matrix. It is assumed to result from the establishment of strong hydrogen bonds between particles that can form during the evaporation process like for chitin whiskers. The structure of starch nanocrystals is completely different but one can assume that above a given volume fraction, starch nanoparticles clusters can connect to form a continuous infinite and open network. This assumption was also supported by SEM observations [27]. The reduction of swelling upon starch nanocrystals addition could also be due to possible interactions between starch and natural rubber, thereby preventing the swelling of the polymeric chains located in the interfacial zone.

The starch nanocrystal-reinforced nanocomposite materials about 1 mm thick were immersed in toluene for 48 h, dried overnight at 40 °C and weighed. The relative weight loss values, RWL, are given in Table 5.5. Data show that about 15 wt% of the unfilled matrix was dissolved in toluene after 48 h immersion. Again, the dissolution of a limited amount of NR can be ascribed to the fact that the experiment was performed at room temperature without any stirring or repetitive manipulations. Furthermore, it is worth noting that the thickness of the films (around 1 mm) was in this case higher than those of the films used for diffusivity measurements (around 0.2 mm). It is observed that RWL increases for starch contents higher than 5 wt%. This result reveals that, contrarily to what was observed for chitin whisker-filled NR, the addition of starch nanocrystals does not prevent the dissolution of the matrix in toluene. RWL is systematically higher than the soluble fraction of the matrix, SFM. Thereby, assuming that the addition of filler does not favor the dissolution of the matrix, it means that the loss in weight should be due to a loss of natural rubber but also of starch nanocrystals. Indeed we have seen that, during toluene immersion, natural rubber swelled. Fillers are then surrounded by a soft matrix and are able to leave the specimen. In addition, this phenomenon should be

Table 5.5 Relative weight loss (RWL), insoluble fraction of the composite (IF), insoluble fraction of the NR matrix (IFM), expected soluble fraction of the matrix (SFM) and starch nanocrystals loss (SL) of starch nanocrystals/NR nanocomposite films immersed for 48 h in toluene or in water and dried overnight at 40 °C. The values are given as percentages

Medium	Toluene					Water	
Sample	RWL[1]	IF[2]	IFM[3]	SFM[4]	SL[5]	RWL[1]	SL[5]
NRev	14.6	85.4	85.4	14.6	0	3.1	0
NRevW5	14.0	86.0	81.1	13.9	0	3.7	0.7
NRevW10	14.0	77.4	76.8	13.2	9.4	4.8	2.0
NRevW20	14.0	77.1	68.3	11.7	11.2	9.8	7.3
NRevW30	14.0	73.7	59.8	10.3	16	10.2	8.0
NRevW40	14.0	76.8	51.2	8.8	18.4	14.1	12.2
NRevW50	14.0	—	—	—	—	15.8	14.3

[1] $\mathrm{RWL} = \frac{M_0 - M'_0}{M_0} \times 100$, where M_0 and M'_0 are the initial and final weights of the sample.

[2] $\mathrm{IF} = 100 - \mathrm{RWL}$.

[3] $\mathrm{IFM} = (100 - \mathrm{RWL}_0) \times (1 - w_s)$, where RWL_0 is the RWL value of the unfilled NR matrix and w_s is the starch nanocrystals content (wt%).

[4] $\mathrm{SFM} = \mathrm{RWL}_0 \times (1 - w_s)$.

[5] $\mathrm{SL} = \mathrm{RWL} - \mathrm{SFM}$.

aggravated for highly filled composites since the probability of appearance of starch nanocrystals on the surface of the film is more significant as the starch content is higher [31]. Observations of the samples clearly prove the migration of starch nanocrystals towards the surface: after extended immersion and drying, the surface is covered by a thin white layer. The values of the starch nanocrystals loss, SL, are given in Table 5.5. We can note that this loss of starch nanocrystals should be gradual during the swelling experiment because no particular break of slope is observed in the evolution of the toluene uptake. This is an indication that although the starch nanocrystals clusters seem to be involved in the formation of a continuous and open network, the interactions between these clusters should be weak and easily broken under NR matrix swelling.

5.5.2 Water Swelling Behavior

In a similar way as for toluene uptake experiments, the water uptake of soaked starch nanocrystal-reinforced NR nanocomposites after immersion in distilled water at room temperature was plotted as a function of time (Figure 5.6b). Similarly to toluene experiments, we noted that all the compositions absorbed water during immersion, even the unfilled matrix. For low starch contents (0 and 2 wt%), the water uptake increased slightly during all the duration of the experiment. For starch contents higher than 2 wt%, the water uptake increased rapidly during the early stage of immersion, that is, during the initial 2–3 h, and then decreased until reaching a plateau after 7 h of immersion. The diminution in the water uptake may be due to the partial release, or leaching, of starch nanoparticles in water, even though starch is insoluble in water. This phenomenon was already reported for polystyrene-co-butyl acrylate filled with potato starch nanocrystals [31].

In order to verify this assumption, samples (1 mm thick) were first weighed, then immersed in distilled water for 2 days, removed from water, dried at 40 °C overnight and weighed again. The relative weight loss, RWL, was calculated for each sample and results are given in Table 5.5. The RWL for NRev equals 3.1% most probably due to the release of low molecular mass NR chains. It was found to increase by adding starch nanoparticles revealing that some starch nanocrystals have previously migrated towards the aqueous phase during soaking, as shown by SL values. The increase in RWL values became more significant above 10 wt% of filler. Indeed, we have seen that during exposure to water, starch domains swelled and the interface between filler and NR matrix weakens. Fillers should be then surrounded by a soft interface and can be able to leave the specimen. Furthermore, like for immersion in toluene, this phenomenon should be magnified for highly filled materials due to the increasing probability of appearance of starch nanocrystals on the surface of the film in direct contact with the liquid medium. Data show that the loss of starch nanocrystals is higher after immersion in toluene than in water. This is attributed to a more extended swelling of the matrix in toluene, favoring the migration of the filler towards the surface and then the liquid phase.

The evolution of the water uptake at equilibrium as a function of starch content is displayed in Figure 5.8a. Up to a starch content of 10 wt%, WU at equilibrium remained roughly constant. Then, it increased more or less linearly from 6% for the 10 wt% filled material (NRevW10) up to 33% for the 50 wt% filled film (NRevW50). For highly filled materials it seems that the loss of unbounded starch nanoparticles was compensated by the swelling of the in bulk starch nanocrystals still bonded to the matrix.

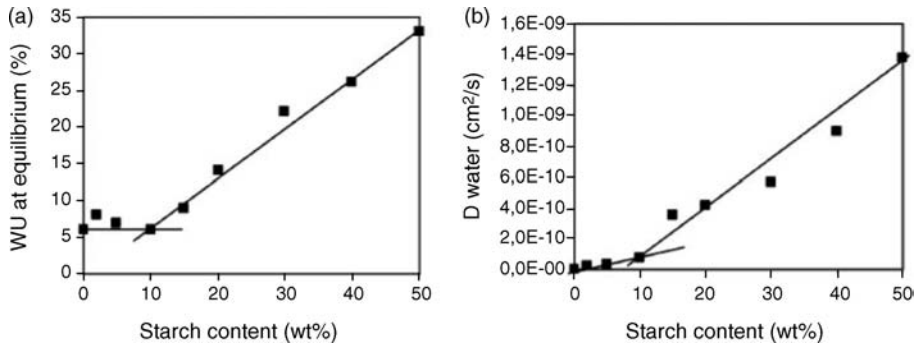

Figure 5.8 Evolution of: (a) the water uptake at equilibrium and (b) the diffusion coefficient of water for starch nanocrystals/NR nanocomposite films as a function of starch content. The solid lines serve to guide the eyes [27] (Reprinted with permission from H. Angellier, S. Molina-Boisseau, L. Lebrun and A. Dufresne, "Processing and structural properties of waxy maize starch nanocrystals reinforced natural rubber," *Macromolecules*, **38**, no. 9, 3783–3792, 2005. © 2005 American Chemical Society.)

The evolution of the water diffusion coefficient values, noted D_{water}, versus starch content is displayed in Figure 5.8b. The unfilled NR matrix displays the lowest value and the addition of starch nanocrystals induces an increase in water diffusivity. Up to a starch content of 10 wt%, D_{water} increases slightly and then increases more rapidly and roughly linearly. Contrarily to toluene swelling experiments and as expected, the formation of a continuous polar network of starch nanocrystals within the NR matrix seems to favor the swelling of the films by water.

A filler content of 10 wt% seems to be a critical value in the swelling behavior. By analogy with materials reinforced with cellulose whiskers, it was assumed that the formation of a rigid network of starch nanocrystals was governed by a percolation mechanism. The critical volume fraction of starch nanocrystals at the percolation is difficult to determine due to the ill defined geometry of the percolating species but should be around 6.7 vol% (that is, 10 wt%). This value is smaller than the value reported for polystyrene-co-butyl acrylate filled with potato starch microcrystals (around 20 vol%) [31]. This difference may be due to a higher surface area of waxy maize starch nanocrystals and to the particular morphology of starch nanocrystals that aggregate by forming a "lace net". This value is of the same order of magnitude (4.4 vol%) than the one observed for NR reinforced with chitin whiskers obtained from crab shell presenting a high specific surface around $180\,m^2\,g^{-1}$ and an aspect ratio close to 16 [19].

5.5.3 Influence of the Chemical Modification of the Filler

After chemical modification the extent of the interactions between the modified crab shell chitin whiskers and the NR matrix and the possibility of chitin-chitin network formation in the matrix were determined by measuring the swelling ratio or diameter variation of the samples before and after swelling in toluene. Figure 5.9 shows photographs of 10 wt% chitin whiskers/NR nanocomposites before and after 24 h swelling in toluene. The extent of swelling is least for NRasaC10 film compared to NRtmiC10 and NRpiC10 samples. The swelling of these two samples are almost the same as observed in Figure 5.9. These observations were quantified by

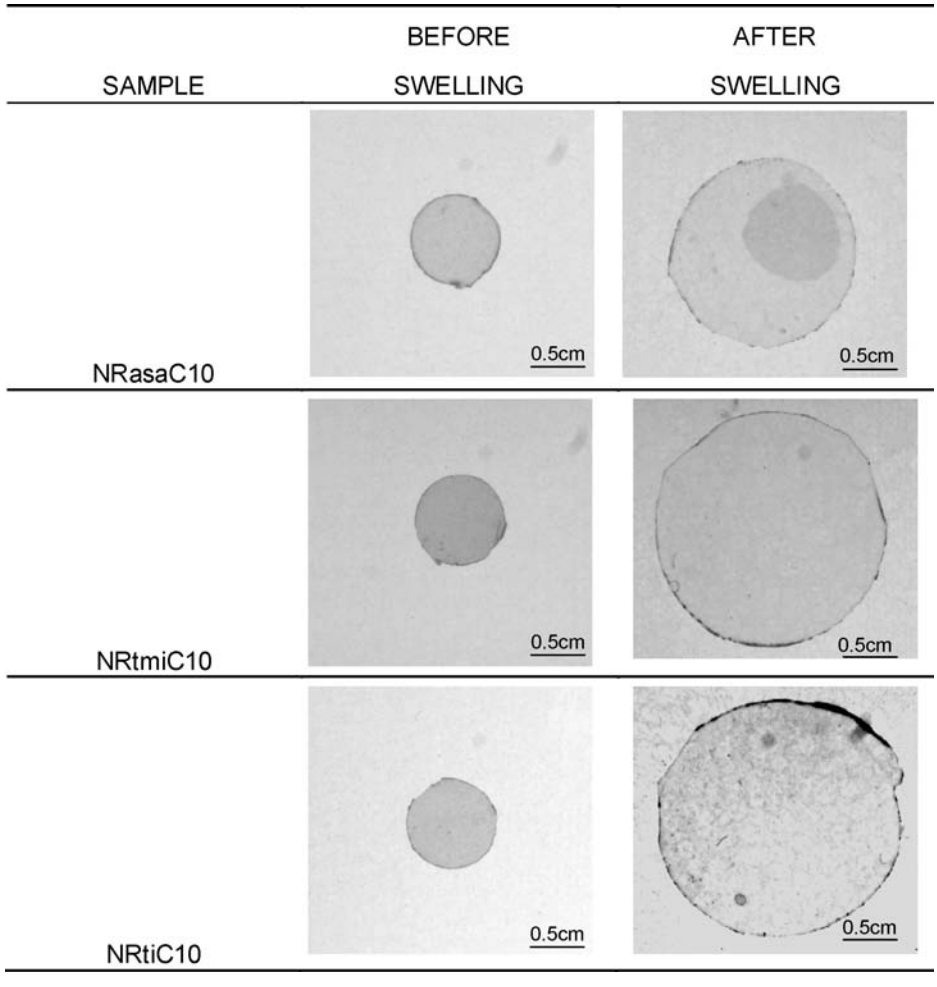

Figure 5.9 Photographs of 10 wt% modified chitin whisker-filled NR films before and just after swelling in toluene for 24 h at room temperature (25 °C). The diameter of all samples before swelling was $d_0 = 7.5$ mm [24] (Reprinted with permission from N.K. Gopalan, A. Dufresne, A. Gandini and M.N. Belgacem, "Crab shells chitin whiskers reinforced natural rubber nanocomposites. 3. Effect of chemical modification of chitin whiskers," *Biomacromolecules*, **4**, no. 6, 1835–1842, 2003. © 2003 American Chemical Society.)

measuring the diameter of the disk after 24 h of swelling in toluene. Results are reported in Table 5.6. The data corresponding to the NR film filled with 10 wt% unmodified chitin whiskers (NRevC10) are included for comparison. The diameter of NRasaC10 is increased by 112% (67% was observed for unmodified composites), whereas for NRtmiC10 and NRpiC10 the increase was around 160% on swelling. It was previously concluded for unmodified whisker-based composites that the formation of a stiff hydrogen-bonded whiskers network within the NR matrix hinders the swelling of the elastomer. It is clear from both Table 5.6 and Figure 5.9

Table 5.6 Diameter (d) of 10 wt% chitin whiskers/NR nanocomposite disks immersed for 24 h in toluene[1]. Relative weight loss (RWL) and fraction of bound matrix (FBR) of chitin whiskers/NR nanocomposite films were determined for samples immersed for 3 days in toluene

Sample	d (mm)	Diameter variation (%)	RWL (%)	FBR (%)
NRev	—	—	77.6	0
NRevC10	12.5	67	11.8	36.6
NRasaC10	15.9	112	36.6	33.2
NRtmiC10	19.8	163	32.8	37.1
NRtiC10	19.7	162	23.6	46.2

[1] The initial sample diameter (before swelling) was $d_0 = 7.5$ mm and the diameter variation was determined by $(d - d_0)/d_0$.

that the swelling of modified chitin whiskers/NR nanocomposites is much higher than the one of unmodified based materials. This could be ascribed to the lower interactions between modified whiskers, part of the surface hydroxyl groups being substituted, and to the lower dispersion level revealed by SEM observations. By comparing ASA and isocyanate modified whiskers, it seems that this effect is more pronounced for the latter.

The bound rubber content and fraction of NR dissolved after immersion in toluene was also measured. The relative weight loss (RWL) and free bonded matrix (FBR) values of composites after 3 days immersion in toluene are collected in Table 5.6. NR used for this experiment was prepared by dissolving freeze-dried NR latex in toluene and evaporating the solvent. Table 5.6 shows that about 78% of the unfilled NR are dissolved in toluene. The dissolution of a limited amount of NR was ascribed again to the fact that the experiments were performed at room temperature without any stirring. For the untreated whiskers based material the RWL value is much lower (11.8%) than for the treated ones. It can be ascribed to the possible chitin-chitin network formed by unmodified whiskers within the NR matrix, which prevents the swelling of the material. The RWL value of NRasaC10 is slightly higher than that of NRtmiC10, which in turn is higher than for NRpiC10 composites. The low RWL value for isocyanate treated composites is due to the stronger interaction between the whiskers and matrix for these materials.

The FBR values determined from RWL data for modified chitin whisker-based composites are also collected in Table 5.6. It is worth remember that FBR values correspond to the NR fraction, which is entrapped within the network of chitin and on the surface of the chitin whiskers. For the unmodified whiskers based material, it was suggested that the nanosized chitin fragments form a 3-D rigid network assumed to be governed by a percolation mechanism. The critical volume fraction of chitin whiskers at the percolation threshold was found to be 4.4 vol% (around 6.4 wt%). For the 10 wt% unmodified whisker-filled NR film, this rigid network is therefore likely to be formed and most of the FBR should originate from the entrapped NR amount. This entrapped NR amount is expected to be much lower in modified whiskers based composites, because of their poorer dispersion in the matrix. However, Table 5.6 shows that the order of magnitude of the FBR values is similar. This could be an indication of comparatively stronger interactions between the whiskers and the matrix in chemically modified systems. It seems that the extent of these interactions is higher in isocyanate treated composites. This is more pronounced for phenyl isocyanate.

Water and toluene absorption experiments were also carried out for unvulcanized NR reinforced with 10 and 30 wt% of ASA- or PI-modified starch nanocrystals (NRasaW10, NRasaW30, NRpiW10 and NRpiW30, respectively). The problem we were faced to was the disruption of films filled with modified starch nanoparticles during the early stage of the swelling experiment after only 1–2 h of immersion in toluene depending on the filler content. This could be attributed to the film processing mode. Indeed, the solubilization step in toluene involved a mechanical stirring, which could result in a decrease of the molecular weight of the sample. For this reason, experiments were carried out by weighing swelled films every 15 min for one hour. The values of TU obtained by weighing the sample after 1 h of immersion and those obtained after four weighing steps every 15 min cannot be compared (samples were removed from the liquid phase for 2 min during each weighing step).

It was shown that regardless the composition, the swelling rate was systematically higher for NR/modified starch than for NR/unmodified nanocrystals [27]. As discussed above, the addition of unmodified filler resulted in a diminution of the nanocomposites swelling. This phenomenon was assumed to be due to the formation of a continuous network of starch nanoparticles supposed to be held through hydrogen bonding forces between starch nanocrystals. In the case of the addition of modified filler, the swelling rate of the composite films is barely higher than for the unfilled NR matrix. This could be due to lower interactions between modified nanocrystals, to higher interactions between the filler and the matrix, or to a higher affinity between the modified filler and toluene. The TU was found to be higher for materials filled with nanocrystals modified by PI than by ASA, revealing either a higher affinity of PI with toluene or lower interactions between modified nanoparticles.

The water uptake was determined for the same materials. As expected, the water uptake is much lower for modified filler-based composites compared with its unmodified counterparts and is also lower for particles modified with PI than with ASA. Indeed, it was shown in a previous paper [25], that the polar component of surface energy was lower for modified nanoparticles and also much lower for particles modified with PI than with ASA.

5.6 Dynamic Mechanical Analysis

In dynamic mechanical analysis the complex modulus (for instance in tension) E^*, that is, the storage component E' and the loss component E'' can be measured. The ratio between these two components, $\tan \delta = E''/E'$, can be also determined. Measurements are generally performed in isochronal conditions at 1 Hz and by varying the temperature.

For instance, Figure 5.10 shows the evolution of $\log(E')$ (Figure 5.10a) and $\tan \delta$ (Figure 5.10b) as a function of temperature for waxy maize starch nanocrystal-reinforced NR nanocomposite films. The curve of $\log(E')$ corresponding to the unfilled matrix is typical of a fully amorphous high molecular weight thermoplastic behavior. For temperatures below the glass transition temperature, NR is in the glassy state: the storage modulus slightly decreases with temperature but remains roughly constant above 1 GPa. Then, a sharp decrease over three decades is observed around $-60\,^{\circ}\mathrm{C}$, corresponding to the primary relaxation process associated with the glass-rubber transition determined by differential scanning calorimetry (DSC) measurements [27]. This modulus drop corresponds to an energy dissipation phenomenon displayed in the concomitant relaxation process where $\tan \delta$ passes through a maximum (Figure 5.10b). Then, the modulus reaches a plateau around 1 MPa, corresponding to the

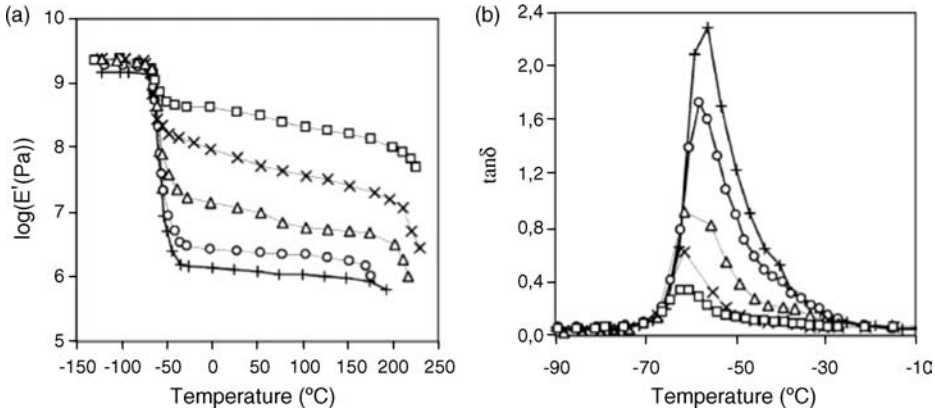

Figure 5.10 (a) Logarithm of the storage tensile modulus E' and (b) tangent of the loss angle tanδ versus temperature at 1 Hz for waxy maize starch nanocrystals/NR nanocomposite films: NRev (+), NRevW5 (○), NRevW10 (△), NRevW20 (×), and NrevW30 (□) [32] (Reprinted with permission from H. Angellier, S. Molina-Boisseau and A. Dufresne, "Mechanical properties of waxy maize starch nanocrystals reinforced natural rubber," *Macromolecules*, **8**, no. 22, 9161–9170, 2005. © 2005 American Chemical Society.)

rubbery state. The broad temperature range from −40 to 180 °C of the rubbery state is ascribed to the high molecular weight of the polymer, resulting in a highly entangled state of the macromolecules. Finally, around 190 °C the modulus decreases more rapidly and the experimental setup fails to measure it. It corresponds to the irreversible flow of the material linked with the disentanglement of polymeric chains.

Starch nanocrystals have a significant reinforcing effect at temperatures higher than T_g. The relative rubbery modulus values, corresponding to the value of the modulus for the composite divided by the one of the neat matrix, estimated at 100 °C are reported in Table 5.7. The values reported for other systems are also listed in Table 5.7. The use of relative data allows a better comparison of values from the literature. No significant improvement of the thermal stability of composites was induced when adding starch nanocrystals within the NR matrix. Actually, the matrix displays a rather high thermal stability and starch begins to degrade at about the same temperature at which NR starts to totally disentangle and flow.

By comparing crab shell chitin whisker-reinforced NR nanocomposites, it is found that the reinforcing effect is slightly higher for unvulcanized (NRevC) than for vulcanized samples (PNRevC), at least for low filler content. Probably the vulcanization process could slightly interfere with the formation of the percolating whiskers network. However, if the real values and not relative modulus values are compared, no significant difference was observed [33]. In contrast the main experimental aspect that alters the reinforcing capability of the nanoparticles seems to be the processing technique. Indeed, for all compositions, the relative relaxed modulus is much lower for the freeze-dried and hot-pressed samples (NRfdC series) than for evaporated ones (NRevC series). This difference was ascribed to the possible formation of a continuous percolating chitin whiskers network within the NR matrix in the evaporated

Table 5.7 Relative rubbery storage rubbery moduli estimated at 100 °C (E_{R100}) for the various NR-based systems. Values in square brackets correspond to real values (MPa)

Sample	E_{R100}	Sample	E_{R100}	Sample	E_{R100}
NRev	1 [1.10]	NRfdC5	2.51	NRevCell2.5	4.17
PNRev	1 [1.51]	NRfdC10	4.57	NRevCell5	7.59
NRfd	1 [1.15]	NRfdC15	13.20	NRevCell10	72.40
NRtolev	1 [1.07]	NRfdC20	22.90	NRevCell15	135.00
NRevC2	7.08	NRasaC10	5.75		
NRevC5	13.50	NRtmiC10	2.04		
NRevC10	44.70	NRpiC10	1.62		
NRevC15	128.00	NRevW5	2.04		
NRevC20	363.00	NRevW10	5.37		
PNRevC2	1.91	NRevW20	39.80		
PNRevC5	9.33	NRevW30	77.60		
PNRevC10	29.50	NRasaW20	1.32		
PNRevC15	79.40	NRpiW20	1.32		
PNRevC20	380.00				

samples [33]. Contrarily to hot-pressing, evaporation is a slow enough process during which filler-filler interactions can occur.

For unvulcanized NR-based composites processed by casting/evaporation, it is also possible to compare the reinforcing effect of crab shell chitin whiskers (NRevC), waxy maize starch nanocrystals (NRevW) and date palm tree cellulose whiskers (NRevCell). Both kinds of rod-like nanoparticles provide similar reinforcing effect whereas starch nanoplatelets provide a much lower reinforcing effect for a given loading level.

The relative modulus of all chemically modified nanoparticles based composites was found to be much lower than that of the unmodified one and more similar to that of the unfilled matrix (Table 5.7). The thermal stability of the composites was also very much reduced after chemical modification [24]. It could be mainly attributed to the negligible presence or absence of the rigid polysaccharidic network as a result of chemical modification onto the particles. For chitin whisker-based nanocomposites, a clear hierarchy is also observed depending on the nature of the chemical coupling agent used. The ASA-treated sample displays a higher rubbery modulus than the isocyanate ones. This result is in agreement with the swelling behavior of the materials and could be an indication of comparatively stronger interactions between the isocyanate modified nanoparticles and the NR matrix. The increase of the filler/matrix interactions results in a decrease in the filler-filler interactions responsible of the high mechanical characteristics of the unmodified nanocrystals filled NR film.

The evolution of tan δ with temperature (Figure 5.10b) displays a peak located in the temperature range of the glass transition of the NR matrix [27]. This relaxation process, labeled α, is associated with the anelastic manifestation of the glass-rubber transition of the polymer. This mechanism involves cooperative motions of long chain sequences. The temperature position (T_α) and magnitude of the peak (I_α) decrease when adding starch nanocrystals (Figure 5.10b) or other nanoparticles [20, 33]. The decrease in T_α becomes significant for the 20 wt% starch reinforced material for which T_α decreases from −56 °C for the unfilled NR down to −61 °C. This is attributed to: (i) the broadening of the glass-rubber transition zone

towards lower temperatures reported from DSC measurements [27] and (ii) to a classical mechanical coupling effect (the shift of the tan δ peak results from the strong decrease of the modulus drop upon filler addition). The reduction of the magnitude of I_α when increasing the starch nanocrystals content, results from: (i) the decrease of the number of mobile units participating to the relaxation process and (ii) the decrease of the magnitude of the modulus drop associated with T_g.

5.7 Tensile Tests

The most classical nonlinear mechanical tests are tensile tests performed at room temperature. In these tests, force (F) - elongation (e) curves are obtained for a given strain rate corresponding to a given crosshead speed. The nominal strain (ε_{nom}) and the nominal stress (σ_{nom}) can be calculated by $\varepsilon_{\text{nom}} = e/L_o$ and $\sigma_{\text{nom}} = F/S_0$, respectively, where S_0 is the initial cross-section. The true strain ($\varepsilon_{\text{true}}$) can be determined by $\varepsilon_{\text{true}} = \ln(L/L_0)$, where L is the length of the sample during the test ($L = L_0 + e$). The true stress (σ_{true}) can be calculated by $\sigma_{\text{true}} = F/S$ where S is the cross-section. S is determined assuming that the total volume of the sample remained constant during the test, so that $S = S_0L_0/L$. This assumption is strictly valid for the unfilled NR matrix at room temperature. Stress versus strain curves can be plotted, and the Young's modulus (E) is measured from the slope of the low strain region. The conventional modulus $E_{100\%}$ can be obtained from the slope of the straight line plotted between the origin $\sigma = \varepsilon = 0$ and the point corresponding to a true strain of 100%. Ultimate mechanical properties, that is, stress at break (σ_b) and elongation at break (ε_b) can also be characterized. Mechanical tensile data are generally averaged over at least five specimens.

Typical stress versus strain curves are shown in Figure 5.11a and b for, respectively, crab shell chitin whisker- (NRevC) and waxy maize starch-reinforced NR (NRevW). For each measurement, it was observed that the strain was macroscopically homogeneous and uniform along the sample, until its break. The lack of any necking phenomenon confirms the homogeneous nature of these composites at the scale of a few hundred cubic nanometers. The samples exhibit an elastic nonlinear behavior typical of amorphous polymer at $T > T_g$. The stress continuously increases with the strain. The polymeric matrix is in the rubbery state and its elasticity from entropic origin is ascribed to the presence of numerous entanglements due to high molecular weight chains.

The tensile modulus, tensile strength and elongation at break of the films were determined from the plot of the true stress versus true strain. The results are collected in Table 5.8. The tensile conventional modulus $E_{100\%}$ is also reported. For a better comparison, relative data are listed in Table 5.8. Indeed, these experimental data were collected from the literature and differences can be induced by the exact nature of the neat matrix and experimental processing conditions.

By comparing crab shell chitin whisker-reinforced NR nanocomposites, it is found again that the stiffness of unvulcanized materials (NRevC) is higher than the one of vulcanized samples (PNRevC) in agreement with DMA experiments. The difference between unvulcanized and crosslinked NR-based systems is more significant from tensile tests than DMA. It could originate from the fact that dynamic mechanical measurements involve weak stresses. The possible interactions between percolating chitin whiskers are not damaged under these weak stresses. Under the higher stress level, as applied in tensile tests, these interactions seem

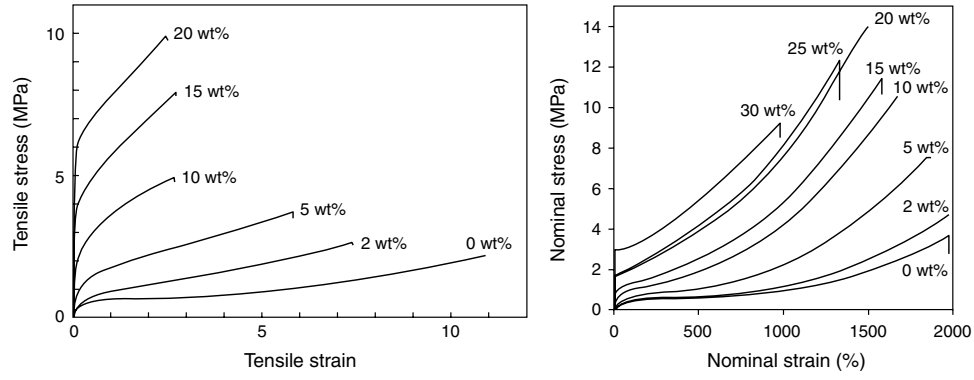

Figure 5.11 Typical stress versus strain curves for: (a) crab shell chitin whiskers [33], and (b) waxy maize starch nanocrystals/NR nanocomposite films [32]. The nanoparticle contents are indicated in the figure (Reprinted with permission from H. Angellier, S. Molina-Boisseau and A. Dufresne, "Mechanical properties of waxy maize starch nanocrystals reinforced natural rubber," *Macromolecules*, **8**, no. 22, 9161–9170, 2005. © 2005 American Chemical Society.)

to be partially destroyed. This is an indication that the strength of the chitin network in the crosslinked NR matrix is lower than that in the unvulcanized one. The chemical crosslinking of the matrix most probably interferes with the formation of the chitin network as already suggested.

The average molecular weight between crosslinks (M_c) and the average number of monomer units between crosslinks were estimated from swelling experiments. For the unfilled vulcanized matrix the average number of monomer units between crosslinks was found to be close to 190. From standard geometry, the monomer length is around 0.47 nm, and assuming that a rubber chain is in a straight, elongated fashion between two adjacent crosslinks, the distance between two adjacent crosslinks should be around 90 nm. This value is of the same order of magnitude, but lower, than the average length of the chitin whiskers obtained from crab shell (around 240 nm). Hence it is reasonable to think that the chemical crosslinking during vulcanization can interfere with the formation of the chitin network in the NR matrix.

For unvulcanized NR-based nanocomposites, the processing technique greatly affects the mechanical behavior. Indeed, the relative modulus is systematically lower for the freeze-dried and hot-pressed samples (NRfdC) than for evaporated ones (NRevC) in agreement with DMA results. In addition, the strength of the evaporated samples first increases and then decreases for highly filled materials whereas it continuously increases for freeze-dried and hot-pressed samples. It is also observed that the elongation at break continuously decreases for evaporated samples whereas it is found to be roughly constant for freeze-dried and hot-pressed composites. This is an indication that the mechanical behavior of evaporated nanocomposite films is mainly governed by the percolating whisker network.

Table 5.8 compares unvulcanized NR-based films reinforced with different sources of polysaccharide nanocrystals, viz. crab shell chitin whiskers (NRevC series), waxy maize starch nanocrystals (NRevW series) and date palm tree cellulose whiskers (NRevCell series). It is clearly seen that for a given composition the higher tensile modulus is observed for cellulose whiskers, then for chitin whiskers and finally for starch nanocrystals. Similarly to DMA

Table 5.8 Relative mechanical properties for the various NR-based systems using data obtained from tensile tests: tensile modulus (E_R), conventional modulus ($E_{R100\%}$), strength (σ_{RB}), and elongation at break (ε_{RB}). Values in square brackets correspond to real values

Sample	E_R	$E_{R100\%}$	σ_{RB}	ε_{RB}
NRev	1 [1.70 Mpa]	1 [1.80 Mpa]	1 [25.50 Mpa]	1 [248%]
PNRev	1 [1.60 Mpa]	1 [1.60 Mpa]	1 [395.00 Mpa]	1 [351%]
NRfd	1 [1.10 Mpa]	1 [0.71 Mpa]	1 [41.60 Mpa]	1 [252%]
Nrtolev	1 [0.42 Mpa]	nd	1 [5.75 Mpa]	1 [274%]
NrevC2	3.30	1.40	0.85	0.86
NrevC5	10.50	2.80	0.98	0.77
NrevC10	nd	nd	nd	nd
NrevC15	75.00	9.40	1.16	0.54
NrevC20	135.00	13.30	0.38	0.51
PNRevC2	1.60	1.30	0.98	0.95
PNRevC5	nd	nd	nd	nd
PNRevC10	16.20	4.30	0.45	0.81
PNRevC15	33.00	7.10	0.32	0.74
PNRevC20	69.00	9.60	0.05	0.37
NRfdC2	1.30	1.40	0.14	0.70
NRfdC5	1.90	2.40	0.37	0.69
NRfdC10	4.20	4.80	0.52	0.63
NRfdC15	7.90	10.10	1.51	0.71
NRfdC20	9.30	13.20	2.02	0.70
NrasaC10	5.70	nd	4.40	0.77
NrtmiC10	2.60	nd	2.30	0.66
NrpiC10	1.80	nd	2.30	0.94
NrevW2	1.60	1.20	1.10	0.98
NrevW5	2.50	1.60	1.80	0.97
NrevW10	7.00	2.50	2.70	0.97
NrevW20	16.60	3.30	2.60	0.93
NrevW30	34.00	5.00	3.00	0.91
NrasaW5	1.30	nd	1.04	0.99
NrasaW10	1.30	nd	1.20	1.00
NrasaW20	2.00	nd	2.20	1.01
NrpiW5	1.10	nd	0.59	0.97
NrpiW10	1.70	nd	0.61	0.93
NrpiW20	2.00	nd	1.20	0.93
NrevCell1	3.40	nd	1.50	0.71
NrevCell2.5	5.60	nd	2.10	0.62
NrevCell5	16.80	nd	4.80	0.40
NrevCell10	236.00	nd	15.90	0.03
NrevCell15	374.00	nd	21.70	0.02

nd: not determined.

experiments, a clear hierarchy is reported between rod-like and platelet-like nanoparticles. However, the tensile tests allow differentiating the two kinds of rod-like nanoparticles. The higher modulus was observed for nanoparticles with the higher aspect ratio as already reported [34]. The strength is found to significantly increase for cellulose whiskers, less for

starch nanocrystals and globally decrease for chitin whiskers. The elongation at break is found to strongly decrease upon cellulose whiskers addition. This trend is less significant for crab shell chitin whiskers and it is observed that the ductility of starch nanocrystal-reinforced NR films remains roughly constant upon filler addition. The strain at break value of a film reinforced with 30 wt% of waxy maize starch is only decreased by a factor lower than 10% whereas its tensile modulus is increased by a factor of 34.

Whatever the nature of the chemical coupling agent is, a reinforcing effect of chitin whiskers is displayed through an increase of the modulus and stress at break (Table 5.8). However, it is much lower than with unmodified nanoparticles and similar to the one observed for freeze-dried and hot-pressed samples. Again a clear hierarchy is observed between ASA and isocyanate modified whiskers. The modulus and ultimate tensile strength of NRasaC10 is found to be higher than that of NRtmiC10 and NRpiC10 composites. The superior tensile properties of NRasaC10 could be attributed to the partial existence of a chitin-chitin network within the NR matrix even after chemical modification of the whiskers. Even though the whisker-matrix interactions in composites are supposed to be greater in NRtmiC10 and NRpiC10, the chance of network formation and thereby a good dispersion of whiskers in these composites is negligible compared to that in NRasaC10.

5.8 Successive Tensile Tests

Successive tensile tests were performed on crab shell chitin whiskers and waxy maize starch nanocrystal-reinforced nanocomposite films to characterize the damage process occurring during tensile tests. At the beginning of each experiment, the sample was first stretched under a load of 2 N. Then, the experiment consisted in stretching the material up to a certain elongation ΔL_1 (cycle 1), then releasing the force down to 2 N and stretching again the material up to a higher elongation $\Delta L_2 = 2 \times \Delta L_1$ (cycle 2). This procedure was repeated with increasing elongation ΔL_i (cycle i), until the sample broke. The tensile modulus E_i for each successive cycle was determined from the initial slope of each stress-strain curve.

Figure 5.12a shows the typical evolution of the force versus elongation for the unvulcanized NR matrix film obtained by the water evaporation technique during successive tensile tests. A significant difference is observed between the curves obtained during stretching (positive elongation rate) and the ones obtained during recovery (negative elongation rate). Moreover after each cycle a residual elongation is reported. During stretching, short macromolecular chains can diffuse within the surrounding entangled lattice but do not tangle again immediately during the recovery step because of the viscous nature of the polymer. Therefore, the curves recorded during positive and negative elongation rate steps do not superimpose and a permanent strain remains, at the time scale of the experiment. Figure 5.12b shows the evolution of the true stress versus true strain for the same sample. The global evolution is similar but the stress level at the beginning of each cycle differs because of the permanent strain induced during each successive cycle.

First, we discuss about the chitin whisker-reinforced unvulcanized NR composite films obtained by the freeze-drying and hot-pressing technique (NRfd series). The effect of the whisker content and successive tensile tests on E_i are shown in Figure 5.13a and experimental data are collected in Table 5.9. Figure 5.13a displays the evolution of the relative tensile modulus, viz. the modulus of the composite measured during cycle i divided by the one

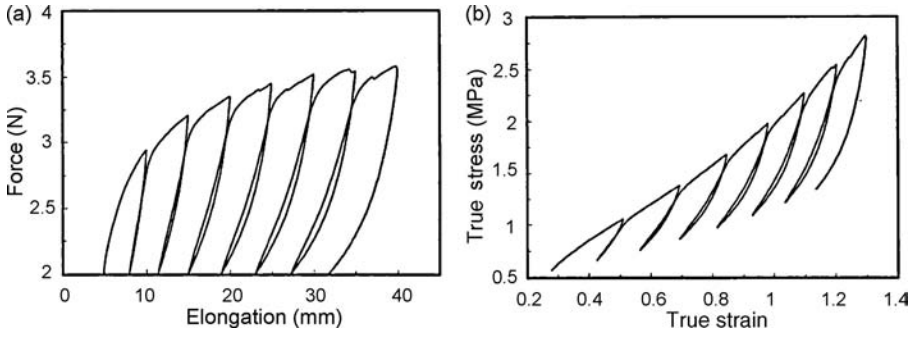

Figure 5.12 Evolution of: (a) the force versus elongation and (b) true stress versus true strain for NRev during successive tensile tests [3] (Reprinted with permission from N.K. Gopalan and A. Dufresne, "Crab shells chitin whiskers reinforced natural rubber nanocomposites. 2. Mechanical behavior," *Biomacromolecules*, **4**, no. 3, 666–674, 2003. © 2003 American Chemical Society.)

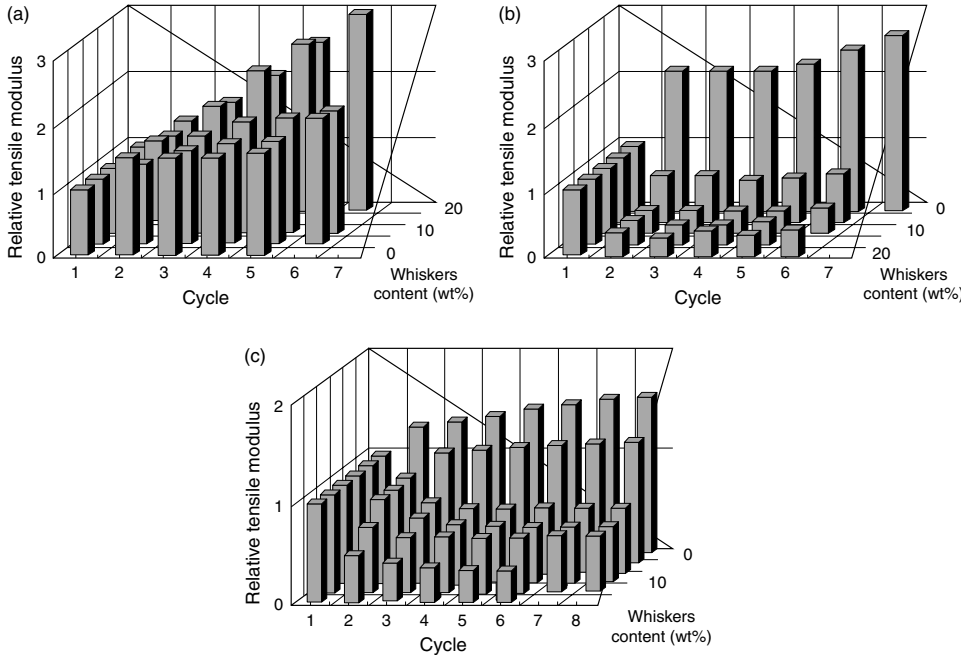

Figure 5.13 Evolution of the relative tensile modulus, viz. the modulus of the composite measured during cycle *i* divided by the one measured for the same sample during the first stretching cycle, E_i/E_1, as a function of *i* and of the whiskers content for: (a) unvulcanized hot-pressed; (b) unvulcanized evaporated; and (c) vulcanized evaporated materials [33] (Reprinted with permission from N.K. Gopalan and A. Dufresne, "Crab shells chitin whiskers reinforced natural rubber nanocomposites. 2. Mechanical behavior," *Biomacromolecules*, **4**, no. 3, 666–674, 2003. © 2003 American Chemical Society.)

Table 5.9 Tensile modulus E_i determined for crab shell chitin whiskers/NR nanocomposite films during the successive tensile tests i

Sample	Processing technique	E_1 (MPa)	E_2 (MPa)	E_3 (MPa)	E_4 (MPa)	E_5 (MPa)	E_6 (MPa)	E_7 (MPa)	E_8 (MPa)
NRev	Water evaporation	1.9	4.1	4.1	4.1	4.3	4.7	5.1	
NRevC5		18.4	13.3	12.9	11.8	12.7	13.7		
NRevC10		48.1	16.9	16.7	16.5	17.0	18.0		
NRevC15		129.7	48.9	38.6	40.5	46.7			
NRevC20		231.5	83.4	69.3	68.1	77.3	88.7		
PNRev	Water evaporation	1.6	2.1	2.1	2.2	2.3	2.4	2.5	2.5
PNRevC2		2.2	1.9	2.5	2.5	2.6	2.7	2.7	2.7
PNRevC5		6.2	5.3	4.5	4.2	4.2	4.2	4.2	4.2
PNRevC10		14.3	12.2	9.5	8.6	8.4	8.2	8.2	8.2
PNRevC15		31.4	21.1	18.0	18.1	17.4	17.5	18.4	18.6
PNRevC20		73.4	35.2	30.2	26.1	24.4	23.9		
NRfd	Freeze-drying and hot-pressing	1.4	2.1	2.1	2.1	2.2			
NRfdC5		2.6	3.2	3.7	4.0	4.1	5.0		
NRfdC10		3.9	5.5	5.8	6.6	6.9	7.3		
NRfdC15		8.5	11.2	15.1	19.6	23.1			
NRfdC20		8.3	11.4	13.7	17.2	21.4	27.2		

measured for the same sample during the first stretching cycle, E_i/E_1. For the unfilled matrix, a continuous increase of E_i is observed for successive cycles. It increases from 1.4 MPa for the first cycle up to 2.2 MPa for the fifth (Table 5.9). The relative tensile modulus increases from 1.0 to 1.57 during successive tests. This phenomenon is ascribed to the well known strain-induced crystallization of rubbers. A group of scientists put forward a new idea about strain induced crystallization of natural rubber during uniaxial deformation [35]. Contrary to the conventional concept their studies revealed that the applied stress induces a network of microfibrillar crystals in NR and that is responsible for the improved elastic properties.

For a given cycle, an increase of the modulus with the chitin whiskers content is observed for all compositions (Table 5.9). This reinforcing effect agrees with the DMA and tensile tests experimental data. As for the unfilled matrix, a continuous increase in the relative modulus is observed for all the compositions (Figure 5.13a). It implies that the behavior of the composites during the successive tensile tests is mainly dominated by the matrix behavior. It could be due to the absence of the formation of a chitin network within the hot-pressed NR matrix.

The successive moduli measured for chitin whisker-reinforced unvulcanized NR composite films obtained by the evaporation technique are reported as absolute values in Table 5.9 and as relative values in Figure 5.13b. For the unfilled matrix, a continuous increase of E_i is observed for successive cycles. It increases from 1.9 MPa for the first cycle up to 5.1 MPa for the seventh (Table 5.9). The relative tensile modulus increases from 1.0 to 2.68 during successive tests. The sharper increase of the modulus during successive cycles for the evaporated matrix compared to the hot-pressed one is an indication of the higher strain-induced crystallization of the former. Similarly as in the case of hot-pressed samples, for a given cycle, the modulus of the composites increases with the chitin whiskers content. In agreement with the previous DMA and tensile tests experimental data, the reinforcing effect is much higher for the composite materials

obtained via water evaporation process compared to that for the materials obtained by freeze-drying and hot-pressing technique. However, it is worth noting that for the evaporated composites the modulus E_i first decreases for the first three or four cycles and then increases. The initial decrease of E_i for composite materials can be ascribed to the progressive damaging of the chitin whisker network. The nonlinear decreasing tendency of modulus values of filled rubber with increasing strain amplitude (Payne effect) has been studied earlier [36, 37]. The Payne effect increases with an increasing filler-filler network factor and decreases with an increasing polymer-filler network [36, 37]. After the complete destruction of the chitin network, the tensile modulus starts to increase slowly as a result of the strain-induced crystallization already observed for the unfilled matrix. The continuous increase of E_i for successive cycles reported for hot-pressed nanocomposites is a clear indication of the absence of any chitin network within these materials. This continuous whiskers network is expected to govern the mechanical behavior of the evaporated composites.

The same experiment was also performed for chitin whisker-reinforced vulcanized NR composites and results are reported in Table 5.9 and Figure 5.13c. It is observed that films containing low percentages of whiskers (0 and 2 wt% filled material) exhibit a continuous increase of E_i for successive cycles. For instance, for the unfilled matrix, it increases from 1.6 MPa for the first cycle up to 2.5 MPa for the seventh (Table 5.9). The relative tensile modulus increases from 1.0 to 1.59 during successive tests. This increase is much lower than the one observed for the unvulcanized evaporated matrix (Figure 5.13b). This can be well understood since for chemically crosslinked polymers the strain-induced crystallization is more restricted. In fact, the network of bridges in vulcanized rubber might have two opposite effects on strain-induced crystallization during stretching [35]. The bridges can improve molecular orientation of chains in the vicinity of crosslinks, thus inducing a crystallization of polymer chains. Conversely these bridges may also hinder the growth of the crystalline structure. The lower increase in modulus of the vulcanized matrix compared to the one observed for the unvulcanized matrix is most probably due to the above-mentioned opposite effects which take place in the former.

For composite materials, a clear decrease in the relative modulus is observed during the successive tensile tests up to the first four cycles and after that it remains almost unchanged. The first decrease in modulus is due to the disruption of chitin whiskers network that is expected to be formed during the slow evaporation step of the composites. However, contrary to the increase in modulus of the unvulcanized evaporated composites, after fourth cycle, it is found that the modulus of vulcanized ones remains unchanged after fourth cycle. It is due to the limited extent of the strain-induced crystallization of crosslinked rubber as a result of the two opposite effects operating during stretching of the material as mentioned above.

Similar experiments were conducted for waxy maize starch nanocrystal-reinforced unvulcanized NR [32]. For these materials both the tensile modulus E_i and the shrinkage r_i corresponding to the difference between the elongation ΔL_i and the residual elongation retained at the end of each cycle were determined for each successive cycle (Figure 5.14). Their evolution as a function of both the starch content and the number of successive cycles are plotted in the 3-D diagrams of Figure 5.15. For the sake of clarity, the modulus scale in Figure 5.15a is restricted to 8 MPa. The whole experimental data are collected in Table 5.10.

For the unfilled NR matrix, the tensile module continuously increases during the successive cycle. This phenomenon is ascribed again to the strain-induced crystallization of NR. Indeed, it was demonstrated that the birefringence and the crystallinity measured by X-ray diffraction of

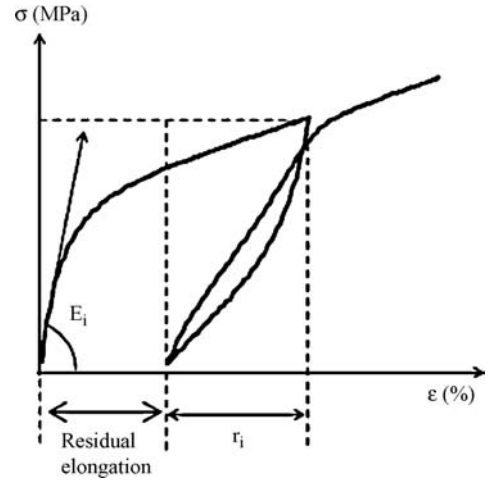

Figure 5.14 Schematic representation of the mechanical properties obtained for each cycle during successive tensile tests [32] (Reprinted with permission from H. Angellier, S. Molina-Boisseau and A. Dufresne, "Mechanical properties of waxy maize starch nanocrystals reinforced natural rubber," *Macromolecules*, **8**, no. 22, 9161–9170, 2005. © 2005 American Chemical Society.)

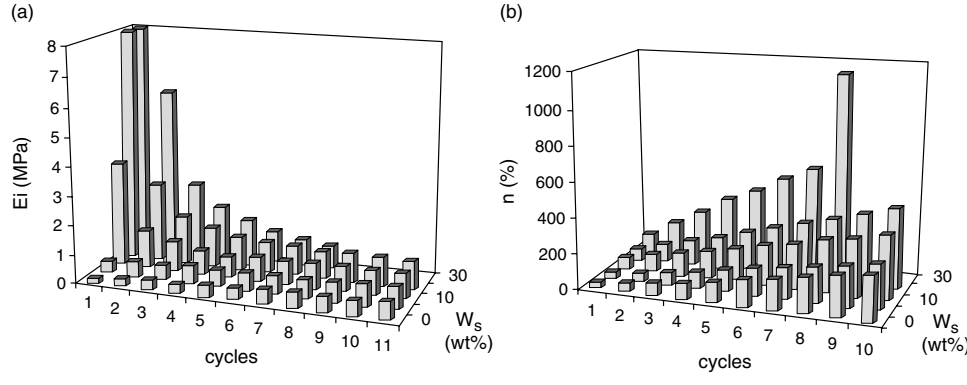

Figure 5.15 Evolution of: (a) the nominal tensile modulus E_i and (b) the shrinkage r_i measured for cycle i for waxy maize starch nanocrystals/NR nanocomposite films during successive tensile tests as a function of i and of the starch nanocrystals content W_s [32] (Reprinted with permission from H. Angellier, S. Molina-Boisseau and A. Dufresne, "Mechanical properties of waxy maize starch nanocrystals reinforced natural rubber," *Macromolecules*, **8**, no. 22, 9161–9170, 2005. © 2005 American Chemical Society.)

NR increased with strain [38, 39]. It was concluded that strain-induced crystallization started for a strain around 400% [40]. The maximum achievable crystallinity was found to be around 30% by WAXS analysis [41] and around 20% by high-resolution solid state ^{13}C NMR spectroscopy [42]. More recently, it was discovered that only a low fraction of the amorphous NR chains are oriented and subsequently crystallized during stretching, carrying most of the applied load [43]. In our case, the modulus increases from the second cycle, revealing that the

Table 5.10 Tensile modulus E_i (MPa) and shrinkage r_i (%) determined for waxy maize starch nanocrystals/NR nanocomposite films during successive tensile tests i

Sample	E_1 (MPa)	E_2 (MPa)	E_3 (MPa)	E_4 (MPa)	E_5 (MPa)	E_6 (MPa)	E_7 (MPa)	E_8 (MPa)	E_9 (MPa)	E_{10} (MPa)	E_{11} (MPa)
NRev	0.1	0.2	0.3	0.3	0.4	0.4	0.5	0.5	0.5	0.5	0.6
NRevW2	0.2	0.3	0.3	0.3	0.4	0.4	0.4	0.5	0.5	0.5	0.5
NRevW5	0.4	0.5	0.5	0.6	0.6	0.6	0.6	0.6	0.6	0.7	0.7
NRevW10	3.6	1.3	1.0	0.8	0.7	0.8	0.8	0.8	0.8	0.8	0.8
NRevW15	6.3	1.7	1.0	0.8	0.7	0.7	0.7	0.6	0.6	0.6	0.6
NRevW20	25.9	2.7	1.6	1.3	1.1	1.0	1.0	0.9	1.0	0.9	0.9
NRevW25	28.8	4.6	2.2	1.7	1.4	1.0	0.9	0.9	0.7	0.6	0.6
NRevW30	59.7	5.8	2.5	1.8	1.4	1.1	0.9	0.8			
Sample	r_1	r_2	r_3	r_4	r_5	r_6	r_7	r_8	r_9	r_{10}	
NRev	22	43	63	86	112	139	171	200	229	253	
NRevW2	38	62	81	102	124	150	181	211	241	269	
NRevW5	21	41	64	89	116	144	173	200	229	257	
NRevW10	53	90	123	156	190	225	258	291	325	361	
NRevW15	55	94	131	168	206	246	285	324	364	406	
NRevW20	59	103	145	186	231	274	321	364	409	456	
NRevW25	91	173	250	323	399	475	557	639	750	798	
NRevW30	97	187	274	359	440	517	594	1143			

crystallization begins before having reached a strain of 400%. Indeed the initial length of the sample, $L_0 = 7$ mm, is of the same order of magnitude as the elongation at each cycle, $\Delta L_1 = 10$ mm. The strain at the beginning of the second cycle is therefore lower than 400%. Such a continuous modulus increase during successive tensile tests is observed for low starch contents composites (up to 5 wt%). This means that the behavior of the poorly filled nanocomposite films is mainly governed by the one of the matrix. It could be ascribed to the absence of a continuous nanocrystals network within the NR matrix.

For highly filled nanocomposite materials (starch content higher than 5 wt%) the tensile modulus decreases during the first five cycles. The higher the starch content is, the stronger the modulus drop is (Table 5.10). This modulus drop during the early successive tensile experiments could be ascribed to the progressive disruption of the continuous starch nanocrystals network. The higher the starch nanoparticles content is, the closer the continuous network is and the stronger the effect of the disruption is. Furthermore, it was already shown that the addition of filler (carbon black for instance) decreases the capability of NR chains to crystallize [43]. After the fifth cycle, the modulus remains roughly constant. This should indicate that complete disruption of the continuous starch network was achieved and that no strain-induced crystallization of the film occurred at this stage. This is an indication that a nominal strain around 700% is necessary for the complete disruption of the percolating nanoparticles network. It was also observed that for a given cycle, the modulus increases with the starch content (Table 5.10). This reinforcing effect agrees with both DMA and tensile tests results.

Regardless the composition, the shrinkage increases for each additional successive tensile cycle. It is about ten times higher for the tenth cycle than for the first (Figure 5.15b and Table 5.10). These data suggest that viscous flow in the samples decreases at each cycle

whereas the elastic recovery component increases. When increasing the starch nanoparticles content, the shrinkage becomes more important, that is, the residual elongation decreases for a given cycle (Figure 5.15b). The presence of the filler induces a more elastic behavior of the material and decreases at the same time its viscoelasticity.

5.9 Barrier Properties

The large interest in nanoparticles for composite applications originates from outstanding mechanical properties. Enhanced properties can often be reached for low filler volume fraction without detrimental effect on other properties such as impact resistance or plastic deformation capability. However, other properties have been shown to undergo substantial improvements, including decreased permeability to gases. Surprisingly, as far as we know, the barrier properties of polysaccharide nanocrystal-reinforced polymer nanocomposites have been reported only late in some recent publications [27, 44–46].

In the first study [27], the authors studied the permeability of natural rubber reinforced with waxy maize starch nanocrystals to both water vapor and oxygen. The water vapor transmission rate of these materials was found to continuously decrease upon starch nanoparticles addition. It decreased from 0.078 g m^{-2} day^{-1} for the unfilled matrix down to 0.043 g m^{-2} day^{-1} for the composite filled with 20 wt% starch. This unobvious result shows that the hydrophilic nature of starch nanocrystals does not increase the permeability of natural rubber to water vapor.

In the same study [27], it was also observed that starch nanocrystals reduced the oxygen diffusion as shown from the decrease of the diffusion coefficient when adding the filler and the oxygen permeability. The latter decreased from 25.7 barrer for the unfilled matrix down to 8.9 barrer for the composite filled with 30 wt% starch. It was checked that this phenomenon was mainly due to the structural modification of the film and not to the decrease of the solubility of oxygen. Both observations were ascribed to the nanoscale platelet-like morphology of starch nanocrystals that increases the tortuosity of the diffusion path of molecules.

The water vapor permeability of starch nanocrystal-reinforced sorbitol plasticized pullulan films was also investigated [44]. The authors reported no significant differences in water vapor permeability of unfilled samples and those containing up to 20 wt% nanocrystals. For higher filler content enhanced barrier properties were observed.

5.10 Conclusions

Polysaccharide nanocrystals are building blocks biosynthesized to provide structural properties to living organisms. They can be isolated from biomass through acid hydrolysis with concentrated mineral acids under strictly controlled conditions varying time and temperature. Acid hydrolysis results in an overall decrease of amorphous material by removing polysaccharide material closely bonded to the crystallite surface and breaks down portions of glucose chains in most accessible, noncrystalline regions. A leveling-off degree of polymerization is achieved corresponding to the residual highly crystalline regions of the original material, that is, cellulose or chitin fiber, or starch granule. Dilution of the acid and dispersion of the individual crystalline nanoparticles complete the process and yield an aqueous suspension of polysaccharide nanoparticles. These nanoparticles occur as rod-like nanocrystals in the case of cellulose- or chitin-based materials, or platelet-like nanoparticles when using starch granules as the raw material.

Polysaccharide nanocrystals are inherently low-cost materials which are available from a variety of natural sources and in a wide variety of aspect ratios, for example, ~200 nm long and 5 nm in lateral dimension and up to several microns long and 18 nm in lateral dimension for cellulose and chitin. They take advantage of both renewable materials, such as abundance, renewability and self-assembly into well defined architectures and nanosized particles, including mechanical properties for example, strength, modulus and dimensional stability, decreased permeability to gases and water, thermal stability and heat distorsion temperature. They are an attractive nanomaterial for the reinforcement of natural rubber.

References

1. Barlow, F.N. (1993) *Rubber compounding principles and techniques*, Marcel Dekker, New York.
2. Bokobza, L. (2004) The reinforcement of elastomeric networks by fillers. *Macromolecular Materials and Engineering*, **289**, 607.
3. Leblanc, J.L. (2002) Rubber-filler interactions and rheological properties in filled compounds. *Progress in Polymer Science*, **27**, 627.
4. Blow, C.M. and Hepburn, C., (1982) *Rubber Technology and Manufacture*, 2nd edn, Butterworth-Heinemann.
5. Liauw, C.M., Allen, N.S., Edge, M., and Lucchese, L. (2001) The role of silica and carbon-silica dual phase filler in a novel approach to the high temperature stabilisation of natural rubber based composites. *Polymer Degradation and Stability*, **74**, 159.
6. De, S.K. and White, J.R. (1996) *Short Fibre-Polymer Composites*, Woodhead Publishing, Cambridge.
7. Ismail, H., Shuhelmy, S., and Edyham, M.R. (2002) The effects of a silane coupling agent on curing characteristics and mechanical properties of bamboo fibre filled natural rubber composites. *European Polymer Journal*, **38**, 39.
8. Ismail, H., Edyham, M.R., and Wirjosentono, B. (2002) Bamboo fibre filled natural rubber composites: the effects of filler loading and bonding agent. *Polymer Testing*, **21**, 139.
9. Geethamma, V.G., Thomas Mathew, K., Lakshminarayanan, R., and Thomas, S. (1998) Composite of short coir fibres and natural rubber: effect of chemical modification, loading and orientation of fibre. *Polymer*, **39**, 1483.
10. Ismail, H., Rozman, H.D., Jaffri, R.M., and Mohd Ishak, Z.A. (1997) Oil palm wood flour reinforced epoxidized natural rubber composites: the effect of filler content and size. *European Polymer Journal*, **33**, 1627.
11. Ismail, H., Jaffri, R.M., and Rozman, H.D. (2000) Oil palm wood flour filled natural rubber composites: fatigue and hysteresis behaviour. *Polymer International*, **49**, 618.
12. Ismail, H. and Jaffri, R.M. (1999) Physico-mechanical properties of oil palm wood flour filled natural rubber composites. *Polymer Testing*, **18**, 381.
13. Azizi Samir, M.A.S., Alloin, F., and Dufresne, A. (2005) Review of recent research into cellulosic whiskers, their properties and their application in nanocomposite field. *Biomacromolecules*, **6**, 612.
14. Dufresne, A., Polymer nanocomposites from biological sources, in *Encyclopedia of Nanoscience and Nanotechnology*, 2nd edn (ed. H.S. Nalwa), in press.
15. Wise, L.E., Murphy, M., and D'Addiecco, A.A. (1946) Chlorite holocellulose, its fractionation and bearing on summative wood analysis and on studies on hemicelluloses. *Paper Trade Journal*, **122**, 35.
16. Marchessault, R.H., Morehead, F.F., and Walter, N.M. (1959) Liquid crystal systems from fibrillar polysaccharides. *Nature*, **184**, 632.
17. Battista, O.A., Coppick, S., Howsmon, J.A. *et al.* (1956) Level-off degree of polymerization: relation to polyphase structure of cellulose fibers. *Industrial & Engineering Chemistry*, **48**, 333.
18. Marchessault, R.H., Morehead, F.F., and Joan Koch, M. (1961) *Journal of Colloid Science*, **16**, 327.
19. Gopalan Nair, K. and Dufresne, A. (2003) Crab shell chitin whisker reinforced natural rubber nanocomposites. 1. processing and swelling behaviour. *Biomacromolecules*, **4**, 657.
20. Bendahou, A., Habibi, Y., Kaddami, H., and Dufresne, A. (2009) *Journal of Biobased Materials and Engineering*, **3**, 81.
21. Angellier, H., Choisnard, L., Molina-Boisseau, S. *et al.* (2004) Optimization of the preparation of aqueous suspensions of waxy maize starch nanocrystals using a response surface methodology. *Biomacromolecules*, **5**, 1545.
22. Araki, J., Wada, M., Kuga, S., and Okano, T. (1998) Flow properties of microcrystalline cellulose suspension prepared by acid treatment of native cellulose. *Colloids Surf A*, **142**, 75.

23. Angellier, H., Putaux, J.L., Molina-Boisseau, S. *et al.* (2005) Starch nanocrystals fillers in an acrylic polymer matrix. *Macromolecular Symposia*, **221**, 95.
24. Gopalan Nair, K., Dufresne, A., Gandini, A., and Belgacem, M.N. (2003) Crab shells chitin whiskers reinforced natural rubber nanocomposites. 3. Effect of chemical modification of chitin whiskers. *Biomacromolecules*, **4**, 1835.
25. Angellier, H., Molina-Boisseau, S., Belgacem, M.N., and Dufresne, A. (2005) Surface chemical modification of waxy maize starch nanocrystals. *Langmuir*, **21**, 2425.
26. Putaux, J.L., Molina-Boisseau, S., Momaur, T., and Dufresne, A. (2003) Platelet nanocrystals resulting from the disruption of waxy maize starch granules by acid hydrolysis. *Biomacromolecules*, **4**, 1198.
27. Angellier, H., Molina-Boisseau, S., Lebrun, L., and Dufresne, A. (2005) Processing and structural properties of waxy maize starch nanocrystals reinforced natural rubber. *Macromolecules*, **38**, 3783.
28. Anglès, M.N. and Dufresne, A. (2000) Plasticized starch/tunicin whiskers nanocomposites: 1. Structural analysis. *Macromolecules*, **33**, 8344.
29. Treloar, L.R.G. (1975) *The Physics of Rubber Elasticity*, Oxford University Press, Oxford.
30. Mathew, A.P. and Dufresne, A. (2002) Morphological investigation of nanocomposites from sorbitol plasticized starch and tunicin whiskers. *Biomacromolecules*, **3**, 609.
31. Dufresne, A. and Cavaillé, J.Y. (1998) Clustering and percolation effect in microcrystalline starch reinforced thermoplastic. *Journal of Polymer Science Part B-Polymer Physics*, **36**, 2211.
32. Angellier, H., Molina-Boisseau, S., and Dufresne, A. (2005) Mechanical properties of waxy maize starch nanocrystals reinforced natural rubber. *Macromolecules*, **38**, 9161.
33. Gopalan Nair, K. and Dufresne, A. (2003) Crab shells chitin whiskers reinforced natural rubber nanocomposites. 2. Mechanical behaviour. *Biomacromolecules*, **4**, 666.
34. Dufresne, A. (2006) Comparing the mechanical properties of high performances polymer nanocomposites from biological sources. *Journal of Nanoscience and Nanotechnology*, **6**, 322.
35. Toki, S., Sics, I., Ran, S. *et al.* (2002) New insights into structural development in natural rubber during uniaxial deformation by in situ synchrotron X-ray diffraction. *Macromolecules*, **35**, 6578.
36. Payne, A.R. (1962) The dynamic properties of carbon black-loaded natural rubber vulcanizates, *Journal of Polymer Science*, **8**, 57.
37. Payne, A.R. and Whittaker, W. (1971) Low strain dynamic properties of filler rubbers. *Rubber Chemistry and Technology*, **44**, 140.
38. Treloar, R.G. (1947) The photo-elastic properties of rubber. Part I: theory of the optical properties of strained rubber. *Transactions of the Faraday Society*, **43**, 277 and 284.
39. Shimomura, Y., White, J.L., and Spruiell, J.E. (1982) A comparative study of stress-induced crystallization of guayule, hevea, and synthetic polyisoprenes. *Journal of Applied Polymer Science*, **27**, 3553.
40. Toki, S., Fujimaki, F., and Okuyama, M. (2000) Strain-induced crystallization of natural rubber as detected real-time by wide-angle X-ray diffraction technique. *Polymer*, **41**, 5423.
41. Mitchell, G.R. (1984) A wide-angle X-ray study of the development of molecular orientation in crosslinked natural rubber. *Polymer*, **25**, 1562.
42. Lin, W., Bian, M., Yang, G., and Chen, Q. (2004) Strain-induced crystallization of natural rubber as studied by high-resolution solid-state 13C NMR spectroscopy. *Polymer*, **45**, 4939.
43. Toki, S., Sics, I., Ran, S. *et al.* (2002) New insights into structural development in natural rubber during uniaxial deformation by in situ synchrotron X-ray diffraction. *Macromolecules*, **35**, 6578.
44. Kristo, E. and Biliaderis, C.G. (2007) Physical properties of starch nanocrystal-reinforced pullulan films. *Carbohydrate Polymers*, **68**, 146.
45. Choi, Y.J. and Simonsen, J. (2006) Cellulose nanocrystal-filled carboxymethyl cellulose nanocomposites. *Journal of Nanoscience and Nanotechnology*, **6**, 633.
46. Petersson, L. and Oksman, K. (2006) Biopolymer based nanocomposites: comparing layered silicates and microcrystalline cellulose as nanoreinforcement. *Composites Science And Technology*, **66**, 2187.

6

Carbon Nanotube Reinforced Rubber Composites

R. Verdejo[1], M.A. Lopez-Manchado[1], L. Valentini[2] and J.M. Kenny[2]
[1] *Institute of Polymer Science and Technology, CSIC, Juan de la Cierva 3, 28006 Madrid, Spain*
[2] *Materials Science and Technology Center, INSTM Unit, University of Perugia, Loc. Pentima Bassa, 21, 05100 Terni, Italy*

6.1 Introduction

Since the early days of the rubber industry, fillers in the form of fine particles like carbon black, silica or calcium carbonate have been used in rubber compounds. These fillers are added in order to get a substantial improvement in the physical and mechanical properties of the compound [1]. However, high concentrations of conventional fillers (above 40 phr, parts per 100 parts of rubber by weight) are required to attain the desired properties, which has a detrimental effect on the processability of the compound, increases the final weight and limits their applications. In the past few years, polymer nanocomposites have aroused widespread interest because of the small particle size and surface activity of nanoparticles, allowing the required properties to be achieved at low filler loadings [2–6]. So, a nanocomposite is a nanostructured material consisting of a homogenous dispersion of nanoparticles inside a polymer matrix. Because of their nanometer filler size, nanocomposites show unique properties typically not shared by their more conventional microcomposite counterparts and, therefore, offer new technology and business opportunities. The main feature of a nanoparticle is that it has at least one dimension in the nanometric range. Among these nanometer-scale reinforcing particles, layered silicates are the most commonly used nanoparticles for the production of polymer nanocomposites. Organoclay/polymer nanocomposites exhibit improved mechanical and physical properties not shared by conventional composites.

Rubber Nanocomposites: Preparation, Properties and Applications Edited by Sabu Thomas and Ranimol Stephen
© 2010 John Wiley & Sons (Asia) Pte Ltd

Over recent years, carbon nanotubes (CNT) have inspired scientists for a range of potential applications [7–12]. Carbon nanotubes are allotropes of carbon with a unique atomic structure consisting in covalently bonded carbon atoms arranged in long cylinders with typical diameters in the range 1–50 nm and a wide variety of lengths. Individual carbon nanotubes are characterized by a high aspect ratio (300–1000), high flexibility [13] and unique combination of mechanical, electrical and thermal properties [14, 15]. The combination of these properties with a very low mass density [16] makes them potentially useful as ideal reinforcing fibers for high-performance polymer composites.

Carbon nanotubes are usually produced by three techniques: arc discharge, laser ablation and chemical vapor deposition. The quality and yield of carbon nanotubes strongly depend on the synthesis and purification techniques and the specific growth conditions used [11]. There are two basic types of CNT: single-walled carbon nanotubes (SWCNT) and multiwalled carbon nanotubes (MWCNT). The structure of a SWCNT is characterized by wrapping a one-atom-thick layer of graphite called graphene (graphene is a monolayer of sp^2-bonded carbon atoms) into a seamless cylinder. The carbon atoms in the cylinder have partial sp^3 character that increases as the radius of curvature of the cylinder decreases. SWCNT exhibit important electric properties that are not shared by the multiwalled carbon nanotubes.

MWCNT consist of multiple layers of graphite arranged in concentric cylinders with an interlayer distance close to the distance between graphene layers in graphite (circa 0.34 nm). Of particular interest are the double-walled carbon nanotubes (DWNT) because they combine a similar morphology and properties in relation to SWCNT, while improving significantly their resistance to chemicals.

This chapter is devoted to a description of the most significant results on carbon nanotubes/elastomer nanocomposites. Although significant advances have been made in recent years in this field, there is still a lack of basic knowledge on the optimum processing conditions. One of the main problems for the effective use of carbon nanotubes as reinforcements of polymer matrices is achieving a good dispersion in the composite, independent of filler shape and aspect ratio. Currently, nanoparticles are incorporated within the polymer matrix by mechanical dispersion in solution or melt processing with several critical issues:

- The nonuniform dispersion of nanoreinforcements within the polymer matrix.
- The increase of the viscosity of the compounds due to the nanofiller high aspect ratio.
- The lack of control of the alignment or orientation of CNTs in the resulting composites.

For this reason, a section of this critical review focuses on the functionalization methods of carbon nanotubes in order to generate an efficient interphase in polymer matrix nanocomposites.

6.2 Functionalized Carbon Nanotubes

Due to their exceptional mechanical, thermal and electrical properties, in addition to their low density with respect to the class of organic and inorganic tubes, carbon nanotubes (CNTs) are extremely promising for the development of high performance nanostructured materials. Since their discovery in 1991 the research in this exciting field has been in continuous evolution, with most of the research focused on the assessment of the CNT properties and the development of

advanced structural composites based on CNTs [17, 18]. Single-walled carbon nanotubes (SWCNTs) are considered as the simplest member of the family of CNTs, consisting of one graphitic sheet, which has been rolled up into a cylindrical shape. Depending on the arrangement of the hexagon rings along the tubular surface, CNT can be metallic or semiconducting. However, the incorporation of nanotubes is not a trivial task mainly if a good dispersion is mandatory to maximize the advantage of nanotube reinforcement. In fact, the affinity to adhere to each other, renders as-grown SWCNTs intractable and indispersable in common solvents [19] (Figure 6.1).

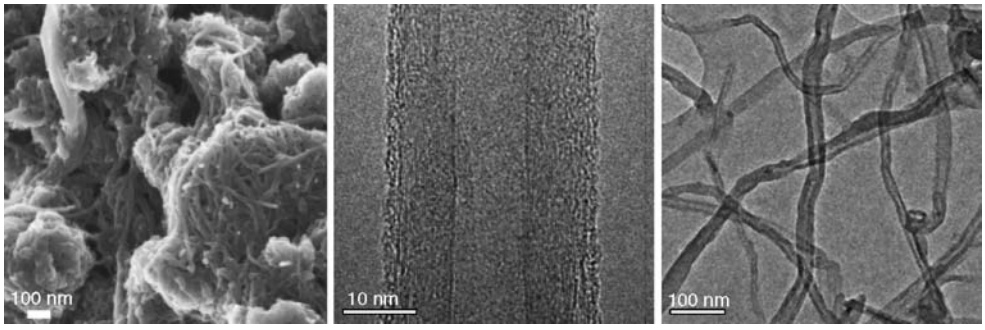

Figure 6.1 Representative SEM and TEM images of CNT

As deposited CNTs can be dispersed in common solvents by sonication, but they precipitate when this treatment is switched off. In order to overcome this problem it was demonstrated the possibility to realize the CNT interaction with different organic compounds [20–36]. This approach renders them able to undergo chemical reactions that make CNTs soluble into polymeric systems. The way of realizing composites made out of carbon nanotubes are securing a reliable control over their surface chemistry through either covalent or noncovalent modification and achieving dispersion.

The development of CNT-based nanocomposites can only be achieved by solving two main problems: (i) the large contact area of CNTs and the strong intertube attraction via van der Waals's forces that make the CNT packed together, thus making more difficult their dispersion in polymeric matrices, and (ii) the poor interfacial adhesion between the CNTs and the matrix. More recently the development of CNT-based nanocomposites has been achieved thanks to approaches that have been used to exfoliate bundles of CNT through the wrapping of the tubular surface by various species of polymers [22, 23], aromatic compounds [37] and surfactants [38].

In this regard interactions between nanotubes and polynuclear species as well as pyrene-modified oxide surfaces have been used for the assembly of single-walled carbon nanomaterials [39]. Surfactants are generally used for the dispersion of neat CNTs [40]. Then, this stable dispersions were used for the compatibilization of the tubes within the polymer matrix [41–43].

CNT are considered ideal materials for reinforcing fibers due to their exceptional mechanical properties. Functionalization of CNTs seems to be the most effective way to incorporate these nanofibers into the polymer matrix. It is generally accepted that the fabrication of high-performance nanotube-polymer composite depends on the efficient load transfer from the host

matrix to the tubes. If the percentage of nanoreinforcements is very low or if it is well dispersed, there are more strong interfaces that slow down the progress of the crack [44, 45].

Therefore, nanotube-polymer composites have potential applications in aerospace science, where lightweight robust materials are needed [44]. To address these issues, several strategies for the preparation of such composites are proposed involving physical mixing in solution, infiltration of monomers in the presence of nanotube sheets and chemical functionalization of CNTs by plasma treatment.

Several years ago it was reported how the selective localization of nanoparticles (that is, carbon black) at the interface of polymer blend [46, 47] represents an alternative route to obtain conductive materials. Following this concept it was recently proposed [48] that the localization of the nanotubes at an interface instead of a homogeneous dispersion within the whole composite volume enhances the conductivity of the material with a low nanotube content. A compromise between the nanotube dispersion and their localization at the interface can be obtained by preparing thin films of carbon nanotubes containing polymers. In this regard more recently it was proposed a novel approach where prealigned arrays of multiwalled carbon nanotubes were grown on a substrate by chemical vapor deposition [49] then a monomer (that is, methyl methacrylate) was infiltrated and polymerized into these arrays. The resulting composite films (Figure 6.2) showed good dispersion of nanotubes in the polymer matrix with an enhanced thermal stability. Similar synthesis approaches have been used to develop composite architectures consisting of intercalated networks of nanotubes and polymers [50–52].

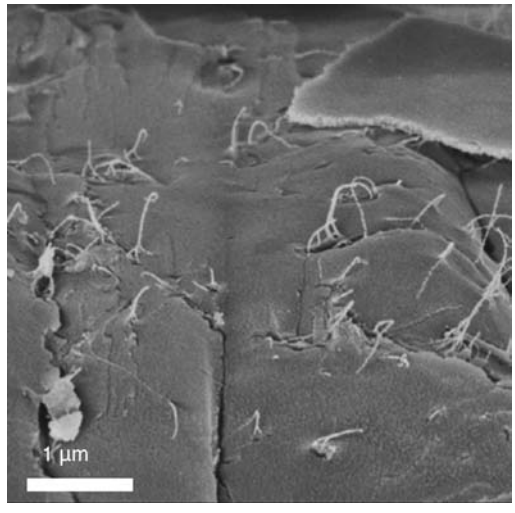

Figure 6.2 Representative SEM image of CNTs dispersed in poly(methyl methacrylate)

One very promising technique being developed for manipulating CNTs is electrophoretic deposition (EPD) [53–55] (Figure 6.3).

EPD is achieved via the motion of charged particles, dispersed in a suitable solvent, towards an electrode under an applied electric field [54]. For example, the presence of carboxylic acid groups onto the nanotube sidewall solubilizes them in water by the development of a negative

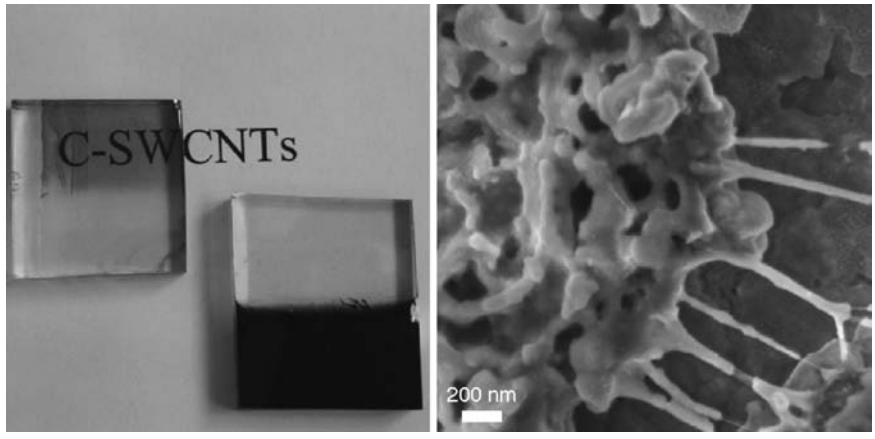

Figure 6.3 Representative optical and SEM images of electrodeposited CNTs (left) and polyfluorene electrodeposited onto CNTs (right)

surface charge. Thus electrophoretic deposition of charged nanotubes moves them towards the anode under an applied electric field [54]. The EPD if compared with other deposition techniques offers advantages of low cost, uniformity of the coatings, and the possibility of depositing on complex-shaped substrates.

Moreover, for the use of carbon nanotubes in devices for practical applications, nanotubes should be in the state of separate nanotubes and small bundles with proper length and functional groups, which can be used for directed self-assembly of nanotubes. For the preparation of such functionalized nanotubes with small bundle size and appropriate length a combined method of multistep oxidation and noncovalent functionalization was previously reported [56, 57].

The direct fluorination of CNTs and their subsequent derivatization provide a versatile tool for the preparation and manipulation of nanotubes with variable sidewall functionalities. Fluorine in CNTs can be efficiently displaced by alkylamino functionalities leading to a nucleophilic substitution that offers an opportunity for CNTs to be integrated into the structure of the epoxy systems through the sidewall amino functional groups.

The plasma treatment for the functionalization of carbon nanotubes represents a novel approach easy to scale up to industrial application. More recently there were a lot of attempts to fluorinate carbon nanotube sidewalls in such manner [58–60]. The CF_4 plasma treatment of CNT sidewall was demonstrated to enhance the reactivity with aliphatic amines.

However for the large-scale integration of CNTs many challenges must be overcome. One important issue remains the selective positioning with predetermined orientations at a large scale on a substrate. Here we propose how a wet chemistry approach can be used to assembly nanotubes in horizontally ordered arrays. This method is based on the control of the wettability of a substrate during a dip coating process.

In suggested mechanisms, as known, during the drying process of the liquid film on the vertical substrate under the gravitational force, the downwardly dewetting liquid film exerts a hydrodynamic drag force defined as $F_h = \eta l V$, where η is the liquid viscosity, l is the nanotube

length, and V is the velocity of the hydrodynamic flow estimated as the rate of dewetting, $V = \gamma\theta 3/6\eta L$ where θ is the contact angle, γ is the surface tension of the liquid and L is a constant of order 10 [61]. From these arguments the evaporation rate versus the dip coating rate induces the nanotube to orient parallel or perpendicular to the solution surface.

More recently, studies on carbon fiber-epoxy composites have shown that process-induced negative surface charges on carbon fibers can be exploited to produce initially charge-stabilized dispersions, which subsequently form oriented filler networks in both direct current (DC) and alternating current (AC) fields [62–64]. Electric fields have been applied to achieve oriented conductive carbon nanotube networks in fully processed nanotube-polymer composites. Experiments aimed at aligning carbon nanotubes have, so far, been carried out only on dispersions of nanotubes in various liquid media. The expectation was that more efficient networks would form if the aggregation process was guided in this way and that interesting anisotropic conductivities might emerge.

Processing methods commonly used to incorporate nanotubes within the polymer matrix include: mixing of nanotubes into the polymer, *in situ* polymerization and melt processing by extrusion. However, the nonuniform dispersion of nanofillers within the polymer matrix and the increasing of the viscosity due to their high aspect ratio render the tubes far from their utilization in nanocomposite.

6.3 Elastomeric Nanocomposites

Even though elastomeric matrices have not been as widely studied as thermoplastic or thermoset matrices, there are a number of interesting reports in the literature. The addition of carbon nanotubes sensibly increases the mechanical, electrical, thermal stability, inflammability and tribological properties of elastomer matrices. In particular, there have been several attempts to incorporate MWCNTs in rubbers to improve their wear resistance [65, 66].

In this review, we have selected the most relevant and studied elastomeric matrices.

6.3.1 Natural Rubber

Natural rubber (NR) is a hydrocarbon diene monomer whose repeating unit is *cis*-isoprene. The outstanding strength of natural rubber has maintained its position as the preferred material in many engineering applications. It has a long fatigue life, good creep and stress relaxation resistance and low cost.

Carbon nanotubes/NR nanocomposites have been successfully prepared by several procedures: melt mixing [67–69], solution blending [70–75] and latex compounding [76].

Lopez-Manchado *et al.* [67] characterized the effects of the incorporation of single-walled carbon nanotubes (SWCNTs) on the physical and mechanical properties of NR. NR compounds were prepared in an open two-roll mill at room temperature and then vulcanized in a hydraulic press at 150 °C. SWCNTs behaved as effective accelerators, decreasing the time of the crosslinking reaction. The authors observed a strong filler-matrix interaction (Figure 6.4), which is reflected in a marked increase of the storage modulus as well as a noticeable shift of the glass transition temperature towards higher temperatures. These effects are more marked in comparison with NR composites filled with carbon black (CB).

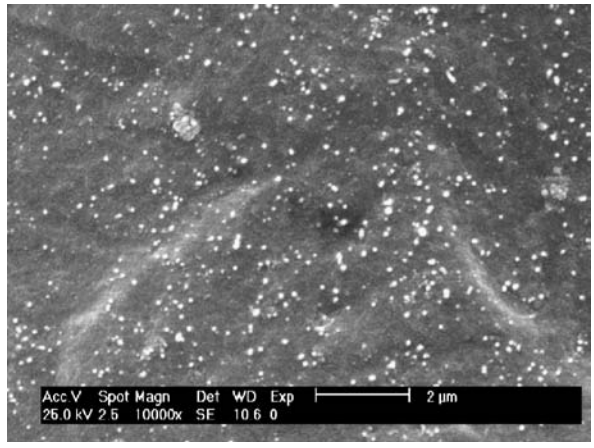

Figure 6.4 Representative SEM image of SWCNTs/NR nanocomposites

This different behavior can be attributed to the dissimilar filler morphology, namely, particle size or surface area and structure. SWCNTs are characterized for a high aspect ratio in relation to CB, such as smaller particle size, larger interfacial area. This implies a stronger filler-matrix interaction at the interface which leads a more immobilized rubber shell compared with large-particle CB. Another interesting aspect for understanding the differences between both fillers is the anisometry of the filler aggregates (shape factor). Guth-Gold [77, 78] defined this factor as the ratio of the longest dimension of the particle to the shortest. It is well known that in compounds containing fillers with identical surface area and chemical nature but different shape, the storage modulus increases with increasing anisometry. The factor shape is larger for SWCNTs than its counterpart CB, which explains the higher hydrodynamic reinforcing of carbon nanotubes. The authors observed by Raman spectroscopy that the load is transferred predominantly along the axis of the nanobundle in elastomer-based composites and, hence, SWCNTs provide load transfer effectiveness.

Bokobza *et al.* [71, 73] prepared multiwall carbon nanotubes (MWCNTs)-NR nanocomposites at several filler concentrations (in the range 1.0–9.1 wt%) by solution blending. Carbon nanotubes were mixed in toluene by sonicating until a homogeneous dispersion was observed in an optical microscope. Natural rubber containing all the vulcanizing ingredients was then dissolved in the suspension of carbon nanotubes with vigorous stirring for about 12 h. After mixing, the toluene was carefully removed at room temperature under vacuum. The results were compared with those obtained with conventional carbon black. Bokobza *et al.* observed that at a given strain level, a noticeable increase in the stress can only be observed from a filler content of 2.4 wt%. The reinforcing effect increased with increasing the CNT loading in the composite. The authors demonstrated that the reinforcement provided by MWCNT is much higher than that by carbon black at the same filler loading. So, at 350% strain, the nominal stress values were, respectively, 2.1 and 3.9 MPa for CB and MWCNT composites. The increase in the stress is usually associated to the hydrodynamic effect, which is more marked by the filler anisotropy and the presence of occluded rubber. However, the incorporation of MWCNTs did not lead to an improvement in the ultimate properties like the stress and strain at break.

Furthermore, the authors studied the influence of CNTs on the electrical properties of these systems. An abrupt decrease of the resistivity by several orders of magnitude by the addition between 2.9 and 3.8 wt% of MWCNTs was observed, indicating the formation of a percolation network. At an equivalent filler loading, samples filled with MWCNTs displayed a higher conductivity than those containing CB, where 3.8 and 9.1 wt% of CB lead to composites that are still insulators. This indicated that the filler-filler network in carbon-filled systems occurs at a filler loading above 9.1 wt%.

When analyzing the dynamic properties, the authors observed a dramatic decrease of the storage modulus with increasing strain amplitude, for composites that contain more than 3.8 wt % of MWCNTs. In general, in the case of filled rubbers the dynamic properties are amplitude-dependent. This phenomenon known as the Payne effect is associated to the breakdown of a filler network formed by filler-filler interactions. This effect depends on several parameters like temperature, concentration, surface characteristics and size of the particles. For the same filler loading, a greater Payne effect is obtained for the MWCNTs/NR composites than for the sample containing CB.

Zhao *et al.* [75] found that by adding 0.25 wt% of SWCNTs, the modulus of the SWCNT/NR composite prepared with toluene as a solvent, increased about 20% compared to the pure NR material. They attributed this improvement to the formation of additional sources of entanglements or physical crosslinks in the network in presence of carbon nanotubes. These extra crosslinks play an important role at the beginning of the deformation, increasing the modulus. At higher deformations, some of the physical crosslinks may dissipate when polymer chains slide on the carbon nanotubes. In addition, comparing the crosslink densities of the NR and SWCNT/NR samples calculated from mechanical and Raman spectroscopy measurements, the authors observed that SWCNTs can be used as Raman sensors to evaluate the crosslinking process of rubbery materials. The D^* peak of SWCNTs was shifted upwards as the extent of vulcanization is increased by increasing the amount of sulfur. So, Raman spectroscopy could be used to determine the degree of crosslinking in rubbery materials.

In order to improve the adhesion between carbon nanotubes and natural rubber at the interface, carbon nanotubes have been superficially modified. Sui *et al.* [69] observed that after being treated with acid and ball-milling, CNTs dispersed well in the rubber matrix and interfacial interaction between them was improved. The vulcanization times, scorch and optimum cure time decreased and the maximum torque increased after adding acid treated and ball milled CNTs into NR. In addition, the over-curing reversion of CNT/NR was alleviated. By adding the treated CNTs, comprehensive performance of the resulting nanocomposites achieved a considerable increase compared to neat NR and CB/NR composites.

Wang *et al.* [76] prepared powder natural rubber composites modified carbon nanotubes by means of spray drying process. CNTs treated in blended acid were fully dispersed in the NR powders and had a good interfacial interaction with the NR matrix. When compared with NR materials prepared by conventional mechanical processes, NR powders modified by CNTs require more vulcanizer. The amount of the vulcanizer to fully vulcanizing the NR powders modified by CNTs was about 1.5 times or more as that for neat NR compound. Moreover, they reported that vulcanizing reversions did not occur in the vulcanized NR powders modified by CNTs. In addition, the mechanical properties of the NR powders were sensibly improved.

Finally, Shanmugharaj *et al.* [68] found that 3-aminopropyltriethoxisilane functionalized CNT increased the scorch time and optimum cure time in the sulfur vulcanization of natural rubber. They attributed this effect to absorption of basic accelerator by acid groups and

quinone-type oxygen atoms of the previous oxidative treatment. NR/silane functionalized carbon nanotubes composites exhibited higher modulus, tensile strength and elongation at break compared to NR vulcanizates due to the higher polymer-filler interaction between the silanized carbon nanotubes and NR vulcanizates.

6.3.2 *Styrene-Butadiene Rubber*

Styrene-butadiene rubber (SBR) is an elastomeric copolymer consisting of styrene and 1,3-butadiene. Most SBR is produced by emulsion polymerization but it is also synthesized by solution polymerization. SBR is the synthetic rubber most widely used in the elastomer industry since it has suitable properties of very good abrasion resistance, aging stability and low-temperature properties. The tire industry constitutes the sector of higher application, consuming approximately 70% of total SBR production. SBR formulations usually require a notable amount of reinforcing filler, being CB the most used. Recently, carbon nanotubes/SBR composites have attracted considerable attention due to the possibility to obtain improved properties at low filler loadings [73, 79–86].

The first reported study on CNT/SBR compounds was carried out by X. Chen *et al.* [80]. They analyzed the effects of different contents of MWCNTs on the performance and microstructure of the SBR composites processing in an open roll mill at room temperature. MWCNTs were modified by refluxing in a HNO_3 solution before blending with SBR rubber. The authors observed a gradual increase of the mechanical properties, tensile and tear strength, shore hardness and abrasion with increasing the MWCNTs content. The performances of MWCNTs/SBR compounds were better than those of carbon black (N330)/SBR composites. The authors suggest the likely application of carbon nanotubes for tires with rolling hysteresis and decreased fatigue loss.

X. Zhou *et al.* [84–86] prepared carbon nanotubes (CNT) and carbon black (CB)-filled powder styrene-butadiene rubber composites by spray drying of the suspension of CNTs and CB in SBR latex. By means of this process, uniform spherules of SBR latex with diameters of less than 10 μm were prepared, in which CNTs were well dispersed. They used CNTs prepared by chemical vapor deposition process and treated by blended acid solution with a volume ratio between sulfuric and nitric acid of 3 : 1. After blended acid treatment, some functional groups such as hydroxyl, carboxyl and carbonyl were loaded on the CNT surface. These functional groups improve the water affinity of CNTs and thus were more suitable for the preparation of a CNT-SBR latex suspension. By the addition of CNTs, a sensible increase of the glass transition temperature (T_g) of the composite was detected due to a strong filler-polymer interaction at the interface. This effect was more marked as the CNT loading in the composite increased (−29.30 °C for pure SBR, −25.65 °C for 10 phr CNTs and −19.56 °C for 60 phr CNTs). In addition, the authors observed that the optimum cure time (t_{90}) and maximum torque of the composites increased gradually with increasing CNT addition. It can be deduced that CNTs decelerated the vulcanization reaction of the SBR compounds probably due to the added functional groups of the CNTs with acid treatment. The acidic functional groups can prevent the formation of vulcanization free action groups. The increase of maximum torque is associated to a higher crosslinking density of the vulcanizates due to high Young's modulus of the added CNTs. The gel fractions measurements confirmed an increase of the crosslinking degrees of the composites with increasing CNTs additives. X. Zhou *et al.* studied also the

influence of CNTs on the dynamic mechanical and mechanical properties of SBR compounds. They observed a sensible increase of the storage modulus with increasing addition of CNTs, due to the hydrodynamic reinforcement upon introduction of fillers. This effect is more marked when the CNTs additions exceed 30 phr. In contrast, the mechanical properties of the composites increase progressively with the increment of the CNTs addition. Compared with the pure SBR, the hardness, tensile and tear strength of the composite filled with 60 phr CNTs were enhanced 73.9%, 327.7% and 191.1%, respectively, reflecting the strong reinforcing effect of CNTs. The authors attributed this increase to the reinforcement of the well dispersed CNTs with high Young's modulus and strength in the rubber matrix.

Furthermore, the authors analyzed the effect of the vulcanizing reagent suspensions (sulfur) addition on the properties of CNT/SBR powder compounds. Compared with the conventional vulcanizing of carbon black/PSBR composites, twice more sulfur additions are needed in the vulcanization of CNT/PSBR compounds. The glass transition temperature of the compound increased gradually with the increment of the vulcanizing reagent and reached the maximum at a sulfur concentration of 4 phr, and then it would decrease slightly at higher sulfur additions. With the increment of the sulfur concentration, the elongation at break of the vulcanized rubber compound decreased gradually, and the tensile strength and hardness reached a maximum when the sulfur addition was 4 phr and kept constant when the addition continued to rise. In contrast, the tear strength reached a maximum value at 2.5 phr of sulfur and then decreased slightly at higher concentrations due to the structure designability of the compounds affected by the sulfur aggregates in the polymer matrix.

L. Bokobza [71, 79] demonstrated the intrinsic potential of multiwalled carbon nanotubes (MWCNT) as a reinforcing filler in elastomer matrices, in particular, styrene-butadiene copolymers. Despite a poor dispersion detected by transmission electron microscopy and atomic force microscopy, sensible improvements in the mechanical and electrical properties of SBR matrix by the addition of MWCNT were observed. The incorporation of 1 phr of carbon nanotubes increases the tensile modulus and strength of the compound, approximately 45% and 70%, respectively. Compared to CB, a small filler loadings of carbon nanotubes is required to reach the same performances due to a stronger interfacial adhesion between the polymer and the nanotubes. So, quite similar hysteresis curves are obtained when SBR is filled with 10 phr of MWCNTs or 50 phr of CB.

However, the authors observed that the carbon nanotubes are able to form a critical concentration of conduction (continuous interconnecting filler network) at a small filler loading: 2–4 phr of CNT are required, against 30–40 phr for CB. By the addition of 2 and 4 phr of CNT, the conductivity of the composite increases by five orders of magnitude, reflecting the formation of a percolation network. However, the aggregation of CNT yields a conductive material at a higher volume fraction that than that expected from individually well dispersed carbon nanotubes. The authors studied the variations in resistivity under uniaxial deformations of up to 200%. They observed a gradual increase in the resistivity of the compound with strain applied. When second stretch was conducted after total unloading of the sample, the resistivity slightly decreased and, when the strain reached the maximum value of the first stretching, the two curves coincided, that is, the sample was now in the same state as it was in the first stretching. The authors studied the changes in the resistivity under uniaxial extension by atomic force microscopy observations of stretched composites. They observed an increase of the roughness of the sample with strain and the filler structures align in the direction of strain. The structure became more slender under deformation, with a loss of contacts between aggregates and an increase in the resistivity.

A second stretching on the sample showed different arrangements in the filler structure: filler aggregates were oriented perpendicularly to the stretching direction. The authors concluded that the strong alignment of the bundles perpendicular to the previous extension axis could be the result of a reequilibration of the stress field. In consequence, new conducting pathways were produced, leading to a weak decrease in resistivity.

De Falco *et al.* [81] developed an easy technique to fabricate cured styrene-butadiene rubber/multiwalled carbon nanotube composites. The compounds were prepared by dissolving the SBR in toluene in a ratio of 25 ml g^{-1}, then adding the filler, previously dispersed in ethanol by sonication, and then drying. Afterwards, the other components, N-t-butyl-2-benzothiazole sulfonamide (TBBS) and sulfur, were added as a cure system and then the system was stirred and put to evaporate for 4 days as films in Petri capsules until constant weight before the cure. This procedure successfully obtained a homogeneous dispersion of the filler into the elastomer matrix without agglomeration. The incorporation of a small quantity of multiwalled carbon nanotubes (0.66 wt%) led to a sensibly increase of the mechanical properties when compared with pristine SBR compound or CB-filled SBR. The authors attributed this higher reinforcing effect to the higher aspect ratio in the MWCNT compared with CB (around 500 times) and the better interface between the two phases in the case of SBR/MWCNT composites.

6.3.3 Polyurethane Rubber

Polyurethane (PU) is one of the largest and most versatile families of polymers. They are generally produced by the polyaddition reactions of higher-molecular-weight diols and diisocyanates, which led to a two-phase morphology of alternating soft and hard segments. The control of parameters such as functionality, chemical composition and molecular weight of the different reactants produces a wide set of materials with significantly different properties. Polyurethanes can be classified according to their production process in: (i) casting rubbers, (ii) thermoplastic rubbers and (iii) vulcanizable rubbers. This versatility has led to the use of polyurethanes as foams, coatings, actuators and adhesive-based products [87] and has made polyurethane-based nanocomposites one of the most widely studied elastomers [88–125].

Most of these studies used previously functionalized CNTs to improve their compatibility and dispersion [89, 91, 93–95, 99, 100, 102–108, 110–112, 116, 119–121, 123–126]. Meanwhile, the addition of as produced CNTs into PU matrices was mainly done by solvent mixing [88, 90, 92, 96–98, 101, 109, 113, 114, 117, 122]. The most frequent functionalization treatment is carried out under oxidizing conditions with acids, which introduce hydroxyl, carbonyl and carboxylic functionalities. These groups would improve the interfacial bonding through the reaction among OH and carboxylic groups on the CNT surface with the NCO groups of the isocyanate.

The majority of the studies have concentrated on either cast [91, 93–97, 100, 101, 103–107, 110, 113, 114, 121, 123–125] or thermoplastic polyurethanes (TPU) [88–92, 98, 99, 102, 108, 111, 116, 120, 122, 124]. Casting systems are composed of liquid or semi-liquid raw materials, polymeric diols, bifunctional or polyfunctional isocyanate and chain extenders. The dispersion procedure in the majority of these studies is carried out by dispersing the CNTs directly into either the polyol or the isocyanate. The polyurethane nanocomposite is finally prepared by the reaction mixing of the reactants. Hence, most of these studies used functionalized CNTs to improve the interaction with the urethane groups. Some authors have also termed this

procedure an *in situ* polymerization. Meanwhile, the preparation procedure of CNT/TPU was mainly carried out by dispersing the CNTs in a solvent, dissolving the polymer in the mixture and subsequently extracting the excess solvent. Cai and Song [109] reported the synthesis of CNT/water-based PU composites by latex compounding, followed by film casting on a polytetrafluoroethylene PTFE substrate.

The first reported studies on CNT/PU systems were independently carried out by Koerner *et al.* [88] and by Sen *et al.* [89]. Koerner *et al.* reported that the uniform dispersion of CNTs in TPU produced a stimuli-responsive material able to store and subsequently release up to 50% more recovery stress than the pristine resin. They attributed this effect to an improvement on the strain induced crystallization due to the CNT presence. The CNTs were thought to absorb infrared photons (light-induced actuation) or electrons (electrically induced actuation) raising the internal temperature, melting strain-induced polymer crystallites (which act as physical crosslinks that secure the deformed shape) and remotely triggering the release of the stored strain energy. Meanwhile, Sen *et al.* reported the fabrication of membranes of SWCNT-filled polyurethane by electrospinning. In the electrospinning technique, polymer nanofibers are produced from an electrostatically driven jet of polymer solution (or melt). They dispersed both as produced and ester-functionalized SWCNTs in dimethylformamide/PU solution and electrospun free-standing membranes 50–100 μm thick. The tensile moduli of as-produced and ester-functionalized SWCNT/PU were found to be respectively 215% and 250% higher than the control polyurethane membranes. Meanwhile, the strength of the ester-modified CNT membranes was improved by up to 104% compared to electruspun pure PU, while the improvement with the as-produced CNT was only of 46%.

The mechanical data of several of these studies show that the tensile modulus of nanotube/PU composites is generally improved, although a detailed comparison of the data is difficult due to the different types of fillers, surface treatments, processing techniques and test methods that have been used. The stiffening effect of the nanotubes was attributed not only to the presence of the CNTs, but also to their impact on soft-segment crystallization, determined by *in situ* X-ray scattering during deformation [88].

Several authors have shown an improvement of the thermal stability of the nanocomposites of as much as 26 °C [93]. Among them, Jana and Cho [123] recently compared as-produced MWCNT/PU prepared by solvent cast and oxidized MWCNT/PU prepared by *in situ* polymerization. The thermal degradation of the samples followed a first-order reaction and took place in two stages, which correspond to the degradation of the soft and hard segments. The study showed that *in situ* nanocomposites outperformed the solvent cast system with a higher degradation temperature and activation energy at 10% degradation. They attributed this behavior to covalent bond formation between the oxidized MWCNTs and PU chains.

The unique electrical conductivity properties of the CNTs suggested their potential use in electrically conductive composites. Thus, the electrical properties of the PU composites have also been studied. In general, the electrical conductivity of a composite reveals a nonlinear increase with the filler concentration, passing through a percolation threshold. Recent studies of functionalised CNT/PU nanocomposites [108, 111, 113] showed a percolation threshold around 0.2 and 0.5 wt% CNTs which was greatly influenced by functionalization treatments [111]. Finally, the electromagnetic interference (EMI) shielding of PU nanocomposites [113] showed that the shielding effectiveness increased with increasing content of SWCNTs, reaching $\sim$17 dB at the SWCNT loading of 20 wt%. The shielding mechanism was found to shift from reflection to an absorption-dominated mechanism.

Even though the main market for PU is as polymeric foams, little effort has been directed towards using CNTs as reinforcements in this system [101, 121, 124]. PU foams are generally obtained from the simultaneous reaction of the polyisocyanate with the polyol in the presence of a blowing agent, usually water [101, 121, 124]. As in bulk systems, the reaction of the polyol with isocyanate produces urethane bonds. Meanwhile, the reaction of the isocyanate with water generates CO_2 which drives the foam expansion.

Park *et al.* [101] reported the used of CNT filled polyurethane foam as the core of a sandwich structure in radar-absorbing structures in the X-band (8.2–12.4 GHz) frequencies. The addition of CNT increased the permittivity of the foam cores, and improved the reflection loss characteristics in the 10.0–10.5 GHz frequency. A second study by Xu *et al.* [121] reported the dependency of the electrical conductivity on foam density. Decreasing the foam density from 0.5 to 0.05 $g\,cm^{-3}$, at a fixed loading fraction of 2 wt%, varied gradually the volume conductivity from $2.4 \times 10^{-2}\,Sm^{-1}$ to $4.3 \times 10^{-5}\,Sm^{-1}$. As the density was further decreased to 0.03 $g\,cm^{-3}$, they observed a nonlinear decrease of eight orders of magnitude. This conductor-insulator change was attributed to a transition from 3-D to 2-D percolation as the CNT distribution concentrated in the cell edges, becoming nonuniform.

Polymer foams have traditionally been used in engineering applications, such as thermal and acoustic insulation, shock absorbers and buoyancy, among others. Recent developments in biomedical applications, in particular in tissue engineering, required the use of 3-D porous structures with appropriate mechanical and mass transport properties, making foams particularly attractive as tissue scaffolds. In this area, CNT/PU foams were investigated as bone tissue scaffolds using two different processing methods. Thermoplastic PU-oxidized CNT foams were manufactured by thermally induced phase separation (TIPS) [124]. The CNT provided a nanotextured surface, changing the surface character of the nanocomposite. Additionally, the CNT significantly improved the compression strength and stiffness of the nanocomposite scaffold. *In vitro* studies revealed that increasing CNT loading fraction did not cause osteoblast cytotoxicity nor had any detrimental effects on osteoblast differentiation or mineralization. Similar results were reported on reactive PU foams [124] (Figure 6.5). These promising results revealed the ability of the CNT to improve simultaneously mechanical performance, surface characteristics and cell phenotype.

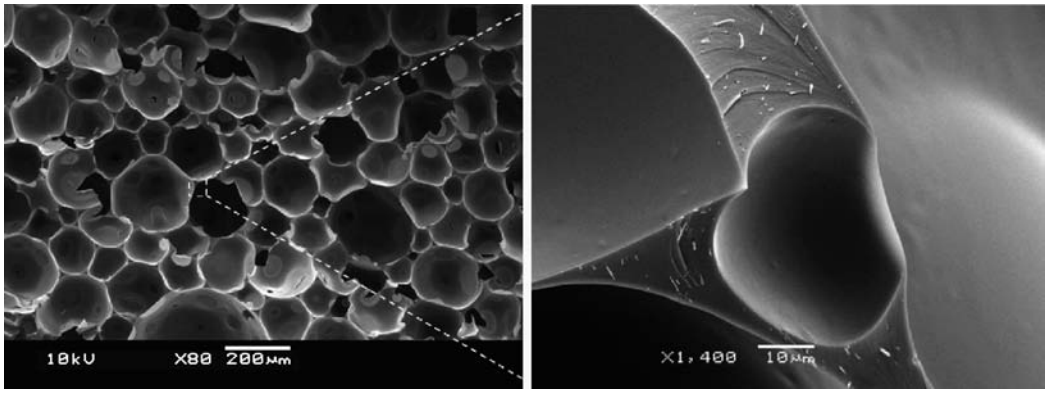

Figure 6.5 Representative SEM images of PU foams reinforced with MWCNTs

6.3.4 Silicone Rubber

Silicone elastomers are unusual synthetic polymers in that their backbone is composed of an "inorganic" repeating unit, that is, silicon to oxygen bonds. In addition, the silicon atoms are attached to organic groups, such as methyl.

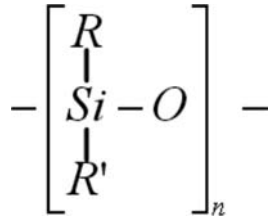

The presence of the inorganic and organic units gives silicones their unique properties and thermal and chemical stability. Hence, silicone nanocomposites have received increasing attention in recent years [127–151].

Most of the studies dispersed as produced CNTs into room-temperature vulcanized (RTV) polydimethylsiloxane (PDMS) by mechanical mixing or ultrasonication. All these studies reported a good dispersion of the CNTs without the need of previous functionalization. It had been suggested that the presence of CH-π interactions could play a role in designing fullerene- and nanotube-based materials [152]. CH-π interactions are a type of hydrogen bond that operates between a soft acid CH and a soft base π-system, as found on the convex surfaces of fullerenes and nanotubes [152]. This suggestion was confirmed experimentally by Baskaran *et al.* [153] and theoretically by Beigdeder *et al.* [149].

The first study on CNT/Silicone nanocomposites was carried out by Frogley *et al.* [127] and compared systems filled with up to 1 wt% SWCNTs and up to 4 wt% CNFs. The mechanical properties showed an approximately linear increase in composite stiffness, but also a reduction in strength and strain to failure for both types of filler, with increasing loading fraction and were more pronounced for the SWCNTs compared to the CNFs. These improvements in mechanical properties were not observed for comparable loading fractions of spherical carbon black. They attributed the modulus increase to the reorientation of nanotubes under strain in the samples.

Several authors have studied new nanocomposite systems to impart *stimuli-responsive* properties to different polymers, among them silicone rubber. The first study on silicone-based nanocomposite as a new photomechanical actuator was reported by Ahir and coworkers [129, 132, 133]. They embedded as produced MWCNTs in PDMS at loading fractions up to 7 wt% and illuminated the samples with infrared source. They measured the strength of photactuator response, at a given radiation intensity, and found it to be in the order of tens of kilopascals, which corresponded to actuation strains of 2–4%. As expected, the response increased with nanotube loading content. Thermal actuation behavior was also observed when the samples were heated by the same amount, but the response was one order of magnitude lower. Chen *et al.* [150] recently reported a similar electrothermal actuator based on a MWCNT/PDMS system. They reported a maximal strain of 4.4% at electric power intensity around 0.03 W mm^{-3}.

Further studies have analyzed the used on these nanocomposites as temperature and pressure sensors [135, 143, 144, 151], humidity sensors [131], strain sensors [137] and gas sensors [148]. Pressure sensors were prepared slightly above the percolation threshold of the material so that the conductivity was low and sensitive to small specific volume change of the composites. Jiang *et al.* [135, 143, 144, 151] dispersed γ-aminopropyltriethoxy silane functionalized CNTs in

methylvinyl silicone rubber and reported a percolation threshold of around 0.01 wt% [142]. Contrary to expectations, they observed a resistance which increased with increasing applied pressure. They attributed this behavior to the loss of the original percolation network original networks under pressure due to nanotube rearrangement perpendicularity to the direction of applied pressure because of the large free volume and low Young's module of the rubber host. Similar results were recently confirmed by Hu *et al.* [151]. A completely different approach was reported by Woo *et al.* [148] to fabricate a gas-sensing system. They made single- walled carbon nanotube (SWCNT) thin films by dispersion and vacuum filtration of 1% sodium dodecyl sulfate (SDS) surfactant solution. These SWCNT films were then transferred onto a flexible substrate by curing a PDMS solution over the films. They obtained a transparent system with high sensitivity to NH_3 gas.

Thermal [128, 130, 139, 141] and electrical [134, 140, 142, 145–147] conductivities were also measured. Thermal conductivities were found to increase by up to 65% with loading fractions of 3.8 wt% of as-produced MWCNTs. Meanwhile the electrical resistivity showed a decreased of more than ten orders of magnitude from 10^{16} to $10^{6}\,\Omega\,\mathrm{cm}^{-2}$ by incorporating 5 wt% of oxidized MWCNT. Among these studies, there were several authors that studied and modeled the anisotropic conductance of aligned CNT impregnated with silicone.

There have been limited studies on functionalization of CNT specially made for a silicone host matrix. Chen *et al.* [134] reported the functionalization of MWCNT with 3-aminopropyltriethoxysilane (APS) which produced a SiO_2 coating around the tubes and produced highly insulating PDMS nanocomposites. Bourlinos *et al.* [154] also reported a surface modification by first oxidizing and then reacting the CNT with an epoxy-terminated silicone. They obtained a carbon-based fluid at ambient conditions combined with the unusually high CNT content.

Finally, CNT were studied as flame retandants in silicone foams [155]. The limiting oxygen index of the nanocomposite increased as a function of nanotube content, attaining the self-extinguishing grade even at low mass fraction of the carbon nanotubes (0.5 wt%). Further thermal characterization revealed increases in thermal dissipation efficiency and thermal degradation temperature. The different thermal and flame retardancy results were attributed to the formation of a CNT network throughout the sample. The formation of this network was attributed to a good dispersion of the CNTs via noncovalent CH-π interactions and to the surface tension of the gas–polymer interface during foaming. However, the nanocomposite foams were found to decrease the acoustic absorption with nanofiller content probably due to the variable foam structure and improved stiffness [156].

6.4 Outlook

The ultimate goal of CNT nanocomposites is to produce materials that are optimally reinforced and multifunctional. In this review, we have provided an overview of the recent advances in carbon nanotube/elastomer composites from synthesis methods and processing to their ultimate properties. As has been shown, the possible applications of carbon nanotube composites range widely, from electrically conductive systems to sensors or biomedical applications. Although much progress has been made, there are still many problems to overcome before the full potential of nanotube containing composites can be achieved. At present, the improvements in the properties are far below the expected values for nanometer-scale reinforcement due to the poor dispersion and lack of interaction of filler/polymer at the

interphase. Further work is required to develop production techniques to achieve the nanostructuration level required to fully exploit the inherent properties of nanoscaled materials. The following critical issues must be developed in the future:

- New commercial synthesis routes of carbon nanotubes to obtain perfectly crystalline nanotubes in large quantities which have a high purity and are cost-effective.
- Optimization of the processing conditions.
- Development of original processing routes to produce carbon nanotubes/polymer nanocomposites.
- Appropriate funcionalizations of carbon nanotubes for their integration in a polymer matrix.
- The provision of sound theoretical models which allow the prediction of the behavior of polymer nanocomposites.

In conclusion, future industrial exploitation of the nanocomposites will depend on how effectively we can handle the mentioned challenges. The significant progress made in the past few years points toward a bright future. Finally, looking to the future, further functional properties may be achieved by using hierarchical reinforced systems or other nanoscale fillers such as nanorods and nanowires.

References

1. Donnet, J.B. (1998) Black and white fillers and tire compound. *Rubber Chemistry and Technology*, **71**(3), 323–341.
2. Pinnavaia, T.J. and Beall, G. (eds) (2001) *Polymer-Clay Nanocomposites*, Wiley.
3. Krishnamoorti, R. and Vaia, R.A. (eds) (2002) *Polymer Nanocomposites: Synthesis, Characterization and Modelling*, American Chemical Society.
4. Ray, S.S. and Okamoto, M. (2003) Polymer/layered silicate nanocomposites: a review from preparation to processing. *Progress in Polymer Science*, **28**(11), 1539–1641.
5. Utracki, L.A. (2004) *Clay-containing Polymeric Nanocomposites*, Rapra Technology Limited.
6. May, Y.W. and Yu, Z.Z. (eds) (2006) *Polymer Nanocomposites*, CRC Press.
7. Ajayan, P.M. *et al.* (1994) Aligned carbon nanotube arrays formed by cutting a polymer resin-nanotube composite. *Science*, **265**(5176), 1212–1214.
8. Saito, R., Dresselhaus, G., and Dresselhaus, M.S. (eds) (1998) *Physical Properties of Carbon Nanotubes*, Imperial College Press.
9. Yu, M.-F. *et al.* (2000) Tensile loading of ropes of single wall carbon nanotubes and their mechanical properties. *Physical Review Letters*, **84**(24), 5552.
10. Moniruzzaman, M. and Winey, K.I. (2006) Polymer nanocomposites containing carbon nanotubes. *Macromolecules*, **39**(16), 5194–5205.
11. Shaffer, M.S.P. and Sandler, J. (2006) Carbon nanotube/nanofibre polymer composites, in *Processing and Properties of Nanocomposites* (ed. S. Advani), World Scientifc, pp. 1–59.
12. Bokobza, L. (2007) Multiwall carbon nanotube elastomeric composites: A review. *Polymer*, **48**(17), 4907–4920.
13. Cooper, C.A., Young, R.J., and Halsall, M. (2001) Investigation into the deformation of carbon nanotubes and their composites through the use of Raman spectroscopy. *Composites Part A: Applied Science and Manufacturing*, **32**(3–4), 401–411.
14. De Heer, W.A. (2004) Nanotubes and the pursuit of applications. *MRS Bulletin*, **29**(4), 281–285.
15. Uchida, T. and Kumar, S. (2005) Single wall carbon nanotube dispersion and exfoliation in polymers. *Journal of Applied Polymer Science*, **98**(3), 985–989.
16. Gao, G.H., Cagin, T., and Goddard, W.A. (1998) Energetics, structure, mechanical and vibrational properties of single-walled carbon nanotubes. *Nanotechnology*, **9**(3), 184–191.
17. Iijima, S. and Ichihashi, T. (1993) Single-shell carbon nanotubes of 1-nm diameter. *Nature*, **363**(6430), 603–605.

18. Kratschmer, W. *et al.* (1990) Solid C-60 - a new form of carbon. *Nature*, **347**(6291), 354–358.
19. Baughman, R.H., Zakhidov, A.A., and de Heer, W.A. (2002) Carbon nanotubes - the route toward applications. *Science*, **297**(5582), 787–792.
20. Dai, L.M. and Mau, A.W.H. (2001) Controlled synthesis and modification of carbon nanotubes and C-60: Carbon nanostructures for advanced polymer composite materials. *Advanced Materials*, **13**(12–13), 899.
21. Rao, C.N.R. *et al.* (2001) Nanotubes. *Chemphyschem*, **2**(2), 78–105.
22. Thostenson, E.T., Ren, Z.F., and Chou, T.W. (2001) Advances in the science and technology of carbon nanotubes and their composites: a review. *Composites Science and Technology*, **61**(13), 1899–1912.
23. Andrews, R. *et al.* (2002) Multiwall carbon nanotubes: synthesis and application. *Accounts of Chemical Research*, **35**(12), 1008–1017.
24. Bahr, J.L. and Tour, J.M. (2002) Covalent chemistry of single-wall carbon nanotubes. *Journal of Materials Chemistry*, **12**(7), 1952–1958.
25. Fischer, J.E. (2002) Chemical doping of single-wall carbon nanotubes. *Accounts of Chemical Research*, **35**(12), 1079–1086.
26. Hirsch, A. (2002) Functionalization of single-walled carbon nanotubes. *Angewandte Chemie-International Edition*, **41**(11), 1853–1859.
27. Niyogi, S. *et al.* (2002) Chemistry of single-walled carbon nanotubes. *Accounts of Chemical Research*, **35**(12), 1105–1113.
28. Sinnott, S.B. (2002) Chemical functionalization of carbon nanotubes. *Journal of Nanoscience and Nanotechnology*, **2**(2), 113–123.
29. Sun, Y.P. *et al.* (2002) Functionalized carbon nanotubes: properties and applications. *Accounts of Chemical Research*, **35**(12), 1096–1104.
30. Davis, J.J. *et al.* (2003) Chemical and biochemical sensing with modified single walled carbon nanotubes. *Chemistry-a European Journal*, **9**(16), 3732–3739.
31. de la Torre, G., Blau, W., and Torres, T. (2003) A survey on the functionalization of single-walled nanotubes. The chemical attachment of phthalocyanine moieties. *Nanotechnology*, **14**(7), 765–771.
32. Tasis, D. *et al.* (2003) Soluble carbon nanotubes. *Chemistry-a European Journal*, **9**(17), 4001–4008.
33. Terrones, M. (2003) Science and technology of the twenty-first century: Synthesis, properties and applications of carbon nanotubes. *Annual Review of Materials Research*, **33**, 419–501.
34. Katz, E. and Willner, I. (2004) Biomolecule-functionalized carbon nanotubes: Applications in nanobioelectronics. *Chemphyschem*, **5**(8), 1085–1104.
35. Banerjee, S., Hemraj-Benny, T., and Wong, S.S. (2005) Covalent surface chemistry of single-walled carbon nanotubes. *Advanced Materials*, **17**(1), 17–29.
36. Lu, X. and Chen, Z.F. (2005) Curved Pi-conjugation, aromaticity, and the related chemistry of small fullerenes (<C-60) and single-walled carbon nanotubes. *Chemical Reviews*, **105**(10), 3643–3696.
37. Nakashima, N., Tomonari, Y., and Murakami, H. (2002) Water-soluble single-walled carbon nanotubes via noncovalent sidewall-functionalization with a pyrene-carrying ammonium ion. *Chemistry Letters* (6), 638–639.
38. Islam, M.F. *et al.* (2003) High weight fraction surfactant solubilization of single-wall carbon nanotubes in water. *Nano Letters*, **3**(2), 269–273.
39. Zhu, J. *et al.* (2003) Surface modification approach to the patterned assembly of single-walled carbon nanomaterials. *Nano Letters*, **3**(9), 1239–1243.
40. Rao, A.M. *et al.* (1997) Diameter-selective Raman scattering from vibrational modes in carbon nanotubes. *Science*, **275**(5297), 187–191.
41. Gong, X.Y. *et al.* (2000) Surfactant-assisted processing of carbon nanotube/polymer composites. *Chemistry of Materials*, **12**(4), 1049–1052.
42. O'Connell, M.J. *et al.* (2002) Band gap fluorescence from individual single-walled carbon nanotubes. *Science*, **297** (5581), 593–596.
43. Yurekli, K., Mitchell, C.A., and Krishnamoorti, R. (2004) Small-angle neutron scattering from surfactant-assisted aqueous dispersions of carbon nanotubes. *Journal of the American Chemical Society*, **126**(32), 9902–9903.
44. Calvert, P. (1999) Nanotube composites - A recipe for strength. *Nature*, **399**(6733), 210–211.
45. Andrews, R. and Weisenberger, M.C. (2004) Carbon nanotube polymer composites. *Current Opinion in Solid State & Materials Science*, **8**(1), 31–37.
46. Gubbels, F. *et al.* (1995) Design of electrical conductive composites - key role of the morphology on the electrical-properties of carbon-black filled polymer blends. *Macromolecules*, **28**(5), 1559–1566.

47. Gubbels, F. *et al.* (1998) Kinetic and thermodynamic control of the selective localization of carbon black at the interface of immiscible polymer blends. *Chemistry of Materials*, **10**(5), 1227–1235.
48. Bocharova, V. *et al.* (2006) Ultrathin transparent conductive films of polymer-modified multiwalled carbon nanotubes. *Journal of Physical Chemistry B*, **110**(30), 14640–14644.
49. Raravikar, N.R. *et al.* (2005) Synthesis and characterization of thickness-aligned carbon nanotube-polymer composite films. *Chemistry of Materials*, **17**(5), 974–983.
50. Vigolo, B. *et al.* (2000) Macroscopic fibers and ribbons of oriented carbon nanotubes. *Science*, **290**(5495), 1331–1334.
51. Coleman, J.N. *et al.* (2003) Improving the mechanical properties of single-walled carbon nanotube sheets by intercalation of polymeric adhesives. *Applied Physics Letters*, **82**(11), 1682–1684.
52. Li, J. *et al.* (2006) Organic light-emitting diodes having carbon nanotube anodes. *Nano Letters*, **6**(11), 2472–2477.
53. Kamat, P.V. *et al.* (2004) Self-assembled linear bundles of single wall carbon nanotubes and their alignment and deposition as a film in a dc field. *Journal of the American Chemical Society*, **126**(34), 10757–10762.
54. Boccaccini, A.R. *et al.* (2006) Electrophoretic deposition of carbon nanotubes. *Carbon*, **44**(15), 3149–3160.
55. Valentini, L. *et al.* (2007) Electrodeposition of polyfluorene on a carbon nanotube electrode. *Nanotechnology*, **18** (11), 115702–115707.
56. Liu, Z.F. *et al.* (2000) Organizing single-walled carbon nanotubes on gold using a wet chemical self-assembling technique. *Langmuir*, **16**(8), 3569–3573.
57. Chattopadhyay, D., Galeska, I., and Papadimitrakopoulos, F. (2001) Metal-assisted organization of shortened carbon nanotubes in monolayer and multilayer forest assemblies. *Journal of the American Chemical Society*, **123** (38), 9451–9452.
58. Stevens, J.L. *et al.* (2003) Sidewall amino-functionalization of single-walled carbon nanotubes through fluorination and subsequent reactions with terminal diamines. *Nano Letters*, **3**(3), 331–336.
59. Khare, B.N., Wilhite, P., and Meyyappan, M. (2004) The fluorination of single wall carbon nanotubes using microwave plasma. *Nanotechnology*, **15**(11), 1650–1654.
60. Valentini, L. *et al.* (2005) Sidewall functionalization of single-walled carbon nanotubes through CF4 plasma treatment and subsequent reaction with aliphatic amines. *Chemical Physics Letters*, **403**(4–6), 385–389.
61. Reiter, G. and Sharma, A. (2001) Auto-optimization of dewetting rates by rim instabilities in slipping polymer films. *Physical Review Letters*, **87**(16), art. no. 166103.
62. Kovacs, J.Z. *et al.* (2007) Two percolation thresholds in carbon nanotube epoxy composites. *Composites Science and Technology*, **67**(5), 922–928.
63. Martin, C.A. *et al.* (2005) Electric field-induced aligned multi-wall carbon nanotube networks in epoxy composites. *Polymer*, **46**(3), 877–886.
64. Schwarz, M.K., Bauhofer, W., and Schulte, K. (2002) Alternating electric field induced agglomeration of carbon black filled resins. *Polymer*, **43**(10), 3079–3082.
65. Felhös, D., Karger-Kocsis, J., and Xu, D. (2008) Tribological testing of peroxide cured HNBR with different MWCNT and silica contents under dry sliding and rolling conditions against steel. *Journal of Applied Polymer Science*, **108**(5), 2840–2851.
66. Karger-Kocsis, J., Felhös, D., and Thomann, R. (2008) Tribological behavior of a carbon-nanofiber-modified santoprene thermoplastic elastomer under dry sliding and fretting conditions against steel. *Journal of Applied Polymer Science*, **108**(2), 724–730.
67. Lopez-Manchado, M.A. *et al.* (2004) Dynamic mechanical and raman spectroscopy studies on interaction between single-walled carbon nanotubes and natural rubber. *Journal of Applied Polymer Science*, **92**(5), 3394–3400.
68. Shanmugharaj, A.M. *et al.* (2007) Physical and chemical characteristics of multiwalled carbon nanotubes functionalized with aminosilane and its influence on the properties of natural rubber composites. *Composites Science and Technology*, **67**(9), 1813–1822.
69. Sui, G. *et al.* (2007) Processing and material characteristics of a carbon-nanotube-reinforced natural rubber. *Macromolecular Materials and Engineering*, **292**(9), 1020–1026.
70. Atieh, M.A. *et al.* (2005) Multi-wall carbon nanotubes/natural rubber nanocomposite. *Journal of Nanotechnology Online*, 1–11. doi: 10.2240/azojono0106
71. Bokobza, L. and Kolodziej, M. (2006) On the use of carbon nanotubes as reinforcing fillers for elastomeric materials. *Polymer International*, **55**(9), 1090–1098.
72. Fakhru'l-Razi, A. *et al.* (2006) Effect of multi-wall carbon nanotubes on the mechanical properties of natural rubber. *Composite Structures*, **75**(1–4), 496–500.

73. Kolodziej, M., Bokobza, L., and Bruneel, J.L. (2007) Investigations on natural rubber filled with multiwall carbon nanotubes. *Composite Interfaces*, **14**(3), 215–228.
74. Kueseng, K. and Jacob, K.I. (2006) Natural rubber nanocomposites with SiC nanoparticles and carbon nanotubes. *European Polymer Journal*, **42**(1), 220–227.
75. Zhao, Q., Tannenbaum, R., and Jacob, K.J. (2006) Carbon nanotubes as Raman sensors of vulcanization in natural rubber. *Carbon*, **44**(9), 1740–1745.
76. Wang, J.D. *et al.* (2006) Preparation and mechanical properties of natural rubber powder modified by carbon nanotubes. *Journal of Applied Polymer Science*, **100**(6), 4697–4702.
77. Guth, E. (1945) Theory of filler reinforcement. *Journal of Applied Physics*, **16**(1), 20–25.
78. Guth, E. and Gold, O. (1938) On the hydrodynamical theory of the viscosity of suspensions. *Physical Review*, **53**, 322.
79. Bokobza, L. and Belin, C. (2007) Effect of strain on the properties of a styrene-butadiene rubber filled with multiwall carbon nanotubes. *Journal of Applied Polymer Science*, **105**(4), 2054–2061.
80. Chen, X.-H. and Song, H.-H. (2004) Multi walled carbon nanotubes filled SBR rubber composites. *New Carbon Materials*, **19**, 214–218.
81. De Falco, A. *et al.* (2007) Carbon nanotubes as reinforcement of styrene-butadiene rubber. *Applied Surface Science*, **254**(1), 262–265.
82. Girun, N. *et al.* (2007) Multi-wall carbon nanotubes/styrene butadiene rubber (SBR) nanocomposite. *Fullerenes Nanotubes and Carbon Nanostructures*, **15**(3), 207–214.
83. Lu, L. *et al.* (2007) Reinforcement of styrene-butadiene-styrene tri-block copolymer by multi-walled carbon nanotubes via melt mixing. *Carbon*, **45**(13), 2621–2627.
84. Zhou, X.W. *et al.* (2006) Preparation and properties of the powder SBR composites filled with CNTs by spray drying process. *Materials Letters*, **60**(29–30), 3769–3775.
85. Zhou, X.W., Zhu, Y.F. and Liang, J. (2007) Effects of the vulcanizing reagent addition on the properties of CNTs/SBR powder composites. *Journal of Applied Polymer Science*, **106**(3), 1836–1841.
86. Zhou, X.W., Zhu, Y.F., and Liang, J. (2007) Preparation and properties of powder styrene-butadiene rubber composites filled with carbon black and carbon nanotubes. *Materials Research Bulletin*, **42**(3), 456–464.
87. Franta, I. (ed.) (1990) *Elastomers and Rubber Compounding Materials. Studies in Polymer Science*, Elsevier.
88. Koerner, H. *et al.* (2005) Deformation-morphology correlations in electrically conductive carbon nanotube thermoplastic polyurethane nanocomposites. *Polymer*, **46**(12), 4405–4420.
89. Sen, R. *et al.* (2004) Preparation of single-walled carbon nanotube reinforced polystyrene and polyurethane nanofibers and membranes by electrospinning. *Nano Letters*, **4**(3), 459–464.
90. Chen, W. and Tao, X.M. (2005) Self-organizing alignment of carbon nanotubes in thermoplastic polyurethane. *Macromolecular Rapid Communications*, **26**(22), 1763–1767.
91. Cho, J.W. *et al.* (2005) Electroactive shape-memory polyurethane composites incorporating carbon nanotubes. *Macromolecular Rapid Communications*, **26**(5), 412–416.
92. Foster, J. *et al.* (2005) Dispersion and phase separation of carbon nanotubes in ultrathin polymer films. *Journal of Colloid and Interface Science*, **287**(1), 167–172.
93. Kuan, H.C. *et al.* (2005) Synthesis, thermal, mechanical and rheological properties of multiwall carbon nano tube/waterborne polyurethane nanocomposite. *Composites Science and Technology*, **65**(11–12), 1703–1710.
94. Kwon, J. and Kim, H. (2005) Comparison of the properties of waterborne polyurethane/multiwalled carbon nanotube and acid-treated multiwalled carbon nanotube composites prepared by in situ polymerization. *Journal of Polymer Science Part a-Polymer Chemistry*, **43**(17), 3973–3985.
95. Kwon, J.Y. and Kim, H.D. (2005) Preparation and properties of acid-treated multiwalled carbon nanotube/waterborne polyurethane nanocomposites. *Journal of Applied Polymer Science*, **96**(2), 595–604.
96. Xia, H.S. and Song, M. (2005) Preparation and characterization of polyurethane-carbon nanotube composites. *Soft Matter*, **1**(5), 386–394.
97. Bliznyuk, V. *et al.* (2006) Surface electrical conductivity in ultrathin single-wall carbon nanotube/polymer nanocomposite films. *Applied Physics Letters*, **88**(16), art. no. 164101.
98. Chen, W. and Tao, X.M. (2006) Production and characterization of polymer nanocomposite with aligned single wall carbon nanotubes. *Applied Surface Science*, **252**(10), 3547–3552.
99. Chen, W., Tao, X.M., and Liu, Y.Y. (2006) Carbon nanotube-reinforced polyurethane composite fibers. *Composites Science and Technology*, **66**(15), 3029–3034.

100. Jung, Y.C., Sahoo, N.G., and Cho, J.W. (2006) Polymeric nanocomposites of polyurethane block copolymers and functionalized multi-walled carbon nanotubes as crosslinkers. *Macromolecular Rapid Communications*, **27**(2), 126–131.
101. Park, K.Y. *et al.* (2006) Fabrication and electromagnetic characteristics of electromagnetic wave absorbing sandwich structures. *Composites Science and Technology*, **66**(3–4), 576–584.
102. Sahoo, N.G. *et al.* (2006) Effect of functionalized carbon nanotubes on molecular interaction and properties of polyurethane composites. *Macromolecular Chemistry and Physics*, **207**(19), 1773–1780.
103. Xia, H.S. and Song, M. (2006) Preparation and characterisation of polyurethane grafted single-walled carbon nanotubes and derived polyurethane nanocomposites. *Journal of Materials Chemistry*, **16**(19), 1843–1851.
104. Xia, H.S. *et al.* (2006) Poly(propylene glycol)-grafted multi-walled carbon nanotube polyurethane. *Macromolecular Chemistry and Physics*, **207**(21), 1945–1952.
105. Xiong, J.W. *et al.* (2006) The thermal and mechanical properties of a polyurethane/multi-walled carbon nanotube composite. *Carbon*, **44**(13), 2701–2707.
106. Xiong, J.W. *et al.* (2006) Fabrication and distribution characteristics of polyurethane/single-walled carbon nanotube composite with anisotropic structure. *Polymer*, **47**(6), 1763–1766.
107. Yoo, H.J. *et al.* (2006) Polyurethane-carbon nanotube nanocomposites prepared by in-situ polymerization with electroactive shape memory. *Journal of Macromolecular Science Part B-Physics*, **45**(4), 441–451.
108. Buffa, F. *et al.* (2007) Effect of nanotube functionalization on the properties of single-walled carbon nanotube/polyurethane composites. *Journal of Polymer Science Part B-Polymer Physics*, **45**(4), 490–501.
109. Cai, D. and Song, M. (2007) Water-based polyurethane filled with multi-walled carbon nanotubes prepared by a colloidal-physics method. *Macromolecular Chemistry and Physics*, **208**(11), 1183–1189.
110. Chen, X.H. *et al.* (2007) Functionalized multi-walled carbon nanotubes prepared by in situ polycondensation of polyurethane. *Macromolecular Chemistry and Physics*, **208**(9), 964–972.
111. Jang, P.G. *et al.* (2007) Electrical behavior of polyurethane composites with acid treatment-induced damage to multiwalled carbon nanotubes. *Journal of Applied Polymer Science*, **106**(1), 110–116.
112. Lee, C.H. *et al.* (2007) Miscibility and properties of acid-treated multi-walled carbon nanotubes/polyurethane nanocomposites. *Polymer Journal*, **39**(2), 138–146.
113. Liu, Z.F. *et al.* (2007) Reflection and absorption contributions to the electromagnetic interference shielding of single-walled carbon nanotube/polyurethane composites. *Carbon*, **45**(4), 821–827.
114. McClory, C. *et al.* (2007) Thermosetting polyurethane multiwalled carbon nanotube composites. *Journal of Applied Polymer Science*, **105**(3), 1003–1011.
115. Meng, Q.H., Hu, J.L., and Yeung, L. (2007) An electro-active shape memory fibre by incorporating multi-walled carbon nanotubes. *Smart Materials & Structures*, **16**(3), 830–836.
116. Meng, Q.H., Hu, J.L., and Zhu, Y. (2007) Shape-memory polyurethane/multiwalled carbon nanotube fibers. *Journal of Applied Polymer Science*, **106**(2), 837–848.
117. Ryszkowska, J. *et al.* (2007) Dispersion of carbon nanotubes in polyurethane matrix. *Physica E-Low-Dimensional Systems & Nanostructures*, **39**(1), 124–127.
118. Shankar, R., Ghosh, T.K., and Spontak, R.J. (2007) Dielectric elastomers as next-generation polymeric actuators. *Soft Matter*, **3**(9), 1116–1129.
119. Song, H.J., Zhang, Z.Z., and Men, X.H. (2007) Surface-modified carbon nanotubes and the effect of their addition on the tribological behavior of a polyurethane coating. *European Polymer Journal*, **43**(10), 4092–4102.
120. Wang, T.L. and Tseng, C.G. (2007) Polymeric carbon nanocomposites from multiwalled carbon nanotubes functionalized with segmented polyurethane. *Journal of Applied Polymer Science*, **105**(3), 1642–1650.
121. Xu, M. *et al.* (2006) Synthesis and properties of novel polyurethane-urea/multiwalled carbon nanotube composites. *Macromolecules*, **39**(10), 3540–3545.
122. Curtzwiler, G. *et al.* (2008) Characterization and compression properties of injection molded carbon nanotube composites. *Journal of Applied Polymer Science*, **109**(1), 218–225.
123. Jana, R.N. and Cho, J.W. (2008) Thermal stability and molecular interaction of polyurethane nanocomposites prepared by in situ polymerization with functionalized multiwalled carbon nanotubes. *Journal of Applied Polymer Science*, **108**(5), 2857–2864.
124. Jell, G. *et al.* (2008) Carbon nanotube-enhanced polyurethane scaffolds fabricated by thermally induced phase separation. *Journal of Materials Chemistry*, **18**(16), 1865–1872.

125. Meng, Q.H. and Hu, J.F. (2008) Self-organizing alignment of carbon nanotube in shape memory segmented fiber prepared by in situ polymerization and melt spinning. *Composites Part A-Applied Science and Manufacturing*, **39**(2), 314–321.
126. Yang, Y. *et al.* (2007) Structure and photoresponsive behaviors of multiwalled carbon nanotubes grafted by polyurethanes containing azobenzene side chains. *J. Phys. Chem. C*, **111**(30), 11231–11239.
127. Frogley, M.D., Ravich, D., and Wagner, H.D. (2003) Mechanical properties of carbon nanoparticle-reinforced elastomers. *Composites Science and Technology*, **63**(11), 1647–1654.
128. Liu, C.H. *et al.* (2004) Thermal conductivity improvement of silicone elastomer with carbon nanotube loading. *Applied Physics Letters*, **84**(21), 4248–4250.
129. Ahir, S.V. and Terentjev, E.M. (2005) Photomechanical actuation in polymer–nanotube composites. *Nature Materials*, **4**, 491–495.
130. Huang, H. *et al.* (2005) Aligned carbon nanotube composite films for thermal management. *Advanced Materials*, **17**(13), 1652–1656.
131. Li, Y., Yang, M.J., and Chen, Y. (2005) Nanocomposites of carbon nanotubes and silicone-containing polyelectrolyte as a candidate for construction of humidity sensor. *Journal of Materials Science*, **40**(1), 245–247.
132. Ahir, S.V. *et al.* (2006) Infrared actuation in aligned polymer-nanotube composites. *Physical Review B*, **73**(8), 085420–085512.
133. Ahir, S.V. and Terentjev, E.M. (2006) Fast relaxation of carbon nanotubes in polymer composite actuators. *Physical Review Letters*, **96**(13), 133902–133904.
134. Chen, G.X. *et al.* (2006) Highly insulating silicone composites with a high carbon nanotube content. *Carbon*, **44**(15), 3373–3375.
135. Jiang, M.J., Dang, Z.M., and Xu, H.P. (2006) Significant temperature and pressure sensitivities of electrical properties in chemically modified multiwall carbon nanotube/methylvinyl silicone rubber nanocomposites. *Applied Physics Letters*, **89**(18), 182902–182903.
136. Kim, S., Pechar, T.W., and Marand, E. (2006) Poly(imide siloxane) and carbon nanotube mixed matrix membranes for gas separation. *Desalination*, **192**(1–3), 330–339.
137. Maune, H. and Bockrath, M. (2006) Elastomeric carbon nanotube circuits for local strain sensing. *Applied Physics Letters*, **89**(17), 173131–173133.
138. Paul, J. *et al.* (2006) Mechanics of prestressed polydimethylsiloxane-carbon nanotube composite. *Applied Physics Letters*, **89**(18), 184101–184103.
139. Song, P.C., Liu, C.H., and Fan, S.S. (2006) Improving the thermal conductivity of nanocomposites by increasing the length efficiency of loading carbon nanotubes. *Applied Physics Letters*, **88**(15), 153111–153113.
140. Yao, Y., Liu, C.H., and Fan, S.S. (2006) Anisotropic conductance of the multiwall carbon nanotube array/silicone elastomer composite film. *Nanotechnology*, **17**(17), 4374–4378.
141. Borca-Tasciuc, T. *et al.* (2007) Anisotropic thermal diffusivity characterization of aligned carbon nanotube-polymer composites. *Journal of Nanoscience and Nanotechnology*, **7**(4–5), 1581–1588.
142. Jiang, M.J., Dang, Z.M., and Xu, H.P. (2007) Enhanced electrical conductivity in chemically modified carbon nanotube/methylvinyl silicone rubber nanocomposite. *European Polymer Journal*, **43**(12), 4924–4930.
143. Jiang, M.J., Dang, Z.M., and Xu, H.P. (2007) Giant dielectric constant and resistance-pressure sensitivity in carbon nanotubes/rubber nanocomposites with low percolation threshold. *Applied Physics Letters*, **90**(4), 042914–42923.
144. Jiang, M.J. *et al.* (2007) Effect of aspect ratio of multiwall carbon nanotubes on resistance-pressure sensitivity of rubber nanocomposites. *Applied Physics Letters*, **91**(7), 072907–72913.
145. Liu, C.H. and Fan, S.S. (2007) Nonlinear electrical conducting behavior of carbon nanotube networks in silicone elastomer. *Applied Physics Letters*, **90**(4), 041905–41913.
146. Park, I.S. *et al.* (2007) Mechanical, dielectric, and magnetic properties of the silicone elastomer with multi-walled carbon a nanotubes as a nanofiller. *Polymer Engineering and Science*, **47**(9), 1396–1405.
147. Vast, L. *et al.* (2007) Preparation and electrical characterization of a silicone elastomer composite charged with multi-wall carbon nanotubes functionalized with 7-octenyltrichlorosilane. *Composites Science and Technology*, **67**(5), 880–889.
148. Woo, C.S. *et al.* (2007) Fabrication of flexible and transparent single-wall carbon nanotube gas sensors by vacuum filtration and poly(dimethyl siloxane) mold transfer. *Microelectronic Engineering*, **84**(5–8), 1610–1613.
149. Beigbeder, A. *et al.* (2008) CH-pi interactions as the driving force for silicone-based nanocomposites with exceptional properties. *Advanced Materials*, **20**(5), 1003–1007.

150. Chen, L.Z. *et al.* (2008) Electrothermal actuation based on carbon nanotube network in silicone elastomer. *Applied Physics Letters*, **92**(26), 263104–263113.
151. Hu, C.H. *et al.* (2008) Resistance-pressure sensitivity and a mechanism study of multiwall carbon nanotube networks/poly(dimethylsiloxane) composites. *Applied Physics Letters*, **93**(3), 033108–33113.
152. Suezawa, H. *et al.* (2003) CH/p interactions as disclosed on the fullerene convex surface. A database study. *Crystal Engineering Communications*, **5**(93), 514–518.
153. Baskaran, D., Mays, J.W., and Bratcher, M.S. (2005) Noncovalent and nonspecific molecular interactions of polymers with multiwalled carbon nanotubes. *Chemistry of Materials*, **17**(13), 3389–3397.
154. Bourlinos, A.B. *et al.* (2007) Silicone-functionalized carbon nanotubes for the production of new carbon-based fluids. *Carbon*, **45**(7), 1583–1585.
155. Verdejo, R. *et al.* (2008) Carbon nanotube provided self-extinguishing grade to silicone-based foams. *Journal of Materials Chemistry*, **18**, 3933–3939.
156. Verdejo, R. *et al.* (2008) Physical properties of silicone foams filled with carbon nanotubes and functionalised graphene sheets. *European Polymer Journal*. doi: 10.1016/j.eurpolymj.2008.06.03

7

Rubber/Clay Nanocomposites: Preparation, Properties and Applications

K.G. Gatos[1] and J. Karger-Kocsis[2,3]

[1] *Megaplast SA, Research & Development Center, 4 Makedonias Str., 16672 Athens, Greece*

[2] *Faculty of Mechanical Engineering and Built Environment, Department of Polymer Technology, Tshwane University of Technology, Pretoria, 0001, Republic of South Africa*

[3] *Faculty of Mechanical Engineering, Department of Polymer Engineering, Budapest University of Technology and Economics, 1111 Budapest, Hungary*

7.1 Introduction

Nanoreinforcement of rubbers has a long and solid background since a plethora of compounding recipes have been developed by both academia and industry which contain particles of nanodimension range, like carbon black and silica grades.

The most popular filler for rubber modification is by far the carbon black, covering all its variants (thermal, furnace, channel and acetylene blacks). Carbon black means elemental carbon (C) in the form of spherical particles of colloidal size. Its particles are coalesced into aggregates and agglomerates as carbon black is obtained by the combustion or thermal decomposition of hydrocarbons [1]. The carbon black grades differ from one another regarding their particle size, aggregate form and aggregate shape. About the terminology: agglomerates are comprised of a large number of aggregates which are physically held together, as opposed to the continuous graphitic structure which links the particles within the aggregates [2]. Silica, which is amorphous, consists of silicon and oxygen arranged in a tetrahedral structure of a three-dimensional lattice. In silica there is no long-range crystal order, only short-range ordered domains may be found sporadically. The presence of the silanol groups (−Si−OH) on

Rubber Nanocomposites: Preparation, Properties and Applications Edited by Sabu Thomas and Ranimol Stephen
© 2010 John Wiley & Sons (Asia) Pte Ltd

the silica surface induces strong particle-particle interaction. By this way, the tendency for filler agglomeration rises [3]. The surface silanol concentration influences the degree of surface hydration. High levels of hydration can adversely affect the physical properties of the final compound. At the same time, clay has been known for many decades as a nonblack filler type for the filling of rubbers [4]. As the property enhancement for rubber/clay compounds was achieved by incorporation of unmodified clay in large amount, microcomposite was the one and only outcome.

The concept of "nanoreinforcement" with layered silicates, credited to researchers at Toyota Central Research Laboratories (Japan), became very popular recently. The ongoing R&D interest is mostly due to the unexpected property improvements when the silicates are dispersed in nanometer- instead of micrometer-scale. Full separation of the clay layers (termed delamination or exfoliation) is usually a combined action of thermodynamical interactions, diffusion and local acting shear stresses. Though these factors prefer rubbers as matrices for clay modification (see the arguments later), far less work addressed the structure–property relationships of rubber/clay nanocomposites compared to thermoplastic- and thermoset-based ones. Therefore, the aim of this chapter is to survey the research works performed on rubber/layered silicate nanocomposites and to derive some future trends.

7.2 Clays and Their Organophilic Modification

In the literature the term clay denotes a textural class of minerals consisting of particles with an equivalent spherical diameter of less than 2 μm, not all of which is crystalline. Majority of the clay minerals belongs to the category of layered silicates or phyllosilicates because their silica layers and alumina sheets joined together in varying proportions and in a certain way [5]. The principal building elements of the clay minerals are two-dimensional arrays of silicon–oxygen tetrahedral and two-dimensional arrays of aluminum– or magnesium–oxygen/hydroxyl octahedral units which are superimposed in different fashions.

Condensation in 1 : 1 ratio of a silica sheet with an alumina one gives rise to a 1 : 1 layer clay (for example, kaolinite). In a 2 : 1 ratio, two silica sheets condense with an alumina one (for example, pyrophyllite, smectite or montmorillonite, vermiculate, illite). Among the 2 : 1 layer clays, the montmorillonite possesses great significance because of its swelling capabilities. Partially replacement of trivalent Al by divalent Mg in the octahedral sheet results to a high negative surface charge of the layer. This fact renders the space between the layer surfaces (that is, intergallery or interlayer) capable of accommodating cations. When montmorillonite clay (MMT) is in contact with water or with water vapor, the water molecules penetrate between the layers (that is, interlayer swelling), increasing the basal spacing. This phenomenon is likely related with the hydration energy. In absence of water van der Waals forces hold the layers together in close packing. Furthermore, the charge compensating cations on the layer surfaces may be easily exchanged by other cations when available in aqueous solution; hence they called "exchangeable cations." The total amount of these cations is expressed in milliequivalents per 100 g of dry clay and is called the "cation exchange capacity" (CEC) of the clay [6].

In the past, kaolins were mainly used for rubber filling (nonactive reinforcement) [7]. Calendering a rubber stock with such anisotropic filler results in the alignment of the filler particles in the direction of the calender gap [4]. In order to yield acceptable mechanical performance, a high degree of clay incorporation is needed.

In general, to enhance the specific properties of the final rubber, the filler (type, characteristics) has to be selected carefully. This involves also the surface treatment of the fillers. For example, carbon blacks used for coloring high-quality coatings have to possess highly polar surfaces for optimum wetting by the binder. On the contrary, conductive applications need carbon black surfaces free from oxides [8]. For controlling the surface energy in case of silica, treatment with glycols, esterification with monofunctional alcohols or silane coupling agents have been extensively used (for example, [9–10]).

Surface treatment of clays has been known since many decades ago [6]. When an amine salt or a quaternary ammonium salt is added to a clay–water suspension, the corresponding organic cations replace the inorganic ones (for example, Na^+, K^+) originally present on the clay surfaces. Because of this exchangeable adsorption, the amino groups are tethered on the clay surface while the hydrocarbon tail is positioned in the gallery space, displacing the previously adsorbed water molecules (cf. Figure 7.1). In this way, the clay becomes compatible with organic molecules and thus is termed organophilic. Note that this treatment expands the intergallery distance at the same time (cf. Figure 7.1). A widely accepted term for the outcoming material is

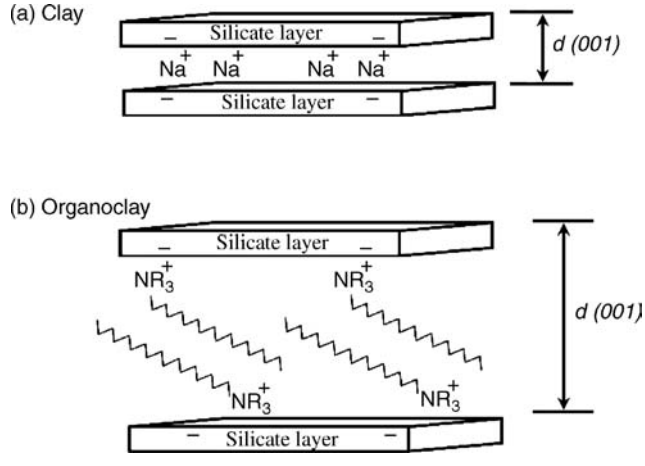

Figure 7.1 Scheme of: (a) clay and (b) modified clay (that is, organoclay). Note that R can be replaced by any chemical unit

"organoclay." Applications of such "clay–organic complexes" were first used in oil dispersions to manufacture lubricating grease. The main advantage of these systems is their better heat stability compared to conventional lubricating greases. Moreover, clay treated with coupling agents, such as isopropyl tristearoyl titanate (TTS) has been also proposed to enhance the heat stability, mechanical performance and processability of rubber [11].

7.3 Preparation of Rubber/Clay Nanocomposites

The special character of rubber, being a multicomponent system (for example, rubber, curing agents, coagents, processing aids, reinforcements, fillers), complicates the analysis of the parameters affecting the rubber/layered silicate nanocomposite formation. This was likely the

reason for its late development compared to thermoplastic or thermoset clay nanocomposites. Note that a nanocomposite is obtained only when the polymer chains are intercalated into the intergallery spacing (cf. "intercalated" nanocomposite) or when the silicate layers are further pulled apart and appear exfoliated in the polymer matrix (cf. "exfoliated" nanocomposite) [12–14]. The possible outcomes are schematically depicted in Figure 7.2. The reinforcing efficiency of the modified clays (that is, organoclays) in the thermoplastic and thermoset matrices was early recognized, even at the beginning of the 1960s [5]. In the case of elastomers, a very successful technique was to let the minerals react with organosilanes. Using aminosilanes, the hydrolyzed silanol group of the reagent was attached onto the clay surface while the pendent amino group, at the other end of the molecule, was free to react with the rubber during vulcanization [5]. The mineral used for such type of rubber reinforcement was mainly nonswellable layered silicate (for example, kaolin).

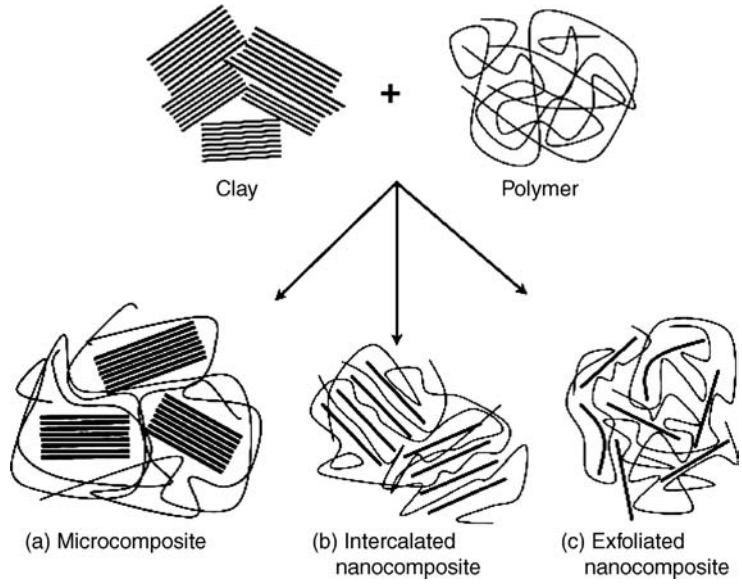

Figure 7.2 Scheme of possible dispersions of layered silicate in a polymer

During the early research activities (that is, during the 1960s to 1970s) on polymer/organoclay nanocomposites less attention was put on rubbers. Even during the "hot" period of the 1990s, only some sporadic works appeared on rubber/layered silicate nanocomposites [15–17]. Since the proof of substantial property upgrade in thermoplastic/organoclay and thermoset/organoclay nanocomposites, research has been initiated on rubber/organoclay nanocomposites [18–23].

In the past ten years, several rubbers served as matrices in organoclay-filled systems. Typical examples are styrene-butadiene-rubbers (SBR) [11, 18, 20, 24–30], ethylene-propylene-diene-rubbers (EPDM) [29, 31–38], fluoro-rubbers (FKM) [39], nitrile-butadiene-rubbers (NBR) [40–42] and natural rubbers (NR) [43–51]. The different methods to prepare a rubber/organoclay nanocomposite include solution mixing (solvent method) [40, 44, 47,

52–53], latex compounding (water-assisted technique) [23, 54–59] and melt mixing (direct method) [26–27, 29–38, 41–43]. The development with rubber/clay nanocomposites was the subject of two review papers in the past [60–61].

7.3.1 Solution Intercalation

For the solution mixing the organoclay is dispersed in the solvent, which is a good solvent for the rubber at the same time. By stirring, followed by evaporation of the solvent, rubber/organoclay nanocomposites are received.

For polar rubbers, like NBR, Hwang *et al.* [40] used a methyl ethyl ketone to blend the NBR with the clay modified with dimethyl dehydrogenated tallow quaternary ammonium salt. After evaporation of the solvent, the curing agents were added on a two-roll open mill and the compounds were vulcanized accordingly. The NBR/organoclay nanocomposite was mainly intercalated (at 10 phr clay loading, where phr = parts per hundred parts rubber) and resulted in increased mechanical performance and decreased water and methanol permeability up to 85% and 42%, respectively. In the solution intercalation method the curatives are usually added in the compound after the evaporation of the solvent. This occurs on an open mill or in an internal mixer. In contrast, addition of the curatives during the solution mixing can also be practiced. Lu *et al.* [62] pointed to a special role of the solvent on the nanocomposite formation. When solvent molecules are still present within the silicate galleries, they can be thermally "activated," which contributes to the formation of exfoliated structures.

Magaraphan *et al.* [45] dissolved natural rubber (NR) in toluene along with MMT modified with primary or quaternary intercalants bearing different hydrocarbon alkyl tails. The curing ingredients were subsequently poured into the mixture and after drying the mix was homogenized on an open mill. It was found that primary amines produced nanocomposites of better mechanical performance than quaternary amine intercalants. López-Manchado *et al.* [47] compared the structure and properties of NR/organophilic MMT nanocomposites produced by solution and melt compounding, respectively. MMT was modified (intercalated initially) with octadecylamine (MMT-ODA). It was found that both methods delivered similar nanocomposite structures. However, the solution technique (toluene served as solvent) yielded a higher amount of bound rubber, improved dynamic mechanical properties and enhanced the compression set and hardness. Similarly Liang *et al.* [63], when studying isobutylene-isoprene rubber (IIR)/clay mixes, attributed the enhanced performance of the solution-produced nanocomposites to the higher aspect ratio of clay therein. The aspect ratio of the clay was maintained after solution mixing, compared to melt compounding whereby the clay was fragmented.

7.3.2 Latex Route

In the latex compounding method the host medium is water. The latex consists of submicron-sized rubber particles which are dispersed in water. To the rubber latex pristine clay can be added directly, or in its aqueous dispersion (slurry). Note that clays are strongly hydrophilic and thus adsorb water molecules, which is associated with an expansion of their intergallery spacing. So, hydration decreases the attractive forces between the silicate layers, making easier their exfoliation under stirring. After mixing/stirring of the clay-containing latices, they are

cast in a mold and left to dry. In this case, the rubber/clay nanocomposite remains unvulcanized. In contrast, suitable rubber curatives, which can be dispersed in water, may also be mixed with the clay-containing rubber latex. After casting and drying, the related articles can be cured accordingly.

Varghese and Karger-Kocsis investigated NR/layered silicate vulcanized nanocomposites [56] and found that sodium fluorohectorite (FHT, a synthetic layered silicate) gave the highest mechanical performance and the lowest toluene swelling compared to clay or bentonite compounds. This was attributed to the high platelet aspect ratio and the prominent water-swelling ability of this FHT. Ma *et al.* [64] produced SBR-clay nanocomposites by mixing SBR latex with modified MMT. In this case, the curatives were added to the dried rubber mix in a melt mixing step that was followed by vulcanization. Jia *et al.* [65] selected another way. After mixing the SBR latex with pristine MMT (cation: Na^+) the mix was dried and subsequently the melt was compounded with a possible intercalant for the MMT (hexadecyl trimethyl ammonium bromide) and coupling agent (3-aminopropyl triethoxy silane) along with curatives. Abdollahi *et al.* [66] produced first an SBR/pristine clay nanocomposite by coagulation of the corresponding latex. Coagulation was achieved by a cation-type coagulation agent (diluted sulfuric acid). This was mixed with sulfuric curatives, vulcanized and tested. It was found that clay exfoliation could only be triggered when the clay content was less than 10 phr. Above this threshold the mechanical properties of the rubbers reached a plateau value.

Blending of rubber latices is a versatile way to produce rubber articles of enhanced performance, at the same time lowering the proportion of the most expensive component. Polyurethane latex (PUR) finds many applications nowadays though it is quite an expensive material. At the same time NR latex is found in abundance in nature. Varghese *et al.* [59] blended PUR and prevulcanized NR latex with clay, producing films of nanocomposite structure with enhanced stiffness characteristics. The property improvement was traced to a skeleton-type ("house of cards") structuring the layered silicate (LS) in the corresponding nanocomposite (cf. Figure 7.3). Infrared spectroscopy (FTIR) and broadband dielectric analysis were adopted to examine the NR/LS, PUR/LS and NR/PUR/LS nanocomposites formed via the latex route [59, 67–68]. It was found that the PUR chains, due to their polar character, facilitate the intercalation/exfoliation of the LS.

7.3.3 Melt Compounding

The most common mixing technique used in both industry and academia for preparing rubber/organoclay nanocomposites is by far melt compounding. This involves equipment like internal mixers and open mills. As presented recently [38], the intercalation/exfoliation phenomena are likely governed by the chemistry involved during compounding and curing. For example, it has been shown that mixing EPDM rubber grafted with maleic anhydride (EPDM-MA) with organoclay (MMT-ODA) on an open mill does not facilitate significant intercalation. Intercalation is, however, promoted after the introduction of curatives in a mix which is not yet cured (Figure 7.4). This finding suggests that the vulcanization curatives migrate into the intergallery space during mixing. This widens the basal spacing and thus supports the nanocomposite formation.

In order to get intercalated/exfoliated nanocomposites with outstanding performance, high shearing provided by an internal mixer (compared to an open mill) should be in action [36].

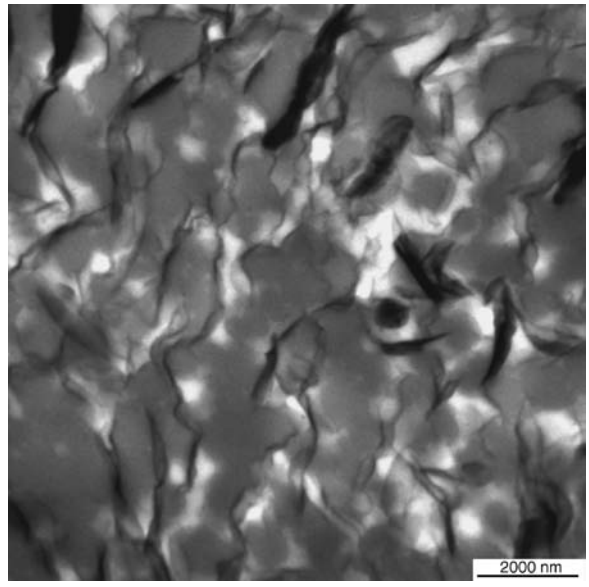

Figure 7.3 TEM picture taken from the film cast of the PUR/NR (1 : 1) latex blend containing 10 phr fluorohectorite (FHT) (Reproduced from *Journal of Applied Polymer Science*, **92**, S. Varghese *et al.*, "Morphology and mechanical properties of layered silicate reinforced natural and polyurethane rubber blends produced by latex compounding," 543–551, copyright Wiley Periodicals Inc., 2004.)

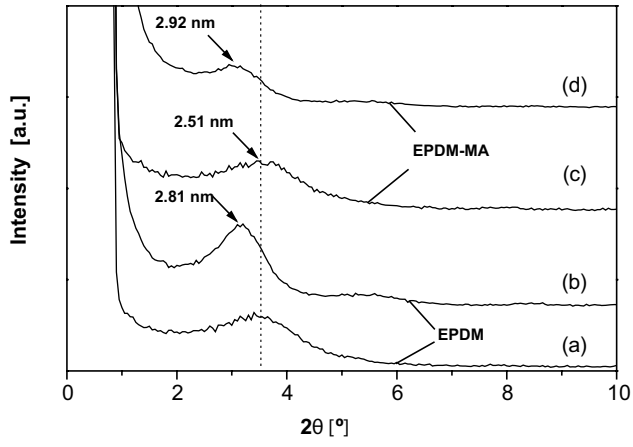

Figure 7.4 XRD patterns of: (a) EPDM mixed with MMT-ODA (10 phr) for 10 min on the open mill; (b) its further addition of the curatives; (c) EPDM-MA mixed with MMT-ODA (10 phr) for 10 min on the open mill; and (d) further addition of curatives (Reproduced from *Polymer*, **46**, K.G. Gatos and J. Karger-Kocsis, "Effects of primary and quaternary amine intercalants on the organoclay dispersion in a sulfur-cured EPDM rubber," 3069–3076, 2005, with permission from Elsevier.)

This is beneficial for shearing off the intercalated stacks and promotes the diffusion of rubber chains into the intergallery space at the same time. The property upgrade can further be enhanced when mixing takes place at high temperature (for example, 100 °C) and in the presence of macromolecular chains of polar character. Needless to say, the latter compound has to show sufficient compatibility with the parent rubber. Table 7.1 presents the mechanical properties of EPDM reinforced by 10 phr organoclay. Note that in all the mixtures presented in Table 7.1, zinc diethyl dithiocarbamate (ZDEC) was used as accelerator. This choice was based on the work of Usuki *et al.* [32], who investigated several types of accelerators and found that the above dithiocarbamate type proved to be the most promising to produce EPDM/clay nanocomposites. The processing conditions, that is, mixing technique and temperature, seem to have some effect on the mechanical properties of the EPDM samples. The tensile moduli at 100%, 200% and 300% elongations are less influenced by the mixing techniques and temperature. However, mixing in the internal mixer at 100 °C increased both the tensile strength and elongation at break (cf. EPDM stocks in Table 7.1). As is obvious in Table 7.1, the use of EPDM-MA compatibilizer resulted in markedly higher values of tensile strength and stiffness at all processing temperatures and mixing methods. This is related to the functional group MA that rendered the rubber chain polar. This "polarity" facilitates further the intercalation/exfoliation phenomena. A clear advantage of MA grafting was observed for compounding in the internal mixer. The tensile strength of EPDM-MA was more than doubled when mixed either at room temperature or at 100 °C. Moreover, the EPDM-MA mixed at 100 °C in the internal mixer possessed the highest tensile strength measured (cf. Table 7.1).

Like the nanocomposites composed of apolar thermoplastics and organophilic clays, the use of polar rubbers as additional modifiers (compatibilizers) is essential to achieve intercalated/exfoliated structures. So, for EPDM-based stocks MA-grafted [36] or glycidyl methacrylate-grafted EPDM versions can be used as suitable compatibilizers [37]; for NR-based ones epoxidized NR (ENR) [43, 48, 51, 69] or ethylene-vinylacetate copolymers [70] can be used as suitable compatibilizers.

Wu *et al.* [29] and Ma *et al.* [71] have demonstrated that the choice of rubber matrix (without considering any modification) is crucial with respect to the final dispersion state of the clay in the related systems. Further, identifying the most reliable melt compounding technique for rubber/organoclay nanocomposites, the proper choice of the type of curatives and organophilic treatment of the layered silicate provide additional property improvement. This was shown by several authors on the example of HNBR/organoclay compounds [72–75].

7.4 Properties of Rubber/Clay Nanocomposites

7.4.1 Crosslinking

The accelerating action of the organoclay on rubber curing has been detected for various stocks [20, 27, 76–78]. Using octadecylamine (ODA) itself, the induction period, scorch time and optimum curing time were decreased in NR mixes [76]. The vulcanization rate was further increased when an ODA-modified clay was introduced in the same NR rubber recipe. This involves a reduction in the activation energy of the vulcanization. This finding underlines that the initial intercalant of the clay may have a strong effect on the vulcanization of rubber.

It was demonstrated on the example of hydrogenated nitrile rubber (HNBR)/organoclay systems that the dispersion of the clay varies with the type of the organophilic modifier (initial

Table 7.1 Mechanical properties of EPDM/organoclay (10 phr) compounds, prepared under different conditions with and without MA-grafted EPDM as compatibilizer

Properties	Processing conditions (mixed with 10 phr MMT-ODA)							
	Open mill				Internal mixer			
	30 °C		100 °C		30 °C		100 °C	
	EPDM	EPDM-MA	EPDM	EPDM-MA	EPDM	EPDM-MA	EPDM	EPDM-MA
Tensile strength (MPa)	3.9	6.6	5.2	8.1	4.9	10.5	7.1	14.9
Modulus (MPa) at:								
100% elongation	1.5	2.0	1.6	2.7	1.5	3.9	1.6	5.4
200% elongation	2.3	3.3	2.3	4.6	2.0	7.3	2.3	9.3
300% elongation	3.0	4.9	2.9	6.9	2.6	9.9	3.0	12.1
Elongation at break (%)	380	395	495	360	520	321	645	403

intercalant) [72]. Results achieved with primary amine-modified clay suggested that the amine compound reacts with the sulfur curatives. As the amines are "pulled out" from the intergallery space, the clay "deintercalates." By contrast, clays with quaternary amine modification preserve their highly intercalated structure [38, 72]. No such phenomenon was noticed for the same rubber when vulcanized with peroxide [73]. As shown in Figure 7.5, using the same organoclay,

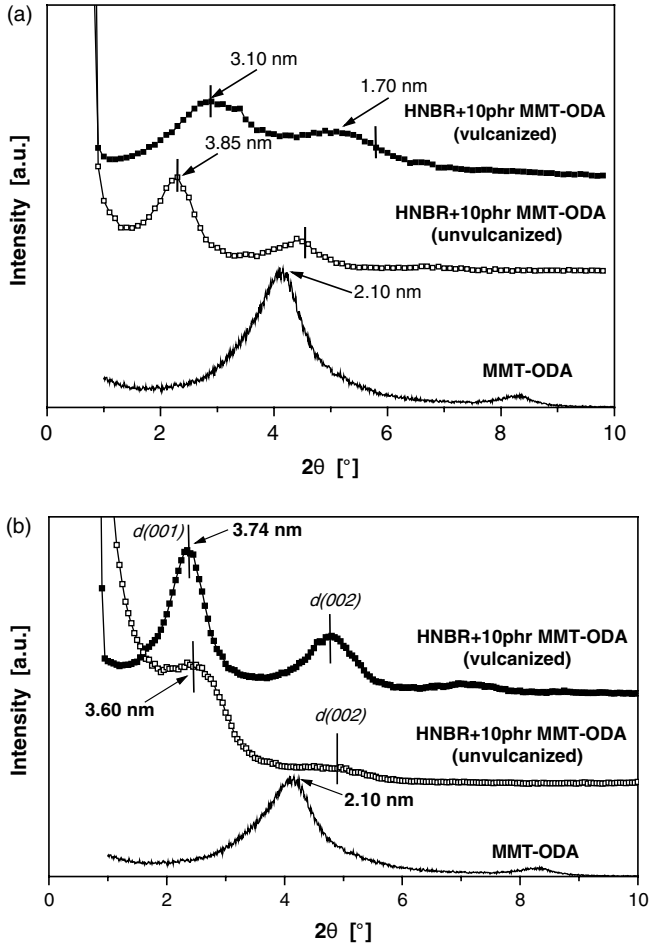

Figure 7.5 XRD spectra of HNBR reinforced with MMT-ODA using different types of curing system, before and after vulcanization: (a) HNBR mixed with sulfur curatives (Reproduced with permission from K.G. Gatos *et al.*, "Nanocomposite formation in hydrogenated nitrile rubber (HNBR)/ organo-montmorillonite as a function of the intercalant type," *Macromolecular Materials and Engineering*, 2004, **289**, 1079–1086. © Wiley-VCH Verlag GmbH & Co. KGaA.) and (b) HNBR mixed with peroxide curatives (Reproduced with permission from K.G. Gatos *et al.*, "Controlling the deintercalation in hydrogenated nitrile rubber (HNBR)/organo-montmorillonite nanocomposites by curing with peroxide," *Macromolecular Rapid Communications*, 2005, **26**, 915–919. © Wiley-VCH Verlag GmbH & Co. KGaA.). Notes: The spectra of the related organoclays are also contained. The positions of the (0 0 1), (0 0 2) and (0 0 3) reflexes are indicated by line marks

viz. MMT-ODA, an intercalated structure was the only outcome after melt compounding and before curing. However, vulcanizing the rubber changed the structural scenario dramatically. Highly intercalated clay populations were identified by X-ray scattering (XRD) in the peroxide-cured system, while intercalated/confined and deintercalated clay populations were found in the sulfur-cured HNBR mixes. The terms confinement and deintercalation are not yet well defined. According to our terminology confinement covers the collapse of the layers up to the initial basal spacing of the organoclay (in the present case up to 2.1 nm; cf. Figure 7.5) in the nanocomposite. A further collapse is termed deintercalation ("extraction," "pull-out" of the initial intercalant). Das *et al.* [75] found for NBR/organoclay systems that even the orientation of the clay particles can be influenced by peroxide or sulfuric curatives.

Based on the general sulfur vulcanization scheme (cf. Figure 7.6), it was suggested that the tethered primary amine of the organoclay leaves the clay surface in order to participate in the

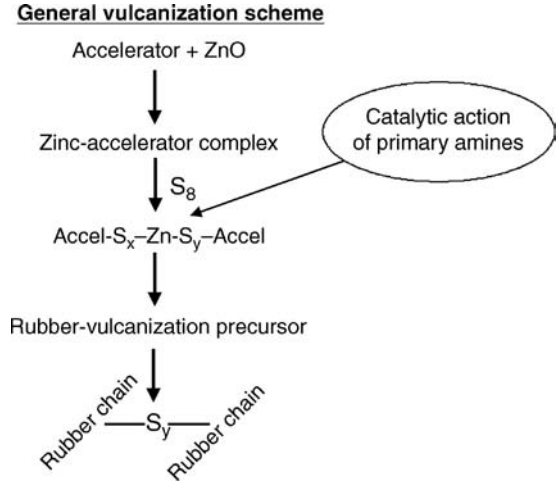

Figure 7.6 Scheme of the vulcanization steps and the stage where a primary amine acts catalytically

formation of a zinc-containing intermediate complex (vulcanization intermediate) having catalytic activity for curing (cf. Figure 7.7) [79]. This occurs either by migration into the rubber matrix (resulting in confinement or deintercalation of the galleries) or by causing rubber crosslinking inside the galleries (inducing better clay dispersion via layers separation or delamination/exfoliation).

Further hints for the importance of the vulcanization procedure were given by Liang *et al.* [80]. The authors found that when high pressure was applied (> 5 MPa) during the curing of an IIR/clay compound the clay became intercalated to a lesser degree (the basal spacing was reduced according to the XRD measurements).

7.4.2 Mechanical Performance

One of the main advantages of rubber/organoclay nanocomposites is the enhancement in the mechanical properties of the rubber matrix at a relatively low inorganic filler content.

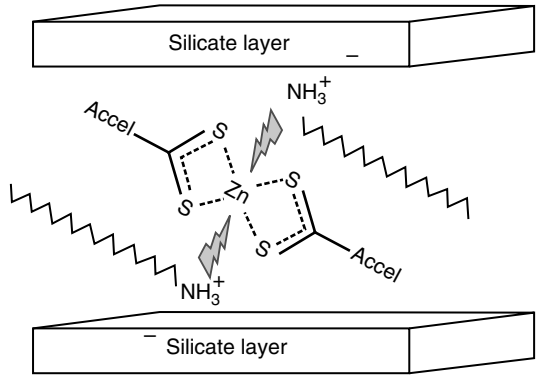

Figure 7.7 Scheme of the interaction between the sulfur-rich Zn complex and the primary amine intercalant within the silicate gallery (Reproduced from *European Polymer Journal*, **43**, K.G. Gatos and J. Karger-Kocsis, "Effect of the aspect ratio of the silicate platelets on the mechanical and barrier properties of hydrogenated acrylonitrile butadiene rubber (HNBR)/layered silicate nanocomposites," 1097–1104, 2007, with permission from Elsevier.)

Thus, layered silicate can be considered as a potential substitute of carbon black and silica, which have to be mixed at high concentrations in order to reach the same performance [50]. Moreover, it has been shown that the organoclay supports the compound to maintain its outstanding mechanical performance also after exposure to various chemical and thermal environments [74].

To monitor the reinforcing ability of layered silicate in the rubber matrix in the temperature range below and above the glass transition temperature (T_g) of the compound, dynamic mechanical thermal analysis (DMTA) appears as an excellent tool. It has been shown for HNBR that the addition of organoclay increased significantly the storage modulus (E') and decreased the mechanical loss factor (tanδ) compared to neat rubber or rubber reinforced with unmodified clay [72]. As shown in Figure 7.8a, the storage modulus (E') of the nanocomposites lies markedly higher than neat HNBR or HNBR filled with unmodified MMT. Having in mind that the working temperature of rubbers is usually above their glass transition temperature (T_g), the plateau values of the E' in this region is of great importance. Similarly, the stiffness of the HNBR/organoMMTs compounds above the T_g is significantly higher than conventional filler (bentonite in this case – cf. Figure 7.8). The best performance is reached when MMT modified with methyl-tallow-*bis*(2-hydroxyethyl) quaternary ammonium (MMT-MTH) is used. Note that this modifier contains hydroxyl groups (OH), capable of creating a stronger interphase between the rubber and the silicate surface via H-bonding.

A further hint for the degree of bonding between the matrix and the nanofiller can be derived from the tan δ versus temperature curves [43]. For NBR filled with carbon black (CB) it was shown that the lowering of the diameter of the CB particle is well reflected in the tan δ peak, which was strongly decreased [81]. As shown in Figure 7.8b, for the unmodified MMT (bentonite) the tan δ peak is identical with that of neat rubber. This finding can be traced to the poor interaction between HNBR and bentonite. For the HNBR/organoMMT mixes the intensity of the tan δ peak was strongly reduced compared to the matrix. This is a manifestation

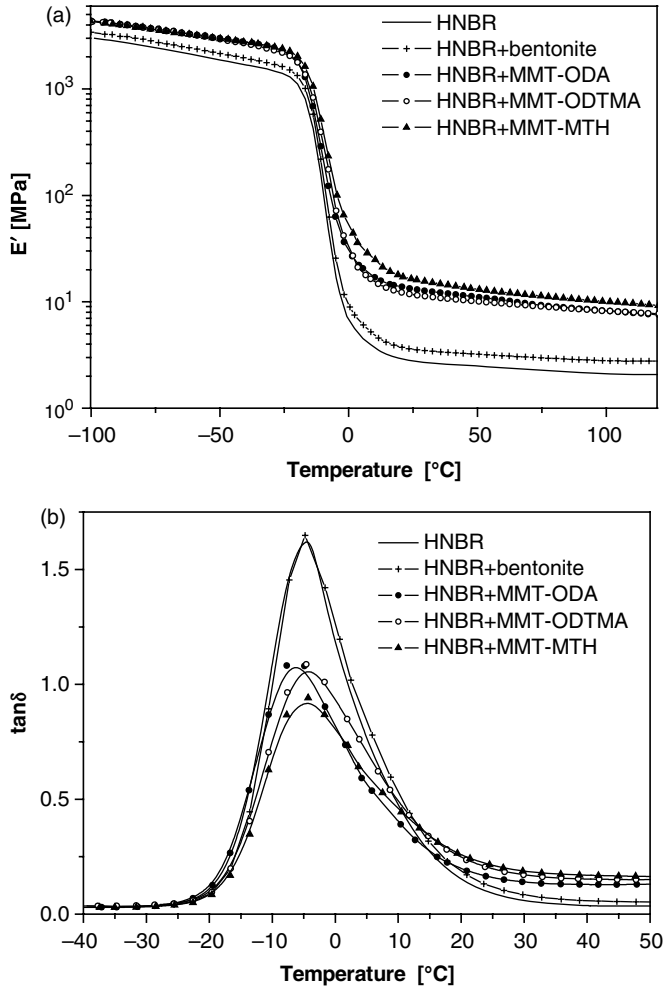

Figure 7.8 (a) Storage modulus (E') and (b) mechanical loss factor (tan δ) as a function of temperature for HNBR and HNBR containing various fillers (10 phr) (Reproduced with permission from K.G. Gatos *et al.*, "Nanocomposite formation in hydrogenated nitrile rubber (HNBR)/organo-montmorillonite as a function of the intercalant type," *Macromolecular Materials and Engineering*, 2004, **289**, 1079–1086. © Wiley-VCH Verlag GmbH & Co. KGaA.)

of the reinforcing effect of the filler [82]. HNBR/MMT-MTH compound presents the lowest T_g peak intensity, indicating that the interphase in this case is the best among the compounds examined. A strong interphase guarantees a good stress transfer from the matrix to the filler. In some systems a further tan δ peak (appearing eventually as a shoulder) above the T_g was revealed. This was assigned to intercalated rubber chains possessing reduced mobility in the related intergallery (confined) space [43].

The tensile properties of rubber nanocomposites are superior to the unfilled counterparts. For an EPDM vulcanizate, containing EPDM-MA compatibilizer (yielding better clay intercala-

tion/exfoliation), and MMT bearing ODA (primary amine) or octadecyl trimethyl ammonium (ODTMA, quaternary amine) type intercalants, the ultimate properties could be markedly improved as shown in Figure 7.9. It appears that at 10 phr organoclay content the tensile strength of the nanocomposites reaches a maximum (cf. Figure 7.9a). It is interesting to observe a different trend with respect to the type of MMT intercalant for the nanocomposites in Figure 7.9a. The EPDM-MA/MMT-ODA presents a plateau as a function of increasing organoclay content, whereas for the EPDM-MA/MMT-ODTMA the ultimate tensile strength goes through a maximum.

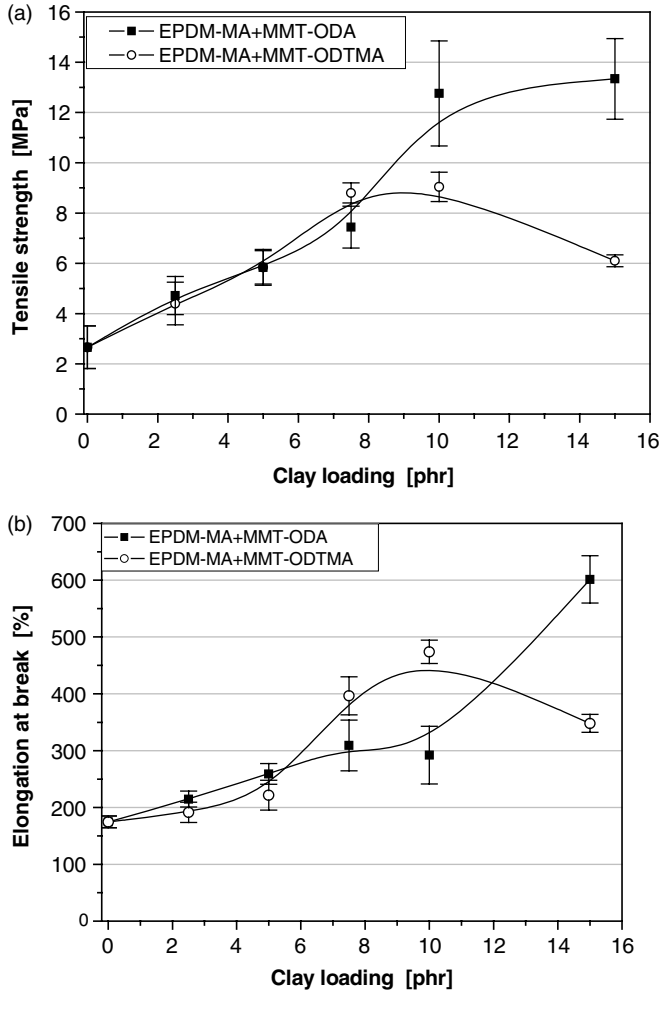

Figure 7.9 (a) Tensile strength and (b) elongation at break versus clay loading for EPDM-MA/MMT-ODA and EPDM-MA/MMT-ODTMA nanocomposites (Reproduced from *Polymer*, **46**, K.G. Gatos and J. Karger–Kocsis, "Effects of primary and quaternary amine intercalants on the organoclay dispersion in a sulfur-cured EPDM rubber," 3069–3076, 2005, with permission from Elsevier.)

A pronounced difference can be observed for the elongation at break values as a function of organoclay type and loading (Figure 7.9b). The EPDM-MA/MMT-ODA nanocomposite, above 10 phr organoclay content, has surprisingly high ultimate strain values. In contrast, the elongation at break of the EPDM-MA/MMT-ODTMA tends to decrease passing 10 phr organoclay content. The latter is likely related with some agglomeration phenomena. Agglomeration causes premature failure, well manifesting in reduced ultimate stress and elongation at break values. Similar stress-strain behavior has been reported for various rubber nanocomposites [16, 20, 35, 40, 42, 49]. Usually, at favorable matrix/organoclay interactions and at relatively low organoclay content, both tensile strength and elongation at break values increase [20, 35, 42]. Further increase of the organoclay content produces a plateau (saturation) or a reduction in the ultimate stress and strain values [35, 40, 42]. This rather typical behavior was found also for the EPDM-MA/MMT-ODTMA nanocomposite (Figure 7.9).

Tensile strength improvement, associated with an increase in the elongation at break values, is a rather unexpected phenomenon for rubber/organoclay nanocomposites [32]. Nevertheless, it was found also in other rubber compounds, and it was explained by a synergistic effect of platelet orientation and chain slippage [29]. In general, the reinforcing efficiency of CB in filled rubbers increases when the CB particles agglomerate (chain-like filler structure at high filler amounts). At the same time, the degree of bound rubber (as measured in the respective uncured specimens) also increases [83]. As typically shown in TEM images, the dispersion of silicate platelets seems to create some "secondary structure" which is analogous to that of CB structuring in highly filled rubbers. However, the organoclay should be well dispersed in the rubber matrix to attain such peculiar morphology at low filler content.

Figure 7.10 shows possible crack growth paths at high deformation of a rubber containing the same amount of layered silicate, but with the latter in either a poor or a good dispersion. Though the filler volume in both cases is the same (cf. same number of plates in Figure 7.10a and b), the effective filler volume values differ from one another as a function of the dispersion grade. The latter may affect the bound rubber content, generate a rubber shell in the vicinity of the silicate platelets (cf. dark gray areas in Figure 7.10 indicate a different rubber crosslinking density compared to the bulk) and influence the occlusion of rubber within the clay galleries. According to this model a modulus increase is expected even at low organoclay content when the clay layers are well dispersed (well intercalated and exfoliated).

The failure of rubber specimens upon tensile loading starts with crack initiation. In rubber/layered silicate nanocomposites, first the orientation of the clay platelets takes place during uniaxial drawing [18]. At sufficient high strain, cracks can be generated by the fillers (via voiding, dewetting phenomena, chain slippage, and so on.). As the dispersion of the platelets allows the creation of voids (subcritical cracks) in their vicinity (Figure 7.10b), the amount of dissipated energy is high enough to withstand higher values of strain than before. Note that shortening the stack-stack distance can lead to greater resistance to crack propagation. Furthermore, the increased length of the crack path, as the crack travels along a "zig-zag" route, can also be considered as a further mechanism of energy dissipation. Although this model can explain the increase in both tensile strength and elongation at break for rubber/layered silicate nanocomposites, it is based on the analogy with discontinuous fiber-reinforced polymers and is a topic of dispute [84]. Furthermore, the deterioration (that usually noticed) or leveling off in the mechanical performance with increasing organoclay loading [20, 35] can be explained by the formation of big agglomerates, which favor the initiation of catastrophic failure.

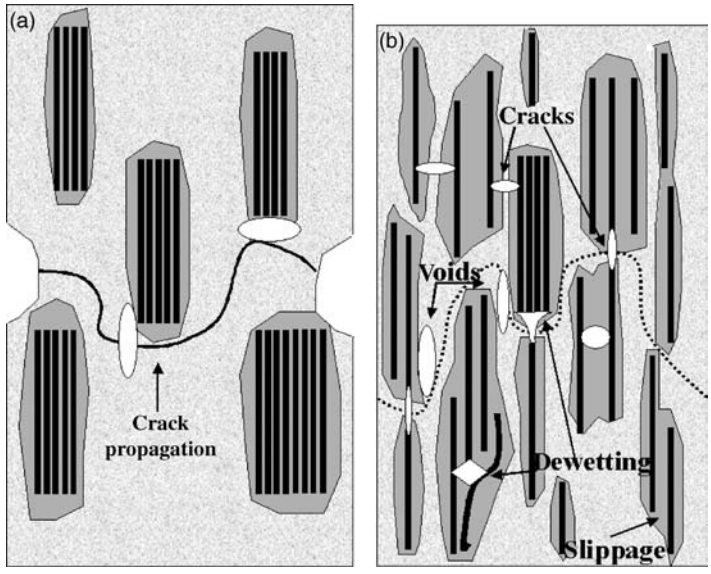

Figure 7.10 Scheme of failure development in rubber/organoclay mixes with poor (a) and good (b) dispersion of the clay layers due to high strain at uniaxial loading: (a) fast crack growth after surface cracking and (b) slow crack growth via void coalescence (Reproduced with permission from K.G. Gatos *et al*., "Nanocomposite formation in hydrogenated nitrile rubber (HNBR)/organo-montmorillonite as a function of the intercalant type," *Macromolecular Materials and Engineering*, 2004, **289**, 1079–1086. © Wiley-VCH Verlag GmbH & Co. KGaA.)

To improve resistance against tearing is one of the main goals for rubber reinforcements. Note that rubber parts often suffer from such a failure mode during their service. The platy, or plate-like, structure of clays blocks the propagation of cracks and thus increases the tear resistance. A good dispersion of silicate layers and a high rubber/clay interphase quality are usually associated with increased tensile strength, increased hardness and enhanced tear resistance [71, 73, 85–87]. López-Manchado *et al.* [88] highlighted the basic difference in the rubber/filler interaction between carbon black and layered silicates. Carbon black forms covalent bonds with the elastomer which is restricted to a given rather small interphase. In contrast, organoclays are physically adsorbed within the rubber chains in a thick interphase. Due to the high aspect ratio of the clays their optimum dispersion is reached at a smaller amount than by carbon black.

7.4.3 Barrier Properties

The superior performance of layered silicates compared to conventional fillers is revealed unambiguously when barrier properties are examined [89]. Hwang *et al.* [40] presented for NBR/organoclay nanocomposites (in 10 phr organoclay) that the relative vapor permeability for water and methanol was reduced up to 85% and 42%, respectively, compared to the neat matrix. Kim *et al.* [90] showed for the same type of rubber that water vapor permeability

decreases not only with the organoclay content but also with the amount of silane coupling agent used. The latter effect was attributed to the enhanced silicate dispersion owing to the increased chain interactions between the silane and the rubber molecules.

The effect of interphase quality on the barrier properties of rubber/layered silicate nanocomposites was investigated using HNBR as matrix [73]. As displayed in Figure 7.11 when MMT-MTH served as organoclay an almost 40% reduction of the oxygen permeation ratio was observed at both 0% and 60% relative humidity. The silica filler, being isometric, only slightly reduced the oxygen transmission rate. For the organoMMTs the aspect ratio is quite high (in the range 100–200) [91–92]. Therefore, the improvement in barrier properties is due to the tortuousity of the penetration path created by impermeable clay layers and stacks. As discussed before, the difference in relative oxygen permeation depends on the dispersion grade of the clay and formed interphase [93–94]. Further, the slight difference between MMT-ODA and MMT-ODTMA (cf. Figure 7.11) suggests that the intercalated part of the clay does not contribute much to barrier improvement. The good dispersion grade and strong interphase for MMT-MTH resulted in the lowest oxygen permeation (cf. Figure 7.11). The oxygen permeability coefficient of the HNBR in dry and wet conditions is 119 and 129 cm^3 mm/m^2.day.atm, respectively. As the humidity increased, the rubber cohesion is weakened because the water molecules are attached to the CN groups. This yields higher oxygen permeations with increasing humidity. As shown in Figure 7.11, the decrease in permeability coefficient ratio in dry and wet conditions is almost the same for all compounds tested. With increasing humidity the rubber nanocomposite films maintain their good barrier properties, as the tortuous path given by the MMT platelets [95] compensates the moisture susceptibility of the matrix [96].

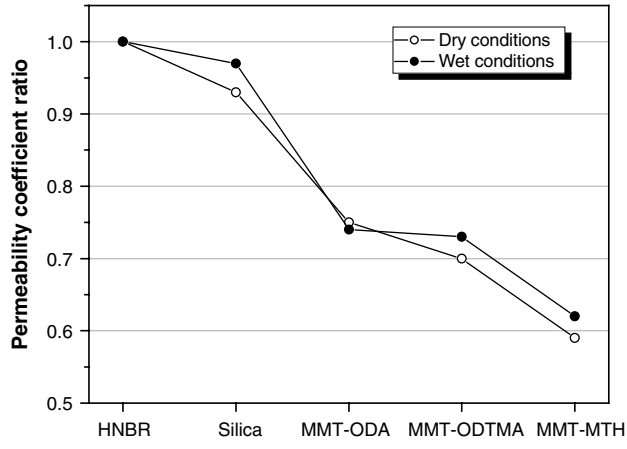

Figure 7.11 Oxygen permeability coefficient ratio for different HNBR films tested at 0% and 60% relative humidity (dry and wet conditions, respectively). Both measurements conducted at room temperature. (Note that the oxygen permeability coefficient values for HNBR were 119 and 129 cm^3.mm/m^2.day.atm for the dry and wet conditions, respectively) (Reproduced with permission from K.G. Gatos *et al.*, "Controlling the deintercalation in hydrogenated nitrile rubber (HNBR)/organo-montmorillonite nanocomposites by curing with peroxide," *Macromolecular Rapid Communications*, 2005, **26**, 915–919. © Wiley-VCH Verlag GmbH & Co. KGaA.)

As it is rather accepted that the labyrinth principle is the main reason for the excellent barrier properties of rubber/layered silicate nanocomposites, a more pronounced tortuous path given by an increased aspect ratio of the silicate platelet would be a decisive clue. To check this, MMT and FHT, bearing the same type of modifier (viz. ODA), were incorporated in HNBR and their barrier properties tested [79]. The silicate dispersion in the rubber matrix is depicted in Figure 7.12, where exfoliated platelets along with stacks of silicate layers are well observable. The TEM pictures present nicely the different aspect ratio of the MMT and FHT platelets. As can be seen in Figure 7.12a, the aspect ratio of the exfoliated MMT layers is in the order of 100, whereas that of the FHT platelets is about 200 (Figure 7.12b). Their different action is well reflected in the oxygen permeation values in Figure 7.13, where the HNBR/FHT-ODA vulcanizate yielded the lowest oxygen permeation coefficient in dry and wet conditions compared to the vulcanizates with unmodified FHT or MMT-ODA. It is noteworthy that the clay dispersion (intercalation/exfoliation) also beneficially affects the solvent transport properties [97–98]. As solvents, for example, methyl ethyl ketone, cyclohexane, chloroform and trichloroethylene were investigated.

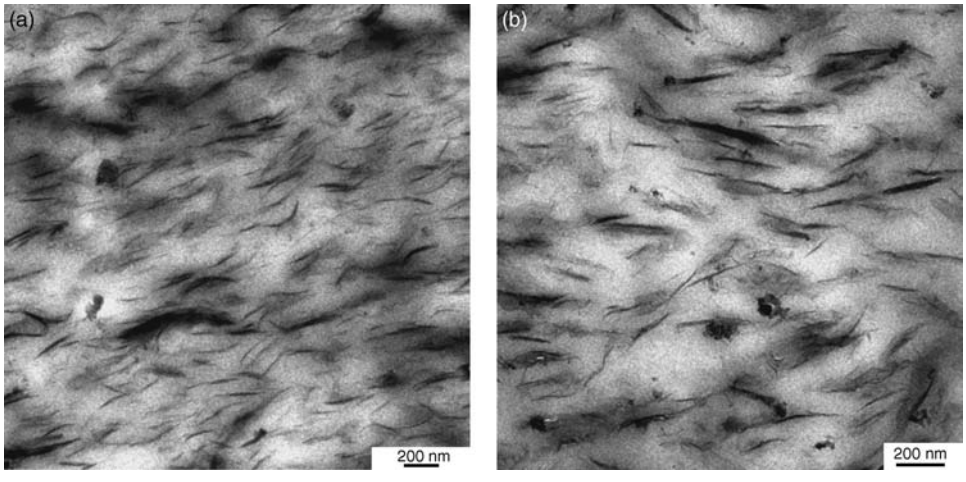

Figure 7.12 TEM images of: (a) HNBR/MMT-ODA and (b) HNBR/FHT-ODA nanocomposites (10 phr filler) (Reproduced from *European Polymer Journal*, **43**, K.G. Gatos and J. Karger-Kocsis, "Effect of the aspect ratio of the silicate platelets on the mechanical and barrier properties of hydrogenated acrylonitrile butadiene rubber (HNBR)/layered silicate nanocomposites," 1097–1104, 2007, with permission from Elsevier.)

7.4.4 Fire Resistance

The dispersion of the inorganic filler in the rubber matrix can improve the fire resistance of the vulcanizate. This is due to a delay in thermal-oxidative degradation and a decrease in the heat release rate.

Kang *et al.* [99] reported that EPDM/organoclay nanocomposites may have increased thermal stability, based on thermogravimetric analysis (TGA). However, this was not accompanied with

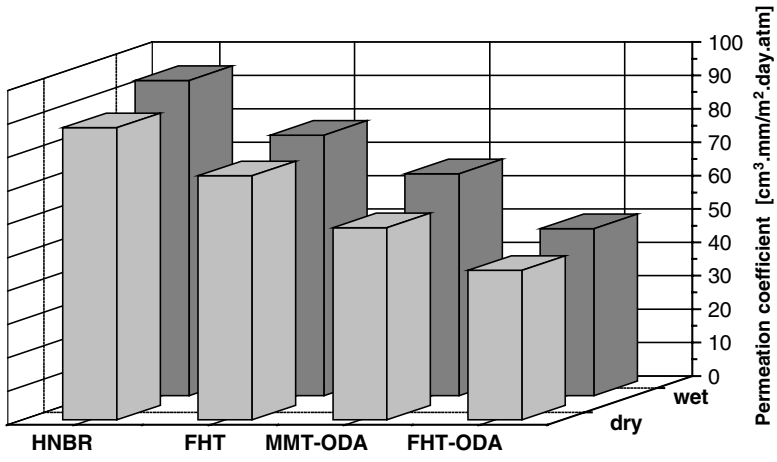

Figure 7.13 Oxygen permeability measurements for the HNBR vulcanizates as a function of the filler aspect ratio (Reproduced from *European Polymer Journal*, **43**, K.G. Gatos and J. Karger-Kocsis, "Effect of the aspect ratio of the silicate platelets on the mechanical and barrier properties of hydrogenated acrylonitrile butadiene rubber (HNBR)/layered silicate nanocomposites," 1097–1104, 2007, with permission from Elsevier.)

improved flame retardance (just the opposite was observed). During the burning process visual inspection revealed that the neat EPDM gave a uniform flame and no char, while the nanocomposites had no uniform flame and produced char. In general, the build-up char on the surface of the vulcanizate should shield the underlying rubber and slow down the decomposition rate. The reduction in the heat release rate, measured in a cone calorimeter, was attributed to a reduction in the gas permeability owing to the clay layering ("labyrinth pathway") [100], as discussed in Section 7.4.3. A widely followed strategy is to combine organoclay with traditional flame retardants, as the outcome is often synergistic [101].

7.4.5 Others

The enhanced performance of rubber/clay nanocomposites involves also properties of great relevance which, however, have received less attention over the past years. The wear behavior of this new class of nanocomposites seems to be a promising topic. Recent experiments on their friction and sliding wear performance have shown that incorporation of layered silicates in rubber may improve or deteriorate the wear behavior of the related vulcanizates [102–104]. The final outcome depends on those parameters which affect the abrasive, fatigue and adhesive wear components [103, 105], similar to "traditionally" filled rubbers. The dispersion and especially the orientation of the silicate platelets in the rubber matrix are crucial. Alignment of the clay platelets in plane (2-D, resulting in an orthotropic character), that is, parallel to the sliding direction is disadvantageous. The 2-D clay alignment triggers a mechanism during sliding, which has some similarities with a "can-opening" process [102]. This markedly reduces resistance to wear. As shown in Figure 7.14, the specific wear rate of HNBR (Figure 7.14a) and EPDM (Figure 7.14b) reinforced by organoclay in 10 phr was reduced

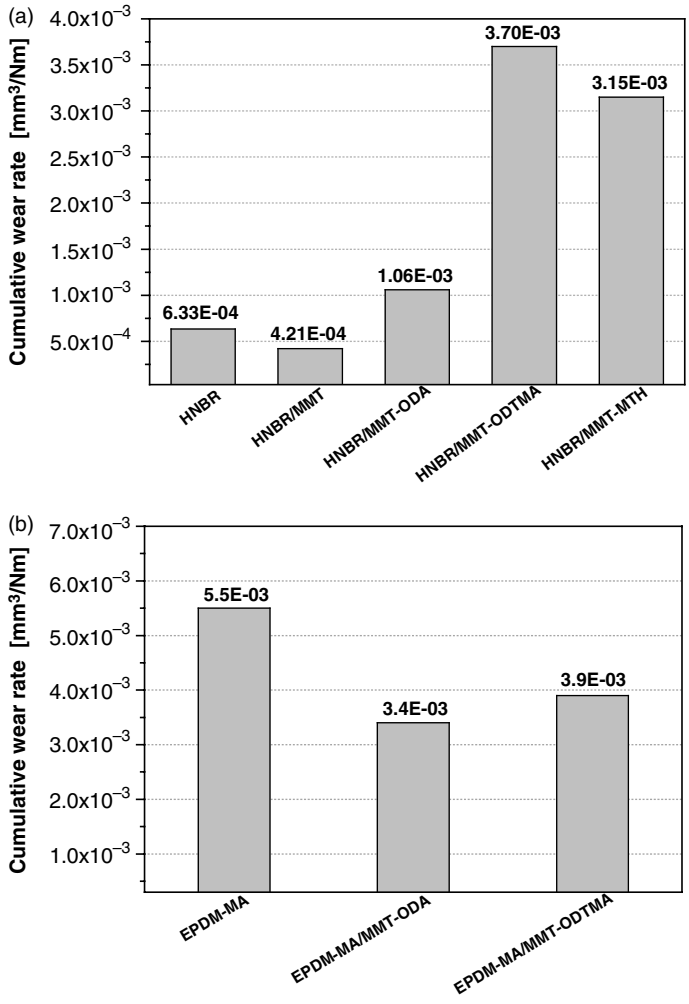

Figure 7.14 Specific wear rate of: (a) HNBR and (b) EPDM-MA, containing various fillers (10 phr) (Reproduced with permission from K.G. Gatos *et al*., "On the friction and sliding wear of rubber/layered silicate nanocomposites," *Express Polymer Letters*, **1**, 27–31, 2007, copyright BME-PT and GTE.)

and enhanced, respectively. In both cases the nanocomposites exhibited outstanding ultimate and dynamic mechanical properties, based on which a better resistance to abrasion and wear was expected. The basic difference between the related rubber compounds lies in their silicate dispersion. As shown in Figure 7.15, HNBR/organoclay has a 2-D (in plane) platelet alignment (cf. Figure 7.15a), whereas EPDM/organoclay exhibits a rather 3-D dispersion (cf. Figure 7.15b). The latter structure was achieved by processing. Unexpectedly, reinforcement with fibrillar silicate (attapulgite, palygorskite) proved to be less efficient than with silica from the viewpoint of abrasion resistance [106].

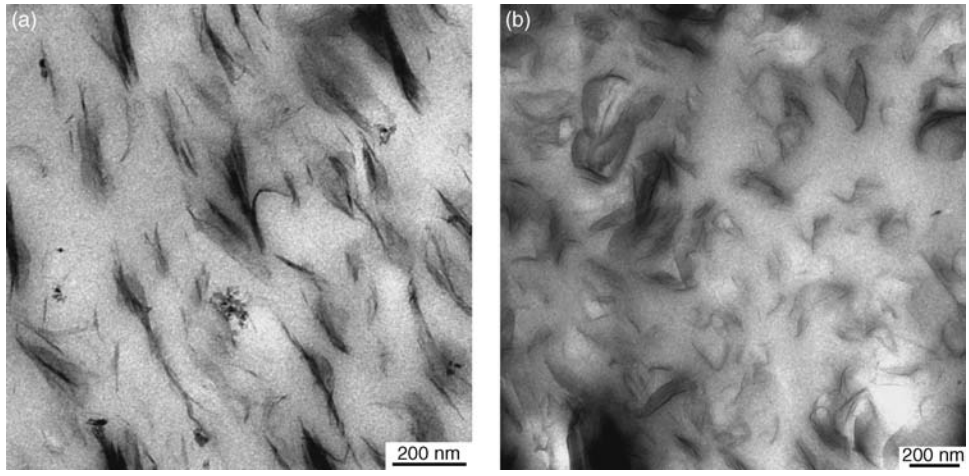

Figure 7.15 TEM images of: (a) HNBR (Reproduced with permission from K.G. Gatos *et al.*, "Nanocomposite formation in hydrogenated nitrile rubber (HNBR)/organo-montmorillonite as a function of the intercalant type," *Macromolecular Materials and Engineering*, 2004, **289**, 1079–1086. © Wiley-VCH Verlag GmbH & Co. KGaA.) and (b) EPDM-MA, containing 10 phr MMT-ODTMA (Reproduced from *Polymer*, **46**, K.G. Gatos and J. Karger-Kocsis, "Effects of primary and quaternary amine intercalants on the organoclay dispersion in a sulfur-cured EPDM rubber," 3069–3076, 2005, with permission from Elsevier.)

7.5 Applications

The application possibilities of this new class of rubber/clay nanocomposites are broad. In applications where a weight decrease of the rubber product is of great significance, substitution of conventional fillers (carbon black and silica) by organoclay may be straightforward as the overall filler content can be highly reduced. Having in mind the superior barrier properties given by the platy nature of the clay, applications demanding low solvent and/or vapor permeations should be favored (for example, tire inlay).

As unreacted curatives usually give rise to blooming (migration to the surface), which is undesirable for commercial rubber articles, clay may also be a helpful additive in this respect. A possible contribution of clay to environmental issues is that, in its presence, the ZnO content of the recipes can be reduced. Note that zinc compounds are ecotoxic.

The most advanced application of organoclays is linked with their flame resistance, fire retardance. Cable jacketing rubber mixes already contain organoclays. It is the right place to call the attention to the fact that the rubber industry is very conservative. Thus, adaptation of new findings occurs with a considerable time lag.

7.6 Outlook

The interest of academia is directed towards producing rubber nanocomposites by *in situ* polymerization techniques. This strategy is parallel with that followed for thermoplastics. In this respect anionic polymerization has been already tried for rubbers [28, 107–108], albeit the

emulsion and suspension polymerization routes seem to be even more promising. Recall that in the latter cases principally the "latex route" is followed.

Attempts have been made to produce rubber nanocomposites by melt compounding of rubber, pristine clay and clay intercalant. Again, this strategy has been adapted from R&D work running with thermoplastics.

Radiation curing of rubber/organoclay systems is an interesting way to overcome cure chemistry-related deintercalation [109]. Wu *et al.* [110] reported that the flex fatigue life of SBR can be improved by the combined use of carbon black and organoclay. Rubber nanocomposites with a very high organoclay loading (up to 60 wt%) have also been prepared. Lu *et al.* [111] reported that such compounds exhibit outstanding gas barrier properties compared to neat rubbers. The clay may serve as a carrier material for various compounds, based on which interesting and even new properties can be triggered, such as electromagnetic shielding [112].

Acknowledgments

Part of this work was performed within the framework of EU project "Kristal" (Contract NMP3-CT-2005-515837; www.kristal-project.org).

References

1. Morgan, P. (2005) *Carbon Fibers and their Composites*, CRC Press, Boca Raton, FL.
2. Hess, W.M. and Herd, C.R. (1993) Microstructure, morphology and general physical properties, in *Carbon Black* (eds J.B. Donnet, R.C. Bansal, and M.J Wang), Dekker, New York, USA, pp. 89–173.
3. Wang, M.J. (1998) Effect of polymer-filler and filler-filler interactions on dynamic properties of filled vulcanizates. *Rubber Chemistry and Technology*, **71**, 520–589.
4. Smallwood, H.M. (1944) Limited law of the reinforcement of rubber. *Journal of Applied Physics*, **15**, 758–766.
5. Theng, B.K.G. (1979) *Formation and Properties of Clay-Polymer Complexes*, Elsevier, Amsterdam.
6. Van Olphen, H. (1977) *An Introduction to Clay Colloid Chemistry*, Wiley, New York.
7. Hofmann, W. (1994) *Rubber Technology Handbook*, Hanser, Munich, pp 230–231.
8. Kühner, G. and Voll, M. (1993) Manufacture of carbon black, in *Carbon Black* (eds J.B. Donnet, R.C. Bansal, and M.J. Wang), Dekker, New York, USA, pp. 1–66.
9. Lin, C.J., Hogan, T.E., and Hergenrother, W.L. (2004) On the filler flocculation in silica and carbon black filled rubbers: Part II. Filler flocculation and polymer-filler interaction. *Rubber Chemistry and Technology*, **76**, 90–114.
10. Sae-Oui, P., Sirisinha, C., Hatthapanit, K., and Thepsuwan, U. (2005) Comparison of reinforcing efficiency between Si-69 and Si-264 in an efficient vulcanization system. *Polymer Testing*, **24**, 439–446.
11. Galanti, A., Laus, M., and Fiorini, M. (1999) Reinforcement of SBS by organophilic clay fillers. *Kautschuk Gummi Kunststoffe*, **52**, 21–25.
12. Alexandre, M. and Dubois, P. (2000) Polymer-layered silicate nanocomposites: Preparation, properties and uses of a new class of materials. *Materials Science and Engineering Reviews*, **28**, 1–63.
13. LeBaron, P.C., Wang, Z., and Pinnavaia, T.J. (1999) Polymer-layered silicate nanocomposites: an overview. *Applied Clay Science*, **15**, 11–29.
14. Sinha Ray, S. and Okamoto, M. (2003) Polymer/layered silicate nanocomposites: a review from preparation to processing. *Progress in Polymer Science*, **28**, 1539–1641.
15. Kojima, Y., Fukumori, K., Usuki, A. *et al.* (1993) Gas permeabilities in rubber-clay hydrid. *Journal of Materials Science Letters*, **12**, 889–890.

16. Burnside, S.D. and Giannelis, E.P. (1995) Synthesis and properties of new poly(dimethylsiloxane) nanocomposites. *Chemistry of Materials*, **7**, 1597–1600.
17. Akelah, A., Salahuddin, N., Hiltner, A. *et al.* (1994) Morphological hierarchy of butadieneacrylonitrile/montmorillonite nanocomposite. *Nanostructured Materials*, **4**, 965–978.
18. Ganter, M., Gronski, W., Reichert, P., and Mülhaupt, R. (2001) Rubber nanocomposites: morphology and mechanical properties of BR and SBR vulcanizates reinforced by organophilic layered silicates. *Rubber Chemistry and Technology*, **74**, 221–235.
19. Burnside, S.D. and Giannelis, E.P. (2000) Nanostructure and properties of polysiloxane-layered silicate nanocomposites. *Journal of Polymer Science: Part B: Polymer Physics*, **38**, 1595–1604.
20. Mousa, A. and Karger-Kocsis, J. (2001) Rheological and thermodynamical behavior of styrene/butadiene rubber-organoclay nanocomposites. *Macromolecular Materials and Engineering*, **286**, 260–266.
21. Vu, Y.T., Mark, J.E., Pham, L.H., and Engelhardt, M. (2001) Clay nanolayer reinforced of cis-1,4-polyisoprene and epoxidized natural rubber. *Journal of Applied Polymer Science*, **82**, 1391–1403.
22. Wang, Y., Zhang, L., Tang, C., and Yu, D. (2000) Preparation and characterization of rubber-clay nanocomposites. *Journal of Applied Polymer Science*, **78**, 1879–1883.
23. Zhang, L., Wang, Y., Wang, Y. *et al.* (2000) Morphology and mechanical properties of clay/styrene-butadiene rubber nanocomposites. *Journal of Applied Polymer Science*, **78**, 1873–1878.
24. Zhang, L., Wang, Y., Wang, Y. *et al.* (2000) Morphology and mechanical properties of clay/styrene-butadiene rubber nanocomposites. *Journal of Applied Polymer Science*, **78**, 1873–1878.
25. Sadhu, S. and Bhowmick, A.K. (2004) Preparation and properties of styrene-butadiene rubber based nanocomposites: the influence of the structural and processing parameters. *Journal of Applied Polymer Science*, **92**, 698–709.
26. Schön, F. and Gronski, W. (2003) Filler networking of silica and organoclay in rubber composites: reinforcement and dynamic-mechanical properties. *Kautschuk Gummi Kunststoffe*, **56**, 166–171.
27. Song, M., Wong, C.W., Jin, J. *et al.* (2005) Preparation and characterization of poly(styrene-co-butadiene) and polybutadiene rubber/clay nanocomposites. *Polymer International*, **54**, 560–568.
28. Zhang, Z., Zhang, L., Li, Y., and Xu, H. (2005) New fabrication of styrene-butadiene rubber/montmorillonite nanocomposites by anionic polymerization. *Polymer*, **46**, 129–136.
29. Wu, Y.P., Ma, Y., Wang, Y.Q., and Zhang, L.Q. (2004) Effects of characteristics of rubber, mixing and vulcanization on the structure and properties of rubber/clay nanocomposites by melt blending. *Macromolecular Materials and Engineering*, **289**, 890–894.
30. Liang, Y.R., Lu, Y.L., Wu, Y.P. *et al.* (2005) Pressure, the critical factor governing final microstructures of cured rubber/clay nanocomposites. *Macromolecular Rapid Communications*, **26**, 926–931.
31. Zheng, H., Zhang, Y., Peng, Z., and Zhang, Y. (2004) Influence of clay modification on the structure and mechanical preperties of EPDM/montmorillonite nanocomposites. *Polymer Testing*, **23**, 217–223.
32. Usuki, A., Tukigase, A., and Kato, M. (2002) Preparation and properties of EPDM-clay hydrids. *Polymer*, **43**, 2185–2189.
33. Zheng, H., Zhang, Y., Peng, Z., and Zhang, Y. (2004) A comparison between cure systems for EPDM/montmorillonite nanocomposites. *Polymers and Polymer Composites*, **12**, 197–206.
34. Ahmadi, S.J., Yudong, H., and Li, W. (2004) Synthesis of EPDM/organoclay nanocomposites: Effect of the clay exfoliation on structure and physical properties. *Iranian Polymer Journal*, **13**, 415–422.
35. Chang, Y.W., Yang, Y., Ryu, S., and Nah, C. (2002) Preparation and properties of EPDM/organomontmorillonite hydrid nanocomposites. *Polymer International*, **51**, 319–324.
36. Gatos, K.G., Thomann, R., and Karger-Kocsis, J. (2004) Characteristics of ethylene propylene diene monomer rubber/organoclay nanocomposites resulting from different processing conditions and formulations. *Polymer International*, **53**, 1191–1197.
37. Gatos, K.G., Apostolov, A.A., and Karger-Kocsis, J. (2005) Compatibilizing effect of grafted glycidyl methacrylate on EPDM/organoclay nanocomposites. *Materials Science Forum*, **482**, 347–350.
38. Gatos, K.G. and Karger-Kocsis, J. (2005) Effects of primary and quaternary amine intercalants on the organoclay dispersion in a sulfur-cured EPDM rubber. *Polymer*, **46**, 3069–3076.
39. Kader, M.A. and Nah, C. (2004) Influence of clay on the vulcanization kinetics of fluoroelastomers. *Polymer*, **45**, 2237–2247.
40. Hwang, W.G., Wei, K.H., and Wu, C.M. (2004) Mechanical, thermal, and barrier properties of NBR/organosilicate nanocomposites. *Polymer Engineering and Science*, **44**, 2117–2124.

41. Nah, C., Ryu, H.J., Han, S.H. *et al.* (2001) Fracture behaviour of acrylonitrile-butadiene rubber/clay nanocomposites. *Polymer International*, **50**, 1265–1268.
42. Kim, J.T., Oh, T.S., and Lee, D.H. (2003) Preparation and characteristics of nitrile rubber (NBR) nanocomposites based on organophilic layered clay. *Polymer International*, **52**, 1058–1063.
43. Varghese, S., Karger-Kocsis, J., and Gatos, K.G. (2003) Melt compounded epoxidized natural rubber/layered silicate nanocomposites: structure-properties relationships. *Polymer*, **44**, 3977–3983.
44. Joly, S., Garnaud, G., Ollitrault, R., and Bokobza, L. (2002) Organically modified layered silicates as reinforcing fillers for natural rubber. *Chemistry of Materials*, **14**, 4202–4208.
45. Magaraphan, R., Thaijaroen, W., and Lim-Ochakun, R. (2003) Structure and properties of natural rubber and modified montmorillonite nanocomposites. *Rubber Chemistry and Technology*, **76**, 406–418.
46. Varghese, S. and Karger-Kocsis, J. (2004) Melt-compounded natural rubber nanocomposites with pristine and organophilic layered silicates of natural and synthetic origin. *Journal of Applied Polymer Science*, **91**, 813–819.
47. López-Manchado, M.A., Herrero, B., and Arroyo, M. (2004) Organoclay-natural rubber nanocomposites synthesized by mechanical and solution mixing methods. *Polymer International*, **53**, 1766–1772.
48. Teh, P.L., Mohd Ishak, Z.A., Hashim, A.S. *et al.* (2004) On the potential of organoclay with respect to conventional fillers (carbon black, silica) for epoxidized natural rubber compatibilized natural rubber vulcanizates. *Journal of Applied Polymer Science*, **94**, 2438–2445.
49. Bala, P., Samantaray, B.K., Srivastava, S.K., and Nando, G.B. (2004) Organomodified montmorillonite as filler in natural and synthetic rubber. *Journal of Applied Polymer Science*, **92**, 3583–3592.
50. Arroyo, M., López-Manchado, M.A., and Herrero, B. (2003) Organo-montmorillonite as substitute of carbon black in natural rubber compounds. *Polymer*, **44**, 2447–2453.
51. Teh, P.L., Mohd Ishak, Z.A., Hashim, A.S. *et al.* (2004) Effects of epoxidized natural rubber as a compatibilizer in melt compounded natural–organoclay nanocomposites. *European Polymer Journal*, **40**, 2513–2521.
52. Pramanik, M., Srivastava, S.K., Samantaray, B.K., and Bhowmick, A.K. (2002) Synthesis and characterization of organosoluble, thermoplastic elastomer/clay nanocomposites. *Journal of Polymer Science: Part B: Polymer Physics*, **40**, 2065–2072.
53. Jeon, H.S., Rameshwaram, J.K., Kim, G., and Weinkauf, D.H. (2003) Characterization of polyisoprene-clay nanocomposites prepared by solution blending. *Polymer*, **44**, 5749–5758.
54. Wang, Y., Zhang, L., Tang, C., and Yu, D. (2000) Preparation and characterization of rubber-clay nanocomposites. *Journal of Applied Polymer Science*, **78**, 1879–1883.
55. Wu, Y.P., Zhang, L.Q., Wang, Y.Q. *et al.* (2001) Structure of carboxylated acrylonitrile-butadiene rubber (CNBR)-clay nanocomposites by co-coagulating rubber latex and clay aqueous suspensions. *Journal of Applied Polymer Science*, **82**, 2842–2848.
56. Varghese, S. and Karger-Kocsis, J. (2003) Natural rubber-based nanocomposites by latex compounding with layered silicates. *Polymer*, **44**, 4921–4927.
57. Wu, Y.P., Wang, Y.Q., Zhang, H.F. *et al.* (2005) Rubber-pristine clay nanocomposites prepared by co-coagulating rubber latex and clay aqueous suspensions. *Composites Science and Technology*, **65**, 1195–1202.
58. Hwang, W.G., Wei, K.H., and Wu, C.M. (2004) Preparation and mechanical properties of nitrile butadiene rubber/silicate nanocomposites. *Polymer*, **45**, 5729–5734.
59. Varghese, S., Gatos, K.G., Apostolov, A.A., and Karger-Kocsis, J. (2004) Morphology and mechanical properties of layered silicate reinforced natural and polyurethane rubber blends produced by latex compounding. *Journal of Applied Polymer Science*, **92**, 543–551.
60. Karger-Kocsis, J. and Wu, C.-M. (2004) Thermoset rubber/layered silicate nanocomposites. Status and future trends. *Polymer Engineering and Science*, **44**, 1083–1093.
61. Sengupta, R., Chakraborty, S., Bandyopadhyay, S. *et al.* (2007) A short review on rubber/clay nanocomposites with emphasis on mechanical properties. *Polymer Engineering and Science*, **47**, 1956–1974.
62. Lu, Y.L., Liang, Y.R., Wu, Y.P., and Zhang, L.Q. (2006) Effects of heat and pressure on microstructures of isobutylene-isoprene rubber (IIR)/clay nanocomposites. *Macromolecular Materials and Engineering*, **291**, 27–36.
63. Liang, Y., Wang, Y., Wu, Y. *et al.* (2005) Preparation and properties of isobutylene-isoprene (IIR)/clay nanocomposites. *Polymer Testing*, **24**, 12–17.
64. Ma, J., Xiang, P., Mai, Y.W., and Zhang, L.Q. (2004) A novel approach to high performance elastomer by using clay. *Macromolecular Rapid Communications*, **25**, 1692–1696.

65. Jia, Q.-X., Wu, Y.-P., Wang, Y.-Q. *et al.* (2007) Organic interfacial tailoring of styrene butadiene rubber-clay nanocomposites prepared by latex compounding method. *Journal of Applied Polymer Science*, **103**, 1826–1833.
66. Abdollahi, M., Rahmatpour, A., Aalaie, J., and Khanli, H.H. (2007) Structure and properties of styrene-butadiene rubber/pristine clay nanocomposites prepared by latex compounding method. *e-Polymers*, Art. No. 074, http://www.e-polymers.org.
67. Psarras, G.C., Gatos, K.G., and Karger-Kocsis, J. (2007) Dielectric properties of layered silicate reinforced natural and polyurethane rubber nanocomposites. *Journal of Applied Polymer Science*, **106**, 1405–1411.
68. Psarras, G.C., Gatos, K.G., Karahaliou, P.K. *et al.* (2007) Relaxation phenomena in rubber/layered silicate nanocomposites. *eXPRESS Polymer Letters*, **1**, 837–845.
69. Arroyo, M., López-Manchado, M.A., Valentín, J.L., and Carretero, J. (2007) Morphology/behaviour relationship of nanocomposites based on natural rubber/epoxidized natural rubber blends. *Composites Science and Technology*, **67**, 1330–1339.
70. Sharif, J., Yunus, W.M.Z.W., Dahlan, K.H., and Ahmad, M.H. (2006) Natural rubber/poly(ethylene-co-vinyl acetate)-blend-based nanocomposites. *Journal of Applied Polymer Science*, **100**, 353–362.
71. Ma, Y., Wu, Y.-P. Wang, Y.-Q., and Zhang, L.-Q. (2006) Structure and properties of organoclay/EPDM nanocomposites: influence of ethylene contents. *Journal of Applied Polymer Science*, **99**, 914–919.
72. Gatos, K.G., Sawanis, N.S., Apostolov, A.A. *et al.* (2004) Nanocomposite formation in hydrogenated nitrile rubber (HNBR)/organo-montmorillonite as a function of the intercalant type. *Macromolecular Materials and Engineering*, **289**, 1079–1086.
73. Gatos, K.G., Százdi, L., Pukánszky, B., and Karger-Kocsis, J. (2005) Controlling the deintercalation in hydrogenated nitrile rubber (HNBR)/organo-montmorillonite nanocomposites by curing with peroxide. *Macromolecular Rapid Communications*, **26**, 915–919.
74. Anmin, H., Xiaoping, W., Demin, J., and Yanmei, L. (2007) Thermal stability and aging characteristics of HNBR/clay nanocomposites in air, water and oil at elevated temperature. *e-Polymers*, Art. No. 051, http://www.e-polymers.org.
75. Das, A., Jurk, R., Stöckelhuber, K.W., and Heinrich, G. (2007) Rubber curing chemistry governing the orientation of layered silicate. *eXPRESS Polymer Letters*, **1**, 717–723.
76. López-Manchado, M.A., Arroyo, M., Herrero, B., and Biagiotti, J. (2003) Vulcanization kinetics of natural rubber-organoclay nanocomposites. *Journal of Applied Polymer Science*, **89**, 1–15.
77. Gatos, K.G. and Karger-Kocsis, J. (2004) Estimation of the vulcanization time for rubbers by considering their linear viscoelastic response assessed by a plate-plate rheometer. *Kautschuk Gummi Kunststoffe*, **57**, 350–354.
78. Kim, M.S., Kim, G.H., and Chowdhury, S.R. (2007) Polybutadiene rubber/organoclay nanocomposites: effect of organoclay with various modifier concetrations on the vulcanization behavior and mechanical properties. *Polymer Engineering and Science*, **47**, 308–313.
79. Gatos, K.G. and Karger-Kocsis, J. (2007) Effect of the aspect ratio of the silicate platelets on the mechanical and barrier properties of hydrogenated acrylonitrile butadiene rubber (HNBR)/layered silicate nanocomposites. *European Polymer Journal*, **43**, 1097–1104.
80. Liang, Y.R., Ma, J., Lu, Y.L. *et al.* (2005) Effects of heat and pressure on the intercalation structures of isobutylene-isoprene rubber/clay nanocomposites. I. Prepared by melt blending. *Journal of Polymer Science: Part B: Polymer Physics*, **43**, 2653–2664.
81. Sirisinha, C. and Prayoonchatphan, N. (2001) Study of carbon black distribution in BR/NBR blends based on damping properties: Influence of carbon black particle size, filler, and rubber polarity. *Journal of Applied Polymer Science*, **81**, 3198–3203.
82. Wolf, S. and Wang, M.J. (1993) Carbon black reinforcement of elastomers, in *Carbon Black*, 2nd edn (eds J.B. Donnet, R.C. Bansal, and M.J. Wang), Marcel Dekker, New York, pp. 289–355.
83. Leblanc, J.L. (2000) Elastomer-filler interactions and the rheology of filled rubber compounds. *Journal of Applied Polymer Science*, **78**, 1541–1550.
84. Herrmann, W., Uhl, C., Heinrich, G., and Jehnichen, D. (2006) Analysis of HNBR-montmorillonite nanocomposites: Morphology, orientation and macroscopic properties. *Polymer Bulletin*, **57**, 395–405.
85. Liu, L., Luo, Y., Jia, D. *et al.* (2007) Structure and properties of natural rubber-organoclay nanocomposites prepared by grafting and intercalating method in latex. *Journal of Elastomers and Plastics*, **38**, 147–161.

86. Kim, M.S., Kim, D.W., Chowdhury, S.R., and Kim, G.H. (2007) Melt-compounded butadiene rubber nanocomposites with improved mechanical properties and abrasion resistance. *Journal of Applied Polymer Science*, **102**, 2062–2066.
87. Jia, Q.X., Wu, Y.P., Wang, Y.Q. *et al.* (2007) Organic interfacial tailoring of styrene butadiene rubber-clay nanocomposites prepared by latex compounding method. *Journal of Applied Polymer Science*, **103**, 1826–1833.
88. López-Manchado, M.A., Valentín, J.L., Carretero, J. *et al.* (2007) Rubber network in elastomer nanocomposites. *European Polymer Journal*, **43**, 4143–4150.
89. Kojima, Y., Fukumori, K., Usuki, A. *et al.* (1993) Gas permeabilities in rubber-clay hybrid. *Journal of Materials Science Letters*, **12**, 889–890.
90. Kim, J.T., Oh, T.S., and Lee, D.H. (2004) Curing and barrier properties of NBR/organo-clay nanocomposites. *Polymer International*, **53**, 406–411.
91. Fornes, T.D. and Paul, D.R. (2003) Modeling properties of nylon 6/clay nanocomposites using composite theories. *Polymer*, **44**, 4993–5013.
92. Chow, W.S., Mohd Ishak, Z.A., and Karger-Kocsis, J. (2005) Atomic force microscopy study on blend morphology and clay dispersion in polyamide-6//polypropylene/organoclay systems. *Journal of Polymer Science Part B:Physics*, **43**, 1198–1204.
93. Osman, M.A., Mittal, V., and Lusti, H.R. (2004) The aspect ratio and gas permeation in polymer-layered silicate nanocomposites. *Macromolecular Rapid Communications*, **25**, 1145–1149.
94. Osman, M.A., Mittal, V., Morbidelli, M., and Suter, U.W. (2004) Epoxy-layered silicate nanocomposites and their gas permeation properties. *Macromolecules*, **37**, 7250–7257.
95. Bharadwaj, R.K. (2001) Modeling the barrier properties of polymer-layered silicate nanocomposites. *Macromolecules*, **34**, 9189–9192.
96. Grunlan, J.C., Grigorian, A., Hamilton, C.B., and Mehrabi, A.R. (2004) Effect of clay concetration on the oxygen permeability and optical properties of a modified poly(vinyl alcohol). *Journal of Applied Polymer Science*, **93**, 1102–1109.
97. Sridhar, V. and Tripathy, D.K. (2006) Barrier properties of chlorobutyl nanoclay composites. *Journal of Applied Polymer Science*, **101**, 3630–3637.
98. Maiti, M. and Bhowmick, A.K. (2007) Effect of polymer-clay interaction on solvent transport behavior of fluoroelastomer-clay nanocomposites and prediction of aspect ratio of nanoclay. *Journal of Applied Polymer Science*, **105**, 435–445.
99. Kang, D., Kim, D., Yoon, S.H. *et al.* (2007) Properties and dispersion of EPDM/modified-organoclay nanocomposites. *Macromolecular Materials and Engineering*, **292**, 329–338.
100. Zhang, H., Wang, Y., Wu, Y. *et al.* (2005) Study on flammability on montmorillonite/styrene-butadiene rubber (SBR) nanocomposites. *Journal of Applied Polymer Science*, **97**, 844–849.
101. Yang, L., Hu, Y., Lu, H., and Song, L. (2006) Morphology, thermal, and mechanical properties of flame-retardant silicone rubber/montmorillonite nanocomposites. *Journal of Applied Polymer Science*, **99**, 3275–3280.
102. Gatos, K.G., Kameo, K., and Karger-Kocsis, J. (2007) On the friction and sliding wear of rubber/layered silicate nanocomposites. *eXPRESS Polymer Letters*, **1**, 27–31.
103. Karger-Kocsis, J. (2006) Dry friction and sliding wear behavior of organoclay reinforced thermoplastic polyurethane rubbers. *Kautschuk, Gummi, Kunststoffe*, **59**, 537–543.
104. Xu, D., Karger-Kocsis, J., and Schlarb, A.K. (2008) Rolling friction and wear of organoclay-modified thermoplastic polyurethane rubbers against steel. *Kautschuk Gummi Kunststoffe*, **61**, 98–106.
105. Karger-Kocsis, J. and Felhös, D. (2008) Friction and sliding wear of "nanomodified" rubbers and their coatings: some new developments, in *Tribology of Polymer Nanocomposites* (eds K. Friedrich and A.K. Schlarb), Elsevier, Amsterdam, pp. 304–324.
106. Tian, M., Cheng, L., Liang, W., and Zhang, L. (2006) Overall properties of fibrillar silicate/styrene-butadiene rubber nanocomposites. *Journal of Applied Polymer Science*, **101**, 2725–2731.
107. Liao, M., Zhang, W., Shan, W., and Zhang, Y. (2006) Structure and properties of polybutadiene/montmorillonite nanocomposites prepared by in situ polymerization. *Journal of Applied Polymer Science*, **99**, 3615–3621.
108. Wang, S., Zhang, Y., Peng, Z., and Zhang, Y. (2006) Morphology and thermal stability of BR/clay composites prepared by a new method. *Journal of Applied Polymer Science*, **99**, 905–913.
109. Cataldo, F., Ursini, O., and Angelini, G. (2007) Radiation-cured nanocomposites based on diene rubber and nanoclay. *Progress in Rubber, Plastics and Recycling Technology*, **23**, 209–221.

110. Wu, Y.-P., Zhao, W., and Zhang, L.-Q. (2006) Improvement of the flex-fatigue life of carbon-black-filled styrene-butadiene rubber by addition of nanodispersed clay. *Macromolecular Materials and Engineering*, **291**, 944–949.
111. Lu, Y.-L., Li, Z., Yu, Z.-Z. *et al.* (2007) Microstructure and properties of highly filled rubber/clay nanocomposites prepared by melt blending. *Composites Science and Technology*, **67**, 2903–2913.
112. Soto-Oviedo, M.A., Araújo, O.A., Faez, R. *et al.* (2006) Antistatic coating and electromagnetic shielding properties of a hybrid materials based on polyaniline/organoclay nanocomposite and EPDM rubber. *Synthetic Metals*, **156**, 1249–1255.

8

Cellulosic Fibril–Rubber Nanocomposites

Maya Jacob John[1] and Sabu Thomas[2]
[1] *CSIR Materials and Science Manufacturing, Polymers and Composites Competence Area, P.O. Box 1124, Port Elizabeth, South Africa*
[2] *School of Chemical Sciences, Mahatma Gandhi University, Priyadarshini Hills P.O., Kottayam, Kerala, 686 560, India*

8.1 Introduction

The interest in developing composite materials containing nanoreinforcement has grown tremendously in recent years. The main advantages are the attractive properties due to the nanometric size of reinforcement. There are two reasons for changes in material properties when the size of the reinforcing phase is reduced down to the nanometer range:

1. The large surface area associated with nanoparticles results in many interfaces between the constituent intermixed phases that play an important role on the macroscopic properties. In addition the mean distance between particles is much lower as their size is reduced, favoring particle/particle interactions.
2. The occurrence of possible quantum effects, viz. changes in magnetic, optical or electrical properties.

When the reinforcing particles are cellulosic materials, there are additional features like biodegradability and renewability, along with the inherent stiffness and high degree of crystallinity. It is also relatively inexpensive and has a much lower density than most fillers that are in use today. The main challenge has been in getting a good dispersion without any agglomerates in a continuous matrix. Another problem lies in the tedious processing steps by means of purification, bleaching, fibrillation and hydrolysis. There are different techniques for

Rubber Nanocomposites: Preparation, Properties and Applications Edited by Sabu Thomas and Ranimol Stephen
© 2010 John Wiley & Sons (Asia) Pte Ltd

the isolation of cellulose whiskers. Acid hydrolysis of cellulose removes amorphous regions and has been adopted by several researchers. Researchers at CERMAV-CNRS have separated cellulose from various sources like wheat straws and tunicin and have used as reinforcements in polymer matrices [1, 2]. Winter of Cellulose Research Institute at ESF found that the addition of an ounce (28.35 g) of cellulose nanocrystal to a pound (0.45 kg) of plastic resulted in a 3000-fold increase in strength [3].

This chapter provides an outlook into nanoreinforcements like cellulosic nanofibers and its reinforcement effects in rubber composites.

8.2 Cellulose

Cellulose is the main constituent of plant structures, bacteria (for example, *Acetobacter*) and tunicates. The annual production of cellulose is about 1.56×10^{12} t [4]. The chain conformation and microfibrillar morphology contribute to a significant load-carrying capability. The axial Young's modulus of cellulose has been measured to be 137 GPa [5], which is similar to aramid fibers. The cellulosic units have a complex, layered structure consisting of a thin primary wall that is the first layer deposited during cell growth encircling a secondary wall. The secondary wall is made up of three layers and the thick middle layer determines the mechanical properties of the fiber. The middle layer consists of a series of helically wound cellular microfibrils formed from long-chain cellulose molecules: the angle between the fiber axis and the microfibrils is called the microfibrillar angle. Such microfibrils have typically a diameter of about 10–30 nm, are made up of 30–100 cellulose molecules in extended chain conformation and provide mechanical strength to the fiber. Figure 8.1 represents the structure of the cellulosic cell wall [6].

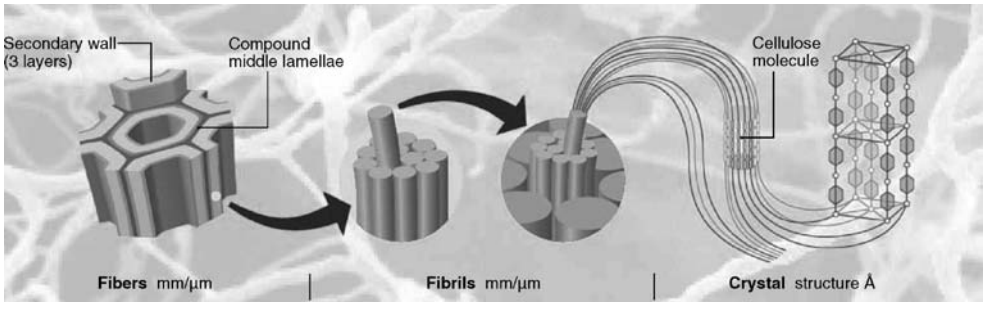

Figure 8.1 Structure of a cell wall [6]

Chemically cellulose is a natural polymer consisting of D-anhydroglucose ($C_6H_{11}O_5$) repeating units joined by β-1,4-glycosidic linkages at C_1 and C_4 position [7]. The degree of polymerization (DP) is around 10 000. Each repeating unit contains three hydroxyl groups at C-2, C-3 and C-6 linkages. Cellulose does not dissolve in common solvents or water at its ordinary state because it crystallizes by intra- and intermolecular hydrogen bond linkages. The presence of these hydrogen bond linkages is responsible for the chain stiffness and stability of the conformation of cellulose. These hydroxyl groups and their ability to hydrogen bond play a

major role in directing the crystalline packing and also govern the physical properties of cellulose. Solid cellulose forms a microcrystalline structure with regions of high order (that is, crystalline regions) and regions of low order (that is, amorphous regions). Cellulose is resistant to strong alkali (17.5 wt%) but is easily hydrolyzed by acid to water-soluble sugars. Cellulose is relatively resistant to oxidizing agents. Although starch has the same basic structure as cellulose – it is also a polysaccharide – the glucose subunits are bonded in such a way that allows the starch molecule to twist. In other words, the starch molecule is flexible, while the cellulose molecule is rigid.

Cellulose exists in several crystal modifications. Naturally occurring cellulose is known as cellulose I which exists in parallel strands without intersheet hydrogen bonding. Cellulose II is thermodynamically more stable and exists in antiparallel strains with intersheet hydrogen bonding. The difference in properties of cellulose I and II arises due to changes in crystal structure [8]. Table 8.1 shows some of the physical properties of cellulose I and II [9].

Cellulose III is amorphous and obtained by treatment of cellulose I or II with amines. Cellulose IV is obtained after treatment of cellulose III with glycerol at very high temperatures. Deguchi *et al.* [10] reported that cellulose undergoes a crystalline to amorphous transition in water at 320 °C and 25 MPa. The transformation is associated with a large change in mechanical and chemical properties, just like the gelatinization of starch. The authors predict that this newly found property of the most abundant and renewable biomass is of significance to its utilization, for example, biomass conversion.

Table 8.1 Some important physical properties of cellulose I and cellulose II

Property	Cellulose I	Cellulose II
DP	103–104	250–240
X-ray crystallinity (%)	50–75	25–40
Density ($g\,cm^{-3}$)	1.53–1.89	1.49–1.55
Breaking strength (dry) $cNtex^{-1}$	26–50	14–61
Elastic modulus (dry) $cNtex^{-1}$	2–11	8–40
Water vapor regained at 65% relative humidity (%)	7–8	12–14

8.3 Cellulosic Nanoreinforcements

8.3.1 Cellulosic Microfibrils

Cellulose microfibrils can be separated by chemical and mechanical treatments. The diameter of cellulose microfibril is about 5–10 nm and the length varies from 100 nm to several microns, depending on the source. Each microfibril consists of monocrystalline cellulose domains linked by amorphous domains. On acid hydrolysis the microfibrils undergo transverse cleavage along the amorphous regions into microcrystalline cellulose or whiskers. The perfect crystalline arrangement of whiskers results in a high modulus and makes them act as efficient reinforcing materials [11–13].

Figure 8.2 represents the microfibrillar arrangement in cellulose [14]. Despite a high Young' modulus, there are problems associated in realizing the full potential of the microfibrils, as the size of agriculturally based fibers varies depending on the isolation procedure and cellulose source. Second, the disintegration of cellulose from a plant cell wall at a reasonable cost and

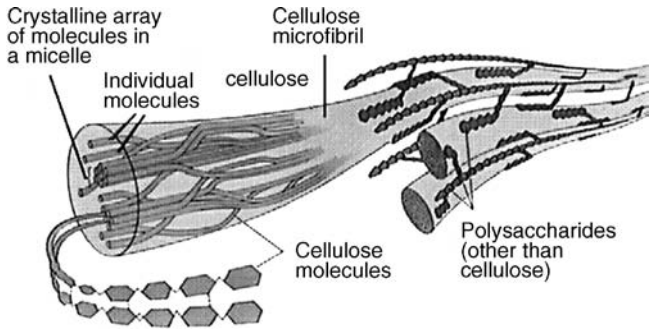

Figure 8.2 Microfibrillar arrangement in cellulose [14]

without severe degradation is a problem. Third, the dispersion of microfibrils in a polymer matrix is difficult as the high density of hydroxyl groups at the microfibril surface induces strong interaction between the microfibrils and they tend to agglomerate [15].

Cellulose microfibrillar surfaces also provide potential for surface modification using well established carbohydrate chemistry [16]. Stenstad *et al.* [17] reported on the chemical modifications of microfibrillated cellulose (MFC) and observed that the surfaces of MFC could be activated and functionalized in both aqueous and organic solvents. The surface modifications used were the grafting of hexamethylene diisocyanate, succinic acid and maleic acid. Alkali treatment was used by Nakagaito and Yano [18] to enhance the toughness of microfibrillated cellulose-reinforced phenolic composites. The improvement was attributed to the transformations in the amorphous regions along the cellulose microfibrils.

In an interesting study, cellulose nanofibril whiskers were synthesized from banana fibers by the process of steam explosion in alkaline medium followed by acidic treatment. This method was found to be very effective in the depolymerization and defibrillation of the fiber to produce banana nanowhiskers. In this study, the authors [19] adopted steam treatment with subsequent explosive defibrillation. This was followed by characterization with X-ray diffraction (XRD) studies and transmission electron microscopy (TEM). XRD studies revealed a reduction in fiber size and an increase in fiber crystallinity. Figure 8.3 shows the TEM of steam exploded banana fibers in acidic medium revealing a needle like structure. The average diameter of the nanofibrils was found to be 4–5 nm and the average length of nanofibrils to be 200–250 nm.

Recently researchers have developed cellulose nanopaper from wood fibrils of high toughness [20]. The high toughness of highly porous nanopaper is related to the nanofibrillar network structure and high mechanical nanofibril performance. The nanopaper exhibits a large strain-to-failure, which indicating mechanisms, such as interfibril slippage, which contribute to inelastic deformation in addition to deformation of the nanofibrils themselves. Figure 8.4 shows a fibrous nanofibril network film which is fine and web-like, with a highly fibrous network structure. The nanofibril length is several microns and nanofibril ends are not apparent. Furthermore, individual nanofibrils are swirled and physically entangled with respect to each other. The nanopaper sample shows very high toughness, the work to fracture being 15 MJ m^{-3}, in uniaxial tension and this was associated with a strain-to-failure as high as 10%. The Young's modulus (13.2 GPa) and tensile strength (214 MPa) were remarkably high although there was a high porosity of 28%.

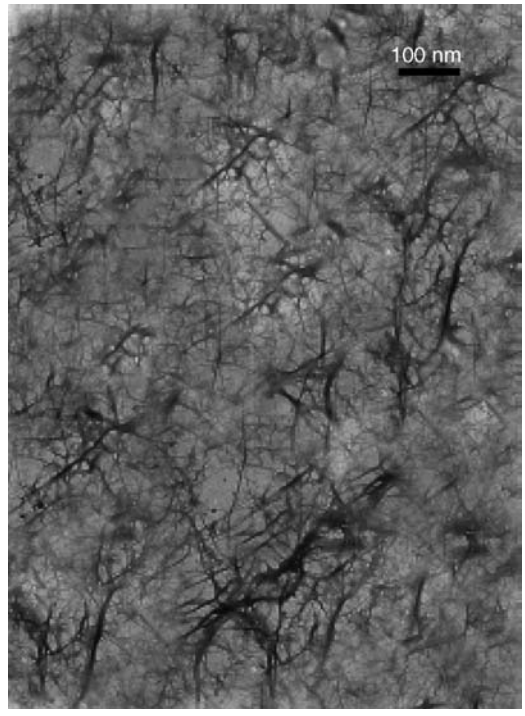

Figure 8.3 Transmission electron micrograph of steam-exploded banana fibers in acidic medium [19] (Reproduced with permission from B.M. Cherian, L.A. Pothan, T. Nguyen-Chung, G. Mennig, M. Kottaisamy and S. Thomas, "A Novel Method for the Synthesis of Cellulose Nanofibril Whiskers from Banana Fibers and Characterization," *Journal of Agricultural and Food Chemistry*, **56**, no. 14, 5617–5627, 2008. © 2008 American Chemical Society.)

Zuluaga *et al.* [21] isolated and characterized cellulose microfibrils from banana rachis using a combination of chemical and mechanical treatments. The morphology and structure of the samples were characterized using transmission electron microscopy, atomic force microscopy and X-ray diffraction. Suspensions of bundled or individualized 5 nm microfibrils were obtained after homogenization whereas an organosolv treatment resulted in shorter aggregates of parallel cellulose microcrystallites. It was also found that microfibrils and microcrystals prepared by both methods can be used as reinforcing filler in nanocomposite materials.

Bhattacharya *et al.* [22] successfully isolated and characterized cellulose microfibrils from bagasse fibers. Bagasse fibers were subjected to conventional pulping to eliminate lignin and hemicellulose. The fibers obtained were separated into constituent microfibrils by a two-stage homogenization process and finally acid hydrolyzed. Atomic force microscopic (AFM) studies revealed that the transverse size of the particles varied between 200 nm to a few microns. Figure 8.5 shows the AFM of the microfibrillar bundles composed of 30 nm nanofibers.

Abraham *et al.* performed a series of experiments in extracting cellulosic nanofibers from various natural fibers. The natural fibers chosen were coir, banana, sisal and pineapple. The fibers were characterized by different techniques like scanning probe microscopy and XRD [23].

The scanning probe micrographs (SPM) of modified fibers are given in Figure 8.6. The results reveal that fiber diameter can be reduced to the nanometer range using steam explosion coupled with acid hydrolysis. Table 8.2 shows the values of the crystallinity index obtained in the case of variously treated fibers. XRD analysis of the alkali-treated fibers revealed an increase in the crystallinity index of the banana and coir. An improvement in the order of the crystallites was observed as the cell wall thickened upon alkali treatment. The crystallinity index initially increased but then declined at high alkali concentrations when damage to the cell wall occurred.

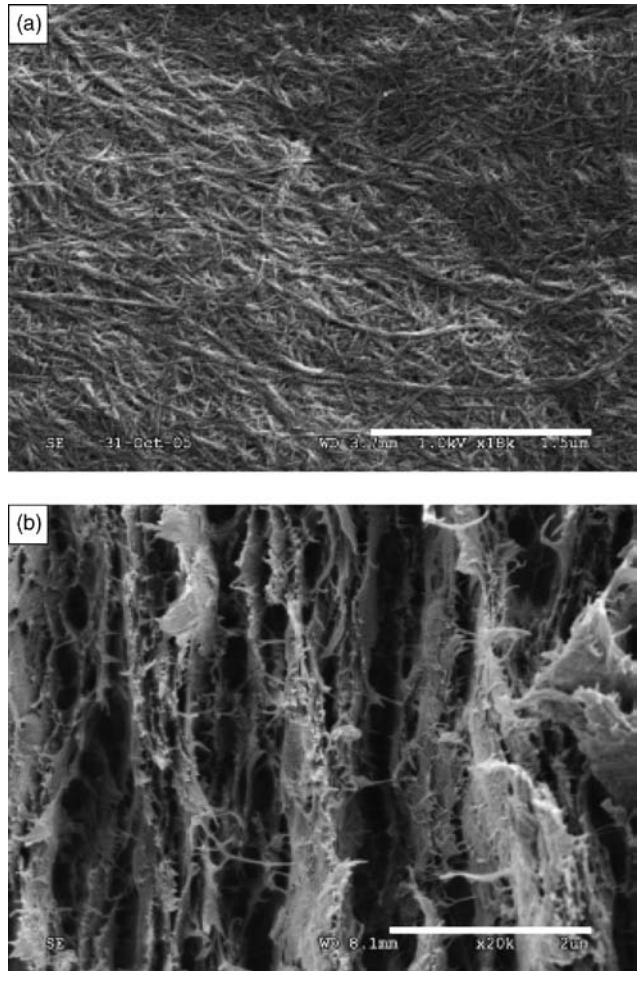

Figure 8.4 FE-SEM micrographs of: (a) a cellulose nanofibril film surface showing a fibrous network (scale bar is 1.5 μm); (b) the cross-section of a fracture surface of a film showing a layered structure (scale bar is 2.0 μm); and (c) a fracture surface viewed perpendicular to the film surface (scale bar is 1.0 μm). These films were dried from water suspension. The film in (a) was prepared from DP-1100 and the other two were prepared from DP-800 [20] (Reproduced with permission from M. Henrickson, L.A. Berglund, P. Isaksson, T. Lindstom and T. Nishino, "Cellulose Nanopaper Structures of High Toughness," *Biomacromolecules*, **9**, 1579–1585, 2008. © 2008 American Chemical Society.)

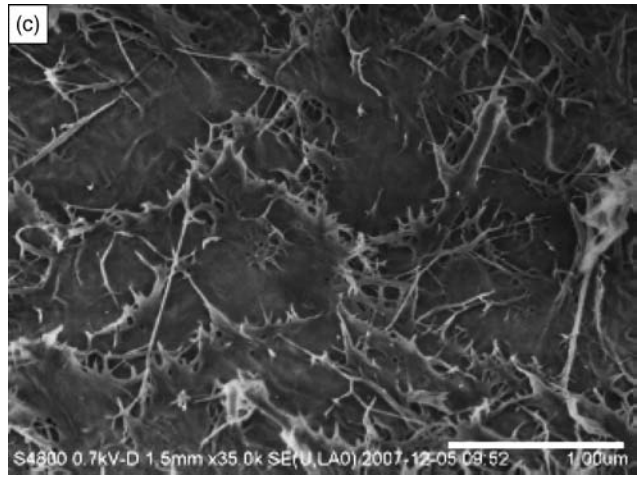

Figure 8.4 *(Continued)*

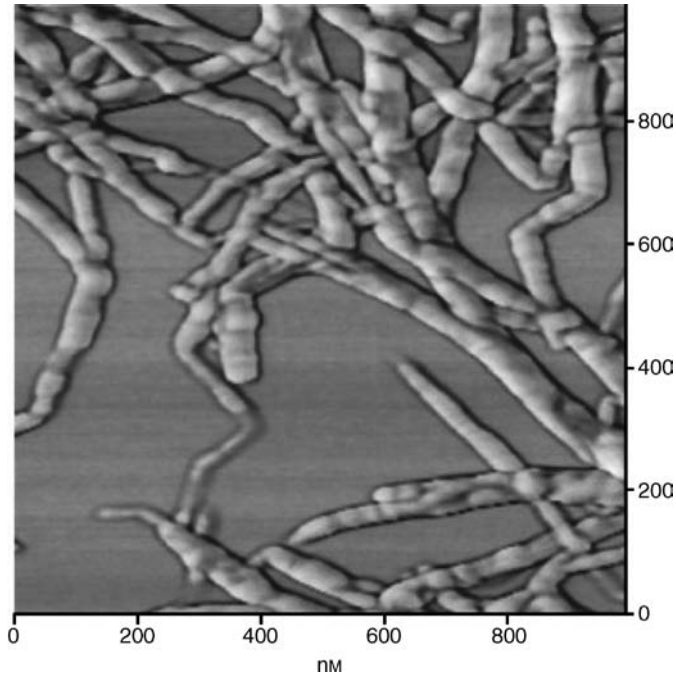

Figure 8.5 Microfibrillar bundles are also observed to be composed of nanofibers (∼30 nm) [22] (Reprinted from *Carbohydrate Polymers*, **73**, D. Bhattacharya, L.T. Germinario and W.T. Winter, "Isolation, preparation and characterization of cellulose microfibers obtained from bagasse," 371–377, © 2008, with permission from Elsevier.)

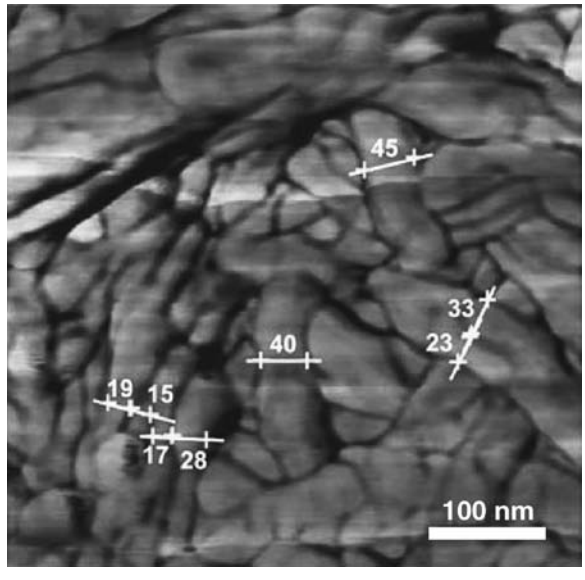

Figure 8.6 Scanning probe micrographs of modified banana fibers [23]

Table 8.2 Crystallinity index values of treated fibers

Fiber stage	I (0,0,2)	I_c (%)
Raw banana fiber	I (0,0,2) = I_{amo} = 10.5	—
Steam-exploded banana fiber	16.4	35.97
Steam-exploded bleached banana fiber	22.9	54.18
5% oxalic acid-treated bleached banana fiber	31.1	66.23
Raw coir fiber	I (0,0,2) = I_{amo} = 4.96	—
Steam-exploded coir fiber	5.19	4.43
5% oxalic acid-treated bleached coir fiber	17.7	71.97

Recently researchers have successfully isolated nanofibers from soybean and analyzed its reinforcing capacity in polymers [24].

8.4 Studies on Cellulosic/Latex Nanocomposites

A survey of the literature has shown that studies on cellulosic nanofiber-reinforced latex composites have been mostly unexplored. With the exception of studies conducted by research groups in France and recently in India, only a limited amount of work is reported in literature.

Orts *et al.* [16] investigated the reinforcements effects of cotton microfibrils at a concentration of 2.5% in latex emulsion. It was observed that the maximum load increased several-fold and the percent elongation at maximum stress increased twofold. Similar results were also observed for latex composites reinforced with straw derived microfibrils [25, 26]. Figure 8.7(a)

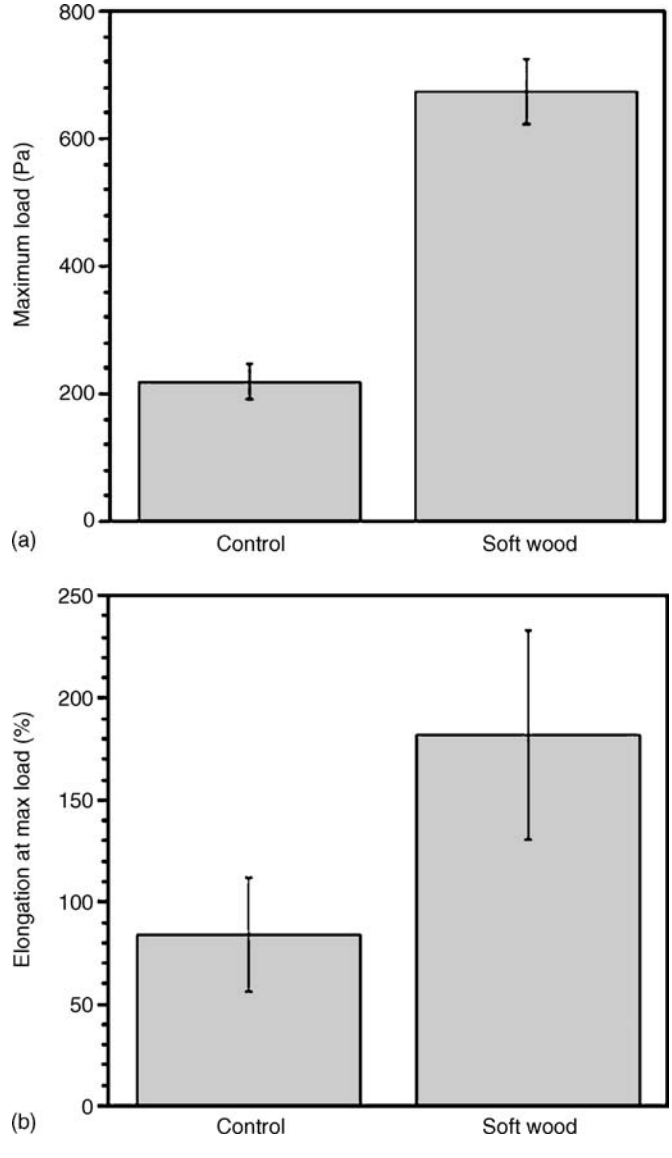

Figure 8.7 Effect of the addition of 2.5% cotton microfibril to a filmcast from latex emulsion. (a) Maximum load and (b) percent elongation at maximum load are shown for untreated and microfibril-reinforced film [16] (With kind permission from Springer Science + Business Media: *Journal of Polymers and the Environment*, "Application of Cellulose Microfibrils in Polymer Nanocomposites," **13**, no. 4, © 2005, 301–306, W.J. Orts, J. Shey, S.H. Imam, G.M. Glenn, M.E. Guttman and J.W. Revol.)

and (b) presents the variation of load and elongation at break on the addition of 2.5% cotton microfibril to latex emulsion.

Favier *et al.* [27] demonstrated the benefits of reinforcing a polymer with cellulose whiskers. The authors used 6% cellulose whiskers derived from tunicate cellulose in a latex polymerized from styrene and butyl acrylate and observed that the composite films exhibited a twofold increase in the shear modulus over control films containing no whiskers. The whiskers were found to form a rigid network linked by hydrogen bonds. The simulation and modeling of the structures were also reported [28].

Hajji *et al.* [29] reported on the tensile behavior of nanocomposites from latex and cellulose whiskers observed significant improvement. The thermomechanical properties of these nanocomposites were investigated, and the influence of processing conditions and the effect of whisker content were considered. Processing conditions were found to have a large influence on the mechanical behavior and can be classified in ascending order of their reinforcement efficiency: It can be attributed to a decrease of the apparent whisker aspect ratio, due to gradual breakage and/or orientation of the whiskers when hot pressing or extrusion is used. Above the glass transition temperature a reinforcing effect was observed, which was related to the presence of a rigid cellulose network, linked by hydrogen bonds.

Recently banana nanofibers obtained by the process of steam explosion were incorporated in matrices like PLA and natural rubber latex to form composites [30]. The main feature observed in the natural rubber composite was a high increase in the mechanical properties after incorporating the nanocellulose. Due to the uniform dispersion of the nanocellulose in rubber latex the prepared composites showed improved stiffness with out any loss of its elastomeric nature. The stress was higher for all systems containing nanofiber composites than the pure natural rubber sample. This is an indication of the effectiveness of reinforcement. XRD analysis of the natural rubber/nanocellulose composite showed the dispersion of nanolayers of cellulose in the polymer matrix (Figure 8.8). The dispersion of the nanocellulose was further confirmed by SEM (Figure 8.9).

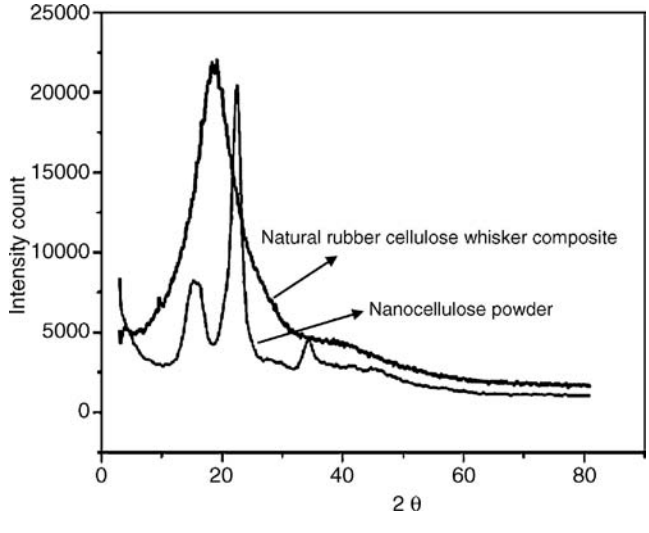

Figure 8.8 XRD curves of the natural rubber/nanocellulose composite [23]

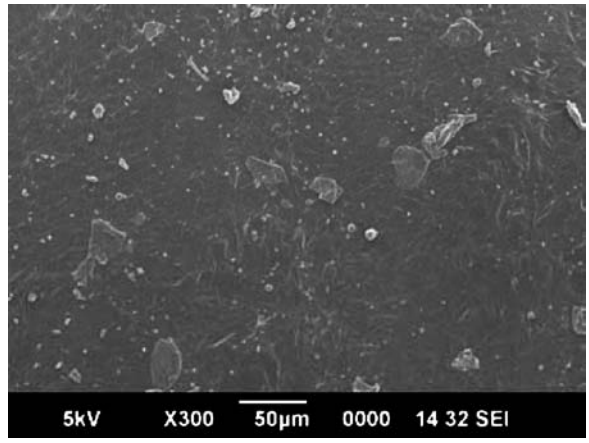

Figure 8.9 SEM of nanocellulose whisker in the natural rubber latex [23]

8.5 Conclusions

This chapter presents an overview of studies on cellulosic nanofiber-reinforced rubber composites. The properties of cellulose and cellulosic microfibrils have been highlighted. Though sufficient data is present on cellulosic fiber-reinforced polymer nanocomposites, studies pertaining to rubber composites are few and need to be addressed in detail. The problems lie in the tedious process of extracting nanofibers from cellulosic sources and their uniform dispersion in a continuous matrix. By addressing certain scientific and technical challenges the possibility of advanced structural materials based on cellulosic nanofibers is likely to be a reality in the near future.

References

1. Morin, A. and Dufresne, A. (2005) Nanocomposites of chitin whiskers from Riftia tubes and poly(caprolactone). *Macromolecules*, **35**, 2190–2199.
2. Dufresne, A. and Cavaille, J.Y. (1999) Nanocomposite materials of thermoplastic polymers reinforced by polysaccharide. *ACS Symposium Series*, **723**, 39–54.
3. Nanowerk (October 2006) Cellulose nanocrystals make plastics 3000 times stronger.
4. Klemm, D., Heublein, B., Fink, H.-P., and Bohn, A. (2005) Cellulose: fascinating biopolymer and sustainable raw material. *Angewandte Chemie-International Edition*, **44**, 3358–3393.
5. Sakurada, I., Nukusina, Y., and Ito, I. (1962) Experimental determination of the elastic modulus of crystalline regions in oriented polymers. *Journal of Polymer Science*, **57**, 651.
6. Pohler, E., Zimmermann, T., and Geiger, Th. (2009) EMPA. www.empa.ch/plugin/template/empa/*/27303/---/l=1.
7. Nevell, T.P. and Zeronian, S.H. (1985) *Cellulose Chemistry and its Applications*, Wiley, New York.
8. Sasaki, M., Adschiri, T., and Arai, K. (2003) Production of cellulose II from native cellulose by near- and supercritical water solubilisation. *Journal of Agricultural and Food Chemistry*, **51**, 5376–5381.
9. Klemm, D., Philipp, B., Heinze, T. *et al.* (1998) *Comprehensive Cellulose Chemistry. Volume I: Fundamentals and Analytical Methods*, Wiley-VCH Verlag GmbH, Weinheim, Germany.

10. Deguchi, S., Tsujji, K., and Horikoshi, K. (2006) Cooking cellulose in hot and compressed water. *Chemical Communications*, 3293–3295.
11. Mathew, A.P., Chakraborty, A., Oksman, K., and Sain, M. (2005) Nanocellulose from lignocellulosic fibres. In *Cellulose Nanocomposites Processing, Characterization and Properties* (eds K. Oksman and M. Sain), ACS, San Diego.
12. Krassig, H.A. (1993) *Cellulose: Structure, Accessibility and Reactivity, Polymer Monographs*, vol. **11**, Gordon and Breach Science Publishers, Yverdon, p. 376.
13. Hamad, W. (2002) *Cellulosic Materials, Fibres, Networks and Composites*, Kluwer Academic Publishers, The Netherlands, p. 47.
14. Modares (2009) www.modares.ac.ir/.../week2/cellulose.
15. Berglund, L. (2005) in *Cellulose Nanocomposites, Natural Fibres, Biopolymers and Biocomposites* (eds A.K. Mohanty, M. Misra, and L.T. Drzal), Taylor and Francis, pp. 807–831.
16. Orts, W.J., Shey, J., Imam, S.H. *et al.* (2005) Application of cellulose microfibrils in polymer nanocomposites. *Journal of Polymers and the Environment*, **13**, 4.
17. Stenstad, P., Andresen, M., Tanem, B.S., and Stenius, P. (2008) Chemical surface modifications of microfibrillated cellulose. *Cellulose*, **15**, 35–45.
18. Nakagaito, A.N. and Yano, H. (2008) Toughness enhancement of cellulose nanocomposites by alkali treatment of the reinforcing cellulose nanofibers. *Cellulose*, **15**, 323–331.
19. Cherian, B.M., Pothan, L.A., Nguyen-Chung, T. *et al.* (2008) Novel method for the synthesis of cellulose nanofibril whiskers from banana fibers and characterization. *Journal of Agricultural and Food Chemistry*, **56**, 5617–5627. doi: 10.1021/jf8003674
20. Henrickson, M., Berglund, L.A., Isaksson, P. *et al.* (2008) Cellulose nanopaper structures of high toughness. *Biomacromolecules*, **9**, 1579–1585.
21. Zuluaga, R., Putaux, J.-L., Restrepo, A. *et al.* (2007) Cellulose microfibrils from banana farming residues: isolation and characterization. *Cellulose*, **14**, 585–592.
22. Bhattacharya, D., Germinario, L.T., and Winter, W.T. (2008) Isolation, preparation and characterization of cellulose microfibers obtained from bagasse. *Carbohydrate Polymers*, **73**, 371–377.
23. Abraham, E., Pothen, L.A., and Thomas, S. (2007) Synthesis and characterization of nano cellulose from lignocellulosic fibres. In Proceedings of the International Conference on Advanced Materials, Bangalore, India, October 6–12, 2007.
24. Wang, B. and Sain, M. (2007) Isolation of nanofibers from soybean source and their reinforcing capability on synthetic polymers. *Composites Science and Technology*, **67**(11–12), 2521–2527.
25. Cavaille, J.Y. and Dufresne, A. (1998) in *Biopolymers: Utilizing Natures Advanced Materials* (eds R.V. Greene and S.H. Imam), ACS Publishing, New York.
26. Dufresne, A. (1998) Recent research. *Developments in Macromolecules Research*, **3**(2), 455–474.
27. Favier, V., Canova, G.R., Cavaille, J.Y. *et al.* (1995) Nanocomposite materials from latex and cellulose whiskers. *Polymers for Advanced Technologies*, **6**(5), 351–355.
28. Favier, V., Dendievel, R., Canova, G. *et al.* (1997) Simulation and modeling of three-dimensional percolating structures: case of a latex matrix reinforced by a network of cellulose fibers. *Acta Materialia*, **45**(4), 1557–1565.
29. Hajji, P., Cavaille, J.Y., Favier, V. *et al.* (1996) Tensile behavior of nanocomposites from latex and cellulose whiskers. *Polymer Composites*, **17**, 4.
30. Abraham, E., Pothen, L.A., and Thomas, S. (2007) Preparation and characterization of green nano composites. In Proceedings of the Fibre Reinforced Composites Conference, Port Elizabeth, South Africa, December 2007.

9

Nanofillers In Rubber–Rubber Blends

Rosamma Alex
Rubber Research Institute of India, Kottayam, Kerala, 686 009, India

9.1 Introduction

Rubbers are used in a wide range of applications and in most of them two or more rubbers are blended to optimize their all-round performance in service conditions. Most of the synthetic rubbers require reinforcement with fillers for practical use. Carbon black (10–30 nm) and precipitated silica (30–100 nm) still remain the conventional fillers for this purpose. Obviously the key factors for reinforcement by fillers are good dispersion and enhanced interaction with the rubber matrix. Recently several other nanofillers have received attention for reinforcement characteristics in rubber, the most promising being organoclay, nanosilica, carbon nanotubes and nano calcium carbonate.

9.2 Types of Nanofillers

Nanofillers are classified into three types based on their dimensions in polymer matrices. The three dimensions of the particle can be in the order of nanometers (isodimensional nanoparticles) and hence appear as spherical particles. Carbon black, silica, aluminum oxide, titanium dioxide, zinc oxide and silicon carbide are examples for nanoparticle fillers. Only two dimensions are in the nanometer scale and the third is larger, forming an elongated structure, as in nanotubes or whiskers or nanofibers. Examples are carbon nanotubes, carbon nanofibers, cellulose whiskers, boron nitride tubes, boron carbon nitride tubes and gold or silver nanotubes. Only one dimension of the filler is in the nanometer range and hence gives a layered appearance, a few nanometers thick but several hundreds of nanometers long. Layered silicates, layered graphite flakes and layered double hydroxides are examples for layered nanofillers. Due to the

Rubber Nanocomposites: Preparation, Properties and Applications Edited by Sabu Thomas and Ranimol Stephen
© 2010 John Wiley & Sons (Asia) Pte Ltd

high adsorption surface energies associated with these nanofillers, they have a strong tendency to form aggregates and agglomerates.

9.2.1 Spherical Fillers

9.2.1.1 Carbon Black

Carbon black fillers are formed from pyrolysis of hydrocarbon materials whilst they are in the vapor phase. Free radicals produced during breakdown of big molecules promote polymerization to liquid droplets and finally to solid particles. In late 1960s the microstructure of carbon black was determined by microscopic techniques. These techniques reveal that carbon black seldom exists as single particles but instead as aggregates. The degree of aggregation is denoted by the term "structure." A low-structure black may have an average of 30 particles while a high-structure black may have as many as about 200 particles per aggregate [1]. The aggregates have a tendency to cluster together to form agglomerates due to van der Waals forces. This agglomeration is called secondary or transient structure. Carbon atoms, on the surface of particles in the aggregates are present in oriented layers. If carbon atoms on the surface have less crystallite orientation they become reactive compared to atoms present in layer planes, more reactive if attached to hydrogen atoms and very reactive if present as a resonance-stabilized free radical. Hence a surface of carbon black can differ in adsorptive capacity and distribution of sites of higher energy. The principal functional groups identified on the surface of carbon black are phenolic, ketonic and carboxylic, together with lactones. Commercially available carbon black fillers have varying levels of structure, particle size, chemical reactivity and pH that lead to different levels of reinforcement.

9.2.1.2 Silica

Silica (silicon dioxide) constitutes 60 wt% of the earth's crust and generally exists alone or in combination with other oxides in silicates. Silica exists in a variety of crystalline and noncrystalline forms. The noncrystalline forms include: (i) vitreous silica (silica glass) formed by fusion and subsequent cooling of crystalline silica and (ii) amorphous silica that are composed of small aggregated particles due to intramolecular hydrogen bonding. The surface of silica and siliceous fillers contain silanol groups which have a higher acidity than hydroxyl groups of aliphatic silanols and a much higher acidity than hydroxyl groups of hydrocarbon alcohols. So they form hydrogen bonds with many compounds like water, amines, alcohols and silanols. The primary aggregated particles act as single units in rubber matrix. They can further agglomerate to the so called secondary aggregates or agglomerates as in the case of carbon black. Technologically important forms of silica are fumed silica and precipitated silica, obtained by coagulation of silica particles from an aqueous medium under the influence of high salt concentration or other coagulants.

9.2.2 Tubular Fillers

Carbon nanotubes and cellulose whiskers are used as reinforcing nanofillers for composites with exceptional properties. Carbon nanotubes contain two or more layers that are closed at

both ends and the diameter range from 3 to 30 nm. Single-walled nanotubes are generally narrower with diameters typically in the range 1–2 nm and tend to be curved rather than straight. The tubes can be considered as rolled-up graphite layers in different manners. They are produced by arc discharge process by vaporizing graphite in a helium atmosphere, chemical vapor deposition or laser ablation. It has amazing mechanical properties and is manyfold stronger than steel.

Cellulose nanofibres are obtained from wood after suitable chemical treatment. Cellulose chains aggregate to form microfibrils, by hydrogen bonds between hydroxyl group and oxygen of adjacent molecules. The diameter of these fibrils ranges from 2 to 20 nm with lengths up to several tens of microns. These microfibrils undergo transverse cleavage into short microcrystals under acid hydrolysis. Cellulose microcrystals can be obtained from wheat straw or cotton by acid hydrolysis.

9.2.3 Layered Clays

Layered clays, composed of platy, or plate-shaped, very fine particles are chemically hydrous silicates of Al, Mg, Fe and other less abundant elements. The individual clay layers are aggregated into discrete particles mainly due to van der Waals forces. The clay particles can be delaminated into discrete nanosized layers in polymer nanocomposites and in absence of delamination or so-called exfoliation, the particles can have dimensions in the micro scale. They are designated as phyllosilicates when silicone oxygen complexes have a two-dimensional infinite layer structure. A layer can have tetrahedral structure when oxygen atoms are bonded to silicon atom or octahedral structure when oxygen atoms are bonded to aluminum atom. Sometimes in the sheets of silicon and aluminum atoms, silicon atoms get substituted by aluminum atoms or aluminum atoms get substituted by magnesium atoms. Such isomorphous substitution generates excess negative charge in the layers. Hence to counterbalance this negative charge, alkali cations like Ca^{2+}, K^{+}, Mg^{2+} and Na^{+} reside in the space between the layers. The cations in the interlayer region can get exchanged by other ions, and the ability for this is related by a term called cation exchange capacity (CEC). It is simply a measure of the quantity of sites on clay surfaces that can retain positively charged ions (cations) by electrostatic forces. The layers of silicates are bound together by weak or strong interactions depending on the chemical structure (Table 9.1).

It is also possible to have positively charged layers with anions intercalated in the interlayer region together with water molecules so as to form anionic clays. Layered double hydroxides (LDHs) which have the structure of mineral brucite, $Mg(OH)_2$ can be considered as anionic clays. In the natural form the hydroxide layers are neutral. When a fraction of the Mg^{2+} ions in brucite is substituted by trivalent cations such as Al^{3+}, the resultant hydroxide layers acquire a positive charge and intercalate various anions, in the interlayer region [2].

Clay minerals are classified by their arrangement of tetrahedral and octahedral sheets, chemical composition of the layers and type of chemical bonds between the layers. Thus, 1 : 1 clay minerals contain one tetrahedral and one octahedral sheet per clay layer; 2 : 1 clay minerals contain two tetrahedral sheets with an octahedral sheet between them. In certain situations an extra aluminum octahedral layer will form in 2 : 1 clay minerals which can be considered to be a 2 : 1 : 1 clay mineral. Such minerals contain an octahedral sheet that is adjacent to a 2 : 1 layer as in chlorite clays. In 1 : 1 clays there can be one sheet of silicon atoms (tetrahedral structure) and one sheet of aluminum atoms (octahedral structure) as in the case of kaolin. Substituting 3 Mg

Table 9.1 The different types of clay used in nanocomposite preparation

Mineral	Type	Interlayer bonding	CEC	Swelling	Specific surface area, $m^2\,g^{-1}$	Basal spacing, nm
Kaolinite	1 : 1 nonexpanding	Lack of interlayer surface, strong hydrogen bonding	3–15	Almost none	5–20	0.72
Montmorillonite	2 : 1 expanding	Very weak bonding	80–150	High	700–800	0.98–1.8 +
Vermiculite	2 : 1 expanding	Weak bonding	100–150	High	500–700	1–1.5
Hydrous mica	2 : 1 nonexpanding	Strong bonding	10–40	Low	500–200	1.0
Chlorite	2 : 1 : 1 nonexpanding	Moderate to strong bonding	10–40	None	—	1.4

(Reproduced with permission from S. Grunwald and K. McSweeney, "Secondary Silicates," University of Wisconsin-Madison, Department of Soil Science, http://www.soils.wisc.edu/courses/SS325/silicates.htm#structsil (accessed February 22, 2008).)

in a kaolin structure [$Al_2Si_2O_5(OH)_4$] results in a serpentine mineral [$Mg_3Si_2O_5(OH)_4$]. In a 2 : 1 assemblage as in the case of a smectic mineral like montmorillonite (MMT), there are three sheets comprising of aluminum atoms (octahedral structure) lying between two sheets of silicon atoms (tetrahedral structure). In smectics substitution is mainly in octahedral layer while the maximum charge deficit in similar clay like mica is in tetrahedral layer. An interlayer sheet in chlorite clay is interpreted as $Mg(OH)_2$ while in vermiculite it is thought to be octahedrally coordinated, $6H_2O$ with Mg^{2+}. Talc {approximate molecular structure: [$Mg_3Si_4O_{10}(OH)_2$]} is also a 2 : 1 layered silicate; the regions between galleries do not contain cations as the layers are neutral. Thus the crystalline layers of talc are loosely superimposed on one another and slide over each other readily giving rise to softness and soapy feeling. Mica {approximate molecular structure: [$KAl_2Si_3O_{10}(OH)_2$]} carries negative charge in crystalline sheets and electrical neutrality is accomplished by alkali cations mostly K^+ (Figure 9.1). Other layered silicates of importance are hectorite and saponite (Table 9.2). Hectorite is mined only in limited locations. Most common synthetic clays are hectorite and fluorohectorite.

In fact the clay sheets stack upon one another like a deck of cards. In the case of smectic minerals when substitution occurs in tetrahedral layers the negative charges form on surface of silicate layers and lead to better interaction with polymer matrix than cases when substitution occur in the octahedral layer.

9.3 Role of Nanofillers in Reinforcement

The addition of general fillers to elastomer matrix affects the viscoelastic character by an increase in viscosity, limitation of chain mobility and improvement in mechanical properties. The extent to which this change occurs strongly depend on: (i) particle size, (ii) rubber-filler interaction, (iii) filler-filler interaction, (iv) filler shape and structure, (v) filler concentration and (vi) filler dispersion in the matrix.

9.3.1 Particle Size

There is a direct relation between surface area and particle size. Surface area can be expressed by $m^2\,g^{-1}$ and particle diameter in nanometers. Fumed silica can have a surface area of $400\,m^2\,g^{-1}$ and carbon black $1000\,m^2\,g^{-1}$. Approximately it can be calculated that a compound with 50 parts per hundred rubber of a reinforcing black like intermediate super abrasion furnace black (ISAF) has a filler elastomer interface of $35\,m^2\,cm^{-3}$. Dimensions of the particulate fillers for reinforcement are generally in the range 10–100 nm.

In the case of layered clays the interlayer distance is around 1 nm. Generally clays are modified to have expansion in layers for use in elastomers, the interlayer distance is generally increased by cation exchange using bigger cations and the corresponding expansion in clay layers depends on the type of cation used (Table 9.3). The alkyl chains of quaternary ammonium ions that replace the cations generally have 3–18 carbon atoms.

The concentration of cation also affects the basal spacing (*d*-spacing) [3]. The basal spacing of the natural sodium montmorillonite clay (Na MMT) is 11.8 Å. Addition of an alkyl ammonium cation at a quantity equal to 50% coverage of the CEC enhances this *d*001 spacing to 13.6 Å while further increase of the surfactant quantity leads to a substantial increase of the clay *d*-spacing up to 18.5 Å at surfactant levels of 150% coverage of the CEC and to 24.2 Å at 250% coverage of the CEC.

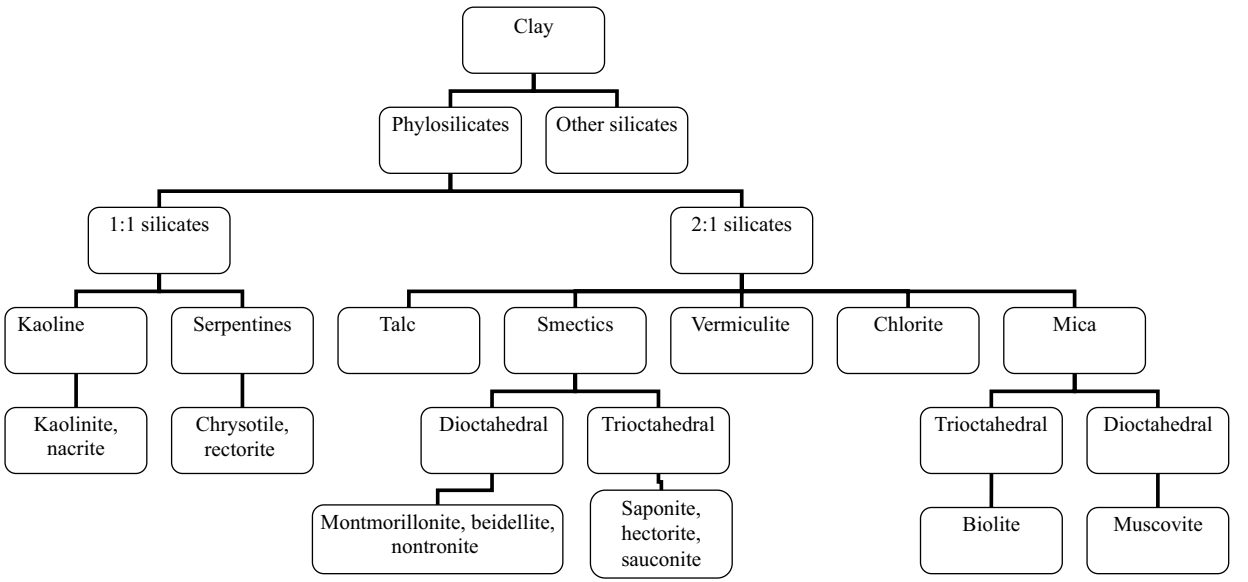

Figure 9.1 Various types of clay (Reproduced from V. Pravdic and I. Sondi, "Electrokinetics of clay mineral surfaces," *Encyclopedia of Surface and Colloid Science* (http://www.informaworld.com), **3**, 2200–2206, © 2006, with permission from Taylor & Francis Ltd.)

Table 9.2 Chemical formula and characteristic parameters of commonly used layered clays

Layered silicate	Chemical formula[1]	CEC milliequivalents/ 100 g	Particle length, nm	Location of isomorphous substitution
Montmorillonite	$[Al_{1.67}\ Mg_{0.33}(Na_{0.33})]Si_4O_{10}\ (OH)_2$	110.0	100–150	Octahedral
Hectorite	$[Mg_{2.67}\ Li_{0.33}]\ (Na_{0.33})]\ O_{10}\ (OH,F)_2$	120.0	200–300	Octahedral
Saponite	$Mg_{3.00}\ [Al_{0.33}\ (Na_{0.33})Si_{3.67}]\ O_{10}\ (OH)_2$	86.6	50–60	Tetrahedral

[1]Reproduced from W.D. Keller, "Clays," *Encyclopedia of Chemical Technologies*, **6**, 198, © 1979, with the permission of John Wiley & Sons, Inc.

Table 9.3 The interlayer *d*-spacing and gallery thickness of alkyl ammonium exchanged MMT

Cation	Interlayer *d*-spacing, nm	Gallery thickness, nm
$CH_3(CH_2)_3NH_3^+$	1.35	0.39
$CH_3(CH_2)_7NH_3^+$	1.38	0.42
$CH_3(CH_2)_9NH_3^+$	1.38	0.42
$CH_3(CH_2)_{11}NH_3^+$	1.56	0.60
$CH_3(CH_2)_{15}NH_3^+$	1.76	0.80
$CH_3(CH_2)_{17}NH_3^+$	1.80	0.84

9.3.2 Rubber–Filler Interaction

Three types of interactions affect the viscoelasticity of rubber compounds. These are interactions between rubber molecules, interaction between rubber and filler and interaction between filler particles. Generally the presence of filler alters the relative segmental mobility only slightly. However, the interaction between polymer and filler strongly influences the flow behavior and mechanical properties.

The general equation for increase in viscosity, η_0, due to hydrodynamic effect of particulate fillers in real rubber filler mixes is governed by the Guth-Gold equation [4, 5]:

$$\eta = \eta_0(1 + 2.5\,c + 14.1c^2) \tag{9.1}$$

where $c =$ volume fraction of particulate filler.

Here it is assumed that there is interaction between filler particles and they are nonuniform in spherical shape. In the case of carbon black-filled vulcanizate the change accompanying filler addition can be denoted by a change in Young's modulus. Thus the Young's modulus of a vulcanizate containing low concentrations of spherical fillers, E, can be treated like Equation 9.1 and can be modified as:

$$E_f = E_g(1 + 2.5\,c + 14.1c^2) \tag{9.2}$$

where E_f and E_g denote the Young's modulii of filled and gum vulcanizates respectively.

Though Equation 9.1 is valid for coarse fillers, for nanosized carbon black fillers the actual increase in modulus is much more than what the equation predicts. So Equation 9.1 is modified

by introducing shape factor (f) which is the ratio of longest dimension of particle to the shortest and given by:

$$E_f = E_g(1 + 0.67fc + 1.62f^2c^2) \tag{9.3}$$

The equation becomes valid when f is assumed to values close to 6, though such anisotropy is not shown by carbon black. However if it is assumed that rubber adsorbed on black surface by way of weak interactions or mechanical entrapment (filler–rubber interaction) is a part of filler then the volume fraction of filler increases and Equation 9.3 becomes more valid. Here the effective volume fraction of filler is volume fraction of filler plus volume fraction of occluded/adsorbed rubber. Thus the actual change in modulus by addition of filler can be related to concentration of filler. The interaction between rubber and filler is quantified by bound rubber content which is the fraction insoluble in a solvent that generally dissolves NR, like toluene. An efficient method of estimating Young's modulus of a rubber vulcanizate is from measurement of hardness.

9.3.3 Filler-Filler Interactions

Filler-filler interactions play a significant role due to breakage of the filler network. In the case of fillers that form aggregates there can be a breakage and recovery of weak physical bonds linking adjacent filler-filler aggregates, called the Payne effect [6].

The Payne effect is reflected under cyclic deformations with small strain amplitudes and is manifest as a dependence of the viscoelastic storage modulus on the amplitude of applied strain. Above approximately 0.1% strain amplitude, the storage modulus decreases rapidly with increasing amplitude. At large amplitudes of about 20% the storage modulus approaches a lower bound. A pure gum vulcanizate shows a constant modulus over this range of amplitude. A similar effect called the Mullins effect [7] occurs at larger deformations due to slippage of polymer chains over the surface of filler particles. Mullins observed that under cyclic loading of high strains, the virgin material exhibits a relatively stiff response. When the material is subsequently unloaded, then reloaded, the stress-strain curve follows a significantly softer path. After several cycles, the stress-strain response stabilizes. If the previous maximum strain is not exceeded, the effect is relatively permanent. The slippage of chains also contributes to frictional loss. So the presence of reinforcing fillers can increase heat build-up under cyclic deformations of high amplitudes along with an increase in permanent set.

The filler particle may serve as physical crosslinks due to physical or chemical interactions involving filler and rubber. The filler can physically be entrapped in the rubber and acts as a part of filler. Due to these factors fillers can share in the load-bearing process when vulcanizate is strained. When fillers contribute in sharing load during deformation their presence in the matrix leads to higher strength. There is a considerable increase in modulus by the incorporation of nanofilllers in rubber, which is considered to be due to the overall effect of crosslinking of polymer network, hydrodynamic effect, polymer-filler interactions which may be physical and chemical and formation of occluded rubber.

9.3.4 Shape and Structure of Filler

There is variation in viscoelasticity and accompanying mechanical properties when the shape and structure of filler vary. Increase in viscosity with filler loading is much greater for acicular

clay (attapulgus clay) than clays which occur as platelets (ASP 400 clay). In comparison the increase in viscosity with spherical fillers (calcium carbonate) is very low. The increase in viscosity due to variation in shape factor arising from any of the factors described above can be approximated by Equation 9.2 by replacing the term viscosity by modulus. Carbon black exists as aggregates which can be compact, voluminous or branched, and all these factors contribute to the definition of structure. Structure is evaluated as void volume using dibutyl phthalate (DBP). On mixing with DBP, when void volumes are filled viscosity shows a sharp increase. The shape and structure of filler also affects barrier properties. Fillers with a high aspect ratio (similar to shape factor *f* used in Equation 9.2) improves barrier properties like air permeability and solvent diffusion, more effectively than spherical fillers. The exfoliated clay layers and intercalated bundles strongly restrict the motion of polymer chains which also reduce the efficient diffusion of gas molecules. The aspect ratio exerts a stronger effect on diffusivity (D) than on permeability. In a system filled with dispersed particles of aspect ratio α, D is related to aspect ratio [8]:

$$D = D_0[1-c/(1+\alpha/2)\,c] \tag{9.4}$$

where D_0 is the diffusivity of amorphous polymer and c is the volume fraction of filler.

Reinforcing fillers resemble additional chemical crosslinks on their effect in a rubber vulcanizate. They increase modulus and decrease swelling by solvents. However they show enhanced creep and compression set.

9.3.5 Filler Reinforcement with Reference to Concentration and Cure

Filler reinforcement is much pronounced with noncrystallizing synthetic rubbers like styrene-co-butadiene (SBR) and acrylonitrile-co-butadiene (NBR) in comparison with NR. There is an optimum loading for reinforcement properties such as tensile strength, tear strength and abrasion resistance whereas stiffness increases steadily with elongation and decreases at higher loading. For layered clays which are used in concentrations of less than 10 parts per hundred rubber (phr) there is also an optimum concentration beyond which there is re-agglomeration of fillers, leading to inferior mechanical properties, and this is around 5 phr in most polymers. In blends of ethylene-co-vinyl acetate (EVA)/natural rubber (NR) there is good dispersion at a loading of 2 phr, while at higher loading of 8 phr there is agglomeration of filler in both peroxide and sulfur cure systems [9]. There is a possibility of good dispersion of nanofillers when the individual clay layers get separated, leading to a structure of exfoliation. In exfoliated condition layered clays improve the mechanical properties very effectively in low doses in the range 0.5–1.0 phr.

Carbon blacks like high-abrasion furnace blacks (HAF) act as catalysts and accelerate the vulcanization reaction. During sulfur vulcanization, it is required that sulfur molecules which exist as rings of eight atoms have to be opened to form active sulfur. Carbon black can help ring opening process of S8 molecules. The dissociation of an accelerator like benzothiazyl disulfide (MBTS) is faster when it is heated together with sulfur, rubber and carbon black [10]. Generally, the acidic nature of filler and a tendency for absorption of accelerators retard vulcanization as in the case of silica filler.

Organoclay generally increases crosslink density in sulfur vulcanization. While organo-clay enhances curing through accelerating effect of quaternary ammonium salt used for modification, unmodified clay shows cure retardation due to absorption of curative by clay for

in situ clay modification. Na MMT can adsorb curatives for modification in fluorocarbon rubber [11]. Amines used for modification of clay can increase the rate of vulcanization in rubber compounds and also due to their interaction with sulfur promote intercalation of rubber molecules into galleries, resulting in reinforcement.

9.4 Methods to Enhance Polymer-Filler Interaction and Reinforcement

Confinement of matrix within filler also promotes reinforcement. The reduction in filler-filler interaction and promotion of rubber filler interaction is the basic concept of reinforcement by nanofillers. They impart reinforcement as long as they are well dispersed, have a polymer-filler interaction and are compatible with the polymer matrix. These conditions are achieved by: (i) micromechanical interlocking, (ii) physical and chemical interactions.

9.4.1 Micromechanical Interlocking

Spherical fillers like silica and carbon black exhibit structure and there is the chance for formation of immobilized rubber leading to reinforcement. In the case of layered silicate, due to intercalation of polymer molecules confined between gallery regions, rubber becomes immobilized to a small degree. In the case of tubular nanofillers like carbon nano tubes due to imperfections in the otherwise smooth surface, there can be mechanical interlocking leading to immobilization in a small degree.

9.4.2 Physical and Chemical Interactions – Modification of Nanofillers

The reactive sites on nanofillers, both those formed during their production and those introduced by suitable modification, help in reinforcement by enhancing the polymer-filler interaction. The functional groups present on fillers like carbon black and silica are able to react with functional groups present on rubbers. In the case of carbon black the filler interaction is mainly of a physical nature, whereas in the case of silane coupling agent a chemical bond between silica and rubber is established. There can be physical adsorption of rubber on the surface of carbon black during processing operations. Polymer free radicals are formed during mixing due to the shear forces generated. Such free radicals react with carbon black to form bound rubber as carbon black acts as radical acceptors. In organoclays polymer can interact with hydroxyl groups present on clay or suitable groups present on the surfactant used for modification.

Nanofillers like silica and layered clays exhibit poor wettability leading to poor dispersion in rubber. This can be improved by: (i) surface modification (through the introduction of suitable functional groups by chemical reactions) and (ii) surface coating. Obviously by these techniques there is introduction of functional groups on filler surface.

9.4.2.1 Surface Modification of Nanofillers

Spherical Fillers

Surface treatment to improve filler polymer interaction has become very common in rubber industry. The material used for surface modification is one which is compatible with chemical

nature of both rubber and filler. Stearic acid and their metallic salts are good examples of surface active agents. For inorganic nanofillers a coating of the filler surface by stearic acid or silanes reduces the tendency to agglomerate and also increases compatibility with the rubber matrix. The surface energy of silica can be reduced by adding glycols or amines in rubber compound. Nano zinc oxide is stabilized by hydroxyl functional oligomers. Calcium carbonate is generally coated with stearic acid or even with (γ-aminopropyl) triethoxysilane. There is a limitation for using a coating to increase compatibility with the rubber matrix. Even though the properties of polymers are improved by addition of surface active agents, the effect does not last in humid conditions or during a long storage period. This is solved by introducing suitable functional groups on the filler surface through chemical reactions.

There are many coupling agents that can be used to enhance polymer-filler interaction and include silanes, phosphorous esters, titanate coupling agents and chromium acid complexes. Organosilanes are widely used for the modification of silica surfaces. Coupling agents may be added directly to polymers or may be fixed to the fillers prior to their addition to polymers. The reaction between organosilane and silica called silanization brings about hydrophobation of silica, reduces the filler network and makes silica compatible with polymer [12]. The reduction depends not only on the degree of hydrophobation but also on the kind of silane used. Long chains cover the silica surface more efficiently and/or form self-oriented layers that shield the surface than short chain silanes. Silane coupling agents have dual reactivity since they are capable of reacting both with polymer and filler. The stability of polymer-filler attachment appears to be related to the strength of covalent bonds between polymer and filler. Surface-treated clay such as kaolin is prepared by a process in which the clay surface is preconditioned by treatment with gaseous hydrogen and then functionalized by reaction with a polymerizable organic moiety of an organic compound. The products are useful as fillers for rubber, resin, plastic and paper.

Layered Silicates

Layered silicates used in production of nanocomposites are also polar and hydrophilic. Some polar polymers like Nylon 6 and some type of epoxies will intercalate into pristine silicates. But elastomers are highly hydrophobic and there is need for suitable modification of layered silicates in order to have good dispersion in the matrix.

The modifier may be associated with silicate by strong interactions (covalent or ionic bonds) so as to make it less hydrophilic. The most commonly used modifiers are alkyl ammonium salts. Other cationic surfactants like phosphonium, pyridinium and imidazolium salts are also used for modification. Not only does the clay become hydrophobic but also the interlayer distance increases by this process. Such modified clays allow rubber molecules to intercalate into the interlayer space or even tear apart the layers leading to exfoliation of layers. The simplest way to reduce hydrophilic nature of silicate layers is by surfactant ion exchange method, wherein the cation of the surfactant enters the layers displacing the ions present in the gallery region and the result is an organosilicate. In a general process for this first a diluted dispersion of layered silicate in deionized water is prepared through a process of sonication by which the layered silicates can be effectively dispersed [13]. To this a solution containing twice the surfactant stoichiometrically necessary for complete exchange is added. The amount of cation is calculated based on CEC. The reaction mixture is held at 70 °C for the reaction to complete. After complete reaction the organosilicate is filtered or centrifuged from reaction mixture and washed repeatedly to remove excess surfactant and dried.

In the "molten surfactant exchange method" the reaction is the same but mobility is given to surfactant by melting it in the presence of silicate. If equilibrium is favorable to start with, the high temperature helps to drive the ion exchange, allowing the use of an approximately stoichiometric amount of surfactant (in some cases slightly higher) for complete exchange. This technique is widely adopted for the large-scale modification of clay. Alternatively functional groups can be introduced by reactions with suitable agents. Laponite clay is modified by grafting either γ-methacryloyloxy propyl dimethyl-methoxysilane (γ-MPDES) or γ-methacryloyloxy propyl triethoxysilane (γ-MPTES) onto the clay edges [12].

A functional group can be introduced along with an increase in interlayer distance by suitable techniques. For instance, MMT is modified with aminosilanes along with surfactants so as to have an increase in layer spacing and also introduction of functional group [14]. Clay-modified aminosilanes are reported to show enhanced mechanical properties as in maleic anhydride-grafted polypropylene clay nanocomposites due to interaction between functional groups on the clay surface and polymer [15].

Tubular Fillers

Generally it is very difficult to get a good dispersion of carbon nanotubes (CNT) in a polymer matrix due to the tendency of nanotubes to form aggregates by van der Waals forces. The absence of functional groups also adversely affects dispersion. Grafting with suitable polymer chains increases compatibility with polymer matrix [16–19]. A breakthrough for the use of tubular nanofillers was achieved by chemical bonding of suitable functional groups onto the surface [20, 21]. Under suitable conditions surfactants, polymers or aromatic compounds get adsorbed on surface of nanotubes and result in enhanced compatibility with polymer matrix [22].

Modification [23] of carbon nanotubes by oxidation was found to give homogeneous dispersion of multiwalled carbon nanotubes (MWCNT) throughout SBR matrix and strong interfacial adhesion between oxidized MWCNT and the matrix, along with considerable enhancement of mechanical properties of the composite.

9.5 Role of Nanofiller as Compatibilizer

The influence of fillers on the miscibility of rubber blends is of immense technological interest for both thermoset rubber blends and thermoplastic vulcanizates used in rubber industry. In rubber blends, there is uneven crosslinking, heterogeneous filler reinforcement and nonuniform elastomer mixing that lead to a narrow interphase and poor physical or chemical interactions between the two phases. All these factors influence the mechanical properties of rubber blends.

Exfoliated clay layers are capable of severely reducing coalescence between dispersed domains in polymer blends due to nano level dispersion of clay layers that act as physical barriers. For instance the dispersed domain size of poly (ethylene-ran-propylene) rubber (EPR) in incompatible polymer blends of nylon 6/EPR decreases significantly in the presence of a small amount of organoclay [24]. The dispersed domain size of ethylene propylene diene monomer rubber (EPDM) in incompatible polypropylene (PP)/EPDM blends is also reduced significantly by the addition of nanoclay [25]. There are several reports to show that organoclay acts as a compatibilizer in immiscible polymer systems [26–28]. Compatibilizers act through a chemical reaction (reactive compatibilization) or by its capability for interaction with blend

components or its interaction with chemicals present at the interface of blend components. Most of the interactions are intermolecular forms of attraction such as van der Waals and hydrogen bonding, based on the polarity of materials (nonreactive compatibilization). The surfactants present in organoclay also contribute in compatibilization. In polystyrene/poly (methylmethacrylate) (PS/PMMA), there is a drastic reduction of domain size in the presence of modified clay which is attributed to the combination of partial compatibilization by excessive surfactants in organoclays and increased viscosity. It is also possible that two immiscible polymer chains can intercalate the same clay platelet and play the role of a block or graft copolymer. Generally graft or block copolymers have similar segments to blend components and hence act as compatibilizers in blends. If the filler has a strong interaction with a particular elastomer of the blend it is enriched in that component while it is depleted in the other.

Carbon black has a stronger interaction with polybutadiene rubber than with butyl rubber due to large number of unsaturated bonds in the former system and the affinity of carbon black generally follows the order, polybutadiene rubber(BR) > SBR > polychloroprene rubber(CR) > NBR > NR > EPDM > isoprene-co-isobutylene rubber (IIR).

Nanoclay also shows preferential migration to specific rubbers when used in blends. The migration depends on the polarity of polymer and type of surfactant used for clay modification. In polyurethane rubber (PUR)/NR) blends layered clay preferentially goes to the PUR phase with which it is more compatible [29, 30]. In NR/EVA blends organoclay has a strong tendency to be located in the EVA phase [31]. In blends of PP and maleated ethylene propylene rubber (EPR-g-MA) organoclay showed preferential migration and significant level of exfoliation in the EPR-g-MA phase.

Organoclay is more compatible with polar rubbers and thus produces intercalated or exfoliated structures. In a polar rubber like NBR the acrylonitrile content influences the morphology of the nanocomposite. Within the nitrile rubbers, the ability for exfoliation decreases as acrylonitrile content increases [32]. In the case of organoclay incorporated SBR with increasing styrene content, the dispersion of clay and hence mechanical properties show an improvement [33]. It is difficult to obtain a completely exfoliated structure in nonpolar systems.

By introducing functional groups the polarity can be changed so as to have better filler dispersion and hence compatibilizing action as when epoxidized natural rubber (ENR) has been used as a compatabilizer in NR clay nanocomposites. In the case of a functionalized rubber like ENR it can affect clay dispersion due to the enhanced interaction and also increased level of vulcanization by reactions involving the epoxy groups. Thus the presence of polar rubbers in small proportions or in large proportions as blend components give intercalated or exfoliated structures. In the case of rubber blends there is the possibility of interfacial crosslinks, and thus an organoclay incorporated blend consisting of a small proportion of polar rubber shows improved mechanical properties. Here at least in a small degree layered clay acts as a compatibilizer. Rubber blends of NR/NBR [34], NR/(carboxylated styrene-co-butadiene rubber) XSBR [35] and NR/PU [30] have intercalated and exfoliated structures.

The interaction of both blend components with suitably modified nanofiller can influence the phase morphology of blends. Nanosized calcium carbonate modified by stearic acid acts as a compatabilizer in blends of styrene-co-acrylonitrile (SAN) and EPDM due to a reduction in surface energy of filler and enhanced polymer-filler interaction [36]. In 50 : 50 PP/EPDM blends the size of dispersed EPDM phase is significantly reduced by addition of nanoclay [25].

The impact properties of PP are considerably improved by incorporation of an ethylene-octene copolymer and nano calcium carbonate due to the synergistic effect of the latter two ingredients [37].

In reactive compatibilization, the compatibilizer acts also through a mechanism as a surfactant by having hydrophobic interaction between hydrophobic parts of both polymer and surfactant. Chemical interactions involving functional groups also enhance clay dispersion. A maleated rubber such as ethylene propylene rubber-grafted malefic anhydride (EPR-g-MA) is known to act as impact modifier and compatibilizer for polyamide 6 (PA6)/PP blends. The synergistic effect of surface modified montmorillonite nanoclay and maleic anhydride-grafted PP (MA-g-PP) could improve the strength and stiffness of PA6/PP nanocomposites, due to a better matrix interfacial interaction between the constituent materials [38].

Unmodified clay can be exfoliated by polar rubbers. In Nylon-6/clay/acrylate rubber ternary nanocomposite, the acrylate rubber particles and clay platelets help each other to disperse or exfoliate in the Nylon-6 matrix. The silicate layers without organic treatment are exfoliated with the aid of irradiated acrylate rubber particles and the irradiated acrylate rubber particles are uniformly dispersed in the matrix with the aid of clay platelets. The novel nanocomposite prepared by spray drying mixture of irradiated rubber latex and clay followed by blending with Nylon-6 shows simultaneously high impact strength, high flexural modulus and high heat distortion temperature [39].

9.6 Structure Compatibility Concept of NR-Based Latex Blends

9.6.1 Forms of NR Suitable for Blend Nanocomposites

9.6.1.1 Fresh NR Latex

Fresh NR latex is a colloidal dispersion of rubber particles in an aqueous serum and stabilized by proteins along with smaller quantities of fatty acid soaps formed through lipid hydrolysis. Fresh latex coagulates by neutralization of the charges present on rubber particles arising from adsorption of proteins and soaps. The proteins adsorbed react very slowly with acids. As fresh latex is predominantly protein stabilized system, coagulation of latex takes several hours. The time of coagulation is reduced by addition of surfactants based on fatty acids to latex before adding coagulants [40, 41]. The added fatty acid soaps get adsorbed on rubber particles and remain in the coagulated rubber. This has the added advantage that the uniformly distributed fatty acids formed during coagulation affect the cure characteristics depending on the type of surfactant used. Laurates impart excellent cure characteristics and mechanical properties while oleates give poor aging characteristics.

There is a very high polydispersity for both particle size and molecular weight in fresh NR latex. Alpha terminal group of rubber chain in fresh latex consists of mono- or di-phosphate groups linked with phospholipids. The association or micelle formation of phospholipids is expected to form long chain branching of molecules [42].

9.6.1.2 Latex Concentrates

Latex concentrates are obtained by centrifugation or creaming process. During the centrifugation of ammonia preserved NR latex comparatively bigger particles separate into the

creamed fraction as centrifuged latex and smaller particles separate into skim fraction. A similar process takes place during the creaming operation performed by the addition of creaming agents like alginates, a small quantity of which remains in the creamed latex. The particles in NR latex concentrates are stabilized predominately by fatty acid soap-based surfactants and consequently coagulate quickly on addition of acids. The rubber molecules are highly entangled and branched. The products prepared directly from latex have high strength due to long chain branching and high molecular weight, as the branched structure of rubber molecules remains even after drying them into films [43].

9.6.1.3 Skim Latex

Skim latex is a protein-rich byproduct obtained during the centrifugal concentration of natural rubber latex. Normally, the rubber content of skim latex is in the range 2–10%. It contains about two-thirds of the total serum from the field latex. The average size of its rubber particles is smaller than that of field latex. In addition to the water soluble substances in serum, latex contains higher quantity of proteins which are mainly distributed as adsorbed ions on the surface of the rubber particles. It contains a higher quantity of fatty acid soaps and has more metallic contaminants like manganese and copper ions. Due to these factors coagulation is difficult, and the rubber recovered has a faster-curing behavior with a higher hardness, modulus and higher compression set along with poor aging characteristics depending on the content of pro-oxidants.

The rubber molecules are found to be linear and have no fatty acid ester groups linked to the chain ends. Due to this chain entanglement involving fatty acid ester group of phospholipids is reduced and consequently shows reduced green strength [43, 44]. Due to these factors there is enhanced ability of intercalation as compared to rubber molecules that show long chain branching due to intermolecular interaction.

9.6.1.4 Prevulcanized Latex

One advantage of latex concentrate is that it can be prevulcanized. Prevulcanization is a modification carried out in NR latex for the production of latex-based goods. On heating latex with curatives added as dispersions it is possible to crosslink the individual particles in latex without destroying the colloidal character. It appears that the crosslinking takes place in individual particles so that after prevulcanization the rubber particles have the same shape, size and distribution as the initial latex. Prevulcanization is carried out by reactions of latex particles with sulfur and accelerators in presence of activators by heating at temperatures around 50 °C for about 2–4 h. Alternatively by heating latex with peroxides and activators at specific temperature for specified time or by exposing latex to high energy radiation like gamma rays, it is possible to prevulcanize latex.

The level of prevulcanization is assessed by coagulation with chloroform. Unvulcanized latex coagulates as a consolidated mass, while fully prevulcanized latex coagulates as a powder. NR vulcanizates in powder form can be obtained by coagulation of fully vulcanized NR. Ultrafine fully vulcanized powdered rubber prepared by irradiation of natural rubber latex containing sensitizers with rubber particles of size 50–150 nm find use as impact modifiers when blended with plastics [45].

9.6.1.5 Dry Natural Rubber

The color of dry NR generally varies from a light honey color to black. However, the pale latex crepe rubber obtained using suitable processing techniques including a bleaching process for the removal of coloring agents, is white in color.

The linked unsaturated fatty acid groups of NR molecules undergo oxidation to form carbonyl groups and produce intermolecular crosslinking involving the proteins. This leads to a storage hardening process for dry NR which is generally quantified by an increase in viscosity. The green strength of natural rubber is attributed to long chain branching, interaction between polar groups, presence of gel and chain entanglement. The rubber molecules undergo crystallization on stretching to about 300%. The difference in these factors account for the difference in green strength within different types of NR or other elastomers [46–48].

9.6.2 Important Synthetic Latices used in Blend Nanocomposites

The majority of synthetic latices of industrial importance contain copolymers based on styrene, butadiene, acrylonitrile and so on and a homopolymer based on chloroprene [49]. Emulsion copolymerization provides a way of fixing dissimilar monomer repeat units to remain in close proximity in the polymer phase. The important types of synthetic latices are: (i) styrene butadiene copolymer latices, (ii) acrylonitrile butadiene copolymer latices, (iii) polychloroprene latices, (iv) vinyl acetate polymer latices, (v) acrylic latices and (vi) vinyl chloride and copolymer latices. A typical aqueous emulsion polymerization is carried out by slowly stirring water, monomer, initiator and surfactant. At a suitable temperature the initiator decomposes to give free radicals that initiate the polymerization reaction. The reaction may be controlled by adjusting temperature and time, by the addition of a short stop and by removal of unreacted monomers.

Synthetic latices are made of spherical particles, much smaller and more uniform in size in comparison with natural rubber latex. They are coagulated by acids, metal salts and certain solvents. Since they have larger quantity of surface adsorbed stabilizers, usually soap, they dry slowly. Mechanical stability of synthetic latex is generally superior to NR latex. Even with high levels of colloidal stabilization rubber particles are rarely saturated with adsorbed stabilizers. Hence when mixed with NR latex there is tendency for adsorption of stabilizers present on NR latex and to cause microflocculation. The wet gel strength of synthetic latex is generally lower than NR latex mainly because interparticle integration is hindered by branching present in polymers along with the presence of high amount of colloid stabilizers. Concentration by centrifugation is usually not possible because particles are too small and in some cases the difference in specific gravity between particle and dispersion medium may not be sufficiently large. Functional groups introduced in rubbers provide additional sites for vulcanization, improves compatibility with NR and also confer special properties to the rubber.

Introduction of functional groups in acrylonitrile butadiene or styrene butadiene copolymers results in rubbers with superior properties as in carboxylated acrylonitrile-co-butadiene rubber (XNBR) and styrene-co-butadiene rubber (XSBR). There is enhancement in mechanical and chemical stability for latex along with improvement in wetting characteristics and adhesion to fibrous fillers. Generally the rubber shows enhanced chemical resistance and improved adhesion to other matrices. The superior resistance of XNBR to oil and solvent along with

abrasion makes it suitable for industrial glove dipping. The degree of carboxylation has significant effect on latex dipping performance. The accepted level of carboxylation is between 3 and 6%. At the highest level, it causes excessive stiffening with ZnO. In XSBR, levels of carboxylation vary from 1% to more than 10% while the styrene content varies from 45 to 60%, which is considered to be the optimum range for good mechanical properties.

Among the additional reagents that react with carboxylated polymers are metal oxides, polyamines and epoxies. Considerable use is made of such reagent for the crosslinking of polymers contained in carboxylated synthetic latices. Vulcanization is generally carried out by sulfur and accelerators. In addition peroxide curing is also employed. Vulcanization by gamma radiation and electron beam is also practiced.

9.7 Solubility Parameter and Mixing of Latices

For mutual solubility or miscibility, the difference between the solubility parameter values of polymers 1 and 2 must be less than 1. In the case of rubbers with a wide difference in polarity, suitable compatibilizers are incorporated in small proportions to enhance miscibility when used in blends. The compatibilizers used generally are those that have segments with chemistry similar to each of the blended components. Methyl methacrylate-grafted natural rubber acts as a compatibilizer in blends of NR and NBR [50].

Polar interactions or any interactions leading to crosslink formation favor compatibility between rubbers during mixing. Functionalized forms of NR are well known to have interactions with suitably functionalized synthetic rubber. For example, blends of carboxylated nitrile rubber and epoxidized natural rubber crosslink without the aid of vulcanizing agents [51].

Along with interactions between rubbers there is the possibility of covulcanization in latex blends. Prevulcanization of one of the phases and covulcanization involving blend components is expected to increase dispersion of nanofillers.

9.7.1 Particle Size and Molecular Weight

The particle size of fresh *Hevea* latex can have a bimodal distribution with a mean diameter of 1.07 μm [52] and in some cases a lower size range of 0.08–0.75 μm [53]. The particle size of skim latex is shown to be about 0.1 μm [54] or in the range 0.07–0.99 μm [55]. This is expected because particles which are small generally separate into skim fraction.

For fresh NR latex particle size varies from 50 to 1300 nm while synthetic latices are smaller in size. The average particle size of high ammonia centrifuged latex is about 510–600 nm, of low ammonia latex concentrate is 480–500 nm and of creamed latex is about 494 nm. With this there is the possibility of selecting NR latex of suitable particle size appropriate for blending with synthetic rubber latices. NR present in latex particles has a number average molecular weight of about $5 \times 10^5\,\mathrm{g\,mol^{-1}}$ while synthetic rubbers generally have a lower molecular weight. It is believed that rubbers present in smaller particles of natural rubber latices have higher molecular weights [53]. However, more extensive analysis is required to understand correlation between rubber particle size and the molecular weight in different rubber yielding plants.

9.7.2 Nonrubber Solids and Total Solids Content

In latex, the interphase of polymer particle-aqueous phase develops an electrostatic charge due to adsorption of ionized surface active materials. In the presence of the preservative, ammonia, the fatty acids obtained from phospholipid hydrolysis form fatty acid soaps and adsorb onto rubber particles. Fatty acid soaps added to latex also get adsorbed onto rubber particles. In synthetic rubber latices in spite of the presence of higher nonrubber solids there is an absence of full coverage of rubber particles by surfactants. In a latex blend system comprising of particles with different chemical structure and size there exists the possibility of a change in the nature of functional groups bound to the surface of rubber particles due to displacement of less-active surfactants by the more-active ones. The fact that by judicious choice of surfactants, the nature of adsorbents, their interaction with modified clay and their sensitivity to coagulants can be controlled plays a major role in production of rubber blend nanocomposites.

9.8 Preparation of Nanocomposites

Two different approaches are generally used for the production of polymer nanocomposites based on layered silicates. One approach involves enhancing the mobility of polymer chains, in the presence of silicate layers due to thermodynamic compatibility between polymer and clay. This technique is employed in melt blending, solvent casting and latex stage compounding. The other approach attempts to literally force the layers apart through the preferential insertion of material in the interlayer galleries by *in situ* polymerization techniques.

9.8.1 Solution Blending

Solution blending is used mostly for composites based on layered and tubular nanofillers. Here also modified clay is effective as compared to unmodified clay. The layered silicate is dispersed in suitable solvents along with the polymer and thoroughly mixed. At the end of the reaction, solvent is allowed to evaporate. The curatives can be added either before solvent removal or in the dry form after solvent removal. The solvent not only helps in increasing the layer spacing but also imparts mobility to the rubber molecules. The dispersion is expected to be enhanced as compared to melt intercalation. Addition of a modifier like silane coupling agent along with clay further enhances the compatibility with rubber matrix [56].

9.8.2 Latex Stage Compounding

In the manufacture of rubber products it is a requirement to add various quantities of fillers, plasticizers, curatives and other ingredients prior to the vulcanization step. Intimate mixing of the ingredients call for energy consuming and expensive equipments like intermix or two roll mixing mill. Further it is very difficult to disperse the different ingredients and there are chances of fine powders going into the surrounding air. This leads to health concerns due to inhalation and environmental pollution. Latex stage compounding offers a potential alternative in rubber product manufacture due to these major concerns of energy consumption, health hazards, increased labor and environmental problems as the method is easy and simple. Being known that a large number of rubbery polymers that need to be used in blends are available commercially as natural, synthetic or artificial latices, there exists the possibility of a simple and environmental friendly means for

production of latex based nanocomposites. By blending with synthetic latices some problems related to protein allergy of NR latex can be alleviated. Low viscosity of latices enables the application of high shear forces during mixing. Suitable modification in the coagulation characteristics and nonrubber solids can be introduced. By latex stage compounding there is the possibility of using prevulcanized latex that can directly be converted into nanocomposites or nanofiller incorporated latex that can be coagulated, dried and then processed conventionally.

Comparatively higher amount of fatty acid soaps are adsorbed on rubber particles of both NR and synthetic latices. Water is a good agent for expansion of clay layers. Hence organoclay gets more uniformly dispersed in latex blends. The coagulation characteristics and interaction between rubber and filler can be enhanced by the type of nonrubber ingredients in latex. Latex stage mixing has been commercially used in the production of carbon black master batch.

9.8.2.1 Mode of Incorporation of Compounding Ingredients

Homogeneous dispersions of polymers, a requirement for enhancement of mechanical properties in polymer blends is easily achieved in polymer blend nanocomposites by mixing the ingredients in emulsion forms. Usually dispersions of nanofillers like carbon black, silica, layered clays, calcium carbonate and so on, prepared using suitable surfactants, are added to the latex under slow stirring. Rather than adding as dispersions, nanosized fillers can be produced in the matrix by a precipitation process.

Carbon Black Master Batches

The advantages of using master batches instead of carbon black itself include improved cleanliness, higher filler loading, improved dispersion, reduced power requirement of mixing, convenience of storage, handling and weighing. Disadvantages are the interference of adsorbed dispersing agents used during preparation of dispersion that may lead to partial deactivation of the filler surface. In addition there are reports of the likely intervention of polymer-filler interaction due to the presence of proteins in latex that adsorb on the surface of carbon black and reduce polymer-filler interaction [57].

The basic method is to mix polymer latex with slurry and then coagulate the mixture with chemicals. With this method there is improvement in filler dispersion as compared to mill mixing. However, the coagulation and mixing times are longer. It is necessary to add acid at an elevated temperature to get a firm coagulum. The pH should be maintained above 7.5.

In a typical process the carbon black slurry is prepared by finely dispersing it in water mechanically without using surfactants. The slurry is injected into the mixer at very high speed and mixed continuously with NR latex stream. Under the highly energetic and turbulent conditions the mixing and coagulation of the polymer with the filler is mechanically completed at room temperature in a very short time. After dewatering, the material is dried with minimum exposure to high temperature to prevent oxidative degradation. It is reported that when filler is well dispersed in polymer, the aggregates tend to re-agglomerate during storage and vulcanization [58–60]. By suitable surface modification this re-agglomeration is reduced to a satisfactory level. A substituted aromatic ring or chain can be attached on the surface of carbon black by decomposition of a dizonium compound derived from a substituted aromatic or aliphatic amine. When carbon black surface is modified with 4-aminophenyl disulfide (APDS) there is an added advantage that sulfide groups are able to react with the polymer during vulcanization, increasing the polymer-filler interaction. This results in excellent dispersibility and stable dispersions of

carbon blacks in aqueous media. Fluffy carbon black received as slurry in water is also directly added. Carbon black master batches are popular with NR, SBR and XSBR.

Nanosilica in situ Formation

The particle size of precipitated silica filler used in rubber industry is in the range 20–80 nm. Because of the small size and the large specific area the incorporation of silica into rubbers by normal mixing techniques gives rise to poor dispersion, increase of viscosity and deactivation of curing agents. These problems are solved to a great extent by *in situ* silica formation. The earlier methods were based on a sol gel process, where silica is formed in the rubber matrix by polymerization of tetraethoxysilane (TEOS). The reaction takes place in two steps: hydrolysis and condensation, to produce silica [61–64]. *In situ* polymerization of TEOS is possible with different elastomers like in silicon rubber, ENR, SBR and NR. The compatibility of *in situ*-formed silica with rubber is improved by using organotriethoxysilane together with TEOS so that alkyl groups can be introduced on silica surfaces.

However this method has a disadvantage of use of large amount of solvent and long reaction time. This can be overcome by suitable *in situ* precipitation methods in the latex stage by addition of sodium silicate followed by precipitation using ammonia or sulfuric acid. On addition of acid to a dilute solution of silicate, silica sol is formed. Silica is precipitated from silica sol by adjusting salt concentration and pH. Precipitating agents include sodium, calcium, other polyvalent metal cations and ammonium ions.

Layered Clay Nanocomposites

Rubber nanocomposites are said to be formed *in situ* within an elastomer matrix by addition of organoclay when there are at least partially exfoliated or intercalated clay platelets. They are also formed by unmodified clay when the rubber molecules separate the clay particles into either individual layers or just silicate layer aggregates of nanometer thickness without the intercalation of rubber molecules into clay galleries. This is owing to the combined effect of clay layer expansions by hydration of intergallery cations like Na^+ or K^+ and shear forces exerted during slurry preparation. Several rubber–clay nanocomposites, NR-clay [18, 65], NBR-clay [66], XNBR-clay [67], SBR-clay [68–70] and so on are prepared by directly co-coagulating the rubber latex and clay aqueous suspension followed by traditional mixing and vulcanization. Owing to good clay dispersion, modulii, tensile strength and barrier property improvements are observed in rubber nanocomposites at comparatively low concentrations of up to 5 phr. However at higher loadings of clay about 10 phr the clay layers inhibit the strain-induced crystallization of NR. Alternatively nanocomposites are also prepared by adding aqueous clay dispersion to prevulcanized latex followed by vulcanization [71].

Latex nanocomposites can also be prepared by carrying out emulsion polymerization of suitable monomers by conventional method in presence of modified clay dispersions [12]. For example a laponite nanofiller can be modified by grafting γ-methacryloyloxy propyl dimethyl-methoxy silane onto clay edges or exchanging interlayer sodium ions by a free radical initiator. This functionalized clay is dispersed in water, and nanocomposite latex is synthesized by using a mixture of styrene and butyl acrylate along with sodium do decyl sulfate as an anionic surfactant.

Carbon Nanotube Latex Blends

Suitably incorporated carbon nanotubes provide a certain level of reinforcement in rubbers. It also provides electrical conductivity depending on the volume fraction of filler in rubber matrices that are generally thermal and electrical insulators.

Dispersion characteristics of carbon nanotubes in NR can be improved by suitable modification [72]. Carbon nanotubes are incorporated in rubber matrices after dissolution of rubber in suitable solvents followed by evaporation of solvent or by direct addition as dispersion to latex followed by conventional processing methods. Twelve-fold modulus enhancements by solution method has been reported [73]. During addition in the latex stage, the type of surfactant plays a major role in controlling the properties of nanocomposites.

9.8.3 Melt Intercalation

To facilitate intercalation and exfoliation usually modified clay rather than unmodified is used. Structure and properties of rubber clay nanocomposites depend on type of rubber, type of intercalant, melt blending conditions and vulcanization process. Better dispersion of clay also imparts transparency in nanocmposites when vulcanized with di-cumyl peroxide. As a large variety of elastomers are available in dry rubber forms and not as latex, melt intercalation provides an easy route for production of nanocomposites. For instance nanocomposites based on EVA, IIR and so on are easily prepared by addition of organoclay as dry powder during the mixing operation [74–77]. Generally rubber molecules that have a low molecular weight and contain functional groups have a greater chance for intercalation than molecules with a low molecular weight and a nonpolar nature [78]. In a nonpolar rubber like EPDM, the presence of stearic acid results in very good dispersion of clay due to the chemical reactions leading to ester formation involving carbonyl groups of acid and hydroxyl group of clay [79]. The level of intercalation also depends on the chemical nature of the surfactants used for modification. For instance a hydroxyl group-containing intercalant like methyl tallow-*bis*-(2 hydroxyethyl) quaternary ammonium ion shows better dispersion in comparison with that which does not contain hydroxyl groups in polymer matrices like hydrogenated nitrile rubber (HNBR) due to the possibility of hydrogen bonding.

With the possibility of interaction between intercalant and vulcanizing agent there can be expulsion of modifiers from the clay galleries, leading to some sort of de-intercalation. Thus, the level of dispersion is lower when there is the possibility for interaction with curatives. For example, in rubber nanocomposites, octadecyltrimethylamine-modified MMT shows a higher level of dispersion than octadecylamine-modified MMT, as the latter is more reactive with curatives [80]. In the case of natural fibrillar silicate minerals, a silane coupling agent improves dispersion in the rubber matrix, especially in SBR. This advantage includes a better interaction with rubber along with enhanced vulcanization as the sulfur atoms of the silane coupling agent (Si 69) also participate in the vulcanization reaction of SBR.

9.9 Rubber Blend Nanocomposites Based on Skim NR Latex and Fresh NR Latex: Preparation, Characterization and Mechanical Properties

As the nonrubber constituents in skim latex are higher, leading to a faster cure, the particle size is small the rubber molecules have a more linear structure, and there is the possibility of

a good interaction with synthetic latices when used in blends with them. A higher interaction with modified clay is also expected due to the ability for linear molecules to intercalate into clay galleries. Skim NR latex has a low dry rubber content of 2–6% and hence limits its use in direct blending of high proportions with synthetic or NR latices owing to problems of handling large volumes of latex and coagulation. Hence it is necessary to increase the dry rubber content by suitable methods for practical purposes. Skim latex undergoes a creaming process easily in the presence of a creaming agent like ammonium alginate. Alternatively creaming also takes place in presence of alkali and surfactant on the general principle of creaming [81]:

$$dh/dt = -(\rho - \sigma)gx^2/18\eta \tag{9.5}$$

where dh/dt is the speed at which rubber particles rise to the surface, ρ is the density of rubber particles, σ is the density of dispersion medium, x is the diameter of rubber particle, η is the viscosity of dispersion medium and g is the acceleration due to gravity. In presence of alkali and surfactant the proteins adsorbed on rubber particles reduce due to alkali hydrolysis and displacement of proteins and natural soaps by active soaps. These changes lead to loose coherence of rubber particles without actual coalescence. Thus there is an apparent increase in rubber particle size and an increase in both the density and viscosity of the dispersion medium, all of which contribute to the creaming process [82].

This method has the advantage that there is not only also an increase in dry rubber content but also reduction in particle size. Blends of skim latex and NBR latex at different proportions can undergo co-creaming (Figure 9.2). Suitably concentrated skim latex can also be used for production of NR nanocomposites either in a pure form or in blends with synthetic latices. In the presence of skim latex there is a displacement of less-active surfactants by the more-active ones, leading to an increased tendency for colloidal destabilization by acids when used in blends with other latices. Due to these changes, the sensitivity of latex blends to coagulation is also improved by the presence of suitable surfactants. The presence of nonrubber ingredients, specifically the fatty acids, help in a better rubber-filler interaction and filler dispersion. Due to

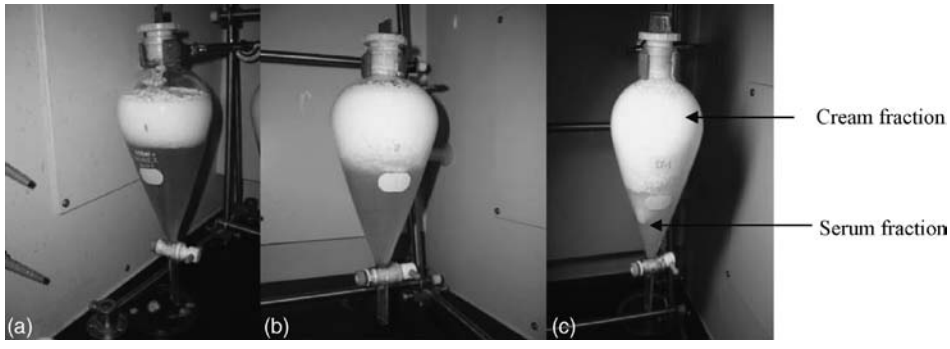

Figure 9.2 Photographs showing the creaming process of skim natural rubber latex/NBR latex with a dry rubber content of NR/NBR of: (a) 75/25; (b) 50/50; and (c) 25/75

good filler dispersion and filler-rubber interaction NR/NBR blends prepared from skim latex show very good mechanical properties. The possibility of intercalation results in enhanced modulus and tensile strength, with comparatively good elongation in skim NR and in blends with NBR (Table 9.4).

Table 9.4 Mechanical properties of NR/NBR blends based on skim NR latex[1]

Parameter	Skim NR	NBR (35% acrylonitrile content)	NR/NBR 25/75 blend	
			Gum	With 5 phr OC
Modulus 100%, MPa	1.05	1.53	1.05	1.42
Modulus 300%, MPa	1.99	3.71	2.04	3.16
Tensile strength, MPa	22	4.1	18.15	20.82
Hardness, shore A	50	50	47	52
Compression set, %	20	35	26.7	27.4
Heat build-up, °C	14	28	24	26
Elongation at break, %	600	380	650	740

ZnO 5 phr, stearic acid 1 phr and antioxidant 1 phr were used for all mixes.
S/CBS for NR was 2.5/0.8 phr, S/CBS/MBTS for NBR was 1/1.7/0.4 phr, S/CBS/MBTS for blend was 1.4/1.5/0.3 phr.
[1]Skim latex is used without creaming.

Quick coagulation of fresh NR latex provides a novel method for the production of nanocomposites. In the case of fresh NR latex, if suitable fatty acid soaps are added, there is a displacement of protein anions by added fatty acid soap anions which sensitize latex to quick coagulation by acids. These fatty acid soaps get precipitated to corresponding fatty acids and remain on the rubber after coagulation. Such fatty acids can enhance filler dispersion. Hence organoclay gets more uniformly dispersed in latex blends due to interactions involving nonrubber ingredients. As a result of quick coagulation the well dispersed clay is expected to remain unaggregated in the latex coagulum (Figure 9.3). NR/NBR or NR/XNBR blends can be easily prepared by a process of quick coagulation of latex blends. The blends have enhanced mechanical properties and oil aging characteristics (Table 9.5).

9.10 Advantages of Nanocomposites and Application of Rubber Nanocomposites

At low concentrations nano particles improve stiffness, strength, abrasion resistance, barrier effect, electrical conductivity and flame behavior in rubber vulcanizates. Improvement in air permeability (Figure 9.4) along with uniform filler dispersion gives more surface finish and fewer rejections in large-scale production of thin-walled goods like thin films, gloves, balloons, medical items and so on (Figure 9.5). Potential industrial applications of

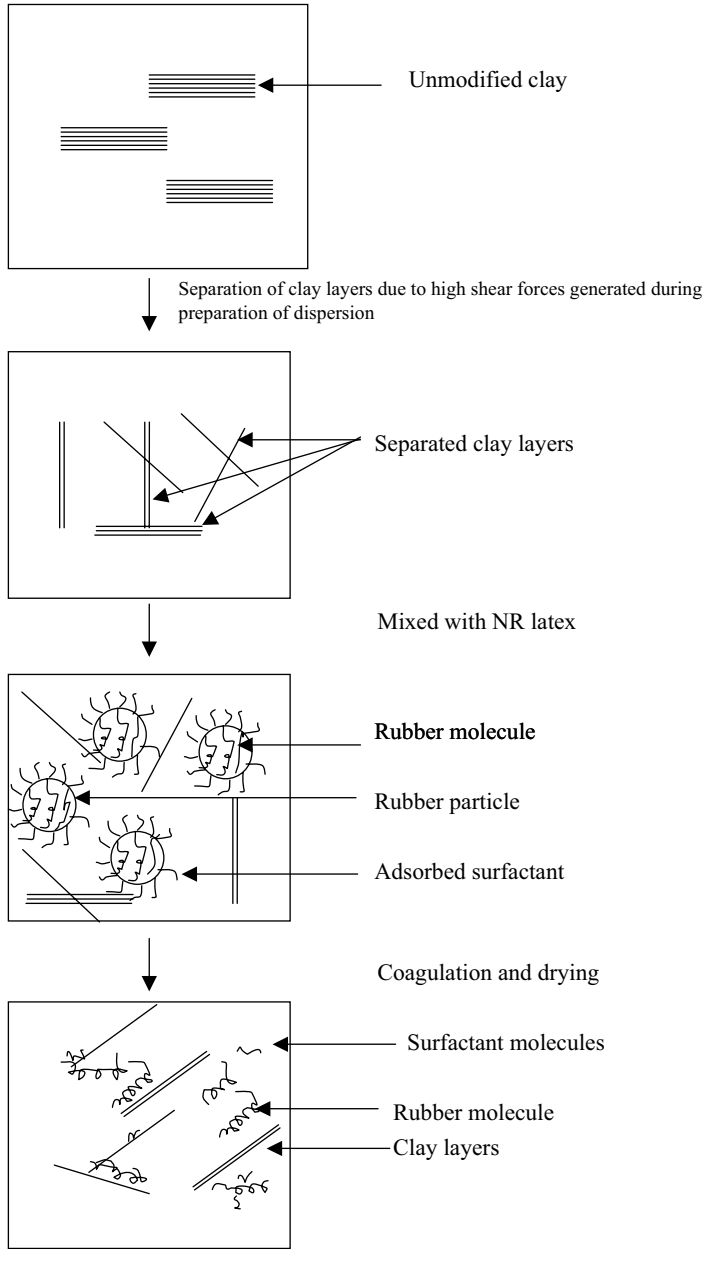

Figure 9.3 Schematic diagram showing formation of rubber nanocomposite from fresh NR latex

Table 9.5 Mechanical properties of NR/NBR and NR/XNBR blends based on fresh NR latex

Parameter	NR[1]	XNBR	NR/NBR[2], 25/75		NR/XNBR, 25/75
			Gum	OC filled	OC filled
Modulus 100%, MPa	0.97	3.25	1.44	1.96	3.26
Modulus 200%, MPa	1.5	7.2	2.50	3.25	6.14
Modulus 300%, MPa	2.4	—	3.73	4.80	11.06
Tensile strength, MPa	23.5	11.8	7.32	8.98	13.9
Hardness, shore A	40	72	59	62	65
Resilience, %	80	6	58.3	51.2	7.0
ASTM fuel c absorption 10 d/33 °C, % weight of oil absorbed	310	127	70	63.89	201

NR was cured by ACS1 formulation, S/CBS/TMTD for NR/NBR blend was 1.15/3.1/0.3 phr, S/MBTS/DCP for NR/XNBR blend and XNBR.
[1]Fresh NR latex.
[2]NBR latex of 40% acrylonitrile content.

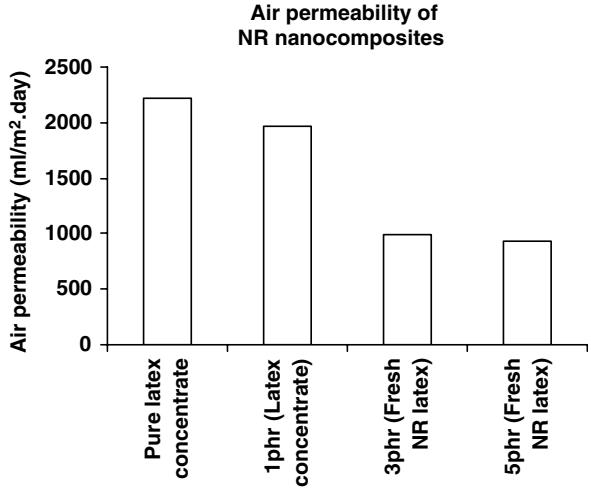

Figure 9.4 Air permeability of NR nanocomposites with nanoclay (Cloysite 91A) from latex concentrate (prevulcanized latex films 0.5 mm thick) and fresh NR latex (compression molded test slabs 2.5 mm thick) as obtained from the Lyssy gas permeability tester (model L 100–5000, Switzerland)

rubber nanocomposites include a large number of latex and dry rubber goods. Some of them are foams, catheters, tubes, packing membranes, tire inner tubes, sports goods, inner bladders of play balls, ball covers, automobile components, electrical devices, applications where electrical heating is required, electrical shielding, sensing devices and related products.

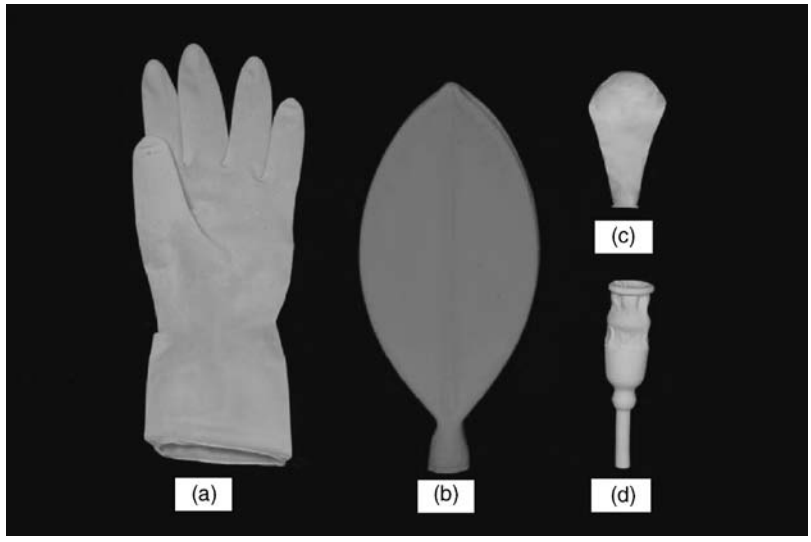

Figure 9.5 Rubber products prepared using nanoclay: (a) glove; (b) football bladder before fixing air valve; (c) toy balloon; and (d) urinary condom

References

1. Byers, J.T. (1987) Fillers, part 1 carbon black, In: *Rubber Technology* (ed. M. Morton), Van Nostrand Reinhold Company, New York, pp. 59–85.
2. Rajamathi, M., Thomas, G.S., and Kamath, P.V. (2001) The many ways of making anionic clays. *Proceedings of the Indian Academy of Sciences-Chemical Sciences*, **113**(5 & 6), 671–680.
3. Marras, S.I., Tsimpliaraki, A., Zuburtikudis, I., and Panayiotou, C. (2007) Surfactant –induced morphology and thermal behavior of polymer layered silicate nanocomposites. *Journal of Physics: Conference Series*, **61**, 1366–1370.
4. Guth, E. (1938) Observation on viscosity of rubber solutions. *Rubber Chemistry and Technology*, **11**(4), 676–679.
5. Guth, E. (1945) Theory of filler reinforcement. *Rubber Chemistry and Technology*, **18**(3), 596–604.
6. Payne, A.R. and Watson, W.F. (1963) Carbon black structure in rubber. *Rubber Chemistry and Technology*, **36**(1), 147–155.
7. Mullins, L. (1969) Softening of rubber by deformation. *Rubber Chemistry and Technology*, **42**(1), 339–362.
8. Nielson, L.E. (1967) Models for the permeability of filled polymer systems. *Journal of Macromolecular Science-Chemistry*, **1**, 929–942.
9. Munusamy, Y., Ismail, H., Mariatti, M., and Ratnam, C.T. (2008) Ethylene vinyl acetate/natural rubber/organoclay nanocomposites: effect of sulphur and peroxide vulcanization. *Journal of Reinforced Plastics and Composites*, **27**, 1925–1945, doi: 10.1177/0731684407084161.
10. Ali, M.S., Gholam Reza, B., and Ghasemzadeh-Barvarz, Massoud. (2005) Effect of carbon black on rate constant and activation energy of vulcanization in EPDM/BR and EPDM/NR blends. *Iranian Polymer Journal*, **14**(6), 573–578.
11. Kader, A.M. and Nah, C. (2004) Influence of clay on the vulcanization kinetics of fluroelastomer nanocomposites. *Polymer*, **45**, 2237–2247.
12. Negrete-Herrera, N., Putaux, J.L., and Bourgeat-Lami, E. (2006) Synthesis of polymer/laponite nanocomposite latex particles via emulsion polymerization using silylated and cation-exchanged laponite clay platelets. *Progress in Solid State Chemistry*, **34**, 121–137.

13. Lapides, I. and Heller-Kallai, L. (2002) Novel features of smectite settling. *Colloid and Polymer Science*, **280**(6), 554–561.
14. Leuteriitz, A., Pospiech, D., Kretzschmar, B. *et al.* (2005) Properties of polypropylene clay nanocomposites modified with difunctional compounds. *Composite interfaces*, **12**, 231–242.
15. Hong, C.H., Bae, J.W., Lee, Y.B. *et al.* (2006) Preparation of polypropylene/clay nanocomposites using aminosilane treated clay. *Polymer (Korea)*, **30**(4), 318–325.
16. Hwang, G.L., Shieh, Y.T., and Hwang, K.C. (2004) Efficient load transfer to polymer-grafted multiwalled carbon nanotubes in polymer composites. *Advanced Functional Materials*, **14**, 487–491.
17. Yang, J., Hu, J., Wang, C. *et al.* (2004) Fabrication and characterization of soluble multi-walled carbon nanotubes reinforced P(MMA-*co*-EMA) composites. *Journal of Applied Polymer Science*, **289**, 828–832.
18. Wang, M., Pramoda, K.P., and Goh, S.H. (2005) Enhancement of the mechanical properties of poly(styrene-co-acrylonitrile) with poly(methyl methacrylate)-grafted multiwalled carbon nanotubes. *Polymer*, **46**, 11510–11516.
19. Kim, K.H. and Jo, W.H. (2007) Synthesis of polythiophene-*graft*-PMMA and Its role as compatibilizer for poly (styrene-*co*-acrylonitrile)/MWCNT nanocomposites. *Macromolecules*, **40**, 3708–3713.
20. Zhang, X.F., Liu, T., Sreekumar, T.V. *et al.* (2003) Poly(vinyl alcohol)/SWNT composite film. *Nanoletters*, **3**, 1285–1288.
21. Rasheed, A., Dadmun, M.D., Ivanov, I. *et al.* (2006) Improving dispersion of single-walled carbon nanotubes in a polymer matrix using specific interactions. *Chemistry of Materials*, **18**, 3513–3522.
22. Islam, M.F., Rojas, E., Bergey, D.M. *et al.* (2003) High weight fraction surfactant solubilization of single-wall carbon nanotubes in water. *Nano Letters*, **3**, 269–273.
23. Harindra, M.S., Choi, Y.C., Kim, G. *et al.* (2004) Surface modification of carbon nanotubes using poly (vinyl alcohol) for sensor applications. Second LACCEI International Latin American and Caribbean Conference for Engineering and Technology, "Challenges and Opportunities for Engineering Education, Research and Development" June, Miami, Florida, USA (Emerging Technologies Track – Paper 062).
24. Khatua, B.B., Lee, D.J., Kim, H.Y., and Kim, J.K. (2004) Effect of organoclay platelets on morphology of nylon -6 anpoly(ethylene-ran-propylene)rubber blends. *Macromolecules*, **37**, 2454–2459.
25. Frounchi, M., Dadbin, S., Salehpour, Z., and Noferesti, M. (2006) Gas barrier properties of PP/EPDM blend nanocomposites. *Journal of Membrane Science*, **282**, 142–148.
26. Voulgaris, D. and Petridis, D. (2002) Emulsifying effect of dimethyldioctadecylammonium-hectorite in polystyrene/poly(ethyl methacrylate) blends. *Polymer*, **43**(8), 2213–2218.
27. Wang, Y., Zhang, Q., and Fu, Q. (2003) Compatibilization of immiscible poly (propylene)/polystyrene blends using clay. *Macromolecular Rapid Communications*, **24**(3), 231–235.
28. Mehrabzadeh, M. and Musa, K.R. (2002) Polymer-clay nanocomposites based on blends of polyamide-6 and polyethylene. *The Canadian Journal of Chemical Engineering*, **80**(6), 1083–1092.
29. Varghese, S., Gatos, K.G., Apostolov, A.A., and Karger- Kocsis, J. (2004) Morphology and mechanical properties of layered silicate reinforced Natural and polyurethane rubber blends produced by latex compounding. *Journal of Applied Polymer Science*, **92**(1), 543–551.
30. Psarras, G.C., Gatos, K.G., and Karger- Koscis, J. (2007) Dielectric properties of layered silicate- reinforced natural and polyurethane nanocomposites. *Journal of Applied Polymer Science*, **106**, 1405–1411.
31. Sharif, J., Yunus, W.M.Z.W., Dahlan, K.H., and Ahmad, M.H. (2006) Natural rubber/poly (ethylene-co-vinyl acetate) blend based nanocomposite. *Journal of Applied Polymer Science*, **100**, 353–362.
32. Sadhu, S. and Bhowmick, A.K. (2005) Morphology study of rubber based nanocomposites by transmission electron microscopy and atomic force microscopy. *Journal of Material Science*, **40**, 1633–1642.
33. Sadhu, S. and Bhowmick, A.K. (2004) Preparation and characterization of styrene butadiene rubber based nanocomposites and study of their mechanical properties. *Advanced Materials Engineering*, **6**(9), 738–741.
34. Alex, R. and Nah, C. (2006) Studies on natural rubber/acrylonitrile butadiene rubber/organoclay nanocomposites. *Plastics Rubber and Composites*, **35**, 219–225.
35. Stephen, R., Varghese, S., Joseph, K. *et al.* (2006) Diffusion and transport through nanocomposites of natural rubber (NR), carboxylated styrene butadiene rubber (XSBR) and their blends. *Journal of Membrane Science*, **282**, 162–170.
36. Zlata, H.M., Jelcic, Z., Kovacevic, V. *et al.* (2002) Molecular and morphological characterization of immiscible SAN/EPDM blends filled by nanofiller. *Macromolecular Materials and Engineering*, **287**, 684–692.
37. Ma, C.G., Mai, Y.L., Rong, M.Z. *et al.* (2007) Phase structure and mechanical properties of ternary polypropylene/elastomer/nano$CaCO_3$ composites. *Composite Science and Technology*, **67**, 2997–3005.

38. Chow, W.S., Abu Baker, A., Mohd Ishak, Z.A. *et al.* (2005) Effect of maleic anhydride-grafted ethylene–propylene rubber on the mechanical, rheological and morphological properties of organoclay reinforced polyamide 6/polypropylene nanocomposites. *European Polymer Journal*, **41**(4), 687–696.
39. Dong, W., Zhang, X., Liu, Y. *et al.* (2007) Process for preparing a nylon-6/clay/acrylate rubber nanocomposite with high toughness and stiffness. *Polymer International*, **56**(7), 870–874.
40. Van Gils, G.E. (1947) Spontaneous coagulation of *Hevea* Latex. *Transaction of Institution of Rubber Industries*, **23**, 74–76.
41. Alex, R., Premalatha, C.K., Nair, R.B., and Kuriakose, B. (2002) Measurement of dry rubber content of fresh natural rubber latex by a titration method. *Journal of Rubber Research*, **6**(4), 221–230.
42. Kawahara, S., Kakubo, T., Sakdapipanich, J.T. *et al.* (2000) Characterization of fatty acids linked to natural rubber-role of linked fatty acids on crystallization of the rubber. *Polymer*, **41**, 7483–7488.
43. Kawahara, S., Kakubo, T., Nishiyama, N. *et al.* (2000) Crystallization behavior and strength of natural rubber: skim rubber, deproteinized natural rubber, and pale crepe. *Journal of Applied Polymer Science*, **78**(8), 1510–1516.
44. Kawahara, S., Isono, Y., Sakdapipanich, J.T. *et al.* (2002) Effect of gel on green strength of natural rubber. *Rubber Chemistry and Technology*, **75**, 739–746.
45. Dong, W.F., Liu, Y.Q., Zhang, X.H. *et al.* (2005) Preparation of high barrier and exfoliated-type nylon-6/ultrafine full-vulcanized powdered rubber/clay nanocomposites. *Macromolecules*, **38**, 4551–4553.
46. Grechanovskii, V.A., Ivanova, L.S., and Poddubnyi, I.Y. (1973) Nature of the cohesional strength of synthetic cis-polyisoprene SKI-3 and carbon black compounds based on it. *Rubber Chemistry and Technology*, **46**, 1234–1238.
47. Grechanovskii, V.A., Poddubnyi, I.Y., and Ivanova, L.S. (1974) Molecular structure and macroscopic properties of synthetic cis poly(isoprene). *Rubber Chemistry and Technology*, **47**(1), 342–356.
48. Hamed, G.R. (1981) Tack and green strength of elastomeric materials. *Rubber Chemistry and Technology*, **54**, 576–595.
49. Feast, A.A.J. (1982) Synthetic latex, in *Polymer Lattices and their Applications* (ed. K.O. Calvert), Applied Science Publishers Ltd, London, pp. 21–46.
50. Karnika de Silva, K.G., and Lewan, MichaelV. (1998) Improving the morphology and properties of NR/NBR blends with NR/PMMA graft copolymers, in *Blends of Natural Rubber, Novel Techniques for Blending with Specialty Polymers* (eds A.J. Tinker and K.P. Jones), Chapman and Hall, U.K., pp. 68–79.
51. Alex, R., De, P.P., and De, S.K. (1989) Self vulcanisable rubber blend system based on epoxidised natural rubber and carboxylated nitrile rubber. *Journal of Polymer Science Part C-Polymer Letters*, **27**, 361–367.
52. Ohya, N., Tanaka, Y., Wittitsuwannakul, R., and Koyama, T. (2000) Activity of rubber transferase and rubber particle size in Hevea latex. *Journal of Rubber Research*, **3**, 214–221.
53. Gomez, J.B. and Hamzah, S. (1989) Particle size distribution in hevea Latex – some observations on electron microscopic method. *Journal of Natural Rubber Research*, **4**(3), 204–211.
54. Sakdapipanich, T., Nawamawati, K., and Tanaka, Y. (2002) Recovery of deproteinised small rubber particles from skim natural rubber latex: effect of some inorganic salts. *Journal of Rubber Research*, **5**(1), 1–10.
55. Rippel, M.M., Lee, L.T., Letite, C.A.P., and Galembeck, F. (2003) Skim and cream natural rubber particles: colloidal properties, coalescence and film formation. *Journal of Colloid and Interface Science*, **268**(2), 330–340.
56. Lopez Menchado, M.A., Herrero, B., and Arroyo, M. (2004) Organoclay-natural rubber nanocomposites synthesized by mechanical and solution mixing methods. *Polymer International*, **53**(11), 1766–1772.
57. Wang, M.J. (2005) New developments in carbon black dispersion. *Kautschuk Gummi Kunststoffe*, **58**(12), 626–637.
58. Bulgin, D. (1945) Electrically conductive rubber. *Transactions, Institution of Rubber Industries*, **21**, 188–218.
59. Bohm, C.G.A., and Nguyen, M.N. (1995) Flocculation of carbon black in filled rubber compounds. I: flocculation occurring in unvulcanized compounds during annealing at elevated temperatures. *Journal of Applied Polymer Science*, **55**, 1041–1050.
60. Wang, T., Wang, M.J., Shell, J., and Tokita, N. (2000) The effect of compound processing on filler dispersion. *Kautschuk Gummi Kunststoffe*, **3**, 497–505.
61. Ikeda, Y., Tanaka, A., and Kohjiya, S. (1997) Reinforcement of styrene butadiene rubber vulcanisate by in situ silica prepared by the sol-gel reaction of tetraethoxy silane. *Journal of Materials Chemistry*, **7**(8), 1497–1503.
62. Kohjiya, S. and Ikeda, Y. (2003) In Situ formation of particulate silica in natural rubber matrix by sol-gel reaction. *Journal of sol gel science and Technology*, **26**(1–3), 495–498.
63. Bokobza, L. and Chauvin, J.-P. (2005) Reinforcement of natural rubber: use of in-situ generated silica and nanofibres of sepiolite. *Polymer*, **46**(12), 4144–4155.

64. Poompradub, S., Kohjiya, S., and Ikeda, Y. (2005) Natural rubber/in situ silica nanocomposite of high silica content. *Chemistry Letters*, **34**(5), 672–673.
65. Wu, Y.P., Wang, Y.Q., Zhang, H.F. *et al.* (2005) Rubber–pristine clay nanocomposites prepared by co-coagulating rubber latex and clay aqueous suspension. *Composite Science and Technology*, **65**(7–8), 1195–1202.
66. Wu, Y.P., Jia, Q.X., Yu, D.S., and Zhang, Li.-Qun (2003) Structure and properties of nitrile rubber (NBR)-clay nanocomposites by co-coagulating NBR latex and clay aqueous suspension. *Journal of Applied Polymer Science*, **89**(14), 3855–3858.
67. Wu, Y.T., Mark, J.E., Pharm, L.H., Englehardt, M. (2001) Clay nanolayer reinforcement of *cis*-1,4-polyisoprene and epoxidized natural rubber. *Journal of Applied Polymer Science*, **82**, 1391–1403.
68. Zhang, L., Wang, Y., Wang, Y. *et al.* (2000) Morphology and mechanical properties of clay/styrene-butadiene rubber nanocomposites. *Journal of Applied Polymer Science*, **78**(11), 1873–1878.
69. Wang, Y., Zhang, H., Wu, Y. *et al.* (2005) Structure and properties of strain-induced crystallization rubber-clay nanocomposites by co-coagulating the rubber latex and clay aqueous suspension. *Journal of Applied Polymer Science*, **96**(2), 318–323.
70. Wang, Y., Zhang, H., Wu, Y. *et al.* (2005) Preparation, structure and properties of novel rectorite/styrene butadiene copolymer nanocomposite. *Journal of Applied Polymer Science*, **96**, 324–328.
71. Varghese, S. and Karger-Kocsis, J. (2003) Natural rubber-based nanocomposites by latex compounding with layered silicates. *Polymer*, **44**(17), 4921–4927.
72. Sui, G., Weihong, Z., Xiaoping, Y., and Suhe, Z. (2007) Processing and material characteristics of a carbon-nanotube-reinforced natural rubber. *Macromolecular Materials Engineering*, **292**(9), 1020–1026.
73. Fakhru'l- Razi, A., Atieh, M.A., Girun, N. *et al.* (2006) Effect of multi-wall carbon nanotubes on the mechanical properties of natural rubber. *Composite Structures*, **75**(1–4), 496–500.
74. Wu, Y.P., Zhang, L.Q., Wang, Y.Q. *et al.* (2001) Structure of carboxylated acrylonitrile-butadiene rubber (CNBR)-clay nanocomposites by co-coagulating rubber latex and clay aqueous suspension. *Journal of Applied Polymer Science*, **82**(11), 2842–2848.
75. Alexandra, M., Beyer, G., Henrist, C. *et al.* (2001) Preparation and properties of layered silicate nanocomposites based on ethylene vinyl acetate copolymers. *Macromolecular Rapid Communications*, **22**, 643–646.
76. Liang, Y., Wang, Y., Wu, Y. *et al.* (2005) Preparation and properties of isobutylene-isoprene rubber (IIR)/clay nanocomposites. *Polymer Testing*, **24**, 12–17.
77. Ray, S. and Bhowmick, A.K. (2001) Synthesis, characterization and properties of montmorillonite clay –poly-acrylate hybrid material and its effect on the properties of engage-clay hybrid composite. *Rubber Chemistry and Technology*, **74**, 835–845.
78. Wu, Y.P., Ma, Yong., Wang, Y.Q., and Zhang, L.Q. (2004) Effects of characteristics of rubber, mixing and vulcanization on the structure and properties of rubber/clay nanocomposites by melt blending. *Macromolecular Materials and Engineering*, **289**, 890–894.
79. Ma S Y., Li, Q.-F. Zhang, L.Q., Wu, Y.-P. (2007) Role of stearic acid in preparing EPDM/clay nanocomposites by melt compounding. *Polymer Journal*, **39**(1), 48–54.
80. Gatos, K.G. and Karger-Kocsis, J. (2005) Effects of primary and quaternary amine intercalants on the organoclay dispersion in a sulfur-cured EPDM rubber. *Polymer*, **46**, 3069–3076.
81. Blackley, D.C. (1997) Natural latices, in *Polymer Latices, Science and Technology, Vol. 2, Type of Latices*, Chapman and Hall, London, pp. 42–105.
82. Alex, R. and Nah, C. (2006) Preparation and characterization of organoclay-rubber nanocomposites via a new route with skim natural rubber latex. *Journal of Applied Polymer Science*, **102**(4), 3277–3285.

10

Thermoplastic Polyurethane Nanocomposites

S.K. Smart[1], G.A. Edwards[3] and D.J. Martin[2,3]

[1] *School of Engineering, University of Queensland, Building 74, College Road, Brisbane, 4072, Australia*

[2] *ARC Centre of Excellence for Functional Nanomaterials, Australian Institute for Bioengineering and Nanotechnology, University of Queensland, Building 75, Cr College and Cooper Rd, Brisbane, 4072, Australia*

[3] *Australian Institute for Bioengineering and Nanotechnology, University of Queensland, Building 75, Cr College and Cooper Rd, Brisbane, 4072, Australia*

10.1 Introduction

Polyurethane chemistry, first discovered by Otto Bayer in 1937, encompasses the series of polymers whose molecular backbone contains a significant number of urethane linkages, regardless of the content of the rest of the macromolecule [1]. The urethane linkage is formed via the reaction between an isocyanate group and a hydroxyl group. Initial studies into these polymers focused on forming linear polyurethanes by reacting diisocyanates with diols; however, it was quickly realized that by varying the structure and molecular weight of the reactants, a series of polymers with wide ranging properties could be produced [2]. Early work focused on polyester-based polyols; however, the enhanced hydrolytic stability and immense versatility afforded by the broader family of polyether-based polyols, quickly saw them become the preferred reactant in polyurethane synthesis [2]. The vast selection of polyols, isocyanates and chain extenders allows polyurethanes to be varied from soft thermoplastic elastomers to adhesives and coatings to flexible foams and rigid thermosets; however, this chapter focuses solely on the elastomeric thermoplastic polyurethanes (TPUs).

Rubber Nanocomposites: Preparation, Properties and Applications Edited by Sabu Thomas and Ranimol Stephen
© 2010 John Wiley & Sons (Asia) Pte Ltd

10.2 Market

TPUs are a member of the broader class of thermoplastic elastomer (TPE) materials. TPEs combine the flexibility and resilience of rubbers with the processability of plastics. Global demand for TPEs is forecast to increase 6.3% annually through 2011 to 3.7 million tonnes (Freedonia, April 2008). TPU materials currently comprise approximately 15% of the volume of TPE sold annually [3].

Some common applications for TPEs include automotive interiors, footwear, asphalt modification, overmoldings such as soft feel grips, cell phones, closures, seals and adhesives, cable jacketing, sport and leisure items, packaging, buttons, building and medical equipment. The various TPE classes compete on the basis of flexibility, ultimate properties, adhesion and compatibility with other part components, chemical resistance and price.

The broader TPE family is comprised of the following five groups of materials.

10.2.1 Styrene Block Copolymers

This group is at the low-cost end as they are produced in a single polymerization step from relatively cheap monomers. The group consists of several major polymers: styrene block copolymers (SBS), SIS and SEBS. The main application for SBS is asphalt modification. SIS is mainly used for adhesives and sealants. SEBS is used for soft feel grips, particularly on low-cost items such as razors and toothbrushes.

10.2.2 Thermoplastic Olefins

Thermoplastic olefins (TPOs) demonstrate a wide range of costs and performances. While a compounding step is generally required, recent developments in catalyst technology allows these polymers to be produced in a single polymerization step. As a result TPOs are challenging higher-priced TPEs in some markets, particularly automotive, where they are used in applications such as fender bars and body side moldings.

10.2.3 Thermoplastic Vulcanizates

These materials consist of a cross-linked rubber phase dispersed in a thermoplastic matrix. The original material (Santoprene) was based on EPDM rubber in polypropylene, but many other combinations now exist. The cross-linked rubber phase gives a significant improvement in compression set (resilience) which allows the use of thermoplastic vulcanizates (TPVs) in more demanding applications. For example, they are widely used in window glazing seals due to long-term sealant properties provided. The cost of these materials is generally higher due to the secondary compounding and cross-linking stage required.

10.2.4 Copolyester Elastomers

Copolyester elastomers (COPEs) are relatively expensive, high-performance materials with outstanding toughness and fatigue properties. They are used in applications such as automotive constant-velocity joint boots, subject to long-term flexing under demanding conditions.

10.2.5 Thermoplastic Polyurethanes

Thermoplastic polyurethanes (TPUs) are very versatile materials with high performance characteristics, although they are typically more expensive than TPVs. Variation of the polyurethane chemistry allows a very wide range of materials to be produced from hard, durable ski boot grades to soft feel grips. A growing application for TPUs is for the production of Spandex elastic fibers via melt spinning rather than solution spinning. Footwear and automotive are the other major areas of application for TPUs. Specialized TPUs have become standard for biomedical applications including implantable device components such as pacemaker lead insulation, where they offer good flexibility, biostability and biocompatibility.

10.3 TPU Chemistry, Morphology and Properties

TPUs are linear, block copolymers of alternating hard and soft segments. The soft segments are composed of long-chain diols (typically polyester- or polyether-based) with a molecular weight of 1000–4000 g mol^{-1}, whilst the hard segments commonly consist of alternating diisocyanates and short-chain extender molecules [1]. Thermodynamic incompatibility between the segments results in phase separation and subsequent organization into hard and soft domains (Figure 10.1) which afford TPUs their distinct mechanical properties [4–6].

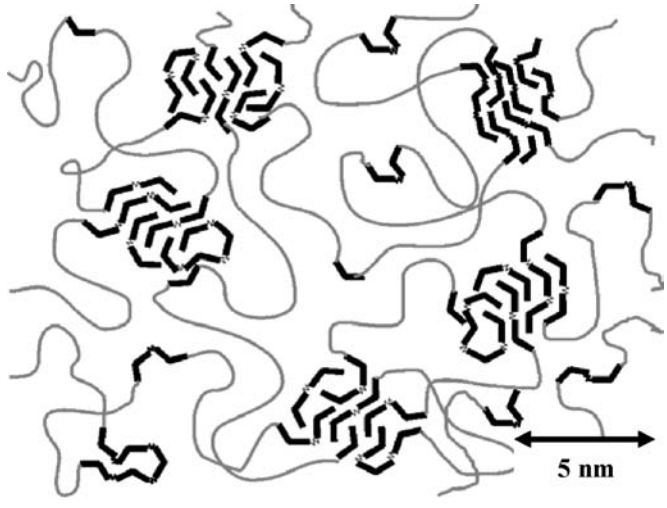

Figure 10.1 Generalized thermoplastic polyurethane morphology (hard segments = black solid lines connected by short chain extenders; soft segments = gray, nonlinear lines)

The flexible, amorphous soft domains primarily influence the elastic nature of the TPU, but still have some influence on the hardness, tear strength and modulus of the polymer. They are typically above their glass transition temperature (Tg) at room temperature and thus control

TPU performance at low temperatures. In contrast the rigid and typically semi-crystalline (as they are below their Tg at room temperature) hard domains primarily influence modulus, hardness, tear strength and melt processability [1]. However, the hard domains also act as physical cross-links, imparting elastomeric properties to the soft domain phase [7]. Thus, the mechanical properties of TPUs are strongly influenced by the exact microphase morphology of the hard and soft domains. These are in turn, dependent on such factors as the composition ratios, the thermodynamic compatibility, molecular weight and polydispersity of the hard and soft segments and the thermal history of the TPU [8–14].

The unique microphase morphology confers TPUs with a higher tensile strength and toughness when compared with most other elastomers [8], and the absence of covalent cross-linking allows TPUs to be both melt and solution processed. However, under continuous and/or cyclic loading the absence of chemical cross-linking allows the hard domains to restructure, which results in large hysteretic losses and poor creep resistance [15, 16]. The clever introduction of nanofillers to this complex nanoscale morphology and the characterization of the level of interplay between the various system components present a fascinating challenge for current researchers.

10.4 TPU Nanocomposites

The polymer industry is continually researching to find new materials that offer increased performance at lower costs, often necessitating the introduction of fillers. There have been various attempts to improve the mechanical performance, creep resistance and permanent set of TPUs, either by varying the composition of the hard and soft segments [11, 17], or by introducing macro- or micro-sized particulate fillers [18, 19], with the majority of these studies yielding suboptimal results. Nanoparticles (particles where at least one dimension is less than 100 nm) offer significant advantages over macro- or micro-sized fillers, including a greater surface area to mass ratio, low percolation threshold and often very high aspect ratios, and as such there has been significant research and investment into the production of polymeric nanocomposites. Recently, a range of nanoparticles have been used in TPU-based composites, with varying levels of success. Figure 10.2 compares several examples of optimum enhancement of TPU mechanical properties afforded by the incorporation of various nanofillers. The bottom of each bar represents the starting property for pure "host" TPU, and the top of each bar represents the increased strength or stiffness achieved after nanofiller addition. An "ideal" property profile is also shown, where the stiffness of the TPU is minimally altered and the ultimate tensile strength is greatly enhanced. Such a property profile has been traditionally very difficult to achieve via the composite approach due to substantial stiffening, and softer TPU formulations tend to suffer from a lack of strength due to the limits of segmental demixing evident at low hard segment composition ratios. Traditionally, if a stiffer, harder and stronger TPU is required, a higher hard segment composition ratio can be formulated.

There are reports in the literature of TPU nanocomposites incorporating nano silica in the form of either fumed silica [20, 21] to improve the mechanical or adhesive properties of TPUs, or in the form of polyhedral oligomeric silsesquioxane (POSS) components to improve either biostability [22] or resistance to thrombosis [22, 23]. However, the vast majority of work on TPU nanocomposites has involved the use of layered silicate or carbon nanotube-based nanofillers. Therefore this chapter focuses upon these two classes.

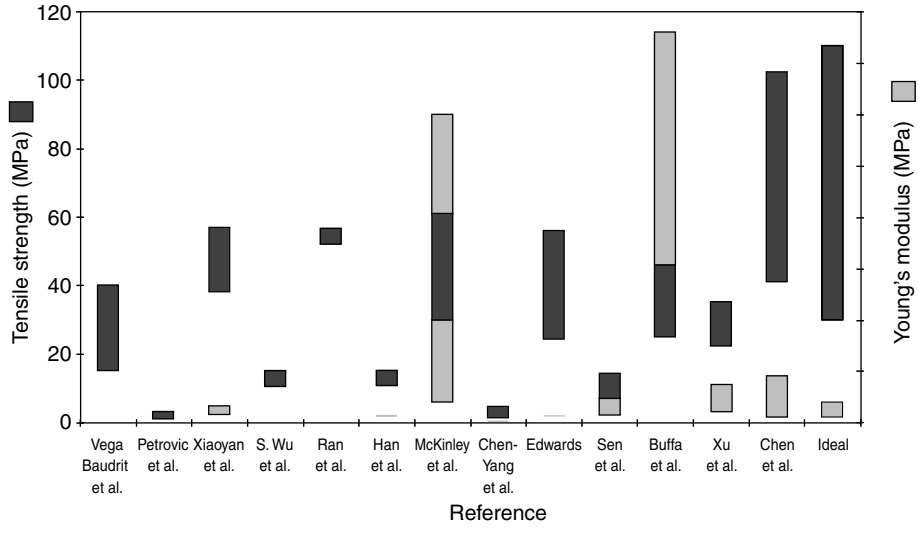

Figure 10.2 Comparison of tensile strength and Young's modulus for various TPU host matrices before and after nanofiller incorporation. The bottom of each bar represents the starting property for pure "host" TPU, and the top of each bar represents the increased strength or stiffness achieved after nanofiller addition. An "ideal" property profile is also shown

10.5 Layered Silicate/TPU Nanocomposites

The layered silicates frequently used in nanocomposites belong to the structural family known as the 2:1 phyllosilicates, which consist of 1 nm platelets, whose lateral dimensions range from 30 nm to several microns [24]. The crystal lattice of each platelet typically consists of an aluminum- or magnesium-rich octahedral layer sandwiched between two silica tetrahedral layers, as depicted in Figure 10.3. The platelets arrange themselves into stacks that are several microns in size. The platelets have a regular van der Waals gap between them known as the interlayer or gallery spacing. Isomorphous substitution of Al^{3+} by Mg^{2+} or Fe^{2+}, or substitution of Mg^{2+} by Li^{+}, results in a net negative surface charge on the platelets. The

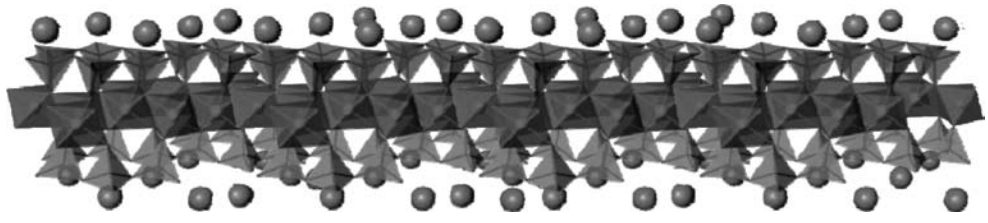

Figure 10.3 Structure of 2 : 1 phyllosilicates [25] (Reprinted with permission from C.S. Hurlbut, W.E. Sharp and E.S. Dana, *Dana's minerals and how to study them*, 4th edn, John Wiley & Sons, Inc., New York. © 1998.)

excess negative charge of the platelets is compensated by hydrated cations (for example, Na+ or Ca+) that reside in interlayer positions.

Natural layered silicates, such as montmorillonite, hectorite, beidellite, saponite, rectorite, nontronite and several less common species, are usually formed when volcanic ash is deposited under marine conditions or in alkaline lakes or through the hydrothermal reaction of volcanic rock at high temperatures [24]. While natural silicates are inexpensive and readily available, their size, purity and chemical structure is inconsistent. Synthetic layered silicates, however, are attractive because their size and composition is more consistent than natural fillers [26]. Synthetic layered silicates are prepared via hydrothermal reactions [26–28] and are commercially available in large quantities. The most commonly employed include trade names such as Laponite™, Lucentite™ and Optigel™ (synthetic hectorites from Rockwood Additives, Kobo Specialty Chemicals and Süd Chemie, respectively), and Somasif™ (a very high aspect ratio synthetic fluoromica from CBC Japan).

The purpose of the nanofiller in a nanocomposite is to be distributed on a nanoscale level and therefore undergo substantial interactions with polymer chains and sequences. There is therefore tremendous potential "reinforcement efficiency" due to the very high nanofiller aspect ratio and surface area, the local confinement of molecular motion [29–31] and the tailoring of specific hard or soft segment interactions with the nanofiller surface [32–34]. However, due to the layered structure of the silicate nanofillers, the organization of the resultant nanocomposite depends on the thermodynamic compatibility of the polymer and the layered silicate, intercalation kinetics and the processing conditions [35, 36]. The types of structures encountered are shown in Figure 10.4. Virgin layered silicate particles are naturally hydrophilic and as such are largely immiscible with TPUs which contain a significant hydrophobic component in form of the soft segments. This natural repulsion between the untreated silicate and the TPU discourages the formation of an exfoliated system as required for an effective nanocomposite. Instead a phase separated or microcomposite is formed whose properties do not exceed those of traditional composites.

In order to prepare effective nanocomposites, the hydrated cations in the interlayer spacing are replaced with organic cations to render the surface more organophilic and improve wetting by the polymer matrix [37, 38]. Furthermore, this substitution allows for swelling of the gallery between silicate layers, which in turn allows the polymer to enter between the galleries during the formation of the nanocomposite. An unswollen silicate has an interlayer spacing in the order of 1 nm, which is smaller than the host polymer's radius of gyration [39, 40]. The control and enhancement of both the polymer/silicate interaction and swelling of the gallery layers, are thus critical factors in the production of any polymeric nanocomposite, particularly so for TPUs which generally possess both hydrophilic components (hard segments) and hydrophobic components (soft segments).

In 1998, Wang and Pinnavaia [41] reported the first examples of TPU/layered silicate nanocomposites. The nanocomposites were prepared via *in situ* polymerization using montmorillonite (ion exchanged with alkylammonium salts) as nanofillers. X-ray diffraction (XRD) patterns indicated that intragallery polymerization contributed to the dispersion of the organosilicates, and improvements in tensile strength, elongation and modulus were observed.

The commercially-available Cloisite™ series of organosilicates have been used in a large number of TPU nanocomposite studies. Earlier studies employed solvent casting [42–45] in order to assist in overcoming some of the abovementioned thermodynamic barriers and also to avoid complications due to thermal degradation of the alkylammonium modifiers [46, 47].

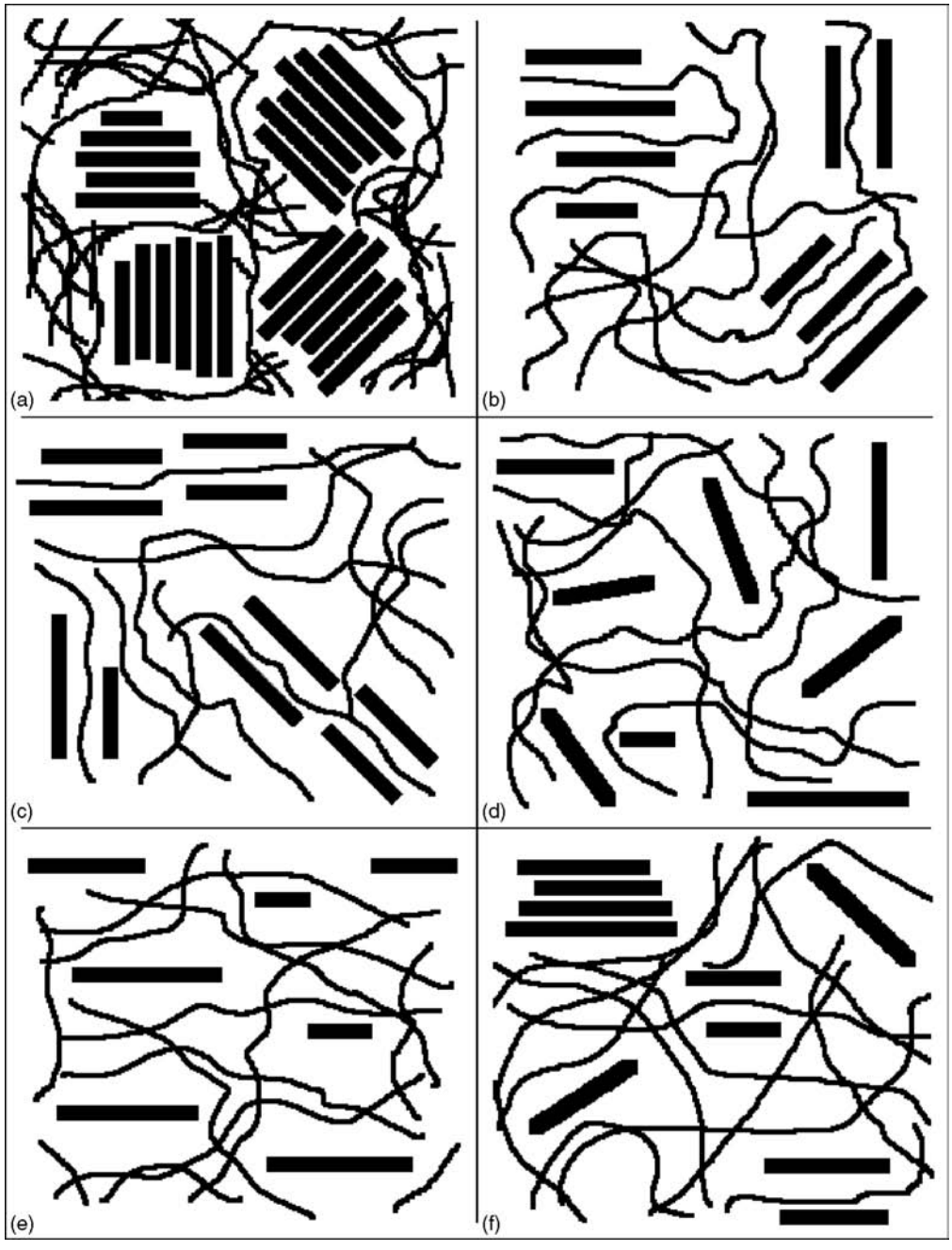

Figure 10.4 Generalized possible polymer-clay nanocomposite structures: (a) phase separated; (b) intercalated; (c) intercalated and flocculated; (d) exfoliated; (e) ordered exfoliated; and (f) mixed

Interestingly, the more hydrophobic Cloisite 15A generally did not offer good dispersion, although increases in tensile and barrier properties [43, 45] were reported with this nanofiller. Finnigan *et al.* reported that the more hydrophilic Cloisite 30B produced nanocomposites with relatively better dispersion, with very large associated increases in stiffness, tensile hysteresis and permanent set [42]. This increase in hysteresis in the nanocomposites is not well documented in the literature but is an important observation because many dynamic applications of TPUs require that resilience is maintained. This study was also the first to directly compare identical TPU nanocomposite formulations prepared via both solution and melt processing. However the very small laboratory-scale conical twin-screw extruder employed was shown to give rise to extreme thermal degradation and loss of ultimate properties.

Due to the more commercially scalable nature of melt compounding, several workers have investigated TPU/Cloisite nanocomposites prepared via melt compounding on a larger scale [42, 48–52]. The relatively hydrophilic Cloisite 30B and Cloisite 10A generally disperse and delaminate well in TPUs [42, 49, 50, 52]. This is due to their respective polar hydroxyl and benzyl functionalities, which promote a thermodynamically favorable enthalpic driving forces, such as H-bonding, for intercalation [32, 42, 53]. Cloisite 25A, in the middle of the hydrophilicity/hydrophobicity range, has also resulted in good dispersion and property enhancement [54, 55]. Dan *et al.* achieved the best property improvements with Cloisite 30B and also found that higher tensile properties could be achieved in an ester-based TPU with respect to an ether-based TPU, despite better dispersion in the latter. They also reported an influence of some nanofillers on the hard/soft segment demixing behavior and morphology, as well as a decrease in observed properties after a second melt processing step, implying thermal degradation.

Chavarria and Paul probed further into the effect of organoclay structure by modifying a series of montmorillonite-based nanofillers with various alkylammonium surfactants and studying the resulting structure/property relationships for a high-hardness ether-based versus a medium-hardness ester-based host TPU. They concluded that for both host TPU systems: (i) one long alkyl tail on the ammonium ion rather than two, (ii) hydroxyl ethyl groups on the amine rather than methyl groups and (iii) a longer alkyl tail as opposed to a shorter one leads to improved clay dispersion and TPU nanocomposite stiffness. However although the harder ether-based (and presumably higher melt viscosity) TPU host polymer resulted in better nanofiller dispersion, the percent increase in properties remained higher in the softer TPU grade. Meng *et al.* [52] also showed that the level of nanofiller (Cloisite 30B) dispersion improved by processing into a higher molecular weight TPU host of higher viscosity due to improved shear. They also showed that an optimum Brabender melt processing time was required in order to achieve the highest combination of nanofiller dispersion and tensile stress at 500% strain, due to excessive thermal degradation at longer processing times. Ma *et al.* organically modified a less well known class of layered silicate, rectorite, and performed melt compounding studies in a polyester-based TPU and reported substantial increases in both tensile strength and tear strength [51]. Most interestingly, the strongest formulations did not necessarily provide the best tear strength, suggesting that toughening mechanisms in these systems are complex and that nondelaminated clay tactoids may play more of a role in toughening than discrete organoclay platelets.

Whilst much of the research has focused on ionic substitution of bulky organic surfactants, several attempts at covalent modification of the silicate surface have been attempted [56, 57]. The initial report from Tien and Wei [56] utilized organosilicates with one to three hydroxyl

groups per surfactant molecule that were capable of participating in the polymerization process and promoting delamination from within the layers. Since this time others have used this approach with Cloisite 30B [57]. The tethering of TPU chains to the organosilicate surface is also performed in order to achieve a strong interfacial bond. However, it is difficult to reach the full potential for property improvements via this route, because the isocyanate groups can also react with bound water in the silicate interlayer and with hydroxyl groups on the silicate edges, which if not correctly accounted for, can lead to reduced molecular weight and increased matrix cross-link density [58].

The size of the layered silicate has been shown to influence the resulting nanocomposite morphology. Due to the relative scale of the hard domains compared with the most common silicates employed, few groups have investigated this area. However, research into smaller silicates has shown tensile strength can be significantly enhanced without significantly altering Young's modulus or resilience [59, 60]. In particular, the number of polymer/filler interactions and entanglements increase as the platelet size decreases, because the smaller platelets have a larger surface area and a smaller interparticle distance. This can have a significant effect on the mechanical properties, particularly at high strains where smaller platelets can more readily rotate without overcrowding, and therefore can more readily interact with the matrix by communicating in shear. Finnigan *et al.* [60] clearly demonstrated this by performing *in situ* strained synchrotron SAXS measurements on a series of solution-cast TPU nanocomposites incorporating organically modified fluoromica nanofillers of controlled aspect ratio which had been prepared via high energy milling. In a followup study they showed that superior resistance to stress relaxation could also be achieved by the incorporation of low aspect ratio organoclays [59]. They explained that as the particle size and aspect ratio of the filler increases, TPU chains in the interfacial region are more restrained and experience greater localized stresses, which results in an increase in strain-induced slippage at the polymer/filler interface. This technology has been patented [61] and a startup company, TenasiTech Pty Ltd, formed to commercialize the technology.

By using a Monte-Carlo simulation, Pandey *et al.* [62] predicted that smaller clay platelets should be more easily delaminated and dispersed in a compatible solvent/host polymer than high aspect ratio clays. Furthermore, computational models by Balazs *et al.* on block copolymers have indicated that a change in microphase texture and properties would be expected at nanofiller scales with the block copolymer phase domain size [63]. McKinley *et al.* [34, 64] incorporated unmodified, low aspect ratio hectorite (Laponite™) into a number of TPUs at up to 20 wt% using a novel solvent exchange technique. They reported remarkable mechanical property, heat distortion temperature and morphological changes in fully delaminated nanocomposite systems. Some degree of "tuned" segmental association of the Laponite™ was demonstrated, depending on the solubility parameter of the chosen soft segment [34].

10.6 Carbon Nanotube/TPU Nanocomposites

Carbon nanotubes are unique, one-dimensional macromolecules of sp2-bonded carbon atoms. Single-walled carbon nanotubes (SWNT) are constructed of a single graphene sheet rolled into a seamless cylinder (diameter 0.4–2.0 nm), while multiwalled carbon nanotubes (MWNT) consist of nested graphene cylinders of increasing diameter (2–100 nm) arranged around a hollow core [65]. Nanotubes can be up to several microns in length, whilst the ends of the

graphene cylinders can be capped [66] or uncapped [67] with hemi-fullerenes depending on synthesis and processing conditions. Both SWNT and MWNT possess high tensile strengths, are ultra-lightweight and have excellent thermal and chemical stability, prompting the explosion of research into CNT-based polymeric nanocomposites. Since the much vaunted discovery of MWNT in 1991 by Iijima [66], there has been much research into efficient and high-yield methods of synthesis for CNT [68]. Currently, there are three main strategies employed for CNT synthesis:

- arc discharge;
- laser ablation;
- chemical vapor deposition (CVD).

These methods have all been extensively reviewed [65, 69, 70] and are not discussed here. Suffice to say each synthesis method (and resultant purification technique) results in different nanotube morphologies, catalyst concentrations, oxidation levels, chirality and structural deformations.

The manipulation and incorporation of large numbers of individual CNT into polymeric systems is a difficult task because high molecular weights and strong intertube forces (both van der Waals and electrostatic) promote the formation of micron-sized bundles and ropes [71], leading to phase separation and poor mechanical properties. As a result both surfactant and covalent functionalisations have been employed in an attempt fragment and disperse these micron-sized inclusions. Since many other applications of CNT require their dispersion in a variety of solvents (for example, organic solvents for polymer interactions, aqueous solvents for drug delivery) there have been numerous investigations [72–77] into surface modification of the CNT sidewall and hence these are not covered here. Significantly, there are several companies that now sell prefunctionalized (for example, Cheap Tubes, Inc., Bayer) and even custom functionalized (for example, Zyvex™ and Baytubes™, as well as unpurified and pristine) nanotubes specifically for nanocomposite applications, underlining the importance of this area.

As with the layered silicates, the interfacial region between nanotube and TPU is a critical parameter in understanding and optimizing the performance of TPU/CNT nanocomposite materials. Computational studies indicate that when there is no chemical bonding present, the interactions are electrostatic and van der Waals in nature [78–80], with several researchers also demonstrating that polymer wrapping of the nanotubes occurs [81] which minimizes energy for geometric reasons [82]. Under such conditions, kinks in the nanotubes, defect sites and diameter changes in the CNT sidewall may result in nanomechanical interlocking, improving interfacial interactions [78]. Covalent functionalization of CNT also has a profound effect on the load transfer from polymer to nanotube, especially when external stress is applied normal to the nanotube axis, with reinforcement scaling roughly with the number of available functionalized sites [83]. These findings suggest that, for purely mechanical applications, highly functionalized nanotubes are preferable to pristine nanotubes, although it remains unclear whether the conformation of the covalent functionalization is important or whether the functional unit spacing plays any role.

Initial experimental interest in TPU/CNT nanocomposites was relatively low, with only two published studies in 2004 [76, 84]; however, this has since jumped to over 43 published studies into TPU/CNT nanocomposites, accounting for approximately 9% of published studies into polymer/CNT nanocomposites and 10% of published studies into polyurethane

nanocomposites. The majority of these TPU/CNT nanocomposites have been formulated via solution processing techniques [76, 84–93], although *in situ* polymerization [91, 94–97] and melt processing techniques [87] have been reported as well. Despite the superior mechanical performance of SWNT, MWNT are the most common variety of CNT studied and a wide variety of surface functionalizations have been investigated. Koerner and coworkers reported the first study into TPU/CNT nanocomposites, in which researchers attempted to improve the stress/recovery characteristics of morthane (a commercially available, shape memory TPU) by adding 1–5 vol% MWNT via a solution-processing technique [84]. Researchers demonstrated that the nanocomposite could store and subsequently release up to 50% more recovery stress than the unmodified TPU. The nanocomposite also demonstrated the ability to recover stress, above that of the host TPU, when exposed to increased temperatures, infrared radiation and electrical current. The authors theorized that the absorption of energy by MWNT caused localized heating, which in turn melted the strain-induced polymer crystals, increasing stress recovery.

Sen and coworkers were the first to investigate the fabrication of TPU nanocomposites incorporating functionalized SWNT [76]. The solution-processed nanocomposites demonstrated significantly increased mechanical properties over the host TPU. Whilst the final material was mechanically inferior to several commercially available TPUs without nanoparticle reinforcement, the study was the first to demonstrate both the possibility of increased dispersion in a TPU/CNT nanocomposite and that TPU/CNT interactions can be enhanced by CNT functionalization.

As a result, the majority of research into TPU/CNT nanocomposites has focused on using functionalized CNT; however, there have been several studies published where pristine CNT have been used [86–88]. Importantly, these investigations have demonstrated poor CNT dispersion and phase separation between SWNT and the host TPU, suggesting that the future of TPU/CNT nanocomposites lies with modification of the CNT surface. There have been a wide variety of functional groups attached to CNT in an attempt to overcome these problems. CNT surface modifiers are typically either short hydrophilic groups like $-$COOH [89, 90], $-NH_2$ [91] and $-$OH [92], capable of significant hydrogen-bonding with the host polymer, or long-chain hydrophobic groups designed to break apart CNT aggregates and increase dispersion [76]. Recently, significant results have been achieved by Deng and coworkers [93, 98], who demonstrated dramatic mechanical enhancements with very small loadings of MWNT modified with novel functional groups. Several research groups have also attempted to use CNT as cross-linking agents, covalently bonding individual CNT to the TPU backbone. However, results have been mixed due to the fine stoichiometric control required to produce nanocomposites with the same molecular weights and hard/soft segment ratios as the control TPU [96, 97].

Despite the abundance of work into TPU/CNT nanocomposites, the only published investigation of TPU/functionalized CNT nanocomposites formulated by melt processing techniques was conducted by Chen and coworkers [87]. The researchers determined that the acid-treated MWNT dramatically increased the mechanical properties, with an eightfold increase in Young's modulus and a 2.4-fold increase in tensile strength due to the strong interfacial interactions and good MWNT dispersion and within the melt-drawn fibers. Significantly this result corroborates computational studies that suggest melt processing may induce a residual thermal radial stress (through differences in coefficients of thermal expansion between the CNT and the host polymer), forcing the polymer into closer contact with the tube surface and thereby enhancing interactions [78].

10.7 Future Perspectives

While the nanocomposite approach has undoubtedly led to several encouraging examples of new functional and mechanical property profiles, most examples have failed to live up to their theoretical potential. An excellent recent review paper by Schaefer and Justice [99] points out that in the majority of polymer nanocomposites today "large scale disorder is ubiquitous." Consistent with some of the reports discussed here, they suggest that the fixation on high aspect ratio nanofillers is unproductive due to: (i) problems with agglomeration and dispersion of high aspect ratio particles and (ii) the potential for tailored molecular self assembly involving a higher degree of "cooperation" between nanofiller and matrix. The nature of more recent investigations suggests that a more systematic and exacting approach is now being adopted by TPU nanocomposites researchers, guided by a growing number of multiscale theoretical modeling efforts. New experimental techniques need to be developed and applied in order to better probe and understand the subtle structures and conformations at the nanofiller/TPU interface. Synchrotron X-ray and neutron scattering will continue to play an important role here. Highly engineered model nanoparticle and TPU systems may be required in order to elucidate these questions. There is also a need for the development of new classes of layered inorganic nanofillers which are more readily delaminated and more thermally stable. Metal phosphonates have been proposed as one possible new class [100], and there have also been some efforts to employ covalent organic modification [101] using silane grafting.

Historically, the mechanical testing performed on polymer nanocomposites has been limited to simple tensile experiments and thereby has largely ignored many of the properties critical to the true service performance of the materials. Therefore long-term mechanical, thermal, or other environmental ageing, tear- or cut-growth resistance and fatigue performance of TPU nanocomposite materials are other areas greatly in need of attention.

The effects of processing on nanocomposite structure and properties and the use of rheology to elucidate the effects of nanocomposite formation are new and exciting fields of research in nanocomposites. Traditionally much work (highlighted above) has focused on the properties of nanocomposites produced from one type of process and/or processing condition. Clearly the effects of processing on nanocomposite formation and the understanding of the rheology of nanocomposites are some of the next key scientific steps needed to fully understand and control TPU nanocomposite properties and performance in various applications. An optimistic perspective would see future applications of TPU nanocomposites in biomedical implants (for example, softer, tougher implantable electrode insulation for pacemakers), more abrasion-resistant mining screens, stronger, lighter melt spun Spandex, thin films (tougher, more scuff-resistant coatings on golf balls and protective wear) and many others. Nanocomposite technology could also see TPUs remain at the "top of their class" with respect to the many other TPEs available.

References

1. Hepburn, C. (1991) *Polyurethane Elastomers*, 2nd edn, Elsevier, London, New York, p. 441.
2. Oertel, G. and Abele, L. (1994) *Polyurethane Handbook: Chemistry, Raw Materials, Processing, Application, Properties*, 2nd edn, vol. **xxii**, Hanser; Hanser/Gardner [distributor], Munich; New York Cincinnati, p. 688.
3. Sullivan, F.a. (2004) U.S. Thermoplastic Elastomers (TPE) Markets, A750-37.
4. Chu, B. *et al.* (1992) Microphase separation kinetics in segmented polyurethanes - effects of soft segment length and structure. *Macromolecules*, **25**(21), 5724–5729.

5. Elwell, M.J. *et al.* (1996) In-situ studies of structure development during the reactive processing of model flexible polyurethane foam systems using FT-IR spectroscopy, synchrotron SAXS, and rheology. *Macromolecules*, **29**(8), 2960–2968.
6. Ryan, A.J. *et al.* (1991) Dynamics of (micro)phase separation during fast, bulk copolymerization - some synchrotron saxs experiments. *Macromolecules*, **24**(10), 2883–2889.
7. Lilaonitkul, A. and Cooper, S.L. (1979) Properties of thermoplastic polyurethane elastomers. *Advances in Urethane Science and Technology*, **7**, 163–183.
8. Speckhard, T.A. and Cooper, S.L. (1986) Ultimate tensile properties of segmented polyurethane elastomers - factors leading to reduced properties for polyurethanes based on nonpolar soft segments. *Rubber Chemistry and Technology*, **59**(3), 405–431.
9. Miller, J.A. *et al.* (1985) Properties of polyether polyurethane block copolymers - effects of hard segment length distribution. *Macromolecules*, **18**(1), 32–44.
10. Wang, C.B. and Cooper, S.L. (1983) Morphology and properties of segmented polyether polyurethaneureas. *Macromolecules*, **16**(5), 775–786.
11. Martin, D.J. *et al.* (1996) Effect of soft-segment CH2/O ratio on morphology and properties of a series of polyurethane elastomers. *Journal of Applied Polymer Science*, **60**(4), 557–571.
12. Abouzahr, S., Wilkes, G.L., and Ophir, Z. (1982) Structure property behavior of segmented polyether Mdi butanediol based urethanes - effect of composition ratio. *Polymer*, **23**(7), 1077–1086.
13. Samuels, S.L. and Wilkes, G.L. (1973) Rheo-optical and mechanical-behavior of a systematic series of hard-soft segmented urethanes. *Journal of Polymer Science Part C-Polymer Symposium* **43**, 149–178.
14. Harrell, L.L. (1969) Segmented polyurethans. Properties as a function of segment size and distribution. *Macromolecules*, **2**(6), 607.
15. Reynolds, N. *et al.* (1994) Structure and Deformation-Behavior of Model Poly(Ether-Urethane) Elastomers. 1. Infrared Studies. *Macromolecular Chemistry and Physics*, **195**(8), 2855–2873.
16. Lee, H.S. and Hsu, S.L. (1994) Structural-Changes and Chain Orientational Behavior During Tensile Deformation of Segmented Polyurethanes. *Journal of Polymer Science Part B-Polymer Physics*, **32**(12), 2085–2098.
17. Martin, D.J. *et al.* (1997) The effect of average soft segment length on morphology and properties of a series of polyurethane elastomers. 2. SAXS-DSC annealing study. *Journal of Applied Polymer Science*, **64**(4), 803–817.
18. Varma, A.J., Deshpande, M.D., and Nadkarni, V.M. (1985) Morphology and mechanical-properties of silicate filled polyurethane elastomers based on castor-oil and polymeric Mdi. *Angewandte Makromolekulare Chemie*, **132**(JUN), 203–209.
19. Torro-Palau, A. *et al.* (1997) Comparison of the properties of polyurethane adhesives containing fumed silica or sepiolite as filler. *Journal of Adhesion*, **61**(1–4), 195–211.
20. Petrovic, Z.S. *et al.* (2000) Structure and properties of polyurethane-silica nanocomposites. *Journal of Applied Polymer Science*, **76**(2), 133–151.
21. Vega-Baudrit, J. *et al.* (2007) Properties of thermoplastic polyurethane adhesives containing nanosilicas with different specific surface area and silanol content. *International Journal of Adhesion and Adhesives*, **27**(6), 469–479.
22. Kannan, R.Y. *et al.* (2006) The antithrombogenic potential of a polyhedral oligomeric silsesquioxane (POSS) nanocomposite. *Biomacromolecules*, **7**(1), 215–223.
23. Kannan, R.Y. *et al.* (2006) The degradative resistance of polyhedral oligomeric silsesquioxane nanocore integrated polyurethanes: An in vitro study. *Biomaterials*, **27**(9), 1971–1979.
24. Gillott, J.E. (1987) Clay in engineering geology, 2nd edn, vol. **xvi**, *Developments in Geotechnical Engineering*, Elsevier, Amsterdam, New York, pp. 468.
25. Hurlbut, C.S., Sharp, W.E., and Dana, E.S. (1998) *Dana's Minerals and how to Study them*, 4th edn, vol. **viii**, Wiley, New York, p. 328.
26. Carrado, K.A. (2000) Synthetic organo- and polymer-clays: preparation, characterization, and materials applications. *Applied Clay Science*, **17**(1–2), 1–23.
27. Carrado, K.A. (1992) Preparation of hectorite clays utilizing organic and organometallic complexes during hydrothermal crystallization. *Industrial & Engineering Chemistry Research*, **31**(7), 1654–1659.
28. Tateyama, H. *et al.* (1998) Interstratification in expandable mica produced by cation-exchange treatment. *Clays and Clay Minerals*, **46**(3), 245–255.
29. Dietsche, F. *et al.* (2000) Plastics and rubber nanocomposites based upon layered silicates. *Plastics Technology*, **1998**, 65–67.

30. Padmanabhan, K.A. (2001) Mechanical properties of nanostructured materials. *Materials Science and Engineering*, **304–306**, 200–205.
31. Pinnavaia, T.J., LeBaron, P.C., and Wang, Z. (1999) Polymer-layered silicate nanocomposites: an overview. *Applied Clay Science*, **15**, 11–29.
32. Balazs, A.C., Singh, C., and Zhulina, E. (1998) Modeling the interactions between polymers and clay surfaces through self-consistent field theory. *Macromolecules*, **31**(23), 8370–8381.
33. Edwards, G. (2007) *Optimisation of Organically Modified Layered Silicate Based Nanofillers for Thermoplastic Polyurethanes, in School of Engineering*, University of Queendland.
34. Korley, L.T.J.L., Shawna, M., Kumar, N. *et al.* (2006) Preferential association of segment blocks in polyurethane nanocomposites. *Macromolecules*, **39**, 7030–7036.
35. Giannelis, E.P., Krishnamoorti, R., and Manias, E. (1999) Polymer-silicate nanocomposites: Model systems for confined polymers and polymer brushes. *Polymers in Confined Environments*, **138**, 107–147.
36. Dennis, H.R. *et al.* (2001) Effect of melt processing conditions on the extent of exfoliation in organoclay-based nanocomposites. *Polymer*, **42**(23), 9513–9522.
37. Giannelis, E.P. (1996) Polymer layered silicate nanocomposites. *Advanced Materials*, **8**(1), 29.
38. Alexandre, M. and Dubois, P. (2000) Polymer-layered silicate nanocomposites: preparation, properties and uses of a new class of materials. *Materials Science & Engineering R-Reports*, **28**(1–2), 1–63.
39. Jürgen, F. *et al.* (1999) Polyurethane nanocomposites containing laminated anisotropic nanoparticles derved from organophilic layered silicates. *Advanced Materials*, **11**(1), 49–52.
40. Lagaly, G. and Bergaya, F. (2001) Introduction: surface modification of clay minerals. *Applied Clay Science*, **19**, 1–3.
41. Wang, Z. and Pinnavaia, T.J. (1998) Nanolayer reinforcement of elastomeric polyurethane. *Chemistry of Materials*, **10**(12), 3769.
42. Finnigan, B. *et al.* (2004) Morphology and properties of thermoplastic polyurethane nanocomposites incorporating hydrophilic layered silicates. *Polymer*, **45**(7), 2249–2260.
43. Finnigan, B. *et al.* (2005) Morphology and properties of thermoplastic polyurethane composites incorporating hydrophobic layered silicates. *Journal of Applied Polymer Science*, **97**(1), 300–309.
44. Xu, R. *et al.* (2003) Low permeability biomedical polyurethane nanocomposite. *Journal of Biomedical Materials Research Part A*, **64**(1), 114–119.
45. Xu, R.J. *et al.* (2001) New biomedical poly(urethane urea) - Layered silicate nanocomposites. *Macromolecules*, **34**(2), 337–339.
46. Edwards, G. *et al.* (2005) Thermal stability analysis of organo-silicates, using solid phase microextraction techniques. *Thermochimica Acta*, **429**, 13–18.
47. He, H. *et al.* (2006) Influence of cationic surfactant removal on the thermal stability of organoclays. *Journal of Colloid and Interface Science*, **295**, 202–208.
48. Chavarria, F. and Paul, D.R. (2006) Morphology and properties of thermoplastic polyurethane composites: Effect of organoclay structur. *Polymer*, **47**, 7760–7773.
49. Cheol, H.D. *et al.* (2006) Effect of clay modifiers on the morphology and physical properties of thermoplastic polyurethane/clay nanocomposites. *Polymer*, **47**, 6718–6730.
50. Dan, C.H. *et al.* (2006) Effect of clay modifiers on the morphology and physical properties of thermoplastic polyurethane/clay nanocomposites. *Polymer*, **47**, 6718–6730.
51. Ma, X. *et al.* (2004) Rectorite/thermoplastic polyurethane nanocomposites: preparation, characterization, and properties. *JAPS*, **93**, 608–614.
52. Meng, X. *et al.* (2008) The investigation of exfoliation process of organic modified montmorillonite in thermoplastic polyurethane with different molecular weight. *Composites Science and Technology*, **68**, 1815–1821.
53. Vaia, R.A. and Giannelis, E.P. (1997) Lattice model of polymer melt intercalation in organically-modified layered silicates. *Macromolecules*, **30**(25), 7990–7999.
54. Chang, J.H. and An, Y.U. (2002) Nanocomposites of polyurethane with various organoclays: Thermomechanical properties, morphology, and gas permeability. *Journal of Polymer Science Part B-Polymer Physics*, **40**(7), 670–677.
55. Kim, B.K., Seo, J.W., and Jeong, H.M. (2003) Morphology and properties of waterborne polyurethane/clay nanocomposites. *European Polymer Journal*, **39**(1), 85–91.
56. Tien, Y.I. and Wei, K.H. (2001) High-tensile-property layered silicates/polyurethane nanocomposites by using reactive silicates as pseudo chain extenders. *Macromolecules*, **34**(26), 9045–9052.

57. Pattanayak, A. and Jana, S.C. (2005) Synthesis of thermoplastic polyurethane nanocomposites of reactive nanoclay by bulk polymerization methods. *Polymer*, **46**(10), 3275–3288.
58. Choi, M.Y. *et al.* (2006) Synthesis and characterization of in situ polymerized segmented thermoplastic elastomeric polyurethane/layered silicate clay nanocomposites. *Journal of Applied Polymer Science*, **102**(3), 3048–3055.
59. Finnigan, B. *et al.* (2007) Impact of controlled particle size nanofillers on the mechanical properties of segmented polyurethane nanocomposites. *International Journal of Nanotechnology*, **4**(5), 496–515.
60. Finnigan, B. *et al.* (2005) Segmented polyurethane nanocomposites: Impact of controlled particle size nanofillers on the morphological response to uniaxial deformation. *Macromolecules*, **38**(17), 7386–7396.
61. University of Queensland (2005) Polymer composite, Patent WO2006/024068.
62. Pandey, R.B., Anderson, K.L., and Farmer, B.L. (2006) Exfoliation of stacked sheets: effects of temperature, platelet size, and quality of solvent by a Monte Carlo simulatio. *Journal of Polymer Science Part B-Polymer Physics*, **44**, 3580–3589.
63. Ginzburg, V.V., Qiu, F., and Balazs, A.C. (2001) Three-dimensional simulations of diblock copolymer/particle composites. *Polymer*, **43**(2), 461–466.
64. Liff, S.M., Nitin, K., and McKinley, G.H. (2007) High-performance elastomeric nanocomposites via solvent-exchange processing. *Nature Materials*, **6**(1), 76–83.
65. Moniruzzaman, M. and Winey, K.I. (2006) Polymer nanocomposites containing carbon nanotubes. *Macromolecules*, **39**(16), 5194–5205.
66. Iijima, S. (1991) Helical microtubules of graphitic carbon. *Nature*, **354**(6348), 56–58.
67. Pierard, N. *et al.* (2001) Production of short carbon nanotubes with open tips by ball milling. *Chemical Physics Letters*, **335**(1–2), 1–8.
68. Dresselhaus, M.S., Dresselhaus, G., and Avouris, P. (eds) (2001) Carbon nanotubes: synthesis, structure, properties and applications, in *Topics in Applied Physics*, vol. **80**, Springer-Verlag, Berlin, p. 447.
69. Thostenson, E.T., Ren, Z., and Chou, T.-W. (2001) Advances in the science and technology of carbon nanotubes and their composites: a review. *Composites Science and Technology*, **61**(13), 1899–1912.
70. Tjong, S.C. (2006) Structural and mechanical properties of polymer nanocomposites. *Materials Science and Engineering: R: Reports*, **53**(3–4), 73–197.
71. Tagmatarchis, N. and Prato, M. (2004) Functionalization of carbon nanotubes via 1,3-dipolar cycloadditions. *Journal of Materials Chemistry*, **14**(4), 437–439.
72. Hilding, J. *et al.* (2003) Dispersion of carbon nanotubes in liquids. *Journal of Dispersion Science and Technology*, **24**(1), 1–41.
73. Barisci, J.N. *et al.* (2004) Properties of carbon nanotube fibers spun from DNA-stabilized dispersions. *Advanced Functional Materials*, **14**(2), 133–138.
74. Dieckmann, G.R. *et al.* (2003) Controlled assembly of carbon nanotubes by designed amphiphilic peptide helices. *Journal of the American Chemical Society*, **125**(7), 1770–1777.
75. Ortiz-Acevedo, A. *et al.* (2005) Diameter-selective solubilization of single-walled carbon nanotubes by reversible cyclic peptides. *Journal of the American Chemical Society*, **127**(26), 9512–9517.
76. Sen, R. *et al.* (2004) Preparation of single-walled carbon nanotube reinforced polystyrene and polyurethane nanofibers and membranes by electrospinning. *Nano Letters*, **4**(3), 459–464.
77. Lin, T. *et al.* (2003) Chemistry of carbon nanotubes. *Australian Journal of Chemistry*, **56**(7), 635–651.
78. Wong, M. *et al.* (2003) Physical interactions at carbon nanotube-polymer interface. *Polymer*, **44**(25), 7757–7764.
79. Desai, A.V. and Haque, M.A. (2005) Mechanics of the interface for carbon nanotube-polymer composites. *Thin-Walled Structures*, **43**(11), 1787–1803.
80. Jiang, L.Y. *et al.* (2006) A cohesive law for carbon nanotube/polymer interfaces based on the van der Waals force. *Journal of the Mechanics and Physics of Solids*, **54**(11), 2436–2452.
81. McCarthy, B. *et al.* (2002) A microscopic and spectroscopic study of interactions between carbon nanotubes and a conjugated polymer. *Journal of Physical Chemistry B*, **106**(9), 2210–2216.
82. Coleman, J.N. and Ferreira, M.S. (2004) Geometric constraints in the growth of nanotube-templated polymer monolayers. *Applied Physics Letters*, **84**(5), 798–800.
83. Grujicic, M., Sun, Y.P., and Koudela, K.L. (2007) The effect of covalent functionalization of carbon nanotube reinforcements on the atomic-level mechanical properties of poly-vinyl-ester-epoxy. *Applied Surface Science*, **253**(6), 3009–3021.

84. Koerner, H. *et al.* (2004) Remotely actuated polymer nanocomposites - stress-recovery of carbon-nanotube-filled thermoplastic elastomers. *Nature Materials*, **3**(2), 115–120.
85. Koerner, H. *et al.* (2005) Deformation-morphology correlations in electrically conductive carbon nanotube thermoplastic polyurethane nanocomposites. *Polymer*, **46**(12), 4405–4420.
86. Foster, J. *et al.* (2005) Dispersion and phase separation of carbon nanotubes in ultrathin polymer films. *Journal of Colloid and Interface Science*, **287**(1), 167–172.
87. Chen, W. and Tao, X.M. (2006) Production and characterization of polymer nanocomposite with aligned single wall carbon nanotubes. *Applied Surface Science*, **252**(10), 3547–3552.
88. Meng, J. *et al.* (2005) Improving the blood compatibility of polyurethane using carbon nanotubes as fillers and its implications to cardiovascular surgery. *Journal of Biomedical Materials Research Part A*, **74A**(2), 208–214.
89. Kwon, J.Y. and Kim, H.D. (2005) Preparation and properties of acid-treated multiwalled carbon nanotube/waterborne polyurethane nanocomposites. *Journal of Applied Polymer Science*, **96**(2), 595–604.
90. Sahoo, N.G. *et al.* (2006) Effect of functionalized carbon nanotubes on molecular interaction and properties of polyurethane composites. *Macromolecular Chemistry and Physics*, **207**(19), 1773–1780.
91. Kuan, H.C. *et al.* (2005) Synthesis, thermal, mechanical and rheological properties of multiwall carbon nano tube/waterborne polyurethane nanocomposite. *Composites Science and Technology*, **65**(11–12), 1703–1710.
92. Buffa, F. *et al.* (2007) Effect of nanotube functionalization on the properties of single-walled carbon nanotube/polyurethane composites. *Journal of Polymer Science Part B-Polymer Physics*, **45**(4), 490–501.
93. Deng, J. *et al.* (2007) Synthesis and properties of poly(ether urethane) membranes filled with isophorone diisocyanate-grafted carbon nanotubes. *Journal of Membrane Science*, **288**(1–2), 261–267.
94. Xiong, J.W. *et al.* (2006) The thermal and mechanical properties of a polyurethane/multi-walled carbon nanotube composite. *Carbon*, **44**(13), 2701–2707.
95. Xia, H.S. *et al.* (2006) Poly(propylene glycol)-grafted multi-walled carbon nanotube polyurethane. *Macromolecular Chemistry and Physics*, **207**(21), 1945–1952.
96. Jung, Y.C., Sahoo, N.G., and Cho, J.W. (2006) Polymeric nanocomposites of polyurethane block copolymers and functionalized multi-walled carbon nanotubes as crosslinkers. *Macromolecular Rapid Communications*, **27**(2), 126–131.
97. Xu, M. *et al.* (2006) Synthesis and properties of novel polyurethane-urea/multiwalled carbon nanotube composites. *Macromolecules*, **39**(10), 3540–3545.
98. Deng, J.N. *et al.* (2008) Mechanical and surface properties of polyurethane/fluorinated multi-walled carbon nanotubes composites. *Journal of Applied Polymer Science*, **108**(3), 2023–2028.
99. Schaefer, D.W. and Justice, R.S. (2007) How nano are nanocomposites? *Macromolecules*, **40**(24), 8501–8517.
100. Plastic Technologies, Inc. (2007) Metal phosphonates and related nanocomposites. Patent WO2005/111131.
101. He, H. *et al.* (2005) Grafting of swelling clay materials with 3-aminopropyltriethoxysilane. *Journal of Colloid and Interface Science*, **288**, 171–176.

11

Microscope Evaluation of the Morphology of Rubber Nanocomposites

Hiroaki Miyagawa
Nitto Denko Technical Corporation, 501 Via Del Monte, Oceanside, CA 92058, USA

11.1 Introduction

Over the past decade, studies utilizing organoclay nanoplatelets in polymers to create nanocomposites having properties greater than their parent constituents have been accelerated. It has been demonstrated that both thermoplastic and thermoset nanocomposites reinforced by organoclay nanoplatelets lead to an excellent increase of elastic modulus [1]. The clay nanoplatelets in their natural state exist as agglomerated tactoids; although an aspect ratio of each silicate nanolayers is extremely large ($\sim$1000). The reinforcing effect of the nanoplatelets on the elastic modulus of nanocomposites is maximized when each individual nanoplatelet is completely separated and homogeneously dispersed in the matrix. Additionally carbon nanotubes (CNT) are another major nanoreinforcement for polymers after CNT were discovered by Iijima in 1991 [2], due to their splendid elastic modulus and strength, [3–8]. Regardless of either clay nanoplatelets or CNT, the nanocomposites with heterogeneously dispersed nanoscale reinforcements possess a lower elastic modulus than a homogeneously dispersed system.

The usefulness of rubber ranges widely from household applications to various industrial products; interestingly, the production of tires and tubes are rubber's highest applications. These rubbers are often reinforced by various reinforcements to substantially improve their mechanical properties [9]. For example, it is known that carbon black (CB) and inorganic fillers are used as additives to rubbers to improve the strength of vehicle tires. Rubbers have a high molecular weight, thus rubber compounds show high viscosity. The volume loading of these

Rubber Nanocomposites: Preparation, Properties and Applications Edited by Sabu Thomas and Ranimol Stephen
© 2010 John Wiley & Sons (Asia) Pte Ltd

reinforcements in highly viscous rubber compounds is extremely high in general, due to the low aspect ratio of the reinforcements. This fact reduces the processability of rubber composite compounds [10]. Considering that the homogeneous dispersion of nanoscale reinforcements having a high aspect ratio in a much smaller volume loading result in the significant improvement of mechanical properties for polymers, nanoscale reinforcements having a high aspect ratio can replace conventional reinforcements for rubber matrix and significantly improve the mechanical properties of rubbers.

This chapter discusses reported recent efforts in observing the morphologies of various rubber nanocomposites using wide range of microscopy techniques, including scanning electron microscopy (SEM), transmission electron microscopy (TEM) and atomic force microscopy (AFM). Morphological observations using various microscopies are extremely important to understand the relation between processing methods and properties of rubber nanocomposites, since the mechanical and electrical properties of the rubber nanocomposites strongly depend on the dispersion level of nanoscale reinforcements. The observed morphological information needs to be used for feedback to improve processing methods that will lead to optimize various properties of rubber nanocomposites. Each microscopy technique has both advantages and disadvantages. Therefore, experimental results are reviewed to discuss the advantages and disadvantages of the different microscopy techniques, and various artifacts are highlighted in each section of this chapter.

11.2 Optical Microscopy

The optical microscope, the oldest and simplest technique in the varieties of microscopes, uses visible light and a system of optical lenses to magnify images of small samples. The advantages of the optical microscopy include simplicity of technique and minimal sample preparation for observations. Theoretically, the magnification of an optical microscope is limited by only the resolution of the lens system. The best possible resolution can be calculated as approximately 200 nm. However, the limit of magnification for most optical microscopes is only 1000×, which is set by the actual resolution of the lenses. Additionally, an optical microscope has a shallow focal depth of only 1 μm at a magnification of 100×, while SEM has a deeper focal depth of about 1 mm at the same magnification. Therefore, optical microscopy has low apparent optical resolution due to the blurriness of objects which are out of focus. Another limitation of the standard optical microscopy is that it can only be applicable to dark or strongly refracting materials. Therefore, due to these limitations, optical microscopy is not suitable to observe the nanoscale dispersion of nanoscale reinforcements in a rubber matrix. In other words, when the dispersion of reinforcements can be seen using optical microscopy, this directly means that the nanoscale homogeneous dispersion of nanoscale reinforcements is not achieved for the sample.

However, optical microscopy is still useful to obtain different morphological information. Liu *et al.* prepared nanocomposites of poly(methylvinylsiloxane) (often called "silicone") elastomers with polyhedral oligomeric silsesquioxane (POSS) by melt blending in a Haake Banbury mixer [11]. POSS has a 3-D and well defined cage-like molecular structure represented by the formula of $(RSiO_{1.5})_n$, where each R is an organic group at a corner of the cage. In other words, the chemical composition of POSS is intermediate between silica (SiO_2) and silicone (R_2SiO). At first, the dispersion conditions of POSS in the blends were

visually observed by optical microscopy, after mixing the blends at different temperatures. For blends prepared at low mixing temperatures, the POSS crystals were dispersed in the silicone rubber matrix as large crystal aggregates of up to 100 μm with irregular shapes. However, the shape of the POSS crystals became hexahedral or flake-like for blends prepared at high mixing temperatures, and it seemed that POSS crystals at higher temperatures (>160 °C) were highly dissolved in the silicone rubber matrix. In order to additionally observe the phase and crystalline morphologies of the blends, a polarizing optical microscope was used while the samples were heated and cooled on a hot-stage. The polarizing optical microscopy can distinguish between materials with different refractive indexes, and thus provides more information in addition to the ordinary benefits of conventional optical microscopy. As a result, the dispersion conditions of POSS in the blends could visually be observed at different temperatures. POSS/silicone rubber mixture blended at 40 °C was placed between two glass plates, heated from 40 to 160 °C, kept at the high temperature for 3 min and then cooled to 40 °C again. The morphological evolution for the sample was recorded using a polarizing optical microscope, as shown in Figure 11.1. The original crystals of POSS in the sample at 40 °C were in irregular shapes, as seen in Figure 11.1(a), and the number of the crystals gradually decreased. The POSS crystals completely disappeared after heating to 160 °C, as seen in Figure 11.1(d), which implied that the POSS was totally dissolved in the silicone matrix. During subsequent cooling, some dissolved POSS molecules crystallized out in hexahedral or flake-like structures again. These results of optical microscopy were useful to observe how the blends became transparent when the processing temperature rose to 160 °C, which was far below the melting point of POSS.

Lim *et al.* processed polyamide (PA) 6-based ternary nanocomposites, which were prepared by melt-compounding of organoclay nanoplatelets as reinforcement and maleic anhydride grafted polyethylene-octene elastomer (POE-g-MA) as the toughening agent while changing the compositions of organoclay nanoplatelets and POE-g-MA [12]. TEM micrograph reveals that nanoscale rubbery phases of POE-g-MA were dispersed in the PA 6 matrix, separate from the organoclay nanoplatelets. Optical microscopy was used to investigate the individual effects of organoclay nanoplatelets and dispersed rubber particles in a PA 6 matrix on the fracture toughness K_{IC} and *J*-integral using single-edge-double-notch four-point bend (SEDN-4PB) technique. Experimental results showed that values of *J*-integral decreased gradually from 52.0 to 31.5 kJ/m^2 with increasing organoclay content from 0 to 10 wt% at a fixed POE-g-MA elastomer content (30 wt%). Optical microscopy as well as TEM were used to understand the influences of rigid organoclay nanoplatelets on the toughness of nanocomposites of PA 6/POE-g-MA blends. The plastic zone in front of the crack tip was observed as numerous line arrays resembling the craze-like feature using optical microscopy. The size of this plastic zone, observed as a craze-like feature by optical microscopy, was reduced with increasing organoclay content, since the nanocomposites lose plasticity with the addition of rigid organoclay nanoplatelets. A tougher specimen showed more plastic behavior; the size of the plastic zone in front of the crack tip of this tougher specimen was larger. Therefore, the decrease of *J*-integral with increasing the organoclay content was well correlated with the smaller plastic zone observed by optical microscopy.

Chiu *et al.* also processed similar organoclay/PA 6,6 nanocomposites with POE-g-MA through a melt-mixing procedure using an intermeshing twin-screw extruder in the co-rotating mode [13]. Instead of fracture toughness, crystalline morphology of PA 6,6 was investigated using polarizing optical microscopy. The thin-film specimens were prepared by first melting

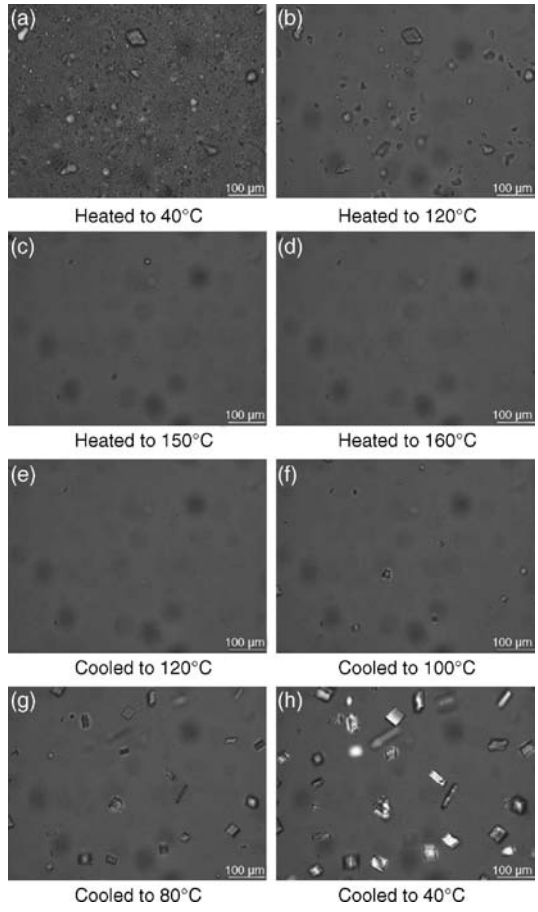

Figure 11.1 Polarizing optical microscope of POSS/silicone nanocomposites during the heating and cooling process (10 °C/min) (Reprinted from *Polymer*, **48**, L. Liu, M. Tian, W. Zhang, L. Zhang and J.E. Mark, "Crystallization and morphology study of polyhedral oligomeric silsesquioxane (POSS)/ polysiloxane elastomer composites prepared by melt blending," 3201–3212, © 2007, with permission from Elsevier.)

the samples and then these were compressed between glass slides. Typical spherulites were grown in a neat PA 6,6 sample. After adding organoclay nanoplatelets, the PA 6,6 spherulites were diffused and became smaller. It was further observed that a lot of dark spots, representing POE-g-MA phases, were exhibited within the PA 6,6 spherulites after the exclusive addition of only POE-g-MA, while the size of the spherulites became slightly smaller than that of neat PA 6,6. This meant that POE-g-MA component could be included within the PA 6,6 spherulites. For the organoclay/PA 6,6/POE-g-MA nanocomposites, broken spherulites containing POE-g-MA were developed; the crystalline boundary became indistinct.

Although optical microscopy still provides useful morphological information of rubber nanocomposites, nanoscale dispersion of nanoscale reinforcements or nanoscale rubber phases cannot directly be observed by optical microscopy.

11.3 Scanning Electron Microscopy

11.3.1 Micrographs with Secondary Electron

SEM provides images while a finely focused high-energy electron beam scans across the specimen surface in a raster scan pattern. When the electron beam strikes the specimen surface, it generates secondary electrons and backscattered electrons at or near the specimen surface. The primary detection mode is secondary electron imaging, which can produce high-resolution images of the specimen's surface with topographic features in about 1–5 nm resolution. SEM has a deep focal depth, resulting in a characteristic 3-D appearance useful for understanding the surface structure of the specimens.

SEM specimens need to be electrically conductive for the electron beam to scan the surface and to have a path to ground. An advantage is that the sample preparation for SEM is minimal, comparing with TEM sample preparation. Fractography conducted by SEM is the observation of fracture and failure surfaces of specimens. The fracture and failure surfaces of rubber nanocomposite specimens need to be cut into a smaller size to fit into the SEM specimen chamber, firmly be mounted on the specimen holder and then be sputter-coated with a ultrathin layer of electrically conductive material, such as Au, Au/Pd or Ir. The dispersed nanoscale reinforcements can often be observed on the fracture and failure surfaces of rubber nanocomposites. However, the disadvantage of the SEM is that only the specimen surface, not the inside of the specimen, can be observed. When nanoscale reinforcements are aggregated in the rubber matrix or when the reinforcement–rubber interaction is poor and interfacial debonding happens on the reinforcement–rubber interfaces, it is easy to recognize nanoscale reinforcements on the fracture and failure surfaces. However, when nanoscale reinforcements are uniformly dispersed and these are well coated with rubber matrix due to a cohesive failure in rubber matrix instead of interfacial debonding on the reinforcement–rubber interface, it is often difficult to distinguish between rubber matrix and nanoscale reinforcements.

SEM was utilized to observe rubber nanocomposites reinforced by organoclay nanoplatelets [14], polyaniline-treated clay nanoplatelets [15], graphite nanoplatelets [16, 17], starch nanocrystals [18], vapor-grown carbon nanofibers (VGCNF) [19, 20], and multiwalled carbon nanotubes (MWCNT) [21, 22]. Sharif reported that each different degree of dispersion of organoclay nanoplatelets was observed with a different roughness of failure surfaces [14]. Soto-Oviedo *et al.* observed aggregates of clay nanoplatelets using SEM [15]. Therefore, preparation of polyaniline/clay nanocomposites before adding these to a rubber matrix did not help to have an excellent nanoscale dispersion of individual clay nanoplatelets, although the utility of polyaniline could add a shielding performance to polymers because of reflecting and absorbing electromagnetic waves by intrinsically conducting polymers [23]. Yang *et al.* observed the graphite platelets dispersed in acrylonitrile butadiene rubber (NBR) matrix on failure surfaces using SEM due to the uncompleted exfoliation of graphene layers [16]. Different sizes and shapes of graphite platelets dispersed in a NBR matrix resulted in different morphologies of worn surfaces of composites after friction testing. Mu *et al.* also observed graphite nanoplatelets on the failure surfaces to see different degree of dispersion of graphite nanoplatelets, depending on different processing methods [17]. Solution method resulted in a relatively larger size of graphite nanoplatelets in silicone rubber matrix, thus the thermal conducting path existed and the relatively larger graphite nanoplatelets were observed on the failure surface by SEM. However, when the nanocomposites were prepared by melt mixing, the size of graphite nanoplatelets was significantly reduced and the thermal conducting path

was not obtained with the same amount of graphite nanoplatelets. Due to the smaller size of graphite nanoplatelets, these could not clearly be observed on the failure surface by SEM. Angellier *et al.* observed different surface morphologies of failure surfaces of starch nanocrystal-reinforced natural rubber nanocomposites, depending on surface treatments on starch nanocrystals [18].

Compared with nanoplatelets or nanoscale spherical reinforcements, nanoscale fibrous reinforcements, such as CNT and VGCNT, provide better possibilities to observe dispersion of the reinforcements in rubber matrix using SEM, because the pulled-out CNT and VGCNT having a length within the micron scale can easily be observed although the diameters of these fibrous reinforcements are in the nanoscale. A good example was reported by Sridhar *et al.* [22]. The failure surface of VGCNF/chlotobutyl rubber nanocomposites was observed by SEM, as seen in Figure 11.2. VGCNF was observed on the entire failure surface, and it seemed that these reinforcements were homogeneously dispersed in the rubber matrix.

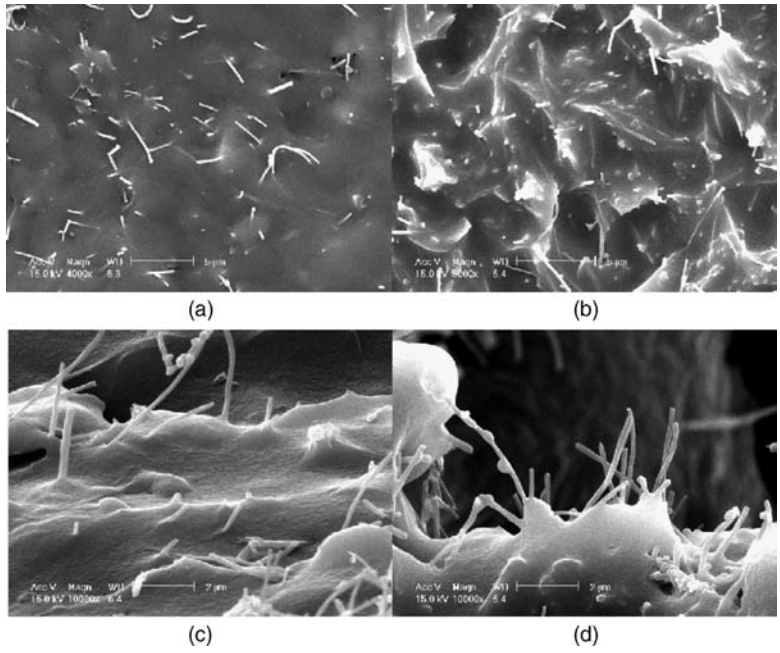

Figure 11.2 SEM microphotographs of VGCNF-reinforced chlorobutyl elastomers at increasing filler loadings: (a) and (c) 3 phr; (b) and (d) 12 phr (Reprinted from V. Sridhar, D. Xu, D.K. Tripathy and J.K. Kim, "Impedance and EMI shielding characteristics of vapor grown carbon nanofiber reinforced chloro-butyl elastomeric composites," *e-Polymers*, no. **44**, © 2008, with permission from e-Polymers Foundation.)

Miyagawa *et al.* processed anhydride-cured biobased epoxy containing 30 wt% epoxidized soybean oil (ESO) and its organoclay nanocomposites, and then the morphologies of fracture and failure surfaces of these specimens were observed by SEM after fracture and Izod impact testing [24]. As shown by arrows in Figure 11.3(a), many ESO-rich rubber phases in the

nanoscale or submicron scale were observed everywhere on the Izod impact failure surface of the epoxy containing 30 wt% ESO when no organoclay nanoplateletes were added. Indeed, the biobased epoxy with 30 wt% ESO was not transparent, due to different refractive indexes of epoxy matrix and ESO-rich rubbery phases. The biobased epoxy with 30 wt% ESO showed a significantly improved Izod impact strength and fracture toughness due to the phase separation. But, no phase separation was observed on the Izod impact failure surfaces after adding either exfoliated or intercalated organoclay nanoplatelets (5.0 wt%) into epoxy containing 30 wt% ESO, as seen in Figure 11.3(b) and (c), although the surfaces were still rough. The lack of ESO-rich rubbery phases also appeared in transparent nanocomposites showing a lower fracture toughness and Izod impact strength. Similarly, there are other reports regarding ESO-toughened phenolic resin [25], acrylic rubber dispersed epoxy nanocomposites reinforced by clay nanoplatelets [26] and carboxyl-randomized liquid butadiene-acrylonitrile rubber modified epoxy nanocomposites reinforced by SiO_2 nanoparticles [27]. The roughness of the fracture and failure surfaces was observed by SEM in these studies. No aggregates of nanoscale reinforcements were observed by SEM, whereas the dispersion of nanoscale reinforcements were observed by TEM in these studies.

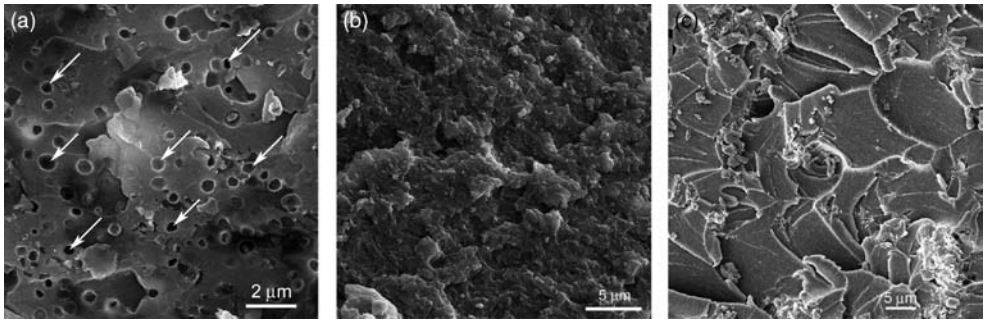

Figure 11.3 SEM micrographs of different Izod impact failure surfaces of epoxy containing 30 wt% ESO: (a) neat epoxy; (b) 5.0 wt% exfoliated clay nanocomposites; and (c) 5.0 wt% intercalated clay nanocomposites

Not only thermoset polymers but also thermoplastic polymers can be toughened with the addition of rubber. For example, polypropylene (PP) [28–31], PA 6 [32–34], PP/PA6 blend [35] and poly(vinyl chloride) [36] are toughened with the addition of rubbers and these are reinforced by clay nanoplatelets [29, 30, 32–36], calcium carbonate nanoparticles [31], or single-walled carbon nanotubes (SWCNT) [28]. In most studies of clay nanocomposites, the morphological changes of rubbery phase with or without the addition of clay nanoplatelets on the failure and fracture surfaces were observed using SEM. Additionally, Bao *et al.* discussed the impact essential work of fracture of clay/PP nanocomposites toughened with maleated rubber [30]. They found that the addition of clay nanoplatelets resulted in decreased impact properties as Miyagawa *et al.* observed in biobased epoxy nanocomposites, and they also observed using SEM that the matrix of rubber-toughened clay/PP nanocomposites showed

plastic behavior. Therefore, they pointed out that the balance between stiffness and toughness can be achieved by properly controlling the contents of clay nanoplatelets and rubbery phases. Ma *et al.* processed calcium carbonate/PP nanocomposites containing poly(butyl acrylate) or ethylene-octene copolymer rubber [31]. They observed the calcium carbonate nanoparticles as well as rubbery phases on the specimen surfaces etched by proper solvents. Based on different thermodynamic characteristics of three different components of nanocomposites, they showed that three different morphologies, (i) encapsulation of calcium carbonate nanoparticles by rubbery phase, (ii) separate dispersions of nanoparticles and rubbery phase and (iii) phase structure of nanoparticles at the PP/rubber interface, can be predicted using thermodynamic considerations [31]. Valentini *et al.* processed SWCNT/PP/ethylene-propylene-diene rubber nanocomposites, and the bundles of SWCNT were observed in low magnification SEM micrographs [28]. This means that individual SWCNT could not homogeneously be dispersed in polymer matrices.

Although SEM is useful to observe different morphologies of fracture and failure surfaces as well as aggregates of nanoscale reinforcements on these surfaces, it should be noted that it is not suitable to observe nanoscale and homogeneous dispersion of individual nanoplatelets and nanoscale spherical reinforcements.

11.3.2 Energy Dispersive X-Ray Spectroscopy (EDX)

The system of energy dispersive X-ray spectroscopy (EDX) is commonly attached to SEM, TEM, or electron probe microanalysis (EPMA). When the electron beam strikes the specimen surface, not only secondary electrons and backscattered electrons but also characteristic X-rays are generated at or near the specimen surface. These characteristic X-rays are used to identify the composition and measure the abundance of elements in the specimens. A solid-state semiconductor detector is used for EDX to accumulate X-rays at all wavelengths produced from the specimens, and the EDX spectrum with identified peaks can be recorded. Elemental maps can also be collected by regions of interest (ROI), which are areas of the EDX spectrum placed around each peak associated with a certain element. A dot is placed on the micrograph every time an X-ray is counted within a pre-established ROI. The maps with dots show the relative concentration of each element; areas with greater numbers of dots directly mean greater concentrations of the element. Ideally the surface of the specimens for EDX analysis needs to be perfectly flat and smooth; the topography of the sample can produce artifacts in EDX data due to nonuniform absorption and blockage of X-rays. When EDX analysis is conducted with bulk SEM samples, not thin-film TEM samples, the size of the specimen–beam interaction of the bulk SEM samples is much larger than that of the thin-film TEM samples. Considering that X-rays are produced from the entire area of specimen–beam interaction, the precision of EDX mapping with bulk SEM samples is poorer than that with thin-film TEM samples. The image acquisition can also be time-consuming when images of EDX mapping are acquired at higher resolution.

There are several examples of EDX mapping to observe the dispersion of nanoscale reinforcements in a rubber matrix. Bandyopadhyay *et al.* processed acrylic rubber/silica nanocomposites, and distribution of silicon was mapped with EDX to investigate the uniformity of dispersed silica [37, 38]. Sahoo *et al.* studied the effect of ZnO nanoparticles as a cure activator of natural rubber and nitrile rubber [39]. After mixing the rubber compounds

and ZnO nanoparticles using a laboratory two-roll mill and then curing at 150 °C, the dispersion of ZnO nanoparticles were observed by EDX mapping for Zn. Aggregated ZnO nanoparticles were observed as concentrated dots in the map, thus different dispersion degrees of ZnO could be detected by EDX mapping.

11.3.3 Electron Probe Microanalysis

EPMA is essentially the same instrument as SEM. EPMA can be used to analyze and determine the chemical composition of small volumes of solid materials. The primary importance of EPMA is the capability to acquire precise and quantitative elemental analyses at very small spot sizes (as little as 1–2 μm), primarily by wavelength dispersive spectroscopy (WDS). Elements from boron to plutonium can be quantitatively analyzed at levels as low as 100 ppm. WDS utilizes Bragg diffraction from crystals to select X-ray wavelengths of interest and direct them to gas-flow or sealed proportional detectors. The main advantage of EPMA is that it has selective elemental scanning capabilities.

Xu *et al.* carried out a carbon scan on the surface of graphite nanoplatelet/fluoroelastomer nanocomposites, as shown in Figure 11.4 [40], whereas Sridhar *et al.* presented a similar carbon scan image on the surface of VGCNF/chlorobutyl rubber nanocomposites [22]. They reported that they could confirm the homogeneous dispersion of graphite nanoplatelets and VGCNF in the rubber matrices. However, the poorer resolution of micrographs acquired by EPMA, compared with SEM micrographs, is a clear drawback of imaging by EPMA.

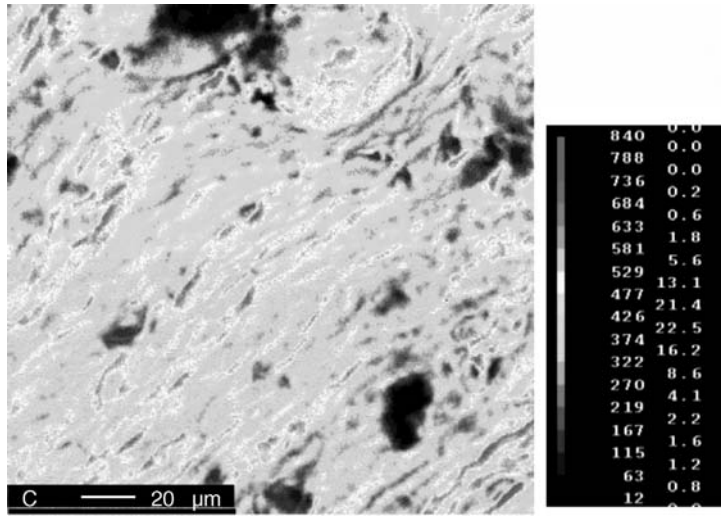

Figure 11.4 2-D distribution of nano graphite platelets in fluoroelastomer matrix: carbon scan (Reprinted from V. Sridhar, D. Xu, T.T. Pham and J.K. Kim, "Dispersion, mechanical and thermal properties of nano graphite platelets reinforced flouroelastomer composites," *e-Polymers*, no. 23, © 2008, with permission from e-Polymers Foundation.)

11.3.4 X-Ray Ultramicroscopy

X-ray ultramicroscopy (XuM) was developed by Mayo *et al.* [41, 42] to observe and determine particle distribution in polymer composites, providing greatly enhanced 2-D image quality. Unfortunately no examples of rubber nanocomposites have been reported. However, XuM provides a clear visualization of dispersion patterns of sub-micron particles in polypropylene and Nylon 6 matrix even with a sample thickness of up to 200 μm. The XuM can be housed in a commercially available SEM, as seen in the schematic diagram of XuM in Figure 11.5. Adding the X-ray detector and target modules is a major modification to the SEM. The technique of XuM has a resolution up to 50 nm. Therefore, XuM offers several advantages over other microscopy techniques, since it can avoid tedious sample preparation, can yield a well contrasted image to enable more accurate quantification of composite microstructure and can provide 2-D and 3-D information of filler distribution in a polymer matrix. Wu *et al.* processed Nylon 6 and polypropylene composites containing 0.5–20 wt% calcium carbonate ($CaCO_3$) at above 200 °C using a HAAKE twin-screw extruder, followed by hot pressing at the same temperature to obtain composite films approximately 150–200 μm thick [43]. $CaCO_3$ particles have an average diameter of 240 nm, a diameter range of 150–350 nm, an average length of 1.2 μm and a length range of 0.8–1.6 μm. Figure 11.6 shows an example of XuM micrograph of the PP composites containing 1 wt% $CaCO_3$. The XuM micrograph could present the size and distribution of the fillers often forming large aggregates. Most of the $CaCO_3$ particles seem to be aligned with the length of the particles perpendicular to the film surface. It was found that the dispersion of the $CaCO_3$ particles was relatively good with

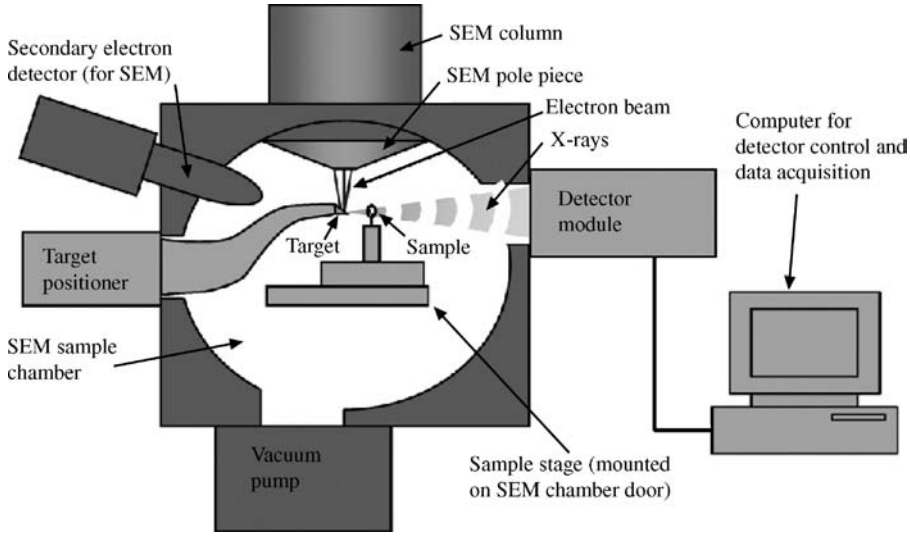

Figure 11.5 Diagram showing the main components of the XuM (Reprinted from *Composites Science and Technology*, **68**, D. Wu, D. Gao, S.C. Mayo et al., "X-ray ultramicroscopy: A new method for observation and measurement of filler dispersion in thermoplastic composites," 178–185, © 2008, with permission from Elsevier.)

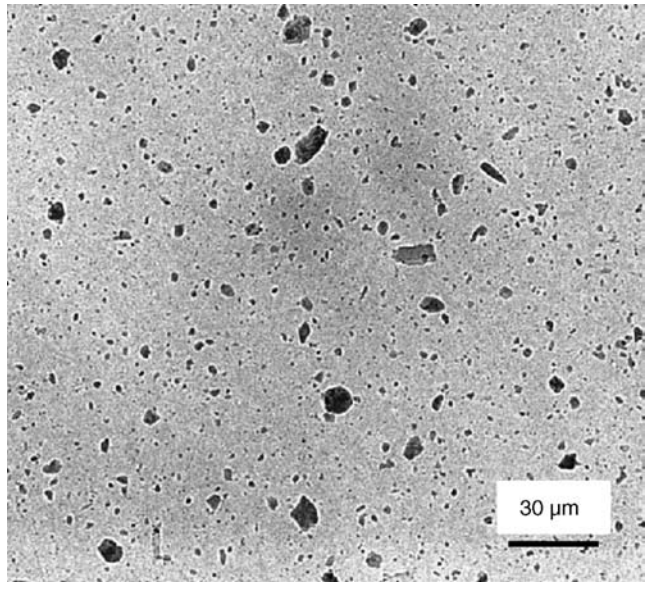

Figure 11.6 XuM image of the sample containing 1 wt% $CaCO_3$ in the PP matrix (Reprinted from *Composites Science and Technology*, **68**, D. Wu, D. Gao, S.C. Mayo et al., "X-ray ultramicroscopy: a new method for observation and measurement of filler dispersion in thermoplastic composites," 178–185, © 2008, with permission from Elsevier.)

loadings less than 1 wt% $CaCO_3$ particles, whereas more $CaCO_3$ loading caused larger number and size of the aggregates. The general methodology of the X-ray microtomography technique involves rotating the specimen around an axis perpendicular to the X-ray beam while collecting radiographs of the specimen at small angular increments. Reconstruction of the series of 2-D micrographs obtained from the entire sample could lead to a 3-D micrograph. 3-D micrographs indicated that there were particle-rich and particle-poor regions throughout the volume of the PP composites, although these observations were not obvious from the 2-D micrograph. 3-D micrographs confirmed the existence of aggregates of the $CaCO_3$ particles in different sizes in the bulk composites.

11.4 Transmission Electron Microscopy

Transmission electron microscopy (TEM) provides images, when an electron beam is transmitted through an ultrathin specimen and interacts with the specimen. Therefore, it can be thought that TEM images contain information inside the specimen. Comparing with SEM, the resolution of TEM is better than that of SEM in general. However, TEM sample preparation is more difficult and often tedious. This section discusses TEM sample preparations, examples of TEM images for rubber nanocomposites, elemental analysis and recent trends with 3-D TEM.

11.4.1 Sample Preparation for TEM Observations

Observations of rubber nanocomposites using TEM are impossible in general without sample preparation and samples need to be thinned for TEM observations. Importantly, the quality of obtained TEM micrographs strongly depends on the uniformity and thickness (preferably approximately 100 nm) of thinned TEM samples. TEM samples from the rubber nanocomposites can be prepared using either cryomicrotomy or the focused ion beam (FIB) technique. Therefore, these TEM sample preparation techniques are briefly explained in the following sections.

11.4.1.1 Cryomicrotomy

Ultramicrotomy is a method for preparing samples for examination using TEM. Since rubber samples are soft at room temperature, they need to be cooled at cryogenic temperature which is below the glass transition temperature of the rubber matrix of nanocomposites. The general procedure is shown in Figure 11.7(a). First, the sample block of rubber nanocomposite is first trimmed to create a block face. Second, thin sections are cut using a diamond or glass knife. The thin cut sections stay on the knife. Finally these thin sections are placed on a TEM grid for TEM observation. The ideal thickness of the thin sections is approximately 100 nm.

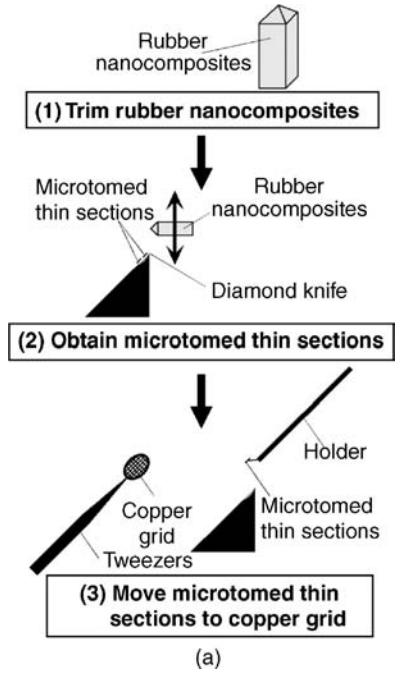

Figure 11.7 TEM sample preparation techniques: (a) using cryomicrotomy; (b) using FIB; and (c) SEM micrograph showing the top view of thinned area for TEM observations

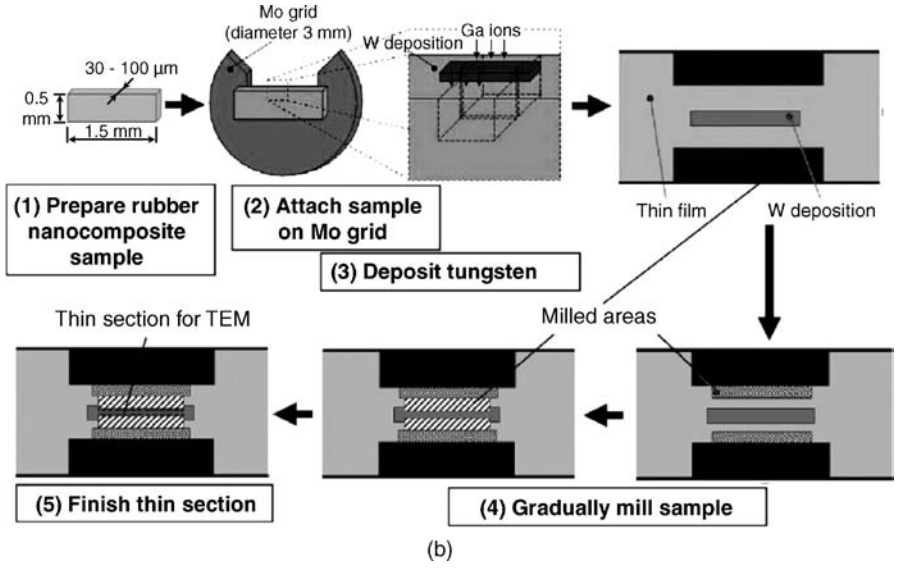

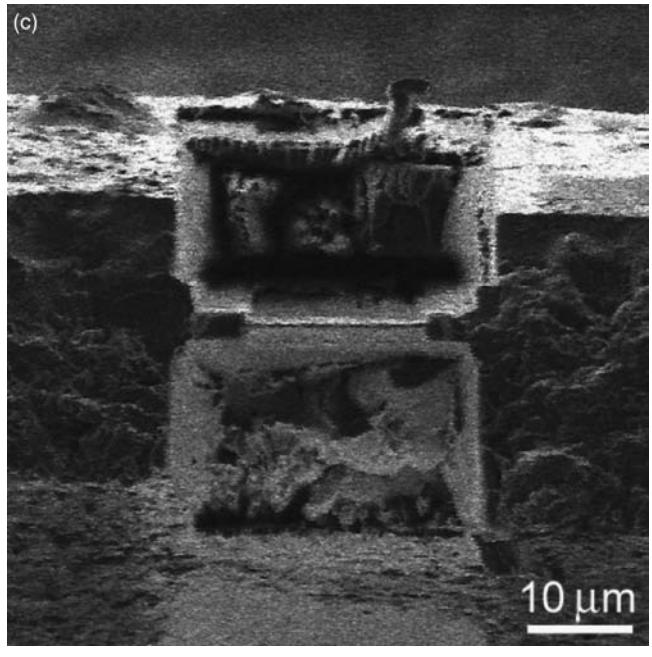

Figure 11.7 (*Continued*)

11.4.1.2 Focused Ion Beam

In the past several years, the focused ion beam (FIB) technique has been used for sample preparation to observe metals and ceramics using TEM and is a relatively new sample

preparation technique from larger specimens [44]. Since FIB can be used to microprocess specimens very precisely, it is possible to mill very thin membranes from a specific area of a polymer sample. There are some examples of how to prepare TEM thin sections for rubber nanocomposites using FIB [45]. Figure 11.7(b) shows the experimental process using the FIB system. First, a small piece is cut from rubber nanocomposite films. Next, the samples are mounted on a Mo grid for FIB thinning, then the samples are continuously milled by Ga ions using different probe sizes and then the thickness of the selected milling area is gradually reduced. This milling process can be stopped when the thickness of electron transparent areas becomes approximately 150 nm and is observed as shown in Figure 11.7(c).

11.4.2 Bright-Field TEM Micrographs

The contrast of bright-field TEM micrographs is not like the contrast of optical micrographs. Although a crystalline material interacts with the electron beam mostly by diffraction rather than absorption, the intensity of the transmitted beam is still affected by the volume and density of the materials through which the transmitted electron beam passes. Since polymer matrix and nanoscale particles have different elements and crystal structures, the nanoparticles dispersed in polymer matrix can be observed with different contrast in bright-field TEM micrographs.

TEM was utilized to observe rubber nanocomposites reinforced by clay nanoplatelets including montmorillonite [46–53], sodium fluorohectorite [10, 53–57], bentonite [50, 54, 56], rectorite [58, 59] and vermiculite [60]. Different morphologies of dispersed clay nanoplatelets were observed, depending on different methods of processing [46], different clay content [46], different organic modifications for clay [48, 50], different rubber matrices [49, 52, 54, 55, 57] and different types of clay nanoplatelets [50, 53, 54, 56]. The actual clay basal spacing in the rubber matrix was also measured directly by TEM micrographs [51], and it was also correlated with the measured results by X-ray diffraction (XRD) [46]. The morphological observations were useful to understand different schemes of material failure [48]. For example, Varghese *et al.* processed sodium fluorohectorite/rubber nanocomposites, whose matrix was either natural rubber (NR), polyurethane rubber (PUR), or a NR/PUR hybrid, via latex compounding [55]. TEM thin sections were prepared by cryomicrotomy at $-120\,^{\circ}C$, and these were observed by TEM without staining. For the PUR nanocomposites, the good intercalation by PUR and partial exfoliation of sodium fluorohectorite nanoplatelets were observed in the TEM micrograph shown in Figure 11.8(a). It was seen in this TEM micrograph that the high-aspect ratio of the sodium fluorohectorite nanoplatelets was also well maintained. In contrast, the dispersion of sodium fluorohectorite nanoplatelets in PUR/NR (1/1) latex blend considerably differed from that in PUR. NR and PUR were not compatible as it was seen that NR and PUR absorbed transmitted electron beam differently; thus the phases of NR and PUR appeared to be dark and light, respectively. The sodium fluorohectorite nanoplatelets were located at the boundary of the PUR and NR phases. Pronounced intercalation and possible exfoliation took place only in the PUR phase, as seen in Figure 11.8(b). The intercalated sodium fluorohectorite nanoplatelets covered the NR particles, resulting in a skeleton structure; sodium fluorohectorite nanoplatelets were less intercalated by NR than by PUR. Therefore in the case of the PUR/NR hybrid, PUR contained a higher amount of intercalated sodium fluorohectorite nanoplatelets, as some sodium fluorohectorite nanoplatelets were excluded by NR. This agreed with the

results from XRD showing that considerably better intercalation was observed for the PUR nanocomposites rather than the NR nanocomposites.

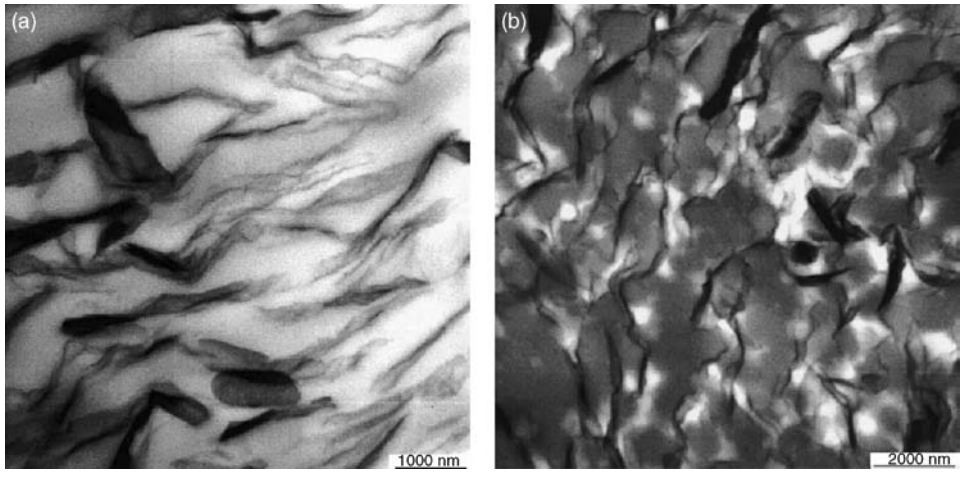

Figure 11.8 TEM micrographs of films containing 10 phr clay nanoplatelets: (a) nanocomposite film cast of PUR latex and (b) nanocomposite film cast of the PUR/NR (1/1) latex blend (Reprinted from S. Varghese, K.G. Gatos, A.A. Apostolov and J. Karger-Kocsis, "Morphology and mechanical properties of layered silicate reinforced natural and polyurethane rubber blends produced by latex compounding," *Journal of Applied Polymer Science*, **92**, no. 1, 543–551, © 2004, with the permission of John Wiley & Sons, Inc.)

Other rubber nanocomposites reinforced by silica nanoparticles [61, 62], MWCNT [63–66], graphite nanoplatelets [40], POSS [67] and europium complex [68] were also observed by TEM. For example, Fakhru'l-Razi *et al.* prepared MWCNT/NR nanocomposites by a solvent casting method using toluene with changing the MWCNT content up to 10 wt% [65]. TEM thin sections were prepared by cryomicrotomy at −120 °C. As seen in Figure 11.9(a), the diameter of the MWCNT was measured to be 2–20 nm, and MWCNT with various lengths homogenously dispersed in the NR matrix were observed. The distance between the MWCNT in the NR matrix was large and the MWCNT were somewhat aligned. After increasing the MWCNT content to 3.0 wt%, as seen in Figure 11.9(b), the orientations of the MWCNT in the NR matrix became more random. A pronounced tendency of random orientations of the MWCNT in the NR matrix was observed when the MWCNT content increased up to 10 wt%. A significant increase in nanocomposite elastic modulus was also observed by tensile testing due to the high aspect ratio of MWCNT observed in these TEM micrographs. It should also be noted that it is much more difficult to observe nanoscale reinforcements when not MWCNT but SWCNT were individually and homogeneously dispersed in rubber matrix, since the diameter of SWCNT (∼1 nm) is much thinner than the thickness of a microtomed thin section (80–100 nm) in general.

Instead of rubber nanocomposites reinforced by nanoscale inorganic reinforcements, there is an example for observing the heterocoagulated phases of two different rubbery materials.

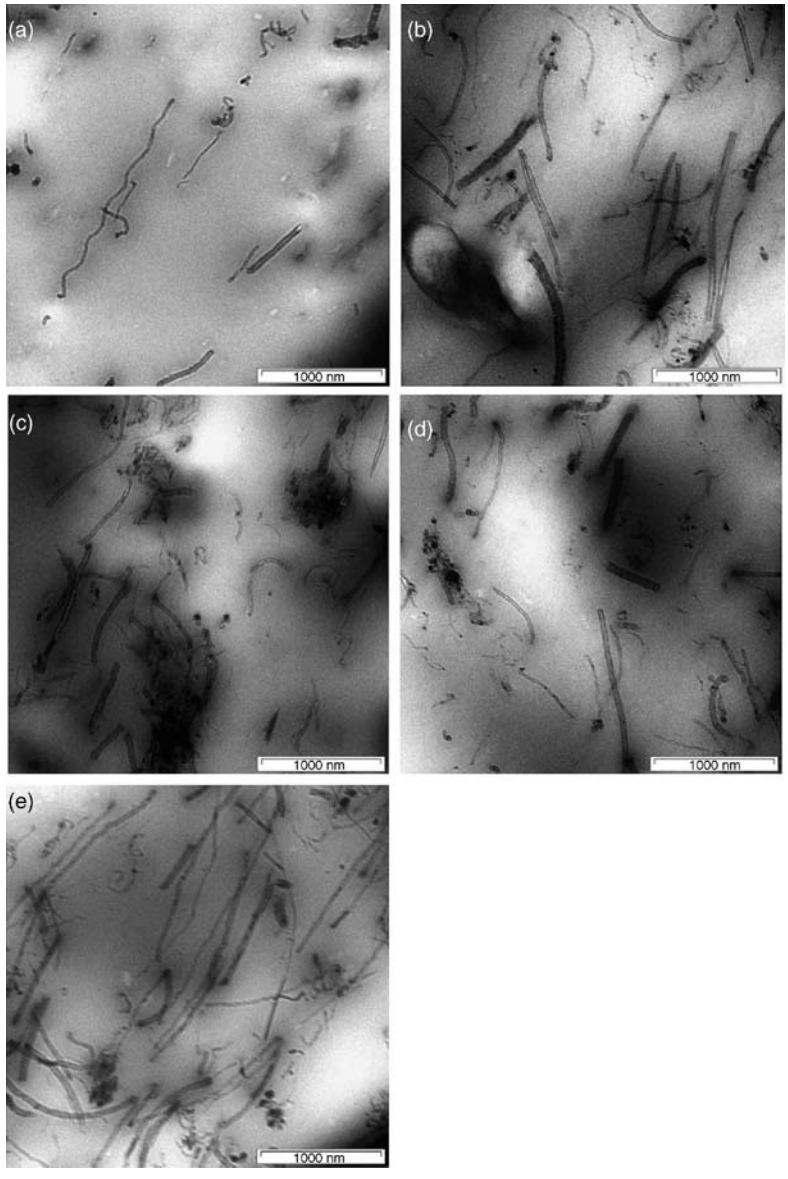

Figure 11.9 TEM images of CNTs in SMR CV60: (a) 1 wt% of CNTs; (b) 3 wt% of CNTs; (c) 5 wt% of CNTs; (d) 7 wt% of CNT; and (e) 10 wt% of CNTs (Reprinted from *Composite Structures*, **75**, A. Fakhru'l-Razi, M.A. Atieh, N. Girun, T.G. Chuah, M. El-Sadig and D.R.A. Biak, "Effect of multi-wall carbon nanotubes on the mechanical properties of natural rubber," 496–500, © 2006, with permission from Elsevier.)

The concentrated mixtures of two rubbery latices of poly(styrene-co-butadiene) (SBR) and poly(butyl acrylate) (PBA) was studied by Maruyama *et al.* [69], and the formation of intermediate aggregates with a core (SBR)/shell (PBA) morphology was observed by TEM; SBR particles were observed as black domains, with PBA particles as white domains with a black edge.

Clay morphologies dispersed in rubber-toughened thermoplastic polyolefin [70–73], PA 6 [74] and PA 66 [75] nanocomposites have also been observed by TEM. For example, Dasari *et al.* produced PA 66/maleic anhydride grafted styrene-ethylene-butylene-styrene block copolymer (SEBS-g-MA)/clay nanocomposites by four different blending protocols, and different morphologies of the nanocomposites depending on different protocols were observed by TEM before and after nanoscale scratch testing [75]. The mixing ratio of PA 66 : SEBS-g-MA : organoclay nanoplatelets was fixed as 80 : 15 :5. The four different protocols for preparing nanocomposites were as follows:

N1. PA 66, SEBS-g-MA and organoclay nanoplatelets were simultaneously blended.
N2. PA 66 was blended with SEBS-g-MA first, and the PA 66/SEBS-g-MA blend was then mixed with the organoclay platelets later.
N3. PA 66 was mixed with organoclay platelets first, and the PA 66/organoclay nanocomposite was then blended with SEBS-g-MA later.
N4. SEBS-g-MA was mixed with organoclay first, and then the SEBS-g-MA/organoclay master batch was blended with PA 66 later.

TEM thin sections of nanocomposites before nanoscale scratch testing were prepared by cryomicrotomy at $-80\,^{\circ}C$, and these were stained with osmium tetroxide (OsO_4) vapor in order to enhance the phase contrast between PA 66, clay nanoplatelets and SEBS-g-MA. It could be seen that the SEBS-g-MA particles were finely dispersed in the PA 66 matrix of nanocomposites prepared by protocols N1 and N2. PA 66 is more polar than SEBS-g-MA, therefore organoclay nanoplatelets were more exfoliated in PA 66, whereas thick clay nanoplatelets were just intercalated in SEBS-g-MA. The percentage of clay nanoplatelets seemed to be distributed equally between the PA 66 matrix and SEBS-g-MA phase of nanocomposites prepared by protocols N1 and N2. By protocol N3, most of the organoclay nanoplatelets seemed to be present in the PA 66 matrix with good dispersion. As a result, the authors judged that protocol N3, preparing the PA 66/clay nanocomposite first and then blending with SEBS-g-MA, was the best route regarding the dispersion quality of organoclay nanoplatelets. In contrast, nanocomposites prepared by protocol N4 showed that most of the organoclay nanoplatelets were present in the SEBS-g-MA phases as organoclay nanoplatelets were blended with SEBS-g-MA first. As indicated above, the result of the relatively low polarity of SEBS-g-MA could be not the exfoliation of organoclay nanoplatelets but intercalation within the SEBS-g-MA phases. These contrasting differences of nanoscale structures depending on protocols N1–N4 significantly affected the testing results of nanoscale scratch testing. TEM thin sections of the subsurface beneath the scratch track were also prepared for some selected samples by cryomicrotomy after conducting nanoscale scratch testing, and those TEM thin sections were observed to understand the damage induced by scratching. Clear differences of the subsurface damage in nanocomposites prepared by protocols N3 and N4, caused by different morphologies of dispersed clay nanoplatelets, were also identified by TEM observations after scratch testing.

11.4.3 Scanning Transmission Electron Microscopy and EDX

Scanning transmission electron microscopy (STEM) is a technique similar to TEM, and the principles of bright-field and dark-field images of STEM are the same as those of TEM. STEM provides images when an electron beam is transmitted through an ultrathin specimen and interacts with the ultrathin specimen. However, the electron optics focuses the beam onto a narrow spot which is scanned over the ultrathin specimen in a raster scan pattern like SEM. The scanning of the beam across the ultrathin specimen makes these microscopes suitable for analysis techniques such as mapping by EDX. These signals can be obtained simultaneously, allowing direct correlation of image and quantitative data of EDX.

Matteucci *et al.* prepared 1,2-polybutadiene rubber (PB)/titanium dioxide (TiO_2) nanocomposites to enhance gas permeability with changing TiO_2 content [76]. Since TiO_2 nanoparticles are expected to have the highest electron density of the phases present in the nanocomposites, the large bright structures in the dark-field STEM micrographs are attributed to aggregates of TiO_2 nanoparticles.

Olivetti *et al.* developed nanocomposite films consisting of a vanadium pentoxide (V_2O_5) phase formed within a rubbery block copolymer for the potential use as nanocomposite cathodes in lithium rechargeable batteries [77]. V_2O_5/rubbery block copolymer nanocomposite films were prepared by sol-gel synthesis from vanadyl triisopropoxide precursor in poly-(oligooxyethylene methacrylate)-*block*-poly(butyl methacrylate), POEM-*b*-PBMA. In order to understand the dispersed V_2O_5 within the rubbery polymer matrix, EDX was used for elemental mapping in the STEM mode. The STEM thin sections of ~50 nm were prepared by cryomicrotomy. Some STEM thin sections with and without vanadium oxide were stained with ruthenium tetraoxide (RuO_4) to obtain better image contrast. Verification of V_2O_5 confinement to the poly-(oligooxyethylene methacrylate) (POEM) domains for lower oxide contents was obtained by elemental mapping for ruthenium and vanadium in a RuO_4-stained thin section using EDX. Figure 11.10(a) shows the bright-field image of a RuO_4-stained film incorporating 24 wt% V_2O_5, whereas Figure 11.10(b) and (c) display the distribution of ruthenium and vanadium, respectively. The strong similarities in the spatial distribution patterns of these two figures confirm the co-location of V_2O_5 and POEM.

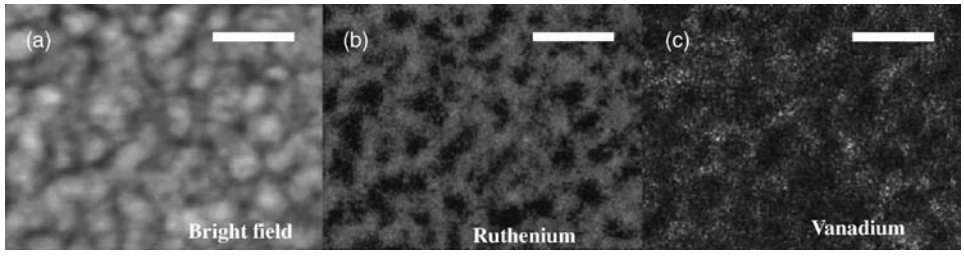

Figure 11.10 STEM micrographs of POEM-*b*-PBMA containing 24 wt% V_2O_5: (a) bright-field stained with RuO_4; (b) ruthenium chemical map; and (c) vanadium chemical map (scale bar = 90 nm) (Reprinted with permission from E.A. Olivetti, J.H. Kim, D.R. Sadoway, A. Asatekin, and A.M. Mayes, "Sol–Gel Synthesis of Vanadium Oxide within a Block Copolymer Matrix," *Chemistry of Materials*, **18**, no. 12, 2828–2833, 2006. © 2006 American Chemical Society.)

11.4.4 Electron Spectroscopy Imaging in Transmission Electron Microscopy

Electron energy loss spectroscopy (EELS) is another spectroscopy technique available with TEM to identify atomic compositions of materials. EELS is especially suitable to identify light elements, whereas the spectral sensitivity of EDX is too low for the light elements that are usually found in polymers. Electron spectroscopy imaging in transmission electron microscopy (ESI-TEM) uses EELS to provide information on particle constituents and their topological distribution. Therefore, ESI-TEM allows the observation of the distribution of light elements (for example, C, O, F, Na, S) in polymer specimens with a high spatial resolution [78, 79].

The research group of Galembeck prepared untreated montmorillonite/NR nanocomposites by a mild dispersion shear blending process [80–82]. TEM samples were prepared by drying a drop of dilute mixture of untreated montmorillonite/NR latex over a TEM grid, and these were observed by ESI-TEM. Characteristic energy losses from interaction of electrons with C (303 eV) and Si (132 eV) were selected, since the carbon and silicon mappings are very useful to identify the location of the NR matrix and the clay nanoplatelets, respectively. The location of the clay nanoplatelets was evident in the dark-field image as the bright areas in the dark-field image coincided with the bright areas in the Si elemental map. The compatibility of clay nanoplatelets with NR matrix was demonstrated by superimposing many bright domains in the C and Si elemental mapping.

The same research group also processed other rubber nanocomposites by mixing a low-T_g styrene-acrylic latex and untreated montmorillonite or ion-exchanged (K-, Li-, Ca-) montmorillonite clay nanoplatelets [83]. TEM thin sections of approximately 50 nm were prepared using cryoultramicrotomy at −140 °C. Figure 11.11 shows ESI-TEM micrographs of microtomed 10 phr Ca-montmorillonite/styrene-acrylic nanocomposites. The adhesion at the interfaces between Ca-montmorillonite and styrene-acrylic polymer was excellent; the corresponding elemental C and Si maps show that the styrene-acrylic polymer and Ca-montmorillonite domains were well connected without any evidence of lack of adhesion. It should be noted that the extent of exfoliation is less pronounced for Ca-montmorillonite, thus the improvements of the mechanical properties are accordingly lower than those using untreated, Li-, or K-montmorillonite clay nanoplatelets.

Horiuchi *et al.* investigated interactions between rubber and ZnO particles in the accelerated vulcanization process using ESI-TEM [84]. Combining elemental mapping and EELS enabled the characterization of the interfaces with spatial resolutions of less than 10 nm and the detection sensitivity for elements was approximately 0.5 at%. ESI-TEM micrographs showed that the mapping of zinc distribution corresponded to the dispersed ZnO particles, and no zinc element was detected from the region in the rubber matrix before vulcanization. ESI-TEM was additionally carried out to identify the chemical structures of the materials surrounding the ZnO particles after vulcanization. It was found from the elemental mapping and image-EELS spectra that a sulfur- and zinc-rich compound was generated around the ZnO particles. As compared to the sample before vulcanization, the sulfur content in the rubber matrix increased after vulcanization. This may suggest that the vulcanization reaction is initiated on the surface of ZnO particles with the adsorbed sulfur compounds. However, the zinc distribution was localized only at the vicinity around the ZnO particles; zinc was not detected in the rubber matrix. Oxygen was equally distributed in the rubber matrix and was not localized in the zinc- and sulfur-rich areas around the ZnO particles. This could lead to the reasonable speculation

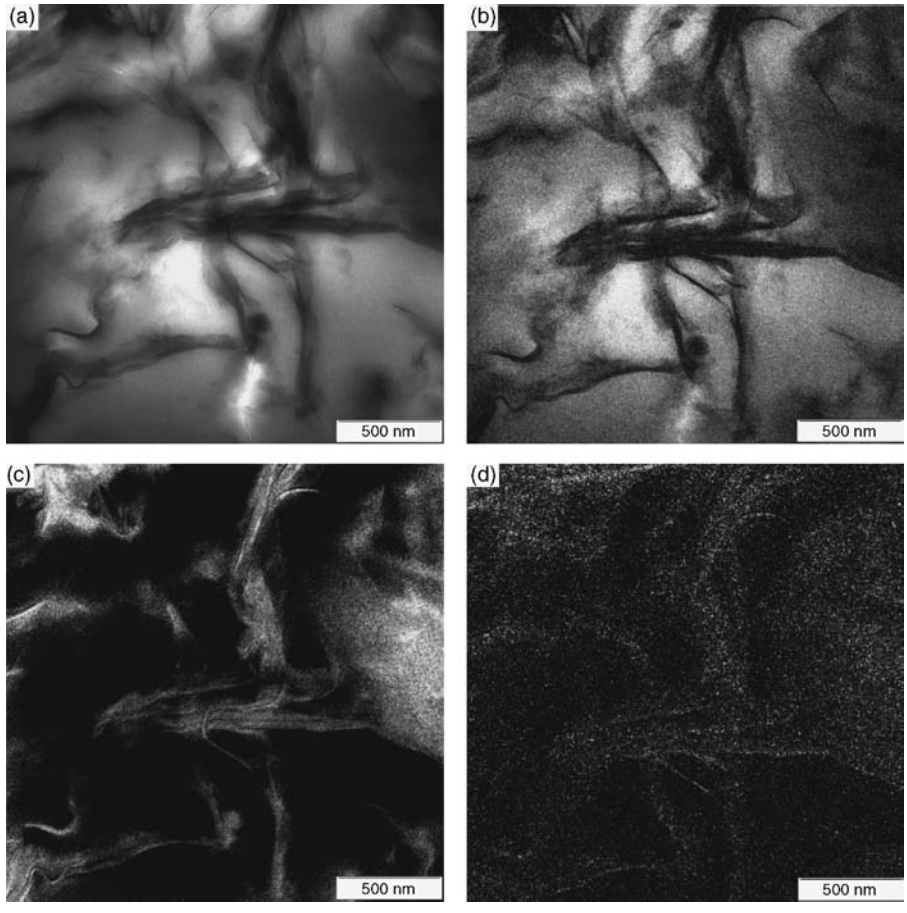

Figure 11.11 ESI-TEM micrographs of 10 phr Ca-MMT styrene-acrylic nanocomposite thin cuts: (a) bright-field image; (b) carbon map; (c) silicon map; and (d) calcium map (Reprinted with permission from Fabio do Carmo Braganca et al., "Counterion Effect on the Morphological and Mechanical Properties of Polymer–Clay Nanocomposites Prepared in an Aqueous Medium," *Chemistry of Materials*, **19**, no. 13, 3334–3342, 2007. © 2007 American Chemical Society.)

that the elemental oxygen distributed in the rubber matrix came from not ZnO nanoparticles but mainly stearic acid. Based on the theory of the chemical reaction, the material found at the vicinity around the ZnO particles was ZnS generated as a byproduct of accelerated vulcanization. The accelerated vulcanization occurs only locally around ZnO particles at a higher reaction rate, not uniformly in the entire rubber matrix. In other words, the rubber network structure can be heterogeneous on the nanoscale.

11.4.5 3-D Transmission Electron Microtomography

Conventional TEM projects a 3-D structural body onto a 2-D plane. In other words, the actual information along the thickness direction of the TEM specimens cannot be acquired by the

conventional TEM. A series of 2-D TEM micrographs at various angles should be obtained by tilting an ultrathin TEM sample, and a 3-D micrograph is produced by backprojection of 2-D TEM micrographs using a technique of computerized tomography. This procedure using transmission electron microtomography (TEMT) to reconstruct 3-D micrographs of the specimens is designated as 3-D TEMT. The resolution of the 3-D TEMT micrographs depends on the number of 2-D TEM micrographs.

Kohjiya *et al.* observed the 3-D structures of dispersed CB [85, 86] and silica nanoparticles [87, 88] in NR matrix. The TEM specimens were prepared at 200 nm, using ultramicrotomy. A total of 66 2-D TEM micrographs were collected at single-axis tilt angles ranged from -65° to $+65^\circ$ in 2° increments by a TEM sample holder. For processing CB/NR nanocomposites, NR was mixed with CB and the other reagents for curing on a two-roll mill in order to prepare NR vulcanizates. The total mixing time was between 20 and 30 min, depending on the loading amount of CB. The CB content was changed from 10 to 80 phr. The mixed compounds were compression-molded at 150 °C for 20 min. It was observed in 3-D TEMT micrographs that all CB nanoparticles were aggregated in NR matrix without any isolated CB nanoparticles, regardless of different CB content. For processing silica/NR nanocomposites, NR was mixed with silica nanoparticles and the other reagents by conventional mechanical mixing and was compression-molded at 150 °C for 20 min. Or, differently from conventional mechanical mixing, *in situ* silica was directly generated in NR matrix based on the sol-gel reaction of tetraethoxysilane (TEOS) as an alternate processing method of silica/NR nanocomposites. The silica/NR sheets were dried under vacuum at 30 °C and were cured with sulfur at 150 °C for 20 min after mixing with curing reagents on a two-roll mill. A lot of silica aggregates were clearly detected in the 3-D TEMT micrographs from various directions, regardless of the two different processing methods. The particle size of *in situ* silica nanoparticles from the sol-gel reaction was larger than that of the conventional silica mechanically mixed with NR matrix, as observed by 2-D TEM. The radius distribution and number of silica aggregates in a definite volume were also quantitatively evaluated from this 3-D TEMT analytical system. It was found that *in situ* silica nanoparticles had an average radius of 13.3 ± 5.6 nm, and the size of *in situ* silica nanoparticles was less uniform than that of the conventional silica nanoparticles. *In situ* silica nanoparticles showed a larger aspect ratio and were less symmetric in shape than conventional silica nanoparticles.

Jinnai *et al.* observed the 3-D morphology of rubber nanocomposites reinforced by both CB and silica nanoparticles using 3-D TEMT [89]. Both CB and silica nanoparticles were dispersed in the mixture of NR and polybutadiene (BR), where the ratio of NR/BR was 60 : 40 wt%. Polymers, fillers, silane coupling agents and curing agents were mechanically mixed and then cured at 145 °C for 40 min. The contents of CB and silica nanoparticles were 6.5 and 6.2 vol%, respectively. TEM thin sections of the rubber nanocomposites were prepared using FIB at cryogenic temperature. Although the distinctions between CB and silica nanoparticles were difficult by conventional 2-D TEM, different morphologies of CB and silica nanoparticles could clearly be observed by 3-D TEMT as the CB and silica nanoparticles appeared to be hollow and solid particles in 3-D TEMT micrographs, respectively. Thus, it could be said that 3-D TEMT provided a unique capability to distinguish two different nanoparticles having different morphological features. EELS was also used together with 3-D TEMT in order to observe the 3-D distribution of silica. Two different nanoscale reinforcements could be directly visualized in the digital slices, as shown in Figure 11.12(a). After such binarization in each digital slice, they are reconstructed into a

3-D TEMT micrographs, as shown in Figure 11.12(b). The vol% of both nanoscale reinforcements experimentally estimated from the 3-D TEMT micrographs closely agreed with the known compositions for processing the nanocomposites. It was also found that the aggregates consisted of only one species of nanoparticle; the CB and silica nanoparticles formed aggregates separately.

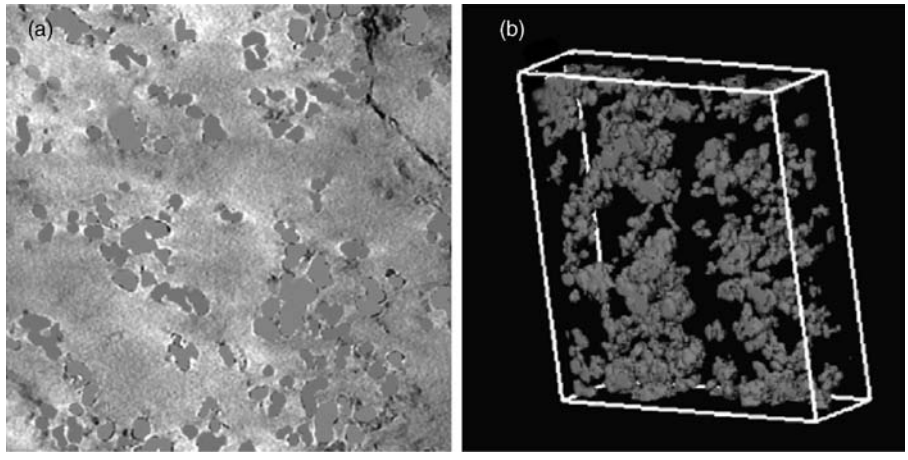

Figure 11.12 (a) Binarization of CB and Si nanoparticles. The digital slice is the same image as Figure 11.4a; and (b) 3-D reconstruction of the CB and Si/NRBR system. Box size is $726 \times 726 \times 107$ nm (Reprinted with permission from H. Jinnai, Y. Shinbori, T. Kitaoka, K. Akutagawa, N. Mashita and T. Nishi, "Three-Dimensional Structure of a Nanocomposite Material Consisting of Two Kinds of Nanofillers and Rubbery Matrix Studied by Transmission Electron Microtomography," *Macromolecules*, **40**, no. 18, 6758−6764, 2007. © 2007 American Chemical Society.)

3-D TEMT provides more information about rubber nanocomposites than conventional 2-D TEM, although the quality of 3-D TEMT micrographs is considerably deteriorated due to the limitation of the tilting angle up to $\pm 70^\circ$ in TEM. It is desired that 3-D TEMT will become a general purpose experimental tool and that the fundamental information from 3-D TEMT will be used to improve various properties of rubber nanocomposites.

11.5 Scanning Probe Microscopy

Scanning probe microscopy (SPM) is a microscopy technique acquiring images of surfaces using a physical probe scanning the surface of specimens. An image of the surface is obtained by mechanically moving the probe on the specimen from scan line to scan line and recording the probe-surface interaction as a function of position. For example, atomic force microscopy (AFM) and scanning tunneling microscopy (STM) are in the category of SPM. An advantage of SPM is that the resolution is only limited by the size of the probe–sample interaction volume.

Furthermore, these specimens do not require a partial vacuum, but can be observed in air at room temperature or while submerged in liquid. Although the resolution varies depending on different SPM techniques, some SPM techniques can reach atomic resolution. In contrast, SPM results may be inaccurate due to the shape and size of the SPM probes when the change of surface height of specimens is steep and more than 10 nm.

11.5.1 Atomic Force Microscopy

AFM consists of a microscale cantilever with a sharp tip (called as a probe) at its end that is used to scan the specimen surface. The cantilever is typically made of silicon or silicon nitride with a tip radius of curvature on the order of nanometers. In general, AFM can be operated in either contact (static) mode or tapping (dynamic) mode. In contact mode operation, the probe is essentially dragged across the sample surface. The tip of the cantilever probe is always in contact with the specimen surface during scanning, while the force between the tip and the surface is maintained as constant in order to maintain a constant deflection. A bend in the cantilever corresponds to a displacement of the probe tip along the z-axis relative to an undeflected cantilever. As the topography of the sample changes, the z-scanner must move the relative position of the tip with respect to the sample to maintain the constant deflection. Using this feedback mechanism, the topography of the sample is thus mapped during scanning by assuming that the motion of the z-scanner directly corresponds to the sample topography. Low stiffness probes are normally used to minimize the amount of applied force for scanning the sample and to boost the deflection signal. However, significant deformation and damage of rubber samples may often occur during this contact mode imaging in air, since significant force is applied to overcome the effects of contamination, including adsorbed moisture, on the specimen surface.

In contrast, tapping mode operation is more applicable particularly to obtain images of rubber-related samples. The resolution is similar to that in contact mode operation. Additionally, the forces applied to the specimens are lower, thus this causes less damage to the specimens. In tapping mode operation, the cantilever is externally oscillated close to its first bending mode resonance frequency by a small piezoelectric element mounted in the AFM tip holder. The amplitude of this oscillation is greater than 10 nm, typically in the range 20–200 nm. The tip makes contact with the sample for a short duration in each oscillation cycle. When the probe tip approaches the specimen surface, the tip–sample interactions alter the amplitude, resonance frequency and phase angle of the oscillating cantilever due to, for example, van der Waals force or electrostatic forces. This change in oscillation with respect to the external reference oscillation provides information for the characteristics of each AFM specimen. Especially, a later development in tapping mode is the use of the changes in phase angle of the cantilever probe to produce a phase contrast image. In general, changes in phase angle of the cantilever probe during scanning are related to energy dissipation by the interaction between the probe tip and the specimen surface. The phase contrast image obtained by the tapping mode often provides significantly more contrast than the topographic image and has been shown to be sensitive to material surface properties, such as elastic modulus and viscoelasticity. The phase contrast image can be concurrently constructed with the topographic image, and this concurrent imaging is another benefit of tapping mode operation in contrast to contact mode operation. The disadvantages of tapping mode operation, relative to contact

mode operation, are that the scan speeds are slightly lower and the operation may also be a little more complex; however, more information from tapping mode operation can certainly cancel such small disadvantages. In practice, the difference between the elastic modulus of the different regions usually needs to be substantially different to obtain a good contrast using tapping mode AFM. Good examples include a rubbery phase surrounded by another polymer matrix with a high glass transition temperature and inorganic reinforcements dispersed in rubber matrix. It should be noted that phase contrast images obtained by tapping mode AFM are qualitative due to inaccurate or unknown spring constant of the probe, unknown contact geometry and contributions from different types of tip–sample interactions.

An advantage of AFM over SEM is that AFM can provide a true 3-D surface profiles, while SEM provides only 2-D micrographs. Although the surfaces of SEM specimens need to be coated with metal or graphite and this coating process as a sample preparation is irreversible and may cause artifacts, such a coating process is not required for AFM. Additionally, most AFM modes can work perfectly in ambient air or even a liquid environment, whereas SEM needs an expensive vacuum environment for proper operation. However, a disadvantage of AFM compared to SEM may be the limited focal depth. AFM has a shallow focal depth on the order of only microns, while SEM has a deeper focal depth on the order of millimeters. Incorrect selection of a probe for the required resolution can also lead to image artifacts. AFM cannot scan images as fast as SEM, thus it is necessary to spend several minutes in a typical scan for an entire image.

AFM was utilized to observe rubber nanocomposites reinforced by montmorillonite clay nanoplatelets [90–97], silica nanoparticles [98, 99], graphite nanoplatelets [40], MWCNT [66, 100], metal nanoparticles [101] and magnetic nanoparticles [102]. For example, Sadhu *et al.* of the Bhowmick group processed rubber nanocomposites reinforced by octadecyl amine-modified montmorillonite clay, whose matrix was either SBR or NBR [90]. The rubber was first dissolved in a solvent. The modified clay was also dispersed in ethyl alcohol, and this was mixed with the rubber solution. After completely removing the solvents, samples were passed through an open two-roll mill and then molded at 160 °C, resulting in 1 mm thick rubber nanocomposite sheets. The AFM specimens were prepared using cryomicrotomy at −140 °C to obtain a truly flat surface for analysis by tapping mode AFM. This sample preparation using ultramicrotomy is common for analyzing polymer nanocomposites by tapping mode AFM. They first measured the dimensions of dispersed clay nanoplatelets in the rubber matrices using TEM, and these dimensions were further confirmed by tapping mode AFM. The bearing analysis of the rubber nanocomposites was conducted as shown in Figure 11.13, revealing the dispersion, dimensions and vol% of the clay nanoplatelets in the rubber matrix. Maiti *et al.* of the Bhowmick group also investigated not only morphological features but also contact and adhesion forces between the clay/fluoroelastomer nanocomposites and the AFM tip by contact mode AFM [92]. These forces were calculated from the force-plots, whose example is shown in Figure 11.14(a)-(e): (a) noncontact range, (b) jump into contact between probe and substrate, (c) maximum position of substrate, (d) maximum interaction force and (e) abrupt separation of probe from substrate [103]. Adhesion force was calculated from the pull-off portion of the retracting curve (Δx) and the contact force was calculated from the horizontal distance traversed by the piezo in the Z-direction, (ΔZ), as shown in Figure 11.14. The contact force was defined by the following equation:

$$F = k\Delta Z$$

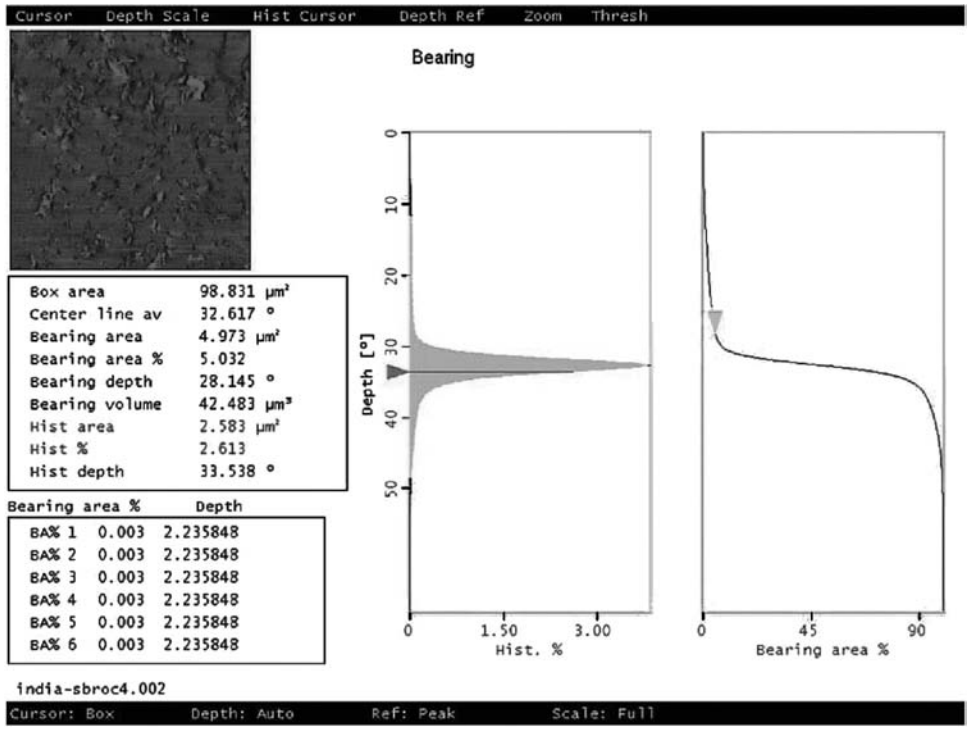

Figure 11.13 Bearing analysis of organoclay/SBR nanocomposites (With kind permission from Springer Science + Business Media: *Journal of Materials Science*, "Morphology study of rubber based nanocomposites by transmission electron microscopy and atomic force microscopy," **40**, © 2005, 1633–1642, S. Sadhu and A.K. Bhowmick, Figure 3.)

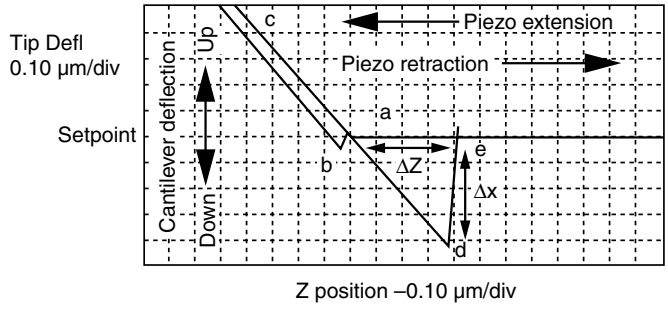

Figure 11.14 A typical force-plot of the atomic force microscope (Reprinted from *Polymer*, **47**, M. Maiti and A.K. Bhowmick, "New insights into rubber–clay nanocomposites by AFM imaging," 6156–6166, © 2006, with permission from Elsevier.)

where k is the spring constant of the probe. Different adhesion and contact forces of clay/fluoroelastomer nanocomposites were measured depending on the fluoroelastomer matrix, the clay/rubber interface and the clay nanoplatelets. The highest values of adhesion and contact forces were observed on the fluoroelastomer matrix, and these values were obviously similar to that of the neat fluoroelastomer. The least adhesion and contact forces were observed on the clay nanoplatelets, as it is the hardest portion on the clay/fluoroelastomer nanocomposites. The intermediate values corresponded to the interface region. Song *et al.* also observed a similar tendency for the adhesion force to decrease when the clay content increased [91]. It was suggested that the surface energy of clay/rubber nanocomposites decreased with increasing clay content.

Bokobza *et al.* observed the morphologies of dispersed MWCNT in a SBR matrix using AFM, when MWCNT/SBR nanocomposites were uniaxially loaded [100]. MWCNT/SBR nanocomposites were processed by the solution technique: SBR and MWCNT were mixed in solvent, solvent was removed under vacuum and then the MWCNT/SBR mixture was cured at 170 °C under a pressure to obtain 200 μm thick sheets. The nanocomposite sheet was placed on a small tensile machine that was fit to the sample holder of the AFM. Phase images obtained by tapping mode AFM for three different extension ratios are represented in Figure 11.15. The roughness of nanocomposite sheet increased with increasing strain and MWCNT were aligned along the loading direction. These MWCNT structures became more slender with increasing strain. However, an increase in strain led to a breakdown of bundles of MWCNT. The most striking results in this AFM investigation were those obtained after total release of the stress. Comparison between the original and prestretched sample, without loading, revealed a pronounced change in the morphology of the material. A second stretch performed on the same specimen did not show the same alignment as that observed for the first-stretched specimen.

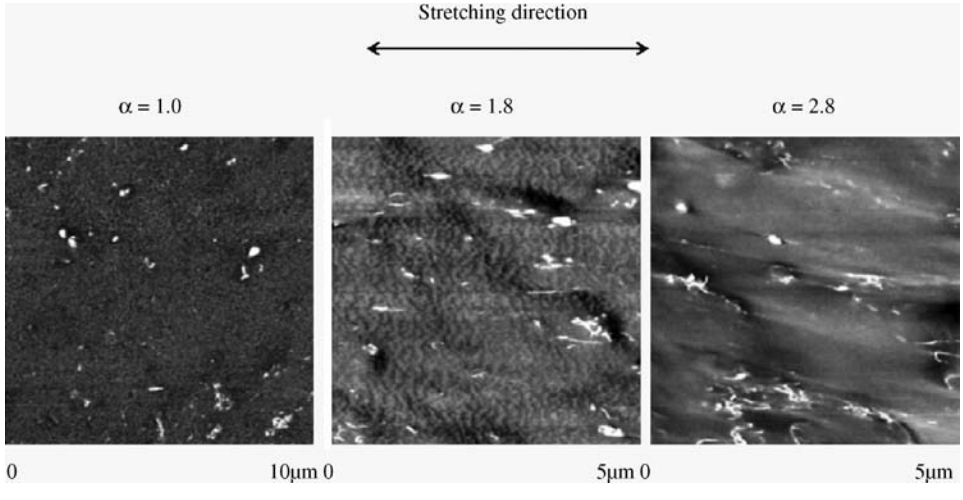

Figure 11.15 AFM images on unstretched and stretched films of SBR filled with 10 phr MWCNT: extension ratio α respectively equals to 1.0, 1.8 and 2.8 (Reprinted from L. Bokobza and C. Belin, "Effect of strain on the properties of a styrene-butadiene rubber filled with multiwall carbon nanotubes," *Journal of Applied Polymer Science*, **105**, no. 4, 2054–2061, © 2007, with the permission of John Wiley & Sons, Inc.)

The second stretch revealed different arrangements of the MWCNT: the MWCNT aggregates seemed to be perpendicularly oriented to the stretching direction. The strong alignment of the MWCNT bundles perpendicular to the previous extension axis could be the result of a re-equilibration of the stress field.

11.5.2 Other AFM-Related Techniques

The combination of AFM with a confocal Raman microscope (CRM) has been used by Schmidt *et al.* to study the composition of various thin films of heterogeneous polymer blends [104]. It is known that CRM combines the chemical sensitivity of Raman spectroscopy and the high resolution of confocal microscopy, providing an ideal tool to characterize various phases with a resolution down to 200 nm. The topographically different structures observed in AFM images can be associated with the chemical composition by using CRM. The combination of AFM and CRM in a single instrument enables the nondestructive and chemical characterization of heterogeneous materials obtained by CRM with the ultrahigh spatial and topographical information acquired by AFM. Schmidt *et al.* investigated three blends composed of immiscible polymers which were in either the rubbery or glassy state at room temperature, and they could obtain surface topographic images at high resolution and chemically identify various materials contributing to the surface composition. Phase separation within the thin films of the poly(methylmethacrylate) (PMMA)-styrene butadiene (SB) copolymer blend was proven by CRM measurements in spectral imaging mode. Figure 11.16(a) shows the basis spectra of SBR, triblock styrene-butadiene-styrene (SBS) copolymer and PMMA used as basis spectra for data analysis of the image spectra. An overlay of the fitted data is shown in Figure 11.16(b) and (c), where bright color represents the PMMA phase and dark color represents the distribution of the SBR or the SBS phase, respectively. The Raman spectral images of the blends of PMMA-SB showed a structure similar to the topographic AFM images in digital pulsed force mode (DPFM). Elevated domains in the topographic DPFM images were associated with the stiffer PMMA and are in good agreement with the distribution of the PMMA phase in the Raman spectral image.

There are other AFM-related techniques which are useful to understand surface properties of polymer materials. For example, friction force microscopy (FFM) is similar to AFM and it has a four-quadrant photodetector; this allows measurement of the frictional force acting on the probing tip. The contrast in FFM of polymer surfaces has been attributed to surface chemistry, molecular orientation, aggregation structure, crystallinity, stiffness and viscoelastic dissipation (molecular relaxation) [105, 106]. Another technique applies a frequency well below the probe tip resonance and is known as force modulation microscopy (FMM) [107]. In FMM, the tip is in contact with the specimen surface, and the sample surface is vibrated at a few kHz. The amplitude of tip oscillation at the modulation frequency provides information about the elasticity of the tip-probed sample region. The phase difference between the modulation signal of the sample position and the modulation response of the tip is related to the viscoelastic property of the sample. FMM was specifically introduced for the study of the elastic and viscoelastic properties of materials with nanoscale resolution.

By combining AFM with acoustic characterization, the techniques of ultrasonic force microscopy (UFM) [108, 109] and heterodyne force microscopy (HFM) [110] solve some of the limitations of conventional AFM. UFM was developed in order to improve the details and

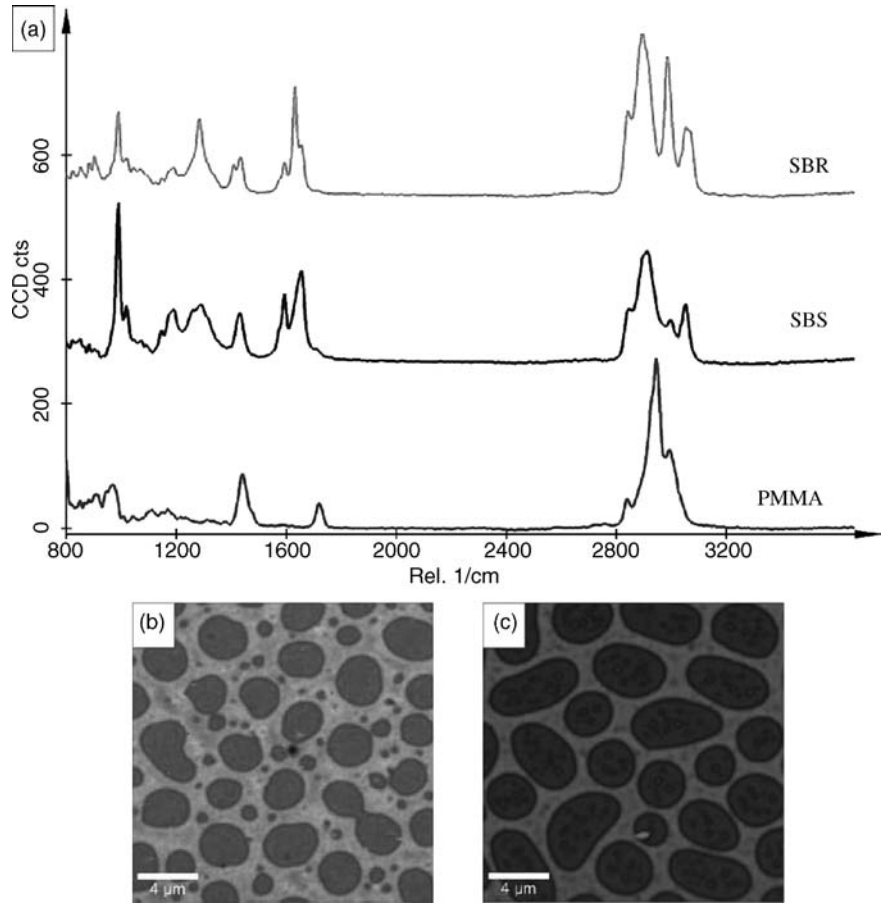

Figure 11.16 (a) Basic spectra of PMMA and SB; (b) phase-separated spectral images with $20 \times 20\,\mu m^2$ scan area of PMMA-SBR; and (c) PMMA-SBS, with PMMA as bright areas. As the Raman spectral images show, the distributions of PMMA and SB are complementary, proving that both polymer phases are formed on the glass substrate (Reproduced from U. Schmidt, S. Hild, W. Ibach and O. Hollricher, "Characterization of Thin Polymer Films on the Nanometer Scale with Confocal Raman AFM," *Macromolecular Symposia*, **230**, no. 1, 133–143, © 2005, Copyright Wiley-VCH Verlag GmbH & Co. KGaA. Reproduced with permission.)

image contrast where it can be seen as "flat" areas by AFM due to its limited contrast. The AFM tip is used to detect the ultrasonic waves and overcomes the limitation of wavelength that occurs in acoustic microscopy. A tip on the end of a cantilever is vibrated in contact with a sample surface at MHz frequencies. HFM is another technique similar to AFM, and this technique provides a means of testing the viscoelastic response of polymers in tip-probed regions at MHz frequencies.

Cuberes *et al.* measured the nanoscale elastic properties of rubber-toughened PMMA using AFM, FFM, FMM, UFM and HFM [111]. The interpretation of these images with respect to the

rather complex local structure of the polymer blend was greatly aided by various AFM-related techniques. Figure 11.17 shows a series of micrographs recorded using these different AFM-related techniques on the same region of the PMMA/rubber specimen. Both micrographs by waveguide UFM (W-UFM) shown in Figure 11.17(b) and amplitude-HFM (A-HFM), in which the vibration of the probe was monitored in amplitude, shown in Figure 11.17(c) revealed similar contrast. However, the image quality shown in Figure 11.17(c) was arguably better than that in Figure 11.17(b). A-HFM resolved differences in local sample stiffness due to the presence of rubber in the near-surface region. FMM micrographs shown in Figure 11.17(e) and (f) were not easy to understand unambiguously as they were strongly affected by frictional effects, presumably accompanied by variations in the tip-sample contact area. It should be noted that friction is strongly reduced by ultrasound in UFM and HFM. The micrograph with phase-HFM (ph-HFM) in which the vibration of the probe was monitored in phase, as shown in Figure 11.17(d) showed different contrast at protrusions that appeared similar in the contact-mode AFM, UFM and A-HFM micrographs. The FMM micrographs shown in Figure 11.17(g) and (h) revealed that those protrusions that gave rise to a darker contrast in Ph-HFM exhibited the characteristic halo-shaped frictional contrast in forward (bright halo) and reversed (dark halo) FFM scans. This was related to the presence of rubber directly exposed at the sample surface. However, the other protrusions could be distinguished from the matrix only by FFM, because of features related to their topography that gave rise to similar contrast in both forward and reversed scans. All the protrusions appeared with the same contrast as the matrix in their central regions when imaged with FFM. This indicated that they all have a PMMA surface.

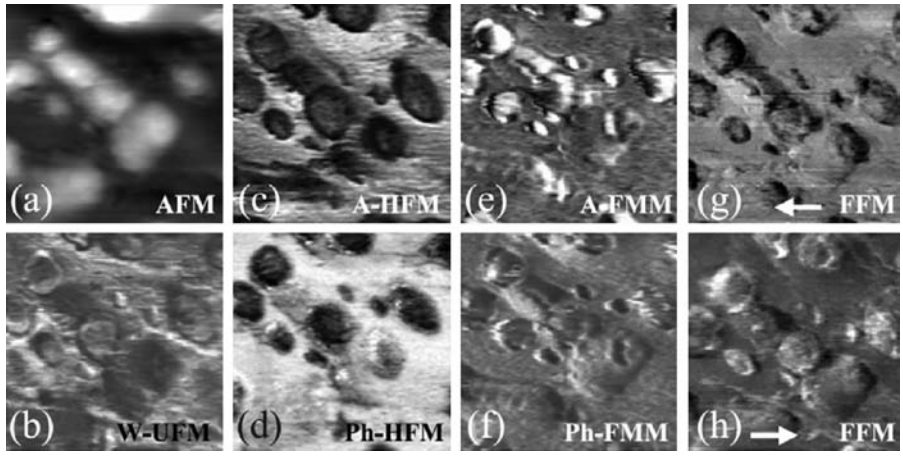

Figure 11.17 (a) Contact-mode AFM (gray scale 140 nm); (b) W-UFM ($f = 5.120$ MHz, modulation frequency 2.4 kHz, gray scale 4 nm); (c) and (d) HFM ($\omega_1 = 5.110$ MHz, $\omega_2 = 5.120$ MHz, gray scale 2 nm in (c) A-HFM, gray scale 5° (2.7 ns) in (d) Ph-HFM). (e) and (f) FMM ($f = 10$ kHz, gray scale 3 nm in (e) A-FMM, gray scale 15° in (f) Ph-FMM); (g) FFM reversed scan; and (h) FFM forward scan: 1.5×1.5 μm; $F_0 = 7$ nN; scan rate = 1 nm/s (2 ms/point) (Reprinted from M.T. Cuberes, H.E. Assender, G.A.D. Briggs and O.V. Kolosov, "Heterodyne force microscopy of PMMA/rubber nanocomposites: nanomapping of viscoelastic response at ultrasonic frequencies," *Journal of Physics D: Applied Physics*, **33**, no. 19, 2347–2355, © 2000, with permission from IOP Publishing Ltd.)

All the protrusions also appeared as dark by UFM and A-HFM which indicated that they have a layer of rubber at the vicinity of the surface. Therefore, it could be concluded that the contrast provided by Ph-HFM provided the capability to distinguish small differences in viscoelastic and/or adhesion hysteresis response time of PMMA on top of rubber, depending on whether or not this PMMA was well adhered to the matrix. Such contrast is unique to Ph-HFM and the differences are not revealed by AFM, UFM, FMM, A-HFM or FFM.

Electrostatic force microscopy (EFM) is a type of dynamic noncontact AFM where the electrostatic force is probed and measures local electrostatic interaction between a electrically conductive tip and a sample through Coulomb forces. A bias voltage is applied on the probe tip while the probe tip scans across the specimen surface. Different responses to the charged probe tip occur depending on the local electrical properties on the specimen's surface. This variation in electrostatic forces can be detected as a change in the oscillation amplitude and phase of the AFM probe. The electrostatic force can be detected 100 nm from the sample. Since this distance influenced by the electrostatic force is much larger than that interacting with van der Waals forces, the information about the electrostatic force can be separated from the surface topography of a flat surface by simply adjusting the distance between probe tip and the sample surface. Thus, the electrical features can be resolved from topographic features. For example, Kader *et al.* showed different EFM micrographs of CB/NBR composites containing 30 phr (14.5 vol%) CB with changing applied voltage, as shown in Figure 11.18 [112]. The topographic image of the sample was plain. Any identifiable features of composite morphology could not be detected at all without voltage, as seen in Figure 11.18(a). However, when the probe tip voltage was increased to 3 and 5 V, the morphology became clearer, with the appearance of bright parts representing the CB particles which were uniformly distributed in the NBR matrix, as shown in Figure 11.18(b) and (c). The appearance of bright parts implied that the current was flowing through these areas at a higher rate, where the CB formed a conducting path between the tip and the sample through electrostatic attraction. Close examination of the sample revealed the presence of circular CB particles having an average particle size of about 60 nm connected with many other particles to form an

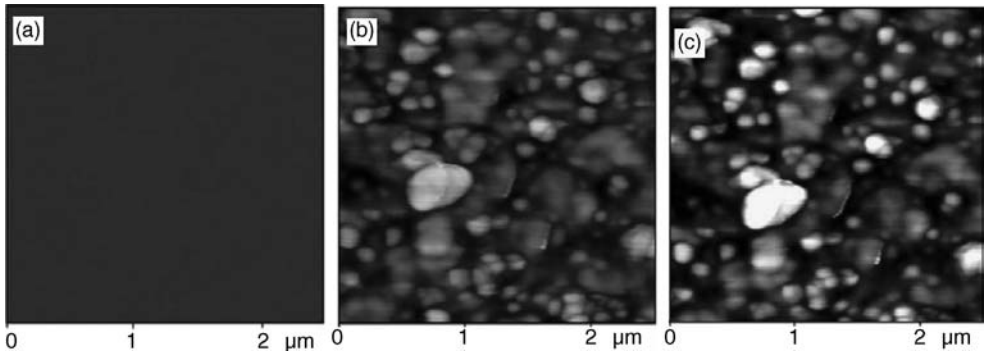

Figure 11.18 Effect of tip voltage on EFM phase images of 30 phr CB/NBR composites: (a) 0 V; (b) 5 V; and (c) 7 V (Reprinted from *Polymer Testing*, **24**, M.A. Kader, D. Choi, S.K. Lee and C. Nah, "Morphology of conducting filler-reinforced nitrile rubber composites by electrostatic force microscopy," 363–366, © 2005, with permission from Elsevier.)

aggregated structure. The application of very high voltage was limited due to electrical damage to the sample, and this may also destroy the morphology of the reinforcements in composite materials.

Since MWCNT are electroconductive, Kader *et al.* also conducted the EFM observations with NBR/MWCNT composites with 11 phr (4.1 vol%) of MWCNT, whose individual outer diameter is in the range of 15–30 nm [112]. The dispersed MWCNT could not be seen clearly with 0 V probe tip voltage. However, EFM images with 7 V probe tip voltage clearly showed the distribution of MWCNT. The dispersed MWCNT observed by EFM were in the form of bundles. More details of MWCNT distribution in the NBR matrix were obtained from the 3-D image and the average diameter of the MWCNT bundles was found to be approximately 50 nm.

As discussed in this section, the developments of various AFM-related techniques started to be applied to rubber nanocomposites and revolutionized to investigate surface properties and morphologies of rubber nanocomposites. Although to understand the acquired images from these new technologies may not often be easy and straightforward, it is desired that more data will be accumulated for observing rubber nanocomposites while these techniques are being improved.

11.6 Summary

This chapter reviews the various microscopy techniques applicable to observe the morphological features of rubber nanocomposites. TEM is the most versatile microscopy technique used for analyzing the nanoscale dispersion of nanoscale reinforcements in the rubber matrix, whereas other microscopy techniques like AFM also provide useful morphological information about rubber nanocomposites. Such morphological observations are important for correlating various properties of rubber nanocomposites with the degree of dispersion, size and aspect ratio of nanoscale reinforcements in rubber matrix. Processing protocols can be improved by understanding such correlations. Additionally, further development of novel microscopy techniques is crucial to easily obtain a range of morphological information about rubber nanocomposites. It is desired that experimental observations for rubber nanocomposites with new functionalities will be even more active in the next decade when researchers continue to obtain new benefits from applying novel microscopy techniques.

References

1. LeBaron, P.C., Wang, Z., and Pinnavaia, T.J. (1999) Polymer-layered silicate nanocomposites. *Applied Clay Science*, **15**(1/2), 11–29.
2. Iijima, S. (1991) Helical microtubules of graphitic carbon. *Nature*, **354**, 56–58.
3. Treacy, M.M.J., Ebbesen, T.W., and Gibson, J.M. (1996) Exceptionally high Young's modulus observed for individual carbon nanotubes. *Nature*, **381**(6584), 678–680.
4. Krishnan, A., Dujardin, E., Ebbesen, T.W. *et al.* (1998) Young's modulus of single-walled nanotubes. *Physical Review B*, **58**(20), 14013–14019.
5. Wong, E.W., Sheehan, P.E., and Lieber, C.M. (1997) Nanobeam mechanics: elasticity, strength, and toughness of nanorods and nanotubes. *Science*, **277**(5334), 1971–1975.
6. Salvetat, J.-P., Briggs, G.A.D., Bonard, J.-M. *et al.* (1999) Elastic and shear moduli of single-walled carbon nanotube ropes. *Physical Review Letters*, **82**(5), 944–947.
7. Yu, M.-F., Files, B.S., Arepalli, S., and Ruoff, R.S. (2000) Tensile loading of ropes of single wall carbon nanotubes and their mechanical properties. *Physical Review Letters*, **84**(24), 5552–5555.

8. Demczyk, B.G., Wang, Y.M., Cumings, J. *et al.* (2002) Direct mechanical measurement of the tensile strength and elastic modulus of multiwalled carbon nanotubes. *Materials Science and Engineering A - Structural Materials Properties Microstructure and Processing*, **334**(1/2), 173–178.
9. Bokobza, L. (2007) Multiwall carbon nanotube elastomeric composites: a review. *Polymer*, **48**(17), 4907–4920.
10. Karger-Kocsis, J. and Wu, C.-M. (2004) Thermoset rubber/layered silicate nanocomposites. Status and future trends. *Polymer Engineering and Science*, **44**(6), 1083–1093.
11. Liu, L., Tian, M., Zhang, W. *et al.* (2007) Crystallization and morphology study of polyhedral oligomeric silsesquioxane (POSS)/polysiloxane elastomer composites prepared by melt blending. *Polymer*, **48**(11), 3201–3212.
12. Lim, S.-H., Dasari, A., Yu, Z.-Z. *et al.* (2007) Fracture toughness of nylon 6/organoclay/elastomer nanocomposites. *Composites Science and Technology*, **67**(14), 2914–2923.
13. Chiu, F.-C., Fu, S.-W., Chuang, W.-T., and Sheu, H.-S. (2008) Fabrication and characterization of polyamide 6,6/organo-montmorillonite nanocomposites with and without a maleated polyolefin elastomer as a toughener. *Polymer*, **49**(4), 1015–1026.
14. Sharif, J., Yunus, W.M.Z.W., Dahlan, K.H., and Ahmad, M.H. (2006) Natural rubber/poly(ethylene-co-vinyl acetate)-blend-based nanocomposites. *Journal of Applied Polymer Science*, **100**(1), 353–362.
15. Soto-Oviedo, M.A., Araújo, O.A., Faez, R. *et al.* (2006) Antistatic coating and electromagnetic shielding properties of a hybrid material based on polyaniline/organoclay nanocomposite and EPDM rubber. *Synthetic Metals*, **156**(18/20), 1249–1255.
16. Yang, J., Tian, M., Jia, Q.-X. *et al.* (2006) Influence of graphite particle size and shape on the properties of NBR. *Journal of Applied Polymer Science*, **102**(4), 4007–4015.
17. Mu, Q. and Feng, S. (2007) Thermal conductivity of graphite/silicone rubber prepared by solution intercalation. *Thermochimica Acta*, **462**(1/2), 70–75.
18. Angellier, H., Molina-Boisseau, S., Lebrun, L., and Dufresne, A. (2005) Processing and structural properties of waxy maize starch nanocrystals reinforced natural rubber. *Macromolecules*, **38**(9), 3783–3792.
19. Karger-Kocsis, J., Felhös, D., and Thomann, R. (2008) Tribological behavior of a carbon-nanofiber-modified santoprene thermoplastic elastomer under dry sliding and fretting conditions against steel. *Journal of Applied Polymer Science*, **108**(2), 724–730.
20. Jiang, M.-J., Dang, Z.-M., and Xu, H.-P. (2006) Significant temperature and pressure sensitivities of electrical properties in multi-walled carbon nanotubes/methylvinyl silicone rubber nanocomposite. *Applied Physics Letters*, **89**, 182902.
21. De Falco, A., Goyanes, S., Rubiolo, G.H. *et al.* (2007) Carbon nanotubes as reinforcement of styrene-butadiene rubber. *Applied Surface Science*, **254**(1), 262–265.
22. Sridhar, V., Xu, D., Tripathy, D.K., and Kim, J.K. (2008) Impedance analysis and electromagnetic interference shielding effectiveness of vapor grown carbon nanofiber reinforced chlorobutyl rubber composites. *e-Polymers*, no. 044.
23. Fauveaux, S. and Miane, J.-L. (2003) Broadband electromagnetic shields using polyaniline composites. *Electromagnetics*, **23**(8), 617–627.
24. Miyagawa, H., Mohanty, A.K., Drzal, L.T., and Misra, M. (2004) Effect of clay and alumina-nanowhisker reinforcements on the mechanical properties of nanocomposites from biobased epoxy: a comparative study. *Industrial & Engineering Chemistry Research*, **43**(22), 7001–7009.
25. Situ, Y., Hu, J., Huang, H. *et al.* (2007) Synthesis, properties and application of a novel epoxidized soybean oil-toughened phenolic resin. *Chinese Journal of Chemical Engineering*, **15**(3), 418–423.
26. Balakrishnan, S., Start, P.R., Raghavan, D., and Hudson, S.D. (2005) The influence of clay and elastomer concentration on the morphology and fracture energy of preformed acrylic rubber dispersed clay filled epoxy nanocomposites. *Polymer*, **46**(25), 11255–11262.
27. Zeng, M., Sun, X., Yao, X. *et al.* (2007) Effects of SiO_2 nanoparticles on the performance of carboxyl-randomized liquid butadiene-acrylonitrile rubber modified epoxy nanocomposites. *Journal of Applied Polymer Science*, **106**(2), 1347–1352.
28. Valentini, L., Biagiotti, J., Kenny, J.M., and López Manchado, M.A. (2003) Physical and mechanical behaviour of single-walled carbon nanotubes/PP-EDPM nanocomposites. *Journal of Applied Polymer Science*, **89**(10), 2657–2663.
29. Mirzazadeh, H. and Katbab, A.A. (2006) PP/EPDM-based thermoplastic dynamic vulcanizates with organoclay: morphology, mechanical and viscoelastic properties. *Polymers for Advanced Technologies*, **17**(11/12), 975–980.

30. Bao, S.P. and Tjong, S.C. (2007) Impact essential work of fracture of polypropylene/montmorillonite nanocomposites toughened with SEBS-g-MA elastomer. *Composites Part A: Applied Science and Manufacturing*, **38**(2), 378–387.
31. Ma, C.G., Zhang, M.Q., and Rong, M.Z. (2007) Morphology prediction of ternary polypropylene composites containing elastomer and calcium carbonate nanoparticles filler. *Journal of Applied Polymer Science*, **103**(3), 1578–1584.
32. Baldi, F., Bignotti, F., Tieghi, G., and Riccò, F.T. (2006) Rubber toughening of polyamide 6/organoclay nanocomposites obtained by melt blending. *Journal of Applied Polymer Science*, **99**(6), 3406–3416.
33. Contreras, V., Cafiero, M., Da Silva, S. *et al.* (2006) Characterization and tensile properties of ternary blends with PA-6 nanocomposites. *Polymer Engineering and Science*, **46**(8), 1111–1120.
34. Wang, K., Wang, C., Li, J. *et al.* (2007) Effects of clay on phase morphology and mechanical properties in polyamide 6/EPDM-g-MA/organoclay ternary nanocomposites. *Polymer*, **48**(7), 2144–2154.
35. Hassan, A., Othman, N., Wahit, M.U. *et al.* (2006) Maleic anhydride polyethylene octene elastomer toughened polyamide 6/polypropylene nanocomposites: mechanical and morphological properties. *Macromolecular Symposia*, **239**(1), 182–191.
36. Wang, Q., Zhang, X., Jin, Y. *et al.* (2006) Preparation and properties of PVC ternary nanocomposites containing elastomeric nanoscale particles and exfoliated sodium-montmorillonite. *Macromolecular Materials and Engineering*, **291**(6), 655–660.
37. Bandyopadhyay, A., Bhowmick, A.K., and De Sarkar, M. (2004) Synthesis and characterization of acrylic rubber/silica hybrid composites prepared by sol-gel technique. *Journal of Applied Polymer Science*, **93**(6), 2579–2589.
38. Bandyopadhyay, A., De Sarkar, M., and Bhowmick, A.K. (2005) Effect of reaction parameters on the structure and properties of acrylic rubber/silica hybrid nanocomposites prepared by sol-gel technique. *Journal of Applied Polymer Science*, **95**(6), 1418–1429.
39. Sahoo, S., Maiti, M., Ganguly, A. *et al.* (2007) Effect of zinc oxide nanoparticles as cure activator on the properties of natural rubber and nitrile rubber. *Journal of Applied Polymer Science*, **105**(4), 2407–2415.
40. Xu, D., Sridhar, V., Pham, T.T., and Kim, J.K. (2008) Dispersion, mechanical and thermal properties of nano graphite platelets reinforced fluoroelastomer composites. *e-Polymers*, no. 023.
41. Mayo, S.C., Miller, P.R., Wilkins, S.W. *et al.* (2002) Quantitative X-ray projection microscopy: phase-contrast and multi-spectral imaging. *Journal of Microscopy*, **207**(2), 79–96.
42. Mayo, S.C., Davis, T.J., Gureyev, T.E. *et al.* (2003) X-ray phase-contrast microscopy and microtomography. *Optics Express*, **11**(19), 2289–2302.
43. Wu, D., Gao, D., Mayo, S.C. *et al.* (2008) X-ray ultramicroscopy: a new method for observation and measurement of filler dispersion in thermoplastic composites. *Composites Science and Technology*, **68**(1), 178–185.
44. Ishitani, T., Tsuboi, H., Yaguchi, T., and Koike, H. (1994) Transmission electron microscope sample preparation using a focused ion beam. *Journal of Electron Microscopy*, **43**(5), 322–326.
45. Niihara, K.-I., Kaneko, T., Suzuki, T. *et al.* (2005) Nanoprocessing and nanofabrication of a structured polymer film by the focused-ion-beam technique. *Macromolecules*, **38**(8), 3048–3050.
46. Wu, Y.-P., Zhang, L.-Q., Wang, Y.-Q. *et al.* (2001) Structure of carboxylated acrylonitrile-butadiene rubber (CNBR)-clay nanocomposites by co-coagulating rubber latex and clay aqueous suspension. *Journal of Applied Polymer Science*, **82**(11), 2842–2848.
47. Li, C.-C., Zhang, D., and Li, Z.-Y. (2002) Synthesis and properties of poly(ester ether) multiblock copolymers/organomontmorillonite hybrid nanocomposite. *Journal of Applied Polymer Science*, **84**(9), 1716–1720.
48. Gatos, K.G., Sawanis, N.S., Apostolov, A.A. *et al.* (2004) Nanocomposite formation in hydrogenated nitrile rubber (HNBR)/organo-montmorillonite as a function of the intercalant type. *Macromolecular Materials and Engineering*, **289**(12), 1079–1086.
49. Zhang, Z., Zhang, L., Li, Y., and Xu, H. (2006) Styrene-butadiene-styrene/montmorillonite nanocomposites synthesized by anionic polymerization. *Journal of Applied Polymer Science*, **99**(5), 2273–2278.
50. Madhusoodanan, K.N. and Varghese, S. (2006) Technological and processing properties of natural rubber layered silicate-nanocomposites by melt intercalation process. *Journal of Applied Polymer Science*, **102**(3), 2537–2543.
51. Han, M., Kim, H., and Kim, E. (2006) Nanocomposites prepared from acrylonitrile–butadiene rubber and organically modified montmorillonite with vinyl groups. *Nanotechnology*, **17**(2), 403–409.
52. Lu, Y.-L., Li, Z., Yu, Z.-Z. *et al.* (2007) Microstructure and properties of highly filled rubber/clay nanocomposites prepared by melt blending. *Composites Science and Technology*, **67**(14), 2903–2913.

53. Gatos, K.G. and Karger-Kocsis, J. (2007) Effect of the aspect ratio of silicate platelets on the mechanical and barrier properties of hydrogenated acrylonitrile butadiene rubber (HNBR)/layered silicate nanocomposites. *European Polymer Journal*, **43**(4), 1097–1104.
54. Varghese, S. and Karger-Kocsis, J. (2003) Natural rubber-based nanocomposites by latex compounding with layered silicates. *Polymer*, **44**(17), 4921–4927.
55. Varghese, S., Gatos, K.G., Apostolov, A.A., and Karger-Kocsis, J. (2004) Morphology and mechanical properties of layered silicate reinforced natural and polyurethane rubber blends produced by latex compounding. *Journal of Applied Polymer Science*, **92**(1), 543–551.
56. Mathew, S., Varghese, S., Rajammal, G., and Thomas, P.C. (2007) Dipping characteristics of layered silicates–natural rubber latex nanocomposites. *Journal of Applied Polymer Science*, **104**(1), 58–65.
57. Psarras, G.C., Gatos, K.G., and Karger-Kocsis, J. (2007) Dielectric properties of layered silicate-reinforced natural and polyurethane rubber nanocomposites. *Journal of Applied Polymer Science*, **106**(2), 1405–1411.
58. Wang, Y., Zhang, H., Wu, Y. *et al.* (2005) Preparation, structure, and properties of a novel rectorite/styrene-butadiene copolymer nanocomposite. *Journal of Applied Polymer Science*, **96**(2), 324–328.
59. Wang, Y., Zhang, H., Wu, Y. *et al.* (2005) Preparation and properties of natural rubber/rectorite nanocomposites. *European Polymer Journal*, **41**(11), 2776–2783.
60. Takahashi, S., Goldberg, H.A., Feeney, C.A. *et al.* (2006) Gas barrier properties of butyl rubber/vermiculite nanocomposite coatings. *Polymer*, **47**(9), 3083–3093.
61. Peng, C.-C., Göpfert, A., Drechsler, M., and Abetz, V. (2005) Smart silica-rubber nanocomposites in virtue of hydrogen bonding interaction. *Polymers for Advanced Technologies*, **16**(11/12), 770–782.
62. Bandyopadhyay, A., Maiti, M., and Bhowmick, A.K. (2006) Synthesis, characterisation and properties of clay and silica based rubber nanocomposites. *Materials Science and Technology*, **22**(7), 818–828.
63. Xiong, J., Zheng, Z., Qin, X. *et al.* (2006) The thermal and mechanical properties of a polyurethane/multi-walled carbon nanotube composite. *Carbon*, **44**(13), 2701–2707.
64. Atieh, M.A., Girun, N., Mahdi, E.-S. *et al.* (2006) Effect of multi-wall carbon nanotubes on the mechanical properties of natural rubber. *Fullerenes, Nanotubes, and Carbon Nanostructures*, **14**(4), 641–649.
65. Fakhru'l-Razi, A., Atieh, M.A., Girun, N. *et al.* (2006) Effect of multi-wall carbon nanotubes on the mechanical properties of natural rubber. *Composite Structures*, **75**(1–4), 496–500.
66. Bokobza, L. and Kolodziej, M. (2006) On the use of carbon nanotubes as reinforcing fillers for elastomeric materials. *Polymer International*, **55**(9), 1090–1098.
67. Fu, B.X., Hsiao, B.S., Pagola, S. *et al.* (2001) Structural development during deformation of polyurethane containing polyhedral oligomeric silsesquioxanes (POSS) molecules. *Polymer*, **42**(2), 599–611.
68. Liu, L., Lu, Y.-L., He, L. *et al.* (2005) Novel europium-complex/nitrile-butadiene rubber composites. *Advanced Functional Materials*, **15**(2), 309–314.
69. Maruyama, K., Kawaguchi, M., and Kato, T. (2001) Heterocoagulation behavior of poly(styrene-co-butadiene) and poly(butyl acrylate) at high particle concentrations. *Colloids and Surfaces A: Physicochemical and Engineering Aspects*, **189**(1/3), 211–223.
70. Lee, H.-S., Fasulo, P.D., Rodgers, W.R., and Paul, D.R. (2005) Thermoplastic olefin based nanocomposites. Part 1. Morphology and mechanical properties. *Polymer*, **46**(25), 11673–11689.
71. Lee, H.-S., Fasulo, P.D., Rodgers, W.R., and Paul, D.R. (2006) TPO based nanocomposites. Part 2. Thermal expansion behavior. *Polymer*, **47**(10), 3528–3539.
72. Kim, D.H., Fasulo, P.D., Rodgers, W.R., and Paul, D.R. (2007) Effect of the ratio of maleated polypropylene to organoclay on the structure and properties of TPO-based nanocomposites. Part I. Morphology and mechanical properties. *Polymer*, **48**(20), 5960–5978.
73. Naderi, G., Lafleur, P.G., and Dubois, C. (2007) Microstructure-properties correlations in dynamically vulcanized nanocomposite thermoplastic elastomers based on PP/EPDM. *Polymer Engineering and Science*, **47**(3), 207–217.
74. Chow, W.S., Bakar, A.A., Ishak, Z.A.M. *et al.* (2005) Effect of maleic anhydride-grafted ethylene–propylene rubber on the mechanical, rheological and morphological properties of organoclay reinforced polyamide 6/polypropylene nano-composites. *European Polymer Journal*, **41**(4), 687–696.
75. Dasari, A., Yu, Z.-Z., and Mai, Y.-W. (2007) Nanoscratching of nylon 66-based ternary nanocomposites. *Acta Materialia*, **55**(2), 635–646.
76. Matteucci, S., Kusuma, V.A., Swinnea, S., and Freeman, B.D. (2008) Gas permeability, solubility and diffusivity in 1,2-polybutadiene containing brookite nanoparticles. *Polymer*, **49**(3), 757–773.
77. Olivetti, E.A., Kim, J.H., Sadoway, D.R. *et al.* (2006) Sol-gel synthesis of vanadium oxide within a block copolymer matrix. *Chemistry of Materials*, **18**(12), 2828–2833.

78. Egerton, R.F. (1996) *Electron Energy-Loss Spectroscopy in the Electron Microscope*, Springer.
79. Crozier, P.A. (1995) Quantitative elemental mapping of materials by energy-filtered imaging. *Ultramicroscopy*, **58**(2), 157–174.
80. Valadares, L.F., Leite, C.A.P., and Galembeck, F. (2006) Preparation of natural rubber–montmorillonite nanocomposite in aqueous medium: evidence for polymer–platelet adhesion. *Polymer*, **47**(2), 672–678.
81. Galembeck, F., Valadares, L., do Carmo Bragança, F. *et al.* (2006) Morphology and microchemistry of colloidal polymers. *Macromolecular Symposia*, **245–246**(1), 307–314.
82. Valadares, L.F., do Carmo Bragança, F., da Silva, C.A. *et al.* (2007) Low-energy-loss EFTEM imaging of thick particles and aggregates. *Journal of Colloid and Interface Science*, **309**(1), 140–148.
83. do Carmo Bragança, F., Valadares, L.F., de Paula Leite, C.A., and Galembeck, F. (2007) Counterion effect on the morphological and mechanical properties of polymer–clay nanocomposites prepared in an aqueous medium. *Chemistry of Materials*, **19**(13), 3334–3342.
84. Horiuchi, S. and Dohi, H. (2006) Nanoimaging and spectroscopic analysis of rubber/ZnO interfaces by energy-filtering transmission electron microscopy. *Langmuir*, **22**(10), 4607–4613.
85. Kohjiya, S., Katoh, A., Shimanuki, J. *et al.* (2005) Nano-structural observation of carbon black dispersion in natural rubber matrix by three-dimensional transmission electron microscopy. *Journal of Materials Science*, **40**(9/10), 2553–2555.
86. Kohjiya, S., Katoh, A., Suda, T. *et al.* (2006) Visualisation of carbon black networks in rubbery matrix by skeletonisation of 3D-TEM image. *Polymer*, **47**(10), 3298–3301.
87. Kohjiya, S., Katoh, A., Shimanuki, J. *et al.* (2005) Three-dimensional nano-structure of in situ silica in natural rubber as revealed by 3D-TEM/electron tomography. *Polymer*, **46**(12), 4440–4446.
88. Ikeda, Y., Katoh, A., Shimanuki, J., and Kohjiya, S. (2004) Nano-structural observation of in situ silica in natural rubber matrix by three dimensional transmission electron microscopy. *Macromolecular Rapid Communications*, **25**(12), 1186–1190.
89. Jinnai, H., Shinbori, Y., Kitaoka, T. *et al.* (2007) Three-dimensional structure of a nanocomposite material consisting of two kinds of nanofillers and rubbery matrix studied by transmission electron microtomography. *Macromolecules*, **40**(18), 6758–6764.
90. Sadhu, S. and Bhowmick, A.K. (2005) Morphology study of rubber based nanocomposites by transmission electron microscopy and atomic force microscopy. *Journal of Materials Science*, **40**(7), 1633–1642.
91. Song, M., Xia, H.S., Yao, K.J., and Hourston, D.J. (2005) A study on phase morphology and surface properties of polyurethane/organoclay nanocomposite. *European Polymer Journal*, **41**(2), 259–266.
92. Maiti, M. and Bhowmick, A.K. (2006) New insights into rubber-clay nanocomposites by AFM imaging. *Polymer*, **47**(17), 6156–6166.
93. Maiti, M. and Bhowmick, A.K. (2006) Structure and properties of some novel fluoroelastomer/clay nanocomposites with special reference to their interaction. *Journal of Polymer Science Part B: Polymer Physics*, **44**(1), 162–176.
94. Ganguly, A., De Sarkar, M., and Bhowmick, A.K. (2006) Thermoplastic elastomeric nanocomposites from poly [styrene-(ethylene-co-butylene)-styrene] triblock copolymer and clay: preparation and characterization. *Journal of Applied Polymer Science*, **100**(3), 2040–2052.
95. Maiti, M. and Bhowmick, A.K. (2006) Effect of solution concentration on the properties of nanocomposites. *Journal of Applied Polymer Science*, **101**(4), 2407–2411.
96. Ganguly, A., De Sarkar, M., and Bhowmick, A.K. (2007) Morphological mapping and analysis of poly[styrene-b-(ethylene-co-butylene)-b-styrene] and its clay nanocomposites by atomic force microscopy. *Journal of Polymer Science Part B: Polymer Physics*, **45**(1), 52–66.
97. Abdollahi, M., Rahmatpour, A., Aalaie, J., and Khanli, F.H.H. (2007) Structure and properties of styrene-butadiene rubber/pristine clay nanocomposites prepared by latex compounding method. *e-Polymers*, no. 074.
98. Ogoshi, T., Fujiwara, T., Bertolucci, M. *et al.* (2004) Tapping mode AFM evidence for an amorphous reticular phase in a condensation-cured hybrid elastomer: b,b-dihydroxypoly(dimethylsiloxane)/poly(diethoxysiloxane)/fumed silica nanoparticles. *Journal of American Chemical Society*, **126**, 12284–12285.
99. Petrovic, Z.S., Cho, Y.J., Javni, I. *et al.* (2004) Effect of silica nanoparticles on morphology of segmented polyurethanes. *Polymer*, **45**(12), 4285–4295.
100. Bokobza, L. and Belin, C. (2007) Effect of strain on the properties of a styrene-butadiene rubber filled with multiwall carbon nanotubes. *Journal of Applied Polymer Science*, **105**(4), 2054–2061.
101. Mohanraj, G.T., Dey, P.K., Chaki, T.K. *et al.* (2007) Effect of temperature, pressure, and composition on DC resistivity and AC conductivity of conductive styrene-butadiene rubber-particulate metal alloy nanocomposites. *Polymer Composites*, **28**(5), 696–704.

102. Song, H.M., Kim, Y.J., and Park, J.H. (2008) Three-dimensional hierarchically organized magnetic nanoparticle polymer composites: achievement of monodispersity and enhanced tensile strength. *The Journal of Physical Chemistry C*, **112**(14), 5397–5404.
103. Sindel, U. and Zimmermann, I. (2001) Measurement of interaction forces between individual powder particles using an atomic force microscope. *Powder Technology*, **117**(3), 247–254.
104. Schmidt, U., Hild, S., Ibach, W., and Hollricher, O. (2005) Characterization of thin polymer films on the nanometer scale with confocal Raman AFM. *Macromolecular Symposia*, **230**(1), 133–143.
105. Haugstad, G., Gladfelter, W.L., Weberg, E.B. *et al.* (1995) Probing molecular relaxation on polymer surfaces with friction force microscopy. *Langmuir*, **11**(9), 3473–3482.
106. Kajiyama, T., Tanaka, K., and Takahara, A. (1997) Surface molecular motion of the monodisperse polystyrene films. *Macromolecules*, **30**(2), 280–285.
107. Maivald, P., Butt, H.J., Gould, S.A.C. *et al.* (1991) Using force modulation to image surface elasticities with the atomic force microscope. *Nanotechnology*, **2**(2), 103–106.
108. Kolosov, O. and Yamanaka, K. (1993) Nonlinear detection of ultrasonic vibrations in an atomic force microscope. *Japanese Journal of Applied Physics, Part 2*, **32**(8A), L1095–L1098.
109. Yamanaka, K., Ogiso, H., and Kolosov, O. (1994) Ultrasonic force microscopy for nanometer resolution subsurface imaging. *Applied Physics Letters*, **64**, 178.
110. Kolosov, O.V. and Briggs, G.A.D. (1996) Atomic force microscopy apparatus and a method thereof. International Patent Application, WO1998008046(A1).
111. Cuberes, M.T., Assender, H.E., Briggs, G.A.D., and Kolosov, O.V. (2000) Heterodyne force microscopy of PMMA/rubber nanocomposites: nanomapping of viscoelastic response at ultrasonic frequencies. *Journal of Physics D: Applied Physics*, **33**(19), 2347–2355.
112. Kader, M.A., Choi, D., Lee, S.K., and Nah, C. (2005) Morphology of conducting filler-reinforced nitrile rubber composites by electrostatic force microscopy. *Polymer Testing*, **24**(3), 363–366.

12

Mechanical Properties of Rubber Nanocomposites: How, Why ... and Then?

L. Chazeau, C. Gauthier and J.M. Chenal
MATEIS (Materials: Engineering and Science), INSA de Lyon, Bât Blaise Pascal, 20 Av. Albert Einstein, 69621, Villeurbanne Cedex, France

12.1 Introduction

Elastomers, also called rubbers, are made of long polymer chains linked to each other by crosslinking nodes. They are largely used in industrial applications, mainly in shoes, pipes and tires. For most applications, they are reinforced by stiff nanofillers [1], mostly carbon blacks or silica particles. These nanocomposites, existing well before the creation of the word "nanocomposites" were first developed on an empirical basis in tire application. Their use has been extended to many other applications, such as seals, because of their very specific viscoelastic properties and wear resistance. Thanks to this large industrial interest, the mechanical properties of filled elastomers have been abundantly studied, as shown by the impressive number of publications on the subject. The development of new nanofillers (nanoclays, carbon nanotubes) [2] and the development of nanoscale characterization techniques, have reactivated the interest of both rubber industry and research community for these materials.

Indeed, the new possibilities of reinforcement offered by the development of nanoscale fillers have lead to new researches in the fields of processing [3], microstructural characterization [4–7], mechanical characterization and the comprehension and modeling of the microstructure/mechanical properties relationships [8–10]. The history of the use of silica nanofillers in rubber is a good illustration. The introduction of silica has been made possible by

Rubber Nanocomposites: Preparation, Properties and Applications Edited by Sabu Thomas and Ranimol Stephen
© 2010 John Wiley & Sons (Asia) Pte Ltd

the synthesis of appropriate compatibilizer of the hydrophilic silica with the hydrophobic polymer matrix. This improvement of nanocomposites processing has lead to the creation of new rubber materials whose microstructure and mechanical properties have been extensively characterized. Then, the discovery of optimized formulations for tire application has lead to the development of the so-called "green tire" which is claimed to decrease car energy consumption compared to equivalent carbon black-filled tires.

Lots of studies on rubber nanocomposites are guided by this success story. This probably explains the extraordinary number of nanocomposite formulations tested, playing with the numerous types of available elastomers and nanofillers. However, a clear evaluation of the interest of each of these formulations is often difficult. This is mainly due to the complex behavior of filled elastomer. Indeed, besides the expected reinforcement it provides, the incorporation of small size fillers to crosslinked elastomeric matrix results in specific nonlinear mechanical behaviors including high hysteresis, stress softening (Mullins effect) and strain-dependent dynamic modulus (Payne effect). Various parameters are known to play a role in these phenomena, that is: (i) geometrical factors such as the shape, the size and the aspect ratio, (ii) intrinsic properties such as modulus and flexibility and (iii) surface characteristics such as specific surface and surface treatments. Most of the articles do not separate these various factors. Consequently, it is necessary to compile the information of the literature to identify and clarify the role of each parameter in rubber nanocomposites reinforcement.

Thus, through a review of the literature, this chapter will first recall the typical mechanical behavior of rubber filled with nanofillers, from the viscoelastic linear behavior to the large deformation one, including the ultimate properties. Then we will highlight the main filler parameters and how they seem to control these properties. In particular, we will focus on the role of filler–filler and filler–matrix interactions, which are necessarily important when dealing with fillers with such high specific surface (up to several hundreds of square meters per gram). We will also see the influence of these fillers on the matrix properties, since, for instance, the filler presence can modify the matrix crosslinking kinetic or induce crystallization. Then, this description will be completed by the introduction of different modeling approaches developed to account for and eventually predict the role of nanofillers in the mechanical behavior of these rubber nanocomposites.

12.2 Typical Mechanical Behavior of Rubber Nanocomposites

This first part presents the different nanofillers used to reinforce rubbers and highlights the specific aspects of the reinforcement induced by them.

12.2.1 The Fillers and Their Main Characteristics

Many types of nanofillers can be incorporated in rubber for reinforcement issue [11]. One of their most important characteristic is their specific surface (generally of the order of several hundreds of square meters per gram) which is directly related to their size, and which controls (at given filler content) the characteristic inter-filler distance. Another important parameter which has to be considered to describe these reinforcing elements is the average length/diameter ratio, known as the "aspect ratio". This aspect ratio may change from one (for spheres, for instance) to values as high as several thousands.

Carbon blacks and precipitated silica are the most common nanofillers used for reinforcing elastomers. Chemically, carbon black is a form of elemental carbon consisting of 90–99% carbon, generally obtained by incomplete combustion or thermal decomposition of hydrocarbons. Amorphous silica, SiO_2, is usually prepared by vapor-phase hydrolysis or precipitation. Both types consist of aggregates of spherical particles (diameter from 10 nm) fused together (Figure 12.1). Note that some papers are devoted to more exotic quasi spherical shaped fillers like SiC [12], Ni and Fe nanoparticles [13, 14] and even carbon–silica dual phase filler (CSDP) [15–17], the latter consisting in a carbon phase including finely divided silica domains herein.

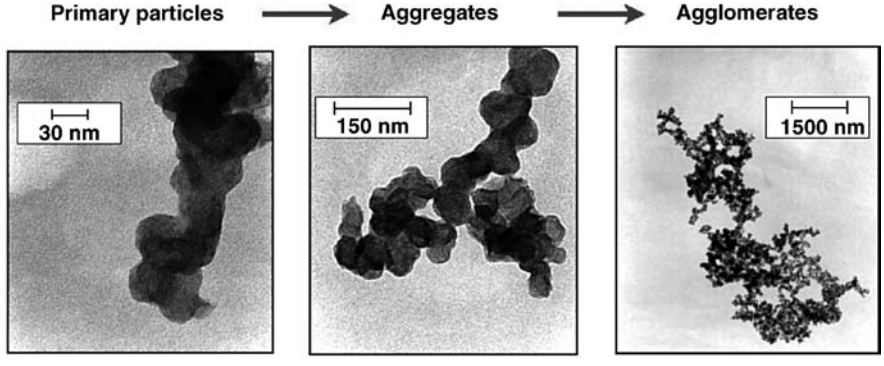

Figure 12.1 Transmission electron microscopy of primary carbon black particles coalesced into primary aggregates and further associated in agglomerates (Reproduced from T. Prasse, "Elektrisch leitfähige polymere Funktions- und Strukturverbundwerkstoffe auf der Basis von Kohlenstoff-Nanopartikeln und-fasern," PhD thesis, Technical University Hamburg-Harburg, 2001.)

The interest of platelet-like fillers such as clays (hydrous alumina-silicates) is also evaluated in many papers. The incorporation of layered silicates in polymers has been actively studied for the past two decades since the pioneer work of Toyota's researchers in the 1980s [18]. Nanosilicates development started when amino acid treatment was found to enable the dispersion of montmorillonite clays $[(OH)_4Si_8(Al_{4-x}\ Mg_x)O_{20}]$ at an individual scale (1 nm thick silicate layers with the lateral dimensions from 0.1 μm to several microns) in polyamide 6. Nowadays, both natural clays and synthetic layered silicates have been used to process polymer nanocomposites (mica, fluoromica, vermiculite, hectorite, fluororhectorite, saponite, ...) [19]. Reports on clay chemical modification and nanocomposite elaboration may be found in the literature (see the chapter written by Karger-Kocsis). The aspect ratio and the dispersion can reach very high values in delaminated composites (aspect ratio ranging from 100 to 1000) (Figure 12.2). Completely exfoliated clay can have a surface area of about $700\,m^2\,g^{-1}$. Clays can have a large modulus anisotropy, this is the case for montmorillonite, in which the longitudinal modulus is about 150 GPa, and the Poisson ratio is assumed to be close to 0.2, that is, close to that of mica crystal.

Recent years have seen an increased interest for rod-shaped nanofillers. Carbon nanotubes, long and thin cylinders of carbons, were discovered in 1991 by the electron microscopist Iijima who was studying the arc-evaporation synthesis of fullerenes [20]. Just few nanometres across, the cylinder can be tens of micron long, and each end is "capped" with half of a fullerene

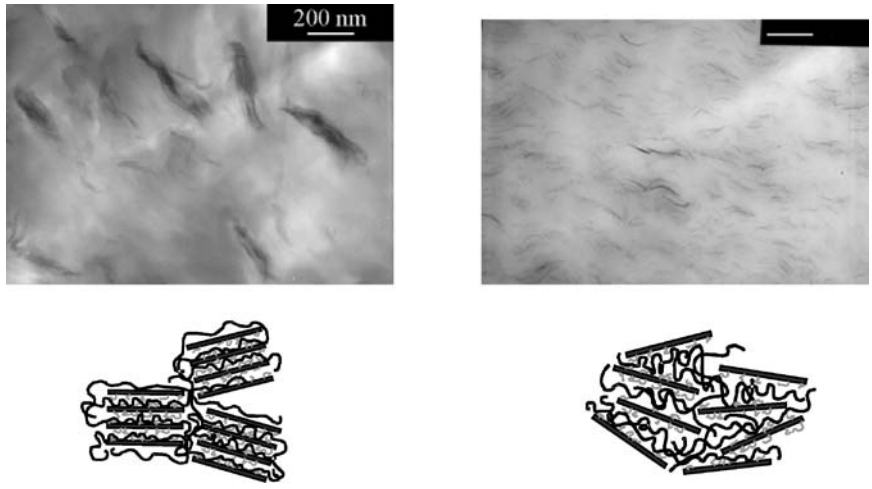

Figure 12.2 Electron microscopy of intercalated and delaminated platelet-like nanofillers in a PA6 matrix (Reproduced from E. Reynaud, "A study on the relationships between structure and mechanical properties in thermoplastics filled with nanoscopic inorganic particles," PhD thesis, Institut National des Sciences Appliquées de Lyon, 2000.)

molecule (Figure 12.3). Nanotubes can have either a unique cylindrical wall (SWNTs) or multiple walls (MWNTs). Their structural properties depend on the diameter, length, and chirality, or twist of the nanotubes. Their predicted mechanical characteristics are remarkable (Young's Modulus $\sim$1 TPa [21, 22], maximum tensile strength $\sim$30 GPa [23]). They have excellent thermal conductivity, are chemically inert and, depending on the details of their atomic arrangement (chirality), behave as metals or semiconductors. Therefore, combined to a low density, these characteristics make them particularly attractive for reinforcement in

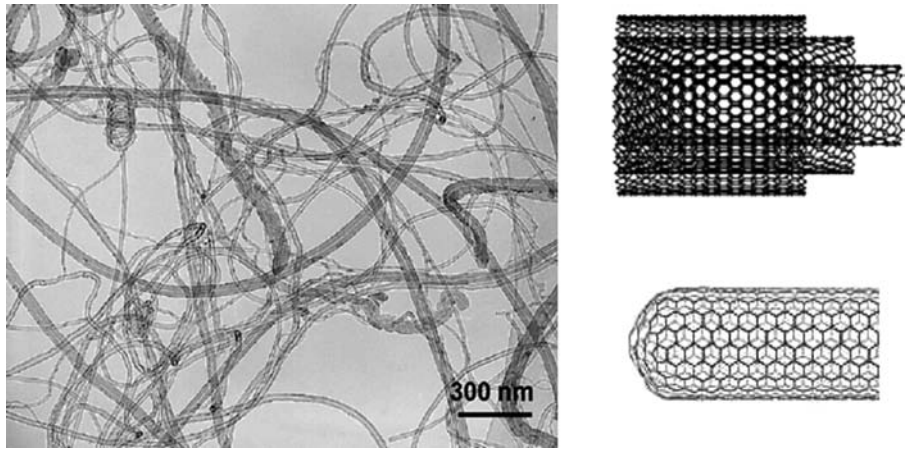

Figure 12.3 Transmission electron microscopy of multiwall carbon nanotube (Reproduced from F. Dalmas, "Composites à matrice polymère et nano-renforts flexible : propriétés mécaniques et électriques," PhD thesis, Institut National des Sciences Appliquées de Lyon, 2005.)

composite materials. Increasing number of publications report their incorporation in rubbery matrices [24] such as NR [25], or silicone [26–28]. Note that these fillers, which enable a very low geometrical percolation threshold, offer the possibility of conductive properties at very low volume fraction compared to carbon blacks [27–29].

Some rodshape fillers with high aspect ratio can also be extracted from the biomass. Cellulose nanofibrils [30] have a typical diameter range of 5–10 nm, with a length of several μm and they consist in the alternation of mono-crystals linked to their neighbors by disordered segments. The hydrolysis of these segments allows the extraction of quasi-perfect mono-crystals in the nano range. These whiskers have been extensively studied in noncrosslinked polymers [31, 32]. Actually, there is an increasing interest for nanofillers from natural origin. For instance, we can cite a recent work with waxy maize starch nanocrystals, which have been incorporated in NR [33].

To complete the picture, we can also evoke particular fillers, which are in between chemical additives and stiff fillers, like polyoxide silesquisiloxane (so-called POSS). These particles are made of few silicium atoms and their surface is generally reactive with the polymer in which they are introduced [34]. They have been for instance incorporated in polydimethyl siloxane elastomer [35] or polyurethane elastomer [36].

To conclude, a large panel of available nanofillers can be introduced in rubbery matrices. Among them, CB, silica and clays are undoubtedly the most studied ones. A large part of literature on new nanocomposites is devoted to the optimization of the filler dispersion in the elastomer. The filler dispersion can be reached through different processing route recalled in different review articles treating of filled nanocomposites: latex route, melt mixing, or solution route [3] (a chapter is devoted to this aspect in the book). The resulting dispersion strongly depends on: (i) the choice of the polymer, which controls the filler/matrix compatibility, (ii) the surface chemistry of the filler, which can change this compatibility, and (iii) the filler morphology, including their shape factor and specific surface area that impacts the amount of interfacial contact area with the polymer, the complex shape of the aggregates and therefore the rheology of the filler/matrix mix. The filler chemical modification is particularly studied, resulting in an impressive increase of the number of nanocomposite systems studied. Moreover, the complex chemistry of crosslinking of the host elastomer can also be chosen as a function of the nanofiller/polymer system [3, 37]. Obviously, all these parameters must be taken into account when one wants to understand the role of the filler incorporation in the mechanical properties of the processed nanocomposites, since they influence the microstructure (filler dispersion, crosslinking) and the different type of interaction (filler/filler, filler/matrix). Before going into the detail of these different effects, one can however note that the first consequence of the introduction of stiff nanofillers, like in the case of micro-scale fillers, is to increase the material modulus. This is described below.

12.2.2 Filler Reinforcement (Modulus Increase)

The commonly accepted definition of an elastomer is an assembly of long polymer chains crosslinked to each other, with a glass transition temperature below the ambient temperature. Like all polymer material, when submitted to a mechanical stimulus, elastomers show a viscoelastic response. Many static or dynamic experimental techniques are used to characterize this behavior. At low strain, unfilled elastomers have a linear behavior, defined by a compliance (or modulus) independent of the applied stress level. Besides, their energy dissipation measured during a strain cycle is low; in other terms, the elastomer shows a low sensitivity

to strain state, in particular at low strain (Figure 12.4). This pseudo-elastic behavior above T_g is also related to a very constant modulus in the rubbery plateau, and can be relatively well described by theory (cf. Section 12.4).

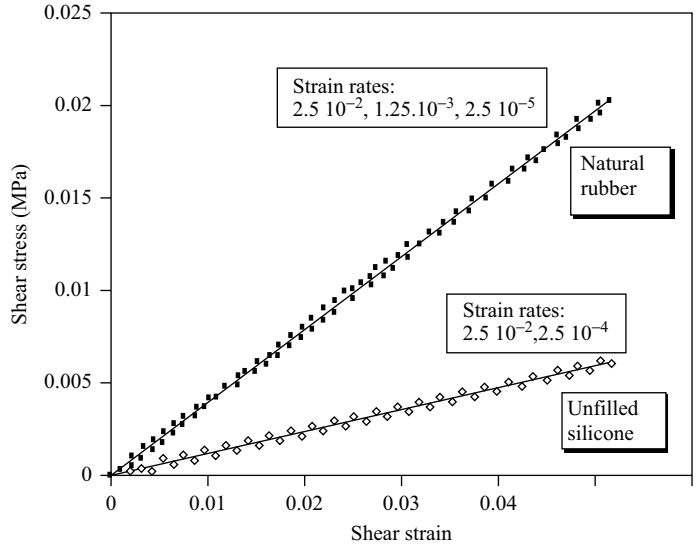

Figure 12.4 Shear stress–strain curve of unfilled NR and silicone (at low strain) at different strain rate, from 2.5×10^{-5} up to $2.5 \times 10^{-2}\,s^{-1}$ (Reprinted with permission from L. Chazeau et al., "Modulus recovery kinetics and other insights into the Payne effect for filled elastomers," *Polymer Composites*, **21**, 202–222, © 2000, Society of Plastics Engineers.)

The stress–strain behavior of unfilled chemically crosslinked elastomers tested at room temperature (that is, above T_α) is proportional to the crosslink density. The latter involves those introduced by the chemical crosslinks created during the crosslinking step (usually by sulfur or peroxide), as well as those created by the entanglements. The contribution of the latter is strongly dependant on the strain rate when they are not trapped during the crosslinking, but can be negligible for highly crosslinked elastomer. The quantity of the trapped entanglements depends on the initial molecular weight of the polymer and the chemical crosslink density (Figure 12.5).

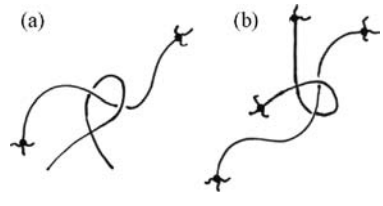

Figure 12.5 Scheme of the molecular structure of an elastomer: crosslinks (black dots), (a) entanglements, and (b) trapped entanglements

As reported in all the articles concerning filled elastomers, when stiff fillers are introduced, the material stiffness increases. Obviously, this is also the case for nanofillers. This reinforcement increases with filler volume fraction, as clearly evidenced in all the papers devoted to nanocomposites. The reinforcement can be evidenced by dynamic mechanical analysis measurements. This technique provides the viscous and elastic part of the complex modulus, as a function of temperature at a given frequency, generally around 1 Hz. Such measurements are suitable as long as the material behavior is linear (otherwise the modulus calculation is wrong). This is clearly the case for strain below 1%. Some articles report also data of modulus measured with large deformation tests. In that case, the modulus is measured at different strain values, depending on the choice of the authors. However, it is noticeable that the strain chosen for such measurement is often above 100%. At these strain levels, as we will see in the next paragraph, many phenomena can occur and complicate the material response. Though these difficulties, some generality can be extracted from literature.

Common filler content for CB or Silica are around 30–50 phr. Content of around 50 phr multiplies the DMA modulus by ten [38]. In the case of spherical Ni and Fe nanoparticles in natural rubber, El'Nashar *et al.* [13] reported a modulus increase of 50% with 30 phr of fillers. Such reinforcement can be obtained for lower nanofiller fraction with high aspect ratio nanofillers such as nanotubes or clays. Atieh *et al.* [25] reported an increase from 0.3 to 2.5 MPa when introducing 10% of multiwall nanotubes (MWNTs) in NR (nanocomposites were processed by evaporation). The introduction of 0, 5 and 10 phr of montmorillonite clay platelet in isobutyl isoprene rubber leads to a modulus equal to 0.8, 3.2 and 4 MPa respectively (measured in tensile test at 100% strain) [39]. Kueseng and Jacob [12] reported a reinforcement of NR matrix from 0.8 to 1.2 MPa with only 2% of SiC nanoparticles. De Falco *et al.* [40] reported also that small quantity of MWCNT is enough to improve significantly the mechanical properties of cured SBR composites when compared to CB-filled SBR. However, due to processing difficulties, the content of filler with higher aspect ratio is generally low, except in few studies such as that of [41]. The latters reported data on a series of rubber/clay nanocomposites with a fraction up to 60 wt% of filler in ethylene-propylene diene rubber (EPDM) styrene butadiene rubber (SBR) and epichlorohydrin rubber (ECO), leading to an important modulus increase measured by dynamic mechanical analysis.

These different examples show clearly that the filler aspect ratio is the main parameter for the reinforcement efficiency, the latter being higher for high aspect ratio filler. Thus, carbon nanotubes or MMT have a much higher reinforcing capability than silica or carbon blacks, except in some few studies where the bad properties obtained with such fillers are probably due to a bad quality of the tested fillers [42]. Literature also suggests that the reinforcement is strongly dependent on the elastomer matrix, the material processing, and the filler surface treatment [26, 43]. Note that a comparison between all the different systems must be cautiously done in the specific case of elastomers since their mechanical properties are also strongly dependent on the crosslinking process of the matrix. Moreover, one can regret in many papers the lack of characterization of the fillers, of precision in the mechanical characterization (for the reason precised above) and of comparison with modeling approach, which would help the clear evaluation of the fillers interest.

12.2.3 Mechanical Behavior at Small Strain: the Payne Effect

Besides a strong reinforcement, the introduction of nanoscopic fillers in a rubbery matrix leads, at intermediate strain level (below 100%) to a nonlinear mechanical behavior. Once again, it

can be shown by two different mechanical experiments (dynamic or classic stress–strain tests). In dynamic mechanical measurements, when submitted to successive sinusoidal deformations with increasing amplitude, rubber nanocomposite samples exhibit a decrease of their measured storage modulus, and the appearance of a maximum for the loss modulus at a deformation level around 0.1. Two plateaux are also visible, as shown in Figure 12.6, with what will be hereafter called low amplitude modulus (LAM) and high amplitude modulus (HAM), respectively. The main features of the Payne effect described above are general to all filled elastomers [38, 44, 45]. Note that this nonlinearity at low deformation – unrevealed in pure elastomer – is equivalently demonstrated in classic shear–stress measurements. The apparent modulus measured as the slope of the stress strain curve decreases strongly when deformation is increased. The composite presents a pseudo-plastic behavior with a strong strain rate dependence of the material response. A decrease of the strain rate of measurement decreases the amplitude of the Payne effect, which quasi-vanishes at a strain rate below 10^{-6}. An increase of temperature has the same influence since it strongly decreases the initial modulus and much less the terminal one [46].

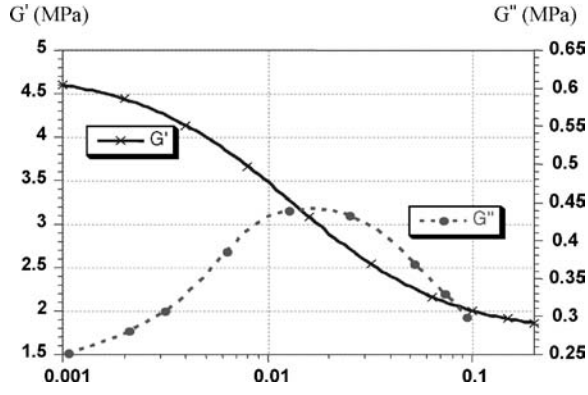

Figure 12.6 Payne effect measurement of a carbon black filled NR: elastic (G′) and viscous (G″) moduli a function of the shear amplitude (at 1 Hz). The measurement is performed at increasing shear amplitude (Reprinted with permission from L. Chazeau et al., "Modulus recovery kinetics and other insights into the Payne effect for filled elastomers," *Polymer Composites*, **21**, 202–222, © 2000, Society of Plastics Engineers.)

It is noteworthy that the DMA measurements presented in Figure 12.6 represent a "fully equilibrated material response": the storage and loss moduli measured at each strain amplitude are steady-state values that would remain constant indefinitely if the strain amplitudes were sustained at a constant value. However, dynamic measurements performed at increasing strain amplitude do not give the same DMA curves when measurements are performed at decreasing amplitude. In other words, the material has the memory of the modulus reduction that occurs at high strain amplitude. This memory effect vanishes with time [44, 47]. Indeed, a material submitted to a static offset, presents, after a sufficient elapsed time, the same DMA curve without a static offset [48]. The curves virtually superpose, even for a deformation of 0.2, that is, much higher than that at which the modulus decrease occurs. However,

this statement is only true when considering material that has been previously submitted to strain as high as the maximum strain seen in the test. Indeed, the original stiffness of a filled elastomer is always higher than that measured in following tests. This is a feature of the so-called Mullins effect.

Both the Payne and Mullins effects are general to all filled elastomers and in particular to elastomers filled with nanofillers, as reported by Ramier *et al.* [38] for silica, by Qian *et al.* [49] for CB, by Ramoniro *et al.* [50] for clays and by Bokobza *et al.* [51] for MWNT. However, the intensity of the phenomenon depends on the filler characteristics for the reason that will be explained further (Section 12.3). This strongly makes more difficult the understanding of the impact of the tested nanofillers and makes more difficult the conclusion that one can have concerning their interest.

12.2.4 Mechanical Behavior at Larger Strains

At higher strain level, rubber exhibits a strain-hardening, that is, a rapid increase of the stress (prior to break). This hardening is related to the limited extensibility of the chains between crosslinks. Crosslinks increase the elastic modulus but induce a decrease of the strain at break. Like at small strain, the introduction of filler leads to an increase of the stress level of the material at a given strain, as shown on Figure 12.7. Different studies report this increase for silica in SBR [52], CB in NR [49], MWNT in NR [51], clay platelets in EPDM [53] and so on. Like at small strain the main filler parameters are the filler aspect ratio and obviously their volume fraction. Moreover, especially for high aspect ratio, one has also to consider the strong influence of the processing which might orient the fibers, like suggested by [54] for fibrillar

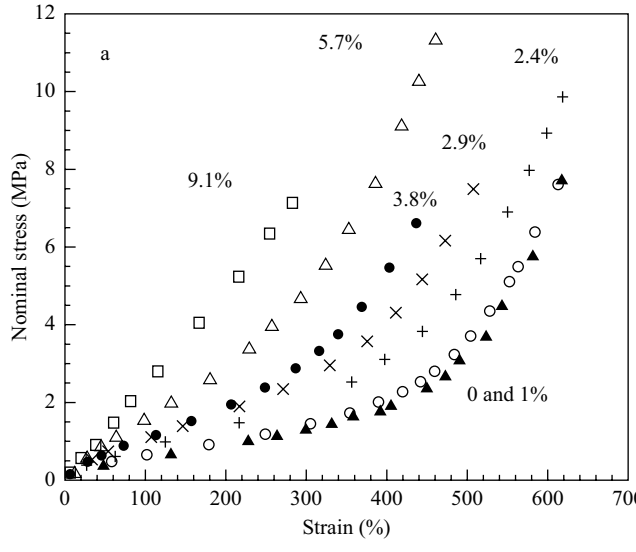

Figure 12.7 Stress–strain curves of pure NR and NR/MWNTs composites (Reprinted from L. Bokobza and M. Kolodziej, "On the use of carbon nanotubes as reinforcing fillers for elastomeric materials," *Polymer International*, **55**, 1090–1098, © 1999–2008, with the permission of John Wiley & Sons, Inc.)

nanosilicate (with length of a few microns and diameters around 10–30 nm) introduced in SBR and NBR by conventional process.

However, as evoked above, filled elastomers exhibit a mechanical behavior modified after a pre-straining. This effect was first shown by Holtz [55] and studied by Mullins [56], whose name was given to the phenomenon. This so-called Mullins effect is illustrated in Figure 12.8. A sample is stretched at a maximum deformation ε_{max}. Then it is unloaded for between half an hour and several days. A new loading of the sample leads to a stress–strain curve which is below the curve obtained during the first loading, for a deformation level below ε_{max}. For a deformation above ε_{max}, the second curve joins the first one. Some experiments suggest that this effect is partly recoverable [56, 57] but for much longer time (in the scale of months) than that involved in the Payne effect (see above). However, a real recovery in the cited experiments is not obvious since it needs heating of the sample at temperature for which a post-crosslinking can occur in the matrix. Interesting features have been shown by Lapra [58]. He confirmed by birefringence the presence of short or strongly stretched chains during the deformation, which do not obey to Gaussian statistic. AFM experiments showed that there is strong heterogeneity of deformation. This confirms the important role of the distribution of the local volume concentration of fillers, this distribution being the result of the nanocomposite processing.

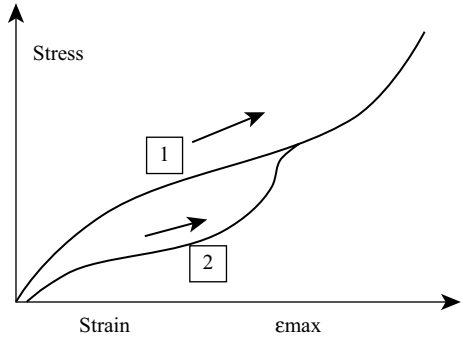

Figure 12.8 The Mullins effect on stress–strain curves in reinforced elastomers. The modulus on second and subsequent curves is lower than obtained on first extension (Reprinted with permission from L. Chazeau et al., "Relationships between microstructural aspects and mechanical properties of polymer-based nanocomposites," *Handbook of organic–inorganic hybrid materials and nanocomposites*, **2**, Hari Singh Nalwa (ed.), 63–111, © 2003, American Scientific Publishers.)

12.2.5 Aging, Fatigue and Ultimate Properties

Conversely to what is generally observed with filled thermoplastic, filled elastomers with nanoscopic particles can exhibit an increase of *both* stress and strain at break. Of course, this is shown when the process enables sufficient filler dispersion and many processing problems can hinder such result. As an example, Figure 12.9a shows stress–strain curves obtained with styrene-butadiene rubber filled with untreated nanoscopic silica [59]. It is also illustrated in the case of carbon MWNTS [24] in Figure 12.9b. The main difference between both examples concerns the amount of nanofiller (10 wt% in the case of carbon nanofibres, 20 vol% in the case

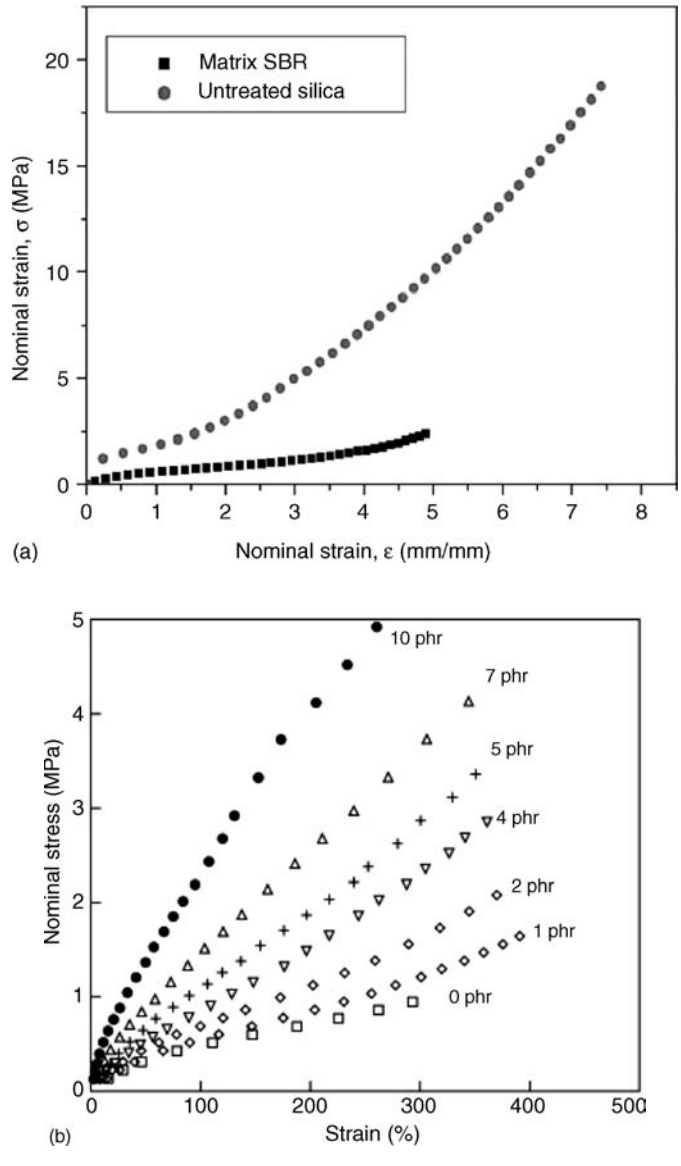

Figure 12.9 (a) Stress strain curve of SBR and 20 vol% silica filled SBR (at 298 K with a strain rate of $4 \cdot 10^{-1}\,s^{-1}$) (Reprinted with permission from L. Chazeau et al., "Relationships between microstructural aspects and mechanical properties of polymer-based nanocomposites," *Handbook of organic–inorganic hybrid materials and nanocomposites*, **2**, Hari Singh Nalwa (ed.), 63–111, © 2003, American Scientific Publishers; and (b) Stress–strain curves for pure SBR and MWNT/SBR composites. The filler content is expressed in parts per hundred parts of rubber (phr) (Reprinted from *Polymer*, **48**, L. Bokobza et al., "Multiwall carbon nanotube elastomeric composites: a review," 4907–4920, © 2007, with permission from Elsevier.)

of silica). However, most of the articles report the existence of an optimum of filler content for the improvement of the ultimate properties. This optimum can often be related to the optimum of dispersion, which is more and more difficult with increasing filler content (see for instance Hwang *et al.* [60]). Thus, a lot of study on clay platelet filled rubber report an optimum around few wt% of clay [61], above which the dispersion is clearly not satisfactory.

The increase of stress can be explained by strain amplification effects [62], that are known to occur in such complex materials. However, this cannot account for the apparent increase of the ultimate strain often reported in rubber nanocomposites. In fact, the total rupture envelope of such composites must be considered. The latter can be obtained by a logarithmic plot of the ultimate stress, corrected by a factor T_{ref}/T, as a function of the ultimate strain, for different testing temperatures and strain rates. T_{ref} is the chosen reference temperature for the curve, while T is the temperature of the test. The correction factor accounts for the temperature dependence of the entropic elasticity. All the tests made at different strain rates and temperature leads to a unique curve (Figure 12.10). The variation of temperature or strain rate only moves the representative point along the envelope, anticlockwise for a decrease of temperature or an increase of strain rate. At high temperature and low strain rate, the reinforcement is limited (low ultimate stress and strain). At low temperature and high strain rate, the ultimate stress increases but the ultimate strain reaches a maximum and then decreases. The rupture properties are optimal in an intermediary region. A maximum ultimate strain can be determined from the envelope curve and will be hereafter call $\varepsilon_{\text{ultm}}$.

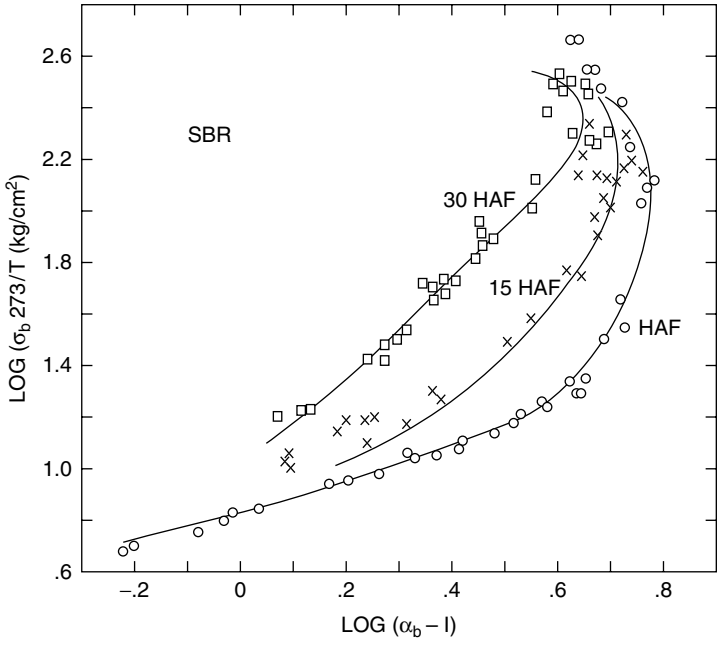

Figure 12.10 Rupture envelope for SBR elastomer filled with different concentrations of carbon black. Theoretical curve (full lines) deduced from the combination of creep curves and the Bueche–Halpin theory (Reprinted with permission from F. Bueche and J.C. Halpin, "Molecular theory for the tensile strength of gum elastomers," *Journal of Applied Physics*, **35**, 36–41, © 1964, American Institute of Physics.)

As shown on Figure 12.10, the addition of filler in the elastomer decreases ε_{ultm}, However, the zone of optimal behavior is shifted toward higher temperature. For instance, Lapra [58] showed that unfilled SBR exhibits, when stretched at a strain rate of 0.1 s^{-1}, a maximum ultimate strain at 273 K when the latter is observed at ambient temperature with the same SBR filled with 20 vol% of untreated silica. The same observation was made with different surface treatments: in all cases, the decrease of the properties for temperature above the ambient is much slower than for unfilled SBR. This leads to an ultimate strain systematically higher in the filled samples than in the unfilled ones at 333 K.

This improvement of the ultimate properties of the fillers is obviously searched when the materials is used in application involving large strain behavior. This is in particular the case when friction is involved. Indeed, even if their macroscopic strain is not necessarily important, elastomer submitted to friction can be submitted to very high local strain. The best example is the tire application where the abrasion resistance of the material is particularly tested. The tribological behavior of elastomers, like for any type of material – because of the very local mechanisms involved- is complex and is strongly dependent of the testing conditions. However, some main characteristics can be recalled here.

Due to the viscoelastic nature of filled elastomers and to their large deformability, the friction behavior of elastomer does not follow the Coulomb rules generally observed for rigid solid. The friction force is not independent of the form and area of the contact surface, this force is not proportional to the normal force, and the sliding of the surface is not independent on the relative displacement rate between the surfaces in contact [63]. Indeed, the elastomer, filled or unfilled can more or less deform following the surface roughness. For this reason, the friction force is higher. Moreover, the latter depends on the physico-chemical nature of the material, that is, its formulation. The viscoelastic nature of the material, complex in the case of filled elastomer, induces a dependence of all the phenomena on the speed and temperature. In addition to its consequence on the direct value of the force resistance to sliding, this has also consequences on the wear behavior, since it is the complex results of the testing conditions.

Given this complexity, it is quite difficult to identify the main parameter deciding the abrasion resistance of rubber nanocomposite. For instance, it appears that the ultimate stress and strain at break obtained in simple tensile test are not consistent with the abrasion resistance properties when comparing a CB-filled SBR and a CB-filled natural rubber [64]. This is the reason why natural rubber, which has better abrasion properties, is preferred to synthetic elastomer for truck tire applications. One property, which is often examined, is the crack growth resistance of the material. Depending on the nature of the elastomer matrix and formulation, the crack propagation can present strong deviation and/or the formation of moustache [65, 66], such as those shown on Figure 12.11. This enables higher energy dissipation and therefore delays the material rupture. This phenomenon is related to some anisotropy development in the vicinity of the crack [67]. It is then obvious that in the case of nanofillers, such phenomenon must be considered at the nanometric scale, or even at the molecular levels. The difference between NR and synthetic rubber is then generally attributed to the crystallization ability of NR, which favors the anisotropy development [68]. Obviously, the addition of nanofiller will have a direct impact on this phenomenon and more generally on the anisotropy development of the material response near the crack tip.

The issue of crack propagation in rubber nanocomposite is obviously a concern in the study of fatigue [69]. The progressive degradation of the material observed in such tests involves all the mechanical aspects previously addressed such as linear and nonlinear (Payne effect)

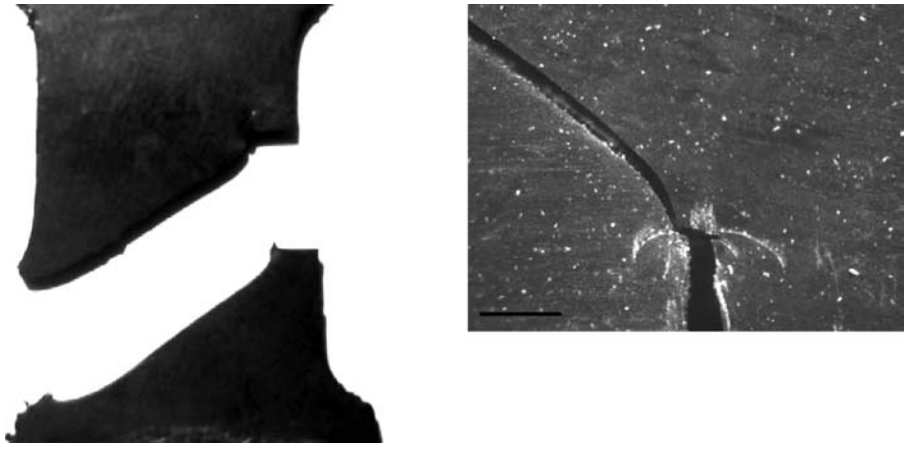

Figure 12.11 Crack propagation in CB-filled NR can present a strong deviation (tensile strain on notched samples performed at room temperature with an initial strain rate $0.01\,s^{-1}$)

viscoelasticity, the Mullins effect and the ultimate properties, in addition to the environmental conditions (temperature, oxygen and ozone concentration, radiation, and so on). The latter can promote the occurrence of complex chemical processes such as polymer chain scissions, additional crosslinking, and byproduct formation, which may occur either in the bulk or at the filler surface. As rubbers are strongly formulated, this degradation strongly depends on the content and nature of antidegradant additives and crosslinking agents, as well as their initial crosslinking state prior to aging. Moreover, given the large specific area of nanoscopic fillers, chemical reactions at the interface can have a large impact on the one hand on the overall chemical processes, that is, their kinetic and their homogeneity and on the other hand on the resulting mechanical behavior of the degraded material. These intricate aspects are covered by Chapter 21 of this book, written by S.K. Srivastava.

12.2.6 Conclusion

Elastomers display specific mechanical properties such as large deformability and small viscoelasticity. The introduction of nanofillers makes this behavior more complex with the occurrence of non linear visco-elasticity, a strong sensitivity to strain history, astonishing ultimate properties such as a possible improvement of both strain and stress at break depending on the testing conditions. This statement is general to all type of nanofillers but their influence is obviously dependent on their intrinsic parameters.

12.3 How to Explain Reinforcement in Rubber Nanocomposite?

After a recall of the typical mechanical behavior of rubber nanocomposites, let us go deeper in the relationships between the microstructure and these mechanical properties. There is no doubt that the filler morphology strongly influences the mechanical reinforcement they provide

to the elastomer matrix. Moreover, this morphology is also involved through the role of the filler surface and the different type of interaction it generates.

12.3.1 Filler Morphology and Filler–Filler Interactions

The increase of the reinforcement with the increase of the aspect ratio can found theoretical explanation that will be recalled in the Section 12.4.2. Aspect ratio has also consequences in the way fillers are spatially distributed in the matrix during the processing. First, that means that the efficiency of high aspect ratio filler such as clays is directly dependent on the way they are dispersed (exfoliated) in the polymer, since a too bad dispersion of the particles means the formation of aggregates or agglomerates, that is, a smaller effective aspect ratio (this effect is illustrated in Figure 12.12). This explains the large variation of the reported reinforcement of elastomer system reinforced by fillers such as clays, or nanotubes since their dispersion is strongly dependent on the material formulation and process. This is also the reason of the very large number of articles devoted to the improvement of the filler/polymer compatibility, via the chemical modification of filler surface [70, 71], the use of compatibilisers [72], or the chemical modification of the polymer matrix [73–75]. Note that other parameters can influence this dispersion such as the vulcanization system and in particular the accelerators [72]. The consequence is that the efficiency of the chemical modifications can only be understood via a deep microstructural characterization of the resulting composite.

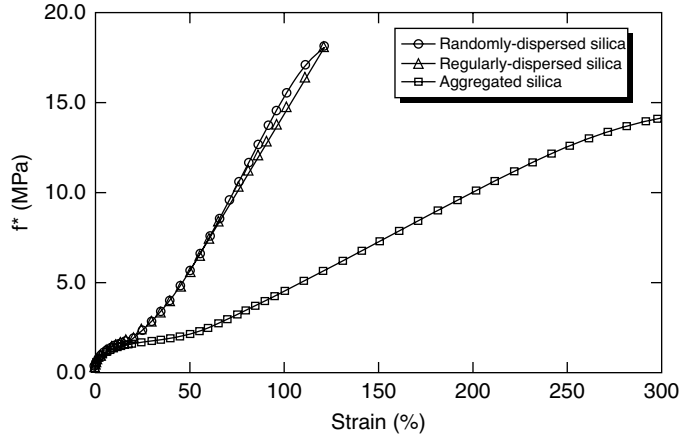

Figure 12.12 Effect of dispersion and aggregation of the silica on the mechanical properties of the composites having a silica content of 35 wt% (Reprinted with permission from Z. Pu et al., "Effects of dispersion and aggregation of silica in the reinforcement of poly(methyl acrylate) elastomers," *Chemistry of Materials*, **9**, 2442–2447, 1997. © 1997 American Chemical Society.)

At that point, one might conclude that a total dispersion of the fillers as individual objects statistically distributed in the material is the optimum to reach. However, different works indicate that such an idea is erroneous. For instance, the influence of the filler dispersion was extensively studied by Pu *et al.* [76]. They prepared model colloidal silica systems in a PMA

matrix (poly methyl-acrylate) in such a way as to obtain particle dispersions that were random, regular or aggregated. The mechanical properties of the three types of sample were tested for both DMA and stress–strain properties (tensile and compression). They observed that the composites with randomly and regularly dispersed silica have almost identical stress-strain behavior (in both dynamic and static uniaxial tests). Conversely, the composites with aggregated silica are seen to exhibit different mechanical properties, particularly higher compressibility and extensibility. These improved mechanical properties relative to the other two types of filler is consistent with frequent observations in the rubber industry that a stop of the compounding process just before the complete filler dispersion can give the best balance of mechanical properties.

Besides, the ability of the fillers to form a sort of continuous phase or network leads to a sharp increase in the reinforcement efficiency [77]. This "percolating" network depends on their aspect ratio, and on their orientation distribution, as described in the literature [78, 79]. Thus it appears that with rigid rods randomly dispersed (in position and orientation), an aspect ratio of 100 should lead to their percolation at a volume fraction of about 1%. Moreover the percolation threshold calculated for a nonuniform length distribution is also found lower than that calculated for a uniform length distribution having the same average length [79–81]. Note that these calculated thresholds are calculated with the assumption of a statistical distribution of the fillers, without account for the interactions between fillers. The latters can strongly modify the statistic spatial distribution of the fillers and therefore can increase or decrease the threshold volume fraction [82]. The process can also favor or inhibit the formation of this network, the evaporation process being likely more favorable than process involving strong mixing.

The question that arises then is the nature of the links creating the continuity of this filler structure [83]. The very high specific surface of nanofillers suggests that filler–filler interactions can form these links. The formation of continuous structure made via filler–filler contacts can be evidenced in the case of conductive fillers such as CB [27, 28, 53, 84, 85]. Indeed, a good correlation was found between LAM value and conductivity, suggesting that this modulus is directly the consequence of a so-called mechanical (and not only geometrical) percolation of the filler. Moreover, conductivity measurement and mechanical characterization have shown the existence of an optimum mixing time to obtain the highest LAM, which allows a macroscopically uniform dispersion of the filler but also the existence of a filler network [84].

Within this frame, the nonlinear behavior of filled elastomers can be explained. The rigidity of the filler structure depends on the rigidity of the filler–filler bonds. The deformation of the composite leads to its breakage and the loss of rigidity. During cycled deformation, as observed by DMA, there is alternately breakage and reformation of the filler bonds, which is a dissipative phenomenon at the origin of the peak of the loss modulus observed in Figure 12.6. Many experiments support this scheme. The decrease of the filler size down to the nanoscale leads to a statistically nanometric distance in between filler, which can favor their interaction, and their agglomeration in complex structure. This "agglomeration–disagglomeration scheme" is also suggested by the analogy between viscoelastic behavior of filled elastomer and the rheology of nanofiller filled suspension. The latter shows a decrease of viscosity with shear rate similar to the decrease of modulus with shear in filled elastomer [86, 87]. A decrease of shear modulus is also observed for suspension of carbon black particles in oil for which the role of polymer chains cannot be evoked. In that case, the only obvious mechanism is a modification of state of aggregation with shear rate [83].

To this direct effect of the filler network stiffness, one must add the role of the structure in its possibility to trap matrix inside cluster of filler agglomerates. This trapped matrix increases the apparent filler fraction, and its unshielding during the deagglomeration of the fillers enhances the modulus decrease [88]. However, the preponderance of the surface of the filler over their structure suggests that the occluded volume theory is not a key mechanism in the Payne effect [89].

However, one might argue that a filler network has a too low modulus to explain the LAM measured in filled elastomer. Moreover, it has been shown that the Payne effect is also observable in carbon black-filled rubber even when they are nonconducting composites, that is, without the presence of a percolating filler structure effect [89]. Figure 12.13 presents the influence of the surface of filler (that is, their size) on the modulus decrease in filled elastomer during the DMA experiment described above (HAM minus LAM). The so-called structure of filler, measured by DPB measurement, and which is characteristic of the complexity of the aggregates geometry, is a very minor parameter compared to their size, that is, to the surface of matrix/filler interface.

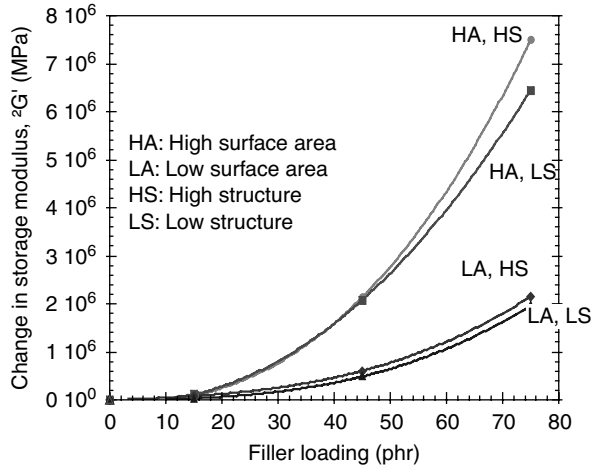

Figure 12.13 Influence of the filler content on the Payne effect amplitude (i.e., the modulus drop value). Carbon blacks with two specific surfaces (GSu for large surface, PSu for small) and two different DBP structures (GSt et PSt) have been studied. The influence of the structure is of second order compared to that of the specific surface (Reprinted with permission from L. Chazeau et al., "Modulus recovery kinetics and other insights into the payne effect for filled elastomers," *Polymer Composites*, **21**, 202–222, © 2000, Society of Plastics Engineers.)

12.3.2 Filler–Matrix Interactions

In fact, the importance of the surface developed by nanoscopic fillers is already noticeable during the composite processing. This can be due to the filler-filler interactions (and the formation of the network previously described) but also to the filler-matrix interactions that occur here on a large surface. The latter can lead to properties of the matrix in the interphase different than in the bulk. Considering the quantity of interface of the order of several hundreds

of square meters per gram, the quantity of polymer involved by the interaction with the filler surface becomes significant. Given generally reported large reinforcements provided by nanoscale filler compared to microscopic ones [9] (though this comparison might be often questionable for different reasons developed in this chapter) many studies have been devoted to the characterization of this assumed immobilized matrix. Different techniques have been proposed to characterize it: bound rubber measurement [7], nuclear magnetic resonance (NMR) [90], positron annihilation light scattering (PALS) [9] and so on. Bound rubber measurement consists in dissolving the uncrosslinked polymer matrix of the composite and extracts the fillers. The rubber bound on the filler surface, that is, the rubber not extractible, is assumed to be characteristic of the quantity of immobilized polymer. The amount of adsorbed polymer depends on the chemical nature of the polymer and of the particle surface, and also of the molecular weight of the polymer [91].

For instance, Burnside and Giannelis [92] studied polysiloxane-layered silicate nanocomposites with filler volume fraction in the range (0, 0.04). They reported that the modulus increase with the filler content correlates with the amount of bound rubber (determined from swelling experiment in toluene). The quantity of bound rubber can be important in such experiments, leading to the calculation of a polymer layer with a modified mobility of several nm thick. More precisely, Dutta [93] has studied by NMR technique the mobility of adsorbed polymer (styrene-butadiene) at the surface of carbon black particles extracted (in solvent) from the composite. They conclude in the presence of three regions with different mobility, a bound rubber region, a loosely bound region and the noninfluenced polymer. This has been supported by other studies on similar or different systems [94, 95]. In the case of silica filled PDMS, Cohen-Addad [96] has shown that the adsorbed polymer involves a multiple link structure. Numerous monomer units are involved in a binding site which is a dynamic system consisting of bonds which form and dissociate permanently. Brinke *et al.* [90] have performed a RMN study of silica filler NR. The fraction of immobilized polymer they found is more important in the case of untreated silica compared to those treated with silane, though the latter enable the formation of covalent bonds. Seemingly, the silanol sites are more efficient to immobilize NR chain than silane. This result is comparable to those found in a silica/polybutadiene system [97].

These results are consistent with the study of Ramier el al. [38]. In his study, different materials with a SBR matrix filled by nanoscopic silica with various surface treatments have been submitted to increasing dynamic strains in the range of the Payne effect. Figure 12.14 synthesizes the behavior observed for the samples with untreated silica, with silica treated by a covering agent with eight carbons, or treated with a coupling agent enabling a covalent bond between the matrix and the filler. The grafting (covering or coupling agents) leads to a decrease of the Payne effect amplitude, that is, basically a decrease of the initial modulus, measured between the modulus drop. It was checked that this could not be due to a modification of the silica dispersion in the material [38]. Bound rubber measurements have shown an expected decrease of the adsorption of polymer chains at the filler surface with the covering agent quantity; note that this characterization also allowed establishing equivalence between the quantity of covering agent and the length of this agent to cover the surface of silica [71]. Moreover, a correlation between the bound rubber value and the initial modulus is found. The modulus drop in the peculiar case of the materials with coupling agents is very similar to that observed with materials with covering agents. Like the work of ten Brinke [90], this could suggest that the formation of covalent bonds between fillers and the matrix does

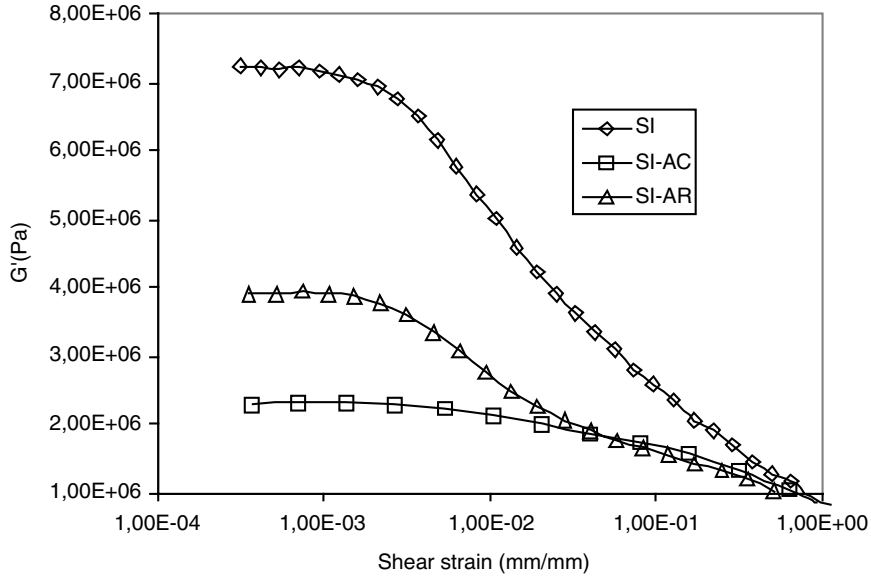

Figure 12.14 Storage modulus versus dynamic amplitude for Si (neat silica), AR (silica grafted with covering agent) and AC (silica grafted with coupling agent) filled SBR (20 vol% silica). Test performed at room temperature and 5 Hz (Reproduced from J. Ramier, "Comportement mécanique d'élastomères chargés, influence de l'adhésion charge - polymère, influence de la morphologie," PhD thesis, Institut National des Sciences Appliquées de Lyon, 2004.)

not counterbalance the decrease of the number of physical bonds induced by the covering of the silica surface.

Another argument for the presence of a large quantity of polymer chains with decreased mobility at the filler surface is the recovery kinetic of the LAM after deformation, at large amplitude or during the application of an offset since it is for some authors, similar to the physical aging of polymer in the glassy state after stretching [98]. The large fraction of polymer involved by adsorption can act through two mechanisms. The first vision is to consider it as a glassy polymer. Within this assumption, the Payne effect can be considered as a decrease of the glass transition temperature of this polymer fraction activated by the deformation [99]. A second possibility is to consider the Payne effect as due to a mechanism of adhesion–desadhesion of the chains at the filler interface [100]. The adsorbed polymer might act as a supplementary crosslink in the elastomer. In addition, the distance between the crosslinks being reduced, linking chains between fillers might not act in the low deformation range as predicted by the Gaussian description but more like chains at the limit of their extensibility [101]. Thus, the desadhesion mechanism would be a return to the normal entropic behavior of these chains [101].

Such assumptions can also be used to explain the Mullins effect (that is, the irreversible modification of the material behavior after a first stretch). For instance, Wagner [102] keeps the idea of a glassy shell of polymer around the particles and proposes that under deformation, this shell deforms quasi-irreversibly (that is, plastically) and does not contribute anymore to the reinforcement. Bueche [57, 103] early assumed the existence of adsorbed polymer chains linking two different filler particles. The distance between particles would be distributed, as

well as the linking segments of chains. An increasing deformation would lead the shortest segments to reach their maximum extensibility. In that case, they would break or they would be debonded from the filler surface. The key parameters in this interpretation are the distance between particles related to their size and the bonding surface. Dannenberg [104] and Boonstra [105] had a very similar interpretation except that they preferred to consider a slipping of the stretched polymer chain on the filler surface (Figure 12.15).

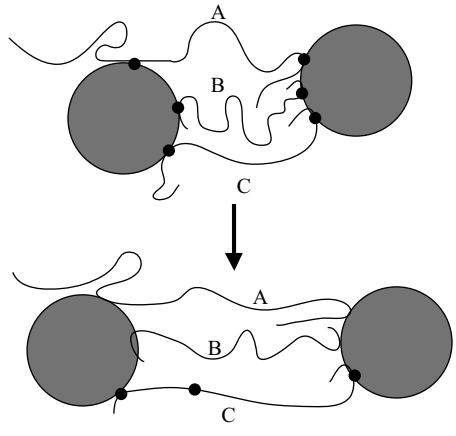

Figure 12.15 Physical interpretation of the Mullins effect as described by Dannenberg (Reprinted with permission from L. Chazeau et al., "Relationships between microstructural aspects and mechanical properties of polymer-based nanocomposites," *Handbook of organic-inorganic hybrid materials and nanocomposites*, **2**, Hari Singh Nalwa (ed.), 63–111, © 2003, American Scientific Publishers.)

Thus, to consider the filler–matrix interactions as the main parameter in the mechanical behavior of rubber nanocomposites could seem appealing. However, some objections exist against a too biased vision. It is noteworthy that all the interpretation of the non linear behavior of filled elastomers in studies which deal with a modification of these interactions via chemical treatment of the filler surface, or via the matrix chemistry, does not always take into account a possible modification of the dispersion. Moreover, the bound rubber quantities generally reported are huge. Ramier reported values up to 40 vol% of matrix in the case of SBR/silica nanocomposites. However, DSC measurements are rarely reported to confirm the modification of the glass transition of the material, or the presence of phase with different glass transition temperature. Some DSC measurements even contradict the assumption of an immobilized phase. The lack of DSC clue is explained by the mobility gradient of the polymer near the surface (with no neat difference of glass transition temperatures), or by the assumed total lack of mobility (that is, of glass transition) of the bound rubber. These receivable arguments at least suggest that more information is needed on the molecular dynamics of the polymer in the vicinity of the filler surface. Moreover, PALS study did not show an effect of the fillers (montmorillonites treated or not with octa-decyl-trimethyl ammonium chloride) in the bulk matrix response (a polystyrene-co-butadiene), whatever the process used to prepare the composite [9]. At last, some authors discuss from dynamic mechanical experiments about the presence of a second loss peak above the main relaxation temperature, (characteristic of a

drop of the rubbery modulus with increasing temperature). But there is no correlation between the intensity of this peak and the quantity of the bound rubber value measured with the same sample [59]. Besides, mechanical spectrometry does not show any modification of the main relaxation peak of G'' of rubber nanocomposites [76], except when they can also be explained by continuum mechanic (that is, without the assumption of the matrix properties), or by a modification of the matrix intrinsic properties by the process (that is, a different crosslinking, copolymerization, degradation, or cure). Indeed, these indirect effects of nanoscopic fillers are important; they will be discussed in the next paragraph.

In any case, whatever the reality of the presence of a matrix with modified properties, filler–matrix interaction has obviously consequences in the behavior at large deformation. Given the Payne effect feature and the fact that it occurs at small strain, the modification of the bulk polymer mobility becomes a negligible phenomenon at large strain. The main characteristic to consider then is indeed the strength of the filler–matrix and filler–filler bonds. Thus, the creation of covalent bonds between the matrix and the filler through the use of appropriate surface treatment is clearly visible at large deformation where it leads to a strong hardening of the material, the fillers then acting as multifunctional crosslinks [59]. The strength of these bonds, as well as the strength of the filler–filler bonds, controls the damage process of the material, and in particular the void formation, and the "desagglomeration" processes, as evidenced in Ramier's work [52]. Consequently, these different phenomena lead to strong heterogeneities in the deformation field and the overall response of the material ... up to the material rupture.

12.3.3 Indirect Influence of Fillers on Matrix Crosslinking

Nanoscopic fillers can also indirectly modify the matrix bulk properties through a perturbation of the crosslinking process. Indeed, these fillers can favor an important and uncontrolled adsorption of activator, accelerator and crosslinking agents that in turn can modify the crosslinking density of the matrix in the filler vicinity [37]. Curing kinetics of rubbers are generally studied using oscillating disc rheometer that measures the torque evolution required to shear the sample (characteristic of the increase of the material rigidity during the crosslinking). Measurements are usually performed versus time at a given temperature and the curing characteristics are often expressed in terms of onset time, optimum cure time and torque value.

It is generally agreed that the incorporation of carbon black in rubber does not modify matrix crosslinking by sulfur but has an influence in the case of peroxide [37]. The results can be extended to the case of nanotubes, as the surface chemistry is close. Untreated silica leads to a strong modification of kinetic. For instance, the introduction of 20 vol% of silica in the SBR matrix leads to a crosslinking reaction which begins earlier with slower kinetics (Figure 12.16). This can be attributed to a strong affinity between silica and common accelerators. The adsorption of accelerators can be significantly reduced by grafting the surface. For instance, increasing grafting quantity of octyl triethoxy silane (noted AR8 on Figure 12.16) leads to kinetics close to those observed in the case of the matrix alone with accelerators (CBS). The same effect is also observed when using silane with alkyl chains of different lengths, the main parameter being the covering of the silica surface. The use of coupling agent has also the same consequences, with the difference that it contributes in the same time to the crosslinking kinetic (accelerating it) by the coupling reaction.

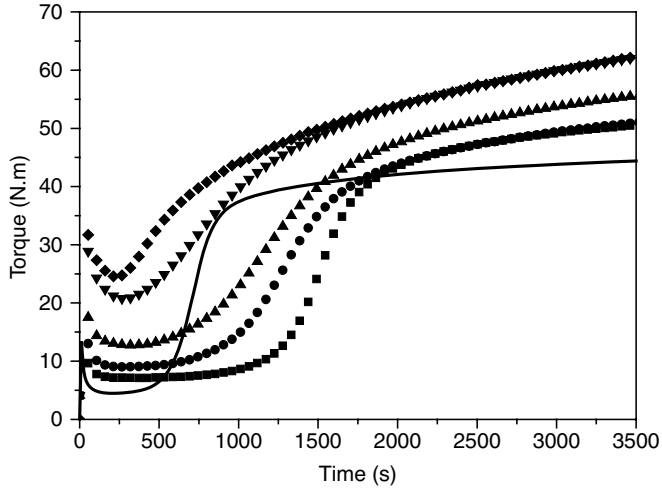

Figure 12.16 Effect of covering agent ratio on vulcanization kinetic: ♦ silica, ▼ AR8-3, ▲ AR8-6, ● AR8-8, ■ AR8-14, = matrix

Let us now consider the case of nanolayered silicates. In order to exfoliate the stacks of platelets, use is often made of ammonium salts [106]. Alex and Nah [107] report that the presence of organoclay in the case of NR matrix leads to a faster crosslinking kinetic. This is attributed to the formation of a transition complex with amine and sulfur. Similar effects have been also reported by Lopez Machado *et al.* [108] and Teh *et al.* [109] in the case of NR and by Varghese *et al.* [110] in the case of epoxidized NR. In the case of silicone matrix, the influence of synthetic Fe MMT on crosslinking kinetic is attributed to the presence of Fe that acts as an antioxidant [14].

Given the fact that it occurs at the filler surface, the consequences are likely a more heterogeneous final crosslinking state (that is, the development of crosslinking gradients in the filler vicinity). However, the characterization of such heterogeneities is difficult to perform. This probably explains why it is generally even not mentioned in articles. Such an omission is obviously not important when studies are devoted to the qualitative aspect of the reinforcement of fillers in rubber nanocomposite; however, it might be a problem when the studies discusses about the modification of elastomer mobility through the filler–matrix interface.

12.3.4 Influence of Fillers on Rubber Crystallization

Creation of specific interactions between polymer and the filler surface can also have consequences on the crystallinity of semi-crystalline polymers. This question is important since a modification of the crystallinity can sometimes explain by itself the change of reinforcement without invoking any other physical mechanisms. This problem is present for some rubbers, such as natural rubber (NR) and polydimethyl siloxane (PDMS). These rubbers are known to crystallize either at a temperature below room temperature (the process called cold crystallization happens around $-25\,^{\circ}C$ for NR and $-70\,^{\circ}C$ for PDMS) or under strain (strain-induced crystallization: SIC). For instance, above a strain level of 300%, NR crystalli-

zation is instantaneous. SIC is often assumed to be to at the origin of the original auto-reinforcing character of natural rubber.

Recent results on SIC in the case of NR have clearly evidenced the critical influence of the crosslink density (see Figure 12.17 where NR2 and NR3 are NR matrices slightly and highly crosslinked, respectively). Crystallization kinetic is ruled by nucleation when the molecular weight between crosslinks is below the molecular weight between entanglements. Conversely, growth is the key factor when the molecular weight between crosslinks is above the molecular

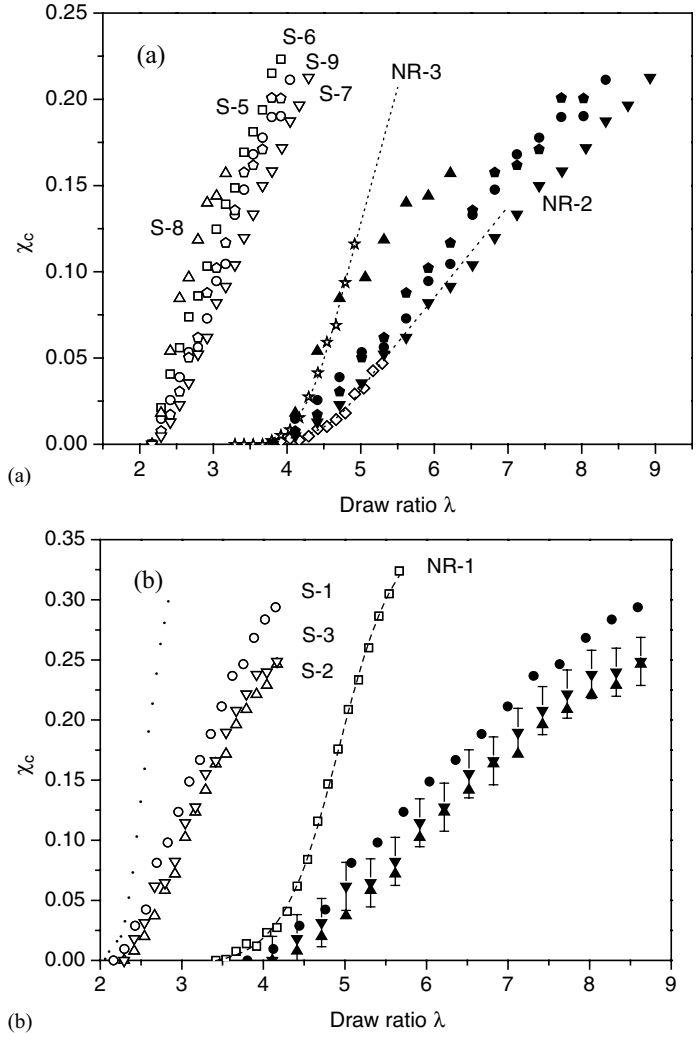

Figure 12.17 Crystallization versus strain for: (a) silica (S-5 to S-9: 50 phr); and (b) carbon black (S-1 to S-3: 45 phr) filled and unfilled NR matrices (NR-1 to NR-3). Tests were performed at room temperature and strain rate 0.25 min^{-1} (Reprinted from *Polymer*, **48**, J.M. Chenal et al., "Parameters governing strain induced crystallization in filled natural rubber," 6893–6901, © 2007, with permission from Elsevier.)

weight between entanglements. That means that the crystallization optimum is reached when the crosslink density corresponds to the physical entanglements density [111].

Besides, it is well established that the addition of nanoscopic fillers in natural rubber can indeed strongly increase rigidity, abrasion resistance, tear strength, and stress at break. The direct relationship between these improvements of the mechanical properties and the influence of the filler on crystallization under strain is still an open debate. Actually, the first role of the filler is the strain amplification of local strain [112]. Therefore, as a first step, it can be interesting to consider the influence of fillers on the cold crystallization (that does not imply strain amplification). For this reason, Dewimille *et al.* [113] studied the cold crystallization of poly dimethyl siloxane (PDMS) networks filled with *in situ* generated silica particles. Chenal *et al.* [114] were interested in the cold crystallization of filled natural rubber (NR) with carbon black (CB) and with silica. In both cases, a reduction in the ability of polymer to crystallize in the presence of filler was observed. The main effects of the fillers are related to the fact that they can create excluded region for crystallization and a region with perturbed mobility where the kinetics of nucleation and/or growth are slowed down, the rest of the matrix being unperturbed. The respective volume of the different regions depends on the filler parameters. The results may also be regarded as the consequence of an increase in the apparent crosslinking density due to polymer–filler interactions. This interpretation is close to that reached by Gent [66] in studies on the effect of the network crosslinking density on the crystallization characteristics of NR.

Let us now discuss the effect of fillers on SIC. Most recent studies are based on Synchrotron wide-angle X-ray scattering (WAXS) during stress–strain measurements performed on NR with different crosslink densities, unfilled or filled with nanoscopic silica, carbon black, clay, or calcium carbonate. Toki *et al.* [115] and Trabelsi *et al.* [116] have explained that the mechanical hysteresis observed, during tensile cycle tests, in all filled and unfilled NR samples is essentially due to the supercooled effect. Chenal *et al.* have demonstrated that the Mullins effect decreases the intensity of the SIC. The Mullins effect being highly dependent on the mechanical history of the material, it is therefore necessary to "demullinize" the samples to study properly the influence of the material parameters on SIC. Another aspect investigated by Poompradub *et al.* [117], Trabelsi *et al.* [116] and Chenal *et al.* [111, 118] using WAXS was the evolution of the crystallite sizes versus strain in the case of filled NR. In each study, it was shown that, when fillers are introduced, the crystallite sizes are decreased as well as the degree of crystallite orientation.

Several teams have demonstrated, regardless of filler nature, that the strain at the crystallization onset decreases with the addition of filler, due to strain amplification. Y. Wang *et al.* [10] have prepared NR-clay nanocomposites by co-coagulating the NR latex and a clay aqueous suspension. From the results of tensile tests, they explained that the presence of nanoclay (more than 10 phr) inhibits the development of crystallization of NR. To understand this result, the nanoparticles must be considered as new effective crosslinks. From this point of view, Rault *et al.* [119] have proposed the concept of effective crosslink density (ν) deduced from the sum of the chemical crosslinks ($\nu_c \sim 1/M_c$), entanglements ($\nu_e \sim 1/M_e$) and elastomer chains adsorption on the filler ($\nu_G \sim 1/M_G$) densities. By using this concept, Chenal *et al.* [118] have given a coherent description of SIC, that is, the evolution of crystallization rate and crystallite size (Figure 12.18a and b). Two different regimes, at weak and high effective crosslink density, were highlighted and the molecular weight between physical entanglements in natural rubber ($M_e \sim 7000$ g mol^{-1} and $\nu_e \sim 1.3 \cdot 10^{-4}$ mol cm^{-3}) seems to correspond to the boundary

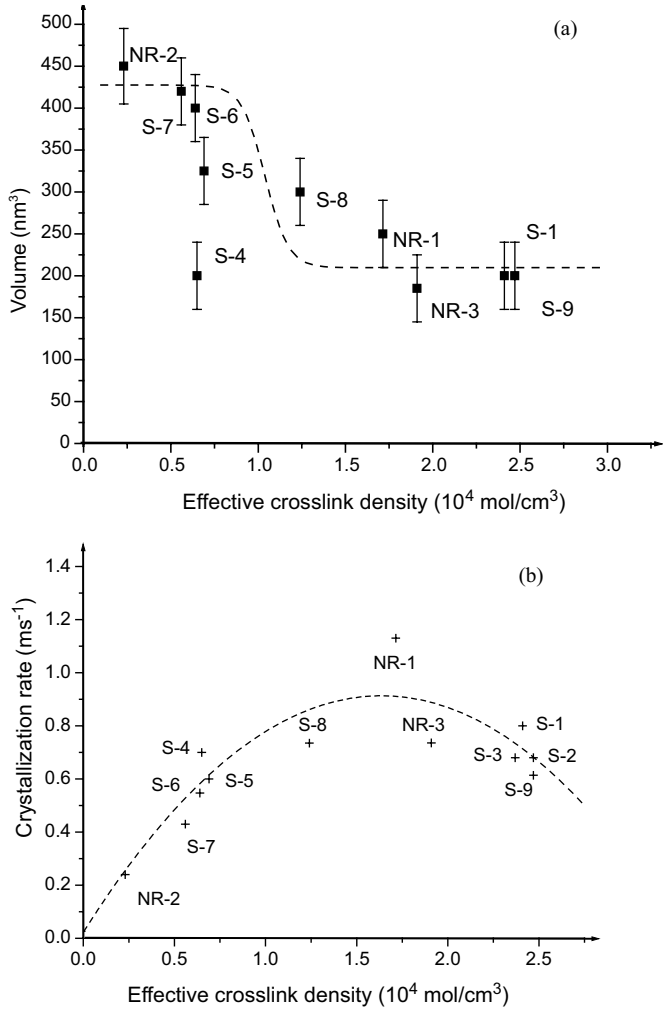

Figure 12.18 Variation of average crystallites' volume versus effective crosslink (a) and crystallization rate versus the effective crosslink density (b) (Reprinted from *Polymer*, **48**, J.M. Chenal et al., "Parameters governing strain induced crystallization in filled natural rubber," 6893–6901, © 2007, with permission from Elsevier.)

between both regimes. Below the critical value (ν_e), when a sample is stretched, nuclei number increases and the medium mobility decreases with the increase of effective crosslink density. Even if the growth step is slightly hindered, the nucleation step is so promoted that the crystallization rate increases. Simultaneously, the crystallites size slowly decreases until it drops at ν_e. Above the critical value, the restriction of the medium mobility becomes significant and hinders not only the growth but also the nucleation step. Thus, the crystallization rate slows down. The origin of this decrease of the nucleation rate can be related to the creation of an excluded volume for crystallization in the filler vicinity because of a reduced mobility.

These modifications of crystallization kinetic are related to the material ultimate properties. Tosaka *et al.* [120] have proposed that SIC induces a microfibrillar structure which can be seen as a network stronger that that created by the sole chemical crosslinks. This structure may significantly contribute to crack growth resistance as suggested by studies that focused on strain-induced crystallization in the crack tip region of CB filled elastomer [68, 121].

12.3.5 Conclusion

As for microscopic particles, the aspect ratio of the nanofiller introduced in rubber appears as a very important parameter for the reinforcement efficiency. Moreover, the very important surface of interface amplifies the problem of dispersion that often needs supplementary chemical step – such as surface treatment and polymer compatibilisation – or more efficient mixing. This dispersion step can first modify the effective aspect ratio of the particles and therefore have a direct effect on the reinforcement efficiency of the fillers. Moreover, the possible interactions of this interface with the complex formulation of the rubber (needed for its vulcanization) can modify the crosslinking kinetics and therefore the spatial distribution of the crosslinks and the matrix intrinsic properties. Besides, different experiments suggest a decrease of the polymer chain dynamic in the vicinity of the filler. At last, due to the small inter-filler distance, the filler–filler and filler–matrix interaction can more easily play a role in the formation of a continuous filler network whose the reinforcement efficiency is much higher than that of the individual particles. Thus, given the difficulty to dissociate the contribution of each type of interaction, the current author opinion, largely accepted in the community, is to consider that the reinforcement of rubber nanocomposites, the mechanisms of the Payne and Mullins effects probably involve *both* the filler structure and the adsorbed chain. As normally expected with fillers, their presence, by strain amplification phenomenon, leads to an earlier occurrence of crystallization (when dealing with crystallizable elastomer), but the interfacial interactions also modify the crystallization kinetic of the materials. Obviously, the ultimate properties of rubber nanocomposites strongly depend on all these phenomena, which control the development of strain anisotropy and damage.

12.4 Modeling Attempts

Given the difficulty to dissociate experimentally all the complex phenomena involved in the mechanical properties of rubber nanocomposite, it seems that a true evaluation of the interest of the introduction of the nanofillers can only be done if some efforts are put in their understanding. Thus, the aim of this last part is to present the different available modeling methods, which can be found in literature, to analyze the mechanical behavior of rubber nanocomposites. The mechanical response of filled rubbers is sometimes seen as the sum of different contributions, that is, that of the polymer network, the hydrodynamic effect and the contribution of filler–filler and/or filler–matrix interactions.

12.4.1 Polymer Network Contribution: Modeling Rubber Behavior

The mechanical response of an elastomer is directly deduced from the modeled behavior of one polymer chain, free from interactions with other chains. The simplest model is the

Gaussian one, which models the chain as an assembly of independent segments free of rotation. The elasticity of the chain is entropic and is deduced from a statistical description of its possible conformations. The behavior of a network of such chains can be done with the affine assumption that the macroscopic deformation of the material is proportional to that of each chain. The simplest theoretical description is based on a three-chain unit and, under simple shear, with the affine deformation of the representative network cell; this leads to the known formula available for low amplitude deformation [122].

$$G = NkT \tag{12.1}$$

where G is the shear modulus, T is the temperature and N is the number of active chains per unit volume.

This model can be refined at different levels: (i) at the level of the chain description by considering its maximal extensibility (the Gaussian description is replaced by the Langevin equation) and (ii) at the level of the network description, by accounting for the crosslink spatial fluctuations [123], by using eight-chain models or a randomly distributed chain model [124, 125], (iii) at the level of the chain environment by accounting also on the entanglements presence and their role in the chain dynamic [126–128]. In the latter case, lateral fluctuations of the polymer strand are limited by the presence of neighboring chains leading to a certain confinement of the individual chain in a determined volume with a tube-like geometry.

For instance, Rubinstein [127] gives the evolution of the Mooney function as a function of the extension ratio λ (length over the initial length):

$$f^*(\lambda^{-1}) = G_c + \frac{G_e}{0.74\lambda + 0.61\lambda^{-0.5} - 0.35} \tag{12.2}$$

where G_c is the modulus contribution of the chemical crosslinks and G_e is related to the entanglement density. f^* is the Mooney ratio defined in tensile testing as:

$$f^*(\lambda^{-1}) = \frac{\sigma}{\lambda^2 - \lambda^{-1}} \tag{12.3}$$

where σ is the tensile stress.

An alternative to these physical models is to adopt a phenomenological description based on the definition of elastic potentials as a function of the different strain invariants, or of the different elongation variables [129, 130]. Note that the number of parameters to evaluate and therefore the number of experiments to perform, depends on the accuracy required for the fit of the experimental curves and the strain range that the model wants to cover.

Some authors proposed to extend the expressions used for unfilled elastomer (Ogden or Mooney type) to composite modeling without accounting explicitly for the specific phenomena induced by the filler presence. Obviously, in such a phenomenological approach, there is no physical meaning of the parameters. The difficulty met by these models (like in the case of more physical based models) is to account for the viscoelastic response of the material when submitted to a complex stress–strain history. This is done through the parameterization of the time-dependence of the parameters. In addition, the account for non linear character of this viscoelasticity (the Payne effect) or the irreversible damage of the material (such as the Mullins effect and cavitation) can be rendered through the introduction of functions giving the evolution of the parameters during deformation [131–133]. An intermediate solution can be

the introduction in the network model of a second network corresponding to the contribution of the filler, as done for instance by Bergstrom *et al.* [134].

All these approaches, even the physically based ones, generally consider the elastomer network as homogeneous. In fact, in elastomers, except when they are processed by cross-linking at the ends of chains whose length distribution is known, intercrosslink distances can be widely distributed. The consequences of this distribution can be very important, especially in the large deformation range, where the nonlinear hyperelastic behavior of the polymer chains is involved. The account for such effects in models needs a more complete description of the network architecture. One can cite in this domain the pioneering work of Termonia [135].

12.4.2 Filler Contribution: How to Describe the Composite Effect?

Of course, the introduction of filler makes more difficult the modeling of the mechanical properties of the material. The first effect of the introduction of the fillers is what we would called the "composite" effect, that is, the reinforcement provided by the introduction of the more rigid filler phase. Different models describe the reinforcement of composite materials. Three general kinds of models can be distinguished.

The first series concerns boundary models, based on variational methods, which define the extreme elastic behaviors of composites [for instance Voigt and Reuss bounds which assume a uniform stress (serial model) or a uniform strain (parallel model) in both phases respectively]. This is possible for elasticity and for linear viscoelasticity too. However, in the case of filled rubbers, the modulus contrast between both phases is huge (for example, shear modulus of silica $\sim$30 GPa, rubber $\sim$1 MPa), so that the obtained bounds (of the first, second and third order using respectively first-, second- and third-order correlation functions) are generally too far apart to be of practical use for comparison with experimental data.

The second set of models involves phenomenological approaches that introduce one or more adjustable parameters. For instance, the serial–parallel model of Takayanagi [136] gives a direct uniaxial representation of the assumed mechanical coupling through an adequate distribution of phases serially or in parallel. This distribution is controlled by one fitting parameter. In specific cases, physical arguments (percolation [137] or filler distribution from morphological observations) can be used to set the adjustable parameter of this type of model.

The last series concerns micromechanical modeling, developed in the framework of homogenization theory. They propose an explicit connection between given morphological information on the microstructure of a "representative volume element" (RVE) of the considered material and the overall mechanical response of the associated "equivalent homogeneous medium" (EHM). In the Christensen and Lo three-phase model [138], the composite is seen as an inclusion surrounded by a matrix immersed in the unknown EHM. The Herve and Zaoui *n*-phase model [139] generalized this so-called self-consistent estimate by an iteration technique, embedding the different phases or more specific patterns in the EHM itself [140]. Three-phase predictions are satisfactory when particles are well dispersed in the matrix and far enough from each other [141]. However, as soon as particle aggregation occurs and especially when the rubbery plateau modulus is concerned, the three-phase model leads to too soft predictions.

This three-phase model for spherical inclusion has an equivalent in the domain of long fibers, then assumed with an infinite length [142]. When these fibers are short, the calculations are

performed using the Eshelby calculation [143] for an ellipsoidal inclusion with the aspect ratio in a matrix taken as the homogenous infinite medium (this calculation was initially proposed by Mori and Tanaka [144]). The general solution for the modulus in the direction of the large axis of the ellipsoid has a strong dependence on the modulus contrast of both phases and on the form factor. One can define a reinforcement factor A with the formula:

$$E_c = E_m(1 + A\phi) \tag{12.4}$$

Its evolution as a function of the form factor and of the modulus ratio is recalled on Figure 12.19. One can notice that for a modulus ratio below 100, fibers with form factor above 100 have the same effect on the predicted reinforcement than infinitely long fibers. Moreover, the highest the form factor, the largest the influence of the modulus contrast. These calculations can be applied to the simple case of composites with unidirectionally oriented fibers. The calculation for a transversely isotropic or totally isotropic material needs the calculation of an average of the reinforcement on all the orientations, calculated in the unidirectional case, as proposed by Tandon and Weng [145].

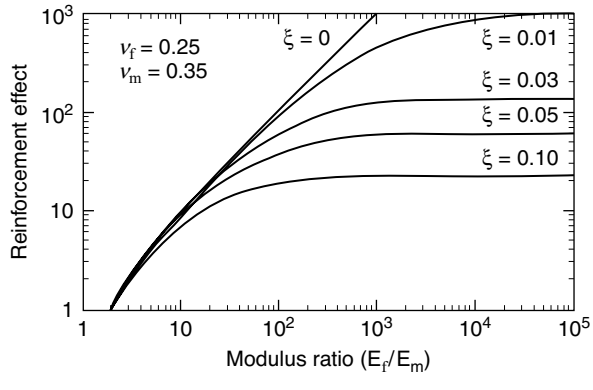

Figure 12.19 Influence of the filler length on the reinforcing factor A (cf. Equation 12.4) as a function of the inverse filler aspect ratio ξ and the filler-to-matrix modulus ratio E_f/E_m (Reprinted from R.M. Christensen, *Mechanics of Composite Materials*, with permission from Dover Publications, Inc., New York. © 2007.)

The absence of an analytical solution for such calculations leads Halpin and Tsai to propose an empirical equation equivalent to the Mori–Tanaka calculation [146]:

$$\frac{M_c}{M_m} = \frac{1 + \zeta\eta\phi}{1 - \eta\phi} \quad \text{where } \eta \text{ writes} \quad \eta = \frac{\frac{M_f}{M_m} - 1}{\frac{M_f}{M_m} + \zeta} \tag{12.5}$$

where ϕ is the filler volume fraction, ζ is a factor depending on the filler form and M is the modulus with indices f for filler, m for matrix and c for composite.

Ashton *et al.* [147] have shown that the equations can be used for the reinforcement of unidirectional fiber composites. They advised the use of $\zeta = 2a/b$ for the calculation, where a is the fiber length and b is the fiber diameter, of the longitudinal modulus E_{11}, $\zeta = 2$ for the

transverse modulus E_{22} or E_{33}, $\zeta = 1/(3–4v_m)$ for the shear modulus G_{23}, and $\zeta = 1$ for shear moduli G_{12} or G_{31} with $v_{31} = v_{12}$.The Halpin and Tsai formula is also often used for the modulus calculation of laminated. In this case, the modulus tensor is the average on all the orientation of the moduli tensor of each ply, weighted by the volume fraction. The Halpin–Kardos model leads to the analytical formula of a four-ply laminate in which fibers are oriented respectively at $0°, 45°, 90°$ and $135°$. Tsai and Pagano, from these calculations, have proposed a simplified expression of a transversely isotropic composite [148]:

$$E_{2D} = 0.375E_{//} + 0.625E_{\perp} \tag{12.6}$$

Where $E_{//}$is the longitudinal modulus of a single ply and $E_{\perp}$ is its transverse modulus.

The modulus of an isotropic composite can be obtained by a three-dimensional average such as that proposed by Van Es [149]:

$$E_{3D} = 0.184E_{//} + 0.816E_{\perp} \tag{12.7}$$

Even if his process is questionable, the results are equivalent to the calculation of Tandon and Weng [145].

All these models have been first developed in the linear domain and they are useful to compare experimental data with predicted modulus values taking into account the filler parameters such as modulus and shape. However, they are adimensional and do not predict any effect of the filler size. Moreover, the interface between filler and matrix is assumed to be perfect. When applied to nanocomposites, they generally underestimate the reinforcement, especially in the case of thermoplastics above T_g or rubbers [150]. This is however not always the case. For example, in the case of CNT filled nanocomposites, even at low nanotubes concentrations, the experimental data can be below predictions from the Halpin–Tsai model [146]. The gap between the predictions and experimental results has been attributed to imperfect dispersion and poor load transfer. Actually, even modest nanotube agglomeration may impact the diameter and length distributions of the filler. This will decrease the aspect ratio, and this can even reduce the modulus of the filler relative to that of isolated nanotubes given the weak interaction forces between nanotubes [151].

To go further in accounting for the complexity of elastomer behavior, two different fields of mechanical modeling were soon developed. First, the impact of agglomeration can be evaluated through the adaptation of the micromechanical approaches cited above. Chabert *et al.* [141] presented a homogenization method based on generalized self-consistent schemes to model polymer-based nanocomposite behavior using different structure patterns. For a silica-filled SBR, Mélé *et al.* [152] defined three phases: silica particles, bound rubber (the rubber close to the particle) and unbound rubber. Their self-consistent model introduced the viscoelastic properties of the different phases in a representative morphological pattern that depends on the particle content. Some authors proposed to apply the self-consistent three-phase model in successive steps [45]. The finite element method (FEM) is sometimes used to calculate stresses and strains in the representative volume element (RVE) containing one [153] or several inclusions with different sizes in random positions for soft inclusions [154] or rigid particles for a nanocomposite [155]. A stochastic and deterministic model was proposed by Minakova *et al.* [156] for the macrostructure geometry of polymer materials containing dispersed fillers and allowed describing the agglomeration and desagglomeration for a filler of complex structure.

The second field concerns larger deformation, for which nonlinearity should be introduced. Because filled rubbers are often used in situations involving large deformations, it is of practical, as well as theoretical interest, to develop adapted constitutive models. But the models must be simple enough to be implemented in standard finite element codes and to be able to carry out simulations at the structural level ("structural" in the sense of piece design). To extend the micromechanical models to higher strains, it is necessary to consider both the nonlinear behavior of the phases and a specific scale transition rule, which takes into account the nonlinear accommodation of stress heterogeneities between the phases. Lopez-Pamies and Ponte Castanada [157] developed nonlinear homogenization modeling (second order) that takes into account the evolution of the microstructure (fiber orientation) and the possible onset of macroscopic instabilities in fiber-reinforced elastomers subjected to finite deformations. Tomita *et al.* [158] propose a computational simulation based on a plane strain rubber unit cell containing CB fillers under monotonic and cyclic strain with a nonaffine molecular chain network model. The results reveal the substantial enhancement of the resistance of the rubber to macroscopic deformation, which is caused by a marked orientation hardening due to highly localized deformation in the rubber. Chain disentanglement during the deformation of the rubber results in the magnification of the hysteresis loss during cyclic deformation processes. Such an approach has also been applied to evaluate the effect of aggregation.

12.4.3 Account for the Filler–Filler and Filler–Matrix Interactions

As seen above, lots of models only introduce the role of interactions through the assumed permanent and perfect load transfer between the matrix and the filler. Nevertheless, filler–filler and filler–matrix interactions are known to play a more complex role in nonlinear manifestations, such as Payne and Mullins effects.

In the filler structure models, the filler–filler interactions are considered as preponderant. Under this assumption, the strain dependencies of both the viscous and elastic moduli have been modeled by Kraus [159], assuming Van der Waals interactions between particles. The contribution given by interaction forces between aggregates to the modulus is proportional to the number of contacts whose rigidity is governed by the size and the form of the aggregates. Their separation occurs at a given strain that corresponds to the maximum restoring force. The concept of occluded elastomer is also often introduced in these filler aggregation models [7]. Nevertheless, the model of Kraus does not predict nor the values of the high and low amplitude moduli, neither the strain necessary for the modulus decrease and the influence of temperature. The estimation of the modulus at high amplitude can be performed using the models presented above (Guth equation, Christensen and Lo three-phase model, and so on). To estimate the low amplitude modulus, some authors prefer to consider the filler structure from the percolation theory [160]. They make the assumption that it has a scale invariance of a fractal object [161]. The reinforcement is deduced from the calculation of the rigidity of the cluster objects forming the network. It is found a power law dependence of the modulus with the filler content. The composite deformation leads to the breakage of the cluster in smaller and smaller units, which lose their effectiveness [162]. This description leads to the same Krauss formula in which the parameters are related to the description of the filler structure: its fractal dimension and its connectivity [160]. Gerspacher [163] uses a different formalism to describe the process of rupture and reformation of contacts between aggregates. He assumes a distribution of pair of

aggregates in the material, from a linked state to a separate state. The alternation, during DMA measurements, of these states (linked–detached–linked) is responsible for energy dissipation.

A second set of models used to describe the Payne effect assumes that the matrix–filler interactions are responsible for this effect [164]. These models are based on the idea of adsorbed polymer chains at the filler surface (bound rubber) that display a decreased molecular mobility and/or may act as supplementary crosslinks in the material. Then, under the increase of strain, a mechanism of adhesion and de-adhesion of polymer chains at the filler interface is proposed. In a purely entropic description of the viscoelastic behavior of the material, Maier and Goritz [100] then assimilate these bonds to supplementary crosslinks; the initial modulus is then the direct consequences of an increase of active chains in the elastomer and its drop is the consequence of a rupture of these bonds. This vision has the advantage to nourish the debate on the importance of matrix–filler interactions on the Payne effect but the model deduced from this is too global (homogenizing) and leads to meaningless theoretical crosslink densities. Indeed, the reinforcement provided by the filler nondeformability (compared to the matrix one) cannot be forgotten.

Besides, the multifunctional crosslinking nature of the fillers might be at the origin of an immobilized polymer phase in their vicinity, or at least a polymer phase with a mobility gradient. Different modeling scales are explored to evidence it. The presence of filler with average distance between them of the same order as the gyration radius of the polymer chain decreases the chain conformational freedom and perturbs the entropic elasticity response of the matrix. Mark has worked for many years on this aspect and has developed Monte Carlo based simulation of filled elastomer [165]. Natural rubber network in presence of saponite or carbon black (N234) [166] has been evaluated by applying the tube model theory. This results in a marked decrease of the tube dimensions due to nanoparticle/elastomer interactions, which restricts the movement of the rubber chains to a lower volume. More and more work is being devoted to molecular dynamics accounting extensively for all the different interactions involved at the atomistic level. We are only at the beginning of these types of simulation whose capabilities increase with the growing calculation efficiency of the computing facilities [167–169].

Instead of describing the material at the molecular level, some might prefer a less refined but more straightforward approach. Thus mesoscopic-scale modeling has been developed in order to capture the complex role of the filler–matrix microstructure in the elastomer nanocomposites: a so-called discrete numerical model simplifies the material description by considering only the mechanical junctions between points. This enables an explicit account of the filler spatial organization in the matrix and the nature of contacts between the filler particles and the filler particles and the matrix [170]. This modeling is easy to handle in the linear domain and therefore can be useful to estimate the material modulus. However, the description of phenomena such as the Payne effect or the Mullins effect needs the introduction of viscoelastic contact and criteria for the rupture of either matrix–filler or filler–filler contacts. If developed, this approach can take benefit from the early work of Bueche et Halpin [171]; for the Mullins effect and material rupture they proposed a molecular model of propagation of rupture of polymer filament, with crack propagation dependent on the viscoelastic properties of the material. Boonstra [172] and Dannenberg [104] added in the interpretation the slipping of chain at the polymer–filler interface, which was included in the modeling of Ambacher *et al.* [173]. These ideas could be advantageously introduced to describe the material behavior from the linear range up to its rupture.

12.4.4 Conclusion

To conclude, all the experimental evidences and theoretical calculations seem to indicate that both filler structure and adsorption of polymer chains are involved in the nonlinear viscoelastic behavior of nanoparticle-filled rubber. The modulus measured is obviously the result of a viscous mechanical coupling of the matrix with a complex structure of more or less aggregated fillers. The deformation of this ensemble is very heterogeneous and involves complex dissipative mechanisms such as rupture of the different type of interactions, filler reorganization and cavitation. Two approaches can be followed to describe this complexity: the first one consists in forgetting it by the use of phenomenological macroscopic constitutive equation. The second approach wants to account for the phenomena occurring at the filler scale (filler spatial repartition, more or less refined) or even at the molecular level (filler–filler and filler–matrix interactions). In addition to the comprehension it brings to the experimental observation, the advantage of this second approach is to feed the macroscopic modeling with meaningful physical parameters. This work is in progress. It is quite advanced in the domain of small deformation but is still a challenge in the domain of large strain, when damage (bond rupture, void formation, spatial reorganization of the fillers) makes the problem very difficult.

12.5 General Conclusions

To conclude, a large number of papers are devoted to rubber nanocomposite mechanical behaviors. Among the different types of filler that have been tested, some are already extensively used in industry (carbon black, silica) whereas others are still under evaluation. Prior to any mechanical studies, fillers have to be dispersed in the host elastomer. To do so, several strategies are reported in the literature, including different processing routes, the use of surface treatments and modification of the matrix. The obtained dispersion state is more or less rigorously controlled, thanks to dedicated characterization techniques at various scales (such as SAXS, TEM, AFM, and so on) or by an indirect approach based on the discussion of mechanical performances.

How nanofillers impact on the mechanical behavior of rubber nanocomposites is the point addressed in numerous papers. Actually, the introduction of a nanoscopic filler strongly modifies the mechanical behavior of unfilled rubbers. In the small deformation range, instead of the quasi-linearity observed in shear with unfilled elastomer, one observes a typical nonlinear viscoelastic behavior, the so-called Payne effect. In the large deformation range, the stress is remarkably increased for a given strain, the hysteretic loss during deformation cycle is enhanced, a strong sensitivity to the first deformation, the so-called Mullins effect, is revealed, and the ultimate properties such as wear resistance and rupture behavior can be improved. Much experimental evidence of the improvement of mechanical behavior of rubber nanocomposites is reported in the literature. However, due to the large number of parameters that can be changed in the formulation and the process, the empirical optimization of the mechanical properties might not be the most relevant approach.

Indeed, to go further, it is important to understand *why* nanofillers are so efficient for rubber reinforcement and why they lead to all these complex nonlinear phenomena. Through the discussion of literature data, several main features can be captured. First of all, as for all heterogeneous materials, the nanocomposite macroscopic behavior depends on the behavior of each phase, their volume fraction, their topological arrangement (dispersion, orientation) and

on interfacial properties. The latter becomes of first importance in nanocomposites because the small size of the filler leads to a high interface/volume ratio, and the average distance between domains, that is, between filler surface can be of the same order as the dimensions of the macromolecule coils. Reinforcement is sometimes attributed to the presence of a rigid phase (immobilized interphase) whose volume fraction can be non-negligible. In addition, the existence of a filler network, which is never discussed for classic, that is, micrometer-scale composites, is often evidenced for nanocomposites and can be analyzed through the percolation concept. The properties of this more or less flexible network is ruled by filler–filler (direct bonding between neighboring fillers) and filler–matrix interactions (when macromolecules that are adsorbed or chemically linked onto the filler surface link together two (or more) fillers). These interactions appear to play a preponderant role at small and large strain. In the later case, the analysis of the mechanical behavior is even more complex as strain heterogeneities, desagglomeration and decohesion processes may take place.

Thus, one can wonder *then* what to do and what are the next challenges. To study more deeply the incidence of the various parameters already mentioned (size, shape, interfacial energy, topological distribution, and so on), one route can be to process model materials trying to modify only one of these parameters. However, this is a tricky task as it is not easy to produce fillers having the same chemical structure with different shapes (rod, platelet, sphere), or even with different sizes and identical surface properties. An alternative way involves the comparison of experimental data with prediction obtained from modeling approaches at different scales (micromechanical approaches, mesoscopic discrete modeling or atomistic Monte Carlo-based simulation). Unfortunately, at the present time, most of the models display insufficient prediction capabilities. Progresses can be expected from development of techniques able to characterize the 3D spatial distribution of filler at a pertinent scale (filler network) and to give an insight on contact force between filler (filler–filler interactions, through or not a matrix layer). Indeed, these data are necessary to improve the modeling of the mechanical behavior especially at large strain, when modification of the filler distribution can no longer be neglected, neither cavitation and decohesion phenomena.

References

1. Hussain, F. *et al.* (2006) Review article: polymer-matrix nanocomposites, processing, manufacturing, and application: an overview. *Journal of Composite Materials*, **40**, 1511–1575.
2. Konecny, P. *et al.* (2007) Dynamic mechanical properties of filled styrene butadiene rubber compounds: comparison of tensile and shear data. *Polymers for Advanced Technologies*, **18**, 122–127.
3. Wypych, G. (2000) *Handbook of Fillers*, Chemtec Publishing.
4. Hainsworth, S. (2007) An environmental scanning electron microscopy investigation of fatigue crack initiation and propagation in elastomers. *Polymer Testing*, **26**, 60–70.
5. Kohjiya, S. *et al.* (2006) Visualisation of carbon black networks in rubbery matrix by skeletonisation of 3D-TEM image. *Polymer*, **47**, 3298–3301.
6. Tscheschel, A., Lacayo, J., and Stoyan, D. (2005) Statistical characterization of TEM images of silica-filled rubber. *Journal of Microscopy*, **217**, 75–82.
7. Leblanc, J.L. (2002) Rubber-filler interactions and rheological properties in filled compounds. *Progress in Polymer Science*, **27**, 627–687.
8. Sengupta, R. *et al.* (2007) A short review on rubber/clay nanocomposites with emphasis on mechanical properties. *Polymer Engineering and Science*, **47**, 1956–1974.
9. Wang, Y. *et al.* (2004) Free volume of montmorillonite/styrene-butadiene rubber nanocomposites estimated by positron annihilation lifetime spectroscopy. *Macromolecular Rapid Communications*, **25**, 1973–1978.

10. Wang, Y. *et al.* (2005) Structure and properties of strain-induced crystallization rubber-clay nanocomposites by co-coagulating the rubber latex and clay aqueous suspension. *Journal of Applied Polymer Science*, **96**, 318–323.
11. Mark, J. (2006) Some novel polymeric nanocomposites. *Accounts of Chemical Research*, **39**, 881–888.
12. Kueseng, K. and Jacob, K. (2006) Natural rubber nanocomposites with SiC nanoparticles and carbon nanotubes. *European Polymer Journal*, **42**, 220–227.
13. El-Nashar, D.E., Mansour, S.H., and Girgis, E. (2006) Nickel and iron nano-particles in natural rubber composites. *Journal of Materials Science*, **41**, 5359–5360.
14. Kong, Q. *et al.* (2006) Influence of Fe-MMT on crosslinking and thermal degradation in silicone rubber/clay nanocomposites. *Polymers for Advanced Technologies*, **17**, 463–467.
15. Wang, M. *et al.* (1998) Carbon-silica dual phase filler, a new generation reinforcing agent for rubber. *Kautschuk und Gummi Kunststoffe*, **51**, 348–360.
16. Wang, M. *et al.* (2000) Carbon-Silica dual phase filler, a new generation reinforcing agent for rubber: Part VIII. Surface characterization by IGC. *Rubber Chemistry and Technology*, **73**, 666–677.
17. Wang, M., Zhang, P., and Mahmud, K. (2001) Carbon-silica dual phase filler, a new generation reinforcing agent for rubber: Part IX. Application to truck tire tread compound. *Rubber Chemistry and Technology*, **74**, 124–137.
18. Alexandre, M. and Dubois, P. (2000) Polymer-layered silicate nanocopposites: preparation, properties and uses of a new class of materials. *Materials Science and Engineering: R: Reports*, **28**, 1–63.
19. Zanetti, M. *et al.* (2001) Synthesis and thermal behaviour of layered silicate-EVA nanocomposites. *Polymer*, **42**, 4501–4507.
20. Iijima, S. (1991) Helical microtubules of graphitic carbon. *Nature*, **354**, 56–58.
21. Krishnan, A. *et al.* (1998) Young's modulus of single-walled nanotubes. *Physical Review B*, **58**, 14013.
22. Thostenson, E.T., Ren, Z., and Chou, T. (2001) Advances in the science and technology of carbon nanotubes and their composites: a review. *Composites Science and Technology*, **61**, 1899–1912.
23. Yu, M. *et al.* (2000) Tensile loading of ropes of single wall carbon nanotubes and their mechanical properties. *Physical Review Letters*, **84**, 5552.
24. Bokobza, L. (2007) Multiwall carbon nanotube elastomeric composites: a review. *Polymer*, **48**, 4907–4920.
25. Atieh, M. *et al.* (2005) Multi-wall carbon nanotubes/natural rubber nanocomposite. *Journal of Nanotechnology*, **1**, 1–11.
26. Jiang, M., Dang, Z., and Xu, H. (2006) Significant temperature and pressure sensitivities of electrical properties in chemically modified multiwall carbon nanotube/methylvinyl silicone rubber nanocomposites. *Applied Physics Letters*, **89**, 182902–182903.
27. Jiang, M., Dang, Z., and Xu, H. (2007) Giant dielectric constant and resistance-pressure sensitivity in carbon nanotubes/rubber nanocomposites with low percolation threshold. *Applied Physics Letters*, **90**, 042914 –3.
28. Jiang, M., Dang, Z., and Xu, H. (2007) Enhanced electrical conductivity in chemically modified carbon nanotube/methylvinyl silicone rubber nanocomposite. *European Polymer Journal*, **43**, 4924–4930.
29. Dalmas, F. *et al.* (2006) Carbon nanotube-filled polymer composites. Numerical simulation of electrical conductivity in three-dimensional entangled fibrous networks. *Acta Materialia*, **54**, 2923–2931.
30. Sassi, J. (1995) Etude ultrastructurale de l'acétylation de la cellulose: Application à la préparation de nanocomposites, PhD Thesis, Grenoble.
31. Chazeau, L. *et al.* (1999) Viscoelastic properties of plasticized PVC reinforecd with cellulose whiskers. *Journal of Applied Polymer Science*, **71**, 1797–1808.
32. Favier, V., Chanzy, H., and Cavaille, J. (1995) Polymer nanocomposites reinforced by cellulose whiskers. *Macromolecules*, **28**, 6365–6367.
33. Angellier, H., Molina-Boisseau, S., and Dufresne, A. (2006) Waxy maize starch nanocrystals as Filler in natural rubber. *Macromolecular Symposia*, **233**, 132–136.
34. Li, G. *et al.* (2001) Polyhedral oligomeric silsesquioxane (POSS) polymers and copolymers: a review. *Journal of Inorganic and Organometallic Polymers*, **11**, 123–154.
35. Liu, L. *et al.* (2006) Preparation, structure and properties of nitrile-butadiene rubber-organoclay nanocomposites by reactive mixing intercalation method. *Journal of Applied Polymer Science*, **100**, 1905–1913.
36. Fu, B.X. *et al.* (2001) Structural development during deformation of polyurethane containing polyhedral oligomeric silsesquioxanes (POSS) molecules. *Polymer*, **42**, 599–611.
37. Wolff, S. (1996) Chemical aspects of rubber reinforcement by fillers. *Rubber Chemistry and Technology*, **69**, 325–345.

38. Ramier, J. *et al.* (2007) Payne effect in silica-filled styrene-butadiene rubber: influence of surface treatment. *Journal of Polymer Science Part B: Polymer Physics*, **45**, 286–298.
39. Kato, M. *et al.* (2006) Preparation and properties of isobutylene-isoprene rubber-clay nanocomposites. *Journal of Polymer Science Part A: Polymer Chemistry*, **44**, 1182–1188.
40. De Falco, A. *et al.* (2007) Carbon nanotubes as reinforcement of styrene-butadiene rubber. *Applied Surface Science*, **254**, 262–265.
41. Lu, Y. *et al.* (2007) Microstructure and properties of highly filled rubber/clay nanocomposites prepared by melt blending. *Composites Science and Technology*, **67**, 2903–2913.
42. Sui, G. *et al.* (2007) Processing and material characteristics of a carbon-nanotube-reinforced natural rubber. *Macromolecular Materials and Engineering*, **292**, 1020–1026.
43. Ramier, J. *et al.* (2007) Influence of silica and its different surface treatments on the vulcanization process of silica filled SBR. *Rubber Chemistry and Technology*, **80**, 183–193.
44. Chazeau, L. *et al.* (2000) Modulus recovery kinetics and other insights into the payne effect for filled elastomers. *Polymer Composites*, **21**, 202–222.
45. Gauthier, C. *et al.* (2004) Analysis of the non-linear viscoelastic behaviour of silica filled styrene butadiene rubber. *Polymer*, **45**, 2761–2771.
46. Arai et, K. and Ferry, J. (1986) Differential dynamic shear moduli of various carbon-black-filled rubbers subjected to large step shear strains. *Rubber Chemistry and Technology*, **59**, 605–614.
47. Roland, C. (1990) Dynamic mechanical behavior of filled rubber at small strains. *Journal of Rheology*, **34**, 25–34.
48. Isono, Y. and Ferry, J. (1984) Stress relaxation and differential dynamic modulus of carbon black-filled styrene-butadiene rubber in large shearing deformations. *Rubber Chemistry and Technology*, **57**, 925–943.
49. Qian, S. *et al.* (2007) Investigation of carbon black network in natural rubber with different bound rubber contents. *Journal of Macromolecular Science, Part B*, **46**, 453.
50. Ramorino, G. *et al.* (2007) Dynamic and viscoelastic behavior of natural rubber/layered silicate nanocomposites obtained by melt blending. *Polymer Engineering and Science*, **47**, 1650–1657.
51. Bokobza, L. and Kolodziej, M. (2006) On the use of carbon nanotubes as reinforcing fillers for elastomeric materials. *Polymer International*, **55**, 1090–1098.
52. Ramier, J. *et al.* (2007) In situ SALS and volume variation measurements during deformatio of treated silica filled SBR. *Journal of Materials Science*, **42**, 8130–8138.
53. Ahmadi, S.J., Huang, Y., and Li, W. (2005) Fabrication and physical properties of EPDM-organoclay nanocomposites. *Composites Science and Technology*, **65**, 1069–1076.
54. Tian, M. *et al.* (2005) The anisotropy of fibrillar silicate/rubber nanocomposites. *Macromolecular Materials and Engineering*, **290**, 681–687.
55. Holt, W. (1932) Behavior of rubber under repeated stresses. *Rubber Chemistry and Technology*, **5**, 79–89.
56. Mullins, L. (1947) Effect of stretching on the properties of rubber. *Journal of Rubber Research*, **16**, 275–289.
57. Bueche, F. (1960) Molecular basis for the Mullins effect. *Journal of Applied Polymer Science*, **4**, 107–114.
58. Lapra, A. (1999) Caractérisation moléculaire et propriétés mécaniques des réseaux élastomères SBR renforcés par de la silice, Ph.D. Thesis, Université Pierre et Marie Curie, Paris VI.
59. Ramier, J. (2004) Comportement mécanique d'élastomères chargé, Influence de l'adhésion charge-polymère, Influence de la morphologie, Ph.D. Thesis, Institut National des Sciences Appliquées de Lyon.
60. Hwang, W., Wei, K., and Wu, C. (2004) Preparation and mechanical properties of nitrile butadiene rubber/silicate nanocomposites. *Polymer*, **45**, 5729–5734.
61. Kader, M. *et al.* (2006) Preparation and properties of nitrile rubber/montmorillonite nanocomposites via latex blending. *Journal of Materials Science*, **41**, 7341–7352.
62. Harwood, J. and Payne, A. (1968) Hysteresis and strength of rubbers. *Journal of Applied Polymer Science*, **12**, 889–901.
63. Schallamach, A. (1952) Abrasion pattern on rubber. *Transactions of the Institute of Rubber Industries*, **28**, 256–268.
64. Hamed, G. and Park, B. (1999) The mechanism of carbon black reinforcement of SBR and NR vulcanizates. *Rubber Chemistry and Technology*, **72**, 946–959.
65. Gent, A.N. and Zhang, L. (2001) Strain-induced crystallization and strength of elastomers. I. cis-1,4-polybutadiene. *Journal of Polymer Science Part B: Polymer Physics*, **39**, 811–817.
66. Gent, A.N. (1954) Crystallization and the relaxation of stress in stretched natural-rubber vulcanizates. *Transaction of the Faraday Society*, **50**, 521–533.

67. Rivlin, R. and Thomas, A. (1953) Characteristic energy for tearing. *Journal of Polymer Science*, **18**, 177–188.
68. Trabelsi, S., Albouy, P., and Rault, J. (2002) Stress-induced crystallization around a crack tip in natural rubber. *Macromolecules*, **35**, 10054–10061.
69. Mars, W.V. and Fatemi, A. (2003) Fatigue crack nucleation and growth in filled natural rubber. *Fatigue & Fracture of Engineering Materials & Structures*, **26**, 779–789.
70. Park, S. and Kim, J. (2000) Role of chemically modified carbon black surfaces in enhancing interfacial adhesion between carbon black and rubber in a composite system. *Journal of Colloid and Interface Science*, **232**, 311–316.
71. Ramier, J. *et al.* (2006) Grafting of silica during the processing of silica-filled SBR: Comparison between length and content of the silane. *Journal of Polymer Science Part B: Polymer Physics*, **44**, 143–152.
72. Usuki, A., Tukigase, A., and Kato, M. (2002) Preparation and properties of EPDM-clay hybrids. *Polymer*, **43**, 2185–2189.
73. Oliveira, P.C. *et al.* (2005) Poly(dimethylaminoethyl methacrylate) grafted natural rubber from seeded emulsion polymerization. *Polymer*, **46**, 1105–1111.
74. Cataldo, F. (2002) Preparation of silica-based rubber compounds without the use of a silane coupling agent through the use of epoxidized natural rubber. *Macromolecular Materials and Engineering*, **287**, 348–352.
75. Peng, C. *et al.* (2005) Smart silica-rubber nanocomposites in virtue of hydrogen bonding interaction. *Polymers for Advanced Technologies*, **16**, 770–782.
76. Pu, Z. *et al.* (1997) Effects of dispersion and aggregation of silica in the reinforcement of poly(methyl acrylate) elastomers. *Chemistry of Materials*, **9**, 2442–2447.
77. Brechet, Y. *et al.* (2001) Polymer based nanocomposites: effect of filler-filler and filler-matrix interactions. *Advanced Engineering Materials*, **3**, 571–577.
78. Stauffer, D. (1992) *Introduction to percolation theory*, Taylor & Francis, London.
79. Balberg, I., Binenbaum, N., and Wagner, N. (1984) Percolation thresholds in the three-dimensional sticks system. *Physical Review Letters*, **52**, 1465–1468.
80. Favier, V. *et al.* (1997) Simulation and modeling of three-dimensional percolating structures: Case of a latex matrix reinforced by a network of cellulose fibers. *Acta Materialia*, **45**, 1557–1565.
81. Balberg, I. and Binenbaum, N. (1983) Computer study of the percolation threshold in a two-dimensional anisotropic system of conducting sticks. *Physical Review B*, **28**, 3799–3812.
82. Richard, P. *et al.* (2003) Reinforcement of rubbery epoxy by carbon nanofibres. *Materials Science and Engineering A*, **352**, 344–348.
83. Payne, A. (1962) The dynamic properties of carbon black-loaded natural rubber vulcanizates. *Journal of Applied Polymer Science*, **6**, 57–63.
84. Hess, W. (1991) Characterization of dispersions. *Rubber Chemistry and Technology*, **64**, 386–449.
85. Dalmas, F. *et al.* (2006) Large deformation mechanical behavior of flexible nanofiber filled polymer nanocomposites. *Polymer*, **47**, 2802–2812.
86. Krieger, I. and Dougherty, T. (1959) A mechanism for non-Newtonian flow in suspensions of rigid spheres. *Tansactions of the society of rheology*, **3**, 137–152.
87. Cross, M. (1970) Kinetic interpretation of non-newtonian flow. *Journal of Colloid and Interface Science*, **33**, 30–35.
88. Yatsuyanagi, F., Kaidou, H., and Ito, M. (1999) Relatioship between viscoelastic properties and characteristics of filler-gel in filled rubber system. *Rubber Chemistry and Technology*, **72**, 657–672.
89. Funt, J. (1988) Dynamic testing and reinforcement of rubber. *Rubber Chemistry and Technology*, **61**, 842–865.
90. ten Brinke, J. *et al.* (2002) Interactions of Stöber silica with natural rubber under the influence of coupling agents, studied by 1H NMR T2 relaxation analysis. *Macromolecules*, **35**, 10026–10037.
91. Meissner, B. (1974) Theory of bound rubber. *Journal of Applied Polymer Science*, **18**, 2483–2491.
92. Burnside, S.D. and Giannelis, E.P. (2000) Nanostructure and properties of polysiloxane-layered silicate nanocomposites. *Journal of Polymer Science Part B: Polymer Physics*, **38**, 1595–1604.
93. Dutta, N. *et al.* (1994) High resolution solid-state N.M.R investigation of the filler-rubber interaction: 1. High speed proton magic-angle spinning N.M.R. spectroscopy in carbon black filled styrene-butadiene rubber. *Polymer*, **35**, 4293–4299.
94. Asai, S. *et al.* (1991) Effect of oxidized carbon black on the mechanical properties and molecular motions of natural rubber studied by pulse NMR. *Journal of Applied Polymer Science*, **43**, 1253–1257.
95. Lin, W. and Blum, F. (2001) Segmental dynamics of interfacial poly(methyl acrylate)-d3 in composites by deuterium NMR spectroscopy, *Journal of the American*, vol. **123**, Chemical Society, pp. 2032–2037.

96. Cohen-Addad, J., Roby, C., and Sauviat, M. (1985) Characterization of chain binding to filler in silicone-silica systems. *Polymer*, **26**, 1231–1233.
97. Legrand, A. *et al.* (1992) Application of NMR spectroscopy to the characterization of elastomer/filler interactions. *Journal of Applied Polymer Science*, **46**, 2223–2232.
98. Haidar, B. *et al.* (1998) *Polymers and Surface: A Versatile Combination*, H. Hommel, Trivandrum.
99. Montes, H., Lequeux, F., and Berriot, L. (2003) Influence of the glass transition temperature gradient on the nonlinear viscoelastic behavior in reinforced elastomers. *Macromolecules*, **36**, 8107–8118.
100. Maier, P. and Goritz, D. (1996) Molecular interpretation of the Payne effect. *Kautschuk und Gummi Kunststoffe*, **49**, 18–21.
101. Sternstein, S. and Zhu, A. (2002) Reinforcement mechanism of nanofilled polymer melts as elucidated by nonlinear viscoelastic behavior. *Macromolecules*, **35**, 7262–7273.
102. Wagner, M.H. (1976) Reinforcing silicas and silicates. *Rubber Chemistry and Technology*, **49**, 703–774.
103. Bueche, F. (1961) Mullins effect and rubber-filler interaction. *Journal of Applied Polymer Science*, **5**, 271–281.
104. Dannenberg, E. (1975) Effects of surface chemical interactions on the properties of filler-reinforced rubbers. *Rubber Chemistry and Technology*, **48**, 410–444.
105. Boonstra, B. (1979) Role of particule fillers in elastomer reinforcement: a review. *Polymer*, **20**, 691–704.
106. Pinnavaia, T. and Beall, G. (2000) *Polymer-Clay Nanocomposites*, John Wiley & Sons, Ltd, Chichester.
107. Alex, R. and Nah, C. (2006) Preparation and characterization of organoclay-rubber nanocomposites via a new route with skim natural rubber latex. *Journal of Applied Polymer Science*, **102**, 3277–3285.
108. Lopez-Manchado, M.A. *et al.* (2004) Novel approach of evaluating polymer nanocomposite structure by measurements of the freezing-point depression. *Macromolecular Rapid Communications*, **25**, 1309–1313.
109. Teh, P. *et al.* (2004) On the potential of organoclay with respect to coventional fillers (carbo blac, silica) for epoxidized natural rubber compatibilized natural rubber vulcanizates. *Journal of Applied Polymer Science*, **94**, 2438–2445.
110. Varghese, S. and Karger-Kocsis, J. (2003) Natural rubber-based nanocomposites by latex compounding with layered silicates. *Polymer*, **44**, 4921–4927.
111. Chenal, J. *et al.* (2007) Molecular weight between physical entanglements in natural rubber: A critical parameter during strain-induced crystallization. *Polymer*, **48**, 1042–1046.
112. Nielsen, L. (1966) Simple theory of stress-strain properties of filled polymers. *Journal of Applied Polymer Science*, **10**, 97–103.
113. Dewimille, L., Bresson, B., and Bokobza, L. (2005) Synthesis, structure and morphology of poly(dimethylsiloxane) networks filled with in situ generated silica particles. *Polymer*, **46**, 4135–4143.
114. Chenal, J.M. *et al.* (2007) New insights into the cold crystallization of filled natural rubber. *Journal of Polymer Science Part B: Polymer Physics*, **45**, 955–962.
115. Toki, S. *et al.* (2003) Molecular orientation and structural development in vulcanized polyisoprene rubbers during uniaxial deformation by in situ synchrotron X-ray diffraction. *Polymer*, **44**, 6003–6011.
116. Trabelsi, S., Albouy, P., and Rault, J. (2003) Crystallization and melting processes in vulcanized stretched natural rubber. *Macromolecules*, **36**, 7624–7639.
117. Poompradub, S. *et al.* (2005) Mechanism of strain-induced crystallization in filled and unfilled natural rubber vulcanizates. *Journal of Applied Physics*, **97**, 103529.
118. Chenal, J. *et al.* (2007) Parameters governing strain induced crystallization in filled natural rubber. *Polymer*, **48**, 6893–6901.
119. Rault, J. *et al.* (2006) Stress-induced crystallization and reinforcement in filled natural rubbers: 2H NMR study. *Macromolecules*, **39**, 8356–8368.
120. Tosaka, M. *et al.* (2004) Orientation and crystallization of natural rubber network as revealed by WAXD using synchrotron radiation. *Macromolecules*, **37**, 3299–3309.
121. Lee, R. and Donovan, J. (1987) Microstrutural changes in the crack tip region of carbon-black filled natural rubber. *Rubber Chemistry and Technology*, **60**, 910–923.
122. Treloar, L. (1976) *The Physics of Rubber Elasticity*, Oxford University Press, Oxford.
123. James, H. and Guth, E. (1943) Theory of the elastic properties of rubber. *The Journal of Chemical Physics*, **11**, 455–481.
124. Arrruda, E. and Boyce, M. (1993) A three-dimensional constitutive model for the large stretch behavior of rubber elastic materials. *Journal of the Mechanics and Physics of Solids*, **41**, 389–412.

125. Wu, P. and Van der Giessen, E. (1992) On improved 3-D non-Gaussian network models for rubber elasticity. *Mechanics Research Communication*, **19**, 427–433.
126. De Gennes, P. (1979) *Scaling Concepts in Polymer Physics*, Cornell University Press, Cornell.
127. Rubinstein, M. and Panyukov, S. (2002) Elasticity of polymer networks. *Macromolecules*, **35**, 6670.
128. Edwards, S. and Vilgis, T. (1988) The effect of entanglements in rubber elasticity. *Polymer*, **27**, 483–492.
129. Rivlin, R. (1948) Large elastic deformations of isotropic materials. I. Fundamental concepts. *Philospphical transactions of the royal society A*, **240**, 459–490.
130. Guo, Z. and Sluys, L. (2006) Application of a new constitutive model for the description of rubber-like materials under monotonic loading. *International Journal of Solids and Structures*, **43**, 2799–2819.
131. Li, J., Mayau, D., and Lagarrigue, V. (2008) A constitutive model dealing with damage due to cavity growth and the Mullins effect in rubber-like materials under triaxial loading. *Journal of the Mechanics and Physics of Solids*, **56**, 953–973.
132. Ogden, R. and Roxburgh, D. (1999) A pseudo-elastic model for the Mullins effect in filled rubber. *Proceedings of the Royal Society of London Series A*, **455**, 2861–2877.
133. Laiarinandrasana, L., Piques, R., and Robisson, A. (2003) Visco-hyperelastic model with internal state variable coupled with discontinuous damage concept under total Lagrangian formulation. *International Journal of Plasticity*, **19**, 977–1000.
134. Bergstrom, J. and Boyce, M. (1999) Mechanical behavior of particle filled elastomers. *Rubber Chemistry and Technology*, **72**, 633–656.
135. Termonia, Y. (1990) Molecular model for the mechanical properties of elastomers. 2. Synergic effects in bimodal cross-linked networks. *Macromolecules*, **23**, 1481–1483.
136. Takayanagi, M., Imada, K., and Tisato, K. (1966) Mechanical properties and fine structure of drawn polymers. *Journal of Polymer Science Part C: Polymer Symposia*, **15**, 263–280.
137. Ouali, N., Cavaille, J.Y., and Perez, J. (1991) Elastic, viscoelastic and plastic behavior of multiphase polymer blends. *Plastics Rubber and Composites Processing and Applications*, **16**, 5560–5572.
138. Christensen, R. and Lo, K. (1979) Solutions for effective shear properties in three phase sphere and cylinder models. *Journal of the Mechanics and Physics of Solids*, **27**, 315–330.
139. Herve, E. and Zaoui, A. (1993) n-layered inclusion-based micromechanical modelling. *International Journal of Engineering Science*, **31**, 1–10.
140. Bornert, M. (1996) A generalized pattern-based self-consistent scheme. *Computational Materials Science*, **5**, 17–31.
141. Chabert, E. *et al.* (2004) Filler–filler interactions and viscoelastic behavior of polymer nanocomposites. *Materials Science and Engineering A*, **381**, 320–330.
142. Hashin, Z. and Rosen, B. (1964) The elastic moduli of fiber-reinforced materials. *Journal of Applied Mechanics*, **31**, 223–232.
143. Eshelby, J. (1957) The determination of the elastic field ... ellipsoidal inclusion, and related problems. *Proceedings of the Royal Society of London Series A*, **241**, 376–396.
144. Mori et, T. and Tanaka, K. (1973) Average stress in matrix and average elastic energy of materials with misfitting inclusions. *Acta Metallurgica et Materialia*, **21**, 597–629.
145. Tandon, G. and Weng, G. (1984) The effect of aspect ratio of inclusions on the elastic properties of unidirectionally aligned composites. *Polymer Composites*, **5**, 327–333.
146. Halpin, J.C. and Tsai, S. (1967) Effects of environmental factors on composite materials. AFML-TR-67-423.
147. Ashton, J., Halpin, J., and Petit, P. (1969) *Primer on Composite Materials: Analysis*, Technomic, Stanford.
148. Tsai, S. and Pagano, N. (1968) *Invariant Properties of Composite Materials, Composite Materials Workshop*, Technomic, Stanford.
149. Van es, M. (2001) Polymer-Clay Nanocomposites: The Importance of Particle Dimensions, Ph.D. Thesis, Technische Universiteit Delft.
150. Chazeau, L. *et al.* (2003) Relationships between microstructural aspects and mechanical properties of polymer-based nanocomposites, *Handbook of organic-inorganic hybrid materials and nanocomposites*, Hari Singh Nalwa, pp. 63–111.
151. Moniruzzaman, M. and Winey, K. (2006) Polymer nanocomposites containing carbon nanotubes. *Macromolecules*, **39**, 5194–5205.
152. Mele, P. *et al.* (2002) Reinforcement effects in fractal-structure-filled rubber. *Polymer*, **43**, 5577–5586.

153. Wang, Q. and Lee, D. (1999) Predictive modelling for rubber-toughened polymers. *Mechanics of Materials*, **31**, 705–716.
154. van Dommelen, J., Brekelmans, W., and Baaijans, F. (2003) Micromechanical modeling of particle-toughening of polymers by locally induced anisotropy. *Mechanics of Materials*, **35**, 845–863.
155. Sheng, N. *et al.* (2004) Multiscale micromechanical modeling of polymer/clay nanocomposites and the effective clay particle. *Polymer*, **45**, 487–506.
156. Minakova, M. and Ushakov, V. (2000) Stochastic and deterministic modeling of spacially orinted structures in dispersion-filled polymers. *Polymer Science Series A*, **42**, 1025–2000.
157. Lopez-Pamies, O. and Ponte-Castaneda, P. (2007) Homogenization-based constitutive models for porous elastomers and implications for macroscopic instabilities: I—Analysis. *Journal of the Mechanics and Physics of Solids*, **55**, 1677–1701.
158. Tomita, Y., Azuma, K., and Naito, M., Computational evaluation of strain-rate-dependent deformation behavior of rubber and carbon-black-filled rubber under monotonic and cyclic straining. *International Journal of Mechanical Sciences*, **50**, 856–868.
159. Kraus, G. (1984) Mechanical losses in carbon black filled rubbers. *Journal of Applied Polymer Science: Applied Polymer Symposia*, **39**, 75–92.
160. Huber, G., Vilgis, T., and Heinrich, G. (1996) Universal properties in the dynamical deformation of filled rubbers. *Journal of Physics: Condensed Materials*, **8**, L409.
161. Witten, T., Rubinstein, M., and Colby, R. (1993) Reinforcement of rubber by fractal aggregates. *Journal de Physique II*, **3**, 367–384.
162. Kluppel, M. (2003) The role of disorder in filler reinforcement of elastomers on various length scales. *Advanced in Polymer Science*, **164**, 1–86.
163. Gerspacher, M., O'Farrell, C., and Yang, H. (1994) A proposed mechanism for the reinforcement of elastomers in the rubbery plateau by carbon black. *Kautschuk und Gummi Kunststoffe*, **47**, 349–353.
164. Van de Wall, A., Tricot, C., and Gerspacher, M. (1996) Modeling of the carbon black reinforcement mechanism in elastomers. *Kautschuk und Gummi Kunststoffe*, **49**, 172–179.
165. Mark, J.E. *et al.* (2005) Some simulations on filler reinforcement in elastomers. *Polymer*, **46**, 8894–8904.
166. Lopez-Manchado, M.A. *et al.* (2003) Vulcanization kinetics of natural rubber-organoclay nanocomposites. *Journal of Applied Polymer Science*, **89**, 1–15.
167. Desai, T. *et al.* (2003) Density fluctuation correlation length in polymer fluids. *Journal of Chemical Physics*, **119**, 7599–7603.
168. Vladkov, M. and Barrat, J. (2007) Local Dynamics and Primitive Path Analysis for a Model Polymer Melt near a Surface. *Macromolecules*, **40**, 3797–3804.
169. Brown, D. *et al.* (2008) Effect of filler particle size on the properties of model nanocomposites. *Macromolecules*, **41**, 1499–1511.
170. Chabert, E. *et al.* (2002) Mechanical behavior of polymer nanocomposites: a discrete simulation approach, in *Nanomaterials for Structural Applications* (eds C.C. Berndt, T.E. Fischer, I. Ovid'ko, G. Skandan, and T. Tsakalakos).
171. Bueche, F. and Halpin, J.C. (1964) Molecular theory for the tensile strength of gum elastomers. *Journal of Applied Physics*, **35**, 36–41.
172. Boonstra, B. (1965) *Reinforcement of Elastomers*, G. Kraus, New York, pp. 529–561.
173. Ambacher, H. *et al.* (1991) Reinforcement in filler-loaded rubbers. *Kautschuk und Gummi Kunststoffe*, **44**, 1111–1118.

13

Nonlinear Viscoelastic Behavior of Rubbery Bionanocomposites

Alireza S. Sarvestani and Esmaiel Jabbari
Biomimetic Materials and Tissue Engineering Laboratories, Department of Chemical Engineering, University of South Carolina, Columbia, SC 29208, USA

13.1 Introduction

Bionanocomposites are a promising class of hybrid nanostructured materials with emerging applications in materials science, life science and nanotechnology [1–3]. *Polymer bionanocomposites* are fabricated by dispersing inorganic/organic fillers, with at least one dimension on the nanometer scale, in biopolymers or synthetic biofunctional polymers [4]. The versatility of these novel materials emanates from the large selection of biopolymers and fillers available to researchers. Existing polymers include, but are not limited to, polysaccharides, aliphatic polyesters, polypeptides, proteins and polynucleic acids, whereas fillers include clay, hydroxyapatite (HA), β-tricalcium phosphates (β-TCP) and metal nanoparticles.

Overwhelming experimental evidence demonstrate that polymer nanocomposites exhibit significantly higher toughness, stiffness, thermal stability, and gas-barrier properties compared to those of conventional composites at same filler volume fraction [5–11]. These desirable properties have made polymer nanocomposites as structural or functional materials with interesting applications in tissue engineering, therapeutics, heterogeneous catalysis and optical, magnetic and electrochemical devices [1, 12].

The interaction between filler and matrix components of nanocomposites at the nanometer scale enables the formation molecular bridges in the polymer matrix. This is the basis for the enhanced mechanical properties of nanocomposite as compared to microcomposites [13–16]. Bionanocomposites add a new dimension to these properties by showing a remarkable advantage in biocompatibility and functional properties provided by the organic or inorganic moieties.

Rubber Nanocomposites: Preparation, Properties and Applications Edited by Sabu Thomas and Ranimol Stephen
© 2010 John Wiley & Sons (Asia) Pte Ltd

Biodegradability is another desirable property of polymer biocomposites. By embedding natural reinforcing fillers [for example, β-TCP, short flax fibers (natural fibers extracted from the Linaceae family of plants), hemp (natural fibers extracted from Cannabis family of plants), ramie (natural fibers extracted from Urticaceae or nettle family of plants)] into biopolymer matrices (for example, cellulose, collagen, chitosan), the resultant hybrid material is expected to degrade and be gradually absorbed and/or eliminated by the body. The degradation is generally caused by hydrolysis or mediated by metabolic processes. Therefore, bionanocomposites are of immense interest in biomedical technologies, such as tissue engineering, bone replacement/repair, dental restoration and controlled drug delivery, as well as the fabrication of environmentally adaptable (that is, *green*) materials.

Natural polymers like collagen [17, 18], chitosan [19] and silk [20], as well as degradable synthetic polymers including poly(L-lactic acid) (PLA) [21–23], poly(glyco1ic acid) (PGA) and poly(lactic-*co*-glycolic acid) (PLGA) copolymer [24], poly(propylene fumarate) [25], poly(ε-caprolactone) [26] degrade to products which can be eliminated from the body either through metabolic pathways such as the citric acid cycle or by renal excretion [27, 28]. In combination with osteoconductive ceramics such as β-TCP and HA, these biodegradable polymers have been used extensively in the fabrication of degradable scaffolds for filling skeletal defects and for the guided regeneration of load-bearing tissues [29, 30]. These scaffolds not only serve as a substrate for the adhesion, spreading, migration, proliferation and differentiation of osteoblastic or chondrogenic cells, but they also provide acceptable mechanical properties. These composite materials exhibit compressive strength in the range 2–30 MPa, suitable for replacement of human trabecular bone.

There are several other advantages in incorporating bioactive ceramics into biodegradable polymers in order to produce hybrid materials. Calcium phosphate particles like HA or β-TCP improve osteoconductivity and bone-bonding properties [31]. Furthermore, biocompatibility could be enhanced with ceramic particles that induce an increased initial spread of serum proteins compared to the more hydrophobic polymer surfaces [32]. Recent *in vitro* studies have demonstrated that the reinforcement of degradable polymers with calcium phosphates improves the attachment, proliferation and osteoblastic differentiation of marrow stromal cells.

Degradable bionanocomposites also show promise in fabrication of eco-sustainable composites. This emanates from the need to replace petroleum-derived synthetic polymers by natural, abundant and low-cost biodegradable products obtained from renewable sources [1, 33–35]. Nature is the source of a wide range of biomacromolecules which can be utilized for fabrication of green bionanocomposites with starch, cellulose and their derivatives [36–39]. Their combination with natural inorganic solids, like clay, gives rise to reinforced plastics that offer the advantages of nanocomposites as well as biocompatibility and biodegradability of natural materials. Microorganisms are able to decompose bionanocomposites in a natural way, producing carbon dioxide that is converted to oxygen by plants. Thus, the use of these new green materials in the food industry, agriculture, or the building industry, among other areas, will help to reduce waste products and environmental pollution, leading to sustainable development.

This chapter focuses on viscoelastic properties of rubbery bionanocomposites (RBNCs). In the next section, we briefly review the general viscoelastic properties of biofiber–natural rubber composites and hydrogel nanocomposites as two important classes of RBNCs used in the fabrication of green materials and biomaterials, respectively. Since we are especially interested in nonlinear aspects of the viscoelastic behavior of RBNCs, we present a predictive model for

nonlinear viscoelastic properties of hydrogel/apatite nanocomposites for the treatment of irregularly shaped degenerated skeletal tissues.

13.2 Rubbery Bionanocomposites

Dispersion of rigid colloidal particles into the crosslinked network of a rubber matrix results in a considerable enhancement in mechanical behavior of the composite. Filled rubbers have been widely used for decades to produce coatings, seals, dampers, cushions, transport belts and automobile tires. A variety of experimental methods are used for characterizing the properties of filled rubbers. Viscoelastic analysis, in particular, proves to be useful for investigating the time-dependent properties of rubber composites. It is shown that the viscoelastic properties of these materials depend on the fiber–matrix interphase, fiber content and the presence of additives like filler and compatabilizer and the mode of testing.

13.2.1 Biofiber–Natural Rubber Composites

The viscoelastic properties of natural rubber biocomposites have been extensively studied by Thomas *et al.* [40]. In natural rubber composites, the effect of fiber reinforcement is to increase modulus, increase strength at high fiber concentrations, decrease elongation at failure, improve creep resistance, increase hardness and substantially improve cut, tear and puncture resistance. Among different natural fibers, sisal (natural fiber extracted from sisal plant or other members of the genus Agaveand plants) and oil palm fibers (natural fiber extracted from palm oil vascular bundles in the empty fruit bunch) are promising materials because of the high tensile strength of sisal fiber and the toughness of palm oil fiber. Therefore, any composite comprising these two fibers will exhibit the above desirable properties of the individual constituents.

Researchers have examined the dynamic mechanical behavior of coir (narrow, hollow, elastic fibers with thick walls made of cellulose extracted from the husk and the outer shell of coconut) fiber-reinforced natural rubber composites [41]. They observed an increase in loss modulus and damping factor which resulted in lower heat dissipation in the gum. It was also observed that composites with poor interfacial bonding tend to dissipate more energy than those with good interfacial bonding. In another study involving biofibers, the dynamic and static mechanical properties of randomly oriented intimately mixed banana (fiber extracted from banana tree bark by peeling the trunk and removing the skin, the white portion is processed into knotted fibers) and sisal hybrid fiber-reinforced polyester composites were reported [42]. Maximum stress transfer between the fiber and matrix was obtained in composites having a 3 : 1 volume ratio of banana to sisal. The storage modulus was found to increase with fiber volume fraction above the glass transition temperature (T_g) of the composites. The viscoelastic properties of palm oil fiber/phenol formaldehyde and palm oil fiber/glass hybrid phenol formaldehyde composites as a function of fiber content and hybrid fiber ratio was investigated by Sreekala *et al.* [43]. The incorporation of palm oil fiber shifted the T_g to lower temperatures. The T_g of the hybrid composites was found to be lower than those of unhybridized composites. Storage modulus of the hybrid composites was also found to be lower than the unhybridized palm oil fiber/phenol formaldehyde composites. Activation energy was found to increase upon fiber reinforcement.

In an innovative approach, a combination of sisal and palm oil fibers in natural rubber has been utilized to design hybrid biocomposites. It was observed that the incorporation of fibers resulted in increased modulus [44, 45]. Chemical modification of both sisal and palm oil fibers was imperative for increased interfacial adhesion [44, 45]. The viscoelastic [46], water sorption [47], dielectric and stress relaxation [48, 49] characteristics were also studied. Research is also being conducted to develop new pathways to synthesize inexpensive biodegradable resins [50] with better mechanical properties and thermal stability using nanotechnology [51]. A typical challenge is the inherent incompatibility between the polymer matrix and the inorganic nanoparticles. To circumvent this problem different methods have been proposed to organically modify the nanoparticles. For example, nanoclays can be ion-exchanged with different alkyl ammonium or phosphonium ions to render them organophilic and thus, more compatible with the polymers like PLA and polyhydroxybutyrate. The resulting nanocomposites exhibit a well ordered intercalated structure with better mechanical properties compared with the neat polymers [51]. Biodegradation can also be controlled by the choice of the nanoclay.

13.2.2 Hydrogel Nanocomposites

Hydrogels are crosslinked polymeric structures which are able to retain a significant fraction of water in their structure without dissolving [52–54]. Small nutrient molecules [55], oxygen [56] and carbon dioxide [57] can readily diffuse through hydrogels [52]. Diffusivity of macromolecules and proteins in hydrogels is 4–5 orders of magnitude higher compared to hydrophobic polymers like PLGA [58–63]. Hydrogels, due to their high water content, exhibit excellent biocompatibility and interact less strongly with immobilized biomolecules than hydrophobic materials [64–67]. Thus, proteins and cells immobilized within hydrogels retain their biological activity [68]. Crosslinkers based on bioactive peptides can be used for the synthesis of hydrogels to fabricate smart cell-responsive hydrogels [69–71]. One of the most desirable properties of hydrogels is their ability to crosslink *in situ* which allows for treating irregularly shaped degenerated tissues [72, 73]. After injection and hardening, the three-dimensional hydrogel matrix guides the organization, differentiation, proliferation and development of the seeded cells into the desired tissue [74].

Recently special attention has been paid to biodegradable hydrogels prepared by copolymers of PLA and poly(ethylene glyco1) PEG [75–78]. These hydrogels, in general, show good biocompatibility, while their swelling behavior and degradation rate can be controlled by the ratio of PLA to PEG in the polymerizing mixture. The fumarate-based macromers have also been utilized to synthesize biodegradable scaffolds for hard and soft tissue regeneration [79–81]. A novel *in situ* crosslinkable Poly(L-lactide-*co*-ethylene oxide-*co*-fumarate) (PLEOF) terpolymer has been developed which consists of ultra low molecular weight PLA (ULMW PLA) and PEG blocks linked by fumarate units [82]. The PLA and PEG are FDA approved for certain clinical applications and fumaric acid occurs naturally in the Kreb's cycle [83]. The unsaturated fumarate groups in PLEOF control the crosslink density in the hydrogel and can be used to covalently attach biologically active peptide sequences to the network [84].

Nonreinforced hydrogels, however, do not possess the stiffness required to replace hard tissues in load-bearing applications. In order to improve their mechanical properties and

enhance their biofunctionality, hydrogels are reinforced with osteoconductive ceramics such as β-TCP and HA. The composites of HA or β-TCP with a variety of natural and synthetic hydrogels have been explored for bone regeneration including collagen type I [85–88], gelatin [89, 90], chitosan and alginate [91, 92], fibrin [93] and poly(ethylene glycol) [94].

Studying the rheological and viscoelastic characteristics of biocomposites as a means to control their injectability and in-situ hardening is of special importance. To develop injectable polymer nanocomposites, accurate models are required to predict the viscoelastic response and to elucidate the underlying mechanisms of reinforcement. These models provide a quantitative approach to design and optimize the properties of reinforced polymer composites for biological applications. Previous experimental studies demonstrate that the matrix structure and molecular weight, the filler size and volume fraction and the interfacial strength between the polymer and filler particles have a significant effect on the viscoelastic properties of polymer/apatite composites [95–112]. In general, composites prepared with nanoparticles ($<$100 nm) exhibit a higher stiffness compared to those with microparticles at the same volume fraction. The mechanical performance of composites is significantly improved by increasing the interfacial adhesion between the polymer matrix and dispersed filler particles.

The unique properties of nanofilled polymer networks are generally rationalized as arising from strong interparticle affinity or thermodynamic interaction between the particle surface and surrounding matrix. The interparticle interactions occur through electrostatic and van der Waals' forces which may result in the formation of particle aggregates and ultimately fractal agglomerated structures [113–117]. The polymer–particle interactions refer to the attachment/detachment of chains to/from the filler surface, a process which is controlled by the effective surface affinity [118–121].

Contrary to extensive experimental studies, theoretical models which are capable to quantitatively elucidate the reinforcement mechanism in filled polymer networks are scarce. Semi-empirical models are proposed for reinforcement of elastomers with aggregated particles based on the concept of fractals [117, 122–124]. The mechanical properties of filled networks with highly interactive polymer particles are modeled by conventional continuum-scale homogenization techniques like the three-phase (core–shell) model [122, 125]. The double network theory has also been used to describe the stress–strain behavior of the networks with active fillers [126].

13.3 Nonlinear Viscoelasticity of Hydrogel Nanocomposites

Biopolymers are generally able to interact with mineral surfaces by polar, van der Waals, or hydrophobic forces [127, 128]. For example, it is believed that the linking of the network of collagen fibers to HA crystals, the mineral phase of the bone, is through a terminal glutamic acid-rich sequence on osteonectin, with high ionic affinity to HA [129, 130]. Osteonectin as a major noncollagenous bone extracellular matrix protein is involved in multiple coordinated functions during bone formation.

To test the effect of ionic interactions between the apatite crystals and gelatinous matrix, a glutamic acid-rich peptide (a sequence of six glutamic acids) derived from osteonectin, functionalized with an acrylate group (Ac-Glu6) for covalent attachment to the matrix, was synthesized by solid-phase – Fmoc chemistry [131]. The Ac-Glu6 sequence was attached to the surface of HA microparticles (mean diameter 50 μm) or nanoparticles (mean diameter 50 nm)

by electrostatic interactions, as shown in Figure 13.1. One end of the peptide was functionalized with an acrylate group to covalently attach the peptide to the aqueous-based poly(lactide-co-ethylene oxide-co-fumarate) (PLEOF) hydrogel matrix. The mixture was injected between the parallel plates of a rheometer and the gelation kinetics was measured [132].

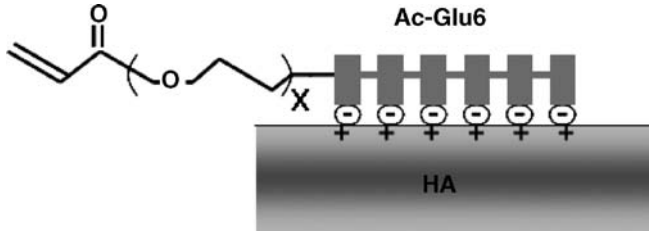

Figure 13.1 Schematic structure of the Ac-Glu6 peptide used for surface-treating HA nanoparticles. The terminal acrylate group of the Ac-Glu6 provides an unsaturated group for covalent crosslinking of the apatite particles to PLEOF matrix

Figure 13.2 shows the dependence of shear modulus of the composite on the size of the dispersed HA particles. Nanoapatite composites (treated and untreated) displayed far larger stiffness compared with microcomposites, at the same volume fraction. The modulus of the composites with micron size particles did not appreciably change with the addition of Ac-Glu6.

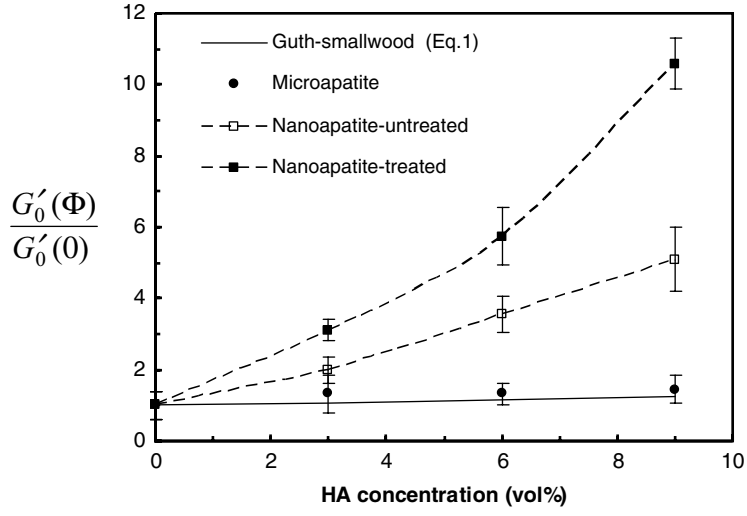

Figure 13.2 The dependence of shear modulus of the PLEOF/Ac-Glu6/apatite composites on size of the dispersed HA particles. Nanoapatite composites displayed far larger stiffness compared with micro-composites, at the same volume fraction. Addition of Ac-Glu6 significantly increased the modulus of the nanocomposites while the modulus of microcomposites did not appreciably change with the addition of Glu6 peptide

The contribution of hydrodynamic effect to the modulus of the composite can be predicted by the Guth–Smallwood equation [133]:

$$G_0'(\Phi) = G_0'(0)(1 + 2.5\,\Phi), \tag{13.1}$$

where $G_0'(0)$and $G_0'(\Phi)$ are the storage modulus of the gel and that of the composite, respectively, and Φ is the HA volume fraction. The storage modulus of the composites prepared with micron-size particles can be reasonably predicted by the Guth–Smallwood equation. However, the large difference between the experimental and predicted results for composites prepared with nanosize HA implies that the reinforcement cannot be explained solely by the hydrodynamic effect in nanoparticulate systems. In what follows, we present a molecular model to predict the viscoelastic behavior of biocomposites that have a crosslinked polymer matrix, in particular with respect to the polymer/mineral interaction energy. To validate the model, its predictions are applied to the viscoelastic response of PLEOF/HA hydrogel nanocomposite as described above [132].

The model is based on the theory of reversible adsorption from a dilute polymer solution [134, 135]. Adsorption of the polymer chains from solution on the solid surface takes place when the chains energetically prefer the surface over the solvent. The average residence time of each monomer on the solid surface is determined by the binding energy between the monomer and particle surface. It has been shown that when the contact energy per monomer, ΔE_{ad}, is less than the thermal energy, k_BT, the adsorption process is reversible, that is, the adsorbed polymer chain detaches from the surface after a finite residence time and the bonding site is replaced with another polymer chain [135]. When the binding energy is somewhat larger than k_BT, the adsorption becomes irreversible, and the adsorbed chains flatten and freeze on the interactive surface [136].

13.3.1 Filler–Gel Interfacial Structure

The equilibrium configuration of a chain segment (between two consecutive crosslink points), near the filler surface with radius R_f, is schematically shown in Figure 13.3. The segment can reversibly adsorb on the colloidal surface and form a polydisperse succession of loops, tails and sequences of bound monomers (trains). In good solvent condition, the effect of excluded volume can be taken into account using the *blob* model for the configuration of polymers in dilute systems [137]. Hence, each segment with N monomers of size a, occupies a spherical volume with a radius comparable to the Flory radius: $R_F = a\,N^{3/5}$.

In order to describe the structure of the adsorbed and fully equilibrated polymer layer on the filler surface, we used a modified version of de Gennes scaling theory [137] for reversible adsorption from dilute solutions under good-solvent conditions. The chain configuration in an adsorbed layer is determined by the competition between excluded volume, surface energy and chain entropic effects. Assuming that the loops are extended to an average thickness D from the surface, the fraction of monomers in direct contact with the particle surface can be approximated by: $f \cong \dfrac{a}{D}$ [134].

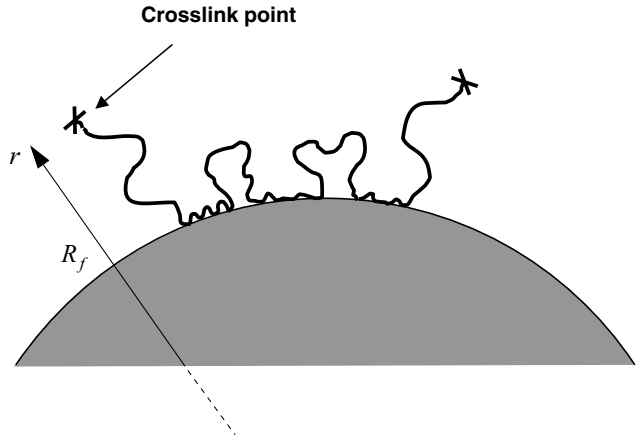

Figure 13.3 Schematic diagram of the equilibrium configuration of an adsorbed polymer segment between two crosslink points on the filler surface. The adsorbed chain consists of loops, tails and sequences of bonded monomers

Assuming that the conformational entropy and energetic affinity with the surface are the only factors that determine the configuration of the adsorbed layer, the free energy per segment, Ψ, can be written as [138]:

$$\Psi \cong k_B T \left(\frac{R_F}{D}\right)^{5/3} - f\, N\, \Delta E_{ad}. \tag{13.2}$$

Minimizing the free energy with respect to D yields:

$$f \cong \left(\frac{\Delta E_{ad}}{k_B T}\right)^{3/2}. \tag{13.3}$$

13.3.2 Dynamics of the Adsorbed Layer

The gel–particle energetic attraction is modeled as a frictional interaction between the adsorbed monomers and particle surface, in addition to the regular monomer–solvent and/or monomer–monomer friction. Therefore, the total friction coefficient due to the hydrodynamic force acting on the *i*th monomer is [139]:

$$(\xi)_i = \xi_1, \; i\text{th monomer is adsorbed}, \tag{13.4a}$$

$$(\xi)_i = \xi_0, \; i\text{th monomer is not adsorbed}, \tag{13.4b}$$

where ξ_1 is the friction coefficient due to monomer–particle interaction and ξ_0 is the friction coefficient corresponding to the self-diffusion of a single monomer and it accounts for its

friction with the solvent molecules and/or other nonadsorbed monomers. Using an Arrhenius type activation model for a monomer of size a, the friction coefficient is approximated by $\xi_0 \cong k_B T\tau_0/a^2$, with time constant τ_0 defined by [139]:

$$\tau_0 = \tau^* \exp\left(\frac{E_0}{k_B T}\right). \tag{13.5}$$

where τ^* is the characteristic time of molecular oscillation. A similar activation model can be used to estimate $\xi_1 \cong k_B T\tau_1/a^2$, where τ_1 is defined as [139]:

$$\tau_1 = \tau^* \exp\left(\frac{E_1}{k_B T}\right). \tag{13.6}$$

Here $E_1 = \Delta E_{ad} + E_0$ is the energy required to detach the adsorbed monomer from the particle surface.

Since a fraction f of the monomers in an adsorbed segment is in contact with the particle surface, the total friction coefficient of the entire adsorbed segment is given by:

$$\xi_a = N(f\,\xi_1 + (1-f)\xi_0), \tag{13.7}$$

where using Equations 13.5 and 13.6:

$$\xi_1 = \xi_0 \exp\frac{\Delta E_{ad}}{k_B T}. \tag{13.8}$$

For weakly attractive surfaces, segments are partially adsorbed to the surface and exhibit their 3-D Rouse dynamics [140]. Hence, the relaxation time of the adsorbed segment is:

$$\tau_a \cong R_F^2 \frac{\xi_a}{k_B T} = \tau_f \left(f \exp\frac{\Delta E_{ad}}{k_B T} + (1-f)\right), \tag{13.9}$$

where $\tau_f \cong R_F^2 \dfrac{\xi_f}{k_B T}$ is the relaxation time of a free segment.

The self-similar grid structure [134], describes the adsorbed layer as a semi-dilute solution of the polymer with continuously varying local concentration of the monomers, such that at any distance r from the surface, the local blob size is equal to r. Therefore, the equilibrium thickness of the layer is on the order of R_F. In a crosslinked system, due to the fixed-end constraint, segments cannot diffuse independently like linear chains. Hence, the adsorption-desorption process takes place between those segments which are located within the interphase region with thickness R_F around the fillers and with total population density equal to $N_f^p + N_a$ (Figure 13.4). Here, N_a is the number density of the adsorbed segments and N_f^p represents the number density of free segments within the interphase zone, which are able to participate in the adsorption–desorption process. The rate of attachment can be shown by the following kinetic equation:

$$\frac{dN_a}{dt} = N_f^p (\tau_{ads})^{-1} - N_a (\tau_{des})^{-1}, \tag{13.10}$$

where τ_{ads} and τ_{des} are the characteristic times of adsorption and desorption of the segments, respectively.

The energy required for detachment of an adsorbed segment is equal to $f\,N\,\Delta E_{ad}$. In the presence of an applied macro-deformation, the tails of each segment move with the bulk

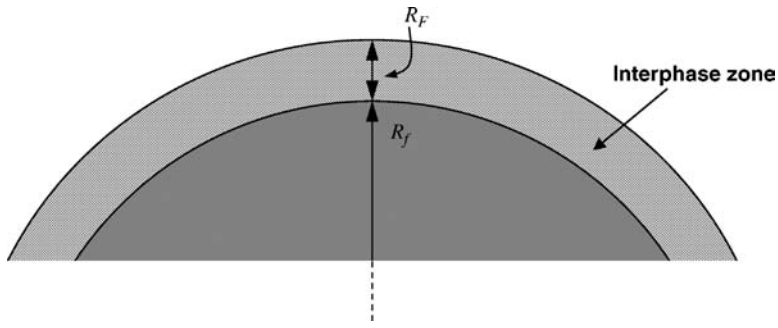

Figure 13.4 The adsorbed chain segments form an interphase zone with thickness R_F around the particle

material (Figure 13.5). The detachment process is thus favored by the resultant entropic tension exerted by the segment. Considering this effect, the time constants associated with attachment and detachment of the segments follow the relation defined by:

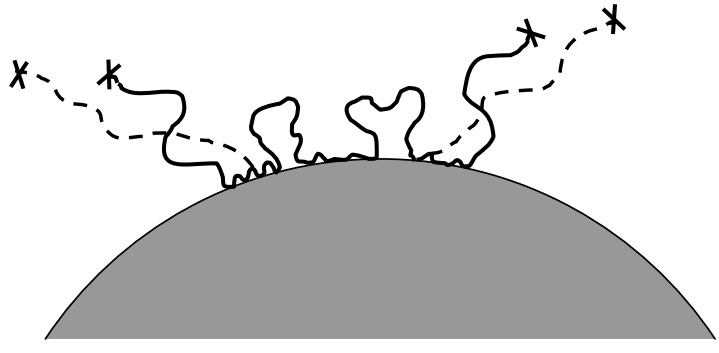

Figure 13.5 The adsorbed segment (solid line) can detach from the surface at a number of points after the application of deformation (dashed line)

$$\tau_{des} = \tau_{ads} \exp\left[\frac{f\,N\,\Delta E_{ad} - \delta\,F_a}{k_B T}\right], \tag{13.11}$$

where F_a is the entropic force in the segment and δ is an activation length on the order of the displacement required to detach the bound segment from the particle surface. The desorption of a bound monomer with weak and short range interaction with the adsorbing surface can be considered as a local process. It takes place when the monomer diffuses a distance on the order of the equilibrium size of the first blob in contact with the wall [141]. According to the self-similar grid structure theory [134], the size of the first blob in contact with the particle surface is on the order of the size of a monomer. Therefore, δ, the total displacement required to separate the entire segment with f fraction of adsorbed monomers is $a \leq \delta \leq R_F$.

13.3.3 Macroscopic Properties

The classical Maxwell model [142] is used to describe the viscoelasticity of the composite matrix. It is assumed that the deformations are relatively small such that geometric nonlinearities can be neglected and only the thixotropic nonlinearities, due to polymer–filler interactions, are considered. At any instant in time, a representative segment is either adsorbed to the surface of the particle or it is free. The total stress in the composite is therefore the sum of the stresses by the adsorbed ($\boldsymbol{\sigma}_a$) and free ($\boldsymbol{\sigma}_f$) segments [119], that is:

$$\boldsymbol{\sigma} = \boldsymbol{\sigma}_a + \boldsymbol{\sigma}_f. \tag{13.12}$$

The contribution of the segments to the stress tensor is given by the Kramers expression:

$$\boldsymbol{\sigma}_a = 3G_a \frac{\langle \boldsymbol{R}_a \boldsymbol{R}_a \rangle}{R_F^2}, \tag{13.13a}$$

$$\boldsymbol{\sigma}_f = 3G_f \frac{\langle \boldsymbol{R}_f \boldsymbol{R}_f \rangle}{R_F^2}, \tag{13.13b}$$

where G_a and G_f represent the stiffness of the adsorbed and free segments, respectively. $\boldsymbol{R}_i$ $(i = a,f)$ is the segment end-to-end vector and $\langle \cdots \rangle$ shows the ensemble average. According to the classical theory of rubber elasticity [143], a linear dependency is introduced between the modulus and number density of the chains at constant temperature, that is, $G_i \propto N_i$ $(i = a,f)$. Therefore, at steady-state conditions, we have:

$$G_a = G_f^p \exp\left[\frac{f\, N\, \Delta E_{ad} - \delta\, F_a}{k_B T}\right], \tag{13.14}$$

where G_f^p shows the stiffness of the free segments within the interphase zone.

The mechanical response of the network can be decoupled into two parts: a rate-independent response and a time-dependent deviation from the equilibrium [144]. That is:

$$\boldsymbol{\sigma}_i = \boldsymbol{\sigma}_i^e + \boldsymbol{\sigma}_i^v \quad i = a,f, \tag{13.15}$$

where $\boldsymbol{\sigma}_i^e$ and $\boldsymbol{\sigma}_i^v$ stand for the rate-independent and rate-dependent components of the stress, respectively. Using Equation 13.13, the time-independent component of stress can be expressed by:

$$\boldsymbol{\sigma}_i^e = G_i \boldsymbol{F} \cdot \boldsymbol{F}^{\mathrm{T}} \quad i = a,f, \tag{13.16}$$

where $\boldsymbol{F}$ is the deformation gradient tensor.

In their simplest form, the constitutive relations for the evolution of the rate-dependent stresses produced by the segments can be expressed by the Maxwell (upper-convected) equations [142]:

$$\tau_a \hat{\boldsymbol{\sigma}}_a^v + \boldsymbol{\sigma}_a^v - G_a \boldsymbol{I} = 0, \tag{13.17a}$$

$$\tau_f \hat{\boldsymbol{\sigma}}_f^v + \boldsymbol{\sigma}_f^v - G_f \boldsymbol{I} = 0, \tag{13.17b}$$

where $\boldsymbol{I}$ is the identity tensor. Here, $\hat{\boldsymbol{\sigma}}$ designates the upper-convected derivative of the stress tensor given by $\hat{\boldsymbol{\sigma}} = \frac{\partial \boldsymbol{\sigma}}{\partial t} - \boldsymbol{\sigma} \cdot \boldsymbol{L}_{ef} - \boldsymbol{L}_{ef}^{\mathrm{T}} \cdot \boldsymbol{\sigma}$, where $\boldsymbol{L}_{ef} = h(\phi)\, \nabla \boldsymbol{v}$ is the effective velocity gradient tensor and $\boldsymbol{v}$ is the velocity field. Here, $h(\phi)$ accounts for the hydrodynamic interaction between the particles with volume fraction ϕ. The contribution of the hydrodynamic effect is determined

by the shape and volume fraction of the particles [145]. At low filler concentrations, it is represented by:

$$h(\phi) = 1 + \zeta\,\phi, \tag{13.18}$$

where the pre-factor parameter ζ accounts for the particle geometry.

13.3.4 Model Predictions

The model is used to predict the effect of surface adsorption energy on the overall steady-state shear modulus of the hydrogel composite. Assuming the material is under oscillatory shear strain with frequency ω, the dynamic strain can be stated as:

$$\lambda(t) = \lambda_0 \sin \omega t. \tag{13.19}$$

For simplicity, only the affine (time independent) part of the deformation is considered for evaluation of the entropic force in Equation 13.14. For oscillatory shear loading with small strain λ_0, the deformation gradient can be written as:

$$\boldsymbol{F} = \begin{pmatrix} 1 & \lambda_0 \sin \omega t & 0 \\ 0 & 1 & 0 \\ 0 & 0 & 1 \end{pmatrix}. \tag{13.20}$$

The average end-to-end vector of an adsorbed segment during a period of oscillation can be obtained by:

$$\bar{\boldsymbol{R}}_a = \bar{\boldsymbol{F}} \cdot \boldsymbol{R}_F, \tag{13.21}$$

where the components of $\bar{\boldsymbol{F}}$ are the average of the absolute values of the corresponding components in $\boldsymbol{F}$ over one period of oscillation. The mean square end-to-end distance, given by Equation 13.21, was used in $F_a = \frac{3\,k_B T}{R_F^2}\bar{R}_a\left(1-\frac{\bar{R}_a^2}{R_{a,\max}^2}\right)^{-1}$, the Warner approximation for the entropic force, to calculate the average entropic tension in an adsorbed segment.

The proposed molecular model is applied to the experimental data of the PLEOF hydrogel/apatite composite under oscillatory shear. The shear storage moduli of the hydrogel composites with increasing content of HA nanoparticles were measured and the results are compared with the model predictions. In the absence of Ac-Glu6, the surface functional groups of the HA nanoparticles interact with the PLEOF hydrogel segments through weak van der Waals and polar interactions. In the presence of Ac-Glu6, the carbonate and phosphate groups on the HA surface can also interact with PLEOF segments by the relatively stronger electrostatic interactions. Spherical HA particles with 50 nm and 5 μm average diameter were used to study the effect of size of the dispersed fillers on the viscoelastic response.

$R_{a,\max}/R_F$, $c = \frac{\Delta E_{ad}}{k_B T}$, and δ/R_F are the model parameters which represent the characteristic length of the polymer segments near the particle surface and the interaction energy between the PLEOF segments and HA nanoparticles. These parameters are independent of the filler concentration. G_f^p/G_f is another fitting parameter which is proportional to the number of those free chains, located in the interphase zone, contributing to the adsorption–desorption kinetics. Therefore, this parameter changes with the concentration of nanoparticles. The magnitude of the shear modulus in the low strain region is found to be sensitive to the values of c, while the onset of nonlinearity in the viscoelastic response is controlled by δ and $R_{a,\max}$.

The Flory radius of the segments between two consecutive fumarate units in PLEOF (that is, potential crosslink points) is approximately 10 nm. The hydrodynamic factor ζ is set equal to 2.5 considering the shape of HA nanoparticles. The best fit of the experimental results to the model was obtained with $G_f \cong 4$ kPa and $\tau_f = 0.001$ sec for free segments. Other extracted fitting parameters are listed in Table 13.1. The value of c for the surface treated samples was found to be higher than that of untreated samples, due to the stronger average monomer–filler interaction in the presence of Ac-Glu6 peptide.

Table 13.1 Fit parameters of the proposed model for hydrogel/nanoapatite composites

Parameters independent from filler concentration		
$\delta/R_F = 0.5$, $R_{a,\max}/R_F = 1.5$	Treated	Untreated
	$c = 0.02$	$c = 0.012$
Parameters variable with filler concentration		
	Treated	Untreated
ϕ (vol%)	G_f^p/G_f	G_f^p/G_f
3	0.25	0.33
6	0.53	0.75
9	0.93	0.76

Figure 13.6 shows the small strain shear modulus of the PLEOF/HA composites versus volume fraction of HA for micro- and nanoapatite particles. As mentioned before, the storage

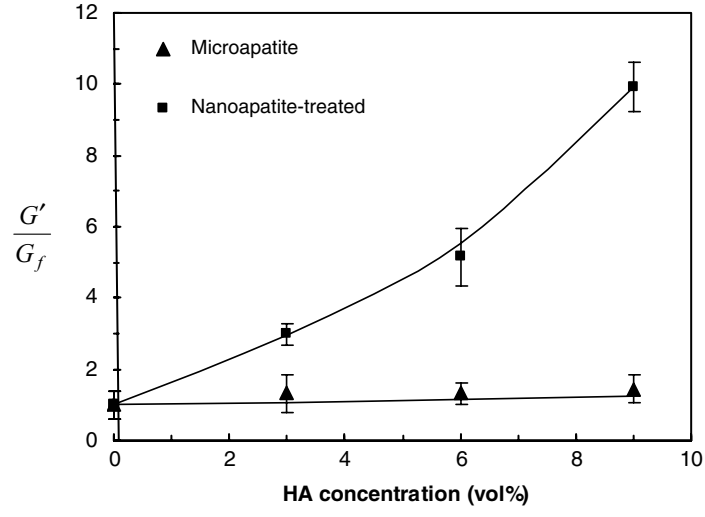

Figure 13.6 Comparison of the experimental results with model predictions (solid lines) for normalized low amplitude shear modulus of the PLEOF/HA hydrogel composites, prepared with micro and nanosize apatite particles (frequency = 1 Hz)

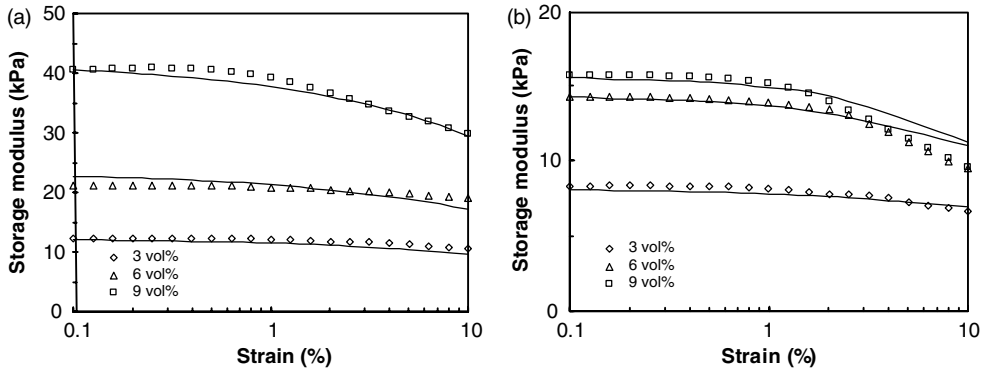

Figure 13.7 Comparison of the experimental results with model predictions (solid lines) for the storage modulus of the PLEOF/HA composites, prepared with 3–9 vol% (a) treated and (b) untreated nanoparticles as a function of strain amplitude (frequency = 1 Hz)

modulus of the composites prepared with microapatite particles fits the well known Guth–Smallwood equation for the suspension of spherical particles in a matrix, that is, $(1 + 2.5\phi)\, G_f$, implying that for large HA particles, relative to the length of the interacting segment, reinforcement is dominated by hydrodynamic effects. The sharp increase in shear storage modulus of the composites reinforced with nanoapatite particles, which is well above the prediction of $h(\phi)\, G_f$, demonstrates that the reinforcement cannot be explained solely by hydrodynamic effects when the particle size is comparable to the size of polymer segments.

The model predictions and experimental values for the shear storage modulus of surface treated and untreated mixtures are shown in Figures 13.7 and 13.8 as a function of strain amplitude and frequency, respectively. The model predictions qualitatively follow the trends in the experimentally measured values; however, there are discrepancies, especially between

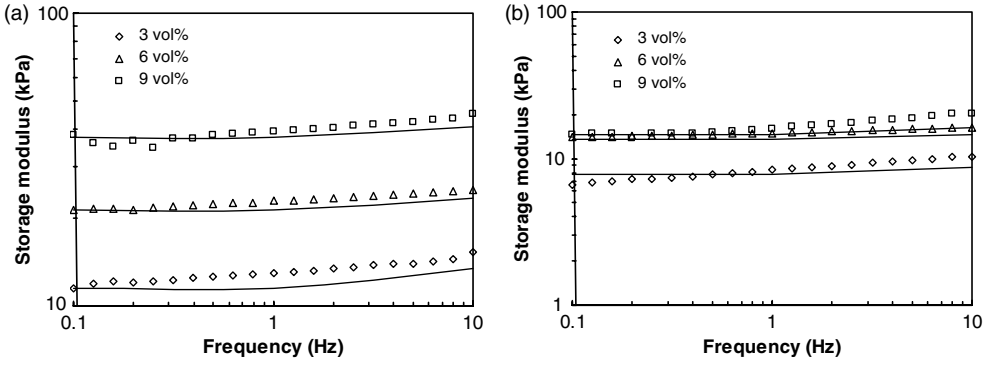

Figure 13.8 Comparison of the experimental results with model predictions (solid lines) for the storage modulus of the PLEOF/HA composites, prepared with 3–9 vol% (a) treated and (b) untreated nanoparticles as a function of frequency (strain = 1%)

the model results and experimental data for untreated samples. In addition, the measured storage modulus shows a slight frequency dependence which is not completely captured by the model.

Although the proposed model and experimental results demonstrate the importance of interfacial bonding on the overall stiffness of the filled hydrogel/nanoapatite composites, the contribution of other reinforcing mechanisms such as filler aggregation cannot be ruled out. HA nanoparticles tend to agglomerate and form larger structures as a result of interparticle electrostatic or van der Waals' interactions. The agglomeration effect is expected to be more pronounced at higher filler concentrations because larger aggregates can form at higher volume fractions. The available surface area for interaction is reduced by the aggregation of filler particles as HA particles, trapped inside the clusters, are unable to interact with the PLEOF chains. Therefore, the lower storage modulus and higher nonlinearity of untreated samples can be attributed to the weaker polymer–filler interaction and stronger tendency for HA to aggregate in these systems. The microsize cluster of particles in untreated mixtures can also orient and anisotropically deform due to the applied shear deformation, leading to a lower overall shear modulus for the composite at higher strains. In addition, the secondary network of locally aggregated particles follows a different kinetic and relaxation pattern rooted in the stored elastic energy in the strained clusters and the failure properties of filler–filler bonds [117] which are not accounted for in this model.

13.4 Conclusions

Bionanocomposites are a promising class of hybrid nanostructured materials with emerging applications in materials science, life science and nanotechnology. Dispersion of rigid colloidal particles in the crosslinked network of a rubber matrix results in considerable enhancement in mechanical behavior of the composite. Contrary to the extensive experimental studies, theoretical models which are capable to quantitatively elucidate the reinforcement mechanism in filled polymer networks are scarce. A molecular model is presented to predict the viscoelastic response of hydrogels reinforced with nonpercolated nanoparticles with emphasize on the role of polymer–particle energetic interaction on viscoelastic response. The structure of the polymer layer adsorbed on the surface of particles is analyzed using a scaling theory for reversible polymer adsorption. The energetic affinity between the monomers and filler surface is assumed to be weak and short range. Due to thermal fluctuations or the applied deformation, the transient junctions between the polymer segments and filler particles break after a finite period of time. The dynamics of the polymer segments is studied by a Maxwell type kinetic model. The results show that monomer–filler energetic affinity can strongly affect the overall viscoelastic response of the hydrogel nanocomposite, even within the range of weak coupling between the mono\mers and filler surface.

Acknowledgments

Preparation of this book chapter was supported by grants from the AO (Arbeitsgemeinschaft Für Osteosynthesefragen) Foundation, the Aircast Foundation and the Oral and Maxillofacial Surgery Foundation.

References

1. Darder, M., Aranda, P., and Ruiz-Hitzky, E. (2007) Bionanocomposites: a new concept of ecological, bioinspired, and functional hybrid materials. *Advanced Materials*, **19**, 1309.
2. Ozin, G. and Arsenault, A. (2005) *Nanochemistry: A Chemical Approach to Nanomaterials*, Royal Society of Chemistry, Cambridge, UK.
3. Dujardin, E. and Mann, S. (2002) Bio-inspired materials chemistry. *Advanced Materials*, **14**, 775.
4. Ruiz-Hitzky, E., Darder, M., and Aranda, P. (2005) Functional biopolymer nanocomposites based on layered solids. *Journal of Materials Chemistry*, **15**, 3650.
5. Sumita, M., Tsukumo, T., Miyasak, K., and Ishikawa, K. (1983) Tensile yield stress of polypropylene composites filled with ultrafine particles. *Journal of Materials Science*, **18**, 1758.
6. Becker, C., Krug, H., and Schmidt, H. (1996) Tailoring of thermomechanical properties of thermoplastic nanocomposite by surface modification of nanoscale silica particles. *Materials Research Society Symposium Proceedings*, **435**, 237.
7. Becker, C., Mueller, P., and Schmidt, H. (1998) Optical and thermomechanical investigations on thermoplastic nanocomposites with surface modified silica nanoparticles. *SPIE*, **346**, 88.
8. Cole, D.H., Shull, K.R., Baldo, P., and Rehn, L. (1999) Dynamic properties of a model polymer/metal nanocomposite: gold particles in poly(t-butyl acrylate). *Macromolecules*, **32**, 771.
9. Dirix, Y., Bastiaansen, C., Caseri, W., and Smith, P. (1999) Preparation, structure and properties of uniaxially oriented polyethylene-silver nanocomposites. *Journal of Materials Science*, **34**, 3859.
10. Oya, A., Kurokawa, Y., and Yasuda, H. (2000) Factors controlling mechanical properties of clay mineral/ polypropylene nanocomposites. *Journal of Materials Science*, **35**, 1045.
11. Zeng, Q.H., Yu, A.B., and Lu, G.Q. (2008) Multiscale modeling and simulation of polymer nanocomposites. *Progress in Polymer Science*, **33**, 191.
12. Frimpong, R.A. and Hilt, J.Z. (2007) *Nanotechnology in Therapeutics: Current Technology and Applications* (eds N.A. Peppas, J.Z. Hilt, and J. Brock Thomas), Horizon Bioscience.
13. Sarvestani, A.S. and Picu, C.R. (2004) Network model for the viscoelastic behavior of polymer nanocomposites. *Polymer*, **45**, 7779.
14. Sarvestani, A.S. and Jabbari, E. (2006) Modeling and experimental investigation of rheological properties of injectable poly(lactide ethylene oxide fumarate)/hydroxyapatite nanocomposites. *Biomacromolecules*, **7**, 1573.
15. Sarvestani, A.S. and Jabbari, E. (2007) Modeling the viscoelastic response of suspension of particles in polymer solution: the effect of polymer-particle interactions. *Macromolecular Theory and Simulations*, **16**, 378.
16. Sarvestani, A.S. and Picu, C.R. (2005) A frictional molecular model for the viscoelasticity of entangled polymer nanocomposites. *Rheologica Acta*, **45**, 132.
17. Liu, L., Zhang, L., Ren, B. *et al.* (2003) Preparation and characterization of collagen-hydroxyapatite composite used for bone tissue engineering scaffold. *Artificial Cells, Blood Substitutes, and Immobilization Biotechnology*, **31**, 435.
18. Rodrigues, V., Serricella, P., Linhares, A.B. *et al.* (2003) Characterization of a bovine collagen–hydroxyapatite composite scaffold for bone tissue engineering. *Biomaterials*, **24**, 4987.
19. Oliveira, M., Rodrigues, M.T., Silva, S.S. *et al.* (2006) Novel hydroxyapatite/chitosan bilayered scaffold for osteochondral tissue-engineering applications: scaffold design and in vitro study. *Biomaterials*, **27**, 6123.
20. Furuzono, T., Yasuda, S., Kimura, T. *et al.* (2004) Nano-scaled hydroxyapatite/polymer composite IV. Fabrication and cell adhesion properties of a three-dimensional scaffold made of composite material with a silk fibroin substrate to develop a percutaneous device. *Journal of Artificial Organs*, **7**, 137.
21. Ajdukovic, Z., Najman, S., Dordevic, L.J. *et al.* (2005) Repair of bone tissue affected by osteoporosis with hydroxyapatite-poly-L-lactide (HAp-PLLA) with and without blood plasma. *Journal of Biomaterials Applications*, **20**, 179.
22. Shikinami, Y. and Okuno, M. (2001) Bioresorbable devices made of forged composites of hydroxyapatite (HA) particles and poly L-lactide (PLLA). Part II: practical properties of miniscrews and miniplates. *Biomaterials*, **22**, 3197.
23. Shikinami, Y. and Okuno, M. (1999) Bioresorbable devices made of forged composites of hydroxyapatite (HA) particles and poly-L-lactide (PLLA) - part I. Basic characteristics. *Biomaterials*, **20**, 859.
24. Kim, S.S., Ahn, K.M., Park, M.S. *et al.* (2007) A poly(lactide-co-glycolide)/hydroxyapatite composite scaffold with enhanced osteoconductivity. *Journal of Biomedical Materials Research*, **80A**, 206.

25. Hakimimehr, D., Liu, D.M., and Troczynski, T. (2005) In-situ preparation of poly(propylene fumarate)-hydroxyapatite composite. *Biomaterials*, **26**, 7297.
26. Wiria, E., Leong, K.F., Chua, C.K., and Liu, Y. (2007) Poly-e-caprolactone/hydroxyapatite for tissue enginering scaffold fabrication via selective laser sintering. *Acta Biomaterialia*, **3**, 1.
27. Dee, K.C. and Bizios, R. (1996) Proactive biomaterials and bone tissue engineering. *Biotechnology and Bioengineering*, **50**, 438.
28. Ishaug, S.L., Yasemski, M.J., Bizios, R., and Mikos, A.G. (1994) Osteoblast function on synthetic biodegradable polymers. *Journal of Biomedical Materials Research*, **28**, 1445.
29. Ramakrishna, S., Mayer, J., Wintermantel, E., and Leong, K.W. (2001) Biomedical applications of polymer-composite materials: a review. *Computer Science and Technology*, **61**, 1189.
30. Mano, J.F., Sousa, R.A., Boesel, L.F. *et al.* (2004) Bioinert, biodegradable and injectable polymeric matrix composites for hard tissue replacement: state of the art and recent developments. *Computer Science and Technology*, **64**, 789.
31. Damien, C.J. and Parsons, J.R. (1991) Bone graft and bone graft substitutes: a review of current technology and applications. *Journal of Applied Biomaterials*, **2**, 187.
32. Hutmacher, D.W. (2000) Scaffolds in tissue engineering of bone and cartilage. *Biomaterials*, **21**, 2529.
33. Sinha Ray, S. and Bousmina, M. (2005) Biodegradable polymers and their layered silicate nanocomposites. *Progress in Materials Science*, **50**, 962.
34. Pandey, J.K., Kumar, A.P., Misra, M. *et al.* (2005) Recent advances in biodegradable nanocomposites. *Journal of Nanoscience and Nanotechnology*, **5**, 497.
35. Yu, L., Dean, K., and Li, L. (2006) Polymer blends and composites from renewable resources. *Progress in Polymer Science*, **31**, 576.
36. Sinha Ray, S. and Okamoto, M. (2003) Biodegradable polylactide and its nanocomposites: opening a new dimension for plastics and composites. *Macromolecular Rapid Communications*, **24**, 815.
37. Park, H.M., Misra, M., Drzal, L.T., and Mohanty, A.K. (2004) Green nanocomposites from cellulose acetate bioplastic and clay: effect of eco-friendly triethyl citrate plasticizer. *Biomacromolecules*, **5**, 2281.
38. Pandey, J.K. and Singh, R.P. (2005) Green nanocomposites from renewable resources: effect of plasticizer on the structure and material properties of clay-filled starch. *Starch*, **57**, 8.
39. Wibowo, A.C., Misra, M., Park, H.-M. *et al.* (2006) Biodegradable nanocomposites from cellulose acetate: mechanical, morphological, and thermal properties. *Compositest A*, **37**, 1428.
40. Jacob, M. and Thomas, S. (2008) Biofibres and biocomposites. *Carbohydrate Polymers*, **71**, 343.
41. Geethamma, V.G., Kalaprasad, G., Groeninckx, G., and Thomas, S. (2005) Dynamic mechanical behavior of short coir fiber reinforced natural rubber composites. *Composites A*, **36**, 1499.
42. Idicula, M., Malhotra, S.K., Joseph, K., and Thomas, S. (2005) Dynamic mechanical analysis of randomly oriented intimately mixed short banana/sisal hybrid fibre reinforced polyester composites. *Composites Science and Technology*, **65**, 1077.
43. Sreekala, M.S., Thomas, S., and Groeninckx, G. (2005) Dynamic mechanical properties of oil palm fiber/phenol formaldehyde and oil palm fiber/glass hybrid phenol formaldehyde composites. *Polymer Composites*, **26**, 388.
44. Jacob, M., Varughese, K.T., and Thomas, S. (2004) Mechanical properties of sisal/oil palm hybrid fiber reinforced natural rubber composites. *Composites Science and Technology*, **64**, 955.
45. Jacob, M., Varughese, K.T., and Thomas, S. (2004) Natural rubber composites reinforced with sisal/oil palm hybrid fibers: tensile and cure characteristics. *Journal of Applied Polymer Science*, **93**, 2305.
46. Jacob, M., Francis, B., Varughese, K.T., and Thomas, S. (2006) Dynamical mechanical analysis of sisal/oil palm hybrid fiber-reinforced natural rubber composites. *Polymer Composites*, **27**, 671.
47. Jacob, M., Varughese, K.T., and Thomas, S. (2005) Water sorption studies of hybrid bio-fiber reinforced natural rubber biocomposites. *Biomacromolecules*, **6**, 2969.
48. Jacob, M., Varughese, K.T., and Thomas, S. (2006) Novel woven sisal fabric reinforced natural rubber composites: tensile and swelling characteristics. *Journal of Composite Materials*, **40**, 1471.
49. Jacob, M., Varughese, K.T., and Thomas, S. (2006) Moisture sorption characteristics in woven sisal fabric reinforced natural rubber composites: a study. *Journal of Applied Polymer Science*, **102**, 416.
50. Allen, S.D., Moore, D.R., Lobkovsky, E.B., and Coates, G.W. (2002) High-activity, single-site catalysts for the alternating copolymerization of co2 and propylene oxide. *Journal of the American Chemical Society*, **124**, 14284.
51. Maiti, P. and Giannelis, E.P. (2002) *Polymer Outreach Program (19)*, Cornell University Press, New York.

52. Peppas, N. and Lustig, S. (1986) *Hydrogels In Medicine and Pharmacy. I. Fundamentals* (ed. P. Na), CRC Press, Boca Raton.
53. Jabbari, E. and Nozari, S. (2000) Swelling behavior of acrylic acid hydrogels prepared by gamma radiation crosslinking of polyacrylic acid in aqueous solution. *European Polymer Journal*, **36**, 2685.
54. Jabbari, E. and Karbasi, S. (2004) Swelling behavior and cell viability of dehydrothermally crosslinked poly(vinyl alcohol) hydrogel grafted with n-vinyl pyrrolidone or acrylic acid using γ-radiation. *Journal of Applied Polymer Science*, **91**, 2862.
55. Dembczynski, R. and Jankowski, T. (2000) Characterisation of small molecules diffusion in hydrogel-membrane liquid-core capsules. *Biochemical Engineering Journal*, **6**, 41.
56. Beruto, D.T. and Botter, R. (2004) Role of the water matrix potential and of equilibrium water content (EWC) on the water self-diffusion coefficient and on the oxygen permeability in hydrogel contact lenses. *Biomaterials*, **25**, 2877.
57. Herber, S., Bomer, J., Olthuis, W. *et al.* (2005) A miniaturized carbon dioxide gas sensor based on sensing of pH-sensitive hydrogel swelling with a pressure sensor. *Biomedical Microdevices*, **7**, 197.
58. Liang, S., Xu, J., Weng, L. *et al.* (2006) Protein diffusion in agarose hydrogel in situ measured by improved refractive index method. *Journal of Controlled Release*, **115**, 189.
59. Zubtsov, D.A., Ivanov, S.M., Rubina, A.Y. *et al.* (2006) Effect of mixing on reaction-diffusion kinetics for protein hydrogel-based microchips. *Journal of Biotechnology*, **122**, 16.
60. Nederberg, F., Watanabe, J., Ishihara, K. *et al.* (2005) Organo hydrogel hybrids. Formation of reservoirs for protein delivery. *Biomacromolecules*, **6**, 3088.
61. Leach, J.B. and Schmidt, C.E. (2005) Characterization of protein release from photocrosslinkable hyaluronic acid-polyethylene glycol hydrogels. *Biomaterials*, **26**, 125.
62. Monteiro, M.J., Hall, G., Gee, S., and Xie, L. (2004) Protein transfer through polyacrylamide hydrogel membranes polymerized in lyotropic phases. *Biomacromolecules*, **5**, 1637.
63. Honiger, J., Balladur, P., Mariani, P. *et al.* (1995) Permeability and biocompatibility of a new hydrogel used for encapsulation of hepatocytes. *Biomaterials*, **16**, 753.
64. Shingel, K.I. and Faure, M.P. (2005) Structure–property relationships in poly(ethylene glycol)–protein hydrogel systems made from various proteins. *Biomacromolecules*, **6**, 1635.
65. Shim, W.S., Kim, J.H., Park, H. *et al.* (2006) Biodegradability and biocompatibility of a pH- and thermo-sensitive hydrogel formed from a sulfonamide-modified poly(epsilon-caprolactone-co-lactide)-poly(ethylene glycol)-poly (epsilon-caprolactone-co-lactide) block copolymer. *Biomaterials*, **27**, 5178.
66. Alexandre, E., Schmitt, B., Boudjema, K. *et al.* (2004) Hydrogel networks of poly(ethylene oxide) star-molecules supported by expanded polytetrafluoroethylene membranes: characterization, biocompatibility evaluation and glucose diffusion characteristics. *Macromolecular Bioscience*, **4**, 639.
67. Risbud, M.V. and Bhat, S.V. (2001) Properties of polyvinyl pyrrolidone/beta-chitosan hydrogel membranes and their biocompatibility evaluation by haemorheological method. *Journal Materials Science Materials Medicine*, **12**, 75.
68. Jabbari, E. (2004) Release characteristics of a model plasmid DNA from synthetic and biodegradable poly(ethylene glycol fumarate)/acrylamide hydrogel microspheres. *Journal of Microencapsulation*, **21**, 525.
69. He, X. and Jabbari, E. (2007) Material properties and cytocompatibility of injectable MMP degradable poly(lactide ethylene oxide fumarate) hydrogel as a carrier for marrow stromal cells. *Biomacromolecules*, **8**, 780.
70. Kim, S. and Healy, K.E. (2003) Synthesis and characterization of injectable poly(n-isopropylacrylamide-co-acrylic acid) hydrogels with proteolytically degradable cross-links. *Biomacromolecules*, **4**, 1214.
71. Tirelli, N., Lutolf, M.P., Napoli, A., and Hubbell, J.A. (2002) Poly(ethylene glycol) block copolymers. *Journal of Biotechnology*, **90**, 3.
72. Peppas, N.A. and Langer, R. (1994) New challenges in biomaterials. *Science*, **263**, 1715.
73. Hou, Q., De Bank, P.A., and Shakesheff, K.M. (2004) Injectable scaffolds for tissue regeneration. *Journal of Materials Chemistry*, **14**, 1915.
74. Hangody, L., Kish, G., Karpati, Z. *et al.* (1998) Mosaicplasty for the treatment of articular cartilage defects: application in clinical practice. *Orthopedics*, **21**, 751.
75. Hill-West, L., Chowdhury, S.M., Slepian, M.J., and Hubbell, J.A. (1994) Inhibition of thrombosis and intimal thickening by in situ photopolymerization of thin hydrogel barriers. *Proceedings of the National Academy of Sciences*, **91**, 5967.

76. Lu, S. and Anseth, K.S. (2000) Release behavior of high molecular weight solutes from poly(ethylene glycol)-based degradable networks. *Macromolecules*, **33**, 2509.
77. Kim, B.S., Hrkach, J.S., and Langer, R. (2000) Biodegradable photo-crosslinked poly(ether-ester) networks for lubricious coatings. *Biomaterials*, **21**, 259.
78. Sawhney, S., Chandrashekhar, P.P., and Hubbell, J.A. (1993) Bioerodible hydrogels based on photopolymerized poly(ethylene glycol)-co-poly(**α**-hydroxy acid) diacrylate macromers. *Macromolecules*, **26**, 581.
79. Jabbari, E., Gruetzmacher, J.A., Lu, L. *et al.* (2003) Development of a novel self-crosslinkable poly(caprolactone fumarate) as a biodegradable and injectable scaffold for bone tissue engineering. *IEEE Transactions on Bio-Medical Engineering*, **2**, 1219.
80. Jabbari, E., Gruetzmacher, J.A., Lu, L. *et al.* (2003) Synthesis and characterization of nano hydroxyapatite grafted with biodegradable and crosslinkable fumaric/adipic acid macromer. *Polymer Preprints*, **44**, 184.
81. Temenoff, J.S., Park, H., Jabbari, E. *et al.* (2004) Thermally cross-linked oligo(poly(ethylene glycol) fumarate) hydrogels support osteogenic differentiation of encapsulated marrow stromal cells in vitro. *Biomacromolecules*, **5**, 5.
82. Sarvestani, S., He, X., and Jabbari, E. (2007) Viscoelastic characterization and modeling of gelation kinetics of injectable in situ crosslinkable poly(lactide-ethylene oxide-fumarate) hydrogels. *Biomacromelcules*, **8**, 406.
83. He, S., Timmer, M.D., Yaszemski, M.J. *et al.* (2001) Synthesis of biodegradable poly(propylene fumarate) networks with poly (propylene fumarate)-diacrylazte macromers as crosslinking agents and characterization of their degradation products. *Polymer*, **42**, 1251.
84. Sarvestani, S., He, X., and Jabbari, E. (2008) Osteonectin-derived peptide increases the modulus of a bone-mimetic nanocomposite. *European Biophysics Journal*, **37**, 229.
85. Nishikawa, T., Masuno, K., Tominaga, K. *et al.* (2005) Bone repair analysis in a novel biodegradable hydroxyapatite/collagen composite implanted in bone. *Implant Dentistry*, **14**, 252.
86. Tampieri, A., Celotti, G., Landi, E. *et al.* (2003) Biologically inspired synthesis of bone-like composite: self-assembled collagen fibers/hydroxyapatite nanocrystals. *Journal of Biomedical Materials Research Part A*, **67**, 618.
87. Rodrigues, C.V., Serricella, P., Linhares, A.B. *et al.* (2003) Characterization of a bovine collagen-hydroxyapatite composite scaffold for bone tissue engineering. *Biomaterials*, **24**, 4987.
88. Lee, S.J., Lim, G.J., Lee, J.W. *et al.* (2006) In vitro evaluation of a poly(lactide-co-glycolide)-collagen composite scaffold for bone regeneration. *Biomaterials*, **27**, 3466.
89. Hillig, W.B., Choi, Y., Murtha, S. *et al.* (2008) An open-pored gelatin/hydroxyapatite composite as a potential bone substitute. *Journal of Materials Science-Materials in Medicine*, **19**, 11.
90. Yao, C.H., Liu, B.S., Hsu, S.H., and Chen, Y.S. (2005) Calvarial bone response to tricalcium phosphate-genipin crosslinked gelatin composite. *Biomaterials*, **26**, 3065.
91. d'Ayala, G.G., De Rosa, A., Laurienzo, P., and Malinconico, M. (2007) Development of a new calcium sulphate-based composite using alginate and chemically modified chitosan for bone regeneration. *Journal of Biomedical Materials Research Part A*, **81**, 811.
92. Zhang, Y., Ni, M., Zhang, M., and Ratner, B. (2003) Calcium phosphate/chitosan composite scaffolds for bone tissue engineering. *Tissue Engineering*, **9**, 337.
93. Le Nihouannen, D., Saffarzadeh, A., Gauthier, O. *et al.* (2007) Osteogenic properties of calcium phosphate ceramics and fibrin glue based composites. *Journal of Materials Science - Materials in Medicine*, **18**, 225.
94. Orgill, D.P., Ehret, F.W., Regan, J.F. *et al.* (1998) Polyethylene glycol/microfibrillar collagen composite as a new resorbable hemostatic bone wax. *Journal of Biomedical Materials Research*, **39**, 358.
95. Bonfield, W., Grynpas, M.D., Tully, A.E. *et al.* (1981) Hydroxyapatite reinforced polyethylene - a mechanically compatible implant material for bone replacement. *Biomaterials*, **2**, 185.
96. Bonfield, W. (1988) Composites for bone replacement. *Journal of Biomedical Engineering*, **10**, 522.
97. Huang, J., Di Silvio, L., Wang, M. *et al.* (1997) In vitro mechanical and biological assessment of hydroxyapatite-reinforced polyethylene composite. *Journal of Materials Science-Materials in Medicine*, **8**, 775.
98. Huang, J., Di Silvio, L., Wang, M. *et al.* (1997) Evaluation of in vitro bioactivity and biocompatibility of bioglass® - reinforced polyethylene composite. *Journal of Materials Science-Materials in Medicine*, **8**, 809.
99. Wang, M., Ladizesky, N.H., Tanner, K.E. *et al.* (2000) Hydrostatically extruded HAPEX. *Journal of Matierals Science*, **35**, 1023.

100. Di Silvio, L., Dalby, M.J., and Bonfield, W. (1998) In vitro response of osteoblasts to hydroxyapatite-reinforced polyethylene composites. *Journal of Materials Science - Materials in Medicine*, **9**, 845.
101. Nazhat, S.N., Joseph, R., Wang, M. *et al.* (2000) Dynamic mechanical characterisation of hydroxyapatite particulate reinforced polyethylene: effect of particle size. *Journal of Materials Science - Materials in Medicine*, **11**, 621.
102. Suwanprateeb, J., Tanner, K.E., Turner, S., and Bonfield, W. (1997) Influence of sterilization by gamma irradiation and of thermal annealing on creep of hydroxyapatite-reinforced polyethylene composites. *Journal of Biomedical Materials Research*, **39**, 16.
103. Suwanprateeb, J., Tanner, K.E., Turner, S., and Bonfield, W. (1997) Influence of Ringer's solution on creep resistance of hydroxyapatite reinforced polyethylene composites. *Journal of Materials Science - Materials in Medicine*, **8**, 469.
104. Guild, J. and Bonfield, W. (1993) Predictive modelling of HAP-polyethylene composite. *Biomaterials*, **14**, 985.
105. Ladizesky, N.H., Ward, I.M., and Bonfield, W. (1997) Hydrostatic extrusion of polyethylene filled with hydroxyapatite. *Advanced Polymer Technology*, **8**, 496.
106. Ladizesky, N.H., Ward, I.M., and Bonfield, W. (1997) Hydroxyapatite/high-performance polyethylene fibre composites for high-load-bearing bone replacement materials. *Journal of Applied Polymer Science*, **65**, 1865.
107. Ladizesky, N.H., Pirhonen, E.M., Appleyard, D.B. *et al.* (1998) Fibre reinforcement of ceramic/polymer composites for a major load bearing bone substitute materials. *Computer Science and Technology*, **58**, 419.
108. Deb, S., Wang, M., Tanner, K.E., and Bonfield, W. (1996) Hydroxyapatite–polyethylene composites: Effect of grafting and surface treatment of hydroxyapatite. *Journal of Materials Science - Materials in Medicine*, **7**, 191.
109. Wang, M., Deb, S., and Bonfield, W. (2000) Chemically coupled hydroxyapatite- polyethelene composites: processing and characterization. *Materials Letters*, **44**, 119.
110. Wang, M. and Bonfield, W. (2001) Chemically coupled hydroxyapatite-polyethylene composites: structure and properties. *Biomaterials*, **22**, 1311.
111. Guild, J. and Bonfield, W. (1998) Predictive modelling of the mechanical properties and failure processes of hydroxyapatite-polyethylene (HAPEX™) composite. *Journal of Materials Science - Materials in Medicine*, **9**, 621.
112. Bonfield, W. (1987) Advances in the fracture mechanics of cortical bone. *Journal of Biomechanics*, **20**, 1071.
113. Wang, X. and Robertson, C.G. (2005) Nature of strain-induced nonlinearity in filled rubbers. *Physical Review E*, **72**, 031406.
114. Payne, R. (1965) *Reinforcement of Elastomers* (ed. G. Kraus), John Wiley & Sons, New York.
115. Donnet, J.-B. (1998) Black and white fillers and tire compound. *Rubber Chemistry and Technology*, **71**, 323.
116. Cassagnau, Ph. (2008) Melt rheology of organoclay and fumed silica nanocomposites. *Polymer*, **49**, 2183.
117. Heinrich, G. and Klüppel, M. (2002) Recent advances in the theory of filler networking in elastomers. *Advances in Polymer Science*, **160**, 1.
118. Maier, P.G. and Göritz, D. (1996) Molecular interpretation on the Payne effect. *Kautsch Gummi Kunstst*, **49**, 18.
119. Joshi, P.R. and Leonov, A.I. (2001) Modeling of steady and time-dependent responses in filled, uncured, and crosslinked rubbers. *Rheologica Acta*, **40**, 350.
120. Chazeau, L., Brown, J.D., Yanyo, L.C., and Sternstein, S.S. (2000) Modulus recovery kinetics and other insights into the payne effect for filled elastomers. *Polymer Composites*, **21**, 202.
121. Bandyopadhyay, A., Sarkar, M.D., and Bhowmick, A.K. (2005) Polymer-filler interactions in sol-gel derived polymer/silica hybrid nanocomposites. *Journal of Polymer Science Part B-Polymer Physics*, **43**, 2399.
122. Huber, G. and Vilgis, T.A. (2002) On the mechanisms of hydrodynamics reinforcement in elastic composites. *Macromolecules*, **35**, 9204.
123. Heinrich, G., Klüppel, M., and Vilgis, T.A. (2002) Reinforcement of elastomers. *Current Opinion in Solid State and Materials Science*, **6**, 195.
124. Kohls, J. and Beaucage, G. (2002) Rational design of reinforced rubber. *Current Opinion in Solid State and Materials Science*, **6**, 183.
125. Colombini, D., Merle, G., and Alberola, N.D. (2001) Use of mechanical modeling to study multiphase polymer materials. *Macromolecules*, **34**, 5916.
126. Reichert, W., Göritz, D., and Duschl, E. (1993) The double network. a model describing filled elastomers. *Polymer*, **34**, 1216.
127. Hansma, P.K., Fantner, G.E., Kindt, J.H. *et al.* (2005) Sacrificial bonds in the interfibrillar matrix of bone. *Journal of Musculoskeletal and Neuronal Interactions*, **5**, 313.

128. Fantner, E., Oroudjev, E., Schitter, G. *et al.* (2006) Sacrificial bonds and hidden length: unraveling molecular mesostructures in tough materials. *Biophysical Journal*, **90**, 1411.
129. Termine, J.D., Kleinman, H.K., Whitson, S.W. *et al.* (1981) Osteonectin, a bone-specific protein linking mineral to collagen. *Cell*, **26**, 99.
130. Romberg, R.W., Werness, P.G., Lollar, P. *et al.* (1985) Isolation and characterization of native adult osteonectin. *The Journal of Biological Chemistry*, **260**, 2728.
131. He, X. and Jabbari, E. (2006) Solid-phase synthesis of reactive peptide crosslinker by selective deprotection. *Protein and Peptide Letters*, **13**, 715.
132. Sarvestani, A.S. and Jabbari, E. (2008) A model for the viscoelastic behavior of nanofilled hydrogel composites under oscillatory shear loading. *Polymer Composites*, **29**, 326.
133. Guth, J. (1945) Theory of filler reinforcement. *Journal of Applied Physics*, **16**, 20.
134. de Gennes, P.G. (1981) Polymer solutions near an interface. 1. Adsorption and depletion layers. *Macromolecules*, **14**, 1637.
135. de Gennes, P.G. (1987) Polymers at an interface: a simplified view. *Advances in Colloid and Interface Science*, **27**, 189.
136. O'Shaughnessy, B. and Vavylonis, D. (2005) Non-equilibrium in adsorbed polymer layers. *Journal of Physics: Condensed Matter*, **17**, R63.
137. de Gennes, P.G. (1985) *Scaling Concepts in Polymer Physics*, Cornell University Press, Ithaca.
138. Gong, J. and Osada, Y. (1998) Gel friction: a model based on surface repulsion and adsorption. *Journal of Chemical Physics*, **109**, 8062.
139. Subbotin, A., Semenov, A., and Doi, M. (1997) Friction in strongly confined polymer melts: effect of polymer bridges. *Physical Review E*, **56**, 623.
140. Ponomarev, L., Sewell, T.D., and Durning, C.J. (2000) Surface diffusion and relaxation of partially adsorbed polymers. *Journal of Polymer Science Part B-Polymer Physics*, **38**, 1146.
141. Wittmer, J., Johner, A., Joanny, J.-F., and Binder, K. (1994) Chain desorption from a semidilute polymer brush: a Monte Carlo simulation. *Journal of Chemical Physics*, **101**, 4379.
142. Larson, R. (1988) *Constitutive Equations for Polymer Melts and Solutions*, Butterworths, Boston.
143. Ferry, J.D. (1980) *Viscoelastic Properties of Polymers*, John Wiley & Sons, New York.
144. Bergeström, J.S. and Boyce, M.C. (2000) Large strain time-dependent behavior of filled elastomers. *Mechanics of Materials*, **32**, 627.
145. Huber, G. and Vilgis, T.A. (2002) On the mechanism of hydrodynamic reinforcement in elastic composites. *Macromolecules*, **35**, 9204.

14

Rheological Behavior of Rubber Nanocomposites

Philippe Cassagnau[1] and Claire Barrès[2]

[1] *Université de Lyon 1, Lyon, F-69003, France; CNRS UMR5223, Ingénierie des Matériaux Polymères: Laboratoire des Matériaux Polymères et Biomatériaux, F-69622 Villeurbanne, France*

[2] *INSA-Lyon, Villeurbanne, F-69621, France; CNRS UMR5223, Ingénierie des Matériaux Polymères: Laboratoire des Matériaux Macromoléculaires, F-69621 Villeurbanne, France*

14.1 Introduction

It has been well known for a century that the addition of fillers, mostly carbon black, to rubber compounds has a strong impact on the properties of materials. In recent years, polymer nanocomposites have been developed as a new class of composites. For example, polymer-layered silicate nanocomposites have attracted great interest as they can attain a higher degree of strength, thermal stability (fire retardance applications) and barrier properties with very low nanofiller content (generally lower than 5%). Furthermore, fumed silica has also recently gained new interest since silica particles have become more important in tire applications. Finally, the development of new generation of nanocomposites filled with carbon nanotubes (CNTs) that exhibit excellent mechanical and electrical properties is promising.

From a rheological point of view, a direct consequence of incorporation of fillers in molten polymers is the significant change in the steady shear viscosity behavior and the viscoelastic properties. For example, the effect of strain-dependence (nonlinearity effect) of the dynamic viscoelastic properties of filled polymers, often referred to as the Payne effect [1, 2], has been well known in elastomers for 40 years. Intensive discussions have been held thereupon but the exact causes of this nonlinear effect, including thixotropic phenomenon, are still a matter of investigations and controversial discussions. The level of filler dispersion is expected to play a

Rubber Nanocomposites: Preparation, Properties and Applications Edited by Sabu Thomas and Ranimol Stephen
© 2010 John Wiley & Sons (Asia) Pte Ltd

major role in determining the filler effects on nonlinear responses of nanocomposites. Generally speaking, elastomers filled with nanoparticles show a solid-like behavior response which includes a nonterminal zone of relaxation, apparent yield stress and a shear-thinning dependence of viscosity on particle concentration and dispersion. This particular rheological behavior arises from the presence of a network structure. Actually, the controversial discussion, or at least the main debate in the open literature, is about the origin of this network structure: Polymer–particle or/and particle–particle interactions.

Since the melt rheological properties of filled polymers are sensitive to the structure, concentration, particle size, shape and surface characteristics of the fillers, rheology offers original means to assess the state of the dispersion in nanocomposites and to investigate the influence of flow conditions upon nanofiller dispersion itself. Interestingly, Leblanc [3] in a review paper on the rheological properties in filled polymers, showed the classification of fillers according to average particle size and their respective consequence on rheological behavior. The present work is dedicated to the review of the present knowledge on rheology of rubber composites filled with carbon black, fumed silica, organoclays and carbon nanotubes. Consequently, a brief description of structure of the most common fillers is addressed in this introductory part.

- Carbon black is produced by thermo-oxidative decomposition of hydrocarbons. It is made of elemental carbon organized in quite spherical elementary particles, which assemble into aggregates. The size of the elementary colloidal particles and the structure of the aggregates depend on the synthesis and manufacturing process and are the parameters that allow carbon blacks to be distinguished and classified. The colloidal particles are made of stacked graphitic layers, which yields a step-like surface topology. The structure and arrangement of the graphitic layers depend on the particle size, therefore both the dimension and the topology are key factors. Average particle sizes range between about 10 and 300 nm. An aggregate comprises coalesced particles, and constitutes the smallest stable form of carbon black that possesses reinforcing properties. Indeed, colloidal blacks have poor, if any, reinforcing capabilities. Aggregates spontaneously agglomerate into micron to millimeter-size clusters, which do not either present reinforcing properties because they are not stable structures. For these reasons, optimal reinforcement of rubber would occur when individual aggregates are well distributed in the bulk. The typical order of magnitude of aggregate dimension is one to several hundreds of nanometers in the longest.

  The complexity of aggregate shape is referred to as "structure", and is characterized by two physical parameters: the surface area in m^2/g, measured by BET method with nitrogen, and the di(n-dibutylphthalate) index (or DBPA value, in $cm^3/100\,g$), which is related to the "inner" volume of the aggregate. This value is determined by incorporation of DBPA into carbon black under shear and corresponds to the quantity of added DBPA that produces a significant increase of viscosity. Three digits are used to characterize the different grades of carbon blacks. In the present ASTM classification, the first one is inversely proportional to the surface area, and the last two form a number that describes the structure (the more intricate the aggregate structure, the higher this number).
- Fumed silica is a finely divided amorphous silicon dioxide which can be seen at three main scales: primary particles of around 1–3 nm fused together in stable aggregates of around 100–250 nm and finally building up large micron-sized agglomerates, generally named clusters. Due to the large surface area (50–400 m^2/g) of these particles, the surface silanol functional groups and the surface siloxane interactions play a major role in the rheological

impact of fumed silica. Actually, this cluster structure can be viewed as an assembly of primary particles in a structure having a fractal dimension. Due to their fractal structure and their high specific area, fumed silica fillers are subjected to self aggregation and can consequently easily form a network of connected or interacting particles in the molten polymer.

- With regard to organoclays based nanocomposites, three layer organization scales are generally differentiated: (i) the clay layers have a micron-size scale in the polymer matrix in the case of weak interaction and/or no appropriate shearing conditions, (ii) a few polymer chains are able to diffuse in the interlayer space, this structure is called intercalated, (iii) all the layers are homogenously dispersed as individual layers at a nanoscale, this structure is called exfoliated. Consequently, the exfoliation of organoclay layers increases the number of frictional interaction between the layers which is consistent with the formation of a network structure of weakly agglomerated particles. Note that the recent developments in the linear and nonlinear viscoelasticity of silica and organoclays nanocomposites has been recently reviewed by Cassagnau [4].
- Carbon nanotubes are members of the fullerene structural family. Their name is derived from their size, since the diameter of a nanotube is in the order of a few nanometers while they can be up to several millimeters or even centimeters in length. Consequently, CNT possess high flexibility, low density and large aspect ratio. However, one of the most important challenges in polymer nanocomposite developments and applications is to obtain a homogeneous dispersion of CNT in polymer matrix by overcoming the van der Waals interaction between elementary tubes. For example, it can be expected that the rheological percolation, and subsequently the nonlinearity effect, depend on nanotube dispersion and aspect ratio. As matter of fact, a great level of activity in the domain of polymer nanocomposites filled with CNT is reported in the more recent scientific literature. Several review papers have been published recently [5–7] on carbon nanotube-based polymer nanocomposites.

A lot of papers, too many to cite them all, and reviews have addressed the rheology of nanofilled polymers. The most recent review was addressed by Litchfield and Baird [124] on the rheology of high aspect ratio nanoparticle-filled liquids. The present work focuses on the rheology of rubber nanocomposites including filler percolation aspects, Payne effect and rheology (shear and elongational) for processing.

14.2 Linear Viscoelasticity

14.2.1 General Trends

Many authors have discussed on the connection which can be made between the filler morphology (structure, particle size, aspect ratio) and the melt viscoselastic properties of polymeric materials. Due to the small size and the high specific surface, nanofillers are prone to self-aggregation and consequently easily form three-dimensional network in molten polymer matrix. Actually, the nature of this network, polymer–filler and/or filler–filler interaction, sustains the controversial discussion on the Payne effect. For example Figure 14.1a–d shows the variation of the linear complex shear modulus $[G^*(\omega) = G'(\omega) + jG''(\omega)]$ at different nanofiller concentrations for respectively: (Figure 14.1a) copolymers of ethylene and vinyl acetate (EVA) filled with hydrophilic silica [8], Styrene butadiene rubber (SBR) filled with carbon black [9], low density polyethylene (LDPE) filled with lamellar organoclay such as

Montmorillonite [10] and (Figure 14.1d) polycarbonate (PC) filled multiwalled carbon nantubes [11]. Therefore, the general rheological trend for nanocomposites reported in most of the works is the appearance of a transition from a liquid-like behavior ($G' \propto \omega^2$ and $G'' \propto \omega^1$) to a solid-like behavior ($G' \propto \omega^0 = \mathrm{Ge}$), that is, the apparition of a plateau (second plateau modulus) of the storage modulus at low frequency which is higher than the loss modulus (tan $\delta < 1$). Remind that the first plateau (rubbery modulus, G_N^0) is attributed to the network of physical entanglements. Obviously, it is admitted that the increase in nanofiller concentration is driving this transition. However, the state of dispersion and/or the surface modification of nanofillers is another parameter driving this transition and more generally transition from linear to nonlinear behavior (see Payne effect part). Since the filler–matrix interactions dictate the nature of shell formation, they play a direct role in the filler agglomeration process. It is evident that poor compatibility, for example untreated silica particles (hydrophilic) in hydrophobic polymer such as polybutadiene or SBR makes the dispersion difficult.

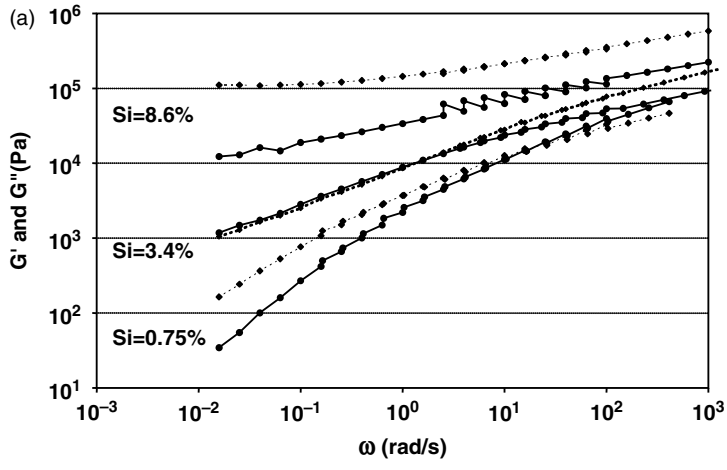

Figure 14.1 Variation of the complex shear modulus of nanocomposites at different nanofiller concentrations. (a) EVA copolymers filled with fumed silica [8] (Reprinted from *Polymer*, **44**, P. Cassagnau, "Payne effect and shear elasticity of silica-filled polymers in concentrated solutions and in molten state," 2455–2462, © 2003, with permission from Elsevier); (b) SBR filled with carbon black [9] (Reproduced with permission from A. Mongruel and M. Cartault, "Nonlinear rheology of styrene-butadiene rubber filled with carbon-black or silica particles," *Journal of Rheology*, **50**, no. 2, 115–135 (Figure 2), © 2006 by The Society of Rheology, Inc.. All rights reserved); (c) LLDPE filled with layer organoclays (Storage modulus variation). Insert caption: MA-x means x phr of organoclay [10] (Reprinted from *Polymer*, **48**, A. Durmus, A. Kasgoz and C.W. Macosko, "Linear low density polyethylene (LLDPE)/clay nanocomposites. Part I: structural characterization and quantifying clay dispersion by melt rheology," 4492–4502, © 2007, with permission from Elsevier); and (d) Polycarbonate filled with multiwalled carbon nanotube (storage modulus variation) [11] (Reprinted from *Polymer*, **45**, P. Pötschke, M. Abdel-Goad, I. Alig et al., "Rheological and dielectrical characterization of melt mixed polycarbonate-multiwalled carbon nanotube composites," 8863–8870, © 2004, with permission from Elsevier.)

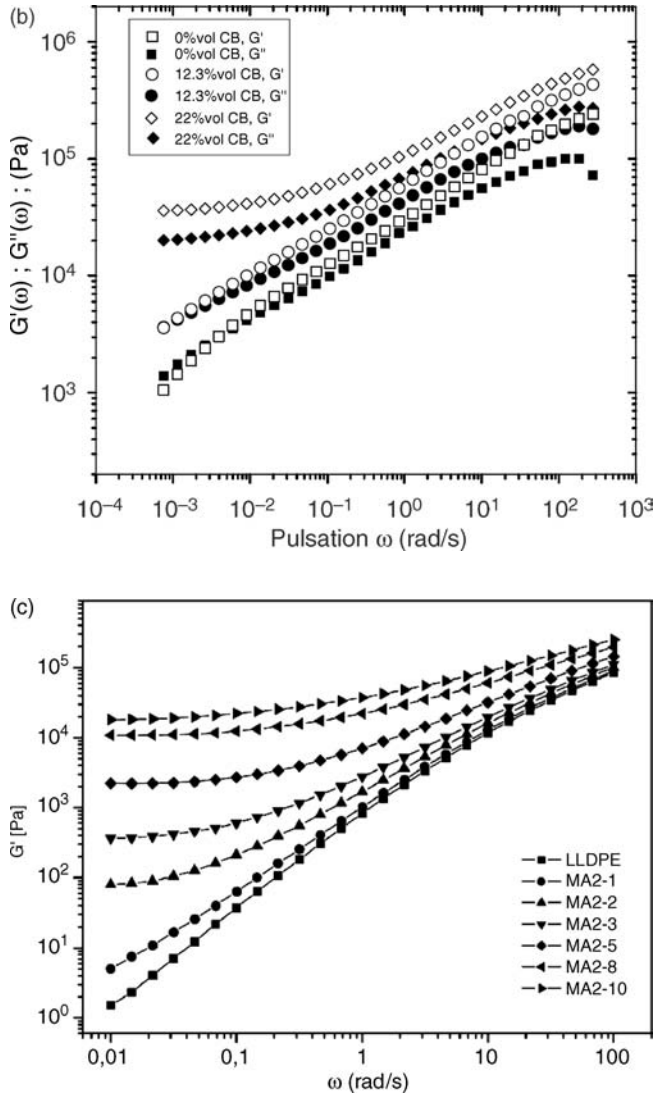

Figure 14.1 (*Continued*)

14.2.2 Percolation Threshold

The sol-gel transition (liquid to solid-like behavior) occurs during a random aggregation process of subunits into larger and larger aggregates at the macroscopic scale. Theoretically, the sol-gel transition for spherical spheres without any interaction (hydrodynamic effect only) should be obtained at the close packing volume fraction of $\phi_c = 0.64$. From a practical point of

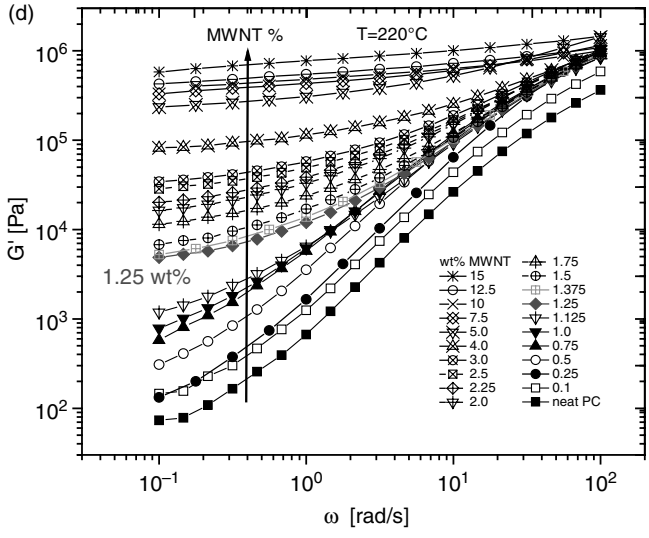

Figure 14.1 (*Continued*)

view, the increase in the effective particle volume fraction due to particle swelling or clustering from inter-particle interaction leads to a drastic decrease in ϕ_c. Scaling relations have been developed to provide the divergence of the properties at the percolation threshold arising from physical interactions. Actually, the sol-gel transition for nanocomposites in which the filler particle aggregates has the same features as chemical gelation, namely the divergence of the longest relaxation time and power law spectrum with negative exponent [12]. As a result, at the percolation threshold, storage and loss moduli have the same power law frequency dependency: $G'(\omega) \propto G''(\omega) \propto \omega^{\Delta}$, where Δ is the relaxation exponent. Moreover, the loss tangent $\tan\delta$ ($\tan\delta = G''/G'$) is independent on the frequency and is given by: $\tan\delta = \tan(\Delta\pi/2)$. For example, Figure 14.1a shows that the silica concentration at the percolation threshold and the relaxation exponent on complex shear modulus are observed to be $\phi_c \approx 0.033$ and $\Delta = 0.5$, respectively. Furthermore, transmission electronic microscopy (TEM) allowed the author [8] to visualize the scale of segregation of silica particles at different concentrations in EVA samples. As shown in Figure 14.2, the fumed silica is aggregated in clusters of elementary silica particles, and these clusters at high concentrations lead to the formation of a percolation-like filler network. Furthermore this percolation threshold was observed to be independent on the polymer chains regimes (entangled or Rouse regime). Inoubli *et al.* [13] observed for a polybutylacrylate nanocomposite filled with $\phi = 0.025$ that G' and G'' vary as $\Delta \approx 0.5$ in the intermediate part of the frequency spectrum. They reasonably estimated that $\phi = 0.025$ of the silica is very close to the percolation threshold. Moreover, Paquien *et al.* [14] concluded that percolation threshold values of fumed silica dispersed in PDMS are between $\phi = 0.01$ and $\phi = 0.02$.

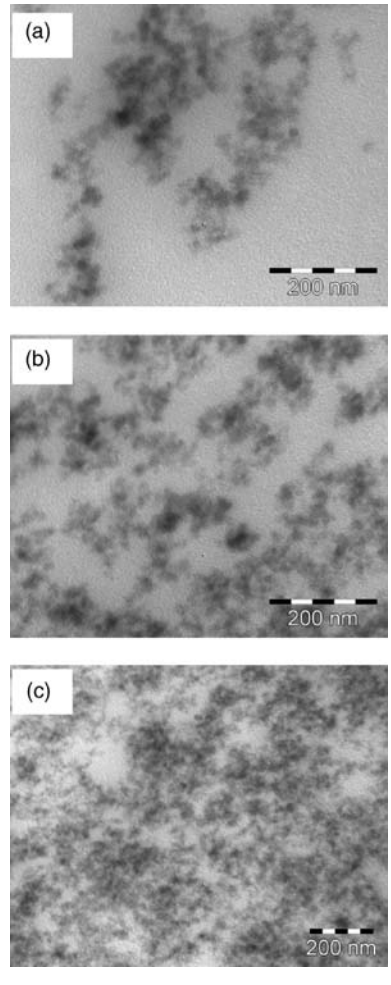

Figure 14.2 TEM pictures for different silica concentrations in EVA nanocomposites: (a) $\phi : 0.0075$ ($<\phi_c$); (b) $\phi : 0.034$ ($\approx\phi_c$); and (c) $\phi : 0.086$ ($>\phi_c$) [8] (Reprinted from *Polymer*, **44**, P. Cassagnau, "Payne effect and shear elasticity of silica-filled polymers in concentrated solutions and in molten state," 2455–2462, © 2003, with permission from Elsevier.)

Regarding carbon black-filled SBR, Mongruel and Cartault [9] and Leboeuf *et al.* [125] observed a percolation threshold situated between $\phi = 0.12$ and $\phi = 0.18$ with $\Delta \approx 0.5$. In contrast, Yurekli *et al.* [15] postulated, on the basis of the linear viscoelastic analysis, that the carbon black filler forms a continuous percolated network structure beyond 9% filler.

The percolation threshold of nanocomposites filled with organoclay platelets appears generally for concentration below $\phi = 0.01$. For example, Loiseau and Tassin [16] obtained for well defined laponite particles dispersed into a PEO matrix the formation of a gel above a critical volume fraction on the order of $\phi_c = 0.002$–0.004 depending on the protection of the particles. From a theoretical point of view, King *et al.* [17] equated the critical percolation threshold with the overlap of randomly oriented tactoids and taking into account the large

transverse dimension of the tactoids. They predicted the percolation threshold to be at or below $\phi = 0.006$ fraction of organoclay, which is consistent with the rheology data. Regarding nanocomposites filled with carbon nanotubes, Du *et al.* [18] and Zhang *et al.* [19] found percolation thresholds around $\phi_c \approx 0.012$ and $\phi_c \approx 0.005$ respectively. However, it is important to point out that some important discrepancies come from the determination methods of the sol-gel threshold. For example, Du *et al.* [18] used a power law function for G' (at a frequency of 0.5 rad/s) versus filler concentration to provide a rheological percolation threshold corresponding to the onset of solid-like behavior. Strictly speaking and according to the Winter and Mours [12] criteria, such method cannot be used to determine the percolation threshold.

Nevertheless, the rheological percolation threshold is actually influenced by several nanofiller factors: aspect ratio, dispersion (processing methods, surface filler treatments, compatibilizing agents), orientation or alignment and temperature. Figure 14.3 clearly shows that the linear viscoelastic response depends strongly on the silica particle interaction. Actually, the trends of storage modulus curves mean that the percolation threshold increases when the silica surface is modified by polymer grafting. Assuming that the original silica network structure at the origin of the percolation threshold can be attributed to particle–particle interactions, these interactions are broken down with steric repulsion of grafted chains. Consequently, the percolation threshold will be observed at higher concentrations due to a better dispersion of silica particles. On the contrary, the percolation threshold was observed to decrease with increasing the exfoliation (dispersion at the tactoïd scale) of nanocomposites filled with lamellar organoclays [10, 16]. Actually, it is a clear fact that the type of surface treatment or compatibilization of organoclays play a crucial role since the rheological behavior of such nanocomposites depends on the effective volume fraction, due to their ability to form large anisotropic structure. Regarding nanocomposites filled with nanotubes, such trends can be also expected. Indeed, the rheological behavior was reported to depend

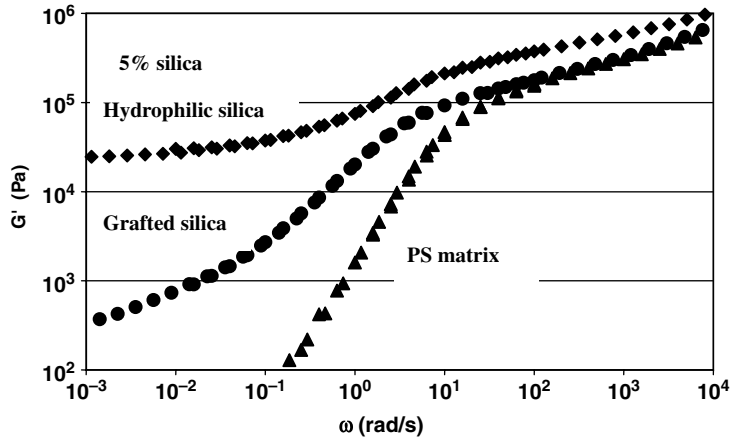

Figure 14.3 Variation of storage modulus versus frequency of PS nanocomposite filled with 5 vol% of silica and PS-grafted silica. Master curve at T = 160 °C [22] (Reprinted from *Polymer*, **46**, C. Bartholome, E. Beyou, E. Bourgeat-Lami et al., "Viscoelastic properties and morphological characterization of silica/polystyrene nanocomposites synthesized by nitroxide-mediated polymerization," 9965–9973, © 2005, with permission from Elsevier.)

on nanotube dispersion, aspect ratio and alignment under flow. By improving the CNT dispersion using functionalized single wall nanotubes, Mitchell *et al.* [20] observed that the percolation threshold dropped from 3 wt% to 1.5% in PS nanocomposites. Interestingly, Pötschke *et al.* [11] found that the percolation threshold is significantly dependent on temperature. Indeed, they observed that rheological percolation threshold decreases from approximately 5.0 to 0.5% carbon nanotubes upon increasing the temperature from 170 to 280 °C. However, their explanation based on the superposition of the entangled polymer network and the combined nanotube–polymer network is questionable. It could be also imagined that the dispersion of CNT is improved via a temperature effect on the miscibility of nanotube in polymer matrix. In a same way, Wang *et al.* [21] showed from polybutadiene/clay nanocomposite systems that the temperature can be a key controlling factor for the exfoliation and orientation-disorientation of clay particles. Actually, the polymer–filler interactions can be temperature-sensitive and therefore the percolation threshold can be also temperature-sensitive.

To conclude, the results on organoclays and carbon nanotubes are opposite to fumed silica and carbon black for which the critical threshold concentration is expected to increase with the dispersion of primary particles. Actually, as previously explained this is coherent with the formation of a gel through a network of aggregated particles dominated by the particle–particle interactions. This finding will be confirmed later by studies on the Payne effect.

14.2.3 Equilibrium Shear Modulus

The growth of the equilibrium elastic modulus after the percolation threshold can be described as a function of the volume concentration ϕ by

$$G_e \propto (\phi - \phi c)^t \quad \text{for } \phi > \phi_c \tag{14.1}$$

Actually, detection of the percolation threshold parameters such as G_e, seems to depend on very difficult and precise criteria which cannot be experimentally validated. However, we observed in a previous work on silica nanocomposites [8] that the predicted power law-dependency $G_e \propto (\phi - \phi c)^t$ with $t \approx 1.5$ is in agreement with some experimental results of the literature on carbon black-filled natural rubber [23], ($t \approx 1.56$) which qualitatively agrees the analogy of De Gennes [24] using a percolation model of a random conductor network ($t \approx 1.9$). Nevertheless, for PMMA filled with single wall carbon nanotubes (SWNT) Du *et al.* [18] found $t \sim 0.7$.

As extensively reported in the literature, the equilibrium elastic modulus (G_e) scales with the filler volume fraction as follows:

$$G_e \propto \Phi^m \tag{14.2}$$

It is expected that this power law exponent depends on particle–particle interaction. Indeed, the elasticity should increase more rapidly and the network become more resistive for elastomers filled with hydrophilic silica than for the hydrophobic ones. For example, Cassagnau [8] observed $m = 4.5$ for suspension of hydrophilic silica in EVA copolymer. Paquien *et al.* [14] observed for silica suspension in PDMS that m decreased from $m = 7.2$ to $m = 3.2$ depending on the silica surface treatment (from hydrophilic to hydrophobic). Zhu *et al.* [25] observed the scaling law $G_e \propto \Phi^{3.4}$ for polybutadiene filled with silica particles. Furthermore, Klüppel [26] and Heinrich and Klüppel [27] reported a power law close

$G_e \propto \Phi^{3.5}$ for carbon black-filled rubber. From works of Moniruzzaman and Winey (Figure 14.9a of their work) on nanocomposites filled with SWNT, the following power law has been derived: $G_e \propto \Phi^{1.35}$. Furthermore from the work of Pötschke *et al.* [11] on nancomposites filled with carbon nanotubes the respective power laws can be calculated: $G_e \propto \Phi^{0.3}$ and $G_e \propto \Phi^{2.0}$. This great discreapancy between these power laws on nanocomposites filled with carbon nanotubes is mainly due to the nanotube nature (purity, aspect ratio, single or multiwall) and their dispersion in the polymer matrix.

Furthermore, the scaling concept based on a fractal dimension, is generally used to study the effect of interparticle forces on the elasticity of aggregated suspensions [28–30]. To model the size dependence, the aggregates of silica particles are described as fractal structure with a characteristic size ξ which is the radius of the smallest particle containing N primary particles of radius a.

$$N(\xi) \approx \left(\frac{\xi}{a}\right)^{d_f}. \tag{14.3}$$

where d_f is the fractal dimension of the aggregate. Following this, the volume fraction of primary particle inside the aggregate is then:

$$\phi \approx \left(\frac{\xi}{a}\right)^{d_f-3} \tag{14.4}$$

Finally, the variation of the equilibrium storage modulus versus the volume fraction of silica can be estimated according to the characteristics of the nonfluctuating fractal structure [31] as follows:

$$G_o \propto \Phi^{\frac{5}{3-d_f}} \tag{14.5}$$

where d_f is the fractal dimension of silica clusters. Wolthers *et al.* [30] found $d_f = 2.25$ for stearyl-coated silica particles. Paquien *et al.* [14] observed a fractal dimension d_f equal to 2.3 for unmodified silica/PDMS composites. Furthermore, they demonstrated that the fractal dimension is very sensitive to the surface modification of silica as d_f can decrease to 1.4. However, Piau *et al.* [31] for silica–silicone physical gel and Cassagnau [8] for EVA/silica composite systems, reported values close to 1.8. This great discrepancy between data is mainly due to the different nature of the samples superposed to the various sample histories in the different experiments.

Heinrich and Klüppel [27] have considered an alternative network structure that refers to a space filling configuration of kinetically aggregated filler clusters: the cluster–cluster aggregation (CCA) model. This model is based upon the assumption that the particles can fluctuate around their mean position in a polymer matrix. Depending on the concentration of filler particles, a flocculation process of particles or clusters leads to a filler network that can be considered as space-filling configuration of fractal CCA clusters. From the calculation of the solid fraction of the fractal CCA clusters and assuming a rigidity condition for reinforcement of the polymer matrix, the authors derived the concentration dependence of the equilibrium elastic modulus:

$$G_e \propto \Phi^{\frac{3+d_{f,B}}{3-d_f}} \tag{14.6}$$

where $d_{f,B} \approx 1.3$ is the fractal dimension of the CCA cluster backbone and $d_f \approx 1.8$ is the fractal dimension due to the characteristic self similar structure of the CCA Clusters. Note that such an expression was already derived by Buscall *et al.* [32] and Shih *et al.* [33]. Equation 14.6 predicts a power law $G_e \propto \Phi^{3.5}$ confirmed [26, 27] by viscoelastic data obtained for carbon black filled rubbers. In the case of fumed silica, Paquien *et al.* [14] observed $G_e \propto \Phi^{4.2-7.2}$ depending on the silica surface nature (from hydrophilic to hydrophobic) and Cassagnau [8] found $G_e \propto \Phi^{4.5}$ for EVA nanocomposites filled with hydrophilic silica. These scaling laws are very close to the values found by Piau *et al.* [31] on silica-silicone gels $G_e \propto \Phi^{4.2}$ in agreement with a formulation of the nonfluctuating fractal concept (Equation 14.5). Nevertheless, it must be pointed out that these power laws are generally measured at a lower constant frequency so that G_e may be not the truly equilibrium elastic modulus. As a consequence, the accuracy and/or the validity of these power laws in some of the works are generally questionable. Furthermore, G_e must not be mistaken for the rubbery plateau modulus G_N^0 at high frequency. The dependence of this modulus on the filler concentration is generally modeled with the Guth-Smallwood equation (for instance, see the work of Yurekli *et al.* [15]).

These results can be completed with some works on thermoplastic nanocomposites filled with organoclays. Vermant *et al.* [34] measured $G_e \propto \phi^{4.8-6.0}$ depending on polymer matrix and Durmus *et al.* [10] observed $G_e \propto \phi^{3.34-3.48}$ depending on the compatibilizer nature. These scaling laws are close, or at least in the same order of magnitude, to those previously reported on silica nanocomposites. Note that these authors [10, 34] used the power law in Equation 14.6 to calculate d_f from experimental variation which allowed them to discuss on clay dispersion with a less or more open fractal structure of the samples. Nevertheless, most of the studies have been focused on the power law variation of equilibrium modulus neglecting the importance of the front factor G_p of this power law ($G_e = G_p \phi^m$). As discussed by Heinrich and Klüppel [27] G_p is the averaged elastic bending-twisting modulus of the different kinds of angular deformation of the cluster units. Actually, G_p depends on the dynamic relaxation regime of the polymer chains and consequently on the particle-particle and particle-polymer interactions. Furthermore, the effect of bound rubber on the elastic modulus can be expressed by introducing an effective solid volume of the clusters. If d is the particle size and Δ the bound rubber layer of a primitive spherical particle, Heinrich and Klüppel derived the following equation:

$$G_e = Gp\left(\frac{(d+2\Delta)^3 - 6d\Delta^2}{d^3}\Phi\right)^{\frac{3+d_{f,B}}{3-d_f}} \tag{14.7}$$

Consequently, more particular attention should be paid to this front factor as a master curve of the variation of the equilibrium modulus versus the effective volume fraction $\frac{(d+2\Delta)^3 - 6d\Delta^2}{d^3}\Phi$ is expected.

14.3 Payne Effect

The famous effect of strain amplitude dependence of the dynamic viscoelastic properties of filled polymers is often referred to as the Payne [1, 2] effect. Actually, the Payne effect was first reported for carbon black reinforced rubbers and extensively studied on filled elastomers [27, 35] and thermoplastic composites [4, 125]. As previously discussed about the linear viscoelastic properties, the mechanism for reinforcement and nonlinearity can be based on two conceptual aspects. The concept of filler networking yields a good interpretation of the Payne

effect for filled elastomers. For example, common features between the phenomenological agglomeration–disagglomeration and recent microscopic networking approaches (particle–particle interaction) were discussed by Heinrich and Klüppel [27]. The excess of dissipated energy is attributed to the breakdown of particle structure. Consequently, filled elastomers can be drastically modified under large deformation and the viscoelastic properties are then governed by filler–structure breakdown and build-up.

A direct experimental support for this concept was reported from electron microscopy studies [36] on elastically stretched chain-like aggregates of inorganic oxides. The concept of the temperature- and deformation-dependence of the modulus as a consequence of the variation of the topological constraint density (polymer-particle interaction) at the filler/polymer interface was reported by Maier and Göritz [37]. Sternstein and Zhu [38] suggested a common mechanism that is rooted in the macromolecular natures of the matrices. Their experimental results demonstrated that the nonlinearity effect is strongly dependent on the filler surface treatment as already suggested by Aranguren *et al.* [39]. Actually, silica fillers have the advantage to be chemically modified and the influence of surface treatment on nonlinearity and polymer reinforcement can be easily studied. Parent *et al.* [40] showed that surface modification of silica reduces the surface energy of the filler leading to a prevention of particle agglomeration. However, the consequence is a decrease in the reinforcing properties resulting from an improvement in filler dispersion. Such a result was also reported for PS/Silica nanocomposites [22, 40]. The authors showed that the modification of precipitated silica with long chains alcohols or amines reduces the surface energy of the filler leading to a reduction in the extent of particle agglomeration. These observations reinforce the idea that the moduli and limit of linearity are related to the fraction of exfoliated layers or silica clusters that form a fractal structure. Figure 14.4 depicts these different contributions to the storage modulus and linear strain limit.

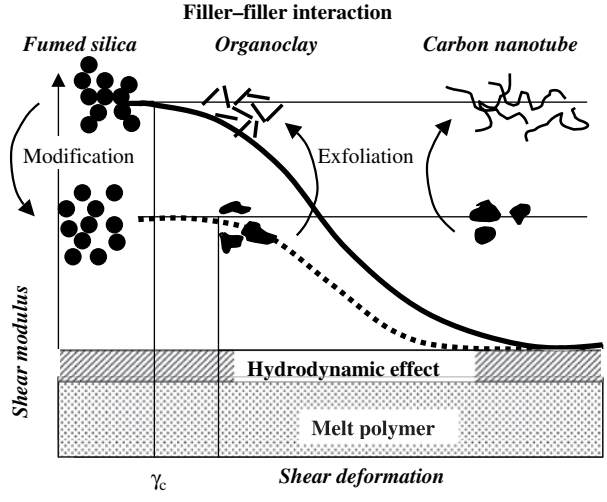

Figure 14.4 Different contributions to the complex shear modulus versus strain for elastomers filled with different types of filler at two levels of dispersion (Adapted from H.D. Luginsland, J. Fröhlich, and A. Wehmeier, "Influence of different silanes on the reinforcement of silica-filled rubber compounds," *Rubber Chemistry and Technology*, **75**, 563–564, 2002. © 2002 American Chemical Society [42].)

Actually, our discussion is consistent with works on elastomer reinforcements [43] and well known practise in rubber industry and compounding control so as to obtain optimal dispersion of fillers without completely suppressing their aggregation into larger structure. In other words, a fractal structure of fillers is required to get the best balance of reinforced properties. Another argument generally put forward to explain this phenomenon is that polymer chains are partly adsorbed on the filler surface and partly entangled with neighboring ones (bound rubber). In the same idea, Parent *et al.* [40] came to the conclusion that the decrease in the reinforcing potential of modified filler was mainly due to excessive molecular slippage under an applied load. This finding was also supported by viscoelastic experiments showing that the linear low frequency modulus of the composites decreased spectacularly when the particles were chemically treated with organosilane [42, 44]. However, the density of chains adsorbed in the bound rubber zone and their conformation at the filler surface are generally quite difficult to access even though measuring bound rubber is a simple technique in principle [3]. With regard to fumed silica, the adsorption of PDMS chains comes from the formation of hydrogen bonds between oxygen atoms belonging to chains sketelons and silanol groups on the surface of the fillers.

If the Payne effect has been deeply studied for carbon black- and silica-filled elastomer nanocomposites, few works have been reported on the organoclay systems and the nonlinearity effect associated with tactoids fillers is generally poorly discussed. Furthermore, as nanocomposites show thixotropic behavior, the value of the maximum strain defining the linear region depends on pre-shear history (intensity and time) of the composite so that rigorous experimental protocols must be applied.

14.3.1 The Limit of Linearity

As a consequence of the Payne effect, the limit of linearity γ_c decreases with increasing the volume fraction of particles according to the following power law:

$$\gamma_c \propto \phi^{-v} \tag{14.8}$$

Regarding silica particles, different experimental works [45, 46] reported on the v exponent values for low viscosity liquid suspensions. For polymer nanocomposites, few power laws have been reported. According to works from Zhu and Sternstein [47] and Sternstein and Zhu [38] we found $v = 2.4$ and $v = 3.0$ for hydrophobic and hydrophilic silica respectively. According to our previous work [41] we calculated $v = 1.7$, as shown in Figure 14.5. Interestingly, Paquien *et al.* [14] observed that, when the silica grafting ratio increases and the silica becomes more hydrophobic, the Payne effect is reduced in PDMS/silica nanocomposites, that is, the critical strain separating the linear and nonlinear regimse increases with increasing the hydrophobic treatment of the silica. Such a result was also reported by Clement *et al.* [48] who showed that the amplitude of the Payne effect is reduced by introducing a permanent treatment of the silica surface or a processing aid.

Only a few works have recently been reported on the nonlinearity of clay–rubber nanocomposites. As expected, the maximum strain to which the linear viscoleastic domain extends was observed to be decreased with increasing clay concentration [49]. However, most of the works have addressed on thermoplastic nanocomposites. Aubry *et al.* [50] first observed $\gamma_c \propto \phi^{-1}$ in polyamide-12 with layered silicate. Such a scaling relation was also reported by

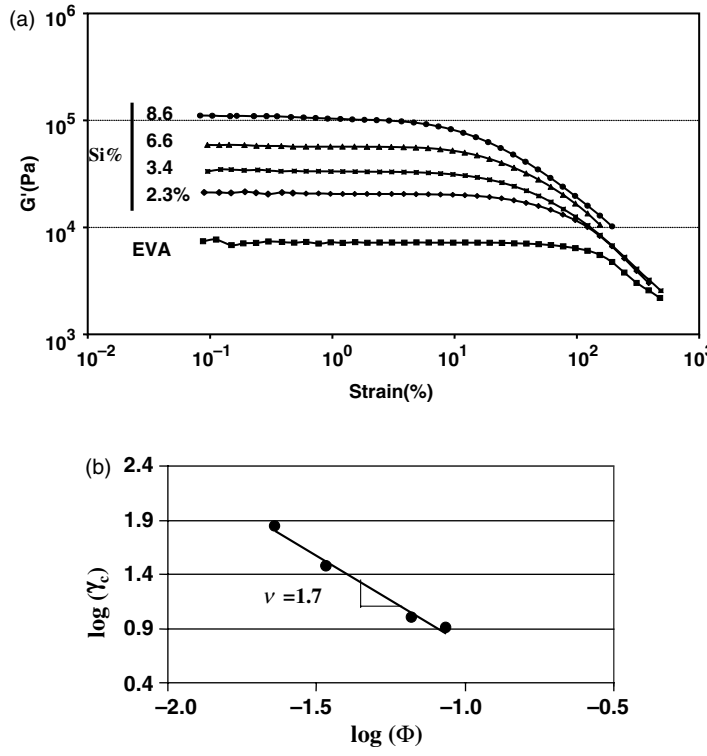

Figure 14.5 Payne effect in fumed silica composites: limit of linearity. (a) Variation of the storage modulus versus deformation at different silica concentrations in a copolymer of ethylene and vinyl acetate. $\omega = 10$ rad/s, T = 140 °C [41] (Reprinted from *Polymer*, **44**, P. Cassagnau and F. Mélis, "Non-linear viscoelastic behaviour and modulus recovery in silica filled polymers," 6607–6615, © 2003, with permission from Elsevier) and (b) Power law on the limit of linearity γ_c

Raghavendra *et al.* [51] in the case of metallocene polyethylene montmorillonite composites. More recently, Durmus *et al.* [10] observed $v = 0.85$–1.1 in LLDPE/montmorillonite nanocomposites depending on the compatibilizers nature. Finally, Vermant *et al.* [34] showed $v = 1.8$–1.9 for the power variation of the limiting strain as a function of particle concentration. Interestingly, Letwimolnun and Vergnes [52] and Letwimolnun *et al.* [53] showed that the linear viscoelastic domain, at the same concentration of organoclay, decreased with increasing the exfoliation degree of tactoids. Consequently, the decrease of linear viscoelasticity can be attributed to the difference in the degree of dispersion and more precisely the degree of exfoliation. This result is of im-portance as it shows again that the linear viscoelastic properties of nanocomposites are governed by the particle–particle interaction of tactoid physical network in the case of organoclay fillers.

According to the paper of Yurekli *et al.* [15] on carbon black-filled elastomer composites, we derived from their work the power law $\gamma_c \propto \phi^{-1.8}$. Finally, Chatterjee and Krishnamoorti [54] reported $\gamma_c \propto \phi^{-2.3}$ for nanotube–poly(ethylene oxide) nanocomposites. The authors concluded that the weak and relatively short-range interactions between nanotubes and the pathways between percolating paths dominate the network properties. This conclusion is consistent with

the mechanism of particle–particle interaction between fillers to explain the nonlinearity effect in nanocomposites.

As previously discussed for the equilibrium shear modulus, Shih *et al.* [33] developed a scaling theory for this limit of linearity γ_c. The critical strain values follow:

$$\gamma_c \propto \phi^{\frac{-(1+d_{f,B})}{3-d_f}} \tag{14.9}$$

The fractal dimension $d_f \approx 2$ is universal for gel aggregate systems whereas $d_{f,b}$, which depends on the number of particles per aggregates, strongly depends on the shape of fillers (spherical or tactoids). Note that these power exponents are extremely sensitive to the experimental criteria used by the authors.

14.3.2 Thixotropy and Recovery

Another important aspect in the mechanisms of nonlinear viscoelasticity in filled polymers is the restoration of moduli of the filler/polymer network following the destruction by a large strain perturbation. Actually, the Payne effect is a reversible process and the material should undergo recovery of its original equilibrium structure. Under steady shear flow, the gel-like particle structures are disrupted and take a long time to recover the original structure. This phenomenon, generally called thixotropy, is really a kind of viscoelasticity [55] but with a long relaxation time of a few hours. Different kinds of rheological experiments are used to quantify the thixotropic effects resulting from the presence of nanofillers. Transient shear flow [56–59], stress relaxation [60] and creep [61] experiments have been successfully developed to investigate the evolution of filler structure under flow. Furthermore, the transient stress in start-up of steady shear combining forward and reverse growth experiments are also useful to characterize the evolution of the fillers microstructure. The recovery of the gel structure is then studied by defining different rest times in forward and reverse growth experiments [53, 56]. The structural recovery can be also measured by measuring the linear viscoelastic properties after cessation of different pre-shear rates and applied rest times. In dynamic conditions, after a step strain experiment the recovery of the complex shear modulus is measured in the linear domain of viscoelasticity. This experiment is generally called subsequent strain sweep experiments [41, 62]. In contrast, Zhu *et al.* [25] used oscillatory shear tests in the sequence of low, high and low amplitude to study the Payne effect of silica nanocomposites All these experiments in steady and/or dynamic conditions aimed at investigating the influence of the relevant parameters (polymer–filler interactions, polymer molecular weight, temperature, and so on) on the dispersion and orientation–disorientation of fillers under flow. Nevertheless, it must be pointed out that transient shear experiment can be only used to investigate the thixotropic behavior of liquid suspensions and the usual thermoplastic polymers. In the case of the reinforcement of elastomers, which generally show complex viscoelastic properties in the terminal relaxation zone combined with strong temporary elasticity, dynamic and subsequent dynamic experiments are generally preferred.

In dynamic conditions, the strain amplitude dependence of the dynamic modulus is caused by a thixotropic change of the filler–network structure. Such process is accompanied by the recovery of the complex shear modulus which is measured in the linear domain of viscoelasticity. Modulus recovery kinetics of elastomers filled with fumed silica have extensively been studied by the Sternstein's group [47, 62]. They proposed that the recovery mechanism is based

entirely on the dynamics of the filler–matrix interface and consequently on the physics of entangled chains. However, the agglomeration or network formation can be invoked especially at high filler concentration. In a same way, Kalfus and Jancar [63] showed that the modulus recovery time was governed by the chain relaxation processes in the polymer matrix near the filler surface. This process was successfully interpreted using the reptation concept of molten entangled chains. Consequently, filler agglomeration and/or network is less important, representing only a secondary contribution to the nonlinear viscoelastic response of a nanocomposite. Nevertheless, we reported in a previous paper [8] viscoelastic behavior of fumed silica particles dispersed in polymer organic solutions, from diluted solution to molten polymer, and the nonlinear behavior could be then imagined [41] to be associated with both mechanisms of chain disentanglements and filler network breakdown, depending on silica concentration, silica surface treatment and amplitude deformation. This point was earlier discussed on linear viscoelastic behavior and our findings confirmed the main conclusion of Bokobza [64] and Sternstein and Zhu [38]. In other words, the nonlinearity effect is probably governed by the filler–network breakdown (particle–particle interaction) combined with a mechanism originating at the polymer–filler interface (polymer–particle interaction). More recently, Zhu *et al.* [25] clearly showed that the particle–particle association is the dominant factor as the filler network broke down during the shear. In addition they observed that the particle–particle dissociation is partially immediately recovered upon switching to dynamic linear deformation. Consequently, the nonlinearity effect is predominantly governed by the filler network breakdown (particle–particle interaction) combined with a second order mechanism originating at the polymer–filler interface (polymer–particle interaction).

In the case of organoclay–elastomer composites few works have been reported in the open literature. However, it can be said that the governing parameter for the structural evolution of the clay network under large deformation is *a priori* the degree of exfoliation which controls the structure of platelet network. Recently, Wang *et al.* [21] showed from liquid polybutadiene/clay nanocomposite systems that the temperature can be also a key controlling factor for the exfoliation and orientation–disorientation of clay particles under large deformation. Actually, the polymer–clay interactions are temperature-sensitive. The system behaves as a system with a liquid–gel transition. This transition depends strongly on the end groups, molecular weight of the liquid rubber and the shear field. The determination of the transition temperature is then very useful for the preparation of liquid rubber/exfoliated clay nanocomposites. At room temperature, the clay is partially exfoliated and complete exfoliation is achieved when heating above this temperature transition ($T \sim 80\,^{\circ}C$) with or without shearing.

14.4 Flow Properties of Rubber Nanocomposites

As demonstrated in Sections 14.2 and 14.3 above, the presence of nanoparticles induces some new features in the linear or nonlinear viscoelastic properties of the elastomer, like the solid-like behavior at low frequencies or the thixotropy and recovery effects, or simply enhances its nonlinear behavior. Such observations have sustained a better understanding of the connexions between microstructure and viscoelastic properties of rubber nanocomposites (although controversial discussion still remains) and have supported the development of models for the description and prediction of these properties. The following sections deal with the present knowledge and understanding of the influence of nanoparticles on the flow properties of an elastomer matrix. It must be noted that the related research work reported in the open literature

mainly concerns carbon black or silica-filled elastomers. Indeed, those have gained for decades a large industrial importance, whereas rubber nanocomposites have been considered only for a few years. As in the preceding sections, general trends will be illustrated and discussed, and more specific aspects, depending on the nature of the matrix-filler system, will be emphasized.

From a practical point of view, polymer-processing tools create steady-state or transient flow conditions in which the material experiences large deformations and large deformation rates. In such situations, filled polymers and more specifically nanocomposites exhibit complex rheological properties, so the description of their flow behavior is still a challenge. From a fundamental point of view, this requires to understand how the nanofiller particles modify the properties of the polymer matrix. Due to the very nature of the flow conditions, the influence of the nanofiller nature or concentration on the shear viscosity, measured either in steady state or in transient conditions like those met in start-up experiments, is expected to be different from the effects described previously on viscoelastic properties measured in oscillatory shear. So, shear viscosity will be addressed first in this section, and next will be extensional viscosity. Then, "new" rheological features (with respect to pure polymer matrix), that is, those features induced by the presence of nanofiller particles which were discussed previously under the angle of linear and nonlinear viscoelasticity, will be briefly dealt with in the framework of steady flow. Finally, other phenomena, like wall slip and extrudate swell will be discussed in terms of the filler influence.

14.4.1 Shear Viscosity

Unlike thermoplastic polymers or soft elastomers that have been the subject of extensive research, relatively few rheological studies are devoted to rubbers. This is due to several experimental problems met during rheological characterization of this class of materials, such as high viscosities, wall slippage and long-time evolution of properties. As a consequence, a limited number of relevant rheological studies on filled rubbers are available in the literature, and rheological data must be analyzed with care. Due to their industrial history, carbon black-filled rubbers have been studied for long, and they induced the development of some specific rheological devices, for the reasons cited above. Thus, prototype instruments such as a sandwich rheometer for low stress creep tests [65], a modified Mooney viscometer [66] or modified Weissenberg rheometer [67], or a sliding cylinder rheometer [68], were built to offer new experimental capacities.

14.4.1.1 Carbon Black- and Silica-Based Rubber (Nano)Composites

As pointed out in a recent review [3], the reinforcing fillers most commonly used with elastomers, namely carbon blacks and high-structure silane-treated silicas, are very different, specifically with regard to their interactions with the polymer, but induce the same qualitative trends of the flow properties, though (see for example the work carried out in parallel with carbon black and silica by Mongruel and Cartault [9]). Therefore, addressing these materials first will help to derive the main lines of the viscous behavior of rubber nanocomposites, before illustrating specific points with other nanofillers in Section 14.4.1.2. Data published by Montes *et al.* [66], displayed in Figure 14.6, illustrate these features which can be summarized as follows:

- At low shear rates (or stresses), the compounds with low filler fractions exhibit a Newtonian plateau and the dependence of the zero-shear viscosity on the volume concentration of

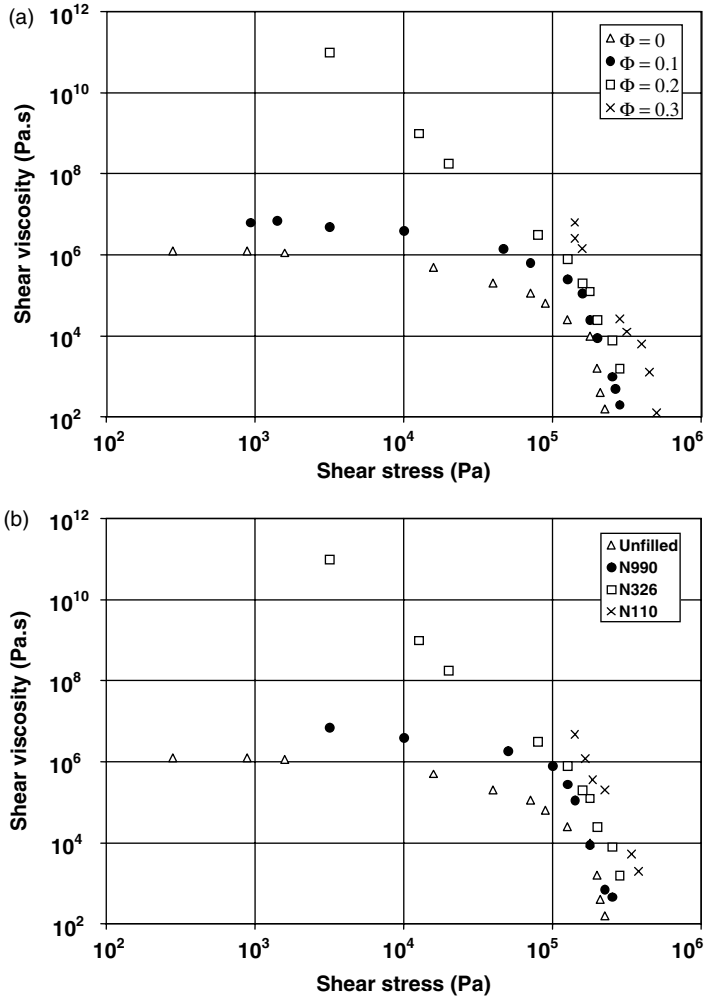

Figure 14.6 Evolution of shear viscosity of natural rubber (NR) compounds versus shear stress, at 100 °C. (a) Unfilled NR and NR compounds with different volume fractions Φ of N326 carbon black (surface area = 80 m^2/g) and (b) Unfilled NR and NR compounds with Φ = 0.2 of carbon blacks with increasing surface area, from 8 m^2/g (N990) to 140 m^2/g (N110) (Data reproduced from *Journal of Non-Newtonian Fluid Mechanics*, **28**, S. Montes, J.L. White and N. Nakajima, "Rheological behavior of rubber carbon-black compounds in various shear-flow histories," 183–212, © 1988, with permission from Elsevier [66].)

particles can be described satisfactorily by hydrodynamic models as those used in suspension rheology. When increasing the filler concentration, the Newtonian plateau is no longer observed and yield behavior occurs (cf. Figure 14.6a).

- At large strain rates or stresses, a shear thinning behavior is observed, and the viscosity is much less sensitive to the filler volume fraction than in the low shear rate range.
- The increase of carbon black surface area (decrease of particle size) at constant loading has qualitatively similar effects as the increase of particle concentration, as shown in

Figure 14.6b: increase of viscosity, and transition towards yielding behavior as particle size decreases.

Influence of the Incorporation of Filler Particles on the Low Shear Rate Viscosity

The occurrence of a yield stress with highly filled compounds will be discussed briefly in Section 14.4.3.

As mentioned above, the incorporation of solid particles strongly influences the low shear rate viscosity. Elastomers filled with carbon blacks comprising large, structureless and roughly spherical aggregates, at volume fractions below the percolation threshold, exhibit Newtonian behavior at low shear rates, and their zero-shear viscosity conforms well to the Guth and Gold relation [69]:

$$\eta_0(\phi) = \eta_{0,\text{polymer}}.\mathrm{F}(\phi) \quad \text{with} \quad \mathrm{F}(\phi) = 1 + 2.5\,\phi + 14.1\,\phi^2 \tag{14.10}$$

However, this equation does not hold for small structured particles black, even in Newtonian polymeric medium. Kraus [70], reviews some attempts to improve the description of viscosity increase in polymers filled with highly reinforcing carbon blacks, by introducing shape factors for example, but also mainly by introducing the concept of effective filler volume concentration, which takes into account the combined volumes of the filler particles and of the unextractible polymer fraction. This concept was extensively developed by Pliskin and Tokita [71], and involves the notion of bound rubber, which is viewed by these authors as a layer of polymer strongly adsorbed on the particle surface and covering the latter as a rigid layer of uniform thickness. The "filler" volume fraction can now be considered as the sum of the respective fractions of the particles and bound rubber, which yields the so-called effective volume fraction (a more detailed analysis of the bound rubber concept is given by [3]). White and Crowder [72] give a general form of the concentration-related factor that they introduce in their continuum mechanics analysis of suspensions of particles (carbon black) in viscoelastic media (synthetic rubbers):

$$\mathrm{F}(\phi) = (1 + \alpha_1 \mathrm{f}\phi_e + \alpha_2 \mathrm{f}\phi_e^2 + \cdots) \tag{14.11}$$

where ϕ_e is the effective volume fraction, f is an anisotropy factor and α_1 and α_2 are empirical coefficients depending on the system under study.

Such relations fail for filler volume fractions increasing beyond the percolation threshold of the particles, because at low shear rates the effects of particles become dominant over those of the matrix: the dynamics of the latter is modified by increasing interparticle forces, and solid-like behavior occurs. This was discussed in detail in Section 14.2 and will be briefly completed in Section 14.4.3.

Influence of the Filler Loading at High Shear Rates

In contrast to the preceding statement, when strain rates are high enough, highly filled polymers demonstrate usual viscoelastic behavior as unfilled polymeric liquids. Several authors illustrate the effects of increasing carbon black or silica concentration on the steady-state, shear thinning viscosity of elastomers, for example (this list is not exhaustive): White and Crowder [72], Osanaiye *et al.* [73], Ertong *et al.* [67], Bandyopadhyay *et al.* [74], Mongruel and Cartault [9]. The general pattern of the plots for different concentrations remains similar, which demonstrates that no qualitative change of rheological behavior occurs. Shifting of the plots over one another is possible. In this respect, the work by Mongruel and Cartault is worth examining in more

details, since it proposes an original analysis of the "concentration scaling" in the nonlinear viscoelastic domain and more specifically of the flow curves.

The authors deal with carbon black- and silica-filled SBR compounds with filler volume fractions ranging between 0.05 and 0.23 (the volume fraction at percolation, ϕ_p, for these fillers lays between 0.12 and 0.16). They first introduce a concentration shift factor $f(\phi)$ defined as the ratio $[G'(\omega,\phi)]/[G'(\omega,\phi=0)]$, where $G'(\omega,\phi)$ is the storage modulus measured in the linear viscoelastic domain for a compound with filler volume fraction ϕ. They demonstrate that $f(\phi)$ is also equal to $[G''(\omega,\phi)]/[G''(\omega,\phi=0)]$ and remains independent upon angular frequency ω. The Guth and Gold equation fails in modeling the evolution of f for $\phi > \phi_p$ whereas the Krieger-type relation $f(\phi) = \left(1-\frac{\phi}{\phi_m}\right)^{-2}$ [75], used in the framework of suspension rheology, succeeds in fitting the data over the whole range of ϕ. This concentration shift factor is then used to rescale the viscosity curves in the nonlinear domain (see Figure 14.7a). Interestingly, when plotting $\eta(\dot{\gamma},\phi,T)/f(\phi)$ versus $\dot{\gamma}\cdot f(\phi)$, a reasonable mastercurve is obtained over the whole range of shear rates for filler volume fractions ϕ below the percolation threshold, whereas for the most filled compounds ($\phi > \phi_p$), the superposition only holds in the low to medium shear rate range. The plots separate in the highest shear rate domain. When plotting the graph of the shear stress versus $\dot{\gamma}.f(\phi)$ (Figure 14.7b), again the superposition fails for the most filled materials at highest shear rates, which correspond to stress values beyond a critical value of about 0.3 MPa. The explanation proposed as most probable is that the data collected for compounds containing filler fractions beyond percolation have been obtained under slip conditions.

Finally, the same shift factor is shown to rescale satisfactorily the damping function $h(\gamma,\phi)$ which is derived from the factorization of the relaxation modulus measured in the nonlinear domain [principle of time strain separability: $G(t,\gamma,\phi) = G_0(t,\phi)\cdot h(\gamma)$]. The authors' conclusions can be summarized as follows:

- At large strains or strain rates, the rheological behavior shows qualitatively the same trends as for unfilled rubber, suggesting that the particles do not alter qualitatively the dynamics of the polymer chains.
- A single concentration shift factor, analogous to the one used for Newtonian suspensions, can rescale different viscoelastic functions of filled materials.
- In practice, this concentration scaling factor can be used to assess the presence or not of slip in capillary rheometer data.

These conclusions emphasize the need for critical analysis of rheometric data which can be altered by slip occurrence. Nevertheless, the latter is scarcely assessed rigorously in published studies concerning rubber nanocomposites.

Influence of the Polymer–Filler Interactions on Flow Properties

In the preceding sections, the rheological properties of filled polymer melts have been shown to be sensitive not only to the concentration, but also to the structure, particle size, shape and surface characteristics of the fillers. In particular, these parameters influence the dispersion and consequently the characteristics of the "filler network" resulting from interparticle interaction. This network in turn affects the viscoelastic and flow properties. A typical illustration comes from the comparison of silica filled composites, either prepared by mixing, or elaborated by *in situ* generation of the nanoparticles. As pointed out by Bandyopadhyay *et al.* [74], the viscosity value of "*in situ*" nanocomposites is not so strongly influenced by filler volume fraction as it is

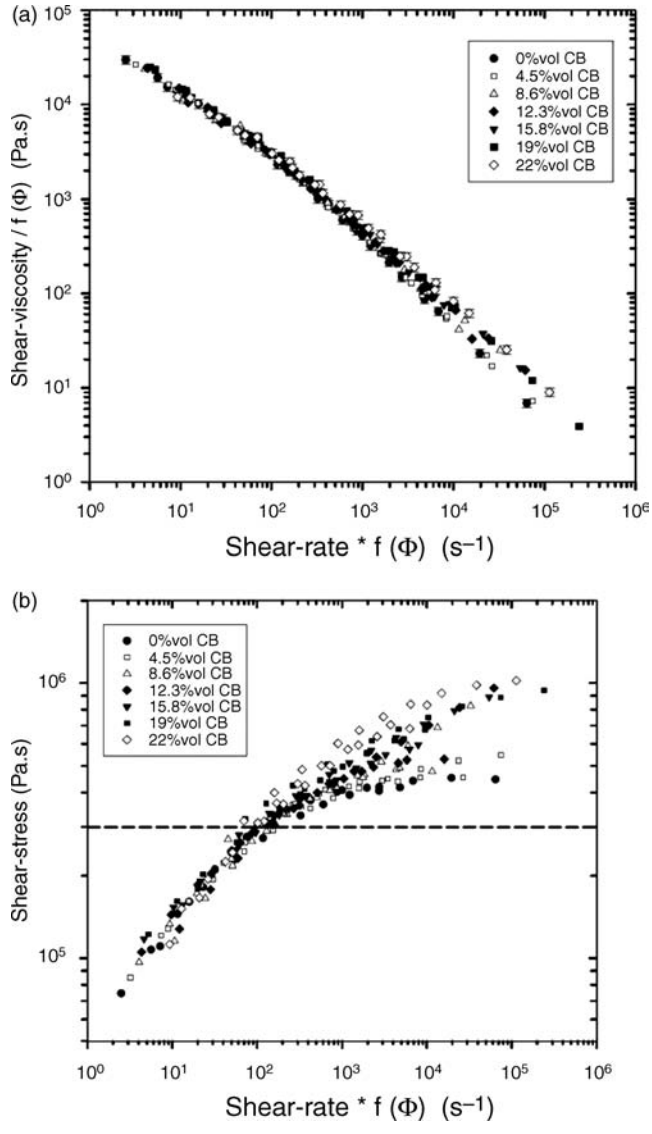

Figure 14.7 Rescaling of time–temperature master curves at 100 °C obtained for SBR1500 compounds with different N330 carbon black volume fractions Φ, using the concentration shift factor $f(\Phi)$: (a) shear viscosity versus shear rate (Reproduced with permission from A. Mongruel and M. Cartault, "Nonlinear rheology of styrene-butadiene rubber filled with carbon-black or silica particles," *Journal of Rheology*, **50**, no. 2, 115–135 (Figure 11a), © 2006 by The Society of Rheology, Inc. All rights reserved) and (b) shear stress versus shear rate [9] (Reproduced with permission from A. Mongruel and M. Cartault, "Nonlinear rheology of styrene-butadiene rubber filled with carbon-black or silica particles," *Journal of Rheology*, **50**, no. 2, 115–135 (Figure 11b), © 2006 by The Society of Rheology, Inc. All rights reserved.)

with composites prepared by mixing. The latter are prone to larger viscosity increase due to agglomeration of the filler.

Leblanc [3] defines bound rubber as the macroscopic result of rubber–filler interactions and discusses its effect on flow properties in the particular case of the Mooney viscometer test which is widespread in the rubber industry. Especially, the initial stage of the test can be considered as a simple shear start-up flow, and induces a stress overshoot with highly filled materials. Leblanc's results with carbon black-filled compounds clearly show a correlation between the height of this peak and the bound rubber fraction, whatever the elastomer considered: the higher the bound rubber, the higher the overshoot, for a given polymer-filler pair. This is corroborated by the results that Schaal and Coran [76] obtained on the same type of measuring device, at a 100-fold lower rotation speed ($\dot{\gamma} = 0.052\,s^{-1}$) and with silica-filled SBR. In a subsequent study, these authors [77] developed a rheological model to predict a simple shear start-up flow with silica-filled tire compounds. Their model describes the effect of the evolution of bound rubber (upon storage) on rheology, and is consistent with the interpretation that the peak stress at low strain rates may be considered as a yield stress, whose existence results from a network structure which develops upon filler incorporation.

Analysis of transient flows can thus be seen as an interesting probe regarding the structure of filled systems, and studies with other nanocomposites (PP + clay) rely on the same approach [53, 56].

However, these works were carried out at low strain rates. In high-strain rate flows, the effect of rubber–filler interaction, visible through the network structure which it creates, is expected to be strongly attenuated if not cancelled due to breakdown of this structure. Indeed, as shows Leonov [78] in his approach of the rheology of highly filled polymers, when strain rates in the filled systems are high enough, the effects of activity of the filler on the rheological behavior of the composites are almost negligible.

Comparisons between different systems must be carried out with care, though, since variations in rubber–filler interaction influence structure and properties via very complex mechanisms. The work of Kim and White [79] typically illustrates this statement. The authors compare untreated silica-filled EPDM with compounds of EPDM and the same silica treated with silanes of different chemical nature or chain length, at the same filler volume fraction and submitted to the same mixing procedure. The viscosity is measured over the $0.1–1.0\,s^{-1}$ decade and exhibits strong shear thinning. The very clear effect of silanization is to reduce significantly the viscosity with respect to untreated silica. Nevertheless, since all parameters vary simultaneously, especially the size of the agglomerates, the state of dispersion, the interparticle interactions and the physicochemical nature of the particle–polymer interactions, no straightforward conclusion regarding the mechanisms of such reduction can be drawn.

Influence of Compound Preparation

The crucial influence of the filler network on the viscoelastic and flow properties of rubber compounds has been emphasized along the preceding sections. The features of this filler network are due obviously to the nature of the polymer and to the chemical and physical characteristics of the filler, but also to the extent of the dispersion achieved. As pointed out by Wang [126], filler networking, that is, the creation of a secondary structure resulting from interaggregate interactions (agglomeration), is governed by the aggregate–aggregate interaction, the aggregate–polymer interaction and the distance between aggregates. Thus, the quality

of the filler microdispersion results from a complex combination of thermodynamic factors (surface energies and interactions between materials), kinetic factors (diffusion mechanisms controlled basically by the polymer viscosity and the size of the particles) and the mechanical and thermal energy input from the mixing operation.

Thermodynamic factors are responsible for example for the fact that in compounds filled with silica or carbon black, with the same surface area and comparable structure, the shear viscosity is higher for the silica-filled compound than for its carbon black counterpart. The most widely accepted explanation, summarized by Wang, considers the strong hydrogen bonds between silica aggregates, which causes a stronger filler network compared to carbon black, and the lower filler–polymer interaction achieved with silica, causing lower bound rubber and thus facilitating filler flocculation.

The relations between the mixing conditions, the morphology of the dispersions and the rheological properties were studied for example by Clarke and Freakley [127], who chose the mixing time as the variable for their analysis of a single system (SBR + N330 carbon black). A reduction in viscosity during the mixing process was observed concomitantly with a disagglomeration of the carbon black, as shown by micrographs of thin sections of the samples collected. Contrary to usual phenomena observed with colloidal suspensions in which the reduction of particle size below 1 μm generally induces an increase in viscosity, Clarke and Freakley's results are interpreted with reference to the notion of effective filler fraction. In the early stage of mixing, the agglomerates are supposed to contain immobilized rubber in the spaces within and between the primary aggregates of carbon black, and this immobilized rubber behaves as part of the filler particle. With mechanical mixing going on, agglomerates are broken down and release aggregates as well as part of the immobilized rubber fraction. This causes the effective filler fraction to decrease and then the viscosity of the blend to decrease, too. Simultaneously, mastication of the elastomer causes reduction in the matrix viscosity. Sirisinha and Sittichokchuchai's results [129] seem to confirm the concept based on immobilized rubber accompanying viscosity reduction with increasing state-of-mix, and show concomitant decrease of bound rubber.

Wang's review [126] also deals with the influence of the mixing process, in a different manner. Traditional mixing and intensive mixing are compared. Traditional mixing consists in a first stage where all components are added except the curatives, which are added in a second stage 24 h later. Intensive mixing involves exactly the same two stages but a third one is added in between, during which the first stage masterbatch is mixed again and maintained 5 min at high temperature, then aged an additional 24 h prior to the final stage of curatives incorporation. Quoting the work carried out by Welsh *et al.* [80], Wang emphasizes the apparent contradiction between the increase in the bound rubber measured on SBR samples mixed intensively and the reduction in viscosity of these compounds, compared to traditionally mixed ones. It is suggested that the effect of increased bound rubber, expected to increase the viscosity, would be overcompensated by a less structured architectural complex of filler aggregates in the polymer matrix. That is to say that the filler networking effect seems to be attenuated when bound rubber is increased.

Whereas the phenomenological interpretations are quite consistent between authors, two majors remarks can be made:

- When comparing Sirisinha and Sittichokchuchai's results [129] on bound rubber evolution during mixing (decrease along time) and the increased bound rubber pointed out by

Welsh *et al.* [80] when intensive mixing is applied, one could feel some contradiction. However, it must be carefully considered that the state of mix achieved is totally different between both studies. In the former, initial samples are poorly mixed and contain a supposedly large fraction of immobilized rubber, which probably takes part in the measured "bound rubber" under different forms, as mentioned by the authors: either occluded within inter- or intra-aggregate spaces, or bound, or both. Due to disagglomeration, part of it is then released and does not contribute any longer to the bound rubber fraction. In Welsh's study [80], intensively mixed compounds have achieved enhanced dispersion and immobilized rubber (occluded) is limited so that bound rubber measurements, which thus include only adsorbed polymer, are shown to increase. This remark raises the question of the significance of bound rubber measurements and emphasizes the difficulty in comparing different rubber systems.

- Additionally, it can be noted that most studies lack a clear criterion for characterizing the mixing process. An indicator based on mixing energy, such as the specific energy (in J/g) mentioned for example by Dimier *et al.* [128] in their study focused on the relationships between mastication conditions and rheological behavior of a natural rubber, might be of interest. This parameter is defined as:

$$E_{\text{spe}} = \frac{2\,\pi\,N\,\int_0^{\text{t}} C(t')\,\mathrm{d}t'}{M} \tag{14.12}$$

where N is the rotation speed, t the mastication time, C the torque and M the mass introduced in the chamber.

Specific energy could be a means for helping in comparisons in the field of rubber compounds and composites in which effects from the matrix, filler and morphology superpose in a very complex manner.

14.4.2 Rubber Nanocomposites Based on Nanoclays

Shear-thinning behavior at high shear rates (or stresses) and the increase of shear viscosity with filler concentration are general features of silica and carbon black-filled elastomers. Shear-thinning is also a feature of nanoclay-based rubber nanocomposites, but the influence of filler loading offers significant contrast with silica or carbon black data.

Different studies of organoclay-based rubber nanocomposites have been reported in literature, involving various polymer matrices: polyepichlorhydrin [81], ethylene-vinyl acetate (EVA, [82]), nitrile rubber (NBR, [83]), fluoroelastomers [84], carboxylated NBR [85]. In most of these composites, intercalated rather than exfoliated morphology was observed. The influence of filler concentration on steady shear viscosity is generally found to be strong at low shear rates: in Lim's and Prasad's works [81, 82], the low shear viscosity increases with filler content, as a result of increased interactions between the silicate layers and the polymer chains. However, the high shear rate behavior of their materials is shown to be almost insensitive to increase in filler content. The authors interpret this as a consequence of orientation and alignment of silicate layers and polymer chains in the flow direction. On the contrary, Ibarra *et al.* [85] notice that, in a carboxylated nitrile rubber matrix, the influence of the nanofiller is maintained even at high shear rate. Sadhu and Bhowmick [83] and Kader *et al.* [84] present data for NBR- and fluoroelastomer-organo-montmorillonite composites, respectively, in overall

contradiction with the preceding ones or with results obtained for conventional fillers like silica or carbon black: they show viscosities that decrease between pure polymer and composites and that go through a minimum upon increase of filler concentration. Kader *et al.* [84] propose some arguments for explaining this effect, which can be summarized as follows:

- The reduction of viscosity upon increasing nanofiller concentration might be partly due to breakdown of platelets stacks and subsequent dispersion and exfoliation under shear, to alignment during flow and to some plasticizing action from the presence of the long chain organic modifier in the clay, possibly causing chain slippage over the clay platelets.
- The viscosity reduction is all the more pronounced as the shear rate decreases. Thus, at lower shear rates, the shear flow seems dominated by the stack and the degree of dispersion of the clay, whereas the high shear rate properties are dominated by the viscoelastic behavior of the polymer matrix. This last aspect is similar to conclusions drawn by Mongruel and Cartault [9] concerning carbon black and silica.
- The occurrence of a minimum viscosity and subsequent increase upon increase of nanofiller concentration is supposed to be due to an optimal state of dispersion followed by aggregation.

As it is clearly shown here, the flow behavior of rubber nanocomposites based on layered organoclays does not exhibit a simple trend because of the miscellaneous and complex influences of polymer-nanofiller interactions, degree of dispersion and orientation-related features during flow. All these effects look enhanced by comparison with traditional rubber composites, making comparisons more difficult. For instance, the magnitude of the influence of filler volume fraction in the high shear rate domain depends on the system, the temperature, the processing history of the composite and so on.

This last point was discussed in Sections 14.2 and 14.3 where the need for very rigorous protocols was strongly emphasized to guarantee the significance of rheological data. In practice, the mixing process is hardly addressed in studies dealing with rubber nanocomposites based on nanoclays and only the resulting morphology is paid attention to. Solution-mixed nanocomposites will not be discussed here, since this method is not representative for the rheological mechanisms involved in "industrial" mixing. In addition to the works by Prasad *et al.* [82], Kader *et al.* [84] and Ibarra *et al.* [85], cited previously in Section 4.1.2., numerous studies exist in which melt blending is carried out [49, 86–95]. Nevertheless, none of them addresses the mixing operation itself. Indeed, no real focus is given on the control and repeatability of the mixing stage. Of course microstructure is analyzed more or less thoroughly in order to connect "rheological" properties with morphological features, but all the works cited just above deal with crosslinked nanocomposites so flow properties are out of their scope. Thus it is clear that the understanding of viscous properties of such materials is lacking at present and that the quantitative analysis of relationships between viscous or viscoelastic properties of uncured rubber nanocomposites and the parameters of their morphology is a wide open research field.

As a consequence, a very careful analysis of published data is needed with these developing rubber nanocomposites. Besides, the comparison of the rheology of different filler/elastomer systems is not straightforward and should be carried out with extreme care. Moreover, the interpretations generally found in the literature rely on the knowledge and on principles developed with carbon black in the 1970s. These have been later extended quite successfully to silica, whose particle shape and structure is close to carbon black. But the question remains

whether newly emerging nanocomposites, based on lamellar nanofillers or on carbon nanotubes, can be addressed with the same concepts.

14.4.3 Extensional Viscosity

Elongational flow situations are met in almost all rubber processing operations, so elongational rheology is an important issue to address. The methods developed to quantify elongational viscosity are based on different types of experiments: filament stretching (that is, "spinning", in which the strain rate varies significantly with position therefore leading to heterogeneous elongation of the sample), homogeneous stretching under constant elongation rate or stress, or at constant sample length, and convergent flows. All these approaches entail strong experimental difficulties, which explains that published data about extensional viscosity of unvulcanized rubber composites are very scarce compared to shear viscosity data.

In filament-stretching experiments, steady-state flow is hardly ever attained. Indeed, a steady elongational strain rate implies that test sample length should grow exponentially, which no material can sustain indefinitely. (Homogeneous) stretching experiments are thus limited to low extension rates and small strains. Cotten and Thiele [96] developed an extensional rheometer dedicated to nonvulcanized elastomers, and published the first data obtained by direct measurement of the elongational viscosity of carbon black-filled rubber compounds, at room temperature, within the 10^{-4}–10^{-1} s^{-1} strain rate range. The device used by Ng [97, 98] was based on a similar concept but placed in a temperature-controlled enclosure which allowed to work at temperatures ranging from 50 to 250 °C.

At present, this technique is still in use with rubber nanocomposites, but the rheometer originally designed by Meissner, based on the rotary clamp technique (see improvements of the concept in [99]), has gained importance. This is mainly due to the facts that this rheometer allows the material to be elongated homogeneously within a zone of constant length between the clamps and that the stress and strain can be measured with accuracy and sensitivity. Moreover, large Hencky strains can be obtained and the Hencky strain rate can be maintained constant by keeping the rotation speed of the rollers constant. Commercial rheometers of this kind were used in recent studies of EVA–clay nanocomposites, as will be reported later.

As an alternative to the different "stretching" techniques, the analysis of convergent flow regimes was preferred by some authors for its better ability to represent real processing conditions but also due to the possibility of achieving a steady flow. However, the occurrence of shear, especially at the wall, makes the analysis complex. After developing a method for deriving extensional viscosity from the analysis of entry pressure loss in capillary flow [100], Cogswell presented the concept of an "ideal" converging flow rheometer [101], whose die walls should be lubricated to eliminate most of the shearing effects and profiled in order to give a uniform extension rate. In later studies, most authors retained these principles, with more or less adaptation. For example, Clarke and Petera [102] used bell-mouthed dies to determine the steady-state elongational viscosity of an SBR compound filled with 30 phr carbon black, but they introduced a correction for shear instead of using lubrication. Rippl *et al.* [103] used an online capillary rheometer to study shear and extensional rheology of EPDM compounds in extrusion, following an improved analysis for the pressure loss on entry to a capillary, as presented by Astarita and Mackay [104].

14.4.3.1 Rubber Nanocomposites Based on Carbon Black

Typical results obtained by Cotten and Thiele [96] for homogeneous, constant strain rate stretching of carbon black-filled SBR compounds are displayed in Figure 14.8. The plots of the elongational stress growth function (that is, elongational viscosity) versus time, measured at different strain rates, superimpose on a single curve up to an almost constant value of strain around 0.8, before rising more rapidly, which reveals strain hardening. This demonstrates that no steady-state flow occurs within the limits of the experiment, which seems to be the general case with carbon black-filled elastomer formulations. The extensional viscosity of these materials is much higher than their shear viscosity, which generally remains within the MPa.s range at low shear rates. The viscosities measured here in elongation increase from a few MPa.s towards values that can reach as high as 1 GPa.s, at low elongation rate, before filament breaks.

The influence of the concentration of carbon blacks, their surface area and particle structure (at constant filler concentration) on extensional viscosities were also addressed by these authors. The elongational viscosity (at a given time in the stretching test) raised upon increase of any of these parameters. Yet, the key factors appeared to be the concentration and surface area, which had more significant influence on viscosities than particle structure. The increase of filler loading strongly modified the initial rate of growth of viscosity (slope of viscosity versus time curve increases with filler concentration), whereas the effect of surface area on the viscosity profiles did not appear from the very first instants of sample stretching, but rather in the later part of the test.

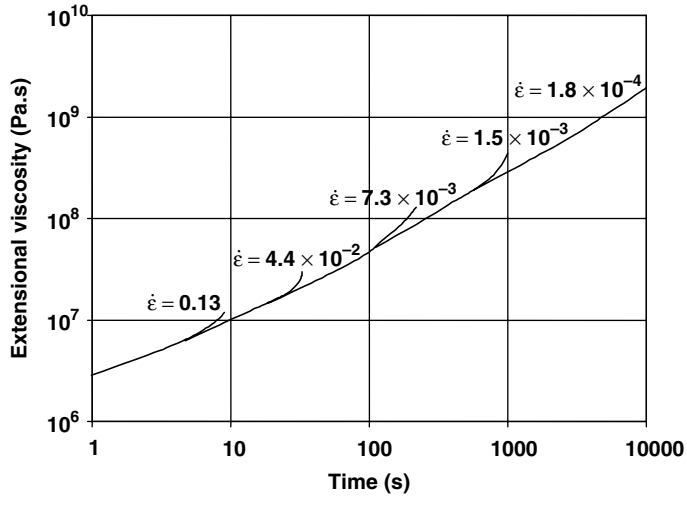

Figure 14.8 Evolution of extensional viscosity (that is, stress growth function $\sigma(t)/\dot{\varepsilon}$) with time, at various elongation rates $\dot{\varepsilon}$ for SBR1500 compounds containing 50 phr N330 carbon black (Data reproduced with permission from G.R. Cotten and J.L. Thiele, "Influence of carbon-black on processability of rubber stocks. 3. Extensional viscosity," *Rubber Chemistry and Technology*, **51**, 749–763, 1978. © 1978 Rubber Division, American Chemical Society, Inc. [96].)

As far as works based on converging flow analysis are concerned, a noticeable feature is that the elongation rates encountered can be much higher than in stretching methods, for example up to $800\,s^{-1}$ in the work by Rippl *et al.* [103]. However, considering a converging geometry

such as the one chosen by these authors (capillary-type geometry mounted online in place of a profile extrusion die) requires some computational treatment of the data consisting in volumetric flow rates and pressures. Indeed, the shear contribution in the entry flow has to be considered, and the model for the developed flow in the capillary must incorporate wall slip. The complete model then involves parameters for shear and elongational viscosities as well as for wall slippage, and the values of these parameters are computed by an inverse method.

In the case of the profile die used by Clarke and Petera [102], the peculiar bell-mouthed geometry allows to derive a very simple expression between the elongational viscosity and the pressure drop, and the correction for the shear contribution to the total pressure drop can also be established simply. The shear properties must be determined separately by regular capillary rheometry. Thus, the experimental equipment in this approach consists only in a capillary rheometer fitted with either classical capillary dies (for shear behavior assessment) or with the bell-mouthed dies (extensional flow + shear flow, with no necessity for lubrication).

14.4.3.2 Rubber Nanocomposites Based on Nanoclays

The melt rheology of composites containing layered silicates are dictated by a combination of mesoscopic structure and the strength of interaction between the polymer and the nanoparticles. Therefore, due to the strong anisometry of nanoclay platelets, the effect of such fillers on the melt viscosity of polymer composites can be expected to be all the more important in elongation. Nevertheless, very few data can be found in literature concerning elongational viscosity layered silicate composites, and most of them deal with ethylene-vinyl acetate (EVA) copolymer-based nanocomposites as in the papers by Bhattacharya and his co-workers [105, 106] and by La Mantia and Dintcheva [107].

In these studies, different clay nanofillers were used (sodium bentonite or montmorillonite) but all were organically modified to provide improved reinforcement of the polymer matrix. The EVA copolymers were different, in terms of vinyl acetate content (9–28 wt%), and so were the elaboration modes of the composites. As a consequence, different morphologies were achieved by the authors: for example, with 5 wt% nanofiller, intercalation was obtained with VA content up to 14 wt%, and exfoliation with EVA containing 18% and more VA. In these papers, the transient elongational viscosity (that is, viscosity versus time at constant elongation rate) is measured at different elongation rates and is discussed with respect to the filler content.

The feature of the plots for the neat polymer appears in Figure 14.9, and is similar for the EVA copolymers used in the works cited, whatever the VA content: at low strain rates, the viscosity gradually increases with time and reaches a plateau in the long time region (steady state). At higher strain rates, these curves exhibit typical strain-hardening behavior: they no longer tend towards a plateau, and viscosity goes up more rapidly after some time.

The results reported by La Mantia and Dintcheva [107] with intercalated composites of EVA (14% VA) and montmorillonite, at loadings of 5 and 10%, show that no plateau is reached whatever the elongation rate, and thus that strain-hardening is emphasized by the presence of the nanofiller. The extensional viscosity of the nanocomposites is higher than that of the neat polymer, and increases with filler content. The effect of the nanoparticles is attenuated, however, as the elongation rate increases.

The transient elongational viscosity of EVA (28% VA) and its nanocomposites with 2.5 and 5.0% bentonite, as presented in Figure 14.9, offers significant contrast. Indeed, it can be noticed that the slope in the strain-hardening part of the curves decreases as filler content increases,

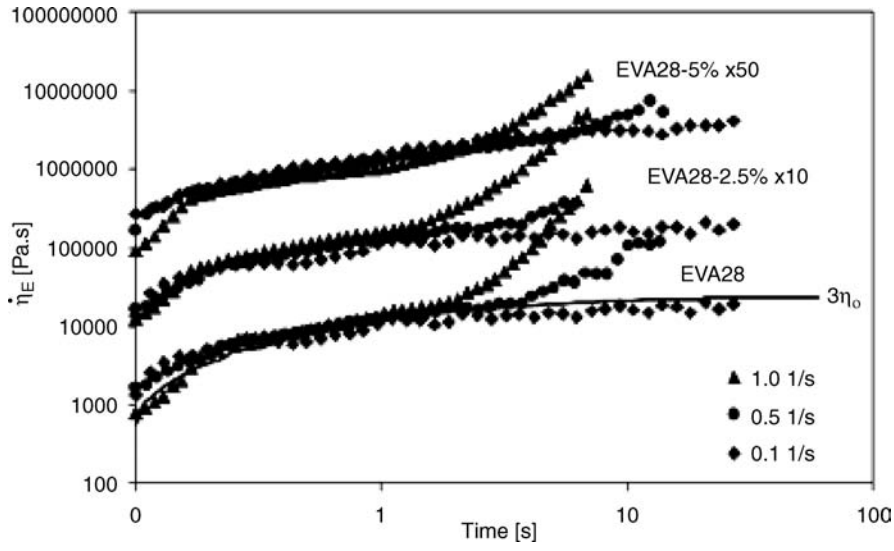

Figure 14.9 Extensional viscosity profiles as a function of time for EVA28 (28% VA) and EVA28 nanocomposites at 130 °C and at different elongation rates. Nanofiller is organomodified bentonite, contents are in wt%. For clarity purposes, the viscosities of EVA28 with 2.5 and 5.0% nanofiller were multiplied by 10 and 50, respectively [105] (Reproduced with permission from V. Pasanovic-Zujo, R.K. Gupta and S.N. Bhattacharya, "Effect of vinyl acetate content and silicate loading on EVA nanocomposites under shear and extensional flow," *Rheologica Acta*, **43**, 99–108 (Figure 15), © 2004, Springer-Verlag Berlin.)

which demonstrates that the strain-hardening effect is reduced in the case of these exfoliated nanocomposites, compared to pure polymer. Microstructural analysis of these strained samples by TEM [106] showed that the extension of the material at large Hencky strains (beyond 3 in the present case), in which the nanoparticles were initially predominantly exfoliated, had resulted in a modification of the dispersion, namely aggregation of the filler material and reformation of the so-called tactoids. This supports the attempt of the authors for a phenomenological explanation: in an exfoliated structure, the interactions between polymer and individual clay layers dominate over the interlayer interactions. The idealized morphology consists in a random dispersion of clay layers with different orientations, forming spheres or ellipsoids of clay surrounded by entangled polymer chains. Gupta *et al.* [106] assume that upon extension, causing axial stretching of the polymer chains, the inter-layer distance decreases due to cross-sectional contraction of the sample, and electrostatic attraction develops between the edge surface of clay (not protected by organic coating) and the flat surfaces, providing a "house of cards" network structure. Van der Waals forces become stronger as clay layers get closer, and flocculated structures (face-to-face associations) eventually form.

Such a mechanism of reduced strain hardening due to the presence of fillers has already been reported in literature for conventional fillers. For instance, Chan *et al.* [108] reported that the strain-hardening properties of high-density polyethylene or polystyrene were decreasing when adding glass fibers. Takahashi *et al.* [109] reported that LDPE composite systems, filled with glass fibers randomly dispersed, had strain-softening properties. Boyaud *et al.* [110] showed

for polymer/polymer composites (the filler was a polymer dispersed phase below its glass or crystallization temperature) that strain-hardening was considerably reduced and that strain-softening appeared. The authors suggested that strain-hardening of such composites was correlated to the homogeneity of the flow at the filler interface. When the elongational flow was disrupted in the interphase region so that the deformation around the particle was not homogeneous, strain-softening occurred.

In conclusion, these results clearly illustrate the importance of the dispersion and polymer–filler interactions in the strain hardening behavior of nanocomposites. In this respect, they can be compared with those obtained by Lee *et al.* [111], with polypropylene/layered silicate nanocomposites: only those composites containing maleic anhydride-grafted PP as a compatibilizer exhibited strain hardening, as a result from the presence of a 3D structure of exfoliated platelets strongly interacting with the polymer, and thus reducing the rate of polymer disentanglement.

14.4.4 Yield Stress

It has long been known that highly filled rubbers exhibit yield stress. Industrial formulations of carbon black or silica filled rubbers such as NR, SBR and EPDM have long been studied for their flow properties, and the occurrence of a solid-like behavior at low shear stress was reported for example by Toki and White [65], Montes *et al.* [66], Shin *et al.* [112], Osanaiye *et al.* [73] and Ertong *et al.* [67]. As previously presented in Sections 14.2 and 14.3 for different types of nanocomposites, this solid-like behavior is clearly observed for filler loadings exceeding the percolation threshold and has been attributed to the filler network.

In the case of elastomers filled with large amounts of carbon black or silica, oscillatory rheometry raises a number of problems already mentioned, thus the evidence of a yield stress is best visible on graphs as those presented in Figure 14.6, in which the value of shear stress below which no flow occurs can be directly seen. The use of different rheometers is necessary for accurate determination of the yield stress σ_c, that is, without extrapolation. The published values of yield stress for different NR, SBR or EPDM-based, carbon black-filled materials were reviewed by Shin *et al.* [112], for example. A $\phi = 0.2$ volume fraction of particle appears to induce a yield stress ranging between 10^4 and $1.3 \cdot 10^5$ Pa at 100 °C. The magnitude of the yield value seems largely dependent on the type and filler volume fraction ϕ of the carbon black rather than on the polymer matrix. Shin *et al.* proposed to correlate σ_c with the ratio ϕ/d, where d is the particle diameter, but this is most unlikely to capture the complexity of the filler influence, whose "efficiency" must depend on its specific surface, geometry and physico-chemical surface characteristics. Nevertheless, no attempt was made for a fundamental approach of such relationships between yield values and microstructure in usual rubber composites. An interesting analysis of elasticity and yield stress of model silica-silicone compounds was presented by Piau *et al.* [31], but no extension to other filled rubber systems can be found in more recent literature.

Thus, the yield stress only appears in some rheological models as a parameter that takes into account the particle network contribution to the total stress. In this respect, Herschel-Bulkley's equation $\left(\eta = \frac{\sigma_c}{\dot{\gamma}} + \mathrm{K}\,\dot{\gamma}^{\mathrm{n}-1}\right)$ provides the simplest approximation for the shear viscosity of concentrated suspensions of small particles in a power-law fluid. While studying temperature influence on carbon black-filled SBR compounds, Ertong *et al.* [67] achieved very satisfactory mastercurves with this model, by applying separate shift factors to the contributions of either

phase of the compound. The polymer contribution was described by the second term in Herschel-Bulkley's equation and was treated with the classical temperature-dependent shift factor a_T. The temperature dependence of the yield stress which resulted from the particle network was introduced via a vertical shift factor on the first term.

More elaborate rheological models are dedicated to filled polymers, like that of Leonov [78] and its derived versions aimed at modeling particle–matrix interactions and, more recently, the chemorheology of filled elastomers [113, 114]. They are able to describe anisotropic yield stresses and thixotropy effects without any externally imposed yield criterion.

From a practical point of view, it can be noted that yield behavior is unlikely to play a significant role in current processing flows of rubber nanocomposites. As noted for example by Rippl *et al.* [103], the magnitude of the shear stresses at the capillary wall of their online rheometric device is 10^6 Pa and widely exceeds the current magnitude of yield stress observed with highly filled rubber compounds.

14.4.5 Wall Slip

A more effective impact is expected from wall slip than from yielding on the flow of filled rubbers. Indeed, wall slippage is often observed with industrial rubber compounds. Ma *et al.* [115] demonstrated with colored markers the occurrence of slip above a critical shear rate. Slip is induced by the presence of filler (above 10 wt% carbon black for example) but can also result from the release of some components like plasticizers, lubricants and processing aids that enter these complex formulations.

It was already mentioned that any rheological characterization of such materials should assess first whether slip is present or not, in order to ensure significance of rheological data. Then, the quantification of slip is a key issue. In the framework of classical assumptions for viscometric measurements, the assessment of a mastercurve for the true wall shear stress σ_w (corrected for entry effects following Bagley's method) versus apparent shear rate $\dot{\gamma}_{app}$, upon variation of the measuring geometry (radius or gap), is a proof of no-slip conditions. By assuming that slip velocity V_s only depended on σ_w, Mooney [116] proposed a method to quantify V_s which is still the most widely used, since it can be applied to most geometries (capillary and slit dies, rotational systems, ...). However, Mooney's method fails in a number of situations and provides slip velocity values with no physical meaning (V_s greater than mean flow velocity $\bar{V}$), which led authors to introduce a dependence of V_s upon the local geometry in addition to σ_w [117, 118].

Other approaches rely on the use of rheological tools with smooth and grooved surfaces. The latter allow to determine slip-free behavior, and comparison with the former leads to the values of slip velocity [119, 120].

Mourniac *et al.* [121] addressed the wall slip velocity of SBR compounds by revisiting Mooney's technique. The first step was to assess the real, slip-free behavior of the material with grooved, nonslippery die surfaces. Then, experimental data collected in the current die provided pressure drop measurements ΔP with corresponding actual flow rate Q. If Q^* represents the theoretical flow rate that would be obtained with the same pressure drop in no-slip conditions, then the wall slip velocity V_s is given by $V_s = (Q - Q^*)/S$, where S is the cross-sectional area of the die. V_s was found to follow a power law upon shear stress in the form $\sigma_w = \alpha K V_s^n$, where K and n are the power law coefficients of the true viscous behavior and α is a slip parameter that depends on the material characteristics and on the local geometry. With this

method, physically sound values of slip velocities were obtained in all cases, and an additional interesting observations could be made: a critical shear stress appeared, showing that the onset of wall slippage was located above 0.1 MPa, which is in good agreement with data published by other authors (except for EPDM compounds).

As a modification to Mooney's method, the consideration for the geometry dependence of the slip velocity gave rise to different expressions (see for example [122, 123]). Similarly, varied interpretations for the increase of $\frac{V_s}{\dot{V}}$ upon gap decrease, all other conditions remaining constant, were given. Mourniac *et al.* suggest that this could result from the increasing weight of surface effects at the expense of volumic effects. Migration of some components is also frequently conjectured.

14.4.6 Extrudate Swell

Reinforcing fillers, in general, reduce the extrudate swell of elastomeric materials. This has been studied for long with carbon black-filled rubbers and was reviewed by Leblanc [3]. Therefore, no exhaustive reporting on extrudate swell is carried out here, but only some complementary aspects, especially dealing with nanoclay- or nanosilica-filled rubbers, are addressed.

Generally admitted mechanisms for extrudate swell combine rearrangement of velocity profile at die exit, partial relaxation of entry tensile stress and recovery of strains associated with normal stress difference within the die. Upon addition of solid filler particles, die swell is reduced not only due to their hydrodynamic effect and the reduction of polymer volume fraction, but also because of the polymer–filler interactions which develop generally higher viscosities at the expense of elasticity.

This point can be illustrated by the evolution of the first normal stress difference N_1, which characterizes the elasticity of viscoelastic materials. For example, Bandyopadhyay *et al.* [74], who prepared nanocomposites of epoxydized natural rubber and *in situ* generated nanosilica by a sol-gel technique, observed a remarkable drop of N_1 when the concentration of nanofiller increased. Similarly, Gupta *et al.* [106] examined the effect of dispersed organobentonite on the melt elasticity of exfoliated EVA-nanocomposites by monitoring the dependence of N_1 on the organoclay concentration. The addition of the nanofiller decreases N_1 at high shear stresses (above 2000 Pa), whereas at low shear stress N_1 appears almost independent on silicate concentration. This behavior contrasts with published data concerning intercalated nanocomposites, whose N_1 was independent of silicate concentration. It shows that strong interactions between clay layers and polymer chains are responsible for the reduced mobility of the latter and thus, reduced elasticity which has direct consequences in decreasing extrudate swell. The effect of dispersion (exfoliation versus intercalation) was confirmed by Sadhu and Bhowmick [83] or Ibarra *et al.* [85], with different polymer matrices like (carboxylated or not) acrylonitrile butadiene, styrene butadiene and butadiene rubbers. All these studies, along with the work by Kader *et al.* [84] on fluoroelastomer/layered clay nanocomposites, demonstrate that the die swell reduces when fillers are added, like in traditional rubber compounds.

14.5 Conclusions

Since the rheological properties of nanocomposites are sensitive to the structure, particle size, shape and surface characteristics of the nanofiller, the rheological tool is intensively used to

assess the features of the dispersion of nanocomposites directly in the molten state. In contrast and from an historical point of view, the determination of flow properties of industrial rubber nanocomposites, that is, basically carbon black- and silica-filled compounds, has been considered for decades in the purposes of quality control and of predicting behavior in processing conditions. The appearance of a novel class of rubber nanocomposites, based on nanoparticles in very low concentrations, has not reached yet this stage of industrial concern. Studies on these materials are much more focused on microstructural analysis through rheological approach, and nonlinear viscoelastic properties or flow features are still often out of scope for these new materials. Determining sound rheological data in processing conditions still remains a challenge with elastomeric materials, because fundamental knowledge on the influence of filler particles, the strongly viscoelastic behavior and slip phenomena, which are inherent to the flow of rubber materials, is only partial. In practice, computational approaches, like inverse methods for the analysis of real processing flows in a rheological context, have gained importance, maybe at the expense of the development of specific tools. Nevertheless, in spite of the progress made in computational rheometry of thermoplastic polymers, the rheology of elastomeric materials still presents enhanced difficulties, which explains that comparatively rather few data are published in literature. As a consequence, very few constitutive models have been derived specifically for rubbers (apart from Leonov and coworkers' model) in spite of crucial need for the use in simulation softwares.

References

1. Payne, A.R. (1962) The dynamic properties of carbon black-loaded natural rubber vulcanizates. Part I. *Journal of Applied Polymer Science*, **6**, 57.
2. Payne, A.R. (1965) Chapter 3, *Reinforcement of Elastomers*, Interscience, New York, pp. 69–123.
3. Leblanc, J.L. (2002) Rubber-filler interactions and rheological properties in filled compounds. *Progress in Polymer Science*, **27**, 627–687.
4. Cassagnau, P. (2008) Melt rheology of organoclay and fumed silica nanocomposites. *Polymer*, **49**, 2183–2196.
5. Szleifer, I. and Yerushalmi-Rozen, R. (2005) Polymers and carbon nanotubes - dimensionality, interactions and nanotechnology. *Polymer*, **46**, 7803–7818.
6. Moniruzzaman, M. and Winey, K.I. (2006) Polymer nanocomposites containing carbon nanotubes. *Macromolecules*, **39**, 5194–5205.
7. Bokobza, L. (2007) Multiwall carbon nanotube elastomeric composites: a review. *Polymer*, **48**, 4907–4920.
8. Cassagnau, P. (2003) Payne effect and shear elasticity of silica-filled polymers in concentrated solutions and in molten state. *Polymer*, **44**, 2455–2462.
9. Mongruel, A. and Cartault, M. (2006) Nonlinear rheology of styrene-butadiene rubber filled with carbon-black or silica particles. *Journal of Rheology*, **50**(2), 115–135.
10. Durmus, A., Kasgoz, A., and Macosko, C.W. (2007) Linear low density polyethylene (LLDPE)/clay nanocomposites. Part I: structural characterization and quantifying clay dispersion by melt rheology. *Polymer*, **48**, 4492–4502.
11. Pötschke, P., Abdel-Goad, M., Alig, I. *et al.* (2004) Rheological and dielectrical characterization of melt mixed polycarbonate-multiwalled carbon nanotube composites. *Polymer*, **45**, 8863–8870.
12. Winter, H.H. and Mours, M. (1997) Rheology of polymers near liquid-solid transitions. *Advances in Polymer Science*, **134**, 165–234.
13. Inoubli, R., Dagréou, S., Khoukh, A. *et al.* (2005) 'Graft from' polymerization on colloidal silica particles: elaboration of alkoxyamine grafted surface by in situ trapping of carbon radicals. *Polymer*, **46**, 2486–2496.
14. Paquien, J.N., Galy, J., Gérard, J.F., and Pouchelon, A. (2005) Rheological studies of fumed silica-polydimethylsiloxane suspensions. *Colloids and Surfaces A-Physicochemical and Engineering Aspects*, **260**, 165–172.
15. Yurekli, K., Krishnamoorti, R., Tse, M.F. *et al.* (2001) Structure and dynamics of carbon black-filled elastomers. *Journal of Polymer Science Part B-Polymer Physics*, **39**, 256–275.

16. Loiseau, A. and Tassin, J.F. (2006) Model nanocomposites based on laponite and poly(ethylene oxide): preparation and rheology. *Macromolecules*, **39**, 9185–9191.
17. King, H.E. Jr, Milner, S.T., Lin, M.Y. *et al.* (2007) Structure and rheology of organoclay suspensions. *Physical Review E*, **75**(021403), 1–20.
18. Du, F., Scogna, R.C., Zhou, W. *et al.* (2004) Nanotube networks in polymer nanocomposites: rheology and electrical conductivity. *Macromolecules*, **37**, 9048–9055.
19. Zhang, Q., Lippits, D.R., and Rastogi, S. (2006) Dispersion and rheological aspects of SWNTs in ultrahigh molecular weight polyethylene. *Macromolecules*, **39**, 658–666.
20. Mitchell, C.A., Bahr, J.L., Arepalli, S. *et al.* (2002) Dispersion of functionalized carbon nanotubes in polystyrene. *Macromolecules*, **35**, 8825–8830.
21. Wang, X., Gao, Y., Mao, K. *et al.* (2006) Unusual rheological behavior of liquid polybutadiene rubber/clay nanocomposite gels: the role of polymer–clay interaction, clay exfoliation, and clay orientation and disorientation. *Macromolecules*, **39**, 6653–6660.
22. Bartholome, C., Beyou, E., Bourgeat-Lami, E. *et al.* (2005) Viscoelastic properties and morphological characterization of silica/polystyrene nanocomposites synthesized by nitroxide-mediated polymerization. *Polymer*, **46**, 9965–9973.
23. Lin, C.R. and Lee, D. (1997) Strain-dependent dynamic properties of filled rubber network systems. 2. The physical meaning of parameters in the L-N-B model and their applicability. *Macromolecular Theory and Simulations*, **6**, 339–347.
24. De Gennes, P.G. (1976) Scaling theory of polymer adsorption. *Journal of Physics*, **37**, 1–2.
25. Zhu, Z., Thompson, T., Wang, S.Q. *et al.* (2005) Investigating linear and nonlinear viscoelastic behavior using model silica-particle-filled polybutadiene. *Macromolecules*, **38**, 8816–8824.
26. Klüppel, M. (2003) Elasticity of fractal filler networks in elastomers. *Macromolecular Symposia*, **194**, 39–45.
27. Heinrich, G. and Klüppel, M. (2002) Recent advances in the theory of filler networking in elastomers. *Advances in Polymer Science*, **160**, 1–44.
28. Mall, S. and Russel, W.B. (1987) Effective medium approximation for an elastic network model of flocculated suspensions. *Journal of Rheology*, **31**, 651–681.
29. Chen, M. and Russel, W.B. (1991) Characteristics of flocculated silica dispersions. *Journal of Colloid and Interface Science*, **141**, 564–577.
30. Wolthers, W., van de Ende, D., Breedveld, V. *et al.* (1997) Linear viscoelastic behavior of aggregated colloidal dispersions. *Physical Review E*, **56**, 5726–5733.
31. Piau, J.M., Dorget, M., Palierne, J.F., and Pouchelon, A. (1999) Shear elasticity and yield stress of silica-silicone physical gels: fractal approach. *Journal of Rheology*, **43**, 305–314.
32. Buscall, R., Mills, P., Goodwin, J.W., and Lawson, D.W. (1988) Scaling behaviour of the rheology of aggregate networks formed from colloidal particles. *Journal of the Chemical Society - Faraday Transactions*, **84**, 4249–4260.
33. Shih, W.H., Shi, W.Y., Kim, S.I., and Aksay, A.I. (1990) Scaling behavior of the elastic properties of colloidal gels. *Physical Review A*, **42**, 4772–4779.
34. Vermant, J., Ceccia, S., Dolgovskij, M.K. *et al.* (2007) Quantifying dispersion of layered nanocomposites via melt rheology. *Journal of Rheology*, **51**, 429–450.
35. Medalia, A.I. (1978) Effect of carbon-black on dynamic properties of rubber vulcanizates. *Rubber Chemistry and Technology*, **51**, 437–440.
36. Friedlander, S.K., Ogawa, K., and Ullmann, M. (2000) Elastic behavior of nanoparticle chain aggregates: A hypothesis for polymer-filler behavior. *Journal of Polymer Science Part B - Polymer Physics*, **38**, 2658–2665.
37. Maier, P.G. and Göritz, D. (1996) Molecular interpretation of the Payne effect. *Kaustchuck Gummi Kunstoffe*, **49**(1), 18–22.
38. Sternstein, S.S. and Zhu, A.J. (2002) Reinforcement mechanism of nanofilled polymer melts as elucidated by nonlinear viscoelastic behavior. *Macromolecules*, **35**, 7262–7273.
39. Aranguren, M.I., Mora, E., DeGroot, J.V., and Macoscko, C.W. (1992) Effect of reinforcing fillers on the rheology of polymer melts. *Journal of Rheology*, **36**, 1165–1182.
40. Parent, J.S., Mrkoci, M.I., and Hennigar, S.L. (2003) Silica agglomeration and elastomer reinforcement - influence of surface modifications. *Plastics, Rubber Composites*, **32**, 114–121.
41. Cassagnau, P. and Mélis, F. (2003) Non-linear viscoelastic behaviour and modulus recovery in silica filled polymers. *Polymer*, **44**, 6607–6615.

42. Luginsland, H.D., Fröhlich, J., and Wehmeier, A. (2002) Influence of different silanes on the reinforcement of silica-filled rubber compounds. *Rubber Chemistry and Technology*, **75**, 563–564.
43. Pu, Z.C., Mark, J.E., Jethmalani, J.M., and Ford, W.T. (1997) Effects of dispersion and aggregation of silica in the reinforcement of poly(methyl acrylate) elastomers. *Chemistry of Materials*, **9**, 2442–2447.
44. Ramier, J., Gauthier, C., Chazeau, L. *et al.* (2007) Payne effect in silica-filled styrene-butadiene rubber: influence of surface treatment. *Journal of Polymer Science Part B - Polymer Physics*, **45**, 286–298.
45. Rueb, C.J. and Zukoski, C.F. (1997) Viscoelastic properties of colloidal gels. *Journal of Rheology*, **41**, 197–218.
46. Yziquel, F., Carreau, P.J., and Tanguy, P.A. (1999) Non-linear viscoelastic behavior of fumed silica suspensions. *Rheologica Acta*, **38**, 14–25.
47. Zhu, A.J. and Sternstein, S.S. (2003) *Composites Science & Technology*, **63**, 1113–1126.
48. Clement, F., Bokobza, L., and Monnerie, L. (2005) Investigation of the Payne effect and its temperature dependence on silica-filled polydimethylsiloxane networks. Part I: experimental results. *Rubber Chemistry and Technology*, **78**, 211–231.
49. Ramorino, G., Bignotti, F., Conzatti, L., and Ricco, T. (2007) Dynamic and viscoelastic behavior of natural rubber/layered silicate nanocomposites obtained by melt blending. *Polymer Engineering and Science*, **47**, 1650–1657.
50. Aubry, T., Razafinimaro, T., and Médéric, P. (2005) Rheological investigation of the melt state elastic and yield properties of a polyamide-12 layered silicate nanocomposite. *Journal of Rheology*, **49**, 425–440.
51. Devendra, D., Hatzkiriakos, S.G., and Vogel, R. (2006) Rheology of metallocene polyethylene-based nanocomposites: Influence of graft modification. *Journal of Rheology*, **50**, 415–434.
52. Lertwilmolnun, W. and Vergnes, B. (2006) Influence of compatibilizer and processing conditions on the dispersion of nanoclay in a polypropylene matrix. *Polymer Engineering and Science*, **46**, 314–323.
53. Lertwilmolnun, W., Vergnes, B., Ausias, G., and Carreau, P.J. (2007) Stress overshoots of organoclay nanocomposites in transient shear flow. *Journal of Non-Newtonian Fluid Mechanics*, **141**, 167–169.
54. Chatterjee, T. and Krishnamoorti, R. (2007) Dynamic consequences of the fractal network of nanotube-poly (ethylene oxide) nanocomposites. *Physical Review E*, **75**(050403), 1–4.
55. Larson, R.G. (1999) Chapter 6.5: Particles in viscoelastic liquids: "Filled melts", *The Structure and Rheology of Complex Fluids*, Oxford University Press, p. 309.
56. Solomon, M.J., Almusallam, A.S., Seefeldt, K.F. *et al.* (2001) Rheology of polypropylene/clay hybrid materials. *Macromolecules*, **34**, 1864–1872.
57. Lele, A., Mackley, M., Galgaly, G., and Ramesh, C. (2002) In situ rheo-x-ray investigation of flow-induced orientation in layered silicate-syndiotactic polypropylene nanocomposite melt. *Journal of Rheology*, **45**, 1091–1110.
58. Lee, K.M. and Han, C.D. (2003) Rheology of organoclay nanocomposites: effects of polymer matrix/organoclay compatibility and the gallery distance of organoclay. *Macromolecules*, **36**, 7165–7178.
59. Lee, K.M. and Han, C.D. (2003) Effect of hydrogen bonding on the rheology of polycarbonate/organoclay nanocomposites. *Polymer*, **44**, 4573–4588.
60. Ren, J.X. and Krishnamoorti, R. (2003) Nonlinear viscoelastic properties of layered-silicate-based intercalated nanocomposites. *Macromolecules*, **36**(12), 4443–4451.
61. Galgali, G., Ramesh, C., and Lele, A. (2001) A rheological study on the kinetics of hybrid formation in polypropylene nanocomposites. *Macromolecules*, **34**, 852–858.
62. Chazeau, L., Brown, J.D., Yanyo, L.C., and Sternstein, S.S. (2000) Modulus recovery kinetics end other insights into the Payne effect for filled elastomers. *Polymer Composites*, **21**, 202–222.
63. Kalfus, J. and Jancar, J. (2007) Relaxation processes in PVAc-HA nanocomposites. *Journal of Polymer Science Part B - Polymer Physics*, **45**, 1380–1388.
64. Bokobza, L. (2001) Reinforcement of elastomeric networks by fillers. *Macromolecular Symposia*, **169**, 243–260.
65. Toki, S. and White, J.L. (1982) Rheological and solid wall boundary-condition characterization of unvulcanized elastomers and their compounds. *Journal of Applied Polymer Science*, **27**, 3171–3184.
66. Montes, S., White, J.L., and Nakajima, N. (1988) Rheological behavior of rubber carbon-black compounds in various shear-flow histories. *Journal of Non-Newtonian Fluid Mechanics*, **28**, 183–212.
67. Ertong, S., Eggers, H., and Schümmer, P. (1994) Steady-state shear-flow properties of carbon-black filled rubber compounds. *Rubber Chemistry and Technology*, **67**, 207–216.
68. Barrès, C. and Leblanc, J.L. (2000) Recent developments in shear rheometry of uncured rubber compounds I. Design, construction and validation of a sliding cylinder rheometer. *Polymer Testing*, **19**, 177–191.

69. Guth, E. and Gold, O. (1938) Analysis about the viscosity of suspensions and solutions. 1. On the viscosity of suspensions. *Physical Review A*, **53**, 322.
70. Kraus, G. (1971) Reinforcement of elastomers by carbon black. *Advances in Polymer Science*, **8**, 155–231.
71. Pliskin, I. and Tokita, N. (1972) Bound rubber in elastomers - analysis of elastomer-filler interaction and its effect on viscosity and modulus of composite systems. *Journal of Applied Polymer Science*, **16**, 473–492.
72. White, J.L. and Crowder, J.W. (1974) Influence of carbon-black on extrusion characteristics and rheological properties of elastomers - polybutadiene and butadiene-styrene copolymer. *Journal of Applied Polymer Science*, **18**, 1013–1038.
73. Osanaiye, G.J., Leonov, A.I., and White, J.L. (1993) Investigations of the rheological behavior of rubber carbon-black compounds over a wide range of stresses including very-low stresses. *Journal of Non-Newtonian Fluid Mechanics*, **49**, 87–101.
74. Bandyopadhyay, A., De Sarkar, M., and Bhowmick, A.K. (2005) Epoxidized natural rubber/silica nanoscale organic-inorganic hybrid composites prepared by sol-gel technique. *Rubber Chemistry and Technology*, **78**, 806–826.
75. Krieger, I.M. and Dougherty, T.J. (1959) A mechanism for non-Newtonian flow in suspensions of rigid spheres. *Transaction of the Society of Rheology*, **3**, 137–152.
76. Schaal, S. and Coran, A.Y. (2000) The rheology and processability of tire compounds. *Rubber Chemistry and Technology*, **73**, 225–239.
77. Schaal, S. and Coran, A.Y. (2002) Rheological model of uncured silica-filled tire compounds: application to a simple shear startup flow. *Rubber Chemistry and Technology*, **75**, 275–286.
78. Leonov, A.I. (1990) On the rheology of filled polymers. *Journal of Rheology*, **34**, 1039–1068.
79. Kim, K.J. and White, J.L. (2002) Silica surface modification using different aliphatic chain length silane coupling agents and their effects on silica agglomerate size and processability. *Composite Interfaces*, **9**, 541–556.
80. Welsh, F.E., Richmond, B.R., Keach, C.B., and Emerson, R.J. (1995) Paper no. 59, Presented at the meeting of the Rubber Division, ACS, Philadelphia, May 2–5.
81. Lim, S.K., Kim, J.W., Chin, I.J., and Choi, H.J. (2002) Rheological properties of a new rubbery nanocomposite: polyepichlorohydrin/organoclay nanocomposites. *Journal of Applied Polymer Science*, **86**, 3735–3739.
82. Prasad, R., Pasanovic-Zujo, V., Gupta, R.K. *et al.* (2004) Morphology of EVA based nanocomposites under shear and extensional flow. *Polymer Engineering and Science*, **44**, 1220–1230.
83. Sadhu, S. and Bhowmick, A.K. (2005) Unique rheological behavior of rubber based nanocomposites. *Journal of Polymer Science Part B Polymer Physics*, **43**, 1854–1864.
84. Kader, M.A., Lyu, M.Y., and Nah, C. (2006) A study on melt processing and thermal properties of fluoroelastomer nanocomposites. *Composites Science and Technology*, **66**, 1431–1443.
85. Ibarra, L., Rodriguez, A., and Mora, I. (2007) Ionic nanocomposites based on XNBR-OMg filled with layered nanoclays. *European Polymer Journal*, **43**, 753–761.
86. Arroyo, M., Lopez-Manchado, M.A., and Herrero, B. (2003) Organo-montmorillonite as substitute of carbon black in natural rubber compounds. *Polymer*, **44**, 2447–2453.
87. Chang, Y.W., Yang, Y., Ryu, S., and Nah, C. (2002) *Polymer International*, **51**, 319–324.
88. Kim, J.T., Oh, T.S., and Lee, D.H. (2003) Preparation and characteristics of nitrite rubber (NBR) nanocomposites based on organophilic layered clay. *Polymer International*, **52**, 1058–1063.
89. Lopez-Manchado, M.A., Arroyo, M., Herrero, B., and Biagiotti, J. (2003) Vulcanization kinetics of natural rubber-organoclay nanocomposites. *Journal of Applied Polymer Science*, **89**, 1–15.
90. Mousa, A. and Karger-Kocsis, J. (2001) Rheological and thermodynamical behavior of styrene/butadiene rubber-organoclay nanocomposites. *Macromolecular Materials and Engineering*, **286**, 260–266.
91. Privalko, V.P., Ponomarenko, S.M., Privalko, E.G. *et al.* (2003) Structure and thermoelastic behavior of synthetic rubber/organoclay nanocomposites. *Macromolecular Chemistry and Physics*, **204**, 1480–1485.
92. Uzuki, A., Tukigase, A., and Kato, M. (2002) *Polymer*, **43**, 2185–2189.
93. Varghese, S., Karger-Kocsis, J., and Gatos, K.G. (2003) Melt compounded epoxidized natural rubber/layered silicate nanocomposites: structure-properties relationships. *Polymer*, **44**, 3977–3983.
94. Vu, Y.T., Mark, J.E., Pham, L.H., and Engelhardt, M. (2001) Clay nanolayer reinforcement of cis-1,4-polyisoprene and epoxidized natural rubber. *Journal of Applied Polymer Science*, **82**, 1391–1403.
95. Zheng, H., Zhang, Y., Peng, Z., and Zhang, Y. (2004) Influence of clay modification on the structure and mechanical properties of EPDM/montmorillonite nanocomposites. *Polymer Testing*, **23**, 217–223.

96. Cotten, G.R. and Thiele, J.L. (1978) Influence of carbon-black on processability of rubber stocks. 3. Extensional viscosity. *Rubber Chemistry and Technology*, **51**, 749–763.
97. Ng, T.S. (1982) Extensional viscosity of rubber mixtures. *Rheologica Acta*, **21**, 456–459.
98. Ng, T.S. (1986) A comparative study of the extensional rheometer results on rubber compounds with values obtained by conventional industrial measuring methods. *Kautschuk Gummi Kunststoffe*, **39**, 830–833.
99. Meissner, J. and Hostettler, J. (1994) A new elongational rheometer for polymer melts and other highly viscoelastic liquids. *Rheologica Acta*, **33**, 1–21.
100. Cogswell, F.N. (1972) *Polymer Engineering and Science*, **12**, 64–73.
101. Cogswell, F.N. (1978) Converging flow and stretching flow - compilation. *Journal of Non-Newtonian Fluid Mechanics*, **4**, 23–38.
102. Clarke, J. and Petera, J. (1997) Determination of steady-state elongational viscosity for rubber compounds using bell-mouthed dies. *Journal of Applied Polymer Science*, **66**, 1139–1150.
103. Rippl, A., Pittman, J., Polynkin, A., and Sienz, J. (2007) Simultaneous determination of shear and extensional viscosities and wall slip by on-line rheometry with parameter fitting: an application to EPDM rubber. *Rheologica Acta*, **46**, 847–860.
104. Astarita, G. and Mackay, M.E. (1997) Analysis of entry flow to determine elongation flow properties revisited. *Journal of Non-Newtonian Fluid Mechanics*, **70**, 219–235.
105. Pasanovic-Zujo, V., Gupta, R.K., and Bhattacharya, S.N. (2004) Effect of vinyl acetate content and silicate loading on EVA nanocomposites under shear and extensional flow. *Rheologica Acta*, **43**, 99–108.
106. Gupta, R.K., Pasanovic-Zujo, V., and Bhattacharya, S.N. (2005) Shear and extensional rheology of EVA/layered silicate-nanocomposites. *Journal of Non-Newtonian Fluid Mechanics*, **128**, 116–125.
107. La Mantia, F.P. and Dintcheva, N.T. (2006) Eva copolymer-based nanocomposites: rheological behavior under shear and isothermal and non-isothermal elongational flow. *Polymer Testing*, **25**, 701–708.
108. Chan, Y., White, J.L., and Oyanagi, Y. (1978) *Journal of Rheology*, **22**, 507–524.
109. Takahashi, T., Takimoto, J., and Koyama, K. (1999) Uniaxial elongational viscosity of various molten polymer composites. *Polymer Composites*, **20**, 357–366.
110. Boyaud, M.F., Cassagnau, P., Michel, A. *et al.* (2001) Transient elongational properties of an in situ generated polymer/polymer composite. *Polymer Engineering and Science*, **41**, 684–695.
111. Lee, S.H., Cho, E.N.R., and Youn, J.R. (2007) Rheological behavior of polypropylene/layered silicate nanocomposites prepared by melt compounding in shear and elongational flows. *Journal of Applied Polymer Science*, **103**, 3506–3515.
112. Shin, K.C., White, J.L., Brzoskowski, R., and Nakajima, N. (1990) A comparative study of characterization methods of carbon-black dispersion in solution and emulsion SBR compounds prepared at various mixing levels. *Kautschuk Gummi Kunststoffe*, **43**, 181–188.
113. Simhambhatla, M. and Leonov, A.I. (1995) On the rheological modeling of filled polymers with particle-matrix interactions. *Rheologica Acta*, **34**, 329–338.
114. Joshi, P.G. and Leonov, A.I. (2001) Modeling of steady and time-dependent responses in filled, uncured, and crosslinked rubbers. *Rheologica Acta*, **40**, 350–365.
115. Ma, C.Y., White, J.L., Weissert, F.C. *et al.* (1985) Flow patterns in elastomers and their carbon-black compounds during extrusion through dies. *Rubber Chemistry and Technology*, **58**, 815–829.
116. Mooney, M. (1931) Explicit formulas for slip and fluidity. *Journal of Rheology*, **2**, 210–222.
117. Geiger, K. (1989) Rheological characterization of epdm rubber compounds with high-pressure capillary rheometer systems. *Kautschuk Gummi Kunststoffe*, **42**, 273–283.
118. Wiegreffe, S. (1991) Influence of the wall slip behavior of rubber compounds on their processability with pin barrel extruders. *Kautschuk Gummi Kunststoffe*, **44**, 216–221.
119. Turner, D.M. and Moore, M.D. (1980) Experimental determination of wall slip. *Plastic and Rubber Processing*, **5**, 81–84.
120. White, J.L., Han, M.H., Nakajima, N., and Brzoskowski, R. (1991) The influence of materials of construction on biconical rotor and capillary measurements of shear viscosity of rubber and its compounds and considerations of slippage. *Journal of Rheology*, **35**, 167–189.
121. Mourniac, P., Agassant, J.F., and Vergnes, B. (1992) Determination of the wall slip velocity in the flow of a SBR compound. *Rheologica Acta*, **31**, 565–574.
122. Malkin, A.Y., Baranov, A.V., and Vickulenkova, M.E. (1993) Experimental estimation of wall slip for filled rubber compounds. *Rheologica Acta*, **32**, 150–155.

123. Crawford, B., Watterson, J.K., Spedding, P.L. *et al.* (2005) Wall slippage with siloxane gum and silicon rubbers. *Journal of Non-Newtonian Fluid Mechanics*, **129**, 38–45.
124. Litchfield, D.W., and Baird, D.G. (2006) The rheology of high aspect ratio nano-particles filled liquids. *Rheology Reviews*, **2006**, 1–60.
125. Leboeuf, M., Ghamri, N., Brulé, B., Coupez, T., Vergnes, B. (2008) Influence of mixing conditions on rheological behavior and electrical conductivity of polyamides filled with carbon black. *Rheologica Acta*, **47**, 201–212.
126. Wang, M.J. (1998) Effect of polymer-filler and filler-filler interactions on dynamic properties of filled vulcanizates. *Rubber Chemistry Technology*, **71**, 520–589.
127. Clarke J., Freakley, P.K. (1994) Reduction in viscosity of an sbr compound caused by mastication and disagglomeration during mixing. *Rubber Chemistry Technology*, **67**, 700–715.
128. Dimier, F., Vergnes, F., Vincent, M. (2004) Relationships between mastication conditions and rheological behavior of a natural rubber. *Rheologica Acta*, **43**, 196–202.
129. Sirisinha, C., Sittichokchuchai, W., (2000) A study of relationships between state of mix, rheological properties, dynamic properties and bound rubber content, *Journal of Applied Polymer Science*, **76**, 1542–1548.

15

Electron Spin Resonance in Studying Nanocomposite Rubber Materials

S. Valić

Department of Chemistry and Biochemistry, School of Medicine, University of Rijeka, Croatia and Rudjer Bošković Institute, Zagreb, Croatia

15.1 An Approach to the Study of Polymer Systems

15.1.1 Introduction

Electron spin resonance (ESR), also known as electron paramagnetic resonance (EPR), is a spectroscopic method able to detect paramagnetic centers (unpaired electrons) [1, 2]. Generally, the nanocomposite rubber materials, as the majority of polymers, possess no intrinsic paramagnetism and therefore do not give rise to an ESR spectrum. However, it is possible to apply this technique as an indirect method in studying these materials. For that reason, it is necessary to introduce stable free radicals into a polymer matrix. The most commonly used free radicals are nitroxides, presented by a general formula in Figure 15.1.

Nitroxide radical possesses a free electron that belongs to the nitroxide group and occupies the p_z orbital of the nitrogen atom. The nitrogen group is often surrounded by four methyl groups, substituted in α positions, which sterically protect the paramagnetic center from a possible attacking reagent and hence contribute to the stability of a free nitroxide radical. The choice of an adequate nitroxide for investigation of a given polymer system is particularly important. Therefore, it is necessary to take care not only of miscibility between the nitroxide and the polymer matrix, but also of nitroxide size, shape, polarity and flexibility [3, 4]. In other words, the chosen nitroxide radical must be compatible with the polymer chain segment in order to be able to follow its motional behavior. Structures of some typical nitroxide radicals frequently used in ESR measurements are shown in Figure 15.2.

Rubber Nanocomposites: Preparation, Properties and Applications Edited by Sabu Thomas and Ranimol Stephen
© 2010 John Wiley & Sons (Asia) Pte Ltd

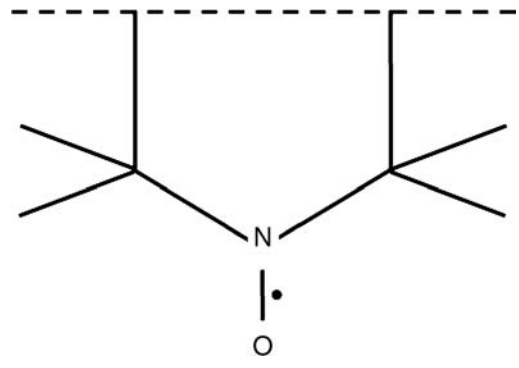

Figure 15.1 Schematic presentation of a stable nitroxide free radical

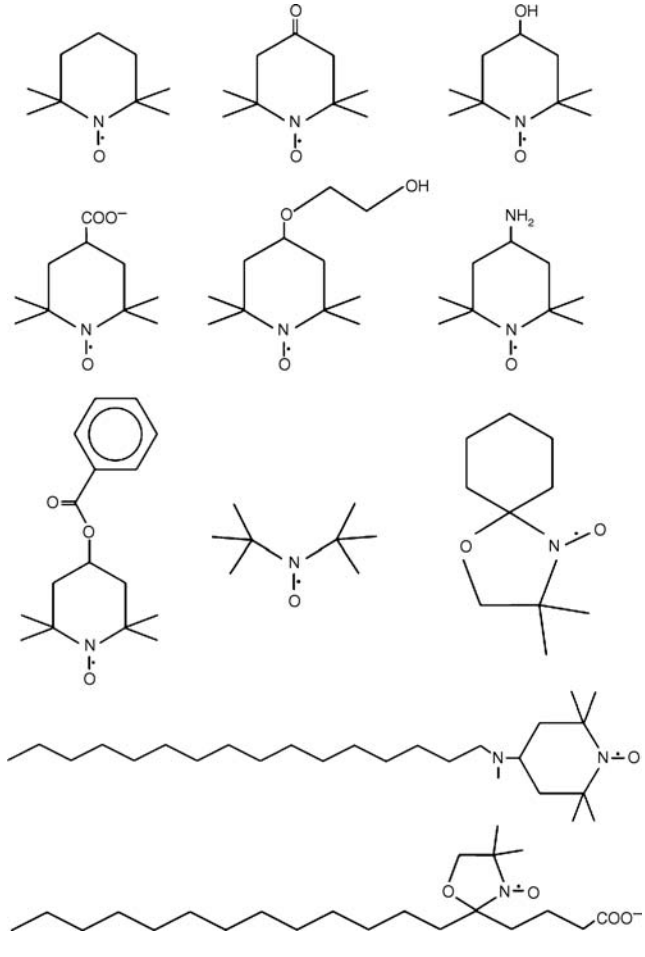

Figure 15.2 Nitroxide free radicals commonly used in ESR of polymers

An example which illustrates the importance of one of the nitroxide parameters described above was reported by C. Cornish and coworkers [5]. They used different doxyl stearic acid-free radicals in studying physical characteristics of rubber particles from various rubber (*cis*-1,4-polyisoprene) producing species. The free electron spin was that of doxyl group, substituted at different positions in stearic chain. Depending on the investigated rubber material, only the spectra of stearic acids with a doxyl group placed at the end (17-doxyl stearic acid) or close to the end (16-doxyl stearic acid) of the stearic chain provide evidence that some doxyl groups are diffusing through a more fluid environment, while the others correspond to doxyl groups strongly immobilized on the ESR time scale. This effect is ascribed to the flexibility gradient as an intrinsic property of the stearic acid chain [5].

There are two common ways of the application of free nitroxide radicals [3]: (i) nitroxides can be covalently attached to polymer chains, or (ii) they can be introduced mechanically (by diffusion) into a polymer matrix. The former method is named spin labeling and the latter is the spin probe method. The advantage of spin labeling is the precisely known position of the nitroxide in a polymer chain [4]. However, this method demands additional synthetic efforts and is rather limited since it cannot be applied to polymer systems without an adequate functional group. The spin probe method is easier and gives the possibility to introduce nitroxides into polymer systems simply by dissolving or swelling the polymer in a probe solution. After the removal of solvent, probes stay incorporated in a polymer matrix. Recent investigation indicates that the temperature of probe incorporation process must be strictly controlled, particularly for inhomogeneous systems [6]. In addition, when the spin probe method is used, it is necessary to take care of a possible attachment of the spin probe to the polymer chain by hydrogen bonding [7].

An advantage of ESR spectroscopy, when compared to other techniques, is that in the cases of spin probe and spin labeling, very low concentrations of nitroxide radicals ($\sim$0.1 wt% or lower) embedded in a polymer matrix result in a good signal-to-noise ratio. Therefore, an introduction of nitroxides into the polymer matrix induces a slight perturbation of the matrix with no significant influence on its properties.

15.1.2 Theoretical Background

Once the nitroxide radical is placed in a static magnetic field, the interaction energy of the magnetic moment associated with the spin **S** with an external magnetic field **B** is described by the Hamiltonian [1, 2]:

$$\mathcal{H} = \mu_B \, \mathbf{B}\,\mathbf{g}\,\mathbf{S} + \mathbf{I}\,\mathbf{A}\,\mathbf{S} \tag{15.1}$$

where μ_B is the Bohr magneton and **I** is the nuclear spin of ^{14}N. The above Hamiltonian consists of two terms: first, known as the Zeeman interaction, which describes the interaction of the electron spin **S** with the static magnetic field **B** and the second, the hyperfine interaction, which describes the interaction between electron and nuclear magnetic moments. Values **g** and **A** are the tensors which parameterize the Zeeman and hyperfine interaction, respectively. The Zeeman interaction splits the energy of a nitroxide molecule in two levels and the hyperfine interaction additionally splits each Zeeman level in three sublevels, as shown in Figure 15.3. Finally, the ESR spectrum of a nitroxide radical shows three absorption lines, registered in the form of the first derivative.

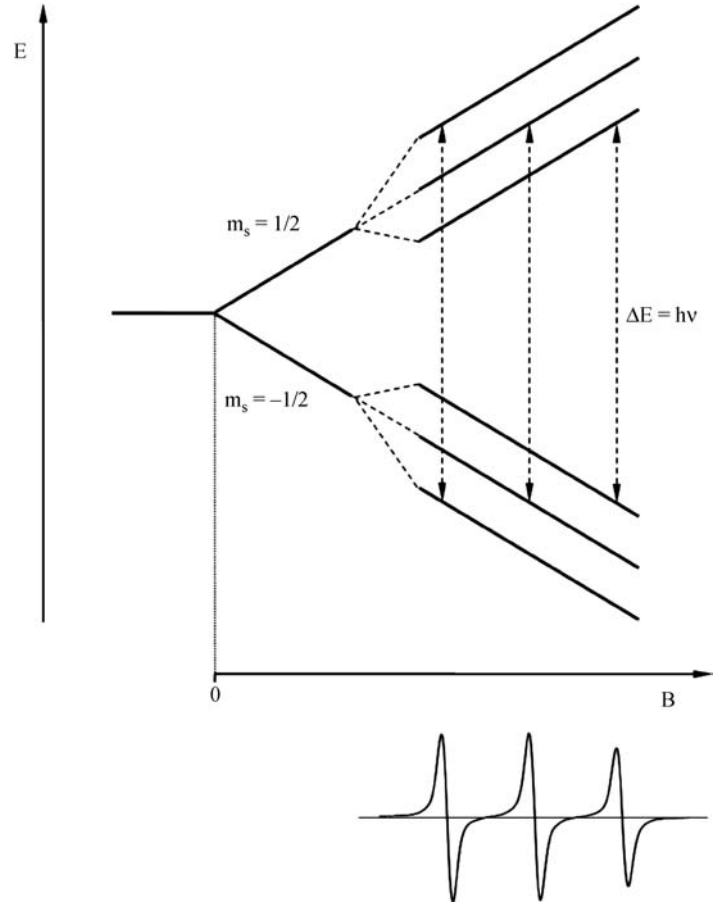

Figure 15.3 Energy levels of a nitroxide radical placed in an external magnetic field

The model ESR spectrum of a spin probe in a polymer matrix measured well above the glass transition temperature is shown in Figure 15.4a. The spectrum consists of three well resolved Lorenzian lines characteristic of the fast molecular motions [3]. Nevertheless, when the segmental motions are frozen ($T < T_g$), the ESR spectrum indicates the slow dynamics of the spin probe determined mostly by the size of free volume holes. However, the motions of side chain groups can also contribute to the slow tumbling of probe molecules. A typical spectrum characteristic of the slow probe motion, composed of three overlapping broad lines, is presented in Figure 15.4b.

In a particular case of an inhomogeneous system, the ESR spectrum observed in the temperature region just above T_g shows a bimodal character [3, 6], which can be seen in Figure 15.4c. Such a bimodal spectrum is composed of two components: the broad component attributed to the slow motion and the narrow one that corresponds to the fast motion of a spin probe. The simplest analysis of a bimodal spectrum can be made by measuring the intensities of broad (I_b) and narrow (I_n) lines. Then the calculated intensity ratio I_n/I_b can be taken as a simple

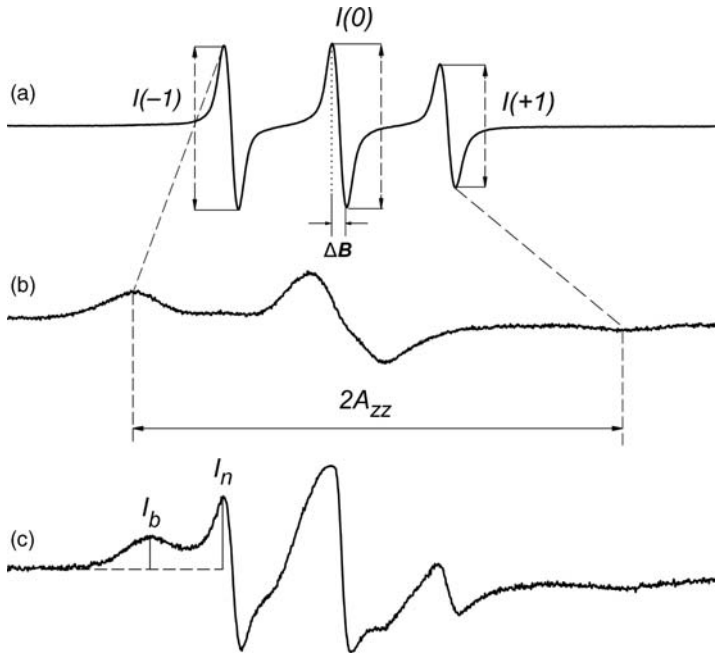

Figure 15.4 Model ESR spectra of a nitroxide radical typical for the polymer: (a) well above T_g; (b) below T_g; and (c) inhomogeneous system just above T_g (Adapted with permission from M. Didović, D. Klepac and S. Valić, "ESR − spin probe method in studying natural rubber: an effect of the probe incorporation temperature," *Macromolecular Symposia*, **265**, 144–147, © 2008, Copyright Wiley-VCH Verlag GmbH & Co. KGaA.)

quantitative measure of the probe dynamics. Higher value of this ratio indicates higher amount of the fast component present in a dynamically inhomogeneous system. The analysis of such composite spectra is often used in the characterization of different heterogeneous systems, particularly elastomers, polymer blends, copolymers, block copolymers, interpenetrating polymer networks and polymer-filler systems [3, 8–14].

Further analysis of ESR spectra makes it possible to deduce useful data about motional behavior of nitroxide molecules, closely related to the dynamics of polymer matrix. Applying the model of an isotropic Brownian motion, relatively precise values of rotational correlation times (τ_R) in the range of fast motions ($10^{-11}\,s < \tau_R < 10^{-9}\,s$) can be estimated using the Kivelson theory [15]:

$$\tau_R = 0.65 \times 10^{-5} \Delta B \left\{ \left[\frac{I(0)}{I(-1)} \right]^{1/2} + \left[\frac{I(0)}{I(+1)} \right]^{1/2} - 2 \right\} \tag{15.2}$$

where $I(-1)$, $I(0)$ and $I(+1)$ are intensities (peak-to-peak amplitudes) of the low, central and high field line, respectively, and $\Delta\mathbf{B}$ is the linewidth of the central line, Figure 15.4a. For slow spin probe motion ($\tau_R > 10^{-9}\,s$), τ_R values can be calculated by:

$$\tau_R = a(1-S)^b \tag{15.3}$$

where a and b are constants depending on the diffusion model, and S is the ratio of outer extrema separation ($2A_{zz}$) of the given spectrum (Figure 15.4b) divided by its maximum value, measured for the completely immobilized nitroxide [16].

The value $2A_{zz}$, when measured as a function of temperature, shows a typical sigmoidal dependence, as presented in Figure 15.5. From the data presented in Figure 15.5, it is possible to determine an additional ESR parameter, known as T_{5mT}. This parameter corresponds to the temperature at which the outer extrema separation reaches the value of 5 mT. Natural rubber (NR) is an inhomogeneous system and, therefore, the broad component is partially present in the ESR spectra at $T > T_g$. Since the decrease of $2A_{zz}$ value with the temperature increase is due to the change in motional probe behavior that reflects the dynamics of surrounding polymer chain segments, T_{5mT} value can be correlated with the glass transition temperature of the investigated polymer system [17]. This correlation, based on the free volume model, is expressed by the equation [18]:

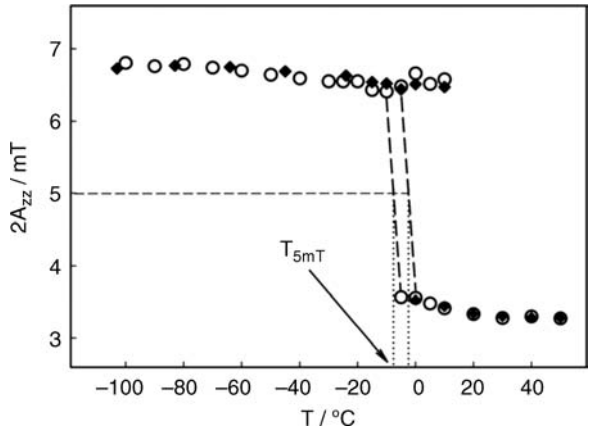

Figure 15.5 Temperature dependence of outer extrema separation ($2A_{zz}$) of uncrosslinked natural rubber (○) and natural rubber crosslinked by γ-irradiation (◆) (Adapted from *Radiation Physics and Chemistry*, **77**, I. Dubrović, D. Klepac, S.Valić and G. Žauhar, "Study of natural rubber crosslinked in the state of uniaxial deformation," 811–817, © 2008, with permission from Elsevier.)

$$T_{5mT} - T_g = 52\{2.9f[\ln(1/f)] - 1\} \tag{15.4}$$

where f is the ratio between the activation volume of a nitroxide probe and a polymer segment undergoing relaxation. The value of T_{5mT}, when compared to T_g measured by differential scanning calorimetry (DSC), is shifted toward higher temperatures. This can be explained by the large difference in the effective frequency of ESR spectroscopy, which ranges from 10^7 to 10^8 Hz at T_{5mT}, and that of calorimetric methods [3], by which T_g values are measured at ~1 Hz. Hence, T_{5mT} values of crosslinked and uncrosslinked sample differ for about 5 °C degrees, even if DSC measurements give the same T_g values (−64 °C) for both samples [17]. This demonstrates the sensitivity of the spin probe on local segmental motions.

On the assumption that the nitroxide molecules are distributed homogeneously in a dynamically inhomogeneous polymer matrix, it is possible to estimate the exact amount

of the mobile and immobile matrix fraction at temperatures in the vicinity of T_{5mT} and above T_{5mT}. In order to obtain such information, it is necessary to make a decomposition of bimodal ESR spectra. This implies the data retrieval of broad and narrow components contained in bimodal ESR spectrum. In fact, spectral decomposition comprises the detection of such broad and narrow components whose superposition (a simple addition of their corresponding intensities) will result in an experimentally observed spectral lineshape. Two programs for calculating ESR spectra, developed by Schneider and Freed [19] and by Stoll and Schweiger [20, 21], are available and they are often used satisfactorily, taking into consideration an isotropic Brownian motion [22]. However, in some inhomogeneous systems the programs have failed to reproduce experimentally observed spectra [3, 23]. Particularly, the main problem in simulating ESR spectra usually occurs when the spectra of slow motion should be reproduced. Consequently, a semiempirical method has been developed and applied for the simulation of bimodal spectra of natural rubber [24]. This method is based on the calculation of fast motional components and their combination with a set of experimentally measured slow motional components of the like systems, as shown in Figure 15.6.

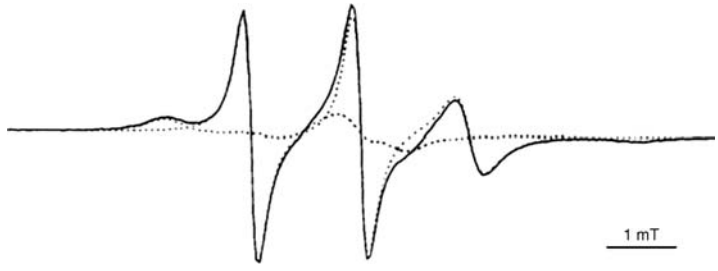

Figure 15.6 Simulated ESR spectrum of 4-hydroxy-2,2,6,6-tetramethylpiperidine-1-oxyl spin probe diffusing in natural rubber crosslinked by γ-irradiation (total dose 250 kGy). The spectrum corresponds to that experimentally observed at 283 K. The broad and narrow components are presented by dotted lines (Adapted from *Radiation Physics and Chemistry*, **51**, Z. Veksli, M. Andreis, S. Valić *et al*., "Different spatial heterogeneity of networks prepared by a two stage irradiation of natural rubber," 207–213, © 1998, with permission from Elsevier.)

15.2 ESR – Spin Probe Study of Nanocomposite Rubber Materials

The application of ESR spectroscopy for the study of nanocomposite materials can be considered as follows: (i) a noticeable number of papers is focused on the use of metallic ions or various agents that give an ESR signal and are present in nanocomposite materials [25–42] and (ii) a significantly lower number of papers reports investigations made by the spin probe and/or spin label techniques [4, 23, 43–45]. In both cases, the results obtained by ESR are related to the changes in material nanostructure. One of the first applications of nitroxide radicals in studying nanocomposite materials was described by M.E. Brik *et al.* [23]. They studied motional heterogeneity in organic–inorganic nanocomposite gels comprising poly(ethylenoxide) chains grafted between silica particles by the spin probe and spin label techniques. The results reported in this work prove that the hindrance of the chain motion in

such a network increases in the vicinity of the silica nodes. Furthermore, the main part of the work in this field was done by G. Jeschke and coworkers [4, 43–48]. They used nitroxide radicals in studying the structure and dynamics of nanocomposite materials [4, 43–45], but also for diffusion measurements [46, 47] and distance measurements in the nanometer range [48].

The first application of spin probe technique in studying nanocomposite rubber materials was carried out recently [49, 50]. Two types of NR samples were prepared: containing (i) nanosilica and (ii) nanoclay particles. These nanofillers are often used as reinforcing agents for different polymer materials [51–54]. The amount of nanofiller varied, while the crosslink density was constant (the samples were crosslinked by an addition of 2.5 phr of sulfur). Additionally, the influence of coupling agent (bis[γ-triethoxysilylpropyl]tetrasulfide, Si-69) on the dynamics of polyisoprene chain segments was investigated for the samples with nanosilica particles. In all measurements, 4-hydroxy-2,2,6,6-tetramethylpiperidine-1-oxyl was used as a spin probe.

The intention of this chapter is to present mainly the qualitative results of the recent work, since the detailed quantitative analysis is currently being developed. ESR spectra of spin probe diffusing in NR matrix doped with 10 phr of nanosilica, measured in a wide temperature range, are presented in Figure 15.7. Spectra obtained in the low-temperature range, that is, below the T_g of NR matrix, consist of three broad lines characteristic of a solid matrix.

Spectral line shapes and line widths change by increasing the temperature and in the high-temperature range ESR spectra consist of three narrow lines indicating the fast probe motion [3]. Particularly interesting are spectra in the middle temperature range, about 0 °C and around room temperature. It is evident that these spectra are composed of three broad and three narrow lines. Such spectra imply the existence of two motionally different spin probe populations that correspond to the slow and fast probe dynamics, as mentioned above.

Figure 15.8 shows the spectra measured at 10 °C for NR samples containing various amounts of nanosilica. Clearly, the fraction of the broad and narrow spectral lines depends on the nanosilica content. The values of the ratio I_n/I_b decrease regularly from 1.72 to 0.92 as the nanosilica amount increases from 0 to 20 phr. However, a significant difference can be observed only between the rubber samples with and without nanosilica, irrespective of the nanosilica content. The glass transition temperatures measured by DSC are almost the same for all samples and oscillate within the limit of experimental error around −57 °C.

A quite strong increase in the fraction of broad component in ESR spectra, when the nanosilica is present in the sample, indicates that the probe molecules sense the presence of the nanofiller. This results in a slower probe motion and should be explained in terms of an interaction between the nanofiller and matrix chains. Such an interaction contributes to the restriction in segmental dynamics. At higher loadings, there is a possibility of agglomeration of particles, which may also have an influence on the probe motion.

The role of the presence of coupling agent was investigated by an addition of 4 phr of coupling agent to NS-10 sample. ESR spectra of the sample with and without the coupling agent are presented in Figure 15.9. It is easy to see that the coupling agent strongly affects the shape of ESR spectra. The spectrum of the sample without coupling agent possesses a quite significant amount of the narrow component. This narrow component almost disappears by the addition of coupling agent. Corresponding values of I_n/I_b ratios are 0.31 and 0.96 for the samples with and without the coupling agent, respectively.

More detailed analysis of ESR results obtained with two samples, with and without the coupling agent is presented in Figure 15.10. This figure shows the change of the outer

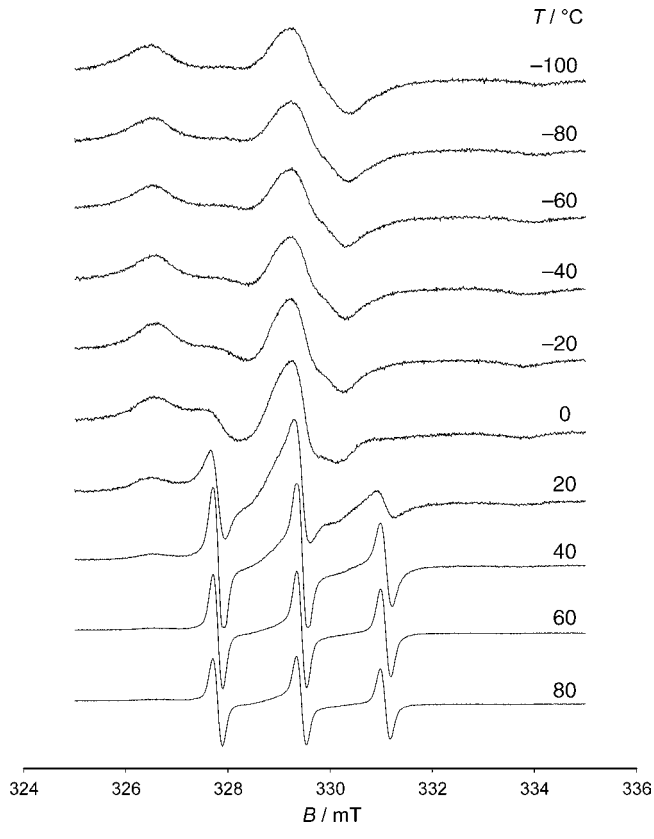

Figure 15.7 ESR spectra of the spin probe diffusing in the matrix of NR sample doped with 10 phr of nanosilica, measured in the temperature range from −100 to 80 °C

extrema of ESR spectra measured as a function of temperature. Two details can be deduced from Figure 15.10: (i) the broad component for the sample containing the coupling agent is present up to 30 °C, while for the sample without coupling agent it disappears at 20 °C, (ii) T_{5mT} values are 16 and 7 °C for the samples with and without the coupling agent, respectively.

As demonstrated in Figures 15.9 and 15.10, the coupling agent has an important influence on the dynamics of chain segments. The changes in the shape of ESR spectra and $T_{5\mathrm{mT}}$ value indicate that the coupling agent makes the interaction between the nanofiller and matrix chains more effective. As a result of the better interaction, the segmental motions become slower. Additional measurements made with the samples containing different amounts of coupling agent, which are not described here, have shown that its presence, even in a very small amount (1 phr), can cause rather intensive changes in segmental motions.

The ESR spectra of the spin probe incorporated in NR containing organically modified nanoclay (Cloisite 20A), when compared to those of NR with nanosilica particles, show strong difference in motional behavior, as shown in Figures 15.7 and 15.11. This difference is

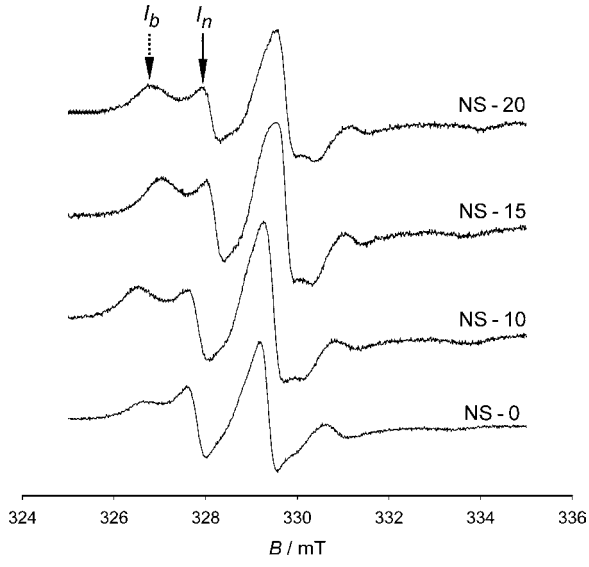

Figure 15.8 ESR spectra of the spin probe measured at 10 °C for the samples containing different amount of nanosilica (the number which follows the sample label "NS" corresponds to the amount of nanosilica, expressed in phr). The dashed and full line arrows indicate the broad and narrow spectral lines, respectively

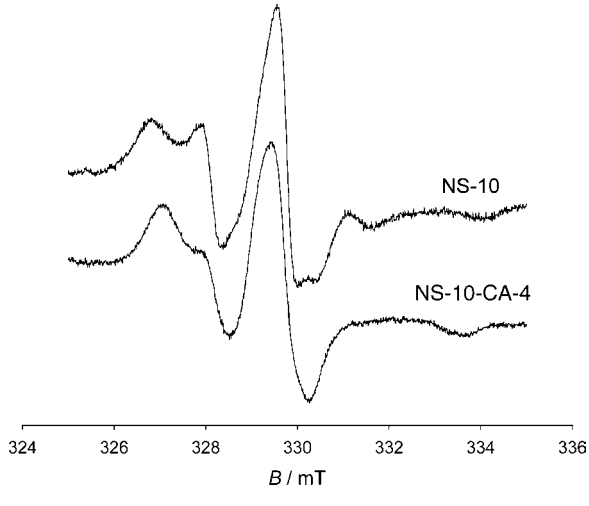

Figure 15.9 The ESR spectra of the spin probe measured at 10 °C for the samples containing the same amount of nanosilica with (NS-10-CA-4) and without (NS-10) coupling agent

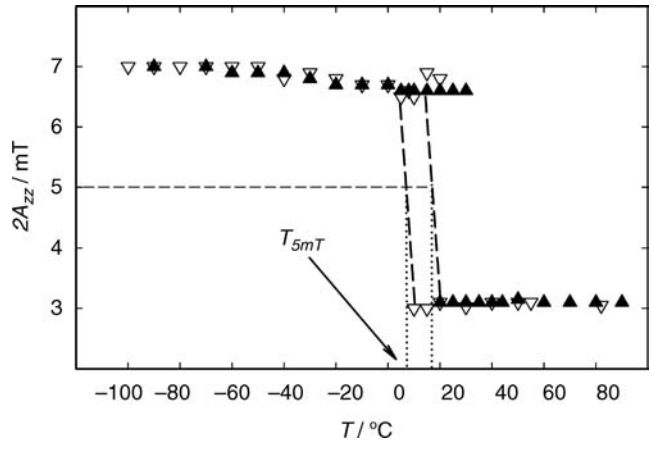

Figure 15.10 Temperature dependence of the outer extrema ($2A_{zz}$) of ESR spectra for the sample with (▲) and without (▽) coupling agent

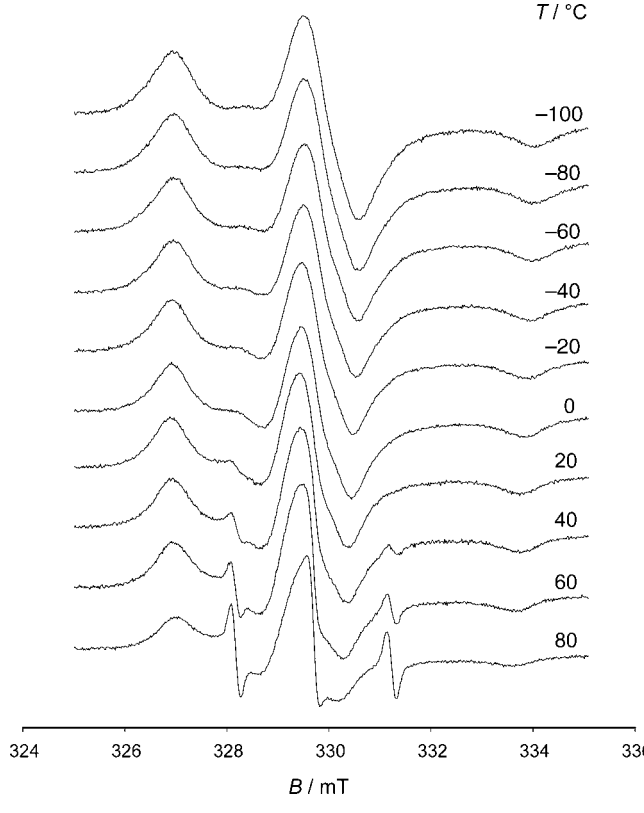

Figure 15.11 ESR spectra of the spin probe diffusing in the matrix of NR sample doped with 10 phr of nanoclay, measured in the temperature range from −100 to 80 °C

particularly evident in the high temperature range (above the room temperature). According to the ESR spectra measured at 80 °C, it is clear that the broad component is well pronounced in NR-nanoclay, while it almost disappears in NR-nanosilica sample. In other words, the restriction in probe motion is much higher in the presence of nanoclay than of nanosilica. The differential scanning calorimetry (DSC) curves of NR-nanoclay composites show T_g around −60 °C, which is close to that of NR-nanosilica composites. This indicates that the interactions between the polyisoprene chains and nanoclay are very intensive and that they introduce an additional restriction in segmental motions. The measurements made by positron annihilation lifetime spectroscopy (PALS) show that nanoparticle–polymer interactions decrease the free volume [55], which can explain the restrictions in segmental motions observed by ESR. The lower free volume also leads to the reduction in gas permeability of such materials [55].

Accordingly, it seems reasonable to expect a positive effect of montmorillonite-based fillers on mechanical properties of the vulcanizates as described in the literature [56–58].

Particularly interesting are the ESR spectra measured at temperatures above 80 °C, Figure 15.12. In this temperature range, three narrow lines indicating fast isotropic motions of spin probe usually occur [3, 22, 24], like with the pure NR and NR-nanosilica samples. However, this is not the case for the NR-nanoclay composites. The broad spectrum implies that even at high temperature probe motions are mainly frozen on the ESR time scale.

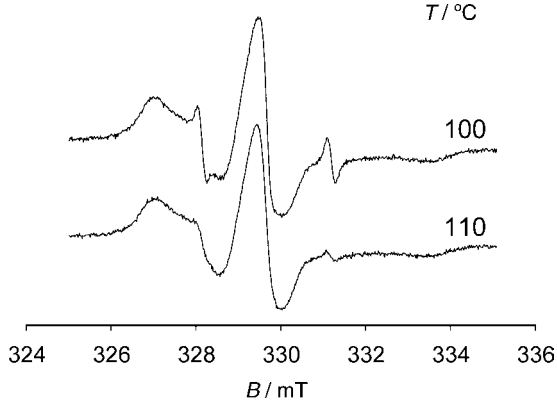

Figure 15.12 ESR spectra of the spin probe measured at high temperatures (100 and 110 °C) for the sample with 10 phr of nanoclay

The DSC results of NR-nanoclay composites, as well as of pure nanoclay, show the first order phase transition in the range from 30 to 60 °C (depending on the weight fraction of the nanoclay in NR). Such a transition, occurring in the low temperature range, should be ascribed to the change in the organic part of nanoclay [59], since it is known that clay nanoparticles are thermally stable in the given temperature range. The appearance of the narrow line in ESR spectra around 40 °C, which indicates that part of the chain segments undergoes fast motions, should be associated with this phase transition whose origin must be

considered in details. In contrast, the decrease of the narrow component at $T > 80\,^{\circ}C$, Figures 15.11 and 15.12, and subsequently its disappearance should be related to the changes in the interaction between the polyisoprene chain segments and nanofiller. Since it is known that organoclays, such as Cloisite 15A and Cloisite 20A, give rise to intercalated nanocomposites [60], one may suppose that such an effect might be the consequence of an extremely strong interaction between the polyisoprene chains and nanoclay particles in the intercalated form. This may result in a very high reduction of the free volume and therefore in slow segmental motions and lower probe dynamics. In order to understand better the described unusual high-temperature line broadening above 80 °C and the disappearance of the narrow component at $T > 110\,^{\circ}C$, additional temperature-dependent X-ray diffraction (XRD) measurements should be performed.

The ESR results, when considered together with XRD measurements, indicate the intercalation of Cloisite 20A by NR matrix chains. In fact, an increase of the interlayer distance for about 1 nm, as measured by XRD, proves the existence of layered clay-NR intercalates. The spectra of the sample containing 5 phr of Cloisite 20A differ from the other samples and suggest that part of Cloisite 20A exfoliates. This is additionally confirmed by the microscopic images (TEM and SEM) and XRD.

15.3 Summary

Electron spin resonance (ESR), known also as electron paramagnetic resonance (EPR), is a powerful tool for the study of molecular motions and structural parameters of various polymer systems. Since the majority of polymers possess no intrinsic paramagnetism, it is necessary to use the stable free radicals (generally nitroxides). Nitroxides can be introduced in a polymer matrix by diffusion (spin probe) or attached by covalent bond to polymer chains (spin label). The advantage of the spin labeling is the precisely known position of the nitroxide in a polymer chain, but this method demands additional synthetic efforts and cannot be applied in the study of polymers without an adequate functional group. The spin probe method is technically very simple; it includes the incorporation of nitroxides in a polymer matrix by dissolving or swelling of polymer in the nitroxide solution. However, the probe incorporation process must be strictly controlled, particularly in the inhomogeneous systems like, for example, natural rubber. It is also necessary to take care of probe size, shape and flexibility as well as of its possible attachment to the polymer chain by a hydrogen bond. In both methods, an introduction of very low concentrations of nitroxide radicals ($\sim$0.1 wt%) results in a good signal-to-noise ratio and has no significant influence on the matrix properties.

An application of spin probe method in studying natural rubber containing the silica and organically modified clay nanoparticles has recently been made. ESR spectra of 4-hydroxy-2,2,6,6-tetramethylpiperidine-1-oxyl measured in a wide temperature range show that segmental motions are hindered in the presence of a nanofiller. This effect is particularly pronounced in the case of nanoclay. For the higher filler loadings nanoparticles agglomerate, which leads to the relative lowering of interaction between the nanofiller and rubber matrix. Natural rubber filled by nanoclay shows an unusual motional behavior in the high-temperature range (above 100 °C); the segmental dynamics seems to be frozen on the ESR time scale. This might be explained by an extremely strong interaction between the polyisoprene chains and nanoclay particles in the intercalated form.

References

1. Berliner, L.J. (ed.) (1976) *Spin Labeling II: Theory and Application*, Academic Press, New York.
2. Marsh, D. (1981) Electron spin resonance: spin labels. In: *Membrane Spectroscopy* (ed. E. Grell), Springer-Verlag, Berlin, pp. 51–142.
3. Veksli, Z., Andreis, M., and Rakvin, B. (2000) ESR spectroscopy for the study of polymer heterogeneity [Review]. *Progress in Polymer Science*, **25**, 949–986.
4. Jeschke, G. (2002) Determination of the nanostructure of polymer materials by electron paramagnetic resonance spectroscopy [Review]. *Macromolecular Rapid Communications*, **23**, 227–246.
5. Cornish, K., Wood, D.F., and Wingle, J.J. (1999) Rubber particles from four different species, examined by transmission electron microscopy and electron-paramagnetic-resonance spin labeling, are found to consist of a homogeneous rubber core enclosed by a contiguous, monolayer biomembrane. *Planta*, **210**, 85–96.
6. Didović, M., Klepac, D., and Valić, S. (2008) ESR - spin probe method in studying natural rubber: an effect of the probe incorporation temperature. *Macromolecular Symposia*, **265**, 144–147.
7. Pace, M.D. and Snow, A.W. (1995) Nitroxide spin probe label study of hydrogen bonding and probe size effects in a linear epoxy polymer. *Macromolecules*, **28**, 5300–5305.
8. Marinović, T., Valić, S., Andreis, M., and Veksli, Z. (1991) Study of matrix inhomogeneity of natural rubber and synthetic polyisoprenes by a spin probe method. *Polymer*, **32**, 2519–2522.
9. Valić, S., Andreis, M., Veksli, Z., and Charlesby, A. (1991) Matrix inhomogeneity in crosslinked rubber and rubber emulsions. *Radiation Physics and Chemistry*, **37**, 257–261.
10. Kovarskii, A.L., Kulish, E.I., Placek, Ya. *et al.* (1993) Aplication of the spin-probe method for the study of 2-phase polymer systems - poly(vinyl chloride) polyethylene blends [in Russian]. *Visokomolekulyarnye Soedineniya A*, **35**, 1669–1673.
11. Hloušková, Z., Tino, J., and Chodák, I. (1994) Study of PE-based composites by the spin-probe method. *European Polymer Journal*, **30**, 175–178.
12. Čulin, J., Andreis, M., Veksli, Z. *et al.* (2005) ESR-spin labelling study of semi-interpenetrating networks and polymer mixtures based on functionalized polyurethanes and polymethacrylates. *European Polymer Journal*, **41**, 1874–1882.
13. Schlick, S., Harvey, R.D., Alonso-Amigo, M.G., and Klempner, D. (1989) Study of phase separation in IPNs using nitroxide spin labels. *Macromolecules*, **22**, 822–830.
14. Cameron, G.G., Qureshi, M.Y., Stewart, D. *et al.* (1994) Spin-label study of immiscible polymers. 5. Blends of labelled poly(2-ethyl hexyl methacrylate) with poly(methyl methacrylate) and polystyrene. *Polymer*, **36**, 3071–3074.
15. Kivelson, D. (1960) Theory of ESR linewidth of free radicals. *Journal of Chemical Physics*, **33**, 1094–1106.
16. Goldman, S.A., Bruno, G.V., and Freed, J.H. (1972) Estimating slow-motion rotational correlation times for nitroxides by electron-spin resonance. *Journal of Physical Chemistry*, **76**, 1858–1860.
17. Dubrović, I., Klepac, D., Valić, S., and Žauhar, G. (2008) Study of natural rubber crosslinked in the state of uniaxial deformation. *Radiation Physics and Chemistry*, **77**, 811–817.
18. Kusumoto, N., Sano, S., Zaitsu, N., and Motozato, Y. (1976) Molecular motions and segmental size of vulcanized natural and acrylonitrile-butadiene rubbers by the spin-probe method. *Polymer*, **17**, 448–454.
19. Schneider, D.J. and Freed, J.H. (1989) Calculating slow motional magnetic resonance spectra: a user's guide. *Biological Magnetic Resonance*, **8**, 1–76.
20. Stoll, S. and Schweiger, A. (2006) EasySpin, a comprehensive software package for spectral simulation and analysis in EPR. *Journal of Magnetic Resonance*, **178**, 42–55.
21. Stoll, S. and Schweiger, A. (2007) EasySpin: simulating cw ESR spectra. *Biological Magnetic Resonance*, **27**, 299–321.
22. Veksli, Z., Andreis, M., and Campbell, D.S. (1998) A spin-probe study of heterogeneity in the natural rubber matrix - the effect of molecular weight, molecular weight distribution and gel phase. *Polymer*, **39**, 2083–2088.
23. Brik, M.E., Titman, J.J., Bayle, J.P., and Judeinstein, P. (1996) Mapping of motional heterogeneity in organic-inorganic nanocomposite gels. *Journal of Polymer Science Part B Polymer Physics*, **34**, 2533–2542.
24. Veksli, Z., Andreis, M., Valić, S. *et al.* (1998) Different spatial heterogeneity of networks prepared by a two stage irradiation of natural rubber. *Radiation Physics and Chemistry*, **51**, 207–213.
25. Kim, B.H., Jung, J.H., Kim, J.W. *et al.* (2001) Physical characterization of polyaniline-Na + -montmorillonite nanocomposite intercalated by emulsion polymerization. *Synthetic Metals*, **117**, 115–118.

26. Kim, B.H., Jung, J.H., Kim, J.W. *et al.* (2001) Effect of dopant and clay on nanocomposites of polyaniline (PAN) intercalated into Na + -montmorillonite (N + -MMT). *Synthetic Metals*, **121**, 1311–1312.
27. Kim, B.H., Hong, S.H., Kim, J.W. *et al.* (2003) EPR signal of nanolayer in conducting polypyrrole (PPy) nanocomposites. *Synthetic Metals*, **135/136**, 1771–1772.
28. Wu, K.H., Li, H.Y., Yang, C.C., and Chen, H.B. (2004) Effect of pH on the EPR properties of NiZn ferrite/SiO2 nanocomposite. *Applied Surface Science*, **228**, 285–291.
29. Wu, K.H., Chang, Y.C., Chen, H.B. *et al.* (2004). Variable temperature electron paramagnetic resonance studies of the NiZn ferrite/SiO_2 nanocomposite *Journal of Magnetism and Magnetic Materials*, **278**, 156–163.
30. Wu, K.H., Ting, T.H., Yang, C.C., and Wang, G.P. (2005) Effect of complexant/fuel on the chemical and electromagnetic properties of SiO_2-doped Ni-Zn ferrite. *Materials Science and Engineering B Solid State Materials for Advanced Technology*, **123**, 227–233.
31. Wu, K.H., Shin, Y.M., Yang, C.C. *et al.* (2006) Preparation and ferromagnetic properties of $Ni_{0.5}Zn_{0.5}Fe_2O_4$/polyaniline core-shell nanocomposites. *Journal of Polymer Science Part A Polymer Chemistry*, **44**, 2657–2664.
32. Maddinelli, G., Montanari, L., Ferrando, A., and Maestrimi, C. (2006) Application of magnetic resonance techniques in investigation of hydrocarbons interaction with composite polymers. *Journal of Applied Polymer Science*, **102**, 2810–2817.
33. Patel, M., Morrell, P.R., Murphy, J.J. *et al.* (2006) Gamma radiation induced effects on silica and on silica-polymer interfacial interactions in filled polysiloxane rubber. *Polymer Degradation and Stability*, **91**, 406–413.
34. Wang, L., and Chen, D. (2006) A one-pot approach to the preparation of silver-PMMA "shell-core" nanocomposite. *Colloid and Polymer Science*, **284**, 449–454.
35. Dridi, C., Haouari, M., Ben Ouada, H. *et al.* (2006) Spectroscopic investigations on hybrid nanocomposites: CdS: Mn nanocrystals in a conjugated polymer. *Materials Science and Engineering C*, **26**, 415–420.
36. Lagadic, I.L. (2006) Schiff base chelate-functionalized organoclays. *Microporous and Mesoporous Materials*, **95**, 226–233.
37. Datta, A., Gorai, S., and Chaudhuri, S. (2006) Synthesis and characterization of sol-gel derived Mn2 + doped In2S3 nanocrystallites embedded in a silica matrix. *Journal of. Nanoparticle Research*, **8**, 919–926.
38. Sarathi, R., Rajesh Kumar, P., and Sahu, R.K. (2007) Analysis of surface degradation of epoxy nanocomposite due to tracking under AC and DC voltages. *Polymer Degradation and Stability*, **92**, 560–568.
39. Cabello, C.I., Botto, I.L., Filace, J. *et al.* (2007) Intercluster porous nanocomposites from combination of $[AlO_4Al_{12}(OH)_{24}(H_2O)_{12}]_7^+$ cation and Anderson-type $[Al_{1-x}Cr_xMo_6O_{24}H_6]_3^-$ anion: XRD, TG-DTA, SEM-EDAX and EPR studies. *Journal of Porous Materials*, **14**, 331–337.
40. Chen, J., Liu, Y., Feng, W., and Cai, W.M. (2008) Structure and photochromism of polyoxometalates nanoparticles in cross-linked polymer networks. *Journal of Materials Science - Materials in Electronics*, **19**, 295–299.
41. Saleta, M.E., Curiale, J., Troiani, H.E. *et al.* (2007) Influence of Ni doping on vanadium oxide/hexadecylamine multiwall nanotubes. *Physica B*, **398**, 333–336.
42. Gonçalves, A.B., Mangrich, A.S., and Zarbin, A.J.G. (2000) Polymerization of pyrrole between the layers of alpha-tin (IV) bis(hydrogenphosphate). *Synthetic Metals*, **114**, 119–124.
43. Vandermeulen, G.W.M., Hinderberger, D., Xu, H. *et al.* (2004) Structure and dynamics of self-assembled poly (ethylene glycol) based coiled-coil nano objects. *ChemPhysChem*, **5**, 488–494.
44. Jeschke, G., Panek, G., Schleidt, S., and Jonas, U. (2004) Addressing the interface in polymer-clay nanocomposites by electron paramagnetic resonance spectroscopy on surfactant probes. *Polymer Engineering and Science*, **44**, 1112–1121.
45. Schleidt, S., Spiess, H.W., and Jeschke, G. (2006) A site-directed spin-labeling study of surfactants in polymer-clay nanocomposites. *Colloid and Polymer Science*, **284**, 1211–1219.
46. Cramer, S.E., Jeschke, G., and Spiess, H.W. (2002) Measurement of diffusion coefficients of additive molecules in colloidal polymer particles by electron paramagnetic resonance. *Colloid and Polymer Science*, **280**, 569–573.
47. Ionita, P., Wolkov, A., Jeschke, G., and Chechik, V. (2008) Lateral diffusion of thiol ligands on the surface of Au nanoparticles: an electron paramagnetic resonance study. *Analytical Chemistry*, **80**, 95–106.
48. Jeschke, G. (2002) Distance measurements in the nanometer range by pulse EPR. *ChemPhysChem*, **3**, 927–932.
49. Lekić, A., Meera, A.P., Valić, S. *et al.* In preparation.
50. Didović, M., Klepac, D. Meera, A.P. *et al.* In preparation.
51. Bandyopadhyay, A., De Sarkar, M., and Bhowmick, A.K. (2005) Rheological behavior of hybrid rubber nanocomposites. *Rubber Chemistry and Technology*, **78**, 806–826.

52. Bandyopadhyay, A., De Sarkar, M., and Bhowmick, A.K. (2005) Poly(vinyl alcohol)/silica hybrid nanocomposites by sol-gel technique: Synthesis and properties. *Journal of Materials Science*, **40**, 53–62.
53. Fiorentini, F., Cakmak, M., and Mowdood, S.K. (2006) Influence of nanosilica particles on hysteresis and strain induced crystallization of natural rubber as investigated by a real time true stress-true strain birefringence system. *Rubber Chemistry and Technology*, **79**, 55–71.
54. Rasid, R., Surip, S.N. Anuar, H. *et al.* (2007) Mechanical and fracture toughness behavior of TPNR nanocomposites. *Journal of Composite Materials*, **41**, 2147–2159.
55. Ammala, A., Pas, S.J. Lawrence, K.A. *et al.* (2008) Poly(m-xylene adipamide)-montmorillonite nanocomposites: effect of organo-modifier structure on free volume and oxygen barrier properties. *Journal of Materials Chemistry*, **18**, 911–916.
56. Hrachová, J., Komadel, P., and Chodák, I. (2008) Effect of montmorillonite modification on mechanical properties of vulcanized natural rubber composites. *Journal of Materials Science*, **43**, 2012–2017.
57. Wang, Y., Zhang, H. Wu, Y. *et al.* (2005) Structure and properties of strain-induced crystallization rubber-clay nanocomposites by co-coagulating the rubber latex and clay aqueous suspension. *Journal of Applied Polymer Science*, **96**, 318–323.
58. Samal, S.K., Nayak, S.K., and Mohanty, S. (2008) Polypropylene nanocomposites: effect of organo-modified layered silicates on mechanical, thermal and morphological performance. *Journal of Thermoplastic Composite Materials*, **21**, 243–263.
59. Carretero-Gonzalez, J., Retsos, H. Verdejo, R. *et al.* (2008) Effect of nanoclay on natural rubber microstructure. *Macromolecules*, **41**, 6763–6772.
60. Silva, S.M.L., Lopez-Manchado, M.A., and Arroyo, M. (2007) Thermoplastic olefin/clay nanocomposites. Effect of matrix composition, and organoclay and compatibilizer structure on morphology/properties relationships. *Journal of Nanoscience and Nanotechnology*, **7**, 4456–4464.

16

Studies on Solid-State NMR and Surface Energetics of Silicas for Improving Filler–Elastomer Interactions in Nanocomposites

Soo-Jin Park[1] and Byung-Joo Kim[2]

[1] *Department of Chemistry, Inha University, 253 Nam-gu, Incheon 402-751, Republic of Korea*

[2] *Nano Material Research Department, Jeonju Institute of Machinery and Carbon Composites, 817 Palbokdong-2ga, Jeonju, Jeollabuk-do 561-844, Republic of Korea*

16.1 Introduction

Knowledge of the surface dynamics of a solid has recently allowed significant progress in many academic and scientific fields: adsorption (solid–gas interaction), wettability (liquid–solid interaction) and adhesion (solid–solid interaction), because it can determine intermolecular interactions at the interface of a solid surface with its environment [1–4]. Recent advances in the understanding of the surface dynamics of a solid have been made on several kinds of the intermolecular interactions at interface in a composite system. This chapter concentrates on the role of filler-elastomer interactions in the solid–solid interface [5–7].

The commercial applications of elastomers often require the use of particulate fillers to obtain the desired reinforcement. In the rubber industry, besides carbon blacks, silicas and alumina powders, other reinforcing fillers are used to impart specific properties to rubber compounds. It is well known that filler-filled rubber composites have multiphase systems which depend on the mobility of rubber molecules and which influence the reinforcement of the composites [8–10].

Extensive works [2–4, 11–14] have also been carried out on structural developments in silica/rubber composites. The surface functional environment of silica particles is quite

Rubber Nanocomposites: Preparation, Properties and Applications Edited by Sabu Thomas and Ranimol Stephen
© 2010 John Wiley & Sons (Asia) Pte Ltd

different from that of other fillers due to the existence of silanol groups in the particles [15, 16]. Thus, the primary discussion on the structural development in the silica/rubber systems focuses on the interactions between silica particles and rubber molecules. Wolff and Wang [17] studied the effects of the surface energies of fillers on rubber reinforcement and reported that the surface energetics of silicas are characterized by a low London dispersive component and a high polar component. On the one hand, the high polar component leads to strong interactions among silica particles; on the other hand, the low London dispersive component causes weak filler–rubber interactions, leading to low moduli of the vulcanizate at a high elongation. Therefore, surface treatments are needed to improve the reinforcement of the composites by increasing the London dispersive component of surface energetics. Various methods used to modify the surface properties of the silicas are largely introduced in terms of thermal, chemical, direct fluorination and coupling agent treatments.

In order to observe surface functional groups and chemical structures of the solid fillers, the solid-state NMR method can give useful data for understanding filler–elastomer interactions in silica–rubber nanocomposites. Solid-state NMR is clearly a very powerful technique capable of looking at a variety of materials. It does not require crystalline materials like diffraction techniques and can still determine local molecular environments [18].

A huge variety of solid-state NMR experiments are available for measuring internuclear distances (dipolar recoupling), the deconvolution of quadrupolar/dipolar influenced spectra, probing site symmetry and chemistry, observing solid-state dynamics and so on [18]. Most of the NMR active nuclei in the periodic table are available for investigation by solid NMR, due to higher magnetic fields, innovative pulse sequences and improved electronics, computer and probe technology.

In this work, we will study the changes of surface chemical structures of silicas by various surface treatments, such as thermal treatment, siliane coupling method and direct fluorination. Solid-state NMR will be applied in order to reveal the relation between the surface functional groups and the surface dynamics of silicas in the elastomer matrix nanocomposite system.

16.2 Surface Modification of Silicas

Silicas are primary used as reinforcing filler in the production of light-colored products. Simply, their white color and, most importantly, their small primary particle size, give rise to a remarkably high reinforcing efficiency compared with other white fillers [19]. However, because silicas have a number of surface silanol groups (Si-OH), on the surface, they are considered to be a highly polar and reactive filler. The presence of silanol groups also brings about strong filler–filler interactions, leading to the inferior filler dispersion of a silica-filled rubber compound compared with that of a carbon black-filled one. As a means of overcoming these drawbacks, surface Si-OH groups can be modified by various nonpolar groups [20, 21].

16.2.1 Thermal Treatment

Thermal treatment is widely applied in real areas, because it is easy to operate, does not require large-scale devices and condensation of surface hydroxyls occurs in the silica surfaces [22–25]. The addition of thermally treated silica to some polymers results in changes in their mechanical properties due to the modification of silanol groups of the silica surface. This treatment can affect

the dispersion and crosslink density of silica/rubber composites by different treatment temperatures. The crosslink density and mechanical interfacial properties of silica/rubber composites can be evaluated by swelling measurements and tearing energy (G_{IIIC}), respectively.

16.2.2 Silane Coupling Method

Silane coupling agents have been used in the rubber industry to improve the performance of silicas and other mineral fillers in rubber compounds. A silane coupling agent contains functional groups that can react with the rubber and the silicas. In this way, the rubber–silicas adhesion is increased and consequently the reinforcing effect of silicas is enhanced.

16.2.3 Direct Fluorination

Direct fluorination is a well established method of modifying fluoropolymers to improve their properties for use, for example, in polymer–membrane gas separation. Therefore it is not necessary to fabricate goods from fluorine-containing polymers; it is simpler, cheaper, and more convenient to apply a surface treatment of articles made from commonly used materials [26–29]. Fluorination is unique in the sense that it represents the sole process by which, in the case of silicas, a bulk addition can be reduced. However, very little attention has been paid to the corresponding fluorinated derivatives [30, 31].

16.3 Solid-State NMR Analyses of Silicas

After various surface treatments, the silica surfaces were confirmed by solid-state ^{29}Si or ^{19}F NMR spectroscopy (Bruker DSX-300 Solid FT-NMR Spectrometer).

16.3.1 Thermally Treated Silicas

Figure 16.1 shows the ^{29}Si-NMR spectroscopy of silicas modified by thermal treatment. Pristine silica shows three peaks, assigned to three possible types of silicon environments, to allow the unambiguous assignment of the measured resonance at −90 (a), −100 (b) and −110 ppm (c) to $(HO)_2Si(OSi\equiv)_2$, $(HO)Si(OSi\equiv)_3$, and $Si(OSi\equiv)$ on the silica surfaces, respectively [32]. After thermal treatments, it is found that $Si(OSi\equiv)$ group at −110 ppm is relatively increased, compared to pristine silicas.

These results can be explained by the thermal treatment causing surface dehydroxylation, resulting in improved siloxane groups on silica surfaces. The disintegrations of hydroxyl groups weaken the strong silica–silica interaction, which reduces the silica agglomeration. These changes lead to an increase of the dispersion of interior silica agglomerates and improvements in the interactions at the interfaces between silica surfaces and rubber matrix.

16.3.2 Silane-Treated Silicas

Figure 16.2 shows the ^{29}Si-NMR spectroscopy of the silicas modified by silane coupling agents. The virgin silicas (pristine or as-received) shows three peaks, assigned to three possible

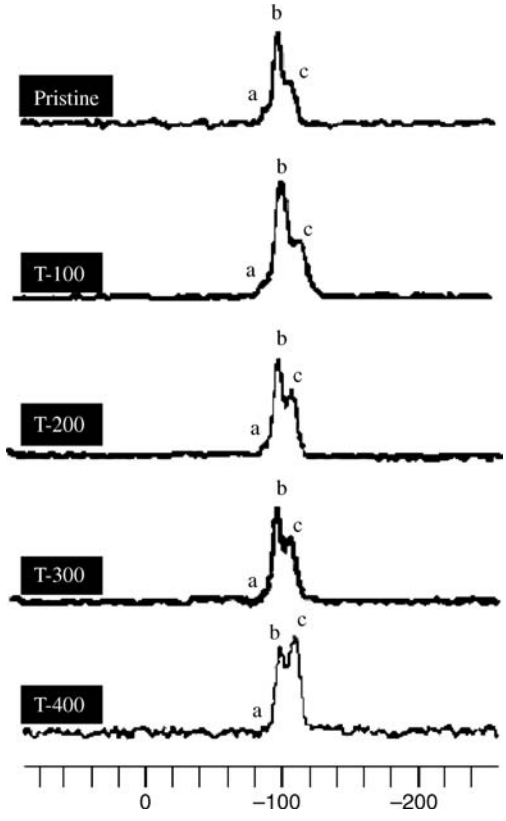

Figure 16.1 Solid-state ^{29}Si NMR spectroscopy of silica as modified by thermal treatment: (a) $(HO)_2Si(OSi\equiv)_2$; (b) $(HO)Si(OSi\equiv)_3$; and (c) $Si(OSi\equiv)$ (Reprinted from *Materials Science and Engineering: A*, **398**, no. 1–2, S-J. Park, S-Y. Jin, S. Kaang, "Influence of thermal treatment of nano-scaled silica on interfacial adhesion properties of the silica/rubber compounding," 137–141, © 2005, with permission from Elsevier.)

types of silicon environments and to allow the unambiguous assignment of the measured resonances at −90 (a), −100 (b) and −110 ppm (c) to $(HO)_2Si(OSi\equiv)_2$, $(HO)Si(OSi\equiv)_3$ and $Si(OSi\equiv)$ on the silica surfaces, respectively [5–7, 32]. After silane coupling agents treatment, γ-amino propyl triethoxy silane (APS), γ-chloro propyl trimethoxy silane (CPS) and γ-methacryloxy propyl trimethoxy silane (MPS) are observed, so that separate ^{29}Si signals from both the surface and the attached silane are able to monitor hydrolysis reactions caused by a cosolvent of methanol (95 wt% in total solvent) and distilled water (5 wt% in total solvent). These are sufficient to distinguish the two signals and show a main peak at −49 (d) and −57 ppm (e) due to $Si(OH)_2R$ and $Si(OSi)(OH)R$ on the surfaces [33], respectively. Also, silane surface treatments increase the intensity of $Si(OSi\equiv)$ groups and decrease the intensity of $(HO)_2Si(OSi\equiv)_2$ and $(HO)Si(OSi\equiv)_3$ groups compared to VS. MPS-treated silicas are observed to give the maximum intensity of $Si(OSi\equiv)$, $Si(OH)_2R$ and $Si(OSi)(OH)R$ groups. The results indicate that silane surface treatments lead to a decrease of the hydroxy groups on silica surfaces through siloxane or hydrogen bonding at the interfaces between silicas and silane coupling agent.

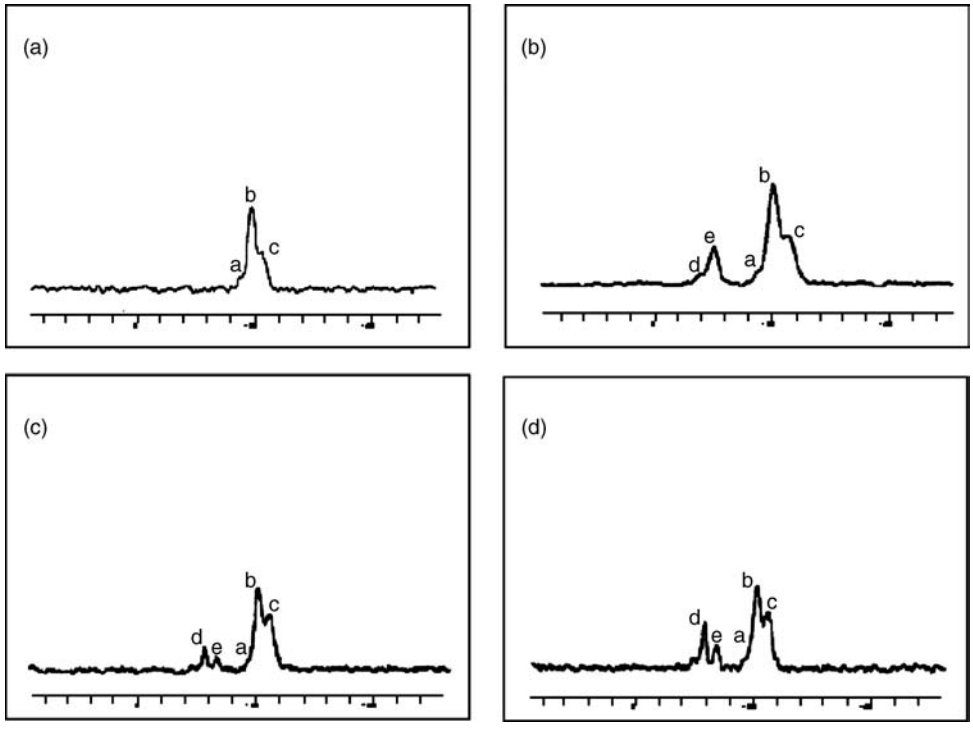

Figure 16.2 Solid-state ^{29}Si-NMR spectroscopy of silicas modified by silane coupling agents (Reprinted from *Journal of Colloid and Interface Science*, **267**, no. 1, S-J. Park and K-S. Cho, "Filler–elastomer interactions: influence of silane coupling agent on crosslink density and thermal stability of silica/rubber composites," 86–91, © 2003, with permission from Elsevier.)

16.3.3 Fluorinated Silicas

To confirm the results, ^{19}F-NMR measurements were performed on the fluorinated silicas, and the results are represented in Figure 16.3. The spectrum of each of the samples includes various peaks of different intensities. The existence of these different peaks means that different types of SiF species interaction occurred on the silica surface. According to Barabash's [19] and Youngman's [20] work, the peaks at −150, −143, −131 and −115 ppm represented O_3Si-F, O_2SiF-OH, O_4Si-F and O_3SiO-F, respectively. According to Barabash's hypothesis, that O_2SiF_2 and O-SiF_3 can be at same position as O_3Si-F, we assumed that the broad and unsymmetrical peak at −150 ppm represented a mixture of O_2SiF_2 and O-SiF_3 [19, 20, 34].

16.4 Surface Energetics of Silicas

To investigate the effect of surface modification, the change of the surface free energy of the thermal treated silica before and after was investigated by contact angle measurements. The surface free energy or surface tension (γ_S) of a solid can be expressed by the sum of the

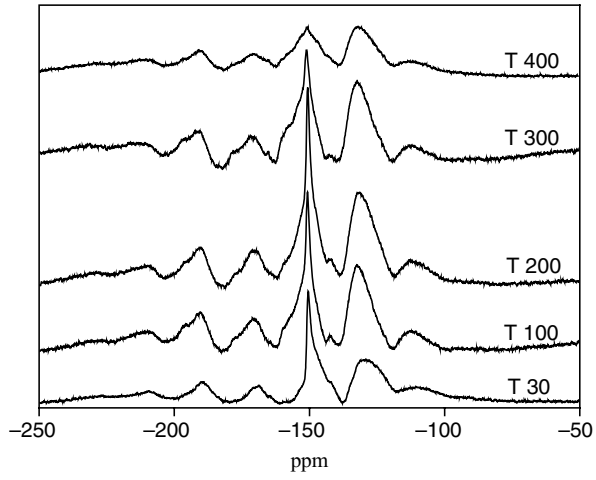

Figure 16.3 ^{19}F solid NMR spectra of fluorine-treated silicas as a function of treatment temperature

London-dispersive (γ_S^L) and specific (γ_S^{SP}) components introduced by Fowkes [1]:

$$\gamma = \gamma^{L} + \gamma^{SP} \tag{16.1}$$

where γ^{L} is the London dispersive component of surface free energy associated with Lifshitz–van der Waals interactions which encompass London dispersion forces, γ^{SP} is the specific (or polar) component of surface free energy related with Debye-inductive polarization, Keesom-orientational polarization forces and hydrogen bonding.

Also, the γ^{SP} component results from electron-acceptor and -donor intermolecular interactions referred to as Lewis acid and base interactions, respectively. The term γ^{SP} is further divided into two parameters using a geometric mean:

$$\gamma^{SP} = 2\sqrt{\gamma^{+} \cdot \gamma^{-}} \tag{16.2}$$

where γ^{+} stands for the electron-acceptor parameter and γ^{-} for the electron-donor parameter of the specific polar component of surface free energy (or tension).

The Young's angle equation can be combined with the Dupré equation to yield the following:

$$\gamma_{L}(1 + \cos\theta) = \gamma_{S} + \gamma_{L} - \gamma_{SL} \tag{16.3}$$

where the subscripts S and L refer to the solid and liquid phases, respectively.

And the interfacial tension, γ_{SL}, can be calculated from the London dispersive and specific polar components of the two substrates as:

$$\gamma_{SL} = \gamma_{S}^{L} + \gamma_{L}^{L} - 2\sqrt{\gamma_{S}^{L}\gamma_{L}^{L}} - 2\sqrt{\gamma_{S}^{SP}\gamma_{L}^{SP}} \tag{16.4}$$

By combining Equations 16.3 and 16.4, the following equation is obtained:

$$\gamma_{L,i}(1 + \cos\theta) = 2\left(\sqrt{\gamma_{S}^{L}\gamma_{L,i}^{L}} + \sqrt{\gamma_{S}^{SP}\gamma_{L,i}^{SP}}\right) \tag{16.5}$$

where the subscript i is the experimental testing liquid, such as water, diiodomethane and ethylene glycol, in Equations 16.2 and 16.5 yielding:

$$\gamma_{L,i}(1+\cos\theta) = 2\left(\sqrt{\gamma_S^L \gamma_{L,i}^L} + \sqrt{\gamma_S^+ \gamma_{L,i}^-} + \sqrt{\gamma_S^- \gamma_{L,i}^+}\right) \tag{16.6}$$

With known values of γ_L^L, γ_L^+, and γ_L^- for three liquids and their contact angles (θ) on the solid, a set of Equation 16.6 can be simultaneously solved to obtain the surface free energy parameters, γ_S^L, γ_S^+ and γ_S^-, for the solid. It is seen from Equation 16.1 that if either the γ^+ or γ^- parameter is zero, that is, there is no polar component contribution to the overall surface free energy ($\gamma = \gamma^L$). And, Equation 16.5 can first determine γ_S^L using a nonpolar liquid ($\gamma_{L,i}^{SP} \cong 0$, i is the diiodomethane) and solve Equation 16.6 to a pair in unknown γ_S^+ and γ_S^- (i is water and ethylene glycol) [1].

In case of thermally treated silicas, the results of surface free energy are shown in Figure 16.4. The elimination of active sites for specific adsorption due to condensation of surface hydroxyls produces an important decrease in the polar component (hydrophilic), γ_S^{SP} and increase in the nonpolar component (hydrophobic), γ_S^L.

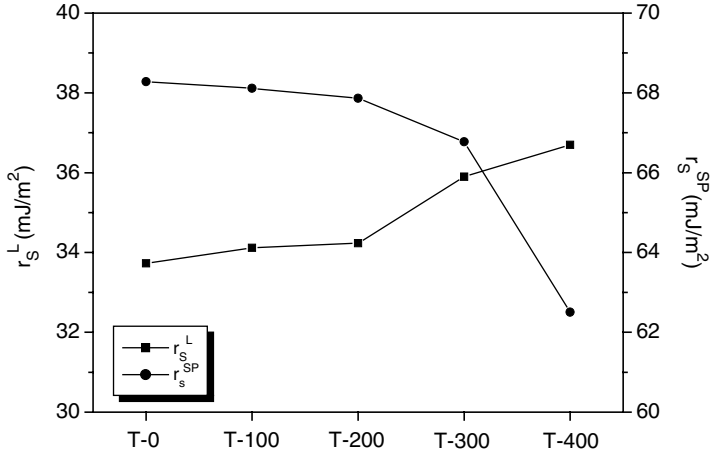

Figure 16.4 Surface free energies of thermally treated silicas as a function of temperature (Reprinted from *Materials Science and Engineering: A*, **398**, no. 1–2, S-J. Park, S-Y. Jin, S. Kaang, "Influence of thermal treatment of nano-scaled silica on interfacial adhesion properties of the silica/rubber compounding," 137–141, © 2005, with permission from Elsevier.)

16.5 Other Surface Analyses of Modified Silicas

16.5.1 Thermally Treated Silicas

The FT-IR spectra of silicas are as shown in Figure 16.5. The peaks at 794 cm^{-1} (Si−O−Si symmetric stretch), 963 cm^{-1} (Si−OH vibration), 1104 cm^{-1} (Si−O−Si asymmetric stretch) and 3800∼3000 cm^{-1} (−OH groups) are shown in the silica surfaces. After thermal treatment, the peak intensities at 3800∼3000 cm^{-1} and 963 cm^{-1} decreased. In contrast, the peak intensities at 794 cm^{-1} and 1104 cm^{-1} increased as the thermal treatment temperature increased. The surface of silica is dehydrated as the temperature of the thermal treatment increases.

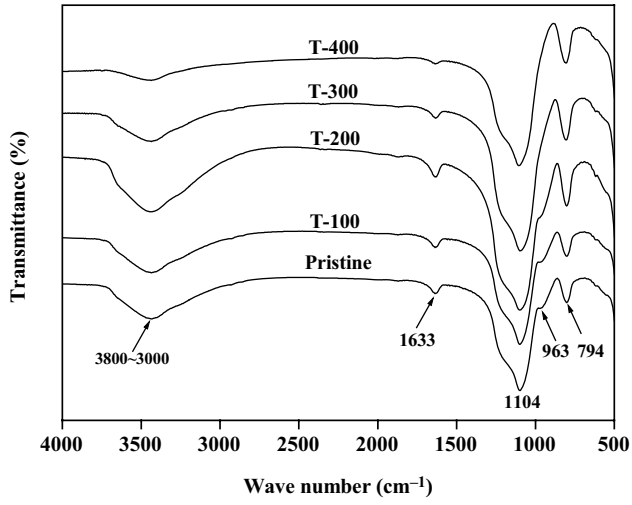

Figure 16.5 FT-IR spectra of thermally treated silicas as a function of temperature (Reprinted from *Materials Science and Engineering: A*, **398**, no. 1–2, S-J. Park, S-Y. Jin, S. Kaang, "Influence of thermal treatment of nano-scaled silica on interfacial adhesion properties of the silica/rubber compounding," 137–141, © 2005, with permission from Elsevier.)

The dehydration comes from the elimination of adsorbed water and thermal dehydration reaction, where two neighboring silanols condense into a siloxane bridge. The experimental results demonstrated that with increasing temperature of heating, the silica surface becomes hydrophobic due to the condensation of surface hydroxyls and the formation of siloxane bridges [35]:

$$(\equiv \mathrm{Sis} - \mathrm{OH}) + (\equiv \mathrm{Si} - \mathrm{OH}) \rightarrow (\equiv \mathrm{Si} - \mathrm{O} - \mathrm{Si} \equiv) + \mathrm{H_2O} \qquad (16.7)$$

Therefore, Si−O−Si (794 $\mathrm{cm^{-1}}$ and 1104 $\mathrm{cm^{-1}}$) peak intensities increase with increasing temperature, compared with pristine silicas. The dehydration occurs under moderate temperature (<200 °C) and consists in the elimination of water adsorbed on the silica surface, and CO double bond (1633 $\mathrm{cm^{-1}}$) peak intensity is increased up to 200 °C. However, it began to decrease after 200 °C due to the acceleration of condensation reactions on the silica surfaces.

16.5.2 Fluorinated Silicas

Figure 16.6 shows the FT-IR spectra of the unfluorinated and fluorinated silicas. After fluorination, peaks, corresponding to the silicon atoms with SiF groups, appeared at approximately 760 $\mathrm{cm^{-1}}$. However, after heating to 300 °C, the peak intensity was noticeably reduced. These results imply that a portion of the silanol groups on the silica surfaces could be exchanged with F [36, 37].

Figure 16.7 shows the XPS spectra of the pure silicas and fluorinated silicas. The peaks located at 100 and 532 eV represent the typical Si and O peaks, respectively, and the new peaks urn up at 682 eV, in response to the F treatment. Like the FT-IR spectra, intensity of the F

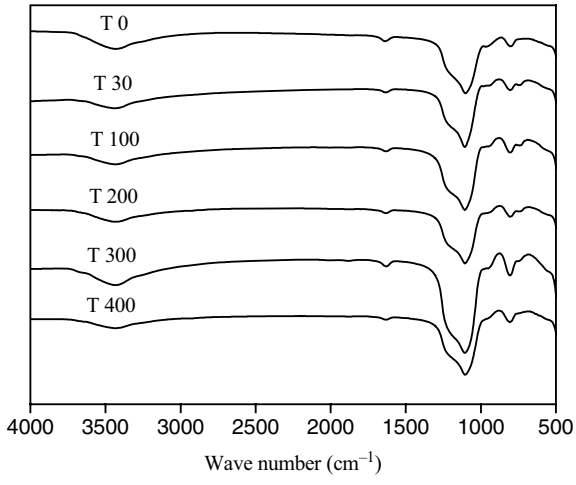

Figure 16.6 FT-IR spectra of fluorine-treated silicas as a function of temperature

peaks was decreased after 300 °C, as can be seen from the relative peak intensities shown in Table 16.1. These results imply that a portion of the silanol groups on the silica surfaces could be replaced with F, forming covalent bonds.

To verify this observation, the silicas spectra of the T 30∼T 400 samples were measured by XPS, as shown in Figure 16.8. Using the Peak fit simulations, the spectra could be decomposed into O_3Si-F, O_4Si-F, and O_3SiO-F, respectively. This shifting means that the interaction between the Si atoms and the F atoms is rather weaker when the number of F groups on silica surfaces is increased. When the temperature was raised to 300 °C, the weak Si-F bonds were broken and the Si-F ratio was decreased.

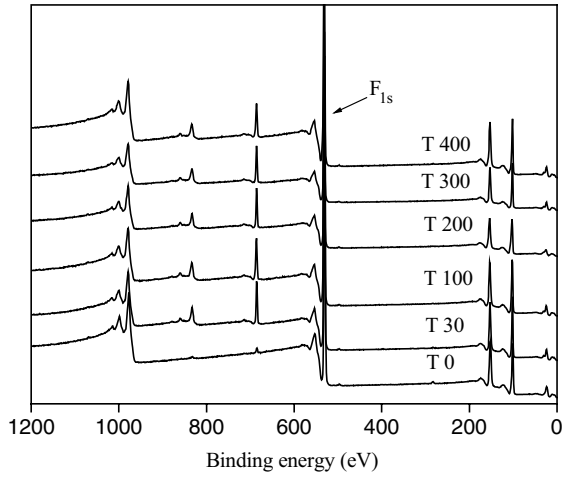

Figure 16.7 XPS survey spectra of fluorine-treated silicas as a function of temperature

Table 16.1 Results for F_{1s} of fluorinated silicas studied as a function of treatment temperature

	T 0	T 30	T 100	T 200	T 300	T 400
F_{1s}	—	8.61	9.62	9.93	9.70	7.09

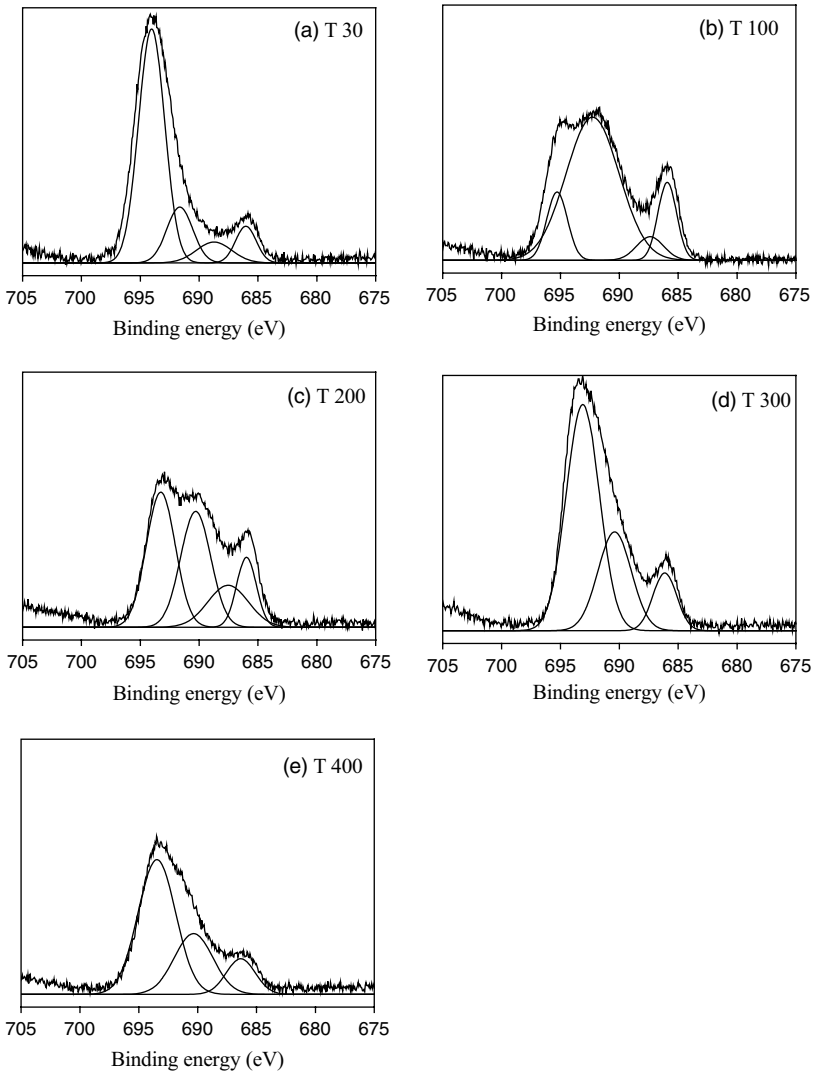

Figure 16.8 Temperature dependence of high-resolution F_{1s} XPS spectra of fluorinated silicas: (a) at room temperature; (b) at 100 °C; (c) at 200 °C; (d) at 300 °C; and (e) at 400 °C

16.6 Mechanical Interfacial Properties of the Compounds

The compounding formulations were listed in Table 16.2. Prior to measuring the mechanical properties of the composites, the filled rubbers were cured for 60 min under a pressure of 1.5 MPa and a temperature of 160 °C for a given period of time, as determined by a torque rheometer (R-100, Monsanto, USA).

Table 16.2 Compounding formulations for rubber nanocomposites

Ingredients	Loading (phr)[1]
Rubber (SBR 1500S)	100
Silica (VN3)	40
Zinc oxide	5
Stearic acid	2
Dispersive agent (EF44)	3
Accelerator[2]	1
Sulfur	2

[1] phr = parts per hundred rubber.
[2] N-oxydiethylene-2-benzothiazole sulfenamide.

Virginal silicas (product name VN3) were prepared by Degussa Co. The thermal treatment for silicas was performed using a pure N_2 under the constant treatment time (1 h) and pressure conditions. SBR (product name SBR1500S; styrene content 23.5%) was obtained by the Kumho Petrochem. Co., and dispersive agent (product name EF44; composition blend of fatty acid derivatives; zinc content 8.5%; density 1070 g/cm^3) was supplied by Struktol Co.

In order to reveal the surface properties of silicas and rubber interactions, we used the swelling and tearing test of silica/rubber compounds by following methods. The cured test pieces of 1 g were swollen in toluene until equilibrium swelling was achieved, which normally took 24 h at room temperature. In this study, the degree of swelling was measured according to ASTM D366-82 and calculated using the relation [38, 39]:

$$Q(\%) = \frac{m - m_0}{m_0} \times 100 \tag{16.8}$$

where m_0 and m were the masses of the sample before and after swelling (measured using an electric balance of sensitivity 10^{-5} g), respectively. The solvent used in this work was toluene [molar volume 107 cm^3/mol; cohesive energy density 37.2 (J/cm^3)$^{0.5}$].

The tearing energy (G_{IIIC}), one of the critical strain energy release rate (G_{C}), was characterized by trouser beam tests for the mechanical interfacial properties of rubber compounding. Rectangular specimens about $70 \times 50 \times 2$ cm^3 were cut from a sheet that was manufactured by a two-roll mill technique. All tests were conducted at a crosshead speed of 2 mm/min.

16.6.1 Thermally Treated Silicas

Swelling of rubber compounds was frequently used for determination of crosslink density. One of the most important structural parameters characterizing a crosslinked polymer is M_c, the

average molecular weight between crosslink, which is directly related to the crosslink density. Early research by Flory and Rehner laid the foundations for the analysis of equilibrium swelling. According to the theory of Flory and Rehner, for a perfect network [38, 39]:

$$M_c = -V_1\rho_p \frac{\left[\phi_p^{1/3} - \frac{\phi_p}{2}\right]}{[\ln(1-\phi_p) + \phi_p + \chi_1\phi_p^2]} \tag{16.9}$$

where M_c is the average molecular weight of the polymer between crosslink, V_1 is the molar volume of the solvent, ρ_p is the polymer density, ϕ_p is the volume fraction of polymer in the swollen gel and χ_1 is the Flory–Huggins interaction parameter between solvent and polymer. The solvent used was toluene [molar volume 107 cm^3/mol; cohesive energy density 37.2 $(J/cm^3)^{0.5}$]. The polymer–solvent interaction parameter χ_1 for the SBR-toluene system was 0.446 [40].

The crosslink density, V_e per unit volume in a perfect network, is given by [38, 39]:

$$V_e = \frac{\rho_P N_A}{M_c} \tag{16.10}$$

where,ρ_p is the polymer density, N_A is Avogadro's number and M_c is the average molecular weight of the polymer between crosslink.

Using Equations 16.9 and 16.10, the average molecular weight of the polymer between crosslink, M_c, the crosslink density, V_e, and the degrees of swelling, Q, are calculated for the silica/rubber compounding, as shown in Table 16.3. As results, with increasing temperature, the crosslink density is slightly increased and the swelling behavior is significantly decreased compared to that of the untreated one. These are explained by the fact that the change of silica surfaces affects the increasing of crosslink density and swelling behaviors, resulting in improvements in the mechanical properties of the silica/rubber compounding.

Table 16.3 Average molecular weight, crosslink density and degree of swelling of the silica/rubber composites as a function of thermal treatment temperature

	Pristine	T-100/SBR	T-200/SBR	T-300/SBR	T-400/SBR
$M_c \times 10$ (g/mol)	3.13	2.64	2.19	1.89	1.36
$V_e \times 10^{28}$ (m^{-3})	8.14	10.98	12.28	14.36	19.71
Q (%)	476	378	356	332	300

According to Kraus [41], the degree of adhesion between the filler surface and the rubber can be assessed from the swelling behavior of the sample in a solvent. Therefore, the importance of tearing energy, G_{IIIC}, as a criterion of the interfacial adhesion relationship can be considered. The tearing energy can be considered to be an interfacial characteristic of the constitutive elements of a material. The tearing energies (G_{IIIC}) are measured by a trouser beam test and are calculated using [42]:

$$G_{\mathrm{IIIC}} = \frac{2 \times F}{t} \tag{16.11}$$

where F is the applied force and t the width of the tear path after tearing is completed.

Figure 16.9 shows the tearing energy (G_{IIIC}) of the silica/rubber composites. As shown in Figure 16.9, the tearing energies (G_{IIIC}) of the compounding made from thermal treatment are largely increased with increasing the thermal treatment temperature. The thermal treatment removes the silane groups and increase siloxane groups on silica surfaces. The surface characteristics of silicas after thermal treatments lead to an increase of the crosslink density of the silica/rubber compounding compared to that of untreated silica/rubber compounding. The increase of the tearing energy then leads to an increase of the resulting mechanical interfacial properties of compounding. The treated silica/rubber compounding has higher crosslink density than that of untreated compounding, resulting in an improvement in the tearing energy (G_{IIIC}). Therefore, it is recognized that the increase of crosslink density of the compounding improves the adhesion at interfaces between silicas and rubber matrices in a compounding system.

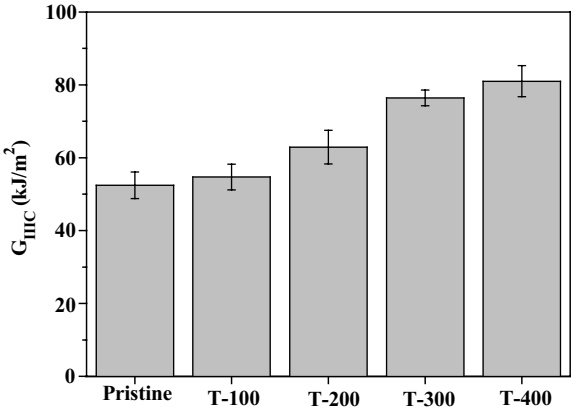

Figure 16.9 Tearing energy (G_{IIIC}) of the silica/rubber compounding as a function of treatment temperature (Reprinted from *Materials Science and Engineering: A*, **398**, no. 1–2, S-J. Park, S-Y. Jin, S. Kaang, "Influence of thermal treatment of nano-scaled silica on interfacial adhesion properties of the silica/rubber compounding," 137–141, © 2005, with permission from Elsevier.)

16.6.2 Silane-Treated Silicas

The degrees of swelling of the silica/rubber composites are listed in Table 16.2. As results, the swelling behaviors of the composites by silane surface treatment are significantly decreased compare to untreated ones. Figure 16.10 shows the weight swelling (g) for the four different composites in toluene with dipping time. The swelling curves of modified silica/rubber composites are similar type to virginal silica/rubber composites. The weight swelling of the composites increases rapidly until dipping time 13 h; after 13 h, it reaches to an equilibrium weight. But, the weight swelling at equilibrium of the composites by silane surface treatments are decreased compare to VS-filled rubber composites. The results could be explained that silane coupling agents form more compacted crosslinking structures in the silane treated silica/rubber composites than untreated ones.

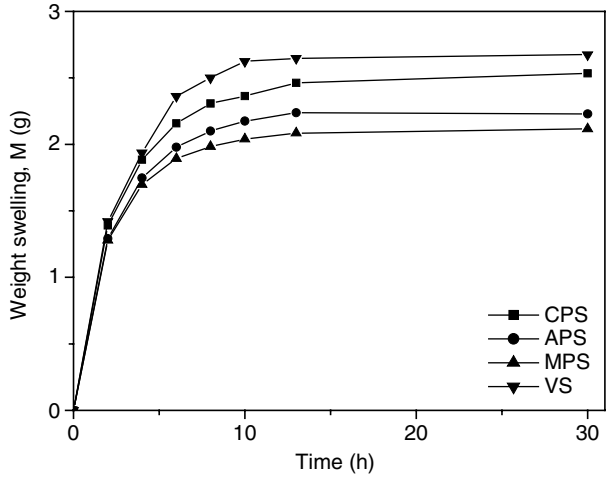

Figure 16.10 Weight of swelling as a function of square root of time for silica/rubber composites with silane coupling agents (Reprinted from *Journal of Colloid and Interface Science*, **267**, no. 1, S-J. Park and K-S. Cho, "Filler–elastomer interactions: influence of silane coupling agent on crosslink density and thermal stability of silica/rubber composites," 86–91, © 2003, with permission from Elsevier.)

The crosslinking density is calculated for the silica/rubber composites, as shown in Table 16.4. The crosslink density of the composites by silane surface treatments is increased compare to untreated silica/rubber composites. In general, when silane coupling agents are introduced onto the silica surfaces in the composites, two interfaces exist between silicas and rubber: the interface between silicas and silane coupling agents and the interface between silane coupling agents and rubber. Therefore, the composites without silane coupling agent show a lower crosslink density than the treated ones due to the lack of cure accelerator by adsorption of accelerator onto the silica surfaces. From the results of NMR studies, MPS-treated silicas are observed in the higher intensity of $Si(OSi\equiv)$, $Si(OH)_2R$, and $Si(OSi)(OH)R$ peaks than VS, APS and CPS. Also, the composites treated by MPS show the superior crosslink density in these systems. It is seen that MPS has organic functional groups, which can react with the double bond of vinyl ester.

Table 16.4 Crosslink density of the silica/rubber composites with silane coupling agents

	VS	APS	CPS	MPS
$V_e \times 10^{29}$ (m^{-3})	0.413	0.464	0.497	0.762

As shown in Figure 16.11, the tearing energies (G_{IIIC}) of the composites made from silane treatments are largely increased as compared to those of VS and increased as a function of the crosslink density, as seen in Table 16.4. Above mentioned the solid-state NMR studies, the silane surface treatments remove silanol groups on silica surfaces and introduce new functional groups on silica surfaces, which can react with the rubber. The surface characteristics of silicas

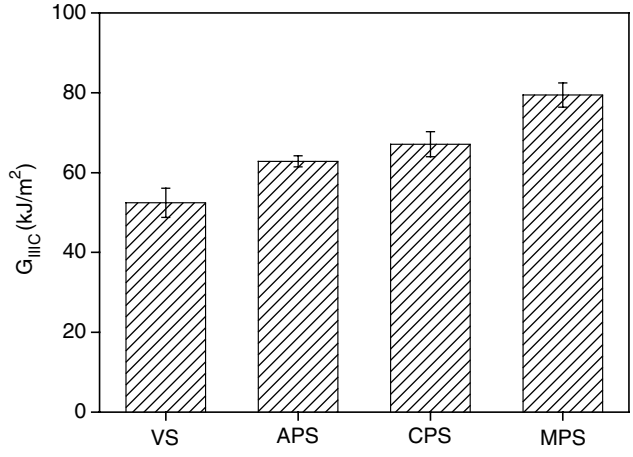

Figure 16.11 Tearing energy (G_{IIIC}) of the silica/rubber composites with silane coupling agents (Reprinted from *Journal of Colloid and Interface Science*, **267**, no. 1, S-J. Park and K-S. Cho, "Filler–elastomer interactions: influence of silane coupling agent on crosslink density and thermal stability of silica/rubber composites," 86–91, © 2003, with permission from Elsevier.)

by silane treatments lead to an increase of the crosslink density of the silica/rubber composites compare to untreated silica/rubber composites, resulting in increasing the tearing energy of the composites. And then, the increasing tearing energy of the composites leads to an increase of the mechanical properties, such as stress and strain, as shown in Figure 16.12. The composites

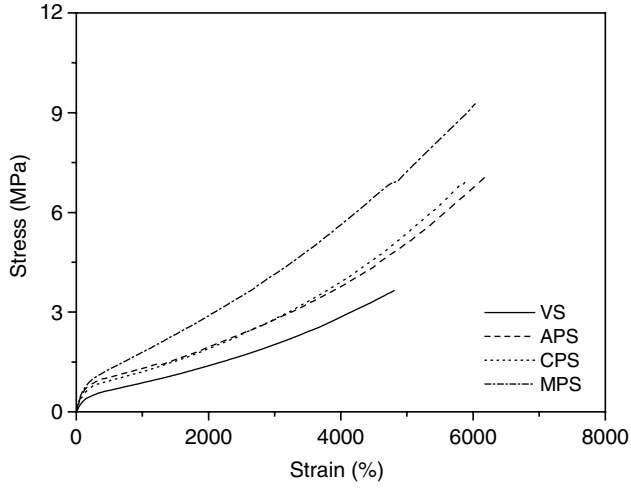

Figure 16.12 Stress-strain curves of the silica/rubber composites with silane coupling agents (Reprinted from *Journal of Colloid and Interface Science*, **267**, no. 1, S-J. Park and K-S. Cho, "Filler–elastomer interactions: influence of silane coupling agent on crosslink density and thermal stability of silica/rubber composites," 86–91, © 2003, with permission from Elsevier.)

treated by MPS, having higher crosslink density than that of the composites made from APS or CPS, are observed to have a higher tearing energy (G_{IIIC}). Therefore, it is recognized that the increase of crosslink density of the composites improves mechanical properties, mainly due to the increase of adhesion at interfaces between silicas and rubber matrix.

16.6.3 Fluorinated Silicas

The mechanical interfacial properties of the fluorinated silicas/NBR nanocomposites were studied. The use of inorganic nanoparticles in elastomer matrices improves the mechanical interfacial properties of composites. Figure 16.13 is a tearing energy graph of the fluorinated silicas/NBR composites. In each case, the same tendency of fluorine on silica surfaces is shown: the fluorine functional groups decease interaction between silicas, which, in turn, increases silicas dispersion in the elastomer matrix.

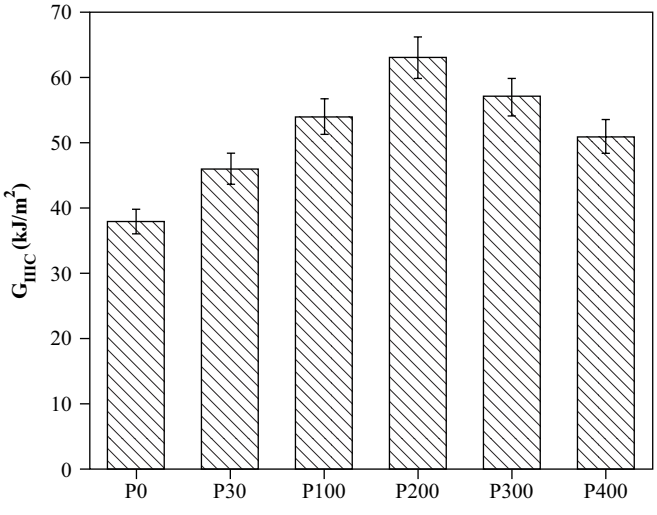

Figure 16.13 Tearing energy (G_{IIIC}) of silica/NBR composites as a function of fluorination temperature

16.7 Conclusions

In this work, various surface treatments, such as thermal, silane coupling agents and fluorination, were applied on silica surfaces and the surface chemical structures were analyzed by solid-state NMR and other methods in order to reveal the relation between surface properties of fillers and filler–elastomer interactions in a nanocomposite system. From this work, it was found that the nonpolar functional groups on the silicas were enhanced after surface treatments and this led to an increase of the adhesion at interfaces between silicas and rubber matrix, resulting in improvements in the crosslink density and mechanical interfacial properties of the composites.

References

1. Park, S.J. (2002) *Encyclopedia of Surface and Colloid Science: Van der Waals Interactions at Surface*, Marcel Dekker, New York.
2. Young, D.M. and Crowell, A.D. (1962) *Physical Adsorption of Gases*, Butterworths, London.
3. Adamson, A.W. (1990) *Physical Chemistry of Surfaces*, 5th edn, John Wiley & Sons, New York.
4. Hwang, S.T. and kammermeyer, K. (1975) *Membranes in Separations*, John Wiley & Sons, New York.
5. Park, S.J. and Cho, K.S. (2003) Filler–elastomer interactions: influence of silane coupling agent on crosslink density and thermal stability of silica/rubber composites. *Journal of Colloid and Interface Science*, **267**, 86–91.
6. Park, S.J., Cho, K.S., and Ryu, S.K. (2003) Filler–elastomer interactions: influence of oxygen plasma treatment on surface and mechanical properties of carbon black/rubber composites. *Carbon*, **41**, 1437.
7. Park, S.J., Jin, S.Y., and Kang, S. (2005) Influence of thermal treatment of nano-scaled silica on interfacial adhesion properties of the silica/rubber compounding. *Materials Science and Engineering A*, **398**, 137–141.
8. Gent, A.N. and Wang, C. (1996) Cutting resistance of polyethylene. *Journal of Polymer Science Part B: Polymer Physics*, **34**, 2231.
9. Park, S.J. and Donnet, J.B. (1998) Anodic surface treatment on carbon fibers: determination of acid-base interaction parameter between two unidentical solid surfaces in a composite system. *Journal of Colloid and Interface Science*, **206**, 29.
10. Park, S.J., Jin, J.S., and Lee, J.R. (2000) Influence of silane coupling agents on the surface energetics of glass fibers and mechanical interfacial properties of glass fiber-reinforced composites. *Journal of Adhesion Science and Technology*, **14**, 1677.
11. Bhadra, S. and Khastgir, D. (2007) In situ preparation of polyaniline coated fumed and precipitated silica fillers and their composites with nitrile rubber (Investigation on structure-property relationship. *European Polymer Journal*, **43**, 4332.
12. Rattanasom, N., Saowapark, T., and Deeprasertkul, C. (2007) Reinforcement of natural rubber with silica/carbon black hybrid filler. *Polymer Testing*, **26**, 369.
13. Liu, Q., Zhang, Y., and Xu, H. (2008) Properties of vulcanized rubber nanocomposites filled with nanokaolin and precipitated silica. *Applied Clay Science*, **42**, 232.
14. Takamura, M., Yamauchi, T., and Tsubokawa, N. (2008) Grafting and crosslinking reaction of carboxyl-terminated liquid rubber with silica nanoparticles and carbon black in the presence of Sc(OTf)3. *Reactive and Functional Polymers*, **68**, 1113.
15. Mélé, P., Marceau, S., Brown, D. *et al.* (2002) Reinforcement effects in fractal-structure-filled rubber. *Polymer*, **43**, 5577.
16. Vigil, G., Xu, Z., Steingerg, S., and Israelachvili, J. (1994) Interactions of silica surfaces. *Journal of Colloid and Interface Science*, **165**, 367.
17. Wolff, S. and Wang, M. (1992) Filler-elastomer interactions. Part IV. The effect of the surface energies of fillers on elastomer reinforcement. *Rubber Chemistry and Technology*, **65**, 65.
18. Massiot, D. (2002) High resolution solid state NMR, in *High Magnetic Fields: Applications in Condensed Matter Physics and Spectroscopy*, LNP, vol. **595** (eds C. Berthier, L.P. Lévy, and G. Martinez), Springer-Verlag.
19. Babarash, R.M., Zaitsev, V.N., Kovalchuk, T.V. *et al.* (2003) Low-temperature fluorination of silica by a nonaqueous solution of NH4F. *Journal of Physical Chemistry*, **107**, 4497.
20. Maebayashi, M., Endo, E., Matsuoka, T. *et al.* (2006) Acoustic analysis of bound rubber formed in silica/SBR compounds. *Ultrasonics*, **44**, e1101.
21. Olejniczak, Z., Leczka, M., Cholewa-Kowalska, K. *et al.* (2005) 29Si MAS NMR and FTIR study of inorganic–organic hybrid gels. *Journal of Molecular Structure*, **744**, 465.
22. Rivera-Utrilla, J. and Sanchez-Polo, M. (2002) The role of dispersive and electrostatic interactions in the aqueous phase adsorption of naphthalenesulphonic acids on ozone-treated activated carbons. *Carbon*, **40**, 2685.
23. Biliński, B. (1998) The influence of thermal treatment of silica gel on surface-molecule interactions I. Finite coverage region. *Journal of Colloid and Interface Science*, **201**, 180.
24. Bonstra, B.B., Cochrane, H., and Dannenberg, E.M. (1975) Reinforcement of silicone rubber by particulate silica. *Rubber Chemistry and Technology*, **48**, 558.
25. Nunes, R.C.R., Fonseca, J.L.C., and Pereira, M.R. (2000) Polymer–filler interactions and mechanical properties of a polyurethane elastomer. *Polymer Testing*, **19**, 93.

26. Solis, D., Ferraro, M.B., and Facelli, J.C. (2002) Modeling NMR chemical shifts: surface charge representation of the electrostatic embedding potential modeling of crystalline intermolecular effects in 19F solid state NMR chemical shifts. *Journal of Molecular Structure*, **602**, 159.
27. Sae-oui, P., Sirisinha, C., Thepsuwan, U., and Hatthapanit, K. (2007) Dependence of mechanical and aging properties of chloroprene rubber on silica and ethylene thiourea loadings. *European Polymer Journal*, **43**, 185.
28. Chamssedine, F. and Claves, D. (2008) A kinetic, morphological and mechanistic approach of the fluorination of multiwall carbon nanotubes. *Chemical Physics Letters*, **454**, 252.
29. Park, S.J., Seo, M.K., and Lee, Y.S. (2003) Surface characteristic of fluorine-modified PAN-based carbon fibers. *Carbon*, **41**, 723.
30. Wang, M., Lu, S.X., and Mahamud, K. (2000) Carbon-silica dual-phase filler, a new-generation reinforcing agent for rubber. Part VI. Time-temperature superposition of dynamic properties of carbon-silica-dual-phase-filler-filled vulcanizates. *Journal of Polymer Science Part B: Polymer Physics*, **38**, 1240.
31. Choi, S.S., Lee, H.M., Ko, J.E., and Kim, M.C. (2007) Recovery behaviors of silica-reinforced SBR vulcanizates using circular deformation test. *Journal of Industrial and Engineering Chemistry*, **13**, 1169.
32. Andre, L. (1990) *The Surface Properties of Silicas*, John Wiley & Sons, New York.
33. Prado, A. and Airoldi, C. (2001) The pesticide 3-(3,4-dichlorophenyl)-1,1-dimethylurea (Diuron) immobilized on silica gel surface. *Journal of Colloid and Interface Science*, **236**, 161.
34. Youngman, R.E. and Sen, S. (2004) Structural role of fluorine in amorphous silica. *Journal of Non-Crystalline Solids*, **349**, 10.
35. Snyder, L.R. (1968) *Principle of Adsorption Chromatography*, Marcel Dekker, New York.
36. Choi, M. and Ryoo, R. (2003) Ordered nanoporous polymer–carbon composites. *Nature Materials*, **2**, 473.
37. Dolbier, W.R. (1993) Fluorination methods. *Science*, **261**, 5125.
38. Flory, P.J. (1950) Statistical mechanics of swelling of network structures. *Journal of Chemical Physics*, **18**, 108.
39. Gwaily, S.E., Badawy, M.M., Hassan, H.H., and Madani, M. (2003) Influence of thermal aging on crosslinking density of boron carbide/natural rubber composites. *Polymer Testing*, **22**, 3.
40. Deng, J.S. and Isayev, I. (1991) Injection molding of rubber compounds: experimentation and simulation. *Rubber Chemistry and Technology*, **64**, 296.
41. Kraus, G. (1963) Swelling of filler-reinforced vulcanizates. *Journal of Colloid and Interface Science*, **7**, 861.
42. Griffith, A.A. (1920) The phenomena of rupture and flow in solids. *Philosophical Transactions of the Royal Society of London, Series A*, **221**, 163.

17

Wide-Angle X-ray Diffraction and Small-Angle X-ray Scattering Studies of Rubber Nanocomposites

Valerio Causin
Dipartimento di Scienze Chimiche, Università di Padova, 35131, Padova, Italy

17.1 Introduction

With their predominantly amorphous nature, elastomers would not seem very prone to X-ray diffraction or scattering studies. As will be shown in the following pages, this is not so true. It must be borne in mind that many elastomers, when stretched, can indeed crystallize. Moreover the preparation of rubber-based nanocomposites consists in the introduction in an elastomeric matrix of fillers, which are crystalline or at least produce a material with fluctuations in electron density within its bulk.

The nanocomposite approach has its roots in the vivid academic and industrial research activity spurred by the increasing demand for high-performance materials. Rather than designing and synthesizing novel polymeric materials employing innovative monomers, it is more convenient under an applicative and industrial point of view to prepare composite materials. The double objective of filler addition is enhancing properties while keeping the cost of the material at an affordable level. Carbon black is nowadays by far the most important filler employed in the rubber industry. It is produced by pyrolyzing oil or natural gas under controlled conditions and is thus associated with pollution. Moreover, it confers a black color to the materials limiting their application in medical, sports and domestic product segments. The quest for other fillers to substitute carbon black in rubber compounds included testing of fillers such as sepiolite, kaolin and silica, but their performance was not adequate and remained

Rubber Nanocomposites: Preparation, Properties and Applications Edited by Sabu Thomas and Ranimol Stephen
© 2010 John Wiley & Sons (Asia) Pte Ltd

below that obtained with carbon black. Due to their inorganic nature, these fillers are not compatible with the polymer matrix and it is therefore very difficult to homogeneously disperse them. More recently, a novel approach has been introduced for the preparation of effective compounds. Clay-based nanocomposites were first discovered by the Toyota group [1, 2]. The dispersion of the reinforcement agents on a nanometer scale and the high aspect ratio of fillers confer to nanocomposites innovative physical and chemical properties with respect to their bulk counterparts [3–5]. A wide variety of nanofillers has thus been tested for reinforcing rubbers, generating the need for techniques that can accurately describe their degree of dispersion in the matrix and the morphology of the obtained composite. This is the aspect that X-ray scattering studies can contribute to shed light on. A quantitative approach to wide-angle X-ray diffraction (WAXD) and small-angle X-ray scattering (SAXS), although somewhat labor intensive, allows to obtain a very thorough description of the structure and morphology of nanocomposites. An especially interesting advantage of X-ray diffraction methods is that, differently from microscopy techniques, they sample the whole bulk of the specimen, thus giving a more generalized picture of its morphology. Being able to exploit this peculiarity at its full extent offers an invaluable tool for a complete characterization of polymer-based nanocomposite materials. This chapter, after a brief introduction on WAXD and SAXS, will present a number of examples of literature works where these techniques were determinant for the investigation. It should not thus be intended as a "textbook" on these techniques (many excellent books of this kind already exist [6–13]) but as a collection of stimulating approaches, among which the reader could find the most suitable solution for his or her particular characterization problem.

17.2 WAXD: An Overview

When X-rays propagate in space, they are accompanied by a periodically changing electric field. If X-rays impinge on a sample, the electrons of the atoms that constitute that sample will be excited to periodic vibrations by this changing field, and will become themselves sources of electromagnetic waves of the same frequency and wavelength. In this instance the phenomenon of incoherent scattering, that is, of diffusion of waves with different frequency than the incident light, will not be considered. New spherical waves are originated then from the electrons of the atoms (which can be treated for our purposes as point sources), which are said to scatter the original beam. The scattered X-ray waves from the atoms can interfere constructively or destructively along certain directions of space, provided that certain geometrical conditions are met. Diffraction is observed when the scattered waves, along a certain direction, have a difference in phase equal to an integer number of wavelengths. When this condition does not hold, destructive interference occurs and scattered radiation is canceled along that direction. Liquids or glasses, that is, amorphous materials, produce diffuse X-ray patterns, whereas when a crystalline order exists in the sample sharp and neat signals due to diffraction appear.

It is beyond the purpose of this contribution to discuss and present the geometrical derivation of the diffraction conditions. A crystal is a regular arrangements of atoms, produced by the periodic repetition of a unit cell. A crystal lattice can be considered as a family of planes extending through the atoms of the lattice, defined by three integer numbers (hkl) known as Miller indices and with a distance between adjacent layers d_{hkl}. Incident X-ray waves are

assumed to be reflected by these planes, and diffraction appears if the Bragg condition is met:

$$n\lambda = 2d_{hkl} \sin\theta \tag{17.1}$$

A family of planes equally spaced by a d_{hkl} distance, impinged by an incident beam of wavelength λ, will give a diffraction signal of order n only at a precise angular value θ given by Bragg law. Along the other directions, destructive interference will occur and no reflections will be observed. Other important concepts, such as the Laue conditions, the reciprocal lattice, the factors that influence the diffracted intensity can be easily found in the specialized literature and will not be discussed here. They will be introduced in the following, when necessary for a more thorough understanding.

17.3 SAXS: An Overview

As may be easily assessed by applying Bragg law, the analysis of aggregates larger than tens of angstroms requires that the investigation be focused in an angular range between 0 and 2° 2θ.

Shifting to SAXS means concentrating on larger dimensional scales, neglecting the minute details of the crystallographic cell, which are the domain of WAXD, to obtain a wider view of the entire system. SAXS is useful whenever, in the material, regions of different electron density with a size between tens and thousands of angstroms exist. For particles immersed in a medium, the parameter that determines the scattered amplitude, and therefore the scattered intensity, is the difference in electron density between the "solute" and the "solvent": $\Delta\rho$. If the dispersed particles have the same electron density than the matrix, the X-ray beam does not distinguish between the two components and the scattered waves will be extinguished in any direction. SAXS is not different from WAXD under a physical point of view: when X-rays impinge upon the sample, the electrons of the materials resonate with the frequency of the incident light and emit coherent secondary waves that interfere with each other.

In the case of a single particle, the scattered intensity $I(q)$ (where $q = \frac{4\pi \sin\theta}{\lambda}$, θ being half the scattering angle, according to the glancing angle used in crystallography) can be calculated taking into account the distribution function of the electrons $p(r)$, which is obtained by geometrical considerations on the particle shape [6]:

$$I(q) = 4\pi \int_0^\infty p(r) \frac{\sin qr}{qr} \mathrm{d}r \tag{17.2}$$

$p(r)$ can be obtained by Fourier inversion of the scattering curve [6]:

$$p(r) = \frac{1}{2\pi^2} \int_0^\infty I(q) \cdot qr \sin qr \cdot dq \tag{17.3}$$

If these single particles are homogeneously dispersed in a dilute system (so that interference between the particles can be neglected), the total scattered intensity will be given by the sum of the intensities scattered by each individual particle. Under this assumption, then, all the independent contributions to the diffracted intensity can be treated as coming from one single particle representative of all the others. SAXS data analysis in these cases thus consists in developing adequate models that allow to reproduce the experimental traces, as a function of morphological parameters, such as size, shape or mass of the particles.

Theoretical $I(q)$ and $p(r)$ have been derived for a number of different geometries, so a fitting based on these models allows to obtain a good picture of the morphology of the system. More complex shapes can be approximated by a collection of primary particles, such as spheres.

What has been said so far applied to dilute systems, but densely packed colloidal particles, such as highly filled nanocomposites, request to take into account interparticle interference effects. Another assumption that is not always valid is that the particles are homogenous and monodisperse in size. Particle anisotropy and polydispersity are very common factors that bring about severe deviations of the system from ideality. A distribution of sizes must therefore usually be included in the theoretical models used to reproduce the experimental SAXS patterns.

As said before, many intensity functions have been calculated for a number of different shapes, for example, spheres, ellipsoids, parallelepipedons, cylinders, that are all similar in the central range. A universal approximation exists for the central part of SAXS traces. Guinier [14] proposed an exponential function only dependent on the radius of gyration R:

$$I(q) = (\Delta\rho)^2 V^2 \exp\left(-\frac{q^2R^2}{3}\right) \tag{17.4}$$

where V is the scattering volume. R is the root-mean square of the distances of all electrons from their center of gravity and is related to the physical dimensions of the particles by geometrical relationships. The Guinier formula holds surprisingly well for a wide variety of cases, failing only for very anisometric particles.

V can be obtained directly from the diffraction pattern by:

$$V = \frac{2\pi^2 I(0)}{\int_0^\infty q^2 I(q)\mathrm{d}q} \tag{17.5}$$

where $I(0)$ is the scattered intensity at zero angle and the integral at the denominator is the invariant Q, which is directly related to the mean square fluctuation of electron density, irrespective of special features of the structure. In other words, alterations or deformations of the structure of part of the system would alter the shape of the diffraction pattern, but the invariant would not change.

A further model-independent parameter can be found in the final slope of the SAXS pattern. In this region, that depends mainly on the fine structure of the particle and not on the mutual arrangement of particles, the intensity $I(q)$ can be approximated by the so called Porod's law [15, 16], $I(q)_{q\to\infty} \frac{(\Delta\rho)^2 2\pi S}{q^4}$, where S is the surface area of the particle. This dependence on q^{-4} holds very well for single particles, densely packed systems and non-particulate structures, as long as a defined internal surface exists. The practical application of this relationship requires the measurements of absolute intensity, but introducing the invariant this problem can be avoided and the specific surface can be determined from the diffraction pattern alone, without any additional data:

$$\frac{S}{V} = \frac{\pi \lim_{q\to\infty} I(q)q^4}{Q} \tag{17.6}$$

17.4 Lamellar Fillers

Clays and clay minerals such as montmorillonite, saponite or hectorite were widely employed as fillers for rubber and plastics for many years, mainly for enhancing properties, saving polymer consumption and reducing the cost [17, 18]. These fillers have lately attracted a renovated interest in the industry and academia, because of the thickness of their layers in the nanometer range, that make these materials ideal for the preparation of nanocomposites.

Montmorillonite is a member of the family of smectites (a group of clay minerals that includes montmorillonite, saponite, sauconite, beidellite, nontronite, and so on) [19]. Smectites occur as minute particles, which, under electron microscopy, appear as aggregates of irregular shapes or hexagonal flakes or, less commonly, of thin laths [20]. Differences in the substitutions within the lattice in terms of position and elemental composition give rise to the various clay minerals.

The molecular formula for montmorillonite is usually given as [21] $(M_x{}^+ \cdot nH_2O)(Al_2{-}yMg_x)Si_4O_{10}(OH)_2$, where $M^+ = Na^+$, K^+, Mg^{2+}, or Ca^{2+}. Ideally, $x = 0.33$. The basic crystal structure of smectites is an octahedral alumina sheet between two tetrahedral silica sheets. These three-layer units are stacked one above another with oxygens in neighboring layers adjacent to each other. This produces a weak bond, allowing water and other polar molecules to enter between layers and induce an expansion of the mineral structure.

The layers are characterized by a high aspect ratio since they have thicknesses of about 1 nm and diameters ranging from 30 nm to several microns or more [4, 22]. Hundreds or thousands of these layers are stacked in clay particles, kept together by weak van der Waals forces. The performance of clay-based nanocomposites is strongly dependent on the breaking-up of clay particles in the polymer matrix. As the degree of interaction between polymer and filler varies, three systems are generally found:

- Clay sheets may remain stacked in structures called tactoids, as in the original mineral. This degree of dispersion does not bring about any improvement compared to usual microcomposites with a low filler loading.
- When polymer chains penetrate into interlayer spacing, an intercalated system is produced, where clay layers are more separated than in the pristine mineral.
- An exfoliated structure appears when the single clay sheets are delaminated and dispersed in the matrix. Strawhecker and Manias proposed that nanocomposites with an interlayer space greater than 5 nm be classified as an exfoliated system, while those with a *d*-spacing below 5 nm should be defined as intercalated [23, 24]. According to some authors a further differentiation is possible into two classes of relative separation of clay layers in the exfoliated state: disorderly exfoliated structure [25–28] and orderly exfoliated structure [29]. In the latter, a layered structure of clay still exists but with a layer spacing larger than 8nm.

The exfoliated system is the most desirable since nanometric dispersion of clay platelets ensures a maximization of the interfacial region between the filler and the polymer matrix, and a consequent improvement in reinforcement effect. If exfoliation occurs, the excellent mechanical properties of the individual clay layers can be effectively exploited and the number of reinforcing components is dramatically increased, since each clay particle contains a very large number of clay sheets. However, it is difficult to achieve exfoliation. Due to the hydrophilic nature of clay, it is generally necessary to modify it, usually by ammonium surfactants, to achieve enough hydrophobicity to be miscible with the polymer matrix.

The WAXD patterns of the types of clays described earlier show two different kinds of signals [21, 30]: symmetrical peaks, usually positioned in the small angle region of the angular range, and asymmetric reflections that show a peculiar shape with a very steep side and a gradual decrease on the other side (Figure 17.1). The former are indexed (00*l*) and are defined as basal signals. They are due to the periodic alternation of the layers in a direction perpendicular to the lateral surface. On the basis of their position, through the application of the Bragg law, it is possible to calculate the spacing between the layers. The asymmetric signals are indexed (*hk*0) and are related to the mean width of the clay layers.

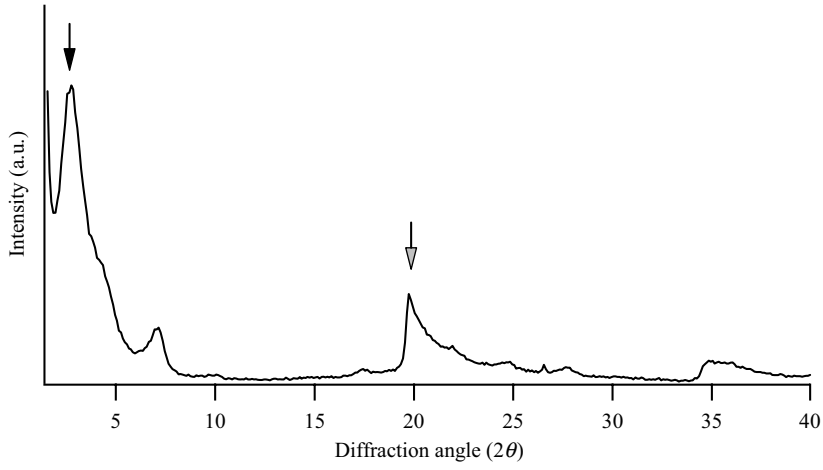

Figure 17.1 Diffraction pattern of an organomodified montmorillonite. The black arrow shows the (001) basal peak, the gray arrow points to a (hk0) peak

It is evident that the position of the basal signal (001) of clay in the X-ray diffractogram of a nanocomposite sample is of great help in defining which degree of dispersion of clay layers in the matrix was attained (Figure 17.2). Generally speaking, a shift of this reflection towards small angles would be associated to a widening of interlayer space, and thus to intercalation. However, if the (001) peak shifts to wider angles, it is a sign that the layers are collapsing one onto the other, usually because of the degradation, exchange or removal of the organomodificant interposed between them.

Zhang's group reported a peculiar and unique nanodispersed structure without macromolecules intercalated into the clay intergallery space, different from the common intercalated or exfoliated structure [31, 32]. In their investigations they found only a marginal increase in *d*-spacing as a consequence of the introduction of clay in several elastomeric matrices. This increase was limited to 0.1 nm for rectorite [31] and was up to about 0.2 nm for montmorillonite [32] and was not large enough to justify the conclusion that rubber molecules had entered the interlayer space and had separated the clay layers. This very slight increase in basal spacings was caused by the processing imposed in the preparation of the samples. First, pristine clay was dispersed in water. In the aqueous medium, the cations already present between the clay layers hydrated, thereby pushing the layers apart. With an increasing water content, in fact, d_{001} increased. Afterwards, rubber latex was added to the aqueous dispersion, avoiding

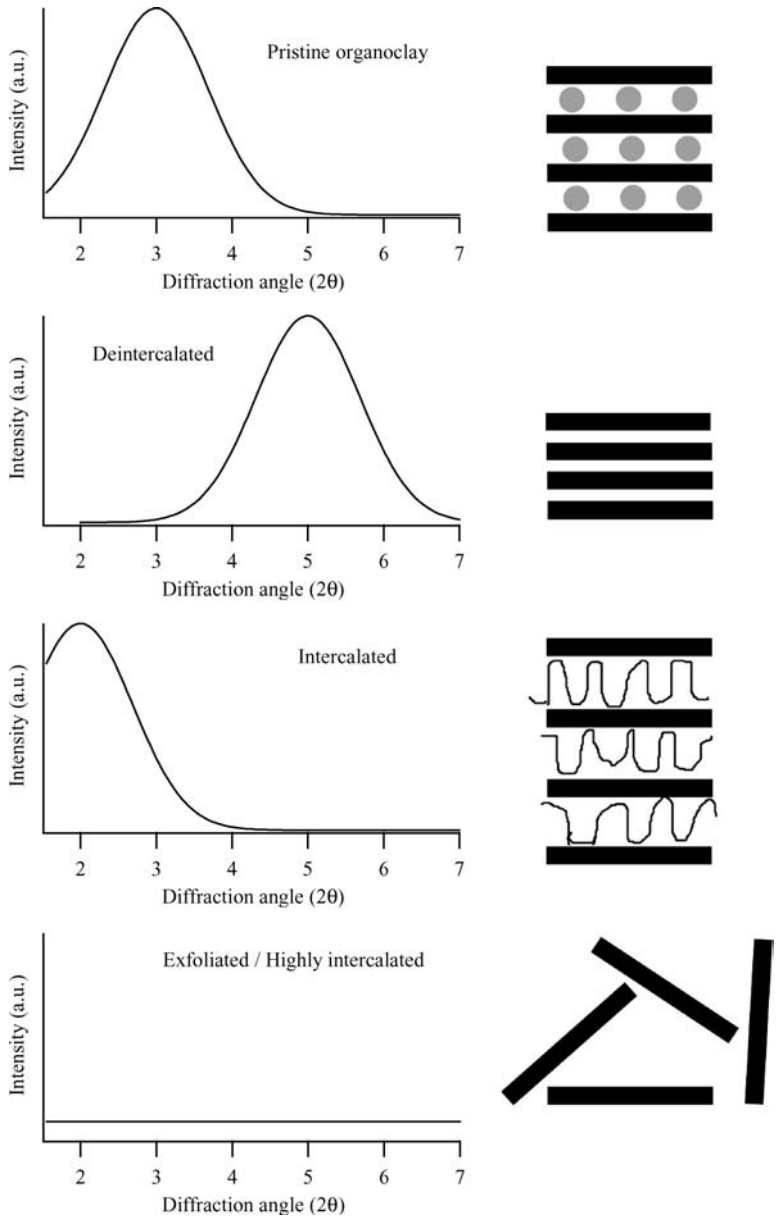

Figure 17.2 Schematic of the WAXD patterns yielded by different filler morphologies. Gray circles in the pristine clay scheme represent the organomodificant molecules

aggregation of clay since both rubber latex particles and clay layers are hydrophilic. Last, a co-coagulation of the mixture by the addition of a flocculant was carried out. Introduction of this agent at this stage determined an exchange of the Na^+ ions existing in the galleries of pristine clay with the cations of the flocculant [31, 32].

The flocculant coagulated both the rubber latex and clay layers, but the intercalation of rubber macromolecules between the clay layers was not observed. The cations in the flocculant tended to enter the interlayer space, obstructing rubber latex particles and preventing intercalation. At the same time, the large amount of latex around the clay layers hindered their re-aggregation, and consequently, the size of clay aggregates was in the nanometer range. Slight increases in interlayer spacing are often observed when characterizing clay-based nanocomposites. Sometimes the shift in the basal peak position is within the experimental error and therefore should not be considered significant. However, when the shift is significant but too limited to be considered the result of intercalation by polymer chains, the most logical and reasonable hypothesis to be done is that some rearrangement of the organomodificant between the layers occurred, due to the change in the environment consequent to the mixing within a polymer matrix.

The studies of Gatos, Karger-Kocsis and coworkers, showed other examples of the potential of WAXD for the thorough description of clay dispersion in a number of rubbers [33–37]. A double population of clay tactoids was frequently found by these authors. In the case of hydrogenated acrylonitrile butadiene rubber (HNBR), they employed two different organoclays, that is, montmorillonite and a synthetic fluorohectorite, with a pristine interlayer spacing of 2.1 and 2.0 nm, respectively [37]. After compounding, the *d*-spacing of the fillers were 3.8 and 3.5 nm for montmorillonite and fluorohectorite, respectively.

As may be seen in Figure 17.3, the diffractograms of the as-compounded, unvulcanized samples showed second and even third order reflections. The presence of such harmonics is associated to very ordered stacking of the intercalated layers [38–45]. After vulcanization, the intercalated structure of the composites underwent dramatic changes, and two populations of tactoids appeared with basal spacings of about 3.0 and 1.7 nm, respectively. Gatos and Karger-Kocsis refer to these two novel populations as deintercalated and confined. According to this terminology, confinement covers the collapse of layers up to the pristine basal spacing of the organoclay in the nanocomposite [33]. Deintercalation, in contrast, is the further collapse due to extraction of the initial intercalant [33]. The presence of two distinct deintercalated and confined populations is evident in Figure 17.3 because the second peak does not fit the predicted position for a (002) reflection. The reason for deintercalation in these nanocomposites is the formation of zinc complexes in which sulfur and the primary amine used as an organomodificant participate. As temperature rises, the amine molecules leave the silicate surface and participate in the formation of vulcanization intermediates [33–35, 37, 46].

In this particular instance, then, the curing procedure brought about a collapse of clay layers. The effects of crosslinking on the dispersion of clay are nevertheless still controversial, due to the complexity of the composite systems that are dependent on the flexibility of rubber chains, differences in crosslinking rate between inner and outer regions of clay galleries and the microstructure and morphology of the composites.

Some authors [42, 47–49] reported that curing reactions could facilitate further intercalation of rubber chains, favoring exfoliated structures. Curing pressure as a critical factor for determining the final microstructure of cured rubber-clay nanocomposites was studied by WAXD [50–53]. In these works, it was shown that X-ray diffractograms of the systems cured under pressure displayed sharp basal signals, also with high order reflections that indicate a very ordered arrangement of the layers. Application of pressure was then found to favor reaggregation of the layers. In contrast, when cure was carried out without applying pressure, no basal signal appeared and exfoliation was attained. The suitability of WAXD to easily follow

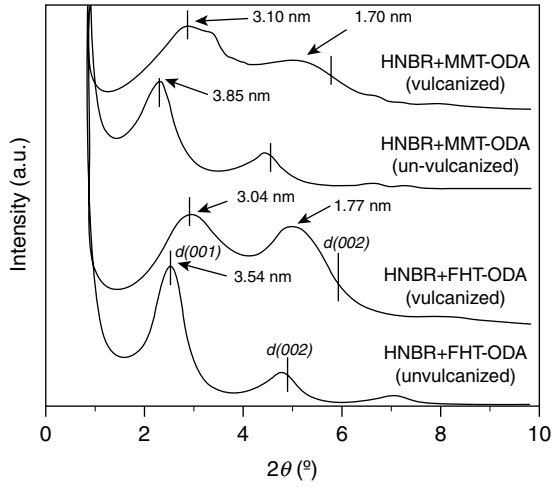

Figure 17.3 WAXD spectra of HNBR-based nanocomposites containing 7.8% organomodified montmorillonite (HNBR/MMT-ODA) and fluorohectorite (HNBR/FHT-ODA) before and after vulcanization. The position of the (001) and (002) reflexes is indicated by vertical lines (Reprinted from *European Polymer Journal*, **43**, K.G. Gatos and J. Karger-Kocsis, "Effect of the aspect ratio of silicate platelets on the mechanical and barrier properties of hydrogenated acrylonitrile butadiene rubber (HNBR)/layered silicate nanocomposites," 1097–1104, © 2007, with permission from Elsevier.)

the effects of processing on the dispersion of clay is evident from the examples given before, and are even more clearly shown in Figure 17.4, where each stage of the preparation process of an EPDM/montmorillonite nanocomposite [54] can be seen.

From the shift of the basal peak towards small angles, it can be concluded that EPDM intercalates into the montmorillonite galleries during the mixing step and that the mechanical shear of the two roll mill further extends this phenomenon. After the curing stage, the basal signal disappears, which is often considered a sign that exfoliation occurred. Considerable attention should be exercised in taking this conclusion, though, because WAXD alone is not sufficient to prove exfoliation [55–58]. In order to correctly assess the degree of interaction between polymer and clay, WAXD and SAXS must be used complementarily. Extensive intercalation could in fact separate clay layers to such an extent to be undetectable by WAXD but that can still be determined by SAXS [59–62]. WAXD instruments have in fact a low angle detection limit, when working in reflection geometry, of 1.5° 2θ at most. Transmission geometry has a higher limit of around 5° 2θ. With the commonly employed X-ray wavelengths, these limits correspond to some tens of Å, often lower than the interlayer distances of intercalated structures. Only the disappearance of SAXS signals and Transmission Electron Microscopy (TEM) observations can confirm that exfoliation has occurred. Moreover a number of possible factors, such as the small sample size, when very low clay loadings are used, or orientation issues, could determine the disappearance or at least a dramatical weakening of the basal signal that could be misinterpreted as exfoliation. Sometimes in the literature, authors tend to overinterpret the decrease of the intensity of basal signals as a sign that exfoliation has occurred at least to some degree. Conclusions taken on these grounds are not sound and reliable, if the previously described factors are not taken into account. This

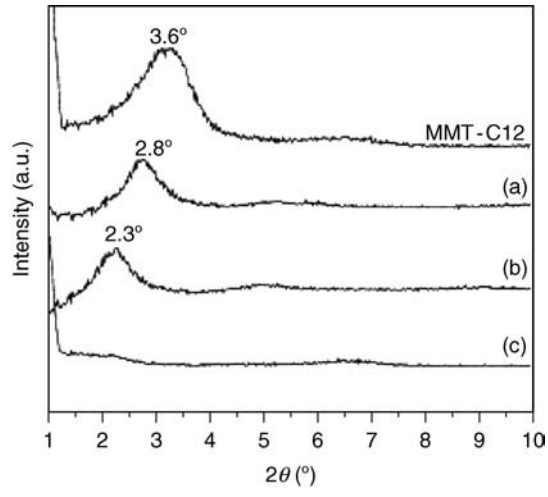

Figure 17.4 WAXD patterns of pristine montmorillonite and of EPDM/MMT composites (a) after mixing in an internal mixer, (b) after pressing in a two-roll mill and (c) after being cured at 175 °C (Reprinted from *Polymer Testing*, **23**, Z. Hua et al., "Influence of clay modification on the structure and mechanical properties of EPDM/montmorillonite nanocomposites," 217–223, © 2004, with permission from Elsevier.)

aspect is very well documented in a paper by Chen and colleagues [63]. They mixed hydroxyl-terminated 1,4-polybutadiene oligomer (HTPB) with montmorillonite modified with octadecyltrimethylammonium chloride (C18-clay). In the WAXD pattern, the absence of the (001) basal reflection peak of HTPB/C18-clay could be explained as a sign of clay being exfoliated. In fact in this case it could be ruled out that the (001) peak disappeared due to the low quantity of clay in the composite, because the (060) in-plane reflection peak of the single-clay sheet [64] could still be detected (Figure 17.5). To complete the characterization of the clay dispersion morphology, SAXS measurements were performed: it can be seen that a weak and broad hump at around 1.2° 2θ is still visible for sample HTPB/C18-clay (10 wt%), consistent with the presence of some swelled tactoids, with an interlayer distance too large to be detected by WAXD.

It frequently happens that WAXD spectra of the nanocomposites display prominent increases in the intensity at lower 2θ values, when compared with those of the unfilled blends. This likely reflects that some degree of intercalation (with the related WAXD peak laying at $2\theta < 2°$) is present in the sample, as can be easily verified by SAXS experiments [65–69].

Very interesting comparisons of WAXD and TEM data, showed moreover that the WAXD signal can disappear even if some intercalation is present. The lack of Bragg scattering can suggest that a wide range of basal layer spacings is present within the tactoids. This variation in persistence lengths (which correspond to regions that have a constant value in the *d*-spacing) can result from a number of different reasons: incomplete exchange of the cations present in the pristine clay galleries with the organomodifier, uneven polymer intercalation, single clay layers organized in tactoids with large interlayer spacing and not regularly ordered [70], variable composition within a tactoid which affects clay surface charge and small tactoid effects [71]. This latter situation, that is, reduction of the size of tactoids to just two or three layers [72], can

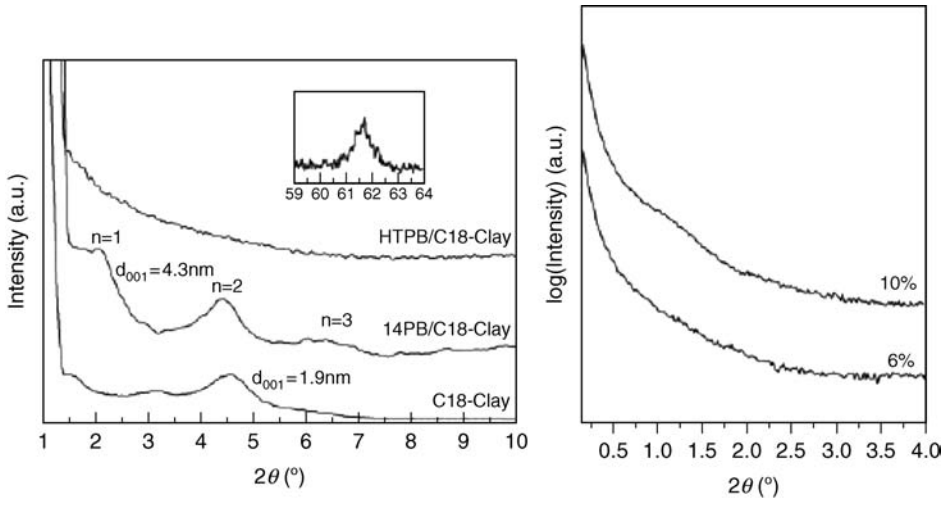

Figure 17.5 Left: WAXD patterns of the organoclay, of the polybutadiene-(14PB/C18-clay) and the HTPB-based nanocomposites (10 wt%). The inset displays the in-plane 060 clay reflection of HTPB/C18-clay (10 wt%). Right: SAXS patterns of HTPB/C18-clay (6 and 10 wt%) (Reprinted with permission from T. Chen, J. Zhu, B. Li et al., "Exfoliation of organo-clay in telechelic liquid polybutadiene rubber," *Macromolecules*, **38**, 4030–4033, 2005. © 2005 American Chemical Society.)

be considered practically equivalent, as far as properties are concerned, to exfoliation [73–76]. As it has already been said, it is very difficult to obtain extensive exfoliation when working with apolar polymers. It is therefore usually much more convenient and worth the effort to aim at a reduction of tactoid size that alone can allow for very interesting increases in properties.

Despite these considerations, WAXD still remains the method of choice for the characterization of polymer–clay nanocomposites. As disorder increases in the sample, WAXD yields less definitive results, though, and should be complemented with other techniques, TEM being probably the most popular one. The main advantage of TEM is that of providing useful data, regardless of the level of order of the system. TEM allows an evaluation by direct visualization of the morphology of nanocomposites, but a great care must be exercised in the selection of representative images. Differently from WAXD and SAXS methods, that sample the whole bulk of the specimen, TEM analyzes just small portions of the material, so it is harder to obtain by this technique a general picture of its morphology. Another drawback in the use of TEM is also the very labor-intensive sample preparation, as opposed to the usually straightforward procedures that are typical in SAXS and WAXD. It is therefore evident that a complementary use of SAXS, WAXD and TEM is necessary for a thorough representation of the morphology of nanocomposites [77, 78]. An advantage of microscopy analysis is immediate information on the spatial distribution and orientation of clay layers in the nanocomposite, but these data are attainable from multiple methods reported on SAXS and WAXD data analysis, the most important ones are discussed below [79–81]. A very simple technique for performing such an investigation is that described by Herrmann and coworkers, who gathered SAXS patterns by a Kratky camera, mounting the sample along three different axes: x, y and z [82].

As can be seen in Figure 17.6, the peaks due to the intercalated structures are detectable in both the x and y dimensions. Therefore it is concluded that the residues of the intercalated

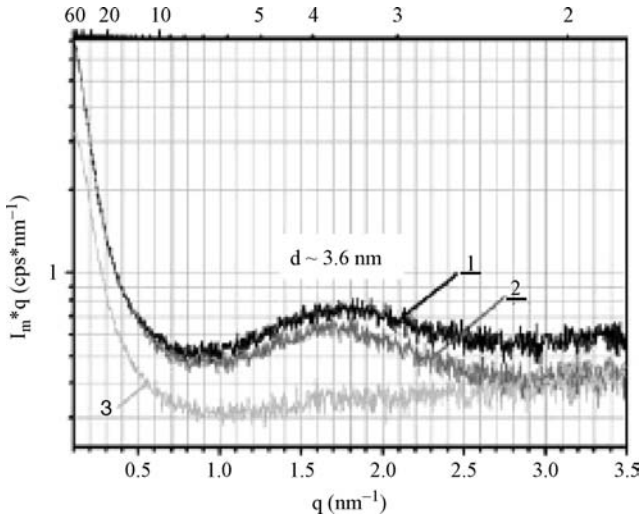

Figure 17.6 SAXS curves of a rubber-clay nanocomposite for different primary beam directions (Reprinted from W. Herrmann, C. Uhl, G. Heinrich and D. Jehnichen, "Analysis of HNBR-montmorillonite nanocomposites: Morphology, orientation and macroscopic properties," *Polymer Bulletin*, **57**, 395–405, © 2006, with kind permission from Springer Science and Business Media.)

structures are orientated in the same direction. This is consistent with an orientation of the layers perpendicular to the *z*-axis, that is, in the *x*-direction.

SAXS and WAXD experiments in two dimensions allow to obtain more detailed information [79, 81]. The possibility of studying the orientation of clay layers is particularly well displayed in Figure 17.7 [79]. The orientation of clay layers is in this case studied as a function of strain. As may be seen, initially the SAXS pattern is isotropic, but it becomes anisotropic as the strain increases. The intensity, that was homogeneously distributed around the circles observed at 0% strain, concentrates along the meridional direction, that is, along the transverse direction, perpendicularly to the strain direction, indicating the alignment of clay layers along the direction of strain.

An advantage of such a 2D approach is the possibility to quantitatively assess the orientation of the layers. A very widely employed parameter used in this case is the Hermans orientation parameter (*f*) [13]:

$$f = \frac{3\langle\cos^2\Theta\rangle - 1}{2} \tag{17.7}$$

where Θ is the azimuthal angle and:

$$\langle\cos^2\Theta\rangle = \frac{\int_0^{\pi/2} I\cos^2\Theta\sin\Theta d\Theta}{\int_0^{\pi/2} I\sin\Theta d\Theta} \tag{17.8}$$

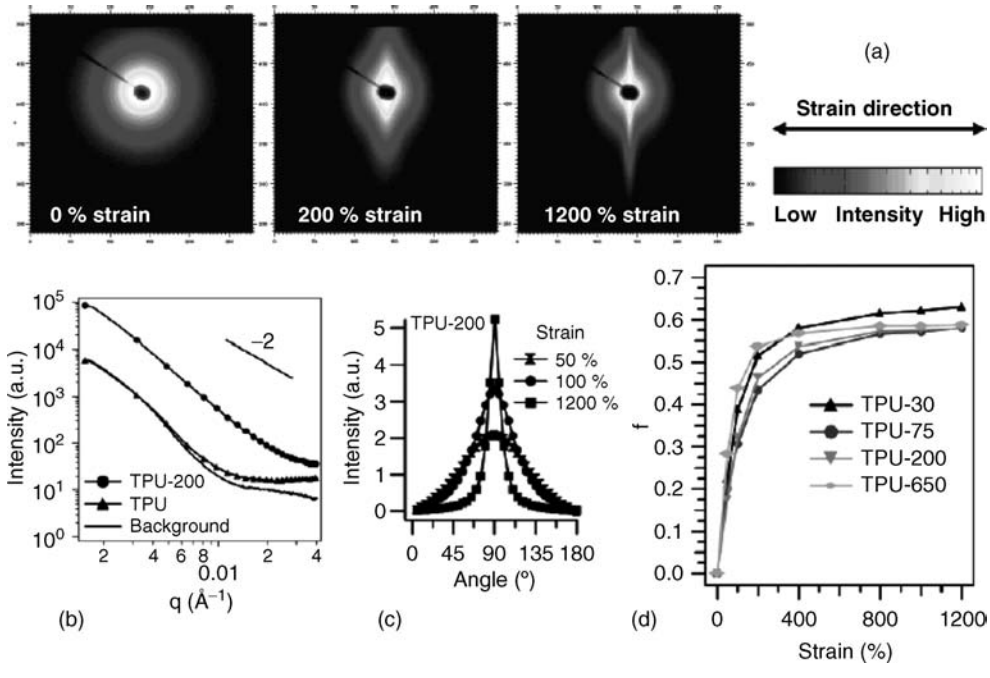

Figure 17.7 (a) 2D SAXS patterns at selected strains for a thermoplastic polyurethane-layered silicate nanocomposite, (b) 1D SAXS profiles illustrating the dominant silicate scattering and power-law behavior, (c) azimuthal scan of scattered intensity at $q = 0.003$ Å^{-1} at selected strains and (d) Hermans orientation parameter as a function of strain (Reprinted with permission from B. Finnigan, K. Jack, K. Campbell et al., "Segmented polyurethane nanocomposites: Impact of controlled particle size nanofillers on the morphological response to uniaxial deformation," *Macromolecules*, **38**, 7386–7396, 2005. © 2005 American Chemical Society.)

f is equal to 1 or $-1/2$ when the system is completely aligned along $\pi/2$ or 0 directions, respectively, whereas it becomes 0 for a completely random system. It should be remembered that the WAXD and SAXS signal may be the sum of different contributions from different structural or morphological elements, for example, different populations of tactoids, present in the system. Each of these possible contributors have scattering maxima at different q values, so f can be a function of q, if these structural elements orient themselves in different ways. The construction of the azimuthally averaged data exemplified in Figure 17.7c should therefore be repeated for several values of q, in order to check if the orientation function is indeed dependent on this parameter.

A very convincing approach for determining the three-dimensional orientation of various hierarchical organic and inorganic structures in polymer-layered silicate nanocomposites was described by Bafna and coworkers [83]. To study the 3D orientation of the structural elements present in the samples, X-ray measurements were gathered with three different orientations of the sample with respect to the X-ray beam. From the azimuthal plots obtained from such patterns and by Equation 17.8, on the basis of a number of trigonometrical relationships, $\langle \cos^2 \Theta_i \rangle$ (i being M, T or N for the machine, transverse and normal direction respectively)

could be calculated and used in a Wilchinsky triangle [7, 13, 84, 85]. This ternary plot, an example of which is shown in Figure 17.8, allows to display the average 3D direction of the structural normal orientation with a single point. For a randomly oriented sample $\cos^2\Theta_M = \cos^2\Theta_N = \cos^2\Theta_T = 1/3$, that correspond to a point in the center of the Wilchinsky triangle. For a structure perfectly orientated in the MT plane, the normal direction points towards the N direction and therefore it is represented by a point at the ND corner. An orientation of a structure normal to the MT plane is represented by a point on the MT axis. A measure of the orientation of a structure along a particular direction, is given by the distance of the point representing the structure from the axis of interest for the particular orientation. The orientation in a planar projection such as the MT plane (any line in the plot reflects a planar projection [84]) is

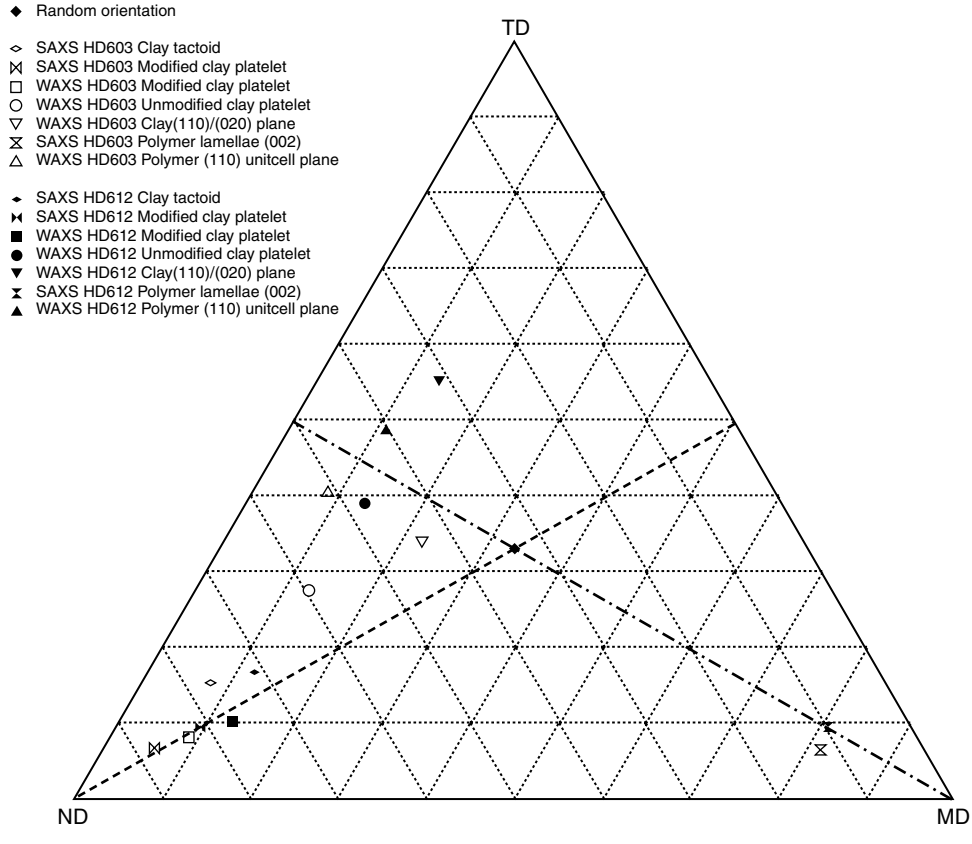

Figure 17.8 Wilchinsky triangle for average normal orientation of clay tactoids, unmodified clay platelets, intercalated clay platelets, clay (110)/(020) plane, polymer lamellae (001) and polymer (110) unit cell plane of two polyethylene-clay nanocomposites. For a completely random oriented sample a point in the center results. (- - -) Points on this line have their normals randomly arranged in a MT projection. Proximity to ND reflects coplanarity with the MT plane. (–·–·–) Points on this line have their normals randomly arranged in the NT projection. Proximity to MD reflects coplanarity with the NT plane (Reprinted from *Polymer*, **44**, A. Bafna et al., "3D Hierarchical orientation in polymer–clay nanocomposite films," 1103–1115, © 2003, with permission from Elsevier.)

determined from the Wilchinsky plot by projecting a line from N to the MT axis through the structural point on the Wilchinsky triangle.

WAXD can yield information on the degree of order and on the dimensions of tactoids. The intensity and breadth of the basal signals are in fact related to the length and order of the repetitive layer structure of clay [41, 70, 79, 86, 87]. There are two possible reasons for the decrease in intensity of the basal reflection: (i) a decrease in the degree of coherent silicate layer stacking and (ii) the occurrence of exfoliation and destruction of some intercalated silicates [41].

A broadening of the diffraction peak suggests a reduction in the size of tactoids that should be associated to the occurrence of partial exfoliation. The Scherrer relationship is very useful for assessing these observations quantitatively. This equation [12] allows to estimate crystallites' thickness on the basis of the full width at half maximum (β_0) of the corresponding WAXD peaks:

$$L_{hkl} = \frac{0.91 \cdot \lambda}{\beta_0 \cos\theta} \tag{17.9}$$

Where L_{hkl} represents the crystallite thickness in a direction perpendicular to that of the crystallographic plane identified by Miller indices *hkl*, 0.91 is a constant used in the case of smectites [21].

Knowing L_{001} values, a further estimation on the number of layers N forming the stacked structures can be derived considering that $N = L_{001}/d_{001}$, where d_{001} is the d-spacing associated to the (001) basal signal of cloisite.

A quantitative approach to WAXD data, extended farther than the simple detection of the position of the basal signals, yields valuable information that can be exploited to improve the design of nanocomposite materials. In a recent work, Galimberti and coworkers [38] deconvoluted the contributions to the WAXD spectrum due to clay and to the rubber matrix. They individuated the trace due to the amorphous halo of rubber and subtracted it from the total WAXD pattern, thereby obtaining clean and neat signals due only to clay. By this approach they could observe a reduction in intensity of the (001) reflection with respect to the (*hk*0) peaks. This phenomenon was more evident for the samples with a lower clay content. As in Ref. [63] described above, also in this study the gradual disappearance of the (001) peak could be positively interpreted as a sign that exfoliation occurred, because the other montmorillonite peaks remained unaltered. In this case, the authors concluded that exfoliation is not always attained through intercalation of polymer chains. In some instances, clay tactoids can be gradually reduced in size until they disappear [38]. Although it is difficult to obtain conclusive results in the absence of *in situ*, time dependent SAXS and WAXD measurements, this mechanism is very reasonable, because it is in accord with the frequently encountered reduction in size of the clay stacks, which as the same time is not coupled to a shift of the corresponding basal peak.

A number of quantitative treatments of SAXS signals produced by clay structures has been proposed. Recently, a fitting model was developed on the basis of a theoretical model [56, 88–91] for the description of the lamellar morphology of semicrystalline polymers. According to this approach, the structure of polymer-layered silicate nanocomposites is represented by high-density clay layers alternated by low density matter, either polymer (in intercalated systems), compatibilizing agent (when intercalation does not occur) or a mix of the two species. This method allowed to calculate the thickness of the low-density regions and the long period

of the one-dimensional lattice, along with their respective variances, and the average number of layers in each stack, in excellent agreement with TEM observations [55, 56, 76]. A similar approach was proposed also by Ruland and Smarsly [92, 93] for the application to inorganic-organic lamellar self-assembled nanocomposite films.

The above technique refers to the Hosemann model [94], that assumes the lateral width of the clay stacks to be much larger than its thickness [4, 95, 96]. On the basis of this assumption a one-dimensional variation along the normal direction to the lamellae is considered for electron density.

Furthermore, the models assume a simplified two-phase structure, where high- and low-density regions are considered, with no transition layer, as schematically represented in Figure 17.9, where the clay layers (Y_i), the low-density regions interposed between the clay platelets (Z_i) and the total periodicity of the ith layer (X_i) are indicated. The statistical fluctuation of the electron density along the normal to the surface of the clay layers can be described by the Hosemann's model [94], where an independent variation is introduced for both the high- and low-density region thicknesses.

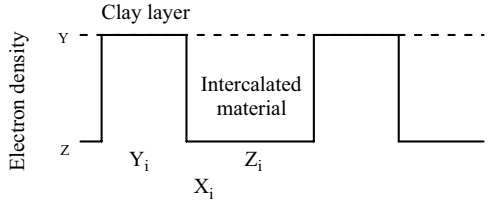

Figure 17.9 Basic model for the tactoid

On the basis of all these assumptions, the one-dimensional SAXS intensity for the ideal lamellar structure [89] can be written as:

$$I^0(s) = I^I(s) + I^{II}(s) \tag{17.10}$$

where:

$$I^I(s) = \frac{(\rho_Y - \rho_Z)^2}{4\pi^2 s^2 X} \times \frac{|1-F_Y|^2(1-|F_Z|^2) + |1-F_Z|^2(1-|F_Y|^2)}{(1-F_Y F_Z)^2} \tag{17.11}$$

$$I^{II}(s) = \frac{(\rho_Y - \rho_Z)^2}{2\pi^2 s^2 XN} \times \mathrm{Re}\left\{\frac{F_Z(1-F_Y)^2(1-(F_Y F_Z)^N)}{(1-F_Y F_Z)^2}\right\} \tag{17.12}$$

In these equations, $s = \frac{2\sin\theta}{\lambda}$, F_Y and F_Z represent the Fourier transforms of the distribution functions of the thicknesses of the clay layers (Y) and of the low-density regions interposed between the clay platelets (Z), ρ_Y and ρ_Z are the electron densities of the clay and low-density

regions, respectively, N is the number of layers and X the average long period. In the fitting procedure, the thickness Y of the layers is fixed, because it does not change during the processing or the mixing in the rubber matrix. In montmorillonite-filled nanocomposites, for example, Y is fixed in 1.0 nm, that corresponds to the thickness of a single layer of this kind of clay [22]. For the distribution of the thicknesses of the low density regions, a symmetric function (Gaussian) or an asymmetric one (exponential) can be used.

When face-to face aggregation of the tactoids occurs, TEM and WAXD can yield inconsistent assessments of the number of platelets in the stacks [97, 98]. This is because in TEM micrographs aggregates appear as single structures, whereas WAXD considers them as separate crystallites. The described model can reproduce the real number of clay layers in the tactoids, in agreement with TEM, because it considers second-kind distortions [91] and thus it corrects the slight differences in the stacking directions of aggregated tactoids, considering them as single stacks [56]. It should be remembered that it is of more practical utility to know the size of aggregates, as these structures are most detrimental for the performance of the material. The effects on the SAXS patterns of second-kind distortions is considered on the basis of Vonk's formula [99]:

$$g(x) = g^0(x)\exp(-2x/\psi) \tag{17.13}$$

where $g(x)$ and $g^0(x)$ are the one-dimensional correlation functions for the distorted and ideal model, respectively, x is the distance perpendicular to the lamellar surface and ψ is the distortion length [99]: the value of ψ increases with decreasing bending of the layers. According to the Wiener-Khintchine theorem [100], the one-dimensional SAXS intensity function $I(s)$, is given as the Fourier cosine transform of the $g(x)$ function:

$$I(s) = F_c[g^0(x)\exp(-2x/\psi)] = F_c[g^0(x)]{*}F_c[\exp(-2x/\psi)] \tag{17.14}$$

where $F_c[\ ]$ and the asterisk denote the Fourier cosine and the convolution respectively, so:

$$I(s) = I^0(s){*}\left[\frac{2/\psi}{s^2 + (2/\psi)^2}\right] \tag{17.15}$$

where $I^0(s)$ is the one-dimensional SAXS intensity for the ideal lamellar structure (Equation 17.10).

The practical usefulness of this approach should be remarked at this point. By a quantitative treatment of SAXS patterns, it is actually possible to count the average number of layers composing the tactoids. This is a very difficult task to be done by other techniques. TEM in fact requires acquisition of a very large number of high definition micrographs and very extensive image analysis. In this case a simple fitting allows to obtain the tactoid size, which is a critical quantity from which most of the properties of the nanocomposite are dependent.

Deconvolution of the intensity $I(q)$ into a form factor $P(q)$ and a structure factor $S(q)$ is another possible approach to the quantitative analysis of SAXS data from polymer-layered silica nanocomposites towards the determination of their morphology [93, 98, 101–104]:

$$I_1(q) = AP(q)S(q) \tag{17.16}$$

Where A consists of both instrument and sample dependent terms and can be treated as a scaling factor. $P(q)$ is a function that describes the interference effects between X-rays scattered by different parts of the same scattering body (microdomain) and is dependent upon both the size and shape of the scattering body [105]. $S(q)$ is a function that describes the interference effects between X-rays scattered by different scattering bodies in the sample and depends on their relative positions [105].

Flat particles of thickness $2H$ yield a small angle scattered intensity of [6]:

$$P(q) = \frac{4B(\Delta\rho)^2H^2}{q^2}\left(\frac{\sin qH}{qH}\right)^2 \tag{17.17}$$

where B is a constant dependent on the surface of the flat particle. If, such as in the real case, a distribution of thicknesses exists in the system, the scattered intensity derives from the sum of the contributions of several populations, each of thickness $2H_i$ [101]:

$$P(q) = \sum \frac{4B_iH_i^2}{q^2}\left(\frac{\sin qH_i}{qH_i}\right)^2 \tag{17.18}$$

The proportion of tactoids of size H_i is yielded by $P_i = B_i/\sum_j B_j$.

The short range interference between the plates (that becomes important as the clay loading increases) can be represented as a one-dimensional lattice [93, 98, 103]. A number of analytical expressions have been derived for the structure factor according to this fundamental assumption. In the ideal case of a perfectly periodic system, all the clay layers would be equidistant and the structure factor would be a series of equidistant peaks, which become infinitely sharp in the limit $N \to \infty$ of infinitely large stacks [103]. In the more realistic case of a disordered system, the distances between the layers in the one-dimensional lattice vary according to some kind of distribution.

Vaia and coworkers proposed two expressions, in terms of the lattice factor $Z(q)$, that described distortions of the first or of the second kind [98]. Distortions of the first kind can be described as the displacement of the scattering layers from an ideal lattice with spacing D, given by the Gaussian probability of a mean-square displacement, $\delta{\cdot}D$. This yields a generalized interference function such as:

$$Z_1(q) = \frac{1}{\langle N\rangle}\left[\langle N\rangle + 2\sum_{N=N_1}^{N=N_2} p(N)\sum_{n=1}^{n=N-1}(N-n)e^{-q^2(\delta D)^2/2}\cos(qDn)\right] \tag{17.19}$$

where $\langle N\rangle$ is the average number of layers in a stack, the first summation accounts for the finite stack size, the second one for the stack size polydispersity ($p(n)$ is the distribution in the number of coherent layers per stack) and the exponential term describes the inhomogeneities in structural order normal to the platelets [98].

For second-kind distortion, not the lattice, but the nearest neighbor correlations are represented by a Gaussian distribution of distance around the mean spacing between adjacent layers [98]. In this case, the exponential term of Equation 17.19 is substituted by the sum of $R(q)$ and $R^*(q)$, the Fourier transform and complex conjugate, respectively, of the probability function $r(z)$, which defines the likelihood of finding a nearest-neighbor pair at a distance

between z and $z + dz$ [106]:

$$Z_2(q) = \frac{1}{\langle N \rangle}\left[\langle N \rangle + 2\sum_{N=N_1}^{N=N_2} p(N) \sum_{n=1}^{n=N-1} (N-n) \times [R^n(q) + R^{*n}(q)]\right] \tag{17.20}$$

The approach to be chosen for a realistic description of the system under investigation is quite case-dependent. Intercalated systems contain the concept of an underlying lattice and are thus most suitably represented by the lattice factor based on distortions of the first kind. As the degree of disorder of the system increases, second-kind distortions reflect the system in a more accurate way.

Hermans' approach [107] can also be followed for the calculation of the lattice factor [93, 103], retaining an arbitrary distance distribution $r(z)$. All higher order distances are given by convolutions of r so that the autocorrelation function can be written in terms of convolution polynomials and the intensity distribution can be expressed in terms of geometric series. Accounting for the finite size of real stacks and for the polydispersity of the stack height N, this expression was obtained for the lattice factor [103]:

$$|Z_N(s)|^2 = \mathrm{Re}\left[\frac{(1-R^2)-2N^{-1}R\{1-\exp[-N(1-R)]\}}{(1-R)^2}\right] \tag{17.21}$$

A number of possible distribution functions $r(z)$ can be used, such as a delta, a shifted exponential [108], a Gaussian, a gamma or a shifted gamma function [103]. In order to further refine the models, the infinitely sharp density transitions at the lamellar interfaces schematized in Figure 17.9 can be modified by an exponential term to account for a more realistic finite interface boundary [93].

A simpler suitable structure factor that takes into account the interactions between different clay tactoids is [101]:

$$S(q) = \frac{1}{1 + k\omega(q)} \tag{17.22}$$

$$\omega(q) = 3\frac{\sin(qd) - qd\cos(qd)}{(qd)^3} \tag{17.23}$$

where d is a correlation length, that is, a pseudo-spatial periodicity, and k describes the magnitude of correlation effects and can be termed as a pseudo order factor [109].

The availability of different models for $P(q)$ and $S(q)$ has the advantage of making this approach more flexible and apt to describing different systems. However, model-dependency can be a drawback for the comparison of data coming from different samples.

The Guinier approximation allows to calculate the dimensions of dispersed particles, in the hypothesis that they are homogenous in size and that the system is dilute, that is, that the distance between the particles is much larger than particle size. Under these assumptions, Equation 17.4 is valid. Equation 17.4 is easily linearized, allowing to obtain R from the slope of a $\ln I(q)$ versus q^2 plot:

$$\ln I(q) = \ln K_0 - \frac{q^2R^2}{3} \tag{17.24}$$

where K_0 is a constant and R is the radius of gyration of the particles. A number of authors [39, 110, 111] suggested that in intercalated polymer/clay nanocomposites, clay particles can be approximated as spheres of radius r, for which the relationship $R = (3/5)^{1/2} r$ holds. Another approximation that could possibly describe clay tactoids could be that of an elliptic cylinder with semi-axes a and b and of height h [6]:

$$R^2 = \frac{a^2 + b^2}{4} + \frac{h^2}{12} \tag{17.25}$$

In inhomogeneous systems, made up of particles with a polydisperse distribution of sizes, the $\ln I(q)$ versus q^2 is no longer linear, but becomes concave. The size and distribution of the particles must therefore be obtained by extracting sequential tangents, as described by Wang and coworkers [110]. According to this method a tangent A′ is drawn at the largest scattering angle in the pristine $\ln I(q)$ versus q^2 plot, from which a radius of gyration R_1 and an intercept K_1 can be obtained by Equation 17.26. This tangent is subtracted from the pristine curve, obtaining curve B. Tangent B' is then drawn, obtaining R_2 and K_2. This tangent is subtracted to B, obtaining curve C and so on. Assuming a spherical shape for clay particles, radii r_1, r_2, r_3 and so on, are calculated for each fraction, and the average radius of the particles is estimated by:

$$\bar{r} = \sum_i r_i W_i \tag{17.26}$$

where $W(r_i)$ is the volume fraction of particles:

$$W(r_i) = \frac{10^{k_i}/r_i^3}{\sum_i 10^{k_i}/r_i^3} \tag{17.27}$$

The main disadvantage of choosing the Guinier approach is that it is based on a dilute system. This hypothesis is rarely satisfied, even in nanocomposites with rather low filler contents.

The Guinier scattering function was used in a quite different way by Koo and coworkers [112, 113]. They chose to reproduce experimental curves by a sum of a Gaussian function and of a Guinier-type exponential decay function:

$$I(q) = \sum_i \frac{A_i}{w_i\sqrt{\pi/2}} \exp\left[-\frac{2(q-q_i)^2}{w_i^2}\right] + B + C\exp\left(-\frac{q}{t}\right) \tag{17.28}$$

The Bragg diffraction peak appearing in the SAXS traces was well approximated by the Gaussian function, whereas the baseline was reproduced by first-order exponential decay. This allowed to accurately measure the d-spacing of the peaks originated by the various periodic structures of the silicate layers. These d-spacings were subsequently compared to those calculated on the basis of geometrical and theoretical considerations [114, 115]:

$$(2R + b)^2 (H + a) = \frac{\pi R^2 H}{\Phi} \tag{17.29}$$

where Φ is the volume fraction of clay, R and H are the radius and the thickness of the disk, respectively, and a and b are the separation gaps between adjacent disks (face-to-face distance) and a lateral separation (edge-to-edge distance), respectively. The expected d-spacing is therefore the sum of a and H.

17.5 Nonlamellar Fillers

17.5.1 Carbon Black

For several decades, high-performance elastomers have been prepared by using carbon black (CB) with a diameter of a few nanometers, somewhat unconsciously pioneering the nanocomposite approach.

Dispersion of the filler in CB-rubber composites is conventionally covered by TEM, but as previously said, among the drawbacks of this technique is the inability to yield statistically averaged information, quantitatively characterized *in situ* over a sufficiently large sample area.

The characterization of the structure and of the degree of dispersion of CB is very important because it has a dramatic effect on polymer chains' mobility: on its surface a "bound rubber" layer can form [116–120] and also it has a tendency to aggregate into structures [121, 122] that trap a part of matrix rubber in the internal void space ("occluded rubber") [123, 124].

Recently ultra-small-angle X-ray scattering measurements (USAXS) proved as a valuable source of information on the arrangement of CB aggregates and on their mutual interpenetration [125, 126]. The results confirm the suspected role of aggregate arrangement in the physical properties of composites and the relationship of the latter with morphology and surface chemistry.

CB offers a good example of a filler with a fractal structure. A fractal is an object which contains self-similarity over different length scales or, in other words, an object whose structure appears similar at different magnifications within some scale range [127, 128]. CB primary particles display a surface fractal structure, and are fused together into spherical aggregate units. These units are further clustered into agglomerates that then form, by organizing on an even superior level, open, multiarmed mass-fractal structures [126, 129].

To model the SAXS intensity of such a structure [130–132], it is assumed to consist of N fractal aggregates per unit volume, built up by the progressive aggregation of primary particles (small primary clusters) of characteristic size a and volume v. The size of the fractal aggregates is defined by a correlation length ξ with $\xi \gg a$. For this model the scattering intensity is given by [133] Equation 17.16.

In the case of very small primary particles ($a \ll \xi$), the form factor $P(q)$ can be approximated by a q-independent value, $(\Delta\rho)^2 v^2$, while the structure factor has a quite complicated analytical form such as [134, 135]:

$$S(q) = 1 + \frac{1}{(q\alpha)^D} \frac{D\Gamma(D-1)}{[1+(1/q^2\xi^2)]^{(D-1)/2}} \sin\left[(D-1)\tan^{-1}(q\xi)\right] \tag{17.30}$$

Where D is the fractal dimension of the aggregates and Γ is the gamma function. For $1/\xi \ll q \ll 1/a$, Equation 17.30 becomes a simple power law $I(q) \propto q^{-D}$ so the parameter D can be obtained by the slope of log-log plots of the experimental scattering intensity $I(q)$ as a function of the modulus of the scattering vector, q. Indeed, on the basis of this slope, different kinds of fractal structures can be distinguished [127, 136]:

$$\text{mass fractal } I(q) \propto q^{-D_m}, 1 < D_m < 3 \tag{17.31}$$

$$\text{surface fractal } I(q) \propto q^{-(6-D_s)}, 3 < 6-D_s < 4 \tag{17.32}$$

where D_m is the mass fractal dimension (which is the exponent that relates the mass M of the object to its size R [137]: $M \approx R^{-D_m}$) and D_s is the surface fractal dimension (which is the

exponent that relates the surface area of the object S to its size R [137]: $S \approx R^{-D_s}$). Koga and coworkers [129] reported for CB dispersed in a SBR matrix an exponent of 3.4 in the high q range ($0.2 < q < 1.5\,\mathrm{nm}^{-1}$), concluding that the surface of the CB primary particles is not smooth, but rough and characterized by surface fractals. This conclusion was confirmed by combined SAXS-WAXD experiments, in which the q range was further extended towards larger q. After subtraction of the amorphous peak due to the (002) reflection of turbostratic graphite-like structures, a power law trend was again found, with an exponent of 3.6, coherent with that of surface fractals. A similar power law was found by the same authors [129] in the q range ($0.0012 < q < 0.012\,\mathrm{nm}^{-1}$) with an exponent 2.3, interpreted as the dimension of the CB mass fractal structure.

At small q ($q \leq 1/\xi$), $I(q)$ exhibits a Gaussian behavior so that the radius of gyration of the fractal aggregates, R_g, can also be determined by applying Guinier's law [6, 133] (Equation 17.4). R_g is related to the correlation length ξ by:

$$R_g = [D(D+1)/2]^{1/2}\xi \tag{17.33}$$

A log $I(q)$ versus q^2 plot of the scattering intensity shows a linear descent with a negative slope from which R_g can be obtained. The radius of gyration obtained by the Guinier relationship in case of a system with a size dispersion, is skewed towards the size of the largest objects. At the other extreme of the validity range of the fractal regime, that is, for q values close to or larger than $1/a$, the Porod regime [6, 133] is entered and so the SAXS intensity is expected to exhibit an asymptotic behavior given by:

$$I(q) \propto 1/q^4 (q \to \infty) \tag{17.34}$$

It frequently happens that CB/elastomer systems do not satisfy the Porod equation. This deviation can have three main causes: a surface fractal structure of pure CB particles [126, 138], the existence of the bound rubber layer at the surface of the CB filler [129] or an internally inhomogeneous, that is, turbostratic, structure of CB [139].

The reciprocal values of the q coordinate corresponding to the crossovers toward the Guinier ($1/q_G$) and Porod ($1/q_P$) regimes yield approximate estimates of the size of the aggregates and of the primary clusters, respectively.

Witten and coworkers [140] proposed a model for the stress-strain properties of rubbers filled with fractal aggregates such as CB, predicting lateral compression of aggregates, similarly to what occurs in polymer gels. This phenomenon is prone to be followed by SAXS, because when swollen polymer networks are uniaxially stretched, they display a SAXS pattern with a "8" or butterfly shape, with the major axis lying parallel to the stretching direction [141, 142].

This phenomenon is determined by the formation of a superstructure in the stretched network, in which zones of higher and lower crosslink density separate into more or less parallel bands lying perpendicular to the stretch axis [143]. An example of such a pattern can be seen in Figure 17.10 for a EPR-based composite with CB.

The sample shows no anisotropy in its initial state, but as a consequence of deformation a clear butterfly pattern develops. As in the case of stretched polymer gels [141], the principal axis of the anisotropic figure is parallel to the stretching axis.

A quantitative exploitation of such SAXS patterns can be obtained by extracting the scattered intensity $I(q)$. In the case of anisotropic traces $I(q)$ can be determined along the

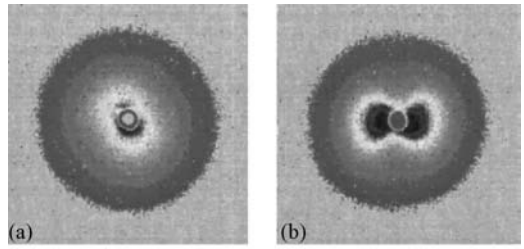

Figure 17.10 Two-dimensional patterns from a EPR-based composite with CB ($\Phi = 0.20$) before elongation ($\lambda = 1$) and elongated by $\lambda = 1.5$. The stretching direction is horizontal (Reprinted with permission from F. Ehrburger-Dolle, M. Hindermann-Bischoff, F. Livet et al., "Anisotropic ultra-small-angle X-ray scattering in carbon black filled polymers," *Langmuir*, **17**, 329–334, 2001. © 2001 American Chemical Society.)

two principal directions $I_{\|}(q)$ and $I_{\perp}(q)$ by radial averaging within two orthogonal sectors ($\pm 5^{\circ}$ from each direction). The trend of $I(q)$ for the initial sample and of $I_{\|}(q)$ and $I_{\perp}(q)$ for a stretched sample are shown as a function of q (Figure 17.11). As may be seen, they exhibit a power law in the fractal regime at low q that commutes into a Porod regime, with a curved crossover region between the two power laws.

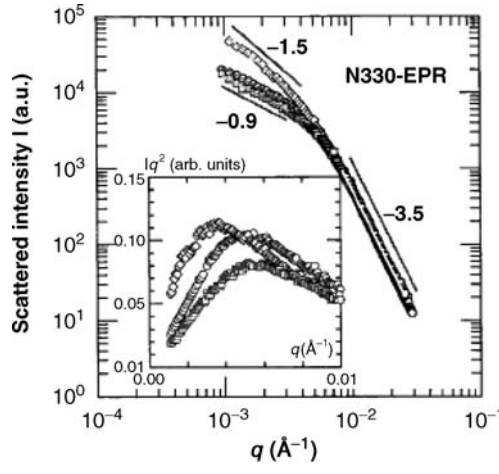

Figure 17.11 Regrouped SAXS curves from the patterns shown in Figure 17.10: (○) before elongation, (◇) $I_{\|}$ and (□) $I_{\perp}$ from the sample elongated by $\lambda = 1.5$. Kratky plots are shown in insert (Reprinted with permission from F. Ehrburger-Dolle, M. Hindermann-Bischoff, F. Livet et al., "Anisotropic ultra-small-angle X-ray scattering in carbon black filled polymers," *Langmuir*, **17**, 329–334, 2001. © 2001 American Chemical Society.)

In the case of the SAXS traces shown in Figure 17.11, the absolute value of the slope in the initial sample, close to that obtained for pelletized CB, and the symmetry of the pattern are consistent with strongly and isotropically interpenetrated aggregates [126]. Upon elongation,

the absolute value of the slope remains almost unchanged in the perpendicular direction, while it increases significantly in the parallel direction. This result implies a decrease in the degree of interpenetration along the direction of the stretch, because it is known that aggregate interpenetration not only decreases the absolute value of the slope in the fractal regime [126], but also shifts the upper limit of the power law domain. Corresponding characteristic cutoff lengths can thus be defined by employing Kratky plots, that is, $I(q)q^2$, $I_{\parallel}(q)q^2$ and $I_{\perp}(q)q^2$ versus q (Inset of Figure 17.11), on the basis of the position of their maximum q_K. As far as aggregates are concerned, ${q_K}^{-1}$ is related to the mean distance between primary particles and not to a mean particle size. The mean size of the primary particles, which is independent of the aggregate arrangement, is related to the onset of the Porod regime [125, 126].

From the Kratky plots, a microscopic Poisson ratio of the CB network can also be deduced [143]:

$$\sigma = -(q_{k\perp} - q_{k0})/(q_{k\parallel} - q_{k0}) \tag{17.35}$$

For the EPR CB-filled samples investigated in Figure 17.11, the obtained σ was 0.20, a result significantly lower than the value for incompressible systems, that is, 0.5, but equal to that for a swollen gel in a good solvent. The features described are fully consistent with the model of reinforcement of rubber by fractal aggregates [140].

Koga and colleagues [129] pursued the aim of reconstructing the scattering pattern of CB on a very large q range, spanning from $q = 0.0001\ \mathrm{nm}^{-1}$ to $q > 1\ \mathrm{nm}^{-1}$ thanks to the application of ultra-small angle neutron scattering (USANS), USAXS, and SAXS such as that shown in Figure 17.12.

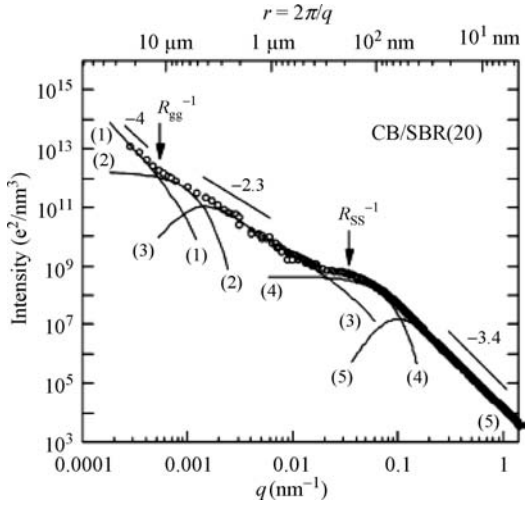

Figure 17.12 Decomposition of the observed SAXS profile for a CB SBR nanocomposite into each scattering component (solid lines numbered 1 to 5) from each structural level comprising the hierarchical structure based on the Beaucage unified fit analysis (Reprinted with permission from T. Koga, T. Hashimoto, M. Takenaka et al., "New insight into hierarchical structures of carbon black dispersed in polymer matrices: a combined small-angle scattering study," *Macromolecules*, **41**, 453–464, 2008. © 2008 American Chemical Society.)

In this pattern, three power law regimes can be seen, along with two discrete form-factor (Guinier scattering) profiles. The authors first applied the unified approach by Beaucage [144]. The unified fit model [144–146] was ideated to describe scattering functions containing multiple length-scales separated by power law regimes. Scattering from a hierarchy of structural levels are merged considering only the four parameters (G, R_i, K_p, p) required to define the single structural levels, each with its radius of gyration, R_i, and power-law exponent $-p$. The actual function used for each level is:

$$I(q) = G\exp(-q^2R_g^2/3) + K_p[(\mathrm{erf}(qR_g/6^{1/2})^3/q]^p \tag{17.36}$$

Where G is the Guinier prefactor, K_p is the Porod prefactor and erf is the error function. This model is effective when it is necessary to extract the parameters associated with each hierarchical level in complex structures that yield many power law regimes. The unified model works best with well separated length scales, but it shows its limits when different structural regimes overlap [147].

On applying the unified fit model, the five profiles shown in Figure 17.12 were obtained. In particular, the profile labeled as "2" represents the Guinier scattering from the mass fractal agglomerates having radius of gyration of R_{gg}, and profile "4" is the Guinier scattering profile for the agglomerates of CB primary particles, with a radius of gyration of R_{ss}. This scattering analysis based on the Beaucage unified approach allowed to quantitatively evaluate the sizes of the aggregates and mass fractal units, but did not yield any information on their shapes, because the Guinier scattering function depends only on R_g values, independently from the particle geometry [148]. These authors, therefore, replaced the Guinier function with a form factor, assuming that the shape of the aggregates was spherical or ellipsoidal [129]. The best fit was obtained with the spherical form factor for CB dispersed in toluene, while the ellipsoid form factor was best suited for CB in SBR or polyisoprene. In other words, a hierarchical structure such as that depicted in Figure 17.13 was proposed for CB dispersed in a rubber medium.

With increasing scale length, the hierarchy starts with monomeric units of the polymers (part a) that form network chains of the elastomers (part b) and interact with primary CB particles giving rise to surface fractal structures (part c). CB particles are fused into aggregates (part d). Aggregates then combine into agglomerates (or agglomerates level 1 or dispersible units) (part e), which are the smallest building block for the formation of the mass-fractal objects (or agglomerates level 2) that are dispersed in the crosslinked bulk rubbers (part g) [129]. When CB was dispersed in toluene, the lack of polymer chains did not allow the formation of the dispersible units, which are linked by the polymer network chains, so mass fractal agglomerates were composed directly by aggregates. It is evident from the examples above that X-ray scattering methods allow a very detailed description of the morphology of the filler in a nanocomposite. This knowledge is paramount for the development of structure-property relationships.

Obviously, in the study of the morphology of filled elastomers, the ideal condition would be being able to single out the contribution of each component of the formulation of the material. Morfin and colleagues tackled this issue by using a technique called anomalous small-angle X-ray scattering (ASAXS) [149]. They studied elastomers filled with carbon black and vulcanized using ZnO. Since ZnO has an electron density close to that of carbon, it produces a strong X-ray scattering that interferes with that due to filler aggregates and does not allow a

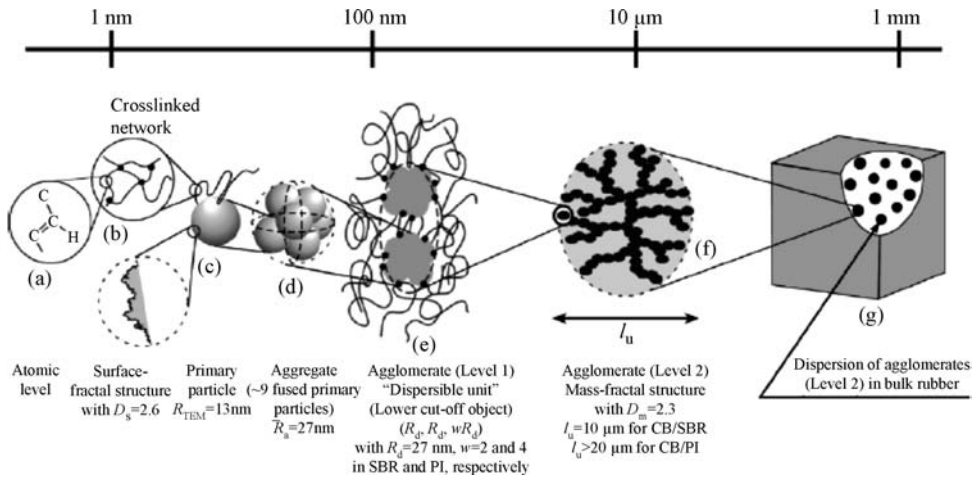

Figure 17.13 Schematic model for the hierarchical structure of the CB filler in the rubber matrices (Reprinted with permission from T. Koga, T. Hashimoto, M. Takenaka et al., "New insight into hierarchical structures of carbon black dispersed in polymer matrices: a combined small-angle scattering study," *Macromolecules*, **41**, 453–464, 2008. © 2008 American Chemical Society.)

correct measurement of their dimensions. ASAXS is based on the anomalous variation of a scattering factor near an absorption edge, and has become increasingly popular in materials science [149 and references therein]. The K-edge of Zn is located at an energy (9661 eV) which is experimentally accessible using synchrotron sources. The scattering curves $I(q, E)$ versus q for a vulcanized sample containing ZnO particles decay differently as a function of the different energies E employed for the measurements (Figure 17.3 of ref. [149]). This anomalous effect is not hidden by the addition of carbon black in the elastomer.

For vulcanized samples containing carbon black, $I(q, E)$ can be written as the sum of three terms, I_{ZnZn}, I_{CC} and I_{ZnC}, that depend on the structure factor of ZnO particles (S_{ZnZn}), the structure factor of carbon black (S_{CC}) and a cross term (S_{ZnC}):

$$I_{ZnZn}(q,E) = [\rho_{Zn}(E) - \rho_P]^2 S_{ZnZn}(q) \tag{17.37}$$

$$I_{CC}(q,E) = (\rho_C - \rho_P)^2 S_{CC}(q) \tag{17.38}$$

$$I_{ZnC}(q,E) = (\rho_C - \rho_P)[\rho_{Zn}(E) - \rho_P] S_{ZnC}(q) \tag{17.39}$$

where ρ_P, ρ_C and $\rho_{Zn}(E)$ are the electronic densities of polymer, carbon black and ZnO, respectively. The elastomer matrix is taken as the reference because its scattering is small compared with that of ZnO or carbon black.

In a sample containing just ZnO but no carbon black, only the I_{ZnZn} term contributes to $I(q, E)$. Equation 17.37 can therefore be exploited to determine the difference $[\rho_{Zn}(E) - \rho_P]$. A correction is necessary, though, because near the Zn absorption K-edge, the electronic density of ZnO varies with energy, according to the anomalous dispersion corrections. Below

the Zn edge, the imaginary anomalous dispersion factor f″(E) is small and can be neglected. It follows that:

$$\rho_{Zn}(E) = \frac{f_O^0 + f_{Zn}^0 + f_0'(E)}{M}\mu \tag{17.40}$$

where f_i^0 is the atomic scattering factor of atom i and $f_i'(E)$ is the real part of the anomalous dispersion factor (anomalous dispersion factors are tabulated [150]), M is the molar mass and μ is the specific gravity of the ZnO particles.

By these equations it is therefore possible to measure $[\rho_{Zn}(E) - \rho_P]$, ρ_P, and ρ_C, since the difference $(\rho_C - \rho_P)^2$ is independent of energy in the energy range employed for data acquisition.

In the case of the system considered by the authors [149], ZnO particles were large and their volume fraction was small compared to carbon black, so the cross term I_{ZnC} could be neglected [151], so $I(q, E)$ was linearly dependent on $[\rho_{Zn}(E) - \rho_P]^2$. The intercept and slope of such a plot yielded the I_{CC} and the I_{ZnZn} contributions, respectively, at a given q. In the cases when the particle size and the volume fraction of the fillers in the matrix are comparable one to each other, the cross term would not be negligible any more and departures from linearity would be observed.

Once I_{ZnZn}, I_{CC} and I_{ZnC} are calculated, the relative structure factors S_{ZnZn}, S_{CC} and S_{ZnC} can be estimated and so the contributions of the two fillers can be successfully deconvoluted [149]. Although quite complicated and necessitating synchrotron radiation sources, ASAXS should be taken into account as an option when deconvolution of the effects of different fillers are sought.

17.5.2 Carbon Nanotubes

Since their discovery more than 15 years ago [152], carbon nanotubes (CNT) have attracted large efforts of academic and industrial research. CNT are long and thin cylinders of covalently bonded carbon atoms. Their outstanding electronic, electric, thermal and mechanical properties make CNT potentially suitable for a very large array of applications. One of the most promising is probably the reinforcement of polymeric materials at very low loadings. While CNT have been widely used with different kinds of polymers, very little work has been done on incorporating the CNT in rubber.

To be effective reinforcing fillers, CNT must meet three main conditions: good dispersion, alignment and good stress transfer from the matrix to the filler [5]. Bundling and aggregation of CNT have been considered the main hindrances for a homogeneous dispersion of the filler in the polymeric matrix. Purity is also a very important issue for the final performance of the materials. Due to these problems, CNT–polymer nanocomposites have so far performed well below expectations.

Microscopy techniques, like TEM or SEM, are widespread for the characterization of individual nanotubes in the nanocomposite. Small-angle scattering techniques, either using neutrons or X-rays, can be useful to evaluate both particle size and average dispersion of these nanoadditives in composite materials. Recent reports on small-angle scattering measurements, on single-walled CNT (SWCNT) dispersed in liquids [153–155] showed that in these cases the scattering intensity follows a power law $I(q) \propto q^{-D}$, typical of scattering by fractals [127], with fractal dimension D. Values of D between 2.0 and 2.5 were reported for SWCNT dispersed in

liquids [153, 156], whereas $D = 1$ would have been predictable for rods ($D = 2$ and $D = 3$ are expected for disks and spheres, respectively) [127, 128, 153–156]. These higher than expected values were due to the formation of SWCNT fractal aggregates [156].

A very accurate study on the interpretation of SAXS data relative to CNT has been recently proposed by Schaefer and colleagues [157]. These authors developed a simplified tube form factor (STFF) to reproduce experimental data on a wide range of q-values. Being L the length of the tube, T its wall thickness, ($T = r_o - r_i$, where r_o and r_i are the outer and inner radius, respectively), the scattering intensity in four distinct regimes could be simulated. For $q \ll 1/L$, $I(q)$ is given by the Guinier prefactor, G. Assuming $L \gg r_o \gg T$:

$$G \equiv I(q \ll L) = (\Delta\rho)^2 v\Phi \tag{17.41}$$

where $\Delta\rho$ is the difference in scattering length density between the tube wall and the pure matrix material, v is the volume of a single tube (excluding the hollow region), and Φ is the volume fraction occupied by the wall material. The Guinier approximation holds as the q values increase up to $q \approx (R_g)^{-1}$, where R_g is the radius of gyration one tube, yielded by:

$$R_g^2 = \frac{L^2}{12} + \frac{r_o^2 + r_i^2}{2} \tag{17.42}$$

In the following q region, comprised in the range $(R_g)^{-1} < q < (r_o)^{-1}$, the rod-like features of the tube predominate and the intensity varies as a power law with the exponent -1, while in the range $(r_o)^{-1} < q < (r_o - r_i)^{-1}$, the intensity varies as q^{-2}.

The final part of the pattern, at high q values, behaves according to Porod's law with an interfacial area per unit volume S_v:

$$S_v = \phi\left[\frac{2\pi(r_o^2 - r_i^2) + 2\pi L(r_o + r_i)}{\pi L(r_o^2 - r_i^2)}\right] \tag{17.43}$$

The STFF employs the Beaucage unified approach to connect the Guinier and power law regimes [144–146] (erf being the error function):

$$I_{tube}(q) = P_G + P_3 + P_2 + P_1 \tag{17.44}$$

$$P_G = G\exp[-(qR_g^2)^2/3] \tag{17.45}$$

$$P_3 = \frac{\pi G}{L} q^{-1} \times [\mathrm{erf}(qR_g^2/\sqrt{6})]^3 \times \exp\left[-(qr_o)^2/3\right] \tag{17.46}$$

$$P_2 = \frac{\pi^2 GT}{v} q^{-2} \times [\mathrm{erf}(qr_o^2/\sqrt{6})]^3 \times \exp\left[-(qT)^2/3\right] \tag{17.47}$$

$$P_1 = \frac{2\pi G}{v^2}\left[2\pi(r_o^2 - r_i^2) + 2\pi L(r_o + r_i)\right] q^{-4} \times [\mathrm{erf}(qT/\sqrt{6})]^3 \tag{17.48}$$

The STFF is adequate for rigid, isolated, monodisperse tubes, and therefore it is not sufficient, per se, to adequately fit experimental data. Polydispersity in tube dimensions, tube flexibility, and/or long-range correlations have been accounted for by the authors of this study by multiplication of the STFF by a fractal–structure factor [157]. They assumed that the morphology of the nanotube is based on fractal ordering of short tube-like segments with a

persistence length L_p. These short ($L_p \ll L$), rigid segments are correlated on larger length scales with a fractal dimension, D. A structure factor such as that of Equation 17.30 can therefore be defined and combined with the STFF obtaining the following expression that describes the flexible tube morphology:

$$I_{F-Tube} = I_{Tube}(q, \Delta\rho, \phi, r_o, L_p, T) \times S(q, D, \xi, L_p) \tag{17.49}$$

where ξ is the correlation range, which should be interpreted as the radius of the "cluster" resulting from the arrangement of the segments.

Such an expression allowed to reproduce experimental SAXS patterns of multiwalled CNT in bismaleimide. The long-range fractal correlations were not necessary to fit well the data relative to a very low content of CNT, consistently with a dispersion, in this case, of single CNT in the matrix. A more complicated morphology, with the formation of aggregates, was observed increasing the CNT content, but it was nevertheless possible, by the use of the described approach, to reproduce SAXS patterns in a wide range of q values, inaccessible to a fractal–rod model or a STFF that does not consider long range fractal correlations. A further advantage of this method is that of being able to determine whether the cylinders are hollow (tubes) or solid (rods) based upon which form factor fits the data more accurately [157]. This attractive approach is surely promising. Applications to systems more similar to CNT-rubber nanocomposites are desired and expected.

Other studies have been reported in which WAXD aided the definition of a detailed picture of the morphology of nanotubes. Hsiao, Chu and colleagues [158, 159] exploited WAXD to describe the orientation of CNT in polymer-based nanocomposites. In the WAXD pattern of nanocomposites containing CNT or carbon nanofibers (CNF),[1] a reflection attributable to the stacking of graphene layers appears with a d-spacing of 0.34 nm. This signal is commonly indexed as (002), in analogy to the similar signal of hexagonal graphite. Azimuthal profiles, such as that of Figure 17.7c, of this reflection allow to study the orientation of the filler.

A flat azimuthal profile of the (002) graphite plane is coherent with a random distribution of the filler, while if it shows a maximum, this means that CNT or CNF are aligned along a preferential direction (for example as a consequence of stretching). A quantification of such anisotropic distributions can be done by the Hermans' orientation parameter. Interestingly, it has been reported that the degree of orientation of CNT or CNF is much less extensive than that of the polymer chains, because the filler particles encounter greater difficulty in adapting to deformation [158, 159].

WAXD and SAXS are useful also for following the modification of CNT when they undergo compatibilization treatments. In order to improve the processability and performance of composites, in fact, several treatments have been proposed to alter the surface of the CNT, for example by acid attacks, plasma, thermal and laser ablation or chemical functionalization, obtaining an increase of the polarity and possible grafting sites. WAXD and SAXS patterns of pure and functionalized CNT may differ, because the peak position, width and intensity can significantly vary upon functionalization [160], due to the variation in d-spacing [161] and lattice distortions [162], and they therefore allow to follow the extent of the modification procedure.

[1] CNF are carbon structures, similar to carbon nanotubes, but with an average diameter of 50–200 nm, in between that of carbon fibers and CNT. Moreover, these kind of fillers show significant advantages, such as the low cost, and the facile surface modification.

17.5.3 Silica

Silica is, along with carbon black, the most industrially employed filler for the rubber industry. Changing the active filler from carbon black to precipitated silica in rubber compounds enhances the rolling resistance and wet grip performance of tires [163, 164]. However, this change requires the introduction of new additives in the filled rubber compounds in order to decrease the strong filler–filler interactions, associated with the hydrogen bonds between silica particles [165, 166]. Recent preparation techniques, such as sol gel, for example, allowed to control the size of the particles and so a number of silica-filled rubber nanocomposites have been presented in the literature. In this case also, SAXS yields useful information on the morphology of the dispersed filler.

The reinforcement effect is mainly due to the development of a percolating network by the filler particles, along with a role of the modified polymer layer at interphase, that is, bound rubber, which is known to be significant in silica as well as in CB [167, 168].

Moreover, the morphology of silica is strongly dependent on the preparation steps. For example the time allowed for the sol gel procedure, the viscosity of the liquid matrix and the microstructure of the polymer have a dramatic effect on the development of the silica particles [131]. The mechanism of aggregation of the precursor colloidal particles is determinant on the size of the outcoming filler. For instance, Chacker and colleagues, exploited fractal dimension to infer the mechanism of aggregation [130, 137, 169, 170].

In analogy to that of CB, the structure of silica is known to be hierarchical as well, and scattering methods are therefore very useful for its thorough description on several length scales, exploiting the same approach in data analysis described for carbon black [130, 131, 167, 168].

The data in Figure 17.14 cover light scattering and USAXS profile of silica over six decades in length scale. Three regimes can be individuated, that draw a picture of the material as composed by three length scales: smooth colloidal particles (Guinier radius, $R_G = 87$ Å) clustered into mass-fractal aggregates of dimension $D_m = 2.5$ that are further clustered into uniformly dense, but porous objects with surface fractal dimension $D_s = 3.35$ and $R_G = 26$ μm [139, 167]. This object with a rough surface can be visualized as a "bunch of grapes," where each grape is actually a fractal aggregate. The grape bunches are further clustered in a fractal structure, whose morphology is mainly dependent on drying conditions. In the hierarchical structure of silica, aggregates are fractal clusters resulting from kinetic growth and agglomerates are clumps of aggregates. Agglomerates, if not broken-down or "dispersed" during rubber processing are very detrimental to performance and the conditions for their formation must therefore be known [171–173]. Schaefer proposed a very simple sequence of processes leading to the structuring of silica. The primary particles grow by nucleation and growth and then aggregate by reaction-limited kinetic growth [137]. By aging, the aggregates fill all the space between the constituting primary particles and toughen them. In solution, aggregates form larger agglomerates dense in the bulk, but rough in the exterior surface. Drying brings about yet a fourth level of structure due to the kinetic clustering of the agglomerates.

In order to investigate the conditions leading to agglomerates, Schaefer and colleagues studied how the morphology of colloidal suspensions of silica changed as they were fastly dried in a spray dryer or more slowly in a vacuum oven [147]. The USAXS patterns of such samples showed, with increasing q, a power law regime and a Guinier regime followed by a Porod behavior. Fitting these traces, the power law exponent and the radius estimated according to

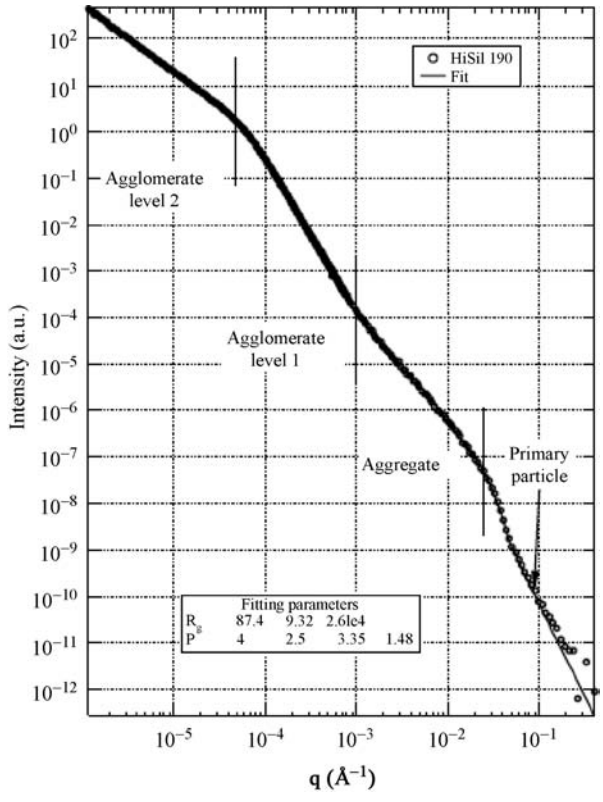

Figure 17.14 Multilevel structure of precipitated silica. The data is a combination of light scattering and USAXS. The data show three-length scales indicated by the vertical lines and four morphologies indicated by the power-law slopes. The Guinier radius (R_g) and the magnitude, P, of the slope are indicated in the inset (Reprinted from *Physica A*, **314**, D.W. Schaefer et al., "Challenges and opportunities in complex materials: silica-reinforced elastomers," 686–695, © 2002, with permission from Elsevier.)

Guinier were obtained [147]. Different drying procedures brought about large changes in the power law exponent. The slope decreased from -1.9 in suspension to -1.6 for spray-dried powder. These small apparent mass fractal dimensions were interpreted as coherent with aggregates with an open structure [147]. The oven dried sample determined a slope of -0.79. Since a connected object can not have a dimension less than one, this value is consistent not with fractal aggregation, but with a structure composed by deeply interpenetrated aggregates. If the aggregates are sufficiently overlapped, the mass fractal domain vanishes, leading to apparent exponents less than one [147]. The slow drying process that takes place in the vacuum oven allows enough time for the aggregates to distort and accommodate interpenetration. Analogous behavior was observed by Reiker [126] for pelletized carbon black.

Significant differences were thus introduced by the processing in the pristine filler, but after its mixing in a SBR matrix, regardless of the drying procedure, the shape of the profile was identical.

The absolute value of the slope in the aggregate regime increased to 2.2, which is probably the actual fractal dimension of the aggregates, because on dispersion into rubber the deeply interpenetrated pristine aggregates regain the colloidal dispersion that they had in the wet state. Confirmation was then found that the interpenetrated powders are apparently stabilized by weak physical forces that are overwhelmed by shear during mixing. Since larger aggregates are softer than the rubber matrix, dispersion in an elastomer leads to complete disruption of the agglomerate, leaving only the aggregate as the highest-level structure [174]. A critical aggregate size is defined as the size at which the bending modulus of the aggregate is equal to that of the rubber matrix; it depends on the size of the primary particles and the modulus of silica and is estimated to be about 1000 Å [174].

Schaefer *et al.* speculated that the agglomerates are soft in the sense that they are physically bonded whereas the aggregates are hard, in the sense that they are formed via strong chemical bridges formed between adjacent primary particles. They proved so by studying the evolution of structure in a sonicated solution. This treatment degraded agglomerates, leaving unaltered the morphology on the lower levels [174]. Some of these examples concerned the study of a "labile" morphology that is lost as a consequence of the introduction of the filler in the matrix. Nevertheless, these studies have a value *per se*, because they show the variegate scales and hierarchy of morphology of silica and can stimulate methods of preparation that preserve them also in the nanocomposites.

The focus has been so far on the characterization of pristine silica and, subsequently, to its introduction in a rubber matrix in so called type I composites. A common classification of composite materials is in fact made on the basis of the type of linking between the inorganic filler and the organic matrix [175]. In class I materials the organic molecules are simply embedded in the inorganic matrix, while in class II materials strong covalent bonds connect the phases. Model compounds based on siloxane-poly(ethylene glycol) or siloxane-poly(propylene glycol) for this class of materials, even though not rubbery, can be useful for possible interesting future applications to elastomers [176, 177]. SAXS spectra of these materials exhibit a single peak associated to the existence of a strong spatial correlation between siloxane heterogeneities or clusters embedded in the polymeric matrix [176, 178]. Under this assumption, the average and most probable distance between siloxane clusters (d_s) can be estimated by the *d*-spacing of the peak maximum located at q_{max} [176, 177]: $d_s = 2\pi/q_{max}$. d_s was observed to increase with increasing molecular weight of the polymer, thereby confirming the assumption made; as the chains get longer, in fact, the clusters are kept farther one from the other. The authors estimated the mean radius of siloxane clusters under the assumption that the spherical particles of siloxane form a compact arrangement [179]:

$$R_S = \left(\frac{3\Phi_S}{8\pi}\right)^{1/3}\left(\frac{d_S}{2}\right) \tag{17.50}$$

where Φ_S is the volume fraction of siloxane particles.

Applying the Scherrer equation to the SAXS peak yields further information on the degree of order of the siloxane clusters arrangement, because by this method an average size of the correlation volume associated with the spatial distribution of siloxane clusters [176, 177], L_C, is obtained:

$$L_C = 4\pi/\beta_0 \tag{17.51}$$

Where β_0 is the full width at half maximum of the correlation peak of the SAXS function.

A broader peak is consistent with a less defined spatial correlation size L_C of siloxane clusters arrangement, probably because of a more complex nature of the composite. It is surprising how very easy and straightforward SAXS analysis yielded in this case the most useful information for applicative purposes.

A further method of interpretation of SAXS data generated by silica dispersed in a polymeric matrix can be the Percus–Yevick hard-sphere, core-shell model [180]. The particle form factor $P(q)$ for a spherical particle of radius r_0 and contrast $\Delta\rho$ is written:

$$P(q) = \Delta\rho^2 v_p^2 \left\{ \frac{3[\sin(qr_0) - qr_0\cos(qr_0)]}{(qr_0)^3} \right\}^2 \tag{17.52}$$

where $v_p = (4/3)\pi r_0^3$ is the volume of a single particle.

The polydispersion in particle size can be accounted for by modifying $P(q)$ by a log-normal distribution, with log-average r_0 and log-variance ε [180]:

$$P(r_0) = \varepsilon^{-1}(2\pi)^{-0.5}\exp[-(\ln(r_0)^{3/2})^2/2\varepsilon^2]d\ln r_0 \tag{17.53}$$

The structure factor $S(q)$ is expressed as the three-dimensional Fourier transform of the particle pair correlation function $g(r)$ (which tends to 1 when $r \to \infty$):

$$S(q) = 1 + 4\pi N_p \int_0^\infty [\sin(qr)/qr][g(r) - 1]r^2 dr \tag{17.54}$$

A "hard-sphere" fluid is assumed, for which the interparticle interactions exclude particles from approaching within a center-center distance r equal to the collision diameter for the interaction, that is, $\sigma_c = 2r_c$. For distances r greater than σ_c the interparticle interactions are assumed to be negligible. The effective volume fraction as determined by the collision radius is $\Phi_c = (4\pi/3)N_p {r_c}^3$. For a hard-sphere fluid at low volume fractions, $g(r)$ has the form $g(r) = 0$ for $r < \sigma_c$ and $g(r) = 1$ for $r > \sigma_c$. At higher volume fractions a liquid-like structure appears, with pronounced coordination spheres that are reflected by maxima in $g(r)$; the first coordination sphere occurs at $r = \sigma_c$. The Percus-Yevick solution to $g(r)$ for a hard-sphere fluid leads to the following structure factor:

$$S(q) = [1 - N_p C(q)]^{-1} \tag{17.55}$$

Where $C(q)$ is the three-dimensional Fourier transform of the direct correlation function:

$$C(q) = -4\pi\sigma_c^3(q\sigma_c)^{-1}\mathrm{Im}[\alpha f_1(q\sigma_c) + \beta f_3(q\sigma_c) + \gamma f_4(q\sigma_c)] \tag{17.56}$$

where:

$$\alpha = (1 + 2\Phi_c)^2/(1 - \Phi_c)^4 \tag{17.57}$$

$$\beta = -6\Phi_c(1 + 0.5\Phi_c)^2/(1 - \Phi)^4 \tag{17.58}$$

$$\gamma = 0.5\Phi_c(1 + 2\Phi_c)^2/(1 - \Phi_c)^4 \tag{17.59}$$

and

$$f_n(q) = \int_0^1 e^{iqs} s^n ds \tag{17.60}$$

Another relationship allows to calculate f_n by a recursive procedure:

$$f_{n+1}(q) = iq^{-1}[f_n(q) - e^{iq}] \tag{17.61}$$

with

$$f_0(q) = iq^{-1}[1 - e^{iq}] \tag{17.62}$$

A possible modeling of a system of silica particles immersed in a rubber matrix could be done assigning a radius $r_c = ½\ \sigma_c$ to silica particles. The SAXS intensity can therefore be reproduced merging these equations in the $I(q) = AP(q)S(q)$. An approach like the one described above allowed Terrill and Crowley to characterize colloidal dispersion of polyaniline-silica particles in water [180]. Models like these seem less prone to an immediate practical application for samples such as rubber-silica nanocomposites, especially due to the complexity of the model and to the assumptions made.

Several studies on the deformation of silica filled nanocomposites have been published, based on SANS, SAXS, USANS, USAXS and AFM, often with comparisons to computer simulations [149, 181–183].

An example of this kind of study was reported by Ikeda and colleagues [184]. They studied the elongation of peroxide-crosslinked isoprene rubber filled with *in situ* generated, spherical silica particles, with an average diameter of about 34 nm. The behavior of the materials as a function of tensile stress was followed by two-dimensional SAXS (Figure 17.15). Before elongation, the obtained patterns were isotropic rings that implied silica particles randomly dispersed in the rubber matrix. An estimate of the average spacing between the particles, d, was calculated according to the Bragg equation on the basis of the maximum of the diffraction signal. Upon stretching, a change in the SAXS data developed, with a shift of the scattered intensity towards the meridional sector, with a significant weakening of the equatorial intensity.

If the pattern shown in Figure 17.15b is compared to that displayed in Figure 17.10, it may be noted that it is different from the butterfly shape that characterizes carbon black [143, 149]. Stretching has the effect of increasing the distance between the filler particles along the stretching direction, while in the perpendicular direction they are forced to come closer, as was predicted by computer simulations [181]. On further stretching the meridional intensity splitted into a four maxima figure, which was more clearly detectable in the SAXS signals gathered during the retracting process (Figure 17.15d–f). This pattern was ascribed to the formation of a buckling structure of silica particles by stretching, as confirmed also by AFM observations [184]. In this case also, the experimental data confirm previous predictions made by computer simulations. It is interesting that the buckling structure of silica particles is retained also when the stress is released. The distance between the silica layers along the stretching direction (D) was calculated as $D = d/\cos\mu$, where μ is the azimuthal angle of the four-spot pattern as shown in Figure 17.15. D values at the same elongation ratio are equal if measured during stretching or retraction and follow linearly the macroscopic elongation ratio, suggesting an affine deformation of the nanocomposite.

Analogous SAXS data were reported by Shinohara and colleagues who followed the morphology of the aggregation under deformation of silica filled SBR samples, in which silica particles and rubber chains are covalently bonded via silane coupling agents [185].

These authors studied the aggregation structure in terms of the structure factor $S(q)$ rather than scattering intensity. $S(q)$ was estimated by calculating the form factor, $P(q)$, of spherical

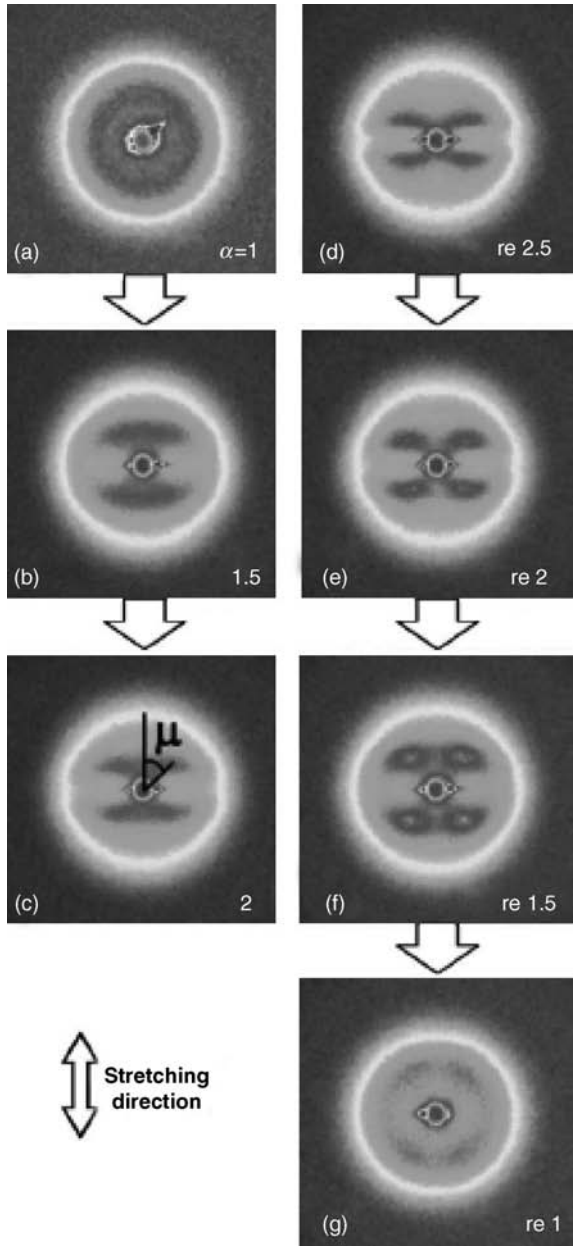

Figure 17.15 Two-dimensional SAXS patterns of an *in situ* silica filled isoprene rubber nanocomposite during tensile deformation (Reprinted with permission from Y. Ikeda, Y. Yasuda, S. Yamamoto and Y. Morita, "Study on two-dimensional small-angle X-ray scattering of in situ silica filled nanocomposite elastomer during deformation," *Journal of Applied Crystallography*, **40**, s1, s549–s552, © 2007, International Union of Crystallography (http://journals.iucr.org).)

silica (Equation 17.52) and by dividing $I(q)$ by $P(q)$ (taking into consideration the size distribution of the particles).

$S(q)$ showed in the undeformed sample an initial peak that was ascribed to the distance between neighboring silica particles. As a consequence of stretching, the peak maximum shifted from the initial $q = 2.2 \times 10^{-3}$ Å^{-1} towards small angles up to $q = 7.95 \times 10^{-4}$ Å^{-1}, consistently with the particles being distanced by stretching. Interestingly, at high strain, an additional peak appeared at higher q (around $q = 2.05 \times 10^{-3}$ Å^{-1}), maintaining its position fixed as strain increased. This new signal corresponded to the distance between spherical silica particles connected via rubber polymers and its appearance was associated to the increase of the elastic modulus, indicating that the polymer chains between the silica could not be stretched any more [185]. This highly stretched rubber was identified as one of the origins of the reinforcement. Studies like these, in which the structure and morphology are studied during deformation, are especially important because they can elucidate the subtle interplay between polymer and filler. Stress transfer from the matrix to the filler is necessary to take full advantage of the superior mechanical properties of the additive. Considering also the behavior of the matrix, such as in the previous example of highly stretched rubber playing a role in the reinforcement, is not often found in the literature, because reports are usually mostly focused just on the filler.

17.5.4 Polyhedral Oligomeric Silsesquioxane

Polyhedral oligomeric silsesquioxane (POSS) are three-dimensional, molecularly precise molecules with an inorganic silica-like core surrounded by organic groups. The empirical formula of POSS is $(RSiO_{1.5})_n$ (where R represents organic groups at the corners of the cage and $n = 6$, 8, 10 or higher). Their diameters range between 1 and 3 nm, depending on the number of silicon atoms in the central cage and the peripheral groups surrounding this core [186, 187]. Their hybrid nature, the tunability of their structure and their nanometer scale size spurred a very active research on POSS as a filler for the preparation of nanocomposites [188–193].

POSS can be incorporated into polymers by simple blending with the matrix, or they can be bonded onto the polymer backbones as side chains, or even inserted into the chains as comonomeric units. The POSS unit can be in this case viewed as a nanoparticle for both its size and filler function and a well defined macromonomer for its ability to undergo polymerization. Three or more reactive groups per molecule can be used to provide crosslinking.

POSS molecules have a tendency to crystallize, inducing a phase separation in the material. Even for POSS containing reactive functional groups, POSS domains often form as aggregates instead of bonding to the polymer backbones or otherwise dispersing into the polymer matrix [194–196].

The most immediate application of WAXD to these systems is in the determination of their crystalline structure. As prepared POSS yield very sharp and intense crystalline reflections, that can be also fit to determine the type and dimensions of the crystalline cell [197]. When an amorphous matrix as rubber is employed, it is often beyond the purpose of the investigation to determine the exact structure of POSS, but it is rather of interest to study how it is dispersed in the nanocomposite.

Addition of POSS into a polymer matrix can bring about very desirable improvements in performance, including increases in maximum use temperature, oxidation resistance, and

surface hardness, improvements in mechanical properties, and reductions in flammability and heat evolution. As common in the field of nanocomposites, the achievement of such enhancements is possible provided that the filler is adequately dispersed in the matrix. The neat signals of crystallized POSS are therefore used as indicators of the aggregation of POSS or of the formation of phase-separated filler domains. Zhang, Mark and colleagues provided a good example of a study of this kind [198]. They studied the WAXD patterns of a polysiloxane elastomer additioned of POSS and prepared in an internal mixer. The diffractograms were characterized by a broad amorphous halo due to the rubber matrix and by sharp reflections due to the presence of POSS crystalline domains. This confirmed microscopy observations that evidenced that in the un-crosslinked blends POSS was dispersed in particle form even for blends made at high temperatures [198]. Interestingly, the intensity and width of the POSS characteristic peaks was found to change with mixing temperature, reflecting changes in the degree of order of the crystals and in the size of crystallites. A sharpening of the peaks is associated to an increase in crystallite dimensions, while an increase in the intensity is due to an increase in the quantity of crystallized POSS. At the highest mixing temperatures, the authors found that the intensity of POSS peaks decreased, because the increasing thermal movement, especially of rubber chains, hindered the POSS molecules from migrating toward each other during cooling so that some POSS molecules were left in silicone matrix and fewer POSS crystals precipitated [198]. Moreover, additional peaks appeared at intermediate mixing temperatures, indicating that POSS gave a different polymorph, in that temperature range [198]. The effect of vulcanization was also investigated by WAXD, finding an increased intensity in the POSS signals, possibly because the formation of the network favored the conditions for crystallization.

As said before, another approach in nanocomposite preparation is that of incorporating POSS into the polymer backbone. Hsiao and coworkers prepared a polyurethane system containing POSS molecules pendant to the polymer chain [197]. The superior properties of segmented polyurethane-based elastomers depend directly on the microphase separation due to the thermodynamic incompatibility (immiscibility) of hard segments and rubbery soft segments. The hard segments usually involve interchain interactions by means of van der Waals forces and hydrogen bonding, providing the macroscopic properties and physical crosslinking to the system. POSS molecules reinforce the hard segment domains at the molecular level.

WAXD was used to follow the evolution of the structure of POSS crystals in the as prepared powder, after substitution of a corner group with 3-(allylbisphenol-A) propyldimethylsiloxy group (BPA-POSS), in order to serve as a comonomer for the polyurethane synthesis, and after incorporation in the polymer backbone (Figures 17.16–17.18).

The BPA-POSS macromonomer yielded most of the reflection peaks characteristic of pristine POSS, although much broader (some of the reflections were even combined together) and with a more intense amorphous halo (Figure 17.17). POSS reflections in the POSS-filled polyurethane appeared to be even weaker, because the amorphous fraction became very large in this sample (Figure 17.18). Nevertheless, the major peaks in the BPA-POSS could be clearly identified in polyurethane, proving that POSS molecules aggregated and formed nanoscale crystals in this system as well. WAXD data were also useful to investigate, during tensile deformation, the crystal structural changes in POSS and strain-induced crystallization of soft segment chains [197]. Stretching brought about strain-induced crystallization of the soft segment and two additional reflection peaks appeared in the 2D WAXD pattern upon the pristine amorphous halo. The width of these soft segment crystals was found to decrease with

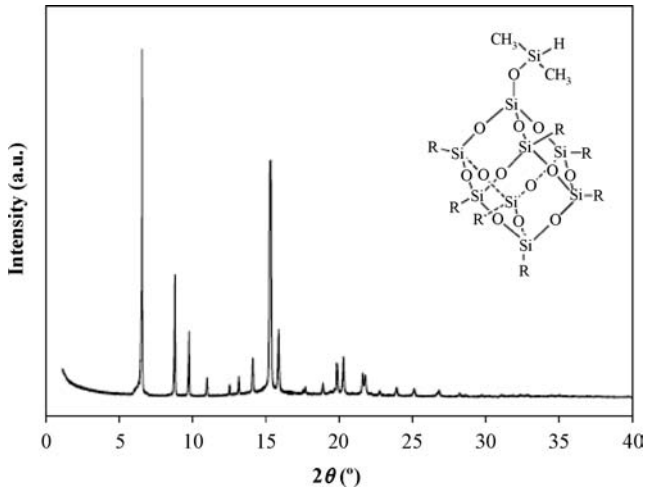

Figure 17.16 WAXD pattern of pristine hydrido-POSS (Reprinted from *Polymer*, **42**, B.X. Fu et al., "Structural development during deformation of polyurethane containing polyhedral oligomeric silsesquioxane (POSS) molecules," 599–611, © 2001, with permission from Elsevier.)

strain, coherently with an enlargement of crystallite size. On the contrary, the POSS crystal reflections became broader with strain, suggesting that partial POSS crystals were destroyed by deformation, probably through the annihilation of some hard segment domains [197].

A further interesting study on the WAXD and SAXS characterization of POSS-containing nanocomposites was published by Coughlin and coworkers [199]. They worked with

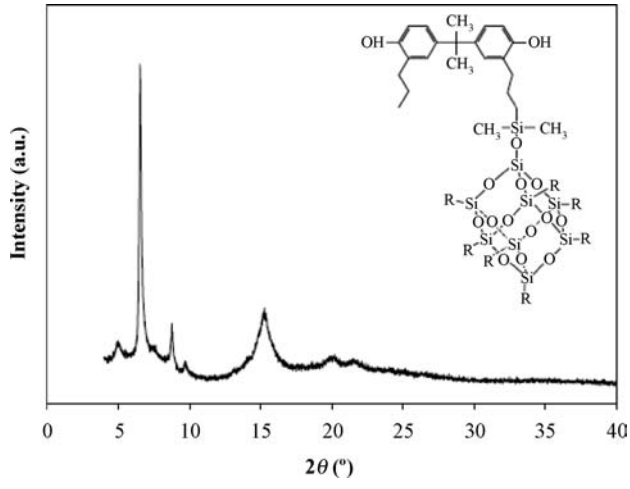

Figure 17.17 WAXD pattern of BPA-POSS (Reprinted from *Polymer*, **42**, B.X. Fu et al., "Structural development during deformation of polyurethane containing polyhedral oligomeric silsesquioxanes (POSS) molecules," 599–611, © 2001, with permission from Elsevier.)

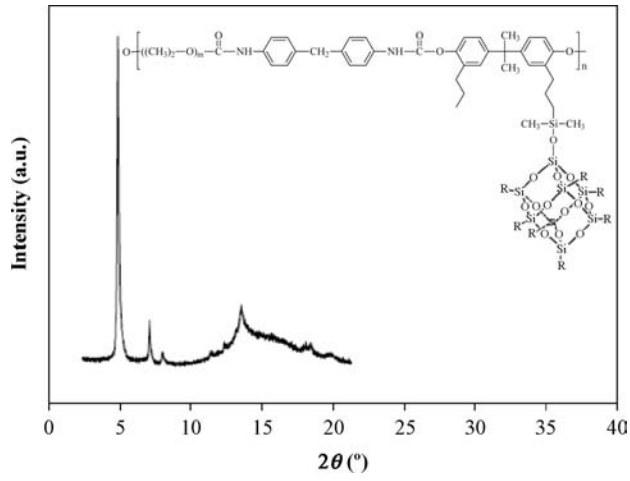

Figure 17.18 WAXD pattern of POSS filled polyurethane (Reprinted from *Polymer*, **42**, B.X. Fu et al., "Structural development during deformation of polyurethane containing polyhedral oligomeric silsesquioxanes (POSS) molecules," 599–611, © 2001, with permission from Elsevier.)

octaalkyl-substituted cubic silsesquioxane nanoparticles $R_8Si_8O_{12}$ that form hexagonal (or equivalently rhombohedral) crystal structures [195, 200, 201]. Regarding cubic silsesquioxane units as approximately spherical, the three-dimensional crystal structure of POSS was shown [201, 202] to be a sequence of stacked planes composed of POSS spheres. When POSS spheres are tethered to polymer chains, the covalently connected chains prevent the development of spherical packing in three dimensions, and as a result, a bilayer or lamella-like structure is formed where POSS spheres are packed hexagonally within planes and two planes are stacked together. Intermolecular van der Waals forces keep the layers stacked in a stable nanolayered structure.

The authors of this work studied copolymers in which POSS was introduced as pendant units onto a polybutadiene backbone, characterizing their structure and morphology by WAXD and SAXS. WAXD patterns showed the superposition of a broad amorphous halo due to the rubbery matrix and of sharp and neat reflections attributable to POSS crystals, as confirmed by the increase in intensity with increasing filler content. Also in this case, the breadth of the peaks was associated to the anisotropic shape of the crystals [195]. In a constrained crystal lattice, the diffraction planes associated with the two long dimensions (length and width in a lamellar structure) showed sharp diffraction, while reflections associated with the one short dimension (thickness) showed the broadest peaks [199].

SAXS data allowed a further characterization of the lamellar morphology formed via controlled self-assembly of POSS particles. Broad maxima were observed in SAXS patterns, originated by the stacked POSS lamellae. The position of the maxima allowed to estimate the spacing d between lamellae, that was found to be dependent on the relative ratio between POSS and polybutadiene.

On the basis of WAXD, SAXS and TEM, the authors proved that morphology depends on composition. At low POSS contents the copolymers assembled into small, randomly oriented lamellae, while a more ordinate lamellar morphology was achieved increasing POSS

concentration. Of course, in the case of these layered POSS, application of the data analysis approaches described in the paragraph on lamellar fillers would have widened the information and allowed a more thorough description of the system.

17.5.5 Rubber as a Filler or Compatibilizer in Nanocomposites

A commonly followed approach for improving the toughness of a thermoplastic polymer, is the preparation of a heterophasic blend with a rubbery component. The introduction of an amorphous phase lowers the glass transition temperature of the system, enabling macromolecular chains to better absorb mechanical energies [203]. In these materials, the two components are immiscible, so a continuous and a disperse phase will appear, and rubber itself can be visualized as a filler. An accurate control of the processing and formulation parameters is critical in determining an optimal morphology, quantity and dimensionality of disperse domains. To obtain the best increase in toughness, the two phases, although immiscible, should have some affinity, so that interfacial adhesion promotes a good phase dispersion, avoiding coalescence of rubber domains or segregation during transformation.

Ternary nanocomposites, composed of a semicrystalline polymer, a rubber and a nanofiller have attracted great attention in both the academic and industrial communities [76, 204–216]. Adding clay as a third component to an heterophasic polymer blend has the effect of reducing the size of the dispersed phase domains [73, 76, 204–207]. Moreover, the presence of rubber can avoid the drawback of worsened impact resistance and of decreased ductility, commonly found when clay is used as a filler. Clay tends in fact to be a stress concentrator, that hinders the elastic deformation of macromolecular chains [73]. WAXD and SAXS are not the methods of choice for studying phase separation, microscopy techniques are more suited for this purpose. However, useful information can be obtained, for systems such as heterophasic semicrystalline polymer blends, from X-ray techniques, focusing on the semicrystalline component of the blend. The modifications of the semicrystalline framework, that is, degree of crystallinity, polymorphism, crystallite size, lamellar morphology, and so on, can be followed as a function of composition by the methods of WAXD and SAXS data analysis typically employed for semicrystalline materials, the description of which are beyond the purpose of this chapter [6–13, 89]. A further interesting aspect for the characterization of ternary nanocomposites is the investigation of the improved compatibilization achieved by the addition of rubber [208]. This improved compatibilization favors the preparation of nanocomposites with a more homogeneous morphology and better clay dispersion than the uncompatibilized counterparts, that implies a significant improvement in the strength and stiffness of composites. The dispersion of clay is studied by the approaches described elsewhere in this chapter.

17.6 Characterization of the Matrix in Polymer-Based Nanocomposites

17.6.1 Strain-Induced Crystallization

The properties of vulcanized natural rubber (NR) make it a yet irreplaceable elastomer for heavy duty applications, especially due to its toughness, high tensile stress and large hysteresis loss. The strength of natural rubber has been attributed to strain-induced crystallizability. Many rubber materials, including synthetic polyisoprene (IR), polybutadiene (BR), and isoprene-isobutylene rubber (IIR or butyl rubber) undergo strain-induced crystallization (SIC). The only

exception is SBR. However, crystallization of natural rubber has been by far the most studied by many researchers [217–226] since the 1940s, using a variety of techniques. Undeformed natural rubber forms spherulitic crystallites below 0 °C [221–226]. The temperature/time-induced crystallites generally form as folded chain lamellae, while no conclusive word has been said on the crystal growth direction in NR with different crosslinking density [227]. The morphology of the strain/stress-induced crystallites has been reported to be various: fibrils, mixed fibrils, folded lamellae and shish kebabs [218, 221–226, 228]. Another unresolved issue has been for many years the role of strain-induced crystallites on the mechanical response of NR. Because crystallization is always accompanied by a considerable increase in modulus, the strain-induced crystallites have been thought to bear the tensile stress. The role of molecular orientation called also for attention because of its expected effect on the final mechanical properties.

Most of the experiments devised to shed light on these topics were done with sequential measurements in which the sample was extended to a desired strain, fixed at that strain, and then removed from the stretching instrument and subsequently mounted on the analyzing instrument and examined. When the stretching was stopped, stress was relaxed and microstructures often changed, which significantly altered the system of interest. In order to understand what occurs during stretching and retraction, though, it is necessary to examine the sample simultaneously with the strain. The use of synchrotron WAXD in combination with *in situ* stretching techniques has allowed to directly follow the development of structure and stress-strain relations during deformation of rubbers in real time [227, 229–235]. An immediate advantage of this technique is that of enabling the study of strain-induced crystallization on a very short time scale. For example it was possible to observe that NR responds to fast deformation by forming strain-induced crystallites more rapidly than its synthetic analog IR [230, 233]. This determines the superior and inimitable toughness of NR.

Two examples of the quality of data yielded by this approach are shown in Figure 17.19 and in Figure 17.20.

Figure 17.19 shows the stress-strain curve and selected 2D and 3D WAXD patterns during deformation (at a 10 mm/min rate) of synthetic IR at 30 °C. It can be seen that at strains up to about 4, stress generally increased with strain. Correspondent WAXD patterns show isotropic amorphous halos, with only some slight tendency to distribute the intensity around the equator (for example, strain 3.0). At about strain 4.5 (vertical bold arrow in Figure 17.19), however, the curve showed a decrease in the rate of stress increase. This marks the onset of strain-induced crystallization, as reflected by the appearance of weak but distinct crystalline signals in the WAXD patterns. The weak intensity of these reflections is to be ascribed to the nascent nature of the crystallites that originate them, which are defective in crystalline ordering or registration but nevertheless highly oriented with respect to the stretching direction [231, 232, 236–238]. As strain increases, crystallites become well developed and give rise to the bright spots revealed by WAXD. It is noteworthy the persistence, even at large strains, of the unoriented amorphous halo.

Figure 17.20 shows analogous WAXD patterns from an NR sample during the stretching (Figure 17.20a–d) and retracting (Figure 17.20d–g) processes. At small strains during stretching, highly oriented reflections of fatty acids [239] were recognized on both sides of the beamstop (arrows in Figure 17.20b and h). Increasing strain, NR starts to crystallize (the indicization of the signals is also shown). In this figure also, the orientation of nascent

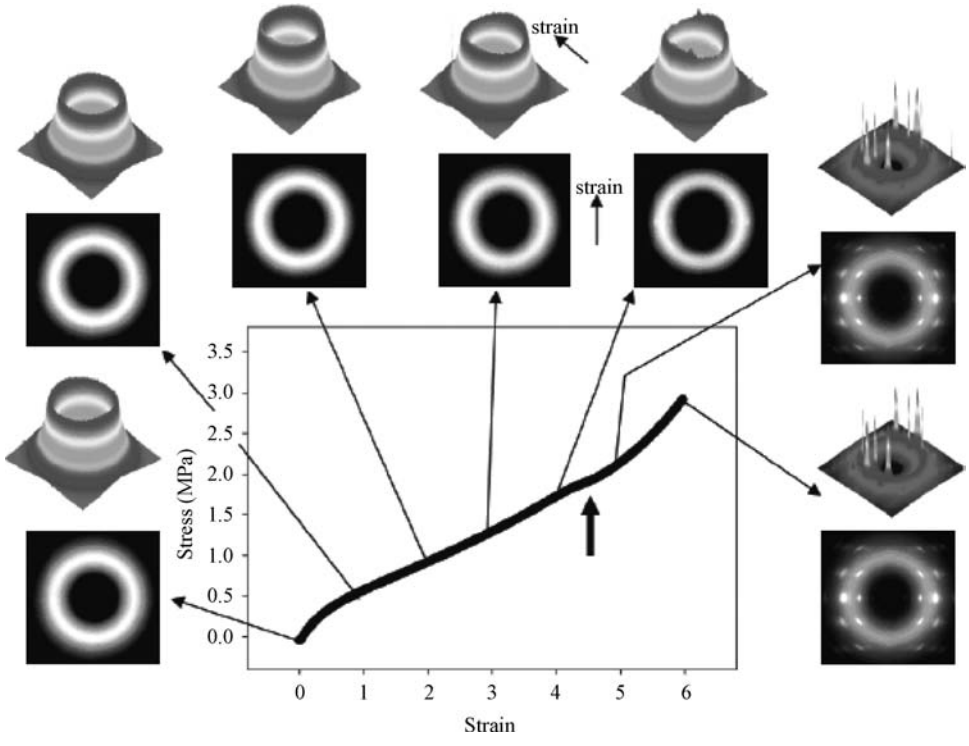

Figure 17.19 Stress–strain relationship and selected 3D and 2D WAXD patterns collected during stretching of IR at 30 °C. Each image was taken at the average strain indicated by the arrow. The bold vertical arrow shows the onset point in the decrease rate of the stress increase (Reprinted with permission from S. Toki, I. Sics, B.S. Hsiao et al., "Probing the nature of strain-induced crystallization in polyisoprene rubber by combined thermomechanical and in situ X-ray diffraction techniques," *Macromolecules*, **38**, 7064–7073, 2005. © 2005 American Chemical Society.)

crystallites (Figure 17.20c) and the persistence of a strong isotropic amorphous halo (Figure 17.20d) can be observed.

This figure allows to follow the retracting process as well, in which the crystalline reflections disappeared gradually, returning to the initial isotropic pattern after total relaxation of the sample. Ringlike (unoriented) crystalline reflections of NR were not observed during the cyclic deformation process, allowing to conclude that strain-induced crystallites always appear in the form of oriented crystals with the chain axis aligned parallel to the stretching direction [227, 232].

The crystal structure of NR is orthorhombic (space group *Pbca*) [240]. A particularly useful reflection is the (002) diffraction line, that is originated by lattice planes perpendicular to the *c* chain axis. The corresponding average crystallite dimension L_{002} is often called in the literature the stem length, used to describe the crystallite size when the chains are folded or extended in the crystallite [235]. The (200) and (120) reflections correspond to lattice planes parallel to the chain direction. A very widespread procedure for measuring the crystallinity is based on the Mitchell method [235, 241–244]:

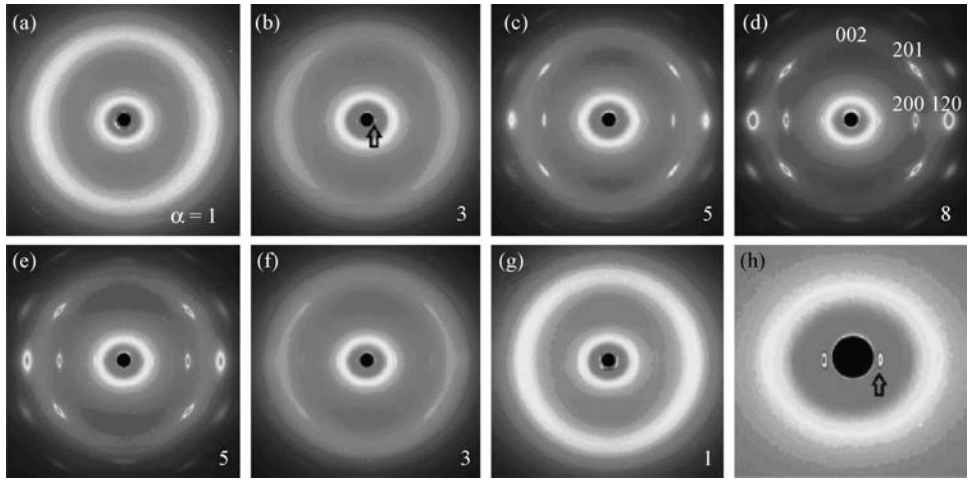

Figure 17.20 Sequential change of WAXD patterns from an NR sample. Stretching direction is vertical. Corresponding strain values are indicated at the right bottom in parts (a–g) of the figure. Indices of crystalline reflections of NR are indicated in part (d). Part (h) shows the enlarged image of the center of part (b). Sharp reflections from fatty acids (indicated by arrows) corresponding to about 4.2 nm in real space are recognized on both sides of the beamstop (Reprinted with permission from M. Tosaka, S. Murakami, S. Poompradub et al., "Orientation and crystallization of natural rubber network as revealed by WAXD using synchrotron radiation," *Macromolecules*, **37**, 3299–3309, 2004. © 2004 American Chemical Society.)

$$\chi = (I_a - I_a^*)/I_a 100 \tag{17.63}$$

where I_a and I_a^* are the scattered intensities of the amorphous halo in the completely amorphous and in the semicrystalline material, respectively.

A very remarkable deconvolution procedure, schematized in Figure 17.21, has been proposed [227, 231, 232, 236, 237], by which it is possible to extract additional structural information (that is, fractions of oriented crystal, unoriented crystal, oriented amorphous, and unoriented amorphous phases) besides the conventional data such as unit cell parameters and crystal dimensions.

As previously seen, the WAXD pattern of the unstretched sample exhibits an anisotropic amorphous halo with no preferred orientation. As deformation is applied, the WAXD pattern shows the superposition of oriented crystal diffraction pattern and a residual amorphous halo. The isotropic contribution at the deformed state is nearly identical to the original amorphous halo appearing in the WAXD pattern before stretching. The de-convoluted anisotropic contribution to the WAXD pattern is composed of oriented crystal reflection peaks and a small amount of oriented amorphous phase, which is conjugated on the equator between the strong (120) and (200) diffraction peaks [231]. After having separated the two contributions, the ratioing of the crystal diffraction intensity over the total scattered intensity is necessary to measure the mass fraction of the strain-induced crystals. To acquire the total scattered intensity volume, the authors transformed the 2D flat-plate geometry to an undistorted geometry in the reciprocal space using the procedure described by Fraser *et al.* [245], then extrapolating the data in the missing meridional region using the expansion of Legendre polynomials [231, 246].

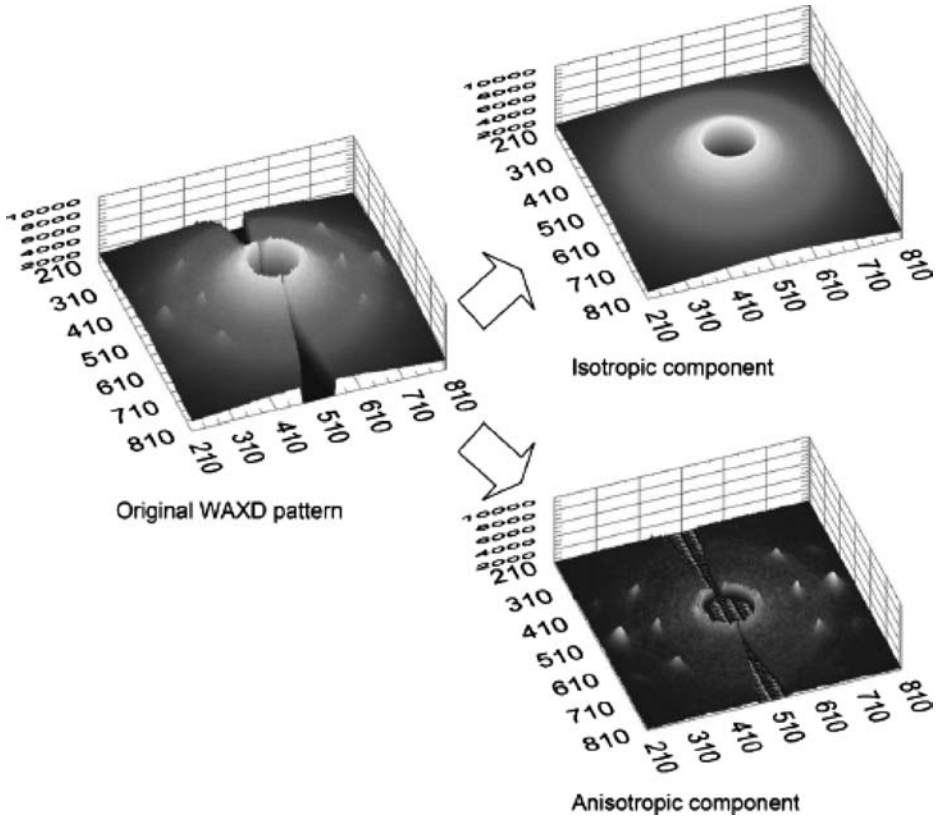

Figure 17.21 Schematic representation of the decomposition of the WAXD pattern into isotropic and anisotropic components (Reprinted with permission from M. Tosaka, K. Senoo, S. Kohjiya and Y. Ikeda, "Crystallization of stretched network chains in cross-linked natural rubber," *Journal of Applied Physics*, **101**, 84909, © 2007, American Institute of Physics.)

A normal peak fitting procedure can then be applied to deconvolute the intensity profile into crystalline peaks and an amorphous halo. On the basis of the data so obtained, it is therefore possible to estimate the amounts of total isotropic and anisotropic mass fractions. The isotropic fraction is composed by the unoriented amorphous fraction Φ_{UA}; the anisotropic fraction is given by the sum of oriented amorphous fraction Φ_{OA} and oriented crystalline fraction Φ_{OC} [231]. As can be observed in Figures 17.19 and 17.20, no unoriented crystalline phase is present during deformation experiments.

This ability to separate the contributions of the oriented and unoriented polymer allowed to show that, during the stretching of natural rubber, only a small fraction of the amorphous chains are oriented and they are subsequently crystallized during stretching, carrying most of the applied load, while the majority of amorphous chains remain unstretched even at very large strains (>500%). This difficulty experienced by the chains in rearranging and aligning according to the stress imposed is mainly due to the presence of crosslinks [232].

The studies that have been previously discussed regard pristine rubber, but the primary technological relevance of filled NR calls for attention from both academic and industrial

viewpoints. Since the discovery of the reinforcement of rubber by carbon blacks in 1904, filled rubbers have been used to manufacture a wide range of materials. Due to the nanometric dimensions attained by CB particles (mean dimension 20–100 nm [124, 247]) it could be asserted that NR/CB have been the first commercial nanocomposites, years before the scientific community even started talking about nanocomposites. Reinforcement of rubber by fillers has been widely studied in the literature [248, 249] but its origin on a molecular scale is still debated. Addition of filler to a rubber matrix changes the stress field, increases the local strain of the chain (a phenomenon also called strain amplification), and leads to local heterogeneities. Thus, a fundamental problem is to understand the influence of the filler, like carbon black (CB) or silica, on the crystallization properties of the NR rubber matrix.

Flory [250] identified the origin of the remarkable performance of pure NR in the formation of crystallites, that played the role of filler, that is, the exceptional properties of filled NR would be due to the presence of both types of solid particles, such as fillers and crystallites. The role of a filler such as carbon black is expected to be that of restricting the polymer chains' mobility, due to the formation of a "bound rubber" layer which is confined both physically and chemically around the filler particle [116–120] and to the appearance of aggregate structures formed by the elementary particles of carbon black [121, 122] that trap a part of matrix rubber in the internal void space ("occluded rubber") [123, 124].

Some reports [243, 244] showed that CB favors SIC in the crack tip region, and suggested that this contributes significantly to crack growth resistance. SIC is also reported to be started at lower strains than in pristine rubber, due to strain amplification [251, 252]. Recent studies carried out by *in situ* synchrotron X-ray measurements during uniaxial deformation allowed to shed light on the effective local deformation in stretched CB filled NR [123, 124, 251, 253].

Figure 17.22 shows an example of XRD patterns for the samples studied by Poompradub *et al.* [123]. These authors worked on NR filled with carbon black (average particle size of 26–30 nm) or ultrafine calcium carbonate $CaCO_3$ (average particle size of 20 nm).

The different orientation of NR and filler crystallites can be observed. Superposed to the highly oriented crystal reflections of NR crystallites, isotropic circular rings due to $CaCO_3$ appear in the diffractogram of Figure 17.22c. This is consistent with the filler particles not having a preferred orientation in the rubber samples upon elongation. This result is very useful to infer the templating and nucleating activity of filler particles on NR crystallites formed upon strain. If some sites on the filler particle were acting as nucleating points, in fact, randomly oriented crystallites of NR would have appeared, resulting in ring-shaped reflections of NR crystallites. Since such ring-shaped reflections of NR have not been reported [123, 227, 254], the nucleating activity of the fillers employed in this study could be ruled out. On the contrary, Rault and coworkers, following by WAXD the degree of crystallinity as a function of strain, concluded that CB particles act as nucleation centers of the SIC [253, 255]. Chenal *et al.*, also on the basis of XRD data on the development of crystallite size and on the crystallization rate, showed that indeed CB or silica can act either as nucleating or as inhibiting agents, depending on the crosslink density of the matrix. They explained this behavior by assuming that, if higher than a threshold critical value, crosslink density restricts the medium mobility and does not allow nucleation in the vicinity of the filler [251].

Crystallinity was evaluated from the 2D WAXD data of Figure 17.22 by integrating the intensity of the (200) and (120) reflections, by a conventional curve-fitting method, from the equatorial intensity distribution in the region included between $\pm 25^{\circ}$ with respect to the

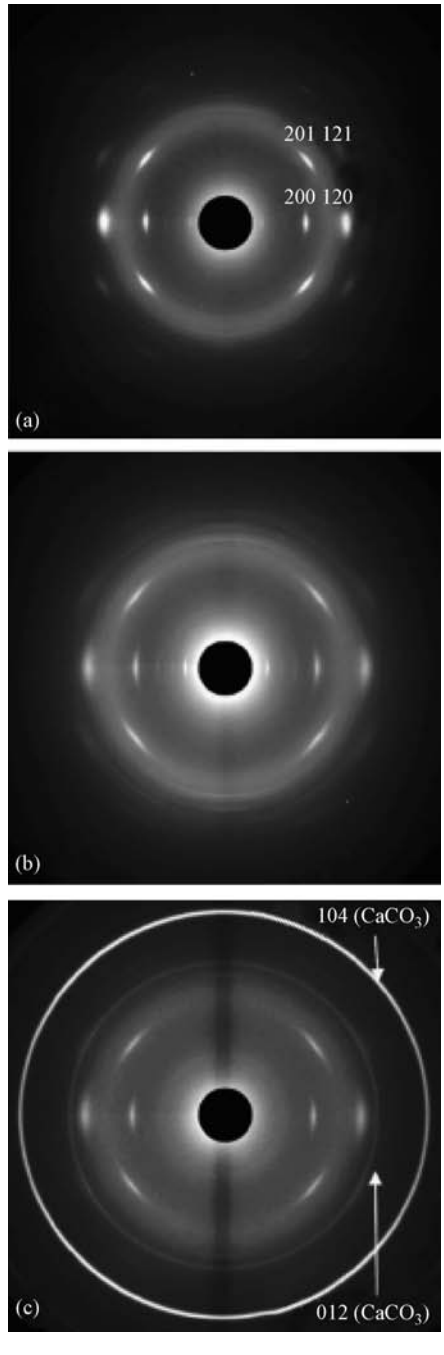

Figure 17.22 WAXD patterns of (a) pristine NR, (b) NR filled with CB, (c) NR filled with $CaCO_3$, at strain ratio 5. Stretching direction is vertical (Reprinted with permission from S. Poompradub, M. Tosaka, S. Kohjiya et al., "Mechanism of strain-induced crystallization in filled and unfilled natural rubber vulcanizates," *Journal of Applied Physics*, **97**, 103529, © 2005, American Institute of Physics.)

equator. On the basis of these intensities, the development of crystallinity as a function of strain was obtained [123].

Furthermore, the degree of orientational fluctuations of crystallites was evaluated from the intensity distribution of the (200) reflection, which was obtained by the azimuthal scan of the peak. This procedure was carried out calculating the width parameter in the azimuthal direction, w_{az}, by fitting the intensity distribution with a Gaussian function. Then w_{az} was converted into half-width β_{az} according to this equation:

$$\beta_{az} = 2w_{az}\sqrt{-2\ln(1/2)} \tag{17.64}$$

The smaller the β_{az}, the smaller are the fluctuations in orientation. The β_{az} for the filled samples were reported by the authors to be larger than in unfilled NR, meaning that the fillers somewhat hinder the orientation of strain-induced crystallites [123].

In pristine rubber, chains can easily adapt along the direction of strain and crystallize, whereas in the presence of carbon black, the stress field is complex and crystallites may grow along complex stress contours [124, 251]. An effect of the filler surface was also postulated as a factor that could affect the orientation of the crystallites, due to a possible nucleating activity of the immobilized rubber-filler interface, and some chain ordering at the surface originated by the adsorption interactions [124].

Another parameter that comes out of WAXD traces is the crystallite size. Employing the Scherrer equation, Poompradub *et al.* [123] and Trabelsi *et al.* [124] followed the variations of crystallite sizes versus strain in the case of CB filled NR, finding that the crystallites' dimensions perpendicular (L_{200} and L_{120}) and parallel (L_{002}) to the stretching direction decrease as filler is added. Chenal and colleagues [251] studied the interplay between crosslink density and filler content, and showed that, regardless of the matrix crosslink density, their CB filled samples had the same crystallites' sizes, close to that obtained for a highly crosslinked unfilled sample (higher crosslink density determined smaller crystallite dimensions).

The assessment of lattice constants is of great importance to study the deformation of the crystalline cell as a consequence of stress or filler addition. Poompradub and colleagues estimated such parameters from WAXD patterns by using the least-square regression method [123, 256]. They assumed that the unit cell was a rectangular parallelepiped, according to the structure analysis by Nyburg [257]. They saw that the lattice was less deformed with the increase in filler content. This trend was stronger for the carbon black-filled samples, and hardly recognizable for the calcium carbonate-filled ones. The smaller degree of lattice deformation in the filled systems indicates that smaller stress is applied to the crystallites due to the presence of filler particles [158, 256], since some local stress is transferred to carbon black, due to the formation of a bound rubber layer and to the aggregate structure of carbon black particles. Both these phenomena are not likely to occur in calcium carbonate [123].

The study of strain-induced crystallization of clay containing rubber-based nanocomposites is definitely underrepresented in the literature. To the knowledge of the author just one study, by Zhang and colleagues, tackled this issue investigating the behavior of nanocomposites based on NR and chloroprene rubber upon stretching [258]. XRD was used in this case to characterize the dispersion of clay in the matrix, finding that the single layers exhibited a mixed exfoliated/unintercalated morphology. Although the presence of clay layers inhibited the crystallization of the matrix on stretching, the modulus of these nanocomposites was higher compared to that of carbon black- or silica-filled rubber, due to the large aspect ratio of clay layers. Clay with

high aspect ratio is more efficient in restricting the rubber chains and in resisting the development of cracks than spherical fillers [258].

17.6.2 Thermoplastic Elastomers

Block copolymers, usually {AB} or {ABA} block sequences, can be prepared if one wishes to widen the gap between the melting temperature T_m and the glass transition temperature T_g, thus covering a property region not easily satisfied by homopolymers or random or statistical copolymers. By synthesizing sequences that are long enough to crystallize independently, composed by a high-melting block A combined with a low-melting block B, one can obtain a material with a high T_m derived from A and a low T_g descending from B. The change in T_g can actually be rather variable, and in a number of cases two T_g's can also appear. The arrangement of blocks is very important. In order to obtain high-tensile-strength materials with elastomeric properties typical of filler-reinforced vulcanizates, it is necessary to accurately calibrate the nature and length of the blocks. Styrenic-based thermoplastic elastomers (TPE) make up approximately 50% of the multibillion dollar TPE industry [259, 260], a rapidly growing market (8%/year), since TPE are viable options to replace conventional vulcanizates. Styrenic TPE are typically based on linear styrene-diene-styrene triblock copolymers with styrene contents ranging from 10 to 90% depending on application. In order to obtain a satisfactory performance, it is necessary that the copolymer contains two or more polystyrene blocks per molecule. In other words, if the structure is {SB} or {BSB} (where S is a styrene block and B a butadiene block) the material is as brittle as polystyrene, while if the structure is {SBS} or {SBSB}, the toughness is much increased and the product behaves as a normal crosslinked rubber. Glassy polystyrene blocks tend to aggregate in domains, that have the double role of crosslink points and of filler particles. The central elastomeric moiety is in fact held fixed by the glassy regions, thereby avoiding the necessity of vulcanization. Keller and coworkers studied highly oriented TPE mechanically and have shown that these systems can be treated as nearly perfect composite materials [261, 262].

When the blocks in such copolymers are not mutually soluble, the system has a natural tendency towards phase segregation. The presence of covalent bonds between the chemically different parts of the molecules, though, prevents a macroscopic phase separation like that seen in polymer–polymer heterogeneous mixtures. The incompatibility between the covalently bonded blocks in such polymers results in self-organized nanostructured materials with peculiar morphologies. The fundamental parameters governing the nature and quality of self-aggregation are the composition and the temperature [263].

At high temperature the entropic contribution is dominant and the blocks mix in a homogenous and disordered state. When temperature is lowered, self-organization can take place in a variety of possible morphologies, the most common of which are a body-centered cubic (bcc) lattice of spheres (S), hexagonally packed cylinders (H), and lamellae (L). More complex morphologies have been identified, such as the bicontinuous structure denominated gyroid phase (G).

For example, in the case of styrenic TPE, with increasing styrene content, one can obtain styrene spheres in a bcc arrangement, followed by hexagonally packed styrene cylinders, a tricontinuous structure, and lamellae. The morphologies invert at high (>50%) styrene content.

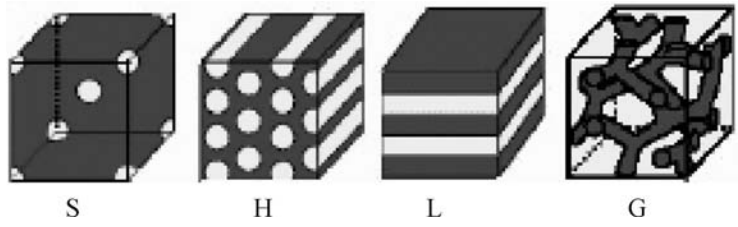

Figure 17.23 Possible morphologies obtained by self-organization of block copolymers

Figure 17.23 schematizes these phases.

SAXS is, along with TEM, the most suitable technique to study the phase behavior of these materials. Typical SAXS patterns of these kind of copolymers consist of an intense principal peak followed by several higher order reflections.

In the case of a lamellar morphology, the higher order signals appear at positions that are integer multiples of the first order reflection. The principal peak is indexed as (001), while the higher order ones as (002), (003). Patterns relative to the H or S morphology are more complicated, as exemplified in Figure 17.24.

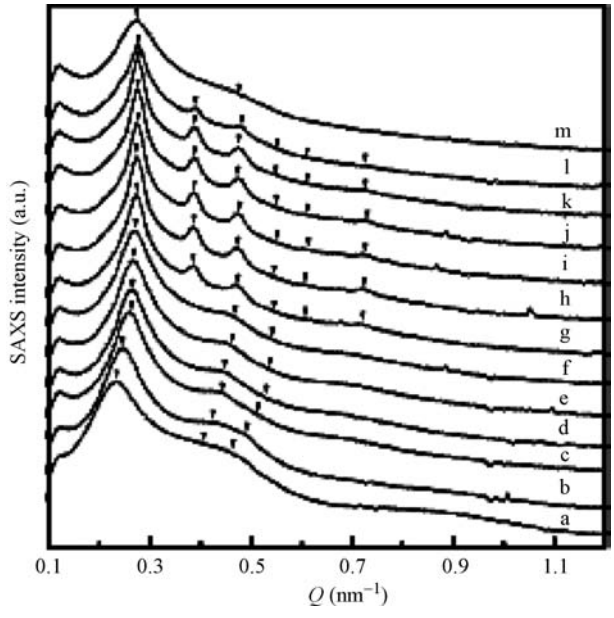

Figure 17.24 SAXS patterns of a SEBS film taken at the following temperatures: (a) 25, (b) 120, (c) 150, (d) 160, (e) 170, (f) 180, (g) 185, (h) 190, (i) 195, (j) 205, (k) 215, (l) 240, and (m) 250 °C. Arrows mark calculated peak positions (Reprinted with permission from C.H. Lee et al., "Ordering Behavior of Layered Silicate Nanocomposites with a Cylindrical Triblock Copolymer," *Macromolecular Chemistry and Physics*, **207**, 444–455, © 2006, Copyright Wiley-VCH Verlag GmbH & Co. KgaA.)

In this figure, 1D SAXS curves obtained at different temperatures on a sample of styrene-(ethylene-co-butylene)-styrene (SEBS) block copolymer are displayed. For the lower temperature patterns, up to 180 °C, the positions of the secondary maxima, relative to the principal peak follow the scaling $1, 3^{1/2}, 4^{1/2}, 7^{1/2}, \ldots$ These ratios indicate that the PS cylinders are packed in a two-dimensional hexagonal lattice [23, 264, 265]. The most intense peak is indexed as a (100) hexagonal peak, and the additional peaks are assigned the (110), (200) and (210) indices [23].

Curves relative to the higher temperatures show that the additional higher order peaks are located approximately according to the ratios $2^{1/2}:4^{1/2}:6^{1/2}:10^{1/2}:12^{1/2}:14^{1/2}$ with respect to the first order peak. This sequence is characteristic of a bcc packing of spherical microdomains [23]. The most intense peak is indexed as a (110) peak and the additional peaks are assigned the (200), (211), (310), (222) and (321) indices.

Another interesting aspect of the data shown in Figure 17.24 is that by temperature-dependent SAXS experiments it is possible to follow the development of the microstructure of the copolymer. The determination of the temperatures of the order-disorder and order-order transition is aided by plotting $I^*(q)^{-1}$ versus T^{-1}, that is, the reciprocal of the absolute temperature, where $I^*(q)$ is the intensity of the main peak such as the (100) peak (cylindrical phase) or (110) peak (spherical phase) in the SAXS pattern. Abrupt decreases of $I^*(q)^{-1}$ with T^{-1} reveal the onset of an order-order or order-disorder transition [23, 266].

SAXS patterns yield additional quantitative results on the morphology of microphase-separated block copolymers. The interdomain distance D is the domain identity period in the case of lamellae, or the nearest neighbor distance between the microdomains for the cylinders and spheres. D can be determined on the basis of the Bragg spacing of the principal peak, according to the following equations:

$$D_{lamellae} = d_{001} \tag{17.65}$$

$$D_{cylinders} = (4/3)^{1/2} d_{100} \tag{17.66}$$

$$D_{spheres} = (3/2)^{1/2} d_{110} \tag{17.67}$$

The indicated $D_{spheres}$ is valid for spherical microdomains in a body centered cubic lattice, while in the case of a simple cubic symmetry $D = d_{100}$.

The radius R of the cylinders or of the spheres can be determined on the basis of space filling considerations, based on the geometry of the microphase, that is, hexagonal cylindrical or cubic, and the volume fraction of the minor phase Φ_B:

$$R_{cylinders} = [d_{100}(3^{1/2}\Phi_B/2\pi)^{1/2}] \tag{17.68}$$

$$R_{spheres} = [(d_{110}/2^{1/2})(3\Phi_B/8\pi)^{1/3}] \tag{17.69}$$

The study of the evolution of the structure of the matrix as a function of the application of mechanical stress is very important for evaluating the performance of these materials and for developing structure-property relationships.

The deformation response of several diblock and triblock copolymer TPE can be studied by various techniques, including SAXS, TEM, AFM, birefringence and rheo-optical techniques. For example, Thomas and coworkers [264] studied the deformation of cylindrical PS domains

of a near single crystal styrene–isoprene–styrene (SIS) triblock copolymer. They carried out deformation experiments normal to the cylinder axis by synchrotron SAXS with the beam both parallel and perpendicular to the cylinder axis. They found that in a first deformation stage the rubber matrix extends along the stretching direction (SD) while contraction occurs almost exclusively along the neutral direction due to the constraint imposed by the aligned PS cylinders. At the onset of a subsequent deformation stage (dependent on the degree of cylinder misorientation, the shear resistance of the rubber matrix, and the bending resistance of the PS cylinders), the initial hexagonal pattern undergoes a continuous distortion through a kinking into a chevron pattern.

The mechanical behavior of elastomeric triblocks with classical microdomain morphologies, that is, H, S and L, has been reported and extensively reviewed [267–269]. An example of a deformation study on a less common morphology, such as the double gyroid phase (G), is shown in Figure 17.25, that shows a typical stress-strain curve of G, with accompanying SAXS patterns recorded at different points along the deformation [143].

Figure 17.25b displays the SAXS pattern of the undeformed sample and consists of an isotropic ring pattern with the characteristic (211) and (220) reflections of the double gyroid. As stress is applied, a fading of the higher-order Bragg rings occurs and the internal diffraction rings lose their isotropy, passing from a circular to an elliptical shape. When necking occurs, in this case at 20% strain, the scattering pattern changes drastically (Figure 17.25c shows the SAXS trace for the X-ray beam directly incident on the necking area). The fading of the isotropic rings is enhanced, the intensity of diffuse low angle scattering increases, and two horizontal streaks appear along the normal to the stretching direction.

A further elongation determines the complete disappearance of the ring, with only the diffuse scatter and streaks remaining (Figure 17.25d). From then on, only the intensity of the streaks changes, while the nature of the pattern remains unaltered. When stress is relieved, that is, upon unloading, the elliptic rings gradually reappear. It is interesting to note that at zero load some degree of anisotropy still remains. Only annealing allows to obtain the same pattern as in the unstretched case, but it is remarkable that any structural consequence of strain deformation is totally recoverable.

A very similar SAXS pattern was also reported for a POSS filled polyurethane [197]. The meridional peaks were attributed in that case to the oriented morphology of the microphase-separated hard and soft segments and the equatorial streak mainly to the extended crystal morphology of the strain-induced soft segment crystals polyurethane [197].

Strain-induced crystallization is observed also in TPE, and a thorough knowledge of this phenomenon is necessary to exploit at their fullest extent the physical mechanical potential of these materials. Strain-induced crystallization, in fact, allows a reduction of flow at high strains and accounts for the retention of the highly elastic behavior of TPE. Among the relatively few studies that were published on this topic a particularly interesting one under the aspect of XRD characterization was presented by Indukuri and Lesser [270]. They studied three SEBS TPE, comparing them to crosslinked natural rubber. The three samples differed by PS content and for the nature of the midblock, that could contain either more ethylene or butylene segments. They showed that especially the nature of the midblock of the TPE had the most important effects on their mechanical properties. On the basis of the internal energy changes from deformation calorimetry and on simultaneous WAXD/SAXD measurements, it was found that strain-induced crystallization occurred only in certain SEBS systems. Figures 17.26 and 17.27 provide examples of the obtained XRD patterns.

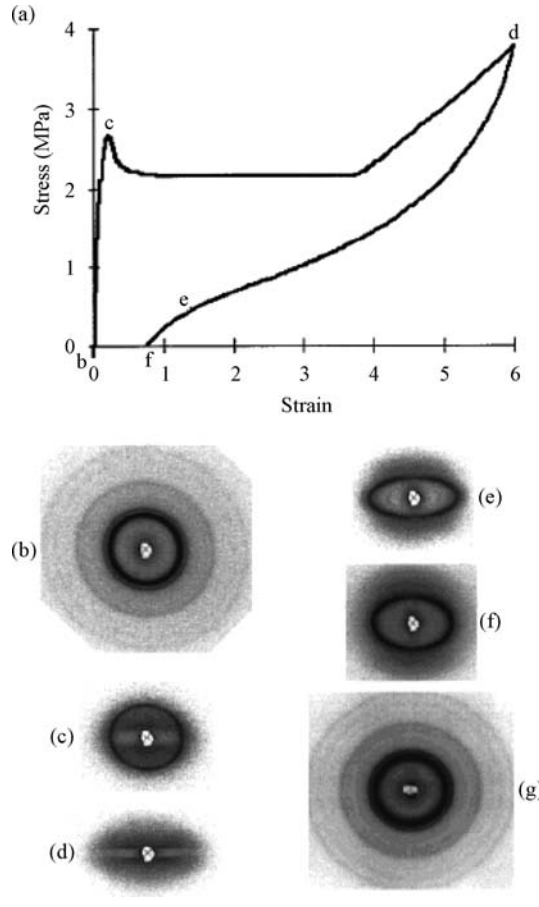

Figure 17.25 (a) Stress-strain curve of a SIS sample in the gyroid morphology, with accompanying SAXS patterns. (b) Pattern before deformation. (c) Pattern at yield, 20% strain. (d) Pattern at 600% strain. (e) Pattern unloaded to 130% strain. (f) Pattern fully unloaded, with 70% residual strain. (g) Pattern upon annealing at 120 °C for 2 weeks (Reprinted with permission from B.J. Dair, C.C. Honeker, D.B. Alward, A. Avgeropoulos, N. Hadjichristidis, L.J. Fetters, M. Capel and E.L. Thomas, "Mechanical Properties and Deformation Behavior of the Double Gyroid Phase in Unoriented Thermoplastic Elastomers," *Macromolecules*, **32**, 8145–8152, 1999. © 1999 American Chemical Society.)

The SAXS patterns of Figure 17.26 allow to follow the deformation of the PS cylinders with strain in the sample containing 20% PS and with a midblock mainly composed of ethylene moieties. The circularly symmetric pattern, showing the characteristic spacings of an hexagonal lattice, was observed before strain is applied. With distortion, the SAXS signal turned into an ellipsoid and then, as strain further increased, into a four-point pattern [271–278]. Figure 17.27 shows the WAXD pattern of the same sample. As strain was increased, bright arches were superimposed to the preexistent amorphous halo, coherently with the formation of crystallites as a consequence of strain. No higher order peaks were observed, not even when the sample underwent further strain, due to the very small dimensions and poor degree of order of

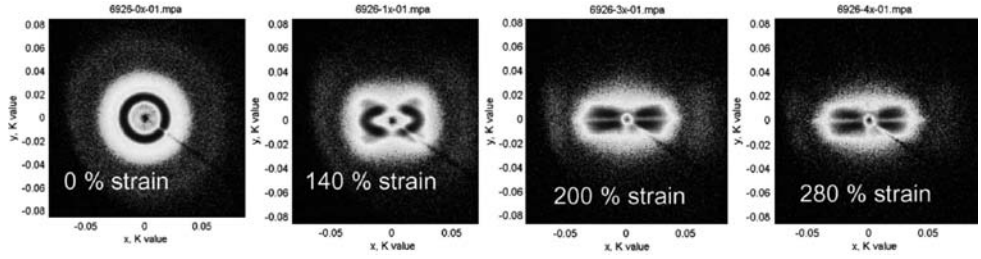

Figure 17.26 SAXS patterns at different strains of a SEBS sample containing 20% PS and with a midblock mainly composed of ethylene moieties (Reprinted from *Polymer*, **46**, K.K. Indukuri and A.J. Lesser, "Comparative deformational characteristics of poly(styrene-b-ethylene-co-butylene-b-styrene) thermoplastic elastomers and cross-linked natural rubber," 7218–7229, 2005. © 2005 with permission from Elsevier.)

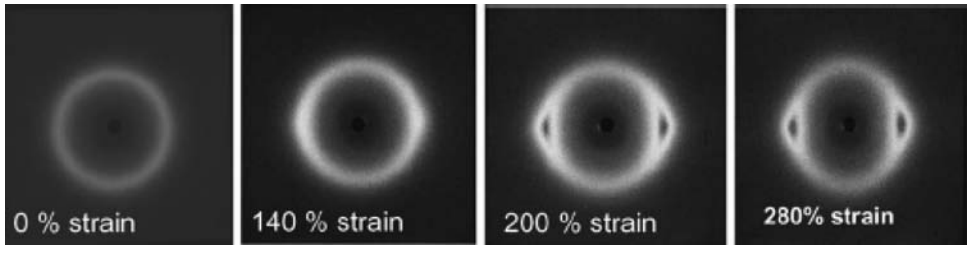

Figure 17.27 WAXD patterns at different strains of a SEBS sample containing 20% PS and with a midblock mainly composed of ethylene moieties (Reprinted from *Polymer*, **46**, K.K. Indukuri and A.J. Lesser, "Comparative deformational characteristics of poly(styrene-b-ethylene-co-butylene-b-styrene) thermoplastic elastomers and cross-linked natural rubber," 7218–7229, © 2005, with permission from Elsevier.)

the crystallites [270]. The same behavior was observed when the PS content was increased to 40%, maintaining the same midblock. When the nature of the midblock was changed, to include predominantly butylene moieties, strain-induced crystallization did not take place, as shown by the persistence in the WAXD diffraction patterns of only the amorphous halo.

It has already been said that TPE can be considered, *per se*, as nanocomposites. The glassy domains, in fact, act as filler particles and, together with the elastomeric microdomains, retain some of the character of their respective homopolymers. Nevertheless, reports have been published in the literature of TPE reinforced with a variety of nanofillers, in particular nanoclays. Under the aspect of XRD characterization of these composite materials, no particular difficulties arise, provided that the contributions to the XRD signal can be adequately singled out. For example, Yamauchi and colleagues investigated the structure of a TPE prepared by blending natural rubber (NR) and high density polyethylene (HDPE) [279]. In this case, the HDPE glassy domains crystallized forming polymeric lamellar stacks, producing a scattering peak in the SAXS pattern that was partially overlapped to the one produced by phase-separated structures between NR and HDPE. When carbon black was added to this polymeric base, scattering by the filler structure was further overlapped on the scattering curve for the

matrix, but the inability to separate the contributions from the different origins, prevented further analysis of the SAXS data [279]. The authors had to complement SAXS data with Small Angle Neutron Scattering. Scattering contrast depends on electron density for X-rays, and on neutron scattering length density for neutrons. The X-ray contrast factors for polyethylene/NR and amorphous/crystalline polyethylene pairs are on the same order whereas the contrast factor of carbon black/NR pair is two orders of magnitudes higher than them. Therefore, both phase-separated structures and crystalline lamellar structures contributed to the SAXS intensity of unfilled samples, while when the filler was added, scattering from carbon black was dominant [279]. On the opposite, the neutron contrast factor for amorphous/crystalline polyethylene pair is negligibly small compared with that for polyethylene/NR pair. In other words, SANS is sensitive just to the phase separated structure and is not influenced by the crystalline structure of HDPE in unfilled samples. Similarly to SAXS, though, due to the very high neutron contrast factor of carbon black/NR pair, the SANS pattern of the filled sample mostly reflects the carbon black structure [279].

The effect of the filler on the structure of the TPE matrix is obviously of interest in the case of nanocomposites. Krishnamoorti and coworkers reported that spherical microdomains of a styrene-isoprene block copolymer arranged on a body-centered cubic (bcc) lattice are templated by the layered silicate, and the kinetics of their growth is accelerated by the presence of a small amount of the filler, whereas the ordering behavior of cylindrical microdomains is essentially unaffected by the addition of layered silicates and the development of three-dimensional mesoscopic order is even disrupted [280].

An effect typically brought about by layered silicate nanofillers is that of influencing the orientation of the matrix. Figure 17.28 shows the SAXS patterns of a SIS triblock copolymer, that show the typically equally spaced signals of a lamellar morphology. The lamellar spacing is in this case approximately $d_{001} = 28$ nm. Knowing the volume fraction of one of the components (in this case it was $\Phi_{PS} = 0.43$), the thickness of the layers of each phase can be calculated as $d_{001}\,\Phi_{PS}$ and $d_{001}(1 - \Phi_{PS})$ and in this case this approximately corresponded to PS layers of 12 nm and PI layers of 16 nm [281]. Preferential orientation of the lamellae can be deduced by the differences in the patterns taken orienting the beam along the flow direction and along its normal. Perpendicularly to the flow direction (beam directed along the x axis), isotropic rings were observed, while if the beam was directed along the y direction the signals were concentrated along the z axis. This anisotropy was attenuated when clay was added, as reflected by the widening of the arches that seem to show a tendency towards circular simmetry. In Figure 17.28e the signal due to silicate layers is displayed: it is oriented and parallel to the lamellar morphology of the block copolymer. Mutual orientation of the silicate and of the block copolymer lamellar microdomains occurs with a uniaxial symmetry in the flow direction.

A similar example of studies on the orientation of TPE-clay nanocomposites was reported by Kim and colleagues [282]. In this case, the microdomains of a SIS block copolymer were organized as hexagonally packed cylinders, preferentially aligned along the flow direction. Also in this work, clay exerted a disrupting role on the orientation of the domains. Clay tactoids in the nanocomposites were mostly oriented along the flow direction, but misaligned tactoids displaced the cylinders nearby, decreasing the Hermans orientation factor in SIS/clay nanocomposites. If the H morphology was attained by a transition from a S morphology, the decrease in the orientational factor from original well aligned H was smaller compared with neat SIS, showing the existence of a memory effect [282].

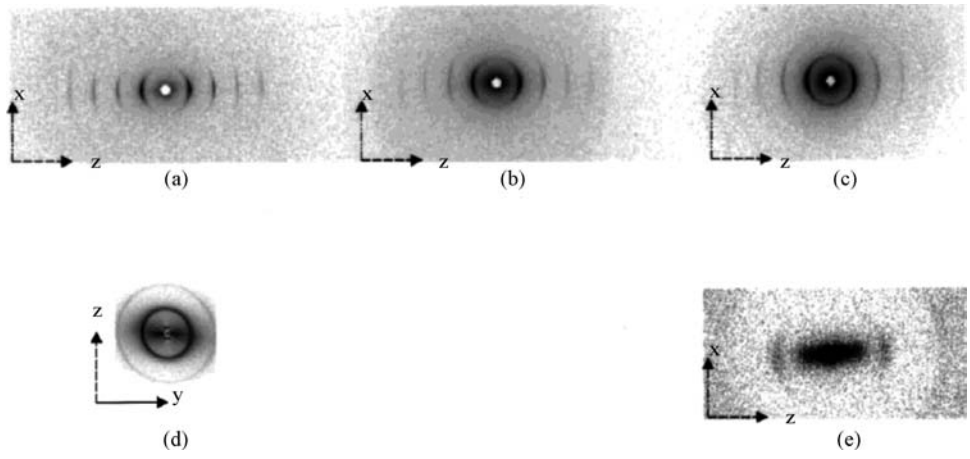

Figure 17.28 Roll-cast samples of (a) 0, (b) 2.5 and (c) 10 wt% SIS block copolymer filled with clay, showing the orientation of the SIS lamellae in SAXS. Note some loss of orientation with increasing amount of the layered-silicate. The lamellar spacing is constant at approximately 28 nm. (d) SAXS pattern of the sample containing 2.5 wt% clay viewed along the roll-cast direction. Note the near isotropic nature of the block copolymer domains. (e) WAXS pattern of the sample containing 10 wt % clay showing preferential orientation of the layered silicates (Reprinted with permission from Y.H. Ha and E.L. Thomas, "Deformation behavior of a roll-cast layered-silicate/lamellar triblock copolymer nanocomposite," *Macromolecules*, **35**, 4419–4428, 2002. © 2002 American Chemical Society.)

The orientation of the polymeric matrix in a poly(butylene terephthalate) (PBT)-block-poly (tetramethylene oxide) (PTMO) TPE filled with carbon nanotubes (CNT) has been also reported [283]. In this study, the structure and morphology of the filled and unfilled material were studied as a function of deformation. For what concerns the pristine polymer, the initial WAXD pattern is an isotropic collection of circular diffraction signals corresponding to the α form of PBT. As strain increased, isotropy was gradually lost and the signal accumulated in the equatorial area (perpendicular to the stretching direction). The structural features that determine the observed WAXD/SAXS signals have been clearly schematized by the authors in Figure 17.29.

The initial isotropic SAXS pattern of the copolymer (pattern A, left in Figure 17.29) is due to a random orientation of the semicrystalline PBT domains in the sample, while the initial SAXS pattern taken from the nanocomposite (pattern A, right in Figure 17.29) reflects their partial orientation due to the templating effect of CNT. Following application of stress in the elastic region, the SAXS signal becomes gradually anisotropic showing an arc on the meridian (pattern B in Figure 17.29), as a consequence of the rotation of the crystal lamellae in order to be aligned along the stretching direction.

At higher strains an irreversible breakage of the PBT crystalline lamellae produces a four point diagram for the copolymer case (Figure 17.29, pattern C, left). The same pattern is present in the nanocomposite (Figure 17.29, pattern C, right), although much less defined, because of a higher degree of disorder, due to the disturbing role of CNT. Later on during the deformation, the fragmented lamellae tend to reassemble themselves along the stretching direction forming

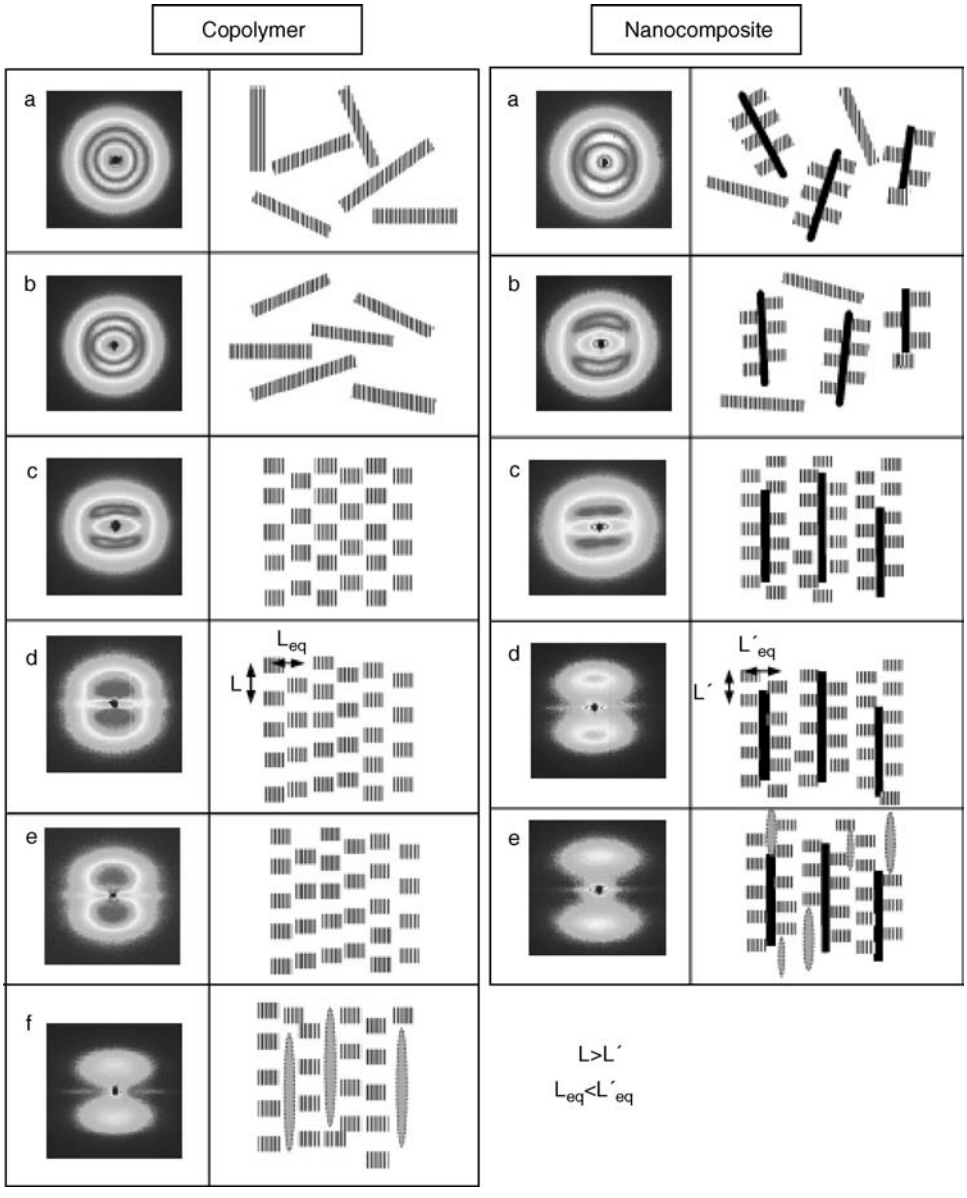

Figure 17.29 2D SAXS patterns together with the schemes of the corresponding microstructure, for the copolymer (left) and for the nanocomposite (right). The patterns have been taken at following strains: (a) 0%, (b) 15%, (c) 35%, (d) 100%, (e) 135%, (f) 300% (Reprinted from *Polymer*, **46**, K.K. Indukuri and A.J. Lesser, "Comparative deformational characteristics of poly(styrene-b-ethylene-co-butylene-b-styrene) thermoplastic elastomers and cross-linked natural rubber," 7218–7229, © 2005, with permission from Elsevier.)

microfibrils through the interconnection by tie molecules, thereby originating an equatorial streak with an intensity maximum in the SAXS patterns that is related to the long period (L_{eq}) in the transverse direction (perpendicular to the applied stress), that is, the average lateral distance between microfibrils.

The appearance of such equatorial maxima upon stretching has been previously reported for PBT-b-PTMO copolymers [284, 285] and the evolution with strain can be explained by the progressive destruction of the semicrystalline domains with increasing strain. This destruction is more efficient in the nanocomposite than in the copolymer, because stress is more efficiently transferred through the nanotubes anchored to the semicrystalline blocks [283]. Last, a further increase in strain smooths the equatorial maxima into an equatorial streak, due to the formation of an elongated soft phase, referred to as soft needles [285], formed by the resulting material of the hard block destruction. CNT favor the appearance of such needles at lower strains than the pristine matrix.

Along with these results, CNT were found to act as nucleating agents in the nanocomposite. Many nanofillers are known to be efficient nucleants. Thus, while the degree of crystallinity was somewhat larger for the nanocomposite, the PBT crystallite size, measured by the Scherrer equation, was considerably reduced by the presence of SWCNT.

The influence of clay on the self-organization of the microphases can be seen by furtherly analyzing the data already shown in Figure 17.24. Analogous experiments done on a clay-containing sample of the same SEBS copolymer, revealed that the observed Bragg peaks became weaker and broader as filler is added. Therefore, clay was found to hinder the regular ordering of the phase-separated domain structure. As seen from the examples above and as clear from the literature, nanofillers are very often associated to a disturbing effect on the crystallization of the matrix. The characteristic peaks of the spherical phase were sharper than those relative to the cylindrical phase. The increase in temperature favored the growth of the grain, and thus the structural perfection of the domain structure. Further heating determined a broadening and weakening of the peak, coherent with an order-disorder transition. It has been observed that in nanocomposites having a strong attractive interaction between the organoclay and block copolymer, the T_{ODT} is increased with respect to the neat matrix [286].

Another possible route for preparing thermoplastic elastomers is by employing polyurethane (PU). PU properties can be adjusted by two approaches: the first is to change the molecular structure of polyurethane by modification of its three basic building blocks: polyether or polyester, diisocyanate, and chain extender. The second is to introduce inorganic fillers into the polyurethane matrix. With the advent of nanocomposite approach, PU/clay hybrids have attracted increasing interest. The XRD characterization of layered fillers has already been discussed elsewhere in this chapter, but in the case of PU-based composites it is of great interest to examine the effect of the filler on the structure of the matrix.

Thermoplastic polyurethanes (TPU) consist of alternating hard and soft segments. The hard segment is composed of alternating diisocyanate and short chain extender molecules (that is, diol or diamine), while the soft segment is a high molecular weight polyester or polyether macrodiol. Phase separation occurs in TPU because of the thermodynamic incompatibility of the hard and soft segments. The segments aggregate into microdomains resulting in a structure consisting of glassy or semicrystalline hard domains and rubbery soft domains that are below or above, respectively, their glass transition temperatures at room temperature.

Mechanical properties for PU/clay nanocomposites are closely related to the phase structures, however, it is not yet clear how the introduction of clay affects the phase morphology of PU.

Through SAXS analysis one can obtain important morphological data such as interdomain spacings, domain size and interfacial thickness [287, 288].

A very common approach for this kind of analysis is that based on the use of the correlation function. As it has already been said, SAXS intensity is a consequence of local heterogeneities in the electron density of the material. For a two-phase system, the invariant quantity Q of overall mean-square electron density fluctuation is obtained by integrating $q^2I(q)$ over the range of scattering angles:

$$Q = \int_0^\infty q^2 I(q) \mathrm{d}q \tag{17.70}$$

The value of invariant Q describes the electron density fluctuation of polymer and is a good approximation to estimate the overall degree of phase separation in segmented polyurethanes. The inter-domain spacing L, defined as the average distance between two hard domains, can be estimated from the q_m corresponding to the maximum of $I(q)q^2$ versus q curves using Bragg's equation.

For systems with a lamellar structure, the one-dimensional correlation function $g_1(r)$ will have a primary local maximum at a position r which corresponds to the inter-lamellar repeat distance L_{1D}. The one-dimensional correlation function (Figure 17.30) is:

$$g_1(r) = \frac{1}{Q} \int_0^\infty q^2 I(q) \cos(qr) \mathrm{d}q \tag{17.71}$$

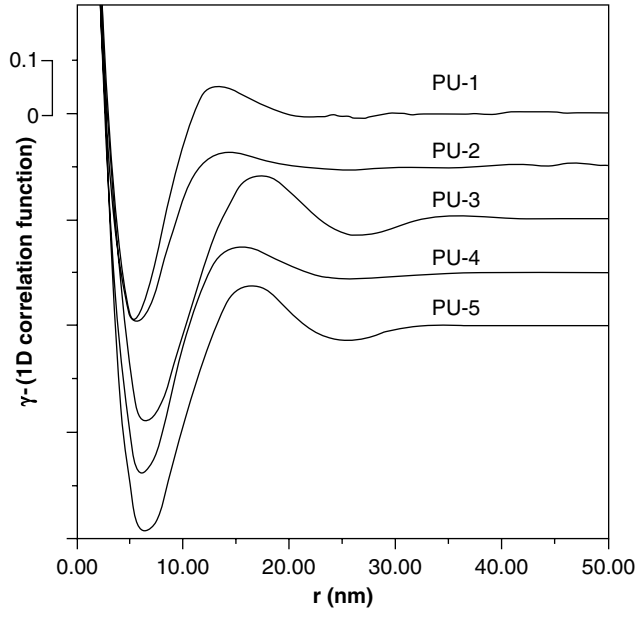

Figure 17.30 Correlation functions $g_1(r)$ obtained from the SAXS profiles of a series of polyurethanes (Reprinted from *Polymer*, **39**, S.L. Chang et al., "Effect of polyester side-chains on the phase segregation of polyurethanes using small-angle X-ray scattering," 3479–3489, © 1998, with permission from Elsevier.)

The domain size can be obtained by interpreting the 1D correlation function [289]. This interpretation assumes that the sample has an ideal lamellar morphology, that is, that it consists of an ensemble of isotropically distributed stacks of alternating crystalline and amorphous lamellae. In the case of PU-clay nanocomposites, the lamellar structure of clay itself can be considered a minor component with respect to the PU matrix and can therefore be neglected.

The inter-domain repeat distance (L or L_{1D}) depends on the molecular length of the polyester soft segment, the number and size of hard segment lamellar crystalline particles and those of polyester crystalline particles. L (or L_{1D}) increases with increasing polyester molecular chain length, and also with decreasing degree of polyester crystallinity. The range of inhomogeneity l_p is a measure of the average size or distance for which all the inhomogeneities in a material exist. According to Debye-Bueche theory [290], the l_p value can be obtained by the slope and intercept of a plot of the left-hand side of Equation 17.72 against q^2 as $q \rightarrow 0$ (Figure 17.31):

$$(I(q)-I_b)^{-1/2} = \left(8\pi\langle\eta^2\rangle l_p^3\right)^{-1/2}(1+l_p^2q^2) \tag{17.72}$$

where $\langle\eta^2\rangle$ is the mean-square electron density fluctuation $(\eta = \rho-\bar{\rho})$ and I_b the background intensity.

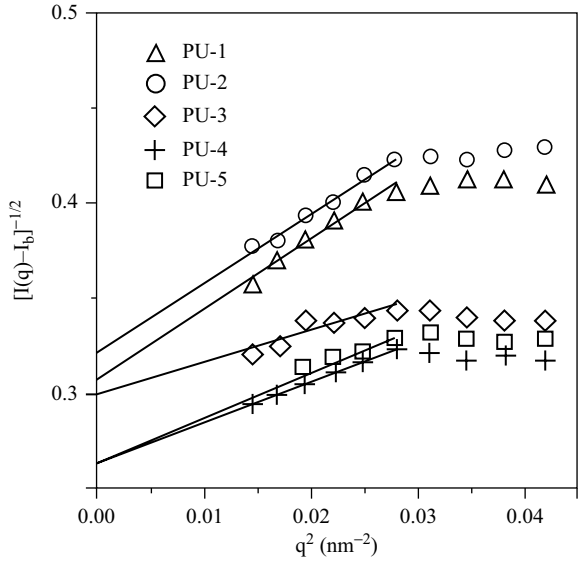

Figure 17.31 Plots of $(I(q)-I_b)^{-1/2}$ versus q^2 at $q \rightarrow 0$ for a series of polyurethanes; full lines are simulated results (Reprinted from *Polymer*, **39**, S.L. Chang et al., "Effect of polyester side-chains on the phase segregation of polyurethanes using small-angle X-ray scattering," 3479–3489, © 1998, with permission from Elsevier.)

The values of the interfacial boundary thickness parameter σ and the Porod's law constant K_p can be obtained from the slope and intercept respectively of a plot of the left-hand side of Equation 17.73 against q^2 as $q \to \infty$ (Figure 17.32):

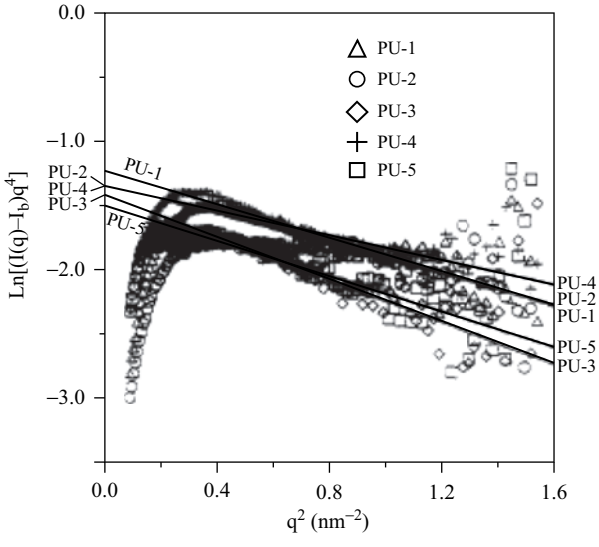

Figure 17.32 Plots of $\ln\{[I(q)-I_b]q^4\}$ versus $q2$ as $q \to \infty$ for a series of polyurethanes; full lines are simulated results (Reprinted from *Polymer*, **39**, S.L. Chang et al., "Effect of polyester side-chains on the phase segregation of polyurethanes using small-angle X-ray scattering," 3479–3489, © 1998, with permission from Elsevier.)

$$\ln\{[I(q)-I_b]q^4\} = \ln K_p - \sigma^2 q^2 \tag{17.73}$$

Porod's law constant K_p is related to the interface surface-to-volume ratio *S/V* by the relation:

$$K_p = 2\pi i_e \langle \eta^2 \rangle (S/V) \tag{17.74}$$

where i_e is the Thompson scattering factor for a single electron. An equivalent thickness E for an inter-phase gradient is given by $E = 12^{1/2}\sigma$.

A furtherly detailed analysis of SAXS data from TPU can be obtained by a method analogous to that described in the case of clay tactoids [56, 88–91]. By this approach, Equations 17.10–17.12 can be used to reproduce experimental SAXS patterns, considering Y and Z as the thicknesses of the hard and soft phase, respectively. This technique was successfully employed by Marigo and Marega [291] to characterize fluorinated PU. These authors also estimated the electron density difference between the two phases ($\rho_h - \rho_s$) and the inner surface *S/V* [6]:

$$2\pi \int_0^\infty sI(s)ds = \left[\Phi_h \Phi_s - \frac{E}{6}\frac{S}{V}\right](\rho_h - \rho_s) \tag{17.75}$$

$$\frac{4}{\pi}\lim_{s\to\infty}\frac{s^3 I(s)}{Q}=\left(\frac{S}{V}\right)\frac{\rho_h-\rho_s}{2\pi^2\Phi_h\Phi_s} \tag{17.76}$$

Where E is the thickness of the transition layer between the hard and the soft regions, evaluated according to the procedure described by Vonk [292], Q is the invariant (Equation 17.70) and Φ_h and Φ_s are the volume fractions of the hard and soft phases.

The inhomogeneity length l_p was evaluated as [293]:

$$l_p=\frac{4\Phi_h\Phi_s}{S/V} \tag{17.77}$$

and the average length of the segments lying within the hard and soft phases, l_h and l_s, respectively, were obtained from $l_h=l_p/\Phi_s$ and $l_s=l_p/\Phi_h$.

The evaluation of such parameters yielded information about the average thickness of the phases.

In the case of the samples examined by the authors [291], the average length of the hard phase l_h and the transition layer thickness did not remarkably change. In contrast, a decreasing trend of the electron density was observed with increasing molecular weight of the fluorinated building blocks, probably because of an increase of melt viscosity of the system, which slows down the expected phase separation. The SAXS patterns obtained for the considered samples showed two partially overlapped peaks, due to the presence of a bimodal distribution of the long period thicknesses. The advantage of the fitting procedure outlined by Equations 17.10–17.12 was that of allowing an independent evaluation of the two overlapped peaks in the SAXS patterns. It was found that the morphological parameters of the first family of structures were dependent on the molecular weight of the fluorinated building block, while the other family had a morphology independent from this parameter. By crossing SAXS and TEM data, it was shown that the studied polymers had a heterogeneous structure, not only at the molecular level, but also at a macroscopic scale. The presence of two families of structures was probably attributable to the synthetic process [291].

The fitting method is moreover preferable because its results are solely based on SAXS. In the correlation function data treatment, in fact, WAXD crystallinity is employed for the estimation of the lamellar thickness, while the fitting technique yields lamellar parameters only on the basis of the SAXS profile. Moreover, the fitting method allows to obtain a larger number of morphological parameters, like the distribution of the thicknesses and of the crystallinity associated to the lamellar stacks, that can not be evaluated by the analysis of the correlation function [76, 294–296]. The reliability of the fitting method was also successfully checked by comparison with transmission electron microscopy measurements [56, 90].

Another alternative approach is that of fitting the data according to other scattering models. Laity *et al.* [297] assessed the ability of a number of scattering models based on different morphologies to reproduce the scattering features observed for TPU with various compositions. Spherical models based on a Zernike-Prins type lattice or a Percus-Yevick liquid type structure were found to most accurately fit the data. The Zernike-Prins model was used by Laity *et al.* to successfully fit SAXS data from TPU subjected to uniaxial deformation [298]. The Zernike-Prins model can also provide a direct estimate of the interdomain distance. The scattering from two-phase systems is represented as the product of the form factor, $P(q)$, and the structure factor, $S(q)$ (Equation 17.16).

In the case of spherical microdomains, the form factor of a sphere is given by Equation 17.52.

The Zernike-Prins model [297] assumes that the positions of the scattering bodies in a medium can be described in any direction by a distorted one-dimensional statistical lattice:

$$S(q) = \frac{1-A^2}{1-2A\cos(qd)+A^2} \tag{17.78}$$

where:

$$A = \exp\left(-\frac{q^2\sigma^2}{2}\right) \tag{17.79}$$

for the case of a Gaussian distribution of nearest-neighbor distances (d) on the lattice, with standard deviation σ.

The effect of clay on the phase morphology of TPU is still open for questions. On one hand there are studies, for example the work of Martin and colleagues [79], that do not report observable effects on the microphase separation due the layered silicates and that do not individuate a role of clay in the morphological response of the TPU to deformation. The improved tensile properties of the nanocomposites containing the smaller nanofillers is ascribed by these authors to the filler particles oriented along the direction of strain, that interact with the TPU sequences via secondary bonding. Large tactoids, that are unable to align in the strain direction, lead to concentrated tensile stresses between the polymer and filler, instead of desirable shear stresses, resulting in void formation and reduced tensile properties.

On the other hand, there are instances where the phase morphology of PU is significantly altered by the presence of clay. Song *et al.* [299] for instance reported that the main interaction sites between polymer and clay are the soft segments and clay appears to influence mostly the inter-domain repeat distance at high soft segment contents, while the hard domain size remains unaltered as filler is added. The addition of clay, moreover, resulted in the decrease in the inter-domain distance as well as the size of the aggregates of the hard domains. The increase in hard segment content leads to the increase in both the inter-domain distance and domain size.

References

1. Kojima, Y., Usuki, A., Kawasumi, M. *et al.* (1993) Mechanical properties of nylon 6-clay hybrid. *Journal of Materials Research*, **8**, 1185.
2. Usuki, A., Kawasumi, M., Kojima, Y. *et al.* (1993) Swelling behavior of montmorillonite cation exchanged for ω-amino acids by ε-caprolactam. *Journal of Materials Research*, **8**, 1174.
3. LeBaron, P.C., Wang, Z., and Pinnavaia, T.J. (1999) Polymer-layered silicate nanocomposites: an overview. *Applied Clay Science*, **15**, 11.
4. Ray, S.S.and Okamoto, M. (2003) Polymer/layered silicate nanocomposites: a review from preparation to processing. *Progress in Polymer Science*, **28**, 1539.
5. Pukánszky, B. (2005) Interfaces and interphases in multicomponent materials: past, present, future. *European Polymer Journal*, **41**, 645.
6. Glatter, O.and Kratky, O. (1982) *Small Angle X-ray Scattering*, Academic Press, London.
7. Alexander, L.E. (1969) *X-ray Diffraction Procedures in Polymer Science*, Wiley, New York.
8. Kakudo, M.and Kasai, N. (1972) *X-ray Diffraction by Polymers*, Kodansha Elsevier, Tokio.
9. Rabek, J.F. (1980) *Experimental Methods in Polymer Chemistry: Physical Principles and Applications*, Wiley, Chichester.
10. Strobl, G. (1997) *The Physics of Polymers*, Springer, Berlin.
11. Vainshtein, B.K. (1981) *Modern Crystallography*, vol. **1**, Springer, Berlin.

12. Klug, H.P.and Alexander, L.E. (1974) *X-ray Diffraction Procedures*, Wiley, New York.
13. Roe, R.J. (2000) *Methods of X-ray and Neutron Scattering in Polymer Science*, Oxford University Press, New York.
14. Guinier, A. (1939) La diffraction des rayons X aux trés petits angles: application à l'étude de phénomènes ultramicroscopiques. *Annals of Physics*, **12**, 161.
15. Porod, G. (1951) The X-ray small angle scattering of close packed colloid systems Part I. *Kolloid-Zeitschrift*, **124**, 83.
16. Debye, P., Anderson, H.R.J., and Brumberger, H. (1957) Scattering by an inhomogeneous solid. II. The correlation function and its application. *Journal of Applied Physics*, **28**, 679.
17. Vaia, R.A., Jandt, K.D., Kramer, E.J., and Giannelis, E.P. (1995) Kinetics of polymer melt intercalation. *Macromolecules*, **28**, 1080.
18. LeBaron, P.C., Wang, Z., and Pinnavaia, T.J. (1999) *Chemistry of Materials*, **1–2**, 11.
19. Bates, R.E.and Jackson, J.A. (1987) *Glossary of Geology*, American Geological Institute, Alexandria, VA.
20. Grim, R.E. (1968) *Clay Mineralogy*, McGraw-Hill, New York.
21. Brindley, G.W. and Brown, G. (1980) *Crystal Structures of Clay Minerals and their X-Ray Identification*, Mineralogical Society, London.
22. Shao, W., Wang, Q., and Ma, H. (2005) Study of polypropylene/montmorillonite nanocomposites prepared by solid-state shear compounding (S3C) using pan-mill equipment: the morphology of montmorillonite and thermal properties of the nanocomposites. *Polymer International*, **54**, 336.
23. Lee, C.H., Kim, H.B., Lim, S.T. *et al.* (2006) Ordering behavior of layered silicate nanocomposites with a cylindrical triblock copolymer. *Macromolecular Chemistry and Physics*, **207**, 444.
24. Strawhecker, K.E. and Manias, E. (2000) Structure and properties of poly(vinyl alcohol)/Na + montmorillonite nanocomposites. *Chemistry of Materials*, **12**, 2943.
25. Ma, J., Yu, Z.Z., Kuan, H.C. *et al.* (2005) A new strategy to exfoliate silicone rubber/clay nanocomposites. *Macromolecular Rapid Communications*, **26**, 830.
26. Jin, Y.H., Park, H.J., Im, S.S. *et al.* (2002) Polyethylene/clay nanocomposite by in-situ exfoliation of montmorillonite during Ziegler-Natta polymerization of ethylene. *Macromolecular Rapid Communications*, **23**, 135.
27. Paul, M.A., Alexandre, M., Degée, P. *et al.* (2003) Exfoliated polylactide/clay nanocomposites by in-situ coordination-insertion polymerization. *Macromolecular Rapid Communications*, **24**, 561.
28. Hoffmann, B., Dietrich, C., Thomann, R. *et al.* (2000) High-output polymer screening: exploiting combinatorial chemistry and data mining tools in catalyst and polymer development. *Macromolecular Rapid Communications*, **24**, 57.
29. Wang, H., Zhao, T., Zhi, L. *et al.* (2002) Synthesis of novolac/layered silicate nanocomposites by reaction exfoliation using acid-modified montmorillonite. *Macromolecular Rapid Communications*, **23**, 44.
30. Brown, G. (1961) *The X-Ray Identification and Crystal Structures of Clay Minerals*, Mineralogical Society, London.
31. Wang, Y., Zhang, H., Wu, Y. *et al.* (2005) Preparation and properties of natural rubber/rectorite nanocomposites. *European Polymer Journal*, **41**, 2776.
32. Wu, Y.P., Wang, Y.Q., Zhang, H.F. *et al.* (2005) Rubber-pristine clay nanocomposites prepared by co-coagulating rubber latex and clay aqueous suspension. *Composites Science and Technology*, **65**, 1195.
33. Gatos, K.G., Százdi, L., Pukánszky, B., and Karger-Kocsis, J. (2005) Controlling the deintercalation in hydrogenated nitrile rubber (HNBR)/organo-montmorillonite nanocomposites by curing with peroxide. *Macromolecular Rapid Communications*, **26**, 915.
34. Gatos, K.G., Sawanis, N.S., Apostolov, A.A. *et al.* (2004) formation in hydrogenated nitrile rubber (HNBR)/organo-montmorillonite as a function of the intercalant type. *Macromolecular Materials and Engineering*, **289**, 1079.
35. Gatos, K.G. and Karger-Kocsis, J. (2005) Effects of primary and quaternary amine intercalants on the organoclay dispersion in a sulfur-cured EPDM rubber. *Polymer*, **46**, 3069.
36. Gatos, K.G., Thomann, R., and Karger-Kocsis, J. (2004) Characteristics of ethylene propylene diene monomer rubber/organoclay nanocomposites resulting from different processing conditions and formulations. *Polymer International*, **53**, 1195.
37. Gatos, K.G. and Karger-Kocsis, J. (2007) Effect of the aspect ratio of silicate platelets on the mechanical and barrier properties of hydrogenated acrylonitrile butadiene rubber (HNBR)/layered silicate nanocomposites. *European Polymer Journal*, **43**, 1097.

38. Galimberti, M., Lostritto, A., Spatola, A., and Guerra, G. (2007) Clay delamination in hydrocarbon rubbers. *Chemistry of Materials*, **19**, 2495.
39. Joly, S., Garnaud, G., Ollitrault, R. *et al.* (2002) Organically modified layered silicates as reinforcing fillers for natural rubber. *Chemistry of Materials*, **14**, 4202.
40. Liang, Y., Wang, Y., Wu, Y. *et al.* (2005) Preparation and properties of isobutylene-isoprene rubber (IIR)/clay nanocomposites. *Polymer Testing*, **24**, 12.
41. Lu, Y.L., Liang, Y.R., Wu, Y.P., and Zhang, L.Q. (2006) Effects of heat and pressure on microstructures of isobutylene-isoprene rubber (IIR)/clay nanocomposites. *Macromolecular Materials and Engineering*, **291**, 27.
42. Ma, Y., Li, Q.F., Zhang, L.Q., and Wu, Y.P. (2007) Role of stearic acid in preparing EPDM/clay nanocomposites by melt compounding. *Polymer Journal*, **39**, 48.
43. Sue, H.-., Gam, K.T., Bestaoui, N. *et al.* (2004) Fracture behavior of α-zirconium phosphate-based epoxy nanocomposites. *Acta Materialia*, **52**, 2239.
44. Vaia, R.A. and Giannelis, E.P. (1997) Lattice model of polymer melt intercalation in organically-modified layered silicates. *Macromolecules*, **30**, 7990.
45. Vaia, R.A. and Giannelis, E.P. (1997) Polymer melt intercalation in organically-modified layered silicates: model predictions and experiment. *Macromolecules*, **30**, 8000.
46. Nieuwenhuizen, P. (2001) Zinc accelerator complexes: versatile homogeneous catalysts in sulfur vulcanization. *Applied Catalysis A General*, **207**, 55.
47. Wu, Y.P., Zhang, L.Q., Wang, Y.Q. *et al.* (2001) Structure of carboxylated acrylonitrile-butadiene rubber (CNBR)-clay nanocomposites by co-coagulating rubber latex and clay aqueous suspension. *Journal of Applied Polymer Science*, **82**, 2842.
48. Usuki, A. and Kato, T.M. (2002) Preparation and properties of EPDM–clay hybrids. *Polymer*, **43**, 2185.
49. LeBaron, P.C. and Pinnavaia, T.J. (2001) Clay nanolayer reinforcement of a silicone elastomer. *Chemistry of Materials*, **13**, 3760.
50. Jia, Q.X., Wu, Y.P., Wang, Y.Q. *et al.* (2007) Organic interfacial tailoring of styrene butadiene rubber-clay nanocomposites prepared by latex compounding method. *Journal of Applied Polymer Science*, **103**, 1826.
51. Liang, Y.R., Lu, Y.L., Wu, Y.P. *et al.* (2005) Pressure, the critical factor governing final microstructures of cured rubber/clay nanocomposites. *Macromolecular Rapid Communications*, **26**, 926.
52. Liang, Y.R., Ma, J., Lu, Y.L. *et al.* (2005) Effects of heat and pressure on intercalation structures of isobutylene-isoprene rubber/clay nanocomposites. I. Prepared by melt blending. *Journal of Polymer Science Part B-Polymer Physics*, **43**, 2653.
53. Maiti, M. and Bhowmick, A.K. (2006) Structure and properties of some novel fluoroelastomer/clay nanocomposites with special reference to their interaction. *Journal of Polymer Science Part B-Polymer Physics*, **44**, 162.
54. Zheng, H., Zhang, Y., Peng, Z., and Zhang, Y. (2004) Influence of clay modification on the structure and mechanical properties of EPDM/montmorillonite nanocomposites. *Polymer Testing*, **23**, 217.
55. Benetti, E.M., Causin, V., Marega, C. *et al.* (2005) Morphological and structural characterization of polypropylene based nanocomposites. *Polymer*, **46**, 8275.
56. Causin, V., Marega, C., Marigo, A., and Ferrara, G. (2005) Assessing organo-clay dispersion in polymer layered silicate nanocomposites: A SAXS approach. *Polymer*, **46**, 9533.
57. Costa, F.R., Abdel-Goad, M., Wagenknecht, U., and Heinrich, G. (2005) Nanocomposites based on polyethylene and Mg-Al layered double hydroxide. I. Synthesis and characterization. *Polymer*, **46**, 4447.
58. Vaia, R.A. and Liu, W. (2002) X-ray powder diffraction of polymer/layered silicate nanocomposites: model and practice. *Journal of Polymer Science Part B-Polymer Physics*, **40**, 1590.
59. Bertini, F., Canetti, M., Audisio, G. *et al.* (2006) Characterization and thermal degradation of polypropylene-montmorillonite nanocomposites. *Polymer Degradation and Stability*, **91**, 600.
60. Chen, C., Khobaib, M., and Curliss, D. (2003) Epoxy layered-silicate nanocomposites. *Progress in Organic Coatings*, **47**, 376.
61. Jeon, H.S., Rameshwaram, J.K., Kim, G., and Weinkauf, D.H. (2003) Characterization of polyisoprene - clay nanocomposites prepared by solution blending. *Polymer*, **44**, 5749.
62. Kim, S.H., Park, S.H., and Kim, S.C. (2005) Novel clay treatment and preparation of poly(ethylene terephthalate)/clay nanocomposite by in-situ polymerization. *Polymer Bulletin*, **53**, 285.
63. Chen, T., Zhu, J., Li, B. *et al.* (2005) Exfoliation of organo-clay in telechelic liquid polybutadiene rubber. *Macromolecules*, **38**, 4030.

64. Triantafillidis, C.S., LeBaron, P.C., and Pinnavaia, T.J. (2002) Homostructured mixed inorganic−organic ion clays: a new approach to epoxy polymer−exfoliated clay nanocomposites with a reduced organic modifier content. *Chemistry of Materials*, **14**, 4088.
65. Chow, W.S., Ishak, Z.A.M., and Karger-Kocsis, J. (2005) Morphological and rheological properties of polyamide 6/poly(propylene)/organoclay nanocomposites. *Macromolecular Materials and Engineering*, **290**, 122.
66. Cho, J.W. and Paul, D.R. (2001) Nylon 6 nanocomposites by melt compounding. *Polymer*, **42**, 1083.
67. Hsiao, S.H., Liou, G.S., and Chang, L.M. (2001) Synthesis and properties of organosoluble polyimide/clay hybrids. *Journal of Applied Polymer Science*, **80**, 2067.
68. Yano, K., Usuki, A., Okada, A. *et al.* (1993) Synthesis and properties of polyimide-clay hybrid. *Journal of Polymer Science Part A-Polymer Chemistry*, **31**, 2493.
69. Chow, W.S., Mohd Ishak, Z.A., Karger-Kocsis, J. *et al.* (2003) Compatibilizing effect of maleated polypropylene on the mechanical properties and morphology of injection molded polyamide 6/polypropylene/organoclay nanocomposites. *Polymer*, **44**, 7427.
70. Fröhlich, J., Thomann, R., and Muölhaupt, R. (2003) Toughened epoxy hybrid nanocomposites containing both an organophilic layered silicate filler and a compatibilized liquid rubber. *Macromolecules*, **36**, 7205.
71. Yoonessi, M., Toghiani, H., Daulton, T.L. *et al.* (2005) Clay delamination in clay/poly(dicyclopentadiene) nanocomposites quantified by small angle neutron scattering and high-resolution transmission electron microscopy. *Macromolecules*, **38**, 818.
72. Zhang, Z., Zhang, L., Li, Y., and Xu, H. (2005) New fabricate of styrene-butadiene rubber/montmorillonite nanocomposites by anionic polymerization. *Polymer*, **46**, 129.
73. Mehta, S., Mirabella, F.M., Rufener, K., and Bafna, A. (2004) Thermoplastic olefin/clay nanocomposites: morphology and mechanical properties. *Journal of Applied Polymer Science*, **92**, 928.
74. Fasulo, P.D., Rodgers, W.R., Ottaviani, R.A., and Hunter, D.L. (2004) Extrusion processing of TPO nanocomposites. *Polymer Engineering and Science*, **44**, 1036.
75. Causin, V., Marega, C., Marigo, A. *et al.* (2006) Morphology, structure and properties of a poly(1-butene)/montmorillonite nanocomposite. *Polymer*, **47**, 4773.
76. Causin, V., Marega, C., Marigo, A. *et al.* (2008) Structure-property relationships in isotactic poly(propylene)/ethylene propylene rubber/montmorillonite nanocomposites. *Journal of Nanoscience and Nanotechnology*, **8**, 1823.
77. Maiti, M. and Bhowmick, A.K. (2006) New insights into rubber-clay nanocomposites by AFM imaging. *Polymer*, **47**, 6156.
78. Sadhu, S. and Bhowmick, A.K. (2005) Morphology study of rubber based nanocomposites by transmission electron microscopy and atomic force microscopy. *Journal of Materials Science*, **40**, 1633.
79. Finnigan, B., Jack, K., Campbell, K. *et al.* (2005) Segmented polyurethane nanocomposites: Impact of controlled particle size nanofillers on the morphological response to uniaxial deformation. *Macromolecules*, **38**, 7386.
80. Ma, Y., Wu, Y.P., Wang, Y.Q., and Zhang, L.Q. (2006) Structure and properties of organoclay/EPDM nanocomposites: influence of ethylene contents. *Journal of Applied Polymer Science*, **99**, 914.
81. Ogata, N., Kawakage, S., and Ogihara, T. (1997) Structure and thermal/mechanical properties of poly(ethylene oxide)-clay mineral blends. *Polymer*, **38**, 5115.
82. Herrmann, W., Uhl, C., Heinrich, G., and Jehnichen, D. (2006) Analysis of HNBR-montmorillonite nanocomposites: Morphology, orientation and macroscopic properties. *Polymer Bulletin*, **57**, 395.
83. Bafna, A., Beaucage, G., Mirabella, F., and Mehta, S. (2003) 3D hierarchical orientation in polymer-clay nanocomposite films. *Polymer*, **44**, 1103.
84. Bafna, A., Beaucage, G., Mirabella, F. *et al.* (2001) Optical properties and orientation in polyethylene blown films. *Journal of Polymer Science Part B-Polymer Physics*, **39**, 2923.
85. Wilchinsky, Z. (1963) Orientation in cold-rolled polypropylene. *Journal of Polymer Science*, **7**, 923.
86. Kaneko, S., Frederick, J.E., and Mcintyre, D. (1981) Void formation in a filled SBR rubber determined by small-angle X-ray scattering. *Journal of Applied Polymer Science*, **26**, 4175.
87. Wu, Y.P., Ma, Y., Wang, Y.Q., and Zhang, L.Q. (2004) Effects of characteristics of rubber, mixing and vulcanization on the structure and properties of rubber/clay nanocomposites by melt blending. *Macromolecular Materials and Engineering*, **289**, 890.
88. Blundell, D. (1978) Models for small-angle X-ray scattering from highly dispersed lamellae. *Polymer*, **19**, 1258.
89. Marega, C., Marigo, A., Cingano, G. *et al.* (1996) Small-angle X-ray scattering from high-density polyethylene: lamellar thickness distributions. *Polymer*, **37**, 5549.

90. Marigo, A., Marega, C., Zannetti, R., and Sgarzi, P. (1998) A study of the lamellar thickness distribution in 1-butene, 4-methyl-1-pentene and 1-hexene LLDPE by small and wide angle X-ray scattering and transmission electron microscopy. *European Polymer Journal*, **34**, 597.
91. Marega, C., Marigo, A., and Causin, V. (2003) Small-angle X-ray scattering from polyethylene: distorted lamellar structures. *Journal of Applied Polymer Science*, **90**, 2400.
92. Garnweitner, G., Smarsly, B., Assink, R. *et al.* (2004) Characterization of self-assembled lamellar thermo-responsive silica-hydrogel nanocomposite films. *Langmuir*, **20**, 9811.
93. Ruland, W. and Smarsly, B. (2004) SAXS of self-assembled oriented lamellar nano-composite films: an advanced method of evaluation. *Journal of Applied Crystallography*, **37**, 575.
94. Hosemann, R. and Bagchi, S.N. (1962) *Direct Analysis of Diffraction by Matter*, North Holland, Amsterdam.
95. Eckel, D.F., Balogh, M.P., Fasulo, P.D., and Rodgers, W.R. (2004) Assessing organo-clay dispersion in polymer nanocomposites. *Journal of Applied Polymer Science*, **93**, 1110.
96. Ray, S.S., Okamoto, M., and Okamoto, M. (2003) Structure–property relationship in biodegradable poly (butylene succinate)/layered silicate nanocomposites. *Macromolecules*, **36**, 2355.
97. Ray, S.S. and Okamoto, M. (2003) Biodegradable polylactide and its nanocomposites: opening a new dimension for plastics and composites. *Macromolecular Rapid Communications*, **24**, 815.
98. Vaia, R.A., Liu, W., and Koerner, H. (2003) Analysis of small-angle scattering of suspensions of organically modified montmorillonite: implications to phase behavior of polymer nanocomposites. *Journal of Polymer Science Part B Polymer Physics*, **41**, 3214.
99. Vonk, C.G. (1978) The small-angle scattering of distorted lamellar structures. *Journal of Applied Crystallography*, **11**, 541.
100. Sasanuma, Y., Abe, A., Sasanuma, T. *et al.* (1993) Small-angle X-ray scattering of distorted lamellar structures. *Journal of Polymer Science Part B Polymer Physics*, **31**, 1179.
101. Hernandez, M., Sixou, B., Duchet, J., and Sautereau, H. (2007) The effect of dispersion state on PMMA-epoxy-clay ternary blends: in situ study and final morphologies. *Polymer*, **48**, 4075.
102. Varlot, K., Reynaud, E., Vigier, G., and Varlet, J. (2002) Mechanical properties of clay-reinforced polyamide. *Journal of Polymer Science Part B Polymer Physics*, **40**, 272.
103. Gelfer, M., Burger, C., Fadeev, A. *et al.* (2004) Thermally induced phase transitions and morphological changes in organoclays. *Langmuir*, **20**, 3746.
104. Gelfer, M.Y., Burger, C., Chu, B. *et al.* (2005) Relationships between structure and rheology in model nanocomposites of ethylene-vinyl-based copolymers and organoclays. *Macromolecules*, **38**, 3765.
105. King, S.M. (1999) Chapter 7, in *Modern Techniques for Polymer Characterisation* (eds R.A. Pethrickand J.V. Dawkins), Wiley, New York.
106. Vainshtein, B.K. (1966) *Diffraction of X-Rays by Chain Molecules*, Elsevier, New York.
107. Hermans, J.J. (1944) Concerning the influence of grid disturbances on the X-ray pattern, particularly in gels. *Recueil des Travaux Chimiques des Pays-Bas*, **63**, 211.
108. Zernike, F. and Prins, J.A. (1927) X-ray diffraction from liquids. *Zeitschrift fur Physik*, **41**, 184.
109. Hajji, P., David, L., Gerard, J.F. *et al.* (1999) Synthesis, structure, and morphology of polymer-silica hybrid nanocomposites based on hydroxyethyl methacrylate. *Journal of Polymer Science Part B Polymer Physics*, **37**, 3172.
110. Wang, S., Zhang, Y., Ren, W. *et al.* (2005) Morphology, mechanical and optical properties of transparent BR/clay nanocomposites. *Polymer Testing*, **24**, 766.
111. Vu, Y.T., Mark, J.E., Pham, L.H., and Engelhardt, M. (2001) Clay nanolayer reinforcement of cis-1,4-polyisoprene and epoxidized natural rubber. *Journal of Applied Polymer Science*, **82**, 1391.
112. Koo, C.M., Ham, H.T., Kim, S.O. *et al.* (2002) Morphology evolution and anisotropic phase formation of the maleated polyethylene-layered silicate nanocomposites. *Macromolecules*, **35**, 5116.
113. Koo, C.M., Kim, S.O., and Chung, I.J. (2003) Study on morphology evolution, orientational behavior, and anisotropic phase formation of highly filled polymer-layered silicate nanocomposites. *Macromolecules*, **36**, 2748.
114. Saunders, J.M., Goodwin, J.W., Richardson, R.M., and Vincent, R. (1999) A small-angle X-ray scattering study of the structure of aqueous laponite dispersions. *The Journal of Physical Chemistry. B*, **103**, 9211.
115. Brown, A.B.D., Clarke, S.M., and Bennie, A.R. (1998) Ordered phase of platelike particles in concentrated dispersions. *Langmuir*, **14**, 3129.
116. Fujiwara, S. and Fujimoto, K. (1971) NMR study of vulcanized rubber. *Rubber Chemistry and Technology*, **44**, 1273.

117. Dannenberg, E.M. (1986) Bound rubber and carbon-black reinforcement. *Rubber Chemistry and Technology*, **59**, 512.
118. Litvinov, V.M. and Spiess, H.W. (1991) H NMR study of molecular motions in polydimethylsiloxane and its mixtures with aerosils. *Makromolekulare Chemie-Macromolecular Chemistry and Physics*, **192**, 3005.
119. Litvinov, V.M. and Spiess, H.W. (1992) Molecular mobility in the adsorption layer and chain orientation in strained poly(dimethylsiloxane) networks by H NMR. *Makromolekulare Chemie-Macromolecular Chemistry and Physics*, **193**, 1181.
120. Litvinov, V.M. and Steeman, P.A.M. (1999) EPDM–carbon black interactions and the reinforcement mechanisms, as studied by low-resolution 1H NMR. *Macromolecules*, **32**, 8476.
121. Medalia, A.I. and Kraus, G. (1994) *Science and Technology of Rubber*, Academic Press, San Diego.
122. Reichert, W.F., Hopfenmuller, M.K., and Goritz, D.J. (1987) Volume change and gas transport at uniaxial deformation of filled natural rubber. *Journal of Materials Science*, **22**, 3470.
123. Poompradub, S., Tosaka, M., Kohjiya, S. *et al.* (2005) Mechanism of strain-induced crystallization in filled and unfilled natural rubber vulcanizates. *Journal of Applied Physics*, **97**, 103529.
124. Trabelsi, S., Albouy, P.A., and Rault, J. (2003) Effective local deformation in stretched filled rubber. *Macromolecules*, **36**, 9093.
125. Rieker, T.P., Misono, S., and Ehrburger-Dolle, F. (1999) Small-angle X-ray scattering from carbon blacks: crossover between the fractal and porod regimes. *Langmuir*, **15**, 914.
126. Rieker, T.P., Hindermann-Bischoff, M., and Ehrburger-Dolle, F. (2000) Small-angle X-ray scattering study of the morphology of carbon black mass fractal aggregates in polymeric composites. *Langmuir*, **16**, 5588.
127. Martin, J.E. and Hurd, A.J. (1987) Scattering from fractals. *Journal of Applied Crystallography*, **20**, 61.
128. Mandelbrot, B.B. (1982) *The Fractal Geometry of Nature*, Freeman, San Francisco.
129. Koga, T., Hashimoto, T., Takenaka, M. *et al.* (2008) New insight into hierarchical structures of carbon black dispersed in polymer matrices: a combined small-angle scattering study. *Macromolecules*, **41**, 453.
130. Chaker, J.A., Dahmouche, K., Craievich, A.F. *et al.* (2000) Structure of weakly bonded PPG-silica nanocomposites. *Journal of Applied Crystallography*, **33**, 700.
131. Chaker, J.A., Dahmouche, K., Santilli, C.V. *et al.* (2003) Gelation and drying of weakly bonded silica-PPO nanocomposites. *Journal of Applied Crystallography*, **36**, 689.
132. Molina, C., Dahmouche, K., Santilli, C.V. *et al.* (2001) Structure and luminescence of Eu3 + -doped class I siloxane-poly(ethylene glycol) hybrids. *Chemistry of Materials*, **13**, 2818.
133. Guinier, A. (1963) *X-ray Diffraction*, Freeman, San Francisco.
134. Freltoft, T., Kjems, J.K., and Sinha, S.K. (1986) Power-law correlations and finite-size effects in silica particle aggregates studied by small-angle neutron scattering. *Physical Review B Condensed Matter*, **33**, 269.
135. Teixeira, J. (1988) Small-angle scattering by fractal systems. *Journal of Applied Crystallography*, **21**, 781.
136. Tian, D., Blacher, S., and Jerome, R. (1999) Biodegradable and biocompatible inorganic-organic hybrid materials: 4. Effect of acid content and water content on the incorporation of aliphatic polyesters into silica by the sol-gel process. *Polymer*, **40**, 951.
137. Schaefer, D.W. (1989) Polymers, fractals, and ceramic materials. *Science*, **243**, 1023.
138. Schmidt, P.W. (1991) Small-angle scattering studies of disordered, porous and fractal systems. *Journal of Applied Crystallography*, **24**, 414.
139. Schaefer, D.W., Rieker, T., Agamalian, M. *et al.* (2000) Multilevel structure of reinforcing silica and carbon. *Journal of Applied Crystallography*, **33**, 587.
140. Witten, T.A., Rubinstein, M., and Colby, R.H. (1993) Reinforcement of rubber by fractal aggregates. *Journal of Physiology, Paris*, **3**, 367.
141. Oeser, R., Picot, C., and Herz, J. (1987) *Polymer Motion in Dense Systems* (eds D. Richterand T. Springer), Springer, Berlin.
142. Mendes, E., Lindner, P., Buzier, M. *et al.* (1991) Experimental evidence for inhomogeneous swelling and deformation in statistical gels. *Physical Review Letters*, **66**, 1595.
143. Ehrburger-Dolle, F., Hindermann-Bischoff, M., Livet, F. *et al.* (2001) Anisotropic ultra-small-angle X-ray scattering in carbon black filled polymers. *Langmuir*, **17**, 329.
144. Beaucage, G. (1995) Approximations leading to a unified exponential/power-law approach to small-angle scattering. *Journal of Applied Crystallography*, **28**, 717.
145. Beaucage, G. and Schaefer, D.W. (1994) Structural studies of complex systems using small-angle scattering: a unified Guinier/power-law approach. *Journal of Non-Crystalline Solids*, **172**, 797.

146. Beaucage, G. (1996) Small-angle scattering from polymeric mass fractals of arbitrary mass-fractal dimension. *Journal of Applied Crystallography*, **29**, 134.
147. Suryawanshi, C.N., Pakdel, P., and Schaefer, D.W. (2003) Effect of drying on the structure and dispersion of precipitated silica. *Journal of Applied Crystallography*, **36**, 573.
148. Guinier, A. and Fournet, G. (1955) *Small-Angle Scattering of X Rays*, Wiley, London.
149. Morfin, I., Ehrburger-Dolle, F., Grillo, I. *et al.* (2006) ASAXS, SAXS and SANS investigations of vulcanized elastomers filled with carbon black. *Journal of Synchrotron Radiation*, **13**, 445.
150. Cromer, D.T. and Liberman, D. (1970) Relativistic calculation of anomalous scattering factors for X rays. *Journal of Chemical Physics*, **53**, 1891.
151. Polizzi, S., Riello, P., Goerick, G., and Benedetti, A. (2002) Quantitative investigations of supported metal catalysts by ASAXS. *Journal of Synchrotron Radiation*, **9**, 65.
152. Iijima, S. (1991) Helical microtubules of graphitic carbon. *Nature*, **354**, 56.
153. Bauer, B.J., Hobbie, E.K., and Becker, M.L. (2006) Small-angle neutron scattering from labeled single-wall carbon nanotubes. *Macromolecules*, **39**, 2637.
154. Schaefer, D.W., Zhao, J., Brown, J.M. *et al.* (2003) Morphology of dispersed carbon single-walled nanotubes. *Chemical Physics Letters*, **375**, 369.
155. Zhou, W., Islam, M.F., Wang, H. *et al.* (2004) Small angle neutron scattering from single-wall carbon nanotube suspensions: evidence for isolated rigid rods and rod networks. *Chemical Physics Letters*, **384**, 185.
156. Hernández, J.J., García-Gutiérrez, M.C., Nogales, A. *et al.* (2006) Small-angle X-ray scattering of single-wall carbon nanotubes dispersed in molten poly(ethylene terephthalate). *Composites Science and Technology*, **66**, 2629.
157. Justice, R.S., Wang, D.H., Tan, L.S., and Schaefer, D.W. (2007) Simplified tube form factor for analysis of small-angle scattering data from carbon nanotube filled systems. *Journal of Applied Crystallography*, **40**, s88.
158. Chen, X., Burger, C., Fang, D. *et al.* (2006) In-situ X-ray deformation study of fluorinated multiwalled carbon nanotube and fluorinated ethylene-propylene nanocomposite fibers. *Macromolecules*, **39**, 5427.
159. Chen, X., Yoon, K., Burger, C. *et al.* (2005) In-situ X-ray scattering studies of a unique toughening mechanism in surface-modified carbon nanofiber/UHMWPE nanocomposite films. *Macromolecules*, **38**, 3883.
160. Shanmugharaj, A.M., Bae, J.H., Lee, K.Y. *et al.* (2007) Physical and chemical characteristics of multiwalled carbon nanotubes functionalized with aminosilane and its influence on the properties of natural rubber composites. *Composites Science and Technology*, **67**, 1813.
161. Reznik, D., Olk, C., Neumann, A., and Copley, J. (1995) X-ray powder diffraction from carbon nanotubes and nanoparticles. *Physical Review B Condensed Matter*, **52**, 116.
162. Burian, A., Dore, J., Fischer, H., and Sloan, J. (1999) Structural studies of multiwalled carbon nanotubes by neutron diffraction. *Physical Review B Condensed Matter*, **59**, 1665.
163. Choi, S. (2001) Filler-polymer interactions in both silica and carbon black-filled styrene-butadiene rubber compounds. *Journal of Applied Polymer Science*, **39**, 439.
164. Wang, M.J., Lu, S.X., and Mahmud, K. (2000) Carbon-silica dual-phase filler, a new-generation reinforcing agent for rubber. Part VI. Time-temperature superposition of dynamic properties of carbon-silica-dual-phase-filler-filled vulcanizates. *Journal of Polymer Science Part B Polymer Physics*, **38**, 1240.
165. Sheng, E., Sutherland, I., Bradley, R.H., and Freakley, P.K. (1996) Effects of a multifunctional additive on bound rubber in carbon black and silica filled natural rubbers. *European Polymer Journal*, **32**, 35.
166. Manna, A.K., Tripathy, D.K., De, P.P., and Peiffer, D.G. (1999) Bonding between precipitated silica and epoxidized natural rubber in the presence of silane coupling agent. *Journal of Applied Polymer Science*, **75**, 389.
167. Mélé, P., Marceau, S., Brown, D. *et al.* (2002) Reinforcement effects in fractal-structure-filled rubber. *Polymer*, **43**, 5577.
168. Matejka, L., Dukh, O., and Kolařík, J. (2000) Reinforcement of crosslinked rubbery epoxies by in-situ formed silica. *Polymer*, **41**, 1449.
169. Brown, W.D. and Ball, C.D. (1985) Computer simulation of chemically limited aggregation. *Journal of Physics A*, **18**, L517.
170. Jullien, R., Kolb, M., and Botet, R. (1984) Diffusion limited aggregation with directed and anisotropic diffusion. *Journal of Physiology*, **45**, L211.
171. Brinker, C.J. and Scherer, G.W. (1990) *Sol-Gel Science: The Physics and Chemistry of Sol-Gel Processing*, Academic Press, New York.

172. Rajeshkumar, S., Anilkumar, G.M., Ananthakumar, S., and Warrier, K.G.K. (1998) Role of drying techniques on the development of porosity in silica gels. *Journal of Porous Materials*, **5**, 59.
173. Rubio, F., Rubio, J., and Oteo, J.L. (1997) A DSC study of the drying process of TEOS derived wet silica gels. *Thermochimica Acta*, **307**, 51.
174. Schaefer, D.W., Suryawanshi, C., Pakdel, P. *et al.* (2002) Challenges and opportunities in complex materials: silica-reinforced elastomers. *Physica A: Statistical Mechanics and Its Applications*, **314**, 686.
175. Sanchez, C. and Ribot, F. (1994) Design of hybrid organic-inorganic materials synthesized via sol-gel chemistry. *New Journal of Chemistry*, **18**, 1007.
176. Chaker, J.A., Dahmouche, K., Santilli, C.V. *et al.* (2005) Effect of salt nature on structure and ionic conductivity of sodium-doped siloxane-PPO ormolytes. *Journal of the European Ceramic Society*, **25**, 2617.
177. Dahmouche, K., Santilli, C.V., Pulcinelli, S.H. and Craievich, A.F. (1999) Small-angle X-ray scattering study of sol-gel-derived siloxane-PEG and siloxane-PPG hybrid materials. *The Journal of Physical Chemistry. B*, **103**, 4937.
178. Chiavacci, L.A., Dahmouche, K., Silva, N.J.O. *et al.* (2004) Effect of presence of an acid catalyst on structure and properties of iron-doped siloxane-polyoxyethylene nanocomposites prepared by sol-gel. *Journal of Non-Crystalline Solids*, **345/346**, 585.
179. Judeinstein, P., Titman, J., Stamm, M., and Schmidt, H. (1994) Investigation of ion-conducting ormolytes: structure-property relationships. *Chemistry of Materials*, **6**, 127.
180. Terrill, N.J., Crowley, T., Gill, M., and Armes, S.P. (1993) Small-angle X-ray scattering studies on colloidal dispersions of polyaniline-silica nanocomposites. *Langmuir*, **9**, 2093.
181. Rharbi, Y., Cabane, B., Vacher, A. *et al.* (1999) Modes of deformation in a soft/hard nanocomposite: a SANS study. *Europhysics Letters*, **46**, 472.
182. Clement, F., Bokobza, L., and Monnerie, L. (2001) On the Mullins effect in silica-filled polydimethylsiloxane networks. *Rubber Chemistry and Technology*, **74**, 847.
183. Oberdisse, J., Rharbi, Y., and Boue, F. (2000) Simulation of aggregate structure and SANS-spectra in filled elastomers. *Computational and Theoretical Polymer Science*, **10**, 207.
184. Ikeda, Y., Yasuda, Y., Yamamoto, S., and Morita, Y. (2007) Study on two-dimensional small-angle X-ray scattering of in situ silica filled nanocomposite elastomer during deformation. *Journal of Applied Crystallography*, **40**, s549.
185. Shinohara, Y., Kishimoto, H., Inoue, K. *et al.* (2007) Characterization of two-dimensional ultra-small-angle X-ray scattering apparatus for application to rubber filled with spherical silica under elongation. *Journal of Applied Crystallography*, **40**, s397.
186. Park, J.U., Choi, Y.S., Cho, K.S. *et al.* (2006) Time-electric field superposition in electrically activated polypropylene/layered silicate nanocomposites. *Polymer*, **47**, 5145.
187. Lichtenhan, J.D. (1996) *Polymeric Materials Encyclopedia* (ed. J.C. Salamone), CRC Press, Boca Raton, FL, p. 7768.
188. Shea, K.J. and Loy, D.A. (2001) Bridged polysilsesquioxanes: molecular engineering of hybrid organic-inorganic materials. *MRS Bulletin*, **26**, 368.
189. Phillips, S.H., Haddad, T.S., and Tomczak, S.J. (2004) Developments in nanoscience: polyhedral oligomeric silsesquioxane (POSS)-polymers. *Current Opinion in Solid State & Materials Science*, **8**, 21.
190. Laine, R.M. (2005) Nanobuilding blocks based on the [OSiO1.5]x (x = 6, 8, 10) octasilsesquioxanes. *Journal of Materials Chemistry*, **15**, 3725.
191. Kannan, R.Y., Salacinski, H.J., Butler, P.E., and Seifalian, A.M. (2005) Polyhedral oligomeric silsesquioxane nanocomposites: the next generation material for biomedical applications. *Accounts of Chemical Research*, **38**, 879.
192. Hillson, S.D., Smith, E., Zeldin, M., and Parish, C.A. (2005) Cages, baskets, ladders, and tubes: conformational studies of polyhedral oligomeric silsesquioxanes. *The Journal of Physical Chemistry. B*, **109**, 8371.
193. Pielichowski, K., Njuguna, J., Janowski, B., and Pielichowski, J. (2006) Polyhedral oligomeric silsesquioxanes (POSS)-containing nanohybrid polymers. *Advances in Polymer Science*, **201**, 225.
194. Zhang, Y., Lee, S., Yoonessi, M. *et al.* (2006) Phenolic resin–trisilanolphenyl polyhedral oligomeric silsesquioxane (POSS) hybrid nanocomposites: structure and properties. *Polymer*, **47**, 2984.
195. Zheng, L., Waddon, A.J., Farris, R.J., and Coughlin, E.B. (2002) X-ray characterizations of polyethylene polyhedral oligomeric silsesquioxane copolymers. *Macromolecules*, **35**, 2375.

196. Strachota, A., Kroutilová, I., Kovářová, J., and Matějka, L. (2004) Epoxy networks reinforced with polyhedral oligomeric silsesquioxanes (POSS). Thermomechanical properties. *Macromolecules*, **37**, 9457.
197. Fu, B.X., Hsiao, B.S., Pagola, S. *et al.* (2001) Structural development during deformation of polyurethane containing polyhedral oligomeric silsesquioxanes (POSS) molecules. *Polymer*, **42**, 599.
198. Liu, L., Tian, M., Zhang, W. *et al.* (2007) Crystallization and morphology study of polyhedral oligomeric silsesquioxane (POSS)/polysiloxane elastomer composites prepared by melt blending. *Polymer*, **48**, 3201.
199. Zheng, L., Hong, S., Cardoen, G. *et al.* (2004) Polymer nanocomposites through controlled self-assembly of cubic silsesquioxane scaffolds. *Macromolecules*, **37**, 8606.
200. Barry, A.J., Daudt, W.H., Domicone, J.J., and Gilkey, J.W. (1955) Crystalline organosilsesquioxanes. *Journal of the American Chemical Society*, **77**, 424.
201. Larsson, K. (1960) The crystal structure of octa-(methylsilsesquioxane) (CH3SiO1.5)8. *Arkiv for Kemi; Utgivet av K. Svenska Vetenskapsakademien*, **16**, 203.
202. Waddon, A.J. and Coughlin, E.B. (2003) Crystal structure of polyhedral oligomeric silsequioxane (POSS) nanomaterials: a study by X-ray diffraction and electron microscopy. *Chemistry of Materials*, **15**, 4555.
203. Moore, E.P. (1996) *Polypropylene Handbook*, Hanser, Cincinnati.
204. Gelfer, M.Y., Song, H.H., Liu, L. *et al.* (2003) Effects of organoclays on morphology and thermal and rheological properties of polystyrene and poly(methyl methacrylate) blends. *Journal of Polymer Science Part B-Polymer Physics*, **41**, 44.
205. Voulgaris, D. and Petridis, D. (2002) Emulsifying effect of dimethyldioctadecylammonium-hectorite in polystyrene/poly(ethyl methacrylate) blends. *Polymer*, **43**, 2213.
206. Wang, Y., Zhang, Q., and Fu, Q. (2003) Compatibilization of immiscible poly(propylene)/polystyrene blends using clay. *Macromolecular Rapid Communications*, **24**, 231.
207. Khatua, B.B., Lee, D.J., Kim, H.Y., and Kim, J.K. (2004) Effect of organoclay platelets on morphology of nylon-6 and poly(ethylene-ran-propylene) rubber blends. *Macromolecules*, **37**, 2454.
208. Chow, W.S., Ishiaku, U.S., Mohd Ishak, Z.A. *et al.* (2004) The effect of organoclay on the mechanical properties and morphology of injection-molded polyamide 6/polypropylene nanocomposites. *Journal of Applied Polymer Science*, **91**, 175.
209. Chiu, F.C., Lai, S.M., Chen, Y.L., and Lee, T.H. (2005) Investigation on the polyamide 6/organoclay nanocomposites with or without a maleated polyolefin elastomer as a toughener. *Polymer*, **46**, 11600.
210. González, I., Eguiazábal, J.I., and Nazábal, J. (2005) Compatibilization level effects on the structure and mechanical properties of rubber-modified polyamide-6/clay nanocomposites. *Journal of Polymer Science Part B-Polymer Physics*, **43**, 3611.
211. Dasari, A., Yu, Z.Z., and Mai, Y.W. (2005) Effect of blending sequence on microstructure of ternary nanocomposites. *Polymer*, **46**, 5986.
212. Denac, M., Šmit, I., and Musil, V. (2005) Polypropylene/talc/SEBS (SEBS-g-MA) composites. Part 1. Structure. *Composites Part A Applied Science and Manufacturing*, **36**, 1094.
213. Trongtorsak, K., Supaphol, P., and Tantayanon, S. (2004) Effect of calcium stearate and pimelic acid addition on mechanical properties of heterophasic isotactic polypropylene/ethylene-propylene rubber blend. *Polymer Testing*, **23**, 533.
214. Wahit, M.U., Hassan, A., Ishak, Z.A.M. *et al.* (2006) Morphology, thermal, and mechanical behavior of ethylene octene copolymer toughened polyamide 6/polypropylene nanocomposites. *Journal of Thermoplastic Composite Materials*, **19**, 545.
215. Wahit, M.U., Hassan, A., Rahmat, A.R., and Mohd Ishak, Z.A. (2006) Morphological and mechanical properties of rubber-toughened polyamide 6/polypropylene nanocomposites prepared by different methods of compounding. *Journal of Elastomers and Plastics*, **38**, 231.
216. Wang, K., Wang, C., Li, J. *et al.* (2007) Effects of clay on phase morphology and mechanical properties in polyamide 6/EPDM-g-MA/organoclay ternary nanocomposites. *Polymer*, **48**, 2144.
217. Treloar, R. (1975) *The Physics of Rubber Elasticity*, Oxford University Press, Oxford.
218. Flory, P. (1947) Thermodynamics of crystallization in high polymers. I. Crystallization induced by stretching. *Journal of Chemical Physics*, **15**, 397.
219. Gent, A.N. (1954) Crystallization and the relaxation of stress in stretched natural rubber vulcanizates. *Transactions of the Faraday Society*, **50**, 521.
220. Smith, K.J.J., Greene, A., and Ciferri, A. (1963) Crystallization under stress and non-Gaussian behavior of macromolecular networks. *Kolloid-Z uZ Polymere*, **194**, 49.

221. Andrews, E.H. (1962) Spherulite morphology in thin films of natural rubber. *Proceedings of the Royal Society of London. Series A, Mathematical and Physical Sciences*, **A270**, 232.
222. Andrews, E.H. (1964) Crystalline morphology in thin films of natural rubber. II. Crystallization under strain. *Proceedings of the Royal Society of London. Series A, Mathematical and Physical Sciences*, **A272**, 562.
223. Andrews, E.H., Owen, P.J., and Singh, A. (1971) Microkinetics of lamellar crystallization in a long chain polymer. *Proceedings of the Royal Society of London. Series A, Mathematical and Physical Sciences*, **324**, 79.
224. Luch, D. and Yeh, G.S.Y. (1972) Morphology of strain-induced crystallization of natural rubber. I. Electron microscopy on uncrosslinked thin film. *Journal of Applied Physics*, **43**, 4326.
225. Luch, D. and Yeh, G.S.Y. (1973) Morphology of strain-induced crystallization of natural rubber. Part II. X-Ray studies on cross-linked vulcanizates. *Journal of Macromolecular Science-Physics*, **B97**, 121.
226. Luch, D. and Yeh, G.S.Y. (1973) Strain-induced crystallization of natural rubber. III. Reexamination of axial-stress changes during oriented crystallization of natural rubber vulcanizates. *Journal of Polymer Science Part B-Polymer Physics*, **11**, 467.
227. Tosaka, M., Murakami, S., Poompradub, S. *et al.* (2004) Orientation and crystallization of natural rubber network as revealed by WAXD using synchrotron radiation. *Macromolecules*, **37**, 3299.
228. Suzuki, A., Oikawa, H., and Murakami, K. (1985) New interpretations for stress-strain behavior of rubber vulcanizates. *Journal of Macromolecular Science-Physics*, **B23**, 535.
229. Toki, S., Fujimaki, T., and Okuyama, M. (2000) Strain-induced crystallization of natural rubber as detected real-time by wide-angle X-ray diffraction technique. *Polymer*, **41**, 5423.
230. Toki, S., Sics, I., Hsiao, B.S. *et al.* (2005) Probing the nature of strain-induced crystallization in polyisoprene rubber by combined thermomechanical and in situ X-ray diffraction techniques. *Macromolecules*, **38**, 7064.
231. Toki, S., Sics, I., Ran, S. *et al.* (2003) Molecular orientation and structural development in vulcanized polyisoprene rubbers during uniaxial deformation by in situ synchrotron X-ray diffraction. *Polymer*, **44**, 6003.
232. Toki, S., Sics, I., Ran, S. *et al.* (2002) New insights into structural development in natural rubber during uniaxial deformation by in situ synchrotron X-ray diffraction. *Macromolecules*, **35**, 6578.
233. Tosaka, M., Kawakami, D., Senoo, K. *et al.* (2006) Crystallization and stress relaxation in highly stretched samples of natural rubber and its synthetic analogue. *Macromolecules*, **39**, 5100.
234. Tosaka, M., Senoo, K., Kohjiya, S., and Ikeda, Y. (2007) Crystallization of stretched network chains in cross-linked natural rubber. *Journal of Applied Physics*, **101**, 84909.
235. Trabelsi, S., Albo uy, P.A., and Rault, J. (2003) Crystallization and melting processes in vulcanized stretched natural rubber. *Macromolecules*, **36**, 7624.
236. Toki, S., Sics, I., Hsiao, B.S. *et al.* (2004) Structural developments in synthetic rubbers during uniaxial deformation by in situ synchrotron X-ray diffraction. *Journal of Polymer Science Part B Polymer Physics*, **42**, 956.
237. Toki, S., Sics, I., Ran, S. *et al.* (2004) Strain-induced molecular orientation and crystallization in natural and synthetic rubbers under uniaxial deformation by in-situ synchrotron X-ray study. *Rubber Chemistry and Technology*, **77**, 317.
238. Toki, S. and Hsiao, B.S. (2003) Nature of strain-induced structures in natural and synthetic rubbers under stretching. *Macromolecules*, **36**, 5915.
239. Schallamach, A. (1942) The long spacing in rubber. *Transactions of the Faraday Society*, **38**, 376.
240. Benedetti, E., Corradini, P., and Pedone, C. (1975) Conformational isomorphism in crystalline 1,4-cis-polyisoprene. *European Polymer Journal*, **11**, 585.
241. Mitchell, G.R. (1984) A wide-angle X-ray study of the development of molecular orientation in crosslinked natural rubber. *Polymer*, **25**, 1562.
242. Dumbleton, B. and Bowles, B. (1966) X-ray determination of crystallinity and orientation in poly(ethylene terephthalate). *Journal of Polymer Science: Part A-2*, **4**, 951.
243. Lee, D.J. and Donovan, J.A. (1987) Microstructural changes in the crack tip region of carbon-black-filled natural rubber. *Rubber Chemistry and Technology*, **60**, 910.
244. Trabelsi, S., Albouy, P.A., and Rault, J. (2002) Stress-induced crystallization around a crack tip in natural rubber. *Macromolecules*, **35**, 10054.
245. Fraser, R.D.B., Marae, T.P., Miller, A., and Rowlands, R.J. (1976) Digital processing of fibre diffraction patterns. *Journal of Applied Crystallography*, **9**, 81.
246. Ruland, W. (1977) Elimination of the effect of orientation distributions in fiber diagrams. *Colloid and Polymer Science*, **255**, 833.

247. Ma, J., Xiang, P., Mai, Y.W., and Zhang, L.Q. (2004) A novel approach to high performance elastomer by using clay. *Macromolecular Rapid Communications*, **25**, 1692.
248. Kraus, G. (1965) *Reinforcement of Elastomers*, Interscience, New York.
249. Gent, A.N. (1992) *Engineering with Rubber*, Oxford University Press, Oxford.
250. Flory, P.J. (1953) *Principles of Polymer Chemistry*, Cornell University Press, Ithaca, NY.
251. Chenal, J.M., Gauthier, C., Chazeau, L. *et al.* (2007) Parameters governing strain induced crystallization in filled natural rubber. *Polymer*, **48**, 6893.
252. Gehman, S.D. and Field, J.E. (1941) *Rubber Chemistry and Technology*, **14**, 85.
253. Rault, J., Marchal, J., Judeinstein, P., and Albouy, P.A. (2006) Stress-induced crystallization and reinforcement in filled natural rubbers:2H NMR study. *Macromolecules*, **39**, 8356.
254. Tosaka, M., Kohjiya, S., Murakami, S. *et al.* (2004) Effect of network-chain length on strain-induced crystallization of NR and IR vulcanizates. *Rubber Chemistry and Technology*, **77**, 711.
255. Rault, J., Marchal, J., Judeinstein, P., and Albouy, P.A. (2006) Chain orientation in natural rubber, Part II: 2H-NMR study. *European Physical Journal E*, **21**, 243.
256. Poompradub, S., Tosaka, M., Kohjiya, S. *et al.* (2004) Lattice deformation of strain-induced crystallites in carbon-filled natural rubber. *Chemistry Letters*, **33**, 220.
257. Nyburg, S.C. (1954) A statistical structure for crystalline rubber. *Acta Crystallographica*, **7**, 385.
258. Wang, Y., Zhang, H., Wu, Y. *et al.* (2005) Structure and properties of strain-induced crystallization rubber-clay nanocomposites by co-coagulating the rubber latex and clay aqueous suspension. *Journal of Applied Polymer Science*, **96**, 318.
259. Creemers, H.M.J.C. (1996) Thermoplastische Elastomere. *Kunststoffe*, **86**, 1845.
260. Rader, C.P. (1996) *Modern Plastics: Encyclopedia*, vol. **73**, McGraw-Hill, New York, p. B51.
261. Arridge, R.G.C. and Folkes, M.J. (1972) The mechanical properties of a 'single crystal' of SBS copolymer - a novel composite material. *Journal of Physics D Applied Physics*, **5**, 344.
262. Folkes, M.J., Keller, A., and Scalisi, F.P. (1973) An extrusion technique for the preparation of 'single-crystals' of block copolymers. *Colloid and Polymer Science*, **251**, 1.
263. Cowie, J.M.G. and Arrighi, V. (2007) *Polymers: Chemistry and Physics of Modern Materials*, CRC Press, Boca Raton, FL.
264. Honeker, C.C., Thomas, E.L., Albalak, R.J. *et al.* (2000) Perpendicular deformation of a near-single-crystal triblock copolymer with a cylindrical morphology. 1. Synchrotron SAXS. *Macromolecules*, **33**, 9395.
265. Hamley, I.W. (1998) *Block Copolymers*, Oxford University Press, Oxford.
266. Leibler, L. (1980) Theory of microphase separation in block copolymers. *Macromolecules*, **13**, 1602.
267. Holden, G. and Legge, N.R. (1996) *Thermoplastic Elastomers* (eds G. Holden, N.R. Legge, R.P. Quirk,and H.E. Schroeder), Hanser, New York, pp. 48–69.
268. Quirk, R.P. and Morton, M. (1996) *Thermoplastic Elastomers*, Hanser, New York, pp. 72–100.
269. Honeker, C.C. and Thomas, E.L. (1996) Impact of morphological orientation in determining mechanical properties in triblock copolymer systems. *Chemistry of Materials*, **8**, 1702.
270. Indukuri, K.K. and Lesser, A.J. (2005) Comparative deformational characteristics of poly(styrene-b-ethylene-co-butylene-b-styrene) thermoplastic elastomers and cross-linked natural rubber. *Polymer*, **46**, 7218.
271. Beecher, J.F., Marker, L., Bradford, R.D., and Aggarwal, S.L. (1969) Morphology and mechanical behavior of block polymers. *Journal of Polymer Science C*, **26**, 117.
272. Inoue, T., Masahiko, M., Hashimoto, T., and Kawai, H. (1971) Deformation mechanism of elastomeric block copolymers having spherical domains of hard segments under uniaxial tensile stress. *Macromolecules*, **4**, 500.
273. Pakula, T., Saijo, K., Kawai, H., and Hashimoto, T. (1985) Deformation behavior of styrene-butadiene-styrene triblock copolymer with cylindrical morphology. *Macromolecules*, **18**, 1294.
274. Agarwal, S.L. (1976) Structure and properties of block polymers and multiphase polymer systems: an overview of present status and future potential. *Polymer*, **17**, 938.
275. Huy, T.A., Adhikari, R., and Michler, G.H. (2003) Deformation behavior of styrene-block-butadiene-block-styrene triblock copolymers having different morphologies. *Polymer*, **44**, 1247.
276. Seguela, R. and Prudhomme, J. (1988) Affinity of grain deformation in mesomorphic block polymers submitted to simple elongation. *Macromolecules*, **21**, 636.
277. Honeker, C.C. and Thomas, E.L. (2000) Perpendicular deformation of a near-single-crystal triblock copolymer with a cylindrical morphology. 2. TEM. *Macromolecules*, **33**, 9407.

278. Honeker, C.C., Thomas, E.L., Albalak, R.J. *et al.* (2000) Perpendicular deformation of a near-single-crystal triblock copolymer with a cylindrical morphology. 1. Synchrotron SAXS. *Macromolecules*, **33**, 9395.
279. Yamauchi, K., Akasaka, S., Hasegawa, H. *et al.* (2005) Structural study of natural rubber thermoplastic elastomers and their composites with carbon black by small-angle neutron scattering and transmission electron microscopy. *Composites Part A Applied Science and Manufacturing*, **36**, 423.
280. Ren, J., Silva, A.S., and Krishnamoorti, R. (2000) Linear viscoelasticity of disordered polystyrene−polyisoprene block copolymer based layered-silicate nanocomposites. *Macromolecules*, **33**, 3739.
281. Ha, Y.H. and Thomas, E.L. (2002) Deformation behavior of a roll-cast layered-silicate/lamellar triblock copolymer nanocomposite. *Macromolecules*, **35**, 4419.
282. Lee, J.Y., Park, M.S., Yang, H.C. *et al.* (2003) Alignment and orientational proliferation of HEX cylinders in a polystyrene-block-polyisoprene-block-polystyrene copolymer in the presence of clay. *Polymer*, **44**, 1705.
283. Hernández, J.J., García-Gutiérrez, M.C., Nogales, A. *et al.* (2007) Deformation behaviour during cold drawing of nanocomposites based on single wall carbon nanotubes and poly(ether ester) copolymers. *Polymer*, **48**, 3286.
284. García-Gutiérrez, M.C., Nogales, A., Rueda, D.R. *et al.* (2007) X-ray microdiffraction and micro-Raman study on an injection moulding SWCNT-polymer nanocomposite. *Composites Science and Technology*, **67**, 798.
285. Stribeck, N. (1999) The equatorial small-angle scattering during the straining of poly(ether ester) and its analysis. *Journal of Polymer Science Part B-Polymer Physics*, **37**, 975.
286. Lee, K.M. and Han, C.D. (2003) Linear dynamic viscoelastic properties of functionalized block copolymer/organoclay nanocomposites. *Macromolecules*, **36**, 804.
287. Chang, S.L., Yu, T.L., Huang, C.C. *et al.* (1998) Effect of polyester side-chains on the phase segregation of polyurethanes using small-angle X-ray scattering. *Polymer*, **39**, 3479.
288. Yu, H., Natnson, A., Singh, M.A., and Plivelic, T. (1999) A comparative study using small-angle X-ray scattering and solid-state NMR of microdomain structures in poly(styrene-butadiene-styrene) triblock copolymers. *Macromolecules*, **32**, 7562.
289. Strobl, G.R. and Schneider, M. (1980) Direct evaluation of the electron density correlation function of partially crystalline polymers. *Journal of Polymer Science*, **18**, 1343.
290. Debye, P. and Bueche, A.M. (1949) Scattering by an inhomogeneous solid. *Journal of Applied Physics*, **20**, 5518.
291. Tonelli, C., Ajroldi, G., Marigo, A. *et al.* (2001) Synthesis methods of fluorinated polyurethanes. 2. Effects on morphology and microstructure. *Polymer*, **42**, 9705.
292. Vonk, C.G. (1973) Investigation of non-ideal two-phase polymer structures by small-angle X-ray scattering. *Journal of Applied Crystallography*, **6**, 81.
293. Ruland, W. (1971) Small-angle scattering of two-phase systems: determination and significance of systematic deviations from Porod's law. *Journal of Applied Crystallography*, **4**, 70.
294. Causin, V., Yang, B.X., Marega, C. *et al.* (2008) Structure-property relationship in polyethylene reinforced by polyethylene-grafted multi-walled carbon nanotubes. *Journal of Nanoscience and Nanotechnology*, **8**, 1790.
295. Marega, C., Causin, V., and Marigo, A. (2008) A SAXS-WAXD study on the mesomorphic-α transition of isotactic polypropylene. *Journal of Applied Polymer Science*, **109**, 32.
296. Causin, V., Carraro, M.L., Marega, C. *et al.* (2008) Structure and morphology of solution blended poly(vinylidene fluoride)/montmorillonite nanocomposites. *Journal of Applied Polymer Science*, **109**, 2354.
297. Laity, P.R., Taylor, J.E., Wong, S.S. *et al.* (2004) A review of small-angle scattering models for random segmented poly(ether-urethane) copolymers. *Polymer*, **45**, 7273.
298. Laity, P.R., Taylor, J.E., Wong, S.S. *et al.* (2004) A 2-dimensional small-angle X-ray scattering study of the microphase-separated morphology exhibited by thermoplastic polyurethanes and its response to deformation. *Polymer*, **45**, 5215.
299. Song, M., Xia, H.S., Yao, K.J., and Hourston, D.J. (2005) A study on phase morphology and surface properties of polyurethane/organoclay nanocomposite. *European Polymer Journal*, **41**, 259.

18

Barrier Properties of Rubber Nanocomposites

Changwoon Nah[1] and M. Abdul Kader[2]

[1] *Department of Polymer-Nano Science and Technology, Chonbuk National University, Jeonju 561-756, Republic of Korea*

[2] *Department of Polymer Technology, B.S.A. Crescent Engineering College, Chennai 600 048, India*

18.1 Introduction

The transport behavior of organic solvents and gases through polymers is of great technological importance, since polymer membranes are increasingly used in applications in biomedical, environmental and agricultural engineering. The migration of gases through materials has been a critical factor in the ability of food packagers to increase the shelf life of products. The migration of carbon dioxide (CO_2) out of soda bottles can reduce shelf life by allowing the soda to become "flat." Oxygen migrating into beer bottles reacts with the beer to make it "stale." The migration of oxygen through auto and truck tires causes the steel to rust, reducing the tire's life. This is particularly important in large industrial truck tires that may be retreaded many times before the "carcass" is discarded. Superior barrier properties of polymer nanocomposites have resulted in applications for barrier liners in storage tanks and fuel lines for cryogenic fuels in aerospace systems, air springs, cure bladders and so on [1]. The selection of a barrier polymer for a particular application typically involves trade offs between permeation, mechanical and esthetic properties as well as economic and recycling considerations.

Excellent air retention properties of butyl/halo butyl is very well known in the tire industries and these rubbers are extensively used in the inner tube (IIR) of tube-type tires and in the inner liner (XIIR) in tubeless tires [2]. The tire industries use approximately $1 billion of butyl rubber just to retain air. There are also some other elastomers, which are not used in the tire industries, but have very good and even better air retention properties, for example, epichlorohydrin

Rubber Nanocomposites: Preparation, Properties and Applications Edited by Sabu Thomas and Ranimol Stephen
© 2010 John Wiley & Sons (Asia) Pte Ltd

rubber (ECO), polysulfide rubber (TM) and polyurethane rubber (AU). Other elastomers like nitrile rubber (NBR) and ethylene/acrylate copolymers (EAM) provide moderate air retention properties. Barrier properties are important for sports balls for feel and bounce due to air retention. Barrier properties are also utilized in chemical protective gloves to protect against chemical warfare agents.

In flexible polymer like elastomers the polymer chains above the glass transition temperature allow microBrownian movement of chain links through various degrees of freedom. Under this condition, the penetrant can diffuse easily through the polymer. Crystalline polymers show impermeability to many liquids and gases due to orderly arrangement of molecular chain and thus prevent the penetration of small molecules. Increased molecular orientation also reduces permeability by making the transportation of permeant more difficult. Improved packing order and increased crystallinity of the barrier material increases its density and, again, decreases permeability. Similarly, crosslinking also prevents the free flow of permeant through the network structure. Physical interaction between penetrant and barrier material such as the formation of hydrogen bonds or the interaction between polar and functional groups may slow down the permeation [3].

It is well known that the barrier properties of a polymer can be improved by the addition of impermeable plate-like structures [4]. When the plates are oriented perpendicular to the diffusion (permeation) direction, the diffusing molecules must go around the plates. This leads to significant reductions in the permeability of the polymer inner tube. The nanocomposite technology can penetrate the automobile sectors especially pneumatic tire, as barrier enhancement is important for air retention in tires. Using butyl as elastomer and clay as filler with high aspect ratio, the air retention properties can be improved to a level 50 times better than that of normal butyl compound.

Improving the performance of polymer products by incorporation inorganic fillers has long been practiced. Elastomers are often reinforced with particulate fillers such as carbon blacks, clays, talc and silica to obtain the desired mechanical, thermal and chemical properties [5]. However, there are many disadvantageous side effects of conventional fillers as these fillers bring down important properties at higher loadings. It is well known that the reinforcing ability of filler is depended on its shape, particle size, particle size distribution and interfacial adhesion [6]. Generally, the presence of active functional groups, surface free energy and energetically different crystallite faces of the filler surfaces influences the interaction between polymer and filler [7]. Recently, the modification of polymer composites using nanosize fillers having a high surface to volumetric ratio has become an attractive method for the development of many industrial products. The use of nanoparticles to alter permeation properties extends beyond reducing permeability with increasing filler content. Nanocomposite improves barrier to gases, such as air, oxygen, carbon dioxide and so on [8]. It also helps to protect migration of moisture and odour. Greater barrier also impedes absorption of flavors and vitamins by the plastic packaging itself.

Outstanding properties of nanocomposites system may arise from large interfacial area per unit volume between the constituent materials at the interface [9]. The interface controls the degree of interaction between different phases thus controlling the overall properties. If the nanocomposites are produced from organic polymers and nanoscale fillers having a high aspect ratio, the increase in the surface area of nanoscale fillers results in a high degree of interfacial interaction, leading to overall improvement in the properties. Thus the greatest challenge in developing polymer nanocomposites lies in managing the interfacial interaction. The interfacial region may be characterized by chemical, structural and molecular environments. The size

of the interface has been reported in the range of 2–50 nm. Additionally the property enhancement is influenced by processing methods that lead to the control of dispersion and distribution of particles of nanoscale dimensions [10].

Many types of nanofiller are currently available and, among these, carbon nanotubes are the most promising, in terms of high performance [11–13], while layered silicates are the most common and established [14–16]. Siliceous filler having a particle size in the range 10–20 nm is a reinforcing particulate filler which finds applications in the polymer industry as dental filling, electronic packaging, thickener for paints and coatings and as a reinforcement for silicones, PVC and many other rubbers [17]. Similarly rod-shaped nanofillers with a high aspect ratio such as cellulose whisker with 18×9 lateral dimensions and an aspect ratio of around 100 nm has been used as reinforcing filler in PP, epoxy and plasticized PVC [18–20].

The focus of this chapter is on the barrier properties of rubber nanocomposites. Recent advances in theoretical and experimental works for the barrier properties are reviewed along with their potential applications.

18.2 Theoretical Consideration

18.2.1 Fundamental Permeation Theories

The barrier properties of a polymeric material refer to its abilities to impede the transportation of small molecules through it. When a polymer is subjected to a high concentration gradient of permeant, the permeant passes through the polymer by several processes, as illustrated in Figure 18.1.

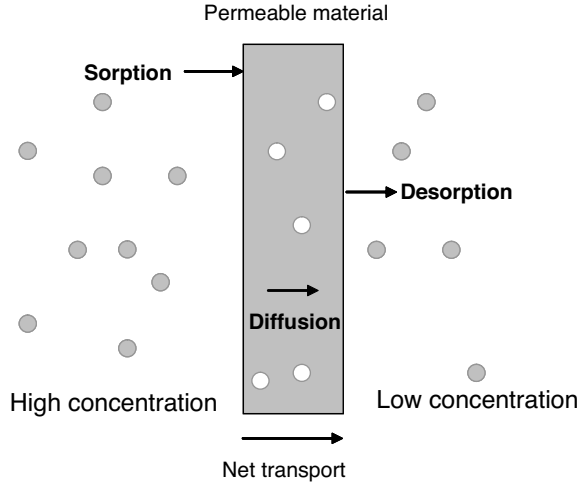

Figure 18.1 Permeation of a substance through a polymeric material

The diffusion of small molecules into polymers is a function of nature of both the polymer and the permeant. There are many factors which influence diffusion process such as the molecular size [21] and physical state of the permeant [22], the morphology of the

polymer [23], the compatibility or solubility limit of the solute within the polymer matrix [24], and the surface or interfacial energies of the monolayer films [21–24]. Additionally, external forces (temperature, pressure, concentration, relative humidity, and so on) also contribute to the diffusion process. In most diffusion processes, permeants plasticize the polymer during the permeation, thereby increasing the chain mobility, leading to stress relaxation, shrinkage, phase ripening and so on [25].

The description of gas/liquid transport across nonporous polymers under the influence of the applied driving force is based on a variety of solution–diffusion models which contain a large number of equilibrium and diffusive parameters [26, 27]. The relative sorption and diffusion rates of gases then lead to separation of the gas mixture. The diffusion of low molecular weight penetrant of varying sizes through the polymeric film or membrane has been extensively studied [27]. A knowledge of thermodynamics and kinetic properties of the gas/liquid-polymer system and experimental study of gas transport through various polymers is an essential requirement for developing suitable models to describe the transport phenomena. The evaluation of the model parameters and discrimination between the various models of membrane transport requires a substantial amount of experimental data, which is not normally available. The model parameters are also often highly system-specific and small changes in the polymer material can cause radical changes in the solubility and/or diffusivity of the permeating species.

Two important parameters used to describe the permeation process, namely the solubility S, which gives the total amount of gas trapped in the membrane, and the diffusion coefficient D of a gas molecule inside the network. For steady-state permeation of simple gases into a homogeneous polymer film, the permeability coefficient (P), a direct measure of the efficiency of the permeation process, is obtained from the product of the solubility and diffusion coefficient [28]

$$P = DS \tag{18.1}$$

The permeation of small molecules through rubbery polymer becomes easier due to higher segmental mobility of the polymer chains and presence of more free volume. The diffusion behavior in the rubbery polymers, represented by permeation, migration and sorption processes, can be described by Fick's laws as given by the equation [29]:

$$J = -D\frac{\partial \phi}{\partial x} \tag{18.2}$$

where J is the flux density of the solute molecules through the membrane, D is the gas diffusion coefficient, $\partial\phi/\partial x$ is the concentration gradient applied across the membrane and ϕ is the concentration of the dissolved gas given as the amount of gas per cubic centimeter of membrane.

In nonsteady or continually changing state diffusion, that is, when the concentration within the diffusion volume changes with respect to time in one direction, Fick's second law of diffusion is given as:

$$\frac{\partial \phi}{\partial t} = -D\frac{\partial^2 \phi}{\partial x^2} \tag{18.3}$$

18.2.2 *Diffusion through Polymer Membrane Filled with Particulate and Layered Fillers*

Polymer film containing aligned flakes or layered fillers show less permeability. The permeability changes with the volume fraction of flakes ϕ and the aspect ratio of the flakes α. This aspect ratio is defined as the intermediate dimension divided by the smallest dimension. Considering the case where the volume fraction of filler is much less than one, often called the dilute limit, the product of concentration and shape, $\phi\alpha$ is also less than one. So, the permeability does not change much. However if the volume fraction of flakes are considerably high (semi-dilute limit), ϕ is much less than one but $\phi\alpha$ is much greater than one. In this case, the permeability of the barrier is dramatically changed. Changes in diffusivity and permeability of nanocomposites with clay content are conventionally explained within the concept of tortuous paths [30]. According to this approach, the path that a small molecule of a penetrant must travel in a polymeric matrix substantially increases in the presence of intercalated and/or exfoliated clay layers (that possess aspect ratios of order of 10^3). This results in a noticeable decrease in the coefficient of diffusion. According to the Nielsen equation [30], the tortuosity factor, defined as the ratio of diffusivity of a composite to that of the pristine polymer, is inversely proportional to a linear function of the volume fraction of filler. The industrial and scientific prospects of using layered mineral filler in polymeric composites is well appreciated and has received much attention recently [31, 32]. Polymer-layered silicate clay nanocomposites containing a small fraction of organically modified layered silicate exhibited reduction in the permeability of small gases, for example, O_2, H_2O, He, CO and ethyl acetate vapors [13]. The clay layers confine the polymer chains around their surrounding through clay-polymer interaction, thus hindering the relaxation of polymer chains, which in turn, reduces the diffusion of small molecules through the nanocomposite. The spherical inorganic particulate fillers such as fumed silica are also considered impenetrable by gas molecules. Hence, the addition of inorganic fillers in the polymer matrix can enhance the barrier properties by forcing the permeant molecules to follow a more tortuous path as they diffuse through the material, slowing down the progress of the phenomenon.

Gas barrier in polymer clay nanocomposites was conventionally explained by the most popular theory originally proposed by Nielsen to describe the tortuosity effect of plate-like particulates on the gas permeability of filled polymer composite structures [30]. In this model, the particles are assumed to be spherical impermeable to a diffusing gas or liquid and are homogeneously dispersed in the polymer matrix. The impermeable nature of filler particles creates a long path for the diffusing molecule by directing them around the particle, leading to an increase in barrier properties. The Nielsen model can be used to determine the effect of filler composition on gas permeability in the model system consisting of uniform platelets homogeneously dispersed in the polymer matrix and oriented parallel to the polymer film surface. A schematic representation of diffusion of permeant is given in Figure 18.2. Parallel platelet orientation presumably gives a better gas barrier performance as compared to random platelet orientation. The general relationship correlating the particle nature and impermeability is given as:

$$P_f = \frac{\phi_p}{\tau} P_u = \frac{1-\phi_f}{\tau} P_u \tag{18.4}$$

where P_f and P_u are the permeabilities of filled and unfilled polymer, respectively, ϕ_p and ϕ_f are volume fraction of polymer and filler respectively and τ is the tortuosity factor.

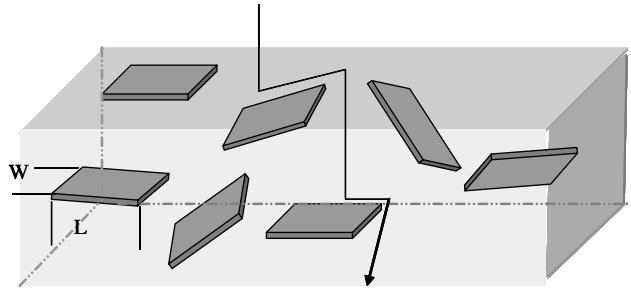

Figure 18.2 Schematic representation of permeant path diffusing through a plate-like particle-filled polymer

The tortuosity factor is defined as the distance that the molecule must travel through the film divided by the thickness of the film. The tortuosity factor, τ, also related to the ratio of diffusivity of a composite to that of the pristine polymer, is inversely proportional to a linear function of the volume fraction of filler. The tortuosity factor is further defined by two other conditions. The first condition requires that the particles are parallel with the surface of the film, while the second condition requires that the particles are perpendicular to the film surface. The tortuosity factor, τ, defined as the ratio of actual distance d' to shortest distance d, is given by:

$$\tau = \frac{d'}{d} = 1 + \left(\frac{L}{2W}\right)\phi_f \tag{18.5}$$

Thus, the relative permeability k, with and without the addition of clay fillers in a polymeric matrix, can be expressed as:

$$k = \frac{k_c}{k_p} = \frac{1-\phi}{\tau} = \left(1 + \frac{L}{2W}\phi\right)^{-1} \tag{18.6}$$

where k_c is the permeability coefficient of gas/liquid molecules in a filled composite and k_p is the permeability coefficient of a polymeric matrix.

However, in the nanocomposite, the clay platelets are randomly oriented and those plates, which are oriented at 90° offer no barrier to the permeant. Thus, the relative permeability may be modified by including the orientation parameter, S:

$$S = \frac{1}{2}(3\cos^2\theta - 1) \tag{18.7}$$

where θ is a range of relative orientations of the plate like filler with respect to each other. Thus the relative permeabilities for nanocomposite is given by:

$$k = \left[1 + \frac{2S+1}{6}\frac{L}{W}\phi\right]^{-1} \tag{18.8}$$

where L and W are the length and width of a particle, respectively (Figure 18.2). The aspect ratio, α, represented as the ratio of width to length (W/L). The effective permeability due to the increased tortuous path length that a molecule must traverse depends on two variables: The

volume fraction of the flakes and the aspect ratio. As the aspect ratio for a flake increases, a permeant such as oxygen experiences a large increase in effective path length. This greatly reduces the rate of movement across the barrier layer. The Nielsen model was recently used to fit experimental data for polyimide–clay [33–36], polyester–clay [37] and nitrile rubber–clay nanocomposites [38].

Xu *et al.* [39] compared the experimental and theoretical values of relative water vapor permeability of poly(urethane urea)/organically modified layered silicate(PUU/OMS) nanocomposites having aspect ratios of 300 and 1000 at different volume fractions of clay (Figure 18.3). It is obvious that the predictions based on these models indicate that Equation 18.6 fits the data somewhat better than Equation 18.8, which as expected, overestimates the barrier properties of nanocomposites. There seems to be a transition of effective aspect ratios from exfoliated platelets ($L/W = 1000$) to intercalated multilayer stacks ($L/W = 300$).

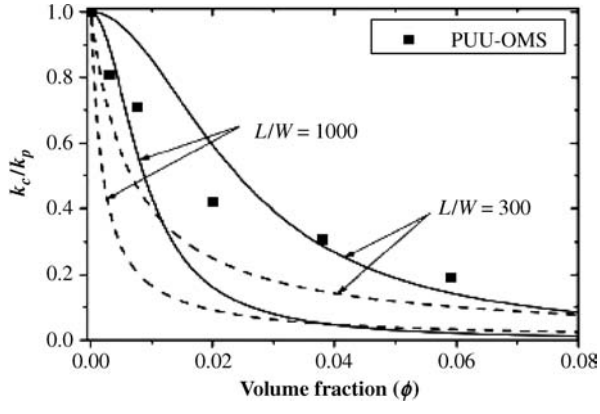

Figure 18.3 Relative water permeability in poly(urethane urea)/organically modified layered silicates (PUU/OMS) nanocomposites (Reprinted with permission from R. Xu, E. Manis, A.J. Snyder and J. Runt, "New Biomedical Poly(urethane urea)-Layered Silicate," *Macromolecules*, **34**, no. 2337, 2001. © 2001 American Chemical Society.)

Under the condition of partial solubility of diffusing molecules in the polymer matrix due to sorption, Nielsen modified the above equation to calculate permeability for the system in which there will be a concentration fluctuation of diffusing species in the matrix and at the polymer filler interface. The difference in the properties of bulk polymer saturated with sorbed molecules and the interfacial layer formed at the filler–polymer interface is given in the form of an equation explaining the total permeability at the bulk and at the interface:

$$\frac{P_f}{P_u} = \frac{P}{P_u\phi^n + P_i(1-\phi^n)}\left(\frac{\phi_i}{\tau^0}\right) + \left(\frac{\phi_p + \phi_l}{\tau}\right) \tag{18.9}$$

P_f, P_u, P_i are the permeabilities of permeant through the filled polymer, the unfilled polymer and the interfacial region, respectively. ϕ_f, ϕ_i, ϕ_p and ϕ_l are the volume fraction of the filler, the liquid collected in the interfacial region in the dry polymer and the liquid dissolved in the bulk

polymer, respectively. τ and τ^0 represent the tortuosity factor for the bulk and the interfacial part, respectively. The constant, n denotes the fractional length of the average diffusional path that crosses the polymer depended upon particle shape and orientation, aggregation of filler particles and so on. Beall [40] proposed a simplified model considering the confinement of polymer chains around the nanoparticles in the interfacial region. The characteristics of confined polymer region depend upon many factors including the nature and shape of nanoparticles and the polymer characteristics. Beall model can explain the relative permeability of different permeant through nanocomposite containing different organic modifier as the model envisage the presence of three different regions at the polymer–filler interface which help in stabilizing the interface through compatibilization.

Bharadwaj [41] proposed a model to explain the permeability of nanocomposites containing randomly oriented plate-like filler. The model is developed by including orientation parameter, S in the Nielsen model:

$$\frac{P_f}{P_u} = \frac{1-\phi_f}{1+\frac{2\tau}{3}\left(S+\frac{1}{2}\right)} \tag{18.10}$$

In the case of random platelet orientation ($S = 0$), the tortuosity decreases with orientation and diffusion is facilitated as opposed to parallel orientation ($S = 1$ or Nielsen model). If the majority of the clay layers appear to be oriented in the same direction (parallel to the membrane surface and perpendicular to the gas flow), rather than randomly oriented, this model fails to describe gas transport thorough the nanocomposites as it does not consider the influence of tortuosity (Figure 18.4).

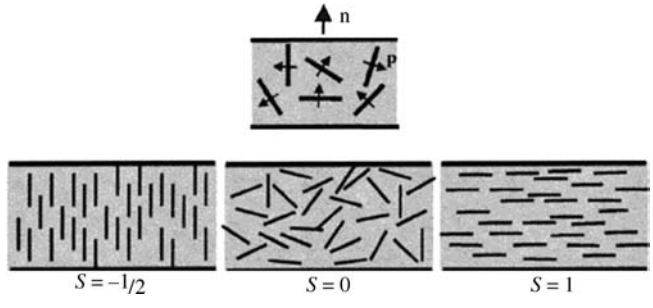

Figure 18.4 Effect of sheet orientation on the relative permeability in exfoliated nanocomposites (**n**) of the silicate sheet normals (Reprinted with permission from R.K. Bharadwaj, "Modelling the Barrier Properties of Polymer-Layered Silicate Nanocomposites," *Macromolecules*, **34**, no. 26, 2289, 2001. © 2001 American Chemical Society.)

Cussler *et al.* developed a model [33, 42, 43] with focus on the diffusion of a small gas molecule through a matrix filled with impermeable flakes oriented perpendicular to the direction of diffusion and having high aspect ratio. This condition leads essentially two-dimensional diffusion. The diffusion is mainly related to three factors: (i) the tortuous wiggles

to get around the flakes, (ii) the tight slits between the flakes and (iii) the resistance of going from the wiggle to the slit.

$$\frac{D_c}{D_0} = \frac{1-\phi_f}{(1-\phi_f)+(\tau-1)^2} = \left(1+\frac{\alpha^2\phi_f^2}{1-\phi_f}\right)^{-1} \tag{18.11}$$

where D_c and D_0 are the diffusion coefficients of the composites and pure polymer, respectively. α is the particle aspect ratio. It was found that the calculated aspect ratio of filler (α) by substituting the experimental permeability values in the above model is lower than the one obtained from the transmission electron microscope. Therefore, Cussler *et al.* modified the model by incorporating a geometric factor (μ) in the previous equation to obtain an actual aspect ratio for the filler:

$$\frac{D_c}{D_o} = \left(1+\mu\frac{\alpha^2\phi_f^2}{1-\phi_f}\right)^{-1} \tag{18.12}$$

μ depends on the distribution of the plate-like material. In either case, the higher the aspect ratio of the filler, the larger is the decrease in permeability. A permeability model can be obtained by multiplying the diffusion by the appropriate solubility. Since the model assumes linear relationship between solubility of filled composites and volume fraction, $S = S_0(1-\phi_f)$, where S is the solubility of the filled composites and S_0 is the solubility of pure polymer. The permeability is expressed as:

$$\frac{P_f}{P_u} = \frac{(1-\phi_f)^2}{(1-\phi_f)+\alpha^2\phi_f^2} \tag{18.13}$$

Aries [45] proposed another model by taking into account the resistance to diffusion in the slits between adjacent flakes in the same horizontal plane:

$$\frac{D_f}{D_u} = 1+\frac{\phi_f^2\alpha^2}{(1-\phi_f)}+\frac{\phi_f\alpha}{\sigma}+\frac{4\phi_f\alpha}{\pi(1-\phi_f)}\ln\left(\frac{\pi\phi_f\alpha^2}{\sigma(1-\phi_f)}\right) \tag{18.14}$$

where σ is the slit shape factor (the ratio between slit width and slit thickness). The first two terms on the right hand side equation are similar to Equation 18.7 and the remaining third and fourth terms are new. The second term, involving α^2, is the resistance to diffusion of the tortuous path around the flakes. It is called "wiggle." This wiggling is the chief contribution to the increased resistance in flake-filled barrier membranes. The third term represents the resistance to diffusion of the slits between adjacent flakes in the same horizontal plane. The fourth term represents the constriction of the solute to pass into and out of the narrow slits. This constriction would represent an additional resistance to diffusion, even when the slit length was extremely short. The result for flakes given by Cussel and Aries models is supported by some experimental results from membrane studies [45–47] and some analytical simulation studies using Monte Carlo simulation [48]. However, a comparison of simulation results with the predictions using Equation 18.6 shows that the Aries model overpredicts the effective diffusion coefficient, especially if compared to the 3D simulation.

Yano *et al.* [36] compared filler aspect ratio with the permeability on clay-filled polyimide containing four different sizes of clay minerals such as hectorite, saponite, montmorillonite and

synthetic mica. The influence of length of clay platelets on permeability is represented in Figure 18.5. They found at constant clay content (2 wt%) that the relative permeability coefficient decreases on increasing the length (related to aspect ratio) of the clay.

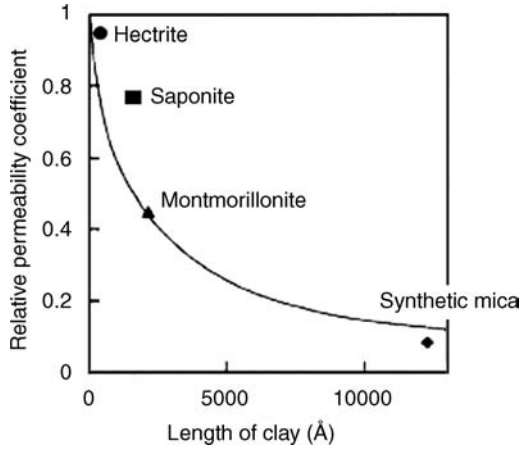

Figure 18.5 Dependency of clay length on relative permeability coefficient. Aspect ratios: hectorite= 50, saponite = 170, montmorillonite = 220, synthetic mica = 1230 (Reprinted from K. Yano, A. Uski and A. Okada, "Synthesis and properties of polyimide-clay hybrid films," *Journal of Polymer Science: Part A, Polymer Chemistry*, **35**, no. 11, 2289, © 1997, with the permission of John Wiley & Sons, Inc.)

Gusev and Lusti [49] developed another model by performing a series of finite-element analyses of a random dispersion of nonoverlapping impermeable round platelets for a number of values of α and ϕ. They found that the results in the form of P_0/P could be represented by the stretched exponential function:

$$\frac{P_f}{P_u} = \frac{\left(1 + \frac{\alpha\phi_f}{3}\right)^2}{(1-\phi_f)} \tag{18.15}$$

Fredrickson [50] developed permeability model for transport properties of dilute and semi-dilute particle dispersions having disk-shaped particles based on multiple scattering expansion. The dilute regime resembles Nielsen model and accounts for low filler content. Fredrickson modified Nielsen model by adding a geometric factor, $K = \pi/\ln\alpha$, into the equation and expressed relationship with diffusion coefficient, D:

$$\frac{D_f}{D_u} = \frac{1}{1 + K\alpha\phi_f} \tag{18.16}$$

Since the volume fraction of filler applied is small (less than 0.1) and thus the solubility can be assumed constant. For the semi-dilute regime, the filler content has increased from the dilute regime, and the system resembles Cussler model. However, Fredrickson model calculates the filler's aspect ratio higher than one predicted by Cussler model.

Meneghetti *et al.* [44] compared the suitability of different models in predicting the aspect ratio of the clay filler from the permeability measurement of SBR/O-MMT nanocomposites at different volume fraction of O-MMT. They used two organic modifiers, viz. octadecyldimethylbetaine (C18DMB) and vinylbenzyl-octadecyldimethylammonium chloride (VODAC) in their study. Figure 18.6 shows the comparison of aspect ratios of O-MMT obtained from various models. The modified Cussler model gives a much higher aspect ratio than the original Cussler model. Fredrickson model curves appear very similar to Nielsen model, and they give the same aspect ratio. The original Nielsen and the modified Nielsen models are very similar to each other, except that the aspect ratio is slightly higher for the modified model. The original Nielsen model gives the closest value of aspect ratio as observed with TEM.

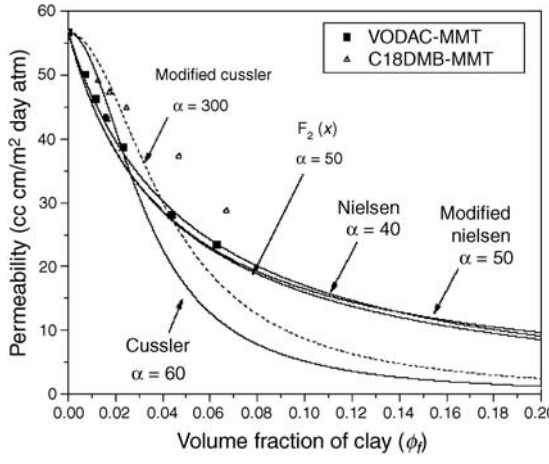

Figure 18.6 Permeability data at different volume fraction of filler and comparison of model fitting (Reprinted with permission from P.C. Meneghetti, "Synthesis and properties of rubber-clay nanocomposites (Figure 4.5)," in PhD Thesis, Case Western Reserve University, 107, © 2005.)

A constitutive equation for the moisture diffusion for an intercalated vinyl ester resin-montmorillonite clay nanocomposite was developed by Drozdov *et al.* [51]. The observed diffusion tests showed that the moisture diffusion in the neat resin is Fickian, whereas it becomes noticeably anomalous (nonFickian) with increasing clay content. This transition is attributed to immobilization of the penetrant molecules on hydrophilic surfaces of clay layers. Fair agreement is demonstrated between the observations and the results obtained from numerical simulation. The moisture uptake by the host matrix increases on increasing the clay content. With reference to the free-volume concept, this observation is explained by the clustering of water molecules in the close vicinity of stacks of platelets, where diffusivity dramatically falls down.

Recently, a model for predicting effective diffusivity in heterogeneous systems with dispersed impermeable domains of variable orientation and distribution was developed by Sorrentino *et al.* [52]. The model is taking into account the formation of an interface region between the polymer bulk and the clay sheets that can influence the barrier properties.

The model also considers the tortuous path way of permeant. The relative diffusivity is given by:

$$\frac{D_f}{D_u} = \frac{(1-\beta\phi_f)}{(1-\phi_f)+\phi_f\left(1+\dfrac{L+2t}{L\sin\theta+2t\cos\theta}\right)^2} \tag{18.17}$$

where θ represents the orientation angle and β is a fitting parameter representing the ratio between the interface diffusivity and the bulk polymer diffusivity.

18.3 Experimental Studies

Research on new materials technology is attracting the attention of studies all over the world. Developments are being made to improve the properties of the materials and also to find alternative precursors that can bestow desirable properties on materials. Great interest has recently been developed in the area of nanostructured reinforcing materials. Reinforcement is especially important for the application of elastomeric materials because the mechanical strength of unfilled elastomers is generally poor. Commonly, isometric fillers like carbon black or fumed silica are used for reinforcing elastomers. New kinds of fillers such as nanoparticles and nanofibers have also been studied and were found to improve the properties of the composites. Commonly used nanoparticles are multiwalled carbon nanotubes (MWNTs), single-walled carbon nanotubes (SWNTs), buckminsterfullerene, carbon nanofibers (CNFs), montmorillonite (MMT) nanoclays, polyhedral oligomeric silsesquioxanes (POSS), nano silica, Al_2O_3, TiO_2 and so on. Rapid advancement in the polymer/nanoparticle nanocomposite technology in the past 15 years have demonstrated a doubling of the tensile modulus and strength without sacrificing impact resistance for numerous thermoplastic (nylon and thermoplastic olefin TPO) and thermosets (urethane, siloxane and epoxy) resins through the addition of as little as 2 vol% nanoparticles. Additionally, reduced thermal expansivity, matrix swellability, gaseous permeability and flammability upon 1–5 vol% addition of nanoparticle will provide new opportunities for various resin systems. Recently, a more efficient approach for reducing the permeability of elastomers has received widespread attention. The permeability of rubber-like substances to gases stands in relation to the solubility and rate of diffusion of the gases in those materials. The differences in permeability of the same elastomer to different gases are caused not only by differences in rate of diffusion but also by differences in solubility. As soon as a fluid is in contact with the surface of an elastomer for a sufficient time, gases and liquids can dissolve into the elastomer and move further by diffusion. These solution and transport processes may cause modifications of the physical properties of the elastomer, which often leads to a decrease in barrier properties. The presence of polar groups in an elastomer reduces the solubility of nonpolar penetrant and increases the solubility of polar gases in the elastomers [53]. It was shown that the chemical structure of the rubber molecules affects the rate of diffusion of gas passing through a series of rubber materials. Moreover, the strain induced crystallization of rubber reduces the rate of diffusion. It is also found that the gas diffusion is related to its molecular size; that is, the bigger the gas molecule, the slower the diffusion. The solubility of the gas in the rubber is determined by its tendency to condense and by the interaction between the rubber and the gas molecules. In the case of permeant gases such as nitrogen, oxygen and hydrogen, the permeability depends on the nature of gas, the membrane

material, temperature and pressure. Inclusion of filler in the elastomeric matrix hinders the transport of fluid by directing the permeant to follow tortuous path. Fillers in general and carbon black in particular are much less permeable than even relatively impermeable elastomers such as the halo butyls currently used in most tire inner liners. Therefore, higher filler loadings in elastomeric components designed to minimize permeability of moisture and gases should lead to a reduction in permeability. However, high loading of fillers may reduce the processability of the rubber compounds and cause the end products to weigh significantly more than the neat rubber, and thus limit their application in some industries. It is expected that dispersing nanoparticles in rubber matrix should effectively reduce the gas permeability.

Engineering products such as tire inner tubes, air springs, cure bladders and so on demand a high barrier to gas permeation. Isobutylene-isoprene rubber (IIR, butyl rubber) has the outstanding gas barrier property among hydrocarbon elastomers. Similarly, the air permeability of styrene-butadiene rubber (SBR) at 65 °C is about 80% that of natural rubber (NR) while butyl rubber shows only 10% permeability on the same scale. Isobutylene-based polymers; particularly halogenated isobutylenes such as chloro- and bromobutyl rubber are the preferred material for tire liners, heat resistant tubes, bladders and pharmaceutical ware due to very high impermeability to gases. Isobutylene have also been blended with numerous compositions such as NR in order to increase its various properties, such as elasticity, strength, air impermeability and so on. Moreover, these elastomers have been functionalized in order to improve compatibility or crosslinkability with other polymers to achieve improved air barrier properties.

A review on selective transport of gases through polymeric membranes has been carried out by Aithel *et al.* [53]. Further extensive studies on permeability of various gases through different elastomers are reported by van Amerogen [54, 55]. Johnson *et al.* [56] investigated the nitrogen and oxygen gas transport properties of natural rubber, epoxidized natural rubber (ENR) and their blends. The permeability of the pure polymers and blends was determined and correlated for oxygen-to-nitrogen selectivity with glass transition temperature. They reported that NR is more permeable to nitrogen and oxygen. In contrast, ENR shows maximum oxygen-to-nitrogen selectivity. In NR/ENR blends, permeability of the penetrant decreases with increasing the volume fraction of ENR in the blend, whereas selectivity increases with volume fraction of ENR

Several studies were realized on the gas barrier properties on rubber–inorganic filler nanocomposites. Many of them are specifically devoted to layered clay-filled rubber systems [38, 57–70]. The variation in gas barrier properties was studied with respect to type and amount of filler, type of polymer matrix and other preparation conditions. The influence of filler particle shape, their aspect ratio, extent of intercalation and/or exfoliation on permeability of gases or liquids was extensively studied. A few others reported the suitability of barrier models for nanocomposites by comparing the experimentally obtained data with the values obtained from models. In many cases there is a broad agreement between the two data validating the models.

Wang *et al.* [57] reported the permeability of the nitrogen gas through pristine NR and its nanocomposites filled with different rectorite contents and measured the nitrogen flux for different time periods (Figure 18.7). According to them, the rectorite content in NR exerted a strong effect on both non-steady state and steady state fluxes of N_2 through the nanocomposites. With the increase of rectorite content, the non-steady state region of flux curve broadens (slower diffusion) and steady-state flux decreases (lower permeability). Further, the permeability of the nanocomposites rapidly decreased with the increase of rectorite content with 50% reduction in permeability for the nanocomposite with 7% rectorite.

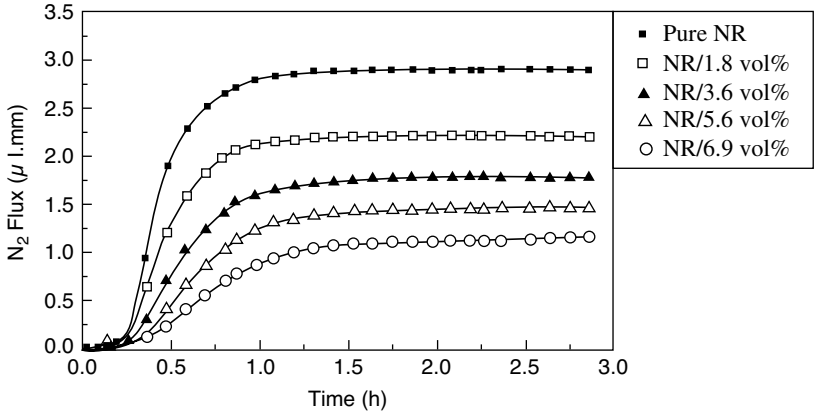

Figure 18.7 Variation of nitrogen gas flux with time for pure NR and its nanocomposites containing different rectorite loading (Reprinted from *European Polymer Journal*, **41**, no. 11, Y. Wang, H. Zhang, Y. Wu, J. Yang and L. Zhang, "Preparation and properties of natural rubber/rectorite composites," 2776, © 2005, with permission from Elsevier.)

Varghese *et al.* [58] reported the swelling behavior of NR nanocomposite obtained from different clay materials in toluene. A plot was drawn by plotting the sorption verses time for different nanocomposite vulcanizates. The amount of toluene absorption at equilibrium swelling is less for the composites containing layered silicate, especially fluorohectorite, compared to that containing commercial clay. The sorption curves of the composites also show the difference in the initial rates of diffusion which is the fastest for gum followed by commercial clay-filled rubber, as shown in Figure 18.8. The relatively lower rates of diffusion at the beginning of the sorption curve for the compounds with layered silicates are due to the strong interface and also due to the orientation of the layers. The authors compared the relative permeability of gum and filled NR. The relative permeability decreases in the order commercial clay (55%) > bentonite (35%) > fluorohectorite (5%).

Stephen *et al.* [59] described the transport properties of nanocomposites derived from the latex blending of natural rubber, carboxylated styrene butadiene rubber and their 70/30 blends with sodium bentonite clay. These layered silicates reinforced rubbers were investigated for permeability using benzene, toluene and *p*-xylene. The nanocomposites displays reduced absorption rate due to increased polymer/filler interaction, which in turn increased the tortuosity of path of the permeant. The diffusion coefficient of layered clay filled rubber decreases as a function of clay loading. The calculated activation energy of diffusion of permeant is found to be higher than that of pristine rubbers. The correlation between the size of penetrant and the permeability shows the inverse relation with increasing the size of the permeant molecule increased, the solvent uptake of nanocomposites decreases in the order benzene > toluene > *p*-xylene. The O_2 and N_2 gas transport properties of nano- and microcomposites latex membranes of NR, XSBR and their blend were investigated [60]. The nanocomposites exhibited lower permeability to oxygen and nitrogen gases due to the enhanced polymer/filler interaction. The gas permeability coefficients have been correlated with type of filler, penetrant gases, filler loading and gas pressure. A comparison between the permeability of layered silicate clays such as sodium bentonite and sodium fluorohectorite and

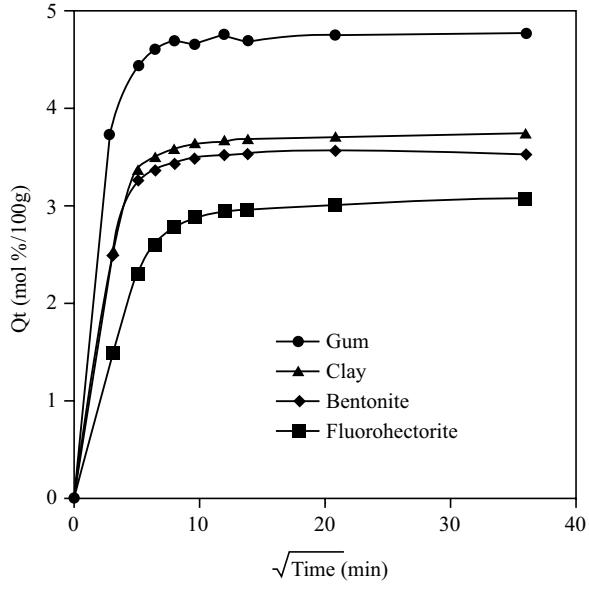

Figure 18.8 Sorption curves for gum and clay-filled NR nanocomposites (Reprinted from *Polymer*, **44**, no. 17, S. Varghese and J. Karger-Kocsis, "Natural rubber based nanocomposites by latex compounding with layered silicates," 4921, © 2003, with permission from Elsevier.)

conventional microfillers such as commercial clay and silica shows the improvement in barrier properties of the nanocomposites. The improvement in gas barrier properties is explained based on the free volume theory. The effect of free volume on the gas barrier properties was investigated by positron annihilation lifetime spectroscopy. It is observed that, due to the presence of platelet-like morphology and high aspect ratio of layered silicates, the gas barrier properties of nanofiller-reinforced latex membranes are remarkably high. The correlation of crosslink density and extent of reinforcement with the gas barrier properties shows an enhancement in barrier properties.

Knite *et al.* [61] discussed the influence of carbon nanotube on the sensing capabilities of polyisoprene rubber for various organic solvent vapors through electrical resistance. They put forward the explanation of the vapors sensing effect. The matrix of polymer soaks up the solvent molecules (solvent molecules are absorbed) and carbon nanoparticles are separated from each other. As a result, the tunneling current between nanoparticles in thin layers of the matrix decreases. During relaxation in air, the change of the sample resistance is thought to follow three processes: (i) diffusion of solvent molecules from internal layers of the matrix to the surface, (ii) relaxation of cross-section connections of the polymer and (iii) relaxation of a volumetric lattice of the electroconductive carbon nanoparticles.

Lu *et al.* [62] prepared various rubber/organoclay nanocomposites from ethylene-propylene diene rubber (EPDM), styrene butadiene rubber (SBR) and epichlorohydrin rubber (ECO). They compared the relative N_2 gas permeability as a function of organo-modified clay content. The gas permeability of the nanocomposites steadily reduces with increasing clay content. The highly filled nanocomposites (with 60 wt% nanoclay) exhibits excellent gas barrier properties

with a reduction of 72∼88% in gas permeability compared to pristine rubbers. They also correlated the experimental values with the models developed by Nielsen, Lu and Mai and Bharadwaj. It is seen from comparison that the filler aspect ratio in rubber nanocomposites increases with organoclay content. However, they were unable to find the real percolation threshold due the presence of interaction between intercalated silicate particles to form a flocculated–intercalated structure with increased aspect ratios at a high clay loading. On the other hand at low clay content the gas molecules mostly prefer to travel through the gap between intercalated structures rather than the intra-galleries between silicate layers. They also observed that ECO nanocomposite showed the most reduced gas permeability.

The gas permeabilities of NBR, NBR/clay nanocomposites and NBR/silica composite showed the reduction in nitrogen permeability with an increase in the amount of filler [63]. Among all filled NBRs, the NBR/clay nanocomposites showed a better gas barrier property than did the NBR filled with the same amounts of silica. This can be attributed to the impermeable filler phase and the large aspect ratio of the silicate layers. Compared with the gum NBR vulcanizate, the nitrogen permeability of the NBR–clay nanocomposites with 10, 20 and 30 phr of clay was reduced by 29%, 41% and 48%, respectively. Similarly, the permeabilities of hydrogen and water vapor through NBR nanocomposite are about 70% those in NBR [64].

Silicone elastomers are important materials for many application areas such as automotive, electric and electronics, gaskets, domestic appliances, fabric coatings (for example, airbags), baby bottle teats, medical devices and in cosmetic applications. Silicone rubbers are one of the most permeable elastomers and have up to 400 times the permeability of butyl rubber at room temperature due to low intermolecular forces and relatively unhindered single bonds. It results in a higher than normal amount of free volume and a high degree of chain mobility. Lebaron [65] reported that insignificant improvement in the barrier properties of silicone/clay nanocomposite even though the tensile and solvent resistance properties of a silicone rubber are greatly enhanced through clay nanolayer reinforcement. Even at an organoclay loading of 8.0 wt%, the oxygen permeability is only reduced by 25%. A thick constrained polymer region can also reduce the permeability by decreasing both the diffusion rate and the solubility of the permeant. Although synthetic fluorohectorite has one of highest nanolayer aspect ratios among smectite clays, it has not been effective in providing substantial reduction in gas permeability of silicone elastomers. This suggests that the nanolayers are not well aligned or that the constrained polymer region is relatively thin. Under the conditions used to form sufficiently thick samples for the permeability measurements, the surface tension forces are too weak to facilitate nanolayer ordering parallel to the sample surface.

Using butyl rubber as matrix and clay as filler with high aspect ratio, the air retention properties could be improved to the level of 50 times better than that of normal butyl compound. Using such filler, therefore, the inner gage of a tubeless tire or the gage of an inner tube could be reduced for identical conditions of service. With carbon black as filler, the passage of air is faster because of spherical nature of the filler. With needle-shaped filler in a nanocomposite, the same air will take a longer time to travel due to the flat shape of the filler. Takahashi *et al.* [66] reported the gas permeation properties of butyl rubber based nanocomposites with 20 and 30 wt% loadings of vermiculite filler. The gas permeability is reduced 20 to 30-fold by the incorporation of vermiculite. The experimental data on diffusion coefficients computed from time lag data for various models for composites containing flake-like fillers were reduced by two orders of magnitude. Liang *et al.* [67] compared the gas barrier properties of butyl rubber/layered clay nanocomposites prepared through melt and solution intercalation process. Both

these methods of preparation showed considerable improvement in impermeability of nanocomposites. The solution method was comparatively effective in improving the nitrogen gas barrier, as shown in Figure 18.9.

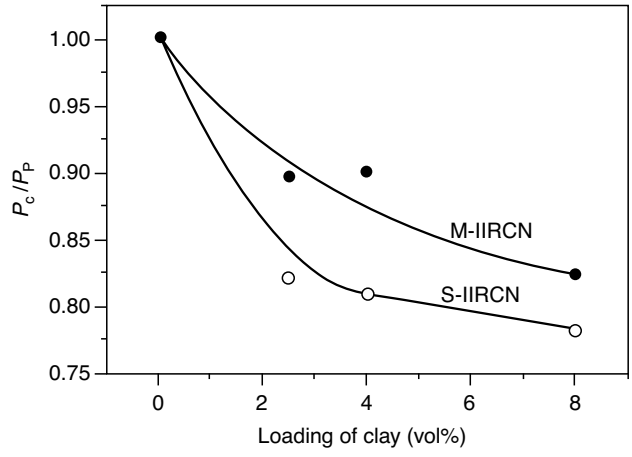

Figure 18.9 Influence of relative permeability of butyl rubber/clay nanocomposite prepared by solution (S-IIRCN) and melt (M-IIRCN) intercalation methods (Reprinted from *Polymer Testing*, **24**, no. 1, Y. Lianga, Y. Wang, Y. Wu, Y. Lu, H. Zhang and L. Zhang, "Preparation and properties of isobutylene-isoprene rubber (IIR)/clay nanocomposites," 12, © 2005, with permission from Elsevier.)

Chang *et al.* [68] showed that the oxygen barrier properties of EPDM/MMT clay nanocomposites are better than that of pristine EPDM. The oxygen permeability of 10 phr layered clay filled EPDM nanocomposite was reduced to 60% as compared with the pristine EPDM compound. The gas permeability was ascribed due to uniform dispersion of the impermeable clay layer with the planar orientation in the EPDM matrix. Comparison of various types of clays with and without organic modification is shown in Table 18.1.

Table 18.1 Oxygen gas permeabilities of EPDM/MMT hybrids containing 10 phr clay

Sample	Permeability of oxygen (cc/m^2 d atm)
EPDM	773
EPDM/Na/MMT	691
EPDM/C-18-MMT	608
EPDM/LEP-C18-MMT	468

(Reprinted from Y.W. Chang, Y. Sang, S. Ryu and C. Nah, "Preparation and properties of EPDM/organomonmorillonite hybrid nanocomposites," *Polymer International*, **51**, no. 4, 319, © 2002, with the permission of John Wiley & Sons, Inc.)

The nitrogen gas permeability of gum SBR vulcanizate, SBR–clay nanocomposites (SBR–clay NC), conventional SBR–clay composites (SBR–clay MC) and SBR-carbon black conventional composites (SBR-N330) are presented in Figure 18.10. It is understood from the

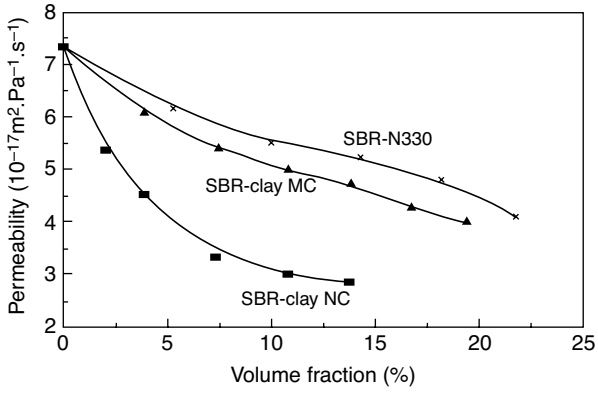

Figure 18.10 The nitrogen gas permeability of gum, clay-filled and carbon black-filled SBR composites (Reprinted from *Composite Science and Technology*, **65**, no. 7-8, Y.P. Wu, Y. Wang, H. Zhang, Y. Wang, D. Yu, L. Zhang and J. Yang, "Rubber-pristine clay nanocomposites prepared by co-coagulating rubber latex and clay aqueous suspension," 1195, © 2005, with permission from Elsevier.)

figure that the nitrogen permeability reduced with the increase in the amount of filler, and SBR–clay nanocomposites showed the best gas barrier property. Compared with the gum SBR vulcanizate, the nitrogen permeability of SBR/clay nanocomposites with 1.96, 7.40 and 13.8 (v/v) clay reduced by 27.3%, 54.1% and 61%, respectively [69]. It can be concluded that the silicate layers having the large aspect ratio and the planar orientation lead to the great increase of the diffusion distance by creating a much more tortuous path for the diffusing gas.

Wu *et al.* [63] also reported the preparation and the gas permeability of nanocomposites prepared by mixing of dispersion of montmorillonite in water with NR, SBR and NBR latex and coagulating the dispersion by dilute triethylenetetrammonium chloride solution. The nitrogen gas permeability of these nanocomposites is given in Table 18.2. When the rubbers were added with 20 wt% clay, the permeability of composites were reduced almost to 50%.

Table 18.2 Nitrogen gas permeability of nanocomposites (clay content: 20 wt%)

Material	Gas permeability (10^{-17} m^2 Pa^{-1} s^{-1})	% reduction in permeability
Pristine NR	13.7	—
NR-clay	7.3	54.1
Pristine NBR	2.3	—
NBR-clay	1.3	47.8
Pristine SBR	7.4	—
SBR-clay	3.4	54.1

(Reprinted from Y.P. Wu, Q.X. Jia, D.S. Yu and L.Q. Zhang, "Structure and properties of nitrile rubber (NBR)/clay nanocomposites by co-coagulating NBR latex and clay aqueous suspension," *Journal of Applied Polymer Science*, **89**, no. 14, 3855, © 2003, with the permission of John Wiley & Sons, Inc.)

The gas permeability of particulate and layered silicate filled composites prepared by blending of NBR latex and with fumed silica and montmorillonite clay with various filler loading decreased with an increase in the amount of filler and that the NBR–clay nanocomposites had a better gas barrier property than did the NBR filled with the same amounts of silica [63]. This was attributed to the impermeable filler phase and the large aspect ratio of the silicate layers. A sheet-like morphology is particularly efficient at maximizing the path length due to the large length-to-width ratio, when compared to other filler shapes such as spheres or cubes. Compared with the gum NBR vulcanizate, the nitrogen permeability of the NBR–clay nanocomposites with 10, 20 and 30 phr of clay was reduced by 29%, 41% and 48%, respectively.

The effect of loading of clay and silane coupling agent on water vapor permeability of NBR/organo-montmorillonite (O-MMT) nanocomposites prepared by a melt intercalation process was determined under steady-state condition at 40 °C and 90% relative humidity (RH). The permeability of all nanocomposites went down slightly with an increase in clay and silane coupling agent content. It was inferred that the dispersion of organic modifier (C18-MMT) decreases the rate of transport by increasing the average path length required to transport the specimen [70]. Figure 18.11 shows the dependence of the permeability of water vapor on clay loading and coupling agent content of NBR/C18-MMT nanocomposites on clay content. The presence of polar or methyl groups in the polymer molecules generally reduces the permeability of polymers while the presence of double bonds has the opposite effect. The coupling agent enhances the clay dispersion and the inter-chain attraction, leading to lower permeability for water vapor.

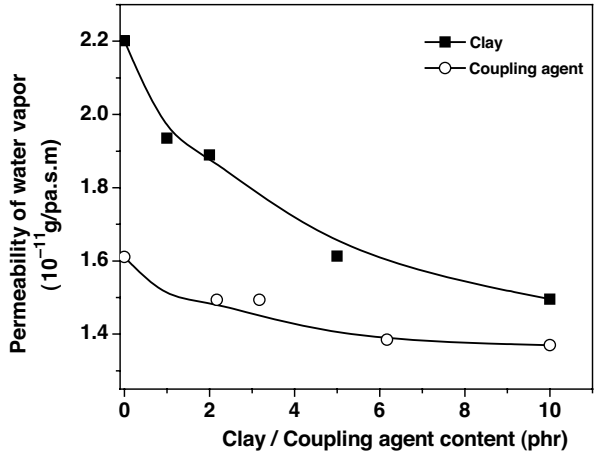

Figure 18.11 Variation of water vapor permeability of NBR/O-MMT nanocomposites with clay content and coupling agent (With kind permission from Springer Science + Business Media: *Journal of Materials Science Letters*, "Gas permeabilities in rubber-clay hybrid," **vol. 12**, no. 12, 889, © 1993, Y. Kojima, K. Fukumori, A. Usuki, A. Okada and T. Kurauchi.)

Kojima *et al.* [64] compared the hydrogen permeability of nitrile rubber (NBR) composite containing ATBN (liquid copolymer of butadiene and acrylonitrile) modified MMT and carbon filler. They found that the hydrogen permeability decreased with increasing MMT content

which is lower than that of carbon filler composite of higher filler loading. Further, the resistance to air permeation was investigated by Nah *et al.* [38] for the NBR/organo-treated montmorillonite nanocomposite prepared by melt mixing and crosslinked with peroxide curative. The air permeability decreases considerably with increase in clay content. Considerable increase in barrier performance was reported with even small amount of clay. A comparison of experimental and theoretical values of relative gas permeability of NBR/clay indicated that the Nielson theory overestimated the gas permeation performance of the nanocomposite. The observed discrepancy between experimental and theoretical values might be due to lack of alignment of clay layers parallel to the direction of rubber sheet.

Brooklite (TiO_2) nanoparticles filled 1,2-polybutadiene nanocomposite prepared via solution processing is reported for negative behavior for gas permeability due to an increase in gas solubility in nanocomposite film and the presence of more voids [71]. These nanocomposites shows large amount of free volumes due to the formation of voids as evidenced from the lower density of filled polymer composites compared to pristine rubber. Figure 18.12 represents the influence of TiO_2 particle loading on the relative permeability of nanocomposites to CO_2, CH_4, N_2 and H_2. The permeability increases with increasing particle content.

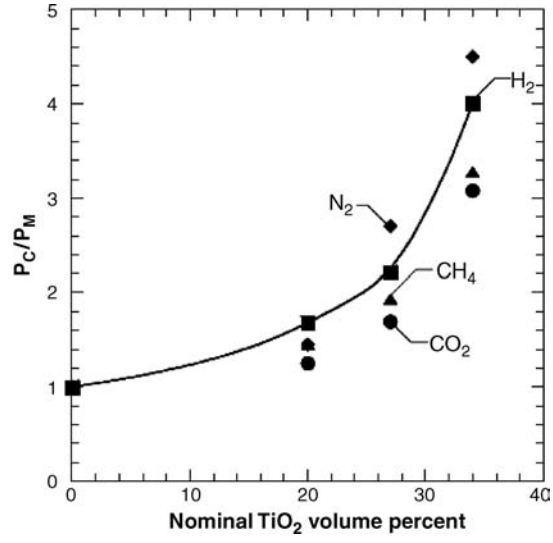

Figure 18.12 Influence of TiO_2 loading on relative permeability of 1,2-BR nanocomposite (Reprinted from *Polymer*, **49**, no. 3, S. Matteucci, V.A. Kusuma, S. Swinnea and B.D. Freemn, "Gas permeability, solubility and diffusivity in 1,2-polybutadiene containing brookite nanoparticles," 757, © 2008, with permission from Elsevier.)

The permeability of all gases increases with increasing void volume, the authors also compared the experimental values with the Bruggeman's permeability model [72] and found deviations as the model does not account for any changes in the continuous phase permeability due to changes in solubility. Deviations are due to many assumption made while formulating the model.

Thermoplastic elastomers (TPEs) combine the benefits of elastomeric properties of thermoset polymers, such as vulcanized rubber, with the processing properties of thermoplastic polymers. Therefore, TPEs are preferred because they can be made into articles such as seals, closures and other articles previously made from butyl rubber using injection molding equipment. But often, TPEs lack gas barrier properties. Styrene-ethylene-butylene-styrene (SEBS) triblock copolymer is extensively used as a thermoplastic elastomer. Sulfonated SEBS-montmorillonite clay-based nanocomposite can be used as a membrane for controlling the proton transfer in the field proton exchange fuel cell due to substitution of polar group in the structure [73]. Water–methanol (80/20) uptake and permeation measurements of sulfonated SEBS and its nanocomposite reveals much improved barrier to the solvent mixture owing to torturous path provided by the finely dispersed clay platelets in the entire matrices. Comparing the water–methanol diffusion through sulfonated SEBS and their nanocomposite film, the nanocomposites show great improvements in permeation of water–methanol under controlled condition due to the proper dispersion of nanoclays in the resulting nanocomposite. Polyethyleneoxide rubbers (PEO) crosslinked with multifunctional acrylates such as poly (ethylene glycol) diacrylate (PEGDA), poly(ethylene glycol) methyl ether acrylate (PEGMEA), PEGDA and poly(ethylene glycol) acrylate (PEGA) were studied to figure out the influence of acrylates on H_2, N_2, CH_4 and CO_2 transport properties [74]. Increasing the PEGMEA content increases CO_2 permeability and CO_2/H_2 selectivity and decreases CO_2/CH4 and CO_2/N_2 selectivity. The pure gas separation performance for CO_2/light gas pairs in crosslinked poly(ethylene oxide) polymers is illustrated by comparison to a nonpolar rubbery polymer (that is, polyethylene) and two rigid glassy polyimides. As the separations moved from those demanding high diffusivity selectivity (for example, H_2/CH_4) to ones benefiting from high solubility selectivity (for example, CO_2/H_2), the performance of the polar rubbers improved dramatically, relative to that of conventional glassy polymers.

Polyurethane (PU) is becoming increasingly important as an engineering material in the form of foams, coatings, adhesives, fibers, rubbers or thermoplastic elastomers because it has excellent abrasion resistance. The gas permeability of a thermoplastic polyurethanes (TPU) is dependent on the chemical structures not only of the soft segments but also of the hard segments. Chang *et al.* [75] compared the influence of type of organic modifiers in the organoclay used to prepare the polyurethane nanocomposite against oxygen gas-barrier properties. The organic modifier C16-MMT shows higher gas barrier than that of DTA-MMT or Cloisite 25A. With the addition of a 0∼4 wt% clay loading, the permeability values decrease from 7214 to 3587 cc for C16-MMT, from 7214 to 6136 cc for DTA-MMT and from 7214 to 4725 cc for Cloisite 25A. The permeability value in the C16–MMT hybrid was about half that of the corresponding pure polyurethane. It is also reported that, with an increase in clay loading from 0 to 4 wt%, regardless of the type of organoclay, the values of the permeability decreased linearly due to the increase in the tortuous paths for gas molecules and also due to increase in rigidity of nanocomposite films containing higher amounts of clay. In a similar study, Osman *et al.* [76] reported the relative permeability of ethylene propylene rubber and polyurethane rubber nanocomposites to oxygen as a function of the volume fraction of filler. In both EP and PU, the transmission rate decreases exponentially with increasing filler volume fraction to level off or slightly increase above 3%, probably due to a decrease in exfoliation or collapse of the layers as the interparticle distance diminish at high concentrations. However, the decrease in transmission rate was larger in PU than in EP, in accordance with the increase in *d*-spacing, pointing to stronger particle matrix interactions in

PU. In a water vapor permeation study, Osman *et al.* [77] observed that the PU nanocomposites adhesive reduced the water vapor transmission to 50%, even at 3 vol% silicate fraction, which is comparatively higher than oxygen transmission at the same filler loading. This is attributed to stronger interactions and hydrogen bonding of the water molecules with the PU matrix as well as to their clustering. Differences in the hydrophobicity of the clay coating influenced the water transmission rate.

The barrier properties of many polymer can be improved by just making laminates of higher barrier polymers and with conventional polymers such as poly(vinylidene chloride) (PVDC), ethylene vinyl alcohol (EVOH), poly(vinyl alcohol) (PVAL) or polyamide (PA) through co-extrusion with a high-barrier polymer. Many of these polymers (for example, PVAL, EVOH, most polyamides) are good oxygen barriers only in the dry state, which means that they have to be sandwiched between water vapor barrier films in order to maintain their oxygen barrier function [78]. In contrast, nanocomposite technology can be used to eliminate the additional step of co-extrusion for such barrier film.

Ethylene-vinyl alcohol (EVOH) copolymers are widely used in the food packaging sector due to their outstanding gas barrier properties to oxygen and organic compounds (solvents, food aromas). It has been reported by Cabedo *et al.* [79] that the barrier property of EVOH can be improved by incorporating the organoclay. The oxygen permeability of EVOH/O-MMT nanocomposites film was too low, that is, below 10^{-5} (cm^3 m)/(m^2 day atm) compared to neat EVOH with a permeability value of 3.6×10^{-5} (cm^3 m)/(m^2 day atm). The authors indicated that they could not measure the permeability due to instruments limitation for detection of very low permeability. The addition of platelet fillers distributed in the polymer film can greatly increase the diffusion pathway; permeating molecules are forced to go around impermeable flakes creating a tortuous path for the diffusing species. The use of mica in ethylene vinyl alcohol (EVOH) copolymers was reported to show a threefold increase in oxygen barrier properties [80]. Oxygen transmission rate of EVOH-kaolinite nanocomposites prepared by melt intercalation process tested at 45 °C under dry conditions showed very low values even at this high temperature. The permeability of all nanocomposites having a different organic modifier showed a considerable decrease in the oxygen permeability compared to pristine EVOH.

Doppers *et al.* [81] showed that ATR-FTIR can be readily applied to monitor the sorption of small molecules into polymeric membranes. The mode of diffusion depends significantly on the chemical interactions between the solvent and the polymer matrix. In the systems examined the diffusion of liquid water into PVOH–nanocomposite is accompanied by polymer salvation which is a dominant process making the diffusion rate determined by the ATR-FTIR method independent of clay loading. Conversely, the rate of diffusion of acetone into the same system reveals a significant dependence on the clay loading, due to the increased path length that an average acetone molecule has to take to reach the evanescent field where it is then detected.

18.4 Applications

Nanocomposite improves the barrier to many gases like air, oxygen, nitrogen, carbon dioxide, helium and so on. It also helps to protect the migration of moisture and odour. Greater barrier also impedes the absorption of flavors and vitamins by plastic packaging itself. Barrier enhancement is important for longer product shelf life where barrier is a limiting factor in

existing packages, where its improvement can lead to lower weight packages and reduced packaging cost. Improved shelf life and lower package cost dominate the uses of nanotechnology in consumer packaging.

The excellent air retention properties of butyl/halo butyl and chemically modified rubbers are very well known in the tire industries as these rubbers are widely used in the inner tube and inner liner in automotive tires. There are also some other elastomers, which are not used in the tire industries, but have very good and even better air retention properties, like, epichlorohydrin rubber (ECO), polysulfide rubber (TM) and polyurethane rubber (AU). There are also some elastomers, like nitrile rubber (NBR) and ethylene/acrylate copolymers (EAM), which provide moderate air retention properties. These polymers can be used for automotive components by incorporating nanofillers. Such fillers, when used in rubbers (NBR, EAM) having moderate air retention properties, can provide a substantial increase in air retention properties. It is known that nanocomposite technology is already commercialized in sports goods (tennis balls) for better durability of the product. It is not surprising that all future tire components may be made with a nanocomposite type of filler, which can produce: (i) low weight tires, (ii) low rolling loss tires, (iii) colored or transparent tires (although a transparent tire is very much for the bicycle and motor cycle categories) and (iv) tubeless tires without a conventional inner liner.

The automotive sector is a heavy user of performance polymers. An average car has over 350 pounds (approx. 160 kg) of polymeric components. Performance polymers are mostly incorporated with reinforcements, thermal stabilizers, chemical resistors and flame resistant additives, each of which increases weight and therefore decreases fuel efficiency. Since nanocomposites contain low nanoclay addition levels, they offer the automotive engineer an opportunity to minimize this weight penalty. The barrier enhancement property of nanocomposites plays a role in transportation by improving fuel vapor emissions in fuel tanks and distribution components. It also contributes greater resistance to common corrosive agents such as gasoline, antifreeze and road salt. Fit-and-finish depends on strength and stability under changing temperature conditions. Nanocomposites resist dimensional changes by reinforcing plastics in all directions and at a submicron level. Barrier is also important for air retention in tires. The initial customer problem is that general purpose rubbers are too permeable for many of its applications. Barrier is important for sports balls for feel and bounce due to air retention. Barrier properties are utilized in chemical protective gloves (which are thick with poor dexterity) in order to protect against chemical warfare agents.

The nanocomposite approach is to target and develop coatings with unique combination of barrier properties and flexibility. At least tenfold improvements in barrier can lead to improved performance at reduced cost. Nanocomposite approach improves air retention properties without weight, rolling resistance and cost penalties. The major driving force of tire companies is reduction of materials and processing costs. Other immediate potential benefits are reduced fuel usage, less generation of solid waste, improved tire safety with reduced maintenance requirement and so on. It is also not surprising that in future, in place of the conventional inner liner of today, only water-based inner paint, based on nanocomposite, may take care of both mold release and the air retention properties of future tires. In the elastomers, when such systems are used they may give rise to distinct improved properties. Nanotechnology creates safer tires and longer-lasting consumer products. The breakthrough can be applied to other elastomers too.

Biomedical applications hold high promise for nanotechnology, which may provide us with a nanopharmacological strategy for the treatment of myriad diseases. Perhaps the only limit of nanotechnology to biomedicine is our imagination. However it is now time to expand the new frontier from imagination and hypotheses to functional reality. Such a change will require relentless work of crossfunctional and multidisciplinary teams focusing on the engineering of nanoparticles to meet biomedical applications and testing potential biomedical applications in controlled environments. It has the unique ability to move the nanotechnology frontier ahead to uninvestigated territory, closer to the ultimate goal of ending disease.

Current sensing in the space-shuttle main engine compartment for hydrogen and oxygen leaks is done using an elaborate and weight-intensive gas-capture mechanism. This space-related system could be replaced with a real-time system at a small fraction of the weight or system cost. The proposed nanoparticle sensor technology extends its usage and investigation in shuttle engine monitoring, on orbit maneuvering systems (OMS) and the reaction control system (RCS) monitoring of hypergolic fuels and oxidizers (MMH and N2O4) to the preflight loading of various cryogenics which can be monitored based on their gaseous emissions in order to enhance safety and system reliability. Additionally a serious need exists for personnel monitoring systems of small size and very low power usage that can detect extremely low levels of various gases. If an astronaut's suit was to become contaminated by hypergolic or ammonia-based contaminants during a space walk, readmission through the air locks would spread the contamination, compounding the impact of the situation. However, as re-pressurization of the airlock occurs, these nanoparticle sensors could warn of the problem before the astronaut's egress from their suits. The sensors would also point to the intensity of contamination at a pressure, which conserves the valuable station atmosphere.

Conventional sensors cannot tolerate extreme cold or the vacuum of space. Nanoparticle sensors can be virtually impervious to either of these extremes. The role of sol-gel process parameters and dopants is being identified in establishing a mechanism of nanoparticle formation and finally, the fabrication, testing and evaluation of gas sensors in various gas environments will be carried out.

Nanocomposite technology can replace conventional materials in food and drink container seals, printer cartridge seals, medical container seals, medical container seals for blood collection tubes, stoppers for medical containers, stoppers for blood collection tubes, baby pacifiers and other products needing both flexibility and barrier properties. Carbon nanotube-filled polymer nanocomposites find useful application in defense. The porous nature of nanotubes allows the rapid diffusion of gases to be detected. The chemical sensors consisting of different type of polymers containing carbon nanotube can be used to detect unknown substances, solvents and so on, through swelling. The detection and identification of gases, pollutants, toxic substances and solvent vapors can be achieved by the use of selective nanocomposites. Polymer nanocomposites find important applications in corrosion protection. A barrier coating with scratch and tear resistance can effectively prevent the diffusion of corrosive gases and liquids. These nanocomposite protective coatings can be applied to the electronic circuits and other components in aerospace.

18.5 Conclusions

Rubber compounds with good barrier properties against gases, vapor and organic solvents are used in wide variety of applications, including tire industries, packagings for foods and

beverages, various sealing products, as air springs for cars, buses/trucks trains and aerospace shuttles and so on. Over the past few years, there have been a lot of developments in the area of barrier technologies. Among them, the use of nanocomposite technologies might give the most significant improvement in the barrier properties. The presence of a nanofiller with a high surface area combined with a large aspect ratio in rubber nanocomposites improves the gas barrier properties by creating a tortuous path for the diffusing species. The degree of dispersion, orientation of filler particle, volume fraction of filler, type of filler modifier and so on greatly influence the permeability of barrier materials. Interestingly, the selective diffusion of permeant through rubbers compels the development of newer barrier materials suitable for particular applications.

The prediction of gas transport behavior through barrier materials can be made by means of various models. The mechanism of sorption and diffusion of permeant depends on the geometry and nature of the barrier material, the solubility of the diffusant, the concentration gradient of the diffusant in bulk and in the interfacial region, the presence of filler modifier and so on. The change in gas barrier properties can be explained based on free volume theory, hole vacancy theory or dual sorption theory.

Various experimental studies are reported in the literature on the barrier properties of different types of barrier material having a flexible and rigid structure. The barrier properties of elastomeric nanocomposites comprising of butyl rubber, NBR, EPDM, PU and so on are found more useful for diversified applications. Possible applications of such excellent barrier performance are suggested at end of this chapter.

Acknowledgments

The authors would like to thank students (J.Y. Lee, J.Y. Lim, Y.H. Kim, G.B. Lee) in our research laboratory at Chonbuk National University for their collecting various literature on the barrier properties of rubber nanocomposites.

References

1. Gent, A.N. (1992) Chapters 1 and 8, in *Engineering with Rubber, How to Design Rubber Components*, Hanser.
2. Aminabhavi, T.M., Harlapur, S.F., and Ortego, J.D. (1997) Solvent resistivity testing of fluoroelastomers using a gravimetric sorption method. *Polymer Testing*, **16**, 91.
3. Mark, H.F. *et al.* (2003) *Encyclopedia for Polymer Science and Technology*, 3rd edn, vol. **2**, Wiley-Interscience, NY, pp. 252–283.
4. Barrer, R.M., Barrie, J.A., and Rogers, M.G. (1963) Heterogeneous membranes: diffusion in filled rubber. *Journal of Polymer Science Part A Polymer Chemistry*, **1**, 2565.
5. Lin, J.H., Chen, H.W., Wang, K.T., and Liaw, F.H. (1998) A novel method for grafting polymers on carbon blacks. *Journal of Materials Chemistry*, **8**, 2169.
6. George, S., Knorgen, M., and Thomus, S. (1999) Effect of nature and extent of crosslinking on swelling and mechanical behavior of styrene–butadiene rubber membranes. *Journal of Membrane Science*, **163**, 1.
7. Park, S.J. (2002) *Encylopedia of Surface and Colloid Science: van der Waals Interactions at Surface*, Marcel Dekker, New York.
8. Matayabas, J., Turner, S., Pinnavaia, T., and Beall, G. (eds) (2001) *Polymer-Clay Nanocomposites*, Wiley, New York, pp. 207–226.
9. Alexandre, M. and Dubois, P. (2000) Polymer-layered silicate nanocomposites: preparation, properties and uses of a new class of materials. *Materials Science and Engineering*, **28**, 1.

10. Kung, H. and Foecke, T. (1999) Special Issue on Mechanical behavior of nanostructured materials. *MRS Bulletin*, **24**(2), 14.
11. Park, S.J., Seo, M.K., and Shim, H.B. (2003) Effect of fiber shapes on physical characteristics of non-circular carbon fibers-reinforced composites. *Materials Science and Engineering A*, **352**, 34.
12. Shi, Q., Wang, L., Yu, H. *et al.* (2006) A novel epoxy resin/CaCO3 nanocomposite and its mechanism of toughness improvement. *Macromolecular Materials and Engineering*, **291**, 53.
13. Meador, M.A.B., Fabrizio, E.F., Ilhan, F. *et al.* (2005) Cross-linking amine-modified silica aerogels with epoxies: mechanically strong lightweight porous materials. *Chemistry of Materials*, **17**, 1085.
14. Kojima, Y., Usuki, A., Kawasumi, M. *et al.* (1993) One-pot synthesis of nylon 6-clay hybrid. *Journal of Polymer Science Part A Polymer Chemistry*, **31**, 1755.
15. Giannelis, E.P. (1996) Polymer layered silicate nanocomposites. *Advanced Materials*, **8**, 29.
16. Yano, K., Usuki, A., Okada, A. *et al.* (1993) Synthesis and properties of polyimide-clay hybrid. *Journal of Polymer Science Part A Polymer Chemistry*, **31**, 2493.
17. Jana, S.C. and Jain, S. (2001) Dispersion of nanofillers in high performance polymers using reactive solvents as processing aids. *Polymer*, **42**, 6897.
18. Chazeau, L., CavaillØ, J.Y., Canova, G. *et al.* (1999) Viscoelastic properties of plasticized PVC reinforced with cellulose whiskers. *Journal of Applied Polymer Science*, **71**, 1979.
19. Matos Ruiz, M., Graillat, C., CavaillØ, J.Y. *et al.* (2000) Processing and characterization of new thermoset nanocomposites based on cellulose whiskers. *Composite Interfaces*, **7**, 117.
20. Bonini, C. (2000) Ph. D. Thesis "Study of the role of fiber/fiber and fiber/matrix interactions in nanocomposites with cellulose reinforcement and apolar matrix", Institut National Polytechnique de Grenoble.
21. Garrido, I.Q., Rienda, J.M.B., and Frutos, G. (1996) Diffusion of erucamide (13-cis-docosenamide) in isotactic polypropylene. *Macromolecules*, **29**, 7164.
22. Földes, E. (1993) Transport of small molecules in polyolefins. II. Diffusion and solubility of irganox 1076 in ethylene polymers. *Journal of Applied Polymer Science*, **48**, 1905.
23. Klein, J. and Briscoe, B.J. (1977) Diffusion of long molecules through solid polyethylene. II. Measurements and results. *Journal of Polymer Science Part B-Polymer Physics Edition*, **15**, 2065.
24. Rawls, A. (1997) MS Thesis "Diffusion of an erucamide slip additive in linear low-density polyethylene film", Clemson University.
25. Maeda, Y. and Paul, D.R. (1987) Effect of antiplasticization on gas sorption and transport. III. Free volume interpretation. *Journal of Polymer Science Part B-Polymer Physics Edition*, **25**, 1005.
26. Strathmann, H., Giorno, L., and Drioli, E. (2006) *An Introduction to Membrane Science and Technology*, CNR Roma, Italy (ISBN 88-8080-063-9).
27. Stannett, V.T., Koros, W.J., Paul, D.R. *et al.* (2006) Recent advances in membrane science and technology. *Advances in Polymer Science*, **32**, 69–121.
28. Kumins, C.A. and Kwei, T.K. (1968) Chap. 4, in *Diffusion in Polymers* (eds J. Crankand C.S. Park), Academic Press, NY.
29. Crank, J. (1968) Methods of measurement, in *Diffusion in Polymers* (eds J. Crankand G.S. Park), Academic Press, NY, pp. 1–3.
30. Nielsen, L.E. (1967) Models for the permeability of filled polymer systems. *Journal of Macromolecular Science*, **A1**(5), 929.
31. Moet, A.S. and Akelah, A. (1993) Polymer-clay nanocomposites: polystyrene grafted onto montmorillonite interlayers. *Materials Letters*, **18**, 97.
32. Vaia, R.A., Ishii, H., and Giannelis, E.P. (1993) Synthesis and properties of two-dimensional nanostructures by direct intercalation of polymer melts in layered silicates. *Chemistry of Materials*, **5**, 1694.
33. Cussler, E.L., Hughes, S.E., Ward, W.J., and Aris, R. (1988) Barrier membranes. *Journal of Membrane Science*, **38**, 161.
34. Lan, T., Padmananda, D.K., and Pinnavaia, T.J. (1994) On the nature of polyimide-clay hybrid composites. *Chemistry of Materials*, **6**, 573.
35. Burnside, S.D. and Giannelis, E.P. (1995) Synthesis and properties of new poly(dimethylsiloxane) nanocomposites. *Chemistry of Materials*, **7**, 1597.
36. Yano, K., Usuki, A., and Okada, A. (1997) Synthesis and properties of polyimide-clay hybrid films. *Journal of Polymer Science Part A Polymer Chemistry*, **35**, 2289.
37. Bharadwaj, R.K., Mehrabi, A.R., Hamilton, C. *et al.* (2002) Structure–property relationships in cross-linked polyester–clay nanocomposites. *Polymer*, **43**, 3699.

38. Nah, C., Ryu, H.J., Kim, W.D., and Choi, S. (2002) Barrier property of clay/acrylonitrile-butadiene copolymer nanocomposite. *Polymers for Advanced Technologies*, **13**, 649.
39. Xu, R., Manias, E., Snyder, A.J., and Runt, J. (2001) New biomedical poly(urethane urea)-layered silicate nanocomposites. *Macromolecules*, **34**, 337.
40. Beall, G.W. (2001) A new model for interpreting nanocomposite behavior. Annual Technical Conference, Society of Plastics Engineers, 59, p. 2195.
41. Bharadwaj, R.K. (2001) New biomedical poly(urethane urea)-layered silicate nanocomposites. *Macromolecules*, **34**, 9189.
42. Lape, N.K., Yang, C., and Cussler, E.L. (2002) Flake-filled reactive membranes. *Journal of Membrane Science*, **209**, 271–282.
43. Lape, N.K. and Cussler, E.L. (2004) Polydisperse flakes in barrier films. *Journal of Membrane Science*, **236**, 29–38.
44. Meneghetti, P.C. (2005) Ph. D. Thesis "Synthesis and properties of rubber-clay nanocomposites", Case Western Reserve University.
45. Aris, R. and Ration, A. (1986) On a problem in hindered diffusion. *Archive for Rational Mechanics and Analysis*, **95**, 83.
46. Alamgir, K., Koray, Y., Carson, M. *et al.* (2002) Combinatorial methods for polymer materials science: phase behavior of nanocomposite blend films. *Polymer Engineering and Science*, **42**, 1836.
47. Kamal, M.R., Jinnah, I.A., and Utracki, L.A. (1984) Permeability of oxygen and water vapor through polyethylene/polyamide films. *Polymer Engineering and Science*, **24**, 1337.
48. Falla, W.R., Mulski, M., and Cussler, E.L. (1996) Estimating diffusion through flake-filled membranes. *Journal of Membrane Science*, **119**, 129.
49. Gusev, A.A. and Lusti, H.R. (2001) Rational design of nanocomposites for barrier applications. *Advanced Materials*, **13**, 1641.
50. Fredrickson, G. and Bicerano, J. (1999) Barrier properties of oriented disk composites. *Journal of Chemical Physics*, **110**, 2181.
51. Drozdov, A.D., Christiansen, J.C., Gupta, R.K., and Shah, A.P. (2003) Model for anomalous moisture diffusion through a polymer-clay nanocomposite. *Journal of Polymer Science Part B Polymer Physics*, **41**, 476.
52. Sorrentino, A., Tortora, M., and Vittoria, V. (2006) Diffusion behavior in polymer-clay nanocomposites. *Journal of Polymer Science Part B Polymer Physics*, **44**, 265.
53. Aithal, U.S., Balundgi, R.H., Aminabhavi, T.M., and Shukla, S.S. (1991) Selective transport of oxygen through polymer films - a review of literature on patents. *Polymer - Plastics Technology and Engineering*, **30**, 299.
54. van Amerongen, G.J. (1947) The permeability of different rubbers to gases and its relation to diffusivity and solubility. *Rubber Chemistry and Technology*, **20**, 494.
55. van Amerongen, G.J. (1951) Influence of structure of elastomers on their permeability to gases. *Rubber Chemistry and Technology*, **24**, 109.
56. Johnson, T. and Thomas, S. (1999) Nitrogen/oxygen permeability of natural rubber, epoxidised natural rubber. *Polymer*, **40**, 3223.
57. Wang, Y., Zhang, H., Wu, Y. *et al.* (2005) Preparation and properties of natural rubber/rectorite nanocomposites. *European Polymer Journal*, **41**, 2776.
58. Varghese, S. and Karger-Kocsis, J. (2003) Natural rubber-based nanocomposites by latex compounding with layered silicates. *Polymer*, **44**, 4921.
59. Stephen, R., Varghese, S., Joseph, K. *et al.* (2006) Diffusion and transport through nanocomposites of natural rubber (NR), carboxylated styrene butadiene rubber (XSBR) and their blends. *Journal of Membrane Science*, **282**, 162.
60. Stephen, R., Ranganathaiah, C., Varghese, S.C. *et al.* (2006) Gas transport though nano and micro composites of natural rubber(NR) and their blends with carboxylated styrene butadiene rubber(XSBR) latex membranes. *Polymer*, **47**, 858.
61. Knite, M., Klemenok, I., Shakale, G. *et al.* (2007) Polyisoprene–carbon nano-composites for application in multifunctional sensors. *Journal of Alloys and Compounds*, **434–435**, 850.
62. Lu, Y.L., Li, Z., Yu, Z.Z. *et al.* (2007) Microstructure and properties of highly filled rubber/clay nanocomposites prepared by melt blending. *Composites Science and Technology*, **67**, 2903.
63. Wu, Y.P., Jia, Q.X., Yu, D.S., and Zhang, L.Q. (2003) Structure and properties of nitrile rubber (NBR)–clay nanocomposites by co-coagulating NBR latex and clay aqueous suspension. *Journal of Applied Polymer Science*, **89**, 3855.

64. Kojima, Y., Fukumori, K., Usuki, A. *et al.* (1993) Gas permeabilities in rubber-clay hybrid. *Journal of Materials Science Letters*, **12**, 889.
65. LeBaron, P.C. and Pinnavaia, T.J. (2001) Clay nanolayer reinforcement of a silicone elastomer. *Chemistry of Materials*, **13**, 3760.
66. Takahashi, S., Goldberg, H.A., Feeney, C.A. *et al.* (2006) Gas barrier properties of butyl rubber/vermiculite nanocomposite coatings. *Polymer*, **47**, 3083.
67. Lianga, Y., Wang, Y., Wu, Y. *et al.* (2005) Preparation and properties of isobutylene–isoprene rubber (IIR)/clay nanocomposites. *Polymer Testing*, **24**, 12.
68. Chang, Y.W., Yang, Y., Ryu, S., and Nah, C. (2002) Preparation and properties of EPDM/organomontmorillonite hybrid nanocomposites. *Polymer International*, **51**, 319.
69. Wu, Y.P., Wang, Y., Zhang, H. *et al.* (2005) Rubber–pristine clay nanocomposites prepared by co-coagulating rubber latex and clay aqueous suspension. *Composites Science and Technology*, **65**, 1195.
70. Kim, J.T., Oh, T.S. and Lee, D.H. (2004) Curing and barrier properties of NBR/organo-clay nanocomposite. *Polymer International*, **53**, 406.
71. Matteucci, S., Kusuma, V.A., Swinnea, S., and Freeman, B.D. (2008) Gas permeability, solubility and diffusivity in 1,2-polybutadiene containing brookite nanoparticles. *Polymer*, **49**, 757.
72. Bouma, R.H., Checchetti, A., Chidichimo, G., and Drioli, E. (1997) Permeation through a heterogeneous membrane: the effect of the dispersed phase. *Journal of Membrane Science*, **128**, 141.
73. Ganguly, A. and Bhowmick, A.K. (2008) Sulfonated styrene-(ethylene-co-butylene)-styrene/montmorillonite clay nanocomposites: synthesis, morphology, and properties. *Nanoscale Research Letters*, **3**, 36.
74. Lin, H., Wagner, E.V., Swinnea, J.S. *et al.* (2006) Transport and structural characteristics of crosslinked poly (ethylene oxide) rubbers and natural rubber/epoxidised natural rubber blends. *Journal of Membrane Science*, **276**, 145.
75. Chang, J.H. and An, Y.U. (2002) Nanocomposites of polyurethane with various organoclays: Thermomechanical properties, morphology, and gas permeability. *Journal of Polymer Science Part B-Polymer Physics*, **40**, 670.
76. Osman, M.A., Mittal, V., and Lusti, H.R. (2004) The aspect ratio and gas permeation in polymer-layered silicate nanocomposites. *Macromolecular Rapid Communications*, **25**, 1145.
77. Osman, M.A., Mittal, V., Morbidelli, M., and Suter, U.W. (2003) Polyurethane adhesive nanocomposites as gas permeation barrier. *Macromolecules*, **36**, 9851.
78. Langed, J. and Wyser, Y. (2003) Recent innovations in barrier technologies for plastic packaging - a review. *Packaging Technology and Science*, **16**, 149.
79. Cabedo, L., Giménez, E., Lagaron, J.M. *et al.* (2004) Development of EVOH-kaolinite nanocomposites. *Polymer*, **45**, 5233.
80. Bissot, T.C. (1990) *Performance of High-Barrier Resins with Platelet-Type Fillers -Effects of Platelet Orientation,* Symposium Series, vol. **423**, American Chemical Society, Washington DC.
81. Doppers, L.M., Breen, C., and Sammon, C. (2004) Diffusion of water and acetone into poly(vinyl alcohol)–clay nanocomposites using ATR-FTIR. *Vibrational Spectroscopy*, **35**, 27.

19

Rubber/Graphite Nanocomposites

Guohua Chen and Weifeng Zhao
Institute of Polymer & Nanomaterials, Huaqiao University, Quanzhou, Fujian 362021, China

19.1 Introduction and Background

Of all the polymeric materials, rubbers are unique. Their characteristics of high reversible extensibility have been fascinating the enquiring mind of people. Rubber materials have been studied extensively in both fundamental and applied research field owing to their advantages of easy processing, remarkable flexibility, corrosion resistant and excellent thermal properties [1–6].

Rubber materials are commonly used in form of composite. Rubber in pure state is extremely nervy (short of mastication) and lack in functions. It is, therefore, usually reinforced with fillers either white or black to help its processability, and with some ingredients with certain functions to confer special properties of physics to rubber matrices. Shiro *et al.* developed a kind of graphitic friction material based on acrylonitrile-butadiene rubber (NBR) with high friction coefficient, high capacity of energy absorption and low wear, which contains aromatic polyamide fiber, carbon fiber, granulated pulp fiber, graphite, rubber-coated exfoliated graphite, CaF_2, SiO_2 and polyimide resin using powder metallurgy [7]. Li *et al.* investigated the influence of graphite particle size and shape on the tribological properties of NBR [8]. The formulation of rubber-based friction material can be optimized using optimization formulation technique on the basis of the golden section principle coupled with relational grade analysis [9, 10]. The mostly used rubber materials under friction research now include NBR, hydrogenated nitrile rubber, acrylic rubber, silicon rubber and fluorocarbon rubber. Solid lubricant-filled rubber composites of good tribological properties (high wear resistance and low friction coefficient) have been extensively used as sealing materials in radial lip seals of shafts, valve shaft seals, reciprocating piston and piston rod seals [8, 11, 12]. Except for the rubber friction materials, flexible conductive rubbers have been of research focus for a long time [13–20]. Conductive rubber composites are frequently manufactured with various conductive fillers

Rubber Nanocomposites: Preparation, Properties and Applications Edited by Sabu Thomas and Ranimol Stephen
© 2010 John Wiley & Sons (Asia) Pte Ltd

incorporated as a second phase into nonconducting rubbers, including metallic particles (Al, Au, Ag, Cu), stainless steel, conductive carbon blacks, carbon and graphite fibers, graphite powders, metal-coated and inorganic oxide particles [21, 22]. By changing the volume fraction of these conductive fillers, not only the mechanical property but also the conductivity of rubber matrix can be easily modified. The electrical conductivity of rubber composites can be varied in a very broad range between the conductivities of rubber matrix and conductive fillers. Conductive rubber composites with good flexibility and processabilily are identified promising candidates for a wide range of industrial applications. Depending on the magnitude of volume electrical resistivity, conductive rubbers can find their applications in electromagnetic interference shielding [23, 24], thermoelectric material [25, 26], electrostatic dissipation [27, 28], lightning-protected aircraft composite panels [29], load or deformation transducers [30, 31], pressure or gas sensitive sensors [32–34], rubber contact switches [35] and other functional applications.

Among the various electrically conducting additives blended with rubbers, graphite has a significant role in imparting functions. Compared with metals which have a high density and tend to oxidize to form an insulating layer on its surface, graphite flake is light weight, oxygen resistance and naturally abundant. Graphite is also well known for its stiffness, excellent thermal/electrical conductivity and lubricant properties, arising from its typical layered structure with anisotropy. These novel properties make graphite a leader conducting filler in composite realm. Graphite has been typically employed in the production of rubber composites to convey conductivity and lubricant to the mix [36–42].

In the past 20 years, tremendous developments have been achieved in many aspects of composites research and technology. Material designers have laid a strong emphasis on producing nanostructured materials with novel properties by designing structures at the nanometer scale. Motivated by the remarkably distinct properties of nanomaterials compared with the bulk ones and recent enthusiasm in nanotechnology, a surge in the development of polymeric nanocomposites is rapidly evolving a significant part in the field of nanotechnology and is greatly facilitated by the development of scanning microscopy along with a rapid growth of computer technology. The polymer nanocomposites can be defined as polymer-based materials in which at least one of the filler dimensions is of nanoscale order although the final product does not have to be in the nanometer size range (<100 nm, generally). Polymer/inorganic nanocomposites have enhanced functions without mechanical compromising.

The adhesion at the filler/rubber interface play crucial roles in determining the performances of the rubber mix [34, 43]. Both the surface area and surface properties of fillers have significant effects on the interface interaction. Compared with fillers of larger dimension, nanoscale additives are more efficient in reinforcement because they have a larger surface area for a given volume. The surface area-to-volume ratio of the reinforcement nanomaterials is a key factor in determining their reinforcing efficiency, and it is of fundamental importance in understanding the structure–property relationship. The ratios of surface area to volume for three kinds of common fillers with different geometries are shown in Figure 19.1 [44]. For graphite of a layered structure, its surface area/volume is dominated by the first term $2/t$ in the equation. The second term which is inversely proportional to the breadth is often omitted compared to the first term. Logically, the transition of graphite thickness from micro to nano scale will yield dramatic increase in the surface area/volume ratio by three orders of magnitude. The high aspect ratio of the resulted graphite nanoplatelets contributes a lot for improvement in reinforcing enhancement for polymer/graphite nanocomposites.

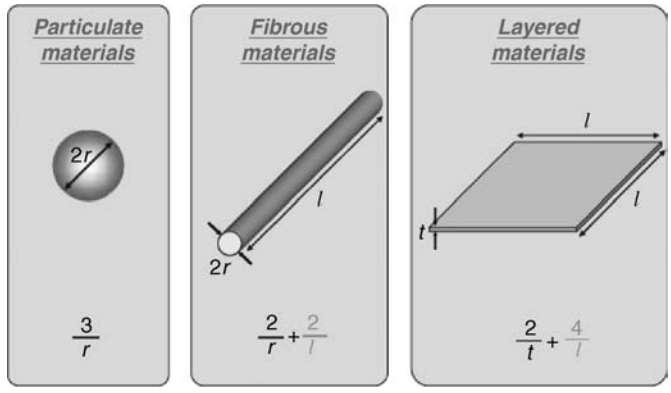

Figure 19.1 Surface area: volume relations for varying reinforcement geometries [44] (Reprinted from *Composites Science and Technology*, **65**, no. 3-4, E.T. Thostenson, C. Li and T-W. Chou, "Nanocomposites in context," 491–516, © 2005, with permission from Elsevier.)

In a word, graphite/rubber nanocomposites with remarkable potentials hold great promise as a particular class of nanocomposites. The focus of this chapter is to highlight the state of knowledge in graphite nanostructures and the processing, characterization, material properties, challenges and potential applications for rubber/graphite nanocomposites.

19.2 Graphite and its Nanostructure

Graphite nanostructures mainly refer to graphite nanoplatelets which have a much larger aspect ratio compared with conventional graphite flakes. The key point to utilizing graphite as a nanoreinforcement is the ability to create graphite nanoplatelets. To maximize the reinforcing efficiency, graphite is favored to be as thin as possible.

Two routes are available for the preparation of nanostructured graphite, one is from acid intercalated graphite, and the other one is from graphite oxide. Graphite has a layered structure similar with the geometry of silicate clay minerals allowing atoms and molecules known as intercalate to reside between its layered galleries. By applying rapid heating, the vaporization of intercalates makes the graphite expand resulting in expanded graphite which comprises graphite sheets with a thickness in nanometer scales. Graphite oxide can readily exfoliate to form graphene oxides in water. After chemical reducement, oxidized carbon atoms are reconverted to the original sp^2 hybridization state in graphite giving birth to conductive graphene.

19.2.1 Basic Issues on Graphite

Graphite is an allotrope of carbon with a lamellar structure. In each carbon layer, the carbon atoms are arranged in a hexagonal pattern through covalence bonding involves sp^2 (trigonal) hybridization. For an isolated carbon atom, the electronic configuration is $1s^22s^2p^2$ where the$1s^2$ electrons belong to the ion core and the other four electrons are valence electrons.

In graphite, the valence electrons positioning 2s, $2p_x$ and $2p_y$ form three hybridized orbitals, leading to the formation of C—C σ-bond directed 120° apart on a layer plane. Whereas, the $2p_z$ electron forms a delocalized orbital of π-symmetry, giving weak van der Waals forces by which the carbon layers are held together. The loosely bound π-electrons of high mobility play a dominant role in the electronic properties of graphite.

The primitive unit cell of graphite crystal contains three carbon layers. As shown schematically in Figure 19.2, the layers in graphite are stacked along the *c*-axis in a staggered array denoted as an . . .ABAB. . . sequence with dimensions $\alpha = 0.246$ and $c = 0.671$ nm [45]; the distance between two neighbor atoms marked ***B*** in adjacent layer planes is 0.335 nm and atoms ***A*** are 0.671 nm away from their neighbors directly above and below in carbon planes.

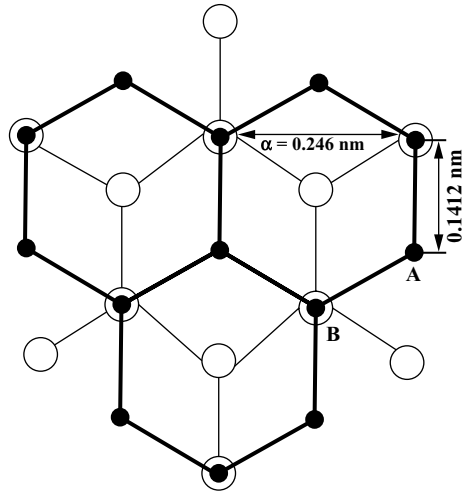

Figure 19.2 The in-plane structure of graphite. The layer plane shown with open circles is adjacent to the layer plane shown with full circles

Corresponding to the layered structure, graphite is anisotropic, showing different properties for in-plane and *c*-axis crystallographic directions. It displays a good electrical and thermal conductivity within the layers and a poor electrical and thermal conduction perpendicular to the layers. Moreover, the carbon layers can slide with respect to one another quite easily, making graphite a good lubricant material.

19.2.2 Graphite Intercalation Compounds

Graphite reacts with many chemical substances to form intercalated compounds which are start materials for graphite nanostructures. Due to the layered structure, graphite is able to undergo chemical reactions by allowing the guest chemical species called intercalate to reside between the interlayer spaces of the graphite lattice [46–48]. Such chemical reactions are known as intercalation, and the products are called graphite intercalation compounds (GICs). Depending on the particular intercalate, the kind of interaction between the carbon

atoms and intercalate can be covalent or partially ionic, according to which GICs can be classified into two groups: covalent intercalation compounds and ionic intercalation compounds. There are only two kinds of covalent intercalation compounds – graphite oxide and graphite fluoride. Both of them are electrical insulators and receive less attention than the ionic ones. Thus, generally, GICs mainly refer to the ionic type such as graphite–acid compounds where the bonding between the intercalate and carbon has a certain degree of ionic or polar character.

Graphite can be intercalated by a large number of acids to form intercalation called "acid salts of graphite." These compounds have received much attention because of their high electrical conductivities [47]. The best known graphite–acid salt is graphite bisulfate (graphite-H_2SO_4) which can be obtained by the spontaneous chemical interaction of graphite with a mixture of concentrated sulfuric acid and an oxidizing agent or by electrolysis [49–55], which can be expressed as follows [56, 57]:

$$n(\text{graphite}) + n\text{H}_2\text{SO4} + n/2[\text{O}] \rightarrow n\,(\text{graphite} \cdot \text{HSO}_4) + n/2\text{H}_2\text{O}$$

(O): Oxidant; $(\text{graphite} \cdot \text{HSO}_4)$: GIC.

The oxidizing agents include nitric acid, chromic oxide, potassium permanganate, ammonium persulfate, manganese dioxide, lead dioxide, arsenic pentoxide, iodic acid, periodic acid and manganese salts. These auxiliary agents induce the intercalate reaction of graphite and sulfuric acid without themselves entering into the final compound, and therefore the oxidation can be performed electrolytically where an external electric battery acting as the oxidizing agent. Therefore graphite bisulfate can also be prepared by electrolysis when concentrated sulfate acid is electrolyzed with graphite as the reference electrode.

It is recognized that the ionic intercalation is accompanied by a charge transfer between the intercalate and graphene layers. The graphite π-bonds can gain electrons from or lose electrons to the intercalate, shifting the position of the Fermi energy from that in pure graphite. That means the intercalates can act as donors or acceptors transferring electrons or holes, respectively, to the graphite sublattice [58]. The bonding in these compounds has some ionic character [59]. Thus, GIC tends to be more conductive electrically than graphite. Depending on the direction of electron transfer, the intercalation compounds of graphite can be classified into donor-GIC and acceptor-GIC. Graphite compounds intercalated by electron donors such as alkali metals which donate electrons to the graphene layer during processing of intercalation are sorted to donor-type GICs whereas compounds formed by the intercalation of molecular species acting as electron acceptors such as halogens, halide and acids, are viewed as acceptor-type GICs. It is important to recognize that although electron transfers really exist between the carbon atoms and the intercalates, it do not mean the interaction between them is scientifically true ionic bonding as same as that in the totally ionic solids. In fact, the degree of the ionicity in GICs is very low, and many of the intercalates retain their molecular form in the graphite lattice.

In GIC, the carbon and intercalate layers always stack on top of one another in a periodic sequence as shown in Figures 19.3 and 19.4 with two different models [60, 61]. This characteristic of GIC is called staging phenomenon. The definite carbon layers number between two intercalate layers is defined as the stage of GIC which can be varied from 1 to n depending on the particular intercalate and intercalation situations as shown in Figure 19.5. The stage can be identified by XRD and by the intercalation isotherms, and it usually decreases with an increasing concentration of the intercalate [60].

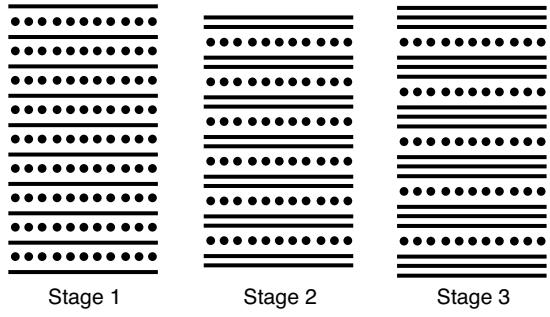

Figure 19.3 Interlayer ordering in lamellar compounds of stages 1, 2, and 3. Lines indicate graphene layers; dots indicate intercalated layers [61] (Reprinted from *European Polymer Journal*, **39**, G-H. Chen, W-G. Weng, D-J. Wu and C-L. Wu, "PMMA/graphite nanosheets composite and its conducting properties," 2329–2335, © 2003, with permission from Elsevier.)

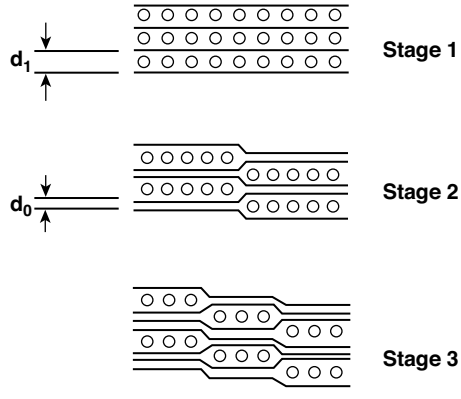

Figure 19.4 Stage ordering of GICs in the pleated layer model. Lines indicate graphene layers; dots indicate intercalated layers (Reprinted from *Synthetic Metals*, **114**, H. Shioyama, "The interactions of two chemical species in the interlayer spacing of graphite," 1–15, © 2000, with permission from Elsevier.)

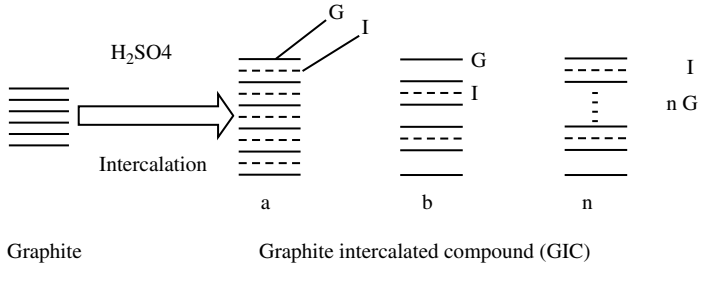

Figure 19.5 Schematic illustration of the stage 1(a), 2(b) and $n(n)$ of graphite bisulfate

19.2.3 Expanded Graphite

GICs are expandable materials which tend to exfoliate upon heating [62]. The exfoliations arise from the vaporization of the intercalate leading to a large expansion of graphite parallel to the *c*-axis. The shear of the graphite layers with respect to another make it possible for the expansion of the gas pockets. The exfoliation is negligible when the graphite particle size is less than 75 μm and when the *c*-axis stack height *Lc* no more than 75 nm [63, 64].

Depending on the heating temperature, the exfoliation can be either reversible or irreversible [65, 66]. At a low temperature, the gas cells do not burst and the heating is not excessive, the exfoliation is reversible upon subsequent cooling. When the gas bubbles burst at a high temperature and the heating is excessive, the exfoliation becomes irreversible. In order to obtain a nanostructure, irreversible exfoliation taking place at a higher temperature is required because irreversibly exfoliated graphite is much more expanded than reversibly exfoliated graphite.

In principle, any intercalate can be used for graphite exfoliation. However, the surface area of exfoliated graphite varies from intercalate to intercalate. The most common choice of GIC is graphite bisulfate obtained through the HNO_3–H_2SO_4 route, as mentioned earlier. In the exfoliation process of graphite bisulfate when suffering an extensive thermal shock at 1050 °C, the graphite expands irreversibly by up to hundreds of times along the *c*-axis (Figure 19.6) [67]. The domestic microwave oven is also a crackajack heating source for the exfoliation. The product with a vermicular or wormlike shape is known as exfoliated or expanded graphite (EG), as shown in Figure 19.7. The expansion ratio, defined as the reciprocal of the apparent density, can yield as high as 300. The typical structure of EG is incompact and porous wormlike shape with many pores of different sizes 10 nm to 10 μm structured with parallel boards, which desultorily collapsed and deformed, possessing an apparent density of about 0.004 g/cm^3 [52]. The surface structure of EG is shown in Figure 19.8 which reveals that the thickness of the graphite sheets on the EG surface ranges from 100 to 400 nm, whereas there are plenty of sheets thinner than 10 nm inside the EG, as revealed by TEM (Figure 19.9). The differences in

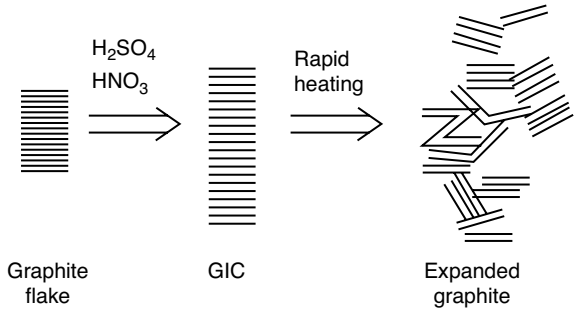

Figure 19.6 Schematic illustration making expanded graphite through the HNO_3–H_2SO_4 route [67] ("Preparation of polystyrene-graphite conducting nanocomposites via intercalation polymerization," G-H. Chen, D-J. Wu, W-G. Weng *et al.*, *Polymer International*, **50**, 980–985, © 2001, Copyright Society of Chemical Industry. Reproduced with permission. Permission is granted by John Wiley & Sons Ltd on behalf of the SCI.)

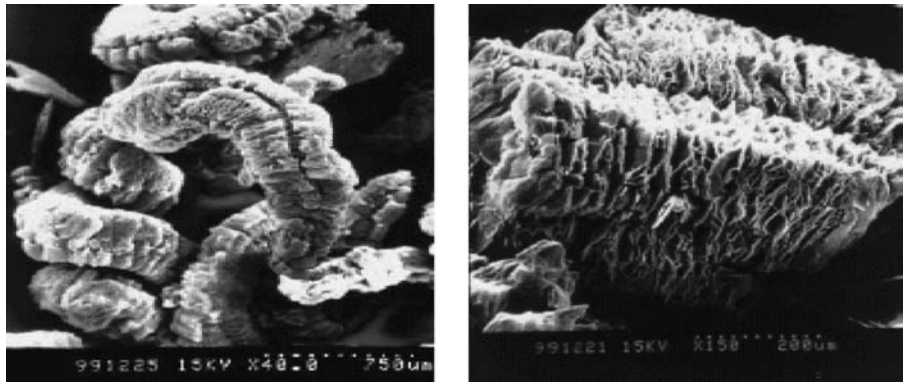

Figure 19.7 Scanning electron micrographs of graphite and expanded graphite [67] ("Preparation of polystyrene-graphite conducting nanocomposites via intercalation polymerization," G-H. Chen, D-J. Wu, W-G. Weng *et al.*, *Polymer International*, **50**, 980–985, © 2001, Copyright Society of Chemical Industry. Reproduced with permission. Permission is granted by John Wiley & Sons Ltd on behalf of the SCI.)

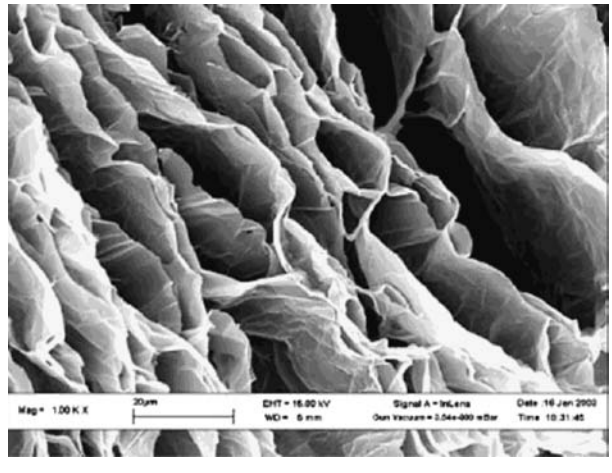

Figure 19.8 SEM of irregular honeycomb network of graphite sheets in expanded graphite [61] (Reprinted from *European Polymer Journal*, **39**, G-H. Chen, W-G. Weng, D-J. Wu and C-L. Wu, "PMMA/graphite nanosheets composite and its conducting properties," 2329–2335, © 2003, with permission from Elsevier.)

graphite sheet thickness observed surfacely and interiorly could largely due to an easier intercalate loss at the GIC surface when GIC is exposed to air.

EG consists of a large number of delaminated graphite sheets most of which have a thickness in nanometer, and it has been identified as conductive nanofillers to develop polymer/graphite nanocomposite. As EG has a high expansion ratio, the galleries of EG can be easily intercalated by monomers or polymer in solution. The EG of nanostructure can be blended with polymer via either the *in situ* polymerization or the solution compounding to achieve nanocomposite of

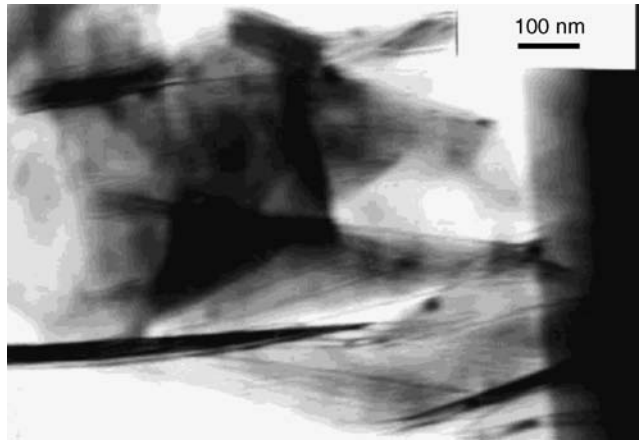

Figure 19.9 TEM of EG embedded in epoxy resin showing the inner nanostructure of EG [67] ("Preparation of polystyrene-graphite conducting nanocomposites via intercalation polymerization," G-H. Chen, D-J. Wu, W-G. Weng et al., *Polymer International*, **50**, 980–985, © 2001, Copyright Society of Chemical Industry. Reproduced with permission. Permission is granted by John Wiley & Sons Ltd on behalf of the SCI.)

polymer with graphite. Many works have been conducted on polymer/EG nanocomposites such as PMMA/EG [68], Nylon6/EG [69], PS/EG [70], PS-PMMA/EG [71] and so on, however studies on rubber-based EG nanocomposite are really much rare now.

19.2.4 Graphite Nanosheets

A crucial aspect in the production of polymer nanocomposites is the filler dispersion, which should be as homogeneously as possible. Aggregates of nanomaterial are proved to degrade the mechanical properties. Although polymer/graphite nanocomposites can be obtained via blending the EG with polymer directly, aggregates of graphite sheets may still exist in the composites, because the graphite sheets on EG interlock with each other firmly. The aggregates may also caused by the closed pores which hinder the penetration of monomers or polymer solution into the EG. As a result, the graphite sheets around such pores cannot be separated by polymer resin and they overlap each other, forming aggregates during processing.

In an attempt to enhance the nanodispersion of graphite in polymer matrix, Chen *et al.* sonicated the EG in an alcohol solution to make isolated graphite nanosheets (GNs) with a thickness range from 30 to 80 nm and a diameter of 5∼20 μm. [72, 73], whose SEM images are shown in Figure 19.10. Their apparent density is 0.015 g/cm^3, much smaller than the density of graphite flakes 2.25 g/cm^3 [52].

TEM observation of Figure 19.11 confirms that the GNs are composed of some thinner sheets with thickness of about 2–5 nm. This is in agreement with the thickness of thinner sheets inside EG. According to the mechanism for the formation of the GIC and EG, the thickness of GN was supposed to be as thin as a single carbon layer if the GNs precursor is GIC of stage 1. When the GIC were in stage 2 to stage 5, the thickness of the sheets in the vermicular graphite

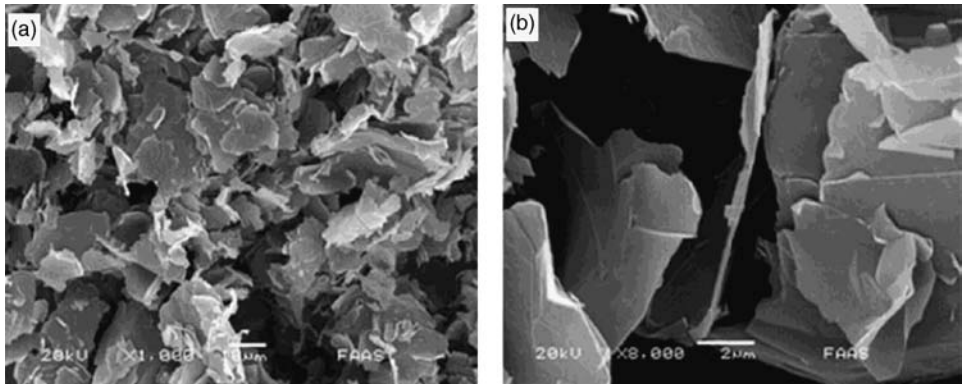

Figure 19.10 SEM of GNs: (a) lower magnification and (b) higher magnification (Reprinted from L. Chen, L. Lu, D-J. Wu et al., "Silicone rubber/graphite nanosheet electrically conducting nanocomposite with a low percolation threshold," *Polymer Composites*, **28**, 493–498, © 2007, with the permission of John Wiley & Sons, Inc.)

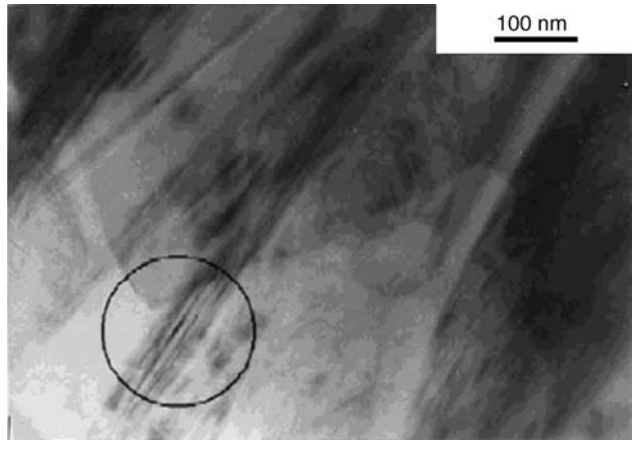

Figure 19.11 TEM of a sample of PMMA/GNs composites showing the thinner sheets inside EG (Reprinted from *Carbon*, **41**, no. 3, G-H. Chen, D-J. Wu, W-G. Weng and C-L. Wu, "Exfoliation of graphite flake and its nanocomposites," 619–621, © 2003, with permission from Elsevier.)

should be 0.5–2.5 nm, assuming the thickness of a single carbon layer was 0.5nm. Actually, When the equilibrium with excess external intercalate is removed, the GIC decomposes in a stepwise manner into a residue compound of higher stage [75–77]. During the process of washing thoroughly the fresh treated GIC with deionized water to remove excess acid, partial desorption of the intercalate was inevitable, strongly depending on the washing condition. The decomposition also occurs by exposing the graphite bisulfate to air [78]. Moreover, when the following thermal shock was brought to bear, there is competition between desorption of

intercalate out of the graphene layers and particle exfoliation [79]. Therefore, only part of the intercalates vaporized during exfoliation, and it must be extremely difficult to expand every graphite sheet from the intercalated layers. This may explain why only a fraction of the GNs have thicknesses ranging from 2 to 5 nm.

Selected area diffraction (SAD) conducted on a graphite nanosheet is very different from the SAD patterns of conventional graphite (Figure 19.12), suggesting the GNs are multicrystalline. The graphite crystals have been broken down into smaller ones by the thermal shock and sonication.

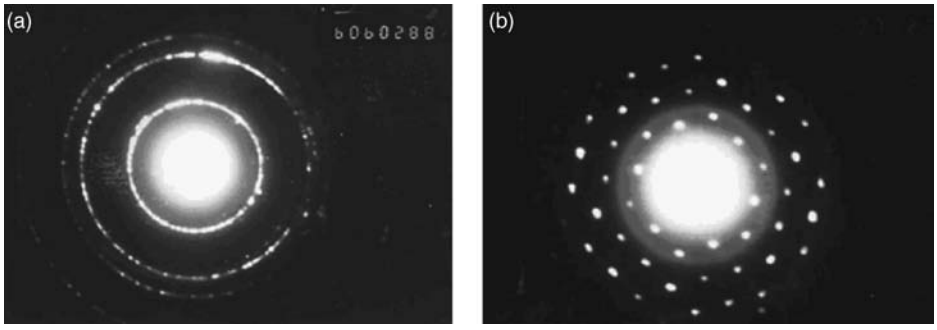

Figure 19.12 SAD on (a) graphite nanosheet; and (b) conventional graphite (Reprinted from *European Polymer Journal*, **39**, G-H. Chen, W-G. Weng, D-J. Wu and C-L. Wu, "PMMA/graphite nanosheets composite and its conducting properties," 2329–2335, © 2003, with permission from Elsevier.)

The high aspect ratio (width:thickness) of GNs around 100–500 gives much advantages in forming the conducting network in a polymer matrix, leading to a higher conductivity at a given loading level. This development offers people a new choice of conductive filler to fabricate conducting polymer nanocomposite.

19.2.5 Graphene and Graphite Oxide

Graphene is the name given to a single carbon layer of graphite. This graphite nanostructure with unique properties were originated newly by A.K. Geim of the University of Manchester, UK, together with his Russian colleagues, in 2004 [80]. In addition to good thermal conductivity, remarkable mechanical stiffness and high fracture strength, graphene has been supposed to be a semiconductor with zero gap which is quite different from conventional silicon semiconductors. In graphene, electrons shoot along with minimal resistance which may allow for low-power, faster-switching transistor and become a candidate to replace silicon in a fresh area of microchip electronics. "But it is difficult to turn graphene off, which will make it hard to use in an electrical switch," says Philip Kim, a physicist from Columbia University in New York [81].

Graphene is the basic structure for many carbon-based materials. It is well known that carbon exists in many forms: fullerene, diamond, multi- or single-wall carbon nanotubes and graphite to name a few. All of them are closely related to the graphene. Crystalline graphite, the most

thermodynamically stable form of carbon, is composed of graphene sheets stacked in an ...ABAB... sequence; the carbon nanotube structure is described as scrolled graphene with joining edges; both diamond and fullerene including five-membered rings can be derived from graphenes.

Two main routes are available to prepare graphene, one is from highly oriented pyrolytic graphite (HOPG) and the other one is from graphite oxide (GO). Heretofore, many material scientists have attempted to create individual graphene sheets using the intercalation/exfoliation method and have demonstrated several evolved procedures from expanded materials such as ball milling and ultrasonic powering [82]. But it is a pity that the resulted products from intercalated graphite typically contain hundreds of stacked graphene layers and yield tens nanometers of an average thickness. Then people realize that graphene should be pulled from a monolith of HOPG [83]. In 2004, A.K. Geim presented originally the micromechanical cleavage method of peeling layers from HOPG using "Scotch" adhesive tape and capturing the monolayers released in acetone on a Si wafer with a SiO_2 layer on its top [80]. However, this approach is severely limited by its very low yield, and it remains difficult and time-consuming to position a suitable single sheet for study, though a detecting technique has been improved somewhat by a combination of optical and atomic force microscopy. Undoubtedly, bulk quantities of product are desirable for industry applications. Starting from GO is a promising methodology to achieve this. The first attempt to produce GO dates from the work of Brodie in 1859 [84]. He obtained GO by treating graphite powder with an oxidation mixture of potassium chlorate and fuming nitric acid, repeatedly. Since then, many procedures have been developed. In the beginning, all were characterized by the use of potassium chlorate and by constant hazards. In 1958, Hummers cooperated with Offeman to present a rapid and relatively safe method of accomplishing the oxidation by treating graphite with a mixture of concentrated sulfuric acid, sodium nitrate and potassium permanganate, which are most commonly used at the present time [85].

In contrast to the pristine graphite, GO is also a layered material but is heavily oxygenated, leading to an enhanced interaction with water. Thus, GO is hydrophilic and water-dispersible due to the presence of hydroxyl and epoxide on their basal planes, in addition to carbonyl and carboxyl groups located on the edge atoms; it readily completely exfoliates into single graphene oxide layers of low electrical conductivity in aqueous media upon sonication. In order to increase its electrical conductivity, the chemical reduction of graphene oxide is usually carried out with hydrazine or their derivatives such as dimethylhydrazine at 80 °C, presumably owing to the restoration of graphitic network of sp^2 bond during the reaction [82, 83, 86].

19.3 Rubber/Graphite Nanocomposites

In Section 19.1, it was mentioned that rubber composites are a particular class of materials and can be widely used in many specialized fields. Although, for the real applications, a set of novel properties, including high strength, good electric and thermal conductivities and improved tribological properties are of interest, rubber/graphite nanocomposites certainly hold tremendous potential in many application fields. Due to the high aspect ratio and the increased relative surface area, graphite nanostructures are idea nanofillers to impart either strength or functions to rubbers. This section discusses the fabrication methodologies, characterization techniques, novel properties and potential applications for rubber/graphite nanocomposites.

19.3.1 Preparation, Processing and Characterization

For preparing rubber/graphite nanocomposites, it is crucial to ensure a fine dispersion of fillers, in addition to a strong interfacial interaction between graphite and rubber which is also very important. Rubber/graphite nanomaterials are mainly prepared by incorporating EG or GNs into the rubber matrix by a proper blending methodology. Various techniques can be selected purposely to determine the structure of rubber/graphite nanocomposites. Techniques including wide-angle X-ray diffraction (WAXD), small-angle X-ray scattering (SAXS), scanning electron microscopy (SEM) and transmission electron microscopy (TEM) are powerful characterization means, and all of them are used extensively nowadays.

19.3.1.1 Rubber Nanocomposites Reinforced by EG

EG is the most intensely used filler for the preparation of polymer/graphite nanocomposites. The EG/polymer systems are believed to be light weight and conductive. As EG is wormlike with delaminated graphite nanosheets building framework with many pores in different size, by proper processing methods, the pores can be readily inhabited by monomers or macromolecules in a liquid state. During subsequent polymerization or solidification, the interlinked nanosheets are separated platelet by platelet, and they reassemble to form a dispersed phase in a matrix whose homogeneity strongly depends on the mixing technique. Moreover, by *in situ* polymerization the galleries of graphite sheets in EG can also be intercalated simultaneously to a certain extent. Li *et al.* investigated influence of graphite particle size and shape on the properties of NBR containing 26 wt% of acrylonitrile. They found that it was difficult to break EG into very small particles when blended with rubber on a twin roller [8]. In fact, for preparing rubber/graphite nanocomposites from EG, it is still a challenge to further exfoliate EG into isolated nanoplatelets completely and ensure a satisfactory dispersion of EG in the rubber matrix, even though a strong force is available during conventional blending processing. This because graphite nanosheets composing EG are interlinked with each other forming a very loose vermicular structure which is easily broken down or compressed to a dense state during the mixing of EG and rubber and also due to the flexibility and high viscosity of rubber materials. It seems not easy to let rubber macromolecules encroach the void space of EG by direct mechanical blending such as melting mixing, not to mention graphite gallery intercalation.

19.3.1.2 Rubber Nanocomposites Reinforced by GNs

As discussed previously, being different from porous EG, GNs are separated graphite platelets with a thickness in the nanometer scale prepared from EG, and they can be more readily dispersed into polymer matrix via *in situ* polymerization, melting bending, solution mixing and other techniques.

Silicon rubber with excellent elastic, thermal and mechanical properties in addition to very good environmental stability has been chosen as a binder by Chen *et al.* to fabricate pressure-sensitive nanocomposites, and a wet mixing method was used to achieve a homogenously dispersion of GNs in the silicon rubber matrix [41]. Zhang' group cooperated with Mai's obtained high-performance nitrile-butadiene rubber (NBR)/GN nanocomposites with improved mechanical and functional properties via a latex compounding method [87].

This method was deemed to contribute to not only a fine nanoscale dispersion of graphite in rubber but also an improved interfacial adhesion between the graphite and the rubber matrix.

19.3.1.3 Characterization

The nanostructure of the final nanocomposites can be verified by a combination of microscopic morphology investigation and XRD structural analysis. Morphologies of freeze-fractured surfaces of NBR/graphite nanocomposites and image of sonicated EG fillers are listed in Figure 19.13a–f; the corresponding XRD patterns at both wide and small angles (Figure 19.13g,h) are also presented.

Observed from SEM images, the distribution states of fillers can be seen clearly. The SEM images also reveal the conditions of interface between the graphite nanosheets and rubber matrix. Figure 19.13a displays the SEM images of the sonicated EG, which are identical with GNs obtained by Chen's group. In contrast to Figure 19.13b, Figure 19.13c–d show a much better dispersion of GNs in rubber matrix and a finer interfacial adhesion between them. The dark line in TEM images corresponds to the nanometer-scale graphite and strongly confirms the nanoscale incorporation of graphite fillers into rubber. Chen *et al.* used SEM to show the state of GNs dispersed in silicon rubber. Meng *et al.* reported the TEM analysis to indicate the separation and delamination of EG within NBR matrix using an internal mixer [88]. In the XRD patterns, compared with the neat rubber (curves of Figure 19.13b1 and c1), the characteristic peak diffracted from the basal plane of graphite still remains at about $2\theta = 26.6^\circ$ after compounding (curves of Figure 19.13b2 and b3) via two different blending techniques; at small angle, the several peaks in curves of Figure 19.13c2 and c3 before and after composition respectively were assigned to exfoliation, intercalation and separation of graphite by Zhang *et al.* [87].

19.3.2 Properties and Applications

To satisfy practical application, composites that combine not only good mechanical properties but also versatile functions are favored. By adding nanofillers into a polymer matrix, the physical properties of polymer composites can be modified and changed dramatically due to the nanomaterials' unique characteristics arising from their much limited size, which can hardly be achieved through conventional microcomposites. In contrast to insulating rubber materials, graphite is rigid with a sound electrical conductivity and is naturally abundant, and both the mechanical and the electrical properties of rubber/graphite nanocomposites are of great interest to materials designers.

19.3.2.1 Mechanical Properties

Meng *et al.* reported their studies on NBR/EG nanocomposites by mixing NBR and EG in an internal mixer. In their work, mechanical properties significant improvement at a loading of only 5.0 wt% EG, the tensile strength increased by 78% with a slightly decrease in elongation at break, and an remarkable enhancement on storage modulus was more than 90% below glass transition temperature for the composite containing 5.0 wt% EG [88]. The mechanical properties of polymer nanocomposites are strongly affected by the degree of filler dispersion. Zhang and Mai [87] incorporated GNs into NBR matrix using a latex compounding method (LCM), where the NBR rubber was used in latex form and the mixture was coagulated by a

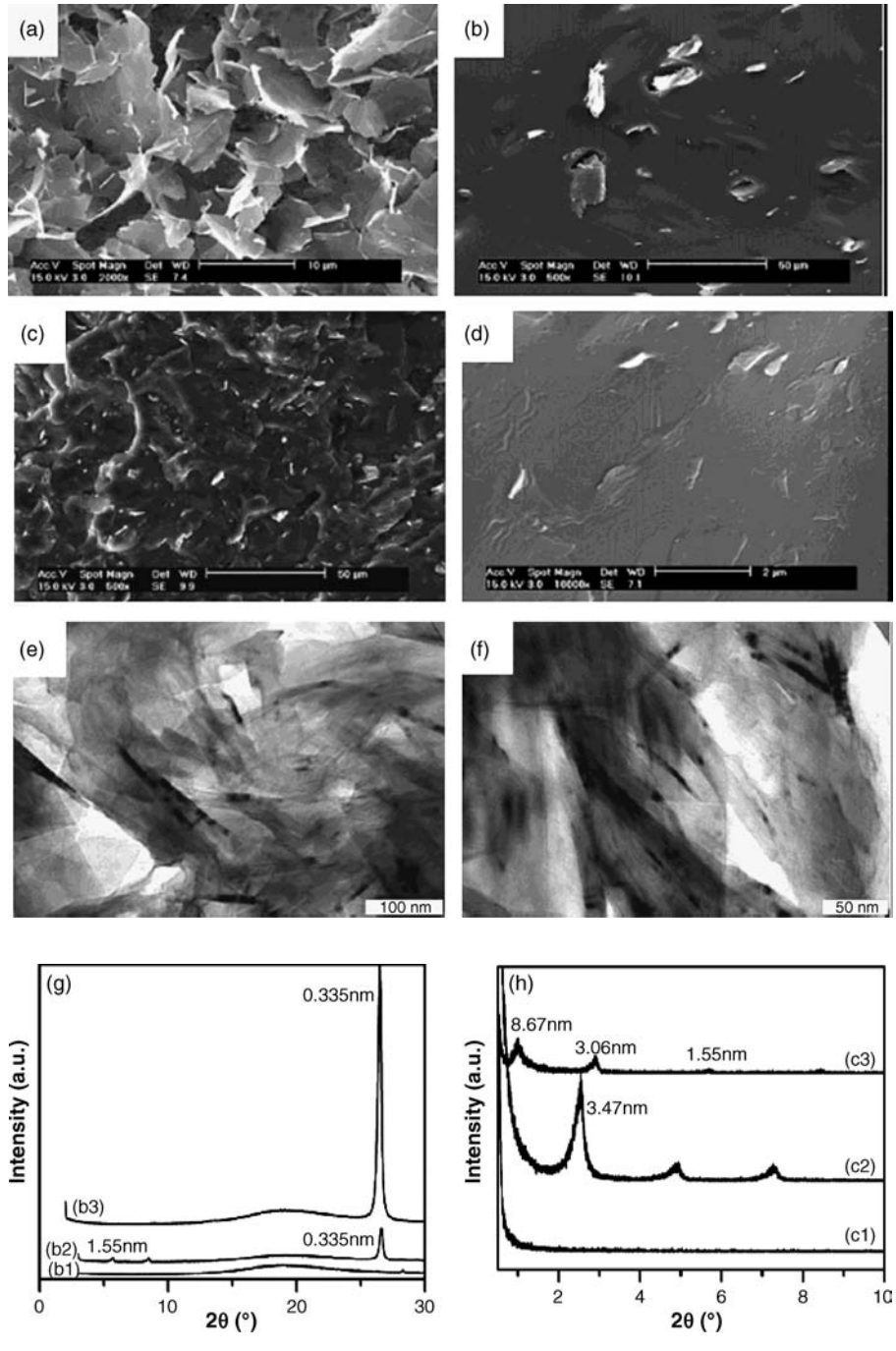

Figure 19.13 (a–f) SEM/TEM images and (g–h) WAXD/SAXD patterns of either GNs or their NBR composites (Reprinted from *Acta Materialia*, **55**, J. Yang, M. Tian, Q-X. Jia, J-H. Shi, L-Q. Zhang, S-H. Lim, Z-Z. Yu and Y-W. Mai, "Improved mechanical and functional properties of elastomer/graphite nanocomposites prepared by latex compounding," 6372–6382, © 2007, with permission from Elsevier.)

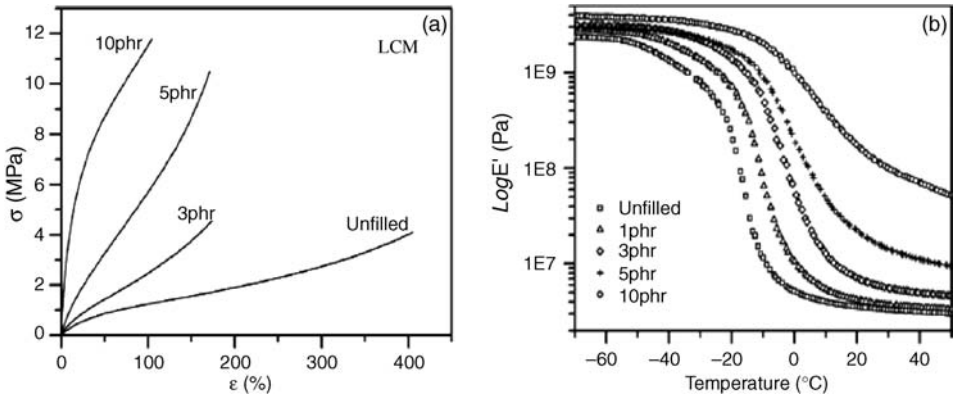

Figure 19.14 (a) Tensile stress–strain curves and (b) storage modulus of NBR/GNs composites prepared by the latex compounding method with different filler content (Reprinted from *Acta Materialia*, **55**, J. Yang, M. Tian, Q-X. Jia, J-H. Shi, L-Q. Zhang, S-H. Lim, Z-Z. Yu and Y-W. Mai, "Improved mechanical and functional properties of elastomer/graphite nanocomposites prepared by latex compounding," 6372–6382, © 2007, with permission from Elsevier.)

subsequent adding of $CaCl_2$ aqueous solution. They demonstrated that LCM is facile to give a fine dispersion of GNs and more interfacial interactions, resulting in greatly increased strength and storage modulus (Figure 19.14). LCM and solution intercalation method display a better effect than melt mixing in improving the mechanical properties of rubber/graphite nanocomposites, as shown in Figure 19.15 [87, 89], the storage modulus of composites prepared by

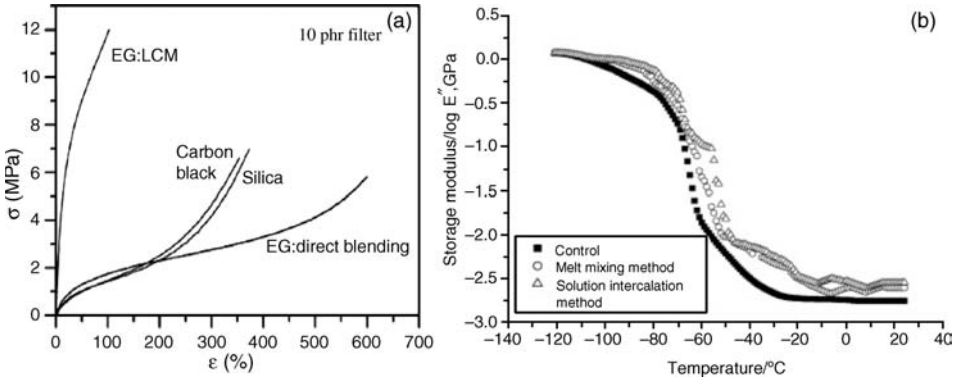

Figure 19.15 (a) Tensile stress–strain curves and (b) storage modulus of rubber/graphite nanocomposites prepared by different compounding techniques. (a) (Reprinted from *Acta Materialia*, **55**, J. Yang, M. Tian, Q-X. Jia, J-H. Shi, L-Q. Zhang, S-H. Lim, Z-Z. Yu and Y-W. Mai, "Improved mechanical and functional properties of elastomer/graphite nanocomposites prepared by latex compounding," 6372–6382, © 2007, with permission from Elsevier.) (b) (Reprinted from *Thermochimica Acta*, **462**, Q. Mu and S. Feng, "Thermal conductivity of graphite/silicone rubber prepared by solution intercalation," 70–75, © 2007, with permission from Elsevier.)

solution intercalation are greater than that of composites fabricated by melt mixing method, and the tensile strength is raised much more remarkably with increasing strain for LCM-prepared composites when compared with the tensile of composites manufactured using a direct melt blending method. Chen *et al.* [74] investigated the mechanical properties of silicon rubber nanocomposites with various GNs content, and their results are presented in Figure 19.16. The elastic modulus of the nanocomposite which is rather sensitive to the speed of applied compression was rised apparently with increasing GNs and could be further enhanced by the addition of Al_2O_3 nanoparticles.

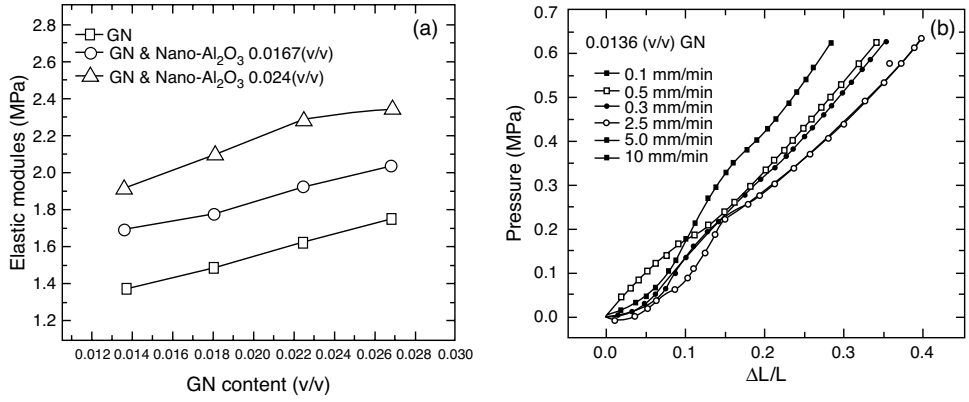

Figure 19.16 (a) Elastic modulus at various GNs fraction and (b) pressure–strain curves under different compression speed for silicon rubber/GNs nanocomposites (Reprinted from L. Chen, L. Lu, D-J. Wu et al., "Silicone rubber/graphite nanosheet electrically conducting nanocomposite with a low percolation threshold," *Polymer Composites*, **28**, 493–498, © 2007, with the permission of John Wiley & Sons, Inc.)

19.3.2.2 Electrical Properties

Great improvement in electrical conductivity is achieved by the incorporation of graphite nanoplatelets into rubber materials [87, 88, 90]. A sharp transition of the rubber from an electrical insulator to electrical conductor with the addition of GNs takes place at a certain filler fraction, which is much lower than the filler content of rubber/conventional graphite composites, as shown in Figure 19.17 [90]. With just a low fillers concentration needed, not only can material redundancy and detrimental mechanical properties be effectively avoided, but also the cost is reduced.

Apart from the high conductivity and low percolation threshold, due to the combination of viscoelastic mechanical properties of rubber and the electrical conductivity from conducting fillers, electrical conductive rubber composites always exhibit variable conductivity in response to varying applied pressure which is known as the piezoresistive effect. Piezoresistive behavior is another interesting property for rubber/graphite nanocomposites. Detailed studies have been carried out on the pressure-sensing properties of silicon rubber/GNs nanocomposites by Chen *et al.* [41]. They demonstrated that the silicon rubber/GNs nanocomposite with 1.36 vol% GNs near the percolation threshold exhibits a super positive pressure coefficient (PPC) effect with good repeatability in the finger-pressure range, as shown in Figure 19.18. The

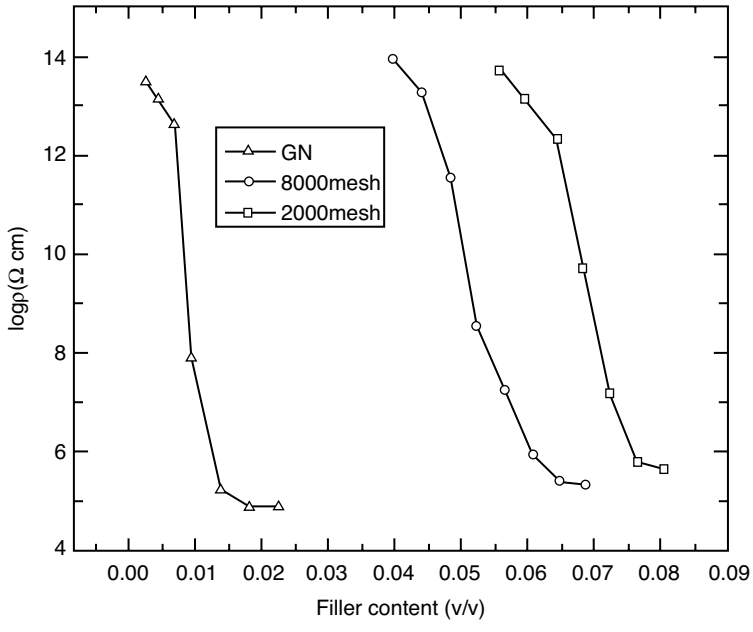

Figure 19.17 Electrical conductivities of rubber reinforced by graphite of different types (Reprinted from L. Chen, L. Lu, D-J. Wu et al., "Silicone rubber/graphite nanosheet electrically conducting nanocomposite with a low percolation threshold," *Polymer Composites*, **28**, 493–498, © 2007, with the permission of John Wiley & Sons, Inc.)

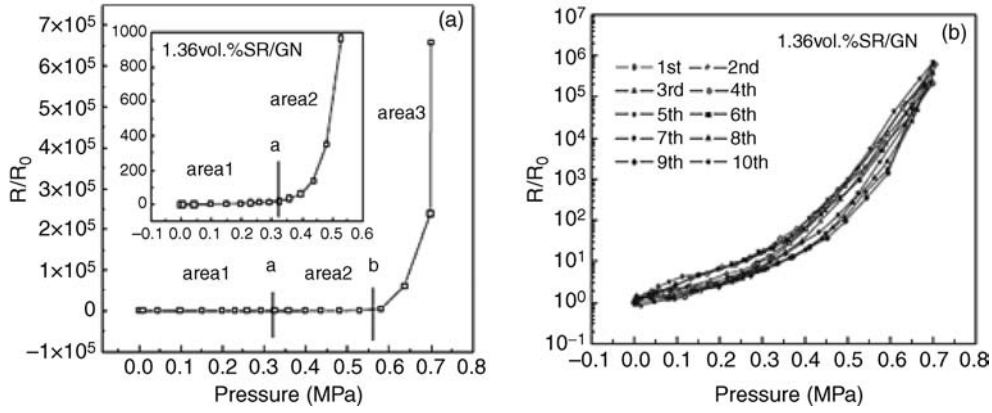

Figure 19.18 (a) Relative resistance of silicon/GNs composite with 1.36 vol% GNs as a function of applied pressure (b) and its repeatable piezoresistive behaviors under cyclic compression (Reproduced with permission from L. Chen, G-H. Chen, L. Lu, "Piezoresistive behavior study on finger-sensing silicone rubber/graphite nanosheet nanocomposites," *Advanced Functional Materials*, **17**, no. 6, 898–904, © 2007, Copyright Wiley-VCH Verlag GmbH & Co. KGaA.)

experimental results can be explained well using the tunneling conduction model, suggesting that under external pressure the charge carrier transport in silicon rubber/GNs composites is mainly controlled by the tunneling-conduction mechanism.

19.3.2.3 Other Properties

Graphite is multifunctional, its lubricant property and thermal conductivity are also well known, except for its stiffness and excellent electrical conductivity. Feng *et al.* paid special attentions on the thermal conductivity of silicon rubber/EG composites and found that the thermal conductivities of silicon rubber/EG nanocomposites improved apparently with increased EG content, and solution intercalation methods were more crackajack than the conventional melt mixing method in improving the thermal conductivity of silicone/EG composites [89]. Zhang and Mai *et al.* achieved NBR/sonicated EG nanocomposites with improved wear resistance, better gas barrier properties and superior thermal conductivity using a latex compounding method [87]. Shen *et al.* reinforced silicon rubber with modified graphite oxides (GO) exfoliated into platelets of nanoscale thickness using a solution intercalation method [90]. The silicon/GO nanocomposite was proved to be a novel anticoagulative biomaterial with good mechanical properties, biocompatibility and longtime blood compatibility from graphite oxide and silicon rubber, which is expected to satisfy wide applications in future medical treatment.

19.3.2.4 Potential Applications

As discussed earlier, graphite holds a significant role in improving the properties of rubber materials. Much research has been conducted with graphite particles and rubbers, purposely focusing on the mechanical, tribological, thermal, electrical and other properties of their composites. Rubber materials containing graphite can find applications in sealing, electromagnetic radiation and electrostatic protection, electrodes, sensors and so on. For example, Cavalheiro *et al.* reported that silicon rubber composite composed of 70 wt% graphite showed a good voltammetric response, making them a favorable material for preparing voltammetric sensor devices. Additionally, they can be used as anodic electrode materials in neutral and acidic medias widely related to their useful potential windows [91]. Ol'shevskij *et al.* developed electric-conducting rubber containing carbon black and graphite with a 3 : 1 ratio to prevent computer hardware being exposed to external electromagnetic waves [92]. Being more advanced than conventional rubber/graphite composites, the nanocomposite materials have great improvements both in performance and potential applications arising from their high aspect ratio of graphite nanoplatelets. Rubber materials can be modified more effectively by adding these graphite nanofillers. For rubber/graphite nanocomposites, both their mechanical and functional properties can be improved remarkably with an addition of small amount of graphite fillers, which seems hard to achieve by adding conventional graphite particles of the micrometer order. Therefore their advantages and potential applications are obvious. There is little doubt that rubber/graphite nanocomposites offer people a superexcellent alternative for fabricating rubber materials of fascinating properties with a favored low filler concentration to fulfill the special requirements of various practical applications. Many believe graphite nanoplatelets will edge aside traditional graphite powders in composites of the future.

19.4 Future Outlook

Realistically, up-to-the-minute, scant literature has been published on rubber/graphite nanocomposites, and the rubber nanomaterials are just underway. However, some of the initial successes have demonstrated that graphite nanoplatelets are idea nanofillers to provide dramatic reinforcement and multifunction to rubbers; the potential of rubber materials loaded graphite nanoplatelets is undoubtedly tremendous and promising. However, people still face many critical issues when creating versatile rubber/graphite compounding materials by designing their structures at the nanometer scale. One of the biggest challenges in the research of rubber/graphite nanocomposites is to develop composition technologies for improving the exfoliation and dispersion of graphite fillers in matrix beside the enhancement of graphite matrix interfacial adhesion, which is equally essential. Graphite is a layered material with unique natural functions, so in order to achieve higher reinforcement efficiency graphite layers should be intercalated, exfoliated and separated as widely as possible, except that a good dispersion throughout the matrix phase is also indispensable. In fact, it seems not very easy to ensure improvements in the separation and dispersion of graphite in ways starting with EG using traditional methods of directly melt blending with rubber as reported by Li *et al.* [8]. Similar results were also noted in other studies using a twin roller or internal mixer for compounding [88, 89]. Furthermore, from the intercalation mechanism viewpoint, the graphite original gallery with 0.335 nm spacing cannot be intercalated by rubber macromolecules, limiting the exfoliation and separation of graphite during direct mix processing. Fortunately, it is hoped this limitation can be overcame by the emergence of graphene, the monolayer of graphite at the atomic scale, which has a great deal of promise as a future conductive graphitic nanofiller for exploiting high-performance rubber materials [86], although their production in quantity has seemed decades away.

Clearly industry and a diverse range of other sectors related to rubber materials will benefit significantly from the introduction of graphite nanofillers, provided excellent techniques for their composition are available. To explore such rubber-based nanocomposite materials of novel properties, deep investigations surrounding the complete exfoliation and dispersion of graphite fillers into matrix, nicer compatibilities, the development of advanced functions, strategy optimization for improved mechanical and functional properties and other fundamental researches will be strongly required in the future.

Acknowledgments

The authors thank the support of the National Natural Science Foundation of China (no. 50373015, 20574025).

References

1. Norman, R.H. (1970) *Conductive Rubbers and Plastics*, Elsevier, Amsterdam, p. 53.
2. Abdel-Bary, E.M. (1979) Factors affecting electrical conductivity of carbon black-loaded rubber-2. Effect of concentration and type of carbon black on electrical conductivity of SBR. *Journal of Polymer Science Part A Polymer Chemistry*, **17**, 2163.
3. Nir, Z., Gilwee, W.J., Kourtides, D.A., and Parker, J.A. (1985) Polyfunctional epoxies: part II. Nonrubber versus rubber-toughened brominated formulations for graphite composites. *Polymer Composites*, **6**(2), 72–81.

4. Herrmann, K.P. and Oshmyan, V.G. (2002) Theoretical study of formation of pores in elastic solids: particulate composites, rubber toughened polymers, crazing. *International Journal of Solids and Structures*, **39**(11), 3079–3104.
5. Wang, J.Y., Vincent, J., and Quarles, C.A. (2005) Review of positron annihilation spectroscopy studies of rubber with carbon black filler. *Nuclear Instruments & Methods in Physics Research Section B Beam Interactions with Materials and Atoms*, **241**(1–4), 271–275.
6. Zhang, W., Dehghani-Sanij, A.A., and Blackburn, R.S. (2007) Carbon based conductive polymer composites. *Journal of Materials Science*, **42**(10), 3408–3418.
7. Shiro, N., Katsuzo, O., and Toshio, K. (1994) Wet friction characteristics of new resilient graphitic friction material. *Transactions of the Japan Society of Mechanical Engineers, Part C*, **60**(572), 1376–1381.
8. Yang, J., Tian, M., Jia, Q.X. *et al.* (2006) Influence of graphite particle size and shape on the properties of NBR. *Journal of Applied Polymer Science*, **102**, 4007–4015.
9. Lu, Y. (2003) A golden section approach to optimization of automotive friction materials. *Journal of Materials Science*, **38**, 1081–1085.
10. Lu, Y., Tang, C.F., and Wright, M.A. (2002) Optimization of a commercial brake pad formulation. *Journal of Applied Polymer Science*, **84**, 2498–2504.
11. Stair, W.K. (1983) *Handbook of Lubrication (Tribology). Vol. II: Dynamic Seals* (ed. E.R. Booser), CRC Press, Boca Raton, FL, pp. 581–622.
12. Schweitz, J.A. and Ahman, L. (1986) Chapter 9, in *Friction and Wear of Polymer Composites* (ed. K. Fredrich), Elsevier, Amsterdam.
13. Norman, R.H. (1970) *Conductive Rubber and Plastics*, EPC, New York, p. 270.
14. Sircar, A.K. (1981) Softer conductive rubber compounds by elastomer blending. Rubber Chemistry and Technology *Rubber Chemistry and Technology*, **54**, 820–834.
15. Gui, V.E. and Shenfil, L.Z. (1984) *Conductive Polymer Compositions*, Khimiya, Moscow, p. 240.
16. Jana, P.B., Mallick, A.K., and De, S.K. (1991) Electromagnetic interference shielding by carbon fibre- filled polychloroprene rubber composites. *Composites*, **22**(6), 451–455.
17. Sau, K.P., Chaki, T.K., and Khastgir, D. (1997) Conductive rubber composites from different blends of ethylene-propylene-diene ubber and nitrile rubber. *Journal of Materials Science*, **32**, 5717–5724.
18. Pramanik, P.K., Khastgir, D., and Saha, T.N. (1992) Effect of some processing parameters on the resistivity of conductive nitrile rubber composites. Plastics, Rubber and Composites Processing and Applications *Plastics, Rubber and Composites Processing and Applcations*, **17**(3), 179–185.
19. Chen, Y.C., Yin, W.S., Zhang, S.X. *et al.* (2000) SBS/LPB/Pan conductive rubber complex. *Polymeric Materials Science and Engineering*, **16**(1), 77–79.
20. Mohanraj, G.T., Chaki, T.K., Chakraborty, A., and Khastgir, D. (2007) Measurement of AC conductivity and dielectric properties of flexible conductive styrene-butadiene rubber-carbon black composites. *Journal of Applied Polymer Science*, **104**(2), 986–995.
21. Sau, K.P., Chaki, T.K., and Khastgir, D. (1998) Carbon fibre filled conductive composites based on nitrile rubber (NBR), ethylene propylene diene rubber (EPDM) and their blend. *Polymer*, **39**, 6461–6471.
22. Park, E.S., Jang, L.W., and Yoon, J.S. (2005) Resistivity and thermal reproducibility of carbon black and metallic powder filled silicone rubber heaters. *Journal of Applied Polymer Science*, **95**, 1122–1128.
23. Housh, R. and Komppa, V. (1987) Overview of plastics development and new commercial plastics. Kemia-Kemi/Finnish Chemical Journal. *Kemia Kemi/Finnish Chemical Journal*, **14**(4), 366–371.
24. Pramanik, P.K., Khastgir, D., and Saha, T.N. (1991) Electromagnetic interference shielding by conductive nitrile rubber composites containing carbon fillers. *Journal of Elastomers and Plastics*, **23**(4), 345–361.
25. Bengt, M. and Bengt, S. (1992) Electrical conductivity of thermo-oxidatively-degraded EPDM rubber. *Rubber Chemistry and Technology*, **65**(2), 315–328.
26. Kowalik, D.P. and Chung, D.D.L. (2002) Carbon black filled silicone as a compliant thermoelectric material. *Journal of Reinforced Plastics and Composites*, **21**(17), 1587–1590.
27. Piazza, S. (1977) electrostatic charges in polymers and the problem of their dissipation. *Poliplasti e Plastici Rinforzati*, **25**(236/237), 49–53.
28. Martins, C.R., Faez, R., Rezende, M.C., and De Paoli, M.A. (2006) Reactive processing and evaluation of butadiene-styrene copolymer/polyamline conductive blends. *Journal of Applied Polymer Science*, **101**(1), 681–685.
29. Anonymous (1995) ESPC has full compliance-precompliance capability. *Electron Engineering*, **67**(825), 19.

30. Kavrak, I. (1970) Conductive rubber pressure transducer for fluids research. *Review of Scientific Instruments*, **41** (5), 628–631.
31. Raper, R.L. and Arriaga, F.J. (2007) Comparing peak and residual soil pressures measured by pressure bulbs and stress-state transducers. *Transactions of the ASABE*, **50**(2), 339–344.
32. Hussain, M., Choa, Y.H., and Niihara, K. (2001) Effects of nano ceramics on electrical resistivity of carbon filled rubber materials. *Scripta Materialia*, **44**(8–9), 1203–1206.
33. Todorova, Z., El-Tantawy, F., Dishovsky, N., and Dimitrov, R. (2007) Investigation of conductivity characteristics of nitrile butadiene rubber vulcanizates filled with semiconducting carbide ceramic. *Journal of Applied Polymer Science*, **103**, 2158–2165.
34. Chen, X.D., Jiang, Y.D., Wu, Z.M. *et al.* (2000) Morphology and gas-sensitive properties of polymer based composite films. *Sensors and Actuators B Chemical*, **66**(1), 37–39.
35. Minns, R.J. (1982) Conductive rubber footswitch design for gait analysis. *Journal of Biomedical Engineering*, **4**(4), 328–330.
36. Vanderbilt, B.M. and Chipps, F.R. (1984) Old and new problems are solved by polymers containing graphite. *Research and Development*, **26**(5), 118–123.
37. Peterson, A.L., Cull, R.A., and McMahon, D.F. (1991) Advances in trapped rubber molding new materials and techniques. *International SAMPE Symposium and Exhibition Proceedings*, **36**, 959–970.
38. Reznikova, L.L., Smorygo, L.N., Tikhomirov, A.F., and Ol'shevskij, O.I. (1992) Electric conducting rubber for computer hardware. *Elektrotekhnika*, **6/7**, 65–66.
39. Anely, J.N. and Khananashvili, L.M. (1994) Effect of technological factors on electric conductivity of filled silicon elastomers. *International Journal of Polymeric Materials*, **25**(3/4), 235–241.
40. Carrillo, A., Martin-Dominguez, I.R., Glossman, D., and Marquez, A. (2005) Study of the effect of solvent induced swelling on the resistivity of butadiene based elastomers filled with carbon particles. Part I. Elucidating second order effects. *Sensors and Actuators A Physical*, **119**(1), 157–168.
41. Chen, L., Chen, G.H., and Lu, L. (2007) Piezoresistive behavior study on finger-sensing silicone rubber/graphite nanosheet nanocomposites. *Advanced Functional Materials*, **17**(6), 898–904.
42. Zhang, J. and Feng, S.Y. (2003) Temperature effects of electrical resistivity of conductive silicone rubber filled with carbon blacks. *Journal of Applied Polymer Science*, **90**(14), 3889–3895.
43. Cataldo, F. (2005) Fullerene-like structures as interaction sites between carbon black and rubber. *Macromolecular Symposia*, **228**, 91–98.
44. Thostenson, E., Li, C., and Chou, T. (2005) Nanocomposites in context. *Composites Science and Technology*, **65**, 491–516.
45. Chung, D.D.L. (2002) Review: graphite. *Journal of Materials Science*, **37**, 1475–1489.
46. Robert, M.C., Oberlin, M., and Mering, J. (1973) *Chemistry and Physics of Carbon*, vol. **10**, Marcel Dekker, New York, p. 141.
47. Ubbelohde, A.R. (1972) Intercalation overpotentials for compound formation by graphite. *Carbon*, **10**(2), 201–206.
48. Shioyama, H. (2000) Interactions of two chemical species in the interlayer spacing of graphite. *Synthetic Metals*, **114**, 1–15.
49. Rudorff, W. and Hofmann, U. (1938) Über Graphitsalze. *Zeitschrift Fur Anorganische und Allgemeine Chemie*, **238**, 1.
50. Henning, G.R. (1959) Interstitial compounds of graphite. *Progress in Inorganic Chemistry*, **1**, 125.
51. Thiele, H. (1932) Über die Quellung von Graphit. *Zeitschrift fur Anorganische und Allgemeine Chemie*, **206**, 407.
52. Berlouis, L.E.A. and Schiffrin, D.J. (1983) Electrochemical formation of graphite–bisulphate intercalation compounds. *Journal of Applied Electro Chemistry*, **13**(2), 147–155.
53. Beck, F., Junge, H., and Krohn, H. (1981) Graphite intercalation compounds as positive electrodes in galvanic cells. *Electrochimica Acta*, **26**, 799–809.
54. Chuan, X., Chen, D., and Zhou, X. (1997) Intercalation of CuCl2 into expanded graphite. *Carbon*, **35**, 311–313.
55. Fukuda, K., Kikuya, K., Isono, K., and Yoshio, M. (1997) Foliated natural graphite as the anode material for rechargeable lithium-ion cells. *Journal of Power Sources*, **69**, 165–218.
56. Hashimoto, K., Sumitomo, H., and Kowasumi, M. (1984) Preparation of a new polyamide macromer having a vinylbenzyl group from bicyclic oxalactam and its radical copolymerization with styrene. *Polymer Bulletin*, **11**, 121–128.

57. Shioyama, H. and Fujii, R. (1987) Electrochemical reactions of state 1 sulfuric acid-graphite intercalation compound. *Carbon*, **25**(6), 771–774.
58. Rigaux, C. and Blinowski, J. (1982) Electronic properties of graphite intercalation compounds. *Lecture Notes in Physics*, **1982**, 352–362.
59. Mcdonnell, F.R.M., Pink, R.C., and Ubbelohde, A.R. (1951) Some physical properties associated with "aromatic" electrons. Part III. The pseudo metallic properties of potassium-graphite and graphite-bromine. *Journal of the Chemical Society*, **1951**, 191.
60. Sasa, T., Takahashi, Y., and Mukaibo, T. (1971) Crystal structure of graphite bromine lamellar compounds. *Carbon*, **9**(4), 407–416.
61. Chen, G.H., Weng, W.G., Wu, D.J., and Wu, C.L. (2003) PMMA/graphite nanosheets composite and its conducting properties. *European Polymer Journal*, **39**, 2329–2335.
62. Thiele, H. (1938) The oxidation of carbon in electrolytes at normal temperature. *Transactions of the Faraday Society*, **34**, 1033.
63. Findeisen, B. and Thomasius, M. (1981) Ger. (East) DD150 739.
64. Dowell, M.B. (1975) Ext. Abstract Programme – *Biennial Conferences on Carbon, American Carbon Society*, vol. 12, pp. 31–32.
65. Martin, W.H. and Brocklehurst, J.E. (1964) The thermal expansion behaviour of pyrolytic graphite-bromine residue compounds. *Carbon*, **1**(2), 133–134.
66. Anderson, S.H. and Chung, D.D.L. (1983) Exfoliation of single crystal graphite and graphite fibers intercalated with halogens. *Synthetic Metals*, **8**, 343–349.
67. Chen, G.H., Wu, D.J., Weng, W.G. *et al.* (2001) Preparation of polystyrene-graphite conducting nanocomposite via intercalation polymerization. *Polymer International*, **50**, 980–985.
68. Zheng, W. and Wong, S.C. (2003) Electrical conductivity and dielectric properties of PMMA/expanded graphite composites. *Composites Science and Technology*, **63**, 225–235.
69. Pan, Y.X., Yu, Z.Z., Ou, Y.C., and Hu, G.H. (2000) New process of fabricating electrically conducting nylon 6/graphite nanocomposites via intercalation polymerization. *Journal of Polymer Science Part B-Polymer Physics*, **38**, 1626–1633.
70. Xiao, P., Xiao, M., and Gong, K. (2001) Preparation of exfoliated graphite/polystyrene composite by polymerization-filling technique. *Polymer*, **42**, 4813–4816.
71. Chen, G.H., Wu, D.J., Weng, W.G., and Yan, W.L. (2001) Preparation of polymer graphite conducting nanocomposite by intercalation polymerization. *Journal of Applied Polymer Science*, **82**, 2506–2513.
72. Chen, G.H., Wu, D.J., Weng, W.G., and Wu, C.L. (2003) Exfoliation of graphite flake and its nanocomposites. *Carbon*, **41**(3), 619–621.
73. Chen, G.H., Wu, C.L., Weng, W.G. *et al.* (2003) Preparation of polystyrene/graphite nanosheet composite polymer. *Polymer*, **44**(6), 1781–1784.
74. Chen, L., Lu, L., Wu, D.J., and Chen, G.H. (2007) Silicone rubber/graphite nanosheet electrically conducting nanocomposite with a low percolation threshold. *Polymer Composites*, **28**, 493–498.
75. Asano, M., Sasaki, T., Abe, T. *et al.* (1996) Mass-spectrometric study of vaporization of FeCl3-graphite intercalation compound. *Journal of Physics and Chemistry of Solids*, **57**, 787.
76. Ho C.T. and Chung, D.D.L. (1990) Kinetics of intercalate desorption from carbon fibers intercalated with bromine. *Carbon*, **28**(6), 825–830.
77. Hennig, G.R. (1952) The properties of the interstitial compounds of graphite. III. The electrical properties of the halogen compounds of graphite. *Journal of Chemical Physics*, **20**, 1438.
78. Frenzel, A. and Hofmann, U.Z. (1934) The constitution of graphite acid and its reactions. *Elektrochemie Angewandte Physics and Chemistry*, **40**, 511.
79. Furdin, G. (1998) Exfoliation process and elaboration of new carbonaceous materials. *Fuel*, **77**, 479–485.
80. Novoselov, K.S., Geim, A.K., Morozov, S.V. *et al.* (2004) Electric field in atomically thin carbon films. *Science*, **306**, 666–669.
81. Noorden, R.V. (2006) Moving towards a graphene world. *Nature*, **442**(20), 228–229.
82. Stankovich, S., Dikin, D.A., Piner, R.D. *et al.* (2007) Synthesis of graphene-based nanosheets via chemical reduction of exfoliated graphite oxide. *Carbon*, **45**, 1558–1565.
83. Gilje, S., Han, S., Wang, M. *et al.* (2007) A chemical route to graphene for device applications. *Nano Letters*, **7**(11), 3394–3398.
84. Brodie, B. (1859) On the atomic weight of graphite. *Philosophical Transactions of the Royal Society*, **149**, 249.

85. Hummers, W. and Offeman, R.E. (1958) Preparation of graphitic oxide. *Journal of the American Chemical Society*, **80**, 1339.
86. Stankovich, S., Dikin 1 D.A., Dommett, G.B. *et al.* (2006) Graphene-based composite materials. *Nature*, **442**(20), 282–286.
87. Yang, J., Tian, M., Jia, Q.X. *et al.* (2007) Improved mechanical and functional properties of elastomer/graphite nanocomposites prepared by latex compounding. *Acta Materialia*, **55**, 6372–6382.
88. Liu, D.W., Du, X.S., and Meng, Y.Z. (2005) Preparation of NBR/expanded graphite nanocomposites by simple mixing. *Polymers & Polymer Composites*, **13**(8), 815–821.
89. Mu, Q. and Feng, S. (2007) Thermal conductivity of graphite/silicone rubber prepared by solution intercalation. *Thermochimica Acta*, **462**, 70–75.
90. Chen, Y.H., Zhou, N.L., Meng, N. *et al.* (2007) Synthesis of polymer/modified graphite oxide biomaterials and in vitro antithrombogenicity assessment. *Journal of Functional Materials*, **38**(3), 438–440.
91. de Oliveira, A.C., dos Santos, S.X., and Cavalheiro, E.T.G. (2008) Graphite-silicone rubber composite electrode: preparation and possibilities of analytical application. *Talanta*, **74**(4), 1043–1049.
92. Reznikova, L.L., Smorygo, L.N., Tikhomirov, A.F., and Ol'shevskij, O.I. (1992) Electric conducting rubber for computer hardware. *Elektrotekhnika*, **6/7**, 65–66.

20

Aging and Degradation Behavior of Rubber Nanocomposites

Suneel Kumar Srivastava and Himadri Acharya
Inorganic Materials and Nanocomposites Laboratory, Department of Chemistry, Indian Institute of Technology, Kharagpur 721302, India

20.1 Introduction

Nanocomposites are multiphase materials containing two or more distinctly dissimilar components mixed at nanometer scale. They belong to inorganic–inorganic, inorganic–organic, or organic–organic nanocomposites where the resulting materials may be amorphous, crystalline or semicrystalline. These nanocomposites very often display new and improved mechanical, catalytic, electronic, magnetic and optical properties not exhibited by the individual phases or by their macrocomposite and microcomposite counterparts. This indeed influences materials scientists to prepare tailor-made advanced materials. The basic reason for the synergistic improvement in their properties is not completely understood to date. It is of particular interest that polymer nanocomposites having inorganic particles of within nanoscale dimensions in the family of organic–inorganic nanocomposites have received considerable attention because of their much improved unique properties and numerous potential applications in automotive, aerospace, construction, electronic purposes and so on [1–3]. Since then nanolevel dispersion of inorganic materials especially clays in the polymer matrix has unfolded a new and interesting chapter in the field of materials science [4]. As a result in recent years, increasing attention has been paid to nanocomposites of rubbers, for example, natural rubber (NR) [5], EVA [6–10], (ethylene-propylene diene monomer (EPDM) [11–13], nitrile-butadiene rubber (NBR) [14], hydrogenated nitrile-butadiene rubber (HNBR) [15], styrene-butadiene rubber (SBR) [16], silicone rubber (SR) [17] and 1,4 polybutadiene (BR) [18] prepared via solution intercalation, melt intercalation and rubber latex compounding.

Rubber Nanocomposites: Preparation, Properties and Applications Edited by Sabu Thomas and Ranimol Stephen
© 2010 John Wiley & Sons (Asia) Pte Ltd

The aging of a polymer is usually due to changes in its chemical structure caused by heat, ultraviolet light, or chemical attack. Natural aging is one such example where polymers exposed can degrade through the action of several agents, UV radiation, water; pollutants and so on. The changes due to aging may also be reflected in the properties of a polymer. The most common form of aging in polymers is physical aging, that is, aging that takes place without any chemical reaction. This phenomenon is very common and is encountered in thermoplastic elastomers at elevated temperature [19]. Thermal aging is the acceleration of physical aging caused by the application of an elevated temperature.

Rubber nanocomposites constitute one of the very important classes of materials because of their unusual improved properties normally unavailable with their pure form or conventional composites. It is therefore necessary to evaluate the property changes of most of these industrially and commercially viable materials, which when subjected to the degradation due to heat could be studied through thermogravimetric analysis (TGA), differential thermal analysis (DTA), and differential scanning calorimetry (DSC). Mechanical aging could be studied after a particular performance life through the changes in the strength, elasticity, toughness, and so on, at a given temperature. Such studies on the thermal stability and degradation behavior of these rubber nanocomposites are extremely useful when they are subjected to heating, allowing the selection of polymeric materials with superior properties for specific applications [20, 21].

20.2 Types of Fillers Used in Rubber Nanocomposites

Fillers in the rubber industry are playing increasingly important roles in the reinforcement of polymers. The filler content in a rubber product is usually more than 40% in total weight. However, the presence of nanofillers in very small amount in the polymers not only remarkably improve the mechanical, thermal properties but also endow polymers with special properties such as electrical conductivity, flame resistance, antibacterial effectiveness and so on [22–27]. The fillers used in the preparation of rubber-based nanocomposites are of the following types.

20.2.1 Clay Minerals

Clay materials, because of their easy availability and well defined intercalation chemistry, have widely been used to prepare polymer–nanocomposites. It is noted that a very small amount of modified clay is enough to exhibit markedly improved mechanical, optical, thermal and physicochemical properties when compared to the neat polymer of conventional microscale composites.

20.2.1.1 Structure of Sodium Montmorillonite

The structure of sodium montmorillonite (Na-MMT) is shown in Figure 20.1. It is composed of units made up of two silica tetrahedral sheets with a central alumina octahedral sheet [28]. The montmorillonite layers consist of negative charges resulting from the isomorphous substitution of Si^{4+} in the tetrahedral lattice by Al^{3+} and of Al^{3+} in the octahedral sheet by Mg^{2+}. These negative charges are counterbalanced by cations such as Na^{+} (Li^{+}, K^{+}, Ca^{2+}), called

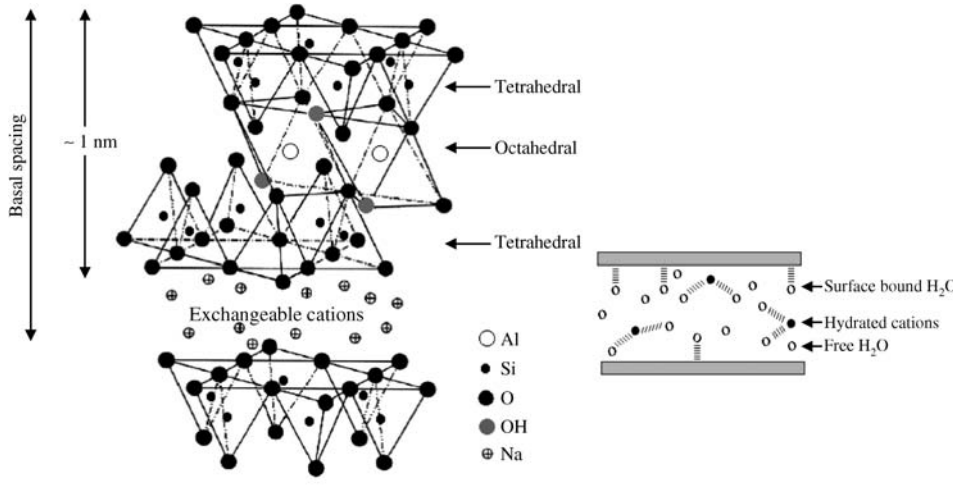

Figure 20.1 Structure of Na^+-montmorillonite

interlayer cations and situated between the layers and remained hydrated. The interlayer cations can be exchanged by organic cations like alkyl ammonium, aryl ammonium and so on to make compatible with organic polymers. The free and surface-bound water molecules are also present between the montmorillonite layers causing the lattice to expand in the *c*-direction [26].

20.2.2 Layered Double Hydroxide

The majority of research work have been focused on cationic clays (montmorillonite; MMT), while the layered double hydroxides (LDH), also known as anionic clays, have been relatively less studied due to their stronger interaction among the hydroxide sheets, small gallery space and the hydrophilic nature of LDH. But due to their highly tunable properties and wide applications, such as catalysts, medical materials and flame retardants, LDHs are considered an emerging class of materials [28–30].

20.2.2.1 Structure of LDH

The general composition of LDHs can be represented by the ideal formula $[M^{II}_{(1-x)}M^{III}_{x}(OH)_2]^{x+}A_{x/m}{}^{m-}\cdot nH_2O$, where M^{2+} is a divalent cation such as Mg^{2+}, Zn^{2+}, Ni^{2+}, Co^{2+}, Fe^{2+}, Mn^{2+}, Cu^{2+}, Ti^{2+}, Cd^{2+}, Ca^{2+} and so on, M^{3+} is a trivalent cation such as Al^{3+}, Cr^{3+}, Fe^{3+}, Mn^{3+}, Ga^{3+}, V^{3+}, In^{3+}, Y^{3+}, La^{3+}, Ru^{3+} and so on, and A is an anion with valency *m* (for example, Cl^-, Br^-, F^-, OH^-, $CO_3{}^{2-}$, $SO_4{}^{2-}$, $NO_3{}^-$). The structure of LDH is closely related to brucite, $Mg(OH)_2$, with the cations at the center of the octahedron, as shown in Figure 20.2 [29]. In the brucite layer, each Mg^{2+} ion is octahedrally surrounded by six OH^- ions and the different octahedrons share the edge to form an infinite two-dimensional layer. The partial replacement of divalent cations by trivalent cations gives the brucite like layer a positive

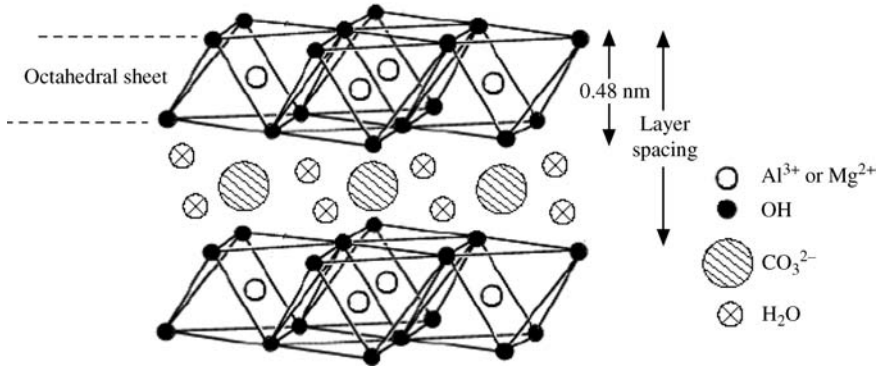

Figure 20.2 Structure of Mg/Al layered double hydroxide (Reprinted from *Composites Science and Technology*, **67**, H. Acharya, S.K. Srivastava and A.K. Bhowmick, "Synthesis of partially exfoliated EPDM/LDH nanocomposites by solution intercalation: structural characterization and properties," 2807–2811 (Figure 1), © 2007, with permission from Elsevier.)

charge which is counterbalanced by the anions in the interlayer region (gallery), resulting in a hydrotalcite-like structure. The gallery also contains water molecules inside, which are hydrogen-bonded in the layer OH and to the interlayer ions. LDH can be organomodified by organic anions, such as dodececyl sulfate, whereby these ions replace the existing anions and in the process increase the gallery space, making the insertion of polymer chains in the interlayer space easier.

20.2.3 Carbon Nanotubes and Other Inorganic Nanofillers

Carbon nanotubes (CNTs), since their discovery in 1991 [31], have received a great deal of interest due to their excellent properties, high strength, heat conductivity and so on. Recent research has shown CNTs as an alternative reinforcing filler in polymer/nanocomposites due to their excellent thermal stability, thermal and electrical conductivity and so on [32]. All present research illustrates that the dispersion of CNTs in a polymer matrix and the interfacial interaction between CNTs and polymer are two critical factors which affect the comprehensive performances of composites. The preparation of CNT/rubber composites has recently received more impetus to explore their extensive applications in many fields, just like conductive rubber composites filled with carbon fiber and carbon black. Nanosized silica, calcium carbonate, titanium dioxide and so on have also been used as another source of fillers for the preparation of rubber nanocomposites.

20.3 Aging of Rubber Nanocomposites

The growing interest in applications of nanocomposite materials in many industrial fields is the driving force for the development of new polymer matrix–nanofiller formulations. However, among the tremendous literature devoted to nanocomposite materials, only very limited work deals with the long-term aging of polymer/clay nanocomposites and more particularly with the

photodegradation of these materials in understanding the changes in appearance, morphology, thermal stability, chemical structures, mechanical and other properties. The aging phenomenon related to some important types of rubber nanocomposites is reviewed as follows:

20.3.1 Natural Rubber

Though many studies have been focused on preparation and investigation of the usual properties of natural as well as synthetic rubber nanocomposites [33], more work on unfolding their aging behavior is needed. Manroshan and Baharin [34] used nanosized calcium carbonate as filler in natural rubber (NR) latex films by casting the prevulcanized latex onto glass substrates. These films are aged in an oven at 70 °C for seven days and tested to examine the effect of filler content on the modulus, tensile strength and elongation at break before and after aging. Figures 20.3 and 20.4 shows the effect of filler loading on the modulus at 100 and 300% elongation of prevulcanized NR latex films before and after aging. The increase in modulus is observed with the increase in filler loading and is due to the stiffening effect caused by the interaction between the filler and rubber particles. In addition, aged films show higher modulus values than unaged filmsat 100% elongation and at 300% elongation. Such a phenomenon is attributed to the heating of the films, which caused enhanced stiffening as a result of the interaction of the curatives with the filler particles and the rubber molecules. Figure 20.5 show the relationship between the filler loading and the tensile strength of the prevulcanized latex

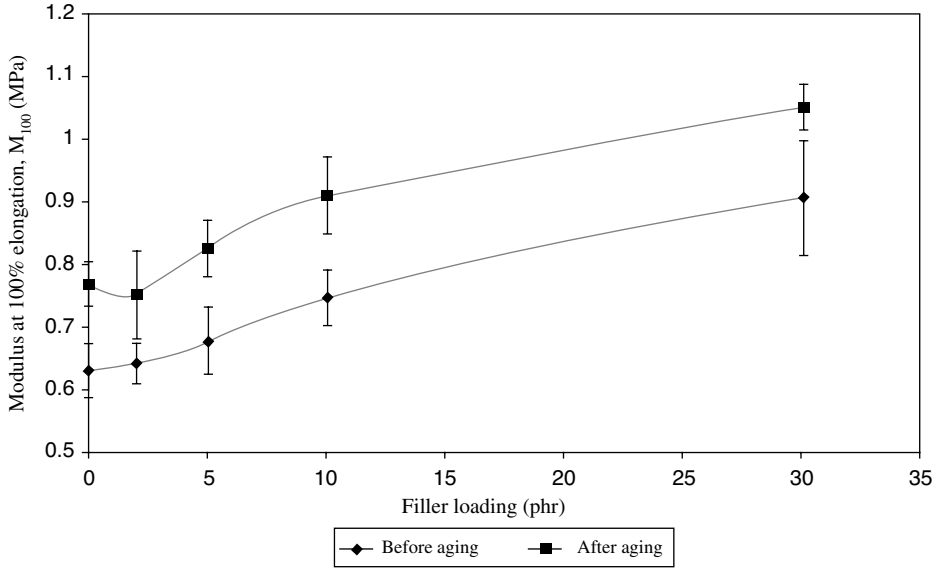

Figure 20.3 Effect of filler loading on the modulus at 100% elongation (M_{100}) of prevulcanized natural rubber latex films before and after aging (Reprinted from S. Manroshan and A. Baharin, "Effect of nanosized calcium carbonate on the mechanical properties of latex films," *Journal of Applied Polymer Science*, **96**, 1550–1556 (Figure 3), © 2005, with the permission of John Wiley & Sons, Inc.)

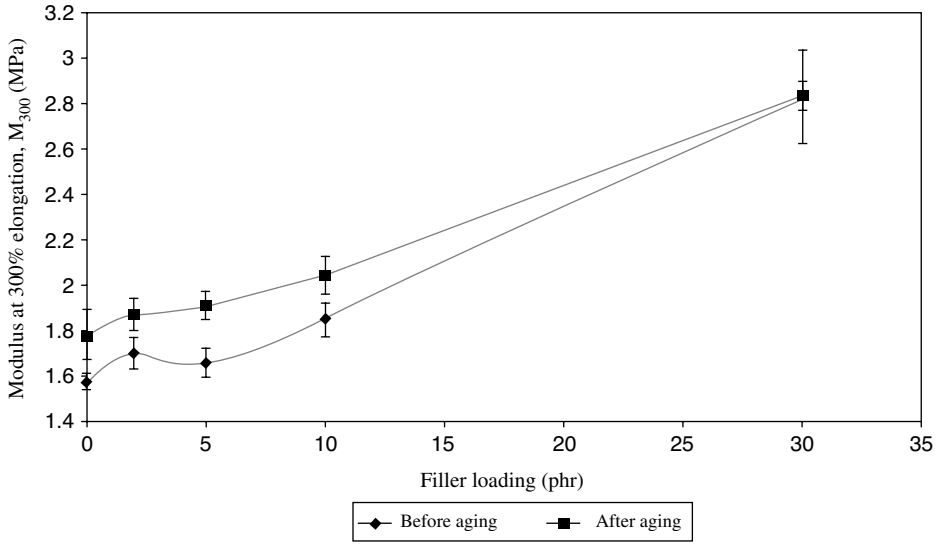

Figure 20.4 Effect of filler loading on the modulus at 300% elongation (M_{300}) of prevulcanized natural rubber latex films before and after aging (Reprinted from S. Manroshan and A. Baharin, "Effect of nanosized calcium carbonate on the mechanical properties of latex films," *Journal of Applied Polymer Science*, **96**, 1550–1556 (Figure 4), © 2005, with the permission of John Wiley & Sons, Inc.)

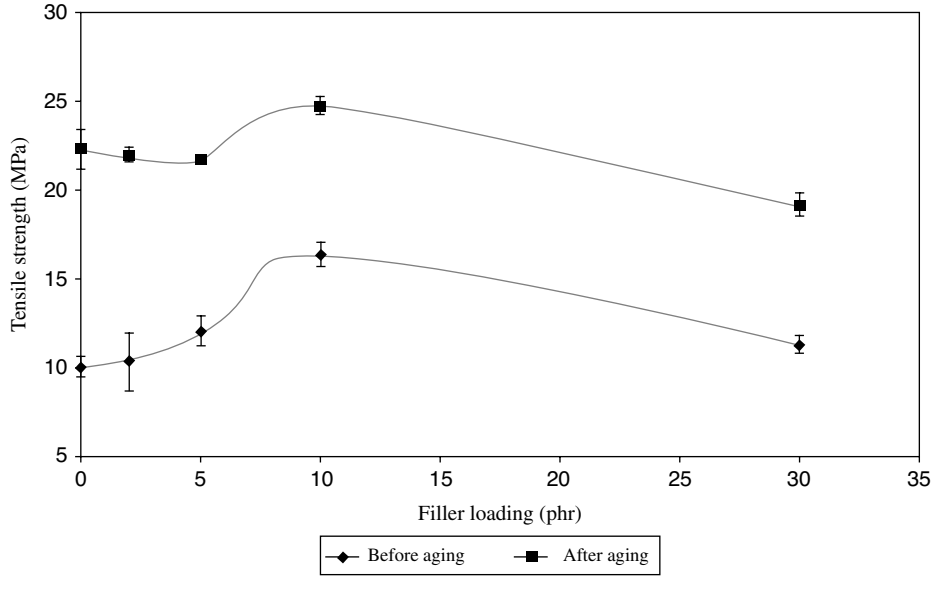

Figure 20.5 Relationship between filler loading and tensile strength of prevulcanized natural rubber latex films before and after aging (Reprinted from S. Manroshan and A. Baharin, "Effect of nanosized calcium carbonate on the mechanical properties of latex films," *Journal of Applied Polymer Science*, **96**, 1550–1556 (Figure 5), © 2005, with the permission of John Wiley & Sons, Inc.)

films, before and after being subjected to aging. According to this, the tensile strength increased with filler loading, reaching a maximum value at 10 phr, which then decreased again for both aged and unaged films. The effect of filler loading on the elongation at break (E_b) of the prevulcanized latex films before and after aging is also shown in Figure 20.6. A similar trend is observed, with E_b reaching a maximum at 10 phr of filler loading and then decreasing with further filler loading. The aged films also show a higher modulus at 100% elongation (M_{100}) and at 300% elongation (M_{300}), higher tensile strength and higher E_b values than unaged films, due to the enhanced interaction between the curatives with the fillers and the rubber molecules as heat is applied to the films.

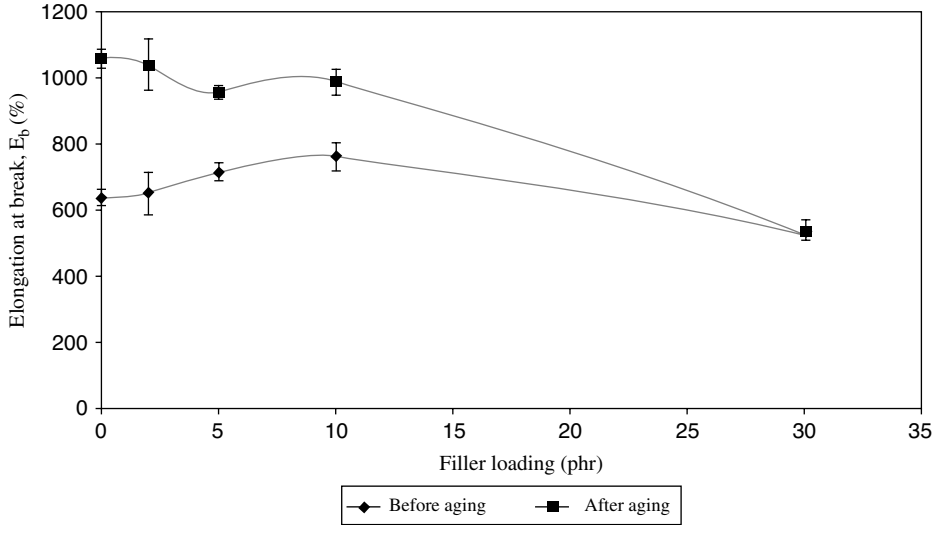

Figure 20.6 Effect of filler loading on the elongation at break of prevulcanized natural rubber latex fIlms before and after aging (Reprinted from S. Manroshan and A. Baharin, "Effect of nanosized calcium carbonate on the mechanical properties of latex films," *Journal of Applied Polymer Science*, **96**, 1550–1556 (Figure 6), © 2005, with the permission of John Wiley & Sons, Inc.)

Alex *et al.* [35] determined the effect of thermal aging on NR nanocomposites. The results in Tables 20.1 and 20.2 compare the changes in modulus, tensile strength and elongation at break between the aged and unaged skim NR samples. A better dispersion of modified clay, together with a higher level of crosslinking, resulted in enhanced mechanical properties and aging characteristics. The resistance to thermal aging and the thermal stability of natural rubber/nano-calcium carbonate (NR/CCR) modified with stearic acid and modified by solid-phase (M-CCR) composites has also been studied [36]. The results showed that the distribution of M-CCR particles in NR vulcanizates was more uniform than that of CCR. The micromorphology, mechanical properties, resistance to aging and thermal stability of NR/M-CCR composites were improved markedly.

Bandyopadhyay and Bhowmick [37] studied low- and high-temperature degradation behavior of epoxidized natural rubber (ENR)/silica and acrylic rubber (ACM)/silica nanocomposites. It was observed that ACM/silica and ENR/silica nanocomposites at 30 wt%

Table 20.1 Mechanical properties of skim NR

Parameter	Loading of clay (phr)				
	0	3	5	10	15
Modulus, 100% (MPa)	1.62	1.98	2.11	2.79	2.98
Modulus, 200% (MPa)	2.24	2.59	2.73	3.63	3.67
Modulus, 300% (MPa)	2.78	3.23	3.30	4.5	4.63
Tensile strength (MPa)	22.54	24.57	25.79	24.8	24.18
Elongation at break (%)	770	730	780	710	700
Hardness (Shore A)	55	60	65	70	76

(Reprinted from R. Alex and C. Nah, "Preparation and characterization of organoclay–rubber nanocomposites via a new route with skim natural rubber latex," *Journal of Applied Polymer Science*, **102**, 3277–3285 (Table VI), © 2006, with the permission of John Wiley & Sons, Inc.)

Table 20.2 Mechanical properties of aged skim NR

	Loading of clay (phr)				
	0	1	3	5	10
Modulus, 100% (MPa)	1.81	2.02	2.14	2.23	2.85
Modulus, 200% (MPa)	2.96	3.27	3.21	3.82	3.69
Modulus, 300% (MPa)	4.02	4.08	4.5	4.8	5.00
Tensile strength (MPa)	24.34	25.5	24.8	24	24.6
Elongation at break (%)	630	700	700	740	650

(Reprinted from R. Alex and C. Nah, "Preparation and characterization of organoclay–rubber nanocomposites via a new route with skim natural rubber latex," *Journal of Applied Polymer Science*, **102**, 3277–3285 (Table VII), © 2006, with the permission of John Wiley & Sons, Inc.)

tetraethoxysilane (TEOS) showed more deterioration in strength on aging at 50, 70 and 90 °C than poly(vinyl alcohol) (PVA)/silica nanocomposites, although in all cases, the control samples showed more deterioration than the respective nanocomposites. It is also noted that the ENR/silica was more resistant in lowering its strength compared with ACM/silica nanocomposite, which is ascribed to a higher gel formation through a greater interaction of silica with polar carbonyl groups in the former on aging than in the latter system.

The effect of ultrafine calcium carbonate (0–30%) to reinforce natural rubber latex film and the physical properties of latex film (for example, tear strength, modulus, tensile strength) before and after aging have been investigated [38]. It was observed that aging of the calcium carbonate-filled reinforced natural rubber latex does not have a great effect on the aging properties. Wang and others [39] studied the effect of air aging on the mechanical properties of NR-montmorillonite nanocomposites prepared by co-coagulating the rubber latex and clay aqueous suspension and compared its properties with carbon black-filled NR composites. It was noted that the tensile strength and elongation at break for both the NR-clay nanocomposite and the NR filled with carbon black decrease with the increase in aging time. Nonetheless, after 7 days of aging, the tensile strength and elongation at break of the NR-clay nanocomposite are 14.7 MPa and 452%, much higher than 9.0 MPa and 388% for the NR filled with carbon black.

20.3.2 Ethylene Propylene Diene Terpolymer

The UV-induced oxidation of ethylene propylene diene terpolymer (EPDM)/montmorillonite nanocomposites has been reported. According to Sandrine Morlat-Therias *et al.* [40], the EPDM/montmorillonite nanocomposites, one with intercalated montmorillonite and the other with exfoliated montmorillonite, are obtained by melt compounding EPDM-g-MA (EPDM grafted with maleic anhydride as compatibilizing agent) and organophilic synthetic clays. It is observed that the photoproducts are the same for EPDM/montmorillonite nanocomposites. Also the formation of these oxidation products occurs after an induction period, which is found to be reduced in the presence of montmorillonite and the effect is enhanced in the case of the exfoliated nanocomposite. After the induction period, oxidation starts with a rate that is independent of the presence of montmorillonite. Gardette and coworkers [41] studied the photooxidation of a vulcanized EPDM/montmorillonite nanocomposite with stabilizers under accelerated UV irradiation ($\lambda \geq 300$ nm, 60 °C) for different times and followed the development of functional groups during oxidation by infrared spectroscopy. The investigations revealed that the photooxidation products are not changed in the presence of the nanofiller. Lonker and others [42] discussed the relationship between the nanoclay reinforcement and stabilizing efficiency in terms of photooxidation and surface morphology for their applicability. However, the aging behavior of EPDM blend nanocomposites has yet to be investigated [43].

20.3.3 Styrene Butadiene Rubber

Ming Tian *et al.* [44] reported for the first time the preparation of styrene butadiene rubber (SBR) nanocomposites by direct blending, using fibrillar silicate (FS) as nanofiller; the corresponding data of their mechanical properties is recorded in Table 20.3. It is noted that FS/SBR nanocomposites possessed higher hardness, tensile stress at 100% strain, tensile strength and very high tear strength, demonstrating the excellent reinforcing effects of modified FS. It is also observed that increasing content of modified FS in SBR is accompanied by an

Table 20.3 Mechanical properties of SBR/fibrillar silicate (FS) nanocomposites

	Amount of modified FS							
	30		40		50		60	
	Unaged	Aged	Unaged	Aged	Unaged	Aged	Unaged	Aged
Hardness (Shore A)	69	78	73	80	75	83	79	85
Tensile stress at 100% strain (MPa)	7.3	8.4	7.6	10.4	7.8	12.2	10.2	13.7
Tensile strength (MPa)	14.1	14.3	14.7	16.0	14.4	17.5	18.8	20.5
Elongation at break (%)	350	260	344	238	336	233	309	233
Permanent set (%)	20	12	20	12	12	8	12	8
Tear strength (kN/m)	58.0		60.8		67.4		64.7	

(Reprinted from M. Tian, L. Cheng, W. Liang and L. Zhang, "Overall properties of fibrillar silicate/styrene-butadiene rubber nanocomposites," *Journal of Applied Polymer Science*, **101**, 2725–2731 (Table 1.3), © 2006, with the permission of John Wiley & Sons, Inc.)

increase in hardness and tear strength but a decrease in elongation at break and permanent set. Table 20.3 also records the properties of FS/SBR composites after 48 h aging at 100 °C. In addition, the composites had a visible increase in hardness, tensile stress and tensile strength, but a small decrease in the elongation at break and permanent set, which indicated that the FS/SBR composites had very good heat-aging resistance. Like unfilled SBR vulcanizate, the main reason is that the crosslinking density of SBR after aging increased when sulfur was chosen as the curing agent.

To understand the effect of aging on SBR/modified clay nanocomposites, Bhowmick and Sandhu [45] made extensive investigations on three different aging conditions (36 h at 100 °C, 36 h at 120 °C, 72 h at 100 °C). The results are reported in Table 20.4. It shows that the aging leads to a significant increase in tensile strength, while elongation at break decreased. The increase in modulus with time or temperature is due to crosslinks through residual peroxide in the initial stage. At higher temperatures or longer times of aging, the strength and modulus improved because of resin formation and gelling. The incorporation of clay deteriorated the aging properties of SBR [16–50% decrease in elongation at break, depending on the aging conditions in SBR with styrene-butadiene (with 23% styrene content + DCP: 1 phr) + OC: 4 phr with respect to the control]. Although the modified clay could not improve the oxidative aging properties significantly, a few aging properties are better in the modified clay system. The extended aging of the samples also led to higher stiffness and higher tensile strength but reduced elongation at break. They indicate that a higher temperature is more effective than a longer aging time in changing the properties in this case.

Table 20.4 Effect of aging conditions (36 h at 100 °C, 36 h at 120 °C, 72 h at 100 °C) on the mechanical properties of SBR modified clay nanocomposites [23SBR = styrene-butadiene with 23% styrene content, 23SBRN4 = 23SBR + DCP (1 phr) + NC (4 phr), 23SBROC4 = 23SBR + DCP (1 phr) + OC (4 phr)]

Sample	Conditions (h/°C)	Tensile strength (MPa)	Elongation at break (%)	Modulus at 5% elongation (MPa)
23SBR	36/100	1.2	84	0.11
23SBRN4		1.9	46	0.16
23SBROC4		2.2	70	0.18
23SBR	36/120	2.3	12	1.17
23SBRN4		5.2	5	5.20
23SBROC4		6.5	6	6.07
23SBR	72/100	2.3	10	1.70
23SBRN4		5.1	5	5.10
23SBROC4		5.6	7	5.20

(Reprinted from S. Sadhu and A.K. Bhowmick, "Preparation and properties of styrene-butadiene rubber based nanocomposites: the influence of the structural and processing parameters," *Journal of Applied Polymer Science*, **92**, 698–709 (Table VIII), © 2004, with the permission of John Wiley & Sons, Inc.)

Zhang and coworkers [46] studied the heat O_2 aging property and O_3 aging property of clay/SBR nanocomposites. These investigations showed that both the heat O_2 aging property and the O_3 aging property of clay/SBR nanocomposite were superior to those of carbon black/SBR composites. The uniformly dispersed nanoclay could improve the heat stability and air isolation of rubber, decrease the diffusion of O_2 and O_3 in rubber and reduce the probability

of an attack on the molecular chain of rubber, improving the heat O_2 aging property and O_3 aging proper of rubber.

The properties and applications of MMT/SBR nanocomposites in the processing of tire tube have also been experimentally investigated and the results showed that the air-tightness and thermal aging properties were improved. [47].

20.3.4 Nitrile Butadiene Rubber

A thorough search of the literature survey reports no studies on the aging of nitrile butadiene rubber (NBR) nanocomposites. However, Varghese *et al.* [48] reported the results of thermal aging of NBR/EVA (ethylene vinyl acetate) blends as a function of blend composition, crosslinking systems, filler type/loading and Young's modulus on the tensile strength. The sample aged at 100 °C also exhibits a lower Young's modulus than those aged at 50 °C and unaged samples. However, the property is not much affected by the mild aging condition. All the systems except sulfur-cured system result in an increase in the property for aged samples at 50 °C. This is due to the additional crosslinks formed during thermal aging. While in the sulfur system the S–S crosslinks are more flexible with the lowest bond energy and can be easily dissociated by thermal energy. Therefore, in the sulfur-cured system, the property decreased because of aging. The property decrease for all the samples after aging at 100 °C is due to the disintegration of crosslinks at an elevated temperature. The crosslink density also decreases after aging at 100 °C. After severe aging condition at 100 °C, the sulfur-cured system retains only 80% of the property. For the peroxide and mixed cure systems, the property retention was 97 and 85%, respectively, implying thereby the peroxide-cured system exhibits the best property retention even after severe aging condition. This is due to the thermal stability of the peroxide-cured system, as evident from the TGA.

Nano-titanium dioxide-filled rubber composites of NBR have been prepared by direct blending and their antimicrobial properties before and after aging have been reported [49]. These results showed that the antimicrobial properties of TiO_2-filled rubber composites are greatly improved compared with those of the unfilled composites. However, thermal aging has no influence on the antimicrobial properties.

ZDMA (zinc methacrylate)/NBR nanocomposite have also been studied and compared to those of a carbon black (CB)/NBR system [50]. The better hot air aging property and hot oil resistance of ZDMA/NBR vulcanizate were obtained when compared to those of the CB/NBR vulcanizate.

20.3.5 Hydrogenated Nitrile Butadiene Rubber

H. Anmin *et al.* [51] studied the aging performance of hydrogenated nitrile butadiene rubber (HNBR)/clay nanocomposites at 178 °C in air, water and oil, respectively. At this temperature, the aging process is accelerated and HNBR/clay nanocomposites can perform better under these severe conditions. Tables 20.5–20.7 summarizes the change of material properties after aging in different media for extended hours. The addition of organoclay significantly improves material performance at high temperature in both air and oil. HNBR/nanocomposites maintain about 80% of tensile strength after aging in air and 50% of tensile strength after aging in oil. Aging performance of HNBR nanocomposites is similar to that of the carbon black filler of

Table 20.5 Material properties of HNBR vulcanizates after air aging at 178 °C for 96 hours

Organoclay (phr)		0	2.5	5	7.5	10	15
Carbon black (phr)	30						
Change in hardness	+15	+4	+7	+7	+8	+8	+9
Tensile strength (MPa)	13.5	4.4	9.5	15.0	15.7	16.5	16.4
Retention of tensile strength (%)	48.2	58.8	88.0	89.3	86.7	80.8	79.2
Elongation at break (%)	130	230	300	375	370	380	370
Retention of elongation at break (%)	30.9	46.5	61.2	75.0	71.2	71.7	70.5
Permanent set (%)	6	2	8	12	14	16	36

(Reproduced from A. Huang, X. Wang, D. Jia and Y. Li, "Thermal stability and aging characteristics of hnbr/clay nanocomposites in air, water and oil at elevated temperature," *e-Polymers*, **051** (Table 2), © 2007, with permission from e-Polymers (http://www.e-polymers.org).)

Table 20.6 Material properties of HNBR vulcanizates after water aging at 178 °C for 96 hours

Organoclay (phr)		0	2.5	5	7.5	10	15
Carbon black (phr)	30						
Change in hardness	+7	−1	+1	+1	+2	+2	+3
Tensile strength (MPa)	24.8	5.3	9.6	14.7	15.4	17.1	16.6
Retention of tensile strength (%)	88.6	71.6	88.9	87.5	84.9	83.6	80.4
Elongation at break (%)	360	470	545	540	530	520	515
Retention of elongation at break (%)	85.7	94.9	111.2	108.0	101.9	98.1	98.1
Permanent set (%)	8	8	16	18	20	24	40

(Reproduced from A. Huang, X. Wang, D. Jia and Y. Li, "Thermal stability and aging characteristics of hnbr/clay nanocomposites in air, water and oil at elevated temperature," *e-Polymers*, **051** (Table 3), © 2007, with permission from e-Polymers (http://www.e-polymers.org).)

Table 20.7 Material properties of HNBR vulcanizates after oil aging at 178 °C for 72 hours

Organoclay (phr)		0	2.5	5	7.5	10	15
Carbon black (phr)	30						
Change in hardness	+19	−1	−2	+1	+3	+2	+1
Tensile strength (MPa)	7.4	3.8	5.5	8.6	10.6	12.1	11.0
Retention of tensile strength (%)	26.4	51.3	50.9	51.2	58.6	59.0	53.1
Elongation at break (%)	135	115	190	255	270	250	235
Retention of elongation at break (%)	32.1	23.2	38.8	50.8	51.9	47.2	44.8
Permanent set (%)	2	4	4	2	4	4	4
Change in mass (%)	12.6	16.5	14.4	13.1	12.9	12.3	11.2

(Reproduced from A. Huang, X. Wang, D. Jia and Y. Li, "Thermal stability and aging characteristics of hnbr/clay nanocomposites in air, water and oil at elevated temperature," *e-Polymers*, **051** (Table 4), © 2007, with permission from e-Polymers (http://www.e-polymers.org).)

HNBR. This may be due to the swelling of the material with the presence of organoclay, which counter-interacts with its reinforcing effect. It is also noted that the retention of material properties is not affected much by clay content when it is greater than 2.5 phr.

20.3.6 Silicone Rubber

Room temperature vulcanized (RTV) silicone rubber (SR) has been used in the form of external coatings to insulate transmission and substation equipment in polluted areas in order to improve their pollution performance, due to water repellency and transferring the water repellency of the silicone rubber materials [52]. Corona is a most important factor that leads to the loss of water repellency in silicone rubber materials, which in the end leads to the further aging of the material, such as cracking and erosion [53]. In order to extend the service life of RTV coatings, the corona aging performance needs to be improved. With the recent advent of organic polymer/inorganic material nanocomposites, it is anticipated that a high and superior performance, for example, better thermal stabilities and endurance to the weather could be achieved [54]. Lei and coworkers [52] have very recently used nanosilica and nanolayered silicate to modify the properties of RTV silicone rubber under corona conditions. According to this, RTV/layered silicate nanocomposites provide special barrier abilities, which can prevent UV and oxygen from going deep inside the material. As a result, these composites have better corona aging properties. In addition, the thermal stabilities of RTV nanocomposites have a much better corona aging performance than the virgin RTV and hence can have a longer service life under the conditions of applied voltage.

20.4 Degradation of Rubber Nanocomposites

20.4.1 Natural Rubber

Early work on the nanolevel dispersion of clay in the natural rubber matrix has been reported by very few workers [55–57]. These studies have shown significant improvements in the mechanical properties of the corresponding nanocomposites, due to the marked reinforcing effect of the nanolayered silicate layers. Varghese and Karger-Kocsis [57] synthesized natural rubber (NR)/layered silicate nanocomposite by latex compounding. It shows that the storage modulus is increased by 400% for fluorohectorite-filled natural rubber and by 450% for bentonite-filled polymer nanocomposites below the glass transition temperature compared to commercially clay-filled polymer composite. The thermal decomposition behavior of NR nanocomposites indicates that, at 400 °C, the percentage of weight retained is higher for the nanocomposites. An improvement in the thermal stability of these nanocomposites is also observed. Such an increase in the thermal stability of the hybrid may result from the dispersion of the clay and from a strong interaction between the clay platelets and rubber molecules. The important feature of this work is related to the thermal property improvement which occurs at a very low filler content, often making the obtained material cheaper, lighter and easier to process than conventional composites.

Sharif *et al.* [58] carried out radiation crosslinking of natural rubber (NR)/clay nanocomposites prepared by melt mixing from natural rubber with sodium montmorillonite (Na-MMT) and Na-MMT modified with cationic surfactants, dodecyl ammonium chloride (DDA) and

octadecylamine ammonium chloride (ODA) to produce NR/Na-MMT, NR/DDA-MMT and NR/ODA-MMT composites. TGA studies showed that NR/DDA-MMT and NR/ODA-MMT nanocomposites have higher decomposition temperatures than NR/Na-MMT. According to Bolland and Orr [59], in the temperature range 200–270 °C of the NR/DDA-MMT thermogram, both scission and crosslinking occur, though no loss of unsaturation of the bulk rubber. The decomposition of natural rubber is accompanied by the volatilization of 39% isoprene, 13.2% dipentene and small amounts of *p*-menthene, as reported by other workers [60, 61]. It is attributed that the presence of silicate layers dispersed homogeneously in natural rubber sheet hinders the permeability of volatile degradation products out from the material and helps delay the degradation of the nanocomposites. Recently, Viet and coworkers [62] prepared organoclay (loading up to 10 phr) filled natural rubber nanocomposites using a laboratory two-roll mill and investigated the thermal behavior. They observed that the thermal degradation shifted to a higher temperature and the weight loss decreased with the incorporation of organoclay.

Alex and Nah [35] provided a simple and environmentally friendly procedure for the production of NR nanocomposites from skim latex produced as a byproduct during the centrifugation of NR latex. The thermal characteristics of NR nanocomposites in Table 20.8 show the maximum degradation temperature to be independent of the presence and concentration of organoclay (OC). However, at 400 °C the percentage retained is higher for the nanocomposites. Higher residue is also retained for all the nanocomposites and this increases in proportion with the clay. The enhanced thermal resistance is attributed to the good dispersion of OC in the rubber matrix as in the rubber matrix, as reported by [63].

Table 20.8 TGA data of NR nanocomposites

Clay loading (phr)	Max. degradation temperature (°C)	Percent weight retained			
		200 °C	300 °C	400 °C	500 °C
0	374.5	98.66	91.84	32.29	10.58
2	375.0	98.57	90.34	33.05	11.30
3	375.0	98.79	91.35	33.28	11.65
5	375.0	98.54	90.79	34.89	12.25
10	375.0	98.61	90.47	36.65	14.95

(Reprinted from R. Alex and C. Nah, "Preparation and characterization of organoclay-rubber nanocomposites via a new route with skim natural rubber latex," *Journal of Applied Polymer Science*, **102**, 3277–3285 (Table VIII), © 2006, with the permission of John Wiley & Sons, Inc.)

Nanosilica has also been used as a nanofiller in studying the thermal stability and degradation of natural rubber by Li *et al.* [64]. According to this, SiO_2 nanoparticles are distributed as spherical nanoclusters homogeneously in a NR matrix. The thermal resistance of the nanocomposites is significantly improved in comparision to neat NR. The degradation temperatures of the nanocomposites are markedly higher than those of pure NR due to the significant retardant effect of SiO_2 nanoparticles.

Sui and coworkers [65] fabricated carbon nanotube/natural rubber (CNT/NR) composites based on a CNT treatment using an acid bath followed by ball-milling with hydrated silica-resorcinol-hexamethylenetetramine (HRH, at a weight ratio of 15 : 10 : 6) bonding systems. After acid treatment and ball-milling, the dispersion of CNTs in the rubber matrix and the

interaction between CNTs and the matrix is improved. In addition, the thermal properties of the CNT/reinforced NR composites are enhanced by the incorporation of the treated CNTs as compared to neat NR and CB/NR composites.

Natural rubber/ethylene vinyl acetate (NR/EVA) blends are very attractive because of the excellent properties of both constituents. Sharif *et al.* [66] prepared a NR/EVA blend (in a ratio of 40 : 60) with dimethyl dihydrogenated tallow ammonium-modified montmorillonite nanocomposites through melt mixing with various amounts of organoclay and described its effect on the degradation steps of NR/EVA blends. Figure 20.7 represents the effect of the organoclay on the degradation steps of the NR/EVA blends. The NR/EVA blend is accompanied by a two-step degradation similar to EVA. The first is due to the NR phase, but the corresponding onset temperature is higher than that observed for pure NR. This behavior suggests the presence of EVA increases the thermal stability of pure NR. In addition, no degradation related to the acetate groups of EVA has been observed, and this indicates that EVA is also stabilized via blending with NR, as reported by Jansen and Soares [67]. The thermal stability of this NR/EVA blends is improved with an increase in the organoclay content from 3 to 5 phr. A further increase in the tallow ammonium-modified montmorillonite content (10 phr) does not further improve the thermal stability of the blends. The thermal degradation behavior with filler content could account for the change in the relative proportions of exfoliated and intercalated species with filler content. At low filler content, exfoliation dominates, but the concentration of exfoliated particles is not high enough to promote thermal stability through char formation. With an increase in filler content, relatively more exfoliated particles are formed and chars form easily and increase the thermal stability of the nanocomposites. At higher levels of clay concentration, the equilibrium between exfoliation and intercalation is drawn toward intercalation, and even if char is still formed in a high quantity, the morphology of the nanocomposites does not allow a good thermal stability to be maintained.

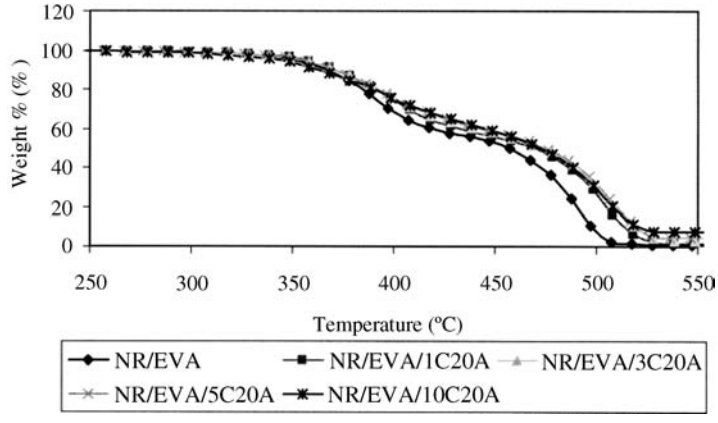

Figure 20.7 TGA results of NR/EVA/C20A nanocomposites (Reprinted from J. Sharif, W.M.Z.W. Yunus, K.H. Dahlan, M.H. Ahmad, "Natural rubber/poly(ethylene-co-vinyl acetate)-blend-based nanocomposites," *Journal of Applied Polymer Science*, **100**, 353–362 (Figure 13), © 2006, with the permission of John Wiley & Sons, Inc.)

20.4.2 Ethylene Vinyl Acetate

Ethylene vinyl acetate polymer is a copolymer and is available with various vinyl acetate contents. Depending on the vinyl acetate content, ethylene vinyl acetate (EVA) copolymers are available as rubbers, thermoplastic elastomers and plastics. Wide applications in electrical insulation, cable jacketing and repair, component encapsulation and water-proofing, corrosion protection, packaging of components and the shoe industry dictate the extent of the industrial importance of these polymers [68]. It is now expected that the nanocomposites of these polymers find applications in the same fields with a better performance.

Thermogravimetric analysis of EVA-45 (vinyl acetate content 45%) and its nanocomposites are depicted in Figure 20.8 and the weight losses at different stages of decomposition are tabulated in Table 20.9 [69]. It is clearly seen that EVA undergoes two-step decomposition [70, 71]. The first step is due to the deacetylation reaction and second step is associated with the formation of transvinylenes accompanied by main-chain scission. The mechanism of this two-step decomposition is represented elsewhere [70, 72] It is also evident from Table 20.9 that the overall weight loss decreases with the filler loading, that is, char formation of the hybrids increases linearly because of the high heat resistance exerted by the clay. It is evident from the TG curves that the weight losses for both the first step and second step decompositions decrease with increasing filler content in the polymer matrix. In the second step decomposition, TG curves for 6 and 8 wt% hybrids run above the pure EVA-45. This is due to the formation of constrained regions originating from the interaction between silicate layers and polymer chains. Additionally, it is also found that the nanocomposites degrade at a faster rate than the pristine polymer. It may be that the previous decomposition of dodecyl ammonium ions induces the deacetylation [49, 73].

Kuila, Srivastava and others reported the formation of nanocomposites of EVA [74] with varying amounts of DS-LDH; and findings are displayed in Figure 20.9. Similar to 12Me-MMT as nanofiller in EVA-45 [69, 75], two-step degradation of EVA is observed. The first and second steps take place in the ranges 214–422 °C and 415–525 °C, respectively. It is evident that the temperature range for the first step is more or less the same as in 12 Me-MMT/EVA-45 nanocomposites, while in the second stage degradation extends to much higher temperature (about 525 °C). It is also seen noted that the decrease in initial decomposition temperature for the nanocomposites is accompanied by a simultaneous increase in initial weight loss. This is possibly due to the early degradation of DS anion present in organo-LDH [76]. Such an initial weight loss in the nanocomposites is anticipated to reinforce the charring process and may be more useful for the fire safety of the nanocomposites. According to Qu *et al.* [77] an efficient charring process in a flame retardant polymer occurs at a temperature higher than its processing temperature but much lower than its decomposition temperature. It is also evident in Figure 20.9 that the final decomposition temperature is ≈10 °C higher for the nanocomposites compared to neat EVA and the weight loss at this stage of degradation significantly decreases with the addition of DS-LDH. This is possibly due to the good dispersion of LDH in these nanocomposites and the degradation perhaps only occurs at the surface of the nanocomposites to form a char between the sheets of LDH, which can effectively prevent the emission of thermally degraded small gaseous molecules, which ultimately enhance the thermal decomposition temperature of the nanocomposites.

Very recently, ethylene vinyl acetate/expanded graphite nanocomposites have been prepared by solution intercalation technique followed by compression molding, and thermal stability

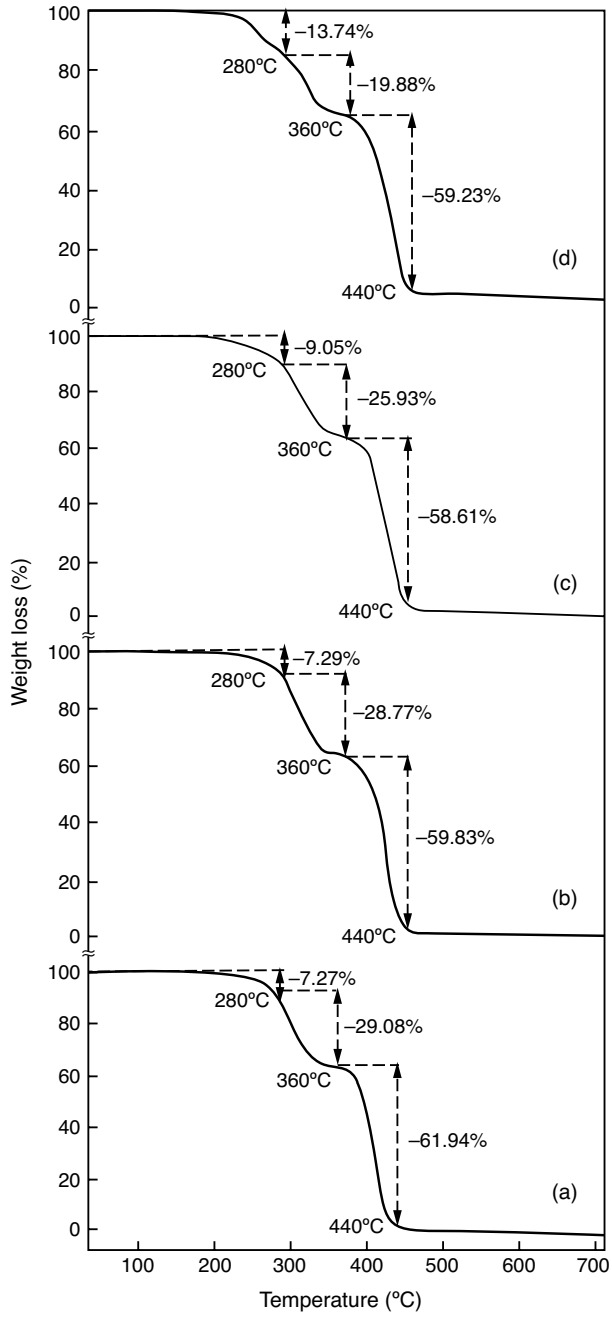

Figure 20.8 TGA of (a) EVA-45, (b) EVA-45 and 2 wt% 12Me-MMT, (c) EVA-45 and 4 wt% 12Me-MMT, (d) EVA-45 and 6 wt% 12Me-MMT, in air atmosphere (Reproduced from M. Pramanik, S.K. Srivastava, B.K. Samantaray and A.K. Bhowmick, "Preparation and properties of ethylene vinyl acetate-clay hybrids," *Journal of Materials Science Letters*, **20**, 1377–1380 (Figure 3), © 2001, with kind permission of Springer Science and Business Media.)

Table 20.9 Thermal properties of EVA and its nanocomposites [68]

Sample[1]	Step-1 weight loss (%) (T_i°−T_f °C)	Step-2 weight loss (%) (T_i°−T_f °C)
EVA-45 + OPC(0)	(227.7–422.7) 38.22	(422.7–501.0) 60.80
EVA-45 + OPC(2)	(219.8–421.7) 37.45	(421.7–502.0) 58.70
EVA-45 + OPC(4)	(215.8–424.5) 36.50	(424.5–501.0) 58.20
EVA-45 + OPC(6)	(213.3–415.1) 33.52	(415.1–502.0) 57.59
EVA-45 + OPC(8)	(210.4–416.2) 32.10	(416.2–500.0) 56.50

[1]OPC = 12Me-MMT; numbers in first bracket in sample column represent respective percentage of 12Me-MMT in the respective EVA matrix.

(Reproduced with permission from M. Pramanik, "Studies on layered materials and polymer nanocomposites," Ph.D thesis, Indian Institute of Technology, Kharagpur, 2005.)

behavior of the resulting nanocomposites have been compared with those of natural graphite-filled EVA composite [78]. It is noted that the incorporation of expanded graphite provides a tremendous improvement in thermal conductivity and thermal degradation resistance. A maximum shift of 14 °C in the maximum rate of degradation was observed for 4 phr expanded graphite addition. This work probably paves the path for preparing stronger, lightweight EVA-based nanocomposites which are cheaper than those based on carbon nanotubes, for use as advanced composites.

20.4.3 Ethylene Propylene Diene Terpolymer

Ethylene propylene diene terpolymer (EPDM) is an unsaturated polyolefin rubber with wide applications. Due to its good mechanical properties, very low unsaturation and associated resistance to aging and ozone deterioration [79], it has become extensively used in making automotive tire sidewalls, cover stripes, wires, cables, hoses, belting, footwear, roofing barriers and sporting goods. EPDM filled with many types of nanofillers often exhibit remarkable improvements in mechanical, thermal and physicochemical properties when compared with neat polymer and their conventional microcomposites, even at very low filler concentration, due to nanolevel interactions with the polymer matrix. The early work on preparation and characterization of EPDM nanocomposites included that of Usuki *et al.* [80], Chang and coworkers [12] and Acharya and Srivastava [81]. Figure 20.10 shows TEM images of EPDM/MMT composites containing 3 wt% (Figure 20.10a) and 8 wt% (Figure 20.10b) of 16Me-MMT (hexadecyl ammonium ion intercalated montmorillonite) [13]. The TEM images clearly indicate the presence of well separated silicate layers in an EPDM matrix, which was also suggested earlier by the X-ray diffraction profiles. The original aggregates of the primary particles are disrupted, resulting in a fine dispersion of silicate layers in the EPDM matrix. Within the primary particles, many of the silicate layers of crystallites are intercalated by EPDM chains to stack with layer expansion, preserving the parallel alignment of layers with nanoscale separation. Additionally, individual layers are also observed outside the crystallites with much finer dispersion. From the figure, it is also observed that the extent of intercalation level increases with increasing 16Me-MMT content from 3 to 8 wt% in EPDM matrix. The average size of the silicate layers dispersed in EPDM matrix is in the range 15–20 nm. These observations on the increasing level of intercalation with increasing 16Me-MMT polymers is nothing unusual and has been observed by other workers. According to Jeon *et al.* [82] the

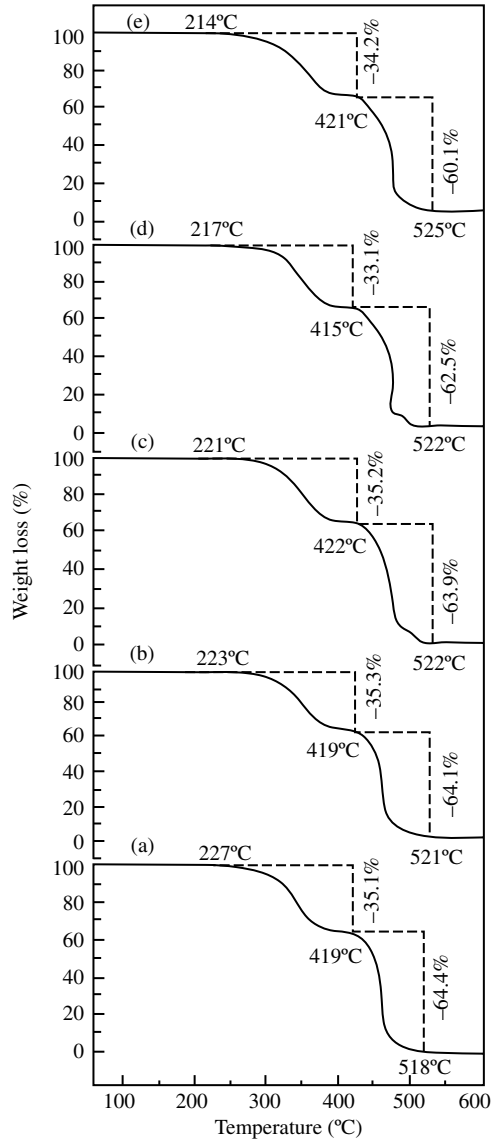

Figure 20.9 TGA curves of (a) EVA-45, (b) EVA-45/DS-LDH (1 wt%), (c) EVA-45/DS-LDH (3 wt%), (d) EVA-45/DS-LDH (5 wt%), (e) EVA-45/DS-LDH (8 wt%) (Reprinted from T. Kuila, H. Acharya, S.K. Srivastava and A.K. Bhowmick, "Rubber/LDH nanocomposites by solution blending," *Journal of Applied Polymer Science*, **108**, 1329–1335, © 2008, with the permission of John Wiley & Sons, Inc.)

distribution of platelets has an intrinsic tendency towards becoming ordered spontaneously from a disordered state with increasing filler contents, with a crossover at which equal amounts of disordered and ordered phases are expected (Figure 20.10). Dimarzio *et al.* [83] also defined a crossover volume fraction (Φc) at which equal amounts of the disordered and ordered phases

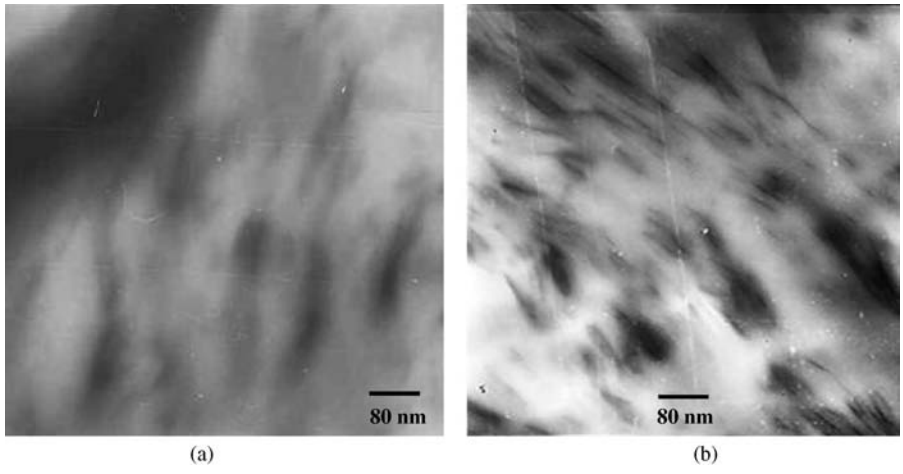

Figure 20.10 TEM images of EPDM nanocomposites containg (a) 3 wt% and (b) 8 wt% of 16Me-MMT [30] (Reproduced from H. Acharya and S.K. Srivastava, "Influence of nanodispersed organoclay on rheological and swelling properties of ethylene propylene diene terpolymer," *Macromolecular Research*, **14**, 132–139 (Figure 2), with permission from the Polymer Society of Korea (2009).)

are expected. At higher filler loading in polymers, the clay undergoes aggregation [84]. Therefore, it can be concluded that the intercalated as well as disordered silicate layers coexist together [85–87].

Typical nonisothermal weight loss curves resulting from the thermal degradation of EPDM and its 16Me-MMT nanocomposites in air are shown in Figure 20.11 [30]. It shows a very sharp one-step weight loss in all the cases corresponding to the thermal degradation of unsaturated organic backbone, accompanied by main-chain scission on oxidation [88]. The thermal

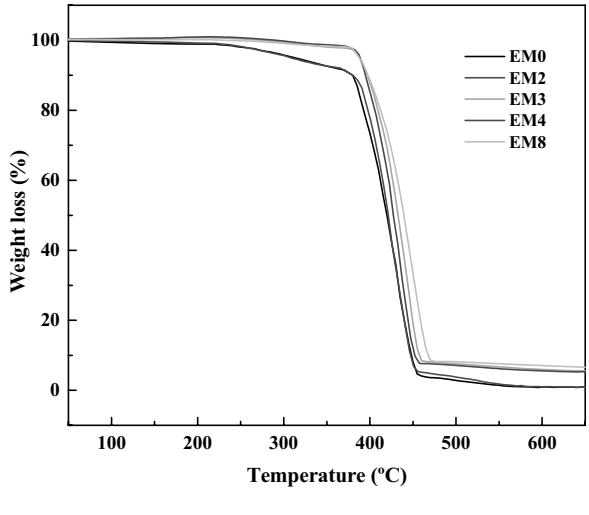

Figure 20.11 TGA of EPDM nanocomposites containing 0, 2, 3, 4 and 8 wt% of 16Me MMT [30]

stability behavior corresponding to the thermal decomposition temperature for 10 wt% loss (T_{10}) in mass improves from 377 to 397 °C for neat EPDM to EPDM/MMT (8 wt%) nanocomposites successively. This significant improvement in thermal stability is more likely due to the presence of silicate layers, which offers a great barrier effect to hinder the formation of small molecules resulting from thermal decomposition and simultaneously resists their movement during desorption from the surface [89]. The coexistence of intercalated and disordered silicate layers in the EPDM matrix increases the (Si-O-C) interfacial interaction to restrict the thermal motion of EPDM chain segments. Furthermore, it is noteworthy that the final thermal decomposition temperature (T_f) at about 460 °C remains more or less the same irrespective of the presence of 16Me-MMT in EPDM. It appears that the final T_f of EPDM is no longer dependent on the effect of silicate layers, suggesting their incapability to hold the polymer chains within themselves. Data relating to the comparison in thermal stability behavior of virgin EPDM and EPDM nanocomposites having 2, 3, 4 and 8 wt% 16Me-MMT as filler is presented in Table 20.10.

Table 20.10 Thermal stability behavior of neat EPDM and its 16-Me-MMT nanocomposites [30]

Sample[1]	10 wt% decomposition temperature (T_{10} °C)	25 wt% decomposition temperature (T_{25} °C)	Final decomposition temperature (T_f °C)
EM0	377	398	460
EM2	379	402	459
EM3	397	416	460
EM4	394	410	461
EM8	397	420	462

[1]EM0, EM2, EM3, EM4 and EM8 refer to EPDM containing 0, 2, 3, 4 and 8 wt% of 16-Me-MMT, respectively.

EPDM-clay nanocomposites with organoclay intercalated with maleic anhydride-grafted EPDM and EPDM-clay composites with pristine clay have been prepared through the melt intercalation technique [90]. The nanoscale silicate layers of organoclay are found to be completely exfoliated in the EPDM matrix and exhibit excellent thermal stability compared with conventional composites. This can be attributed to a decrease in the diffusion of volatile gases from the polymer matrix due to the homogeneous distribution of the nanoparticles, which lengthens the total path.

Kang *et al.* [91] in their work used several compatibilization approaches including the addition of EPDM modified with maleic anhydride and the use of organoclay modified with maleic anhydride-grafted liquid vinyl polybutadiene (LVPB-g-MA). It was observed that the use of LVPB-g-MA modifled organoclay gives increased thermal stability.

LDH is another very important type of filler used in EPDM. Scanning electron micrographs of pure LDH, calcined LDH and DS-LDH are shown in Figure 20.12 [29]. Pure LDH shows the presence of hexagonal platy particles stacked on top of each other. The calcined LDH shows a flake-like structure due to the breaking of the patterned grains in pure uncalcined LDH. The DS-LDH again develops the clear grain boundary with a nonuniform round-edged hexagonal plate-like morphology. Figure 20.13 shows the TEM images of EPDM/LDH nanocomposite with 3 wt% DS-LDH. The lower magnification image (Figure 20.13a) clearly reveals that the DS-LDH particles are mostly dispersed throughout the polymer matrix. However, TEM at the higher magnification (Figure 20.13b) shows the diffused nature of the particles, which vary

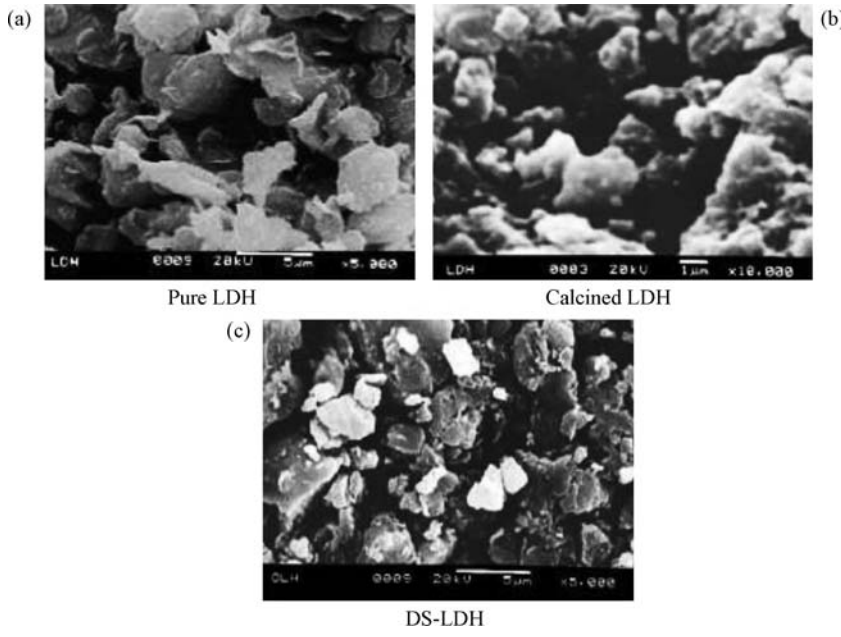

Figure 20.12 SEM images of (a) pure Al-LDH; (b) calcined LDH; and (c) DS-LDH (Reproduced from *Composites Science and Technology*, **67**, H. Acharya, S.K. Srivastava and A.K. Bowmick, "Synthesis of partially exfoliated EPDM/LDH nanocomposites by solution intercalation: structural characterization and properties," 2807–2816 (Figure 6), © 2007, with permission from Elsevier.)

widely in sizes and shape. These are associated with stacks of few layers as well as in the monolayer form in the EPDM matrix, as evident from Figure 20.13(c and d). The average thickness and lateral dimension of the DS-LDH layers varies from 2 to 4 nm and 50 to 100 nm, respectively.

Figure 20.14 shows topographic and phase contrast images of EPDM/LDH nanocomposites by tapping mode AFM [29]. In this, the dispersion nature of LDH particles (3 wt% of DS-LDH) in EPDM matrix can be observed directly. The structural hierarchies of the surface of nanocomposite films indicate sufficient mechanical (intrinsic) contrast between the inorganic LDH particles and the EPDM matrix. The brighter phase contrast and the darker areas in Figure 20.14a correspond to the LDH particles and EPDM matrix, respectively. It is also evident from the phase image of surface morphology that te LDH particles are randomly well dispersed in the skin layer of nanocomposite EPDM matrix, which is in good agreement with XRD patterns. The large sheet (50–100 nm in the horizontal direction) in the higher magnification of topographic image area in Figure 20.14b shows an average thickness of $\approx$18 nm. It is also observed from a three-dimensional image that the thickness of the LDH platelets in the nanocomposite is somewhat higher than their individual platelets. The apparent broadening feature of height in the LDH particle distribution is possibly due to the interaction of the tip with submerged LDH platelets in nanocomposite [41] which are not perfectly perpendicular to the EPDM matrix.

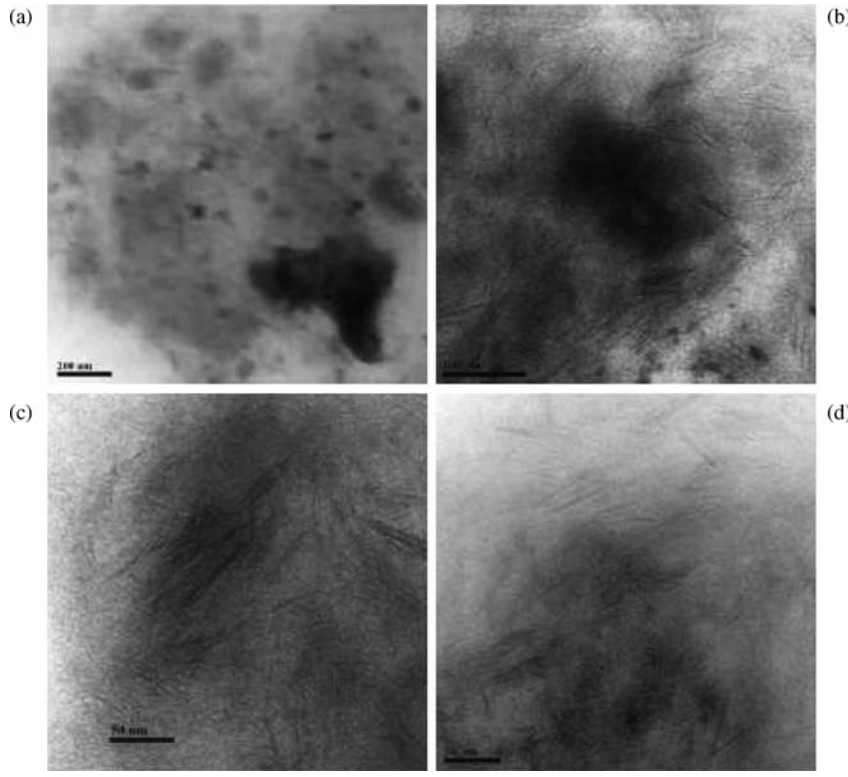

Figure 20.13 TEM images of EPDM nanocomposite containing 3 wt% of DS-LDH (a) at low magnification; (b) at high magnification; (c) stacks of LDH layers; and (d) LDH monolayer (Reproduced from *Composites Science and Technology*, **67**, H. Acharya, S.K. Srivastava and A.K. Bowmick, "Synthesis of partially exfoliated EPDM/LDH nanocomposites by solution intercalation: structural characterization and properties," 2807–2816 (Figure 7), © 2007, with permission from Elsevier.)

Figure 20.15 [92] represents the TG curves of pure EPDM and EPDM/LDH nanocomposites with different wt% of DS-LDH content; and the results are summarized in Table 20.11 [30]. They clearly demonstrate that the thermal decomposition temperature of nanocomposites is relatively higher than its pure counterpart. The degradation rate for pure EPDM is faster above 380 °C while, in the case of its nanocomposites, it is much slower up to 405 °C. Such a slow rate of degradation towards 10% weight loss in EPDM/LDH nanocomposites is possibly due to dehydration and thermal decomposition of DS-LDH. The weight loss in the TG before the onset of oxidative thermal decomposition of unsaturated organic backbone of the pure EPDM in its LDH nanocomposites promotes the charring process and plays an important role for fire safety, where the efficient charring process occurs between the processing temperature and the decomposition temperature [42]. Figure 20.15 and data presented in Table 20.11 also indicate that the thermal stability of EPDM nanocomposite containing 3 wt% of LDH is about 40 °C

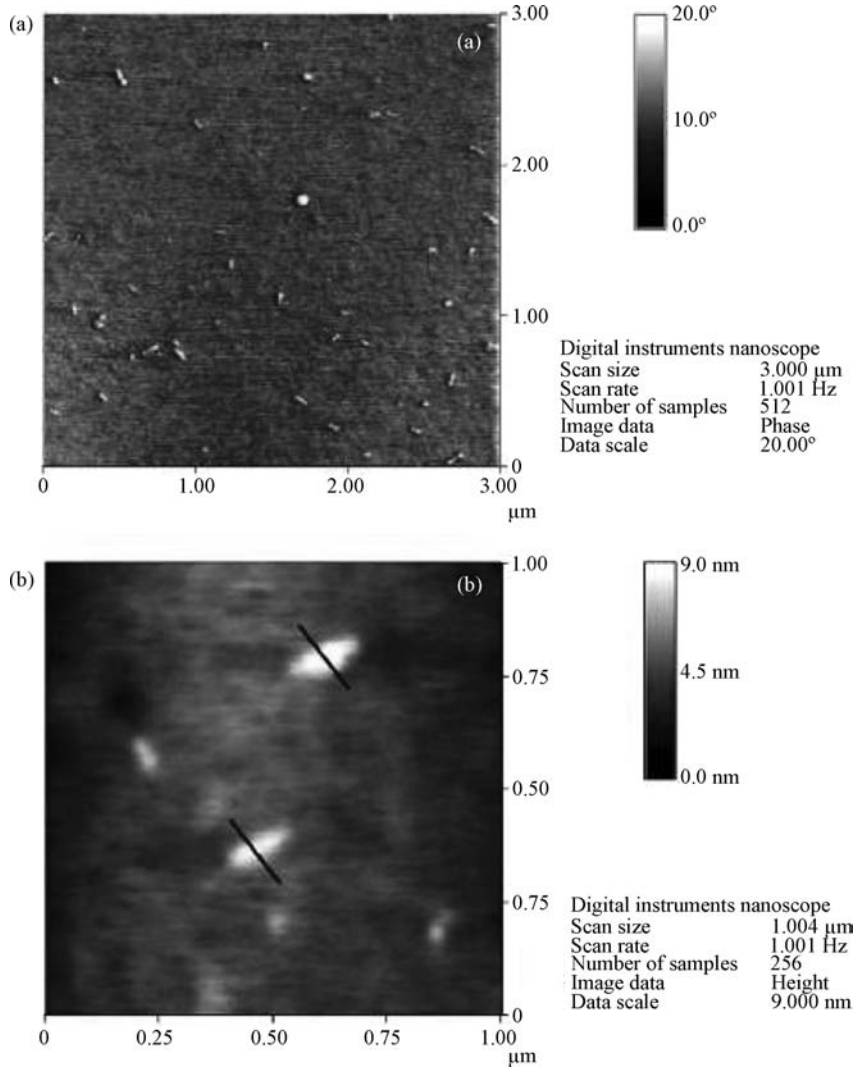

Figure 20.14 Tapping mode AFM phase (a) height and (b) images of EPDM/LDH nanocomposite (Reproduced from *Composites Science and Technology*, **67**, H. Acharya, S.K. Srivastava and A.K. Bowmick, "Synthesis of partially exfoliated EPDM/LDH nanocomposites by solution intercalation: structural characterization and properties," 2807–2816 (Figure 8), © 2007, with permission from Elsevier.)

higher than pure EPDM when 10% weight loss was selected as a point of comparison [30]. This is due to the fine dispersion of DS-LDH nanolayer which, in turn, obstructs the internal diffusion of heat and gaseous small molecules formed during thermal oxidation. Above 3 wt% of DS-LDH loading, the thermal stability of the nanocomposites decreases, possibly due to the presence of DS-LDH aggregates in the EPDM matrix. The enhanced thermal stability of the

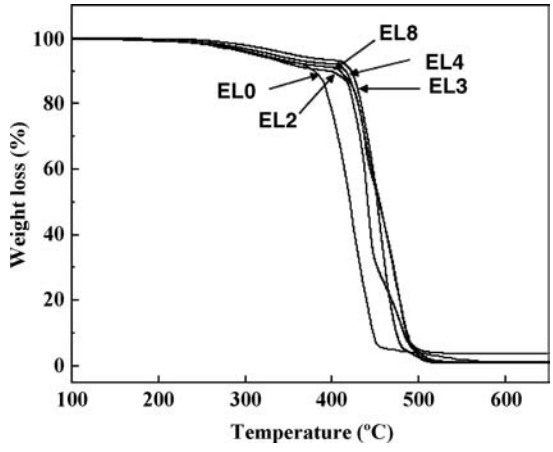

Figure 20.15 TGA profiles EPDM/LDH nanocomposites; EL0, EL2, EL3, EL4 and EL8 refer to EPDM containing 0, 2, 3, 4 and 8 wt% DS-LDH content in EPDM (Reproduced from H. Acharya, T. Kuila, S.K. Srivastava and A.K. Bhowmick, "A solution blending route to ethylene propylene diene terpolymer/layered double hydroxide nanocomposites," *Nanoscale Research Letters*, **2**, 1–5 (Figure 7), © 2007, with kind permission of Springer Science and Business Media.)

polymer-LDH nanocomposites is attributed to the lower permeability of oxygen and the diffusibility of the degradation products from the bulk of the polymer caused by the exfoliated LDH in the composites [93]. It is also interesting to note that the thermal stability of nanocomposites increases with DS-LDH content above the degradation temperature when the selected point of comparison was taken on 50% weight loss. This in all probability is due to the uniform molecular dispersion of a small amount of DS-LDH layers in the EPDM matrix.

Table 20.11 Thermal stability data of neat EPDM and its LDH nanocomposites [30]

Sample[1]	10 wt% decomposition temperature (T_{10} °C)	25 wt% decomposition temperature (T_{25} °C)	50 wt% decomposition temperature (T_{50} °C)
EL0	377	398	417
EL2	393	428	441
EL3	422	438	452
EL4	416	435	454
EL8	408	435	454

[1]EL0, EL2, EL3, EL4 and EL8 refer to EPDM containing 0, 2, 3, 4 and 8 wt% of DS-LDH, respectively.

TG curves of neat EPDM and EPDM mesoporous silica nanocomposites are shown in Figure 20.16 and the related enhancements are recorded in Table 20.12 [30]. It is known that EPDM undergoes a very sharp one-step weight loss corresponding to the thermal degradation of unsaturated organic backbone accompanied by main-chain scission on oxidation [94–96]. The thermal stability corresponding to thermal decomposition temperature for 25 wt% loss in mass (T_{10}) improves successively from 380 to 440 °C from neat EPDM to 10 wt%

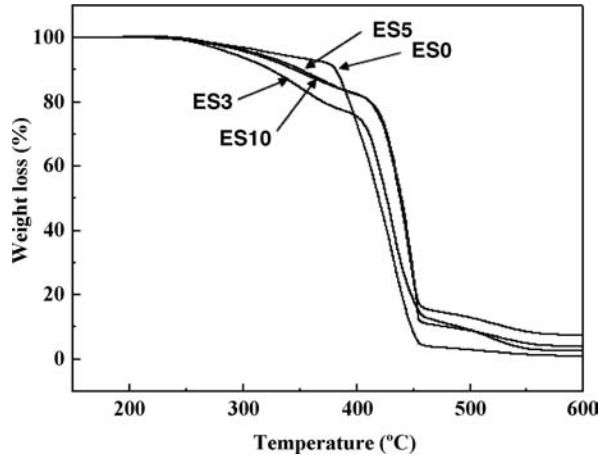

Figure 20.16 TGA profile of EPDM nanocomposites containing 0, 3, 5 and 10 wt% of organomodified mesoporous silica [30]

silica-containing EPDM nanocomposites. Such a significant improvement in thermal stability of EPDM/mesoporous silica nanocomposites is more likely due to the presence of silica mesopore, which offers a great barrier effect to hinder the formation of small molecules during thermal decomposition and simultaneously resists their movement during desorption from the surface.

Table 20.12 Thermal stability behavior of neat EPDM organomodified mesoporous silica nanocomposites [30]

Sample[1]	10 wt% decomposition temperature (T_{10} °C)	25 wt% decomposition temperature (T_{25} °C)	50 wt% decomposition temperature (T_f °C)
ES0	377	398	417
ES3	323	404	427
ES5	351	423	440
ES10	345	421	438

[1]ES0, ES3, ES5 and ES10 refer to EPDM containing 0, 3, 5 and 10 wt% of mesoporous silica, respectively.

Figure 20.17 shows TG/DTG curves of nonoxidative (under nitrogen flow) thermal degradation of EPDM/EVA nanocomposites with varying EPDM/EVA in the ratio of 50/50 and 16Me-MMT contents [97]. Similar to neat EPDM/EVA, the blended nanocomposites also undergo two-step decomposition. The first step between 300 and 400 °C corresponds to the emission of the acetic acid (deacetylation), while the second step is associated with the polyolefinic (polyethylenic and polypropylinic) main-chain scission. The process of deacetylation of EPDM/EVA/layered silicate blend nanocomposites in the first step is accelerated by 16Me-MMT, which corresponds to an initial additional step because of the previous decomposition of hexadecyl ammonium ions. According to Zanetti *et al.* [98], the acceleration is due

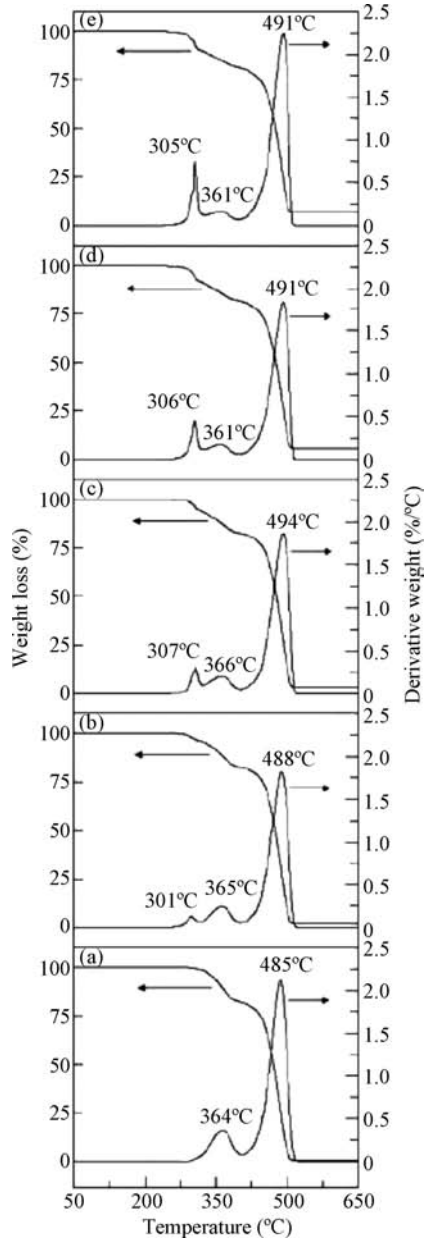

Figure 20.17 TG/DTG of (a) neat EVA/EPDM; (b) EVA/EPDM and 2 wt% 16Me-MMT; (c) EVA/EPDM and 4 wt% 16Me-MMT; (d) EVA/EPDM and 6 wt% 16Me-MMT; and (e) EVA/EPDM and 8 wt% 16Me-MMT [97] (Reprinted from H. Acharya, S.K. Srivastava and A.K. Bhowmick, "Ethylene propylene diene terpolymer/ethylene vinyl acetate/layered silicate ternary nanocomposite by solution method," *Polymer Engineering and Science*, **46**, 837–843 (Figure 6), with the permission of John Wiley & Sons, Inc.)

to the catalyzing effect of protonated silicate layers owing to the initial decomposition of organoclay. In addition, first-step weight loss increases with increasing filler concentration in the EPDM/EVA matrix due to the presence of an increasing amount of hexadecyl ammonium ion. The unsaturated backbone of EPDM/EVA in the second step involves radical scission for nonoxidative degradation and thermal combustion for oxidative degradation [99]. It is also clearly observed that the initial thermal decomposition temperature slightly decreases in the presence of 16Me-MMT, while the weight loss corresponding to the different steps for pure blend and its nanocomposites indicates improved thermal stability during main-chain degradation compared to the neat EPDM/EVA blend. This in all probability is due to the barrier effect of montmorillonite, which inhibits the cooperative motion of the small molecules formed as decomposition products. It is also observed that the thermal stability of EPDM/EVA blend nanocomposites in air is relatively much higher than that of the pure polymer blend itself. This is invariably due to the formation of char under oxidative degradation, which acts as a physical barrier and prevents the permeation of air. However, the possibility of a strong interaction between the MMT layers and elastomer chains because of the uniform dispersion of MMT particles in the thermoplastic elastomer matrix also cannot be ruled out. Table 20.13 shows that, in either case (oxidative vs nonoxidative degradation), stability is highest for the nanocomposites containing 4 wt% 16Me-MMT, suggesting a better dispersion of layered silicate in the polymer matrix. The hybrid containing 8 wt% 12Me-MMT exhibits no further increase, rather it shows some decrease in the initial thermal decomposition temperature, probably due to a weak interaction between the 16Me-MMT layers and the polymer blend matrix because of the aggregation of 16Me-MMT particles. Such behavior could be explained on the basis of the relative proportion of exfoliated and intercalated species with 16Me-MMT content [99].

Table 20.13 Degradation temperature of EPDM/EVA/MMT nanocomposites at 10, 25 and 50 wt% loss in mass [97]

Sample[1]	In air atmosphere			In nitrogen atmosphere		
	T (°C) for 10 wt% loss	T (°C) for 25 wt% loss	T (°C) for 50 wt% loss	T (°C) for 10 wt% loss	T (°C) for 25 wt% loss	T (°C) for 50 wt% loss
EEC110	341	387	453	357	438	471
EEC112	339	421	455	351	446	474
EEC114	339	433	460	338	446	475
EEC118	327	428	456	309	437	475

[1]EEC110, EEC112, EEC114 and EEC118 refer to EPDM/EVA containing 0, 2, 4 and 8 wt% of 16-Me-MMT, respectively.

(Reproduced from H. Acharya, S.K. Srivastava and A.K. Bhowmick, "Ethylene propylene diene terpolymer/ethylene vinyl acetate/layered silicate ternary nanocomposite by solution method," *Polymer Engineering & Science*, **46**, 837–843, © 2006, with the permission of John Wiley & Sons, Inc.)

The thermal degradation behavior of LDPE/EPDM composites containing nano-kaolin and nano-HAO (nanosized hydroxyl aluminum oxalate) has been explored by Chang *et al.* [100]. TG of the LDPE/EPDM blends indicates the two-step thermooxidative degradation in an oxygen atmosphere. However, when nano-HAO is added to this blend, the mechanism of the thermooxidative degradation reaction composite is changed. It is also noted that the nano-

kaolin together with nano-HAO had little effect on the mechanism of the thermooxidative degradation reaction of nano-HAO/LDPE/EPDM composites. When 10% nano-kaolin is replaced by 10% nano-HAO in the composites, the decomposition temperature at 5 wt% loss of the composites is enhanced from 289.2 to 305.7 °C, indicating the enhanced thermal stability of the composites in the presence of nano-kaolin. The investigations have been made using EPDM rubber and nano-SiO_2 particles simultaneously to modify polypropylene (PP) [101–103]. This is mainly due to the fact that the appplication of PP (though one of the important commodity polymers widely used in automobiles, household appliances and the construction industry due to its balanced mechanical properties) is limited by its brittleness, especially at low temperature, as well as its low stiffness at elevated temperature.

20.4.4 Acrylonitrile Butadiene Rubber

Elastomer nanocomposites consisting of nitrile butadiene rubber (NBR) latex and layered silicates have been prepared by a modified latex shear blending process aided with ball milling [104]. The mode of dispersion of layered silicates in NBR is partially exfoliated and intercalated when the concentration of layered silicates is below 7.5 wt%, as evidenced by transmission electron microscopy and X-ray diffraction results. These nanocomposites display higher thermal stabilities than neat rubber.

M.A. Kader *et al.* [105] reported similar work for NBR and its nanocomposites containing 5 and 10 phr Na-MMT. The initiation of degradation of pristine NBR was found to occur at around 367 °C and maximum degradation occurred at 467 °C. However, the maximum degradation temperatures were slightly increased to 471 and 473 °C for NBR nanocomposites containing 5 and 10 wt% Na-MMT respectively. The presence of residue beyond 600 °C in the TGA curves is due to the presence of compounding ingredient in addition to the inorganic clay in nanocomposites. The observed increase in the thermal stability of NBR/MMT may be due to the high thermal stability of clay and the interaction between clay layers and polymer matrix through intercalation/exfoliation.

Jin-Tae *et al.* [106] prepared nanocomposites of octadecyl-modified organophilic montmorillonite (C18-MMT), nitrile-butadiene rubber (NBR) and a coupling agent during a melt compounding process at room temperature. Figures 20.18 and 20.19 show TG and derivative curves of C18-MMT/NBR/coupling agent (3-mercapto-propyl trimethoxy silane) nanocomposites, respectively. It is evident that pure NBR and C18-MMT show a decomposition onset temperature (DOT, the temperature at which 5% of the weight loss appears) of 351.8 and 400.1 °C, respectively. In the presence of the coupling agent, DOT and maximum decomposition temperature (MDT, at which maximum weight loss occurs) depend on the concentration of the coupling agent. It is observed that a large weight loss occurs in C18-MMT/NBR/coupling agent nanocomposites at a higher temperature, which ranges from 412.7 to above 600 °C. In the case of pure NBR, the temperature ranges between 351.8 and 496 °C. For the C18-MMT/NBR nanocomposite without a coupling agent, the temperature ranges from 400.1 to 558.1 °C. This clearly suggests that the coupling agent affects the thermal stability of the C18-MMT/NBR nanocomposite. The higher thermal stability in the presence of the coupling agent is attributed to the formation of coupling bonds. Optimal thermal stabilization is obtained at a coupling agent content of about 1–5 parts per hundred filler (phf). At 10 phf the thermal stabilization is slightly decreased.

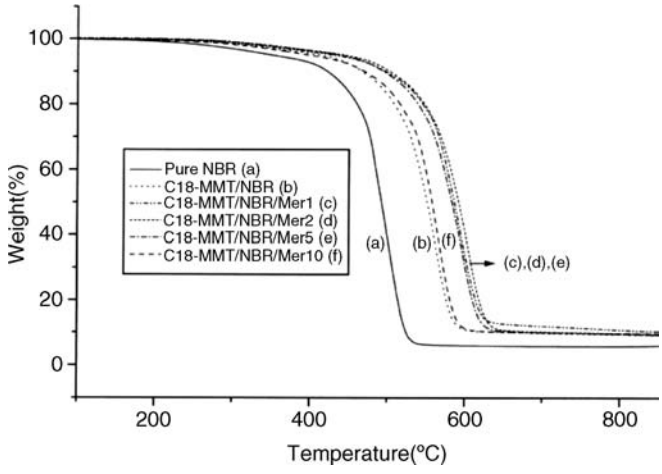

Figure 20.18 Thermogravimetric analysis of C18-MMT/NBR/coupling agent nanocomposites. MER1, −2, −5, −10 indicate the contents (phf) of 3-(mercaptopropyl)trimethoxy silane (Reproduced from J-T. Kim, D-Y. Lee, T-S. Oh, D-H. Lee, "Characteristics of nitrile-butadiene rubber layered silicate nanocomposites with silane coupling agent," *Journal of Applied Polymer Science*, **89**, 2633–2640 (Figure 4), © 2003, with the permission of John Wiley & Sons, Inc.)

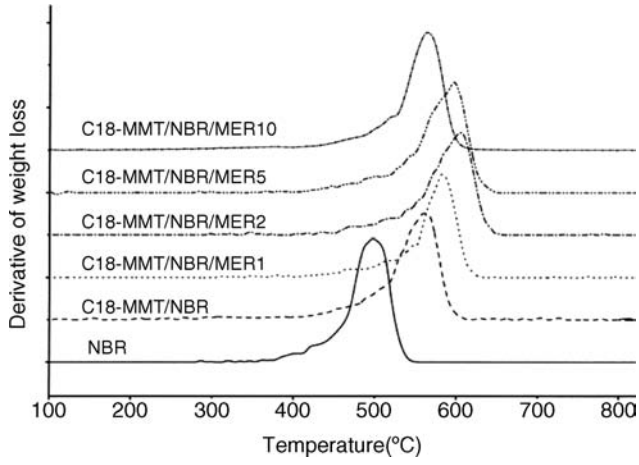

Figure 20.19 Derivatives of weight loss with respect to temperature. MER1, −2, −5, −10 indicate the contents (phf) of 3-(mercaptopropyl)trimethoxy silane (Reproduced from J-T. Kim, D-Y. Lee, T-S. Oh, D-H. Lee, "Characteristics of nitrile-butadiene rubber layered silicate nanocomposites with silane coupling agent," *Journal of Applied Polymer Science*, **89**, 2633–2640 (Figure 5), © 2003, with the permission of John Wiley & Sons, Inc.)

20.4.5 Hydrogenated Nitrile Butadiene Rubber

Huang and coworkers [51] performed thermal degradation analysis of HNBR vulcanizates is in both nitrogen and air atmospheres, respectively. The TGA curves of different HNBR vulcanizates in nitrogen in Figure 20.20a exhibit one major degradation step around 733 K, which is associated with decomposition of the polymer chain. However, in air, the TGA curves shown in Figure 20.20b exhibit two major degradation steps around 738 and 768 K, respectively. For the purpose of comparison, temperatures at the maximum rate of decomposition for different materials in the derivative thermograms (DTG) are designated as T_p and summarized in Table 20.14. It should be noted that T_p is higher in air than in nitrogen. This is caused by the faster heating rate in air. From Table 20.14, it can be seen that T_p is greatly improved with the addition of organoclay, and it is increased with clay content. It is believed that layered clay particles can insulate underlying materials and provide a tortuous path for heat/gas transportation [107]. This, in turn, significantly slows down the degradation process. A second degradation step observed at higher temperature in air suggests a different degradation mechanism [108]. It is suspected that a –CN group in the decomposition product from Step I can react with oxygen to form a more stable condensation product via condensation reaction. This condensation product then decomposes at a higher temperature in Step II. With the addition of organoclay, both T_p and T_i^a (starting degradation temperature) are increased significantly.

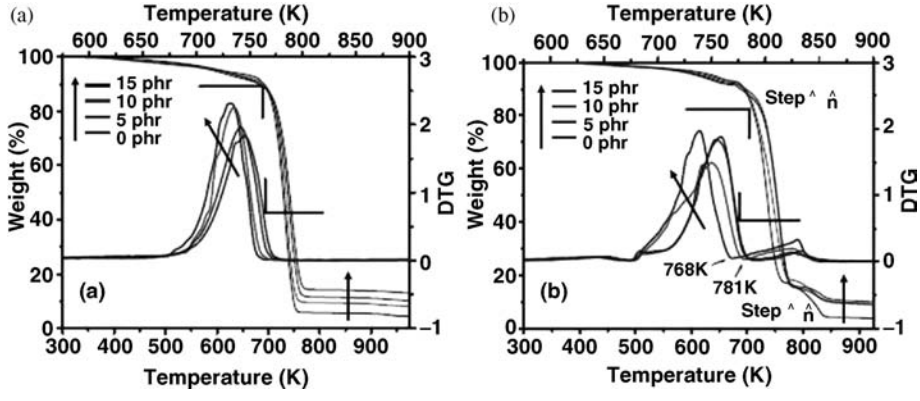

Figure 20.20 TGA and DTG curves of HNBR vulcanizates with different clay content in (a) nitrogen (heating rate, 10 K/min) and (b) air (heating rate 20 K/min) (Reproduced from A. Huang, X. Wang, D. Jia, Y. Li, "Thermal stability and aging characteristics of hnbr/clay nanocomposites in air, water and oil at elevated temperature," *e-Polymers*, **051** (Figure 3), © 2007, with permission from e-Polymers (http://www.e-polymers.org).)

Recently, two methods have been described for the preparation of hydrogenated nitrile rubber (HNBR)/carbon nanotube (CNT) nanocomposites and the mechanical properties of the composites have been studied [109]. However, the thermal behavior of these composites is yet to be investigated.

Table 20.14 T_p of different HNBR vulcanizates in N_2 and air atmospheres

Organoclay/phr	T_p in N_2 atmosphere/K	T_p of step I in air atmosphere/K	T_i[1] of step II in air atmosphere/K
0	731	738	768
5	736	749	781
10	742	754	787
15	745	759	787

[1] T_i: Starting decomposition temperature of step II in air atmosphere.

(Reproduced from A. Huang, X. Wang, D. Jia and Y. Li, "Thermal stability and aging characteristics of hnbr/clay nanocomposites in air, water and oil at elevated temperature," *e-Polymers*, **051** (Table 5), © 2007, with permission from e-Polymers (http://www.e-polymers.org).)

20.4.6 Styrene Butadiene Rubber

Mousa and Karger-Kocsis [110] reported the formation of SBR nanocomposites with organophilic montmorillonite (OMMT) having intercalated and partly exfoliated structure with improved viscoelastic and mechanical properties. However, a completely exfoliated SBR/MMT nanocomposite prepared by Zhang *et al.* [111] reported the formation of exfoliated SBR/MMT nanocomposites by anionic polymerization. The DSC shows that SBR/MMT nanocomposites show a higher T_g than SB (styrene: butadiene, 25 : 75). These findings are also confirmed by Sandhu and Bhowmick [112], where clay-modified rubber nanocomposites show that T_g is shifted by a few degrees to the higher temperature, suggesting that it is due to filler–polymer interaction. TGA and DTG studies on these samples have been carried out to determine the onset decomposition temperatures and peak temperatures of the samples. The value of onset decomposition temperatures of SBR/MMT nanocomposites containing 0, 1.0, 2.0, 2.5, 3.0 and 4.0 wt% OMMT are found to be 384.1, 385.8, 393.5, 399.6, 402.8 and 394.5. It is also observed that the initial degradation temperature is shifted for SBR + sodium montmorillonite (1%) + DCP (1%) and SBR + octdecylamine-modified sodium montmorillonite (4%) + DCP (1%) by about 25 °C in the case of modified SBR/clay nanocomposites. The corresponding values for peak temperature (°C) are 431.9, 442.7, 454.4, 456.3, 454.4 and 451.4 for SBR/MMT nanocomposites containing 0, 1.0, 2.0, 2.5, 3.0 and 4.0 wt% OMMT respectively. According to Bhowmick and Sandhu [112], the position of T_{max} is the same for almost all the samples, but the rate of degradation decreases 1.6% per °C to 1.2% per °C for modified clay rubber nanocomposites. In either case, the thermal stability of the SBR/MMT nanocomposites is improved with the addition of OMMT.

Nano-kaolin-filled and precipitated silica when used as a filler in SBR (and NR, BR, EPDM) vulcanized rubber composites effectively improves the operational safety of prophase vulcanizing rubbers, quickens the vulcanization rate and notably advances the production efficiency [113]. The rubber composites filled with nano-kaolin are of outstanding elasticity, and its tensile strength is close to that of precipitated silica, but the tear strength and the modulus is not superior to that of precipitated silica. The nano-kaolin sheets are well dispersed in the rubber matrix in a parallel direction and are less than 100 nm. The good interface links between nano-kaolin and rubber contributes to the excellent thermal stability of the rubber composites.

Styrene butadiene rubber (SBR) as matrix has been reinforced separately with 9, 15 and 21 nm $CaCO_3$ by mixing and compounding on a two-roll mill and has been investigated to study

the effect and loading of nano-$CaCO_3$ on these rubber nanocomposites by TGA and DSC [114]. An appreciable increase in glass transition temperature has been observed from DSC and is attributed to the restricted mobility of nano-$CaCO_3$-filled SBR nanocomposites. TGA shows that, as the size of $CaCO_3$ reduces, the thermal stability increases as compared to pristine SBR.

Venter *et al.* [115] studied the thermal stability of a silica-filled SBR/BR composite. In the presence of silica particles, the decomposition temperature is shifted to a higher temperature, which indicates a better polymer/filler interaction.

20.4.7 Silicone Rubber

Very limited work has been extended on the preparation of silicone rubber nanocomposites [116–122]. Kong [116] focused their work on the synthesis of silicone rubber (SR)/clay nanocomposites by a melt-intercalation process using synthetic Fe-montmorillonite (Fe-MMT) and natural Na-MMT which were modified by cetyltrimethylammoniumbromide (CTAB). The TEM image in Figure 20.21a shows the SR/Fe-MMT nanocomposite image, the nanolayers generated by the exfoliation of clay tactoids tending to orient parallel to one another. However, the TEM image in Figure 20.21b shows the SR/Na-MMT nanocomposites, wherein the nanolayers emanating from different tactoids were nearly orthogonal to each other, and there was little or no tendency for the nanolayers to orient uniformly throughout the matrix. The results are also in accordance with the XRD patterns. The thermal stability of pure

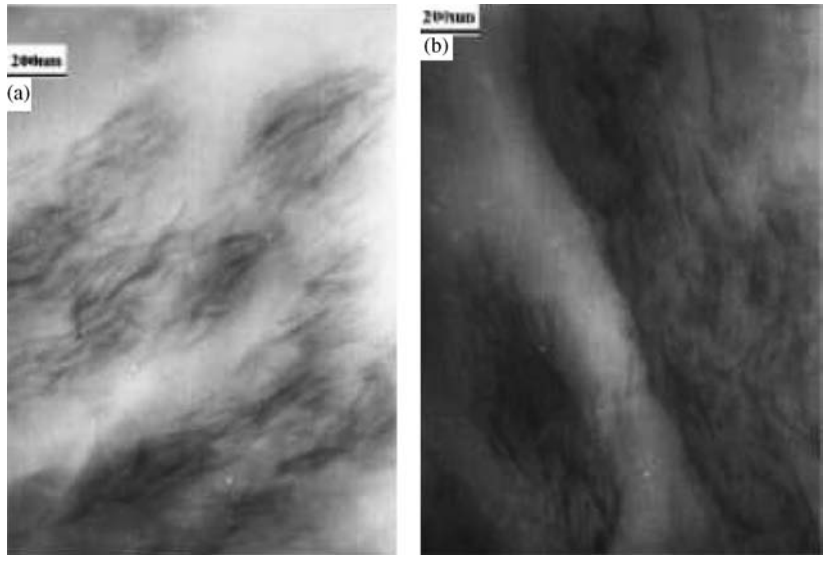

Figure 20.21 TEM micrographs of SR/clay nanocomposites: (a) 4% Fe-OMT/SR nanocomposites and (b) 4% Na-OMT/SR nanocomposites (Reprinted from Q. Kong, Y. Hu, L. Song, Y. Wang, Z. Chen and W. Fan, "Influence of Fe-MMT on crosslinking and thermal degradation in silicone rubber/clay nanocomposites," *Polymers for Advanced Technologies*, **17**, 463–467 (Figure 2), © 2006, with the permission of John Wiley & Sons, Inc.)

SR, SR/Fe-MMT and SR/Na-MMT nanocomposites has also been investigated and the results are shown in Figure 20.22. It is noted that the thermal stability of the SR/clay nanocomposites is noticeably improved by adding MMT into the SR matrix. The results show the temperatures at which 10% degradation occurs, $T_{0.1}$, as a measure of the onset of the degradation, and at which 50% degradation occurs, $T_{0.5}$, as the midpoint of the degradation process. These temperatures and the amount of residue that is nonvolatile at 700 °C are higher with clay content in the nanocomposites than pure SR. TGA curves of SR/clay are given in Figure 20.22. The two kinds of SR/clay nanocomposites have a similar process of degradation below about 200 °C. Thermal decomposition of the OMT took place at around 200 °C and proceeded according to the Hofmann degradation mechanism [117]. The initial step was the loss of an olefin, followed by the loss of the amine, leaving an acid proton on the surface of the MMT in the place of the ammonium cation. In modified clay, adsorptive water and interlamellar water were lost before 200 °C. At nearly 240 °C, the weight loss of the two kinds of modified clay was equivalent. And the intercalant CTAB decomposed and/or vaporized from MMT. The TGA data in Table 20.15 and TGA curves in Figure 20.22 clearly show that the SR/clay nanocomposites enhanced thermal stability compared to virgin SR. Table 20.15 shows the values for $T_{0.1}$, $T_{0.5}$, and residue at 700 °C. The onset temperature of the degradation was obviously higher for the SR/clay than for pure SR. The onset temperature of pure SR was 415 °C. And thoset of the SR/Fe-MMT and the SR/Na-MMT were 462 and 423 °C, respectively. The midpoint temperature of the degradation for pure SR was 488 °C, and the midpoint temperature of the degradation for 4% Fe-OMT of SR/Fe-MMT was 556 °C and that of SR/Na-MMT was 524 °C. These results indicate that the thermal stability of the SR/clay nanocomposites was obviously improved with the addition of OMT. This could be explained by the fact

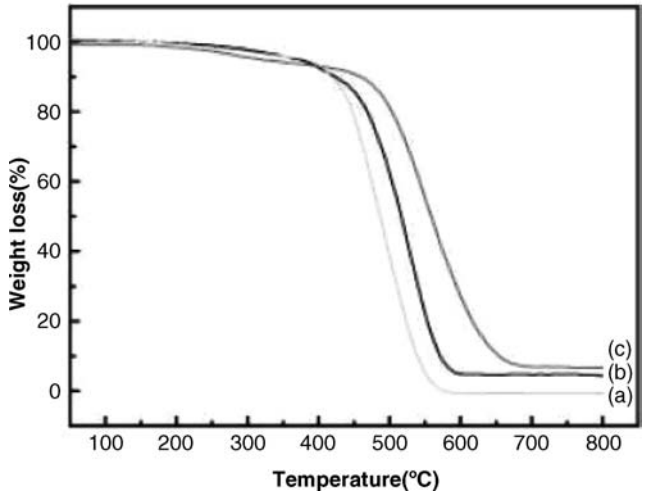

Figure 20.22 TGA curves of SR and their nanocomposites under nitrogen flow: (a) pure SR; (b) 4% Na-OMT/SR/clay nanocomposites; and (c) 4% Fe-OMT/SR/claynanocomposites (Reprinted from Q. Kong, Y. Hu, L. Song, Y. Wang, Z. Chen and W. Fan, "Influence of Fe-MMT on crosslinking and thermal degradation in silicone rubber/clay nanocomposites," *Polymers for Advanced Technologies*, **17**, 463–467 (Figure 3), © 2006, with the permission of John Wiley & Sons, Inc.)

Table 20.15 TGA results of SR/clay nanocomposites and SR

Contents	$T_{(0.1)}$ (°C)	$T_{(0.5)}$ (°C)	Residue at 700 °C (wt%)
Pure SBR	415	488	0.3
1% Fe-MMT	453	543	2.4
4% Fe-MMT	462	556	6.0
7% Fe-MMT	460	558	8.5
4% Na-MMT	427	524	4.9

(Reprinted from Q. Kong, Y. Hu, L. Song, Y. Wang, Z. Chen and W. Fan, "Influence of Fe-MMT on crosslinking and thermal degradation in silicone rubber/clay nanocomposites," *Polymers for Advanced Technologies*, **17**, 463–467 (Table 1), © 2006, with the permission of John Wiley & Sons, Inc.)

that strong interaction between OMT and polymer chains prevented the segmental motion of the macromolecules.

Wang *et. al.* [120] also reported the synthesis and properties of silicone rubber–organomontmorillonite hybrid nanocomposites prepared by a melt intercalation process. TGA traces of silicone rubber and its composites with 8.1 vol% of filler (organoMMT and aerosilica) have been studied [121]. These results have shown improvements in the decomposition temperatures of filled silicone rubber–organoMMT hybrids (433 °C) and aerosilica-filled silicone rubber (440 °C) compared to unfilled silicone rubber (381 °C). The comparison of TGA data of SR/organomodified MMT and SR/aerosilica nanocomposites prepared by solution blending [122] have shown the best reinforcing effect for SR nanocomposite with 1 wt% of organomodified MMT. This has the highest center temperature of thermal degradation (535.98 °C) with respect to the neat SR (526.34 °C).

El-Hag *et al.* [118] prepared vulcanized silicone rubbers filled with 3, 5, 7 and 10% of 12 nm hydrophobic fumed silica by weight (wt%) and subjected them to TGA in a 5% oxygen and 95% helium environment from 100 to 800 °C, as shown in Figure 20.23. The weight loss for the fumed silica is also shown for the same temperature range for comparison. The weight loss for

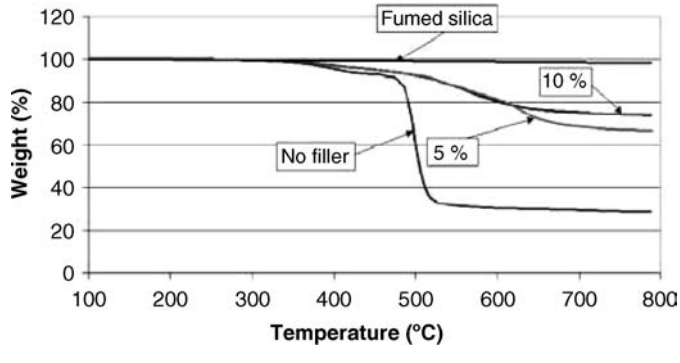

Figure 20.23 TGA analysis of different silicone rubber compositions (© 2004 IEEE. Reproduced from A.H. El-Hag, L.C. Simon, S.H. Jayaram, and E.A. Cherney, Annual Report – Conference on Electrical Insulation and Dielectric Phenomena, 688–691 (Figure 4), © 2004, with permission from Institute of Electrical and Electronics Engineers (IEEE).)

unfilled silicone is about 66.5%, whereas it is only 28.5% for 5% filled sample. The first derivative of the TGA curves in Figure 20.24 provides an idea about the temperature at which decomposition began for both filled and unfilled silicone rubber. The first peak, which is not very strong, was noticed for both the filled and unfilled silicone rubber around 400 °C. The second peak, which appears around 500 °C, showed a significant difference in terms of the steepness that corresponds to the weight loss to filler amount. While the rate of weight change (%/°C) is around 0.15 for both 5 and 10% nanofilled silicone rubber, it exceeds 2.25 for unfilled silicone rubber. All these observations suggest the possibility of strong chemical bonding between the fumed silica and the silicone rubber matrix. The estimated weight loss of the composites under investigation when compared suggested that addition of fumed silica improves the chemical bonding of composites and accounts for the lesser weight loss in TG.

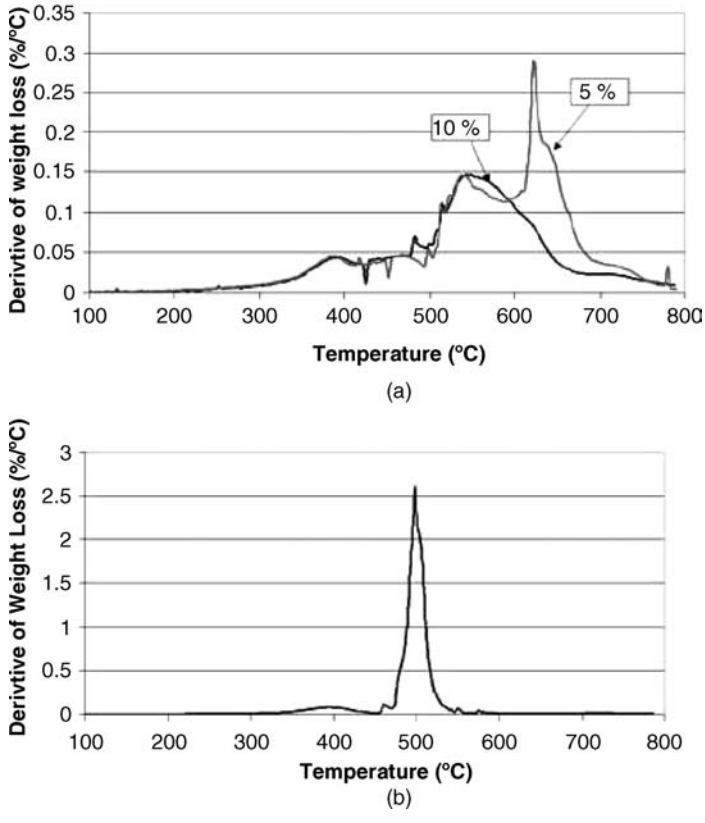

Figure 20.24 Derivative of weight loss for (a) both 10 and 5% nanofilled silicone rubber and (b) unfilled silicone rubber (© 2004 IEEE. Reproduced from A.H. El-Hag, L.C. Simon, S.H. Jayaram and E.A. Cherney, Annual Report – Conference on Electrical Insulation and Dielectric Phenomena, 688–691 (Figure 5), © 2004, with permission from Institute of Electrical and Electronics Engineers (IEEE).)

20.4.8 Butyl Rubber

High *cis*-1,4-polybutadiene or butyl rubber (BR) is widely used in the tire industry due to its superior dynamic mechanical properties, abrasion resistance, elasticity and flex crack resistance [119]. BR cannot form crystals at room temperature unless it is sufficiently stretched (stress-induced crystallization). Moreover, the stress-induced crystallization of BR is obviously less than that of natural rubber (NR) [123]. That is why the tensile strength of BR is much lower than that of NR and, therefore, BR must be reinforced by filler in order to obtain adequate strength. Carbon black is an effective reinforcing filler for BR but the carbon black-reinforced BR is always black in color, which limits its applications in medical, sports and domestic products. However, not much work has been reported on the development and characterization of BR nanocomposites [124–126].

Hwang *et al.* [124] prepared nanocomposites of intercalated and exfoliated organosilicates in butadiene rubber (BR) by using a two-stage melt blending process and examined them by TGA. Marked enhancements in the thermal properties of BR occurred when it incorporated <10 parts of organosilicates and the loading ratio of the organosilicate to dicarboxylic acid-terminated butadiene oligomer was approximately three. The degradation temperature for the BR nanocomposite containing only a ten-part loading of organosilicate (561 °C) is 51 °C higher than that of neat BR (510 °C), but it increased only slightly (9–13 °C) upon the addition of CTB compatibilizer. Wang and others [125] also prepared butadiene rubber (BR)/organoclay nanocomposites were prepared by direct melt mixing of BR and clay modified with different primary and quaternary ammonium salts and also extended their work on BR/clay/dimethyl dihydrogenated tallow ammonium chloride (DDAC) nanocomposites [126] prepared by *in situ* organic modification. Figure 20.25 represents the results of TGA of gum BR, BR/pristine clay, BR/organoclay modified with about 40% DDAC and BR/clay/DDAC (75%) vulcanizates [126]. It indicated a slight increase in thermal decomposition temperature for the BR/pristine/40% DDAC and BR/pristine clay vulcanizates with respect to the gum BR. However,

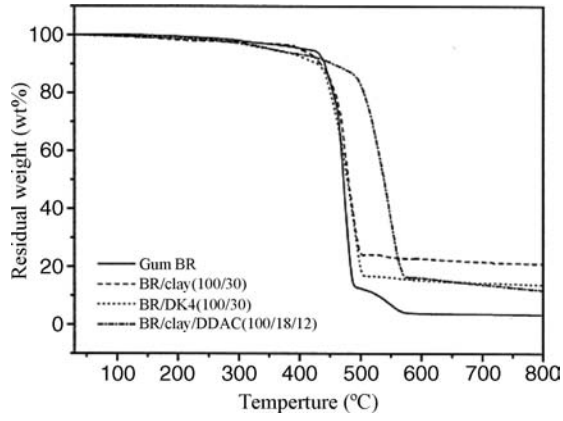

Figure 20.25 TGA thermograms of gum BR, BR/pristine clay, BR/DK4 and BR/clay/DDAC vulcanizates (Reprinted from S. Wang, Y. Zhang, Z. Peng and Y. Zhang, "Morphology and thermal stability of BR/clay composites prepared by a new method," *Journal of Applied Polymer Science*, **99**, 905–913 (Figure 7), © 2006, with the permission of John Wiley & Sons, Inc.)

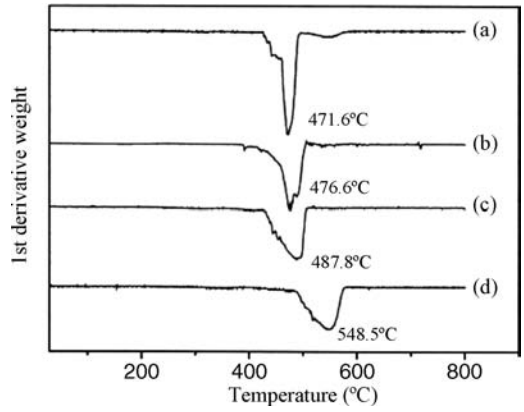

Figure 20.26 DTG curves of (a) gum BR vulcanizate; (b) BR/clay (100/30) vulcanizate; (c) BR/DK4 (100/30) vulcanizate; and (d) BR/clay/DDAC (100/18/12) vulcanizate (Reprinted from S. Wang, Y. Zhang, Z. Peng and Y. Zhang, "Morphology and thermal stability of BR/clay composites prepared by a new method," *Journal of Applied Polymer Science*, **99**, 905–913 (Figure 8), © 2006, with the permission of John Wiley & Sons, Inc.)

the decomposition temperature increased for the BR/clay/DDAC vulcanizates. DTG in Figure 20.26 shows an increase in degradation temperature by 5 °C, when clay was added to BR. For 40% DDAC and clay/DDAC, the temperature increased between 16 and 77 °C, respectively. It is inferred that the clay/DDAC is much more effective in improving the thermal decomposition temperature of BR. This is attributed to the good dispersion of clay particles in the rubber matrix. The good thermal stability of the BR/clay/DDAC composite is due to the hindered out-diffusion of the volatile decomposition products.

20.5 Summary

The most important aspect of these rubber nanocomposites is that all these improvements are obtained at very low filler loading in the polymer matrix. Among the various fillers used, 2-D layered montmorillonite, layered double hydroxide and 3-D framework mesoporous silica offer the richest intercalation chemistry because of their stability and well ordered vacant sites. The fillers used are not only easy to prepare but also, interestingly, the presence of their small amount provides a high extent of improvement in the physicomechanical properties of rubber nanocomposites. In this chapter, we reviewed up-to-date research work related to the thermal degradation of important types of rubber nanocomposites and their aging properties under various temperatures and atmospheres.

References

1. Principia Partners (1999) Nanocomposites 1999: Polymer Technology for the Next Century, Principia Partners, Exton, PA.
2. Vaia, R.A.and Kishnamoorti, R. (eds) (2001) *Polymer Nanocomposites*, vol. **804**, American Chemical Society, Washington, DC.

3. Merkel, T.C., Freeman, B.D., Spontak, R.J. *et al.* (2002) Ultrapermeable, reverse-selective nanocomposite membranes. *Science*, **296**, 519–522.
4. SinhaRay, S. and Okamoto, M. (2003) Polymer/layered silicate nanocomposites: a review from preparation to processing. *Progress in Polymer Science*, **28**, 1539–1641.
5. Varghese, S. and Karger-Kocsis, J. (2003) Melt-compounded natural rubber nanocomposites with pristine and organophilic layered silicates of natural and synthetic origin. *Journal of Applied Polymer Science*, **91**, 813–819.
6. Zanetti, M., Camino, G., and Mülhaupt, R. (2001) Combustion behaviour of EVA/fluorohectorite nanocomposites. *Polymer Degradation and Stability*, **74**, 413–417.
7. Srivastava, S.K., Pramanik, M., and Acharya, H. (2006) Ethylene/vinyl acetate copolymer/clay nanocomposites. *Journal of Polymer Science Part B Polymer Physics*, **44**, 471–480.
8. Pramanik, M., Srivastava, S.K., Samantaray, B.K., and Bhowmick, A.K. (2002) Synthesis and characterization of organosoluble, thermoplastic elastomer/clay nanocomposites. *Journal of Polymer Science Part B Polymer Physics*, **40**, 2065–2072.
9. Pramanik, M., Srivastava, S.K., Samantaray, B.K., and Bhowmick, A.K. (2003) EVA/clay nanocomposite by solution blending: effect of aluminosilicate layers on mechanical and thermal properties. *Macromolecular Research*, **11**, 260–266.
10. Tang, Y., Hu, Y., Wang, S.F. *et al.* (2002) Preparation and flammability of ethylene-vinyl acetate copolymer/montmorillonite nanocomposites. *Polymer Degradation and Stability*, **78**, 555.
11. Zheng, H., Zhang, Y., Peng, Z. *et al.* (2004) Influence of clay modification on the structure and mechanical properties of EPDM/montmorillonite nanocomposites, *Polymer Testing*, **23**, 217–223.
12. Chang, Y.W., Yang, Y., Ryu, S., and Nah, C. (2002) Preparation and properties of EPDM/organomontmorillonite hybrid nanocomposites. *Polymer International*, **51**, 319–324.
13. Acharya, H.and Srivastava, S.K. (2006) Influence of nanodispersed organoclay on rheological and swelling properties of ethylene propylene diene terpolymer. *Macromolecular Research*, **14**, 132–139.
14. Nah, C., Ryu, H.J., Kim, W.D., and Chang, Y.W. (2003) Preparation and properties of acrylonitrile-butadiene copolymer hybrid nanocomposites with organoclays. *Polymer International*, **52**, 1359–1364.
15. Gatos, K.G., and Karger-Kocsis, J. (2007) Effect of the aspect ratio of silicate platelets on the mechanical and barrier properties of hydrogenated acrylonitrile butadiene rubber (HNBR)/layered silicate nanocomposites. *European Polymer Journal*, **43**, 1097–1104.
16. Lu, Y.-L., Li, Z., Yu, Z.-Z. *et al.* (2007) Microstructure and properties of highly filled rubber/clay nanocomposites prepared by melt blending. *Composites Science and Technology*, **67**, 2903–2913.
17. Jiang, M.-J., Dang, Z.-M., and Xu, H.-P. (2007) Enhanced electrical conductivity in chemically modified carbon nanotube/methylvinyl silicone rubber nanocomposite. *European Polymer Journal*, **43**, 4924–4930.
18. Wang, S.H., Zhang, Y., Ren, W.T. *et al.* (2005) Morphology, mechanical and optical properties of transparent BR/clay nanocomposites. *Polymer Testing*, **24**, 766–674.
19. Bhowmick, A.K., and White, J.R. (2002) Thermal, UV-and sunlight ageing of thermoplastic elastomeric natural rubber-polyethylene blends. *Journal of Materials Science*, **37**, 5141–5151.
20. Still, R.H. (1981) *Developments in Polymer Degradtion*, vol. **1** (ed. N. Grassie), Applied Science, London.
21. Stephen, R., Siddique, A.M., Singh, F. *et al.* (2007) Thermal degradation and ageing behavior of microcomposites of natural rubber, carboxylated styrene butadiene rubber latices, and their blends. *Journal of Applied Polymer Science*, **105**, 105–351.
22. Pinnavaia, T.J.and Beall, G.W. (eds) (2001) *Polymer-clay Nanocomposites*, John Wiley & Sons, Ltd.
23. Giannelis, E.P. (1996) Polymer layered silicate nanocomposites. *Advanced Materials*, **8**, 29–35.
24. Gilman. J.W., Jackson, C.L., Morgan, A.B. *et al.* (2000) Flammability properties of polymer-layered-silicate nanocomposites. polypropylene and polystyrene nanocomposites. *Chemistry of Materials*, **12**, 1866.
25. Duan, X.and Evans, D.G.(eds) (2006) *Layered Double Hydroxides*, Springer.
26. Bala, P., Samantaray, B.K., Srivastava, S.K., and Haueseler, H. (2000) Microstructural parameters and layer disorder accompanying dehydration transformation in Na-montmorillonite. *Zeitschrift fur Kristallographie*, **215**, 235–239.
27. Rives, V. (ed.) (2001) *Layered Double Hydroxide: Present and Future*, Nova publishers.
28. Hoffman, U., Endell, K., and Wilm, D. (1933) Kristallstruktur und Quellung von Montmorillonit. *Zeitschrift fur Kristallographie*, **86**, 340–348.
29. Acharya, H., Srivastava, S.K., and Bowmick, A.K. (2007) Synthesis of partially exfoliated EPDM/LDH nanocomposites by solution intercalation: structural characterization and properties. *Composites Science and Technology*, **67**, 2807–2816.

30. Acharya, H. (2007) Synthesis, Characterization and Properties of Polyolefinic Elastomer Nanocomposites, Ph.D Thesis, I.I.T. Kharagpur.
31. Iijima, S., G.A. (1991) Helical microtubules of graphitic carbon. *Nature*, **354**, 56–58.
32. Ajayan, P.M. (2000) *Nanostructural Materials and Nanotechnology* (ed. H.R. Singh), Academic Press, pp. 329–360.
33. Bala, P. (2001) Studies on variation of structural and electrical properties during dehydration and intercalation in 2:1 layered clay minerals and their application of the intercalated clay as filler material, Ph.D Thesis, I.I.T. Kharagpur, India.
34. Manroshan, S. and Baharin, A. (2005) Effect of nanosized calcium carbonate on the mechanical properties of latex films. *Journal of Applied Polymer Science*, **96**, 1550–1556.
35. Alex, R.and Nah, C. (2006) Preparation and characterization of organoclay-rubber nanocomposites via a new route with skim natural rubber latex. *Journal of Applied Polymer Science*, **102**, 3277–3285.
36. Gu, J., Jia, D., Luo, Y., and Cheng, R. (2005) Micromorphology and mechanical properties of natural rubber/nano-calcium carbonate modified by solid phase composites. *Hecheng Xiangjiao Gongye*, **28**, 374–377.
37. Bandyopadhyay, A.and Bhowmick, A.K. (2006) Low and high temperature degradation of polymer/in situ silica hybrid nanocomposites. *Plastics, Rubber and Composites*, **35**, 210–218.
38. Cai, H.-H., Li, S.-D., Tian, G.-R. *et al.* (2003) Reinforcement of natural rubber latex film by ultrafine calcium carbonate. *Journal of Applied Polymer Science*, **87**, 982–985.
39. Wang, Y., Zhang, H., Wu, Y. *et al.* (2005) Structure and properties of strain-induced crystallization rubber–clay nanocomposites by co-coagulating the rubber latex and clay aqueous suspension. *Journal of Applied Polymer Science*, **96**, 318–323.
40. Morlat-Therias, S., Mailhot, B., Gardette, J.-L. *et al.* (2005) Photooxidation of ethylene-propylene-diene/montmorillonite nanocomposites. *Polymer Degradation and Stability*, **90**, 78–85.
41. Morlat-Therias, S., Fanton, E., Tomer, N.S. *et al.* (2006) Photooxidation of vulcanized EPDM/montmorillonite nanocomposites. *Polymer Degradation and Stability*, **91**, 3033–3039.
42. Lonkar, S.P., Kumar, A.P., and Singh, R.P. (2007) Photo-stabilization of EPDM-clay nanocomposites: effect of antioxidant on the preparation and durability. *Polymers for Advanced Technologies*, **18**, 891–900.
43. Valentini, L., Biagiotti, J., Kenny, J.M. *et al*, (2003) Physical and mechanical behavior of single-walled carbon nanotube/polypropylene/ethylene-propylene-diene rubber nanocomposites, *Journal of Applied Polymer Science*, **89**, 2657–2663.
44. Tian, M., Cheng, L., Liang, W., and Zhang, L. (2006) Overall properties of fibrillar silicate/styrene-butadiene rubber nanocomposites. *Journal of Applied Polymer Science*, **101**, 2725–2731.
45. Sadhu, S.and Bhowmick, A.K. (2004) Preparation and properties of styrene-butadiene rubber based nanocomposites: the influence of the structural and processing parameters. *Journal of Applied Polymer Science*, **92**, 698–709.
46. Zhang, H., Wang, Y., Wu, Y. *et al.* (2004) Study on aging properties of clay/rubber nanocomposite. *Xiangjiao Gongye*, **51**, 453–459.
47. Zhao, W., Wu, Y., Wang, Y., and Zhang, L. (2007) Application of montmorillonite/SBR nanocomposites in tire tube. *Xiangjiao Gongye*, **54**, 275–278.
48. Varghese, H., Bhagawan, S.S., and Thomas, S. (2001) Thermogravimetric analysis and thermal ageing of crosslinked nitrile rubber/poly-(ethylene-co-vinyl acetate) blends. *Journal of Thermal Analysis and Calorimetry*, **63**, 749–763.
49. Lin, G., Qian, Y., Zhang, P. *et al.* (2005) Dispersion morphology and mechanical properties of nano-titanium dioxide filled rubber composites. *Hecheng Xiangjiao Gongye*, **28**, 98–104.
50. Zhao, Y., Feng, Y., Liu, L. *et al.* (2002) Study on properties of ZDMA/NBR nanocomposite. *Xiangjiao Gongye*, **49**, 9–14.
51. Huang, A., Wang, X., Jia, D., and Li, Y. (2007) Thermal stability and aging characteristics of hnbr/clay nanocomposites in air, water and oil at elevated temperature. *e-Polymers*, **051**, http://www.e-polymers.org.
52. Lan, L., Wen, X., and Cai, D. (2004) Corona ageing tests of RTV and RTV nanocomposite materials, Eighth IEEE International Congress on Solid Dielectrics, Toulous, France, July 5–9, 2004.
53. IEEE (2003) Std 1523 TM. *Guide for the Application, Maintenance and Evaluation of RTV Silicone Rubber Coatings for Outdoor Ceramic Insulators*, IEEE.
54. Chow, G.M. (2000) *Nanostructured Films and Coatings*, Kluwer Academic Publishers.
55. Lopez-Manchado, M.A., Arroyo, M., Herrero, B., and Biagiotti, J. (2003) Vulcanization kinetics of natural rubber-organoclay nanocomposites. *Journal of Applied Polymer Science*, **89**, 1–15.

56. Bala, P., Samantaray, B.K., Srivastava, S.K., and Nando, G.B. (2004) Organomodified montmorillonite as filler in natural and synthetic rubber. *Journal of Applied Polymer Science*, **92**, 3583–3592.
57. Varghese, S. and Karger-Kocsis, J. (2003) Natural rubber-based nanocomposites by latex compounding with layered silicates. *Polymer*, **44**, 4921–4927.
58. Sharifa, J., Yunus, W.M., Dahlan, K.Z.H., and Ahmad, M.H. (2005) Preparation and properties of radiation crosslinked natural rubber/clay nanocomposites. *Polymer Testing*, **24**, 211–217.
59. Bolland, J.L.and Orr, W.J.C. (1945) Thermal breakdown of rubber. *Transactions of the Institute for the Rubber Industries*, **21**, 133.
60. Straus, S. and Madorsky, S.L. (1953) Pyrolysis of styrene, acrylate, and isoprene polymers in a vacuum. *Journal Research National Bureau Standards*, **50**, 165.
61. Madorsky, S.L., Straus, S., Thompson, D., and Williamson, L. (1949) Pyrolysis of polyisobutene (vistanex), polyisoprene, polybutadiene,GR-S1 and polyethylene in a high vacuum. *Journal Research National Bureau Standards*, **42**, 499.
62. Viet, W., Ismail, H., Rashid, A.A., Takeichi, T., and Thao, V.H. (2008) Organoclay filled natural rubber nanocomposites: the effects of filler loading. *Polymer Plastics Technology and Engineering*, **47**, 1090–1096.
63. Ganter, M., Gronski, W., Reichert, P., and Mulhaupt, R. (2001) Rubber nanocomposites: morphology and mechanical properties of BR and SBR vulcanizates reinforced by organophilic layered silicates. *Rubber Chemistry and Technology*, **74**, 221–235.
64. Li, S.-D., Peng, Z., Kong, L.X., and Zhong, J.-P. (2006) Thermal degradation kinetics and morphology of natural rubber/silica nanocomposites. *Journal of Nanoscience and Nanotechnology*, **6**, 541–546.
65. Sui, G., Zhong, W., Yang, X., and Zhao, S. (2007) Processing and material characteristics of a carbon-nanotube-reinforced natural rubber. *Macromolecular Materials and Engineering*, **292**, 1020–1026.
66. Sharif, J., Yunus, W.M.Z.W., Dahlan, K.H., and Ahmad, M.H. (2006) Natural rubber/poly(ethylene-co-vinyl acetate)-blend-based nanocomposites. *Journal of Applied Polymer Science*, **100**, 353–362.
67. Jansen, P. and Soares, B.G. (1996) Effect of compatibilizer and curing system on the thermal degradation of natural rubber/EVA copolymer blends. *Polymer Degradation and Stability*, **52**, 95–99.
68. Pramanik, M. (2005) Studies on layered materials and polymer nanocomposites, Ph.D Thesis, I.I.T. Kharagpur.
69. Pramanik, M., Srivastava, S.K., Samantaray, B.K., and Bhowmick, A.K. (2001) Preparation and properties of ethylene vinyl acetate-clay hybrids. *Journal of Materials Science Letters*, **20**, 1377–1380.
70. Zanetti, M., Camino, G., Thomann, R., and Mulhaupt, R. (2001) Synthesis and thermal behaviour of layered silicate-EVA nanocomposites. *Polymer*, **42**, 4501–4507.
71. Tang, Y., Hu, Y., Wang, J. *et al.* (2004) Influence of organophilic clay and preparation methods on EVA/montmorillonite nanocomposites. *Journal of Applied Polymer Science*, **91**, 2416–2421.
72. Dutta, J.K., Bhowmick, A.K., Mukunda, P.G., and Chaki, T.K. (1995) Thermal degradation studies of electron beam cured ethylene-vinyl acetate copolymer. *Polymer Degradation and Stability*, **50**, 75–82.
73. Zhang, W., Chen, D., Zhao, Q., and Fang, Y. (2003) Effects of different kinds of clay and different vinyl acetate content on the morphology and properties of EVA/clay nanocomposites. *Polymer*, **44**, 7953–7961.
74. Kuila, T., Acharya, H., Srivastava, S.K., and Bhowmick, A.K. (2008) Rubber/LDH nanocomposites by solution blending. *Journal of Applied Polymer Science*, **108**, 1329–1335.
75. Pramanik, M., Srivastava, S.K., Samantaray, B.K., and Bhowmick, A.K. (2003) Rubber clay nanocomposite by solution blending. *Journal of Applied Polymer Science*, **87**, 2216–2220.
76. Chen, W.and Qu, B. (2004) LLDPE/ZnAl LDH-exfoliated nanocomposites: effects of nanolayers on thermal and mechanical properties. *Journal of Materials Chemistry*, **14**, 1705–1710.
77. Qiu, L., Chen, W., and Qu, B. (2005) Morphology and thermal stabilization mechanism of LLDPE/MMT and LLDPE/LDH nanocomposites. *Polymer*, **47**, 922–930.
78. George, J.J.and Bhowmick, A.K. (2008) Ethylene vinyl acetate/expanded graphite nanocomposites by solution intercalation: preparation, characterization and properties. *Journal of Materials Science*, **43**, 702–708.
79. Teisseidre, G., Pilichowski, J.F., Chmela, S., and Lacoste, J. (1996) Ageing of EPDM-I: photo and thermal stability of EPDM hydroperoxides. *Polymer Degradation and Stability*, **53**, 207.
80. Usuki, A., Tukigase, A., and Kato, M. (2002) Preparation and properties of EPDM–clay hybrids. *Polymer*, **43**, 2185–2198.
81. Acharya, H., Pramanik, M., Srivastava, S.K., and Bhowmick, A.K. (2004) Synthesis and evaluation of high-performance ethylene-propylene-diene terpolymer/organoclay nanoscale composites. *Journal of Applied Polymer Science*, **93**, 2429–2436.

82. Jeon, H.S., Rameshwaram, J.K., Kim, G., and Weinkauf, D.H. (2003) Characterization of polyisoprene–clay nanocomposites prepared by solution blending. *Polymer*, **44**, 5749.
83. DiMarzio, E.A., Yang, A.J.M., and Glotzer, S.C. (1995) *Journal of Research of the National Institute of Standards and Technology*, **100**, 173.
84. Xiao, J., Hu, Y., Wang, Z. *et al.* (2005) Preparation and characterization of poly(butylene terephthalate) nanocomposites from thermally stable organic-modified montmorillonite. *European Polymer Journal*, **41**, 1030–1035.
85. Lee, Y.H., Park, C.B., Sain, M. *et al.* (2007) Effects of clay dispersion and content on the rheological, mechanical properties, and flame retardance of HDPE/clay nanocomposites. *Journal of Applied Polymer Science*, **105**, 1993–1999.
86. Chan, C.-M., Wu, J., Li, J.-X., and Cheung, Y.-K. (2002) Polypropylene calcium carbonate nanocomposites. *Polymer*, **43**, 2981–2992.
87. Zanetti, M., Camino, G., Canavese, D. *et al.* (2002) Fire retardant halogen−antimony−clay synergism in polypropylene layered silicate nanocomposites. *Chemistry of Materials*, **14**, 189–193.
88. Gilman, J.W., Kashivagi, T.C.L., Giannelis, E.P. *et al.* (eds) (1998) *Fire Retardancy of Polymer*, The Royal Sociaty of Chemistry, Cambridge.
89. Wang, Z.and Pinnavaia, T.J. (1998) Hybrid organic−inorganic nanocomposites: exfoliation of magadiite nanolayers in an elastomeric epoxy polymer. *Chemistry of Materials*, **10**, 1820–1826.
90. Ahmadi, S.J., Huang, Y., and Li, W. (2005) Fabrication and physical properties of EPDM–organoclay nanocomposites. *Composites Science and Technology*, **65**, 1069–1076.
91. Kang, D., Kim, D., Yoon, S. *et al.* (2007) Properties and dispersion of EPDM/modified-organoclay nanocomposites. *Macromolecular Materials and Engineering*, **292**, 329–338.
92. Acharya, H., Kuila, T., Srivastava, S.K., and Bhowmick, A.K. (2007) A solution blending route to ethylene propylene diene terpolymer/layered double hydroxide nanocomposites. *Nanoscale Research Letters*, **2**, 1–5.
93. Costa, F.R., Satapathy, B.K., Wagenknecht, U. *et al.* (2006) Morphology and fracture behaviour of polyethylene/Mg–Al layered double hydroxide (LDH) nanocomposites. *European Polymer Journal*, **42**, 2140.
94. Wu, C.L., Zhang, M.Q., Rong, M.Z., and Friedrich, K. (2002) Tensile performance improvement of low nanoparticles filled-polypropylene composites. *Composites Science and Technology*, **62**, 1327–1340.
95. Marcilla, A., Gómez-Siurana, A., Menargues, S. *et al.* (2006) Oxidative degradation of EVA copolymers in the presence of MCM-41. *Journal of Analytical and Applied Pyrolysis*, **76**, 138–143.
96. Hassanpour, S.and Khoylou, F. (2007) Synergistic effect of combination of Irganox 1010 and zinc stearate on thermal stabilization of electron beam irradiated HDPE/EVA both in hot water and oven. *Radiation Physics and Chemistry*, **76**, 1671–1675.
97. Acharya, H., Srivastava, S.K., and Bhowmick, A.K. (2006) Ethylene propylene diene terpolymer/ethylene vinyl acetate/layered silicate ternary nanocomposite by solution method. *Polymer Engineering and Science*, **46**, 837–843.
98. Zanetti, M.and Costa, L. (2004) Preparation and combustion behaviour of polymer/layered silicate nanocomposites based upon PE and EVA. *Polymer*, **45**, 4367–4373.
99. Zhang, W., Chen, D., Zhao, Q., and Fang, Y. (2003) Effects of different kinds of clay and different vinyl acetate content on the morphology and properties of EVA/clay nanocomposites. *Polymer*, **44**, 7953–7961.
100. Chang, Z., Guo, F., Chen, J. *et al.* (2007) Synergistic flame retardant effects of nano-kaolin and nano-HAO on LDPE/EPDM composites. *Polymer Degradation and Stability*, **92**, 1204–1212.
101. Yang, H., Zhang, Q., Guo, M. *et al.* (2006) Study on the phase structures and toughening mechanism in PP/EPDM/SiO2 ternary composites. *Polymer*, **47**, 2106–2115.
102. Yang, H., Zhang, X., Qu, C. *et al.* (2007) Largely improved toughness of PP/EPDM blends by adding nano-SiO_2 particles. *Polymer*, **48**, 860–869.
103. Yang, H., Li, B., Wang, K. *et al.* (2008) Rheology and phase structure of PP/EPDM/SiO_2 ternary composites. *European Polymer Journal*, **44**, 113–123.
104. Hwang, W., Wei, K., and Wu, C.-M. (2004) Preparation and mechanical properties of nitrile butadiene rubber/silicate nanocomposites. *Polymer*, **45**, 5729–5734.
105. Kader, M.A., Kim, K., Lee, Y.-S., and Nah, C. (2006) Preparation and properties of nitrile rubber/montmorillonite nanocomposites via latex blending *Journal of Materials Science*, **41**, 7341–7352.
106. Kim, J.-T., Lee, D.-Y., Oh, T.-S., and Lee, D.-H. (2003) Characteristics of nitrile-butadiene rubber layered silicate nanocomposites with silane coupling agent. *Journal of Applied Polymer Science*, **89**, 2633–2640.

107. Li, F.X., Xu, X.J., Li, Q.B. *et al.* (2006) Thermal degradation and their kinetics of biodegradable poly(butylene succinate-co-butylene terephthate)s under nitrogen and air atmospheres. *Polymer Degradation and Stability*, **91**, 1685.
108. Park, J.W., Oh, S.C., Lee, H.P. *et al.* (2000) A kinetic analysis of thermal degradation of polymers using a dynamic method. *Polymer Degradation and Stability*, **67**, 535–540.
109. Liu, D.Y., Yunfang, S., and Zengmin, Z. (2006) Study on preparation and properties of carbon nanotubes/rubber composites. *Journal of Materials Science*, **41**, 2541–2544.
110. Mousa, A.and Karger-Kocsis, J. (2001) Rheological and thermodynamical behavior of styrene/butadiene rubber-organoclay nanocomposites. *Macromolecular Materials and Engineering*, **286**, 260–266.
111. Zhang, Z., Zhang, L., Li, Y., and Xu, H. (2005) New fabricate of styrene–butadiene rubber/montmorillonite nanocomposites by anionic polymerization. *Polymer*, **46**, 129–136.
112. Sandhu, S.and Bhowmick, A.K. (2003) Effect of chain length of amine and nature and loading of clay on styrene-butadiene rubber-clay nanocomposites. *Rubber Chemistry and Technology*, **76**, 860–875.
113. Zhang, Y., Liu, Q., Wu, Z. *et al.* (2006) Vulcanized rubber composites filled with nano kaolin and precipitated silica. *Hunan Keji Daxue Xuebao, Ziran Kexueban*, **21**, 73–76.
114. Mishra, S., Shimpi, N.G., and Patil, U.D. (2007) Effect of nano CaCO3 on thermal properties of styrene butadiene rubber (SBR). *Journal of Polymer Research*, **14**, 449–459.
115. Venter, S.A.S., Kunita, M.H., R Matos, R. *et al.* (2005) Thermal and scanning electron microscopy/energy-dispersive spectroscopy analysis of styrene-butadiene rubber-butadiene rubber/silicon dioxide and styrene-butadiene rubber-butadiene rubber/carbon black-silicon dioxide composites. *Journal of Applied Polymer Science*, **96**, 2273.
116. Kong, Q., Hu, Y., Song, L. *et al.* (2006) Influence of Fe-MMT on crosslinking and thermal degradation in silicone rubber/clay nanocomposites. *Polymers for Advanced Technologies*, **17**, 463–467.
117. Nyden, M.R.and Gilman, J.W. (1997) Molecular dynamics simulations of the thermal degradation of nano-confined polypropylene. *Computational and Theoretical Polymer Science*, **7**, 191–198.
118. El-Hag, A.H., Simon, L.C., Jayaram, S.H., and Cherney, E.A. (2004) Annual Report – Conference on Electrical Insulation and Dielectric Phenomena, pp. 688–691.
119. Xie, S.Z. (1989) *Handbook of Rubber Industry*, vol. **1**, Chemical Industry Press, Beijing.
120. Wang, S., Long, C., Wang, X., Li, Q., and Qi, Z. (1998) Synthesis and properties of silicone rubber/organomontmorillonite hybrid nanocomposites. *Journal of Applied Polymer Science*, **69**, 1557–1561.
121. Wang, J., Chen, Y., and Jin, Q. (2005) Organic montmorillonite as substitute of aerosilica in addition-type liquid silicone rubber systems. *Macromolecular Chemistry and Physics*, **206**, 2512–2520.
122. Lewicki, J.P., Liggat, J.J., Pethrick, R.A., Patel, M., and Rhoney, I. (2008) Investigating the ageing behavior of polysiloxane nanocomposites by degradative thermal analysis. *Polymer Degradation and Stability*, **93**, 158–168.
123. Göritz, D.and Kiss, M. (1986) On the origin of styrene induced crystallization. *Rubber Chemistry and Technology*, **59**, 40–45.
124. Hwang, W., Wei, K., and Wu, C. (2006) Synergistic effect of compatibilizer in organo-modified layered silicate reinforced butadiene rubber nanocomposites. *Polymer Engineering and Science*, **46**, 80–88.
125. Wang, S., Peng, Z., Zhang, Y., and Zhang, Y. (2005) Structure and properties of BR nanocomposites reinforced with organoclay. *Polymers & Polymer Composites*, **13**, 371–384.
126. Wang, S., Zhang, Y., Peng, Z., and Zhang, Y. (2006) Morphology and thermal stability of BR/clay composites prepared by a new method. *Journal of Applied Polymer Science*, **99**, 905–913.

21

Positron Annihilation Lifetime Spectroscopy (PALS) and Nanoindentation (NI)

Dariusz M. Bieliński[1,2] and Ludomir Ślusarski[1]

[1] *Technical University of Łódź, Institute of Polymer & Dye Technology, Stefanowskiego 12/16, 90-924 Łódź, Poland*

[2] *Institute for Engineering of Polymer Materials & Dyes, Division of Elastomers & Rubber Technology, Harcerska 30, 05-820 Piastów, Poland*

21.1 Introduction

Rubber belongs to very particular group of polymers. Its properties, that is, an ability to reversible, high elongation ranging up to 1000%, are unique. Similar feature cannot be found among any other class of materials. To limit plastic deformations rubber should be slightly crosslinked (vulcanized). To emphasize its particular properties it is often called an elastomer. According to the kinetic and statistical theories of elasticity the mechanism of elastic deformation consists of transitions of coiled macromolecules under stress to a form of linear zig-zag ones. When an external force is removed they return to their previous conformation. A dependence between structure and properties of elastomers has been systematically investigated, initially on an example of natural rubber. However, simultaneously, based on the results of those studies, methods describing the synthesis of different rubbers have been developed and great progress in technology of rubbers processing has been achieved as well. Considerable amounts of fillers are introduced to contemporary applied elastomers, and beyond them different processing aids and auxiliary chemicals are used. Such compositions could be treated as composite materials, strengthen with dispersed particles or in some cases – fibers. During

Rubber Nanocomposites: Preparation, Properties and Applications Edited by Sabu Thomas and Ranimol Stephen
© 2010 John Wiley & Sons (Asia) Pte Ltd

prolonged studies of such systems it has been recognized that their structure is extremely complicated. The properties of rubber depend on many factors, for example: (i) microstructure of rubber macromolecules (stereoregular or irregular configuration), (ii) energy of free rotation in skeletons of macromolecules, (iii) chemical composition (homopolymers, copolymers, therpolymers, block copolymers, presence and location of functional groups), (iv) molecular weight and its distribution, (v) degree of crosslinking and type of crosslinks, (vi) activity and concentration of fillers, (vii) morphology of mixes, (viii) type and energy of intermolecular and interphase interactions, (ix) degree of matrix solvatation by softeners and (x) migration of low molecular weight components toward the surface of samples. It should be stressed that complications arise if two or three rubbers are mixed together, because as a rule they are thermodynamically immiscible and form heterogeneous blends. Other components of the mixes are usually also nonuniformly distributed between the polymer phases. Recently, in the period of the past 20 years, nanofillers have been applied in rubber technology. It was announced that their addition, even in quite small quantities ranging from one to a few phr, influences very positively mechanical, thermal and barrier properties of vulcanizates, decreasing also their flammability. Positive effects can be achieved if the morphology of rubber nanocomposites is perfectly uniform. However, because of the high surface energy of the dispersed phase and its tendency to form aggregates and agglomerates during mixing, it is extremely difficult to prepare such a mix. This in particular concerns the preparation of mixes composed of layered silicates, for example, montmorillonite, intercalated most often with quaternary ammonium salts, and unpolar rubbers of highly coiled macromolecules. In such conditions exfoliation of the filler as a rule is not observed. From our calculations it follows that steric aspects are a reason for insufficient dispersion of the filler, because the medium diameter of coiled macromolecules is greater than the distance between parallel platelets of the filler structure [1]. This is why layered silicates are usually incorporated to solutions of nonpolar rubbers [2].

This chapter presents the application of two modern methods, and namely positron annihilation lifetime spectroscopy (PALS) and nanoindentation (NI) to study elastomers and their filled composites. PALS used to be applied to determine the size of the free volume present in polymer materials. The parameter depends on the segmental mobility of macromolecules and their mutual interactions as well as those between them and particles of filler dispersed in a rubber matrix. However, the annihilation of positrons occurs also inside filler particles, which enables us to draw conclusions concerning their aggregation and agglomeration. A subject literature study points out an oversimplification of a problem of nanofillers aggregation and agglomeration. We have found that the behavior of aggregates and agglomerates in vulcanizates under stress depends not only on their size and the presence of voids inside them. Of great importance is also whether agglomerates and also smaller aggregates are infiltrated by a rubber matrix [3]. The free volume is also important from the point of view of diffusion of low molecular weight species through rubbers. PALS has been also successfully used to study the effect of nanofiller addition on the barrier properties of vulcanizates [4, 5].

Nanoindentation is a technique adapted approximately 30 years ago to determine the hardness of thin coatings and surface layer of engineering materials. Alternatively it enables determination of friction, topography and scratch resistance when a probe, instead of vertical penetration, is dragged horizontally over the scanned surface. In this chapter the application of the method toward filled rubbers is demonstrated.

21.2 Positron Annihilation Lifetime Spectroscopy

21.2.1 Introduction

The phenomenon of positron annihilation has been used extensively for the determination of defects in crystalline materials like metals and ceramics. However, due to the development of polymer science, resulting in a significant increase in engineering applications, the technique has also been tried to probe polymer materials. At the beginning its application to characterize polymers was focused on their unique properties like glass transition. Recently, our knowledge on the influence of macromolecules on the mechanisms of annihilation makes it possible to study more complicated filled systems or polymer blends. Information on what positron annihilation can tell us about the physical properties of polymers can be found in the exhaustive review by Pethrick [6].

21.2.1.1 Positron and Positronium

The positron (e^+) is the anti-particle of the electron, generated by the decay of some unstable isotopes, for example, ^{22}Na, with the simultaneous emission of e^+ and photons of 1.28 MeV. The emitted positrons, of the energy distribution from 0 to 540 keV (with a maximum at about 200 keV), are thermalized by inelastic collisions with the surrounding media being studied. The thermalization causes ionization of the media, resulting in the production of secondary electrons, which in turn can form a bound positron-electron pair called the positronium (Ps).

Ps exhibits two spin states:

1. *Ortho* - (o-Ps), about 75% being formed in solids,
2. *Para* - (p-Ps), present in the rest, 25%.

Their existence depends on the presence of regions of low electron density in the materials studied. The lifetime of p-Ps in vacuum is of the order of 0.125 ns, whereas o-Ps decays with characteristic emission of two photons after approximately 100 ns [7]. The latter can be enhanced by the presence of electrons and spins with which o-Ps is able to interact or exchange. The occurrence of so-called pick-off annihilation reduces the lifetime to about 0.5–5.0 ns. Positrons not forming Ps have a lifetime of about 0.4 ns through interactions with the outer electrons of molecules with which they collide.

21.2.1.2 Ps Formation and Annihilation

There are three models describing the Ps formation:

1. Spur [8],
2. Ore [9],
3. The so-called free volume model [10].

These assume that Ps are mostly trapped in the areas of low electron density and account for 20–70% of all positrons probing the material studied. In materials of high electron density, for example, metals, Ps cannot be formed unless defects are present. The free volume in an

amorphous material can be considered as a cluster of defects, in the case of macromolecular systems embracing a small number of backbone units.

In macromolecular solids three annihilation processes are possible, namely:

1. Free positron annihilation – e^+ annihilates directly with e^- from the surrounding medium with the generation of two γ-rays of energy 511 keV and occurs in a timescale of 0.125–0.4 ns,
2. p-Ps,
3. o-Ps annihilation – being mostly trapped in the regions of low electron density and high "defects" concentration.

The ability of Ps to characterize the morphology of materials lies in the assumptions associated with the pick-off annihilation in molecular size voids. Measuring o-Ps annihilation rate and yield provides a direct measure of the microvoids in the material. In the case of amorphous polymer systems it has been commonly accepted that these microvoids correlate with free volume. A simplified free volume model relates the change of the o-Ps lifetime in such a "hole" to the change of the total volume of the material [11, 12]. An alternative approach proposed, based on the Ore gap model [13] assumes that Ps can be formed if a free volume present in the matrix is larger than a certain critical value.

Many theories have been proposed to describe the properties of microvoids. Values of microvoids or free volume have been calculated using the group contribution method [14] or estimation of the occupied volume (van der Waal's) [15]. The radius (R) of the free volume [nm], assumed to be a sphere, can be calculated using the semi-empirical Equation 21.1 proposed by Tao [16]:

$$\tau_3[ns] = 0.5\left[1 - \frac{R}{R + 0.1656\,\text{nm}} + \frac{1}{2\pi}\sin\left(\frac{2\pi R}{R + 0.1656\,\text{nm}}\right)\right]^{-1} \tag{21.1}$$

where: τ_3 is attributed to o-Ps pick-off annihilation.

21.2.1.3 Principles of Positron Lifetime Spectroscopy (PALS)

PALS involves detection of the γ-photon associated with the creation of e^+ – as a zero time reference and the subsequent observation of two coincident 0.54 MeV γ-photons to give the annihilation lifetime. A small spot of ^{22}NaCl, typically below 50 μCi, sandwiched between two thin Kapton or Ni foils, usually serves as a e^+ source. The sample, placed on its both sides, should be thick enough for all the positrons emitted to be stopped inside the material, which for polymers is about 10 mm. The γ-ray detection allows energy resolution and timing and a lifetime is determined using a time to amplitude converter. A typical spectrum consists of at least three main annihilation components, corresponding to expotentially decaying e^+, p-Ps and o-Ps. Each component is determined by a mean lifetime and probability for annihilation. In addition the spectrum may contain components resulted from background radiation and statistical fluctuations. In order to deconvolute the signal and to "extract" various lifetime components the least-squares analysis is used. The computer software [17]

fits a sum of decaying expotentials to a spectrum using lifetimes and intensities as fitting parameters (21.2):

$$y(t) = R(t) \, (N_t \, \Sigma \alpha_i \, \lambda_i e^{-\lambda i t} + B) \tag{21.2}$$

where $y(t)$ is an experimental raw datum, $R(t)$ is the instrument time-resolution function (usually represented as a Gaussian curve), N_t is the normalized total count, B is the background, λ_i is the inverse of the ith lifetime component (τ_i) and $\alpha_i \, \lambda_i$ is its intensity.

An experimental spectrum $y(t)$ is then least-squares fitted to Equation 21.2 in order to obtain lifetimes $\tau_i = 1/\lambda_i$ and corresponding intensities $\alpha_i \, \lambda_i$.

21.2.2 Application of PALS to Study Rubber Morphology

21.2.2.1 Introduction

Plenty of investigations on positron annihilation in polymers show large deviations, in both lifetime and intensity results. The reason for that is because unfortunately most of the works were done on commercial materials of unknown molecular weight, structure and chemical purity. It is only since the early 1970s that the importance of working with well characterized samples has been appreciated. A brief review of the results on polymers [18] has been published, emphasizing the problems of origin and history of sample preparation.

In most polymers positron annihilation occurs via three distinct processes and possibly four in crystalline materials [19, 20], which can be associated with:

1. Amorphous part of polymer matrix,
2. Crystalline part of polymer matrix,
3. Internal structure of filler agglomerates,
4. Polymer–filler interphase.

The positron studies can provide information on the size of voids in the system, which however may be influenced (usually the short time components) by the chemistry of polymer materials and the presence of trapped radicals or the build up of trapped electrons. The former may arise from the presence of free radicals or halogens in the system, being responsible for the complex shape of voids. The data have to be considered in the terms of a distribution of free volume rather than asuming that the free volume value is a single and discrete number. Nevertheless o-Ps annihilation studies can provide a unique chance to access the microstructure at a nanoscale and in principle can allow the free volume distribution to be probed in complex polymer materials.

21.2.2.2 State of the Art

Investigations of various copolymers, polymer blends and of filled polymers have been carried out and reflect the presence of the incorporated phase [20–24].

Studies on carbon black (CB)-filled polybutadiene (BR) were reported for the first time in 1979 [22]. The decrease in the longtime component intensity with CB loading has been confirmed. It has been found to go in the opposite direction for the size of CB particles, which was attributed to the increase in the amount of bound rubber (BdR) as the particle size was

reduced and the consequent increase in the number of annihilation sites. Dlubek *et al.* [25] determined the number density distributions of holes for polycarbonate and polystyrene by positron lifetime measurements. Experimental data fit very well with calculations based on theoretical model of Bueche [26], in which local fluctuations of free volume correspond to fluctuations of the hole volume around average value. Wang *et al.* [27] found free volume distribution for poly(ethyleneterephtalate), determined by PALS, broadened with increase of temperature. Similarly, the size distributions of holes present in copolymers of styrene and maleic anhydride were found to follow the compressibility of the free volume, as predicted by the theory of thermal volume fluctuations [28]. Positron lifetime studies of styrene-butadiene rubber (SBR) filled with intercalated montmorillonite (MMT) or carbon black demonstrate narrower distribution of free volume hole size for SBR/MMT nanocomposites in comparison to SBR/CB mix or unfilled SBR vulcanizate [29]. It correlates with differential scanning calorimetry (DSC) data, showed the highest value of glass transition temperature for SBR filled with MMT. The highest value of a specific surface area for nanoparticles is responsible for the most distinct inhibition of chain motion around separated platelets dispersed in rubber.

Despite there being many studies on the influence of filler dispersion and distribution on the properties of rubber, contributions discussing the effect of the internal structure of solid phase agglomerates have appeared recently [30, 31].

21.2.2.3 The Influence of Mixing on Rubber Morphology

Mixing is one of the most important operations in rubber technology. It should ensure optimal morphology of rubber mixes, which influences a quality of rubber goods. However it should be taken into consideration that at the end of the process a state of thermodynamic, chemical and rheological equilibrium is not achieved. As a consequence the morphology of mixes also depends on factors acting after completing the mixing process. The term "morphology" is complex and among others it includes: the content of a filler, the sizes and shape of its primary particles, aggregates and agglomerates, their distribution in a matrix, the content of loosely and tightly bounded rubber and structures formed from interacting filler particles. The dispersion index (DI) [32] is commonly accepted by the rubber industry as a measure of rubber mix quality. It is assumed that big agglomerates, composed of loosely packed aggregates, exert a particularly detrimental effect on properties of vulcanizates [33]. Under external stresses they break, initiating the formation of microcracks, whose propagation in a matrix leads finally to a rubber rupture. During the preparation of a rubber mix, the following steps can be distinguished: (i) distributive mixing – filler in form of agglomerates or pellets at the early stage is wetted with rubber and distributed in the matrix, (ii) dispersive mixing – simultaneously transformation of agglomerates into aggregates takes place, accompanied by formation of a bound rubber and 3D structure of filler particles [34–36]. If the viscosity of the matrix is low and interfacial tension high a flocculation of aggregates and restoration of agglomerates is possible. The mechanism of disagglomeration and infiltration was thoroughly studied [37, 38]. It has been recognized that three different phenomena could be responsible for lowering the agglomerates' size, namely: erosion, breaking and collision of particles.

To date, filler agglomerates were treated as rather loosely packed clusters of aggregates, which break under high shear stresses, being responsible for rubber failure. This approach seems to be oversimplified. There are a few factors influencing strength of agglomerates, namely: internal (submicron structure), filler–filler and filler–rubber interactions, being related

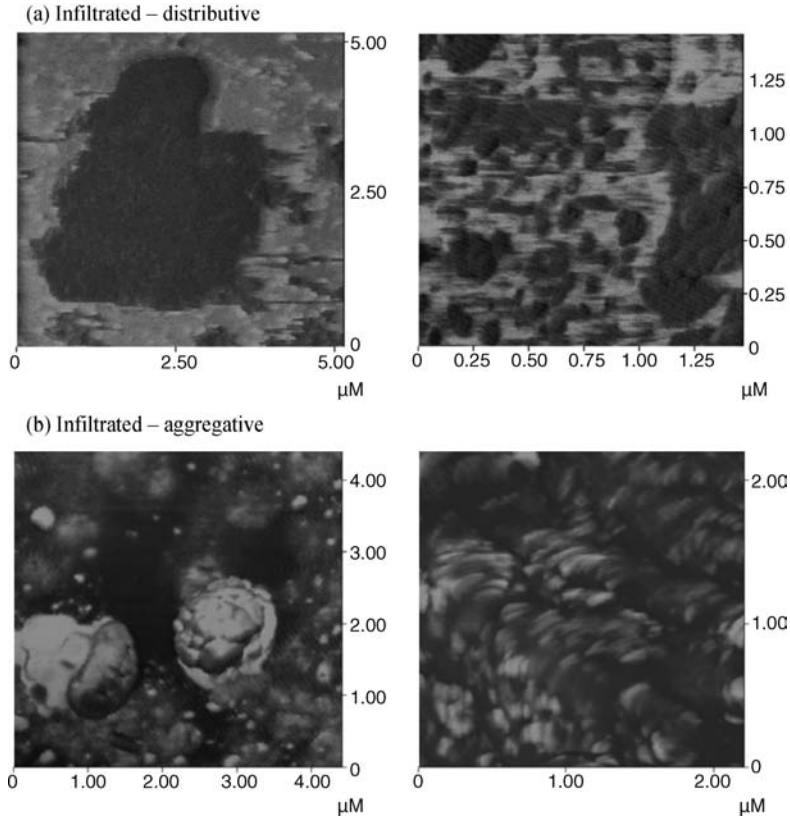

Figure 21.1 Classification of filler agglomerates according to their internal structure (AFM): (a) infiltrated – distributive; (b) infiltrated – aggregative; (c) infiltrated – trapped rubber; and (d) non-infiltrated (Reprinted from D.M. Bieliński, O. Dobrowolski and G. Przybytniak, "Morphological aspects of rubber fracture and wear," *Journal of Applied Polymer Science*, **110**, 55, © 2008, with the permission of John Wiley & Sons, Inc.)

to parameters of mixing process. A classification of filler agglomerates according to their internal structure is presented in Figure 21.1 [39, 40].

Apart from the submicron structure of filler particles, also the character of microscale interactions between their surface and rubber macromolecules is important. It can be measured by the so-called bound rubber (BdR) content. Another classification of rubber morphology, taking into consideration structural ability of filler is presented in Figure 21.2.

21.2.2.4 Correlation Between Morphology and PALS Data for Rubber

Generally, the worse the macroscale filler dispersion (lower DI value) the higher the average positron lifetime ($\bar{\tau}$) – Figure 21.3. A significantly higher value of $\bar{\tau}$, observed for unfilled rubber suggests that presence of filler influences the number of sites where Ps can be formed.

All spectra were deconvoluted into three lifetime components (assuming that it is enough to calculate three components of the spectra to obtain value of χ^2 close to 1). The shortest one – τ_1

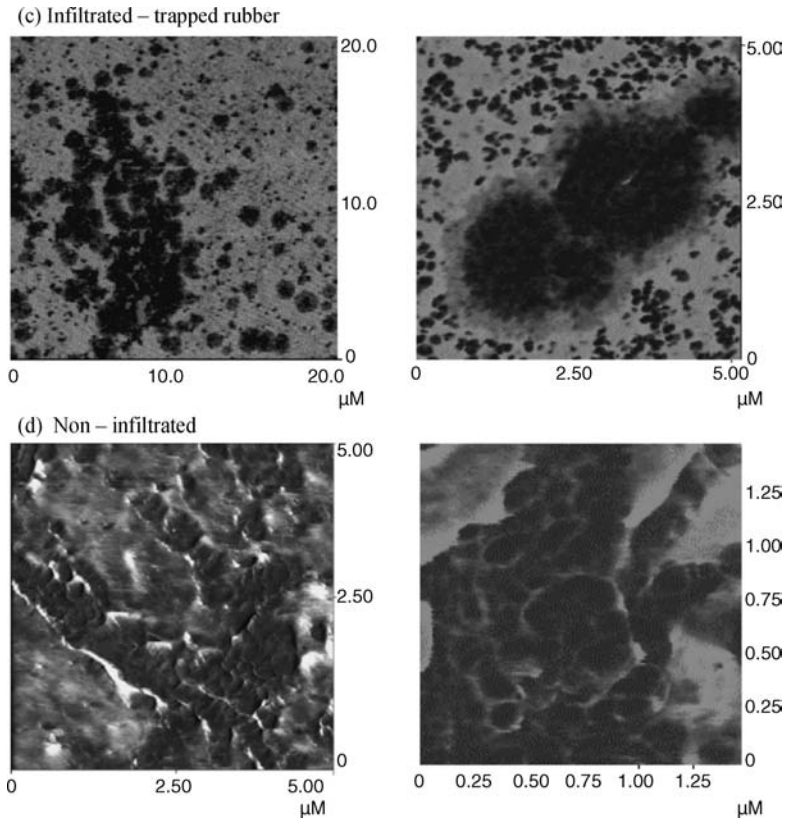

Figure 21.1 (*Continued*)

equals to 125 ps, originated from the annihilation of the p-Ps and was fixed in all cases. The data was accounted for the source and background correction. An average positron lifetime was calculated as:

$$\bar{\tau} = I_1\tau_1 + I_2\tau_2 + I_3\tau_3 \tag{21.3}$$

where τ_1, τ_2, τ_3 are components of the positron lifetime and I_1, I_2, I_3 are adequate intensities of the lifetime components.

Admixing of filler to amorphous elastomer matrix changes conditions for positron annihilation. In all positron lifetime spectra the creation of positronium (Ps), which is the bound state of an electron and positron, was detected. Such a state can be created in the free space between molecules, the internal structures of the filler agglomerates as well as in the filler-matrix interface. In the experiment the third component, τ_3, is attributed to o-Ps pick-off annihilation taking place in the amorphous phase of polymers, in free volume regions. In our consideration we assume that the intensity of the third component, I_3 [%], is related to the volumetric fraction of the free volume, according to the following equation [41]:

$$f = \frac{V_f}{V_{\text{total}}} 100\% = 1.8 \times V_f \times I_3 \tag{21.4}$$

where $V_f = 4\pi R^3/3$ is the free volume [nm^3], obtained from τ_3 (21.3).

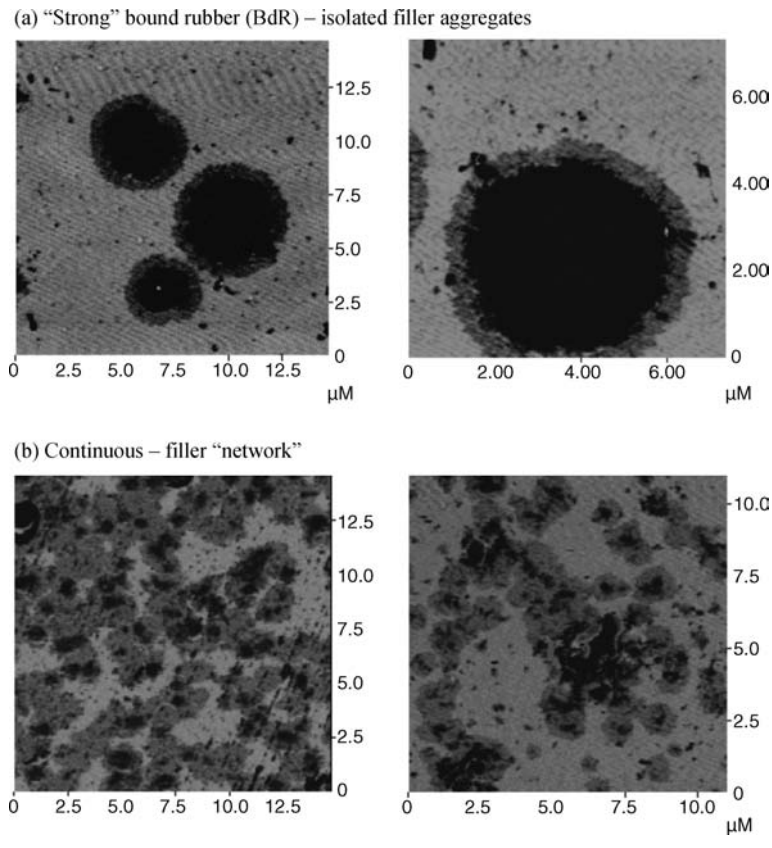

Figure 21.2 Classification of filler agglomerates according to their structural ability (AFM): (a) "strong" bound rubber (BdR) – isolated filler aggregates; and (b) continuous – filler "network" (Reprinted from D.M. Bieliński, O. Dobrowolski and G. Przybytniak, "Morphological aspects of rubber fracture and wear," *Journal of Applied Polymer Science*, **110**, 55, © 2008, with the permission of John Wiley & Sons, Inc.)

The positron annihilation in the free state is attributed to the intermediate component (τ_2, I_2). In the subject literature one can also find the report subscribing I_2 to the thickness of the interface present very often in polymer materials [42] containing trapping sites for Ps.

AFM analysis of the EPDM/silica system suggests that changes of average positron lifetime (τ) from mix to mix must have been the result of the microscale filler distribution and different sub-agglomerate structures rather than associated with a negligible silica–elastomer interface [43]. Complete PALS analysis for a series of EPDM/Coupsil VP 6411 mixes is presented in Figure 21.4.

Unfilled rubber contains more free volumes of bigger radius (higher τ_3), suitable for positronium formation. Admixing of silica reduces significantly the value of the third component of intensity, I_3, by up to about 25%, which is followed by changes in the third positron lifetime component, τ_3. The differences between filled samples, according to the second component of positron lifetime, τ_2, are negligible, however its value is obviously higher than for unfilled rubber. Significantly higher values of I_2 for rubber mixes in comparison to

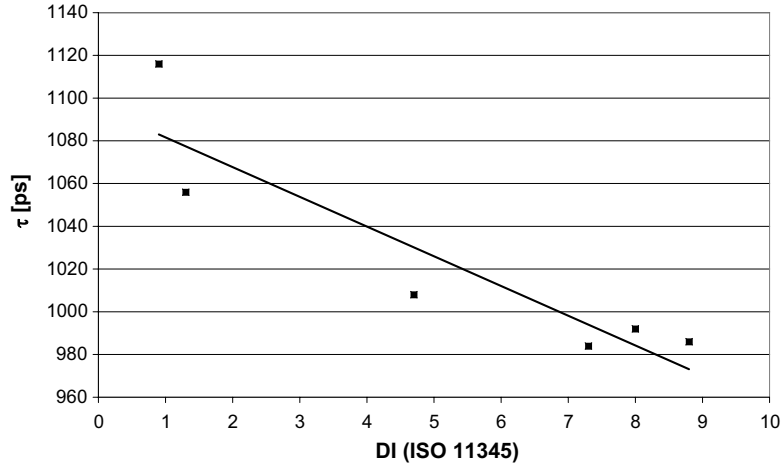

Figure 21.3 Correlation between average positron lifetime ($\bar{\tau}$) and value of dispersion index (DI) for a series of EPDM/Coupsil VP 641 mixes prepared on a roll-mill [40] (Reprinted from D.M. Bieliński, L. Ślusarski, O. Dobrowolski *et al.*, "Studies of filler agglomeration by atomic force microscopy and positron annihilation spectroscopy. Part I: silica filled compounds," *Kautschuk Gummi Kunststoffe*, **57**, 579–586, © 2004, with the permission of KGK Kautschuk Gummi Kunststoffe, Hüthing GmbH.)

unfilled EPDM indicate a higher contribution of positron annihilation in the free state. I_2 is highest for rubber mixes of a very good degree of macroscale filler dispersion: 50/100 and 60/100, exhibiting lower values for the others. This can be connected with positron annihilation inside filler agglomerates. However, the decrease of I_2 for "bad" mixes 100/100, 120/100 and 150/100 shows that the filler–matrix interface (the so-called bound rubber) has its part in the second lifetime component. The worse dispersion of silica aggregates results in a lower surface area of filler particles and a lower volume contribution of the interface region. The effect is significantly reduced by agglomeration of filler particles.

There is a general tendency of lower I_2 values for vulcanizates in comparison to rubber mixes, pointing at a possible microscale filler distribution and the structure effect on the number, geometry and dimensions of free volumes.

Additionally, measurements of Doppler's broadening of the annihilation line were carried out – Figure 21.5. Two parameters of positron annihilation were extracted, namely: (i) the *S* parameter, the ratio of counts in the fixed, central part of annihilation line to all number of counts detected for the whole line, and (ii) the *W* parameter, the ratio of counts in the wing region of annihilation line to all number of counts detected for the whole line. They reflect part of positrons annihilating with electrons of low (mainly p-Ps self-annihilation) and high momentum adequately.

For the samples studied the S parameter increases monotonically, which is more distinct in comparison to the mean lifetime – Figure 21.3. The linear correlation between *S* parameter and dispersion index (DI) has been detected. Again the value of the S parameter determined for EPDM differs significantly from that for filled samples. The interpretation of the relation $S = f(W)$ is more complicated; however its linear character could be a proof of the same character of the free volumes present in the filled rubber mixes.

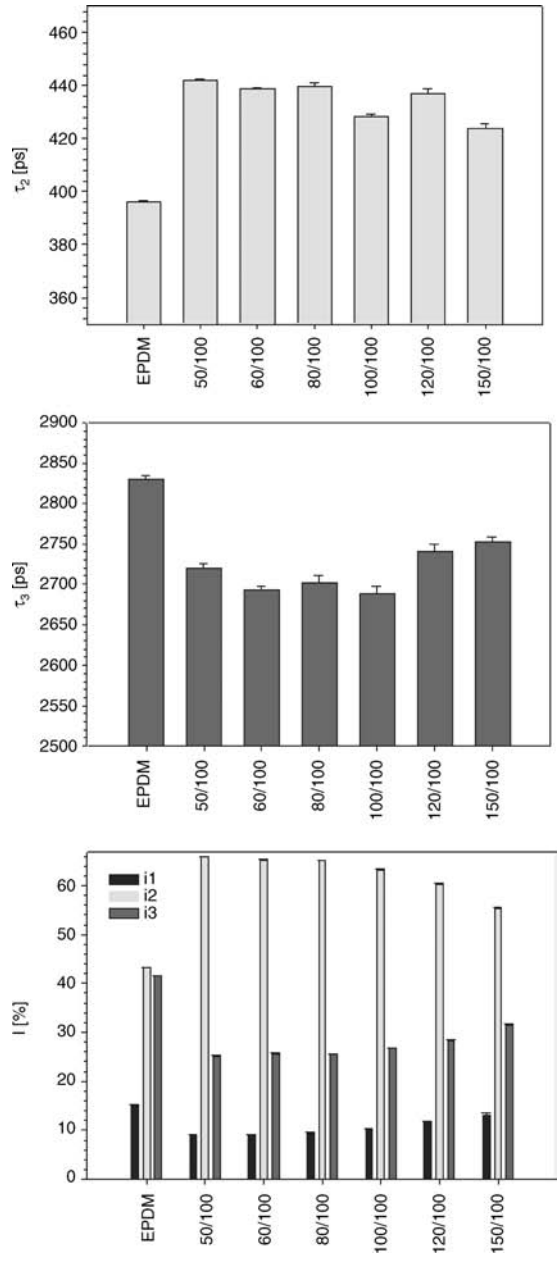

Figure 21.4 Discrete PALS analysis for a series of EPDM/Coupsil VP 6411 mixes. Numbers assigned to samples stand for silica content [phr] [40] (Reprinted from D.M. Bieliński, L. Ślusarski, O. Dobrowolski *et al*., "Studies of filler agglomeration by atomic force microscopy and positron annihilation spectroscopy. Part I: silica filled compounds," *Kautschuk Gummi Kunststoffe*, **57**, 579–586, © 2004, with the permission of KGK Kautschuk Gummi Kunststoffe, Hüthing GmbH.)

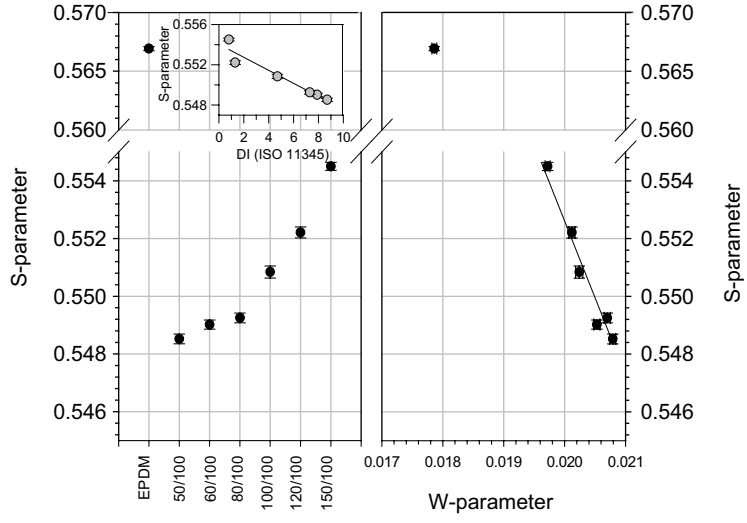

Figure 21.5 Values of *S* parameter (left) for a series of EPDM/Coupsil VP 6411 mixes. Dependence of *S* in a function of *W* parameter (right). Numbers assigned to samples stand for silica content [phr] [40] (Reprinted from D.M. Bieliński, L. Ślusarski, O. Dobrowolski *et al*., "Studies of filler agglomeration by atomic force microscopy and positron annihilation spectroscopy. Part I: silica filled compounds," *Kautschuk Gummi Kunststoffe*, **57**, 579–586, © 2004, with the permission of KGK Kautschuk Gummi Kunststoffe, Hüthing GmbH.)

One can ask what happens to filler distribution and agglomerates due to vulcanization. The subject literature suggests possible phenomenon of filler flocculation during the vulcanization of rubber [35, 36]. Indeed, the third component of the positron lifetime (τ_3) for the series of EPDM/silica mixes prepared on the roll-mill is lower in comparison to their vulcanizates – Figure 21.6.

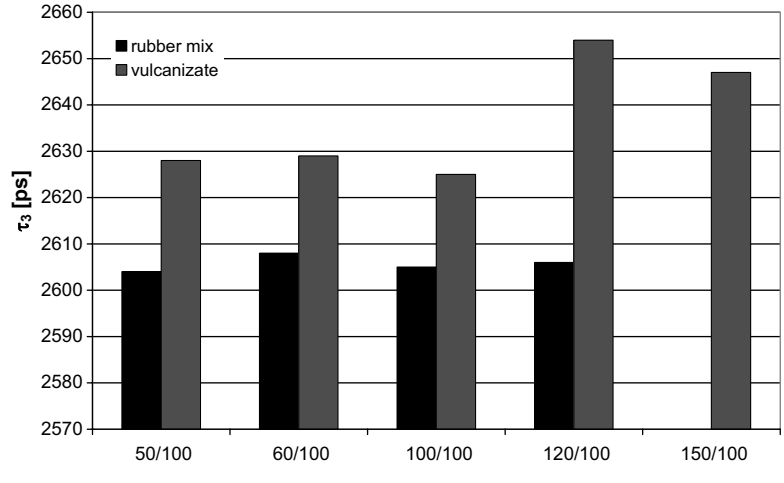

Figure 21.6 Influence of vulcanization on the third positron lifetime component (τ_3) for EPDM/Coupsil VP 6411 mixes. Numbers assigned to samples stand for silica content [phr]

The changes are the highest for the rubber mix of the worst degree of macroscale filler dispersion (150/100), whereas very good and good mixes (50/100, 60/100 or 80/100) exhibit very small but systematic differences. An adequate intensity component, I_3, follows the changes of the annihilation lifetime one.

PALS analysis carried out for carbon black filled rubber confirms data for silica systems – Figure 21.7. The difference in average positron lifetime ($\bar{\tau}$) between rubber mixes and their vulcanizates reaches about 15%.

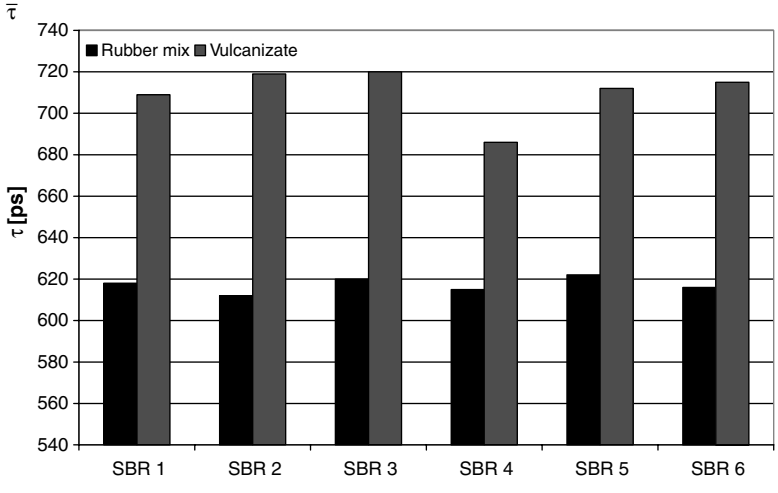

Figure 21.7 Influence of vulcanization on average positron lifetime ($\bar{\tau}$) for SBR/50 phr of N 234 mixes. Rubber mixes vary according to the degree of filler dispersion (DI) (Reprinted from D.M. Bieliński, L. Ślusarski, O. Dobrowolski *et al.*, "Studies of filler agglomeration by atomic force microscopy and positron annihilation spectroscopy. Part II: carbon black mixes," *Kautschuk Gummi Kunststoffe*, **58**, 239–245, © 2005, with the permission of KGK Kautschuk Gummi Kunststoffe, Hüthing GmbH.)

Contrary to the silica-filled vulcanizates, differences in DI are not reflected by $\bar{\tau}$ values for the carbon black-containing rubber. Only the worst one, SBR 4, varies from the others. Deconvolution of the positron lifetime has revealed that the difference has to be subscribed mainly to its third component of intensity, being associated with o-Ps pick-off annihilation taking place in the amorphous phase of polymers, within free volume regions. Complete PALS analysis for series of SBR/50 phr of N 234 mixes is presented in Figure 21.8.

The value of the third component of lifetime (τ_3) increases slightly as a result of vulcanization, which indicates on the increase of an average free volume "hole" radius (maximum increase of about 2% for SBR 5). The change is very small but present for all samples, except SBR 4. It could be the result of filler flocculation during vulcanization.

Similarly to I_3, the second component of intensity (I_2) also exhibits different values for the mixes and vulcanizates – the decrease reaches 10%. Again sample SBR 4 differs from the others, revealing the smallest variation of I_2. It seems likely that the vulcanization of carbon black mixes, producing filler flocullation, results in a decrease of the volume

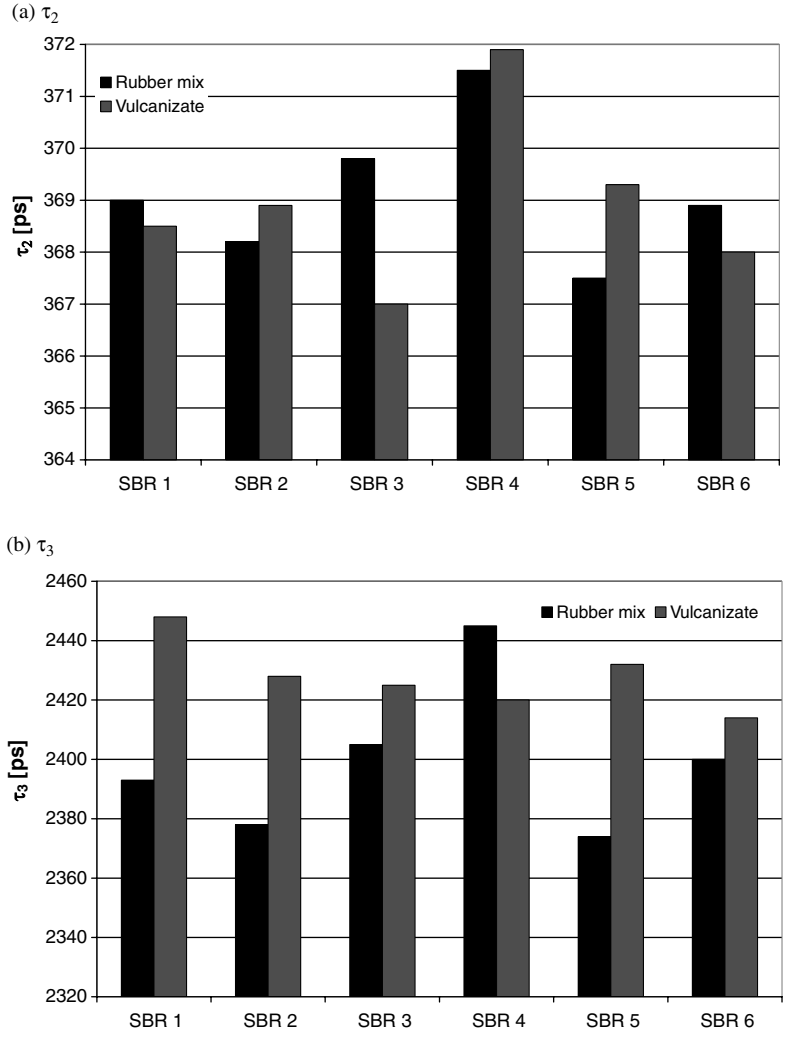

Figure 21.8 Discrete PALS analysis for series of SBR/50 phr of N 234 mixes. Rubber mixes vary according to the degree of filler dispersion (DI): (a) τ_2; (b) τ_3; (c) I_2; and (d) I_3 (Reprinted from D.M. Bieliński, L. Ślusarski, O. Dobrowolski *et al.*, "Studies of filler agglomeration by atomic force microscopy and positron annihilation spectroscopy. Part II: carbon black mixes," *Kautschuk Gummi Kunststoffe*, **58**, 239–245, © 2005, with the permission of KGK Kautschuk Gummi Kunststoffe, Hüthing GmbH.)

contribution of the filler–matrix interphase layer, which is reflected by an increase of I_3. A considerable increase of the crosslink density in the carbon black-rubber matrix interphase layer [44] is probably responsible for changes detected by PALS. Microheterogeneity of rubber vulcanization is well demonstrated in the subject literature. The average positron lifetime of the unfilled SBR has practically no chance to be altered by its vulcanization.

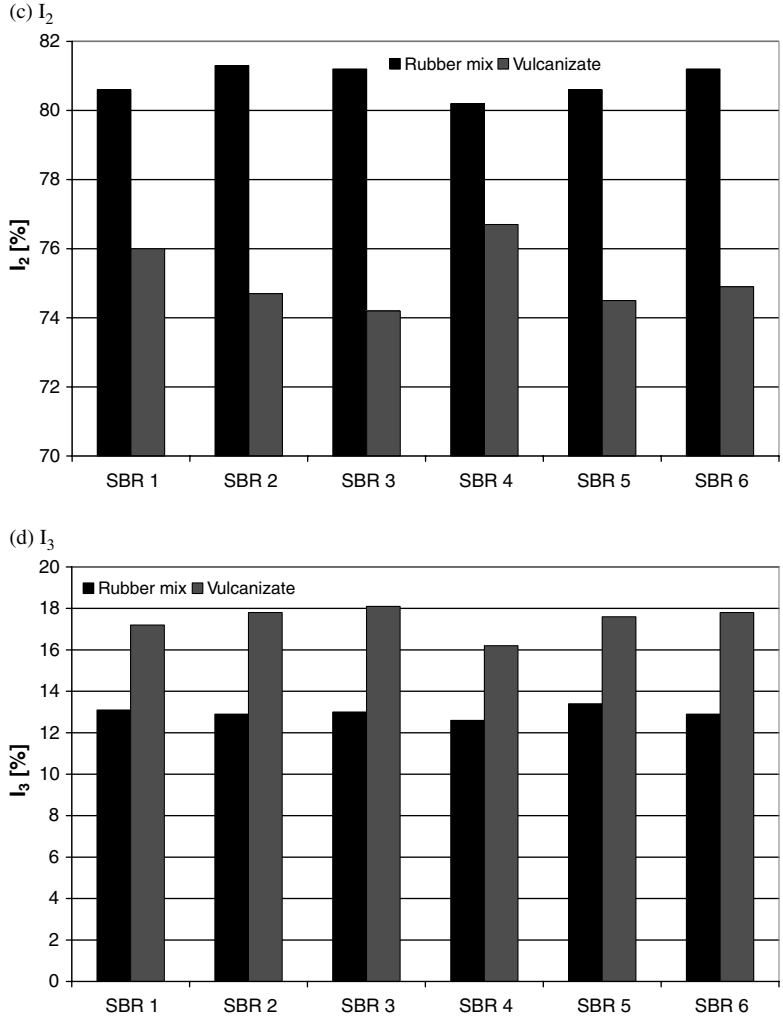

Figure 21.8 (*Continued*)

The positron lifetime spectrum can be conventionally described by a sum of discrete exponentials:

$$s(t) = \sum_{i=1}^{k} \frac{I_i}{\tau_i} \exp\left(-\frac{t}{\tau_i}\right) \tag{21.5}$$

where k is the number of lifetime components and τ_i is mean the lifetime of the i th component with the relative intensity of I_i, $\sum I_i = 1$. As already mentioned, the *ortho*-Ps lifetime is

related to the radius of the spherical hole r, in which the *ortho*-Ps are annihilated in the *pick-off* process [16]:

$$\tau_{pick-off} = \frac{1}{2}\left[1-r(r+\Delta r)+\left(\frac{1}{2\pi}\right)\sin\left(\frac{2\pi r}{(r+\Delta r)}\right)\right]^{-1} \tag{21.6}$$

where $\Delta r = 1.656$ Å is an empirical parameter obtained by fitting the measured *ortho*-Ps lifetimes to known free volume sizes in molecular crystals or zeolites [45, 46]. In the case of heterogeneous materials in which a distribution of *ortho*-Ps lifetimes is expected, the lifetime spectrum may be described by a continuous decay form:

$$s(t) = \int_0^\infty I(\tau)\exp\left(\frac{-t}{\tau}\right) d\tau \tag{21.7}$$

where $I(\tau)$ represents the intensity which allows to deduce the free volume hole radius from probability density function $f(r)$:

$$f(r) = -2\Delta r\left\{\cos\left[\frac{2\pi r}{r+\Delta r}\right]-1\right\}\frac{I(\tau)}{\lambda^2(r+\Delta r)^2} \tag{21.8}$$

where $\lambda = \frac{1}{\tau}$. The hole radius density distribution corresponds to a hole volume v density distribution:

$$g(v) = \frac{f(v)}{4\pi R^2} \tag{21.9}$$

From this the number density distribution of holes $g_n(v) = g(v)/v$ may be calculated. The distribution function may be deduced to be a Gaussian:

$$g_n(v) = g_0 \exp\left[-\frac{(v-\langle v_n\rangle)^2}{2\sigma^2}\right] \tag{21.10}$$

where g_0 is a proportionality constant.

Application of the MELT routine makes the lifetime spectrum inverted into a continuous lifetime distribution using a quantified entropy method [47]. The characteristic lifetimes τ_i have been calculated as the mass centers of peaks and the intensities I_i as the relative areas under the peaks. No assumptions with respect of the numbers and shape of components were necessary. In the case of the measured lifetime spectra for SBR/50 phr of N 234 vulcanizates four peaks appeared in the obtained lifetime distributions – Figure 21.9.

First located close to $\tau_1 \approx 130$ ps originating from annihilation of *para*-Ps, second at $\tau_2 \approx 370$ ps coming from the annihilation of free positrons, third at $\tau_3 \approx 1000$ ps having small intensity of about 2% and fourth at $\tau_4 \approx 2500$ ps with intensity about 15%, originating from *pick-off* annihilation of *ortho*-Ps. The additional medium peak close to 1000 ps could be interpreted as coming from the *ortho*-Ps annihilation in more densely packed regions [48]. Due to instability of medium lifetime τ_3, which seems to be affected by the artifacts, further analysis concerns the fourth lifetime τ_4. Figure 21.10 presents the number density distributions $g_n(v)$ of free-volume holes in the SBR/carbon black vulcanizates.

The centers of mass of the obtained distributions for the samples SBR 3 and SBR 6 are slightly shifted to lower values of free-volume hole size in comparison to other samples. The

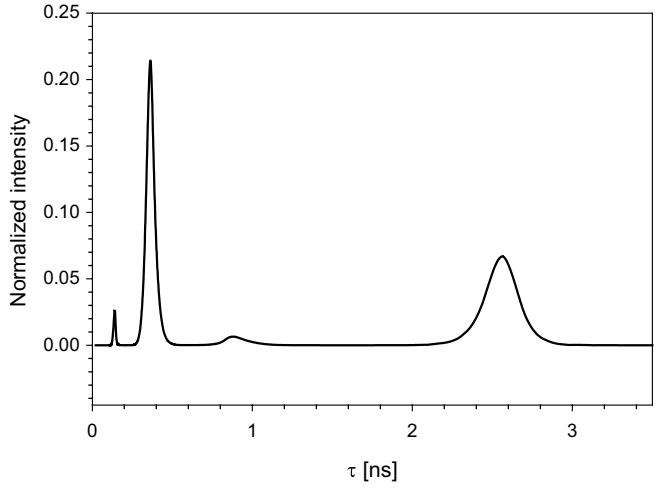

Figure 21.9 Positron lifetime distribution for SBR 2 sample (Reprinted from D.M. Bieliński, O. Dobrowolski and E. Dryzek, "Application of PALS to study rubber morphology" (in Polish), in Elastomers and Rubber Industry, W. Parasiewicz and W.M. Rzymski (Eds.), 291–299, © 2006, with permission from Rubber Research Institute "STOMIL" and Technical University of Lodz.)

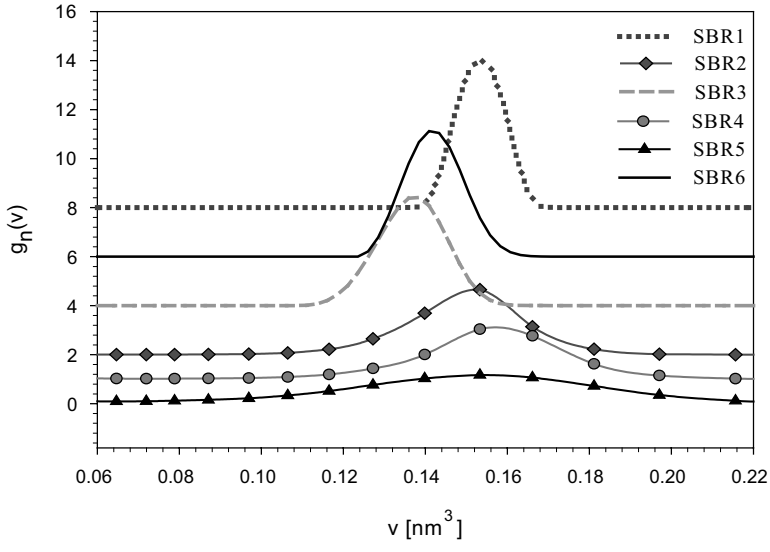

Figure 21.10 Number density distributions $g_n(v)$ of free volume holes in SBR/50 phr of N 234 vucanizates. The curves are shifted vertically to be more visible. Rubber mixes vary according to the degree of filler dispersion (DI) (Reprinted from D.M. Bieliński, O. Dobrowolski and E. Dryzek, "Application of PALS to study rubber morphology" (in Polish), in Elastomers and Rubber Industry, W. Parasiewicz and W.M. Rzymski (Eds.), 291–299, © 2006, with permission from Rubber Research Institute "STOMIL" and Technical University of Lodz.)

widths of the distributions differ visibly. The broadest distribution is for the sample SBR 5. Samples SBR 1, SBR 3 and SBR 6 constitute a group exhibited narrower distributions. Taking into account interpretation of the positron lifetime distribution width in SBR given in [29], the narrower lifetime or hole volume density distribution should indicate a higher contribution of bound rubber and better filler dispersion. However, this dependence may be more complex because of the presence of free radicals [49] in carbon black particles, which influences Ps formation and annihilation.

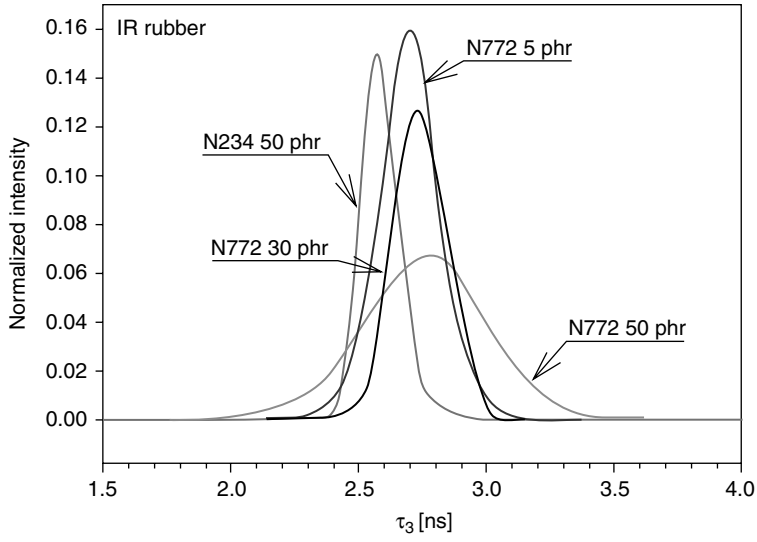

Figure 21.11 Influence of filler loading on *ortho*-Ps lifetime distribution for IR/N 772 vulcanizates. Data for SBR/N 234 is given for comparison

Ortho-Ps lifetime distribution was also determined for vulcanizates of different filler loading (IR/N 772) – Figure 21.11.

The highest value of FWHM for rubber of the highest filler content (IR/50 phr of N 772) can be explained by 3D filler network, which is not able to be created for lower carbon black loading. Different morphology of SBR filled with carbon black of various activity is also well represented by MELT studies – Figure 21.12.

Isolation of filler particles in rubber matrix is well visualized by FWHM of *ortho*-Ps lifetime distribution for SBR/carbon black systems. It is about two times thinner (see Figure 21.12) for SBR loaded with N 110 in comparison to other carbon blacks studied.

Complete PALS analysis for IR/N 772 system is presented in Figure 21.13.

The longest lifetime component (τ_3) does not depend on filler content, but its intensity (I_3) reduces with carbon black loading. Small increase of the second lifetime component (τ_2) can be observed, but this time accompanied by significant increase of intensity (I_2). Experimental data stay in agreement with literature on SBR/N 326 system [29]. The authors explain the lowering of I_3 as a consequence of two factors: (i) a decrease of rubber content in a system and (ii) an increase of filler–matrix interactions, limiting the mobility of macromolecular segments,

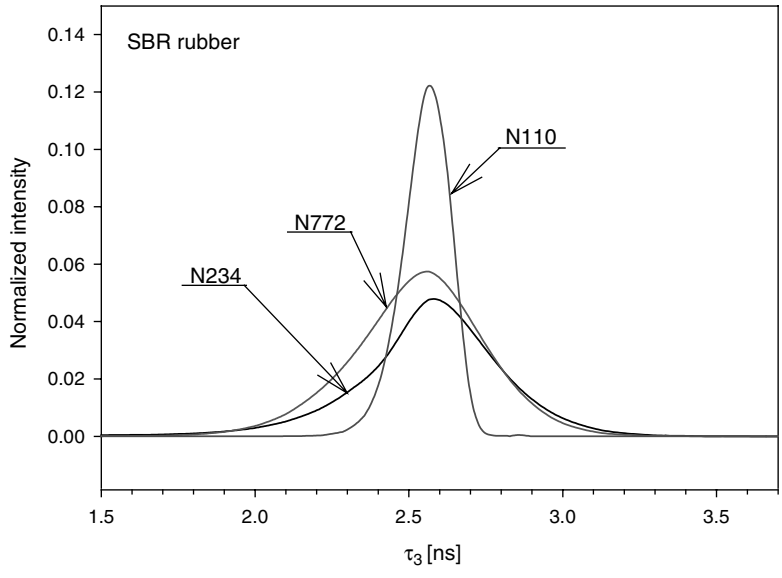

Figure 21.12 Influence of filler activity on *ortho*-Ps lifetime distribution for SBR/50 phr of carbon black vulcanizates

which in turn reflects the concentration of free volumes. Simultaneous increase of I_2 probably points on annihilation taking place in a filler-matrix interphase. A lower value of I_3 and higher value of I_2, for IR filled with N 234 in comparison to rubber containing N 772, seems to be connected with the higher BdR content for the former.

The hypothesis has been confirmed by PALS study on SBR filled with carbon black of various average grain sizes – Figure 21.14.

Positron annihilation lifetime components τ_2 and τ_3 for SBR containing 50 phr of carbon black do not depend on filler grain size. According to expectations a significant influence of grain size on I_2 and I_3 intensities is visible when comparing active (N 110 or N 234) to structural (N 772) carbon black. Rubber containing filler of bigger particles, having a smaller specific surface, exhibits a lower ability for interphase positron annihilation (lower value of I_2), but presents a higher concentration of free volumes (higher value of I_3).

21.2.2.5 The Influence of Exploitation on PALS Data for Rubber

In the light of our experience on the influence of filler dispersion on mechanical and tribological properties of rubber, PALS data seems to be more relevant to filler agglomeration than Philips' test. Positron annihilation spectroscopy can differentiate between rubber samples of various microscale filler dispersions and the dominating structure of agglomerates, being more suitable for the estimation of rubber mix quality.

Subjected to intensive friction, filled vulcanizates undergo structural changes, as reflected by PALS experiments – Figure 21.15.

The third component of the positron lifetime, τ_3, for EPDM/silica vulcanizates decreases in comparison to the values for the same samples before friction; however it does not reach the

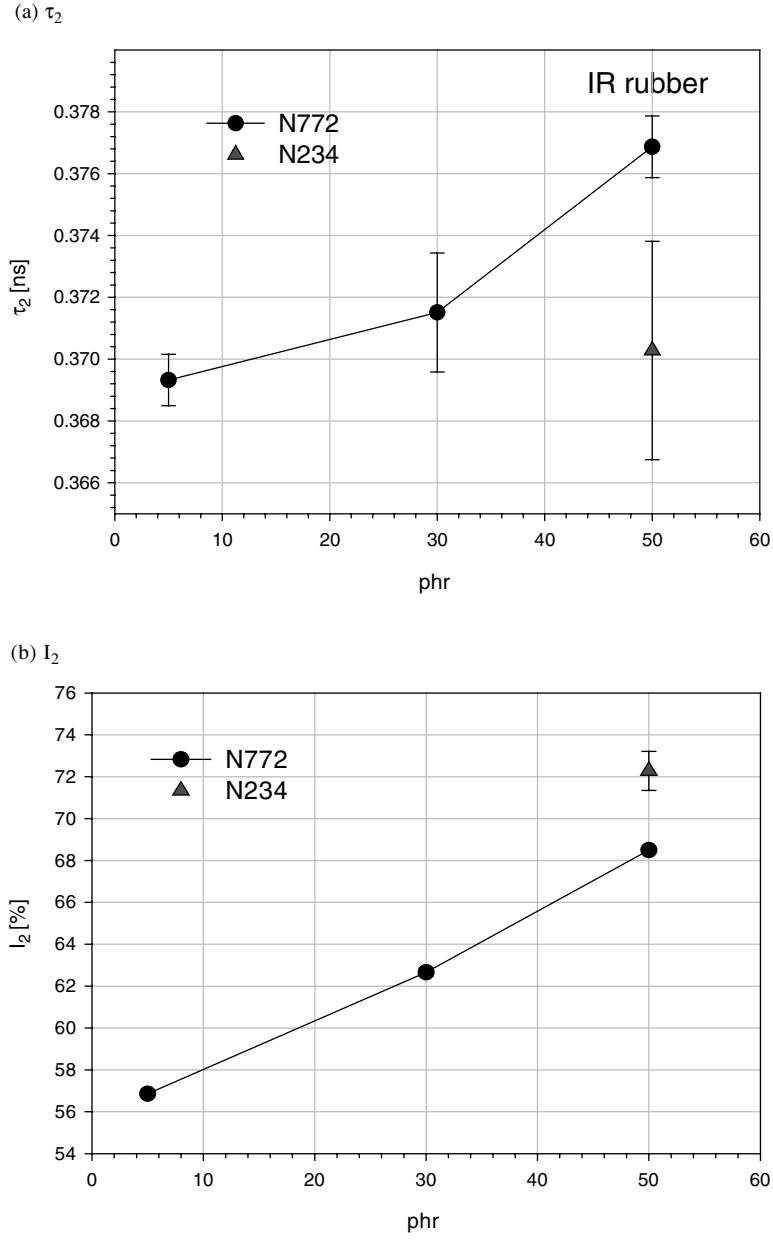

Figure 21.13 Discrete PALS analysis for IR/N 772 vulcanizates of various filler content. Data for SBR/N 234 is given for comparison: (a) τ_2; (b) I_2; (c) τ_3; and (d) I_3

level of adequate rubber mix. It can be either the result of generation of microcracks in the elastomer matrix or breaking of the filler network and possibly tearing silica particles out. No changes to the second component of positron annihilation intensity, I_2, in agreement with expectations, point rather to the former mechanism.

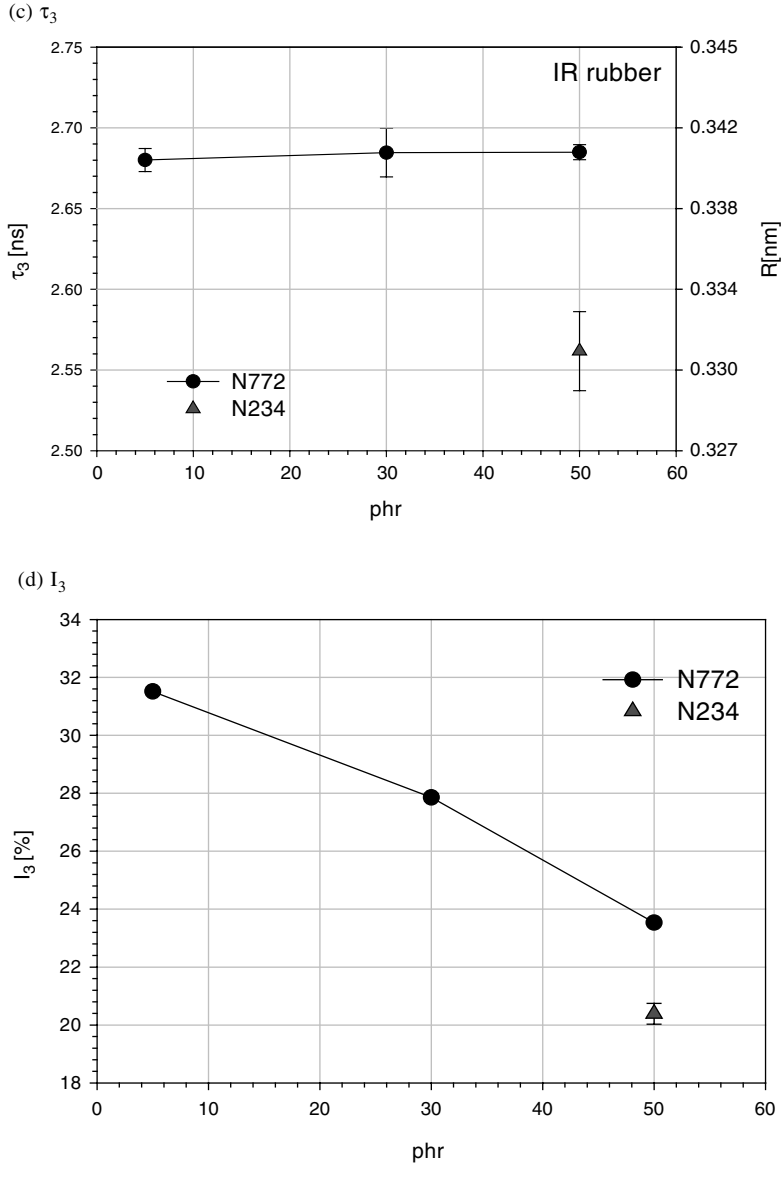

Figure 21.13 (*Continued*)

Positron annihilation in carbon black-filled rubber differs from silica-containing ones. Complete PALS spectra for SBR/50 phr of N 234 vulcanizates subjected to friction and fatigue are presented in Figure 21.16.

Fatigue makes τ_3 of vulcanizates significantly increased, but its intensity (I_3) only slightly decreased. The average value of free volume holes is the highest for the M 4 sample, exhibiting

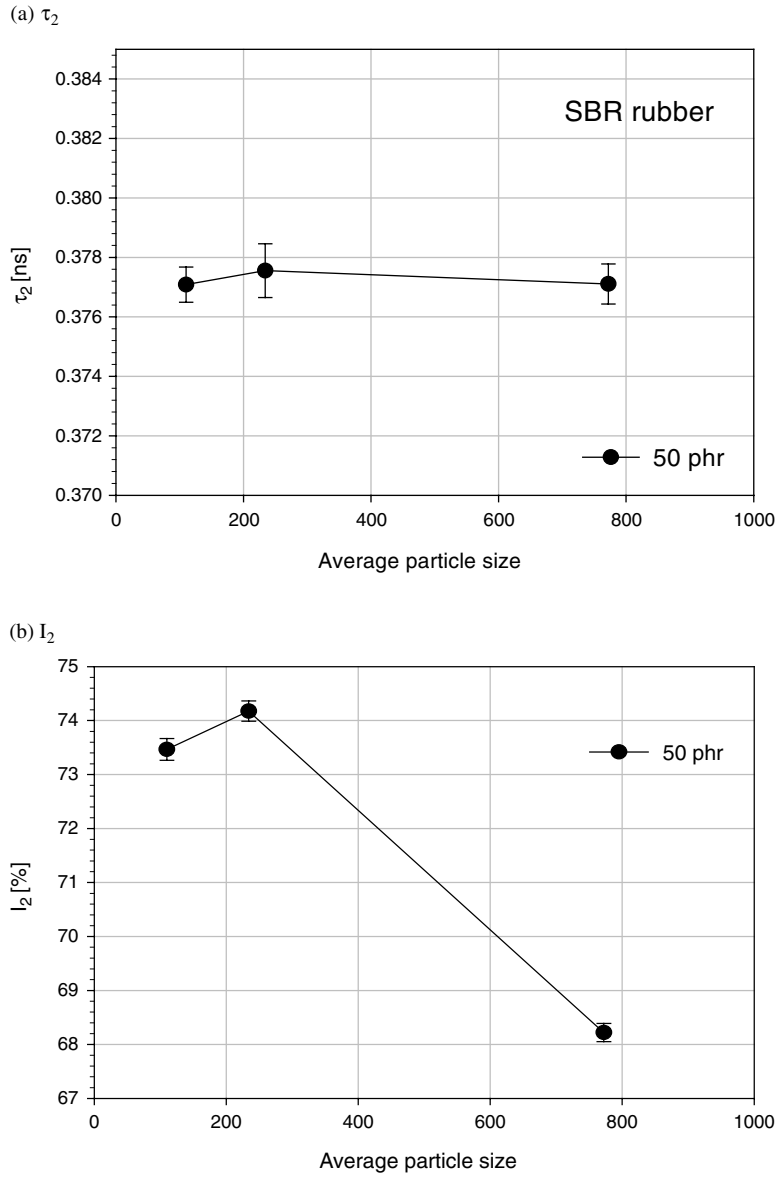

Figure 21.14 Discrete PALS analysis for SBR/50 phr of carbon black vulcanizates: (a) τ_2; (b) I_2; (c) τ_3; and (d) I_3

the worst filler dispersion. Friction introduces structural changes different from fatigue. This time moderate changes of *ortho*-Ps lifetime are accompanied by changes to its intensity. Probably a slightly increasing free volumes content is compensated by a decrease of their concentration. Apart from M 4 vulcanizate, exploitation does not influence significantly the average positron lifetime ($\bar{\tau}$).

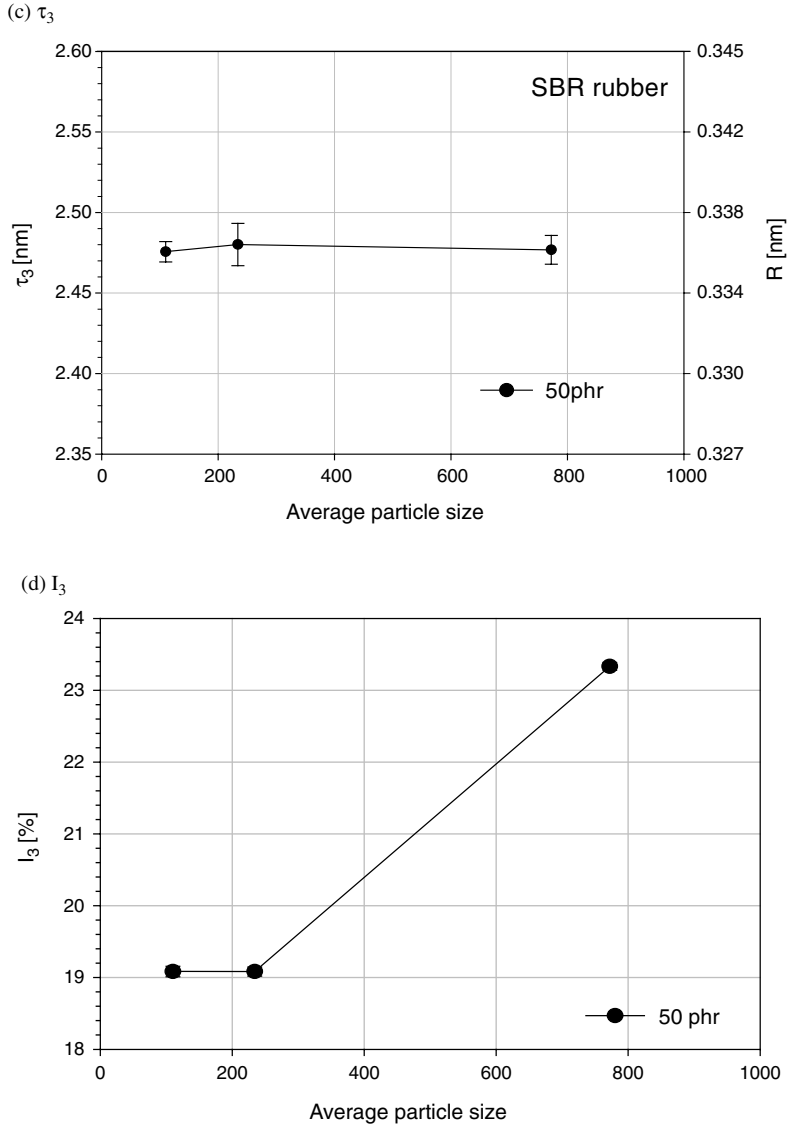

Figure 21.14 (*Continued*)

The number density distributions of holes, $g_n(v)$, were fitted by Gaussian functions. According to Equation 21.10 the standard deviation of the Gaussian functions should be related to the bulk modulus of elasticity or other mechanical properties of material. Figure 21.17 presents the dependence of FWHM (full width at half maximum; for a Gaussian FWHM $= 2\sqrt{2 \ln 2}\sigma$) on the increase of mechanical modulus under elongation ($\Delta\sigma_{100-300}$).

The experimental points are scattered, though it seems that the higher value of the $\Delta\sigma_{100-300}$ parameter corresponds to the narrower number density distribution of holes. The dashed line is

(a) EPDM/Coupsil VP 6411

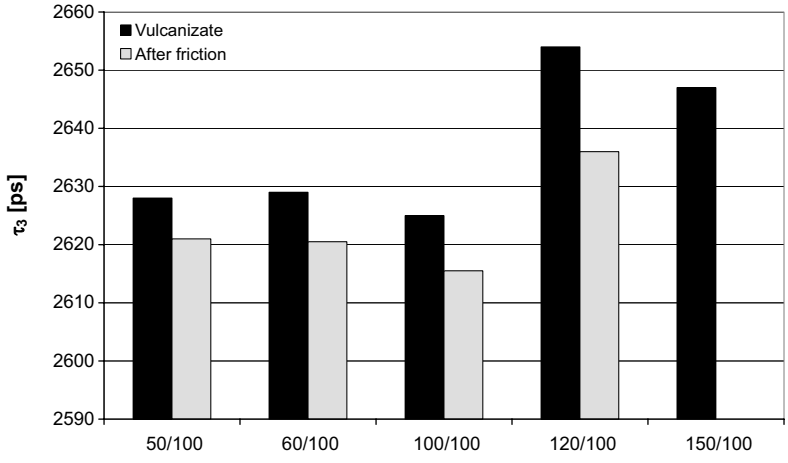

(b) SBR/50 phr of N 234

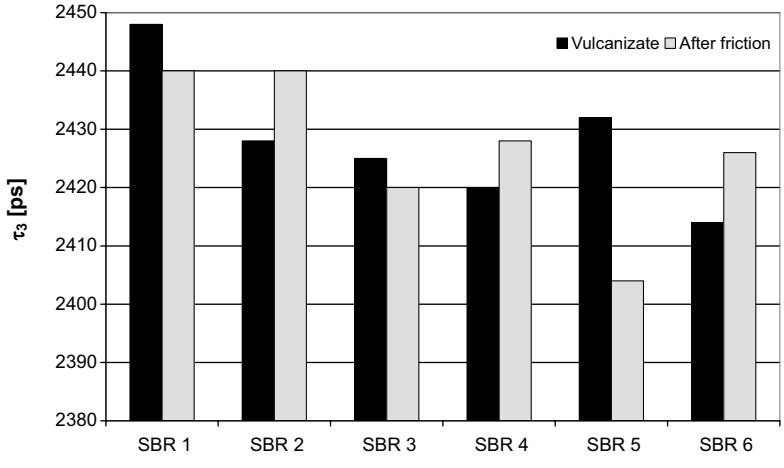

Figure 21.15 Influence of friction on *o*-Ps annihilation in free volumes: (a) EPDM/Coupsil VP 6411 and (b) SBR/50 phr of N 234

the least-squares fit of the equation FWHM $= A(\Delta S_{100-300})^{-\frac{1}{2}} + B$ to the experimental points with the fitted parameters $A = 0.39 \pm 0.13$, $B = -0.14 \pm 0.06$.

21.2.3 Final Remarks

Despite its sophistication PALS is a very useful analytical technique which enables us to recognize subtle details of rubber mixes morphology. They either could be hardly recognized or their detection requires complicated sample preparation procedure if other contemporary

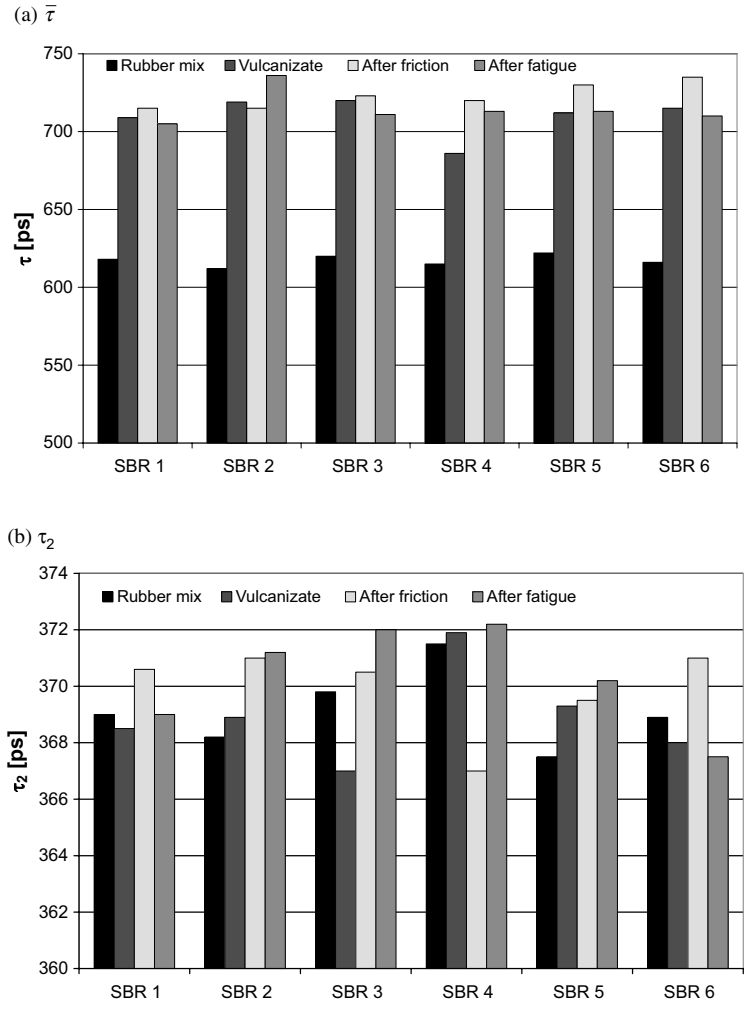

Figure 21.16 Influence of exploitation conditions on PALS spectra for SBR/50 phr of N 234 vulcanizates: (a) $\bar{\tau}$; (b) τ_2; (c) I_2; (d) τ_3; and (e) I_3

techniques are used. However until now PALS has not been used very often because of the difficult interpretation of experimental data. Most of the papers published on the application of PALS for studying rubber concern the morphology of filled mixes and the number and sizes of nano- and microholes, forming the so-called free volume. However, the effect of these parameters on the properties of elastomers has not been well enough recognized. Most often particles of fillers used in rubber technology are microsized, although it should be stressed that analysis of phenomena occurring during the preparation of rubber mixes is very often oversimplified. In general it is accepted that agglomerates have a detrimental effect on the properties of filled vulcanizates but the reason for this has not been recognized. Recently we

(c) I_2

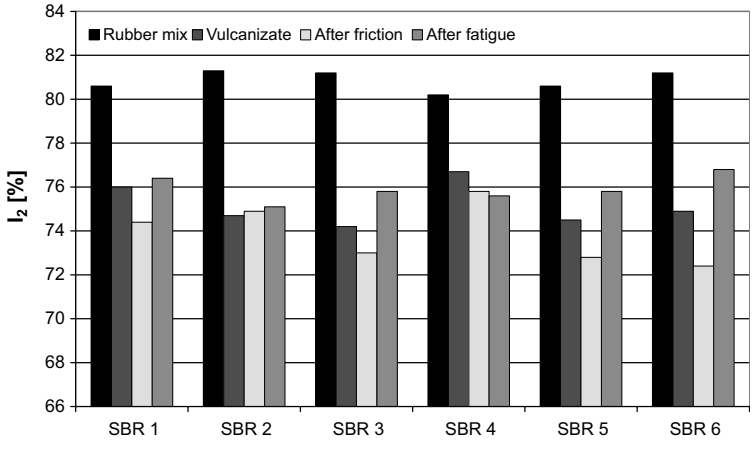

(d) τ_3

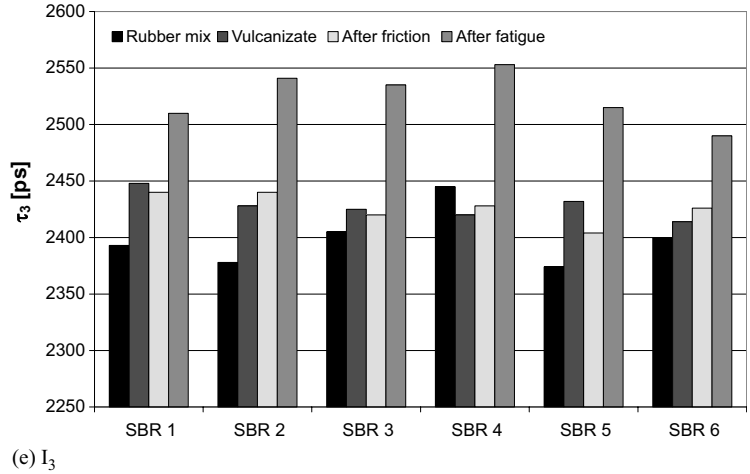

(e) I_3

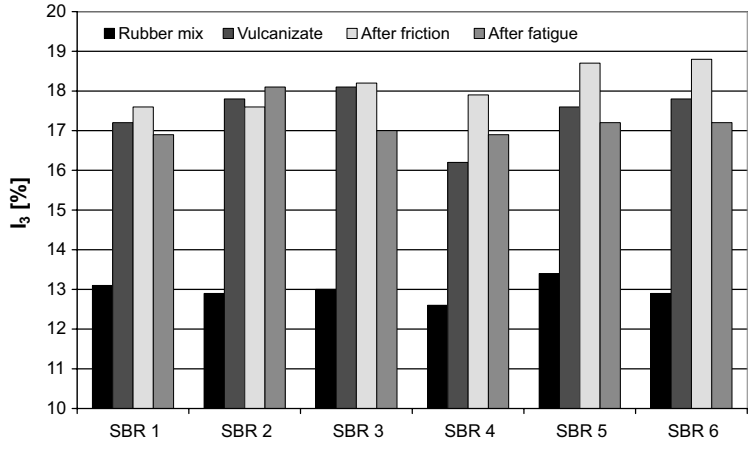

Figure 21.16 (*Continued*)

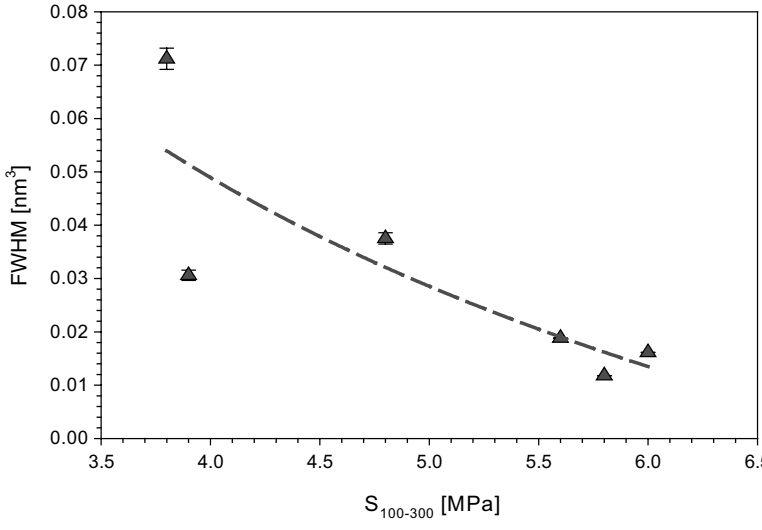

Figure 21.17 Dependence of FWHM values of number density distribution of holes – $g_n(V)$, calculated from Figure 21.10, on $\Delta\sigma_{100-300}$ parameter for SBR/50 phr of N 234 vulcanizates (Reprinted from D.M. Bieliński, O. Dobrowolski and E. Dryzek, "Application of PALS to study rubber morphology" (in Polish), in Elastomers and Rubber Industry, W. Parasiewicz and W.M. Rzymski (Eds.), 291–299, © 2006, with permission from Rubber Research Institute "STOMIL" and Technical University of Lodz.)

have investigated with the use of AFM and SEM techniques morphology of rubber mixes and behavior of stressed vulcanizates [30, 31, 39]. On the basis of results obtained, the original classification of agglomerates has been proposed and the particular role of non-infiltrated agglomerates (called "fatal") disclosed. It is worthy of mention that particles of commonly used fillers, for example, silica or carbon black are composed of nanosized primary particles, of very high surface energy, responsible for their ability towards aggregation and agglomeration. For that instance it is so difficult to prepare rubber mixes filled with nanofillers of satisfactory morphology and mechanical properties of their vulcanizates. Undoubtedly examination of such systems with the use of the PALS technique is very promissing and creates an opportunity for further progress in recognition of nanofillers effect on properties of elastomers.

21.3 Nanoindentation

21.3.1 Introduction

Because polymer materials are being used in thinner films and smaller volumes (for example, electronics, packaging) it is becoming increasingly important to test the actual material rather than to infer performance from results on bulk specimens. The surface layer of polymers can differ significantly from their bulk, which is the result of processing or further modification of materials [50]. Despite this, the role of the surface layer in the exploitation of polymer materials is very often underestimated or even neglected.

21.3.1.1 Principles of Nanoindentation

Nanoindentation (NI) differs from classic measurement of hardness, where the impressions are first generated and then imaged with a microscope. Load and penetration depths are recorded simultaneously during both loading and unloading, producing a force–depth diagram – Figure 21.18.

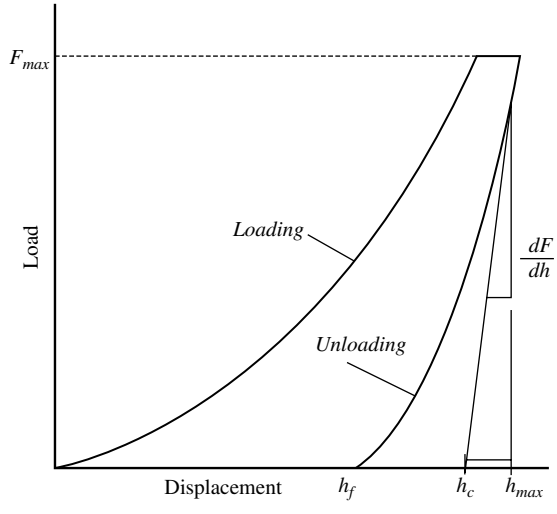

Figure 21.18 Schematic representation of the force-depth curve for a nanoindentation procedure

The technique permits the determination of hardness and Young modulus as a function of penetration depth. The maximum indentation depth ($h_{\max}$) includes elastic and plastic deformation. The symbol δ represents an elastic deformation part of the indent. The depth at which the applied force becomes zero on unloading is called plastic depth (h_p), whereas h_c is the contact depth at which the cross-section area (A_c) is taken to calculate hardness and mechanical modulus. Nanohardness (H) is calculated from the following formula:

$$H = \frac{F_{\max}}{A_c} \tag{21.11}$$

According to Oliver and Pharr [51], the contact depth (h_c) is given by:

$$h_c = h_{\max} - 0.75\frac{F_{\max}}{S} \tag{21.12}$$

where S is the contact stiffness,

$$S = \frac{dF}{dh} \tag{21.13}$$

with $\frac{dF}{dh}$ being the slope of the unloading curve at the initial point of unloading. The reduced Young modulus (E_r) is a measure of the elastic properties of the tip-sample system and can be

calculated from the force-depth curves, according to the following formula:

$$E_r = \frac{1}{2}\sqrt{\frac{\pi}{A_c}}\frac{dF}{dh} \tag{21.14}$$

For a diamond tip of Berkovitch geometry (ideal cube corner pyramid), the relation between indentation depth (h) and cross-section area (tip area function – A_c) is $A_c = 2.598h^2$.

It has been suggested that the so-called plastic work function (PWF) may serve as a guide to toughness of polymer materials [52]. The plastic work function is a dimensionless quantity defined as the ratio of the plastic (dissipated) energy, W_p (area between the loading and unloading curves), to the total energy, $W_t = W_p + W_e$ (area under the loading curve):

$$PWF = \frac{W_p}{W_p + W_e} \tag{21.15}$$

Cheng *et al.* [53] have determined that WPF is approximately linearly related to both the ratio of hardness to reduced modulus and to the ratio of residual depth to maximum depth. The latter ratio is in turn closely linked to the degree of elastic recovery in indentation (ERP):

$$ERP = \frac{h_{\max} - h_p}{h_p} \tag{21.16}$$

Nanoindentation can be also applied for analyzing creep of materials. Although several complex models have been proposed to describe the phenomenon in viscoelastic materials, in the case of elastomers and elastomeric composites a satisfactory approach [54] is to model the nanoindentation creep data with a general logarithmic creep formula, as proposed by Chudoba and Richter [55]:

$$h = A \ln (Bt + 1) \tag{21.17}$$

where h is the increase in depth at maximum load, t is time and A and B are fitting parameters.

A is an extent term, responsible for enhanced initial creep, whereas B is a rate term, with a smaller value indicating that the creep process occurs over a longer timescale.

21.3.2 Application of Nanoindentation to Study Rubber Morphology

21.3.2.1 Introduction

Nanoindentation allows to determine surface profile of hardness, mechanical modulus and ERP, being the result of changes to composition, morphology and structure of polymer materials. The changes can also be reflected by creep parameters, but in this case deformation process is strongly influenced by the strain rate. Assuming a relation between morphology of rubber and its mechano-rheological characteristics, one can apply nanoindentation for determination of the quality of filler dispersion, degree of crosslinking, modification or aging of the material.

21.3.2.2 State of the Art

Depth sensing indentation (DSI) made it possible to determine mechanical properties of silicone rubber coatings on substrates and freestanding films at submicron penetration depth [55]. For the first time authors observed complete elastic behavior for rubber-like films.

The calculated from DSI measurements mechanical moduli of the silicone rubber films were in good agreement with those measured by dynamic mechanical analysis (DMA).

In order to compare properties of rubber containing filler agglomerates to homogeneous rubber matrix Petitet *et al.* also carried out a nanoindentation experiment [56]. They used the continuous stiffness measurement with two kinds of indenters: (i) Berkovitch and (ii) trigonal geometry (average imposed strain of 7% of the elastoplastic limit [57]), superimposing a small oscillation onto a large-scale DC loading. The results showed that no residual strain was found in the rubber matrix when using both indenters nor was any found in the carbon black agglomerate when using the Berkovitch indenter. However, a residual strain was observed in the agglomerate when using the trigonal indenter. The presence of a residual strain means that elastoplastic limit of the agglomerate is between 7 and 14% and the Young modulus is around 300 MPa, while the Young modulus of homogeneous rubber matrix is about 30 MPa. Nanoindentation experiments have shown that rubber compound is heterogeneous from mechanical point of view. Agglomerates are closely linked to the rubber matrix. As a consequence, mechanical plasticizing of agglomerates causes craters on the rubber surface. It has been found that it is the exact influence of carbon black agglomerates on the wear of rubber.

A depth-sensing and frequency-specific dynamic indentation technique was used by researchers from Exxon Mobil Chemical Company to detect the spatial distribution of dynamic moduli (including storage, E', and loss, E'') in synthetic rubbers with varying degrees of cure and with or without carbon black fillers, as a function of penetration depth [58]. Combining experimental data with AFM pictures provided quantitative cure distribution maps for rubber blends and compounds. Atomic force microscopy and indentation mapping were also applied for studying the morphology of silicone rubber filled with $CaCO_3$ [59] and the detection of SiO_2 in polyethylene terephthalate matrix [60]. Nanohardness images revealed boundary regions of increased softness surrounded protruding particles.

The highest attention has been devoted to polymer blends, which have been studied under quasi-static conditions – using compliance nanoindentation method [61, 62] or under repetitive contact – using nanoscale impact testing [52, 63], producing mapping of mechanical parameters of materials. In the subject literature there are also many contributions on the application of nanoindentation for monitoring changes produced by various kinds of chemical or physical treatment to the surface of polymer materials [64–67].

21.3.2.3 The Influence of Rubber Morphology on Stress Relaxation Behavior

The presence of filler agglomerates of different internal structure and various kinds of interaction with rubber matrix makes it possible to classify vulcanizates according to their quality using nanoindentation. A comparison between stress relaxation courses for good and bad rubber mixes is given in Figure 21.19.

Due to an averaging approach, the method cannot be applied to distinguish between materials of similar degree of filler distribution, but it works perfectly in the case of bad material which has to be eliminated.

21.3.3 Application of Nanotribology to Study Rubber Morphology

21.3.3.1 Introduction

The difference between filler agglomerates and elastomer matrix can also be revealed during friction. The bigger the difference between the phases, according to the stiffness of the materials,

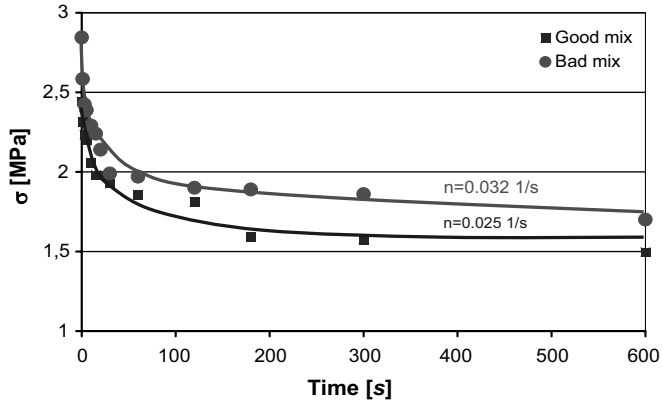

Figure 21.19 Comparison between stress relaxation courses for vulcanizates made of good and bad rubber mixes (SBR/50 phr of N 234)

the better the maps of filler distribution that can be obtained. This is why AFM pictures acquired applying friction mode are generally better for silica than carbon black mixes. From our experience it follows that the friction mode applied to silica filled vulcanizates can sometimes bring even better results than the recommended tapping mode. Nanofriction run simultaneously with microroughness makes it easy to eliminate effects coming from surface artifacts [68].

21.3.3.2 State of the Art

ASTM D 2663-95a describes an experimental procedure for determining the degree of filler agglomeration in rubber. By moving the 1 μm indenter over the surface of a rubber cross-section, it is possible to reflect the hills and valleys resulting from agglomerates and the craters after this part of them has been removed, respectively – Figure 21.20.

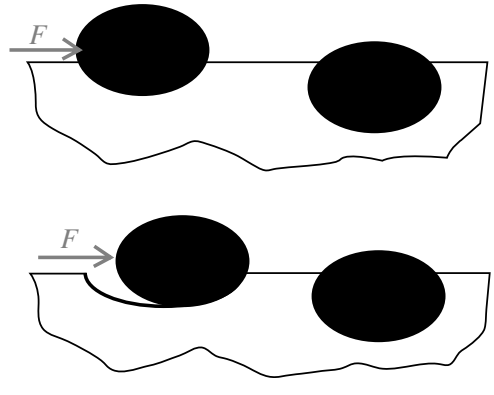

Figure 21.20 Principle of creation of a surface profile due to cross-section cutting

The results of microprofilometry are then analyzed and the degree of filler dispersion (DI) calculated, according to the formula [69]:

$$DI = 100\text{–}10 \exp(A \log F^2H + B) \tag{21.18}$$

where F is the number of roughness peaks per "cm", H is the number average peak height in "μm" and A and B are constants for each specific rubber formulation, which may vary with the kind of elastomer, carbon black type and loading, as well as state of cure. The values for DI are inversely proportional to F^2H.

Statistic analysis makes it possible to filter the geometrical signal from artifacts which are the result of surface preparation by cutting. The experimental procedure describing the determination of carbon black agglomeration in rubber has been validated in the thesis by Wehmeier [70]. The author compared results derived from microroughness profiles to values obtained using other methods.

21.3.3.3 The Influence of Rubber Morphology on Surface Microroughness and Nanofriction

The presence of filler agglomerate, arising from rubber matrix or its lack resulting in a hole, makes it possible to classify vulcanizates according to their quality using microprofilometry – Figure 21.21.

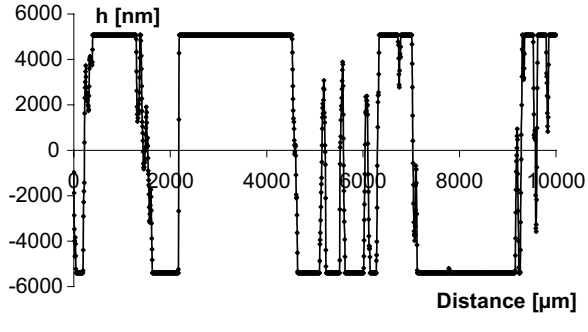

Figure 21.21 Example of the surface geometry profile of rubber vulcanizate

Microfriction profiles of vulcanizates having various morphology are also different, but their analysis is more complicated – Figure 21.22.

Both microprofilometry and nanofriction are time-consuming experiments, additionally demanding samples of perfectly prepared surface. They cannot compete with easier and cheaper rheological or microscopic methods, which makes them seldom applied for the determination of rubber mix quality (the degree of filler agglomeration) in industrial practice.

21.3.4 Final Remarks

Nanoindentation (NI) is broadly used for examining the surface layer of different materials: metals, ceramics, polymers and composites. It allows determination of real stress at shallow

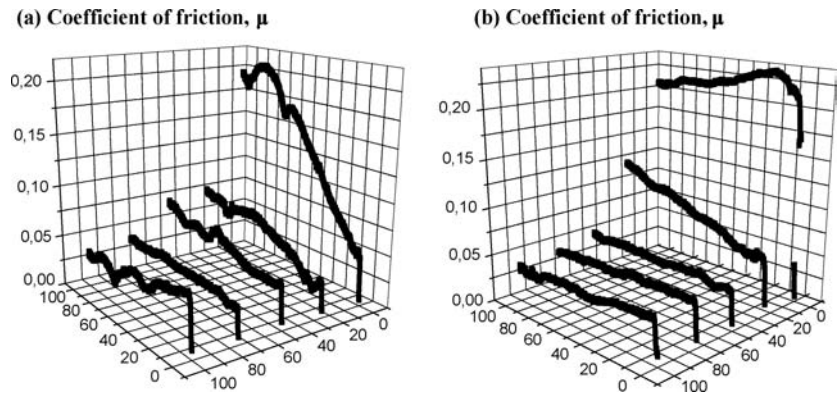

Figure 21.22 Microfriction characteristics for vulcanizates made of good and bad rubber mixes: (a) very bad dispersion, DI = 2.4 μ = 0.042 ± 0.004; and (b) good dispersion, DI = 6.8 μ = 0.056 ± 0.009

depths, where the plastic component of deformation is very small. The method is permanently improved, which concerns both mode of action as well as steering systems and registration of results. It is well known that the structure of polymer material surfaces including polymer composites differs in comparison to their bulk. What is particularly important in the surface layer are, for example, the initiation process of crack formation, ageing, burning, friction and others influencing the exploitation properties of polymer goods. Therefore, information obtained by the use of NI is of great practical importance, giving an early indication of the beginning of the phenomena. It should be stressed that nanofillers introduced to rubber very often exert their effect mainly on the surface. This concerns, for example, barrier properties, thermal stability and antipiretic action. Until now not many papers on the application of NI for studying rubber nanocomposites have been published. However, undoubtedly their number will increase in the near future. Generally speaking, the importance of the surface layer of polymer materials has until now been underestimated or even neglected.

References

1. Ślusarski, L. (2006) Modification of polymer materials by nanoparticles, a current status and perspectives of progress. Proceedings of the E-MRS Fall Meeting, Symposium D, Warsaw, p. 108.
2. Pramanik, M., Srivastawa, S.K., Samantaray, B.K., and Bhowmick, A.K. (2003) Rubber-clay nanocomposite by solution blending. *Journal of Applied Polymer Science*, **87**, 2216.
3. Bieliński, D., Głąb, P., Dobrowolski, O., and Ślusarski, L. (2005) Dispersion of fillers and its effect on properties of rubber. *Elastomery*, **9**, 42.
4. Wang, Z.F., Wang, B., Qi, N. *et al.* (2005) Influence of fillers on free volume and gas barrier properties in styrene-butadiene rubber studied by positrons. *Polymer*, **46**, 719.
5. Ranimol, S., Ranganathaiah, C., Varghese, S. *et al.* (2006) Gas transport through nano and micro composites of natural rubber (NR) and their blends with carboxylated styrene butadiene rubber (XSBR) latex membranes. *Polymer*, **47**, 858.
6. Pethrick, R.A. (1997) Positron annihilation – a probe for nanoscale voids and free volume? *Progress in Polymer Science*, **22**, 1.
7. Dirac, P.A.M. (1930) On the annihilation of electrons and protons. *Mathematical Proceedings of the Cambridge Philosophical Society*, **26**, 361.

8. Mogensen, O.E. (1974) Spur reaction model of positronium formation. *Journal of Chemical Physics*, **60**, 998.
9. Ore, A. and Powell, J.L. (1949) Three-photon annihilation of an electron-positron pair. *Physical Review*, **75**, 1969.
10. Brandt, W., Berko, S., and Walker, W.W. (1960) Positronium decay in molecular substances. *Physical Review*, **120**, 1289.
11. Brandt, W. and Wilkenfeld, J. (1975) Electric field dependence of positronium formation in condensed matter. *Physical Review*, **B12**, 2579.
12. Brandt, W. and Wilkenfeld, J. (1976) Erratum: Electric field dependence of positronium formation in condensed matter. *Physical Review*, **B13**, 2243.
13. Levay, B. (1979) Chemical structure studies with positrons and mesons. *Atomic Energy Review*, **17**, 413.
14. van Krevelen, D.W. and Hoftzer, P.J. (1976) *Properties of Polymers*, 2nd edn, Elsevier, New York, pp. 51–79.
15. Lee, W.M. (1980) Selection of barrier materials from molecular structure. *Polymer Engineering and Science*, **20**, 65.
16. Tao, S. (1972) Positronium annihilation in molecular substances. *Chemical Physics*, **56**, 5499.
17. Kirkgaard, P. and Eldrup, M. (1972) POSITRONIFIT: a versatile program for analyzing positron lifetime spectra. *Computer Physics Communications*, **3**, 240.
18. Hamielec, A.E., Eldrup, M., Mogensen, O., and Jansen, P. (1973) Positron annihilation techniques (PAT) in polymer science and engineering. *Journal of Macromolecular Science-Reviews in Macromolecular Chemistry and Physics*, **9**, 305.
19. Brandt, W. and Fahs, J.H. (1970) Positronium decay in condensed matter. *Physical Review*, **B2**, 1425.
20. Bielinski, D.M., Włochowicz, A., Dryzek, J., and Ślusarczyk, Cz. (2001) Differences between crystallization of LDPE and iPP in EPDM matrix. *Composite Interfaces*, **8**, 1.
21. Belov, G.P., Esipov, YuK., Zherdev, YuV. *et al.* (1977) *Plasticheskie Massy*, **10**, 54.
22. West, D.H.D., McBrierty, V.J., and Delaney, C.F.G. (1979) A positron annihilation study of carbon black and carbon-black-filled polybutadiene. *Applied Physics*, **18**, 85.
23. Morgensen, O.E., Jacobsen, F.M., and Pethrick, R.A. (1979) Positron annihilation in a rubber modified epoxy resin. *Polymer*, **20**, 1034.
24. Djermouni, B. and Ache, H.J. (1980) Effect of casting solvents on the properties of styrene-butadiene-styrene block copolymers studied by positron annihilation techniques. *Macromolecules*, **13**, 168.
25. Dlubek, G., Clarke, A.P., Fretwell, H.M. *et al.* (1996) Positron lifetime studies of free volume hole size distribution in amorphous and in semi-crystalline polymers. *Journal of Radioanalytical and Nuclear Chemistry*, **211**, 69.
26. Bueche, F. (1953) Segmental mobility of polymers near their glass temperature. *Journal of Chemical Physics*, **21**, 1850.
27. Wang, B., Wang, Z.F., Zhang, M. *et al.* (2002) Effect of temperature on the free volume in glassy poly(ethylene terephthalate). *Macromolecules*, **35**, 3993.
28. Kilbum, D., Dlubek, G., Pionteck, J. *et al.* (2005) Microstructure of free volume in SMA copolymers. I. Free volume from Simha-Somcynsky analysis of PVT experiments. *Polymer*, **46**, 869.
29. Wang, Z.F., Wang, B., Qi, N. *et al.* (2005) Application of PALS to study rubber micromorphology in elastomers and rubber industry. *Polymer*, **46**, 719.
30. Bieliński, D.M., Ślusarski, L., Dobrowolski, O. *et al.* (2004) Morphological aspects of rubber fracture and wear. *Kautschuk Gummi Kunststoffe*, **57**, 579.
31. Bieliński, D.M., Ślusarski, L., Dobrowolski, O. *et al.* (2005) Studies of filler agglomeration by AFM and PAS. Part II: carbon black mixes. *Kautschuk Gummi Kunststoffe*, **58**, 239.
32. ISO (2006) 11345, *Rubber. Assessment of Carbon Black and Carbon Black/Silica Dispersion. Rapid Comparative Methods*, ISO.
33. *DisperGrader 1000, Instrument for determination of filler dispersion and the presence of large agglomerates in all black rubber*, Optigrade A.B., Sweden.
34. Grossman, R.F. (ed.) (1997) *The mixing of Rubber*, Chapman & Hall, London.
35. Leblanc, J.L. (2001) Some considerations on optimum mixing with respect to the full development of rubber – carbon black morphology. *Kautschuk Gummi Kunststoffe*, **54**, 327.
36. Gerspacher, M., Nikiel, L., Yang, H.H. *et al.* (2002) Flocculation in carbon black filled rubber compounds. *Kautschuk Gummi Kunststoffe*, **55**, 596.
37. Qi, L., Feke, D.L., and Manas-Zloczower, I. (1995) Influence of aggregate structure and matrix infiltration on the dispersion behavior of carbon black agglomerates. *Rubber Chemistry and Technology*, **68**, 836.

38. Collins, V. (2004) Etude rheo-optique des mecanismes de dispersion du noir de carbone dans des elastomeres, Docteur these, l'Ecole des Mines de Paris.
39. Bieliński, D.M., Dobrowolski, O., and Przybytniak, G. (2008) Morphological aspects of rubber fracture and wear. *Journal of Applied Polymer Science*, **110**, 55.
40. Bieliński, D.M., Ślusarski, L., Dobrowolski, O. *et al.* (2004) Studies of filler agglomeration by atomic force microscopy and positron annihilation spectroscopy. Part I: silica filled compounds. *Kautschuk Gummi Kunststoffe*, **57**, 579.
41. Wang, Y.Y., Nakanishi, H., Yean, Y.C., and Sandreczki, T.C. (1986) Positronium annihilation in amine-cured epoxy polymers. *Journal of Polymer Science Part B*, **24**, 1247.
42. Baltá Calleja, F.J., Serna, F.J., and Segovia, M.A. (1985) Structural implications on positron lifetimes in lamellar polyethylene with chain defects. *Journal of Applied Physiology (Bethesda, Md: 1985)*, **58**, 253.
43. Bokobza, L. (2001) Reinforced elastomeric network by fillers. *Macromolecular Symposia*, **169**, 243.
44. Zaborski, M., Baryń, W., and Ślusarski, L. (1991) The effect of structure of elastomer matrix on activity of fillers. Pt.1: behaviour of carbon black in the rubber filler systems. *Polimery*, **36**, 66.
45. Jean, Y.C. (1990) Positron anihilation spectroscopy for chemical analysis: a novel probe for microstructural analysis of polymers. *Microchem Journal*, **42**, 72.
46. Eldrup, M. (1982) *Positron Annihilation* (eds P.G. Coleman, S.C. Sharma, and L.M. Diana), North-Holland Publishing Company, Amsterdam, New York, Oxford, p. 753.
47. Shukla, A., Peter, M., and Hoffmann, L. (1993) Analysis of positron lifetime spectra using qualified maximum entropy and linear filter. *Nuclear Instruments & Methods in Physics Research Section A - Accelerators Spectrometers Detectors and Associated Equipment*, **335**, 310.
48. Dlubek, G., Hübner, Ch., and Eichler, S. (1999) Do MELT or CONTIN programs accurately reveal the o-Ps lifetime distribution in polymers *Physica Status Solidi A - Applied Research*, **172**, 303.
49. Ito, Y. (1998) *Positron and Positronium Chemistry* (eds D.M. Schrader and Y.C. Jean), Elsevier, Amsterdam, p. 151.
50. Bieliński, D.M. (2001) The surface layer and friction of elastomers. *Polimery*, **46**, 684.
51. Oliver, W.C. and Pharr, G.M. (1992) An improved technique for determining hardness and elastic modulus using load and displacement sensing indentation experiments. *Journal of Materials Research*, **7**, 1564.
52. Beake, B.D., Goodes, S.R., and Smith, J.F. (2004) Nanoscale repetitive impact testing of polymer films. *Journal of Materials Research*, **19**, 237.
53. Cheng, Y.-T., Li, Z., and Cheng, C.-M. (2002) Scaling relationships for indentation measurements. *Philosophical Magazine A - Physics of Condensed Matter Structure Defects and Mechanical Properties*, **82**, 1821.
54. Bieliński, D.M. (2007) Proc. of the 11th Int. Seminar on Elastomers ISE'07, Freiburg (Germany) 23-27.09.2007 p. 57.
55. Li, Z., Brokken-Zijp, J.C.M., and de With, G. (2004) Determination of the elastic moduli of silicone rubber coatings and films using depth-sensing indentation. *Polymer*, **45**, 5403.
56. Petitet, G., Loubet, J.-L., Zahouani, H., and Mazuyer, D. (2005) A contribution to the understanding of elementary wear mechanisms of rubber filled compounds. *Rubber Chemistry and Technology*, **78**, 312.
57. Kendall, K. (1988) Agglomerate strength. *Powder Metallurgy*, **31**, 28.
58. Hsou, A.H., Westwood, A.D., Schulze, J.S., and Herbert, E.G. (2004) Cure state distributions in rubbers by dynamic nano-indentation. *Rubber Chemistry and Technology*, **77**, 678.
59. Eaton, P., Fernandez, E.F., Ewen, R.J. *et al.* (2002) Combined nanoindentation and adhesion force mapping using the atomic force microscope: investigations of a filled polysiloxane coating. *Langmuir*, **18**, 10011.
60. Nowicki, M. and Susła, B. (2003) Nanoindentation as a tool for recognition of composites components. *Acta Physica Polonica A*, **104**, 365.
61. Zhu, S.-H., Chan, Ch.-M., and Mai, Y.-W. (2004) Micromechanical properties on the surface of PVC/SBR blends spatially resolved by a nanoindentation technique. *Polymer Engineering and Science*, **44**, 609.
62. Achalla, P., McCormick, J., Hodge, T. *et al.* (2006) Characterization of elastomeric blends by atomic force microscopy. *Journal of Polymer Science Part B - Polymer Physics*, **44**, 492.
63. White, C.C., Drzal, P.L., and Van Landingham, M.R. (2005) Fundamentals on nanoindentation and nanotribology III. *Materials Research Society Symposium Proceedings*, **841**, 187.
64. Brun, C., Fromm, M., Berger, F. *et al.* (2003) Modifications of polypropylene surface properties by He + ion implantation. *Journal of Polymer Science Part B-Polymer Physics*, **41**, 1183.
65. Qasmi, M., Delobelle, P., Richard, F. *et al.* (2004) Viscoelastic mechanical properties determined by nanoindentation tests and its numerical modeling of polypropylene modified by He + particle implantation and e- irradiation. *Progress in Organic Coatings*, **51**, 195.

66. Bieliński, D.M., Pieczyńska, D., and Jagielski, J. (2007) Modification of elastomer friction by ion bombardment. Proc. of the 4th Int. Conf. on "High Performance and Speciality Elastomers, HPE'07", Paper 20, Frankfurt, 5–6.12.2007.
67. Bieliński, D.M., Ślusarski, L., and Gąb, P. (2007) Modification of rubber by iodoform. *Journal of Applied Polymer Science*, **105**, 177.
68. Micro Materials Ltd (2009) www.micromaterials.com.
69. ASTM (2000) D 2663-95a, *Standard Test Methods for Carbon Black – Dispersion in Rubber*, ASTM.
70. Wehmeier, A. (1998) Entwicklung eines Verfahrens zur Charakterisierung der Füllstoffdispersion in Gummimischungen mittels einer Oberflächentopografie, Diplomarbeit, Fachbereich Chemieingenieurwesen, Fachhochschule Münster, Abteilung Steinfurt, Germany November.

22

Thermoelasticity and Stress Relaxation Behavior of Synthetic Rubber/Organoclay Nanocomposites

K.M. Sukhyy[1], E.G. Privalko[2], V.P. Privalko[2], and M.V. Burmistr[1]
[1] *Ukrainian State Chemical Technology University, Pr. Gagarina 8, Dnepropetrovsk, 49005, Ukraine*
[2] *Institute for Macromolecular Chemistry, National Academy of Sciences of Ukraine, Kharkiv Chaussee 48, Kyiv, 02160, Ukraine*

22.1 Introduction

The quasi-static mechanical properties of filled elastomers have been the object of extensive experimental studies over many decades (for example, [1–3]); the main results can be summarized as follows:

1. The increasing "overshoot" of elasticity moduli, the smaller the filler particle size, above the values predicted by pragmatic phenomenological models (that is, those assuming that the moduli of a matrix and of a filler remain size- and composition-invariant, so that the volume fraction of inclusions φ is the only factor responsible for the composition dependence of the modulus of a composite).
2. Pronounced "stress-softening" phenomena setting on after the first uniaxial stretching and gradually leveling-off during subsequent stretching/contraction cycles (the so-called Mullins-Patrikeev effect).

Rubber Nanocomposites: Preparation, Properties and Applications Edited by Sabu Thomas and Ranimol Stephen
© 2010 John Wiley & Sons (Asia) Pte Ltd

Our previous thermoelastic studies of several series of elastomeric nanocomposites (ENC) prepared by melt-compounding of synthetic rubber with different fillers [4–7] have shown that both above phenomena can be quantitatively treated using the concept of hydrodynamic strain amplification. In fact, the first phenomenon listed above is accounted for through the strain amplification factor $X = \varepsilon_{int}/\varepsilon$ which relates the microscopic intrinsic strain of the rubber matrix ε_{int} to the macroscopic extension of the filled sample, $\lambda = 1 + \varepsilon$ [8, 9]. The second phenomenon listed above implies the prestrain dependence of the strain amplification factor. This means that with increasing strain the initial spatial aggregates of filler particles spanning the entire sample volume (infinite clusters, InC) would decay to smaller-size fragments (isolated clusters, IsC); however, the sizes of the latter are believed to be frozen in subsequent stretching/contraction cycles, provided the eventual strains would not exceed the maximum prestrain [10–12]. Moreover, the exothermal effects of external friction between particles generated during a successive decay of a spatial network of filler particles with increasing strain were shown to depend on the nature of a filler and on the interaction energy at the rubber/filler interface [4–7].

22.2 Experimental

22.2.1 Materials

Two elastomeric matrices are investigated: (i) mercaptan-type polychloroprene rubber CR (Baypren 110, Bayer AG) with very good aging properties, flame retardance, high weather resistance, resistance against ozone, different chemicals and oils and so on and (ii) styrene-*co*-butadiene rubber with styrene content 18% (BUNA-SL18; Bayer AG).

The nanoparticles of the commercial organoclay OC_2 (Nanofil, Süd-Chemie AG) were pretreated with dioctadecyl-dimethyl ammonium salt. The crosslinking reagents and stabilizers (stearic acid SA, zinc oxide ZnO, magnesium oxide MgO, Rhenogran ETU-80) were supplied by Bayer AG.

The polychloroprene/organoclay nanocomposites were prepared in two steps. In the first step, CR was melt compounded with OC_2 at 353 K, using an internal mixer (Haake Rheocord 90); after 7 min the vulcanization reagents were added and the mixing continued during the next 3 min; finally, each composition was homogenized in a three-roll mill (Exakt 80S) at 333–353 K. In the second step, the samples were crosslinked by sulfur vulcanization of the matrix in a hot stage vacuum press (Collin) under a pressure of 30 bar at 433 K during about 50 min, as described in detail elsewhere [4, 13]. The sample codings and compositions are shown in Table 22.1. The volume content of the inorganic nanophase (fifth column) was calculated assuming 35 wt% as the total amount of an organic modifier in the OC_2 (information from the supplier), and 2.65 g/cm^3 as the density of SiO_2.

The styrene-*co*-butadiene rubber/organoclay nanocomposites were prepared by melt compounding by using an internal mixer and a three-roll mill, followed by sulfur vulcanization of the matrix in a hot press under a pressure of 20 bar, as reported elsewhere [10]. The reference sample with weak interfacial interactions (RS) contained 30 phr of clay nanoparticles pretreated with dioctadecyl-dimethyl ammonium salt (Nanocor 1.42 E). The test sample with strong interfacial interactions (TS) contained the same amount of the same clay nanoparticles that were, however, chemically bonded to the rubber matrix with the silane-coupling agent, bis(triethoxysilyl)-tetrasulfan (Si69; Degussa AG) [11].

Table 22.1 Sample composition and coding

No.	Sample	CR [phr]	OC_2 [phr]	SiO_2 [vol.%]	SA [phr]	ZnO [phr]	ETU-80 [phr]	MgO [phr]
1	CR	100	0	0	0.5	5	0.5	4
2	CR/OC2-2,5	100	2.5	0.6	0.5	5	0.5	4
3	CR/OC2-5	100	5.0	1.2	0.5	5	0.5	4
4	CR/OC2-7,5	100	7.5	1.7	0.5	5	0.5	4
5	CR/OC2-10	100	10.0	2.3	0.5	5	0.5	4
6	CR/OC2-12,5	100	12.5	2.8	0.5	5	0.5	4
7	CR/OC2-15	100	15.0	3.4	0.5	5	0.5	4
8	CR/OC2-20	100	20.0	4.4	0.5	5	0.5	4
9	CR/OC2-30	100	30.0	6.2	0.5	5	0.5	4
10	CR/OC2-40	100	40.0	7.9	0.5	5	0.5	4

22.2.2 Methods

Wide-angle X-ray scattering (WAXS) patterns in the range of scattering angles (2θ) 5–40° were measured with a DRON-2,0 diffractometer. As usual, the scattering curves were normalized by thickness and X-ray absorption.

SAXS measurements were performed using a Kratky compact small-angle system (PAAR, Graz, Austria) equipped with a scintillation counter operating in a step-scanning mode [6], as well as a KRM-type diffractometer [5, 7].

Specific heat capacity c_p was measured (temperature interval: 215–380 K; heating rate: 10 K/min) with the temperature-modulated DSC instrument (Perkin Elmer DSC-2 upgraded and supplied with signal processing software by IFA GmbH, Ulm).

The mechanical work (W) and concomitant heat effects (Q) in the stepwise loading (stretching)/unloading (contraction) cycles were measured (with the estimated mean errors below 2%) at room temperature with the stretching calorimeter described in detail elsewhere [14, 15]. In the range of small relative extensions λ (<1.10–1.20), each specimen was stretched at a constant velocity q^+ (10% of the total specimen length per minute) to a predetermined λ_i, kept at fixed λ_i to the full completion of mechanical and thermal relaxations, and thereafter allowed to contract at the same velocity q^- to zero force. The typical difference between fixed extensions in two successive steps, $\Delta\lambda = \lambda_{i+1} - \lambda_i$, varied from several digits in the fourth place to a few digits in the third place. At higher elongations, the mechanical work and heat effects were measured only in the regime of successive step-wise stretching at larger $\Delta\lambda$ (a few digits in the second place).

The same experimental set-up was used for stress relaxation measurements [7]. Prior to each measurement, the previous mechanical history was erased by several successive prestretchings to the maximum extension λ_{lim}, free relaxation to zero stress and subsequent storage in an unloaded state overnight. Then the specimen was stretched to a predetermined fixed extension $\lambda_f < \lambda_{lim}$, and the time dependence of the stress σ was monitored at $\lambda_f = const$.

22.3 Polychloroprene/Organoclay Nanocomposites

22.3.1 Structural Characterization of Unstretched Samples

The main features of the WAXS patterns for the neat CR (Figure 22.1a) were the major diffuse amorphous halo with a maximum near the scattering vector $q_0 \approx 13.2\,\mathrm{nm}^{-1}$ (which can be

attributed to the interchain spacing $d_0 = 2\pi/q_0 \approx 0.48$ nm), and several sharp reflections at higher q (as argued elsewhere [5], the latter reflections are due to stabilizer inclusions). The WAXS profiles for the RNC were essentially similar; however, three additional reflections due to the organoclay appeared near $q \approx 15.3$, 14.2 and 3.4 nm^{-1} and tended to gain intensity with the filler content w (Figure 22.1a).

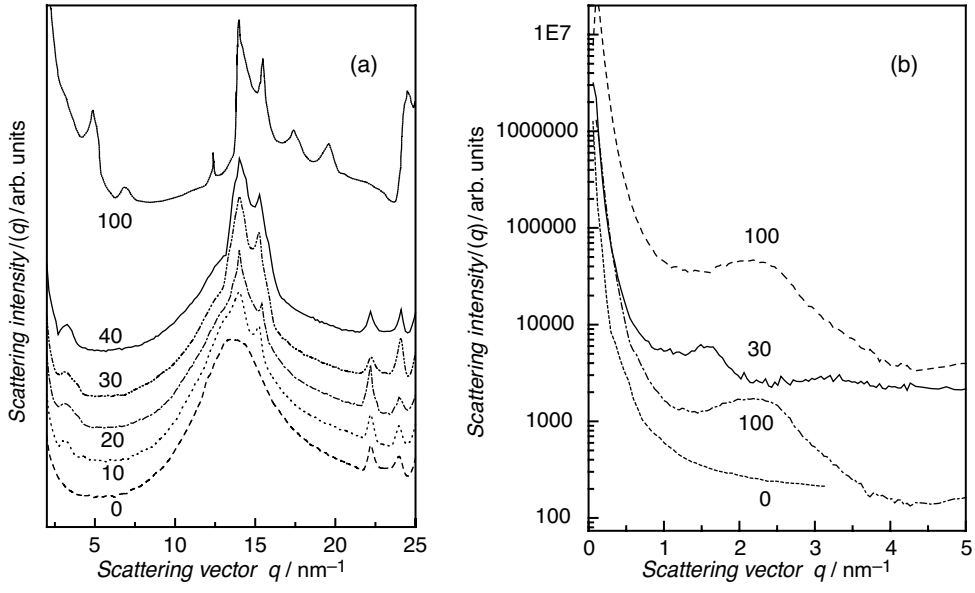

Figure 22.1 (a) WAXS and (b) SAXS profiles for studied samples. Numbers at the curves indicate the organoclay content (phr)

No evidence for large-scale heterogeneities could be detected on the SAXS curves for the neat CR (Figure 22.1b). A single SAXS maximum at $q \approx 2.25$ nm^{-1} observed for a pure Nanofil both in the bulk state and in a thin layer corresponded to the interlayer distance $d \approx 2.8$ nm. A significantly larger spacing of $d \approx 4.0$ nm calculated from the angular position of a single well-resolved SAXS reflection at $q \approx 1.56$ nm^{-1} on the representative SAXS curve for the sample CR/OC2-30 (Figure 22.1b) suggested a reasonably high degree of organoclay exfoliation.

The absence of crystallinity in the neat CR was also evident from the DSC traces (Figure 22.2), in which no endothermal effects of crystal melting were observed in the temperature interval above the specific heat capacity jump $\Delta c_p \approx 0.30$ J/g K at the glass transition temperature $T_g = 243$ K. As could be expected, the apparent values of Δc_p for the ENC continuously decreased, while the glass transition temperatures tended to increase, the higher the filler content up to $T_g = 248$ K for the sample CR/OC2-40.

22.3.2 Thermoelastic Behavior

As expected, both the mechanical work and the heat effects in the stretching/contraction cycles for the neat CR were completely reversible. The experimental values of specific (per unit of

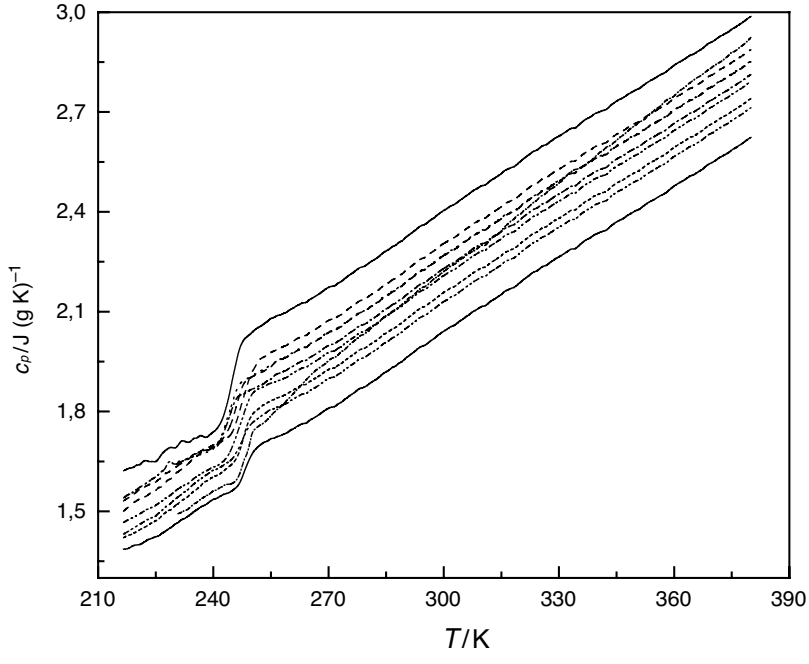

Figure 22.2 DSC heating traces for all studied samples (the organoclay content increases from the top to the bottom as shown in Table 22.1)

mass m) mechanical work W/m and specific heat effects Q/m (Figure 22.3a) were fitted to the standard equations of elasticity for real rubbers [16],

$$W/m = A(E/6\rho)f_1(\lambda), \tag{22.1a}$$

$$Q/m = -(W/m)\,[1-T\beta-2\alpha T/f_2(\lambda)], \tag{22.1b}$$

where $A = \langle h_0^2\rangle/\langle h^2\rangle$ is the front factor (usually, $A = 1$ is assumed); $\langle h_0^2\rangle$ and $\langle h^2\rangle$ are the mean-square end-to-end distances of an isolated, unperturbed chain and of an identical chain in the network, respectively; E is the elasticity modulus in the simple stretch regime; ρ is the density; $\beta = d \ln \langle h_0^2\rangle/dT$ is the temperature coefficient of unperturbed chain dimensions; $\alpha = -d \ln \rho/dT$ is the thermal expansion coefficient of bulk rubber; $f_1(\lambda) = \lambda^2 + 2/\lambda - 3$ and $f_2(\lambda) = \lambda^2 + \lambda - 2$.

First, the best-fit value $E = 1.94$ MPa was derived from Equation 22.1a; next, the relevant experimental data were fitted to Equation 22.1b treating β and α as adjustable parameters. The excellent quality of the data fits to both Equations 22.1a and 22.1b over the entire range of relative elongations at the best-fit values of $E = 1.94$ MPa, $\beta = 1.56 \times 10^{-3}\,\mathrm{K}^{-1}$ and $\alpha = 0.98 \times 10^{-3}\,\mathrm{K}^{-1}$ can be assessed from Figure 22.3a.

In contrast to the neat CR, for all RNC the irreversible effects (manifesting themselves as divergencies between both W/m and Q/m in stretching/contraction cycles) proved to set on at fairly low elongations. Therefore, these data were treated according to the following procedure:

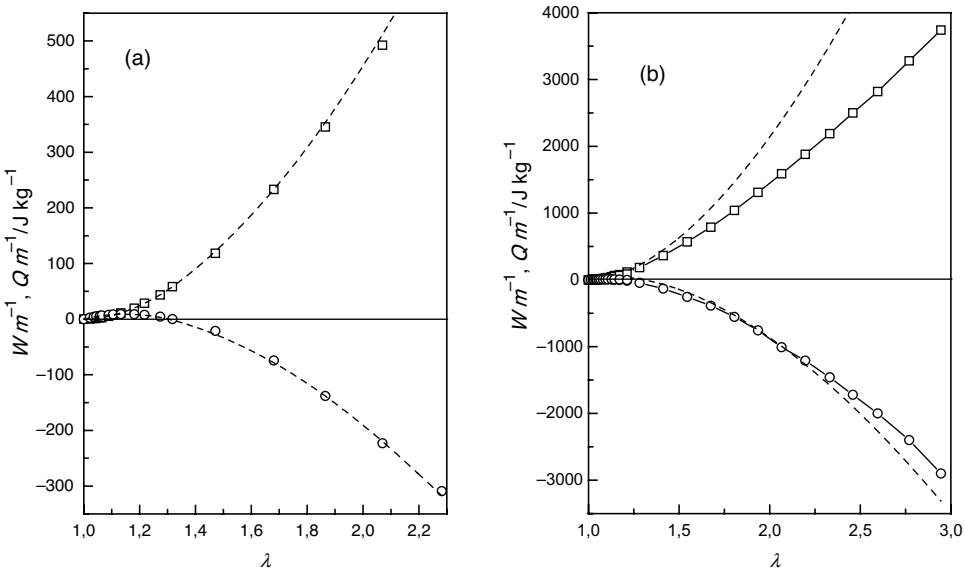

Figure 22.3 Dependencies on relative elongation of specific mechanical work (squares) and specific heat effects (circles) for (a) neat CR and (b) sample CR/OC2-30. Dashed and solid lines indicate the best nonlinear fits to Equations 22.1 and 22.3, respectively

first, the best-fit values of the apparent modulus (hereafter referred to as E') were derived by Equation 22.1a for the range of reversible deformations ($\lambda < 1.2$); then, the theoretical curves of W/m and Q/m were calculated by Equations 22.1a and 22.1b assuming reversibility (that is, keeping unchanged the material parameters β and α for the CR matrix).

The relatively large "overshoot" of the apparent Young's modulus of the sample CR/OC2-2.5 with the lowest organoclay content (2.5 wt%) above that for the neat CR and subsequent continuous increase of E' with the filler weight content w (Table 22.2) suggest a considerable reinforcement effect by the infinite clusters (InC) of organoclay particles. According to the cluster-cluster aggregation (CCA) model [17], a fingerprint for the onset of an InC of filler

Table 22.2 Thermoelastic parameters

Sample	E′, MPa	X_0	X_∞	z	C
CR	1.94	...	...	...	...
CR/OC2-2,5	2.12	22.20	16.96	0.60	0.10
CR/OC2-5	2.24	24.03	18.85	0.60	0.21
CR/OC2-7,5	3.05	28.01	22.07	0.60	0.28
CR/OC2-10	3.74	28.13	22.95	0.61	0.35
CR/OC2-12,5	4.06	33.56	25.82	0.60	0.24
CR/OC2-15	5.34	33.88	26.38	0.60	0.29
CR/OC2-20	7.22	40.41	29.59	0.60	0.26
CR/OC2-30	8.91	43.39	33.01	0.62	0.25
CR/OC2-40	11.54	51.01	39.92	0.61	0.16

particles above the apparent "gel point" φ^* is the following scaling relationship for the elasticity modulus,

$$E' \sim \varphi^{\alpha}, \tag{22.2}$$

where φ is the filler volume fraction, $\alpha = (3 + d_{f,B})/(3 - d_f)$ and d_f and $d_{f,B}$ are the fractal dimensions of a CCA-cluster and of a CCA-cluster backbone, respectively. The experimental tests of Equation 22.2 for a series of RNC containing isometric filler particles (like carbon blacks or model organic nanospheres) at $\varphi ? \varphi^* \approx 0.2$ yielded $\alpha \approx 3.5$ [17] which is consistent with the typical fractal dimensions of $d_{f,B} \approx 1.3$ and $d_f \approx 1.8$.

As can be seen from Figure 22.4, the experimental values of E' for the RNC studied in this work also quantitatively obey Equation 22.2. However, the applicability of this equation to the data obtained in the range of filler fractions $\varphi < 0.25$ is not immediately obvious; moreover, the nearly fourfold smaller value of the relevant exponent ($\alpha \approx 0.87$) also can not be readily rationalized.

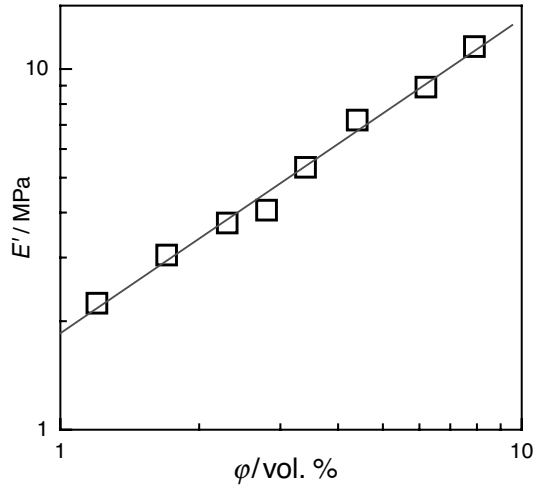

Figure 22.4 E' versus φ plot for the ENC

In our opinion, the origin of the observed discrepancy is in the basically different shapes of filler particles (nearly isometric carbon black particles of aspect ratio $l/d \approx 1$, and highly anisometric organoclay particles of aspect ratio $l/d \ll 1$). In fact, the geometrical percolation threshold for the onset of an InC of overlapping ellipsoids was shown [18] to decrease from $\varphi^* \approx 0.28$ expected for $l/d \approx 1$ down to $\varphi^* \approx 0.04$ for $l/d \approx 1/20$. Hence, the onset of an InC of highly anisometric organoclay particles at volume fractions as low as $\varphi \leq 0.04$ (Figure 22.4) seems both theoretically possible [18] and experimentally proved (for example, by melt viscoelasticity studies of polyamide 6/organoclay nanocomposites [19]). In this context, space-filling conditions for clusters in carbon black-filled elastomers and in the RNC studied in this work may be also basically different; in other words, the observed differences between the exponents α

suggest different fractal structures and/or properties of the InC (for example, the lengths of the spanning arms and the relevant force constants for bending/twisting).

As can be seen from the representative plots for the sample CR/OC2-30 (Figure 22.3b), as well as from similar data obtained for all other RNC, the deviations between the experimental values of both W/m and Q/m and the theoretical curves which were calculated by Equations 22.1a and 22.1b assuming reversibility (dashed lines) steadily increased, the higher the relative extension. These deviations can be attributed to irreversible structural changes in the InC of filler particles, as implicit in the following equations [5–7]:

$$W/m = A(E/6\rho)(\lambda_{\text{int}}^2 + 2/\lambda_{\text{int}} - 3), \tag{22.3a}$$

$$Q/m = -(W/m)[1 - T\beta - 2\alpha T/(\lambda_{\text{int}}^2 + \lambda_{\text{int}} - 2) + C]. \tag{22.3b}$$

Here $\lambda_{\text{int}} = 1 + \varepsilon X$ is the normalized relative extension, $X = X_\infty + (X_0 - X_\infty)\exp(-z\varepsilon_{\max})$, X_0, X_∞ and z are the fitting parameters, $\varepsilon_{\max}$ is the maximum strain at each successive loading step and C is the empirical correction for the heat generated by external friction between nanoparticles during the deformation/fragmentation processes of an InC.

As can be seen from Figure 22.3b (solid lines), the relevant experimental data proved to quantitatively obey Equations 22.3a and 22.3b; the best-fit values of fitting parameters are listed in Table 22.2. These results provide additional support for the concept of prestrain-dependent strain amplification factor as the major parameter controlling the thermoelastic behavior of ENC [5–7]. Nearly identical values of z imply similar fractal dimensions [11] of the initial InC of organoclay nanoparticles in all studied RNC, while the observed trend for the increase of both the initial (X_0) and the final (X_∞) strain amplification factors with organoclay content also seems physically reasonable. However, the rather low values of the correction term C are more difficult to explain. As shown elsewhere for several series of the BUNA SL19-based RNC [5–7], the values of C tended to increase, the weaker the interactions at the rubber/filler interface (that is, the larger the scale of interparticle motions during the successive breakdown of the initial InC of nanoparticles into the small IsC, as measured by the difference between X_0 and X_∞). In terms of this criterion, for the values of C as low as 0.10–0.35 one could expect [5] $(X_0 - X_\infty) \rightarrow 0$, which is definitely not the case (Table 22.2).

In our opinion, this apparent discrepancy reflects the influence of strong CR/filler interfacial interactions on the initial structure and deformation behavior of the InC of organoclay nanoparticles. In fact, strong interfacial interactions are the necessary prerequisite for a build-up of a layer of sterically immobilized polymer chain segments ("boundary interphase", BI) around filler particles [17, 20]. Judging by the rather high values of both X_0 and X_∞ for studied ENC (Table 22.2), large-scale displacements of organoclay nanoparticles should remain the basic mechanism of fragmentation of the initial InC into the IsC; however, such displacements will be mediated by the BI coatings. In this context, the low values of the fitting parameter C in Equation 22.3b should be regarded as evidence for the reduced exothermal effects of external friction between organoclay nanoparticles coated with the BI.

22.3.3 Stress Relaxation

As could be expected, the stress relaxation after stretching the neat CR to several fixed extensions λ_f proved to be negligibly small. In contrast, significant decays were observed on

the plots of the uniaxial stress σ_t (normalized by the initial stress σ_0 at time $t = 0$) versus time t at different fixed extensions λ_f for the RNC. These experimental data were fitted to the stretched-exponential Kohlrausch Equation 22.4 [21]

$$\sigma_t/\sigma_0 = \sigma_\infty/\sigma_0 + (\sigma_1/\sigma_0)\exp\left[-(t/\tau)^\beta\right]; \tag{22.4}$$

the best-fit values of parameters σ_∞/σ_0, σ_1/σ_0, τ and β are given in the Table 22.3.

Table 22.3 Fitting parameters of Equation 22.4

λ_f	σ_∞/σ_0	σ_1/σ_0	β	τ/s
CR/OC2-2.5				
1.9	0.95	0.047	0.42	205.0
2.5	0.95	0.049	0.40	206.8
2.9*	0.95	0.051	0.46	335.9
CR/OC2-5				
1.7	0.92	0.077	0.42	202.3
2.6	0.92	0.079	0.40	204.6
2.9*	0.92	0.080	0.40	204.9
CR/OC2-7.5				
1.5	0.89	0.103	0.40	551.4
2.4	0.89	0.109	0.40	569.7
3.0*	0.89	0.111	0.40	581.2
CR/OC2-10				
1.5	0.87	0.129	0.38	661.1
1.9	0.86	0.135	0.40	653.6
2.5	0.86	0.139	0.40	621.5
3.0*	0.81	0.188	0.38	1105.8
CR/OC2-12.5				
1.8	0.83	0.165	0.40	606.0
2.2	0.83	0.169	0.40	609.3
2.6	0.83	0.172	0.40	613.1
3.1*	0.78	0.221	0.40	1121.4
CR/OC2-15				
1.6	0.82	0.182	0.41	547.6
2.0	0.81	0.189	0.40	591.8
2.6	0.80	0.194	0.45	599.2
3.2*	0.75	0.243	0.40	1136.6
CR/OC2-20				
1.8	0.82	0.179	0.46	564.1
2.1	0.81	0.189	0.41	553.0
2.6	0.79	0.202	0.40	549.1
3.2*	0.73	0.261	0.40	1154.4
CR/OC2-30				
1.6	0.79	0.208	0.36	510.3
1.9	0.78	0.217	0.30	473.2
2.7	0.78	0.219	0.40	439.0
3.3*	0.68	0.315	0.33	1200.4

(*Continued*)

Table 22.3 (*Continued*)

λ_f	σ_∞/σ_0	σ_1/σ_0	β	τ/s
CR/OC2-40				
1.5	0.76	0.231	0.36	402.2
2.0	0.76	0.234	0.39	393.7
2.6	0.76	0.239	0.39	321.6
3.5*	0.62	0.379	0.38	1229.8

$\lambda_f = \lambda_{\lim}$.

As can be seen from the representative data for the sample CR/OC2-30 (Figure 22.5), as well as from similar data obtained for all other RNC, the plots of reduced stress, $(\sigma - \sigma_\infty)/\sigma_\infty$, versus t for the relaxations at $\lambda_f < \lambda_{\lim}$ nicely superpose on the same master curve, as expected for a linear viscoelastic body [21], whereas a similar plot for $\lambda_f = \lambda_{\lim}$ is shifted considerably upwards. These results are reflected by the values of σ_∞/σ_0, σ_1/σ_0 and τ for each ENC sample which are nearly identical at $\lambda_f < \lambda_{\lim}$ but significantly different at $\lambda_f = \lambda_{\lim}$. The patterns of composition dependencies of the latter parameters (Figure 22.6a–c) suggest that the structure and/or properties of an infinite cluster of organoclay nanoparticles may change around $w = 10$ wt% (that is, $\varphi \approx 0.04$). Anyway, the above results are qualitatively consistent with the original assumption [11] that after initial stretching to $\lambda_{\lim}$ the pre-existing infinite clusters of filler particles are broken into the isolated clusters which remain structurally similar, whatever the subsequent stretching to $\lambda_f < \lambda_{\lim}$.

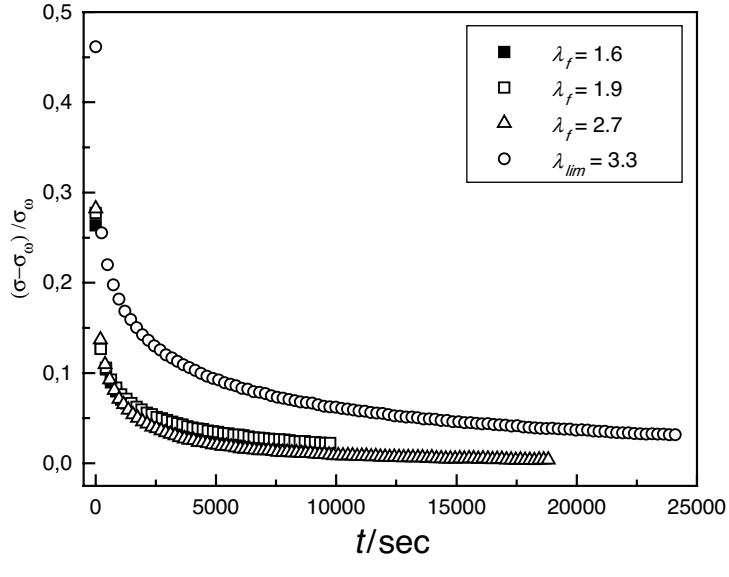

Figure 22.5 Time dependencies of the reduced stress for the sample CR/OC2-30

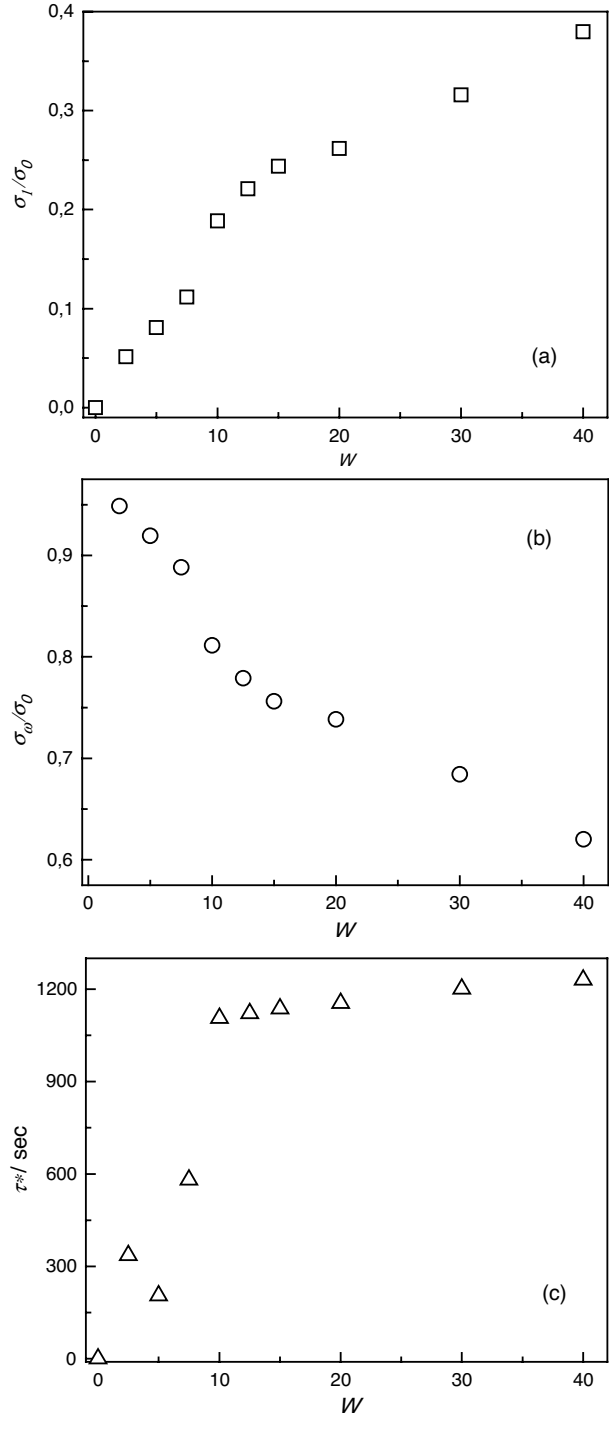

Figure 22.6 Composition dependencies of the fitting parameters: (a) σ_1/σ_0; (b) σ_∞/σ_0; and (c) τ at $\lambda_f = \lambda_{\lim}$

22.3.4 Conclusions

1. The infinite clustering of highly anisometric organoclay particles is likely to set on at filler volume fraction as low as $\varphi \leq 0.04$.
2. Quantitative analysis of thermoelastic behavior over the entire range of relative elongations provides additional support for the concept of a prestrain-dependent strain amplification factor as the major parameter controlling the thermomechanical properties of the RNC.
3. Low values of the fitting parameter C in Equation 22.3b should be regarded as evidence for reduced exothermal effects of external friction between organoclay nanoparticles coated with the BI.
4. The stress relaxation behavior of the RNC is qualitatively consistent with the original assumption that after initial stretching to the highest elongation (λ_{lim}) the pre-existing infinite clusters of filler particles are broken into the isolated clusters which remain structurally similar, whatever the subsequent stretching to $\lambda_f < \lambda_{\text{lim}}$.

22.4 Styrene-*co*-Butadiene Rubber/Organoclay Nanocomposites

22.4.1 Structural Characterization of Unstretched Samples

The main features of the WAXS patterns for the pristine rubber (Figure 22.7a) are the diffuse amorphous halo with a maximum near the scattering vector $q = (4\pi/\lambda) \sin(\theta) \approx 14.0\,\text{nm}^{-1}$ (which can be attributed to the interchain spacing $d_0 = 2\pi/q_0 \approx 0.45\,\text{nm}$) and several sharp reflections at higher q (presumably from stabilizer inclusions).

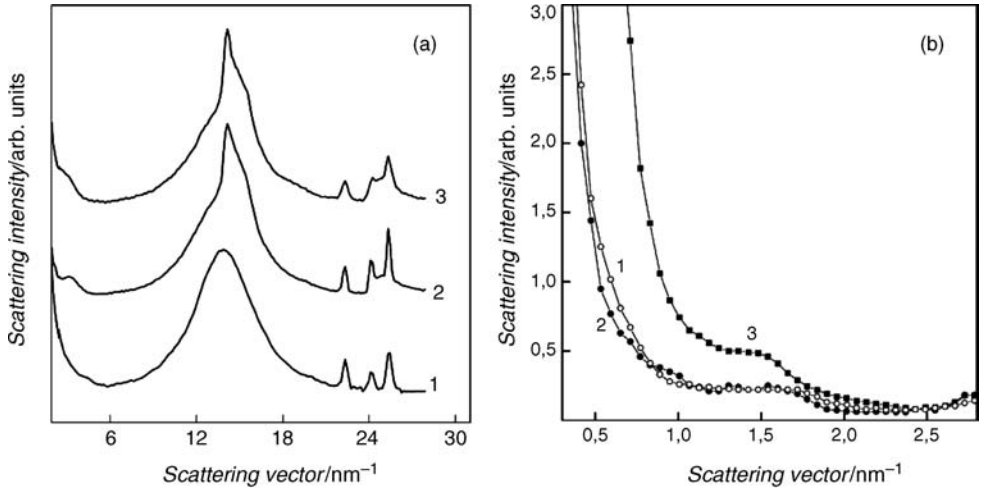

Figure 22.7 (a) WAXS and (b) SAXS patterns for (1) pristine rubber, (2) RS and (3) TS [5] (Reprinted from V.P. Privalko, S.M. Ponomarenko, E.G. Privalko, F. Schön and W. Gronski, "Interfacial interactions – controlled thermoelasticity and stress relaxation behavior of synthetic rubber/organoclay nanocomposites," *Journal of Macromolecular Science – Physics* (http://www.informaworld.com), **B42**, 1183–1196, © 2003, with permission from Taylor & Francis Ltd.)

Apparently, it is these nanoparticles of a stabilizer that also are responsible for a slight inflection at $q \approx 1.75\,\mathrm{nm}^{-1}$ on the SAXS pattern (Figure 22.7b), which implies a very weak structural heterogeneity with periodicity on the scale $D \approx 3.6\,\mathrm{nm}$.

The WAXS profiles for both nanocomposites (Figure 22.7a) reveal a few extra reflections (presumably due to clay modifiers) superposed on the major amorphous halo for the matrix rubber and the weak reflections around $q \approx 3.3\,\mathrm{nm}^{-1}$ (corresponding to the WAXS periodicity $d \approx 1.9\,\mathrm{nm}$), which can be associated with the interlayer spacing of organoclays. A nearly identical value was reported for the interlayer spacing of MMT-Alk organoclay [14]. This finding suggests that a non-negligible fraction of internal galleries in the initial organoclay tactoids remained inaccessible to penetration of rubber chains.

In contrast, the SAXS patterns for nanocomposites (Figure 22.7b) are typical for intercalated/exfoliated polymer-clay systems; in fact, no extra reflections can be detected on the SAXS curve 2 for the RS, while the SAXS periodicity $D \approx 4.2\,\mathrm{nm}$ for the TS calculated from the angular position of SAXS reflection (curve 3) is considerably higher than the interlayer spacing of the initial organoclay (see above). The higher overall SAXS intensity for the TS suggests a somewhat more ordered inner structure of a spatial network of nanoparticles.

22.4.2 *Thermoelastic Behavior*

As expected, both the mechanical work and the heat effects in the stretching/contraction cycles for the pristine rubber were completely reversible. The experimental values of specific (per unit of mass m) mechanical work W/m, specific heat effects Q/m and of the ratio Q/W (Figure 22.8)

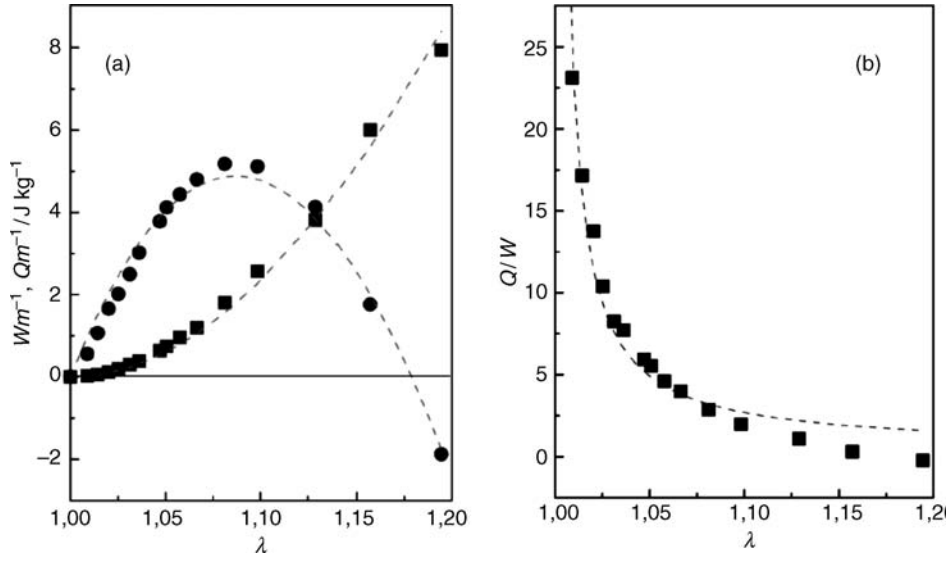

Figure 22.8 Dependencies on relative elongation of (a) specific mechanical work (squares) and specific heat effects (circles); and (b) the $Q = W$ ratio for pristine rubber. Dashed lines are the best nonlinear fits to Equation 22.1 [5] (Reprinted from V.P. Privalko, S.M. Ponomarenko, E.G. Privalko, F. Schön and W. Gronski, "Interfacial interactions – controlled thermoelasticity and stress relaxation behavior of synthetic rubber/organoclay nanocomposites," *Journal of Macromolecular Science – Physics* (http://www.informaworld.com), **B42**, 1183–1196, © 2003, with permission from Taylor & Francis Ltd.)

could be quantitatively fitted to the standard equations of elasticity of real rubbers, assuming $E = 0.515$ MPa, $\beta = -5 \times 10^{-3}\,K^{-1}$ and $\alpha = 2.4 \times 10^{-3}\,K^{-1}$.

As judged by the best-fit value of the apparent modulus $E = 2.9$ MPa for the RS (which was derived by Equation 22.1a for the range of reversible deformations, $\lambda < 1.15$), the organoclay nanoparticles provide a significant mechanical reinforcement effect to the pristine rubber. However, the glaring deviations between the experimental values of $W = m$ for the RS and the theoretical curve, which was calculated by Equation 22.1a assuming reversibility (curve 1 in Figure 22.9a), steadily increased, the higher the λ. As mentioned in the introductory paragraph, it is the violation of this latter assumption that is believed to be at the root of the observed discrepancies. Formally, such effects can be accounted for through the strain amplification factor $X = \varepsilon_{int}/\varepsilon$ which relates the microscopic intrinsic strain of the rubber ε_{int} to the macroscopic extension, $\lambda = 1 + \varepsilon$ [11]. In this context, for filled rubbers Equation 22.1a should be rewritten as Equation 22.3a.

It could be easily verified that the values of $W = m$ for the RS did not quantitatively fit Equation 22.3a, whereas the quality of the data fit to Equation 22.3a was reasonably good (dashed line 2 in Figure 22.9a calculated assuming the same value $E = 0.515$ MPa as that for the pristine rubber, and $X_0 = 11.5$, $X_\infty = 8.5$ and $z = 0.6$). This result supports the concept of strain-dependent strain amplification factor as the major parameter controlling the stress-strain behavior of nanocomposites with weak interfacial interactions [11].

Incidentally, the theoretical curve 1 calculated by Equation 22.1a assuming $E = 2.9$ MPa for the RS, roughly fit to the experimental values of $W = m$ for the TS (Figure 22.9a). Moreover, a nearly identical curve proved to be the best fit of these latter data to Equation 22.3a (assuming $E = 0.515$ MPa and $X = 28.2$). A slightly better fit (curve 3 in Figure 22.9a) could be achieved by the use of Equation 22.3a assuming $E = 0.515$ MPa, $X_0 = 26.7$, $X_\infty = 30.2$ and $z = 0.6$; however, this fit should be discarded in view of its physically unreasonable result ($X_\infty \,?\, X_0$). Thus, these data can be regarded as evidence for the strain amplification-induced mechanical reinforcement of the rubber matrix by filler aggregates and for the negligible (if any) decay of the latter with increasing extension (that is, for the vanishingly small MP effect) in a nanocomposite with strong interfacial interactions.

In view of the above results, it could be expected that the original Equation 22.1b also would apply for the specific heat effects in stretching of nanocomposites, provided the strain-dependent strain amplification factor would be properly accounted for, that is:

$$Q/m = -(W/m)\,[1 - T\beta - 2\alpha T/(\lambda_{int}^2 + \lambda_{int} - 2)] \tag{22.5}$$

It turned out, however, that Equation 22.5 badly overestimated (dashed lines 1 and 2 in Figure 22.9b) the experimental values of $Q = m$ for both nanocomposites, whereas reasonably good fits (dash-dotted lines 3 and 4 in Figure 22.9b calculated by Equation 22.3b assuming $C = 4.0$ and 0.8 for the RS and TS, respectively) could be achieved through the introduction of an additional, dimensionless fitting parameter C into Equation 22.5.

This important result is considered as experimental evidence for additional, intrinsically similar exothermal effects set in during the uniaxial stretching of nanocomposites in the range of relative extensions where the strain amplification factor becomes operative. Most probably, these exothermal effects are related to the heat generated by the mechanism of interparticle friction within the filler aggregates. As expected, the rather high value of the fitting parameter C for the RS suggests a significant contribution of large-scale interparticle motions during the successive breakdown of the initial, infinite clusters of nanoparticles into small, isolated clusters, while the fivefold lower value

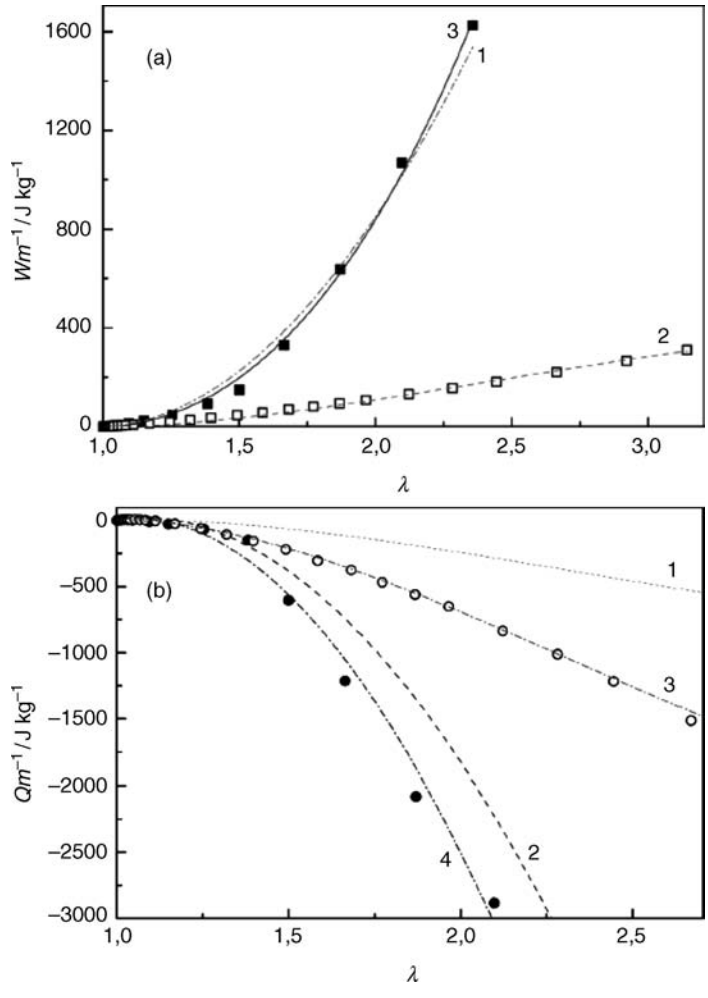

Figure 22.9 Dependencies on relative elongation of (a) specific mechanical work and (b) specific heat effects for the RS (open symbols) and TS (filled symbols) [5] (Reprinted from V.P. Privalko, S.M. Ponomarenko, E.G. Privalko, F. Schön and W. Gronski, "Interfacial interactions – controlled thermoelasticity and stress relaxation behavior of synthetic rubber/organoclay nanocomposites," *Journal of Macromolecular Science – Physics* (http://www.informaworld.com), **B42**, 1183–1196, © 2003, with permission from Taylor & Francis Ltd.)

of C for the TS implies small-scale (presumably, reversible) displacements of nanoparticles within the infinite filler clusters, which leave the latter essentially undestroyed. Thus, these conclusions are totally consistent with those derived from the preceding analysis of specific mechanical work.

22.4.3 Stress Relaxation

As could be already inferred from the complete reversibility of both specific mechanical work and specific heat effects in the stretching/contraction cycles (see the preceding section), the

stress relaxation after stretching the pristine rubber to several fixed extensions λ_f proved to be negligibly small. In contrast, significant decays were observed on the plots of the uniaxial stress σ (normalized by the initial stress σ_0 at time $t = 0$) versus time t at different fixed extensions λ_f for the RS (Figure 22.10a); however, the initial rates of stress relaxation proved to decrease, the higher the λ_f, which was directly opposite to the behavior expected for simple, exponential processes [21].

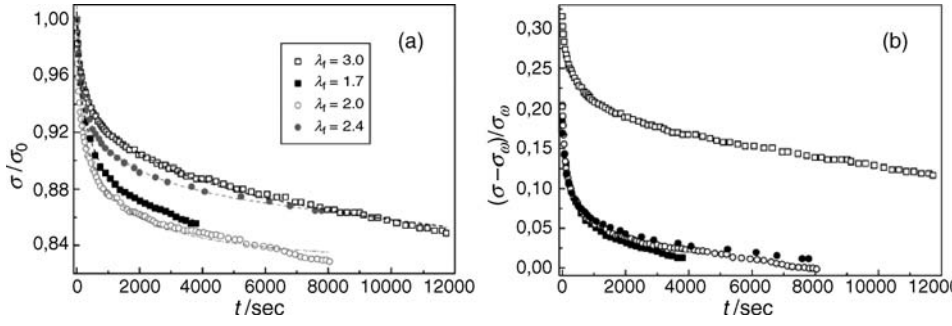

Figure 22.10 Time dependencies of (a) normalized stress and (b) reduced stress for the RS [5] (Reprinted from V.P. Privalko, S.M. Ponomarenko, E.G. Privalko, F. Schön and W. Gronski, "Interfacial interactions – controlled thermoelasticity and stress relaxation behavior of synthetic rubber/organoclay nanocomposites," *Journal of Macromolecular Science – Physics* (http://www.informaworld.com), **B42**, 1183–1196, © 2003, with permission from Taylor & Francis Ltd.)

These empirical observations were quantified by fitting the experimental data to the stretched-exponential Kohlrausch Equation 22.4 [16].

The quality of the data fit to Equation 22.4 can be assessed from the representative plots for the RS (dashed lines in Figure 22.10a); the best-fit values of the parameters of Equation 22.4 are given in the Table 22.4.

Table 22.4 Fitting parameters of Equation 22.4

λ_f	σ_∞/σ_0	σ_1/σ_0	β	τ/s
Samples RS				
1.70	0.85	0.15	0.56	630
2.00	0.83	0.19	0.42	550
2.40	0.85	0.21	0.31	520
3.05	0.76	0.24	0.35	1111
Samples TS				
1.40	0.89	0.13	0.47	480
1.56	0.91	0.10	0.54	280
1.85	0.93	0.07	0.52	280
2.25	0.94	0.07	0.45	0.65

As can be seen from Figure 22.10b, the plots of reduced stress, $(\sigma - \sigma_\infty)/\sigma_\infty$, versus t for the relaxations at $\lambda_f < \lambda_{\text{lim}}$, nicely superpose on the same master curve, as expected for a linear viscoelastic body [21], whereas a similar plot for $\lambda_f = \lambda_{\text{lim}} = 3.05$ is shifted considerably

upward. Thus, these results are qualitatively consistent with the original assumption [11] that, after initial stretching of a nanocomposite with weak interfacial interactions to λ_{lim}, the preexisting clusters of nanoparticles are broken into isolated clusters, which remain structurally similar, whatever the subsequent stretching to $\lambda_f < \lambda_{lim}$.

The stress relaxation patterns at different λ_f for the TS (Figure 22.11a) also quantitatively obeyed (dashed lines) the Kohlrausch Equation 22.4 for the best-fit values of fitting parameters reported in Table 22.4; moreover, all four $(\sigma - \sigma_\infty)/\sigma_\infty$, versus t plots reasonably superposed on the same master curve (Figure 22.11b). In these aspects, the patterns of stress relaxation in

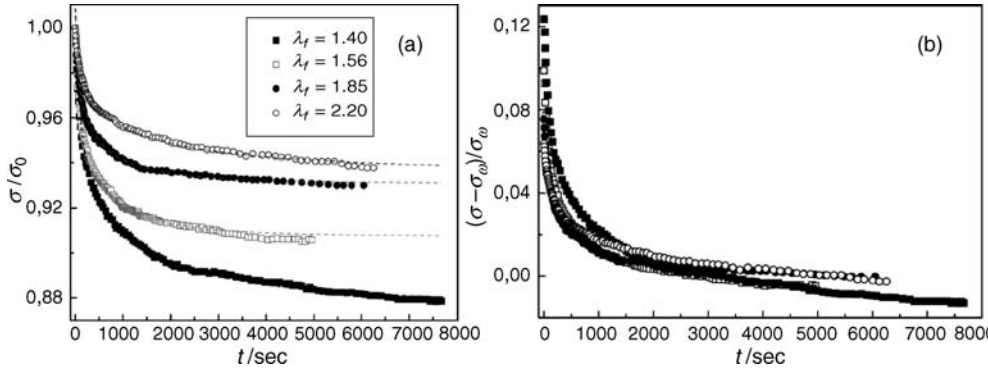

Figure 22.11 Time dependencies of (a) normalized stress and (b) reduced stress for the TS [5] (Reprinted from V.P. Privalko, S.M. Ponomarenko, E.G. Privalko, F. Schön and W. Gronski, "Interfacial interactions – controlled thermoelasticity and stress relaxation behavior of synthetic rubber/organoclay nanocomposites," *Journal of Macromolecular Science – Physics* (http://www.informaworld.com), **B42**, 1183–1196, © 2003, with permission from Taylor & Francis Ltd.)

samples TS and RS are qualitatively similar; however, the quantitative differences are revealing and can be traced back to the underlying differences in the structural states of filler aggregates (that is, infinite clusters in the former, isolated clusters in the latter; see Figure 22.12).

As can be seen from Table 22.4, the values of the stretching exponent β for the TS, on the average, were of the same order of magnitude as those for the RS, while the values of the characteristic relaxation time τ and of the transient stress, σ_1/σ_0, on the one hand, and those of the limiting stress, σ_∞/σ_0, on the other hand, proved to be considerably lower and higher, respectively, for the former. The observed trends imply smaller-scale structural rearrangements in the course of stress relaxation in the TS compared with the RS. In fact, the low values of the limiting (quasi-equilibrium) stress σ_1/σ_0 (that is, high relaxation amplitudes, $1 - \sigma_1/\sigma_0$) combined with the long relaxation times, t, for the RS can be regarded as evidence for a mechanism of structural relaxation involving large-scale displacements of isolated clusters of nanoparticles within the rubber matrix. In contrast, shorter relaxation times τ, significantly higher levels of σ_1/σ_0 and their regular increase with λ_f for the TS can be explained by the finite extensibility of chemically bonded rubber-chain strands in the interstitial space between neighboring nanoparticles, thus reducing the eventual structural rearrangements to the small-scale displacements of nanoparticles within the infinite clusters.

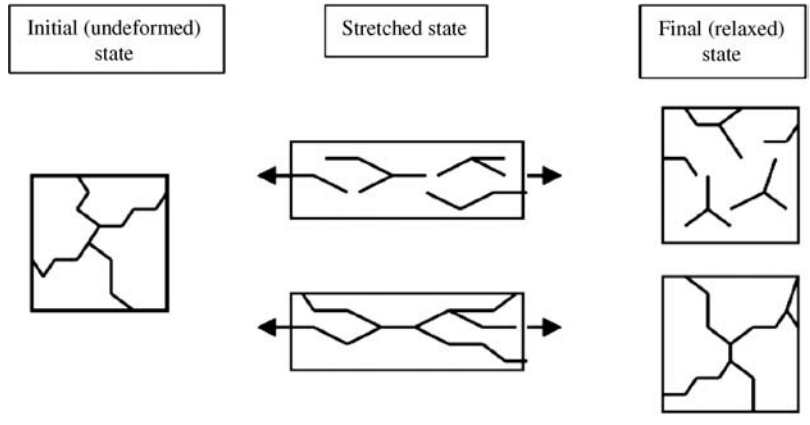

Figure 22.12 Schematics of assumed structural changes in the initial infinite cluster after stretching of rubber/organoclay nanocomposites with weak (upper part) and strong (lower part) interfacial interactions (Reprinted from V.P. Privalko, S.M. Ponomarenko, E.G. Privalko, F. Schön and W. Gronski, "Interfacial interactions – controlled thermoelasticity and stress relaxation behavior of synthetic rubber/organoclay nanocomposites," *Journal of Macromolecular Science – Physics* (http://www.informaworld.com), **B42**, 1183–1196, © 2003, with permission from Taylor & Francis Ltd.)

22.4.4 Conclusions

1. Strain amplification is a common mechanism of reinforcement of the rubber matrix by spatial aggregates of nanoparticles in both RS and TS samples.
2. Breakdown of the initial infinite clusters of nanoparticles into small, isolated clusters at high extensions of the RS manifests itself as a strain dependence of the strain amplification factor concomitant to the generation of the large excess exothermal heat effects of external friction between nanoparticles.
3. The strain-invariant strain amplification factor for the TS, combined with much smaller excess exothermal heat effects of external friction between nanoparticles, is regarded as evidence for the survival of the initial infinite clusters of nanoparticles even at high extensions.
4. Long relaxation times and high amplitudes of stress relaxation for the RS suggest the mechanism of structural relaxation involving large-scale displacements of isolated clusters of nanoparticles within the rubber matrix.
5. Shorter relaxation times, signicantly smaller relaxation amplitudes, and their regular decrease with λ_f for the TS can be explained by the finite extensibility of chemically bonded rubber-chain strands in the interstitial space between neighboring nanoparticles, thus reducing the eventual structural rearrangements to the small-scale displacements of nanoparticles within the infinite clusters.

References

1. Kraus, G. (ed.) (1965) *Reinforcement of Elastomers*, Interscience Publication, New York.
2. Bartenev, G.M. (1979) *Structure and Relaxation Behavior of Elastomers*, Khimia, Moscow (in Russian).

3. Mark, J.E., Erman, D., and Eirich F.R. (eds) (1994) *Science and Technlogy of Rubber*, Academic Press, San Diego.
4. Privalko, V.P., Ponomarenko, S.M., Privalko, E.G. *et al.* (2003) Thermoelastic behavior of synthetic rubber/organoclay nanocomposites at low elongations. *Advanced Composites Letters*, **12**, 57–60.
5. Privalko, V.P., Ponomarenko, S.M., Privalko, E.G. *et al.* (2003) Interfacial interactions-controlled thermoelasticity and stress relaxation behavior of synthetic rubber/organoclay nanocomposites. *Journal of Macromolecular Science Physics*, **B42**, 1183–1196.
6. Privalko, V.P., Ponomarenko, S.M., Privalko, E.G. *et al.* (2003) Structure and thermoelastic behavior of synthetic rubber/organoclay nanocomposites. *Macromolecular Chemistry and Physics*, **204**, 1480–1485.
7. Ponomarenko, S.M., Privalko, E.G., Privalko, V.P. *et al.* (2004) Structure and thermoelasticity of synthetic rubber/silica nanocomposites. *Journal of Macromolecular Science-Physics*, **43**, 1231–1242.
8. Mullins, L. and Tobin, N.R. (1965) Stress softening in rubber vulcanizates. Part I. Use of a strain amplification factor to describe the elastic behavior of filler-reinforced vulcanized rubber. *Journal of Applied Polymer Science*, **9**, 2993–3009.
9. Harwood, J.A., Mullins, L., and Payne, A.R. (1965) Stress softening in rubber vulcanizates. Part II. Stress softening effects in pure gum and filler loaded rubbers. *Journal of Applied Polymer Science*, **9**, 3011–3021.
10. Witten, T.A., Rubinstein, M., and Colby, R.H. (1993) Reinforcement of rubber by fractal aggregates. *Journal De Physique II (France)*, **3**, 367–383.
11. Klueppel, M. and Schramm, J. (2000) A generalized tube model of rubber elasticity and stress softening of filler reinforced elastomer systems. *Macromolecular Theory and Simulations*, **9**, 742–754.
12. Klueppel, M., Schuster, R.H., and Heinrich, G. (1997) Structure and properties of reinforcing fractal filler networks in elastomers. *Rubber Chemistry and Technology*, **70**, 243–258.
13. Schön, F. (2004) PhD Thesis. Institut für Makromolekulare Chemie, Universität Freiburg.
14. Privalko, V.P., Lipatov, Yu.S., Mirontsov, L.I., and Dashevskii, L.I. (1985) Thermoelastic properties of segmented polyurethaneureas. *Colloid and Polymer Science*, **263**, 691–696.
15. Privalko, V.P., Sukhorukov, D.I., and Karger-Kocsis, J. (1999) Thermoelastic behavior of carbon fiber/polycarbonate model composites. *Polymer Engineering and Science*, **39**, 1525–1533.
16. Godovsky, Yu.K. (1991) *Thermal Physics of Polymers*, Springer Verlag, Munich.
17. Heinrich, G. and Klueppel, M. (2002) Recent advances in the theory of filler networking in elastomers. *Advances in Polymer Science*, **160**, 1–44.
18. Garboczi, E.J., Snyder, K.A., Douglas, J.F., and Thorpe, M.F. (1995) Geometrical percolation threshold of overlapping ellipsoids. *Physical Review E*, **52**, 819–828.
19. Karaman, V.M., Shumsky, V.F., Privalko, E.G. *et al.* (2003) Melt viscoelasticity of polyamide 6/organoclay nanocomposites. *Polymers & Polymer Composites*, **11**, 663–668.
20. Privalko, V.P. and Novikov, V.V. (1995) *The Science of Heterogeneous Polymers*, John Wiley & Sons, Chichester.
21. Ferry, J.D. (1970) *Viscoelastic Properties of Polymers*, John Wiley & Sons, New York.
22. Govingee, S. and Simo, J. (1991) Micro-mechanically based continuum damage model for carbon black-filled rubbers incorporating Mullins effect. *Journal of the Mechanics and Physics of Solids*, **39**, 87–112.

23

Theoretical Modeling and Simulation of Rubber Nanocomposites

Jan Kalfus and Josef Jancar
Institute of Materials Chemistry, Brno University of Technology, Brno, Czech Republic

23.1 Introduction

Over the past 20 years, polymer matrix nanocomposites have attracted considerable attention of the research community. It has been proposed that advanced structural materials can be developed employing the design of polymer composites on the nanoscale. A large portion of the research has been devoted to amorphous matrix nanocomposites and, especially, to nanosize filler-reinforced rubbers. In addition to the interpretation of the well known phenomena, this research has discovered number of new phenomena not encountered at the coarser length scales. Reliable models capable of linking large-scale mechanical properties of rubber nanocomposites with their nanoscale structure are scarce and not generally accepted. However, the need to establish reliable prediction algorithms for large-scale mechanical properties required for practical applications of nanoscale engineered rubbers are highly desired.

The understanding of the mechanism of the rubber reinforcement on the nanoscale belongs among the most important topics. In general, there are two groups of models considered. Historically first and still relatively widely accepted by the industrial community is the model considering the percolation of solid particles to be responsible for reinforcing rubbery matrices. Over the past few years, neutron scattering experiments [1], modulus recovery experiments [2, 3] and theoretical models [4] have provided strong evidence supporting the second group of models interpreting the reinforcing mechanism in rubbery nanocomposites in terms of reduced chain mobility due to interactions of matrix molecules with solid nanoparticles. The role of nanoparticles is to provide a "supporting template" allowing the connecting of the immobilized

Rubber Nanocomposites: Preparation, Properties and Applications Edited by Sabu Thomas and Ranimol Stephen
© 2010 John Wiley & Sons (Asia) Pte Ltd

chains over the entire solid. It has been shown [2, 5, 6], that this approach can explain the Payne effect in both chemically and physically X-linked systems as well as the effects of particle shape and, moreover, provides a conceptual framework for modeling the transition from discrete nanoscale to continuum macro scale [7].

Generally, modeling of the structure–property relationships is based on developing mathematical description of the behavior of a small volume element of the material termed the representative volume element (RVE), exhibiting all the structural features of the complete solid. On the micro- and longer scales, the approach based on the RVE to deduce the properties of composite materials has been a common approach since the early 1970s. One of the uncertainties when using the RVE for computational simulation of nonperiodic composites is determining its minimal required size. There are two main strategies used to determine the minimum required size of the RVE. The first one is based on a convergence of some effective mechanical property requiring the RVE to obey a mechanical criterion. The second approach defines RVEs statistically concerning the inclusion volume fraction, establishing confidence intervals for mean values of mechanical variables and analyzing the statistical distribution of the stress or the statistical distribution of the inclusion distribution within the composite. It is necessary for the SRVE to represent properly the random distribution of inclusions (distance to first neighbors, occurrence of clusters of particles, and so on). Recently, correct evaluation of the minimal size of the RVE has become pivotal in an effort to develop reliable multiscale modeling scheme capable of predicting macroscale properties considering the nanoscale structure. On the microscale, the minimal suitable length scale, L_c, of the statistical RVE (SRVE) has been estimated as $L_c = 50R$, where R is the particle radius [8–10]. The minimal size of the SRVE should also be determined considering the nanoscale inclusions, since the discrete nature of both the matrix and the inclusions at the nanoscale prohibit simple scaling down the existing micromechanics models. In addition to structural inhomogeneities, which prohibit the use of the ergodic principle for volumes smaller than the lower limiting size of the SRVE, the characteristic length and time scales in polymer nanocomposites are also strongly dependent on temperature and molecular structure, which further complicates theoretical treatment.

Polymers are unique systems with macroscopic viscoelastic response driven by the relaxation processes on the molecular level. These relaxation processes represent particular molecular motions occurring in some characteristic volume, V_c. The V_c depends on the type of the relaxation process and temperature. The characteristic volumes vary from 10^{-3} nm^3 for localized bond vibrations to 10^6 nm for the nonlocal normal mode of relaxation. In the case of the nonlocal normal mode of relaxation, its characteristic volume is the upper limit for V_c displaying strong dependence on the chain size. Below this upper limiting characteristic volume, $V_c \sim r^3 \sim N^{3/2}$, where r is the chain end-to-end distance and N is the number of monomer units in the chain. The characteristic time for each particular relaxation process varies from 10^{-12} to 10^{-14} s for bond vibrations above T_g to the infinitely long times below T_g. Thus, the macroscopic viscoelastic response of a polymer is a manifestation of a range of molecular motions localized in some characteristic volume and the rate of the relaxation mode is indirectly proportional to its locality [7]. A recent work by Nikolov *et al.* [10] estimated that neat rubbers above their T_g should have a nonlocal length scale of approximately 5 nm and the network deformation is not affine. The high nonlocality in polymers most probably stems from a cooperative behavior of large number of chain segments characteristic for entangled polymers. As a result, parts of the material system may undergo considerable non-affine deformation associated with occurrence of high moment stresses.

23.2 Brief Theory of Conformation Statistics and Chain Dynamics

One can identify a number of structural length scales in an amorphous polymer from atomic constitution (~0.1 nm), monomer unit configuration (~1.0 nm) and conformation of the whole molecule (~10 nm). At length scales greater than a few hundred nanometers, multiple chains are involved and one can consider the system a continuum. In addition to the length scale, one has to take into consideration also time scales related to the various relaxations observed at these length scales. As briefly outlined in the previous paragraph, the addition of solid nanoparticles into a polymer affects considerably both the supermolecular structure as well as the chain dynamics. Since the effects on the polymer segmental mobility, conformation statistics are of primary importance and some aspects of conformation statistics and conformation dynamics of chain molecules will be discussed in this paragraph.

The most successful theoretical model of a polymer chain is the one-dimensional Ising model [11, 12] taking the interdependence of conformational states into account. Considering molecular structure of a simple polymer chain in general terms, rotation of a single backbone bond around its axis leads to the change of the chain end-to-end distance. Due to the interaction among electron clouds of atoms constituting the monomer units in a polymer chain, a number of minima exist in the angular dependence of the bond rotation potential. Some of these minima can be energetically non-equivalent. In case of model PE chain, this leads to the partition of rotation states into *gauche* +, *gauche*− and *trans* positions. Due to the interdependency of these states, the energy of at least two neighboring bonds has to be taken into account. In other words, the rotation of one bond can induce conformation transitions of its neighbors along the chain, termed cooperative rotations. The mathematical procedure of the Ising model includes complex combinatorial or matrix calculations giving reasonable values of the chain characteristic ratio, partition function and thermodynamic quantities. The characteristic ratio, C_N, represents a very useful quantity relating the root mean square end-to-end distance of a real chain to the random walk model approximation, *rwm*, where the fixed bond length, b, is the only restriction. The fixed bond angle and preferred rotation positions are neglected in the *rwm*. The C_N can simply be expressed as:

$$C_N = \langle r^2 \rangle_{\text{real}} / \langle r^2 \rangle_{rwm}, \tag{23.1}$$

where the *rwm* mean square end-to-end separation $\langle r^2 \rangle_{rwm} = Nb^2$ and $\langle r^2 \rangle_{\text{real}}$ is the mean square end-to-end distance of a real polymer chain. Thus, real polymer coil is considerably larger compared to the random walk model due to the intramolecular interactions. The parameter C_N exhibits strong temperature dependence and, as has been shown by Boyd and Phillips [12], it is affected by the molecular weight of a polymer. It increases with increasing number of monomer units in a chain, N, until a plateau value is reached at sufficiently high N. In spite of the fact that the random walk model does not provide results in a satisfactory agreement with experimental data, it is of pivotal conceptual importance in the chain conformation statistics. The random walk model is mathematically treated using the Gaussian statistics and provides some kind of a reference state. Usually, the real polymer chain dimension is calculated from this reference state using the parameter C_N known for each polymer [13].

The probability of the end-to-end separation in the three dimensional random flight individual chain is given by the Gaussian distribution function, $P(r)$, in the form:

$$P(r)\mathrm{d}x\mathrm{d}y\mathrm{d}z = (3/2\pi Nb^2)^{3/2} \exp(-3r^2/2Nb^2)\mathrm{d}x\mathrm{d}y\mathrm{d}z. \tag{23.2}$$

Since the Gaussian distribution function is spherically symmetrical, the volume element dxdydz is replaced by spherical shell of thickness dr. It results in the radial distribution function, $P(rdf)$, having maximum at the root mean square end-to-end separation $0 < \langle r^2 \rangle^{1/2} \ll Nb$:

$$P(rdf)\mathrm{d}r = 4\pi r^2 P(3d, r)\mathrm{d}r. \tag{23.3}$$

As a result, polymer chain is often called the random coil. One has to be, however, very cautious when considering the size and shape of a real chain which may exhibit features very distinct from those described by the simple Gaussian random coil statistics. This became of serious importance especially in considering viscoelasticity of polymer matrix nanocomposites involving segmental immobilization by large specific surface area fillers.

Let us first consider Figure 23.1, where a snapshot of the united atom model of polyethylene (PE) chain is presented. The chain discrete structure is composed of coiled sequences of segments and far less resembles the random coil as a whole. At each instant, it assumes very irregular shape, however, as the exposition time of the snapshot is extended, the chain shape becomes closer to a regular random coil. If the exposition time of the snapshot would equal to tens of nanoseconds, under conditions considered in Figure 23.1, the PE chain would resemble a spherical domain – the random coil. This can clearly be illustrated using the dependence shown in Figure 23.2, where the length of the exposition time is simulated using an averaging procedure. As a result, the Gaussian average – the root mean square end-to-end separation, $\langle C_N N b^2 \rangle^{1/2}$ – is obtained after a sufficiently large statistical ensemble is achieved, that is, at a high enough N and sufficiently long time. However, in many physical phenomena related to polymers, this nonideal behavior is not considered. For instance, short chain segments are far from Gaussian behavior due to the discrete nature of attainable chain states [12]. Similar situation exists when the chain segments are kinetically constrained preventing them to achieve the equilibrium $\langle r^2 \rangle^{1/2}_{\text{segment}}$ on a common time scale.

Figure 23.1 Snapshot of one isolated united atom model of PE ($N = 1000$) obtained from molecular dynamics simulation after 10 ns equilibration at temperature 400 K

Dependences shown in Figure 23.2 also demonstrate one very essential phenomenon of polymers on the molecular level – thermally induced fluctuations. Due to thermal energy given by the factor $k_B T$ (k_B is the Boltzmann constant, T is temperature), each atom, monomer unit and polymer molecule executes thermally activated random oscillations. Consequently, one

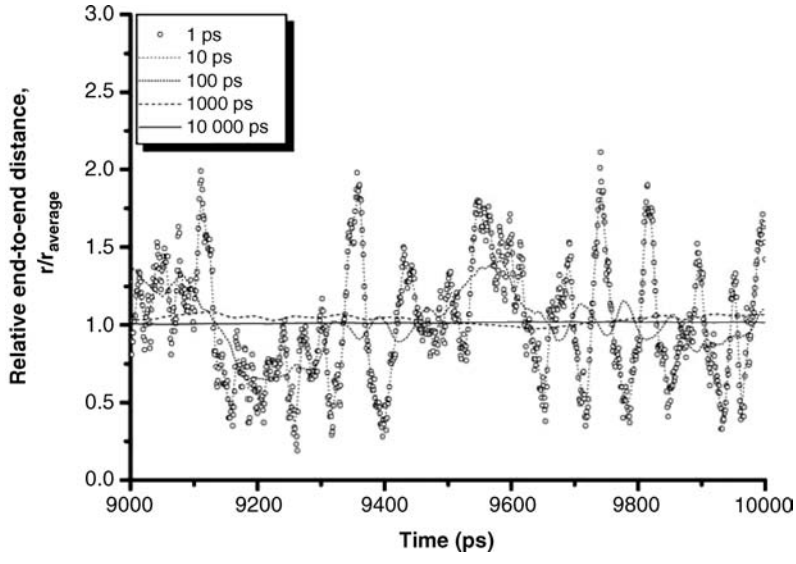

Figure 23.2 Time evolution of end-to-end distance of one isolated united atom PE chain ($N = 100$) related to 10 ns average at 400 K from molecular dynamics simulation. As the time interval for adjacent averaging increases from 10 to 10 000 ps, the structure becomes homogenized

can observe fluctuations of the chain ends belonging to the normal mode relaxations. This nonlocal motion is composed of large number of local relaxation modes – jumps of bonds between various rotation isomeric states. These motions are again composed of more localized torsional vibrations. Hence, one can identify some kind of structural hierarchy in the isolated chain dynamics. Obviously, in an ensemble of long chains, the diffusion of the whole chain, that is, the reptation dynamics are considerably retarded due to the nonlocal chain entanglements acting as an effective tube under given conditions. This can further be altered by the interactions with solid particles, especially in the case of large specific surface area nanofillers.

All the fluctuations can be characterized by a characteristic frequency or time and amplitude. The time characteristic of torsion vibrations, τ^*, can be simply estimated as [14, 15]:

$$\tau^* \approx b(m_0/k_BT)^{1/2}, \tag{23.4}$$

where m_0 is the monomer unit molar weight. The torsional vibrations represent motion, which is localized to volumes less than 10^{-3} nm^3. The dynamics of local rotation isomeric jumps can be characterized by the average time between two consecutive jumps, τ_c. In contrast to the torsional vibrations, the jumps between two rotation isomeric states are typical of energy barrier separating them. Therefore, the modified Vogel–Fulcher–Tamann (VFT) equation can be used to estimate this characteristic relaxation time for a chain unit in a melt [16]:

$$\tau_c = \tau^* \exp\left(\frac{zE_A^{\text{intra}}}{k_BT}\right)\exp\left(-\frac{E_A^{\text{intra}}}{k_BT^*}\right), \tag{23.5}$$

where:

$$z = \frac{T^* - T_0}{T^*} \cdot \frac{T}{T - T_0}. \tag{23.6}$$

T_0 is the Vogel temperature, typically expected to be approximately 50 °C below the experimentally measured glass transition temperature, T_g. T^* is the empirical activation temperature denoting a hypothetical temperature, where the cooperativity of segmental motion vanishes. E_A^{intra} is the activation energy of intramolecular barriers of rotation (for PE at 160 °C $zE_A^{\text{intra}} \cong 25$ kJ/mol). As seen in Figure 23.3, τ_c is an average value for a given ensemble and its local value within the chain becomes very heterogeneous at low temperatures or short times of "observation." Hence, the ensemble can be considered non-ergodic.

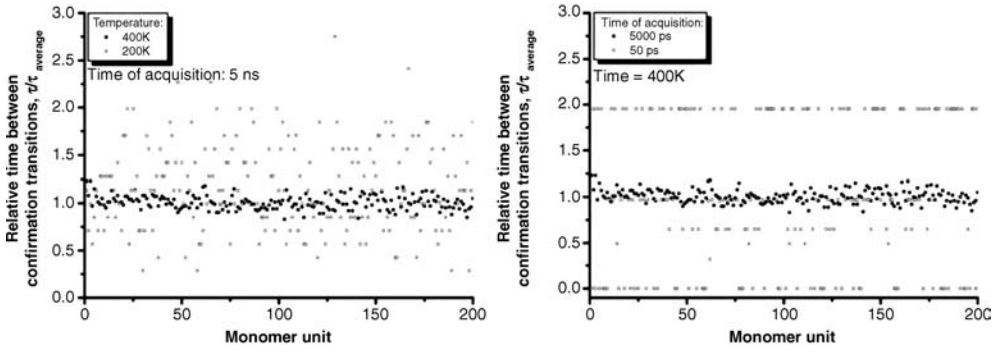

Figure 23.3 Relative time between rotation isomeric transitions related to the 5 ns average over the whole ensemble, for selected 200 bonds of single united atom PE chain ($N = 1000$) from molecular dynamics simulation. The left graph represents one acquisition time at two temperatures; and the graph on the right contains results acquisited for two different periods at one temperature

According to Bueche [17], the monomer friction coefficient, ζ_0, can be estimated according to the following simple equation, which gives reasonable values for the temperature region $T > T_g$:

$$\zeta_0 = k_B T \tau_c / b^2, \tag{23.7}$$

where b is the length of a link between two Brownian particles (in case of simple chains, b is of the order of the bond length). Consequently, one can establish the monomer unit mobility, μ_0, as follows [18]:

$$\mu_0 = \zeta_0^{-1}. \tag{23.8}$$

In a melt of long chains, each chain is entangled with its neighbors and the characteristic relaxation time of movement of the whole chain is given by the time of the chain to diffuse trajectory equal to its length. According to deGennes [18], the relaxation time of the chain reptation motion, τ_{rep}, can be expressed as:

$$\tau_{\text{rep}} \cong \frac{NL^2}{D_0}, \tag{23.9}$$

where L is the chain length and D_0 is the monomer unit diffusion coefficient ($D_0 = k_BT/\zeta_0$). The reptation motion of an entangled chain can be written in the approximate form proposed by Doi and Edwards [19]:

$$\tau_{\text{rep}} = \frac{b^4\zeta_0 N^3}{\pi^2 k_B T a_T^2}, \tag{23.10}$$

where a_T is the tube diameter. Supposing the a_T equal to the distance between the entanglement points yields the relation: $\tau_{\text{rep}} = b^2\zeta_0 N^3/\pi^2 k_B T N_e$ (N_e is the number of monomer units per an effective entanglement strand). Characteristic volume of a domain in which the reptation motion of an entangled Gaussian chain occurs is: $V_c^{\text{reptation}} = 4\pi(C_N N b^2/6)^{3/2}/3$.

Considering the normal mode motion of chain segments between chemical crosslinks or effective entanglement points, the Rouse relaxation time has to be used. For a given segment, its end-to-end distance fluctuation can be characterized by the Rouse time, τ_R, where the parameter $p = 1$ [20]:

$$\tau_R = \frac{b^2\zeta_0 N^2}{3\pi^2 k_B T p^2}. \tag{23.11}$$

Characteristic volume of one strand between two entanglement points or chemical crosslinks in a Gaussian network is $V_c^{\text{ent}} = (M_e C_N b^2/M_0)^{3/2}\pi/6$ or $V_e^x = (M_c C_N b^2/M_0)^{3/2}\pi/6$ (M_e is the molecular weight of an effective entanglement strand and M_c is the mean molecular weight of chains between network junctions). Average fluctuation of the distance between two ends of a chain segment, Δr^2, can attain significant amplitude relative to the value of the root mean square end-to-end separation.

Mark and coworkers [21] have precisely developed theory of fluctuation of chain strands in a Gaussian network. For a chain in an unstrained Gaussian network, the average amplitude of the thermally fluctuating end-to-end distance, Δr_0^2, can be approximated as [22]:

$$\Delta r^2 \cong Nb^2/15. \tag{23.12}$$

Only a schematic illustration of this fluctuation phenomenon is shown in Figure 23.4, which presents a molecular dynamics simulation of single united atom PE chain.

23.3 Basic Aspects of Rubber Elasticity

The elastic properties of a single chain in equilibrium can simply be derived from the first and second law of thermodynamics. Considering $pdV/fdl \approx 10^{-4}$, the retractive force, f, can be expressed as [23]:

$$f = \left(\frac{\mathrm{d}U}{\mathrm{d}r}\right)_T - T\left(\frac{\mathrm{d}S}{\mathrm{d}r}\right)_T = f_E + f_S. \tag{23.13}$$

The f_E and f_S, respectively, express the energy and entropy contribution to the rubber retractive force, respectively. The change of the end-to-end distance, r, causes the conformation entropy decrease resulting in an increase of the chain retractive force. For the finite chain length with $(\mathrm{d}U/\mathrm{d}r)_T = 0$, the retractive force can be expressed on the basis of the Langevin inverse

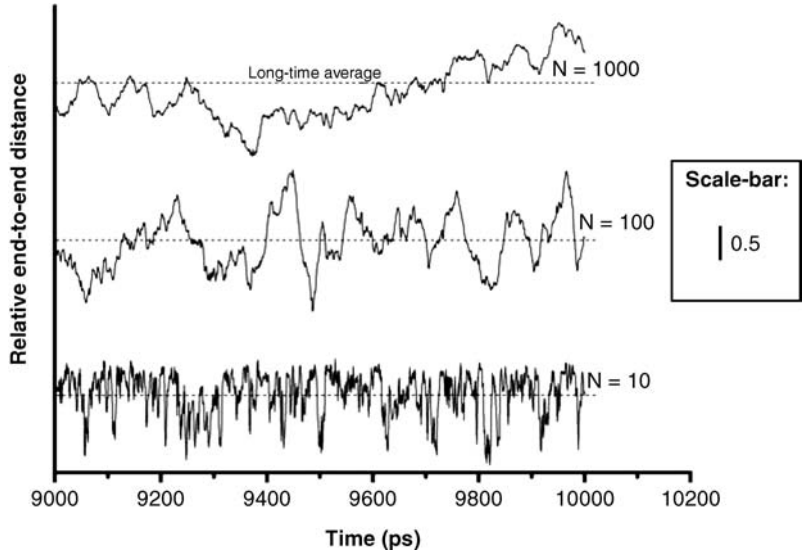

Figure 23.4 Illustration of time evolution of end-to-end distance of chain segments with $N = 10$ and 100 and of the whole chain $N = 1000$. From molecular dynamics simulation of single united atom PE chain at 400 K

function, L^{-1} [23, 24]:

$$f_S^{\text{chain}} = \frac{k_B T}{b} L^{-1}\frac{r}{Nb} = \frac{k_B T}{b}\left\{3\left(\frac{r}{Nb}\right) + \left[\frac{9}{5}\left(\frac{r}{Nb}\right)^3 + \frac{297}{175}\left(\frac{r}{Nb}\right)^5 + \frac{1539}{875}\left(\frac{r}{Nb}\right)^7 + \cdots\right]\right\}. \tag{23.14}$$

The first term of Equation 23.14 represents the response of a purely Gaussian (infinitely long) chain, $f_S^{\text{chain}} = 3k_B T/Nb^2$. The stress–strain relation in a Gaussian network can be derived using the simple thermodynamics from the system free energy. The entropy-based stress–strain relation for a simple shear loading of a Gaussian network can be written in the general form [12]:

$$\sigma_{\text{shear}} = \bar{\nu} F k_B T \gamma, \tag{23.15}$$

where σ_{shear} is the shear stress, $\bar{\nu}$ is the total number of chains in a network and F is the front factor. Parameter γ is the shear strain equal to $(\lambda - \lambda^{-1})$, where λ is the relative strain. For the affine network of phantom chains, $F = 1$ and for fluctuation junction network of phantom chains, $F = 1 - 2/f_x$, where f_x is the network junctions functionality [12].

To obtain a more realistic prediction of a deformation response of rubber network, the stress–strain relation of a network involving the finite Langevin chains has to be taken into account. Moreover, the internal energy of a chain connected to transition of rotation isomers, corresponding to the more tightly coiled conformations of a chain, into the rotation isomers, pertaining more elongated conformations upon network strain can occur [11]. Generally, the energy term in the Equation 23.13 depends on the intramolecular interactions and, hence, it can

be expressed in the form [11]:

$$f_E = f\,T\,\frac{d\ln r^2}{\mathrm{d}T}. \tag{23.16}$$

Further factors complicating the prediction of the network stress–strain response are nonrandom packing effects and irreversible changes of a network upon loading.

Considering purely entropic behavior in the rubbery region, the shear elastic modulus of an entangled and crosslinked polymer network, G_e and G_x, respectively, can be estimated as follows [25]:

$$G_e = 4\rho RT/5M_e \quad \text{and} \quad G_x = \rho RT/M_c, \tag{23.17}$$

where ρ is the polymer density, R is the universal gas constant.

As it has already been outlined above, positions of chain segments, ends and X-links in a network fluctuate significantly above the glass transition temperature. The normal mode fluctuations occur by virtue of large number of local rotation isomeric state jumps. However, the local conformation dynamics displays substantially heterogeneous distribution over the entire network. These heterogeneities are localized close to the X-links – chemical crosslinks or physical crosslinks such as filler surface adsorbed chain segments. Conformation dynamics of various polyethylens has been investigated by the NMR method by Ediger and Qiu [26]. They clearly showed that the time characteristic of conformation jumps is considerably increased close to the branching points. Effects of this kind in connection with deviation from purely Gaussian structure may become critical in nanofilled rubbers, as will be shown below.

23.4 Mechanisms of Nanocomposite Reinforcement

Above the neat matrix T_g, immobilization of polymer chains becomes the primary reinforcing effect exhibiting a rate given by the large nanofiller surface. Nanocomposites represent systems typical of a high filler–polymer interface area, which is analogous in many aspects to the thin polymer layers deposited on solid substrates. This can be justified considering nanocomposite as a result of virtual reaction, where the degree of conversion depends on the fraction of chain segments adsorbed onto the filler surface:

$$xP + yF \xleftrightarrow{k(\text{desorption})-k(\text{adsorption})} P_n{-}F_m + (x{-}n)P + (y{-}m)F, \tag{23.18}$$

In Equation 23.18, P and F express the number of polymer segments and filler adsorption sites, respectively. In general, *the filler surface-to-volume ratio* and *the filler–polymer interaction energy*, among other effects, primarily affect the amount of the P_n-F_m "complex". Due to the high filler–matrix contact area, the portion of the P_n-F_m complex becomes of pivotal importance in the nanocomposite reinforcement.

However, polymer microcomposites represent systems which are very much the opposite of what has been outlined above. The specific surface area, A_f, of a micron-sized filler is below $10\,\mathrm{m}^2/\mathrm{g}$, providing a very low contact area between filler and polymer matrix. Moreover, the filler diameter is a number of orders of magnitude higher than the chain dimensions as well as characteristic volumes of particular relaxation processes (for example, Rouse or reptation relaxations). Hence, continuum mechanics approach may be used to predict composite properties. Typical examples of continuum mechanics models are the Halpin–Tsai model [27], the Kerner–Nielsen model [27] or the Guth model [28].

In polymer nanocomposites, the contact area between nanofiller and matrix is considerably larger. The particle dimensions, as well as the average interparticle distance are of the same order as the dimensions of polymer chains and characteristic relaxation volumes (see Figure 23.5). Hence, the continuum models fail in the prediction of nanocomposite reinforcement. Moreover, one has to keep in mind that objects on this level exhibit intensive fluctuations and deviation from the Gaussian statistics may easily occur as well. In general, one can approximate the nanocomposite reinforcement using the relation taking into account the particle size independent mechanical contribution due to filler, $f(v_f, A_r, \ldots)$, and particle size dependent segmental immobilization, $F(A_f, \ldots)$, in the following form:

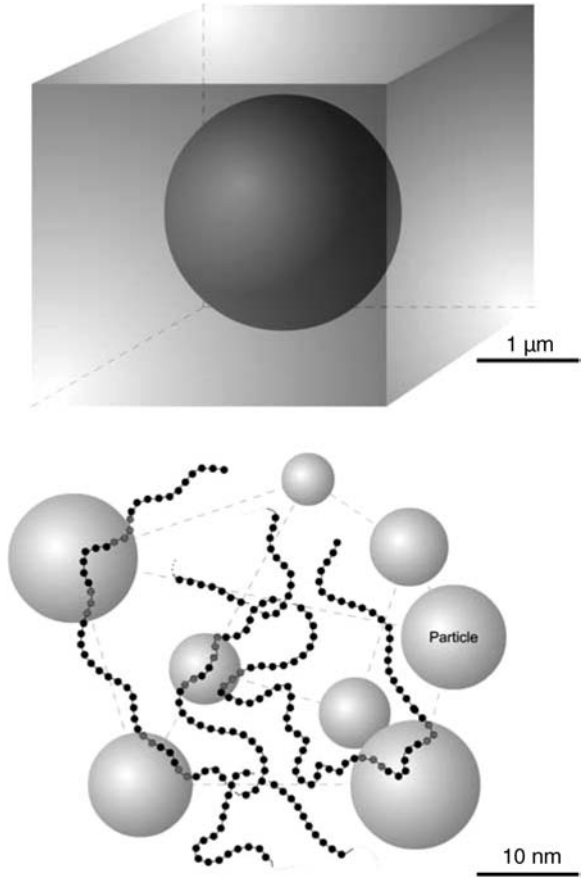

Figure 23.5 Sketch of continuum structure of a microcomposite (upper) and of discrete structure considered in an entangled polymer nanocomposite (lower)

$$G_r = G_{\text{composite}}/G_{\text{matrix}} = f(v_f, A_r, \ldots)_{\text{mechanical}} + F(A_f, \ldots)_{\text{immobilization}}, \tag{23.19}$$

where v_f is the filler volume fraction, A_r is the filler aspect ration and A_f is the filler specific surface area. Droste and DiBenedetto have identified similar relation in their contribution

published in 1969 [29]. Below neat matrix glass transition temperature, T_g, the equation term $F(A_f, \ldots)_{\text{immobilization}}$ becomes zero. Above matrix T_g, $F(A_f, \ldots)_{\text{immobilization}} \gg f(v_f, A_r, \ldots)_{\text{mechanical}}$. An example of the experimentally measured data of rubbery nanocomposite reinforcement is shown in Figure 23.6.

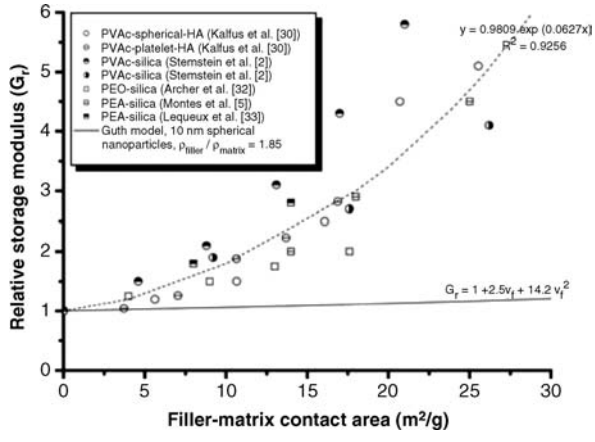

Figure 23.6 Experimentally measured relative storage modulus as a function of the filler-matrix contact area calculated from filler specific surface area and filler weight fraction. Abbreviations used: PVAc – poly(vinylacetate), HA – hydroxyapatite, PEO – poly(ethyleneoxide), PEA – crosslinked poly (ethylacrylate)

In systems, where negligibly small portion of polymer molecules is in direct interaction with the filler surface (microcomposites) or in nanocomposites below their T_g the continuum mechanics approach can successfully be used for the prediction of their reinforcement. It is possible because the volumes characteristic of local relaxation modes are several orders of magnitude smaller compared to the dimensions of the filler particles. Chains in a nanocomposite below the matrix T_g exist in their non-equilibrium conformations exhibiting low conformational entropy regardless of the distance from the particle surface. Moreover, the dynamics of rotation isomerization is extremely low and most monomer units execute solely the vibration motion within the given time scale. Hence, providing that torsion vibration is the primary microscopic motion in a glassy polymer, the characteristic volume of local relaxation process is very low in comparison to the filler particle volume. Thus, the glassy nanocomposite behaves as a true two-component system, where the effect of nanofiller is merely the replacement of a portion of softer polymer matrix with more rigid filler nanoparticles. Hence, the dependence of the relative modulus on filler volume fraction is in accordance with the existing Kerner-Nielsen model [7] for spherical particles or the Halpin–Tsai model for nonspherical particles [30]. The simple continuum mechanics K-N model can be expressed in the form [27]:

$$\frac{G_c}{G_m} = \frac{1 + AB v_f}{1 - B\psi v_f}, \tag{23.20}$$

where:

$$A = (7-5\mu_1)(8-10\mu_1)^{-1} \tag{23.21}$$

and:

$$B = \left(\frac{G_f}{G_m}-1\right)\left(\frac{G_f}{G_m}+A\right)^{-1}. \tag{23.22}$$

The A is a factor depending on the matrix Poisson's ratio, μ_1, B is a factor primarily related to the filler/matrix stiffness ratio and G_m and G_f are moduli of matrix and filler particles, respectively. The factor ψ represents boundary condition and can be expressed using empirical function taking into account the maximum filler volume fraction, $v_{\max}$:

$$\psi = 1 + v_f(1-v_{\max})v_{\max}^{-2}. \tag{23.23}$$

The K-N model represents the substitution mechanism of the composite reinforcement.

To include further mechanical reinforcing effect – the stress transfer from matrix to the surface of anisometric particles, the Halpin–Tsai model [27] can be used providing reasonable predictions:

$$\frac{G_c}{G_m}|_{L,T} = \frac{1+\zeta\eta v_f}{1-\eta v_f}, \tag{23.24}$$

and:

$$\eta_{L,T} = \left(\frac{G_f}{G_m}-1\right)\left(\frac{G_f}{G_m}+\zeta_{L,T}\right)^{-1}. \tag{23.25}$$

The $\zeta_{L,T}$ is the semi-empirical shape related factor and $\eta_{L,T}$ is the factor related to the relative stiffness of the filler and the matrix. For ribbon-shaped reinforcement with rectangular cross-section, $\zeta = 2A_r = 2\times$(length/thickness). The elastic modulus for randomly oriented anisometric inclusions can be expressed using a simple Tsai randomization procedure [27]:

$$G_c^{\text{random}} = \frac{3}{8}G_{cL} + \frac{5}{8}G_{cT}. \tag{23.26}$$

In Equation 23.25, G_{cL} and G_{cT} are the longitudinal and transverse elastic modulus of a composite with unidirectionally aligned anisotropic inclusions, respectively.

The immobilization contribution to the nanocomposite reinforcement is given by the topological constraint imposed on the chains by the impermeable filler surface. The constraint results in the three separate effects of primary importance for the reinforcement of polymers filled with low volume fraction of nanoparticles: the Langevin effect [2], the reference state bias [2] and decreased segmental dynamics connected with the loss of dynamical ergodicity within the interphase [5, 31]. Effects modifying the manifestations of the immobilization phenomenon are as follows: test conditions (time/frequency, temperature, strain), matrix molecular parameters, structural heterogeneity, thermal history, strength of the surface–chain interaction in various systems, preparation procedure and others. This can be illustrated by the dependence in Figure 23.6, which presents reinforcement in various nanofilled rubbers. The trend of the dependence in this graph is obvious – above a neat matrix T_g, the reinforcement is primarily governed by the extent of the filler–matrix interaction area. The scatter of experi-

mental points is given by different test conditions, sample history, molecular structure of the matrix and so on.

To bring a deeper insight into the physical meaning of the immobilization phenomenon as the dominating reinforcing mechanism, let us consider a general situation – the entangled polymer chain attached to the surfaces of nanoparticles resulting in the train-loop-bridge-tail structure illustrated in Figure 23.5. The chain is trapped by both nonlocal entanglements (effective tube) with surrounding chains and by the localized trains situated on particle surfaces each with very different persistence time characteristic of the physical bond lifetime. In crosslinked rubbers, well localized chemical junctions are also present in the nanocomposite structure in addition to entanglements, which are considered as temporary X-links. Furthermore, the impermeable and adsorbing filler surface affects considerably the dynamics of rotation isomerisation as well as normal mode relaxation motions. The effect of lowered rate of conformational transformation is rather localized to the regions close to the trains. In general, the slowed dynamics can be well characterized by the effectively increased activation energy of diffusive motion and monomer friction coefficient ($\ln\zeta_0 \sim E_A/k_BT$).

The trains can act as additional semi-permanent crosslinks above the matrix T_g at times and temperatures, where the train life time is substantially longer compared to the time of experiment. Due to the substantial mass and stiffness of nanoparticles, the fluctuation of these temporary junctions is negligible. Chain loops and bridges between these junctions represent segments exhibiting the so-called Langevin effect, which has been precisely described by Sternstein *et al.* [2]. Such bridges and loops are of finite length and much shorter than the entire chain clearly resulting in considerably increased incremental stiffness: $\mathrm{d}(f_S b/3k_BT)/\mathrm{d}(r/Nb)$. Nevertheless, the nonGaussian behavior represents a general property of a chain regardless of whether it is free or adsorbed; but within the adsorbed chain these short segments have ends "fixed" to the filler surfaces. Filler surface adsorption makes the chain bridges and loops connecting the filer surfaces mechanically active and, as such, able to contribute significantly to the nanocomposite reinforcement [34–36]. Furthermore, one may take into account the effect of the reference state bias involving those parts of chains situated at the filler–polymer interface. They can be in a state r/Nb higher than $\langle r^2_{\mathrm{reference}}\rangle^{1/2}/Nb$ leading to the further enhancement of the interface chain stiffness and consequently of the complete transient filler–polymer network (Figure 23.7) [2].

Lequeux *et al.* [33] and other authors [37, 38] have shown that the nanocomposite contains a phase at the filler–polymer interface exhibiting dynamics substantially retarded in comparison to neat polymer above T_g. The time constant of segmental relaxation motion, T_2, determined by the solid state NMR of the immobilized phase was comparable to that of the neat matrix below its T_g. Thus, it seems necessary to extend the structural effects by the dynamics effects, which are constrained to the diffuse shell of nanometer "thickness" surrounding each particle. This is, in principle, similar to the slowed dynamics of monomer units close to chain branches or junctions mentioned above; however, this effect is expected to be substantially stronger on filler surface. Chakraborty *et al.* [31] have summarized the kinetic constraints caused by the adsorbing surface as follows: (i) the nearest-neighbor interactions, (ii) the specific segment–surface interactions, (iii) the entropic constraint due to impermeable surface, (iv) the topological barriers due to other adsorbed chains and (v) the competition for surface sites. Whilst the first two effects are typical of strongly adsorbed chains, the other effects are generic to all polymer systems.

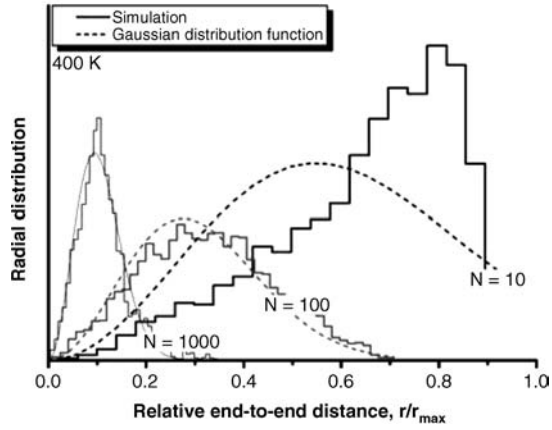

Figure 23.7 Radial distribution of the chain end-to-end distance as a function of the relative extension. Simulation data were obtained from molecular dynamics simulation of single united atom polyethylene chains with $N = 10$, 100 and 1000 at 400 K (statistical ensemble contained 10^4 ps/1 ps $= 10^4$ counts). As seen, short chains exhibit substantially nonGaussian behavior

23.5 Chains at Rubber–Filler Interfaces

23.5.1 Structural Aspects

Pioneering statistical–mechanical theories describing conformation structure of a chain adsorbed on a filler surface have been published by Chandrasekhar [39] and DiMarzio and McCrackin [40]. DiMarzio and McCrackin [40] have verified the statistical–mechanical calculations by computer simulations utilizing the Monte-Carlo method (MC). They showed that in the case of no attraction the mean number of chain-surface contacts, $\langle v \rangle = 1$. As the polymer–surface attraction increases above the critical value equal to $\varepsilon/k_BT = \ln 2$, where $\langle v \rangle = N^{1/2}$ the fraction of adsorbed chain segments $\langle v \rangle / N$ becomes 1/2 for infinitely long one-dimensional *rwm* chain. Moreover, they showed that the obtained results on a one-dimensional *rwm* are universally valid even in case of the chains in three dimensions. The adsorbed chain exhibits a so-called train-loop-tail structure and as the segment–wall interaction energy, ε, increases the size of loops and tails decreases in favor of trains. Furthermore, the adsorption of a chain was shown to be a second-order transition in the sense of the Ehrenfest definition [15]. The chain end-to-end distance was shown to be decreasing with increasinge polymer–surface attraction.

A large ensemble of noticeable results obtained from Monte-Carlo simulations of chains in presence of nanoparticles has been presented by Vacatello [41–43]. He carried out a simulation of dense polymer melt composed of coarse-grained rotation isomeric state chains in a cubic cell containing adsorbing randomly located nanoparticles. His simulations confirmed the formation of the train-loop-bridge-tail structure (Figure 23.5) of chains in the nanofilled system, where the interparticle distance approaches the chain end-to-end distance. Thus, the nanofilled system can be characterized by the fraction of monomer units in trains, loops, bridges and tails. Especially, the average length of a bridge changes significantly as the filler volume increases, as well as the average number of chain connections to the surfaces of filler nanoparticles.

Moreover, the bridging effect becomes more pronounced as the filler particle diameter decreases – the specific filler surface area increases. Vacatello [43] also presented results for chains of varying stiffness involved through the bending potential between two monomer units. This simulation revealed that even ratio of the chain flexibility to the particle diameter is an important factor. As the flexibility of a chain decreases the average length of loops and bridges increases, while the length of trains changes less.

Kumar *et al.* [35] have performed MC simulations of chains in the presence of nanoparticles on a simple cubic lattice. In their simulations, simple self-avoiding chains with no rotation isomeric states of internal rotation and phantom *rwm* chains were considered. In general, their data are in agreement with those of Vacatello [41, 42]. However, in contrast to Vacatello [41, 42] Kumar *et al.* [35] have stressed especially the conformation structure of chain segments (bridges, loops, and so on). Their results support theoretical analysis published by Sternstein and Zhu [2]. As the interparticle distance decreases (filler volume fraction increases) the chain segments bridging the nanofiller particles gain in the effect depicted as the reference state bias [2] and the increased total number of bridging segments per nanoparticle. However, the most important finding is that the strong nonGaussian statistics of short chain segments is a general property independent of the nanoparticle presence. The bridges and loops are attached to the filler surface for a period given by the filler-matrix interaction energy and, hence, are mechanically active.

Deeper insight into the mechanisms by which mechanically active bridging segments and chain loops contribute to the nanocomposite reinforcement above matrix T_g has been published by Keblinski *et al.* [36]. They used a coarse-grained bead-spring approximation as a model of polymer chain. The results clearly showed that the transient filler–polymer network forms in systems, where substantially attractive filler–polymer interaction occurs. However, the strong filler–polymer interaction results in slowing down the segmental dynamics given by the long average lifetime of filler–polymer contacts. It was clearly illustrated on two nanocomposite systems prepared utilizing two distinct methods. In the first method, the system was prepared without attractive interactions and, in the second method, attractive interactions were active during the system preparation. In spite of the fact that the state of filler dispersion was almost the same in both cases, as verified from the radial distribution function, the stress autocorrelation function displayed a very different nature. The system prepared by the first method displayed very slow dynamics and did not equilibrate in given period in contrast to the system prepared by method 2. Based on the analysis of the transient network structure the concentration of chain units in loops, bridges and trains was considerably higher in the system prepared by method 1. Hence, one can see that the differences in the structure of the transient filler–polymer network are the first order parameters affecting the rubbery nanocomposite behavior. Unfortunately, systematic investigation of the effect of the preparation procedure and formation of the interphases of various structures on the nanocomposite properties has not been published, yet.

Perturbation of chain dimensions in the presence of nanoparticles has been simulated and discussed extensively by Mark *et al.* [44]. They used the MC simulation method of chains using the rotation isomeric state model. Their results revealed that the effect of nanoparticles on chain swelling or collapse cannot be simply generalized and depends on the particle diameter, particle volume fraction and so on. According to Mark *et al.* [44] the chain swelling or collapse obtained from the MC simulation can be responsible for the rubbery nanocomposite reinforcement. Thus, they used the average end-to-end distance of a whole chain, simulated by the

MC method, for the Helmhotz free energy calculation. Consequently, the stress and elastic modulus were calculated. However, their theory approach does not offer a satisfactory explanation of the experimentally observed behavior in contrast to the Sternsteins theory analysis [2] in connection with the considerations of the dynamics effects [5, 33].

As it has been mentioned above, the primary reinforcing entity in rubbery nanocomposites is the filler-rubber network. Schweizer and Hooper [45, 46] have investigated the supermolecular structure and phase behavior of the nanofiller-polymer systems utilizing a microscopic polymer reference interaction model simulations. In this model, the polymer chain is represented by the freely jointed chain composed of N spherical interacting units of diameter d. Nanofiller particles are rigid spheres of diameter D. The primary variables affecting the phase behavior of polymer nanocomposite are the strength of filler–polymer interaction ε/k_BT, spatial range of monomer–surface attraction and the ratio D/d. The polymer length plays a lesser role. Generally, they showed that below $\varepsilon/k_BT = 0.5$ the entropy driven separation occurs, which is consistent with calculations by DiMarzio and McCrackin [40]. Above the value $\varepsilon/k_BT = 2$–3, the enthalpy driven formation of transient polymer–filler network involving interparticle chain bridging occurs. The intermediate state is a state of miscibility, where stabilized nanoparticle dispersion can be obtained. In real systems, however, mixture of these three states is often obtained due to kinetic effects. Obviously, the inhomogeneous nanofiller dispersion can modify the overall nanocomposite deformation response due to inhomogeneous stress–strain field leading to the stress and strain concentration or localized screening of the applied load.

23.5.2 Dynamical Aspects

Dynamical aspects of the filler-polymer interface in rubbery nanocomposites represent an issue being more difficult compared to the above structural properties outlined above. The characteristic times of structural relaxation of chains in presence of adsorbing surfaces represent time scale often higher than is the usual time scale of the experiment as well as simulation. Hence, one can find principal similarity between the segmental immobilization due to polymer-filler adsorption and behavior of native polymers at low temperatures. Unfortunately, physicists are still far from the complete understanding of slowed dynamics of polymer chains below the glass transition temperature in native polymers. Moreover, as it has been shown in literature [47] polymer glasses are dynamically very heterogeneous systems. It results in the phenomenon that the physical manifestations of localized subsystems of a glassy polymer solid are very dissimilar to the measured macroscopic and, hence, averaged material response designated as dynamical heterogeneity. Similar situation one may find in the nanofilled rubbers and thin polymer layers deposited on solid substrates.

An excellent approach to the simulation of the local conformational dynamics of chains, both strongly and weakly, interacting with the adsorbing substrate has been presented by Chakraborty *et al.* [31, 48, 49]. Because of the fact that the relaxation times of chains adsorbed on an attractive solid substrate, $E_A/k_BT > 2$–3, attain so high values to be included in the molecular dynamics (MD) simulations, the new stochastic model had to be developed. Their model can be designated as the kinetic Ising model considering polymer chain as a system composed of N interacting units, each containing either two or one specifically interacting pendant groups – two sticker and one sticker kinetic Ising model, respectively. The local energy interactions were estimated utilizing the quantum mechanics calculations [49]. In their kinetic

Ising model, the spin up is assigned to the adsorbed pendant group while the spin down belongs to the desorbed pendant group. The time evolution of the spin states was included to the master equation based on known transition probabilities. These probabilities were determined utilizing the transition-state theory concept. The rate constant characteristic of local transition process was considered to be affected by the activation energy, frequency of molecular oscillations, steric constraint due to the neighboring chain segments, intramolecular torsional strain, and configuration entropy decrease. The intrinsic time scale (clock time) was involved into the kinetic Ising model utilizing the MD simulations from which the base time of oscillation $\tau^* \cong 10^{-13}$ s was obtained.

In the two sticker model situation considered by Chakraborty *et al.* [48] ($N = 500$) above the critical attraction between polymer and surface, $E_A/k_BT \cong 0.3$, the equilibrium fraction of chain segments adsorbed on surface successively increased. However, at the limiting $E_A/k_BT \cong 0.8$, the system becomes unable to achieve equilibrium configuration on a given time scale and the fraction of adsorbed units changes only slightly with increasing E_A/k_BT. For infinitely long time – equilibrium conditions, the fraction of adsorbed units should be unity above $E_A/k_BT \cong 2$. Hence, the interface polymer chains can be taken as entities trapped in their non-equilibrium states at $E_A/k_BT > 1$. At higher temperature, lower value of E_A/k_BT enables the chain to equilibrate, but the kinetics of equilibration adopts the non-exponential form so common for polymer at low temperature. This behavior can be well described by the Kolraush-Williams-Watt (KWW) function, $\sim \exp-(t/\tau)^{\beta}$, where τ is the average relaxation constant and β is the stretching exponent being of value less than unity. Hence, this equilibration represents a nonDebye highly cooperative relaxation process, where the rate of conformation dynamics of one unit is "caged" by its neighbors. For the case of one sticker model, the behavior was very similar to the two-sticker version over broad range of N, but the equilibrium limit was identified at higher values of $E_A/k_BT \cong 2$. Worthy of note that the slow conformation dynamics simulated by Chakraborty *et al.* [31, 48, 49] correlates well with the experimentally measured data [5, 33, 37, 38, 50]. Segmental dynamics of polymer chains close to the adsorption sites on the nanofiller surface exhibits manifestations resembling behavior of polymers at low temperature even for the case of relatively weakly interacting systems. This involves loss of ergodicity within the particle-polymer interphase.

On the other hand, one should keep in mind that the decreased conformational dynamics is rather localized to the units close to the sites on filler surface, where adsorption occurred. According to MD simulation results published by Adolf and Ediger [51] the transmition of rotational cooperativity should be of the order of 10 backbone bonds along the chain giving the extent around 1 nm. Secondly, the sites of filler-polymer adsorption in real systems represent temporary junctions with lifetime given not only by the ratio E_A/k_BT, but also affected by the mechanical bias (Payne effect) [2, 52].

The presence of temporary junctions in form of the adsorbed trains of monomer units on the nanofiller surface has an effect even on the normal mode relaxations of bridging chain segments, chain loops and other chains trapped by the adsorbed chains due to their uncrossability. This has been proved both experimentally [32, 53–55] and by computer simulations [56, 57]. Pryamitsin and Ganesan [56] have used a coarse-grained model of polymer melt of chains of various lengths simulated using the dissipative particle dynamics method. In addition to the immobilization phenomenon, they also investigated the effect of particle jamming and inhomogeneous stress–strain field in detail. The particle jamming is, however, an effect becoming important only if the filler volume exceeds $v_f \cong 0.5$ (even in the

sense of local inhomogeneity of filler concentration). Within the frame of the bead-spring approximation considered in Rouse as well as reptation model, the term E_A/k_BT can be conveniently involved in the effective monomer friction coefficient, ζ. The effectively increased friction due to the chain-surface interaction is responsible for the slowing down the normal relaxation modes. Rubinstein and coworkers [54] have brought a successful concept for the description of the normal mode relaxation of long polystyrene chains in presence of silica and poly(2-vinylpiridine) surface. The suggested theory concept was shown to be in good agreement with experimental results based on the secondary ion mass spectroscopy measurements of the tracer diffusion coefficient. In their theory analysis, the chain friction coefficient was shown to be composed of two contributions – free and adsorbed monomer units:

$$\zeta_{\text{chain}} \cong \zeta_{\text{adsorbed}} N^{1/2} + \zeta_0 N. \tag{23.27}$$

Resulting characteristic time of the chain diffusion – the time of chain reptation motion was estimated as follows:

$$\tau_{\text{rep}} \cong \frac{NL^2}{D_0} \cong \frac{b^2 N^{5/2}}{2k_B T N_e} (\zeta_{\text{adsorbed}} + \zeta_0 N^{1/2}). \tag{23.28}$$

It was demonstrated that this kind of relaxation is responsible for the recovery after the high strain amplitude perturbation of the nanocomposite structure – the Payne effect [55]. The high strain oscillations lead to the chain mobilization at the filler-polymer interface. This is evidenced by the decreased storage modulus of elasticity [52]. As the interphase structure recovers after this mechanical excitation, the value of the nanocomposite storage modulus increases to the original value on the time scale well estimated by the Rubinstein model [54].

It has been shown that the chain adsorption followed by the chain immobilization is the primary mechanism leading to the rubbery nanocomposite reinforcement. The immobilization makes the nonGaussian chain behavior mechanically active in the form of interphase regions commonly forming the stiff transient filler-polymer network. The attractive interaction between nanofiller and polymer leads to the break of dynamical ergodicity resembling to the dynamics of polymers at low temperatures. This is connected with strong spatial heterogeneity of segmental dynamics. This property of rubbery nanocomposites represents current issue in the field of computer simulations leading to the discussion about the connection between continuum and discrete matter, representative volume of matter and so on. These aspects will be discussed in the following section.

23.6 Structural Peculiarities of Rubbery Nanocomposites

Microscopic relaxation processes occurring on the molecular level govern the macroscopic viscoelastic response of an amorphous polymer. These molecular relaxation modes range from local vibrations being the primary mode in the glassy state to the nonlocal normal mode relaxations operating above the T_g of the amorphous polymer (Figure 23.8). Above T_g, the enormous number of conformation transitions allows the chain to be in a high entropy state. As a result, the chain size and shape can greatly fluctuate. In the case of stiff filler nanoparticles dispersed in an amorphous polymer matrix, one can compare the characteristic volumes of relaxation modes with those of filler particles (Figure 23.8).

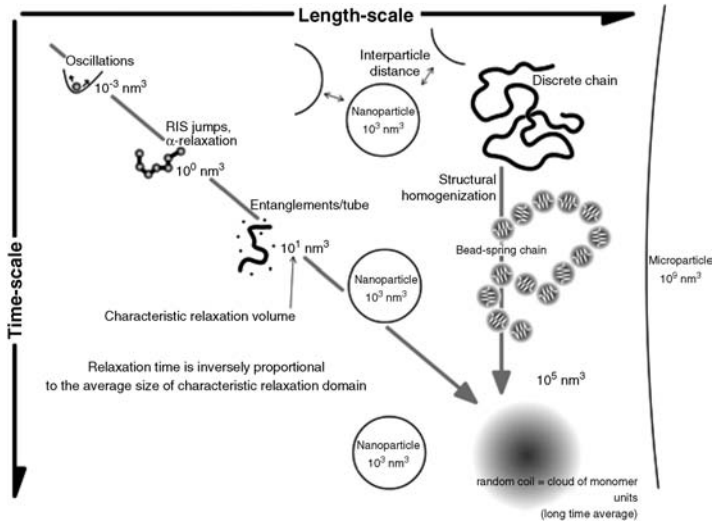

Figure 23.8 Schematic scaling of the structural and dynamical entities in a polymer composite

In order to account for the structural features of a given material, the representative volume element (RVE) is defined. The RVE can be defined as the smallest volume of the material possessing the average properties of a macroscopic solid made of the same material. The size of the RVE (SRVE) is related to the structural heterogeneity of the material, and, thus, determining the RVE (SRVE) becomes a crucial task in developing reliable models capable of predicting mechanical properties as a function of structural variables.

In ordered systems such as metal crystals, the RVE is of the order of Angstroms and the classical continuum mechanics was developed as a local theory. The average strain, $\langle\varepsilon\rangle$, and stress, $\langle\sigma\rangle$, in a representative volume element, V, can be expressed as follows:

$$\langle\sigma\rangle = \frac{1}{V}\int_V \sigma(x)\mathrm{d}V, \tag{23.29}$$

$$\langle\varepsilon\rangle = \frac{1}{V}\int_V \varepsilon(x)\mathrm{d}V. \tag{23.30}$$

In disordered solids, and, especially, in amorphous polymers, the extent of nonlocality is several orders of magnitude greater than in the ordered media [10]. This results in substantially larger RVE which can further be increased by adding filler particles, especially in the case when the size of the filler particles is of the order of the average end-to-end distance of the polymer chains.

Above the glass transition temperature of polymer matrix, the reinforcement is primarily given by the immobilization contribution, $F(A_f, \ldots)_{\text{immobilization}}$, involving mechanically active network of nonGaussian segments in form of the interparticle bridges and surface loops + decreased segmental dynamics due to the surface–polymer interaction occurring on the extensive filler–polymer contact area. Under these conditions, it is difficult to define both

the average stress and strain, since for volumes smaller than approximately 1000 nm^3, the matter has to be considered discrete.

An attempt to make a multiscale modeling of polymer nanocomposites involving the immobilization effect has been published by Borodin *et al.* [58]. Their methodology was composed of MD simulations of coarse-grained chains to obtain the shear modulus of elasticity from the analysis of the polymer-bead mean square displacement. The dependence of the shear modulus versus position from nanofiller surface, bulk polymer and solid particle shear modulus was further used for the calculation of the average composite properties. This was carried out based on the material-point-method (MPM) simulation representing a continuum-based numerical model. The transition from the discrete molecular structure to the continuum-based structure composed of a single nanoparticle surrounded by isotropic layers of varying stiffness was achieved by replacing the continuous polymer density profile by a series of discrete isotropic layers. The model qualitatively describes well the experimentally observed trends shown in Figure 23.6.

However, real polymer nanocomposites usually exhibit a very heterogeneous structure involving filler agglomerates and a transient polymer–filler network. Within the transient polymer–filler network, a broad distribution of interparticle distances can be recognized. Moreover, in the case of X-linked matrices, significant heterogeneities in the matrix molecular structure can be identified as well. In such a case, it is very difficult to determine the correct size of the representative volume element. Consequently, deformation within the network will become significantly non-affine. Seeking the RVE is important in molecular simulations (MC or MD), because the selection of suitable RVE and averaging procedure to determine an average property of a dynamically changing system. The averaging represents some kind of homogenization bringing mean value of a property, which itself can fluctuate in the system very substantially.

The structural homogenization of a matrix occurs due to high number of conformation transitions (RIS jumps) of chain bonds. The conformation transitions hierarchically build the normal mode fluctuations of chain segments as well as chain as a whole. Thus, the length of chains in given system affects the homogenization time, because the normal mode relaxations are scaled as $\tau_{nm} \propto N^{2-3.7}$. If a part or several parts of a chain are kinetically constrained the structural homogenization is greatly retarded and exhibits spatially heterogeneous nature. This, of course, leads to the loss of matrix ergodicity (bonds become kinetically non-equivalent). The stronger is the constraint (average energy barrier related to the constraint) the stronger is this effect.

In nanocomposites, the structural inhomogeneities and fluctuations can survive over long-time scale even above the matrix T_g. For instance, in polymer nanocomposite there are regions typical of very different values of the following structural ratio being very important for the formation of the transient filler–polymer network:

$$r_0/d_{pp}, \tag{23.31}$$

where d_{pp} is the average particle-to-particle distance and r_0 is the end-to-end distance of a chain or a strand of crosslinked network. The average value of the ratio r_0/d_{pp} can vary depending on the averaging procedure involving time, ensemble over many realizations or other. The distribution of interparticle distances in nanocomposite is far from the case of ideal simple cubic lattice distribution [2]. Rather broad range of the r_0/d_{pp} ratios can be expected in the nanocomposite structure and its fluctuation can achieve very large amplitudes. Hence, it is

a question, whether the average value of the ratio r_0/d_{pp} is sufficiently representative for the simulation of the viscoelastic response of polymer nanocomposites.

Furthermore, one can consider for instance the chain normal mode of $p=1$ (23.11) of relaxation time given by the relation:

$$\text{and} \quad \ln \tau_{nm} \propto \ln \zeta_0 \propto E_A/k_B(T-T_0), \tag{23.32}$$

where E_A is the activation energy of relaxation transition. The average time constant $\langle \tau_{nm} \rangle$ can be taken as a limit of the transient filler–polymer network lifetime. Similar as before, the distribution of energy barriers can vary very substantially especially at the filler–polymer interface [31]. Spatially heterogeneous distribution of activation barriers of diffusive motion of chain units and segments, E_A, can be very broad.

In conclusion, various structural as well as dynamical units in a polymer can be recognized. Some of them are a consequence of equilibrium between contending repulsive and attractive physical forces acting among various structural assemblies of matter and some of them are a result of kinetically driven processes. These structural units involve hierarchically atoms, monomer units, chain segments, network strands or nonlocal chain entanglements (effective tube), polymer coils and filler particles. Fluctuations on each particular submicroscopic level are characteristic of respective relaxation times needed for the unit positional or shape rearrangement. Thus, in considering heterogeneity of rubbery nanocomposites one has to involve filler-dispersion heterogeneity, molecular heterogeneity as well as dynamical heterogeneity of polymer matrix (Figure 23.9). Bridging the gap between the small-scale mechanics of the discrete level being of statistical nature (and tending to be non-affine) on one hand and continuum mechanics on the other hand represents current issue for composite scientists.

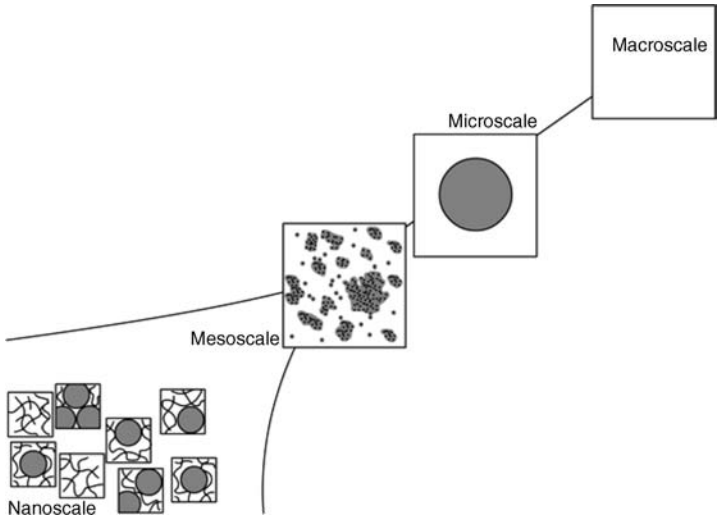

Figure 23.9 What is the representative structural element on the nanoscale?

23.7 Concluding Remarks

In this chapter, a brief introduction of basic aspects of reinforcement of rubbery nanocomposites was presented. Above the matrix T_g, polymer chains near the nanofiller surface become extensively perturbed in respect to their dynamics. This constraint occurring on the nanometer (molecular) level causes severe effects detectable on the micro- and macroscopic levels. Due to the large nanofiller surface–polymer matrix interaction area, the filler nanoparticles are able to cause significant effects even at very low filler loadings. Interestingly, Droste and DiBenedetto [29] have already addressed the immobilization phenomenon in polymers filled with high specific surface area fillers in 1960s although very poor computer simulation possibilities were available at that time.

Currently, no universal theory is available to predict quantitatively the effects of chain immobilization on the reinforcement of nanocomposites above their T_g. Methods of molecular simulations advanced very substantially during the past 20 years. Now we are able to model behavior of polymer chains at the nanoscale. Unfortunately, the gap between the discrete molecular levels covered by molecular models and continuum models operating on the micro- and macroscopic levels has not been overcome. Moreover, the reduced and spatially heterogeneous dynamics of interphase chains in rubbery nanocomposites is principally connected with the glass transition phenomenon, which is an issue still unresolved yet.

Undoubtedly, routes to reinforcing polymers with nanometer-sized particles and exploring the various possibilities given by the selection of the polymer/filler combination represent very attractive field for both academic scientists and industrial engineers bringing both experimental and theoretical challenge. Theoretical modeling of the actual reinforcing mechanisms introduced by adding nano sized solid particles into both crosslinked and linear polymer matrices usable above their T_g represents the first step in a deeper understanding of the structure–property relationships in these industrially important materials. Very likely, the viscoelasticity of a large rubber nanocomposite article such as a tire will not directly reflect the peculiarities of the nanoscale effects due to property "homogenization" occurring during the transition from the nano- to the macroscale. Hence, the classical models assuming uniform "average" affine deformation of a network can successfully be used in predicting short term behavior of large filled rubber articles. However, due to the heterogeneity of both localized chain relaxation and composition, a locally non-affine deformation field has been predicted, which may result in wear, fatigue and degradation being directly controlled by the nanoscale effects similarly to the behavior of thin polymer nanocomposite films and polymer melts. Hence, it seems realistic to assume that in the foreseeable future, successful products in the rubber industry will be developed using the modeling strategies considering the nanoscale peculiarities described above.

Acknowledgments

The authors are very grateful to Ms. Katerina Hynštová for providing results from molecular dynamics simulations. The authors are also very thankful to Prof. S.S. Sternstein and Dr. Jaroslav Kučera for many fruitful discussions.

References

1. Narayanan, R.A., Thiyagarajan, P., Zhu, A.J. *et al.* (2007) Nanostructural features in silica-polyvinyl acetate nanocomposites characterized by small-angle scattering. *Polymer*, **48**, 5734–5741.

2. Sternstein, S.S. and Zhu, A.J. (2002) Reinforcement mechanism of nanofilled polymer melts as elucidated by nonlinear viscoelastic behavior. *Macromolecules*, **35**, 7262–7273.
3. Zhu, A.J. and Sternstein, S.S. (2003) Nonlinear viscoelasticity of nanofilled polymers: interfaces, chain statistics and properties recovery kinetics. *CompositeS Science and Technology*, **63**, 1113–1126.
4. Kalfus, J. and Jancar, J. (2007) Relaxation processes in PVAc-HA nanocomposites. *Journal of Polymer Science Part B-Polymer Physics*, **45**, 1380–1388.
5. Montes, H., Lequeux, F., and Berriot, J. (2003) Influence of the glass transition temperature gradient on the nonlinear viscoelastic behavior in reinforced elastomers. *Macromolecules*, **36**, 8107–8118.
6. Kalfus, J. and Jancar, J. (2007) Viscoelastic response of nanocomposite poly(vinyl acetate)-hydroxyapatite with varying particle shape - dynamic strain softening and modulus recovery. *Polymer Composites*, **28**, 743–747.
7. Kalfus, J. and Jancar, J. (2008) Reinforcing mechanisms in amorphous polymer nanocomposites. *Composites Science and Technology*, **68**, 3444–3447.
8. Chen, Y., Lee, J.D., and Eskandarian, A. (2004) Atomistic viewpoint of the applicability of microcontinuum theories. *International Journal of Solids and Structures*, **41**, 2085–2097.
9. Marangati, R. and Sharma, P.J. (2007) A novel atomistic approach to determine strain-gradient elasticity constants: Tabulation and comparison for various metals, semiconductors, silica, polymers and the (Ir) relevance for nanotechnologies. *Journal of the Mechanics and Physics of Solids*, **55**, 1823–1852.
10. Nikolov, S., Han, C.S., and Raabe, D. (2007) On the origin of size effects in small-strain elasticity of solid polymers. *International Journal of Solids and Structures*, **44**, 1582–1592.
11. Birshtein, T.M. and Ptytsin, O.B. (1966) *Conformations of Macromolecules*, John Wiley & Sons, New York.
12. Boyd, R.H. and Phillips, P.J. (1996) *The Science of Polymer Molecules*, Cambridge Universtity Press, Cambridge.
13. Wu, S. (1992) Predicting chain conformation and entanglement of polymers from chemical structure. *Polymer Engineering and Science*, **32**, 823–830.
14. Donth, E. (1996) Exhausting of fluctuating free volume of dynamics glass transition at low temperatures. *Journal of Physics I France*, **6**, 1189–1202.
15. Hill, T.L. (1986) *An Introduction to Statistical Thermodynamics*, Dover, New York.
16. Matsuoka, S. (1997) Entropy, free volume, and cooperative relaxation. *Journal of Research of the National Institute of Standards and Technology*, **102**, 213–228.
17. Bueche, F. (1962) *Physical Properties of Polymers*, Interscience Publishers, New York.
18. deGennes, P.G. (1979) *Scaling Concepts in Polymer Physics*, Cornell University Press, Cornell.
19. Doi, M. and Edwards, S.F. (2003) *The Theory of Polymer Dynamics*, Oxford University Press, Oxford.
20. Kawakatsu, T. (2001) *Statistical Physics of Polymers, An Introduction*, Springer, Berlin.
21. Erman, B., Kloczkowski, A., and Mark, J.E. (1989) Chain dimensions and fluctuations in random elastomeric networks. 2. Dependence of chain dimensions and fluctuations on macroscopic strain. *Macromolecules*, **22**, 1432–1437.
22. Brereton, M.G. (1991) Cross-link fluctuations and the NMR properties of strained poly)dimethylsiloxane) networks. *Macromolecules*, **24**, 6160–6163.
23. Treloar, L.R.G. (2005) *The Physics of Rubber Elasticity*, Clarendon Press, Oxford.
24. Ward, I.M. (1971) *Mechanical Properties of Solid Polymers*, John Wiley & Sons, Bristol.
25. Lin, Y.H. (2003) *Polymer Viscoelasticity, Basics, Molecular Theories, Experiments*, World Scientific.
26. Qiu, X. and Ediger, M.D. (2000) Branching effects on the segmental dynamics of polyethylene melts. *Journal of Polymer Science Part B-Polymer Physics*, **38**, 2634–2643.
27. Nielsen, L.E. and Landel, R.F. (1994) *Mechanical Properties of Polymers and Composites*, Dekker, New York.
28. Guth, E. (1945) Theory of filler reinforcement. *Journal of Applied Physics*, **16**, 20–25.
29. Droste, D.H. and DiBenedetto, A.T. (1969) The glass transition temperature of filled polymers and its effect on their physical properties. *Journal of Applied Polymer Science*, **13**, 2149–2168.
30. Kalfus, J. and Jancar, J. (2007) Elastic response of nanocomposite poly(vinylacetate)-hydroxyapatite with varying particle shape. *Polymer Composites*, **28**, 365–371.
31. Shaffer, J.S. and Chakraborty, A.K. (1993) Dynamics of poly(methyl methacrylate) chains adsorbed on aluminum surfaces. *Macromolecules*, **26**, 1120–1136.
32. Zhang, Q. and Archer, L.A. (2002) Poly(ethylene oxide)/silica nanocomposites: structure and rheology. *Langmuir*, **18**, 10435–10442.
33. Berriot, J., Montes, H., Lequeux, F. *et al.* (2002) Evidence for the shift of the glass transition near the particles in silica-filled elastomers. *Macromolecules*, **35**, 9756–9762.

34. Gaylord, R.J. (1979) The confined chain approach to the deformation behavior of bulk polymers. *Polymer Engineering and Science*, **19**, 955–965.
35. Ozmusul, M.S., Picu, C.R., Sternstein, S.S., and Kumar, S.K. (2005) Lattice Monte Carlo simulations of chain conformations in polymer nanocomposites. *Macromolecules*, **38**, 4495–4500.
36. Sen, S., Thomin, J.D., Kumar, S.K., and Keblinski, P. (2007) Molecular underpinnings of the mechanical reinforcement in polymer nanocomposites. *Macromolecules*, **40**, 4059–4067.
37. Kaufman, S., Slichter, W.P., and Davis, D.D. (1971) Nuclear magnetic resonance study of rubber-carbon black interactions. *Journal of Polymer Science: Part A-2*, **9**, 829–839.
38. Asai, S., Kaneki, H., Sumita, M., and Miyasaka, K. (1991) Effect of oxidized carbon black on the mechanical properties and molecular motions of natural rubber studied by pulse NMR. *Journal of Applied Polymer Science*, **43**, 1253–1257.
39. Chandrasekhar, S. (1943) Stochastic problems in physics and astronomy. *Reviews of Modern Physics*, **15**, 1–89.
40. DiMarzio, E.A. and McCrackin, F.L. (1965) One-dimensional model of polymer adsorption. *Journal of Chemical Physics*, **43**, 539–547.
41. Vacatello, M. (2002) Molecular arrangements in polymer-based nanocomposites. *Macromolecular Theory and Simulations*, **11**, 757–765.
42. Vacatello, M. (2003) Predicting the molecular arrangements in polymer-based nanocomposites. *Macromolecular Theory and Simulations*, **12**, 86–91.
43. Vacatello, M. (2003) Monte-Carlo simulations of the interface between polymer melts and solids. effect of chain stiffness. *Macromolecular Theory and Simulations*, **10**, 187–195.
44. Sharaf, M.A., Kloczkowski, A., Sen, T.Z. *et al.* (2006) Filler-induced deformations of amorphous polyethylene chains. The effects of the deformations on elastomeric properties, and some comparisons with experiments. *European Polymer Journal*, **42**, 796–806.
45. Hooper, J.B. and Schweizer, K.S. (2007) Real space structure and scattering patterns of model polymer nanocomposites. *Macromolecules*, **40**, 6998–7008.
46. Hooper, J.B. and Schweizer, K.S. (2006) Theory of phase separation in polymer nanocomposites. *Macromolecules*, **39**, 5133–5142.
47. Ediger, M.D., Angell, C.A., and Nagel, S.R. (1996) Supercooled liquids and glasses. *The Journal of Physical Chemistry*, **100**, 13200–13212.
48. Adriani, P.M. and Chakraborty, A.K. (1993) Dynamics of relaxation at strongly interacting polymer-solid interfaces, Effects of chain architecture. *Journal of Chemical Physics*, **98**, 4263–4274.
49. Shaffer, J.S., Chakraborty, A.K., Davis, H.T. *et al.* (1991) The nature of the interactions of poly(methyl methacrylate) oligomers with an aluminum surface. *Journal of Chemical Physics*, **95**, 8616–8630.
50. Berriot, J., Lequeux, F., Monnerie, L. *et al.* (2002) Filler-elastomer interaction in model filled rubbers, a 1H NMR study. *Journal of Non-Crystalline Solids*, **307–310**, 719–724.
51. Adolf, A.B. and Ediger, M.D. (1992) Cooperativity of local conformational dynamics in simulations of polyisoprene and polyethylene. *Macromolecules*, **25**, 1074–1078.
52. Lin, E.K., Kolb, R., Sajita, S.K., and Wu, W. (1999) Enhanced polymer segment exchange kinetics due to an applied shear field. *Macromolecules*, **32**, 4741–4744.
53. Zhang, Q. and Archer, L. (2003) Effect of surface confinement on chain relaxation of entangled cis-polyisoprene. *Langmuir*, **19**, 8094–8101.
54. Zheng, X., Sauer, B.B., Van Alsten, J.G. *et al.* (1995) Reptation dynamics of a polymer melt near an attractive solid surface. *Physical Review Letters*, **74**, 407–410.
55. Kalfus, J. and Jancar, J. (2007) Relaxation processes in PVAc-HA nanocomposites. *Journal of Polymer Science Part B-Polymer Physics*, **45**, 1380–1388.
56. Pryamitsyn, V. and Ganesan, V. (2006) Origins of linear viscoelastic behavior of polymer-nanoparticle composites. *Macromolecules*, **39**, 844–856.
57. Dionne, P.J., Picu, C.R., and Ozisik, R. (2006) Adsorption and desorption dynamics of linear polymer chains to spherical nanoparticles: a Monte Carlo investigation. *Macromolecules*, **39**, 3089–3092.
58. Borodin, O., Bedrov, D., Smith, G.D. *et al.* (2005) Multiscale modeling of viscoelastic properties of polymer nanocomposites. *Journal of Polymer Science Part B-Polymer Physics*, **43**, 1005–1013.

24

Application of Rubber Nanocomposites

Miroslawa El Fray[1] and Lloyd A. Goettler[2]

[1] *West Pomeranian University of Technology in Szczecin, Polymer Institute, ul. Pulaskiego 10, 70-322, Szczecin, Poland*

[2] *Professor of Polymer Engineering (retired), The University of Akron, Akron, Ohio, USA*

24.1 Introduction

Rubber nanocomposites have gained increased attention in both academic and industrial research in recent years. From the definition, a nanocomposite is considered as a polymer composite in which the occluded phase has at least one nanoscale dimension, that is, one measuring from 1 to 100 nanometers (nm). In keeping with the definition of a composite as a multiphase material comprising a continuous matrix embedding another material that has more desirable properties, any application of such a material should utilize some synergistic combination of the component properties of the two major components, the matrix polymer and the reinforcement. Nanocomposites have already showed improved performance (compared to matrices containing conventional, micron-sized fillers) due to their high surface area and significant aspect ratios. Improved properties (increased stiffness and, to some extent, strength, reduced elongation to failure, improved resistance to crack growth and tearing and, finally, various modifications of abrasion, dynamic and fatigue properties) are being achieved at much lower additive concentrations compared to conventional systems. Particulate conventional fillers such as carbon black and fumed silica are incorporated in the rubber as reinforcing fillers to enhance the mechanical properties, to improve the barrier properties or to increase the resistance to fire and ignition [1].

Rubber Nanocomposites: Preparation, Properties and Applications Edited by Sabu Thomas and Ranimol Stephen
© 2010 John Wiley & Sons (Asia) Pte Ltd

24.1.1 Rubbery Matrices

Rubbery polymers serving as matrices in nanocomposite materials can be categorized as crosslinked systems (chemically crosslinked during a curing process) and thermoplastic elastomers, TPEs (physically crosslinked elastomeric materials). Classic elastomers, such as polybutadiene rubber and polyisoprene rubber, are used as general purpose rubbers in high volume products such as tyres, hoses, belting while styrene-butadiene TPEs are special rubbers for footwear applications, sound-deadening materials, wire insulation and flexible automotive parts [2].

World rubber consumption in 2006 was in a range of 21.5×10^6 t, including 8.95×10^6 t of natural rubber and 12.55×10^6 t of synthetic rubber (Figure 24.1). The largest consumption market is in the tire industry (59–63% synthetic rubbers, 68–71% natural rubbers). Other industrial sectors (mainly automotive) consume 25% of the total annual production.

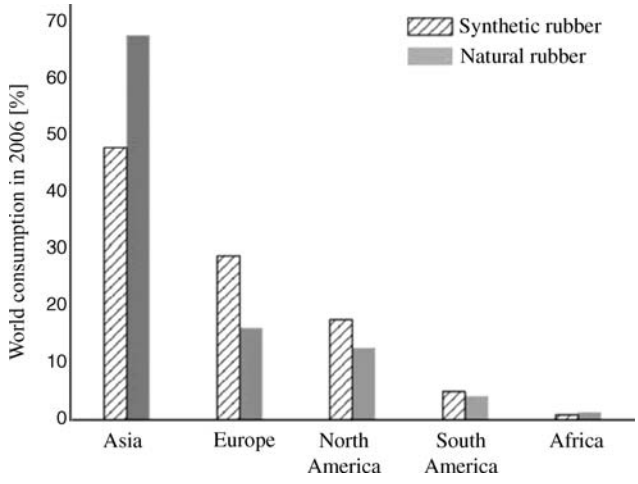

Figure 24.1 Rubber consumption worldwide in 2006

The largest world production of rubbery goods is constantly growing, mainly in China (Figures 24.2 and 24.3), while total production in other large countries is rather stable.

An increasing trend in consumption is also observed for thermoplastic elastomers (4.5% per year in Europe). Almost 30% is used in automotive industry. The world production of thermoplastic polyurethanes was 13×10^6 t in 2005, predominantly in rigid and elastic foams.

24.1.2 Nanofillers

The conventional fillers most highly used in the rubber industry include carbon black and silicone dioxide (silica), while organically modified layered clays, carbon nanotubes or polyhedral oligomeric silsesquioxanes are opening up new points of access [3].

An obvious example is carbon black-reinforced rubber, since the primary carbon black particles, and even some aggregates, fall within the nanoscale range. SAF, the highest

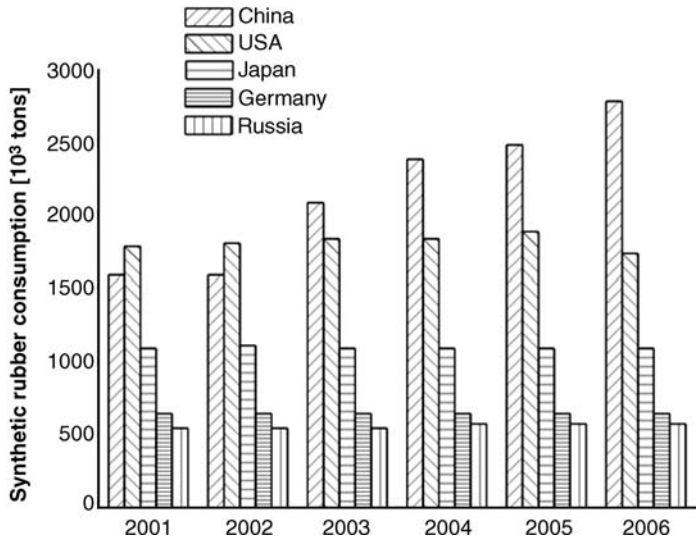

Figure 24.2 Synthetic rubber consumption 2001–2006

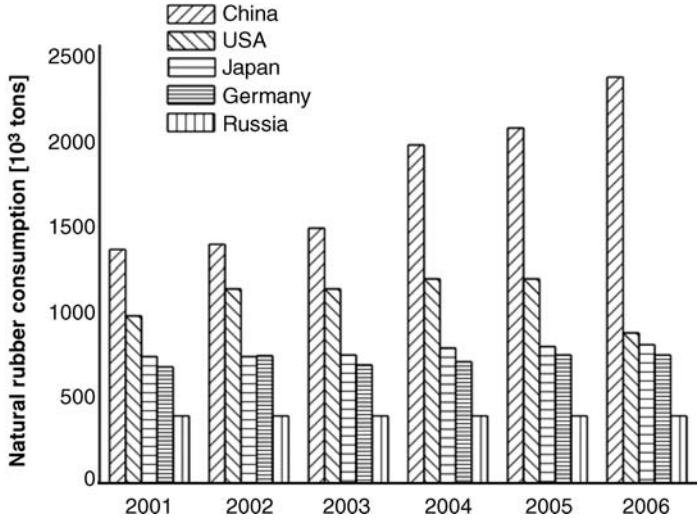

Figure 24.3 Natural rubber consumption 2001–2006

reinforcing type of carbon black, has a particle size of only 20 nm [4]. Some other potential nanoscale reinforcements include particulate silica and other metal oxides, silsesquioxane molecular cages and silica-based molecular networks [5], smectic-layered silicates (either intercalated or exfoliated), haloysite tubular silicates, fullerenes, carbon nanotubes, carbon nanofibrils and graphite platelets.

The common and traditional rubber reinforcement, carbon black, can be varied in both its aggregate structure and particle size. While a higher structure leads to higher modulus at lower loading and therefore less hysteresis, producing a high resilience and low rolling resistance, a smaller particle size, especially in grades with a more active surface chemistry, leads to greater interfacial effects that ultimately enhance traction and abrasion resistance, though with the penalty of greater hysteresis (due to molecular slippage at the interface under high stresses). Thus, strong tethering of polymer chains to the surface would be desirable to reduce hysteresis, which results in high heat build-up and rolling resistance. It has long been, and still currently is, a high objective of tire rubber formulators to achieve all of these beneficial performance criteria simultaneously. Perhaps nanotechnology can play a role.

The fullerenes, another form of particulate carbon, can potentially provide good reinforcement and a low Payne effect in rubber from high rubber bonding (producing physical crosslinks) due to their highly curved active surface. Unfortunately, they are toxic and at this point of development are very expensive. There is still interest in utilizing their potential by synergistic blending with more conventional carbon black or silica reinforcements to cost-effectively extend the "magic triangle" of tread performance.

Multiwall carbon nanotubes ranging from 2 to 20 nm in diameter, present the ultimate in carbon-based nanoscale reinforcement, having a 1 TPa modulus and about 60 GPa tensile strength. While still quite pricey, their cost is going down as volume production increases with more efficient manufacturing processes. They can be best incorporated into rubber matrices by solution processing. Their high reinforcing efficiency can increase modulus dramatically along with simultaneously increasing elongation to fail, thus resulting in a compound that is both stiffer, stronger and more ductile, up to about 3 wt% concentration; at higher levels the modulus actually accelerates its increase, but elongation diminishes.

Silica reinforcement is available in a size range between fumed (nanoscale) and ground (microscale) as a potential replacement for carbon black. BET surface area of commercial products varies from 150 to 230 m^2/g. In the finer grades a high viscosity results from strong particle–particle forces, making dispersion and flow processing difficult. Furthermore, its high acidity retards the sulfur vulcanization of the rubber formulation. Fortunately, silane treatment of the particles can be employed to reduce the particle–particle interactions and increase particle–polymer interactions to improve dispersion (HDS grades) and enhance reinforcement (to even higher levels than carbon black, producing a high modulus at high strain even while modulus is kept low at low strain) and abrasion resistance without increasing hysteresis (Payne effect), rendering it suitable for tire treads. A typical silane for bonding silica while also preventing interference with rubber cure is TESPT, bis(3-triethoxysilylpropyl)-tetrasulfide. It should be noted that the silane gives some property improvement on its own, even without the presence of silica. While a successful treatment, its cost is unfortunately high.

The typical layered silicate employed in commercial applications is montmorillonite, which has a high surface area ($\sim$800 m^2/g) and a high aspect ratio ($\sim$100–200), both of which contribute to efficient reinforcing potential. The gallery surfaces are commonly treated with cationic surfactants to tailor the interfaces for compatibility with the polymer matrix. Polarity matching should be observed, so that a nonpolar ammonium cation, substituted for example with hydrogenated tallow, is preferred for nonpolar rubbers, such as EP, EPDM, BR, isoprene, IR and even SBR or NR, while a more polar hydroxyethyl substituent is better suited to polar rubbers like NBR and BIIR [3]. The nonpolar organoclays (whose gallery walls are decorated with primary or tertiary ammonium cations) readily exfoliate in BIMS,

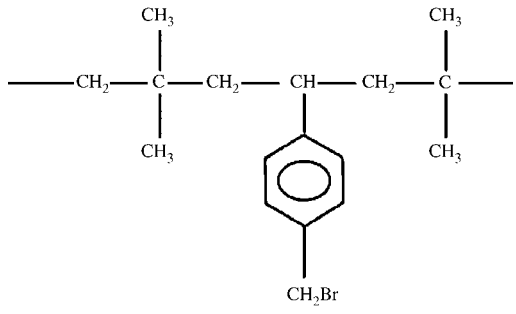

producing increased mechanical properties and glass transition temperature with decreases in tanδ and cure time [6]. They also exfoliate in maleic anhydride-grafted IIR to generate a 5× increase in tensile strength and 60% reduction in nitrogen transmission rate. In highly nonpolar rubbers like BR, the use of a carboxylic acid-terminated rubber compatibilizer is helpful, producing in BR, for example, an 80% reduction in water vapor transmission rate. While montmorillonite usage in plastic polymers predates and overshadows rubber applications, the latter are now in an accelerating pattern of development.

Since layered silicates, while efficient polymer reinforcements in general, are less effective than carbon black in strengthening rubber, and in addition are subject to high hysteresis [7] they are typically not selected for structural applications, such as stress-supporting tire components. In addition, the flexing experienced in rotating tires causing repetitive high strains would result in cracking of components containing layered silicates. In this sense, they resemble discontinuous microfiber reinforcement despite their overall smaller size, perhaps because of their microscale dimensions in two spatial directions. In both cases, the high aspect ratio (macroscale length/microscale diameter for fibers, microscale width/nanoscale thickness for layered silicate platelets) makes them more suitable for stiffening than strengthening of the polymer matrix.

Nanocomposite attributes that drive commercial applications include:

- Efficient reinforcement;
- Low density, as property development obtains at low concentration levels;
- Good balance of stiffness with toughness and tear resistance;
- Good dimensional stability;
- Permeation and absorption resistance;
- Flame retardancy;
- Chemical resistance;
- Easy flow processing with low abrasiveness (nanocomposite viscosity is typically high relative to that of the polymer matrix at low shear rates, but diminishes significantly under typical flow processing conditions);
- Good appearance with smooth surfaces, as exemplified by the scanning electron micrograph in Figure 24.4.

As the processing of thermoset rubbers inevitably involves vulcanization, the effects of embedded nanoplatelets of surfactant-modified montmorillonite on the rate of cure as well

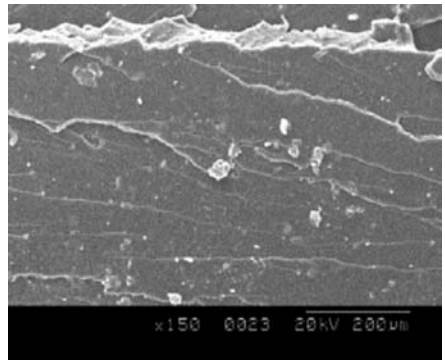

Figure 24.4 Scanning electron micrograph of a cryofractured nanocomposite of montmorillonite in nitrile rubber [10]

as the ultimate density of the crosslinked network must be taken into account. It is now known that the presence of ammonium ions on the gallery surfaces has an accelerating effect upon sulfur vulcanization, as demonstrated by the data reported in Table 24.1 [8] and Figure 24.5.

Table 24.1 Comparative cure properties of an SBR rubber and its nanocomposite

Cure property	SBR rubber	SBR + 20A clay
t_{90}, min	10.5	8.8
G', MPa	1.50	1.33
t_1, min	0.35	0.38
t_2, min	0.45	0.53

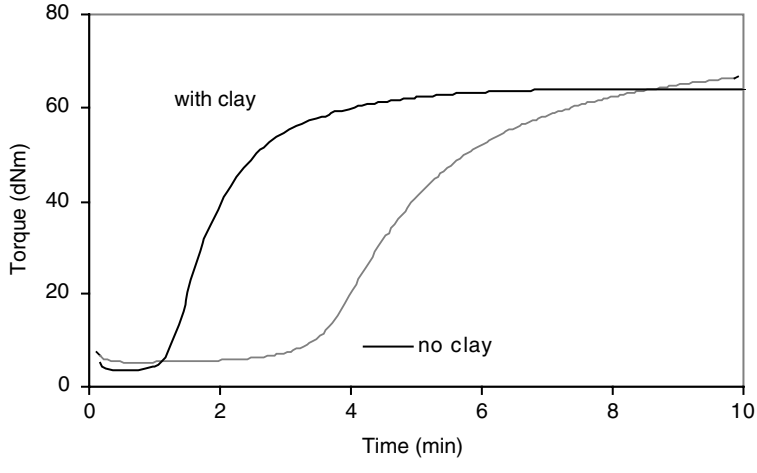

Figure 24.5 Comparative cure of another SBR rubber and its nanocomposite [10]

Thus, cure time is reduced, and the shear modulus at cure temperature is also reduced by the presence of the treated clay, indicating a looser crosslink network. Interestingly, the scorch time is slightly lengthened.

Another study [9] found octadecyl amine to accelerate the vulcanization by itself, though even more effectively as a cation in the clay gallery; there was no change in vulcanization characteristics of a pristine clay composite.

Reinforcement depends upon the degree of delamination and dispersion of the layered silicates in the rubber matrix. Al-Yamani and Goettler [8] report the addition of a dispersion agent to the treated clay that serves to increase M_{400} rubber modulus an additional 20% by promoting the degree of dispersion of the clay platelets. Since they possess two mesoscale dimensions (between 100 and 1000 nm) in the plane of the platelet, montmorillonite can be added as a secondary reinforcement to nanoscale carbon black or silica. Unfortunately, while tensile strength of a gum rubber may be increased by some 400% at a volume loading of only 2%, layered silicates confer little further reinforcement in black rubber compounds. Furthermore, hysteresis loss is generally increased, perhaps due to incomplete tethering of the rubber chains to the large interfacial areas representing the walls of the silicate galleries.

Synergy, however, is achieved in nanoscale–microscale hybrid composites, such as the dual reinforcement of nitrile rubber with layered silicates and wood cellulose pulp fibers [10], with regard to tear resistance. Layered silicate inclusions enhance tear resistance with or without the presence of microscale cellulose fibers, which by themselves are detrimental to tear resistance at high concentration when the tears can easily propagate parallel to the direction of locally aligned fibers. The nonlinearity of the tear dependence on clay and cellulose content indicates a synergistic effect that exceeds linear additivity. However, cellulose fibers provide more reinforcement for tensile strength than do nanoscale platelets. Thus, the combination of these two reinforcements produces a multiscale composite with both enhanced strength and tear resistance.

With their similar discontinuous nature characterized by high aspect ratio, layered silicate nanoplatelets can be expected to open up design and processing opportunities in reinforced rubber analogous to microscale short fibers, with the additional advantage of maintaining a less heterogeneous structure due to their smaller size. Thus, applications in industrial rubber goods such as hosing, belts, seals and moldings should be feasible, although these are largely yet to be satisfactorily demonstrated for commercial manufacture. Two important differences, however, need to be taken into account: mechanically, the layered silicates have the potential for imparting higher stiffness due to their higher modulus (versus flexible cellulose fibers) or greater aspect ratio (versus brittle glass fibers), while imparting a lesser degree of strengthening that can be attributed to their smaller size and generally inadequate adhesion to the rubber matrix. Furthermore, while both forms of reinforcement improve dimensional stability, the layered silicate's two-dimensional shape will develop less anisotropy in the fabricated part than the one-dimensional fiber that is more easily oriented by the fabrication flows. In both cases, the benefits of the resiliency and elasticity of the rubber matrix may be sacrificed [11].

Any type of discontinuously reinforced composite will benefit from the good economics of flow processing, although some aspects of processability such as mill banding (due to reduced shrinkage) and drawability (due to reduced die swell and extension in the green state) may be impeded at higher concentration level [12]. For application as a filler in transmission v-belts, the layered silicate platelets could serve to resist compressional stresses in the pulley grooves, while still allowing some measure of axial flexibility. Orienting the platelets in the plane of sheeting material would impart longitudinal stability in die cut nanocomposite seals, while

facilitating swell in thickness in order to maintain a tight joint. Such an orientation should result naturally from the squeezing flow used to form the sheet. In hoses, the orientation should be transverse to the extrusion direction to provide the necessary resistance to hoop and swelling stresses, while maintaining hose flexibility. Extrusion dies like those demonstrated by Goettler *et al.* [13] for forming effective short fiber reinforced rubber hoses may be similarly operative with layered silicate nanocomposite rubber stock.

24.2 Rubber Nanocomposites in Tire Engineering Applications

The incorporation of nanocomposites into tire components is driven by potentially higher overall performance, especially focused on fuel efficiency through reduced weight and energy absorption from rolling resistance and more favorable economics deriving from easier processing, reduced complexity of construction and substitution of less expensive polymers. These general motivations translate into specific development targets regarding:

- Extension of the *magic triangle* of tire tread performance:
  - Reduced heat build-up (rolling resistance);
  - Improved traction;
  - Better wear.
- Enhanced air retention;
- Colorability/transparency;
- Reduced heat build-up, leading to fewer tire failures;
- Elimination of halogenated butyl resulting in easier disposal and/or recyclability.

While specialty rubber types are usually employed in specific tire components, a generic formulation for an SBR rubber nanocomposite matrix might comprise (see Table 24.2):

Table 24.2 Baseline formulation for SBR nanocomposite

Ingredient	Phr
Rubber	100
Carbon black	50
Oil	15
Stearic acid	1
Zinc oxide	5
Sulfur	2
Accelerators	2

24.2.1 Tread

Incorporation of silica, Boehmite (alumina) and fullerene black into tire tread formulations allow relaxation of formulation constraints in balancing heat build-up, traction and abrasion resistance, thus allowing greater latitude in composition and better optimization of overall tire performance.

In SBR tread compounds, AlOOH produces 8–20% hysteresis reduction, about the same as for silica reinforcement. It is estimated that a 20% reduction in hysteresis yields 4% fuel

savings, which amounts to about 5×10^9 gallons (19×10^9 l) or US$ 10×10^9 savings to consumers annually [14]. As a consequence, there are also reduced CO_2 emissions.

Fumed silica particles are used in tire applications, but they have become more important since the introduction of the Green Tire premium product by Michelin Europe in 1992 [15], representing a combination of HDS silica, TESPT silane, high T_g solution SBR and low T_g BR in the tire tread. As a filler, silica has greater reinforcing power, such as improving tear strength, abrasion resistance, age resistance and adhesion properties, compared to carbon black [16–18]. However, due to the strong interparticle hydrogen bonds between hydroxyl groups, the agglomeration nature of silica is generally believed to be responsible for considerable rolling resistance in tire applications. To improve silica–rubber interaction and, in turn, to reduce the rolling resistance, different strategies were developed including chemical modifications of rubbers by attaching functional groups interacting with silica and surface treatments of silica with different silane coupling agents. Compounding with silica enables tire technicians to reduce the filler content due to great reinforcing power of silica. A decrease in filler content corresponds to a higher amount of elastic rubber in proportion to the damping filler phase in the compound and is an effective way to reduce rolling resistance by 20%, fuel usage by 3–4% and hysteresis by 50%.

Carbon blacks of high surface area provide good traction and abrasion resistance in tire treads; those of large particle diameter or wide range of aggregate size (structure) reduce rolling resistance. Fullerene carbons having a lower specific gravity than conventional carbon black can be used economically along with carbon black to optimize the performance characteristics of tread compounds [19].

NanoProducts Corporation had reported in 2003 the successful use of its nanoscale materials to produce tires (currently commercially available) with improved skid resistance and reduced abrasion [20]. According to the inventors, silicon carbide was used to prepare elastomeric nanocomposites that exhibit superior properties over conventional materials [20]. The performance data published in the patent demonstrated the successful dispersion of nanoscale materials in elastomers as well as the highest improvement in wet skid resistance (over other tested materials) and a nearly 50% reduction in abrasion. As reported by the inventors, silicon carbide-derived nanocomposites perform better than products with no additives or composites with conventional additives such as nanoscale fumed silica. Improved wet skid resistance resulted in superior safety, and reduced abrasion provided extended life.

It has been already demonstrated that the use of brominated isobutylene-co-paramethylstyrene (BIMS) improved dynamic properties of wet and winter traction tire treads [21]. Silane-coupled and silica-filled compounds were prepared with BIMS, *cis*-polybutadiene (BR) and natural rubber (NR). It has been found that vehicles having tires with BIMS winter treads showed reduced braking distances on an indoor ice surface, on a snowy glacier, on a wet asphalt surface and on a dry surface compared to both the control and reference winter treads.

Innovative carbon blacks, silicas and a new rubber silane were used in tire systems for improved rolling resistance [22, 23]. In particular with the new silane VP Si363 a significant reduction of the rolling resistance of passenger tires by more than 10% was achieved. Simultaneously the emission of volatile organic compounds (VOCs) was cut by up to 80%. A new class of silicas with an exceptional morphology provided also a significant drop in hysteresis and simultaneously improved the reinforcement of rubber compounds. It has been also found that carbon black with extremely low surface area provided an excellent compromise between hysteresis and abrasion resistance and therefore was especially dedicated for application in truck tire treads.

Natural rubber vulcanizates were reinforced with *in situ* formed nanoscale silica particles of around 40 nm diameter using a sol-gel process [24]. The prepared sol-gel nanocomposites showed much higher London dispersive component of free energy compared with conventional melt-mixed composites. Also, much lower frictional coefficients were found for the sol-gel nanocomposites. The abrasion resistance of the nanocomposites was proven to be superior to that of meltmixed composites. Similar behavior in terms of significantly improved modulus and tensile strength was found for natural rubber or SBR rubber matrix vulcanizates prepared with organoclay (fluorohectorite modified by octadecylammonium with interlayer distance 2.24 nm) [25, 26], suggesting that reinforcement and hysteresis are related to the anisotropic nature of the aggregates and concomittant orientation during strain.

24.2.2 Innerliner

The room temperature gas permeability of classical elastomers (Table 24.3) is high relative to glassy polymers. Nevertheless, many pneumatic products, including tire innerliners, are made from elastomers and they must be periodically refilled with air.

Table 24.3 Oxygen permeability of selected rubbers

Rubber	O_2 [$cmm^3{*}mm/m^{2*}day^{*}atm$]
Silicone rubber	100 000
Natural rubber	5000
SBR	1000
Neoprene	500
Butyl rubber	100

Therefore, many attempts have been made to improve the barrier properties of elastomers by incorporating high aspect ratio fillers (such as exfoliated clay minerals) [27–29]. Their high asperity planar geometry makes exfoliated layered silicates ideal barriers for permeation, as in retarding air loss through the tire innerliner. A commonly accepted mechanism for this accomplishment is the increase in path tortuosity experienced by a permeating small molecule species, thus lengthening the diffusion path and so reducing the concentration gradient and hence the diffusive flux (Figure 24.6).

A two-dimensional idealized model for the permeation rate reduction according to these concepts is given by Nielsen [30] as $P_f/P_p = V_p/[1 + (L/2W)V_f]$. Following earlier work by Kojima *et al.*, [31] the permeability of intercalated layered silicate NBR nanocomposites has been found [32] to decrease substantially with increasing clay loading according to this model, though barrier enhancement can be further augmented through optimal selection of the cationic surface treatment. Another model, for aligned randomly dispersed platelets [33], is $P/P_o = \exp(-(x/x_o)\beta)$, where x is the product of platelet aspect ratio and its volume fraction, f. The authors found a good data fit using $\beta = 0.71$ and $x_0 = 3.47$. If the platelets are in addition randomly oriented, their barrier efficiency drops to around 50% [32, 34].

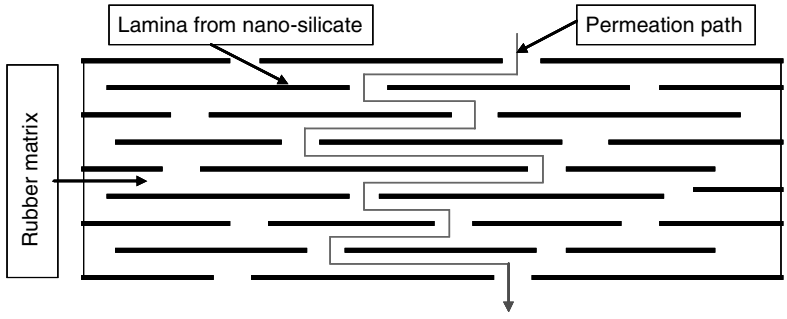

Figure 24.6 Increased path tortuosity for permeation through a layered silicate nanocomposite containing exfoliated platelets

A secondary effect on permeability derives from molecular changes in the matrix in the vicinity of the platelet interface. In addition, the cross-sectional area available for transport through the film is reduced.

By using exfoliated vermiculite as a layered silicate filler, for example, elastomeric dispersions have been developed as a new class of elastomeric nanocomposite barrier coatings [35, 36] with good dispersion and stability of the exfoliated vermiculite in butyl rubber. In this way, coatings that maintain a high degree of flexibly along with excellent barrier properties have been developed. These coatings will enable rubber products to be developed with good barrier properties.

Isobutylene-based polymers are well known to exhibit a high resistance to small molecule permeation from their tight molecular packing that finds application in tire innertubes and innerliners. A baseline bromobutyl rubber innerliner formulation is given in Table 24.4 (TDA Research [14]). Inclusion of usually an alkyl-based organomontmorillonite clay further enhances the permeation barrier through its favorable, though restricted dispersion. Organoclay effects on the vulcanization of these like other rubbers can be problematic.

Table 24.4 Innerliner formulation

Ingredient	Phr
Bromobutyl resin	100
Carbon black	55
Naphthenic oil	6.0
Stearic acid	1.0
Phenolic resin tackifier	4.0
Struktol 40 MS	8.0
Magnesium oxide	0.15
Zinc oxide	2.0
Sulfur	0.5
MBTS	1.5

As developed by ExxonMobil using Exxpro polymers, a brominated isobutyl methylstyrene (BIMS) rubber blend nanocomposite with montmorillonite reduces air permeation by 38%

below that of a totally bromobultyl rubber formulation without the smectic clay [37]. Moreover, this technique is less expensive and offers weight savings of up to 1 kg for large truck tires that results in a higher fuel efficiency. Additional benefits are that tire curing is speeded up by the higher thermal conductivity induced by the clay, which also dissipates hot spots at local failure points in service; and the resulting tires are 20% more durable due to the improved inflation retention. Further, thermal stability is enhanced by the clay simultaneously limiting oxygen diffusion through the liner into the internal tire rubber.

In another publication, by Tsou and Measmer [38], ExxonMobil reports on the permeation barrier generated by organolayered silicate dispersion in BIMSM and BIIR rubbers. Aspect ratios of the dispersed silicates back-calculated from permeation data according to the Gusev–Lusti equation showed BIMSM to be the preferred dispersant and the presence of carbon black to be inconsequential.

Butyl rubber nanocomposites made by exfoliating octadecyl primary ammonium organophilic clay via melt intercalation with MA-g-IIR compatibilizer produced a 2.5× gas barrier at 15 phr clay concentration [39].

TDA Reseach, Inc. (Wheat Ridge, Colo., USA) reports [14] that Boehmite AlOOH nanoparticles measuring 1–2 nm thick, 10–20 nm wide and 2–200 nm long incorporated at 5–10% loading in BIIR can produce 20% OTR reduction with little change in mechanical properties. It should be noted that oxygen permeation rates are controlling for air retention since the nitrogen component's permeation is considerably slower. While carbon nanotubes are considered to engage in network formation within rubber nanocomposites, they would not be as effective in permeation resistance as platy montmorillonite inclusions.

Novel SBR copolymer nanocomposites comprising rectorite, a 1 : 1 type layered structure with aspect ratio higher than montmorillonite, prepared by co-coagulating latex and the layered silicate in a water suspension achieve a good permeation barrier in comparison to N330 carbon black reinforcement [40].

The technology developed in 1996 between Michelin and Hoechst Celanese, further patented by InMat [41] gave more potential in the tire market through special tire liners containing smectic silicates enabling tires to hold air longer with reduced weight, which led to better gas mileage. InMat's Air D-Fense product combines butyl rubber with exfoliated vermiculite in a 20-μm coating that can be applied in tire innerliners. Thinner coating that used less butyl rubber also made recycling tires easier and more environmentally friendly.

Different layered clay minerals in the range 100–1400 μm dispersed in the elastomer matrix [42] allows the production of tire innerliners having sufficiently low air permeability. The polymer matrix suitable for preparation of such innerliners can be made of natural rubber, polybutadiene and its copolymers, copolymers of isobutylene, isoprene, paramethyl styrene, to mention only a few. Layered materials useful for preparation of such systems include natural and synthetic minerals capable of being intercalated and having individual layer thickness up to 20 nm and a diameter up to 10 μm, such as montmorillonite, hectorite and vermiculite, to mention only a few. Importantly, these clay minerals should have a cation exchange capacity up to 150 milliequivalents per 100 g. Such layered minerals can be modified with swelling agents by contacting the layered mineral with the swelling agent in an appropriate liquid or flowable dispersant.

Mulhaupt and coworkers prepared rubber nanocomposites based on butadiene rubber (BR) and styrene/butadiene rubber (SBR) containing organophilic-layered silicates [43]. The authors prepared organophilic silicates swollen in a rubber/toluene solution, thus achieving

an interlayer distance increased from 1.26 nm for montmorillonite to 2.59 nm for the organoclay.

Intercalation of a montmorillonite nanoclay with a tetralkylammonium salt gave a rubber compound (a carbon black filled NR/SBR) with lower hysteresis, lower heat build up under dynamic conditions and significantly reduced compression set [44]. Good results in terms of well dispersed silicate layers in the rubber matrix were obtained by Kojima who prepared montmorillonite cation-exchanged with amine terminated butadiene oligomer (ATBN) in a solvent mixture of N,N′-dimethylsulfoxide, ethanol and water [45]. After this, organophilic montmorillonite was blended with acrylonitrile/butadiene rubber (NBR) by roll milling, and the rubber was vulcanized with sulfur. According to TEM observations, the silicate layers were well dispersed in the rubber matrix. The tensile stress at 100% elongation of this rubber–clay nanocomposite, containing 10 phr of montmorillonite, was equal to that of rubber containing 40 phr of carbon black. In this rubber-clay nanocomposite, the permeability of hydrogen and water decreased by 70% by means of adding 3.9 vol% montmorillonite. In general, the benefits achievable through the use of nanocomposites in innerliners, particularly in the area of permeability reduction, are one of the most important considerations for advanced rubber technology [46].

Exfoliated graphite dispersed into nanosheets having a thickness from 100 to 400 nm was intercalated with polybutadiene, styrene-butadiene rubber, and polyisoprene elastomers to produce pneumatic tires (for passenger cars, motorcycles and trucks) [47]. Other related pneumatic applications utilizing the permeation reduction produced by incorporation of layered silicates could include tire innertubes, air springs and curing bladders [48].

The various mechanisms of rubber reinforcement by active fillers and related to the specific properties of high performance elastomer goods were considered [49]. In particular, an analysis of filler flocculation and clustering on nanoscopic and mesoscopic length scales gave some quantitative insight into the morphology of filler networks. Based on this analysis, a scaling approach for the variation of the small strain modulus with filler concentration was described as well as a recently developed micromechanical material model of stress softening and filler induced hysteresis of reinforced rubbers, considering the breakdown and reaggregation of filler clusters.

24.2.3 Other

Layered silicate nanoscale reinforcements are also applicable to bead filler and chafer strips for stiffening of the upper sidewall, and to belt edge stiffening [37]. There are no benefits mentioned to chipping and chunking resistance in heavy duty tires, unlike the case for cellulose short fibers. There are similarly no reports of layered silicates reducing cord shadowing in tire innerliner applications.

24.3 Rubber Nanocomposite Membranes

Traditionally, the addition of impermeable particles to rubbery polymeric membranes reduces light gas and vapor permeability as particle loading increases. This phenomenon is well known for barrier materials. The reduced gas and liquid permeability of nanofilled polymers makes them attractive membrane materials. According to theoretical predictions [50], the higher the

aspect ratio of the filler, the larger is the decrease in permeability. The effect of the different aspect ratio of organoclays such as montmorillonite (MMT) and fluorohectorite (FHT) bearing the same type of intercalant (that is, octadecylamine, ODA) was best reflected in the oxygen permeation measurements for hydrogenated nitrile rubber (HNBR)/organophilically layered silicate nanocomposites [51]. Increasing aspect ratio (MMT < FHT) resulted in higher stiffness under uniaxial tensile loading. The dispersion state ("secondary structure") of the organophilic layered silicates reduced dramatically the oxygen permeability of the rubber matrix based on the labyrinth principle. The lowest oxygen permeability was measured for the HNBR/FHT-ODA films in which the layered silicates had the highest aspect ratio. According to the authors, the organo fluorohectorite created a more extended tortuous path against gas penetration compared to organomontmorillonite, thus, lower permeation values.

Recently, nonporous metal oxide nanoparticles (primary particle diameter as low as 2.5 nm) have been dispersed in rubbery polymer to make membranes that have over an order of magnitude higher light gas (that is, CO_2, N_2, O_2, H_2) permeability with little or no change in selectivity relative to the neat polymer, which runs counter to traditional filler rubbery polymers [52]. For example, the CO_2 permeability was 1100 barrers in filled 1,2-butadiene, as compared to 52 barrers for the unfilled polymer. For both materials, the CO_2/N_2 selectivity was 14, at 35 °C and 3.4 atm. Furthermore, nanocomposites with rubbery matrices often exhibit significantly improved gas transport behavior at low temperatures. Both light gas permeability and selectivity increases substantially with decreasing temperature. However, in some of these materials the gas transport enhancements are limited by the onset of nanoparticle-induced polymer crystallization, as characterized by permeation and DSC experiments.

Nanocomposite films of polypropylene/styrene-ethylene-butylene-styrene (PP/SEBS) and organoclay were sheet-extruded with differing clay concentrations [53]. Blends were compounded using a high shear single screw reciprocating kneader. Results demonstrated that higher clay content increased the Shore A hardness of the films but induced a significant improvement in both O_2 and CO_2 barrier performance.

NBR/graphite nanocomposites possess significantly improved wear resistance and gas barrier properties, and superior electrical/thermal conductivity [54]. Such versatile functional properties make NBR nanocomposites a promising new class of advanced materials. Rubber–pristine clay nanocomposites prepared by co-coagulating rubber latex and clay aqueous suspension prepared by latex compounding containing graphite nanosheets into elastomeric polymer matrix gave high-performance elastomeric nanocomposites with improved mechanical and functional properties.

Nanostructured layered silicates compounded with natural rubber (NR), carboxylated styrene butadiene rubber (XSBR) and their 70/30 latex blend were investigated for membrane applications and their solvent resistance properties were measured by the equilibrium swelling method using benzene, toluene and *p*-xylene [55]. The layered nanostructured sodium bentonite and sodium fluorohectorite were used as nanofillers. Nanocomposite of natural rubber (NR), carboxylated styrene butadiene rubber (XSBR) and their blends showed reduced swelling rate due to the tortuosity of the path and the reduced transport area in polymeric membrane.

Excellent gas barrier properties were found for butyl rubber/vermiculite nanocomposites [56]. The formulations consisting of a butyl rubber latex (the rubber particles are about 1 μm in diameter) to which exfoliated vermiculite was added (at 30 wt%) for which an independent gas sorption isotherm experiments for CO_2 were measured and found to be larger

than that in butyl rubber possibly due to adsorption on the vermiculite. It was also found that the transient tortuosity factor defined by the time lag was significantly larger than the steady-state tortuosity factor defined by permeability.

Significantly decreased gas permeability was found for several rubber–clay nanocomposites, including styrene butadiene rubber (SBR)–clay, natural rubber (NR)–clay, nitrile butadiene rubber (NBR)–clay, carboxylated acrylonitrile butadiene rubber (CNBR)–clay nanocomposites, prepared by directly co-coagulating the rubber latex and clay aqueous suspension [57]. X-ray diffraction (XRD) patterns and transmission electron microscopy (TEM) micrographs showed that these nanocomposites possessed a unique structure, in which the rubber molecules "separated" the clay particles into either individual layers or just silicate layer aggregates of nanometer thickness without the intercalation of rubber molecules into clay galleries, different from intercalated and exfoliated clay nanocomposites. According to the authors, this unique structure resulted in increased glass transition temperature and the tensile strength, where for the SBR–clay nanocomposite containing 20 phr clay, the strength was 6.0 times higher than that of the conventional SBR–clay composite. The gas permeability of separated rubber–clay nanocomposites containing 20 phr decreased 50% as compared with the corresponding gum vulcanizates.

24.4 Applications of Rubber Nanocomposites in Sporting Goods

Using butyl rubber as the matrix, and very high aspect ratio vermiculite filler, flexible coatings with gas permeability 30–300 times lower than butyl rubber have been produced. These coatings have been shown to be undamaged by strains up to 20%. The first commercial application of this technology (sold under InMat's trademark Air D-Fense) is in Wilson's new, longer life, Double Core tennis ball, the official ball of the Davis Cup [39, 58]. With its functional nanocomposite coating approach, InMat implemented solutions to a generic problem in the rubber industry – too high a permeability for most of its applications. A thin, flexible coating that combines butyl rubber polymers with vermiculite forms the unique coating. The new tennis balls using this coating retain air longer, and are able to bounce twice as long as ordinary balls (improvement in air retention).

Another interesting solution for sport applications is nanosized $CaCO_3$ used in combination with different elastomers [59]. The reinforcing effect of nano$CaCO_3$ in different compounds – NR and NR/NBR blends was used in sports goods such as laminated sheet for inflated balls and NR based cycle tubes with improved barrier properties and air retention.

A golf ball with an intermediate nanocomposite layer contains exfoliated graphite nanostructures having a thickness <5 nm dispersed in elastomeric matrix of NR, polyisoprene, polybutadiene, SBR, styrene-propylene or ethylene-diene block copolymer rubbers, to mention only few [60].

Thermoplastic elastomer polyurethanes (TPU) used for footwear applications as shoe soles have already well established position on the market. However, different new formulations containing nanoparticles were developed to improve the dry sliding behavior of TPU of various types and hardness values [61]. Organoclays with various intercalants were incorporated at 5 wt% in the TPUs. It was found that the friction and wear characteristics were moderately influenced by the type of the organoclay albeit the dispersion state of the latter was highly different in the corresponding TPU nanocomposites. The organoclay reinforcement altered the wear mechanisms,

compared to the neat versions. TPU systems with high hardness showed lower friction coefficient and higher resistance to wear than those of lower hardness. The fact that friction and wear characteristics did not change much by contrast to the clay dispersion were attributed to changes in the (super)molecular structure of the TPU owing to the organoclay modification.

24.5 Advanced Nanocomposites for Airspace Applications

With rapid advancement of nanotechnology in rubber industry, organoclay and other nano fillers are introduced to HNBR elastomers as a new filler system leading to high-performance nanocomposites to meet the increasing demand of aerospace industry [62] for extremely high operating temperatures and extended material service lifetime (improved thermal stability and air/water/oil resistance of HNBR elastomer at extremely high temperatures) [63]. In HNBR/clay nanocomposites exposed to high temperature the organoclay layers provide effective barriers and tortuous path to heat, oxygen, water and oil evolved, thus slowing the rate of mass loss during thermal decomposition of HNBR/clay nanocomposites.

Metal Rubber is the first material of its kind, a self-assembled free-standing electrically conductive elastomer in aerospace areas [64]. Metal Rubber is a novel nanocomposite formed via the self-assembly processing of metal nanoparticles and elastomeric polyectrolytes. This type of processing allows for control over bulk mechanical and electrical properties and requires only ppm quantities of metal to achieve percolation. The use of nanostructured precursors also results in transparent, electrically conductive nanocomposites. Metal Rubber elastomers are being developed as sensors to detect fatigue, impact and large strain for aerospace applications. This novel material may be formed as a conformal coating on nearly any substrate or as free standing films [65]. There are other aspects of using nanocomposites in aerospace applications.

Polymer composites containing ferrites are increasingly replacing conventional ceramic magnetic materials because of their moldability and reduction in cost [66]. They are also potential materials for microwave absorbers, sensors and other aerospace applications. These flexible magnets or rubber ferrite composites are made possible by the incorporation of magnetic powders in various elastomer matrices. This modifies the physical properties of the polymer matrix considerably. γ-Fe_2O_3 dispersed natural rubber exhibited fine dispersion of iron oxide particles in the rubber matrix. The dispersed particles had irregular shape and showed agglomeration.

Electromagnetic absorbers are a critical part of electronic systems in applications such as electromagnetic shielding for air vehicles and wireless communications [67]. However, the existing electromagnetic absorption materials have several drawbacks: heavy, less durable and effective only over fixed frequency bands. One way to improve the current electromagnetic absorbers is to exploit polymer composites reinforced with magnetic nanoparticles (NPs). The polyurethane (PU) composites reinforced with magnetic NPs having an iron core/iron oxide shell structure were fabricated by the surface-initiated polymerization (SIP) method. SIP was observed to fabricate a high particle loading of up to 65 wt% in a polyurethane matrix while still maintaining the structural integrity. The calculated metal-backed reflection loss indicated that the Fe-PU nanocomposite can be used at a substantial weight savings in a discrete frequency absorption application, when compared with the CIP-PU composite and the commercially available electromagnetic absorbers. These findings offer the feasibility of developing lighter-weight microwave absorbers by using magnetic nanocomposites.

24.6 Nanorubbers in Medicine and Healthcare

One of the best known example of elastomer used in medicine is a medical grade silicone elastomer filled with silica and saline-filled mammary prostheses for breast augmentation and reconstruction [68]. Different data, however, confirmed that silicone implant patients responded immunologically to the silicon dioxide contained in mammary prostheses and used as a reinforcing agent [69]; therefore their usage, although again approved by FDA, is still controversial.

Milliken Chemical Speciality Elastomers offers an Elastoguard, a pro-active antimicrobial rubber (HNBR- or EPDM-based) that provides residual protection against microbial contamination due to silver nanoparticles, thereby dramatically reducing the necessity for a traditional routine decontamination service agenda [70]. It incorporates a zirconium phosphate-based ceramic, ion-exchange resin containing silver, which is acknowledged to be safe for human contact, and it recognised for its antimicrobial effectiveness against a broad spectrum of microorganisms. Unlike most organic biocides, Elastoguard can be used in food contact situations and is designed for use in pharmaceutical and medical industries.

InMat's elastomer nanocomposite is also tested as coatings for medical packaging. Metal Rubber, successfully tested for airspace applications has also been evaluated at NASA's Jet Propulsion Laboratory to determine its suitability for artificial muscles [71]. Another interesting material for medical applications is natural rubber latex (NRL) containing silver salt. Silver nanoparticles are formed in a natural rubber matrix via photo reduction of film cast. The nanoparticles, diameters ranging between 4 and 10 nm, are dispersed within distinct interfaces which correspond to the interparticle boundaries of the NRL particles that form the matrix. A comparison with the results of formation of silver in different rubber matrices suggests that the protein in natural rubber is responsible for the formation of stable silver nanoparticles in the natural rubber (NR) matrix [72].

A novel nanocomposite coating was developed by researchers from Dundee University to create antibacterial coatings [73]. The coating applied on a polymer by a low-temperature plasma deposition technique consisted of silver (Ag) and platinum (Pt). The Ag-Pt together act as "nanoelectrodes", using the body fluids or mucosa as electrolyte to control silver ion release. The negatively charged biocompatible polymer attracts silver cations to the device surface to kill any local or approaching bacteria and inhibit silver ions releasing into the body fluids, providing extended protection. Such an Ag-Pt polymer system is very promising for urinary catheters since it can provide greatly improved antimicrobial efficacy and much longer duration antimicrobial efficacy.

Inherent properties of elastomers such as elasticity which allows good sealing properties, low gas and water permeability, excellent oil resistance and a low level of migrating substances from rubber products are relevant for the application of NBR rubbers in food, pharmaceutical and cosmetics [74].

Nanocomposites comprising biocompatible thermoplastic elastomer matrices and inorganic nanoparticle fillers represent a new group of composite biomaterials for tissue engineering scaffolds and biomedical implants and devices. It has been demonstrated that addition of ceramic nanoparticles, such as alumina or titania, to polymer matrices greatly influences their mechanical, physical and biological properties [75, 76]. Recently, thermoplastic multiblock polyester elastomers were fabricated by *in situ* polycondensation with TiO_2 (0.2 wt%) nanoparticles giving an impressive improvement of fracture strength (100%) and elongation at fracture (300%; Figure 24.7). The potential of these elastomeric nanocomposites is seen in soft tissue engineering (tendon implants or shells of breast implants after additional modification).

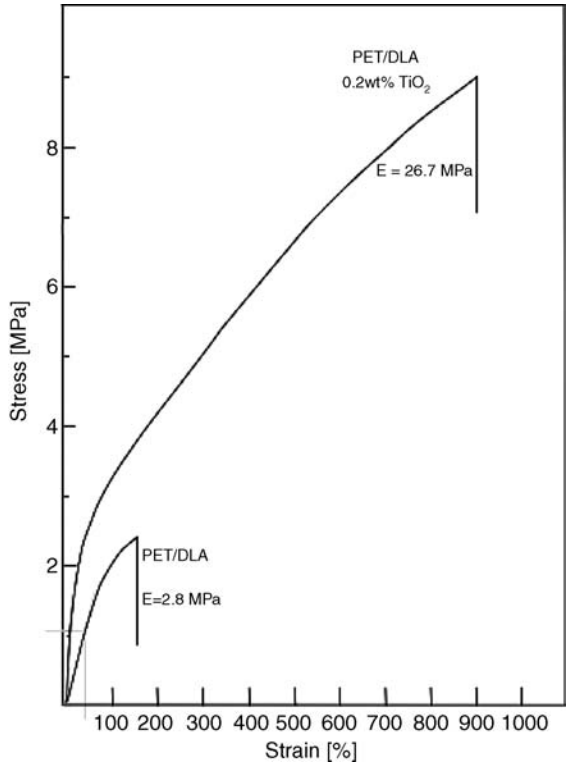

Figure 24.7 Stress–strain curves for thermoplastic elastomer (poly(ethylene terephthalate)PET/ester of dilinoleic acid, DLA) and its nanocomposite with 0.2 wt% TiO_2

Table 24.5 Some trade names of rubber nanocomposites

Trade name (supplier)	Rubber	Nanofiller	Note
Air D-Fense, Willson Double Core (InMat LLC)	Butyl rubber	Vermiculite	Innerliners and sporting goods
NanoTech Elite H-D + (Zhermack)	Vinylpolysiloxanes	Silicate	Dentistry
Metal Rubber (NanoSonic Inc.)	Piezoelectric or conductive rubber	Nanoclusters of Pt, Pd, Ni, Ti and metal clusters	Electrically conductive elastomer for aerospace applications
Elastoguard® (Milliken Chemical Speciality Elastomers)	H-NBR, EPDM	Silver	Antimicrobial properties, medical and pharmaceutical applications

24.7 Conclusions

Although much progress has been made in nanocomposite development (Table 24.5), continuing advances would facilitate a broader range of applications. Further commercialization of rubber nanocomposites will likely depend on optimizing their structure, dispersion and interfacial properties for broader mechanical and physicochemical performance. Better economics will ensue as volumes grow along with methodolgies for efficient and consistent manufacturing. But enhanced reliability in applications will depend on rapid and accurate characterization procedures that can be used for quality assurance and control. Finally, health and environmental issues must be identified and addressed.

References

1. Mai, Y-.W. and Yu, Z-.Z. (eds) (2006) *Polymer Nanocomposites*, Woodhead Publishing Limited, Cambridge, pp. 297–325.
2. Holden, G., Kricheldorf, H.R., and Quirk, R.P. (eds) (2004) *Thermoplastic Elastomers*, Hanser, Munich, pp. 493–520.
3. Goettler, L.A., Lee, K.Y., and Thakkar, H. (2007) Layered silicate reinforced polymer nanocomposites: development and applications. *Polymer Reviews*, **47**(2), 291–317.
4. Kastein, B. (1982) A historical view – carbon black in tire treads. *Rubber World*, **187**, 44–46.
5. Kalkan, Z.S. and Goettler, L.A. (2006) Co-in-situ polymerization of polyamide 66 nanocomposites via interfacial polycondensation using sol-gel chemistry. Society of Plastics Engineers Annual Technical Conference May 2006.
6. Maiti, M., Sadhu, S., and Bhowmick, A.K. (2004) Brominated poly(isobutylene-co-paramethylstyrene) (BIMS)–clay nanocomposites: synthesis and characterization. *Journal of Polymer Science Part B-Polymer Physics*, **42**, 4489–4502.
7. Kato, M., Tsukigase, A., Tanaka, H. *et al.* (2006) Preparation and properties of isobutylene-isoprene rubber–clay nanocomposites. *Journal of Polymer Science Part A – Polymer Chemistry*, **44**, 1182–1188.
8. Al-Yamani, F. and Goettler, L.A. (2007) Nanoscale rubber reinforcement: a route to enhanced intercalation in rubber-silicate nanocomposites. *Rubber Chemistry and Technology*, **80**(1), 100, presentation at ACS Rubber Division, 168th Technical Meeting, Pittsburg, PA USA, Nov. 1–3, 2007, Paper No. 43.
9. Lopez-Manchado, M.A., Arroyo, M., Herrero, B., and Biagiotti, J. (2003) Vulcanization kinetics of natural rubber–organoclay nanocomposites. *Journal of Applied Polymer Science*, **89**, 1–15.
10. Benes, M. and Goettler, L.A. (2002) Improved properties of short fiber rubber composites through nanoscale co-reinforcement. ACS Rubber Division, Savannah, Georgia, USA; April 29-May 1, Paper No. 5.
11. De, S.K. and Murty, V.M. (1984) Short fiber–rubber composites. *Polymer Engineering Reviews*, **4**(4), 313–343.
12. Goettler, L.A., Sezna, J.A., and DiMauro, P.K. (1982) Short fiber reinforcement of extruded rubber profiles. *Rubber World*, **187**, 33.
13. Goettler, L.A., Leib, R.I., and Lambright, A.J. (1979) Short fiber reinforced hose – a new concept in production and performance. *Rubber Chemistry and Technology*, **52**, 838–863.
14. Myers, A., Cook, R., Kreutzer, C. *et al.* (2008) "Rocks in the road: nanoparticle design for improved tire performance", report on SBIR Project, US Department of Energy.
15. Peng, Ch.-Ch., Gopfert, A., Drechsler, M., and Abetz, V. (2005) "Smart" silica-rubber nanocomposites in virtue of hydrogen bonding interaction. *Polymers for Advanced Technologies*, **16**, 770–782.
16. Cochet, L., Barriquand, Y., Bomal, S., and Touzet, S. (1995) Precipitated silica in tire tread. Paper presented at a meeting of ACS, Rubber Division, Cleveland, Ohio.
17. Ou, Y.C., Yu, Z.Z., Vidal, A., and Donnet, J.B. (1996) Effects of alkylation of silicas on interfacial interaction and molecular motions between silicas and rubbers. *Journal of Applied Polymer Science*, **59**, 1321–1325.
18. Gatti, L. (2001) Compounding techniques to reduce silane in green tire formulations. *Tire Technology International Annual Review*, **2001**, 39.
19. Lukich, L.T. *et al.* (1998) Use of fullerene carbon in curable rubber compounds, US Patent 5750615, to Goodyear Tire and Rubber Co.

20. Wang, M., Kutsovsky, Y., Reznek, S.R., and Mahmud, K. (2002) Elastomeric compounds with improved wet skid resistance and methods to improve wet skid resistance, US Patent 6469089, to Cabot Corp.
21. Waddell, W.H., Rouckhout, D.F., and Steurs, M. (2003) Isobutylene elastomer compound optimization for winter tire tread applications. *Kautschuk Gummi Kunststoffe*, **10**, 525–532.
22. Niedermeier, W. and Schwaiger, B. (2007) Performance enhancement in rubber by modern filler systems. *Kautschuk Gummi Kunststoffe*, **04**, 184–187.
23. Klockmann, O. and Hasse, A. (2007) A new rubber silane for future requirements – lower rolling resistance; lower VOCs. *Kautschuk Gummi Kunststoffe*, **03**, 82–84.
24. Nah, C., Kim, D.H., Kim, W.D. *et al.* (2004) Friction and abrasion properties of in-situ silica-filled natural rubber nanocomposites using sol-gel process. *Kautschuk Gummi Kunststoffe*, **05**, 224–226.
25. Wu, You-Ping, Ma, Yong, Wang, Yi-Qing, and Hang, Li-Qun (2004) Effects of characteristics of rubber, mixing and vulcanization on the structure and properties of rubber/clay nanocomposites by melt blending. *Macromolecular Materials and Engineering*, **289**, 890–894.
26. Ganter, M., Gronski, W., Semke, H. *et al.* (2001) Surface-compatibilized layered silicates – a novel class of nanofillers for rubbers with improved mechanical properties. *Kautschuk Gummi Kunststoffe*, **04**, 166–171.
27. Kresge, E.N. and Lohse, D.J. (1996) Composite tire innerliners and inner tubs. US Patent 5,576,372.
28. Usuki, A., Tukigase, A., and Kato, M. (2002) Preparation and properties of EPDM-clay hybrids. *Polymer*, **43**, 2185–2189.
29. Kojima, Y. *et al.* (1993) Gas permeabilities in rubber–clay hybrid. *Journal of Materials Science Letters*, **12**, 889–890.
30. Nielsen, L.E. (1967) Models for the permeability of filled polymer systems. *Journal of Macromolecular Science – Chemistry*, **A1**(5), 929.
31. Bandyopadhyay, A., Maiti, M., Bhowmick, A.K. (2006) Synthesis, characterisation and properties of clay and silica based rubber nanocomposites. *Materials Science and Technology*, **22**, 818–828.
32. Nah, C., Ryu, H.R., Kim, W.D., and Choi, S.-S. (2002) Barrier property of clay/acrylonitrile-butadiene copolymer nanocomposite. *Polymers for Advanced Technologies*, **13**, 649–652.
33. Gusev, A.A. and Lusti, H.R. (2001) Rational design of nanocomposites for barrier applications. *Advanced Materials*, **13**, 1641–1643.
34. Lusti, H.R., Gusev, A.A., and Guseva, O. (2004) The influence of platelet disorientation on the barrier properties of composites: a numerical study. *Modelling and Simulation in Materials Science and Engineering*, **12**, 1201–1207.
35. Goldberg, H.A., Feeney, C.A., Karim, D.P., and Farrell, M. (2002) Elastomeric barrier coatings for sporting goods. *Materials Research Society Symposium Proceedings*, **733E**, T.4.7.1–T.4.7.6.
36. Takahashi, S., Goldberg, H.A., Feeney, C.A. *et al.* (2006) Gas barrier properties of butyl rubber/vermiculite nanocomposite coatings. *Polymer*, **47**, 3083–3093.
37. Rogers, B., Webb, R., and Wang, W. (2006) Nanocomposite technology in tire innerliners. ACS Central Regional Meeting, Frankenmuth, Mich.; 16–20 May, Paper No. 140.
38. Tsou, A.H. and Measmer, M.B. (2006) Dispersion of layered organosilicates in isobutylene-based elastomers. *Rubber Chemistry and Technology*, **79**, 281–306.
39. Kato, M., Tsukigase, A., Tanaka, H. *et al.* (2006) *Journal of Polymer Science*, **44A**, 1182–1188.
40. Wang, Y., Zhang, H., Wu, Y. *et al.* (2005) Preparation, structure and properties of a novel rectorite/SBR copolymer nanocomposite. *Journal of Applied Polymer Science*, **96**, 324–328.
41. Feeney, C.A., Goldberg, H.A., Farrell, M. *et al.* (2006) Barrier coating of a non-butyl elastomer and a dispersed layered filler in a liquid carrier and coated articles, US Patent 10741251, to InMat Inc.
42. Elspass, C.W., Peiffer, D.G., Kresge, E.N. *et al.* (1996) Tactoidal elastomer nanocomposites, US Patent 5807629, to Exxon Research Engineering Co.
43. Zigl, C., Mulhaupt, R., and Finter, J. (1999) Morphology and toughness/stiffness balance of nanocomposites based upon anhydride-cured epoxy resins and layered silicates. *Macromolecular Chemistry and Physics*, **200**, 661.
44. Cataldo, F. (2007) Preparation and properties of nanostructured rubber composites with montmorillonite. *Macromolecular Symposia*, **247**, 67–77.
45. Kojima, Y., Fukumori, K., Ususki, A. *et al.* (1993) Gas permeabilities in rubber–clay hybrid. *Journal of Materials Science Letters*, **12**, 884.
46. Rodgers, B., Webb, R.N., and Weiqing, W. (2006) Nanocomposite technology in tire innerliners. *Rubber World*, **234**, 36–41.

47. Lechtenboehmer, A. (2006) Pneumatic tire having a rubber component containing exfoliated graphite, USPTO Patent Application 20060229404, to Goodyear.
48. Gent, A.N. (ed.) (1992) Chapters 1 and 8, in *Engineering with Rubber. How to Design Rubber Components*, Hanser.
49. Klüppel, M. and Heinrich, G. (2005) Physics and engineering of reinforced elastomers: from molecular mechanisms to industrial applications. *Kautschuk Gummi Kunststoffe*, **58**, 217–224.
50. Cussler, E.I., Hughes, S.E., Ward, W.J. III, and Aris, R. (1988) Barrier membranes. *Journal of Membrane Science*, **38**, 161.
51. Gatos, K.G. and Karger-Kocsis, J. (2007) Effect of the aspect ratio of silicate platelets on the mechanical and barrier properties of hydrogenated acrylonitrile butadiene rubber (HNBR)/layered silicate nanocomposites. *European Polymer Journal*, **43**, 1097–1104.
52. Barrer, R.M., Barrie, J.A., and Rogers, M.G. (1963) Heterogenous membranes: diffusion in filled rubber. *Journal of Polymer Science Part A – Polymer Chemistry*, **1**, 2565–2586.
53. Small, C.M., McNally, G.M., McShane, P., and Kenny, I. (2007) Polypropylene/styrene-ethylene-butylene-styrene thermoplastic elastomer nanocomposite films. *Journal of Vinyl & Additive Technology*, **13**, 46–52.
54. Yang, J., Tian, M., Jia, Q.-X. *et al.* (2007) Improved mechanical and functional properties of elastomer/graphite nanocomposites. *Acta Materialia*, **55**, 6372–6382.
55. Stephen, R., Varghese, S., Joseph, K. *et al.* (2006) Diffusion and transport through nanocomposites of natural rubber (NR), carboxylated styrene butadiene rubber (XSBR) and their blends. *Journal of Membrane Science*, **282**, 162–170.
56. Choudalakis, G., Gotsis, A.D (2009) Permeability of polymer/clay nanocomposites: a review. *European Polymer Journal*, **45**, 967–984.
57. Wu, Y.-P., Wang, Y.-Q., Zhang, H.-F. *et al.* (2001) Structure of carboxylated acrylonitrile-butadiene rubber (CNBR)-clay nanocomposites by co-coagulating rubber latex and clay aqueous suspension. *Journal of Applied Polymer Science*, **82**, 2842–2848.
58. Goldberg, H.A., Feeney, C.A., Karim, D.P., and Farrell, M. (2002) Nanocomposite barrier coatings for elastomeric applications. *Materials Research Society Symposium Proceedings*, **733E**, T.4.7.1–T.4.7.6
59. Chakravarty, S.N. and Chakravarty, A. (2007) Reinforcement of rubber compounds with nano-filler. *KGK – Kautschuk Gummi Kunststoffe*, **11**, 619–622.
60. Sullivan, M.J. and Ladd, D.A. (2006) Golf ball containing graphite nanosheets in a polymeric network, US Patent 715756 issued on 11 April, to Acushnet Co.
61. Karger-Kocsis, J. (2006) Dry friction and sliding behavior of organoclay reinforced thermoplastic polyurethane rubbers. *Kautschuk Gummi Kunststoffe*, **10**, 537–543.
62. Gatos, K.G., Sawanis, N.S., Apostolov, A.A. *et al.* (2004) Nanocomposite formation in hydrogenated nitrile rubber (HNBR)/organo-montmorillonite nanocomposites as a function of the intercalant type. *Macromolecular Materials and Engineering*, **289**, 1079.
63. Anmin, H., Xiaoping, W., Demin, J., and Yanmei, L. (2007) Thermal stability and aging characteristics of HNBR/clay nanocomposites in air, water and oil at elevated temperature. *e-Polymers*, **051**, 1–11.
64. Lalli, J.H., Claus, R.O., Hill, A.B. *et al.* (2005) Commercial applications of Metal Rubber™. *Proceedings of SPIE – The International Society for Optical Engineering*, **5762**, 1–7.
65. Claus, R.O., Zeng, T., and Liu, Y. (2002) Electrostrictive and piezoelectric thin film assemblies and method of fabrication therefore, US Patent 6447887.
66. Lagashetty, A. and Venkataraman, A. (2005) Polymer nanocomposites. *Resonance*, **5**, 49–60.
67. Guo, Zhanhu, Park, Sung, Thomas Hahn, H. *et al.* (2007) Magnetic and electromagnetic evaluation of the iron nanoparticle filled polyurethane nanocomposites. *Journal of Applied Physiology*, **101**, 09M511–09M511-3.
68. Brody, G.S. (1997) On the safety of breast implants. *Plastic and Reconstructive Surgery*, **100**, 1314.
69. Smalley, D.L., Shanklin, D.R., Hall, M.F. *et al.* (1995) Immunologic stimulation of T lymphocytes by silica after use of silicone mammary implants. *The FASEB Journal*, **9**, 424–427.
70. Antimicrobial Rubber Technology (2008) http://www.milliken2.com
71. Metal/rubber nanocomposite evaluated for artificial muscles. *Advanced Materials & Processes,* April (2005).
72. Abu Bakar, N.H.H., Ismail, J., and Abu Bakar, M. (2007) Synthesis and characterization of silver nanoparticles in natural rubber. *Materials Chemistry and Physics*, **104**, 276–283.
73. De Coster, N. and Magg, H. (2003) NBR in contact with food, potable water, pharmaceutical and cosmetic applications. *Kautschuk Gummi Kunststoffe*, **07–08**, 405–411.

74. Myers, A.W. (2007) Antimicrobial nanocomposites for plastics and coatings. SPX Leadership Technology Forum, Charlotte, N.C., 15 November.
75. El Fray, M. and Boccaccini, A.R. (2005) Novel hybrid PET/DFA–TiO2 nanocomposites by in situ polycondensation. *Materials Letters*, **59**(18), 2300–2304.
76. Piegat, A., El Fray, M., Jawad, H. *et al.* (2008) Inhibition of calcification of polymer–ceramic composites incorporating nanocrystalline TiO_2. *Advanced Applied Ceramics*, **107**(5), 287–292.

Index

abrasion resistance, 303
acicular clay, 216
acid salts of graphite, 531
  graphite bisulfate, 531
activation model, 339
adhesion, 407
adhesion-deadhesion, 309
adsorption, 407
affine part, 342
agglomerates, 210
agglomeration-deagglomeration mechanism, 75, 306
aggregate-aggregate interaction, 374
aggregate-polymer interaction, 374
aging, 552
aging of rubber nanocomposites, 554
  ethylene propylene diene terpolymer (EPDM), 559
  hydrogenated nitrile butadiene rubber (HNBR), 561
  natural rubber (NR), 555
  nitrile butadiene rubber (NBR), 561
  silicone rubber (SR), 563
  styrene butadiene rubber (SBR), 559
Air D-Fense, 686, 689
amorphous silica, 210
anionic clays, 553
annihilation, 598
  free positron annihilation, 598
  o-Ps annihilation, 598
  p-Ps annihilation, 598
applications of rubber nanocomposites, 189, 682
  air space, 690
  medicine and health care, 691
  membranes, 687
  sporting goods, 689
  tire engineering, 682
    innerliner, 684
    tread, 682
aspect ratio, 292, 297, 678
aspect ratio of flakes, 503
attapulgite (AT), 25, 34
average molecular weight between crosslinks (Mc), 418
average positron life time, 602

barrier properties, 500, 684
barrier properties of various rubber nanocomposites, 510–520
  applications, 520
BET surface area, 678
biocompatibility, 334
biodegradability, 332
bionanocomposites, 332
biopolymers, 331, 335
block copolymers, 472
  SAXS, 473
bound rubber, 308, 365, 469
boundary model, 318
Bragg equation, 427
brucite, 211, 553

can-opening process, 187
carbon black, 88, 210, 293, 354, 678
carbon black masterbatches, 227

Rubber Nanocomposites: Preparation, Properties and Applications Edited by Sabu Thomas and Ranimol Stephen
© 2010 John Wiley & Sons (Asia) Pte Ltd

carbon nanotube latex blends, 228
carbon nanotube/elastomeric nanocomposites, 152
  natural rubber, 152–155
  polyurethane rubber, 157–159
  silicone rubber, 160–161
  styrene butadiene rubber, 155–157
carbon nanotubes (CNTs), 148, 210–211, 293, 355
  double-walled carbon nanotubes (DWNTs), 148
  multi-walled carbon nanotubes (MWCNTs), 148
  single-walled carbon nanotubes (SWCNTs), 148
cation exchange capacity (CEC), 170, 211
cellulose, 198
  cellulose I, 199
  cellulose III, 199
  cellulose IV, 199
  properties, 199
  structure, 198
cellulose microfibrils, 199, 201
cellulose nanofiber-reinforced latex composites, 204–207
cellulose nanofibers, 211, 295
cellulose nanofibril whiskers, 200
cellulosic materials, 197
cellulosic whiskers, 114
centrifugation process, 222
chain friction coefficient, 668
chain reptation motion, 656, 668
characteristics of fillers, 292
chemical crosslink density, 296
clays, 170
cluster-cluster-aggregation (CCA) model, 362, 636
cold crystallization, 312
compliance, 295
compounding formulation, 417
conductive rubber composites, 527
contact angle measurements, 411
contact mode, 277
continuous decay form, 610
continuum mechanics models, 659
conventional composites, 25
conventional fillers, 676
copolyester elastomers (COPEs), 240
corona, 563
coupling agent, 308
crab shell chitin, 116
creaming principle, 230
crosslink density, 296, 417, 418
crosslinked systems, 676
crosslinks, 299
crossover volume fraction (ϕc), 569
cryomicrotomy, 266
crystallinity index, 202–204
cure temperature, 681
cure time, 681

degradable scaffolds, 332
degradation of rubber nanocomposites, 563
  acrylonitrile butadiene rubber (NBR), 579
  butyl rubber, 587
  ethylene propylene diene terpolymer (EPDM), 568
  ethylene vinyl acetate (EVA), 566
  hydrogenated nitrile butadiene rubber (HNBR), 581
  natural rubber (NR), 563
  silicone rubber (SR), 583
  styrene butadiene rubber (SBR), 582
degree of elastic recovery in indentation, 623
degree of filler dispersion, 626
degree of swelling, 417
delamination, 681
depth sensing indentation (DSI), 623
die swell, 384
diffusion coefficient, 119
dilute limit, 503
dispersion index (DI), 600
dispersive mixing, 600
distributive mixing, 600
double network theory, 335
dry natural rubber, 224
Dupre equation, 412
dynamic mechanical analysis, 297

effective crosslink density, 314
effective tube, 663
effective volume fraction, 371
Elastoguard, 691
electron paramagnetic resonance (EPR), 391
electron spin resonance (ESR), 391
electrophoretic deposition (EPD), 150
elongational rheology, 378
end-to-end distance, 653
entanglements, 296
entropic force, 342
equilibrium shear modulus, 361

ESR spectra of NR, 397
exfoliated, 26, 172
exfoliation mechanism, 102
expanded graphite, 533
extension ratio, 317
extensional viscosity, 378
  CB/rubber nanocomposite, 379
  nanoclay/rubber nanocomposite, 380
extrudate swell, 384
Exxpro polymers, 685

factors influencing matrix reinforcement, 63
fibrillar silicate (FS), 34–35, 300
  FS/SBR composite, 35
    preparation, 35
    properties, 35–38
Fickian, 509
Ficks law, 502
  Ficks second law of diffusion, 502
Ficks model, 67
filler in elastomers, 113
filler surface modification, 34–35
filler-elastomer interactions, 407
finite element method (FEM), 320
Flory-Huggins interaction parameter, 418
Flory radius, 337, 343
Flory-Rehner equation, 418
fluorohectorite, 213
focused ion beam (FIB), 267
Fourier inversion, 427
fractal structure, 362, 364, 445
fraction of bounded rubber (FBR), 119, 124
free volume, 109, 596, 602
free volume model, 396
friction behavior, 303
friction coefficient, 338
front factor, Gp, 363
FT-IR spectra of silicas, 413
fuel efficiency, 682
fullerenes, 678
fumed silica, 210, 354
functionalised carbon nanotubes, 148

gaussian average, 654
gaussian distribution function, 653
Gaussian model, 317
gel-particle energetic attraction, 338
Gennes scaling theory, 337
graphene, 537
  preparation, 538
graphite, 528, 529
graphite intercalation compounds (GICs), 530
  acceptor GIC, 531
  covalent intercalation compounds, 531
  donor GIC, 531
  ionic intercalation compounds, 531
graphite nanosheets, 535
graphite oxide (GO), 538
green bionanocomposites, 332
green strength, 8, 224
green tire, 11, 292, 683
Guinier formula, 428
Guth and Gold equation, 73, 215, 371
Guth-Smallwood equation, 337

Halpin-Tsai equation, 319, 662
Hamiltonian, 393
hectorite, 213
Heinrich and Kluppel equation, 363
Hermans orientation parameter, 436
heterogeneous elongation, 378
high-amplitude modulus (HAM), 298
high-structure black, 210
homogeneous stretching, 378
house of cards network structure, 381
hybrid biocomposites, 334
hydrodynamic effect, 337
hydrodynamic factor, 343
hydrogel nanocomposites, 334
hydrogels, 334
hydroxyapatite (HA), 331, 332
hyperfine interaction, 393
hysteresis, 292, 678

immiscible rubber nanocomposites, 89
immobilization phenomenon, 663
interaction of filler-elastomer depends on,
  particle size, 87
  surface activity, 87
intercalated, 25, 172
  influence of heat/temperature, 26, 28, 39–43
  influence of pressure, 28, 31, 43, 46
interface adhesion, 88
interface characterization, 104
  direct methods, 104–106
  indirect methods, 104, 106–109
interface modification, 89
  non-reactive route, 89, 93
  reactive route, 89, 100

kinetic constraints, 663
kinetic factors, 375
kinetic Ising model, 666
Kivelson theory, 395
K-N model, 661
Kohlrausch equation, 639
Kohlrausch-Williams Watt function, 667
Kramers equation, 341
Kratky plots, 448
Kraus model, 75

labyrinth principle, 688
lamellar fillers, 429
Langevin effect, 663
Langevin inverse function, 658
latex coagulating method (LCM), 89, 96
latex compounding, 47, 226
latex concentrates, 222
lattice factor, 443
layered clay nanocomposites, 228
layered double hydroxides (LDH), 211, 553
  structure, 553
layered silicates, 170, 678
limit of linearity, γc, 365
linear viscoelasticity, 355
London dispersive component, 408, 412
Lorenzian lines, 394
low amplitude modulus (LAM), 298
low structure black, 210

magic triangle, 678, 682
magnetic nanoparticles, 690
Maier and Goritz model, 75
manufacturing techniques, 22
  conventional, 22
    forming, 22
    mixing, 22
      internal mixer, 22
      two-roll mill, 22
    vulcanizing, 22
mass fractal, 445
mastication, 375
material-point-method (MPM), 670
maximum indentation depth, 622
Maxwell model, 341
mechanical properties, 292
  aging, 300
  fatigue, 300
  filler characteristics, 292
  mechanical behavior at high strain, 299
  mechanical behavior at low strain, 297
  modulus, 295
  ultimate properties, 300
mechanism of rubber reinforcement, 651, 659
  interaction of matrix with solid nanoparticles, 651
  percolation of solid particles, 651
melt compounding, 25
melt intercalation, 229
melt rheological properties, 354
metal rubber, 690, 691
mica, 213
microfibrillar angle, 198
microfibrillated cellulose (MFC), 198
micromechanical interlocking, 218
micromechanical model, 318
microprofilometry, 626
microscopic polymer reference interaction model, 666
microscopy techniques, 256
  3-D transmission electron microtomography (TEMT), 274
  amplitude heterodyne force microscopy (A-HFM), 283
  atomic force microscopy (AFM), 277
  confocal Raman microscopy (CRM), 281
  electron energy loss spectroscopy (EELS), 273
  electron probe microanalysis (EPMA), 263
  electron spectroscopy imaging in TEM (ESI-TEM), 273
  electrostatic force microscopy (EFM), 284
  energy dispersive X-ray spectroscopy (EDX), 262
  force modulation microscopy (FMM), 281
  friction force microscopy (FFM), 281
  heterodyne force microscopy (HFM), 282
  optical microscopy (OM), 256
  scanning electron microscopy (SEM), 259
  scanning probe microscopy (SPM), 216
  scanning transmission electron microscopy (STEM), 272
  transmission electron microscopy (TEM), 265
  ultrasonic force microscopy (UFM), 281
  wavelength dispersive spectroscopy (WDS), 263
  X-ray ultramicroscopy (XuM), 264
microvoids, 598
mill banding, 681
Miller indices, 439
miscible rubber nanocomposites, 88–89

mixing, 600
modification of layered silicates, 219
modification of spherical fillers, 219
modified clay, 100–103
modulus, 295
molecular weight of latex, 225
molten surfactant exchange method, 220
monomer friction coefficient, 656, 668
montmorillonite (MMT), 213, 678
Mooney function, 317
Mooney ratio, 317
morphology of rubber nanocomposites, 256
  acrylic rubber/silica, 262
  epoxidised soybean oil (ESO)/organoclay, 260–261
  MWCNT/SBR, 280
  NR/MWCNT, 269
  organoclay/PA6, 6, 257
  organoclay/PA6, 6/POE-g-MA, 258
  POSS/silicone, 256
  PUR/clay nanoplatelets, 268
  PUR/NR/clay nanoplatelets, 268
  VGCNF/chlorobutyl rubber, 260, 263
morthane, 249
Mullins effect, 216, 292, 299, 300
Mullins-Patrikeev effect, 631
multiphase systems, 407
multiwall carbon nanotubes, 678

nano silica, 228, 293
nanoapatite, 336
nanoelectrodes, 691
nanofibril, 200
nanofiller as compatibilizer, 220
  in blends, 220
    NR/NBR, 221
    NR/PU, 221
    NR/XSBR, 221
    nylon 6/poly (ethylene-ran-propylene rubber) (EPR), 220
    poly (propylene)/EPDM, 220
    PS/PMMA, 221
nanofillers, 2, 209, 676
  bionanofillers, 7
  layered silicates, 2, 209, 211
    phyllosilicates, 2
      compatibilising agent, 3
  nanotubes, 3, 209–211
    carbon nanotubes (CNTs), 3
      chemical modification, 5
      composites, 4
      multiwalled nanotubes (MWNTs), 4
      single walled nanotubes (SWNTs), 4
      synthesis, 4
    halloysite (HNTs), 5
  polyhedral oligomeric silsesquioxanes (POSS), 6
  spherical particles, 5, 209–210
    synthesis, 5
      sol-gel process, 5
      Stöber synthesis, 5
nanofillers in reinforcement depends on, 213
  filler-filler interactions, 216
  particle size, 213–215
  rubber-filler interaction, 216
  shape structure of fillers, 216
nanofriction, 625
nanohardness, 622
nanoindentation, 596, 621
  applications, 623
  principles, 622
    maximum indentation dept, 622
    plastic depth, 622
nanopaper, 200
nanoparticle dispersion, 88
nanoscience, 1
nanostructured graphite, 529
nanotechnology, 1
nanotribology, 624
natural and synthetic hydrogels, 335
natural polymers, 332
natural reinforcing fillers, 332
natural rubber (NR), 113
natural rubber latex, 222
network model, 318
Newtonian behavior, 371
Newtonian plateau, 370
Nielsen equation, 684
nitroxide radical, 391
nominal strain, 134
nominal stress, 134
non-Fickian, 509
nonlamellar fillers, 445
  carbon black, 445
  carbon nanotubes, 451
  polyhedral oligomeric silsesquioxanes (POSS), 460
non-rubber solids, 226
NR green nanocomposites, 113–143
NR/chitin whisker, 119
NR/starch nanocrystal, 124

one sticker model, 667
one-dimensional Ising model, 653
optimum filler content, 302
organic-inorganic hybrid, 63
  sol-gel process, 63–64
organo clay, 171, 355
organo clay/rubber-rubber blends, 217
  EVA/NR, 217
orientation parameter, 504
osteoconductive ceramics, 335
osteoconductivity, 332
osteonectin, 335
overshoot of elastic moduli, 631

parallel model, 318
particle size, 87, 88
  particle mass, 88
  surface area, 87
particle size of latex, 225
particle-matrix interface, 63
path tortuosity, 684
Payne effect, 53, 72, 74, 75, 154, 216, 292, 309, 353, 363, 668
percolation network, 161
percolation threshold, 161, 295, 306, 357, 359
permeability coefficient (P), 502
permeability models, 507
  Aries model, 507
  Cussler *et al.* model, 507
  Fredrickson model, 508
  Gusev and Lusti model, 508
permeability of nanocomposite, 503
  aspect ratio, 505
  tortuous path, 503
permeation theories, 501
phyllosilicates, 170, 211, 243
physical aging, 552
physical and chemical interactions, 218
physical properties of cellulose, 198
piezoresistive effect, 543
plastic depth, 622
plastic work function (PWF), 623
pneumatic tires, 687
Pn-Fm complex, 659
Poisson ratio, 448
polar component, 408
poly (butadiene rubber) (PBR), 676
poly (isoprene rubber), 676
poly (L-lactide-co-ethylene oxide-co-fumarate) (PLEOF), 334, 336
polychloroprene/organoclay nanocomposites, 633
  stress relaxation, 638
  structural characterisation, 633
    SAXS, 634
    WAXD, 634
  thermoelastic behavior, 634
polydimethyl siloxanes (PDMS), 64
  composite preparation, 66
    in situ filling process after network formation, 66
      characterisation, 67–69
    in situ filling process before crosslinking, 69
  synthesis of unfilled networks, 65–66
polymer bionanocomposites, 331
polymer nanocomposites (PNCs), 1
polymer-filler interface, 68, 78
  characterization, 78
    FTIR, 78
    1HNMR, 79
    DSC, 79
polyoxide silsesquioxane (POSS), 295, *see also* nanofillers
polysaccharide nanocrystals, 114
  chemical modification, 128
  preparation, 114
  reinforced rubber nanocomposites, 115
    barrier properties, 143
    dynamic mechanical analysis, 131–134
    morphology, 116, 118
    successive tensile tests, 131–143
    swelling behavior, 118–131
    tensile tests, 134–137
polyurethanes, 239
Porods' law, 428
positron, 597
positron annihilation lifetime spectroscopy (PALS), 109, 596, 597
  application, 598
  principles, 598
positronium (Ps), 597
  formation models, 597
    free volume model, 597
    ore, 597
    spur, 597
  o-Ps, 597
  p-Ps, 597
power law, 361
precipitated silica, 210

preferential migration, 221
preparation of,
  modified clay, 97
  polymer/clay nanocomposites, 93
  SBR/clay composite, 100
  silicone rubber/clay nanocomposites, 97
pressure sensors, 160
prevulcanized latex, 223
probability density function, 610
pseudo-elastic behavior, 296
pseudo-plastic behavior, 298

random coil, 654
random walk model, rwm, 653
reinforcement, 88, 113, 297
reinforcement efficiency, 244
reinforcement in rubber nanocomposites
    depends on, 304
  aspect ratio, 305
  filler-filler interaction, 306
  filler-matrix interaction, 307
  filler-polymer compatibility, 305
  percolating network, 306
reinforcing agents, 23
  carbon black, 23
  clay minerals, 24
  clays, 24
relative diffusivity, 510
relative permeability, 504
relative storage modulus equation, 660
representative volume element (RVE), 318,
    652, 669
reptation concept, 368
rheological percolation threshold, 360
rolling resistance, 682
rotation isomeric state model, 665
rubber elasticity, 657
rubber nanocomposites, 2, 8, 22, 89
  advantages, 23
  challenges, 23
  conventional, 2
  exfoliated, 2, 3
  intercalated, 2, 3
  rubber/biofiller, 11
  rubber/LS, 9
  rubber/NT, 10
  rubber/POSS, 11
  rubber/spherical particles, 11
  without interface modification, 89
    advantages, 92
    disadvantages, 92
    mechanical properties, 89–92
rubber retractive force, 657
rubber/clay nanocomposites (RCNs),
    25, 171
  isobutyl-isoprene rubber/clay (IIRCNs),
    26–34, 39–46
  NBR/ODA-modified MMT, 25
  NR/organoclay, 25
  preparation, 171
    latex route, 173–174
    melt compounding, 174–176
    solution intercalation, 173
  properties, 176
    barrier properties, 184
      labyrinth principle, 186
      tortuous path, 186
    crosslinking, 176, 178–179
    fire resistance, 186
    mechanical performance, 179–184
    wear behavior, 187
  SBR/attapulgite, 25
  SBR/clay, 47, 48, 57
rubber-filler interfaces, 664
  dynamical aspects, 666
  structural aspects, 664
rubber/graphite nanocomposites, 538
  applications, 545
  characterisation, 540
  preparation, 539
  properties, 540
    electrical, 543
    mechanical, 540
    thermal conductivity, 545
rubbery bionanocomposites (RBNCs), 32

SAF, 676
SAXS, 427, *see also* WAXD
SBR/attapulgite, 25
scaffolds, 332
scaling law, 361
scattered intensity (Iq), 427
scorch time, 681
secondary structure, 210
self-consistent model, 320
self-similar grid structure theory, 340
separated structure, 59–60
serial model, 315
serial-parallel model, 318
shape factor (f), 216

shear elastic modulus of crosslinked polymer network, 659
shear elastic modulus of entangled polymer network, 659
shear mixing, 101, 104
shear thinning, 370
shear viscosity, 369
  CB/rubber nanocomposites, 369
  nanoclay/rubber nanocomposites, 376
  silica/rubber nanocomposites, 369
sil clay, 97
silanization, 219
silanol groups, 408
silica, 210, 293, 678
skim latex, 223, 229, 230
slippage of polymer chain, 216
smectites, 213
sol fraction, 124
sol-gel process, 64
  properties of hybrid materials, 71
    dispersion, 71
    low strain dynamic properties, 74
    stress-strain, 71
sol-gel transition, 357
solid-solid interface, 407
solid-state NMR, 408
solid-state NMR of silicas, 409
  fluorinated, 411
  silane treated, 409
  thermally treated, 409
solubility parameter, 225
solution blending, 39, 226
specific energy, 376
spin labelling, 393
spin probe, 393
spin probe ESR of NR nanocomposite, 398
statistical RVE, 652
stochastic and deterministic model, 320
strain amplification effects, 302
strain amplification factor, 632, 644
strain hardening, 299, 380
strain-induced crystallization, 312
stress softening, 631
structure of Na-montmorillonite, 552
structure of rubber nanocomposites, 668
styrene block copolymers (SBS), 240
styrene butadiene rubber (SBR), 113
styrene-co-butadiene rubber (SBR)/organoclay nanocomposites, 642
  stress relaxation, 645
  structural characterisation, 642
    SAXS, 643
    thermoelastic behavior, 643
    WAXD, 643
surface activity, 88
surface dynamics, 407
surface energetics of silicas, 411
  Debye-inductive polarization, 412
  Keesom-orientation polarization forces, 412
  London dispersive component, 412
  specific component, 412
surface energy, 408
surface fractal, 445
surface free energy, 413
surface modification of silica, 408
  direct fluorination, 409
  silane coupling method, 409
  thermal treatment, 408
surface-to-volume ratio (S/V), 484
surfactants, 100
swelling test, 417
synthetic latices, 224

tactoids, 381
Tao equation, 598
tapping mode, 277
tearing energy, 417-418
tetraethoxy silane (TEOS), 64
thermal aging, 552
thermal properties, 80
  TGA, 80
thermodynamic factors, 375
thermoplastic elastomers (TPEs), 472
thermoplastic olefins (TPOs), 240
thermoplastic polyurethane nanocomposites, 242
  carbon nanotube/TPU, 247–249
  layered silicate/TPU, 243–247
thermoplastic polyurethanes (TPU), 240, 241
  chemistry, 241
  morphology, 240–241
  properties, 240–241
thermoplastic vulcanizates (TPVs), 240
thixotropic non-linearities, 341
thixotropy, 367
three-phase model, 318, 335
titania, 66
torsion vibrations, 655
tortuosity factor, 503, 504
  Nielsen model, 503, 506

total permeability equation, 505
total solids content (TSC), 226
traditional rubber reinforcement, 678
train-loop-bridge-tail, 663
transient filler-polymer network, 665, 670, 671
transient shear flow, 367
transient structure, 210
trapped entanglements, 296
treated clay solution, 93
tribological behavior, 303
β-tricalcium phosphate (TCP), 331, 332
true strain, 134
true stress, 134
Tsai-Pagano equation, 320
two sticker model, 667
types of fillers, 552 (*see also* in nanofillers)

ultimate strain, 302
ultimate stress, 302
ultramicrotomy, 266

Van Es equation, 320
vapour-grown carbon nanofibers (VGCNF), 259
vermiculite, 213
viscoelastic properties of biocomposites, 333
  biofiber/NR composites, 333
  PLEOF/HA composites, 343
vitreous silica (silica glass), 210
Vogel-Fulcher-Tamann (VFT) equation, 655
volume fraction, 299
volume fraction of flakes (ϕ), 503
Vonks' formula, 441
vulcanization, 21

wall slip, 383
Warner approximation, 342
WAXD, 426
  lamellar fillers, 429
  POSS, 460
  POSS containing nanocomposites, 461
  rubber/CB composite, 445
  rubber/clay nanocomposite, 432
  rubber/CNT nanocomposite, 451
  silica, 454
  strain induced crystallization, 464
  thermoplastic elastomers, 472
  TPE nanocomposites, 477
wet gel strength, 224
wet skid resistance, 683
wettability, 407
whiskers, 114
wiggle, 507
Wilchinsky triangle, 438

XPS spectra of silicas, 414

yield stress, 371, 382
Young angle equation, 412

Zeeman interaction, 393
Zernike-Prins model, 486
zero-shear viscosity, 369